TRANSIENT ANALYSIS OF POWER SYSTEMS

SOLUTION TECHNIQUES, TOOLS AND APPLICATIONS

EDITOR

JUAN A. MARTINEZ-VELASCO

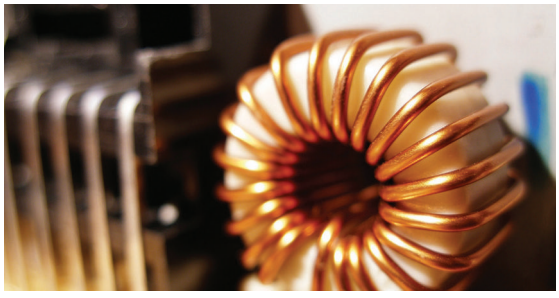

IEEE
IEEE PRESS

WILEY

TRANSIENT ANALYSIS OF POWER SYSTEMS

TRANSIENT ANALYSIS OF POWER SYSTEMS

SOLUTION TECHNIQUES, TOOLS AND APPLICATIONS

Edited by

Juan A. Martinez-Velasco
Universitat Politecnica de Catalunya
Barcelona, Spain

IEEE
IEEE PRESS
WILEY

This edition first published 2015

Registered office
John Wiley & Sons Ltd, The Atrium, Southern Gate, Chichester, West Sussex, PO19 8SQ, United Kingdom

Library of Congress Cataloging-in-Publication Data

Martinez-Velasco, Juan A.
Transient analysis of power systems : solution techniques, tools, and applications / Dr. Juan A. Martinez-Velasco.
pages cm
Includes bibliographical references and index.
ISBN 978-1-118-35234-2 (hardback)
1. Electric power system stability. 2. Transients (Electricity)–Mathematical models. I. Title.
TK1010.M37 2014
621.319′21–dc23 2014029300

A catalogue record for this book is available from the British Library.

ISBN: 9781118352342

Set in 9/11pt Times by Aptara Inc., New Delhi, India

1 2015

Contents

Preface

The simulation of electromagnetic transients is a mature field that plays an important role in the design of modern power systems. From the first steps in this field up to today, a significant effort has been dedicated to the development of new techniques and more powerful software tools. Sophisticated models, complex solution techniques and powerful simulation tools have been developed to perform studies that are of paramount importance in the design of modern power systems. The first developments of transients tools were mostly aimed at calculating overvoltages. Presently, these tools are applied into a myriad of studies (e.g. FACTS and custom power applications, protective relay performance, power quality studies) for which detailed models and fast solution methods can be of huge importance.

The story of this book may be traced back to the General Meeting that the IEEE Power and Energy Society held in July 2010, when the Analysis of System Transients using Digital Programs Working Group gave a tutorial course on 'Transient analysis of power systems. Solution techniques, tools and applications'. The tutorial provided a basic background to the main aspects to be considered when performing electromagnetic transients studies (solution techniques, parameter determination, modelling guidelines), detailed some of the main applications of present transients tools (overvoltage calculation, power electronics applications, protection) and discussed more recent developments (e.g. dynamic average models and interfacing techniques) mostly aimed at overcoming some of the current limitations.

This book was initially thought of as an expanded version of the material used in the tutorial; however, several important fields were not covered in the tutorial, such as smart grid simulation, HVDC analysis distributed energy resources and custom power modelling. Therefore, rather than expanding the tutorial chapters, this book has incorporated new material by adding chapters and providing a broader coverage of fields related to transient analysis of power systems.

Although this is a book on electromagnetic transients, some important topics related to this field are not well covered or not covered at all. For instance, parallel computing will become a very important aspect in the future development of software tools for simulating transients in power systems; except in those chapters that deal with real-time simulation, nothing on this field has been included in this book. Another aspect that will be fundamental to the analysis and design of the future smart grid is the combined simulation of communication and power systems; the book includes a chapter dedicated to analysing the possibilities that time-domain simulation offers in the analysis of smart grid technologies without considering the representation of the communication system.

It is also worth mentioning that the topics covered in most chapters require a previous background on electromagnetic transient analysis. The book is mainly addressed to graduate students and professionals involved in transient studies.

As with any other previous book in which I have been involved, I want to finish this Preface thanking members of the IEEE WG, friends and relatives for their help and, in many circumstances, for their patience.

Juan A. Martinez-Velasco
Barcelona, Spain
March 2014

About the Editor

Juan A. Martinez-Velasco was born in Barcelona, Spain. He received the Ingeniero Industrial and Doctor Ingeniero Industrial degrees from the Universitat Politècnica de Catalunya (UPC), Spain. He is currently with the Departament d'Enginyeria Elèctrica of the UPC.

He has authored and coauthored more than 200 journal and conference papers, most of them on transient analysis of power systems. He has been involved in several EMTP (ElectroMagnetic Transients Program) courses and worked as a consultant for some Spanish companies. His teaching and research areas cover power systems analysis, transmission and distribution, power quality and electromagnetic transients. He is an active member of several IEEE and CIGRE Working Groups. Presently, he is the chair of the IEEE General Systems Subcommittee.

He has been involved as editor or co-author of several books. He is also coeditor of the IEEE publication "Modeling and Analysis of System Transients Using Digital Programs" (1999). In 2010, he was the coordinator of the tutorial course "Transient Analysis of Power Systems. Solution Techniques, Tools, and Applications", given at the 2010 IEEE PES General Meeting, July 2010, and held in Minneapolis.

In 1999, he got the "1999 PES Working Group Award for Technical Report", for his participation in the tasks performed by the IEEE Task Force on Modeling and Analysis of Slow Transients. In 2000, he got the "2000 PES Working Group Award for Technical Report", for his participation in the edition of the special publication "Modeling and Analysis of System Transients using Digital Programs". In 2009, he got the "Technical Committee Working Group Award" of the IEEE PES Transmission and Distribution Committee.

List of Contributors

Omid Alizadeh, Ryerson University, Toronto, ON, Canada

Udaya D. Annakkage, University of Manitoba, Winnipeg, MB, Canada

Hamid Atighechi, BC Hydro, Vancouver, BC, Canada

Tarek Ould-Bachir, École Polytechnique de Montréal, Montréal, QC, Canada

Jean Bélanger, OPAL-RT Technologies, Montréal, QC, Canada

Sina Chiniforoosh, BC Hydro, Burnaby, BC, Canada

Jean-Pierre David, École Polytechnique de Montréal, Montréal, QC, Canada

Francisco de León, NYU Polytechnic School of Engineering, Brooklyn, NY, USA

Sébastien Dennetière, Réseau de Transport d'Electricité (RTE), Paris, France

Christian Dufour, OPAL-RT Technologies, Montréal, QC, Canada

Shaahin Filizadeh, University of Manitoba, Winnipeg, MB, Canada

Arindam Ghosh, Curtin University, Perth, Australia

Francisco González-Molina, Universitat Rovira i Virgili, Tarragona, Spain

Bjørn Gustavsen, SINTEF Energy Research, Trondheim, Norway

José A. Gutiérrez-Robles, Universidad de Guadalajara, Guadalajara, Mexico

Juri Jatskevich, University of British Columbia, Vancouver, BC, Canada

Ulas Karaagac, École Polytechnique de Montréal, Montréal, QC, Canada

Ilhan Kocar, École Polytechnique de Montréal, Montréal, QC, Canada

Jean Mahseredjian, École Polytechnique de Montréal, Montréal, QC, Canada

José L. Naredo, CINVESTAV, Guadalajara, Mexico

Xuanchang Ran, NYU Polytechnic School of Engineering, Brooklyn, NY, USA

Hani Saad, École Polytechnique de Montréal, Montréal, QC, Canada

Reynaldo Salcedo, NYU Polytechnic School of Engineering, Brooklyn, NY, USA

Kalyan K. Sen, Sen Engineering Solutions, Monroeville, PA, USA

Farhad Shahnia, Curtin University, Perth, Australia

Amirnaser Yazdani, Ryerson University, Toronto, ON, Canada

1

Introduction to Electromagnetic Transient Analysis of Power Systems

Juan A. Martinez-Velasco

1.1 Overview

Electrical power systems are among the most complex, extensive and efficient systems designed to date. The goal of a power system is to generate, transport and distribute the electrical energy demanded by consumers in a safe and reliable way.

Power systems play a crucial role in modern society, and their operation is based on some specific principles. Since electricity cannot be stored in large quantities, the operation of the power system must achieve a permanent balance between its production in power stations and its consumption by loads in order to maintain frequency within narrow limits and ensure a reliable service.

Even when the power system is running under normal operation, loads are continually connected and disconnected, and some control actions are required to maintain voltage and frequency within limits. This means that the power system is never operating in a steady state. In addition, unscheduled disturbances can alter the normal operation of the power system, force a change in its configuration, cause failure of some power equipment or cause an interruption of service that can affect a significant percentage of the system demand, such as a blackout.

The analysis and simulation of electromagnetic transients has become a fundamental methodology for understanding the performance of power systems, determining power component ratings, explaining equipment failures or testing protection devices. The study of transients is a mature field that can be used in the design of modern power systems. Since the first steps in this field, a significant effort has been dedicated to the development of new techniques and more powerful software tools. Sophisticated models, complex solution techniques and powerful simulation tools have been developed to perform studies that are of paramount importance in the design of modern power systems. The first developments of transients tools were mostly aimed at calculating overvoltages. Presently, these tools are applied in a myriad of studies (e.g. FACTS and custom power applications, protective relay

Transient Analysis of Power Systems: Solution Techniques, Tools and Applications, First Edition.
Edited by Juan A. Martinez-Velasco.

performance, power quality studies) for which detailed models and accurate solutions can be extremely important.

Transient phenomena in power systems are associated with disturbances caused by faults, switching operations, lightning strikes or load variations. These phenomena can stress and damage power equipment. The paramount importance of their study relates to the effects they can have on system performance or the failures they can cause to power equipment.

Two types of stress can be caused by transient phenomena in power systems: (1) overcurrents, which can damage power equipment due to excessive heat dissipation, and (2) overvoltages, which can cause insulation breakdown (failure through solid or liquid insulation) or flashovers (insulation failure through air). Protection against these stresses is therefore necessary. This protection can be provided by specialized equipment whose operation is aimed at either isolating the power system section where the disturbance has occurred (e.g. a power component failure that causes short-circuit) or limiting the stress across power equipment terminals (e.g. by installing a surge arrester that will mitigate voltage stresses). In addition, a better ability to handle stresses caused by transient phenomena can be also achieved through good design of power equipment (e.g. by shielding overhead transmission lines to limit flashovers caused by direct lightning strikes). That is, although the power system operates most of the time under normal operating conditions, its design must enable it to cope with the consequences of transient phenomena.

In order to provide adequate protection against both types of stresses, it is fundamental to know their origin, calculate their main characteristics and estimate the most adverse operating conditions. A rigorous and accurate analysis of transients in power systems is difficult due to the size of the system, the complexity of the interaction between power devices and the physical phenomena that need to be analysed. Presently, the study and simulation of transients in actual power systems is carried out with the aid of a computer.

Aspects that contribute to this complexity are the variety of causes, the nature of the physical phenomena and the timescale of the power system transients.

Disturbances can be external (lightning strikes) or internal (faults, switching operations, load variations).

Power system transients can be electromagnetic, when it is necessary to analyse the interaction between the (electric) energy stored in capacitors and the (magnetic) energy stored in inductors, or electromechanical, when the analysis involves the interaction between the electric energy stored in circuit elements and the mechanical energy stored in rotating machines.

Physical phenomena associated with transients make it necessary to examine the power system over a time interval as short as a few nanoseconds or as long as several minutes.

This latter aspect is a challenge for the analysis and simulation of power system transients, since the behaviour of power equipment is very dependent on the transient phenomena: it depends on the range of frequencies associated to transients. An accurate mathematical representation of any power device over the whole frequency range of transients is very difficult, and for most components is not practically possible.

Despite the powerful numerical techniques, simulation tools and graphical user interfaces currently available, those involved in electromagnetic transients studies, sooner or later, face the limitations of models available in transients packages, the lack of reliable data and conversion procedures for parameter estimation or insufficient studies for validating models.

Figure 1.1 presents a typical procedure when simulating electromagnetic transients in power systems. The entire procedure implies four steps, that are summarized as follows:

1. The selection of the study zone and the most adequate representation of each component involved in the transient

   The system zone is selected, taking into account the frequency range of the transients to be simulated: the higher the frequencies, the smaller the zone modelled. In general, it is advisable to minimize the study zone, because a larger number of components does not necessarily increase

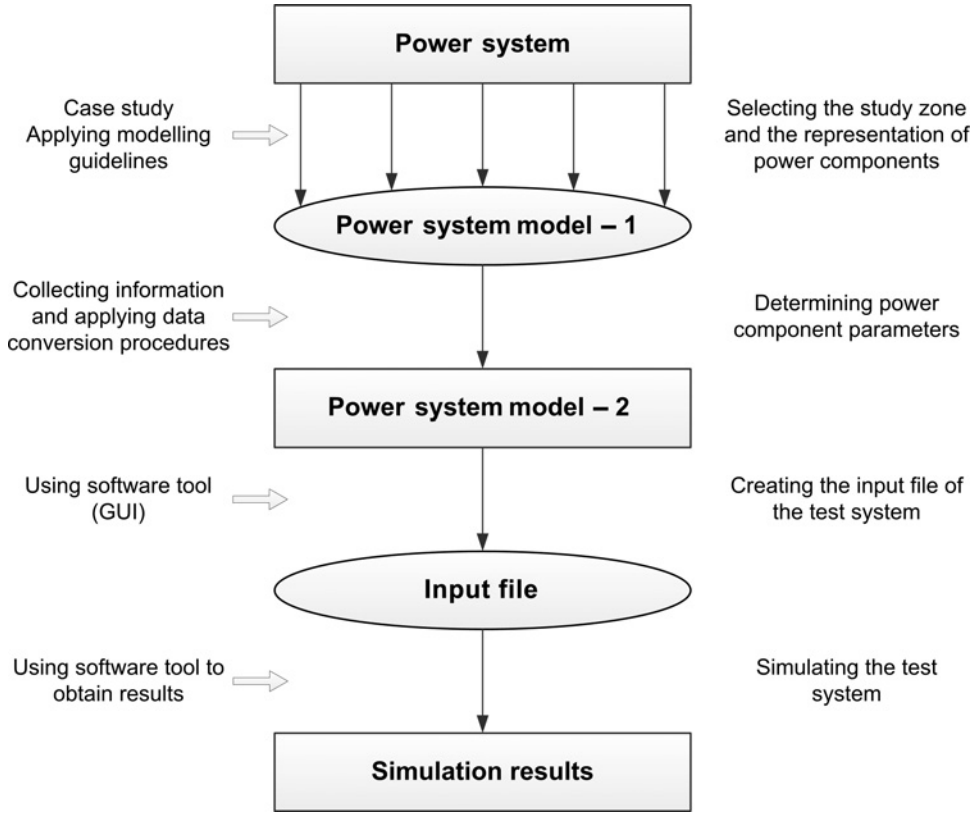

Figure 1.1 Simulation of electromagnetic transients in power systems.

accuracy; instead it will increase the simulation time, and there will be a higher probability of insufficient or incorrect modelling. Although many works have been dedicated to providing guidelines on these aspects [1–3], some expertise is usually needed to choose the study zone and the models.

2. The estimation of parameters to be specified in the mathematical models

   Once the mathematical model has been selected, it is necessary to collect the information that could be useful for obtaining the values of parameters to be specified. For some components, these values can be derived from the geometry; for other components these values are not readily available and they must be deduced by testing the component in the laboratory or carrying out field measurements. In such case, a data conversion procedure will be required to derive the final parameter values. Details of parameter determination for some power components were presented in [4].

   Interestingly, an idealized/simplified representation of some components may be considered when the system to be simulated is too complex. This representation will enable the data file to be edited and the analysis of the simulation results to be simplified.

   A sensitivity study should be carried out if one or several parameters cannot be accurately determined. Results derived from such a study will show what parameters are of concern.

3. The application of a simulation tool

   The steadily increasing capabilities of hardware and software tools have led to the development of powerful simulation tools that can cope with large and complex power systems. Modern software for

transient analysis incorporates powerful and friendly graphical user interfaces that can be very useful when creating the input file of the test system model.

4. The analysis of simulation results

   Simulation of electromagnetic transients can be used, among other things, for determining component ratings (e.g. insulation levels or energy absorption capabilities), testing control and protection systems, validating power component representations or understanding equipment failures. A deep analysis of simulation results is an important aspect of the entire procedure, since each of these studies may involve an iterative procedure in which models and parameters values must be adjusted.

Pioneering work in this field was presented in [2, 5, 6]; see also [7]. Readers interested in electromagnetic transient analysis can consult other specialized literature [8–15].

1.2 Scope of the Book

This book provides a basic background to the main solution techniques presently applied to the calculation of electromagnetic transients, gives details of the main applications of the most popular transient tools (insulation coordination, power electronics applications, protection) and discusses new developments (e.g. dynamic average models, interfacing techniques) mostly aimed at overcoming some limitations of the present software tools.

The main topics to be covered by this book are as follows:

Solution Methods and Simulation Tools: The analysis of electromagnetic transients in power systems can be performed in either the time or the frequency domain. Although time-domain solution methods are the most common option, frequency-domain analysis offers certain features that complement the advantages of time-domain analysis [16–18]. In addition, the calculation of the steady state of a power system, prior to the calculation of a transient process, is usually performed in the frequency domain.

Tools for electromagnetic transient simulation are classified into two main categories [19]: off-line and real-time. The purpose of an off-line simulation tool is to conduct simulations on a generic computer. Off-line tools are designed to use numerical methods and programming techniques without any time constraint and can be made as precise as possible within the available data, models and related mathematics. Real-time (on-line) simulation tools are capable of generating results in synchronism with a real-time clock, and have the advantage of being capable of interfacing with physical devices and of maintaining data exchanges within the real-time clock [20, 21]. Computations in real time, imposes important restrictions on the design of such tools, but they can be extremely useful for testing and designing power equipment.

The chapters dedicated to these topics detail currently applied methods for steady-state and transient solution of power systems and control systems, they provide an overview of simulation tools and methods for the computation of electromagnetic transients, including practical examples, and they discuss limitations.

Although parallel computation is covered in the chapters related to real-time simulation, readers interested in the computation of electromagnetic transients using a multicore environment are advised to consult reference [22].

Modelling and Parameter Determination: Despite the powerful numerical techniques, simulation tools and graphical user interfaces currently available, a lack of reliable data, standard tests and conversion procedures generally makes the determination of parameters one of the most challenging aspects of creating a model [4]. Although there is no specific chapter of this book dedicated to these topics, many issues connected to modelling guidelines are presented in several chapters, and two annexes covering

aspects related to the development of models and calculation of parameters for electromagnetic transients studies have been included:

- ***Fitting Techniques***: When parameter determination is based on a frequency response test, a data conversion procedure is usually required, in which a fitting procedure is always needed. Although similar fitting techniques can be used for all power components whose behaviour can be derived from a frequency response test, the optimal procedure to be applied in each case is different. Annex A presents the application of fitting techniques for extracting rational models of lines, cables and transformers from frequency response tests [23].
- ***Dynamic System Equivalents***: A common practice when dealing with large power systems in transient studies is to divide the system into a study zone, where transient phenomena occur, and an external system encompassing the rest of the system. The study zone is represented in detail, while the rest of the system is modelled by an equivalent. Given the frequency range with which transients are generated, there is a need for suitable techniques that could accurately determine the parameters of the external equivalent system from low- to high-frequency behaviours. Annex B reviews current techniques for obtaining dynamic system equivalents [24].

Readers interested in modelling guidelines and parameter determination for electromagnetic transients studies can consult references [1–7].

Overvoltage Calculations: An overvoltage is a voltage having a crest value exceeding the corresponding crest of the maximum system voltage. Overvoltages can occur with very wide range of waveshapes and durations. Types and shapes of overvoltages, as well as their causes, are well known; they are classified in standards (IEC, IEEE). The magnitude of external lightning overvoltages remains essentially independent of the system design, whereas that of internal switching overvoltages increases with the operating voltage of the system. The estimation of overvoltages is fundamental to the insulation design of power components, and to the selection of protection devices [25, 26]. Chapter 5 summarizes the different types of overvoltages and their causes, provides modelling guidelines for digital simulation using a time-domain tool (e.g. an EMTP-like tool) and presents some illustrative cases of any type of voltage stress in power systems.

Power Electronics Applications: Power electronics applications have quickly spread to all voltage levels, from extra high voltage (EHV) transmission to low voltage circuits in end-user facilities. They include high-voltage DC (HVDC) systems [27], flexible AC transmission systems (FACTS) [28], custom power devices [29], high-power AC to DC converters, converter-based drive technologies, instantaneous backup power systems and power-electronic interfaces for integration of distributed energy resources (DER) [30]. Power electronics modelling and simulation are especially important for a concept validation and design iteration during new product development. Four chapters of this book have been dedicated to the simulation of power electronics components. They provide general modelling guidelines and procedures for simulation of the main power electronics applications using a time-domain tool (e.g. an EMTP-like tool), and present several case studies.

Dynamic Average Modelling: Detailed switching models of power electronics converters are computationally intensive and can be the bottleneck for system-level studies with a large number of components and controllers. These drawbacks have led to the development of the so-called dynamic average-value models (AVM) in which the effect of fast switching is neglected or averaged within a prototypical switching interval [31]. The resulting models are computationally efficient and can run orders of magnitudes faster than the original models. Chapter 10 describes methods of constructing AVMs and demonstrates their advantages with some practical examples.

Protection Systems: Protection systems are critical power system components and their behaviour is an important part of power system response to a transient event. A system aimed at protecting against overcurrents consists of three major parts: instrument transformers (current, wound electromagnetic voltage, and coupling capacitor voltage transformers), protective relays, and circuit breakers [32–34]. Chapter 11 summarizes models for instrument transformers and different types of relays (electromechanical, static/electronic, microprocessor-based), and presents some illustrative cases of protection systems.

Smart Grids: The smart grid may be seen as an upgrade of the current power system, in which present and new functionalities will monitor, protect and automatically optimize the operation of its interconnected elements to maintain a reliable and secure environment. The smart grid will offer better management of energy consumption by the use of advanced two-way metering infrastructure and real-time communication; improved power reliability and quality; enhanced security by reducing outages and cascading problems; and better integration of DERs. Although the smart grid will build upon the basic design of the current power grid, it will have features essential to its operation that will involve monitors, sensors, switching devices and sophisticated two-way communication systems that will allow it to be a highly automated power delivery system [35, 36].

The complete model of an actual smart grid should include the representation of: (1) conventional power components that will generate and transmit the electric energy, (2) various types of power-electronic interfaces, loads and DERs, plus their corresponding controllers, and (3) the two-way communication system. To date, there is no software tool capable of coping with such a complex model, although some work is in progress [37].

Chapter 12 presents the application of time-domain solution techniques to the study of large actual distribution systems. The chapter covers the study of DER integration and its possible effects on system reliability and voltage violations, the application of system reconfigurations by large numbers of switching operations to exploit the advantage of automation and self-healing capabilities and the analysis of distribution system overvoltages. The chapter also describes some experiences with the development of industrial-grade translators for interfacing Power-Flow programs with EMTP-like tools, which can facilitate the simulation of electromagnetic transients to utilities.

Interfacing Techniques: Interfacing an electromagnetic transient tool with external programs or algorithms expands their applicability to areas where techniques are available through the external agent (program or algorithm) [38–40]. Chapter 13 describes methods for interfacing a transient simulation tool with other mathematical algorithms to extend their application for both analysis and design of complex power systems.

References

[1] CIGRE WG 33.02 (1990) Guidelines for Representation of Network Elements when Calculating Transients. CIGRE Brochure 39.

[2] Gole, A., Martinez-Velasco, J.A. and Keri, A. (eds) (1998) Modeling and Analysis of Power System Transients Using Digital Programs. IEEE Special Publication TP133.

[3] IEC TR 60071-4 (2004) Insulation Co-ordination – Part 4: Computational Guide to Insulation Co-ordination and Modeling of Electrical Networks.

[4] Martinez-Velasco, J.A. (ed.) (2009) *Power System Transients. Parameter Determination*, CRC Press, Boca Raton, FL, USA.

[5] Phadke, A.G. (Course Coord.) (1980) Digital Simulation of Electrical Transient Phenomena. IEEE Publication 81 EHO173-5-PWR.

[6] Tziouvaras, D.A. (Course Coord.) (1999) Electromagnetic Transient Program Applications to Power System Protection. IEEE Special Publication TP150.

[7] Martinez-Velasco, J.A. (Course Coord.) (2011) Transient Analysis of Power Systems: Solutions Techniques, Tools and Applications. IEEE Special Publication 11TP255E.

[8] Dommel, H.W. (1986) *ElectroMagnetic Transients Program Reference Manual (EMTP Theory Book)*, Bonneville Power Administration, Portland, OR, USA.
[9] Greenwood, A. (1991) *Electrical Transients in Power Systems*, 2nd edn, John Wiley & Sons, Inc., New York, NY, USA.
[10] van der Sluis, L. (2001) *Transients in Power Systems*, John Wiley & Sons, Ltd, Chichester, UK.
[11] Chowdhuri, P. (2003) *Electromagnetic Transients in Power Systems*, 2nd edn, RS Press-John Wiley & Sons, Ltd, Taunton, UK.
[12] Watson, N. and Arrillaga, J. (2003) *Power Systems Electromagnetic Transients Simulation*, The Institution of Electrical Engineers, Stevenage, UK.
[13] Shenkman, A.L. (2005) *Transient Analysis of Electric Power Circuits Handbook*, Springer, Dordrecht, The Netherlands.
[14] Das, J.C. (2010) *Transients in Electrical Systems. Analysis, Recognition, and Mitigation*, McGraw-Hill, New York, NY, USA.
[15] Ametani, A., Nagaoka, N., Baba, Y. and Ohno, T. (2013) *Power System Transients: Theory and Applications*, CRC Press, Boca Raton, FL, USA.
[16] Bickford, J.P., Mullineux, N. and Reed, J.R. (1976) *Computation of Power System Transients*, Peter Peregrinus Ltd, London, UK.
[17] Noda, T. and Ramirez, A. (2007) z-transform-based methods for electromagnetic transient simulations. *IEEE Transactions on Power Delivery*, **22**, 3, 1799–1805.
[18] Moreno, P. and Ramirez, A. (2008) Implementation of the Numerical Laplace Transform: A review. *IEEE Transactions on Power Delivery*, **23**(4), 2599–2609.
[19] Mahseredjian, J., Dinavahi, V. and Martinez, J.A. (2009) Simulation tools for electromagnetic transients in power systems: Overview and challenges. *IEEE Transactions on Power Delivery*, **24**(3), 1657–1669.
[20] Dufour, C., Ould Bachir, T., Grégoire, L.-A. and Bélanger, J. (2012) Real-time simulation of power electronic systems and devices, Chapter 15, in *Dynamics and Control of Switched Electronic Systems: Advanced Perspectives for Modeling, Simulation and Control of Power Converters* (eds F. Vasca and L. Iannelli), Springer, London, UK.
[21] Bélanger, J. and Dufour, C. (2013) Modern methodology of electric system design using rapid-control prototyping and hardware-in-the-loop, Chapter 9, in *Real-Time Simulation Technologies: Principles, Methodologies, and Applications* (eds K. Popovici and P.J. Mosterman), CRC Press, Boca Raton, FL, USA.
[22] Uriarte, F. (2013) *Multicore Simulation of Power System Transients*, The Institution of Engineering and Technology, Stevenage, UK.
[23] Gustavsen, B. (2002) Computer code for rational approximation of frequency dependent admittance matrices. *IEEE Transactions Power Delivery*, **17**(4), 1093–1098.
[24] Annakkage, U.D., Nair, N.K.C., Liang, Y., *et al.* (2012) Dynamic system equivalents: A survey of available techniques. *IEEE Transactions on Power Delivery*, **27**(1), 411–420.
[25] Ragaller, K. (ed.) (1980) *Surges in High-Voltage Networks*, Plenum Press, New York, NY, USA.
[26] Hileman, A.R. (1999) *Insulation Coordination for Power Systems*, Marcel Dekker, New York, NY, USA.
[27] Kim, C.K., Sood, V.K., Jang, G.S., *et al.* (2009) *HVDC Transmission: Power Conversion Applications in Power Systems*, John Wiley & Sons (Asia) Pte Ltd, Singapore.
[28] Sen, K.K. and Sen, M.L. (2009) *Introduction to FACTS Controller: Theory, Modeling, and Applications*, John Wiley & Sons, Inc.-IEEE Press, Hoboken, NJ, USA.
[29] Ghosh, A. and Ledwich, G. (2002) *Power Quality Enhancement using Custom Power Devices*, Kluwer Academic Publishers, Norwell, MA, USA.
[30] Yazdani, A. and Iravani, R. (2010) *Voltage-Sourced Converters: Modeling, Control, and Applications*, John Wiley & Sons, Inc., Hoboken, NJ, USA.
[31] Chiniforoosh, S., Jatskevich, J., Yazdani, A., *et al.* (2010) Definitions and applications of dynamic average models for analysis of power systems. *IEEE Transactions on Power Delivery*, **25**(4), 2655–2669.
[32] Anderson, P.M. (1998) *Power System Protection*, Mc-Graw Hill-IEEE Press, New York, NY, USA.
[33] Phadke, A.G. and Thorp, J.S. (2009) *Computer Relaying for Power Systems*, 2nd edn, John Wiley & Sons, Ltd, Chichester, UK.
[34] Ziegler, G. (2011) *Numerical Distance Protection. Principles and Applications*, 4th edn, Siemens-Publicis Publishing, Erlangen, Germany.
[35] Hadjsaïd, N. and Sabonnadière, J.C. (eds) (2012) *Smart Grids*, John Wiley & Sons, Ltd-ISTE, London (UK) – Hoboken (NJ, USA).

[36] Momoh, J. (2012) *Smart Grid. Fundamentals of Design and Analysis*, John Wiley & Sons, Inc.-IEEE Press, Hoboken, NJ, USA.

[37] Nutaro, J., Kuruganti, P.T., Shankar, M., *et al.* (2008) Integrated modeling of the electric grid, communications, and control. *International Journal of Energy Sector Management*, **2**(3), 420–438.

[38] Gole, A.M., Filizadeh, S., Menzies, R.W. and Wilson, P.L. (2005) Optimization-enabled electromagnetic transient simulation. *IEEE Transactions on Power Delivery*, **20**(1), 512–518.

[39] Filizadeh, S., Heidari, M., Mehrizi-Sani, A., *et al.* (2008) Techniques for interfacing electromagnetic transient simulation programs with general mathematical tools. *IEEE Transactions on Power Delivery*, **23**(4), 2610–2622.

[40] Jalili-Marandi, V., Dinavahi, V., Strunz, K., *et al.* (2009) Interfacing techniques for transient stability and electromagnetic transient programs. *IEEE Transactions on Power Delivery*, **24**(4), 2385–2395.

2

Solution Techniques for Electromagnetic Transients in Power Systems

Jean Mahseredjian, Ilhan Kocar and Ulas Karaagac

2.1 Introduction

Modern power systems are complex and require advanced mathematical analysis methods for their design and operation. Numerical techniques are used to simulate and analyse power systems. Such numerical techniques are programmed in specialized software packages. The power system simulation and analysis tools can be subdivided into three main categories: steady-state, electromechanical transients and electromagnetic transients.

The computation of a power system load-flow falls into the steady-state category. It is often based on the positive sequence approximation of the studied network. The positive sequence approximation uses the balanced network assumption: balanced loads and continuously transposed transmission lines. It is often an acceptable approximation for balanced transmission systems, but in some systems transmission lines may not be balanced, and unbalanced loading may occur. Distribution systems are not balanced by nature and require multiphase and unbalanced load-flow calculation methods. The load-flow solution is the first initialization stage of a power system. It determines all the voltage phasors in the studied system and establishes all the initial conditions.

The load-flow solution of a power system is a nonlinear problem that can be solved using Jacobian matrices and iterations. When all the load-flow constraints are converted into lumped branch equivalent models, it is possible to achieve a linear steady-state solution without iterations.

Electromechanical transients assume low-frequency perturbations and are conventionally solved using the positive sequence network approximation. The power system is assumed to remain in quasi steady-state, whereas the generating units (synchronous or asynchronous machines) are solved using differential equations in the time-domain. Such methods can be efficiently used to simulate and study very-large-scale systems for rotor angle stability problems, including large disturbances and small-signal stability problems.

Transient Analysis of Power Systems: Solution Techniques, Tools and Applications, First Edition.
Edited by Juan A. Martinez-Velasco.

The category of electromagnetic transients avoids approximations and becomes applicable to the widest range of frequencies. Studied phenomenon signals are visualized in the time-domain at the waveform level and can contain frequencies from 0 Hz to 100 kHz or higher. Using such a wideband of frequencies requires detailed circuit-based calculation methods and models. The modelling sophistication is linked to the frequency content. Electromagnetic transients include electromechanical transients and require load-flow solution for initialization. Due to the detailed representation of circuit components and increased precision, the computation of electromagnetic transients requires more computing resources and consequently significantly more computing time.

Software packages and methods used for computing electromagnetic transients are called electromagnetic transient-type (EMT) tools. EMT-type simulation methods are classified into two main categories: off-line and real-time. The purpose of an off-line simulation tool is to conduct simulations on a generic computer. Off-line tools are designed for high efficiency using powerful graphical user interfaces, numerical methods and programming techniques. Such tools do not have any computing time constraints and can be made as precise as needed within the available data, models and related mathematics.

Real-time simulation tools are capable of generating results in synchronism with a real-time clock. Such tools are capable of interfacing with physical devices and maintaining data exchanges within the real-time clock. The capability to compute and interface in real time, imposes restrictions on the design of such tools. Computing technologies and numerical methods are, however, evolving rapidly, and the gap between real-time and off-line methods is constantly reducing.

This chapter targets mainly off-line solution methods and tools. The objective is to provide an overview of off-line simulation tools and methods for the computation and analysis of electromagnetic transients. This chapter focuses on the most widely recognized and available groups of methods applied in industrial grade computer software packages

This chapter follows the initial work presented in [1–4].

2.2 Application Field for the Computation of Electromagnetic Transients

The initial application of EMT-type tools was the computation of overvoltages in power systems. There are four main categories of overvoltages: very fast front, fast front, slow front and temporary. The very fast front category is related mainly to restrikes in gas-insulated substations. The frequencies range from 100 kHz to 50 MHz. Lightning overvoltages fall into the fast front category, their typical frequency content being from 10 kHz to 3 MHz. Switching overvoltages fall into the slow front category with frequencies ranging from fundamental frequency to 20 kHz. Switching events are internal controlled or uncontrolled events. For example, controlled events are line switching actions. Faults on buses or in transmission lines fall into the list of uncontrolled events. For temporary overvoltages, the typical causes are: single-line-to-ground faults causing overvoltages on live phases, open line energization and load-shedding. In some cases, temporary overvoltages are combined with ferroresonance. The frequency content for temporary overvoltages is typically from 0.1 Hz to 1 kHz.

Frequencies above the fundamental frequency usually involve electromagnetic phenomena. Frequencies below the fundamental frequency may also include electromechanical modes (synchronous or asynchronous machines).

The above categories can be expanded to list specific important study topics in power systems:

- switchgear, TRV, shunt compensation, current chopping, delayed-current zero conditions
- insulation coordination
- saturation and surge arrester influences
- harmonic propagation, power quality
- interaction between compensation and control
- wind generation, distributed generation
- precise determination of short-circuit currents

- detailed behaviour of synchronous machines and related controls, auto-excitation, subsynchronous resonance, power oscillations
- protection systems
- HVDC systems, power electronics, FACTS and custom power controllers

These applications are in a wideband range of frequencies, from DC to 50 MHz. EMT-type methods are also applicable to the simulation and analysis of electromechanical transients. EMT-type programs can produce more precise simulation results for such studies due to inherent modelling capabilities to account for network nonlinearities and unbalanced conditions. Frequency-dependent and voltage-dependent load models can also be incorporated in EMT-type tools.

Since EMT-type programs are able to represent the actual circuit of a power network, they are more general than traditional power system analysis tools. EMT-type methods constitute the precision reference for power system analysis.

2.3 The Main Modules

The main modules of an EMT-type simulation tool are:

1. graphical user interface (GUI)
2. load-flow solution
3. steady-state solution
4. initialization: automatic or manual initial conditions
5. time-domain solution
6. waveforms and outputs.

These modules are described in the following sections. The steady-state solution is based on lumped component models with parameters derived from the load-flow solution phasors. As shown below, the load-flow solution is based on constraints at various buses and requires a nonlinear system solver.

In addition to the above fundamental modules, EMT-type tools may include an external interface for user-defined models and communication with other solution methods or complete software packages. Statistical analysis modules can be included to generate, for example, random switching timings for estimating the worst overvoltage conditions. A set of defined parameters may be perturbed using specific rules or random numbers, to perform parametric studies where the simulations are executed for each set of parameters to present an ensemble of results submitted to various analysis options and optimizations [5, 6].

2.4 Graphical User Interface

The graphical user interface is the first entry level to the simulation process. It is the simulated network data input method. Modern applications rely on GUIs for preparing data and controlling the simulation process. GUIs with various levels of flexibility and visualization capabilities allow us to draw the circuit diagram of the simulated system and enter all the appropriate data for selected models. In most cases the GUI is just used to generate a data file that is submitted directly to the computational engine. The GUI may also maintain a permanent and dynamic link with the computational engine for exchanging data, visualization of intermediate results and manipulating parameters.

An example of a GUI-based design is shown in Figure 2.1. Modern GUIs are based on the hierarchical design approach with subnetworks and masking. Subnetworks allow us to simplify the drawing and hide details while masking provides data encapsulation. The design of Figure 2.1 uses several subnetworks. The 230 kV network is interconnected with a 500 kV network evacuated with all its details into the subnetwork shown in Figure 2.1. In a hierarchical design subnetworks can also contain other subnetworks. Subnetworks can be also used to develop models. The three-phase transformers shown in Figure 2.1 are

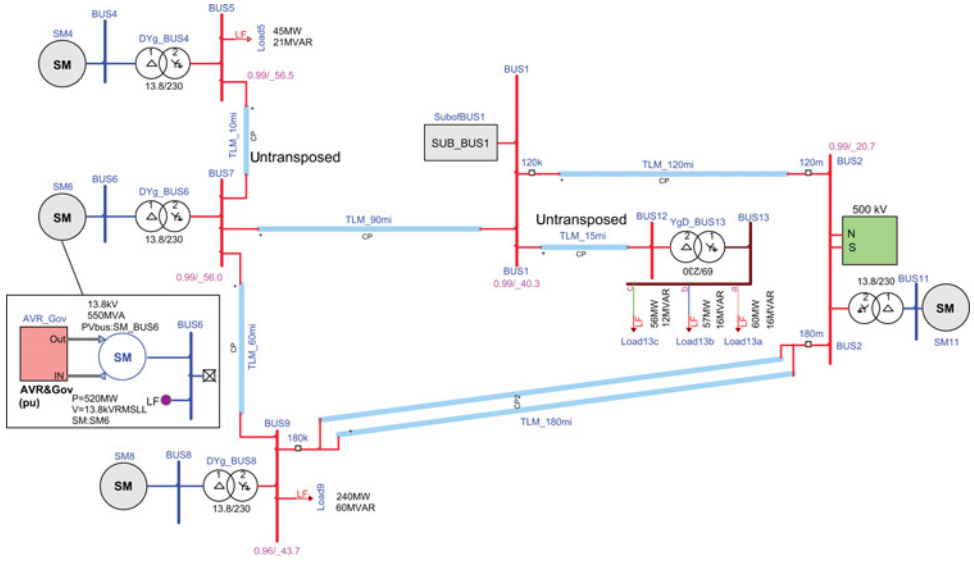

Figure 2.1 Sample 230 kV network simulation presented in a GUI.

based on the interconnection of single-phase units. The synchronous machine subnetworks contain the load-flow constraints, machine models and the subnetwork composed of voltage regulator and governor control subnetworks, as shown in Figure 2.1.

Although several advanced GUIs [7–9] are currently available, the industry lacks interoperability standards between various software applications. Currently there are no applicable standards for transient (EMT-type) model data fields. This means that the GUIs and related data files are based on proprietary formats that cannot be decoded by other applications. This situation creates major bottlenecks when different software tools are used within a given organization or when different applications are used in one or more collaborating organizations. Some applications provide external access functions and might be called directly from other applications for performing simulations on assembled networks. The programming aspects of such applications are not complex, but interfacing networks solved in different computational engines may become error prone or create numerical instabilities due to inherent lack of simultaneous solution capability.

A possible solution to data portability between applications is the utilization of the common information model [10] (CIM) format in the simulation of electromagnetic transients. The CIM format is an open standard for representing power system components. It could be used for electromagnetic transients if augmented with the needed data fields related to such models. An experiment with CIM/XML data translation into a proprietary format and GUI drawing is presented in [11].

Standardization of data is also an important part of the solution for creating portability with other conventional power system applications. Standardization should result in significant benefits to the power industry.

2.5 Formulation of Network Equations for Steady-State and Time-Domain Solutions

EMT-type programs are based on the representation of the actual electrical circuit equivalent of the studied power system. The most common network equation formulation methods fall into two main categories: nodal analysis and state-space.

Bold characters are used hereafter for the representation of vectors and matrices.

2.5.1 Nodal Analysis and Modified-Augmented-Nodal-Analysis

The nodal analysis approach is based on Kirchhoff's current law. The network admittance matrix $\mathbf{Y_n}$ is used for computing the sum of currents entering each electrical node

$$\mathbf{Y_n}\,\mathbf{v_n} = \mathbf{i_n} \tag{2.1}$$

where $\mathbf{v_n}$ is the vector of node voltages and the members of $\mathbf{i_n}$ hold the sum of currents entering each node. It is assumed that the network has a ground node at zero voltage which is not included in equation (2.1). Since the network may contain voltage sources (known node voltages), equation (2.1) must be partitioned to keep only the unknown voltages on the left-hand side:

$$\mathbf{Y'_n}\,\mathbf{v'_n} = \mathbf{i'_n} - \mathbf{Y_s}\,\mathbf{v_s} \tag{2.2}$$

where $\mathbf{Y'_n}$ is the coefficient matrix of unknown node voltages $\mathbf{v'_n}$, $\mathbf{i'_n}$ holds the sum of currents entering nodes with unknown voltage, $\mathbf{Y_s} \in \mathbf{Y_n}$ and relates to known voltages $\mathbf{v_s}$. Note that $\mathbf{v_n} = \begin{bmatrix}\mathbf{v'_n} & \mathbf{v_s}\end{bmatrix}^T$.

The automatic formulation of $\mathbf{Y_n}$ is very simple and extremely efficient. It is sufficient to combine individual device (network component) admittance matrices at each node. A given device (network component) connected between left node *k* and right node *m*, is described through its generic admittance matrix in

$$\begin{bmatrix}\mathbf{i_k}\\ \mathbf{i_m}\end{bmatrix} = \begin{bmatrix}\mathbf{Y_{kk}} & \mathbf{Y_{km}}\\ \mathbf{Y_{mk}} & \mathbf{Y_{mm}}\end{bmatrix}\begin{bmatrix}\mathbf{v_k}\\ \mathbf{v_m}\end{bmatrix}, \tag{2.3}$$

where $\mathbf{i_k}$ and $\mathbf{i_m}$ represent the current vectors for the sum of currents entering the *k* side and *m* side nodes respectively and the vectors $\mathbf{v_k}$ and $\mathbf{v_m}$ represent the voltages on the k side and m side nodes respectively. In most cases $\mathbf{Y_{km}} = \mathbf{Y_{mk}}$ and the resulting matrix $\mathbf{Y_n}$ is symmetric. Equation (2.3) is generic and may accommodate any number of phases and coupling between phases. If the device model includes current sources, such sources will contribute (summation) directly to $\mathbf{i_n}$ (or $\mathbf{i'_n}$) in (2.1).

Equation (2.1) has several limitations. It is restricted to modelling devices with the admittance matrix representation of (2.3) and ideal voltage sources connected to ground. It is not possible, for example, to directly model branch relations such as ideal transformer units or ideal sources without a ground node. Ideal transformer units are used as primitive devices for building three-phase transformer models. It is not possible to model ideal switches in (2.2) using a fixed rank $\mathbf{Y'_n}$ matrix. Devices with voltage and current relations cannot be represented directly.

The above limitations can be eliminated using modified-augmented-nodal analysis (MANA) introduced in [12] for an EMT-type solution method and improved in [13, 14]. Equation (2.1) is augmented to include generic device equations, and the complete system of network equations can be rewritten in the more generic form:

$$\mathbf{A_N}\,\mathbf{x_N} = \mathbf{b_N} \tag{2.4}$$

Now $\mathbf{Y_n} \in \mathbf{A_N}$, $\mathbf{x_N}$ contains both unknown voltage and current quantities, and $\mathbf{b_N}$ contains known current and voltage quantities. The matrix $\mathbf{A_N}$ is not necessarily symmetric. Equation (2.4) can be also written explicitly as

$$\begin{bmatrix}\mathbf{Y_n} & \mathbf{A_c}\\ \mathbf{A_r} & \mathbf{A_d}\end{bmatrix}\begin{bmatrix}\mathbf{v_n}\\ \mathbf{i_x}\end{bmatrix} = \begin{bmatrix}\mathbf{i_n}\\ \mathbf{v_x}\end{bmatrix}, \tag{2.5}$$

where: the matrices $\mathbf{A_r}$, $\mathbf{A_c}$ and $\mathbf{A_d}$ (augmented portion, row, column and diagonal coefficients) are used to enter network model equations which are not or cannot be included in $\mathbf{Y_n}$; $\mathbf{i_x}$ is the vector of unknown

currents in device models; $\mathbf{v_x}$ is the vector of known voltages; $\mathbf{x_N} = \begin{bmatrix} \mathbf{v_n} & \mathbf{i_x} \end{bmatrix}^T$ and $\mathbf{b_N} = \begin{bmatrix} \mathbf{i_n} & \mathbf{v_x} \end{bmatrix}^T$. In reality the network component equations can be entered in any order in equation (2.4) and other types of unknown/known variables can be used, but the partitioning presented in (2.5) allows us to simplify the explanations. Further details can be found in [13, 14].

As will be shown below, (2.4) (or (2.5)) can be used for both steady-state and time-domain solutions of a generic network and allows us to integrate generic model equations such as

$$k_1 v_k + k_2 v_m + k_3 i_x + k_4 i_y + \cdots = b_z, \tag{2.6}$$

where the unknown node voltages (v_k,v_m) and branch currents (i_k,i_m) are members of $\mathbf{x_N}$, while b_z is entered into $\mathbf{b_N}$. Any number of unknown node voltages and branch currents can be used, and (2.6) can also include coupling by rewriting it with vectors and matrices. A three-phase voltage source, for example, connected between two arbitrary nodes k and m is expressed as

$$\mathbf{v_k} - \mathbf{v_m} - \mathbf{Z_s i_{km}} = \mathbf{v_{b\ km}}, \tag{2.7}$$

where $\mathbf{Z_s}$ is the source impedance, $\mathbf{i_{km}} \in \mathbf{i_x}$ representing source currents (entering node k), and $\mathbf{v_{b\ km}} \in \mathbf{v_x}$ is the known source voltage. This equation contributes its own row into $\mathbf{A_r}$ with coefficients 1 and -1 in the columns k and m respectively. The impedance $\mathbf{Z_s}$ (which can be set to zero) is entered in a diagonal block of $\mathbf{A_d}$. The row contributed into $\mathbf{A_r}$ is transposed and placed in the corresponding column of $\mathbf{A_c}$. Equation (2.7) can be rewritten in its single-phase form using scalars.

For a single-phase switch model there are two states. In the closed state

$$v_k - v_m - R_S\, i_{km} = 0, \tag{2.8}$$

with R_S being the switch resistance. The contributions of this equation to (2.5) are similar to the voltage source case. The resistance R_S can be zero for the ideal case. For the open state condition the resistance R_S in (2.8) can be replaced by a very high value or in the ideal switch case $i_{km} = 0$, and the corresponding diagonal cell of $\mathbf{A_d}$ is set to 1, whereas the switch row terms in $\mathbf{A_r}$ are nullified and the matrix $\mathbf{A_N}$ becomes non-symmetric. For both states, the corresponding $\mathbf{v_x}$ element is 0, unless a fixed voltage source is appearing in series with the switch. It is noticed that changes in switch status in the time-domain require updates (reformulation) in $\mathbf{A_N}$, and constitute a computational bottleneck.

Single-phase and three-phase transformers can be built using the ideal transformer unit representation shown in Figure 2.2. It consists of dependent voltage and current sources. The secondary branch equation is given by

$$v_{k2} - v_{m2} - g\, v_{k1} + g\, v_{m1} = 0, \tag{2.9}$$

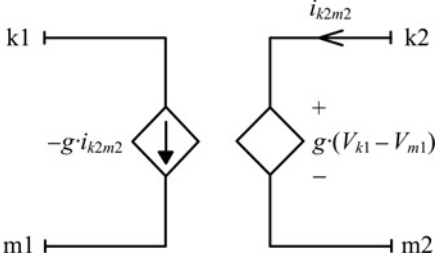

Figure 2.2 Ideal transformer model.

where g is the transformation ratio. This equation contributes its own row to the matrix $\mathbf{A_r}$, whereas the matrix $\mathbf{A_c}$ contains the transposed version of that row. A phase-shifting function can be created in a similar manner, with a complex g in the steady-state formulation. It is possible to extend to multiple secondary windings using parallel-connected current sources on the primary side and series-connected voltage sources on the secondary side. Leakage losses and the magnetization branch are added externally to the ideal transformer nodes.

Three-legged core-form transformer models – or any other types – can be included, using coupled leakage matrices and magnetization branches.

The MANA formulation (2.4) is completely generic and can easily accommodate the juxtaposition of arbitrary component models in arbitrary network topologies with any number of wires and nodes. It is not limited to the usage of the unknown variables presented in (2.5) and can be augmented to use different types of unknown and known variables. It is conceptually simple to realize.

2.5.1.1 Steady-State Solution

The steady-state version of equation (2.4) is based on complex numbers. Equation (2.4) is simply rewritten using capital letters to represent complex numbers (phasors). If a network contains sources at different frequencies, then (2.4) can be solved at each frequency and assuming that the network is linear (linear models are used for all devices), the solutions of $\mathbf{x_N}$ can be combined to derive the harmonic steady-state solution in the form of a Fourier series.

2.5.1.2 Time-Domain Solution

The time-domain module is the heart of an EMT-type program. It starts from 0-state (all devices are initially de-energized) or from given automatic or manual initial conditions and computes all variables as a function of time using a time-step Δt.

Since component models may have differential equations, we need to select and apply a numerical integration technique for their solution. Since many electrical circuits result in a stiff system of equations, the chosen numerical integration method must be stiffly stable. Such a need excludes explicit methods. In the list of implicit numerical integration methods, the most popular method in industrial applications remains the trapezoidal integration method. It is an A-stable polynomial method that can be programmed very efficiently. If an ordinary differential equation is written as

$$\begin{aligned} \frac{dx}{dt} &= f(x,t) \\ x(0) &= x_0, \end{aligned} \tag{2.10}$$

then the trapezoidal integration rule gives

$$x_t = \frac{\Delta t}{2} f_t + \frac{\Delta t}{2} f_{t-\Delta t} + x_{t-\Delta t}. \tag{2.11}$$

The terms found at $t - \Delta t$ constitute history terms, and all quantities at time-point t are also related through network equations. The computation process finds a solution at discrete time-points, as illustrated in Figure 2.3.

The trapezoidal rule is the most widely used method for performing numerical integration in EMT-type programs.

In the time-domain solution, the objective is to use the real version of equation (2.4) for solving the algebraic-differential equations of the network. This is achieved simply by converting or discretizing the

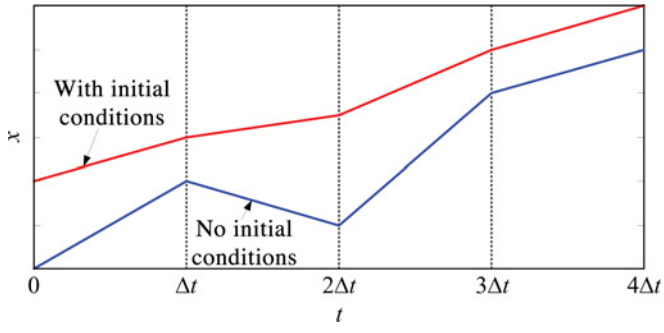

Figure 2.3 Discrete solution time-points.

device equations using a numerical integration technique such as equation (2.11). For a pure inductor branch connected between two nodes k and m

$$v_{km} = L\frac{di_{km}}{dt}, \tag{2.12}$$

and the discretized version (equivalent circuit model or companion branch) [15–17] is given by

$$i_t = \frac{\Delta t}{2L}v_t + \frac{\Delta t}{2L}v_{t-\Delta t} + i_{t-\Delta t}, \tag{2.13}$$

where the km subscript is dropped to simplify the notation. Since the last two terms of this equation represent computations available from a previous time-point, it can be written as

$$i_t = \frac{\Delta t}{2L}v_t + i_{h_t}, \tag{2.14}$$

where i_{h_t} is a history term for the solution at time-point t. This term contributes to the right-hand side of equation (2.4). The coefficient of voltage v_t is the branch admittance that contributes four elements to the matrix $\mathbf{A_N}$ of equation (2.4). The integration time-step Δt becomes embedded in $\mathbf{A_N}$, and if Δt is modified we need to reformulate $\mathbf{A_N}$.

An equation similar to (2.14) can be written for capacitor branches. The inductor, capacitor and resistor are primitive elements for building other models. All discretized device equations are entered into (2.4) which must be written as

$$\mathbf{A}_{\mathbf{N}_t}\,\mathbf{x}_{\mathbf{N}_t} = \mathbf{b}_{\mathbf{N}_t} \tag{2.15}$$

for the solution at the time-point t.

The matrix $\mathbf{A_N}$ of an arbitrary network is normally sparse. A block diagonal structure results when the network contains transmission lines or cables. The models of such devices have a propagation delay which creates a natural decoupling of the studied network into subnetworks that can be solved in parallel.

The companion branch approach is used in several EMT-type tools [13, 16–18].

2.5.1.3 Nonlinear Devices

An important problem in the time-domain computation of power system transients is the solution of nonlinearities. Such nonlinearities occur due to nonlinear functions being used in some network device

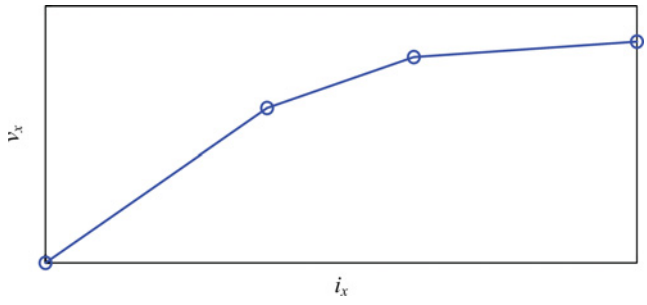

Figure 2.4 Sample nonlinear symmetric function.

models. In most cases, a nonlinear function can be modelled using piecewise linear segments. The positive part of a sample nonlinear function with three segments is shown in Figure 2.4 for a voltage $v_x(t)$ and a current $i_x(t)$. In EMT-type applications such functions are monotonically increasing, since it is assumed that there is a unique solution for a given voltage. Each segment j can be represented by a liner equation

$$i_{x_j} = K_j v_{x_j} + i_{q_j}, \tag{2.16}$$

which is in fact a Norton equivalent with admittance K_j and Norton current source i_{q_j}. This relation can be directly included in equation (2.5). It constitutes a linearization of the nonlinear function at the operation point for the voltage solution at the time-point t.

Equation (2.16) can be also written in its vector-matrix form for coupled nonlinearities.

In some cases, the piecewise linear representation is not realizable beforehand. In such cases, the linearization equation (2.16) must be recalculated at each network solution time-point. A typical example is the breaker arc model, the nonlinear function based arrester model or the case of a generic black-box device.

There are two main categories of methods for solving nonlinear functions: with and without solution delays. The delay is a numerical integration time-step delay. In some methods the nonlinear model is represented through a voltage-dependent current source. Such methods may encounter numerical instabilities. More robust methods rely on linearization at the operating point. As explained above, the linearization results in an equivalent Norton circuit. Norton equivalents can also be used for interfacing with more complex nonlinear devices and rotating machine models [19].

In delay-based methods the Norton equivalent is updated with a time-step delay. The delay-based methods are also called pseudo-nonlinear methods [20], whereas methods without delays are called true-nonlinear methods.

If there is no artificial delay, then in a coupled subnetwork all nonlinear devices must be solved simultaneously. A coupled subnetwork is defined here as a physical subnetwork in which all devices are related to each other at a given solution time-point and there are no delay elements, such as distributed parameter transmission lines or cables. Such a subnetwork actually creates an independent set of equations or matrix blocks in equation (2.5). The simultaneous solution means that if at a given solution time-point the node voltage of a device modifies its current (or equivalent model) then it is necessary to update and resolve the subnetwork nodal equations until all voltages stop changing within a given tolerance. The convergence of voltages must occur before moving to the next solution time-point.

In delay-based methods the device equations (or currents) are updated without recalculating their voltages at the same time-point and through the coupled subnetwork. The solution is advanced to the next time-point without recalculating the voltages in the subnetwork. If the time-step is sufficiently small,

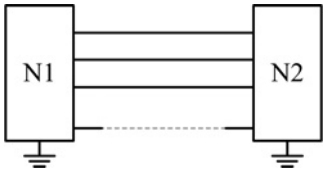

Figure 2.5 Two networks separated using the compensation method.

this method can become sufficiently precise, but in some cases it may still create numerical problems or force abnormally small time-steps.

Simultaneous solution methods are more precise and are almost unavoidable in most cases.

2.5.1.3.1 Compensation Method

A powerful and efficient method applied in some programs is the compensation method. For historical reasons this method is poorly understood in the literature, and its limitations are not well known. It is also often reused or reinvented without recognizing or referring to the original idea.

The compensation method was originally introduced in [21,22] and applied to EMT-type simulations in [20]. The basic idea is the separation of a network into two parts, as shown in Figure 2.5, networks N1 and N2. This separation can be also used in independent subnetworks. As explained above, these subnetworks are created naturally due to propagation delay decoupling of transmission line or cable models.

If the network N1 is a linear network, then N2 can be the compensation-based network. The network N2 can have the following properties:

- N2 can contain one or more devices or a complete network.
- N2 can be linear or nonlinear.
- N2 can contain any number of devices and its nonlinear functions can be of any type.

The basic principle is the computation of a Thevenin equivalent for the network N1. The following steps are applied in the compensation process at a given solution time-point t:

1. The network N1 is solved first without N2 (N2 is disconnected). This results in the computation of all node voltages in N1.
2. The Thevenin equivalent of N1 is established from the voltage computations in the previous step and followed by the computation of the Thevenin impedance matrix $\mathbf{Z_{th}}$.
3. The network N2 is solved with the Thevenin equivalent of N1.
4. All active sources in N1 are killed, and the currents entering N2 are used to find all network voltages in N1.
5. The network voltages found in step 1 are added to the network voltages found in the previous step. This is the compensation step. It is based on the superposition theorem.

The above steps can be expressed symbolically through the following equations. Either the classical nodal analysis system (2.2) or the more generic formulation of equation (2.15) can be used with similar results. If $\mathbf{v_n}$ is the vector of voltages found from the solution of (2.2) in the time-domain for the network N1 due to its internal sources only (N2 is disconnected), then the compensated solution becomes (at a given time-point)

$$\mathbf{v}_\mathbf{n}^{final} = \mathbf{v_n} + \mathbf{v}_{\mathbf{n}\phi}, \tag{2.17}$$

where $\mathbf{v}_{\mathbf{n}}^{final}$ is the final solution at time-point t and $\mathbf{v}_{\mathbf{n}\phi}$ is the contribution from the currents entering the network N2. The time variable subscript is not shown in (2.17) and the following equations, for the purpose of simplifying the notation. If equation (2.15) is used instead of (2.2), then equation (2.17) should be applied to $\mathbf{x}_{\mathbf{N}}$.

The Thevenin voltages are found from

$$\mathbf{v}_{\mathbf{th}} = \mathbf{A}_{\mathbf{n}\phi}^{T}\, \mathbf{v}_{\mathbf{n}}, \tag{2.18}$$

where $\mathbf{A}_{\mathbf{n}\phi}$ is the node incidence matrix ($a_{\mathbf{ij}} \in \mathbf{A}_{\mathbf{n}\phi}$,$a_{\mathbf{ij}} = 1$ if current of branch j is leaving node i, $a_{\mathbf{ij}} = -1$ if current of branch j is entering node i, $a_{\mathbf{ij}} = 0$ if branch j is not connected to node i) for the connection points with N2.

The Thevenin impedance matrix is found from the solution of equation (2.15) by first replacing the right-hand side with the currents $\mathbf{i}_{\phi}$ entering the network N2:

$$\mathbf{v}_{\mathbf{n}\phi} = \mathbf{Z}_{\phi}\, \mathbf{i}_{\phi} \tag{2.19}$$

Since the nonlinear branch voltages are found from

$$\mathbf{v}_{\phi} = \mathbf{A}_{\mathbf{n}\phi}^{T}\, \mathbf{v}_{\mathbf{n}}^{final}, \tag{2.20}$$

its combination with equations (2.17) and (2.19) results in

$$\mathbf{v}_{\phi} = \mathbf{v}_{\mathbf{th}} + \mathbf{A}_{\mathbf{n}\phi}^{T}\, \mathbf{Z}_{\phi}\, \mathbf{i}_{\phi} = \mathbf{v}_{\mathbf{th}} + \mathbf{Z}_{\mathbf{th}}\, \mathbf{i}_{\phi}, \tag{2.21}$$

where

$$\mathbf{Z}_{\mathbf{th}} = \mathbf{A}_{\mathbf{n}\phi}^{T}\, \mathbf{Z}_{\phi}. \tag{2.22}$$

It is not necessary to recalculate $\mathbf{Z}_{\mathbf{th}}$ at each time-point if the network N1 topology does not change.

Generally speaking, the voltages and currents in N2 can be related to each other through a function $\mathbf{\Phi}$:

$$\mathbf{\Phi}\left(\mathbf{v}_{\phi}, \mathbf{i}_{\phi}\right) = \mathbf{0} \tag{2.23}$$

This function can be linear or nonlinear. If it is nonlinear then the combination of equations (2.21) and (2.23) is solved iteratively using the Newton method. Once $\mathbf{i}_{\phi}$ is found, equation (2.19) is used to calculate $\mathbf{v}_{\mathbf{n}\phi}$ and to update equation (2.17).

In practical implementations, the matrix $\mathbf{A}_{n\phi}$ is not used explicitly and the computation of $\mathbf{Z}_{\phi}$ requires as many forward–backward substitutions as the number of independent currents interfacing N1 with N2.

If N2 does not contain nonlinearities, then the compensation method is a non-iterative method.

The compensation method can be readily used for decoupling networks for parallel solutions. One approach is to use several linear networks represented through Thevenin equivalents (as in equation (2.21)) and connected to the main network. The Thevenin equivalents can be converted to Norton equivalents and included in the nodal system of equations of the main network. All such networks can be solved in parallel and also compensated in parallel at the completion of the solution of the main network.

Although the compensation method is an efficient method since it iterates with a reduced network N1, it has some important limitations, mainly because of the Thevenin impedance matrix $\mathbf{Z}_{\mathbf{th}}$. This matrix can have dependent rows (rank deficiency) when the devices located in N2 form a voltage loop. Since the $\mathbf{Z}_{\mathbf{th}}$ calculation is based on current injections, if nonlinear devices are connected in series, the columns of $\mathbf{Z}_{\mathbf{th}}$ may result in infinite numbers. The updating of $\mathbf{Z}_{\mathbf{th}}$ can become extremely inefficient if the network

N1 has repetitive topological changes due to switching devices, which is another important handicap in the compensation method.

2.5.1.3.2 Linearization with Full Matrix Updating Method

This linearization with full matrix updating (LFMA) method is more generic and does not have any of the limitations of the compensation method. It also results in better convergence properties. At each time-point, the linearized model equations (such as (2.16)) are updated through an iterative process until convergence. The updating of each device equation requires the main system of equations to be updated. In this approach, the matrix $\mathbf{A_N}$ is actually the Jacobian matrix. Despite the fact that the iterations are performed with the full system matrix, this approach is more general and can be programmed much more efficiently than the compensation method.

In the compensation method presented in the previous section, the network N1 is solved separately from network N2 before compensation and unlike the LFMA method, this condition disables voltage solution movement on the linearized equations and weakens convergence. The LFMA method is used in [13].

2.5.2 State-Space Analysis

State-space equations are given by

$$\dot{\mathbf{x}} = \mathbf{A}\,\mathbf{x} + \mathbf{B}\,\mathbf{u} \tag{2.24}$$

$$\mathbf{y} = \mathbf{C}\,\mathbf{x} + \mathbf{D}\,\mathbf{u}, \tag{2.25}$$

where $\mathbf{x}$ is the vector of state variables, $\mathbf{u}$ is the vector of inputs and $\mathbf{y}$ is the vector of outputs. The matrices $\mathbf{A}$, $\mathbf{B}$, $\mathbf{C}$ and $\mathbf{D}$ are called the state matrices. These matrices can be calculated for given ideal switch positions and piecewise linear device segments. Each topological change requires the state matrices to be updated. It is also possible to use the more generic version

$$\mathbf{y} = \mathbf{C}\,\mathbf{x} + \mathbf{D}\,\mathbf{u} + \mathbf{D}_1\,\dot{\mathbf{u}} \tag{2.26}$$

for output equations.

As for the case of nodal analysis, the state-space equations (2.24) and (2.25) can be solved in both steady-state and time-domain. Some EMT-type tools are based on the network representation of (2.24)–(2.25) [23].

2.5.2.1 Steady-State Solution

In steady-state conditions the differential of $\mathbf{x}$ is transformed into $s \cdot \tilde{\mathbf{X}}$ with the Laplace operator $s = j\omega$ (ω is the steady-state frequency in rad/s and j is the complex operator),

$$\tilde{\mathbf{X}} = (s\,\mathbf{I} - \mathbf{A})^{-1}\left(\mathbf{B}\,\tilde{\mathbf{U}}\right), \tag{2.27}$$

where tilde-uppercase vectors are used to denote phasors and $\mathbf{I}$ is the identity matrix. Equation (2.26) can be written in steady-state as

$$\tilde{\mathbf{Y}} = \left[\mathbf{C}\ (s\,\mathbf{I} - \mathbf{A})^{-1}\ \mathbf{B} + \mathbf{D}\ + s\,\mathbf{D}_1\right]\ \tilde{\mathbf{U}}. \tag{2.28}$$

2.5.2.2 Time-Domain Solution

For the time-domain solution the state-space equations can also be discretized with a numerical integration technique. It can be shown that equation (2.24) results in

$$\mathbf{x}_t = \left(\mathbf{I} - \frac{\Delta t}{2}\mathbf{A}\right)^{-1}\left(\mathbf{I} + \frac{\Delta t}{2}\mathbf{A}\right)\mathbf{x}_{t-\Delta t} + \left(\mathbf{I} - \frac{\Delta t}{2}\mathbf{A}\right)^{-1}\frac{\Delta t}{2}\mathbf{B}\left(\mathbf{u}_t + \mathbf{u}_{t-\Delta t}\right), \tag{2.29}$$

when discretized through the trapezoidal integration method of equation (2.11). The above equation can be written as

$$\mathbf{x}_t = \hat{\mathbf{A}}\,\mathbf{x}_{t-\Delta t} + \hat{\mathbf{B}}\,\mathbf{u}_{t-\Delta t} + \hat{\mathbf{B}}\,\mathbf{u}_t, \tag{2.30}$$

where hatted matrices result from the discretization process.

It is possible to include switches and nonlinear devices in (2.30) by rewriting it for the kth combination of switch statuses and piecewise linear device segments,

$$\dot{\mathbf{x}} = \mathbf{A}_k\,\mathbf{x} + \mathbf{B}_k\,\mathbf{u}, \tag{2.31}$$

with (2.25) becoming

$$\mathbf{y} = \mathbf{C}_k\,\mathbf{x} + \mathbf{D}_k\,\mathbf{u}. \tag{2.32}$$

Unlike with nodal analysis, the automatic formulation of state-space equations is significantly more time-consuming and requires the computation of the network topological proper-tree. That is why it is limited to the simulation of smaller systems. Reformulating matrices for the above kth combination creates further complications and may become extremely inefficient. That is why in many state-space solvers, the nonlinearities are extracted and modelled with delay-based current sources. In some cases – and especially for power electronics applications – the matrices for all switch combinations k can be precomputed and retrieved from memory to avoid major computational bottlenecks.

2.5.3 Hybrid Analysis

Hybrid analysis [24, 25] is a generic method for formulating network equations. It can be used to derive other formulations and, more importantly, to relate and combine different formulation methods for eliminating numerical limitations. The equations characterizing an N-port through the hybrid matrix $\mathbf{H}$ are

$$\begin{bmatrix} \hat{\mathbf{I}}_\mathbf{v} \\ \hat{\mathbf{V}}_\mathbf{i} \end{bmatrix} = \begin{bmatrix} \mathbf{H}_{\mathbf{vv}} & \mathbf{H}_{\mathbf{vi}} \\ \mathbf{H}_{\mathbf{iv}} & \mathbf{H}_{\mathbf{ii}} \end{bmatrix} \begin{bmatrix} \hat{\mathbf{V}}_\mathbf{v} \\ \hat{\mathbf{I}}_\mathbf{i} \end{bmatrix} + \begin{bmatrix} \mathbf{H}_{\mathbf{va}} & \mathbf{H}_{\mathbf{vb}} \\ \mathbf{H}_{\mathbf{ia}} & \mathbf{H}_{\mathbf{ib}} \end{bmatrix} \begin{bmatrix} \hat{\mathbf{V}}_\mathbf{a} \\ \hat{\mathbf{I}}_\mathbf{b} \end{bmatrix}, \tag{2.33}$$

where the vector $\hat{\mathbf{V}}$ is for extracted port voltages, and the vector $\hat{\mathbf{I}}$ stands for extracted port currents. The subscripts a, b, v and i are used to denote independent voltage source ports, independent current source ports, voltage ports and current ports respectively. The extracted ports can be of either type, linear or nonlinear. The matrix $\mathbf{H}$ is used to relate port variables through network connectivity. The ports are generic components, either capacitors, inductors or nonlinear devices. The term nonlinear includes linear functions or particular cases, such as short-circuits and open-circuits. It can also contain entire circuits.

If it is considered that all extracted ports are nonlinear, then it is possible to relate them through a nonlinear function,

$$\hat{\mathbf{\Phi}}\left(\hat{\mathbf{I}}_{\phi}, \hat{\mathbf{V}}_{\phi}\right) = \mathbf{0}, \tag{2.34}$$

with $\mathbf{I}_{\phi} = \begin{bmatrix} \hat{\mathbf{I}}_{\mathbf{v}} & \hat{\mathbf{I}}_{\mathbf{i}} \end{bmatrix}^T$ and $\mathbf{V}_{\phi} = \begin{bmatrix} \hat{\mathbf{V}}_{\mathbf{v}} & \hat{\mathbf{V}}_{\mathbf{i}} \end{bmatrix}^T$ when ports are identified. Port identity is related to topological proper-tree. If all nonlinear branches are modelled as current ports, then according to equation (2.33)

$$\hat{\mathbf{V}}_{\mathbf{i}} = \mathbf{H}_{\mathbf{ii}}\hat{\mathbf{I}}_{\mathbf{i}} + \begin{bmatrix} \mathbf{H}_{\mathbf{ia}} & \mathbf{H}_{\mathbf{ib}} \end{bmatrix} \begin{bmatrix} \hat{\mathbf{V}}_{\mathbf{a}} \\ \hat{\mathbf{I}}_{\mathbf{b}} \end{bmatrix}. \tag{2.35}$$

This equation is identical to (2.21) of the compensation method with $\mathbf{Z}_{\mathbf{th}} = \mathbf{H}_{\mathbf{ii}}$ and $\mathbf{V}_{\mathbf{th}} = \begin{bmatrix} \mathbf{H}_{\mathbf{ia}} & \mathbf{H}_{\mathbf{ib}} \end{bmatrix} \begin{bmatrix} \hat{\mathbf{V}}_{\mathbf{a}} & \hat{\mathbf{I}}_{\mathbf{b}} \end{bmatrix}^T$. It means that the compensation method can only use current ports for representing nonlinear devices, it may not be conformal to network's topological proper-tree and $\mathbf{H}_{\mathbf{ii}}$ may become ill-conditioned. It also means that hybrid analysis is more generic than the compensation method and can avoid ill-conditioning problems by remaining conformal to the topological proper-tree through the usage of a combination of nonlinear voltage and current ports.

2.5.3.1 Automatic Formulation from MANA

Hybrid analysis equations can be automatically formulated from MANA equations. If equation (2.5) is augmented to extract and include nonlinear port currents $\mathbf{I}_{\phi}$ and nonlinear port voltages $\mathbf{V}_{\phi}$, then (2.5) is modified to

$$\begin{bmatrix} \mathbf{Y}_{\mathbf{n}} & \mathbf{A}_{\mathbf{c}} & \mathbf{A}_{\mathbf{n}\phi} \\ \mathbf{A}_{\mathbf{r}} & \mathbf{A}_{\mathbf{d}} & \mathbf{0} \\ \mathbf{A}_{\mathbf{n}\phi}^T & \mathbf{0} & \mathbf{0} \end{bmatrix} \begin{bmatrix} \mathbf{x}_{\mathbf{N}} \\ \mathbf{I}_{\phi} \end{bmatrix} = \begin{bmatrix} \mathbf{b}_{\mathbf{N}} \\ \mathbf{V}_{\phi} \end{bmatrix}, \tag{2.36}$$

and $\mathbf{A}_{\mathbf{n}\phi}$ is the adjacency matrix of ports. Gaussian elimination is applied at this stage in (2.36) to extract the network relations between $\mathbf{I}_{\phi}$, $\mathbf{V}_{\phi}$ and independent variables. The extracted equations are written symbolically as

$$\mathbf{P}\,\mathbf{I}_{\phi} = \mathbf{M}\,\mathbf{V}_{\phi} + \mathbf{S}\,\mathbf{b}_{\mathbf{N}}. \tag{2.37}$$

The above equation (2.37) can be written as (2.33) by simply identifying the ports and regrouping the voltage and current variables accordingly. Port identity (voltage or current) is related to the conditioning of the matrices **P** and **M**. It may not be possible to assume that all ports are voltage or current ports since **P** or **M** may have an infinite condition number. It is possible to derive port identity from the topological tree of the network, but that is normally a time-consuming process. A more efficient approach [26] is to apply diagonalization or reduced row echelon form computation. Since port identity is not unique, a decision must be taken beforehand on the desired number of voltage or current ports. If, for example, the desired number of voltage ports is minimal, then the solution process starts by the reduction of **M**. By letting the ports classified in the first columns of **M** be more susceptible to becoming voltage ports, the reduction of **M** is applied from right to left. At the end of the diagonalization process, equation (2.37) takes the following shape:

$$\mathbf{P}'\,\mathbf{I}_{\phi} = \mathbf{M}'\,\mathbf{V}_{\phi} + \mathbf{S}'\,\mathbf{b}_{\mathbf{N}}, \tag{2.38}$$

where $\mathbf{P}' = \begin{bmatrix} \mathbf{P}'_{\mathbf{v}} & \mathbf{P}'_{\mathbf{i}} \end{bmatrix}$ and $\mathbf{M}' = \begin{bmatrix} \mathbf{M}'_{\mathbf{v}} & \mathbf{M}'_{\mathbf{i}} \end{bmatrix}$ with

$$\begin{aligned} \mathbf{M}'_{\mathbf{v}_{ij}} &= 0 \quad i = 1, \ldots, m_1, \quad \forall j \\ \mathbf{M}'_{\mathbf{i}_{ij}} &= 0 \quad i \neq m_1 + j, \quad \forall j \\ \mathbf{M}'_{\mathbf{i}_{ij}} &= 1 \quad i = m_1 + j, \quad j = 1, \ldots, m_2. \end{aligned} \tag{2.39}$$

Matrices $\mathbf{M}'_{\mathbf{v}}$ and $\mathbf{M}'_{\mathbf{i}}$ are $m \times m_1$ and $m \times m_2$, respectively and $m = m_1 + m_2$. The m_1 ports with null pivots in $\mathbf{M}'_{\mathbf{v}}$ are voltage ports. Since the diagonalization of $\mathbf{M}$ is performed from right to left, it is clear that ports classified in the first columns of $\mathbf{M}$ have a greater probability of remaining in $\mathbf{M}'_{\mathbf{v}}$ during the diagonalization process and becoming voltage ports. To finalize the solution of (2.38) it is necessary to first exchange $\mathbf{P}'_{\mathbf{v}}$ with $\mathbf{M}'_{\mathbf{v}}$ to give

$$\begin{bmatrix} -\mathbf{M}'_{\mathbf{v}} & \mathbf{P}'_{\mathbf{i}} \end{bmatrix} \begin{bmatrix} \hat{\mathbf{V}}_{\mathbf{v}} \\ \hat{\mathbf{I}}_{\mathbf{i}} \end{bmatrix} = \begin{bmatrix} -\mathbf{P}'_{\mathbf{v}} & \mathbf{M}'_{\mathbf{i}} \end{bmatrix} \begin{bmatrix} \hat{\mathbf{I}}_{\mathbf{v}} \\ \hat{\mathbf{V}}_{\mathbf{i}} \end{bmatrix} + \mathbf{S}' \begin{bmatrix} \hat{\mathbf{V}}_{\mathbf{a}} \\ \hat{\mathbf{I}}_{\mathbf{b}} \end{bmatrix}, \tag{2.40}$$

and pursue the reduction to identity matrix of $\begin{bmatrix} -\mathbf{P}'_{\mathbf{v}} & \mathbf{M}'_{\mathbf{i}} \end{bmatrix}$ until the hybrid port variables on the left-hand side of (2.33) become isolated:

$$\begin{bmatrix} \hat{\mathbf{I}}_{\mathbf{v}} \\ \hat{\mathbf{V}}_{\mathbf{i}} \end{bmatrix} = \begin{bmatrix} \mathbf{M}''_{\mathbf{v}} & \mathbf{P}''_{\mathbf{i}} \end{bmatrix} \begin{bmatrix} \hat{\mathbf{V}}_{\mathbf{v}} \\ \hat{\mathbf{I}}_{\mathbf{i}} \end{bmatrix} + \mathbf{S}'' \begin{bmatrix} \hat{\mathbf{V}}_{\mathbf{a}} \\ \hat{\mathbf{I}}_{\mathbf{b}} \end{bmatrix} \tag{2.41}$$

The same idea is applicable to the diagonalization of $\mathbf{P}$, for maximizing the number of voltage ports. The classification procedure discussed above can be related to the type of device. If, for example, the objective is to generate state-space equations (discussed below), then all capacitor branches must be classified first in $\mathbf{V}_{\phi}$ to preferably (topological proper-tree) become voltage ports, and all inductor branches must be classified last to result in being current ports. In reality, there are no restrictions, and any valid combination will enable the derivation of (2.41), but port identity may be forced according to the application.

2.5.3.2 Generation of State-Space Equations

If nonlinear and linear components are separated in (2.33), then it can be rewritten as

$$\begin{bmatrix} \mathbf{I}_{\mathbf{v}_\mathbf{x}} \\ \mathbf{V}_{\mathbf{i}_\mathbf{x}} \\ \mathbf{I}_{\mathbf{v}_\mathbf{n}} \\ \mathbf{V}_{\mathbf{i}_\mathbf{n}} \end{bmatrix} = \begin{bmatrix} \mathbf{H}_{\mathbf{v}_\mathbf{x}\mathbf{v}_\mathbf{x}} & \mathbf{H}_{\mathbf{v}_\mathbf{x}\mathbf{i}_\mathbf{x}} & \mathbf{H}_{\mathbf{v}_\mathbf{x}\mathbf{v}_\mathbf{n}} & \mathbf{H}_{\mathbf{v}_\mathbf{x}\mathbf{i}_\mathbf{n}} \\ \mathbf{H}_{\mathbf{i}_\mathbf{x}\mathbf{v}_\mathbf{x}} & \mathbf{H}_{\mathbf{i}_\mathbf{x}\mathbf{i}_\mathbf{x}} & \mathbf{H}_{\mathbf{i}_\mathbf{x}\mathbf{v}_\mathbf{n}} & \mathbf{H}_{\mathbf{i}_\mathbf{x}\mathbf{i}_\mathbf{n}} \\ \mathbf{H}_{\mathbf{v}_\mathbf{n}\mathbf{v}_\mathbf{x}} & \mathbf{H}_{\mathbf{v}_\mathbf{n}\mathbf{i}_\mathbf{x}} & \mathbf{H}_{\mathbf{v}_\mathbf{n}\mathbf{v}_\mathbf{n}} & \mathbf{H}_{\mathbf{v}_\mathbf{n}\mathbf{i}_\mathbf{n}} \\ \mathbf{H}_{\mathbf{i}_\mathbf{n}\mathbf{v}_\mathbf{x}} & \mathbf{H}_{\mathbf{i}_\mathbf{n}\mathbf{i}_\mathbf{x}} & \mathbf{H}_{\mathbf{i}_\mathbf{n}\mathbf{v}_\mathbf{n}} & \mathbf{H}_{\mathbf{i}_\mathbf{n}\mathbf{i}_\mathbf{n}} \end{bmatrix} \begin{bmatrix} \mathbf{V}_{\mathbf{v}_\mathbf{x}} \\ \mathbf{I}_{\mathbf{i}_\mathbf{x}} \\ \mathbf{V}_{\mathbf{v}_\mathbf{n}} \\ \mathbf{I}_{\mathbf{i}_\mathbf{n}} \end{bmatrix} + \begin{bmatrix} \mathbf{H}_{\mathbf{v}_\mathbf{x}\mathbf{a}} & \mathbf{H}_{\mathbf{v}_\mathbf{x}\mathbf{b}} \\ \mathbf{H}_{\mathbf{i}_\mathbf{x}\mathbf{a}} & \mathbf{H}_{\mathbf{i}_\mathbf{x}\mathbf{b}} \\ \mathbf{H}_{\mathbf{v}_\mathbf{n}\mathbf{a}} & \mathbf{H}_{\mathbf{v}_\mathbf{n}\mathbf{b}} \\ \mathbf{H}_{\mathbf{i}_\mathbf{n}\mathbf{a}} & \mathbf{H}_{\mathbf{i}_\mathbf{n}\mathbf{b}} \end{bmatrix} \begin{bmatrix} \mathbf{V}_{\mathbf{a}} \\ \mathbf{I}_{\mathbf{b}} \end{bmatrix}, \tag{2.42}$$

where the hatted notation is dropped to simplify the presentation. The above hybrid analysis formulation allows us to separate nonlinear components from linear components. The subscripts are defined as follows: n stands for generic nonlinear or nodal in the particular case, x stands for state variables, v is for voltage ports, i is for current ports, a indicates independent voltage sources and b indicates independent current sources. The vector $\mathbf{I}_{\mathbf{v}_\mathbf{x}}$, for example, holds the currents of all voltage ports that are extracted from the network as state variables, whereas the vector $\mathbf{I}_{\mathbf{v}_\mathbf{n}}$ holds the currents of all voltage ports identified as generic nonlinear.

Although equation (2.42) is generic, it is assumed here, for simplification, that the solved network has a topological proper-tree. Equation (2.42) can be separated into two parts. The first part is for state variable equations:

$$\begin{bmatrix} \mathbf{I}_{\mathbf{v}_x} \\ \mathbf{V}_{\mathbf{i}_x} \end{bmatrix} = \begin{bmatrix} \mathbf{H}_{\mathbf{v}_x\mathbf{v}_x} & \mathbf{H}_{\mathbf{v}_x\mathbf{i}_x} \\ \mathbf{H}_{\mathbf{i}_x\mathbf{v}_x} & \mathbf{H}_{\mathbf{i}_x\mathbf{i}_x} \end{bmatrix} \begin{bmatrix} \mathbf{V}_{\mathbf{v}_x} \\ \mathbf{I}_{\mathbf{i}_x} \end{bmatrix} + \begin{bmatrix} \mathbf{H}_{\mathbf{v}_x\mathbf{v}_n} & \mathbf{H}_{\mathbf{v}_x\mathbf{i}_n} \\ \mathbf{H}_{\mathbf{i}_x\mathbf{v}_n} & \mathbf{H}_{\mathbf{i}_x\mathbf{i}_n} \end{bmatrix} \begin{bmatrix} \mathbf{V}_{\mathbf{v}_n} \\ \mathbf{I}_{\mathbf{i}_n} \end{bmatrix} + \begin{bmatrix} \mathbf{H}_{\mathbf{v}_x\mathbf{a}} & \mathbf{H}_{\mathbf{v}_x\mathbf{b}} \\ \mathbf{H}_{\mathbf{i}_x\mathbf{a}} & \mathbf{H}_{\mathbf{i}_x\mathbf{b}} \end{bmatrix} \begin{bmatrix} \mathbf{V}_{\mathbf{a}} \\ \mathbf{I}_{\mathbf{b}} \end{bmatrix} \tag{2.43}$$

If the inductance and capacitance matrices are included, equation (2.43) results in the classic state variable equations:

$$\begin{bmatrix} \dot{\mathbf{V}}_{\mathbf{v}_x} \\ \dot{\mathbf{I}}_{\mathbf{i}_x} \end{bmatrix} = \begin{bmatrix} \mathbf{A}_{\mathbf{v}_x\mathbf{v}_x} & \mathbf{A}_{\mathbf{v}_x\mathbf{i}_x} \\ \mathbf{A}_{\mathbf{i}_x\mathbf{v}_x} & \mathbf{A}_{\mathbf{i}_x\mathbf{i}_x} \end{bmatrix} \begin{bmatrix} \mathbf{V}_{\mathbf{v}_x} \\ \mathbf{I}_{\mathbf{i}_x} \end{bmatrix} + \begin{bmatrix} \mathbf{B}_{\mathbf{v}_x\mathbf{v}_n} & \mathbf{B}_{\mathbf{v}_x\mathbf{i}_n} \\ \mathbf{B}_{\mathbf{i}_x\mathbf{v}_n} & \mathbf{B}_{\mathbf{i}_x\mathbf{i}_n} \end{bmatrix} \begin{bmatrix} \mathbf{V}_{\mathbf{v}_n} \\ \mathbf{I}_{\mathbf{i}_n} \end{bmatrix} + \begin{bmatrix} \mathbf{B}_{\mathbf{v}_x\mathbf{a}} & \mathbf{B}_{\mathbf{v}_x\mathbf{b}} \\ \mathbf{B}_{\mathbf{i}_x\mathbf{a}} & \mathbf{B}_{\mathbf{i}_x\mathbf{b}} \end{bmatrix} \begin{bmatrix} \mathbf{V}_{\mathbf{a}} \\ \mathbf{I}_{\mathbf{b}} \end{bmatrix} \tag{2.44}$$

The second part holds the nonlinear equations:

$$\begin{bmatrix} \mathbf{I}_{\mathbf{v}_n} \\ \mathbf{V}_{\mathbf{i}_n} \end{bmatrix} = \begin{bmatrix} \mathbf{H}_{\mathbf{v}_n\mathbf{v}_x} & \mathbf{H}_{\mathbf{v}_n\mathbf{i}_x} \\ \mathbf{H}_{\mathbf{i}_n\mathbf{v}_x} & \mathbf{H}_{\mathbf{i}_n\mathbf{i}_x} \end{bmatrix} \begin{bmatrix} \mathbf{V}_{\mathbf{v}_x} \\ \mathbf{I}_{\mathbf{i}_x} \end{bmatrix} + \begin{bmatrix} \mathbf{H}_{\mathbf{v}_n\mathbf{v}_n} & \mathbf{H}_{\mathbf{v}_n\mathbf{i}_n} \\ \mathbf{H}_{\mathbf{i}_n\mathbf{v}_n} & \mathbf{H}_{\mathbf{i}_n\mathbf{i}_n} \end{bmatrix} \begin{bmatrix} \mathbf{V}_{\mathbf{v}_n} \\ \mathbf{I}_{\mathbf{i}_n} \end{bmatrix} + \begin{bmatrix} \mathbf{H}_{\mathbf{v}_n\mathbf{a}} & \mathbf{H}_{\mathbf{v}_n\mathbf{b}} \\ \mathbf{H}_{\mathbf{i}_n\mathbf{a}} & \mathbf{H}_{\mathbf{i}_n\mathbf{b}} \end{bmatrix} \begin{bmatrix} \mathbf{V}_{\mathbf{a}} \\ \mathbf{I}_{\mathbf{b}} \end{bmatrix} \tag{2.45}$$

Note here that hybrid analysis allows us to generate state-space equations (2.24). Equation (2.44) can also be derived when capacitive loops or inductive nodes (only inductors connected to a node) exist in a network.

At this stage (2.44) is discretized using trapezoidal integration to give

$$\begin{bmatrix} \mathbf{V}_{\mathbf{v}_x} \\ \mathbf{I}_{\mathbf{i}_x} \end{bmatrix}_{t+\Delta t} = \hat{\mathbf{A}} \begin{bmatrix} \mathbf{V}_{\mathbf{v}_x} \\ \mathbf{I}_{\mathbf{i}_x} \end{bmatrix}_t + \hat{\mathbf{B}}_{\mathbf{s}} \begin{bmatrix} \mathbf{V}_{\mathbf{a}} \\ \mathbf{I}_{\mathbf{b}} \end{bmatrix}_t + \hat{\mathbf{B}}_{\mathbf{n}} \begin{bmatrix} \mathbf{V}_{\mathbf{v}_n} \\ \mathbf{I}_{\mathbf{i}_n} \end{bmatrix}_t + \hat{\mathbf{B}}_{\mathbf{s}} \begin{bmatrix} \mathbf{V}_{\mathbf{a}} \\ \mathbf{I}_{\mathbf{b}} \end{bmatrix}_{t+\Delta t} + \hat{\mathbf{B}}_{\mathbf{n}} \begin{bmatrix} \mathbf{V}_{\mathbf{v}_n} \\ \mathbf{I}_{\mathbf{i}_n} \end{bmatrix}_{t+\Delta t}, \tag{2.46}$$

where Δt is the integration time-step and the hatted matrices result from the discretization process (as it did for (2.30)). Equation (2.45) for the nonlinear ports is combined with equation (2.46) to give

$$\begin{aligned} \begin{bmatrix} \mathbf{I}_{\mathbf{v}_n} \\ \mathbf{V}_{\mathbf{i}_n} \end{bmatrix}_{t+\Delta t} = \hat{\mathbf{H}}_1 \begin{bmatrix} \mathbf{V}_{\mathbf{v}_x} \\ \mathbf{I}_{\mathbf{i}_x} \end{bmatrix}_t + \hat{\mathbf{H}}_2 \begin{bmatrix} \mathbf{V}_{\mathbf{a}} \\ \mathbf{I}_{\mathbf{b}} \end{bmatrix}_t + \hat{\mathbf{H}}_3 \begin{bmatrix} \mathbf{V}_{\mathbf{v}_n} \\ \mathbf{I}_{\mathbf{i}_n} \end{bmatrix}_t + \begin{bmatrix} \hat{\mathbf{H}}_4 & \mathbf{H}_{\mathbf{nab}} \end{bmatrix} \begin{bmatrix} \mathbf{V}_{\mathbf{a}} \\ \mathbf{I}_{\mathbf{b}} \end{bmatrix}_{t+\Delta t} \\ + \begin{bmatrix} \hat{\mathbf{H}}_5 & \mathbf{H}_{\mathbf{nn}} \end{bmatrix} \begin{bmatrix} \mathbf{V}_{\mathbf{v}_n} \\ \mathbf{I}_{\mathbf{i}_n} \end{bmatrix}_{t+\Delta t}. \end{aligned} \tag{2.47}$$

At the solution time-point $t + \Delta t$, the history terms and independent source values are known and allow the rewriting of equation (2.47) as

$$\begin{bmatrix} \mathbf{I}_{\mathbf{v}_n} \\ \mathbf{V}_{\mathbf{i}_n} \end{bmatrix}_{t+\Delta t} = \begin{bmatrix} \mathbf{I}_{hist} \\ \mathbf{V}_{hist} \end{bmatrix} + \mathbf{Q}_{\mathbf{n}} \begin{bmatrix} \mathbf{V}_{\mathbf{v}_n} \\ \mathbf{I}_{\mathbf{i}_n} \end{bmatrix}_{t+\Delta t}, \tag{2.48}$$

where *hist* (history) terms are known variables and the matrix $\mathbf{Q}_{\mathbf{n}}$ is the equivalent system matrix. Equation (2.48) can be solved independently for the vector $\begin{bmatrix} \mathbf{V}_{\mathbf{v}_n} & \mathbf{I}_{\mathbf{i}_n} \end{bmatrix}^T$, and once this vector is determined, equation (2.46) can follow with its solution procedure for calculating all state variables at the time-point $t + \Delta t$. Equation (2.42) can also be applied to a network portion instead of the entire network.

2.5.4 State-Space Groups and MANA

2.5.4.1 State-Space Groups

This section demonstrates that it is possible to create a group of circuit elements combined with the complete network MANA equations using group equation (2.48). This method is named the state-space-nodal (SSN) [27, 28] method since it combines state-space groups with nodal (MANA) equations.

Equations (2.24) and (2.25) are refined as follows:

$$\mathbf{x}_{t+\Delta t} = \hat{\mathbf{A}}_k \, \mathbf{x}_t + \hat{\mathbf{B}}_k \, \mathbf{u}_t + \begin{bmatrix} \hat{\mathbf{B}}_{k_i} & \hat{\mathbf{B}}_{k_n} \end{bmatrix} \begin{bmatrix} \mathbf{u}_{i_{t+\Delta t}} \\ \mathbf{u}_{n_{t+\Delta t}} \end{bmatrix} \tag{2.49}$$

$$\begin{bmatrix} \mathbf{y}_{i_{t+\Delta t}} \\ \mathbf{y}_{n_{t+\Delta t}} \end{bmatrix} = \begin{bmatrix} \mathbf{C}_{k_i} \\ \mathbf{C}_{k_n} \end{bmatrix} \mathbf{x}_{t+\Delta t} + \begin{bmatrix} \mathbf{D}_{k_{ii}} & \mathbf{D}_{k_{in}} \\ \mathbf{D}_{k_{ni}} & \mathbf{D}_{k_{nn}} \end{bmatrix} \begin{bmatrix} \mathbf{u}_{i_{t+\Delta t}} \\ \mathbf{u}_{n_{t+\Delta t}} \end{bmatrix} \tag{2.50}$$

The subscript character *i* refers to internal sources (injections) and the subscript *n* refers to external nodal injections. The combination of the lower row of equation (2.50) with equation (2.49) gives

$$\begin{aligned} \mathbf{y}_{n_{t+\Delta t}} = \mathbf{C}_{k_n} \left(\hat{\mathbf{A}}_k \, \mathbf{x}_t + \hat{\mathbf{B}}_k \, \mathbf{u}_t + \hat{\mathbf{B}}_{k_i} \mathbf{u}_{i_{t+\Delta t}} \right) + \mathbf{D}_{k_{ni}} \mathbf{u}_{i_{t+\Delta t}} \\ + \left(\mathbf{C}_{k_n} \hat{\mathbf{B}}_{k_n} + \mathbf{D}_{k_{nn}} \right) \mathbf{u}_{n_{t+\Delta t}}. \end{aligned} \tag{2.51}$$

It is apparent that the above equation has an independent term (known variables before solving for $\mathbf{y}_{n_{t+\Delta t}}$) and can be written as

$$\mathbf{y}_{n_{t+\Delta t}} = \mathbf{y}_{k_{hist}} + \mathbf{W}_{k_n} \, \mathbf{u}_{n_{t+\Delta t}}, \tag{2.52}$$

where the subscript *hist* denotes known variables.

When $\mathbf{y}_n$ represents current injections (entering a group) and $\mathbf{u}_n$ is for node voltages, then $\mathbf{y}_{k_{hist}}$ represents history current sources ($\mathbf{i}_{k_{hist}}$) and $\mathbf{W}_{k_n}$ is an admittance matrix. This is called a V-type SSN group and it is a Norton equivalent.

When $\mathbf{y}_n$ represents voltages and $\mathbf{u}_n$ holds currents entering a group, then $\mathbf{y}_{k_{hist}}$ represents history voltage sources ($\mathbf{v}_{k_{hist}}$) and $\mathbf{W}_{k_n}$ is an impedance matrix. This is referred to as an I-type SSN group and it is a Thevenin equivalent.

In general, it is possible to have both types of groups (V-type and I-type) by rewriting equation (2.52) as

$$\begin{bmatrix} \mathbf{i}_n^{\mathrm{V}} \\ \mathbf{v}_n^{\mathrm{I}} \end{bmatrix}_{t+\Delta t} = \begin{bmatrix} \mathbf{i}_{k_{hist}} \\ \mathbf{v}_{k_{hist}} \end{bmatrix} + \mathbf{W}_{k_n} \begin{bmatrix} \mathbf{v}_n^{\mathrm{V}} \\ \mathbf{i}_n^{\mathrm{I}} \end{bmatrix}_{t+\Delta t}, \tag{2.53}$$

where the superscripts V and I denote V-type and I-type relations respectively. This equation is referred to as a mixed-type group equation. It is equivalent to equation (2.48) by noticing that V-type relations are voltage ports, I-type relations are current ports and $\mathbf{W}_{k_n} = \mathbf{Q_n}$. This fact confirms once again the generality of hybrid analysis and confirms the theoretical foundations of the SSN method.

2.5.4.2 Interfacing the Groups

Once equation (2.53) is defined for a given group, it can be inserted into the main network equations and simultaneously interfaced with other group equations. This is done using equation (2.15). The upper (V-type) rows of equation (2.53) can be inserted directly into equation (2.53) by mapping the group

nodes. The lower row (I-type) variables $\mathbf{v}^{\mathrm{I}}_{n_{t+\Delta t}}$ and $\mathbf{i}^{\mathrm{I}}_{n_{t+\Delta t}}$ can be regrouped on the right-hand side and listed in $\mathbf{x_N}$ with coefficients inserted in equation rows of $\mathbf{A_N}$. The history terms of (2.53) participate in $\mathbf{b_N}$ with a negative sign.

The matrix $\mathbf{A_N}$ can change between solution time-points if the $\mathbf{W}_{k_n}$ matrix of any group changes due to changes in switch positions or in segment positions for piecewise linear devices.

If the more general equation (2.26) is used instead of (2.50)

$$\mathbf{y} = \mathbf{C}_k\,\mathbf{x} + \mathbf{D}_k\,\mathbf{u} + \mathbf{D}_{1k}\,\dot{\mathbf{u}}, \tag{2.54}$$

then the I-type groups can be avoided. However, the capability of using I-type groups remains useful since in many state-space solvers the matrix $\mathbf{D}_{1k}$ is not readily available. Note that (2.54) can be rewritten at a solution time-point t in terms of current injections $\mathbf{i}_t$ and nodal voltages $\mathbf{v}_t$

$$\mathbf{i}_t = \mathbf{C}_k\,\mathbf{x}_t + \mathbf{D}_k\,\mathbf{v}_t + \mathbf{i}^c_t, \tag{2.55}$$

where trapezoidal integration for the capacitive current ($\mathbf{i}^c_t$) results in

$$\mathbf{i}^c_t = \frac{2}{\Delta t}\mathbf{D}_{1_k}\,v_t - \frac{2}{\Delta t}\mathbf{D}_{1_k}\,\mathbf{v}_{t-\Delta t} - \mathbf{i}^c_{t-\Delta t}. \tag{2.56}$$

The state equations are written with input voltage

$$\mathbf{x}_t = \hat{\mathbf{A}}_k\,\mathbf{x}_{t-\Delta t} + \hat{\mathbf{B}}_k\,\mathbf{v}_{t-\Delta t} + \hat{\mathbf{B}}_k\,\mathbf{v}_t. \tag{2.57}$$

Equations (2.56) and (2.57) can be replaced in (2.55) to create a nodal formulation that can be directly integrated into (2.15). The above example is a much simpler presentation of the theory of state-space groups in MANA.

Equation (2.15) does not make any assumptions of the combined group equations. Any number (including zero) of groups can use state-space equations and any number of groups can use MANA equations. A group may contain an arbitrary number of devices. Moreover, MANA equations can contain nonlinear devices solved through an iterative process and independently from state-space equations. The capability of evacuating the solution of nonlinear devices from state-space groups into MANA groups is another important contribution in the proposed method since the simultaneous solution of nonlinear equation in MANA is much more efficient than in state-space groups.

The method presented in this section offers several advantages [27, 28], the most important being the capability of achieving a simultaneous and parallel solution with independent state-space blocks. Such network tearing capability is advantageous when delay-based transmission line models are not available. Moreover, the number of stored switch combinations in the matrices of (2.31) can be dramatically reduced [27] by separating a given circuit into smaller parts.

2.5.4.3 Steady-State Solution

The steady-state solution is found for initializing the time-domain solution. In addition to the complex version of (2.4), the state-space groups are solved using the complex versions of (2.27) and (2.28):

$$\tilde{\mathbf{X}} = \left(s\mathbf{I} - \mathbf{A}_k\right)^{-1}\left(\mathbf{B}_{k_i}\,\tilde{\mathbf{U}}_i + \mathbf{B}_{k_n}\,\tilde{\mathbf{U}}_n\right) \tag{2.58}$$

$$\tilde{\mathbf{Y}}_i = \left(\mathbf{C}_{k_i}\,\mathbf{H}\,\mathbf{B}_{k_i} + \mathbf{D}_{k_{ii}}\right)\tilde{\mathbf{U}}_i + \left(\mathbf{C}_{k_i}\,\mathbf{H}\,\mathbf{B}_{k_n} + \mathbf{D}_{k_{in}}\right)\tilde{\mathbf{U}}_n \tag{2.59}$$

$$\tilde{\mathbf{Y}}_n = \left(\mathbf{C}_{k_n}\,\mathbf{H}\,\mathbf{B}_{k_i} + \mathbf{D}_{k_{ni}}\right)\tilde{\mathbf{U}}_i + \left(\mathbf{C}_{k_n}\,\mathbf{H}\,\mathbf{B}_{k_n} + \mathbf{D}_{k_{nn}}\right)\tilde{\mathbf{U}}_n, \tag{2.60}$$

where tilde-uppercase vectors are used to denote phasors, $\mathbf{I}$ is the identity matrix and $\mathbf{H} = \left(s\mathbf{I} - \mathbf{A}_k\right)^{-1}$. Equation (2.60) is first inserted into the complex version of (2.4) for finding the MANA solution. It is followed by the solution of equations (2.58) and (2.59). The solution of state variables at the time-point $t = 0$ is found by taking the real part of the corresponding phasors. This solution is used to initialize history terms for the following time-point solution with discretized equations (2.49) and (2.50).

2.5.5 *Integration Time-Step*

The integration time-step Δt can be fixed or variable. The fixed (set by the user) approach has several advantages in power systems. It avoids the time-consuming reformulation of system equations and programming issues related to the models. In the case of transmission line models, for example, it is necessary to maintain history buffers for interpolating for propagation delays. The time-step variability will affect the buffer sizes continuously, thus slowing down the computations. Fixing the size for the smallest time-step will create memory problems for large cases.

The automatic computation of time-steps can be based on the local truncation error [4, 17]. If it is assumed that $\hat{x}(t)$ is the exact solution to equation (2.10), then Taylor series expansion at $t = t_k$ gives

$$\hat{x}\left(t_{k+1}\right) = \hat{x}\left(t_k\right) + \frac{\hat{x}^{(1)}\left(t_k\right)}{1!}\left(t_{k+1} - t_k\right) + \frac{\hat{x}^{(2)}\left(t_k\right)}{2!}\left(t_{k+1} - t_k\right)^2 + \cdots + \frac{\hat{x}^{(p)}\left(t_k\right)}{p!}\left(t_{k+1} - t_k\right)^p + \theta, \tag{2.61}$$

where $\hat{x}^{(j)}\left(t_k\right)$ is the jth time derivative of $\hat{x}(t)$ at $t = t_k$, $\Delta t_k = t_{k+1} - t_k$ and θ is the truncated term. Trapezoidal integration can be derived from the above equation using $p = 2$:

$$x_{k+1} = x_k + \frac{\Delta t_k}{2}\left[\dot{x}_{k+1} + \dot{x}_k\right] - \frac{\Delta t_k^3}{12}\frac{d^3x(\xi)}{dt^3}, \tag{2.62}$$

where the third derivative term is the local truncation error of the trapezoidal method, with $t_k \le \xi \le t_{k+1}$. One approach for estimating the third-order derivative is to fit a third-order polynomial of the form

$$x(t) = a_0 + a_1(t_{k+1} - t) + a_2(t_{k+1} - t)^2 + a_3(t_{k+1} - t)^3 \tag{2.63}$$

for $t_{k-2} \le t \le t_{k+1}$ to the found solutions x_{k+1}, x_k, x_{k-1} and x_{k-2}. In a large system, the number of state variables can become very high. A possible approach is to use equation (2.63) for the entire set of unknowns in a nodal analysis type method. Once the third-order derivative is approximated and the local truncation error is found, it can be checked against preset bounds for selecting the time-step Δt_{k+1}.

The variable time-step approach provides an important advantage for riding through various system time-constants with the required precision. Another advantage is for the solution of nonlinear functions. Reducing the time-step may help convergence. It also provides more precise function fitting in the time-domain. Changing the time-step can, however, become significantly time-consuming as explained above. An alternative, applicable specifically to the stiffest problems, is to use a set of predefined time-steps. The breaker arc model, for example, is an extremely nonlinear function that requires the use of time-steps in the range of nanoseconds. Since the breaker arc acts only for a short duration of the entire simulation period, the simulation method could revert only temporarily to a reduced time-step. This will not affect overall efficiency since the time-steps will be user-defined and two or three system matrices can be precalculated.

Using a variable time-step does not solve the numerical oscillation problems (see references in [29]), but it can minimize them. It will also minimize errors related to interpolation issues (see [29] and its references), but may become extremely time-consuming for such problems. A complete solution for

numerical oscillations due to discontinuities and interpolation for events occurring within the fixed time-step must be able to correctly account for nonlinear functions and distributed parameter models. The efficient and precise treatment of discontinuities remains an ongoing research topic.

There are other numerical integration methods, such as multistep methods and the backward-differentiation formula [30]. Some of these methods can be more precise or provide other advantages over the trapezoidal method for a given integration time-step. The backward-differentiation formula, for example, has the advantage of providing an extremely simple equation for evaluating the local truncation error.

The polynomial Gear methods can be used in a variable-order setup to increase the integration time-step. However, they must be restarted at each breakpoint and require the maintenance of more history terms. The difficulty is with the added computational burden due to added number of coefficients, history terms and restarting procedures. The theoretical advantages become overshadowed by the computational overhead, especially since lowering the integration time-step in the trapezoidal method provides similar precision while still remaining more efficient in most cases.

A promising approach is the use of multiple time-steps in the same simulation [31,32]. Using different time-steps in different regions of the same network and according to the frequency of transients can be used to accelerate computations. The automatic scheduling of time-steps and decoupling methods in the absence of distributed parameter transmission line models, are ongoing research activities.

2.6 Control Systems

The simulation of control system dynamics is fundamental to the study of power system transients. The development of control system solution algorithms based on the block-diagram approach was initially triggered by the modelling of synchronous machine exciter systems. It was then extensively used in HVDC applications. Control elements can be transfer functions, limiters, gains, summers, integrators and many other mathematical functions. In many applications the block-diagram approach is also used to build and interface user-defined models with the built-in power system components.

A typical control diagram taken from the AVR_Gov block shown in Figure 2.1 is shown in Figure 2.6. Such diagrams are drawn in the GUI and solved directly. The GUI must allow the drawing of arbitrary control systems.

A complicated problem in oriented-graph systems is the capability of solving the complete system simultaneously without inserting artificial (one time-step) delays in feedback loops. A solution to this problem is available in some programs [33, 34]. The approach presented in [33] is similar to equation (2.15). All linear functions (blocks) are entered directly into (2.15). All nonlinear blocks are linearized at the operating point and then written into (2.15). Numerical perturbation can be applied to derive the

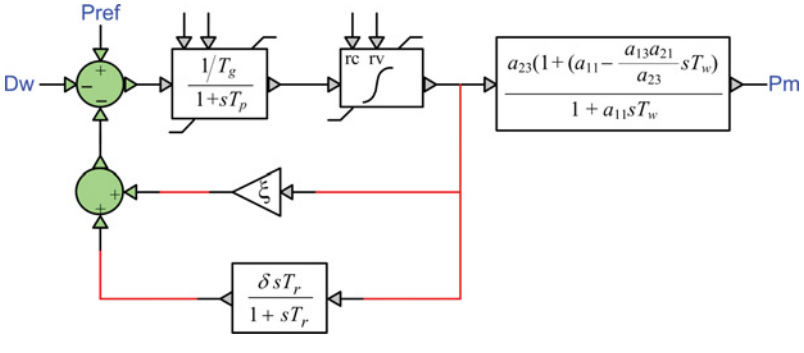

Figure 2.6 Example of control system diagram.

linearization of complex nonlinear and multivariable functions and black-box devices. As for electrical network equations, the control system matrix $\mathbf{A_N}$ is the Jacobian matrix, and the complete system is solved iteratively at each time-point with successive updates of $\mathbf{A_N}$ and $\mathbf{b_N}$ for each nonlinear device. As shown in [33], it is possible to avoid iterations at each time-point in the majority of cases, for improving computational performance by limiting the reformulations of $\mathbf{A_N}$ only to each new time-point (single iteration).

The automatic initialization of control system equations is an important research topic. Semi-automatic methods allow the propagation of the required output values backwards in the control system diagram for the establishment of initial conditions in all blocks.

In most applications the control system diagram equations are solved separately from the network equations. Although this is not a significant source of errors in most cases, it can become an important drawback for user-defined network models and in the simulation of power electronic systems. The combination of both systems into a unique system of iteratively solved equations is complex. A fixed-point approach where both systems are solved sequentially is more efficient and acceptable in many cases [33].

2.7 Multiphase Load-Flow Solution and Initialization

The importance of initialization in the simulation of electromagnetic transients in power systems can be illustrated through the simple example of Figure 2.7. The presented waveforms are the voltages at the receiving end of an arrester-protected transmission line. The solid line shows the waveform solution without any initial conditions and the second dashed line is with automatic initialization from steady-state solution. Even if frequency-dependent line models (increased damping over constant parameter models) are used, the transients without initialization require more than 150 ms for attaining the actual steady-state response. This will have dramatic computing time consequences on large systems. In most cases the study of transients is conducted from a given steady-state condition in the network.

The initialization problem becomes more complex in the presence of synchronous or asynchronous machines within multiple generator networks. Machine phasors can be made available from an external load-flow program, but since the actual network may be unbalanced or may use models specific to the simulation of transients, the best approach is the implementation of a load-flow method directly before the steady-state solution and within the same simulation tool [13].

As demonstrated in Figure 2.8 (test case of Figure 2.1, machines SM6 and SM3 in SubofBUS1), without automatic initialization, and even after 5 s of simulation, the shown machines do not reach

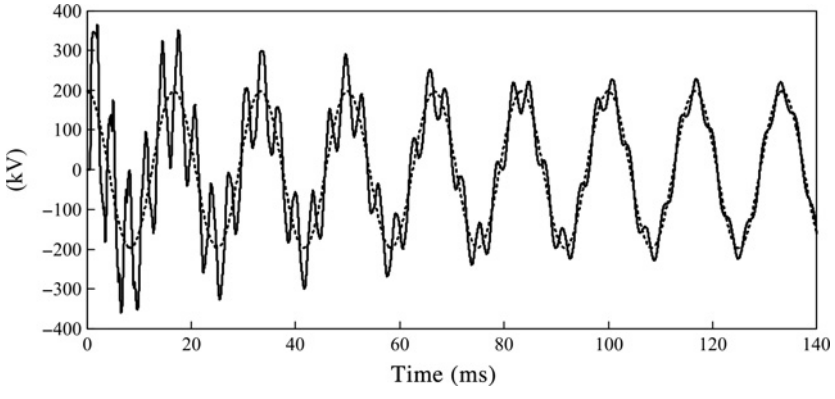

Figure 2.7 Transmission line voltage at the receiving end: with (dashed line) and without (solid line) initialization.

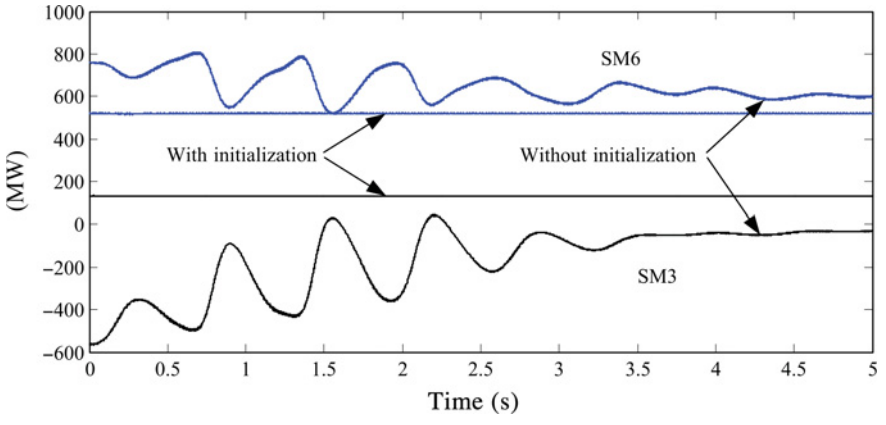

Figure 2.8 Two synchronous machine powers in MW, with (straight lines) and without initialization (oscillations).

steady state, whereas the automatic initialization starts from the load-flow solution, where the machines are given PV constraints. In some cases, if no proper initialization is applied, the simulation may reach abnormal operating modes for an otherwise obtainable load-flow solution.

The load-flow module in an EMT-type program is used to compute the operating conditions of the power system. It must employ a multiphase solution since the objective is to use the same network topology and data, and initialize the time-domain network. There are several multiphase load-flow methods in the literature, but most of them are not suitable for EMT-type solvers. In EMT-type solvers the network is not necessarily balanced, the applied models are usually more complex and there could be a variation of models that must be correctly initialized for smooth transition into time-domain. The methodology presented below is the one used in [13, 14] (see other details in [35]).

The load-flow solution is based on constraints. The sources (synchronous machines or other types of generation) are replaced by PQ, PV or slack bus constraints. The loads are replaced by PQ constraints. These are the main load-flow devices. All network components must provide a load-flow solution model. In some cases it is the same as the one used in the steady-state representation.

The system of equations (2.4) is used for representing the passive network equations, but it must be augmented with load-flow constraint equations. This is another major advantage of the augmented formulation approach. The modified-augmented load-flow equations are given by

$$\begin{bmatrix} \mathbf{A}_{\mathbf{N}}^{\mathbf{LF}} & \mathbf{A}_{\mathbf{I}} \\ \mathbf{L}_{\mathbf{LA}} & \mathbf{L}_{\mathbf{d}} \end{bmatrix} \begin{bmatrix} \Delta\mathbf{x} \\ \Delta\mathbf{x}_{\mathbf{LF}} \end{bmatrix} = -\mathbf{f}_{\mathbf{LF}}. \tag{2.64}$$

Equation (2.64) is real, since real and imaginary parts must be represented separately for load-flow constraints. $\mathbf{A}_{\mathbf{N}}^{\mathbf{LF}}$ is constructed from the original complex version of $\mathbf{A}_{\mathbf{N}}$ by separating real and imaginary parts of each element, $\mathbf{A}_{\mathbf{I}}$ is a connectivity matrix for accounting for load-flow devices and $\mathbf{L}_{\mathbf{LA}}$ and $\mathbf{L}_{\mathbf{d}}$ provide load-flow device constraint equations. The vector function $\mathbf{f}_{\mathbf{LF}}$ must be minimized (zero) for finding the load-flow solution. Recall that the solution of $\mathbf{f}_{\mathbf{LF}}(\mathbf{x}) = \mathbf{0}$ can be found using the Newton method

$$\mathbf{J}^{(j)}\Delta\mathbf{x}^{(j)} = -\mathbf{f}_{\mathbf{LF}}(\mathbf{x}^{(j)}), \tag{2.65}$$

where (j) is the iteration count, $\mathbf{J}$ is the Jacobian matrix and $\mathbf{\Delta x}$ is used for updating the vector $\mathbf{x}$

$$\mathbf{x}^{(j+1)} = \mathbf{x}^{(j)} + \mathbf{\Delta x}^{(j)}. \tag{2.66}$$

For the basic set of load-flow constraints, equation (2.64), can be expanded and rewritten as

$$\begin{bmatrix} \mathbf{Y_n} & \mathbf{A_c} & \mathbf{A_{IL}} & \mathbf{A_{IG}} & \mathbf{0} \\ \mathbf{A_r} & \mathbf{A_d} & \mathbf{0} & \mathbf{0} & \mathbf{0} \\ \mathbf{J_L} & \mathbf{0} & \mathbf{J_{LI}} & \mathbf{0} & \mathbf{0} \\ \mathbf{Y_G} & \mathbf{0} & \mathbf{0} & \mathbf{B_{GI}} & \mathbf{B_{GE}} \\ \mathbf{J_{GPQ}} & \mathbf{0} & \mathbf{0} & \mathbf{J_{GPQI}} & \mathbf{0} \\ \mathbf{J_{GPV}} & \mathbf{0} & \mathbf{0} & \mathbf{0} & \mathbf{0} \\ \mathbf{J_{GSL}} & \mathbf{0} & \mathbf{0} & \mathbf{0} & \mathbf{0} \end{bmatrix}^{(j)} \begin{bmatrix} \Delta\mathbf{V_n} \\ \Delta\mathbf{I_x} \\ \Delta\mathbf{I_L} \\ \Delta\mathbf{I_G} \\ \Delta\mathbf{E_G} \end{bmatrix} = - \begin{bmatrix} \mathbf{f_n} \\ \mathbf{f_x} \\ \mathbf{f_L} \\ \mathbf{f_{GI}} \\ \mathbf{f_{GPQ}} \\ \mathbf{f_{GPV}} \\ \mathbf{f_{GSL}} \end{bmatrix}^{(j)}, \tag{2.67}$$

where the submatrices $\mathbf{A_{IL}}$ and $\mathbf{A_{IG}}$ are adjacency matrices for interfacing the load ($\mathbf{I_L}$) and generator ($\mathbf{I_G}$) currents with the corresponding passive network nodes. The following submatrices are used to include load-flow constraints for any number of phases: $\mathbf{J_L}$ and $\mathbf{J_{LI}}$ for PQ-loads, $\mathbf{Y_G}$, $\mathbf{B_{GI}}$ and $\mathbf{B_{GE}}$ for generator current equations, $\mathbf{J_{GPQ}}$ and $\mathbf{J_{GPQI}}$ for PQ-type generators, $\mathbf{J_{GPV}}$ for PV-type generators and $\mathbf{J_{GSL}}$ for slack-type generators (buses). The unknown supplementary vectors are defined as follows: $\mathbf{I_L}$ is for PQ-load currents, $\mathbf{I_G}$ is for generator currents and $\mathbf{E_G}$ represents generator internal voltages.

Equation (2.67) is the expanded version of (2.65) and the left-hand-side matrix is the Jacobian matrix of the solved nonlinear function $\mathbf{f_{LF}}$.

The linear network coefficient submatrices are taken directly from the real version (2.5) and remain unchanged, except that now the right-hand side of (2.5) is eliminated due to the differentiation process for the derivation of the Jacobian matrix. There is no need to derive separate equations for linear network devices. For the ideal transformer case, for example, the constraint equation is taken directly from (2.9):

$$V_{k2} - V_{m2} - gV_{k1} + gV_{m1} = f_x \tag{2.68}$$

and results in

$$\Delta V_{k2} - \Delta V_{m2} - g\,\Delta V_{k1} + g\,\Delta V_{m1} = -f_x^{(j)}. \tag{2.69}$$

This means that the existing submatrices $\mathbf{A_r}$ and $\mathbf{A_c}$ are not affected and already constitute the Jacobian terms allowing us to account for all single-phase and three-phase transformer configurations. When the tap positions are not defined, it is also possible to represent the transformation ratio g in (2.69) as a variable and introduce additional Jacobian terms in (2.67). All submatrices used for the construction of (2.5) are directly reused in (2.67).

2.7.1 Load-Flow Constraints

The constraint equations of load-flow devices are presented in this section to demonstrate how such arbitrary equations are entered into (2.67).

In the case of a single-phase load, the PQ constraint can be expressed in terms of load voltage and current. If a load numbered as p in the list of load devices and connected between the nodes k and m, its voltage V_{L_p} and current I_{L_p} are given by

$$\begin{aligned} V_{L_p} &= V_k^R + jV_k^I - V_m^R - jV_m^I = V_{km}^R + jV_{km}^I \\ I_{L_p} &= I_{p_{km}}^R + jI_{p_{km}}^I, \end{aligned} \tag{2.70}$$

where the superscripts R and I stand for real and imaginary parts respectively, and the subscript km means from k to m. The constraint equations become

$$\begin{aligned} P_p - V_{km}^R I_{p_{km}}^R - V_{km}^I I_{p_{km}}^I &= f_{L_p}^R = 0 \\ Q_p - V_{km}^I I_{p_{km}}^R + V_{km}^R I_{p_{km}}^I &= f_{L_p}^I = 0, \end{aligned} \tag{2.71}$$

and the Jacobian terms can now be written as

$$\begin{bmatrix} -I_{p_{km}}^{R(j)} & -I_{p_{km}}^{I(j)} \\ I_{p_{km}}^{I(j)} & -I_{p_{km}}^{R(j)} \end{bmatrix} \begin{bmatrix} \Delta V_{km}^R \\ \Delta V_{km}^I \end{bmatrix} + \begin{bmatrix} -V_{km}^{R(j)} & -V_{km}^{I(j)} \\ -V_{km}^{I(j)} & V_{km}^{R(j)} \end{bmatrix} \begin{bmatrix} \Delta I_{p_{km}}^R \\ \Delta I_{p_{km}}^I \end{bmatrix} = \begin{bmatrix} -f_{L_p}^{R(j)} \\ -f_{L_p}^{I(j)} \end{bmatrix}. \tag{2.72}$$

The voltage and current coefficient matrices populate the matrices $\mathbf{J_L}$ and $\mathbf{J_{LI}}$ of equation (2.67), respectively. The right-hand side is entered into the vector $\mathbf{f_L}$ of (2.67). A three-phase load device is a combination of three single-phase loads. The loads can be connected in arbitrary configurations.

The current constraint of a three-phase generator numbered as p in the list of generators and connected between buses $\mathbf{k}$ and $\mathbf{m}$ takes the following form:

$$\mathbf{Y}_{\mathbf{G}_p}\left(\mathbf{V_k} - \mathbf{V_m} - \tilde{\mathbf{E}}_{\mathbf{G}_p}\right) - \mathbf{I}_{\mathbf{G}_p} = \mathbf{f}_{\mathbf{GI}p} = \mathbf{0} \tag{2.73}$$

This is a three-phase and complex system of equations. The generator currents in the vector $\mathbf{I}_{\mathbf{G}p}$ are entering bus $\mathbf{k}$, the matrix $\mathbf{Y}_{\mathbf{G}_p}$ is the internal admittance matrix and the vector $\tilde{\mathbf{E}}_{\mathbf{G}_p}$ holds the internal positive sequence voltages and can be written as $\mathbf{E}_{\mathbf{G}p} = \begin{bmatrix} 1 & a^2 & a \end{bmatrix}^T E_{G_p}$ with $a = 1\angle 120°$ and the scalar E_{G_p} is the voltage of phase A. Equation (2.73) is rewritten as

$$\mathbf{Y}_{\mathbf{G}_p}\Delta\mathbf{V_k} - \mathbf{Y}_{\mathbf{G}_p}\Delta\mathbf{V_m} - \mathbf{B}_{\mathbf{GE}_p}\Delta E_{G_p} - \Delta\mathbf{I}_{\mathbf{G}_p} = -\mathbf{f}_{\mathbf{GI}_p}^{(j)}. \tag{2.74}$$

In this case $\mathbf{Y}_{\mathbf{G}_p}$ populates $\mathbf{Y_G}$, $\mathbf{B}_{\mathbf{GE}_p}$ is entered into $\mathbf{B_{GE}}$ and the identity coefficient matrix of $\Delta\mathbf{I}_{\mathbf{G}_p}$ contributes to $\mathbf{B_{GI}}$. In addition, $\Delta E_{G_p} \in \Delta\mathbf{E_G}$, $\Delta\mathbf{I}_{\mathbf{G}_p} \in \Delta\mathbf{I_G}$ and $\mathbf{f}_{\mathbf{GI}_p} \in \mathbf{f_{GI}}$.

In addition to (2.73) each generator must provide its equations for controlled quantities. In the case of PQ control, the Jacobian terms are similar to (2.72), except that now the left-hand side voltage and current vectors are three-phase, which results in two 6×6 coefficient matrices contributing to $\mathbf{J_{GPQ}}$ and $\mathbf{J_{GPQI}}$. The right-hand side is now related to $\mathbf{f_{GPQ}}$.

For PV control, the Q row of PQ control is replaced by the voltage constraint equation. The control is on the voltage magnitude V_p (pth generator) of one phase and gives

$$V_p - \sqrt{\left(V_p^R\right)^2 + \left(V_p^I\right)^2} = f_{GPV_p} = 0. \tag{2.75}$$

The contribution to (2.67) is found from

$$-\left[\left(V_p^R\right)^2+\left(V_p^I\right)^2\right]^{-\frac{1}{2}}\left(V_p^{R\,(j)}\,\Delta V_p^R+V_p^{I\,(j)}\,V_p^I\right)=-f_{GPV_p}^{(k)} \tag{2.76}$$

and affects $\mathbf{J_{GPV}}$ and $\mathbf{f_{GPV}}$. It is not complicated to extend (2.75) to control the positive sequence voltage magnitude by calculating it from the Fortescue transformation for positive sequence.

For the slack bus case it is necessary to write two equations (real and imaginary parts) for controlling the positive sequence voltage magnitude and phase.

In the case of single-phase generators (or generic sources), it is sufficient to use the single-phase version of (2.73) and to include single-phase control equations.

2.7.2 Initialization of Load-Flow Equations

Initialization is performed by reverting (2.67) to its linearized version (2.5). All loads are replaced by equivalent impedances calculated at nominal voltages, and all generators are replaced by ideal sources behind their impedances. This approach yields sufficiently good initial conditions for the fast convergence of (2.67).

2.7.3 Initialization from Steady-State Solution

Upon convergence of (2.67), all steady-state phasors become available. The synchronous machine phasors are used to calculate internal state variables. The asynchronous machine requires the calculation of slip for a given mechanical power or torque.

The steady-state module starts with the load-flow solution and replaces all devices by lumped equivalents to proceed with a phasor solution. This is achieved with the complex version of (2.5). The resulting solution is the same as with the load-flow module, except that now the device models have access to internal phasors for proceeding with initialization. The steady-state solution phasors are used for initializing all state-variables at the time-point $t = 0$. The solution at $t = 0$ is only from the steady-state, and all history terms for all devices are initialized for the first solution time-point.

In some cases the network may contain harmonic sources or nonlinearities, in which cases it is necessary to perform a harmonic load-flow. It is feasible to program such a method [35], but it has a narrower application field. Finding the harmonic steady-state solution can have a significant impact on computing time under some particular conditions [36, 37].

When the solved network is linear or in linear operating conditions, then the initialization with harmonics through the linear steady-state constitutes a simple superposition of all harmonic solutions. In some special conditions, such as different rotor frequencies, initialization is still possible by solving the rotor networks independently.

If there is no calculated steady-state solution, there could be manual initial conditions, such as trapped charge, or all variables could be at 0-state. Manual initial conditions are also useful for reproducing complex conditions such as ferroresonance.

A complex subject in automatic initialization is the initialization of systems with power electronics switching devices. It is not possible to automatically predict commutation patterns in a given operating mode and initialize all state-variables for harmonic steady-state solution. A programmed initialization method should find steady-state conditions in significantly less computing time than the brute force approach. In some cases, such as wind generation installations with power electronics devices connected on the rotor side, the best approach is to start with mean-value models or tricked equivalents, and to switch onto actual commutating functions after establishing steady-state operation.

To complete the picture it is important to mention that initialization also concerns the control system diagrams. It is usually a more complex but essential feature, since, for example, initialization of synchronous machine variables without initialization of its controls can become worthless. Fully automatic methods do not yet exist, but backward propagation of variables in control blocks from specified initial condition variables is a practical option. This problem remains complex.

2.8 Implementation

Sparse matrix solvers are used for the efficient computation of large network equations. Such solvers can be divided into two groups: direct and iterative solvers. Due to the typical structure of electrical network matrices, the direct approach is currently the most popular. A list of available software for sparse direct methods can be found in [38]. The direct approach is based on LU factorization. For a given sparse matrix $\mathbf{A_N}$ in (2.4)

$$\mathbf{A_N x_N} = \mathbf{L}(\mathbf{U x_N}) = \mathbf{b_N}, \tag{2.77}$$

where $\mathbf{L}$ and $\mathbf{U}$ are lower and upper triangular matrices, respectively. Equation (2.77) is a generic version of (2.4). Special ordering techniques can be used to generate row and column permutations and reduce fill-in during factorization. Minimum degree orderings such as approximate minimum degree (AMD) ordering [39, 40] or column approximate minimum degree (COLAMD) ordering [41, 42] can be applied to obtain sparser $\mathbf{L}$ and $\mathbf{U}$ matrices.

Recently the KLU solver has been established as one of the most effective solvers for circuit simulation problems [43, 44]. The KLU solver permutes the matrix $\mathbf{A_N}$ to obtain the block triangular form (BTF) before ordering. The BTF of $\mathbf{A_N}$ results in the new matrix $\mathbf{A'_N}$

$$\mathbf{PAQ} = \begin{bmatrix} \mathbf{A'_{N11}} & \mathbf{A'_{N12}} & \cdots & \mathbf{A'_{N1n}} \\ \mathbf{0} & \mathbf{A'_{N22}} & & \vdots \\ \mathbf{0} & \mathbf{0} & \ddots & \vdots \\ \mathbf{0} & \mathbf{0} & \mathbf{0} & \mathbf{A'_{Nnn}} \end{bmatrix}, \tag{2.78}$$

where $\mathbf{P}$ and $\mathbf{Q}$ are column and row permutation matrices, respectively and n denotes the number of block. The BTF provides important advantages. The diagonal blocks can become independent and hence only these blocks require factorization. The off-diagonal non-zeroes do not contribute to any fill-in. When a network contains delay based line/cable models, the BTF can then automatically formulate the block-diagonal version of $\mathbf{A_N}$

$$\mathbf{A'_N} = \begin{bmatrix} \mathbf{A'_{N11}} & \mathbf{0} & \cdots & \mathbf{0} \\ \mathbf{0} & \mathbf{A'_{N22}} & & \vdots \\ \mathbf{0} & \mathbf{0} & \ddots & \vdots \\ \mathbf{0} & \mathbf{0} & \mathbf{0} & \mathbf{A'_{Nnn}} \end{bmatrix}. \tag{2.79}$$

The independent blocks can be solved in parallel and the BTF method can automatically derive (2.79) when all resulting subnetworks are separated by propagation delay-based transmission line modes. This is not the case when the transmission lines are modelled by coupled pi-sections.

The KLU method employs AMD or COLAMD (option) for ordering before factoring each diagonal block. In [45], AMD is found to provide better results on circuit matrices. KLU performs a factorization based on the Gilbert–Peierls left-looking algorithm [45].

An important computational bottleneck is created by the fact that nonlinear devices solved through the LFMA approach and switch models may require repetitive updates and thus refactorization of $\mathbf{A_N}$ at each solution time-point. The usage of $\mathbf{A'_N}$ in (2.79) can confine the refactorization process to smaller matrices and consequently increases performance.

For some networks, instead of the block-diagonal version of $\mathbf{A_N}$, it is possible to obtain its bordered-block-diagonal form

$$\mathbf{A'_N} = \begin{bmatrix} \mathbf{A'_{N11}} & \mathbf{0} & \dots & \mathbf{S_1^T} \\ \mathbf{0} & \mathbf{A'_{N22}} & \dots & \mathbf{S_2^T} \\ \vdots & \vdots & \ddots & \vdots \\ \mathbf{S_1} & \mathbf{S_2} & \dots & \mathbf{S_d} \end{bmatrix}, \tag{2.80}$$

which is also suitable for parallel programming in the solution of network equations. Equation (2.80) is related to diakoptic analysis theory [46–48]. Equation (2.80) and the concept of tearing a network at an arbitrary location are actually related to MANA. If closed switches are used to separate a network into several parts by cutting it at arbitrary locations, then if the resulting subnetworks are identified (matrix reordering) and the switch equations (2.8) are assembled at the bottom of $\mathbf{A_N}$, equation (2.4) allows us to write

$$\begin{bmatrix} \mathbf{A'_{N_{11}}} & \mathbf{0} & \dots & \mathbf{S_1^T} \\ \mathbf{0} & \mathbf{A'_{N_{22}}} & \dots & \mathbf{S_2^T} \\ \vdots & \vdots & \ddots & \vdots \\ \mathbf{S_1} & \mathbf{S_2} & \dots & \mathbf{S_d} \end{bmatrix} \begin{bmatrix} \mathbf{x'_N} \\ \mathbf{i_S} \end{bmatrix} = \begin{bmatrix} \mathbf{b'_N} \\ \mathbf{0} \end{bmatrix}, \tag{2.81}$$

where the switch submatrices $\mathbf{S}$ contain closed switch equations (as (2.8)) and the vector $\mathbf{i_S}$ holds unknown switch currents. When all the network tearing switches are ideal, $\mathbf{S_d} = \mathbf{0}$. In theory it is possible to solve for $\mathbf{i_S}$ before solving for $\mathbf{x'_N}$, but complexities arise when it is necessary to refactor the matrices $\mathbf{A_{N_{ii}}}$ for switching devices or nonlinear functions.

Iterative matrix solution methods [49] can scale well to significantly larger problem sizes. Although the conventional wisdom is that direct solvers are not effective for circuit simulation problems, some experiments with specific parallel matrix preconditioners have been demonstrated to outperform direct solvers [50].

Parallel programming of EMT-type solutions methods is a new trend for accelerating computations and also for extending the range of applications. There are two fundamental approaches to express parallelism in programs: message passing and multithreading. The message passing approach is suitable for distributed memory systems. Message passing interface (MPI) is a communication library used as the message passing platform on distributed systems. The multithreading approach can be implemented on shared memory systems and multicore technologies supporting thread programming. OpenMP has become an industry standard API for shared-memory programming.

As explained above, the basic concept of network partitioning (for parallelization) in EMT-type solvers is based on the natural decoupling introduced by travelling wave propagation on transmission lines. The same approach can be used in both real-time and off-line simulation tools to achieve coarse-grain parallelization. The recently introduced SSN [27, 28] method also offers a direct method for tearing and parallelizing a network at arbitrary locations.

Computational accelerators are used in order to enable higher performance when exploiting fine-grained parallelism. The most popular accelerators are graphical processing units (GPUs) and field programmable gate arrays (FPGAs). These hardware accelerators can provide fast computations for certain classes of problems. GPU and FPGA accelerators are used as an alternative to accelerate the

circuit simulation besides distributed and shared memory architectures. Several approaches have been developed on hardware accelerators for circuit simulation. By using FPGAs, the KLU matrix solver in the matrix-solve phase of the SPICE simulation is parallelized in [51]. A parallel CPU+FPGA based architecture for sparse matrix LU factorization is developed in [52]. The computational power of FPGAs can be used to extend the processing potential of CPU-based simulators and even expect faster-than-real-time [53] computations.

Several papers present work based on multithreading through OpenMP for the SPICE program. Two levels (fine-grained and coarse-grained) of parallelism on multicore systems are presented in [54].

2.9 Conclusions

This chapter has presented an overview of the numerical methods applied to the simulation of electromagnetic transients in power systems. It focused on the most widely accepted and recognized solution methods available in industrial grade applications.

Computer programs based on the off-line EMT-type algorithms are today the most widely used simulation tools for power system transients. They are also the most precise and provide the largest library of models specific to power system transients.

The EMT-type tools now offer many new advantages, including convergence of environments from load-flow to time-domain and increased computational speeds for simulating over an even wider range of frequencies.

References

[1] Mahseredjian, J., Naredo, J.L., Karaagac, U. and Martinez–Velasco, J.A. (2010) Off-line simulation methods and tools for electromagnetic transients in power systems: Overview and challenges. IEEE/PES Tutorial on *Transient Analysis of Power Systems. Solution Techniques, Tools and Applications*, IEEE Catalog Nr. 11TP255E, ISBN 978-1-4577-1501-3, July 2010.

[2] Mahseredjian, J., Dinavahi, V. and Martinez, J.A. (2009) Simulation tools for electromagnetic transients in power systems: Overview and challenges. *IEEE Transactions on Power Delivery*, **24**(3), 1657–1669.

[3] Mahseredjian, J., Dinavahi, V. and Martinez, J.A. (2007) An overview of simulation tools for electromagnetic transients in power systems. Proceedings of IEEE Power Engineering Society General Meeting, Tampa, FL, 24–28 June 2007, pp. 1–6.

[4] Mahseredjian, J. (2007) Computation of power system transients: Overview and challenges. Proceedings of IEEE Power Engineering Society General Meeting, Tampa, FL, 24–28 June 2007, pp. 1–7.

[5] Kragh, H., Blaabjerg, F. and Pedersen, J.K. (1998) An advanced tool for optimized design of power electronic circuits. Proceedings of IEEE Industry Applications Conference, St Louis, MO, October 1998, pp. 991–998.

[6] Gole, A.M., Filizadeh, S., Menzies, R.W. and Wilson, P.L. (2005) Optimization-enabled electromagnetic transient simulation. *IEEE Transactions Power Delivery*, **20**(1), 512–518.

[7] www.pscad.com.

[8] http://www.mathworks.com/.

[9] www.emtp.com.

[10] Common Information Model (CIM): CIM 10 version, EPRI, Palo Alto, CA, 2001.

[11] Mahseredjian, J., Saad, O. and Dennetière, S. (2009) Computation of power system transients: modeling portability. Proceedings of IEEE Power and Energy Society General Meeting, Calgary, 26–30 July 2009.

[12] Mahseredjian, J. and Alvarado, F. (1997) Creating an electromagnetic transients program in MATLAB: MatEMTP. *IEEE Transactions on Power Delivery*, **12**(1), 380–388.

[13] Mahseredjian, J., Dennetière, S., Dubé, L., *et al.* (2007) On a new approach for the simulation of transients in power systems. *Electric Power Systems Research*, **77**(11), 1514–1520.

[14] Mahseredjian, J. (2008) Simulation des transitoires électromagnétiques dans les réseaux électriques. Édition 'Les Techniques de l'Ingénieur', 10 February 2008, Dossier D4130, 12 pages.

[15] Branin, F.H. (1967) Computer methods of network analysis. *Proceedings of IEEE*, **55**(11), 1787–1801.

[16] Dommel, H.W. (1969) Digital computer solution of electromagnetic transients in single- and multiphase networks. *IEEE Transactions on Power Apparatus and Systems*, **88**(4), 734–741.
[17] Nagel, L.W. (1975) SPICE2 A computer program to simulate semiconductor circuits. Memorandum No. UCB/ERL M520, 9 May 1975.
[18] Woodford, D.A., Gole, A.M. and Menzies, R.Z. (1983) Digital simulation of DC links and AC machines. *IEEE Transactions on Power Apparatus and Systems*, **102**(6), 1616–1623.
[19] Karaagac, U., Mahseredjian, J. and Saad, O. (2011) An efficient synchronous machine model for electromagnetic transients. *IEEE Transactions on Power Delivery*, **26**(4), 2456–2465.
[20] Dommel, H.W. (1971) Nonlinear and time-varying elements in digital simulation of electromagnetic transients. *IEEE Transactions on Power Apparatus and Systems*, **90**(6), 2561–2567.
[21] Tinney, W.F. (1971) Compensation methods for network solutions by triangular factorization. Proceedings of Power Industry Computer Applications Conference, Boston, MA, May 24–26, 1971.
[22] Tinney, W.F. (1972) Compensation methods for network solutions by optimally ordered triangular factorization. *IEEE Transactions on Power Apparatus and Systems*, **91**(1), 123–127.
[23] SimPowerSystems User's guide, The MathWorks, Inc., 2012.
[24] Chua, L.O. and Lin, P.M. (1975) *Computer Aided Analysis of Electronic Circuits: Algorithms and Computational Techniques*, Prentice Hall, Englewood Cliffs, CA.
[25] So, H.C. (1965) On the hybrid description of a linear n-port resulting from the extraction of arbitrarily specified elements. *IEEE Transactions on Circuit Theory*, **12**(3), 381–387.
[26] Mahseredjian, J., Lefebvre, S. and Do, X.-D. (1993) A new method for time-domain modeling of nonlinear circuits in large linear networks. Proceedings of 11th Power Systems Computation Conference (PSCC), Vol. 2, August 1993, pp. 915–922.
[27] Dufour, C., Mahseredjian, J. and Bélanger, J. (2011) A combined state-space nodal method for the simulation of power system transients. *IEEE Transactions on Power Delivery*, **26**(2), 928–935.
[28] Mahseredjian, J., Dufour, C., Karaagac, U. and Bélanger, J. (2011) Simulation of power system transients using state-space grouping through nodal analysis. Proceedings of International Conference on Power Systems Transients, IPST 2011, Delft, Netherlands, 14–17 June 2011.
[29] Zou, M., Mahseredjian, J., Joos, G., *et al.* (2006) Interpolation and reinitialization in time-domain simulation of power electronic circuits. *Electric Power Systems Research*, **76**(8), 688–694.
[30] Brayton, R.K., Gustavson, F.G. and Hachtel, G.D. (1972) A new efficient algorithm for solving differential-algebraic systems using implicit backward-differentiation formulas. *Proceedings of IEEE*, **60**(1), 98–108.
[31] Semlyen, A. and de León, F. (1993) Computation of electromagnetic transients using dual or multiple time steps. *IEEE Transactions Power Systems*, **8**(3), 1274–1281.
[32] Moreira, F.A., Martí, J.R., Zaneta, L.C. and Linares, L. (2006) Multirate simulations with simultaneous-solution using direct integration methods in a partitioned network environment. *IEEE Transactions on Circuits and Systems*, **53**(12), 2765–2778.
[33] Mahseredjian, J., Dubé, L., Zou, M., *et al.* (2006) Simultaneous solution of control system equations in EMTP. *IEEE Transactions Power Systems*, **21**(1), 117–124.
[34] Simulink, 1994–2014 The MathWorks, Inc.
[35] Kocar, I., Mahseredjian, J., Karaagac, U., *et al.* (2014) Multiphase load flow solution of large scale distribution systems using the MANA approach. *IEEE Transactions on Power Delivery*, **29**(2), 908–915.
[36] Xu, W., Martí, J. and Dommel, H.W. (1991) A multiphase harmonic load flow solution technique. *IEEE Transactions on Power Systems*, **6**(1), 174–182.
[37] Lombard, X., Mahseredjian, J., Lefebvre, S. and Kieny, C. (1995) Implementation of a new harmonic initialization method in the EMTP. *IEEE Transactions on Power Delivery*, **10**(3), 1343–1352.
[38] Davis, T.A. (2012) Summary of available software for sparse direct methods. http://www.cise.ufl.edu/research/sparse/codes/codes.pdf, April 2012.
[39] Amestoy, P.R., Davis, T.A. and Du, I.S. (1996) An approximate minimum degree ordering algorithm. *SIAM Journal on Matrix Analysis and Applications*, **17**(4), 886–905.
[40] Amestoy, P.R., Davis, T.A. and Du, I.S. (2004) Algorithm 837: AMD, an approximate minimum degree ordering algorithm. *ACM Transactions on Mathematical Software*, **30**(3), 381–388.
[41] Davis, T.A., Gilbert, J.R., Larimore, S.I. and Ng, E.G. (2004) A column approximate minimum degree ordering algorithm. *ACM Transactions on Mathematical Software*, **30**(3), 353–376.
[42] Davis, T.A., Gilbert, J.R., Larimore, S.I. and Ng, E.G. (2004) Algorithm 836: COLAMD, a column approximate minimum degree ordering algorithm. *ACM Transactions on Mathematical Software*, **30**(3), 377–380.

[43] Davis, T.A. and Natarajan, E.P. (2010) Algorithm 907: KLU, a direct sparse solver for circuit simulations problems. *ACM Transactions on Mathematical Software*, **37**(3), 36:1–36:17.

[44] Hutchinson, S.A., Keiter, E.R., Hoekstra, R.J., *et al.* (2000) The XyceTM parallel electronic simulator – An overview. Proceedings of IEEE International Symposium on Circuits and Systems, Sydney (AU), May 2000.

[45] Natarajan, E.P. (2005) KLU A high performance sparse linear solver for circuit simulation problems. Master's Thesis, University of Florida.

[46] Chua, L.O. and Chen, L.-K. (1976) Diakoptic and generalized hybrid analysis. *IEEE Transactions on Circuits and Systems*, **23**(12), 694–705.

[47] Kron, G. (1953) A set of principles to interconnect the solution of physical systems. *Journal of Applied Physics*, **24**(8), 965–980.

[48] Kron, G. (1963) *Diakoptics-Piecewise Solution of Large-Scale Systems*, MacDonald, London, England.

[49] Saad, Y. (2003) *Iterative Methods for Sparse Linear Systems*, SIAM, Philadelphia, PA.

[50] Thornquist, H.K., Keiter, E.R., Hoekstra, R.J., *et al.* (2009) A parallel preconditioning strategy for efficient transistor-level circuit simulation. Proceedings of IEEE/ACM International Conference on Computer-Aided Design, ICCAD 2009, San Jose, CA, November 2009, pp. 410–417.

[51] Kapre, N. (2010) SPICE2 A spatial parallel architecture for accelerating the SPICE circuit simulator. Ph.D. dissertation, California Institute of Technology.

[52] Wu, W., Shan, Y., Chen, X., *et al.* (2011) FPGA accelerated parallel sparse matrix factorization for circuit simulations. Proceedings of the 7th International Conference on Reconfigurable Computing: Architectures, Tools and Applications, Belfast, UK, 23–25 March 2011.

[53] Matar, M. and Iravani, R. (2013) The reconfigurable-hardware real-time and faster-than-real-time simulator for the analysis of electromagnetic transients in power systems. *IEEE Transactions on Power Delivery*, **28**(2), 619–627.

[54] Ye, X., Dong, W., Li, P. and Nassif, S. (2011) Hierarchical multialgorithm parallel circuit simulation. *IEEE Transactions on Computer-Aided Design of Integrated Circuits and Systems*, **30**(1), 45–48.

3

Frequency Domain Aspects of Electromagnetic Transient Analysis of Power Systems

José L. Naredo, Jean Mahseredjian, Ilhan Kocar, José A. Gutiérrez–Robles and Juan A. Martinez-Velasco

3.1 Introduction

The electromagnetic transient (EMT) response of a power system can be determined either by time-domain (TD) or by frequency-domain (FD) methods. A common belief in the 1980s was that these two approaches were in competition and that, in the end, only one of these would prevail. Instead, nowadays, TD and FD methods complement each other. Devices whose parameters depend on frequency are treated more conveniently in the frequency domain, whereas those elements exhibiting strong nonlinear behaviour can be better analysed by means of time-domain techniques.

In practice TD-based methods, like EMTP, are the most used. These methods are much more intuitive than those based on FD analysis, and they also usually require much less computer resource. However, deep knowledge of FD techniques has become essential for modern power system analysis. Often the synthesis of models and of network equivalents is conducted in the frequency domain. In addition, time-domain analysis by digital computer requires the sampling of all the time-dependent variables. When this sampling is not done properly, it can produce erroneous results. In this respect, FD analysis provides valuable references to check TD results. Side-effects of sampling processes are also better understood and handled in the frequency domain.

This chapter deals with those aspects of frequency domain analysis and of digital signal processing that have become essential for the analysis of transients in modern power systems. The first section of the chapter provides a brief review of basic concepts of FD methods. Continuous-time Fourier analysis is introduced as an extension of phasor analysis which is more familiar to power engineers. The second section of the chapter presents the basic differences between continuous-time and discrete-time Fourier analysis. Of special interest here are: (1) the effect of aliasing, (2) the sampling theorem and (3) the principle of conservation of information. The third section provides a brief overview of transient analysis methods based on the discrete Fourier transform (DFT) and the numerical Laplace transform (NLT).

Transient Analysis of Power Systems: Solution Techniques, Tools and Applications, First Edition.
Edited by Juan A. Martinez-Velasco.

Power systems are increasing substantially in both, size and complexity. Even though transient events usually occur locally, one often needs to analyse their effects on a large network. In these circumstances some parts of the network will be subject to fast dynamics, while others will continue operating at slow dynamics, and even close to steady state. It is, therefore, highly attractive to simulate the various parts of a system at different sampling rates [1], each one chosen in accordance with its local dynamics. An important issue in multirate transient analysis is the interfacing of various simulation processes running at different sampling rates. Interface variables from slower to faster processes should be interpolated, whereas those from faster to slower processes must be decimated [2–5]. These two processes, interpolation and decimation introduce aliasing errors that can be treated by frequency-domain and signal-processing techniques [6]. The fourth section of the chapter deals with multirate transient analysis.

3.2 Frequency Domain Basics

3.2.1 Phasors and FD Representation of Signals

Figure 3.1 represents a linear time-invariant (LTI) system. Consider first that its input is a pure sinusoid with constant amplitude A, frequency Ω_0 and phase ϕ:

$$x_0(t) = A\cos\left(\Omega_0 t + \phi\right) \tag{3.1}$$

The input/output relationship for the system is expressed symbolically as follows:

$$x_0(t) \xrightarrow{LTI} = y_0(t)$$

A well-established fact for LTI systems is that the output $y(t)$ is always a pure sinusoid with the same frequency Ω_0 [7]:

$$y_0(t) = \alpha A\cos\left(\Omega_0 t + \phi + \theta\right) \tag{3.2}$$

Only the amplitude and phase angle of an input sinusoid are changed by the system. Sinusoids are therefore said to be *characteristic functions* (or eigenfunctions) of LTI systems.

Complex exponentials offer a convenient alternative to sinusoids in the analysis of LTI systems. Consider the following equivalences for $x_0(t)$ in (3.1):

$$x_0(t) = \Re e\left\{Ae^{j(\Omega_0 t+\phi)}\right\} \tag{3.3}$$

and

$$x_0(t) = \tfrac{A}{2}e^{-j(\Omega_0 t+\phi)} + \tfrac{A}{2}e^{j(\Omega_0 t+\phi)} \tag{3.4}$$

Figures 3.2(a) and (b) provide illustrations of expressions (3.3) and (3.4), respectively. Whereas (3.3) leads to phasor representations of sinusoidal waves, (3.4) provides Fourier-type representations for signals that are not necessarily sinusoidal.

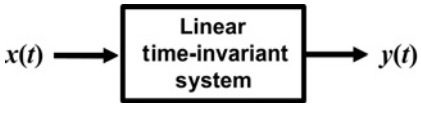

Figure 3.1 Linear time-invariant (LTI) system.

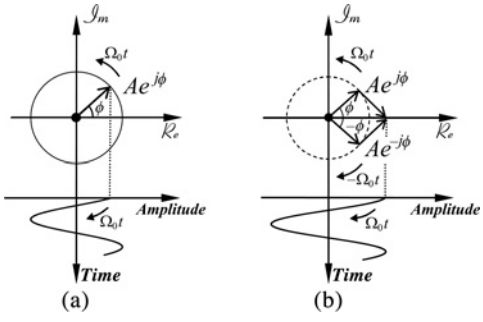

Figure 3.2 Sinusoidal signal representation: (a) real-axis projection of complex exponential signal; (b) sum of two complex conjugate exponential signals.

Recall that the phasor representation of $x_0(t)$ in (3.1) is by the complex exponential function at the right-hand side of (3.3) with its factor $e^{j\Omega_0 t}$ being removed (see Figure 3.2(a)):

$$x_0(t) \rightarrow X_0 = Ae^{j\phi} \tag{3.5}$$

The underlying assumption in phasor analysis is that systems operate in steady state. That is, signal $x_0(t)$ has always been an input to the system in Figure 3.1. Since frequency Ω_0 remains constant, there is no need to refer explicitly the factor $e^{j\Omega_0 t}$ in phasor representation (3.5).

Input/output relation (3.2) can be stated in phasor form as follows:

$$Y_0 = \alpha A e^{j(\phi+\theta)} = \alpha e^{j\theta} \times Ae^{j\phi}, \tag{3.6a}$$

where

$$y_0(t) = \Re e\left\{Y_0 \times e^{j\Omega_0 t}\right\} \tag{3.6b}$$

Two advantages of phasor representation become apparent from the comparison of equations (3.6a) and (3.2). The first is that the input/output relations are given by the multiplication of two complex numbers (i.e. phasors). The second is that, at the particular frequency Ω_0, the LTI system of Figure 3.1 is fully characterized by the complex number $\alpha e^{j\theta}$ and this number can also be regarded as a phasor.

Now consider the representation of $x_0(t)$ by (3.4). The first term on the right-hand side is associated to a phasor A_{-1} of negative frequency $-\Omega_0$, while the second term is to a phasor A_{+1} of positive frequency $+\Omega_0$; see Figure 3.2(b):

$$\tfrac{A}{2}e^{-j(\Omega_0 t+\phi)} \rightarrow A_{-1} = \tfrac{A}{2}e^{-j\phi}$$

and

$$\tfrac{A}{2}e^{j(\Omega_0 t+\phi)} \rightarrow A_{+1} = \tfrac{A}{2}e^{j\phi}$$

Sinusoid $x_0(t)$ is further represented by the following vector whose elements are phasors:

$$x_0(t) = A\cos\left(\Omega_0 t + \phi\right) \rightarrow \mathbf{X} = \left\{A_{-1}, 0, A_{+1}\right\} \tag{3.7}$$

Note here that the frequency associated with each element is determined by its vector position-index; that is, $(-1)\boldsymbol{\Omega}_0$ for the first, $(0)\boldsymbol{\Omega}_0$ for the second, and $(+1)\boldsymbol{\Omega}_0$ for the third. Note also the introduction of a zero element as place-holder for a zero-frequency component which, for $x_0(t)$ in (3.3), certainly is null.

Vector representation (3.7) is readily extended to signals composed of a number of *harmonically related* sinusoids. Recall that two sinusoids are said to be harmonically related when their frequencies are multiples of a third one Ω_0 called the fundamental. Consider the following signal:

$$x_K(t) = A_0 + \sum_{k=1}^{K} A_k \cos\left(k\Omega_0 t + \phi_k\right) \tag{3.8}$$

By extension of (3.7), a phasor-vector representation for $x_K(t)$ is

$$x_K(t) \rightarrow \mathbf{X}_K = \left\{X_{-K}, \ldots, X_{-1}, X_0, X_1, \ldots, X_K\right\}, \tag{3.9a}$$

where

$$X_0 = A_0, \tag{3.9b}$$

$$X_k = \begin{cases} \frac{1}{2}A_k e^{j\phi_k}, & k = +1, +2, \ldots, +K \\ \frac{1}{2}A_{-k} e^{-j\phi_{-k}}, & k = -1, -2, \ldots, -K. \end{cases} \tag{3.9c}$$

The original signal $x_K(t)$ (3.8) is readily recovered from vector representation (3.9a) as

$$x_K(t) = \sum_{k=-K}^{+K} X_k e^{jk\Omega_0 t}. \tag{3.10}$$

A large class of signals in engineering can be represented, or at least approximated, by expressions (3.8), (3.9a) or (3.10). If $x_K(t)$ of (3.8) is an input to the LTI system of Figure 3.1, the output can be expressed as

$$y_K(t) = \alpha_0 A_0 + \sum_{k=1}^{K} \alpha_k A_k \cos\left(k\Omega_0 t + \phi_k + \theta_k\right). \tag{3.11}$$

For excitations of the form in (3.8), the LTI system is characterized by the vector

$$\mathbf{H}_K = \left\{H_{-K}, \ldots, H_{-1}, H_0, H_1, \ldots, H_K\right\}, \tag{3.12a}$$

where

$$H_k = \alpha_k e^{j\theta_k} \quad k = 0, \pm 1, \pm 2, \ldots, \pm K. \tag{3.12b}$$

The input/output relation can thus be expressed in phasor-vector form as

$$\mathbf{Y}_K = \mathbf{H}_K \otimes \mathbf{X}_K, \tag{3.13a}$$

where

$$\mathbf{Y}_K = \left\{Y_{-K}, \ldots, Y_{-1}, Y_0, Y_1, \ldots, Y_K\right\}, \tag{3.13b}$$

$$Y_k = X_k \times H_k \quad k = 0, \pm 1, \pm 2, \ldots, \pm K, \tag{3.13c}$$

and the symbol $\otimes$ represents the element-by-element product of two vectors.

The time-domain output waveform $y_K(t)$ is obtained from (3.13b) as

$$y_K(t) = \sum_{k=-K}^{K} Y_k e^{jk\Omega_0 t}. \tag{3.14}$$

The equivalence between expressions (3.14) and (3.11) can easily be verified. Expressions (3.12) and (3.13) extend phasor analysis to signals composed by harmonically related sinusoids. Note that for the signal $y_K(t)$ in (3.14) to be real-valued, the following conditions must hold:

$$\alpha_k = \alpha_{-k} \quad \text{and} \quad \theta_k = -\theta_{-k} \tag{3.15}$$

3.2.2 Fourier Series

A signal $x_p(t)$ is said to be periodic when it repeats itself at constant time intervals T:

$$x_p(t) = x_p(t+T) \tag{3.16}$$

Figure 3.3 depicts a periodic signal. The minimum value of $T > 0$ for which property (3.16) holds is called the *fundamental period*.

A periodic waveform $x_p(t)$ is further said to be a *power signal* when its mean power is finite; that is

$$P_{xp} = \frac{1}{T}\int_T \left|x_p(t)\right|^2 dt < \infty.$$

It is straightforward to show that signal $x_K(t)$ in (3.8), and in (3.10), is periodic and has fundamental period $T = 2\pi/\Omega_0$. The Fourier theorem establishes that a periodic signal of power $x_p(t)$ can always be approximated by a series $x_K(t)$, as in (3.8) or in (3.10), in such way that the power of the difference between $x_p(t)$ and $x_K(t)$ tends to zero as the number of series terms K increases towards infinity [8], that is

$$\lim_{K\to\infty} \frac{1}{T}\int_T \left|x_p(t) - x_K(t)\right|^2 dt = 0. \tag{3.17}$$

On the grounds of the Fourier theorem, the following equivalence is stated for a periodic signal of power:

$$x_p(t) = \sum_{k=-\infty}^{+\infty} X_k e^{jk\Omega_0 t} \tag{3.18}$$

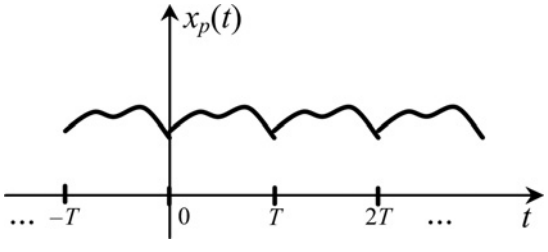

Figure 3.3 Example of a periodic signal.

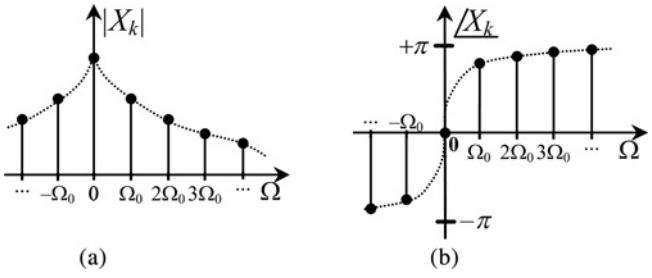

Figure 3.4 Periodic signal spectrum: (a) magnitude spectrum; (b) phase angle spectrum.

This expression corresponds to the Fourier series in its complex exponential form. Since $x_p(t)$ is assumed real-valued, the coefficients X_k of (3.18) with negative index should be complex-conjugates of their positive-index counterparts [8]:

$$X_{-k} = X_k^*$$

Fourier coefficients are obtained through using [7–9]

$$X_k = \frac{1}{T}\int_T x_p(t)\, e^{-jk\Omega_0 t} dt. \tag{3.19}$$

In the same form as signal $x_K(t)$ in (3.10), $x_p(t)$ in (3.18) can be represented in vector form, only that now the dimensions are infinite:

$$x_p(t) \rightarrow \mathbf{X} = \left\{\ldots, X_{-2}, X_{-1}, X_0, X_1, X_2, \ldots\right\}$$

A plot of the magnitudes of elements in **X** against their corresponding frequencies is illustrated in Figure 3.4(a). A similar plot for the angles of elements in **X** is shown in Figure 3.4(b). Vector **X**, as well as its associated graphs in Figures 3.4, are referred to as the *spectrum* of $x_p(t)$. Since the components of **X** are complex, a full graphical representation of its spectrum requires two plots, one for phasor magnitudes and the other for phasor angles. An alternative spectrum specification consists in providing one plot for the real parts of the phasor elements and a second plot for the corresponding imaginary parts.

In summary, the Fourier (series) theorem permits the extension of phasor analysis to the treatment of linear systems being excited by periodic signals of power. This is illustrated next by means of an application example.

Example 3.1 A single-phase aerial line is 10 km long and it is excited by a voltage source that produces a square wave with a period of $T = 2$ ms. The line is terminated in its characteristic impedance. The voltage waveform is to be determined at the line termination, assuming that the source has been connected for a long enough time to consider steady-state operation; so, the Fourier series method can be used. Figure 3.5(a) provides the transverse geometry of the line along with the electrical data required to determine the line parameters, Figure 3.5(b) shows a longitudinal diagram of the line and its connections and Figure 3.5(c) depicts the input waveform.

Line admittance in per unit length (p.u.l.) is calculated through the following expression [10]:

$$Y = \frac{j\Omega 2\pi\varepsilon_0}{\log_e(2h/r)}$$

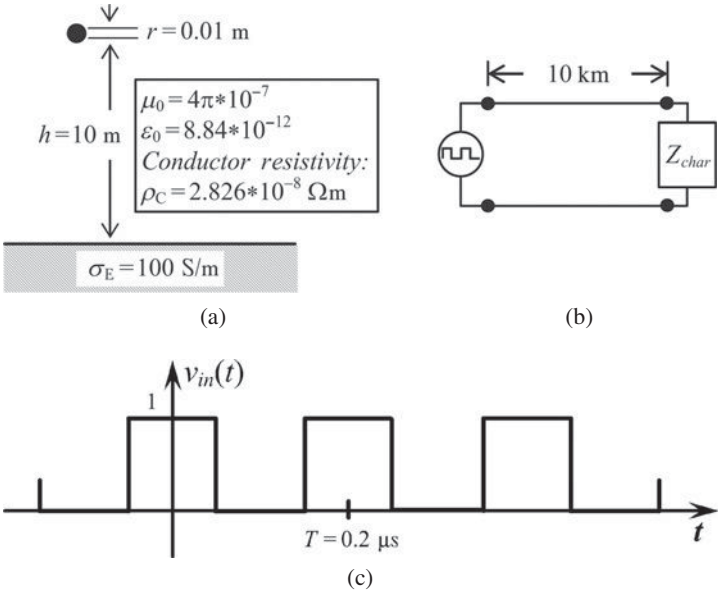

Figure 3.5 Example 3.1 – Single-phase transmission line excited by periodic signal: (a) transversal geometry; (b) line layout; (c) input waveform.

The line impedance parameter in p.u.l. is calculated as follows:

$$Z = Z_G + Z_E + Z_C,$$

where Z_G is the geometric impedance in p.u.l.:

$$Z_G = \frac{j\Omega\mu_0}{2\pi} \log_e\left(\frac{2h}{r}\right)$$

Z_E is the earth impedance in p.u.l.:

$$Z_E = \frac{j\Omega\mu_0}{2\pi} \log_e\left(1 + \frac{1}{h\sqrt{j\Omega\mu\sigma_E}}\right)$$

and Z_C is the conductor impedance in p.u.l.:

$$Z_C = \sqrt{\left(\frac{\rho_c}{\pi r^2}\right)^2 + \frac{j\Omega\mu_0\rho_c}{(2\pi r)^2}}$$

The transfer function for the line setup is

$$V_{out}/V_{in} = e^{-\sqrt{ZY}\times length}.$$

Figure 3.6(a) shows a plot of the input voltage $v_{in}(t)$ being approximated by partial series with $K = 17$. Figure 3.6(b) shows a plot of the output voltage $v_{out}(t)$ obtained from the above transfer function along

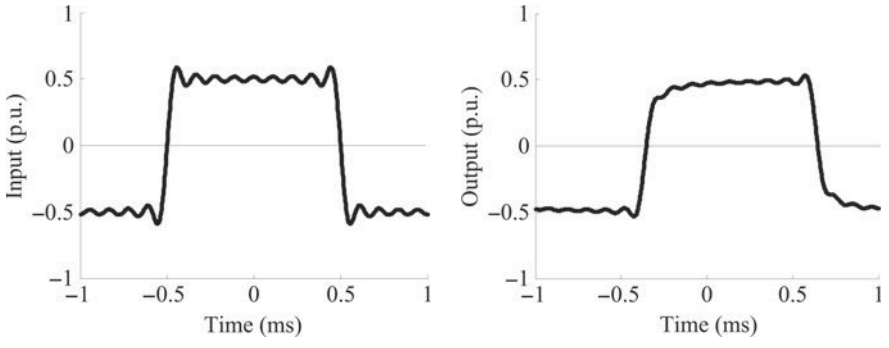

Figure 3.6 Example 3.1: (a) Fourier series approximation of square wave input signal; (b) output signal as obtained by the Fourier series method.

with expressions (3.13), (3.14) and (3.19). Note that the use of partial Fourier series produces oscillation errors in both Figures 3.6(a) and (b). If better precision is required, the window techniques described in Section 3.5.1.1 can be employed here as well.

3.2.3 Fourier Transform

Fourier series decomposition of a signal into harmonic sinusoids, or into complex exponentials, is extended next to non-periodic waveforms.

A signal $x(t)$ is said to be of *energy* if its total energy is finite, that is, if

$$E_x = \int_{-\infty}^{\infty} |x(t)|^2 \, dt < \infty.$$

Consider a signal $x(t)$ of finite duration, starting at $t = 0$ and ending at $t = t_0$, as the input to the LTI system of Figure 3.1. A periodic extension for this signal is given by

$$x_p(t) = \sum_{n=-\infty}^{+\infty} x(t - nT).$$

Figure 3.7 provides the respective representations for finite duration signal $x(t)$ and its periodic extension $x_p(t)$. Note in these figures that, as $T > t_0$, $x_p(t)$ reproduces $x(t)$ inside the interval $[0,T]$. It is clear also that $x_p(t)$ becomes equal to $x(t)$ when T approaches infinity.

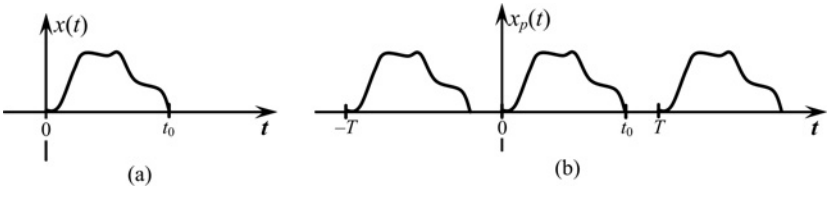

Figure 3.7 (a) Signal of finite duration $x(t)$; (b) periodic extension of $x(t)$.

Back to finite values of T, when $x(t)$ is an energy signal, $x_p(t)$ is a signal of power with Fourier series representation as in (3.18) and coefficients given by (3.19). To extend Fourier analysis to non-periodic $x(t)$, first (3.18) and (3.19) are applied to $x_p(t)$ and combined as

$$x_p(t) = \sum_{k=-\infty}^{+\infty} \frac{1}{T} \left[\int_{-T/2}^{T/2} x_p(t)\, e^{-jk\Omega_0 t} dt \right] e^{jk\Omega_0 t}.$$

Then, consideration of $(1/T) = (\Omega_0/2\pi)$ is introduced to give

$$x_p(t) = \sum_{k=-\infty}^{+\infty} \frac{\Omega_0}{2\pi} \left[\int_{-T/2}^{T/2} x_p(t)\, e^{-jk\Omega_0 t} dt \right] e^{jk\Omega_0 t}.$$

Next, as the limit of T approaching infinity is taken, Ω_0 becomes an infinitesimal and is denoted by $d\Omega$; $k\Omega_0$ becomes a continuous variable and is denoted by Ω; $x_p(t)$ becomes $x(t)$ and the summation becomes the integral [9]

$$x(t) = \frac{1}{2\pi} \int_{-\infty}^{\infty} \left[\int_{-\infty}^{\infty} x(t)\, e^{-j\Omega t} dt \right] e^{j\Omega t} d\Omega. \tag{3.20}$$

Note that (3.20) is an identity and that the integral inside braces corresponds to a function of Ω that hereafter is denoted by $X(\Omega)$. Hence

$$X(\Omega) = \int_{-\infty}^{\infty} x(t)\, e^{-j\Omega t} dt \tag{3.21a}$$

and

$$x(t) = \frac{1}{2\pi} \int_{-\infty}^{\infty} X(\Omega)\, e^{j\Omega t} d\Omega. \tag{3.21b}$$

Expression (3.21a) corresponds to the Fourier transform and (3.21b) corresponds to the inverse Fourier transform (IFT) [7–9]. The Fourier transform decomposes non-periodic signal $x(t)$ into a continuous frequency spectrum $X(\Omega)$. Figures 3.8(a) and 3.8(b) present typical plots of $X(\Omega)$. Since it has been

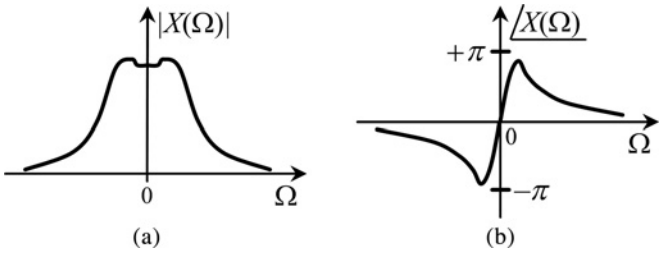

Figure 3.8 Spectrum of non-periodic signal: (a) magnitude spectrum; (b) phase-angle spectrum.

assumed that $x(t)$ is an energy signal, the existence of its Fourier transform is ensured [8, 9]. The relationship between $x(t)$ and its spectrum $X(\Omega)$ is stated symbolically as

$$x(t) \xrightarrow{\text{FT}} X(\Omega).$$

The output of LTI system in Figure 3.1, when it is excited by non-periodic input $x(t)$, is expressed in the frequency domain by the product of two complex functions as

$$Y(\Omega) = H(\Omega) \times X(\Omega). \tag{3.22}$$

As before, $X(\Omega)$ is the spectrum (or Fourier transform) of $x(t)$. $H(\Omega)$ is a function characterizing the LTI system and is referred to as its *frequency response*. The time-domain output (or system response) is obtained by applying the inverse Fourier transform (3.21b) to $Y(\Omega)$ in (3.22):

$$y(t) = \frac{1}{2\pi} \int_{-\infty}^{\infty} X(\Omega) H(\Omega) e^{jk\Omega t} d\Omega \tag{3.23}$$

It can be shown that (3.23) is equivalent to [9]

$$y(t) = \int_{-\infty}^{\infty} x(\tau) h(t-\tau)\, d\tau, \tag{3.24a}$$

where $h(t)$ is the inverse Fourier transform of $H(\Omega)$. Expression (3.24a) defines the *convolution* operation between two functions, $x(t)$ and $h(t)$. This operation is also represented symbolically as

$$y(t) = x(t) * h(t). \tag{3.24b}$$

The *Convolution theorem* states that the convolution of two time-domain functions is equivalent to the product of their Fourier transforms, or spectra [8,9]. It can also be shown that the product of two TD signals is equivalent to the convolution of their Fourier transforms.

The Convolution theorem is a convenient property of the Fourier transform. Nevertheless, there are two major difficulties for its direct application to practical transient problems. The first comes from the fact that Fourier transforms are guaranteed only for signals of energy, and this excludes several cases of practical interest, such as periodic waves. The second difficulty is due to the Fourier transform being an analytical method, and analytical functions that represent practical signals usually are very difficult to obtain and handle. Nevertheless, the Fourier transform provides the basis for other more practical FD methodologies, including the discrete Fourier transform (DFT), the numerical Laplace transform (NLT) and the Z-transform.

3.3 Discrete-Time Frequency Analysis

In the analysis of systems by digital computer, continuous time signals must be sampled – usually at regular intervals – and must be represented by means of ordered sequences of their samples. A convenient way to analyse the sampling process is through impulse functions. Recall that an impulse $\delta(t - t_0)$ is a generalized function which is zero all over t, except at $t = t_0$, where it takes a very large and undetermined

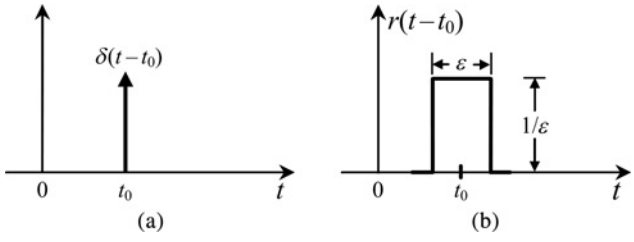

Figure 3.9 (a) Impulse function; (b) rectangular pulse.

value – see Figure 3.9(a). Figure 3.9(b) provides the plot of a rectangular function $r(t - t_0)$ of width ε, height $1/\varepsilon$ and centred at time $t = t_0$:

$$r\left(t-t_0\right)=\begin{cases}1/\varepsilon, & \left|t-t_0\right|\le\varepsilon/2\\ 0, & \left|t-t_0\right|>\varepsilon/2\end{cases}$$

The impulse function $\delta(t - t_0)$ in Figure 3.9(a) is seen as the limit of $r(t - t_0)$ when ε approaches zero.

Consider now a continuous-time function $x(t)$ as the one shown in Figure 3.10(a). The sifting (or sampling) property of the impulse function states that [8, 9]

$$\int_{-\infty}^{\infty} x\left(t\right)\delta\left(t-t_0\right)dt=x\left(t_0\right).$$

Another important (generalized) function is the train of pulses denoted by $\delta_{\Delta t}(t)$ and consisting of an infinite sequence of pulses occurring at time intervals of size Δt:

$$\delta_{\Delta t}\left(t\right)=\sum_{k=-\infty}^{+\infty}\delta\left(t-k\Delta t\right)$$

Figure 3.10b provides a plot for $\delta_{\Delta t}(t)$.

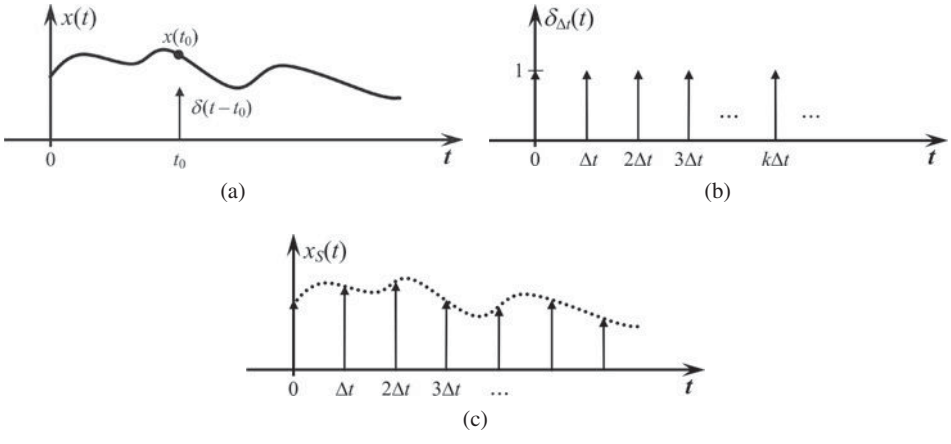

Figure 3.10 Sampling a signal by a train of pulses: (a) continuous-time signal; (b) train of pulses; (c) sampled signal.

3.3.1 Aliasing Effect

The sampling of $x(t)$ at regular intervals Δt can be represented mathematically by its product with $\delta_{\Delta t}(t)$:

$$x_S(t) = x(t) \times \delta_{\Delta t}(t) \tag{3.25a}$$

or

$$x_S(t) = \sum_{k=-\infty}^{+\infty} x(k\Delta t)\,\delta(t - k\Delta t) \tag{3.25b}$$

This is illustrated in Figure 3.10(c).

Figure 3.11(a) shows the spectrum of $x(t)$ being denoted by $X(\Omega)$, and Figure 3.11(b) shows the spectrum of $\delta_{\Delta t}(t)$ that also is a train of pulses along the Ω-axis [7]:

$$\delta_{\Delta t}(t) \xrightarrow{\text{FT}} \Omega_S \delta_{\Omega_S}(\Omega), \tag{3.26a}$$

where

$$\delta_{\Omega_S}(\Omega) = \sum_{k=-\infty}^{\infty} \delta\left(\Omega - k\Omega_S\right) \tag{3.26b}$$

and

$$\Omega_S = \frac{2\pi}{\Delta t}. \tag{3.26c}$$

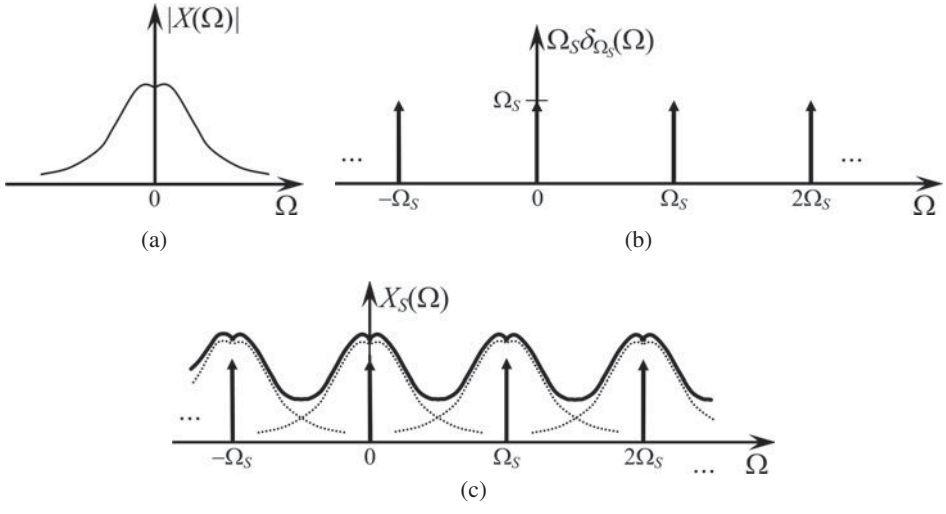

Figure 3.11 Effect of sampling on the spectrum of a signal: (a) spectrum of a continuous–time signal; (b) spectrum of a train of pulses; (c) spectrum of sampled signal.

Note that Ω_S is the frequency interval between pulses. In agreement with the convolution theorem, the spectrum of sampled signal $x_S(t)$ is obtained by the convolution of $X(\Omega)$ with $\Omega_S \delta_{\Omega s}(\Omega)$ whose result is:

$$X_S(\Omega) = \Omega_S \sum_{k=-\infty}^{+\infty} X\left(\Omega - k\Omega_S\right) \tag{3.27}$$

Figure 3.11(c) illustrates the plot of $X_S(\Omega)$ according to (3.27). Note from this figure that time-domain sampling causes the repetition of shifted (or frequency modulated) replicas of the original spectrum $X(\Omega)$. This is the effect of *aliasing* in the *frequency domain*. The overlapping of frequency components from replicas provokes sampling or aliasing errors. In extreme cases, poor choice of a sampling rate results in the original signal not being recoverable from its samples.

In signal analysis, time-to-frequency relations are usually symmetric. This has been already observed with the convolution theorem, and it is also the case with the aliasing effect; that is, the sampling of a signal spectrum creates superposition of time-shifted replicas of the signal, or TD aliasing.

3.3.2 Sampling Theorem

A signal $x(t)$ is said to be band-limited if there is a maximum frequency Ω_M above which its spectrum $X(\Omega)$ is zero – see Figure 3.12(a):

$$|X(\Omega)| = 0, \quad |\Omega| > \Omega_M$$

For this type of signal, one can select a sampling interval that avoids the overlapping of frequency replicas. This is illustrated in Figure 3.12(b) and it follows from (3.26b) that the required sampling interval is

$$\Delta t \leq \pi/\Omega_M. \tag{3.28a}$$

The inverse of Δt is the sampling frequency or rate. Its units are 'samples per second':

$$F_S = 1/\Delta t \tag{3.28b}$$

The equality option in (3.28a) (i.e. $\Delta t = \pi/\Omega_M$) corresponds to the Nyquist sampling interval Δt_{Nyq}, and its inverse $F_{Nyq} = 1/\Delta t_{Nyq}$ is known as the *Nyquist frequency* [7–9].

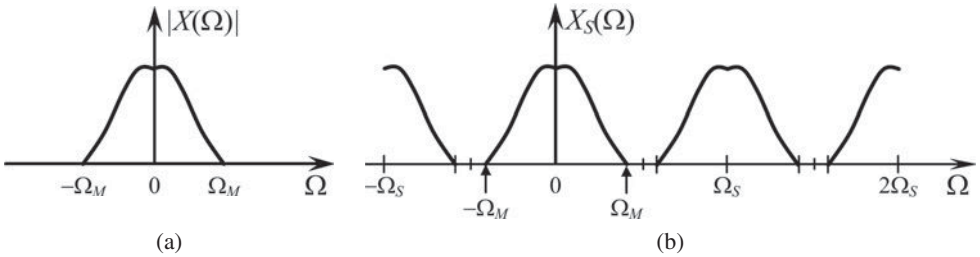

(a) (b)

Figure 3.12 (a) Spectrum of band-limited signal; (b) spectrum of sampled band-limited signal.

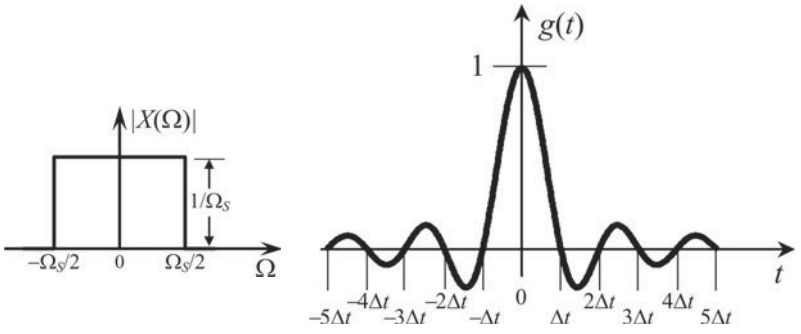

(a) (b)

Figure 3.13 (a) Frequency response $G(\Omega)$ *of* low-pass ideal filter. (b) time-domain image of $G(\Omega)$.

Consider now that a signal with band-limited spectrum $X_S(\Omega)$ has been sampled with an interval complying with (3.28a). The original signal is readily recovered by passing its samples through a low-pass filter with a frequency response of

$$G(\Omega) = \begin{cases} 1/\Omega_S & |\Omega| \le \Omega_S/2 \\ 0 & |\Omega| > \Omega_S/2. \end{cases} \tag{3.29}$$

This filter response is plotted in Figure 3.13(a). From (3.27) and (3.29)

$$X(\Omega) = X_S(\Omega) \times G(\Omega). \tag{3.30}$$

The inverse Fourier transform of $G(\Omega)$ is obtained as follows and its plot is shown in Figure 3.13(b):

$$g(t) = \frac{\sin(\pi t/\Delta t)}{(\pi t/\Delta t)} \tag{3.31}$$

On applying the convolution theorem to (3.30) we have

$$x(t) = \int_{-\infty}^{\infty} x_S(\tau)\, g(t-\tau)\, d\tau,$$

then replacing $x_S(t)$ from (3.25b), and performing the above integration gives

$$x(t) = \sum_{k=-\infty}^{+\infty} x(k\Delta t)\, g(t - k\Delta t). \tag{3.32}$$

Figure 3.14 provides a plot of $x(t)$ in accordance with (3.32). This figure shows that the reconstruction of $x(t)$ is done by superposing replicas of $g(t)$, each one scaled by a sample value and shifted by an amount of time that is a multiple of the sampling interval Δt. Note that, for instance, $g(t - k\Delta t)$ is zero at all sampling instants, except at the kth one. The implication of this is that the value of $x(t)$ at $t = k\Delta t$ is determined only by the corresponding sample $x(k\Delta t)$, whereas a value of $x(t)$ between sampling points is given by a combination of all the samples, each weighted by its corresponding shifted function $g(t)$.

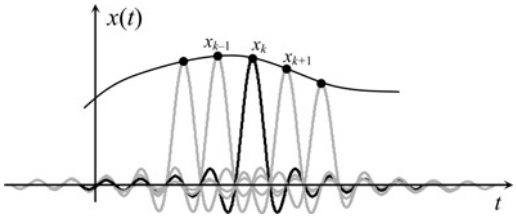

Figure 3.14 Reconstruction of a signal from its samples.

It follows from (3.32) and from Figure 3.14 that the role of $g(t)$ is that of an interpolating function. This is known as the *ideal interpolator* [8, 9]. Function $g(t)$ is essentially a theoretical tool. Its practical realization as a filter is impossible since, as can be observed from Figure 3.13, it would have to start acting at time $t = -\infty$. Nevertheless, practical signal recuperation is usually achieved satisfactorily with a well-designed non-ideal low-pass filter.

The results expressed by (3.28a) and (3.32) conform the *sampling theorem* that can be worded as follows:

A band-limited signal $x(t)$ with maximum frequency $F_M = \Omega_M/(2\pi)$ can be fully recovered from its samples, provided it has been sampled at a frequency F_S that is equal at least to double the maximum frequency F_M; i.e. sampling frequency F_S must be at least equal to the Nyquist frequency F_{Nyq}. The original signal can be fully reconstructed from its samples through the ideal interpolator function $g(t)$ defined by (3.31).

3.3.3 Conservation of Information and the DFT

In addition to (3.27), the spectrum of sampled signal $x_S(t)$ can be obtained from

$$X_S(\Omega) = \sum_{k=-\infty}^{+\infty} x(k\Delta t)\, e^{-jk\Omega\Delta t}. \tag{3.33}$$

This expression is obtained by applying the Fourier transform to (3.25a). It can be shown, either through (3.27) or (3.33), that $X_S(\Omega)$ is periodic with a repetition interval $\Omega_S = 2\pi/\Delta t$. The discrete representation of $X_S(\Omega)$ can be accomplished by sampling only one period. First suppose that this is done with N samples:

$$\Delta\Omega = \Omega_S/N = 2\pi/(N\Delta t)$$

and the continuous variable Ω in (3.33) is replaced by $m\Delta\Omega$ as

$$X_S(m\Delta\Omega) = \sum_{k=-\infty}^{+\infty} x(k\Delta t)\, e^{-j2\pi km/N}.$$

Then, the sum at the right-hand side is carried out in groups of N terms. This is done by expressing the summation variable k as $k = n + lN$:

$$X_S(m\Delta\Omega) = \sum_{l=-\infty}^{+\infty} \sum_{n=0}^{N-1} x((n+lN)\Delta t)\, \underbrace{e^{-j2\pi ml}}_{1}\, e^{-j2\pi mn/N}$$

Next, the order of summations is interchanged:

$$X_S(m\Delta\Omega) = \sum_{n=0}^{N-1} \left[\sum_{l=-\infty}^{+\infty} x((n+lN)\Delta t) \right] e^{-j2\pi nm/N}$$

Afterwards, a new discrete-time signal $x'(n\Delta t)$ is defined as

$$x'(n\Delta t) = \sum_{l=-\infty}^{+\infty} x((n+lN)\Delta t),$$

hence

$$X_S(m\Delta\Omega) = \sum_{n=0}^{N-1} x'(n\Delta t)\, e^{-j2\pi nm/N}.$$

Note that $x'(n\Delta t)$ is a periodized version of $x(n\Delta t)$ with aliasing. Finally, by assuming that $x(n\Delta t)$ is a finite sequence of N or less terms, $x'(n\Delta t)$ equals $x(n\Delta t)$ for samples between $n = 0$ to $n = N - 1$:

$$X_S(m\Delta\Omega) = \sum_{n=0}^{N-1} x(n\Delta t)\, e^{-j2\pi nm/N} \tag{3.34}$$

Recall that the derivation of (3.34) started with the assumption of a discrete spectrum consisting of N samples, and it ended up establishing the correspondence with N TD samples at the most. This is in agreement with the principle of information conservation.

Expression (3.34) is also readily identified as the discrete Fourier transform. Its inverse, the IDFT, is as [8, 9]

$$x(n\Delta t) = \frac{1}{N} \sum_{m=0}^{N-1} X_S(m\Delta\Omega)\, e^{j2\pi nm/N}. \tag{3.35}$$

Expressions (3.34) and (3.35) establish a unique relation between one finite sequence of N samples, say in the time domain, and another length-N sequence of 'spectral' samples. Note that sequences $X_S(m\Delta\Omega)$ and $x(n\Delta t)$ can be extended beyond their original lengths N through (3.34) and (3.35); nevertheless, these extensions are mere periodic repetitions.

3.3.4 Fast Fourier Transform

Numerical approaches to spectral or frequency-domain analysis usually end up with DFT (3.34) and IDFT (3.35) evaluations. It is customary for (3.34) and (3.35) to omit the term Δt in the argument of $x(n\Delta t)$ and to denote this variable simply as $x(n)$, or as x_n. Similarly for $X_S(m\Delta\Omega)$, $\Delta\Omega$ and subscript 's' are omitted, and this variable is written as $X(m)$, or as X_m. It is also customary to denote the complex exponentials as follows:

$$e^{-2\pi jmn/N} = W_N^{mn}$$

Expressions (3.34) for the DFT and (3.35) for the IDFT take the respective forms

$$X(m) = \sum_{n=0}^{N-1} x(n)\ W_N^{mn} \quad m = 0, 1, 2, \ldots, N-1 \tag{3.36}$$

and

$$x(n) = \frac{1}{N} \sum_{m=0}^{N-1} X(m)\ W_N^{-mn} \quad m = 0, 1, 2, \ldots, N-1. \tag{3.37}$$

Clearly from (3.36) and (3.37), the evaluation of the DFT and the IDFT is essentially through the same procedure. It is clear also that direct evaluation of (3.36) or (3.37) takes N^2 complex multiplications and $N(N–1)$ complex sums. The fast Fourier transform (FFT) is an algorithm for evaluating the DFT and the IDFT with very high computational efficiency. Its working principle is outlined as follows.

As N, the number of samples, is decomposed in its prime factors, the DFT or the IDFT can be evaluated in partial groups of sizes determined by these factors. The evaluation by partial groups requires fewer operations than direct calculations by (3.36) or (3.37). The highest numerical efficiency is obtained when N is a power of 2, that is, $N = 2^i$.

Assuming that this is the case, (3.36) is organized in two groups of sums. One is for even-indexed samples and other is for odd-indexed ones. An auxiliary integer variable k running from 0 to $(N/2) – 1$ is introduced, so $n = 2k$ is for even-indexed samples and $n = 2k + 1$ is for odd-indexed ones. With these changes (3.36) yields

$$X(m) = \sum_{k=0}^{(N/2)-1} x(2k)\, W_{N/2}^{mk} + W_N^m \sum_{k=0}^{(N/2)-1} x(2k+1)\, W_{N/2}^{mk},\ m = 0,\ 1,\ 2, \ldots,\ (N/2) - 1 \tag{3.38a}$$

$$X\left(\frac{N}{2} + m\right) = \sum_{k=0}^{(N/2)-1} x(2k)\, W_{N/2}^{mk} - W_N^m \sum_{k=0}^{(N/2)-1} x(2k+1)\, W_{N/2}^{mk},\ m = 0,\ 1,\ 2, \ldots,\ (N/2) - 1. \tag{3.38b}$$

The original DFT with N samples can thus be evaluated by two DFTs with $(N/2)$ samples. The number of multiplications involved in (3.38a) and (3.38b) is

$$2 \times (N/2)^2 + N/2 = \left(N^2/2\right) + N/2.$$

This number is approximately one half of the multiplications required by the direct evaluation of the N-sample DFT. Each $(N/2)$-samples DFT in (3.38a) and (3.38b) can be further evaluated by two $(N/4)$-sample DFTs, and the required number of multiplications for this is $(N^2/4) + N/2$. Since N is a power of 2, the subdivisions can continue until one ends up with $N/2$ DFTs, each one with two samples and this requires $N/2$ multiplications. The FFT algorithm evaluates DFTs and IDFTs by continued subdivisions until it ends up with $N/2$ two-sample transforms. The number of multiplications is thus

$$\left(\frac{N}{2}\right) \log_2(N).$$

From this expression, it can be observed that the number of operations required by the FFT algorithm increases almost in linear proportion to the number of samples N, whereas in the direct evaluation of the DFT by (3.36), or of the IDFT by (3.37), the number of multiplications increases in quadratic proportion

Table 3.1 Comparing number of multiplications required by the direct DFT and the FFT algorithms.

Number of samples N	DFT N^2	FFT $(N/2) \times \log_2(N)$	Ratio DFT/FFT
4	16	4	4
8	64	12	5.33
16	256	32	8
32	1024	80	12.8
64	4096	192	21.3
128	16 384	448	36.57
256	65 536	1024	64
512	262 144	2304	113.77
1024	1 048 576	5120	204.8

to N. Table 3.1 provides a comparison between the number of multiplications required by the FFT and the one by direct evaluation [11].

3.4 Frequency-Domain Transient Analysis

The time-domain description of power systems for the analysis of transients is through relations involving integrals, differentials and convolutions. In the frequency domain these relations take an algebraic form. FD transient analysis is performed first by building a system model in the Fourier [12], Laplace [13] or Z domain [14–16], and then FD transient responses are obtained solving the corresponding algebraic relations. Finally, the TD-response waveforms are derived from their FD counterparts by applying the corresponding inverse transform. An additional advantage of FD methods is that often system elements are synthesized in the frequency domain; their incorporation into FD system models is thus direct.

The FD technique described next is referred to as the numerical Laplace transform (NLT) [17, 18]. It is very robust and offers unprecedented numerical accuracy. First, the problems associated with the numerical inversion of the Fourier transform are addressed. Then, the processes developed in the solution of these problems lead in a natural way to the NLT technique. Finally, the usefulness of NLT is demonstrated with two application examples.

3.4.1 Fourier Transforms and Transients

Consider that the spectrum of a transient signal is available as N samples of the form $Y(m\Delta\Omega)$, with $m = -N/2, \ldots, -1, 0, 1, N/2-1$. To obtain the corresponding TD waveform $y(t)$, the inverse Fourier integral (3.21b) is approximated numerically as follows:

$$y(t) \cong y_1(t) = \frac{\Delta\Omega}{2\pi} \sum_{m=-N/2}^{(N/2)-1} Y(m\Delta\Omega)\, e^{j(m\Delta\Omega)t}. \tag{3.39}$$

This approximation involves two steps. The first is the truncation of the integration range of Ω in (3.21b), from the infinite range $[-\infty,\infty]$ to the finite one $[-\Omega_M,\Omega_M]$:

$$y(t) \cong y_2(t) = \frac{1}{2\pi} \int_{-\Omega_M}^{\Omega_M} Y(\Omega)\, e^{j\Omega t} d\Omega \tag{3.40a}$$

with

$$\Omega_M = \Delta\Omega \times (N/2). \tag{3.40b}$$

The second step is the discretization of the integrand, both in (3.21b) and in (3.40a). Continuous variable Ω is replaced by the discrete one, $m\Delta\Omega$. In addition, $Y(\Omega)$ and $e^{j\Omega t}$ are represented by their samples at these discrete values. Then, the application of rectangular integration to (3.40a) yields (3.39).

A detailed analysis of the two steps, truncation and discretization, is provided below.

3.4.1.1 Frequency Range Truncation

Expression (3.40a) is equivalent to [19]

$$y_2(t) = \frac{1}{2\pi}\int_{-\infty}^{\infty} Y(\Omega)\, H_R(\Omega)\, e^{j\Omega t} d\Omega, \tag{3.41}$$

with

$$H_R(\Omega) = \begin{cases} 1, & |\Omega| \le \Omega_M \\ 0, & |\Omega| > \Omega_M \end{cases}. \tag{3.42}$$

$H_R(\Omega)$ is a rectangular (truncation) window and is plotted in Figure 3.15(a). Its time domain image is given by the following expression and is plotted in Figure 3.15(b):

$$h_R(t) = \left(\frac{\Omega_M}{2\pi}\right)\frac{\sin\left(\Omega_M t\right)}{\left(\Omega_M t\right)} \tag{3.43}$$

Figures 3.15(a) and (b) should be compared with Figures 3.13(a) and (b). Note from Figure 3.15(b) that the zeros of $h_R(t)$ occur at regular intervals of size $t_0 = \pi/(2\Omega_M)$. If the truncation frequency Ω_M is made larger (i.e. wider bandwidth), the main lobe of $h_R(t)$ becomes taller and, at the same time, narrower. In the limit, as $\Omega_M \to \infty$, $h_R(t)$ approaches the impulse function $\delta(t)$ in much the same manner as with $R(t)$ in Figure 3.9(b).

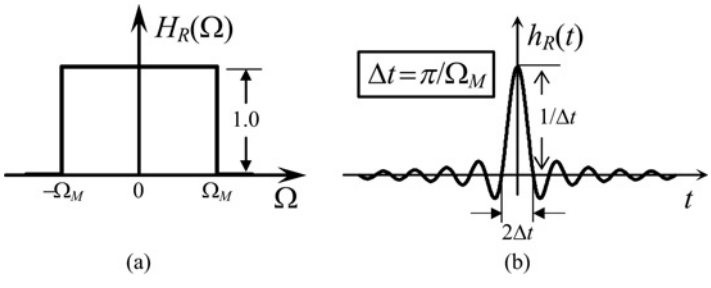

Figure 3.15 Rectangular (truncating) window: (a) frequency response $H_R(\Omega)$; (b) time-domain image $h_R(t)$.

The time-domain relation between $y(t)$ and its approximation $y_2(t)$ is obtained by applying the convolution theorem to (3.41) to give

$$y_2(t) = y(t) * h_R(t). \tag{3.44}$$

The effect of truncating the frequency range is observed at its best on signals with discontinuities. Suppose that the original signal $y(t)$ is the unit step function $u(t)$ defined as

$$u(t) = \begin{cases} 0, & t < 0 \\ 1, & t \geq 0 \end{cases}. \tag{3.45}$$

Figure 3.16(a) provides a plot of $u(t)$, while Figures 3.16(b) and (c) illustrate its convolution with $h_R(t)$ as given by (3.43). The latter figure depicts the approximation to $u(t)$ obtained by truncating its spectrum. Four important features of this approximation should be noted. The first is that, as a filter, the rectangular window is non-causal. It is clear from the comparison of Figures 3.16(a) and (c) that the window output $y_2(t)$ starts responding before $t = 0$; that is, before the input $y(t) = u(t)$ starts acting. The second feature is that the discontinuity at $t = 0$ is approximated by a continuous segment with a non-zero rise time amounting to $0.42\Delta t$. The third is the presence of oscillations that are most pronounced near the instant of the discontinuity. These oscillations are referred to as the Gibbs phenomenon. The fourth feature is the overshoot after the discontinuity, which reaches a peak value in the order of 9.0%.

The step function approximation of Figure 3.16(c) is of special interest for transient analysis. Every signal with an isolated discontinuity is equivalent to a continuous one with a superimposed step function. A major concern in FD transient analysis is the 9.0% level of overshoot that cannot be decreased by making the truncation frequency Ω_M larger [7]. In practice, it is decreased and a better approximation to $y(t)$ is obtained by applying a smoothing filter. By observing that the Gibbs errors have an oscillation interval $t_{Gibbs} = \pi/\Omega_M$, one can see that an effective smoother is a sliding window of duration π/Ω_M – see Figure 3.16(c). For an improved estimate of $y(t)$, first the sliding window is centred at each point t_x of the time range, then a weighted average is performed with all the values of $y_2(t)$ inside the window, next the result of this average is assigned to the new estimate of $y(t)$ at t_x, finally, the process is applied to all values of t in the range.

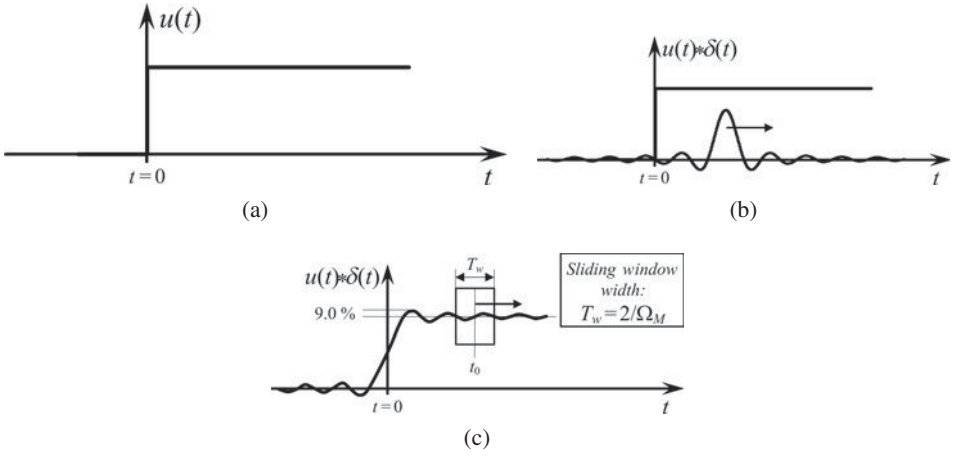

Figure 3.16 Effects of frequency truncation: (a) unit step function $u(t)$; (b) convolving signals $u(t)$ and $h_R(t)$; (c) convolution result and sliding window.

The Lanczos window is a smoothing filter that applies pure averaging (or constant weight) along its aperture. Its frequency response is [19]

$$\sigma_L(\Omega) = \begin{cases} \dfrac{\sin\left(\pi\Omega/\Omega_M\right)}{\left(\pi\Omega/\Omega_M\right)}, & |\Omega| \le \Omega_M \\ 0, & |\Omega| > \Omega_M. \end{cases} \tag{3.46}$$

Figure 3.17(a) shows a plot of $\sigma_L(\Omega)$ that should be compared with the rectangular window in Figure 3.15(a). This comparison shows that the time-domain averaging is equivalent to a continuous and gradual truncation of the signal spectrum. The truncation of the spectrum of unit step (3.43) by the Lanczos window results in the waveform plotted in Figure 3.17(b). It can be seen that Lanczos window reduces the overshoot to 1.2%. This reduction comes at the expense of introducing a slightly larger delay in the estimated signal; that is, the rise time amounts now to $0.73\Delta t$.

A highly recommended window for transient analysis is the one by Von Hann (or Hanning). Apparently, its use for this purpose was first proposed in [20]. The frequency response of the Hanning window is

$$\sigma_{VH}(\Omega) = \begin{cases} \dfrac{1}{2} + \dfrac{\cos\left(\pi\Omega/\Omega_M\right)}{2}, & |\Omega| \le \Omega_M \\ 0, & |\Omega| > \Omega_M \end{cases} \tag{3.47}$$

and the corresponding plot is shown in Figure 3.17(c). In addition to applying a continuous and gradual truncation, $\sigma_{VH}(\Omega)$ presents a continuous first derivative at the cut-off frequencies $\pm\Omega_M$.

The Hanning window further reduces the overshoot to 0.63%; the rise time, however, is increased to $0.87\Delta t$.

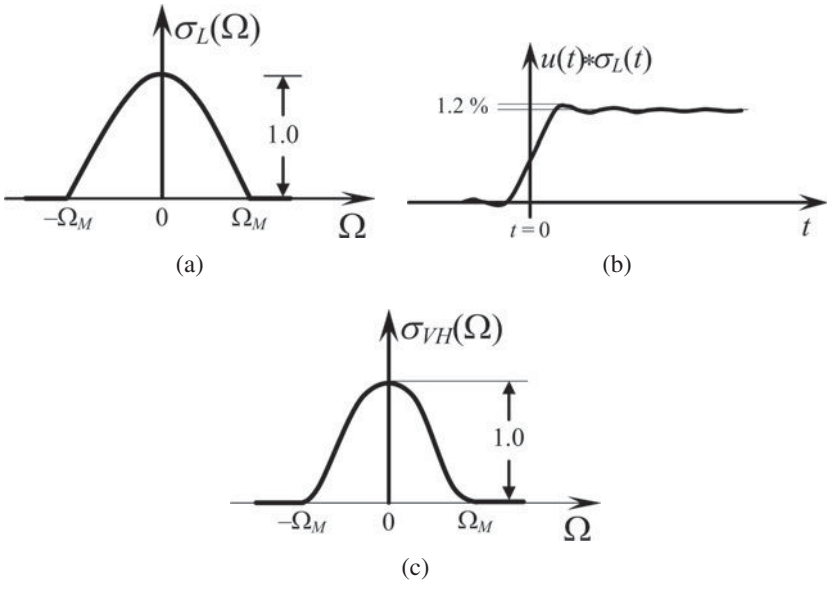

Figure 3.17 Lanczos Window: (a) frequency response; (b) time response when applied to a step function; (c) Von Hann or Hanning window.

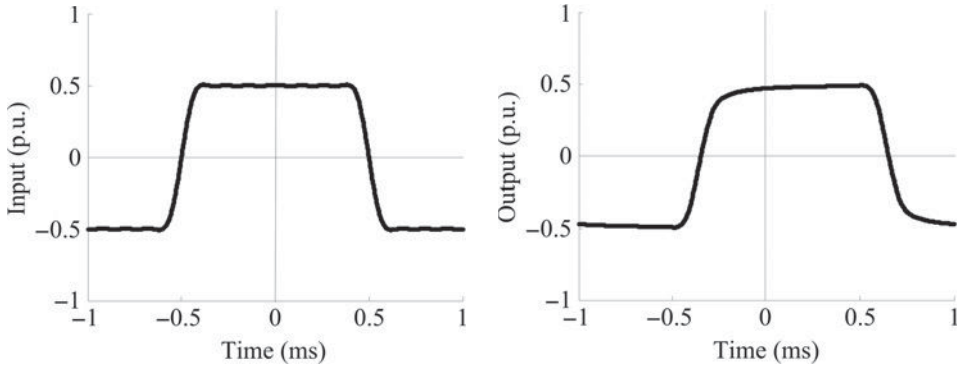

Figure 3.18 Example 3.2: (a) approximating square wave signal of Figure 3.5(c) by a partial Fourier series with coefficients weighted by the Hanning window; (b) response of system in Figure 3.5(b) obtained by the modified Fourier series.

Example 3.2 Consider again the transmission system described in Figures 3.5(a) and (b), as well as the input signal in Figure 3.5(c). Again $v_{in}(t)$ is approximated by the finite Fourier series (3.10) with $K = 17$. This time, however, the series coefficients are multiplied by $\sigma_{VH}(\Omega)$ as given by (3.47). Figure 3.18(a) shows a plot of the reconstruction of $v_{in}(t)$ through partial series (3.10) with its coefficients further modified by the Hanning window. Compare this plot with the one in Figure 3.6(a). Figure 3.18(b) shows a plot of the new system output. Note the practical absence of the Gibbs errors and compare this last plot with the one in Figure 3.6(b).

The finite Fourier series will approximate periodic waveforms by minimizing the power of the error signal (i.e. least mean square error of the difference). However, a series approximation with minimum overshoot error is preferable in transient analysis. The reason is that the main objective here is usually to determine overvoltage and overcurrent levels.

3.4.1.2 Discrete Frequency Range

Consider now that a transient signal $y(t)$ is to be synthesized from samples of its spectrum $Y(\Omega)$, and that the frequency range is not truncated. By applying rectangular integration in (3.21b), the following approximation is obtained:

$$y(t) \cong y_3(t) = \frac{\Delta\Omega}{2\pi} \sum_{m=-\infty}^{\infty} Y(m\Delta\Omega)\, e^{j(m\Delta\Omega)t}$$

This expression is also obtained by multiplying $Y(\Omega)$ by $\Delta\Omega\delta_{\Delta\Omega}(\Omega)$ and applying the inverse Fourier transform to the product. Recall from (3.26b) that $\delta_{\Delta\Omega}(\Omega)$ is a train of unit pulses placed at regular intervals of length $\Delta\Omega$ along the frequency axis:

$$y_3(t) = \frac{1}{2\pi} \int_{-\infty}^{\infty} Y(\Omega) \left[\Delta\Omega \sum_{k=-\infty}^{\infty} \delta(\Omega - k\Delta\Omega) \right] e^{j\Omega t} d\Omega$$

From (3.26a) and from the convolution theorem

$$y_3(t) = \int_{-\infty}^{\infty} \left[\sum_{k=-\infty}^{\infty} \delta(\tau - kT) \right] y(t-\tau)\, d\tau,$$

where $T = 2\pi/\Delta\Omega$. By exchanging the order between the integral and the summation, and by further performing the integral, the following relation between $y_3(t)$ and $y(t)$ is obtained:

$$y_3(t) = \left[\sum_{k=-\infty}^{\infty} y(t-kT) \right] \tag{3.48}$$

This shows that the discretization of $Y(\Omega)$ produces time-domain aliasing. As transient signals are generally not time-limited, the question here is: what are the conditions to obtain good approximations to $y(t)$ by $y_3(t)$ given in (3.48)? Clearly, since $y_3(t)$ is periodic the useful range of the approximation has to be confined to the interval $[0,T]$.

To address the previous question consider first the case of $y(t)$ being a unit step $u(t)$. According to (3.48), direct sampling of its spectrum of $u(t)$ results in an excessive aliasing error; that is, the value for approximation $y_3(t)$ turns out to be infinite. Let now the unit step be multiplied by a damping exponential [21]:

$$y(t) = u(t) \times e^{-ct}$$

and the spectrum of the resulting function $y(t)$ be sampled. From (3.48):

$$y_3(t) = \sum_{k=-\infty}^{\infty} u(t-kT)\, e^{-c(t-kT)} \tag{3.49}$$

Figure 3.19 depicts $y_3(t)$ as in (3.49). Notice that if attention is restricted to interval $[0,T]$, $y_3(t)$ is composed only of $y(t)$ and all its past replicas:

$$y_3(t) = \sum_{k=-\infty}^{0} u(t)\, e^{-c(t-kT)}$$

Reordering and then factoring terms gives

$$y_3(t) = u(t)\, e^{-ct} \sum_{k=0}^{\infty} \left(e^{-cT}\right)^k.$$

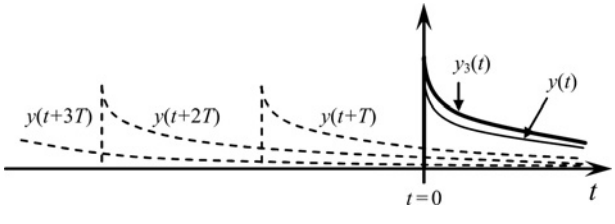

Figure 3.19 Aliasing effect on an exponentially decaying step function.

This expression is a geometric series and $0 < e^{-cT} < 1$; hence

$$y_3(t) = u(t)\, e^{-c\,t} \frac{1}{1 - e^{-cT}}. \tag{3.50}$$

It follows from (3.50) that the aliasing error is given by the factor $1/(1 - e^{-cT})$. In addition, if $e^{-cT} \ll 1$, then

$$y_3(t) \cong u(t)\, e^{-ct} \left(1 + e^{-cT}\right),$$

and the relative aliasing error is

$$\varepsilon_{rel} = \frac{y_3(t) - y(t)}{y(t)} \cong e^{-cT}. \tag{3.51}$$

Finally, the original signal $u(t)$ is recuperated with some aliasing error after multiplying $y_3(t)$ by undamping exponential e^{+ct} as

$$u(t) \cong y_3(t)\, e^{ct} = u(t) + u(t)\, e^{-cT}.$$

This example illustrates the technique for controlling aliasing errors by introducing exponential damping. Despite its simplicity, the case of a step function is highly relevant for transient analysis. Power systems are composed by passive elements, so their natural responses are bounded, and mostly decaying. One can therefore assume that the step function is a good representative of the worst case of natural responses and of excitation signals. A highly convenient form to introduce the damping coefficient c in FD transient studies is by working directly in the Laplace domain. The result in (3.51) is useful for fixing this coefficient that is incorporated in the Laplace variable as $s = c + j\Omega$.

3.4.2 Fourier and Laplace Transforms

While the Fourier transform is appropriate for steady-state analysis, the Laplace transform is far better suited for transient studies. It is thus convenient to establish the relationship between these two transforms. Many signals of practical interest are not of energy, and their Fourier transforms cannot be assured. Often, however, when these signals are damped by a decaying exponential factor – as has been shown above – the Fourier transform becomes applicable.

Consider a signal $x(t)$, along with the modification

$$x_{MOD}(t) = x(t) \times u(t) \times e^{-ct}. \tag{3.52}$$

Assume that $x_{MOD}(t)$ is an energy signal and obtain its Fourier transform as

$$X_{MOD}(\Omega) = \int_{-\infty}^{\infty} x(t)u(t)e^{-ct}e^{-j\Omega t}dt = \int_{0}^{\infty} x(t)\, e^{-(c+j\Omega)t}dt. \tag{3.53}$$

By introducing the Laplace variable $s = c + j\Omega$ we obtain

$$X_{MOD}(j(c - s)) = \int_{0}^{\infty} x(t)e^{-st}dt.$$

Based on this last result, the one-sided Laplace transform is introduced as [8]

$$X_L^+(s) \stackrel{\Delta}{=} \int_{0-}^{\infty} x(t)e^{-st}dt \stackrel{\Delta}{=} X_{MOD}(\Omega). \tag{3.54}$$

Note that the lower bound of the integral is taken as '0–'. This choice is convenient for resolving ambiguities that can arise from signals with a discontinuity at $t = 0$ [8]. Such discontinuities occur commonly in transient analysis.

The corresponding Laplace inversion integral is now obtained. First, the inverse Fourier transform is applied to (3.53) as

$$x(t)u(t)e^{-ct} = \frac{1}{2\pi}\int_{-\infty}^{\infty} X_{MOD}(\Omega)\, e^{j\Omega t}d\Omega. \tag{3.55}$$

Then, both sides of (3.55) are multiplied by e^{ct}. Next, the Laplace variable $s = c + j\Omega$ is introduced and the assumption is made of $x(t)$ being zero as $t < 0$. Finally, all these changes lead to the inverse (one-sided) Laplace transform

$$x(t) = \frac{1}{2\pi j}\int_{c-j\infty}^{c+j\infty} X_L^+(s)e^{st}ds. \tag{3.56}$$

For ease of notation reasons, here as in most texts on the subject the symbol $X()$ is hereafter used indistinctly to denote the Laplace or the Fourier transform of $x(t)$. To avoid the confusion that this may bring, the strong recommendation is made to always keep in mind that $X(s)$ is a shorthand notation for $X_L^+()$ in (3.54) and in (3.56).

3.4.3 The Numerical Laplace Transform

One of the major advantages of analysing transients in the frequency domain is that signal relations involving integrals, derivatives and convolutions become algebraic expressions. For practical analysis, Fourier and Laplace transforms must be applied in discrete form, and it has been shown already that FD discretization produces TD aliasing errors. These errors can be controlled by introducing a damping coefficient, and this is most conveniently done with the Laplace transform.

Now let $X(s)$ denote the (one-sided) Laplace transform of transient signal $x(t)$. A first approximation to the numerical solution of the inverse Laplace transform (3.56) is

$$x(n\Delta t) = \frac{\Delta\Omega}{2\pi}\sum_{m=-(N/2)}^{(N/2)-1} X(c + jm\Delta\Omega)e^{cn\Delta t}e^{jmn\Delta\Omega\Delta t} \quad n = 0,\ 1,\ 2, \ldots,\ N-1. \tag{3.57}$$

In agreement with the principle of conservation of information, the number of TD samples in (3.57) has been made equal to N, which is the number of samples in FD. In addition, N determines the observation time for $x(t)$ as

$$T = N\Delta t. \tag{3.58}$$

Recall that a maximum value for the observation time has already been established by virtue of T being the repetition (or aliasing) period in (3.48):

$$T = 2\pi/\Delta\Omega \tag{3.59}$$

The combination of (3.58) and (3.59) yields the relation

$$\Delta t \Delta\Omega = 2\pi/N. \tag{3.60}$$

The introduction of (3.60) into (3.57) yields

$$x(n\Delta t) = \frac{e^{cn\Delta t}}{\Delta t}\left[\frac{1}{N}\sum_{m=-(N/2)}^{(N/2)-1} X(c + jm\Delta\Omega)\, e^{2\pi jmn/N}\right] \quad n = 0,\ 1,\ 2, \ldots,\ N-1. \tag{3.61}$$

Note in (3.61) that the term inside the braces is an IDFT. It is thus convenient to modify the summation index as

$$x(n\Delta t) = \frac{e^{cn\Delta t}}{\Delta t}\left[\frac{1}{N}\sum_{m=0}^{N-1} X(c + jm\Delta\Omega)\, e^{2\pi jmn/N}\right] \quad n = 0,\ 1,\ 2, \ldots,\ N-1, \tag{3.62}$$

where, for $m > N/2$

$$X(c + jm\Delta\Omega) = X^*(c + j(N-m)\Delta\Omega),$$

and $X^*()$ denotes the complex conjugate of $X()$.

To minimize the Gibbs (frequency truncation) errors in (3.62), the discrete FD samples $X(c + jm\Delta\Omega)$ are multiplied by a data window. The Hanning window is recommended here [20], and:

$$x(n\Delta t) = \frac{e^{cn\Delta t}}{\Delta t}\, ifft\left\{\left[X(c + jm\Delta\Omega) \times \sigma_{VH}(m\Delta\Omega)\right]_{m=0}^{N-1}\right\}. \tag{3.63}$$

where *ifft* stands for inverse fast Fourier transform.

This expression is the inverse numerical Laplace transform. Note that the summation of (3.62) is performed in (3.63) through the FFT algorithm. Aliasing error minimization is attained here by a proper choice of damping coefficient c.

It follows from (3.51) that the relation between the overall relative aliasing error and the damping coefficient is

$$c = -\left[\log_e\left(\varepsilon_{rel}\right)\right]/T. \tag{3.64}$$

Ideally, one would like to specify an arbitrary small value for ε_{rel}, but there are practical limits to this. For the frequency sampling used in (3.57), Wedepohl reports in [18] the following rule, which has been found by experience,

$$\varepsilon_{rel} = 1/N. \tag{3.65}$$

In summary, numerical Laplace transform inversion is attained through (3.63). In practice, we have to choose two or at most three parameters to apply this expression. By setting the maximum observation time T, the frequency resolution $\Delta\Omega$ is fixed automatically by (3.59). Choice of maximum or cut-off frequency Ω_M automatically determines Δt as the Nyquist sampling interval in (3.28a). In power system

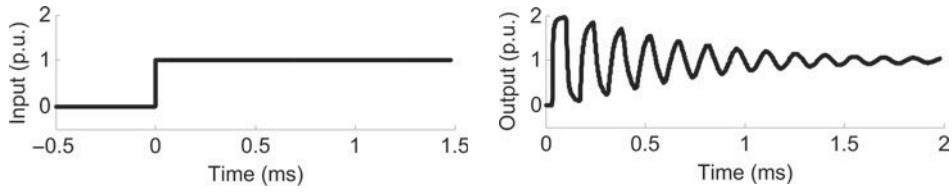

Figure 3.20 Example 3.3: (a) excitation signal; (b) response.

analysis the bandwidth for the different types of transient events is generally well established. As T and Δt (or Ω_M and $\Delta\Omega$) are given, the number of samples N is determined. When N is not of the form 2^i, it is recommended here to choose the next largest value that is an integer power of 2. To select a suitable value for damping coefficient c, recommendation is made here for the use of Wedepohl's relation (3.65). As an observation time T is being set for a specific analysis, we have to take into consideration that 3–5% of the last samples obtained by (3.58) are useless due to amplification of runaway aliasing and Gibbs errors.

3.4.4 Application Examples with the NLT

Example 3.3 Consider again the transmission line studied in Example 3.1. The line data is given in Figure 3.5(a), and the longitudinal layout is provided by Figure 3.5(b). This time, however, the line is terminated in a three-phase open circuit and the input signal is a step function starting at $t = 0$. Unlike Example 3.1, the system response now includes a transient component. Figure 3.20(a) depicts the input step function, while Figure 3.20(b) shows the far-end response obtained with the NLT using $N = 2048$ samples. In Figure 3.20(b) observe the response delay due to the travel time of the line. Observe also the transient oscillations caused by the reflection at the line open end. Note that the oscillation period is four times the line travel time.

Example 3.4 Figure 3.21(a) shows the connection diagram for the line in Figure 3.21(b) [22,23]. The transient recovery voltage of switch t_2 is to be obtained. The simulation starts at $t = 0$, with the simultaneous phase energizing and with a permanent fault at the line end. The fault condition is represented by the three 0.1 Ω shunt resistances. After 2 ms of energizing, the switches open simultaneously.

The transient recovery voltage at switch t_2 is shown in Figure 3.21(c) as calculated with the NLT using a resolution of $\Delta t = 20$ μs. Figure 3.21(c) shows also the results obtained with the EMTP using the FD line model with two integration steps: $\Delta t = 20$ μs and $\Delta t = 2$ μs. It can be observed in this figure that when the resolution of $\Delta t = 20$ μs is used, the NLT and EMTP result differ substantially. As the resolution is increased ten times in EMTP ($\Delta t = 2$ μs), the result becomes closer to the one with the NLT. It should be stressed here that essentially the same results are obtained by using the universal line model (ULM) [24] with the EMTP.

Currently, the NLT cannot produce sequential real-time and off-line simulations. In these cases, we have to rely on advanced TD-EMTP models. Nevertheless, this last example illustrates the form in which frequency-domain methods assist in the development and fine-tuning of EMTP study cases.

3.4.5 Brief History of NLT Development

In addition to the NLT technique that is described here, various other methods have been developed for applying Laplace transforms to transient system analysis. The one presented in [13] deserves special

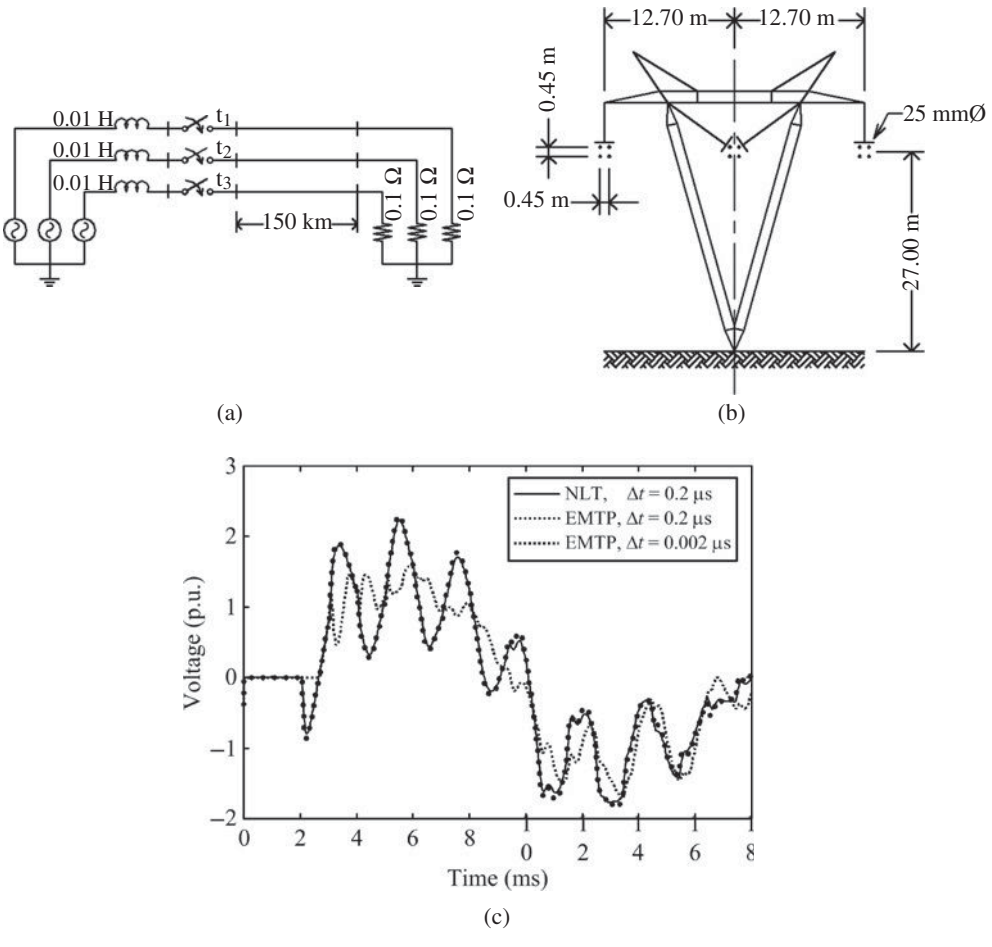

Figure 3.21 Example 3.4: (a) system Layout; (b) line data; (c) comparing NLT and EMTP results: NLT ($\Delta t = 20$ μs), EMTP1 ($\Delta t = 2$ μs), EMTP2 ($\Delta t = 20$ μs).

attention, although it still is at a very early stage of development. The technique described here originated in the early 1960s by the works of Mullineux *et al.* [21, 25, 26]. It then evolved in the late 1960s through the work of Wedepohl *et al.* [27–30]. At that time, the technique was referred to as the modified Fourier transform. In the early 1970s, Ametani introduced the use of the FFT algorithm [31]. In the late 1970s, Wilcox produced a systematic view of the methodology relating it to Laplace transform theory, and he provided important criteria for its practical application [17]. In the early 1980s, Wedepohl introduced into the technique further refinements that have enabled very high accuracy [18]. More recent work on the NLT can be found in [10, 11, 15, 20, 22, 23, 32–34].

3.5 Multirate Transient Analysis

Consider a large network in which two regions can be distinguished: region 1 with an ongoing fast disturbance and region 2 with operation close to the steady state. The network may be conveniently

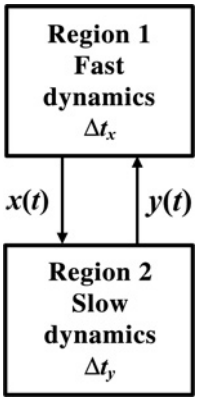

Figure 3.22 Subdivision of a large network into two regions operating with different dynamics.

subdivided for its analysis in these two regions as illustrated in Figure 3.22. The interface between the regions is through the exchange variables $x(t)$ and $y(t)$. The first conveys the necessary information from the fast to the slow dynamics region. The second carries this information from the slow to the fast region. The network can be simulated digitally with two different sampling rates. A high rate $F_{XS} = 1/\Delta t_x$ is assigned to the simulation of region 1 and it has to be in agreement with its fast dynamics. The other is a slower rate $F_{YS} = 1/\Delta t_y$ used for region 2. In practical situations these two rates can be up to three orders of magnitude apart, and the savings in computational time make it highly attractive to pursue two-rate and even multirate simulation techniques.

Signal $x(t)$ is produced by the ongoing processes in region 1. Digital simulation of this region delivers a discrete version of $x(t)$ as

$$x_d(n) = x(n\Delta t_x) \quad n = 0, 1, 2, \ldots .$$

The spectrum of $x_d(n)$, denoted here as $X_d(\Omega)$, has to be periodic with repetition interval $2\Omega_{XM} = 2\pi F_{XS}$. This is illustrated in Figure 3.23(a). The maximum frequency Ω_{XM} must be chosen sufficiently high so that $x_d(n)$ provides an accurate representation of $x(t)$.

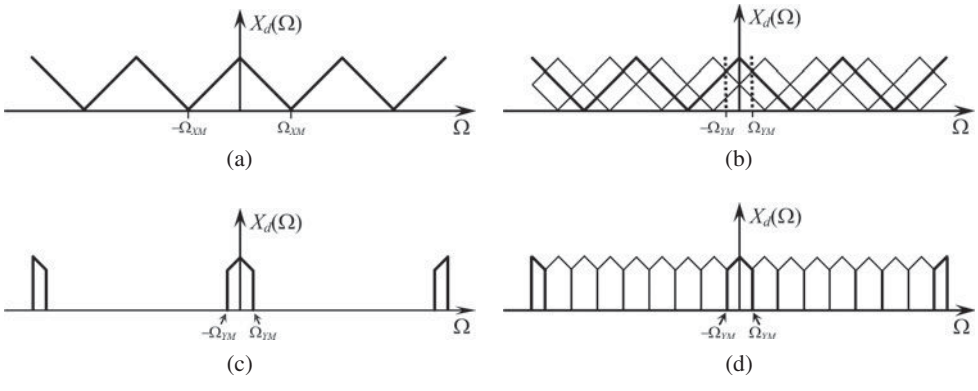

Figure 3.23 (a) Spectrum of signal $x_d(n)$; (b) spectrum of $x_d(n)$ after decimation by an L-factor; (c) filtering of by an ideal filter; (d) spectrum of $x_d(n)$ after being filtered and before decimated.

Consider now that the samples of $x_d(n)$ are produced at the rate F_{XS}. Region 2 simulation cannot accept all these samples, as it runs at the lower rate F_{YS}. Suppose that F_{XS} is L times faster than F_{YS}, or that time-step Δt_y is L times larger than Δt_x. Signal $x_d(n)$ must thus be decimated by an L-factor; that is, for every L samples of $x_d(n)$ one is kept and the other $L-1$ are discarded. A new signal $x'_d(n) = x_d(nL)$ is produced by this decimation process that is represented as

$$(\downarrow L)\, x_d(n) = x'_d(n) = x_d(nL).$$

The spectrum of $x'_d(n)$ is a further periodization of $X_d(\Omega)$, now with a repetition interval $2\Omega_{YM} = 2\Omega_{XM}/L$. Figure 3.23(b) illustrates this, and it can be seen that aliasing errors could be severe. To avoid these errors, signal $x_d(n)$ should be filtered before the decimation [35]. Figure 3.23(c) illustrates the filtering of $x_d(n)$ by an ideal low-pass filter (LPF). Now the maximum frequency of the filtered signal is Ω_{YM}. Figure 3.23(d) shows the spectrum of the new signal after being decimated by an L-factor – note the absence of aliasing. Although ideal filters are non-realizable, good results can be obtained in practice from a real filter with cut-off frequency Ω_{YM} and with sufficient attenuation in its transition band [35].

Concerning signal $y(t)$, being produced by the ongoing processes in region 2, suppose that it is reproduced in discrete form as $y_d(n)$ by digital simulation. The following time-step is used:

$$\Delta t_y = \pi/\Omega_{YM}$$

with $\Omega_{YM} = \Omega_{XM}/L$. Hence

$$y_d(n) = y(n\Delta t_y) \quad n = 0, 1, 2, \ldots .$$

In the same form as with signal $x_d(n)$, the spectrum of $y_d(n)$ is periodic with repetition interval $2\Omega_{YM}$. This is depicted graphically in Figure 3.24(a). The samples of signal $y_d(n)$ are produced at a much lower rate than that required by region 1 simulation. The rate of $y_d(n)$ has to be increased L times by interpolating $L-1$ samples in between every two consecutive values. The interpolation is performed conveniently first by inserting $L-1$ zeros between the consecutive samples, and then by low-pass filtering the new signal with cut-off frequency Ω_{YM} [35]. The process of interpolation is represented as

$$(\uparrow L)\, y_d(n) = y'_d(n) = \begin{cases} y_d(n/L) & n = 0, \pm L, \pm 2L, \ldots \\ 0 & \textit{otherwise} \end{cases}.$$

The insertion of zeros in $y_d(n)$ increases the signal sampling rate by L times without modifying the information content of the signal. This means that now the repetition interval is $2\Omega_{XM}$ and the effective bandwidth has been increased to $\pm\Omega_{XM}$. This new bandwidth is also marked in Figure 3.24(a). Note that

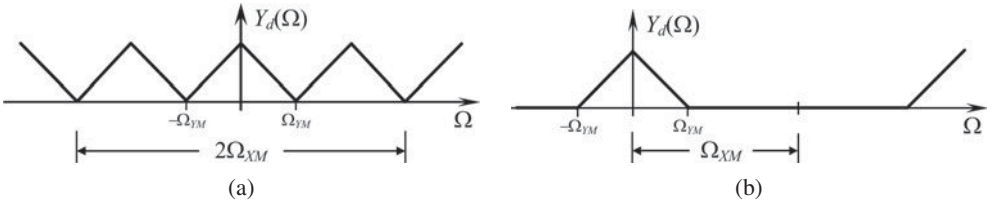

Figure 3.24 (a) Spectrum of signal $y_d(n)$; (b) spectrum of signal $y_d(n)$ after the interpolation and filtering processes.

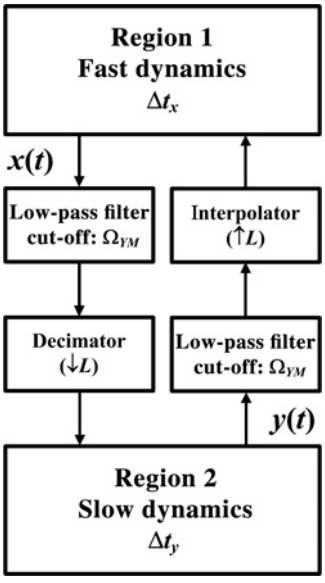

Figure 3.25 Interconnection of a two-rate process with an interface to avoid aliasing errors.

the spectral components outside the range $\pm\Omega_{YM}$ are unwanted aliasing replicas. Their removal by an ideal LPF with Ω_{YM} cut-off frequency is illustrated in Figure 3.24(b).

Finally, Figure 3.25 provides a modification to the diagram of Figure 3.22, where the required interfaces have been included to avoid the aliasing errors that would otherwise be caused by interconnecting two simulation processes running at different rates. This interfacing is based on the assumption that the faster rate is an integer multiple of the slower one.

3.6 Conclusions

Transient analysis of power systems can be done by different methods, in either the time domain or the frequency domain. It has been stated here that time-domain methods, such as the EMTP, are the most used in practical applications. Two important reasons for this are (1) they are easier to understand and apply to a very wide class of problems, and (2) their requirements in terms of computation resources are moderate. However, it has been shown here that frequency-domain methods are valuable complements to the time-domain ones. Most times, power system element models and power system equivalents are synthesized in the frequency domain, and their frequency-domain analysis can attain unmatched numerical accuracies. Frequency-domain methods can thus be used to verify and fine-tune the time domain models and procedures.

The increasing size and complexity of modern power systems requires correspondingly more powerful tools for analysis, and power system engineers must be well acquainted now with frequency-domain analysis (FDA) and digital signal processing (DSP) disciplines. In this chapter, first FDA was introduced as an extension of phasor analysis, as this is more familiar to power engineers. Then, the differences between continuous time and discrete time FDA was examined. A central topic here is sampling theorem and its implications in the simulation and analysis of power system transients. Next, the numerical Laplace transform method for analysing power transients was explained and its application illustrated by two examples. Finally, the possibility of conducting multirate transient analysis in the time domain was examined through frequency-domain analysis.

Acknowledgement

The authors gratefully acknowledge the assistance of Octavio Ramos Leaños and Efraín Cruz Chan in preparing the examples.

References

[1] Semlyen, A. and de León, F. (1993) Computation of electromagnetic transients using dual or multiple time-steps. *IEEE Transactions on Power Systems*, **8**(3), 1274–1281.

[2] Szczupak, J. (1999) Real time, oscillation free network digital simulation. Proceedings of International Conference on Power Systems Transients, Paper 032, Budapest, Hungary, June 1999.

[3] Pöller, M. and Schiemieg, M. (1999) Exploiting multiple timescale properties for fast simulation algorithms. Proceedings of the 13th Power Systems Computation Conference, Trondheim, Norway, 1999.

[4] Szczupak, J., Facerolli, S.T. and Guedes, K.B. (2003) Electrical network simulation by multirate parallel digital filter structures. Proceedings of IEEE Power Tech Conference, Bologna, Italy, June 2003.

[5] Zini, H. and Ratta, G. (2004) Multirate modeling scheme for electromagnetic transients calculation. *IEEE Transactions on Power Delivery*, **19**(1), 240–247.

[6] Naredo, J.L., Guardado, J.L., Gutiérrez-Robles, J.A., *et al.* (2009) Trends in the frequency domain analysis of electromagnetic transients. Proceedings of IEEE Power & Energy Society General Meeting, Calgary, AB, Canada, July 2009, pp. 1–5.

[7] Hsu, H.P. (1970) *Fourier Analysis*, Simon & Schuster, Inc.

[8] Proakis, J.G. and Manolakis, D.G. (2007) *Digital Signal Processing. Principles, Algorithms and Applications*, 4th edn, Prentice-Hall.

[9] Lathi, B.P. (1992) *Linear Systems and Signals*, Berkeley Cambridge Press.

[10] Ramirez, A., Gómez, P., Moreno, P. and Gutiérrez, A. (2004) Frequency domain analysis of electromagnetic transients through the numerical Laplace transforms. Proceedings of IEEE Power Eng. Society General Meeting, June 2004, pp. 1136–1139.

[11] Naredo, J.L., Gutiérrez, J.A., Uribe, F.A., *et al.* (2007) Frequency domain methods for electromagnetic transient analysis. Proceedings of IEEE Power Eng. Society General Meeting, Tampa, FL, June 2007, pp. 1–7.

[12] Gustavsen, B. (2005) Validation of frequency-dependent line models. *IEEE Transactions on Power Delivery*, **20**(2), 925–933.

[13] Vlach, J. and Singhal, K. (2003) *Computer Methods for Circuit Analysis and Design*, 2nd edn, Kluwer Academic Publishers.

[14] Humpage, W.D. and Wong, K.P. (1982) Electromagnetic transient analysis in EHV power networks. *Proceedings of the IEEE*, **70**(4), 379–402.

[15] Watson, N.R. and Irwin, G.D. (2000) Comparison of root-matching techniques for electromagnetic transient simulation. *IEEE Transactions on Power Delivery*, **15**(2), 629–634.

[16] Noda, T. and Ramirez, A. (2007) z-Transform-based methods for electromagnetic transient simulations. *IEEE Transactions on Power Delivery*, **22**(3), 1799–1805.

[17] Wilcox, D.J. (1978) Numerical Laplace transformation and inversion. *International Journal of Electrical Engineering Education*, **15**, 247–265.

[18] Wedepohl, L.M. (1983) Power system transients: Errors incurred in the numerical inversion of the Laplace Transform. Proceedings of the Twenty-Sixth Midwest Symposium on Circuits and Systems, pp. 174–178.

[19] Day, S.J., Mullineux, N. and Reed, J.R. (1965) Developments in obtaining transient response using Fourier transforms. Part I: Gibbs phenomena and Fourier integrals. *International Journal of Electrical Engineering Education*, **3**, 501–506.

[20] Naredo, J.L., Moreno, P., Guardado, J.L. and Gutiérrez, J.A. (1998) The numerical Laplace transform as a tool for research and development in electrical engineering (in Spanish). Proceedings of the 2nd International Conference on Electrical and Electronics Conference, Aguascalientes, Mexico, September 1998.

[21] Day, S.J., Mullineux, N. and Reed, J.R. (1966) Developments in obtaining transient response using Fourier transforms. Part II: Use of the Modified Fourier transform. *International Journal of Electrical Engineering Education*, **4**, 31–40.

[22] Gómez, P., Moreno, P., Naredo, J.L. and Guardado, J.L. (2003) Frequency domain transient analysis of transmission networks including nonlinear conditions. Proceedings of IEEE PowerTech Conference, Paper BPT03–115, Bologna, Italy, June 2003.

[23] Moreno, P., Gómez, P., Naredo, J.L. and Guardado, J.L. (2005) Frequency domain transient analysis of transmission networks including nonlinear conditions. *International Journal of Electrical Power and Energy Systems*, **27**(2), 139–146.

[24] Morched, A., Gustavsen, B. and Tartibi, M. (1999) A universal model for accurate calculation of electromagnetic transients in overhead lines and underground cables. *IEEE Transactions on Power Delivery*, **14**(3), 1032–1038.

[25] Day, S.J., Battisson, M.J., Mullineux, N. and Reed, J.R. (1968) Developments in obtaining transient response using Fourier transforms. Part III: global response. *International Journal of Electrical Engineering Education*, **6**, 259–265.

[26] Mullineux, N. and Reed, J.R. (1973) Developments in obtaining transient response using Fourier transforms: Part IV: survey of the theory. *International Journal of Electrical Engineering Education*, **10**, 259–265.

[27] Wedepohl, L.M. and Mohamed, S.E.T. (1969) Multiconductor transmission lines. Theory of natural modes and Fourier integral applied to transient analysis. *Proceedings of the IEEE*, **116**(9), 1553–1563.

[28] Wedepohl, L.M. and Mohamed, S.E.T. (1970) Transient analysis of multiconductor transmission lines with special reference to nonlinear problems. *Proceedings of the IEEE*, **117**(5), 979–988.

[29] Wedepohl, L.M. and Indulkar, C.S.I. (1975) Switching overvoltages in short crossbonded cable systems using the Fourier transform. *Proceedings of the IEEE*, **122**(11), 1217–1221.

[30] Wedepohl, L.M. and Indulkar, C.S.I. (1979) Switching overvoltages in long crossbonded cable systems using the Fourier transform. *IEEE Transactions on Power Apparatus and Systems*, **98**(4), 1476–1480.

[31] Ametani, A. (1973) The application of the fast Fourier transform to electrical transient phenomena. *International Journal of Electrical Power and Energy Systems*, **10**, 277–287.

[32] Uribe, F.A., Naredo, J.L., Moreno, P. and Guardado, J.L. (2002) Electromagnetic transients in underground transmission systems through the Numerical Laplace Transform. *International Journal of Electrical Power and Energy Systems*, **24**(3), 215–221.

[33] Moreno, P. and Ramirez, A. (2008) Implementation of the Numerical Laplace Transform: A review. *IEEE Transactions on Power Delivery*, **23**(4), 2599–2609.

[34] Gómez, P. and Uribe, F.A. (2009) The Numerical Laplace Transform: An accurate technique for analyzing electromagnetic transients on power system devices. *International Journal of Electrical Power and Energy Systems*, **31**(2–3), 116–123.

[35] Strang, G. and Nguyen, T. (1997) *Wavelets and Filter Banks*, Wellesley-Cambridge Press.

4

Real-Time Simulation Technologies in Engineering

Christian Dufour and Jean Bélanger

4.1 Introduction

Real-time simulators have always been used to design and test control and protection equipment performance before their installation on actual power systems. Protection and control equipment was usually interfaced with analogue benches emulating the real power systems in order to perform tests under realistic steady-state and faulty operating conditions. Actual control systems as well as analogue benches were, by definition, operating in real time, meaning that control and protection systems under test were exchanging signals at the same speed as when the tested equipment was installed on the actual power systems. The same technique was and is still applied in all industries including automotive, aircraft and aerospace.

Over the past two decades, commercially available computers have become both increasingly powerful and more affordable. This, in turn, has led to the emergence of highly sophisticated simulation software tools enabling high-fidelity real-time simulation of dynamic systems, as well as of fast electromagnetic transients (EMT) expected in electrical and power electronic systems. The consequence is that several expensive analogue test benches and simulators have been replaced by more affordable, very flexible and accurate, fully digital real-time simulators (RTS). The RTS can then be connected in closed-loop with control and protection systems under design and test, as was the case with former analogue simulators. This is called hardware-in-the-loop (HIL) simulation and test. Of course, the RTS must have the bandwidth and the very small latency required to simulate the high-frequency components of the phenomena that can affect the performance of the control and protection systems under test. The RTS must then have the ability to simulate all phenomena within a specified time-step, from μs to milliseconds, depending on the application, as discussed in following sections. But in all cases, the RTS must maintain its real-time performance, that is, all signals must be updated *exactly* at the specified time-step. Otherwise, an overrun or a failure to update its outputs and inputs at the specified time-step will cause unacceptable signal distortion affecting the performance of the equipment under test. Consequently, at the terminals of systems under test, we should not be able to see any difference between the signals generated by the simulator and the real plant systems within a specified bandwidth.

Transient Analysis of Power Systems: Solution Techniques, Tools and Applications, First Edition.
Edited by Juan A. Martinez-Velasco.

Automatic code generation tools are used in conjunction with the current generation of a real-time simulators for implementation in industrial controllers. These simulation software tools, including off-line and real-time tools as well as automatic code generators, form the basis of the 'model-based design' paradigm; a control design methodology that is centred on the use of reference system models and simulation at each design step. In the model-based design (MBD) approach, described in greater detail in the next section, initial modelling and requirements, early controller prototypes, production code generation, production controller testing and integration are all derived from reference models. The approach aims to accelerate the design cycle and reduce total design cost through the early detection of design flaws and other problems. In the automotive industry in particular the MBD method is a de facto standard. MBD is also quickly gaining acceptance and being adopted by design engineers in many different industries.

Real-time controller prototypes, whose development is based on automatic code generation, are being used in many engineering fields and applications, such as aircraft flight control design and validation, industrial motor drive design, complex robotic controller design and power grids. In several cases, the same controller code used for the prototyping phase is also used for the final hardware implementation.

The controller developed for these applications can be tested with scaled-down analogue benches, as was common 15–20 years ago. However, these applications can now benefit from the use of fully digital real-time simulators in a number of ways:

- Real-time simulation produces a set of requirements and specifications that can be used by all teams/subcontractors involved in a project.
- It enables testing of prototypes and actual controllers at or beyond their normal operating limits without the risks involved in testing real devices connected to the actual systems being controlled, especially when high power levels are present. It is easier and less risky to test fault responses on a simulated plant model.
- The simulation acceleration factor obtained by the use of compiled code (instead of the interpreted code used by most simulation tools), as well as by specialized parallel electrical solvers and hardware, enables the realization of rapid batch simulations. More tests can be done in less time.

Fast and real-time simulation can be used for statistical studies using the Monte Carlo simulation method for power grid applications such as finding the statistical distribution of amplitude of overvoltages and overcurrents caused by a series of random events. This analysis can be performed with prototypes or actual fast controller and protection equipment connected to the simulator (HIL). Data fitting/curve matching in the case of aircraft dynamic model parameter identification is another example of the use of fast simulation.

4.2 Model-Based Design and Real-Time Simulation

Model-based design is an engineering process that addresses problems associated with the design of complex systems, and it is based on the extensive use of models and simulation at each design phase. MBD is a methodology based on a workflow known as the 'V' diagram, as illustrated in Figure 4.1. It allows multiple engineers involved in a design and modelling project to use models to communicate knowledge of the system under development in an efficient and organized manner.

The left side of the V-cycle leads to the development of a production-type controller. The right side consists of steps to deploy this controller gradually until the final release.

MBD offers many advantages. By using models, a common design environment is available to every engineer involved in creating a system from beginning to end. Indeed, the use of a common set of tools facilitates communication and data exchange. Reusing older designs is also easier because the design environment can remain homogeneous through different projects. In addition to MBD, graphical

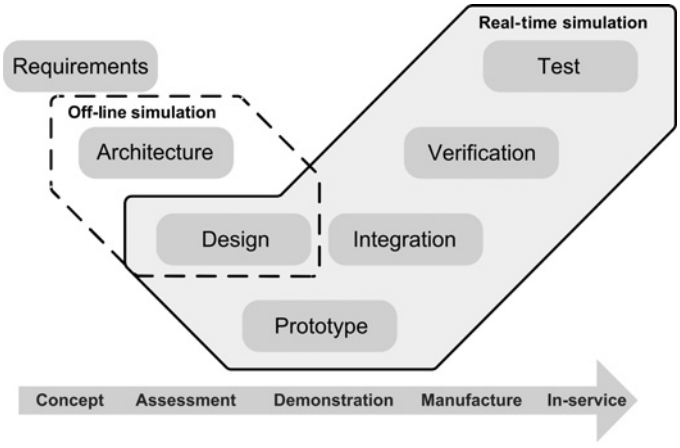

Figure 4.1 Model-based design workflow.

modelling tools, such as the SimPowerSystems toolbox for Simulink from The MathWorks, simplify the design task by reducing the complexity of models through the use of a hierarchical approach.

Most commercial simulation tools provide an automatic code generator (ACG) that facilitates the transition from controller model to controller implementation. The added value of real-time simulation in MBD emerges from the use of an ACG, which translates graphical simulation models into C code. By using an ACG with a real-time simulator, a hardware prototype of the controller – this is called rapid control prototyping (RCP) – can be implemented from a model with minimal effort. The prototype can then be used to accelerate integration and verification testing, something that cannot be done using off-line simulation. The same holds true for HIL testing. By using an HIL test bench, test engineers become part of the design workflow early in the process, sometimes before an actual plant becomes available. For example, by using the HIL methodology, automotive test engineers can start testing of a car or power system controller before a physical test bench is available. Combining RCP and HIL, while using the MBD approach, has many advantages:

- Design issues can be discovered earlier in the process, enabling required trade-offs to be determined and applied, thereby reducing development costs.
- The development cycle duration is reduced, due to parallelization in the workflow.
- Testing costs can be reduced in the mid to long term since HIL test setups often cost less than physical setups, and the real-time simulator can typically be used for multiple applications and projects.
- Test results are more repeatable because real-time simulator dynamics do not change through time the way physical systems do.
- It can replace risky or expensive tests that use physical test benches.

4.3 General Considerations about Real-Time Simulation

4.3.1 The Constraint of Real-Time

The most important aspect of real-time simulation technologies is that they need to make their computations fast enough to keep up with real-world time. Moreover, this constraint must be respected at all times and, specifically in terms of solvers, at all time-steps. This means that the solver used to compute the equations of the phenomenon under study must be optimized with this in mind.

Typically, the differential-algebraic equations (DAE) of the simulated system will be discretized and computed along a sequence of equal time-spaced points. Then, all these points must be computed and completed within the specified time-step. If a time-step is not completed in time, we get what is called an 'overrun', meaning that the simulated process is late compared to real time. Such overruns create distortion of the waveforms injected into the controller under test, which is not acceptable.

4.3.2 Stiffness Issues

One other problem that occurs in simulating electric circuits is that their equations often exhibit stiffness. Stiffness occurs when one simulates a DAE with a spread in the eigenvalues or natural frequencies – let's say high, medium and low – but with a special interest in the medium or 'mid-range' bandwidth phenomena. Non-stiff solvers (e.g. explicit Runge–Kutta) will be unstable because of the higher-frequency components of the DAE. In other words, to simulate these systems with a non-stiff solver, you will be forced to adapt the time-step to the higher frequency component, and the simulation will become extremely long for the frequency of interest. But a certain category of solvers called 'stiff solvers' are able to 'cut through' the high-frequency components and be less influenced by frequency components that are higher than the sampling frequency. Mathematically speaking, the solver stiffness property refers to A-stability or L-stability.

For power systems switching transient studies, people are typically interested in components below 2 kHz. But the equations may have eigenvalues in the MHz range that cannot easily be eliminated. For example, modelling switches with small and high resistance values to simulate the on and off states have a tendency to create stiff systems. This is why most power system simulator solvers are based on the A-stable order-2 trapezoidal rule of integration, as in RTDS [1] or Hypersim [2]. However, in most cases users must still use snubber resistors and capacitors across the switches to improve numerical stability.

The order-5 L-stable discretization rules of ARTEMiS [3] are, however, more stable for many situations. Because of its higher order, ARTEMiS order-5 is usually more accurate than an order-2 solver for the same time-step value. Such features enable the use of larger time-step values, which facilitate real-time simulation of difficult cases. Furthermore, while the trapezoidal integration rule can be applied with the classic nodal technique used in most simulation tools, higher-order solvers like ARTEMiS order-5 can only be used with a state-space formulation as in the state-space-nodal (SSN) solver algorithm of ARTEMiS.

4.3.3 Simulator Bandwidth Considerations

Another important aspect of a real-time simulator is its bandwidth; the definition of the simulation (the selected time-step) must be compatible with the speed or bandwidth of the phenomena that we want to simulate. For example, simulating electric circuits requires a much smaller time-step than mechanical ones because the former is much faster by nature. This is one reason why electrical systems are difficult to simulate: their bandwidth is high, imposing smaller time-steps and thus more powerful computers are needed to simulate them.

Because the simulation is a sampled process, the appropriate bandwidth of a simulator refers to the Shannon theorem, which requires a minimum of two samples within the period of the largest frequency of interest. But in practice, the simulation sampling frequency (inverse of the time-step) will be selected between 5 and 10 times the frequency of the phenomenon that the user wants to study.

4.3.4 Simulation Bandwidth vs. Applications

Figure 4.2 outlines typical time-step and computing power requirements for a variety of applications. The left side of the chart illustrates mechanical systems with slow dynamics that generally require a simulation time-step between 1 and 10 ms, using the rule of thumb that the simulation step should be

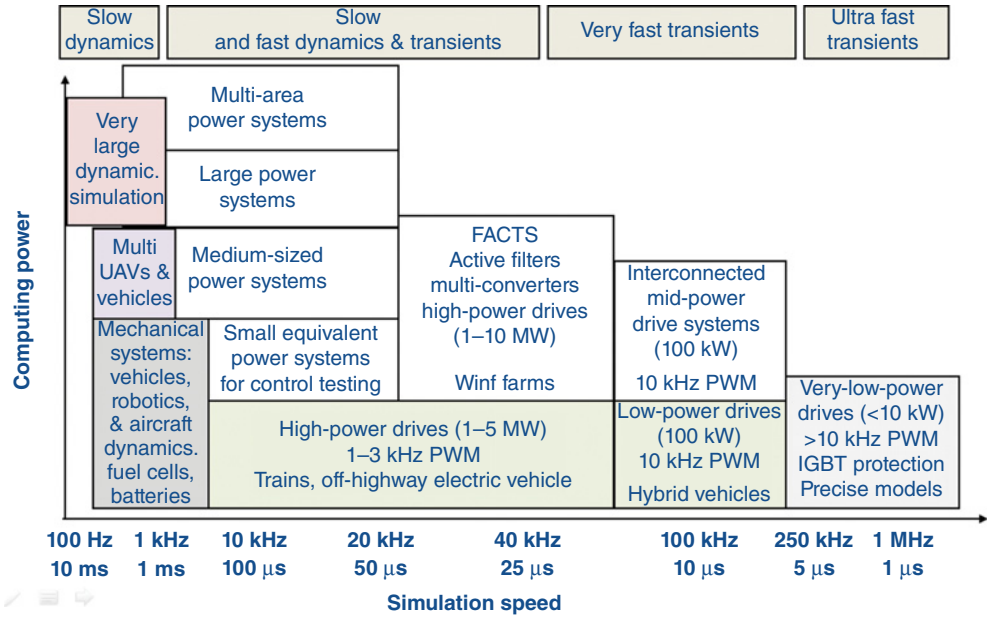

Figure 4.2 Simulation bandwidth by application.

smaller than 5–10% of the smallest time constant of the system. A smaller time-step may be required to maintain numerical stability in stiff systems. When friction phenomena are present, simulation time-steps as low as 100–500 µs may be required.

It is a common practice with EMT simulators to use a simulation time-step of 30–50 µs to provide acceptable results for transients up to 2 kHz. Because greater precision can be achieved with smaller time-steps, simulation of EMT phenomena with frequency content up to 10 kHz typically requires a simulation time-step of approximately 10 µs.

Accurate simulation of fast-switching power electronic devices requires the use of very small time-steps to solve system equations. Off-line simulation is widely used, but is time-consuming if no precision compromise is made on models (i.e. the use of average models). Power electronic converters with a higher PWM carrier frequency in the range of 10 kHz, such as those used in low-power converters, require time-steps of less than 250 nanoseconds without interpolation, or 10 µs with an interpolation technique. AC circuits with higher resonance frequency and very short lines, as expected in low-voltage distribution circuits and electric rail power feeding systems, may require time-steps below 20 µs. Tests that use practical system configurations and parameters are necessary to determine minimum time-step size and computing power required to achieve the desired time-step.

4.3.5 Achieving Very Low Latency for HIL Application

One of the main applications of real-time simulators is to develop and test protection and control systems by interconnecting the equipment in closed-loop with the simulator. This is called Hardware-In-the-Loop (HIL) or Controller-in-the-Loop (CIL). In such application, the total system must react like the real system, implying that the simulator delays are small compared to the delays and time constant of the actual controller, which is usually the case for typical thyristor-based power electronic controllers when the simulator time-step values are 25 to 50 µs.

However, the use of fast voltage source converters with PWM frequency larger than 10 kHz as well as modular multilevel converters (MMC) with a very large number of levels may require time-step values below 1 to 2 μs to achieve a total latency below 2–4 μs. The latency is defined as the time elapsed between the IGBT firing pulses sent by the controller under tests and the reception, by the controller, of voltage and current signals sent back by the simulator. Reaching such a low latency requires the use of field programmable gate array (FPGA) chips that are available in most modern simulators.

4.3.6 Effective Parallel Processing for Fast EMT Simulation

Conventional off-line simulation tools such as EMTP, EMTP-RV, ATP and PSCAD typically use only one processor to compute the total system, which means that the time to compute one time-step can exceed the wall-clock time when the size of the simulated system increases. However, real-time constraints also require the use of highly optimized solvers, taking advantage of parallel processing to reach the specified time-step, even if the complexity and size of the simulated system increases.

An important improvement in simulation speed was achieved in the 1990s by using the transmission lines modelled with distributed parameters to make the admittance matrix block-diagonal, creating subsystems that can be solved independently of each other. This property allows the network to be divided into subsystems with smaller admittance matrices which can be solved in much shorter time. The resulting simulation model structure is illustrated in Figure 4.3 where the line equations serve as links between the decoupled set of equations.

However, the effective implementation of this technique implies that the processing time for data exchange between processors is much smaller than the time used to simulate each subsystem. Fifteen years ago, only high-end commercial or very expensive custom-made supercomputers were able to implement such parallel simulation effectively with time-steps as low as 50 μs. The main impediment was the difficulty in implementing a low-latency interprocessor communication capable of transferring data with a delay below 50 μs without overloading each processor. In the early 1990s, organizations such IREQ (Hydro-Quebec's R&D centre), EDF (ARENE simulator [4]) and Manitoba HVDC R&D centres (and RTDS Technologies Inc.) developed their own custom-made supercomputers to implement real-time digital parallel simulators. Such supercomputers were expensive to develop and maintain.

By contrast, ubiquitous PC and laptop computers are equipped with processors that have up to eight cores. Standard PC servers can be equipped with up to 32 processor cores, tightly interconnected by a fast shared memory. They are able to run several threads in parallel with fast interprocessor communication, provided that the software uses these features.

Traditional EMT off-line simulation software packages, such as EMTP and PSCAD, are being modified by their respective development teams to take advantage of parallel processing. The EMT simulation

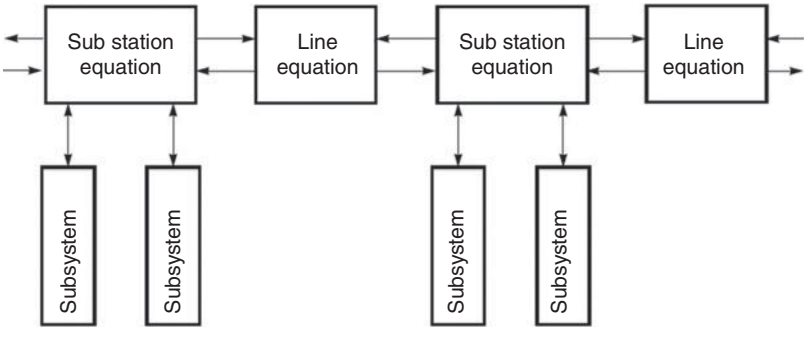

Figure 4.3 Program execution structure for EMT parallel simulation.

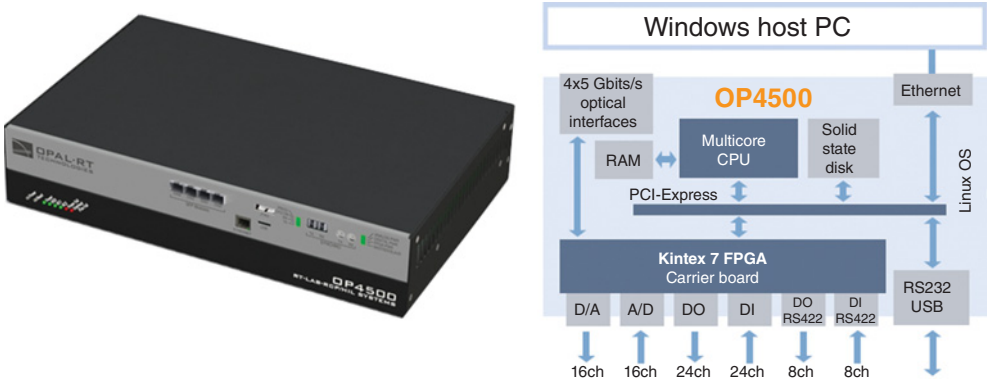

Figure 4.4 A multiprocessor desktop computer for fast simulation of complex systems.

software packages, Hypersim, eMEGAsim and RTDS, have been specifically developed, from the beginning, to take advantage of parallel and distributed processing, with great improvements in simulation speed. To perform this, Hypersim and RTDS partition the network at the connection points to transmission lines, creating subsystems, as illustrated in Figure 4.3.

Hypersim and eMEGAsim generate C code for each subsystem and compile them individually. Linkage is performed, depending on the commercial hardware used for the simulation, so that different executable modules are generated to be assigned to different processor cores. In this way, the simulation speed is increased according to the number of assigned processor cores.

Over the past 20 years, RTDS Inc. has developed ever-more-powerful custom computer boards optimized for real-time simulation of power grids. At the same time, the same Hypersim EMT parallel code has been ported from a custom supercomputer to the SGI supercomputer and now to standard multicore PCs.

Figure 4.4 illustrates an example of a small but powerful four-core simulator that can simulate a power grid with about 220 electrical nodes (single-phase) at 50 μs, using a standard low-cost Intel i7 four-core processor such as can be found in typical PCs. This small desktop simulator is also equipped with a powerful Kintex-7 FPGA to simulate fast power-electronic converter systems and controllers with time-step below 1 μs [5]. This setup can run a small system model in real time, for testing purposes, with HIL.

Although Hypersim is adequate for regular PCs, an interesting alternative for large, complex simulations is to use server-grade multiprocessor computers, which are now available at costs comparable to normal workstations. In this case, a 32-core Intel-based server can be used to simulate grids with more than 2000 electrical nodes with hundreds of generators, transformers and loads and several HVDC transmission systems with a time-step of 50 μs. This capability is very useful for integrating tests of power grids equipped with several HVDC, FACTS and distributed generation.

For very large grids, Hypersim can also take advantage of large SGI supercomputers with hundreds of processors cores. The ability to run the same simulation software on laptops or on commercial servers, supercomputers and on the cloud is certainly an advantage for large utilities, R&D centres and universities.

It must also be noted that using parallel processing for EMT simulation is essential not only for real-time HIL simulation but also to accelerate simulation studies performed in off-line mode. A faster simulation speed improves user interaction and enables the analysis of more contingencies in less time. For such applications, Hypersim can take advantage of commercial or in-house cloud computing.

Of course, using hundreds of processor cores to simulate very large grids requires the use of efficient and automatic processor allocation software to facilitate the use of such powerful parallel computers. Hypersim provides this essential feature with the ability to calculate all initial conditions.

4.3.7 FPGA-Based Multirate Simulators

The simulation of complex voltage source converters used in transmission and distribution systems such a modular multilevel converter (MMC) – as well as fast converters found in distributed generation systems such as PVs, wind farms and microgrids – often requires simulation time-steps below 1 μs. Such a small time-step cannot be achieved by today's standard computers. Specialized processor technologies such as FPGA processors must be used for simulation time-steps down to 200 ns, and to interface simulation results with external equipment using fast I/O converters. One such simulator architecture is that of the OPAL-RT OP4500 simulator in Figure 4.4. In this case the slower subsystems are simulated with a time-step of 10–50 μs on standard Intel i7 processors, while the fast power-electronic systems are simulated with a time-step below 1 μs. A general nodal solver, called eHS (**e**lectrical **H**ardware **S**olver) has been implemented directly on FPGA chips to facilitate the simulation of complex power electronic systems [5, 6]. Users can simply draw the circuit diagram, and the FPGA will automatically simulate it without any need to learn complex FPGA programming.

A powerful multi-FPGA simulator has also been delivered for the real-time simulation of MMC HVDC power grids using a total of 7500 MMC cell models and five converter terminals [7]. Such FPGA simulators are interfaced with eMEGAsim and Hypersim multicore simulators to allow the simulation of very large power grids, integrating fast power-electronic systems for transmission, distribution and microgrid systems.

4.3.8 Advanced Parallel Solvers without Artificial Delays or Stublines: Application to Active Distribution Networks

The parallel solver implementation described above is based on the availability of transmission lines or cables to separate the system into small independent subsystems, which can be simulated within the specified time-step, using only one processor. If the computational time for one of these subsystems becomes too large because it has too many nodes, then the common practice is to add artificial delays to enable parallel processing to reduce the computational time.

An artificial delay is usually implemented with a stub line, which is a line with its length adjusted to obtain a propagation time of one time-step. Large capacitors and inductors can also be used to split a large system into several smaller subsystems to take advantage of parallel processing. However, adding artificial delays also adds parasitic series inductances and parasitic shunt capacitances. Users must then compare results obtained without the addition of artificial delays using off-line simulation with results obtained using the artificial delays to reach the specified time-step. These parasitic L and C can be tolerated in many applications, depending on the values of these elements with respect to the other circuit impedances. This technique is used successfully by users of RTDS, eMEGAsim and Hypersim for many cases.

However, in some cases, such as large distribution circuits simulated with several pi circuits, the addition of artificial delays may be problematic because parasitic L and C will be large compared to actual component values and therefore *the standard decoupling methods cannot be used in distribution systems*. Simulating large converter systems interconnected with a large number of AC and DC switchable filters may also be problematic to reach time-step values below 25 to 50 μs even with the fastest available processors. Steady-state and transient values may be affected by the addition of artificial delays. Consequently, the use of circuit solvers that can simulate large circuits in parallel without adding any parasitic L and C can be very useful to increase simulation speed and accuracy. This is the key feature of the state-space-nodal algorithm described in detail in [3, 8].

SSN is a nodal admittance-based solver that allows us to minimize the number of nodes and thus the size of the nodal admittance matrix. This, in turn, can help increase the speed of simulation because the LU solution of the admittance equation requires a number of operations that is proportional to N^3, the cube of the size N of the nodal matrix. It does so by letting users choose the node locations and the corresponding groups of elements.

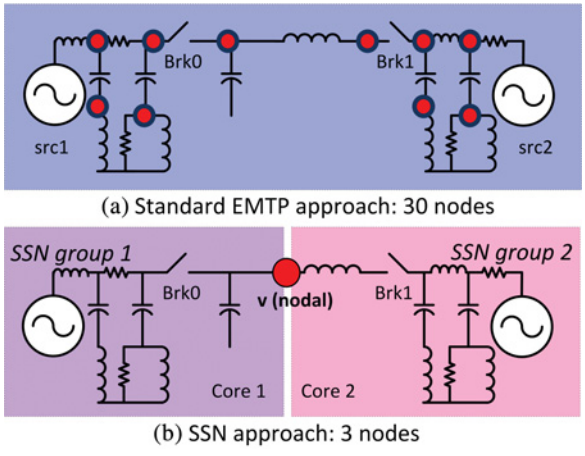

Figure 4.5 Comparison of node number for standard nodal admittance method and SSN.

As a simple example, we show the single-line circuit of Figure 4.5. In this circuit, the classic method to build the nodal admittance matrix, using standard RLC branches, would result in 30 nodes. By comparison, the SSN method can result in only three nodes. The reduction of the size of the nodal admittance matrix comes with an increased complexity in the resulting SSN group equations (a group is a multiterminal generalization of a branch).

When the SSN group equations are large enough, they can also be computed in parallel on different processor cores, without delays, thus accelerating the simulation even more. The SSN algorithm is more complex to compute than the simple nodal technique but actual results show a performance gain when using up to four processors, which can be very useful for the simulation of difficult cases where too many R, L and C components are tightly interconnected without lines or cables. This is depicted in Figure 4.7 (in the next section about the iterative MOV feature) where we can observe that the SSN group history source calculation and update stages are threaded on different cores without delays. Note that a similar delay-free parallelization could, in theory, be done with the standard EMTP approach. However, in practice, if the branch size is too small and their number is too high, the parallelization gains would be nullified by interprocessor communication overheads and other phenomena such as CPU cache trashing.

Using the SSN approach and the principles shown in Figure 4.5, it is possible to simulate in real time a radial distribution system with more than 700 nodes (with 980 LC states from short pi-lines) at a time-step under 65 μs, *without algorithmic delay or stub lines*, using four cores of a standard Xeon multicore server running RT-LAB. This performance is possible because the SSN reduces the network to a system with only six nodes and six multiterminal branches (i.e. SSN groups), and uses a threaded process to compute the SSN group equation in parallel, without any delay. A similar distribution system (Figure 4.6) with an on-load tap changer (OLTC) at the feeder point and more than 650 equivalent EMTP nodes can also be simulated in real time with the SSN solver. Using SSN and an 18 SSN nodes separation of the network (the six large dots in the figure), this model can be simulated in real-time at a time-step of 85 μs on a 3.3 GHz i7 Intel PC, without any delays or stub lines. In [9], this network was simulated without the SSN solver, and some delays were added to parallelize the simulation.

4.3.9 The Need for Iterations in Real-Time

When simulating, in real time, highly nonlinear devices such as surge arresters and metal oxide varistors (MOV), it is often necessary to use iterations in the standard nodal admittance solver. Hypersim [10] and

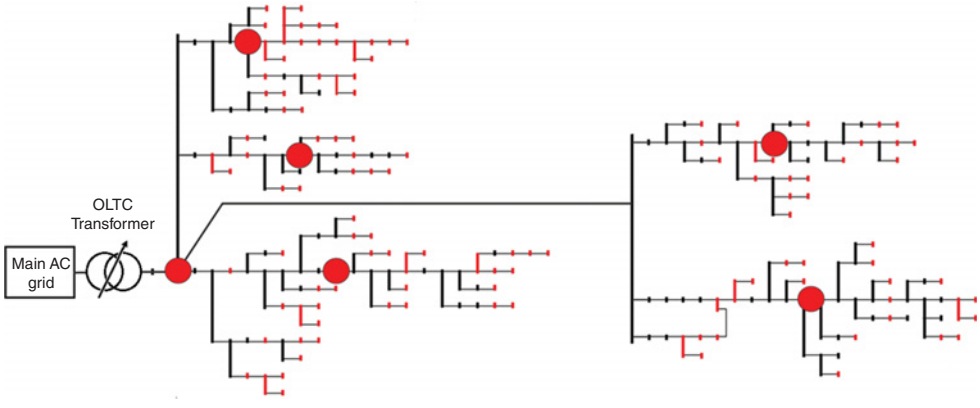

Figure 4.6 Large distribution network with more than 650 'EMTP-type' nodes.

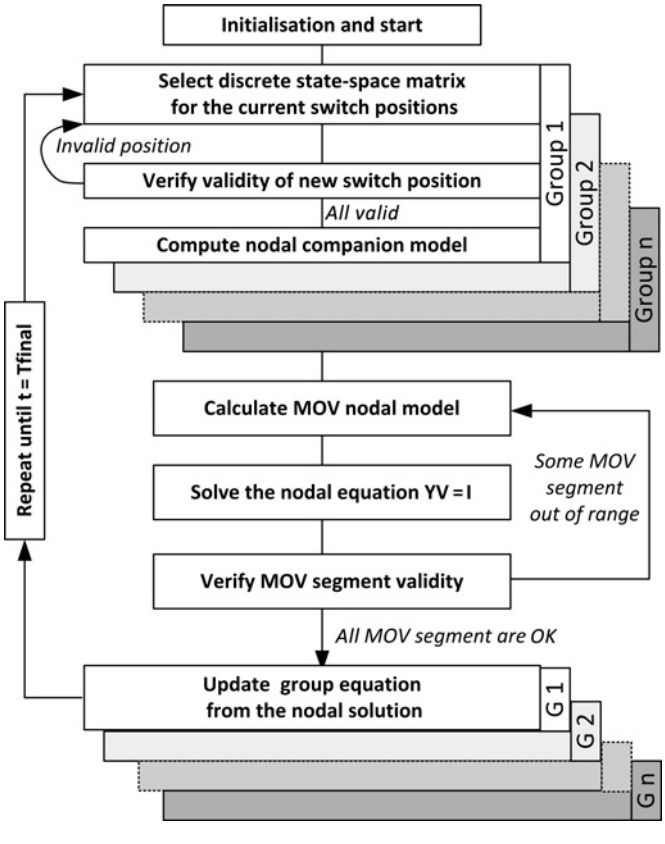

Figure 4.7 SSN algorithm with iterative MOV.

ARTEMiS [11] implement this type of iterative algorithm. The previous reference clearly shows realistic cases in which iterations are required to obtain accurate results.

Making iterations in a real-time simulator can be done efficiently because MOV only modifies the nodal equations of the solver, without history source computations, as shown in Figure 4.7.

Similar iterative principles are currently being applied to switches and also, for Hypersim only, saturable transformers.

4.4 Phasor-Mode Real-Time Simulation

Real-time simulation for EMT studies in power systems is well established. As discussed in previous sections, the fundamentals of most power-grid real-time simulations are based on the mathematics of EMT-type analysis. This includes the hardware/power/model-in-the-loop simulations. However, power system experts have long since realized that besides the real-time EMT domain simulation, they also need tools for off-line real-time phasor-domain simulation. These types of tools can be used to test the functionality of hardware such as global control and special protection devices in large-scale power systems. Furthermore, it can be utilized for training purposes in academic laboratories, or as an operator training tool in energy management centres. Some organizations are contemplating the use of faster-than-real-time phasor-type simulators for on-line prediction of system instability and implementing corrective actions to prevent system collapse or to minimize damage.

The ePHASORsim from OPAL-RT Technologies Inc. is a simulation environment for both transmission and distribution power systems and for balanced and unbalanced systems. The mathematics of ePHASORsim is based on a set of differential-algebraic equations [12]:

$$\dot{x}(t) = f(x, V) \tag{4.1}$$

$$YV = I(x, V) \tag{4.2}$$

$$x(t_0) = x_0, \tag{4.3}$$

where x is the vector of state variables, V and I are the vector of bus voltages and currents, Y is the nodal admittance matrix of the network, and x_0 is the initial values of state variables. The solver core is built as a Matlab/Simulink S-function, and its library of models is coded in C++, which can also be used in standalone mode. The built-in library includes major and most common components that are used for this type of simulation in power systems, such as synchronous machines and their controllers, different type of loads and transformers with on-load tap changers. An interface with Modelica FMI enables users to implement their own models. User models can also be implemented in C++ or with Simulink.

As of 2014, ePHASORsim can simulate systems with up to 10 000 nodes with a time-step of 10 ms with only one Intel processor core [13]. The systems can include about 3000 synchronous machines (six states), 5000 controllers and 20 000 other components. Faults, line switching and OLTC can also be simulated.

Similar research is being done, for example by PNNL in the USA [14] and PEGASE in Europe [15], to develop real-time and faster-than-real-time parallel transient stability simulators.

4.5 Modern Real-Time Simulator Requirements

Modern real-time simulators are typically built around multicore multiprocessor PCs with extensive I/O capabilities based on FPGA technology. Some simulators use custom-made computer boards.

A central processing unit (CPU) is a highly serialized arithmetic processing unit with a very flexible code flow architecture that enables it to implement very complex algorithms such as advanced ODE solvers. In modern PCs, it is commonly made with several computing cores and interfaced with other I/O components through a bus structure, such as PCIe in PCs.

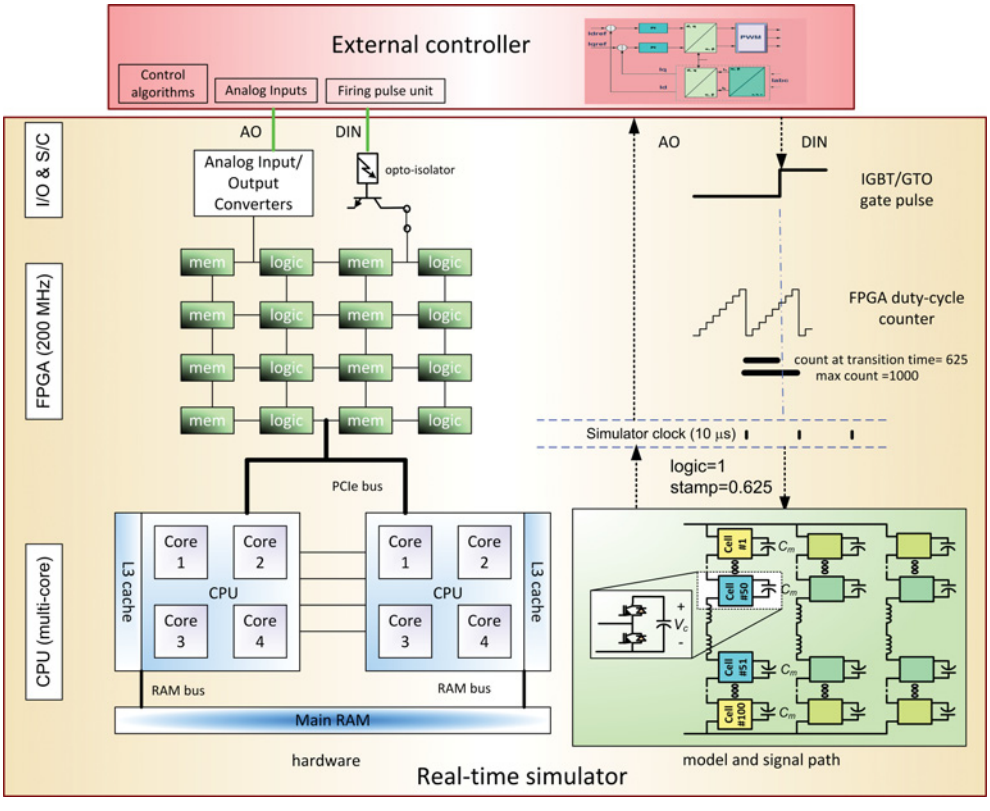

Figure 4.8 Simulator hardware and model paths.

A field-programmable gate array is a massively parallel structure of basic logic and memory elements that can be assembled into computing units from a user specification. Typical FPGA chips are mounted on electronic boards that, in addition to RAM memory and SSD hard disk, provide a direct and rapid interface with I/O points. It can also implement models and solvers of moderate complexity, especially for power electronics [5], as well as fast control systems and signal processing.

In Figure 4.8, we see the simulator hardware composed of CPUs and FPGA, along with the model path for MMC circuits. It shows that the I/O signals driving the IGBTs of the MMC cells are first captured by some timing on the FPGA card. This allows the precise timing of the IGBT gate pulse to be recorded. This timing, a time stamp, is then sent to the complete MMC model on the CPUs, where the time stamp is used to correctly compute the model voltages and currents.

In other cases, the MMC models can be simulated directly in the FPGA chips [7] using a very small time-step value, below 1 µs, to increase overall accuracy and to decrease the total latency.

4.5.1 Simulator I/O Requirements

I/O requirements are increasing for real-time simulation. Today's power electronics systems are getting more complex as new topologies, such as the MMC, gain acceptance. In order to perform HIL simulation of power electronic devices, real-time simulators must have various I/O types such as: (1) time-stamped

digital input, capable of sampling switching device gate signals with a resolution better than 100 nanoseconds (these types of inputs are sometimes referred as PWM inputs); (2) analogue output (1 μs sampling time), to emulate the device current, voltage and sensors as viewed by the controller under test; (3) digital input and output to for routing various signals between the controller under test and the real-time emulated power electronic devices.

The FPGA also provides the capacity to easily code and emulate various sensors, such as motor resolvers, quadrature encoders, RVDT and fault sensors.

Modern power electronic devices and controllers can also communicate through high-level communication links, such as Ethernet-based IEC-61850, DNP3 protocols for power system relays and substations, C37.118, the IEEE standard for using synchro-phasors in power systems, CAN protocol for automotive or the TCN protocol for trains. The simulator must be able to physically interface with such protocols with an appropriate driver. For this purpose, on PC-based real-time simulators, the simulator can be equipped with a PCI/PCIe interface board and/or a simple Ethernet board for IEC-61850. Alternately, the user can also program the FPGA board to interface to the desired protocol.

The simulator must also provide proper signal conditioning for all I/Os such as filtering and isolation. Additionally, the simulator should provide easy access to I/O interfaces between the simulator and the device under test. Typical real-time simulators provide such probing points on the front panel of the simulator, as does the OPAL-RT OP5600 simulator, Figure 4.9, or with a more complete patch panel. Figure 4.9 shows the probing connection points on the front of the simulator. The controller under test is interfaced with the simulator through the I/O interface on the back of the simulator.

The ability to provide a very large number of I/O points is also very important in certain applications. The MMC is a good example of a device with a very large number of I/Os.

As an example, a dual three-phase 100 cells/arms MMC simulator was recently commissioned by OPAL-RT with a total of 2788 I/O points with three digital signals per cells (1800), one analogue output per capacitor (600) and various other voltage and current sensors and well as breaker signals. The time to manage all these I/O channels and to compute the models was 25 μs using parallel processors and several FPGA chips.

A large MMC system, with up to five converters with 2400 cells each (120 000 cells in total) to simulate a DC grid, was also delivered to the China Institute, using 10 FPGA systems – OP7020 Virtex-7 FPGA racks that basically extend the number of I/Os for the OP5600 simulator – to simulate all the MMCs in less than 500 ns and to interface thousands of signals to customer controllers using optical fibres.

Figure 4.9 OP5600 real-time simulator (right) with a controller under test (left).

4.6 Rapid Control Prototyping and Hardware-in-the-Loop Testing

Various applications of real-time simulation are detailed in this section. These applications can be broken into five important categories:

- rapid control prototyping (RCP)
- hardware-in-the-loop testing (HIL) or controller-in-the-loop (CIL)
- software-in-the-loop (SIL)
- power-hardware-in-the-loop (PHIL)
- rapid simulation (RS)

Consider a controlled process that is composed of a plant with a controller acting upon it. In RCP applications, an engineer will use a real-time simulator to quickly implement a controller and connect it to the real plant or to a simulated plant. HIL (or CIL) acts in an opposite manner: its main purpose is to test actual controllers connected to a simulated plant.

Software-in-the-loop can be done when controller object code can be embedded in the simulator to analyse the global system performance and to perform tests prior to use of the actual controller hardware (HIL or CIL).

Power-hardware-in-the-loop (PHIL) consists of using real power components in the loop with the simulator. An example is a high-power motor emulator used to test actual inverter systems. The motor emulator uses a real-time simulator controlling a power amplifier to output the simulated motor current with the same amplitude as the actual motors. PHIL is also used for battery emulator and microgrid laboratories [16–19].

Rapid simulation take advantage of parallel processing to accelerate simulation in massive batch run tests, such as aircraft parameter identification using aircraft flight data or in Monte Carlo simulation used in power system analysis. RS is very useful for simulating large MMC HVDC grids using detailed converter models to reduce simulation time by several orders of magnitude depending on system complexity and size.

4.7 Power Grid Real-Time Simulation Applications

4.7.1 Statistical Protection System Study

Protection and insulation coordination techniques make use of statistical (Monte Carlo) studies to deal with inherent random events, such as the electrical angle at which a breaker closes, or the point-on-wave at which a fault is applied. For protection coordination studies, multiple fault scenarios are required to determine appropriate protective relay settings and correct equipment sizing. By testing multiple fault occurrences, the measured quantities are identified, recorded and stored in a database for later retrieval, analysis and study.

Protection relay development and testing is one of the most traditional uses of real-time simulators. Actual protection relay equipment is interfaced to the simulator using voltage and current amplifiers in such a way that the relays receive the same signals as they would if connected to actual power systems. Protection relay breaker tripping signals are connected to the simulated breaker through logical inputs. Faults can then be applied to the simulated network to test relay performance (i.e. its operating speed and accuracy) as well as to test the relay security (i.e. to determine the number of erroneous operations).

Figure 4.10 presents a typical setup for testing modern relays interfaced with the IEC 61850 Ethernet protocol replacing hard-wired connections.

Data measured by the PT and CT is sent by the simulator using Ethernet protocol IEC 61850-9-2 sampled values to the MiCOM P444 relay. The relay backup overcurrent function detects the fault and the relay sends an IEC 61850-8-1 GOOSE message back to the simulator in order to control the circuit breakers at each end of the transmission line.

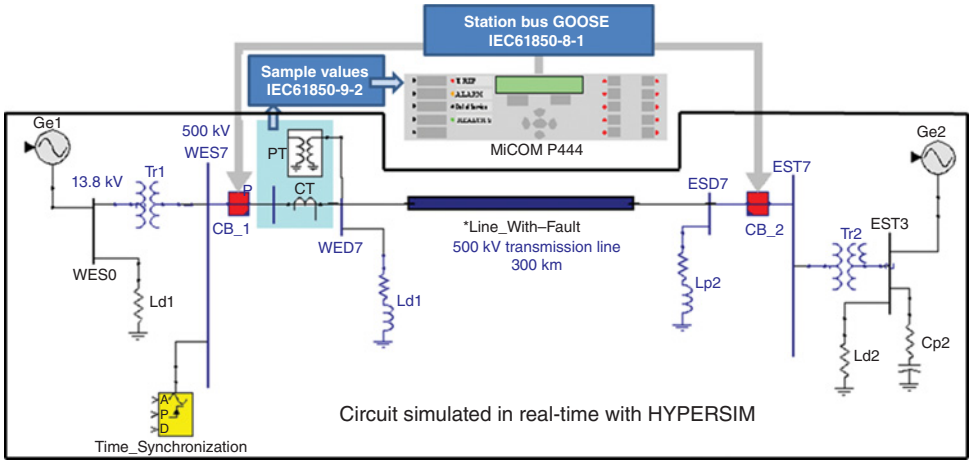

Figure 4.10 Typical protection relay testing setup with IEC61850 and HYPERSIM.

Many automated tests must be executed to evaluate the relay performance as a function of the fault impedance, duration and incidence angle.

Figure 4.11 presents such statistical results, executed with TestView, the Hypersim test automation software, by modifying all these parameters so that a fault is provoked at 50 km from the west bus on the 500 kV transmission line. In this test, the incidence angle varied between 0° and 359° and 332 tests were run in order to characterize the reaction time of the relay. The average value was 21.25 ms and the standard deviation was 1.08 ms. Several tests must also be performed to test the capability of the relay to not operate for transient voltages and current values outside its specified operating range. Of course, more complex tests can be performed using several relays installed on several lines and transformers, to evaluate the risk of cascaded relay misoperations caused by the effect of previous relay operation. Such tests are often performed to test new relay design or new network topologies. The integration of new HVDC and FACTS technologies, as well as distributed generations and microgrids, may require more sophisticated tests.

In several cases, transients overvoltage and overcurrent waveforms can be recorded and played back later to test the relays in open loop mode. This testing method is very popular when it is not necessary to evaluate the effect of relay operation on the performance of other relays. Waveform recording can be performed by standard off-line simulation software, such as EMTP-RV and PSCAD. Real-time simulators are also used in faster-than-real-time mode, when the grid is very large, to reduce the time to record thousands of waveforms.

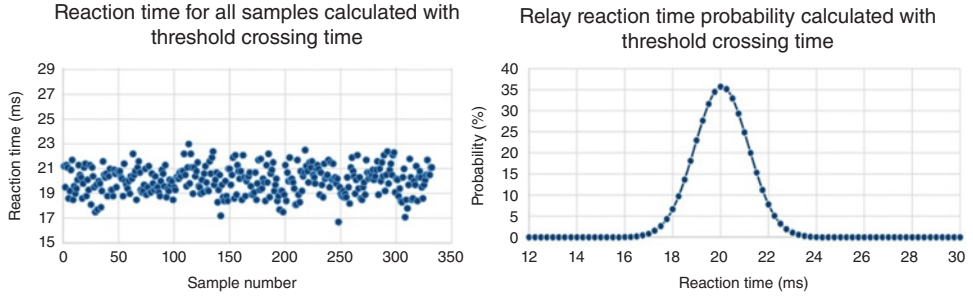

Figure 4.11 Protection relay testing results showing the probabilistic reaction time.

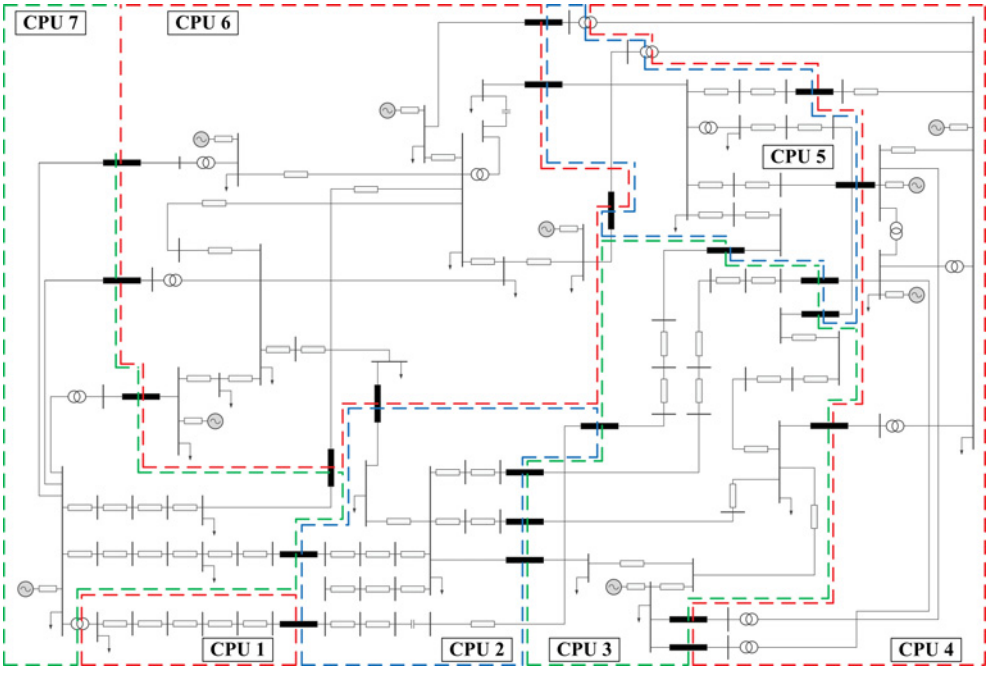

Figure 4.12 Schematic diagram of the network model – Courtesy of Entergy.

4.7.2 Monte Carlo Tests for Power Grid Switching Surge System Studies

The Monte Carlo technique has been used in the past for practical studies, such as the evaluation of the probable overvoltage at a substation [20], using traditional off-line simulation software such as ATP, PSCAD or EMTP-RV, as well as real-time simulators.

The large power system model depicted in Figure 4.12 illustrates a network with a very large number of busses and short lines. It was first built and tested in the EMTP-RV environment and then converted to the SimPowerSystems/Simulink environment as a distributed model, ready to use with the RT-LAB real-time simulator to perform statistical tests in less time but also to analyse the impact of SVC and future HVDC systems using actual control equipment.

The 60 Hz, 138/230 kV HVAC power system model is an 86-bus electrical network. Its large number of transmission lines supply power to a total of 23 loads, and nine ideal voltage sources with lumped equivalent impedance represent the generators. Full machine dynamics can easily be added, as these models are available in SimPowerSystems.

Figure 4.12 also describes the simulated power system along with CPU task separation for the eight-core target used in this test. Just a decade ago, simulation of such a model would not have been possible. A model of such complexity would have required a supercomputer composed of proprietary hardware. Today, this model can be simulated in real time at a time-step under 50 μs on commercial-off-the-shelf (COTS) PC computer hardware equipped with the RT-LAB real-time simulation platform. This particular 86-bus model can now be run on four 3 GHz Pentium cores under the Linux real-time OS.

The Monte Carlo test is designed using the Python script language, and uses the RT-LAB API to control simulation runs, data acquisition and post-treatment [21]. As can be observed in Figure 4.13(a), at the point where two different fault durations are applied (one cycle versus three cycles), the overvoltage measured during certain contingencies is dependent on fault timing. This comparison shows the necessity

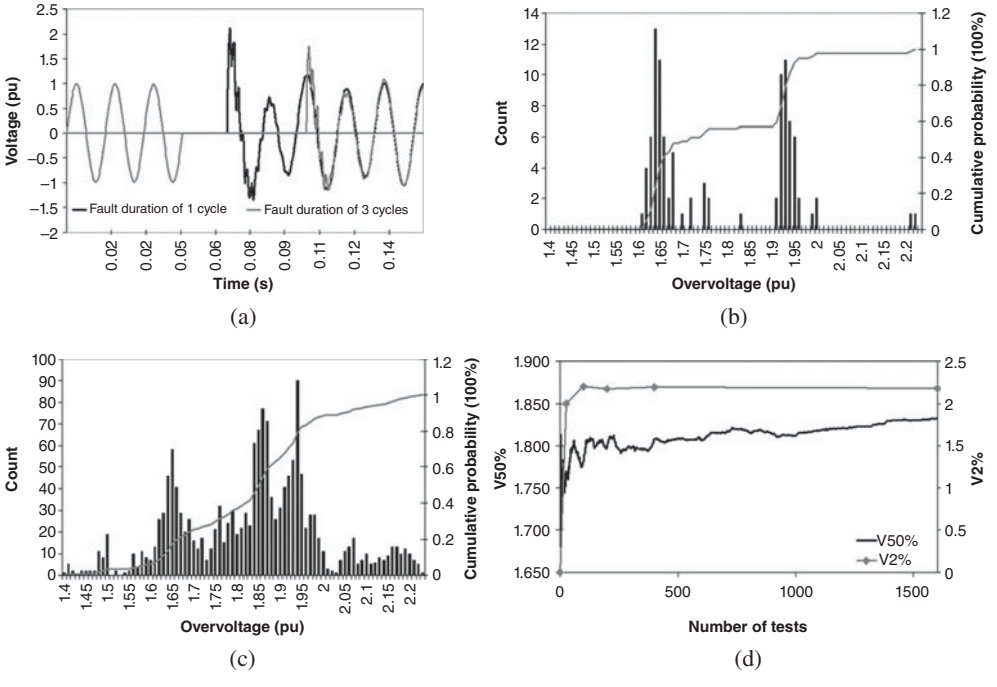

Figure 4.13 Monte-Carlo Study results. (a) Phase-a voltage for one-cycle and a three-cycle fault duration (Tstart = 50 ms). (b) and (c) Overvoltage statistic distribution for 100 and 1600 tests. (d) Mean value and standard deviation evolution with respect to number of samples.

of using statistical methods to calculate the maximum overvoltage to achieve an efficient design of the power system under study. It is also important to understand that a significant number of tests may be needed, depending on the study. The total number of tests needs to be large enough to obtain acceptable precision on the statistic distribution. The criteria used to determine the number of tests can be decided upon by calculating the evolution of the mean value (V50%) and/or, for instance, the evolution of the maximum overvoltage having a 2% probability of occurring (V2%). The evolution of these two quantities, according to the number of tests performed, is illustrated in Figure 4.13(d).

The above study can be performed in off-line mode using conventional software or with parallel software such as Hypersim or eMEGAsim to execute more tests in less time. However, in several cases, actual protection or controller hardware must be interconnected with the simulator to analyse the effect of fast control and protection actions on system overvoltage, overcurrent and arrester energy. Such real-time statistical tests also enable testing of control and protection system performance under realistic transient conditions and discovering unwanted random controller operations.

4.7.3 Modular Multilevel Converter in HVDC Applications

The inclusion of high voltage direct current (HVDC) and Flexible AC Transmission System (FACTS) devices in electric power grids is expanding rapidly. Also relatively recently, the use of voltage source converters (VSCs) based on insulated gate bipolar transistors (IGBTs) is becoming more attractive, mainly due to their cost and higher performance. The recent modular multilevel converter (MMC) topology, based on half-bridge modules connected in series [22], offers significant benefits compared to

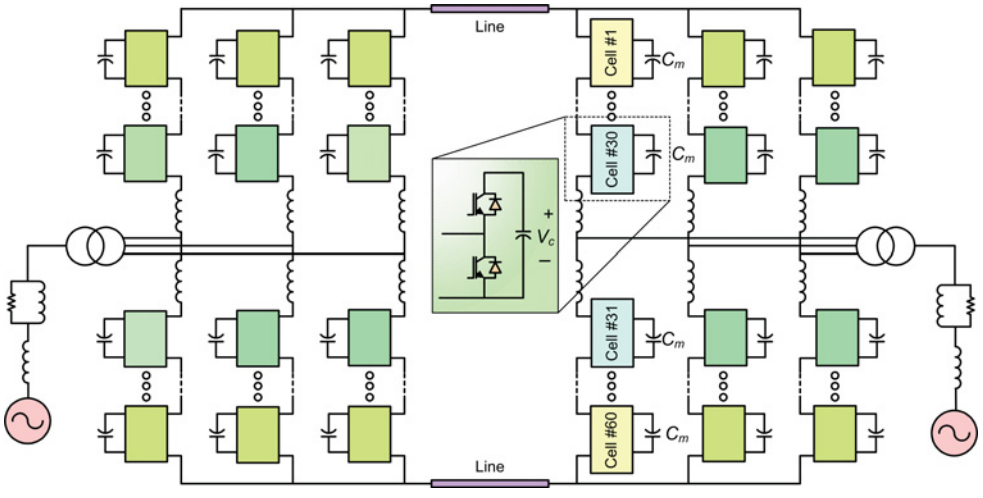

Figure 4.14 An MMC-based HVDC link.

previous VSC technologies, such as two-three level and neutral-point diode-clamped (NPC) topologies. By using a significant number of levels per phase in the MMC, the filter requirements can be eliminated. Moreover, switching frequency and transient peak voltages on IGBT devices are lower in the MMC, which reduces converter losses. An HVDC systems made of MMCs is shown in Figure 4.14. Scalability to higher voltages is easily achieved and reliability is improved by increasing the number of submodules (SMs) per phase.

The excessive number of power switches in the MMC, creates significant computational difficulties in EMT-type simulation tools. The numerous and nonlinear devices in the converter require an iterative process to solve the global matrix, which significantly increases the computational burden. Thus, in real-time simulations, modelling a highly accurate switching device is out of reach with current computational technology and some form of simplification is required to accomplish network integration and hardware-in-the-loop studies.

Real-time simulation of these large MMC systems enables users to develop and test actual controller equipment by interfacing them to the simulator in closed-loop. Such an HIL setup makes it possible to test the control system performance under several operating conditions before its installation in the real power grid. Real-time simulators with the ability to simulate MMC systems and HVDC grids are therefore essential and are used by MMC manufacturers, R&D centres and utilities.

In [23], full real-time digital simulation of a static MMC HVDC link interconnecting two AC networks is discussed. The converter has 60 cells per arm; each cell has two power switches with antiparallel diodes and one capacitor. The simulated model can be used to study the natural rectifying mode, which is very important in the energizing process of the converter, whether a ramping voltage or a charging resistance is used. Current injection with delay is the method used in this approach. This facilitates the use of HIL in realistic-sized MMC systems that can have more than a thousand cells.

In [24], the MMC is simulated using the SSN approach. The advantage of this approach is to avoid injection delays that can destabilize the simulation. The difficulty in using this approach is to effectively include the I/O signals with small latency when the cell number increases.

4.7.4 High-End Super-Large Power Grid Simulations

Because of the importance of grid reliability, utilities have very stringent testing requirements, and many of them have developed their own real-time simulator for these purposes. Hypersim, the Hydro-Quebec

Figure 4.15 Quebec grid simulated in real-time by Hypersim.

Research Institute (IREQ) real-time simulator, is a good example of these high-end simulators, which have been developed and used over the past 20 years.

As an example, the complete power network of the Province of Quebec, depicted in Figure 4.15, including 25 DFIG-based wind power plants, was simulated in real time on the Hypersim real-time simulator [2]. The network contained the following elements: 643 three-phase buses, 34 hydroelectric generators (turbine, AVR, stabilizer), one steam turbine generator, 25 wind power plants with DFIG generators, seven static VAr compensators, six synchronous condensers, 167 three-phase lines, on multiterminal DC-link and 150 three-phase transformer with saturation modelling.

Hypersim used 72 processors in an SGI supercomputer to perform the real-time simulation of this network at a time-step of 50 μs. Larger systems are simulated by China State Grid using Hypersim [25].

One key aspect of this type of 'super-large' EMT simulations is that the Hypersim simulator comes with automatic task allocation. The Hypersim GUI is also designed to cope with super-large grid diagrams including single-line schematics as only one example. Continuously developed and improved internally at IREQ since the mid 1990s, Hypersim has been marketed by OPAL-RT Technologies since 2012.

4.8 Motor Drive and FPGA-Based Real-Time Simulation Applications

4.8.1 Industrial Motor Drive Design and Testing Using CPU Models

Mitsubishi Electric Co. has used real-time simulation technologies to design motor drives for machine tool applications. The challenge faced on this project was that the motor itself, a permanent magnet

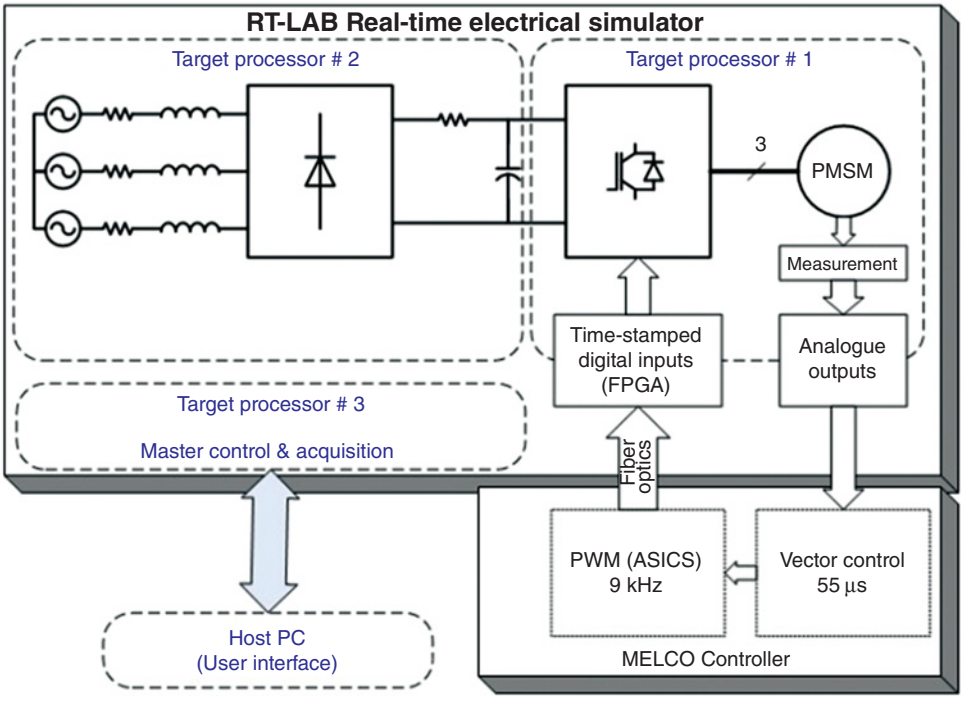

Figure 4.16 Real-Time Simulation of a PMSM drive.

synchronous motor and its related controllers were designed simultaneously. Therefore, a physical motor was not available for controller tests. The solution was to use a virtual motor, simulated in real time, during the controller testing phase [26].

The setup, depicted in Figure 4.16, consists of two main parts: the controller and the motor drive circuit. The controller includes a control module and PWM generator board. The vector control runs at 55 µs, and the PWM carrier frequency can be varied up to 9 kHz. The motor drive circuit was implemented in Simulink and simulated in real time on an RT-LAB electrical simulator. The motor drive was simulated more than 10 years ago by two Pentium 4 target processors, each operating at 2.8 GHz: one for the AC-DC part, and one for the DC-AC part, including the motor. A third Pentium processor was used for master control of the simulator, and for data acquisition sent to a remote host by a 100 Mb Ethernet link.

The simulator used a blockset called RTeDRIVE, designed by OPAL-RT, which uses interpolation techniques to solve under-sampling problems of the PWM waveform by the real-time simulator. As can be seen in Figure 4.17, HIL simulations closely match actual system results despite a 10 µs sample time and a nominal 9 kHz PWM frequency. Furthermore, one can observe that the current ripple amplitude decreases when PWM frequency is increased, just as in a real drive system.

Note that, today, such HIL simulation can be done with a time-step of less than 1 µs, using a complex finite element motor model implemented on a single FPGA chip, as discussed in the following sections.

4.8.2 FPGA Modelling of SRM and PMSM Motor Drives

In [27], an FPGA implementation of a switched reluctance motor drive (SRM drive) and an H-bridge Buck-Boost converter targeted for HIL testing of modern SRM controllers.

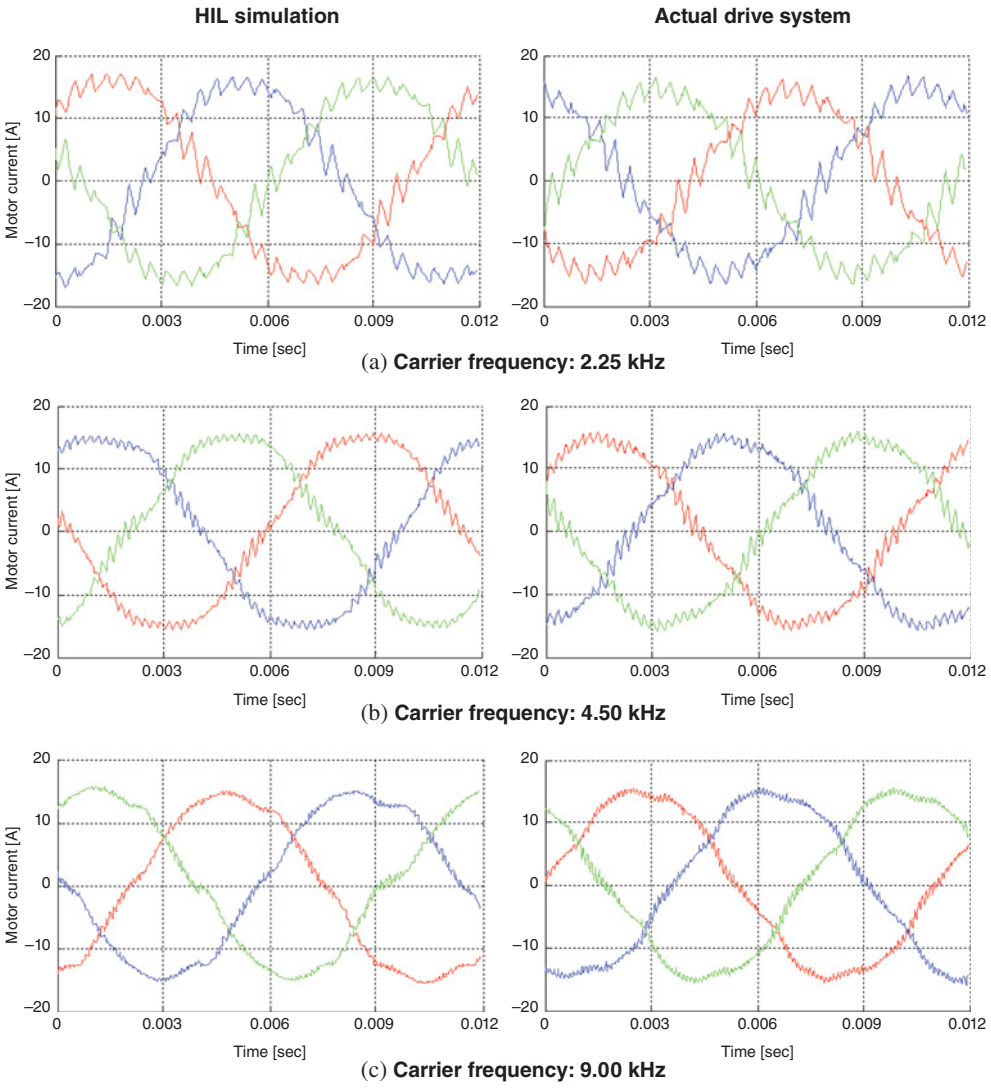

Figure 4.17 Effect of PWM carrier frequency.

These FPGA models, shown in Figure 4.18, allow the HIL simulation of SRM drive and boost converter with switching frequencies in the 50–100 kHz range because of the very high sampling rate of the FPGA. The models are also integrated into the RT-LAB real-time environment and directly linked with the simulator I/Os, providing ultra-low HIL gate-in-to-current-out latency, suitable for testing motor controllers with ultra-low latency requirements.

Similar FPGA models have also been designed for PMSM drive [28]. This type of model is used to test hybrid vehicle drivelines, similar to the Prius car, composed of two PMSMs, depicted in Figure 4.19. These PMSM models include finite element analysis (FEA) data and are sufficiently accurate to replace the real driveline, as tests made by the OEM show – see Figure 4.20.

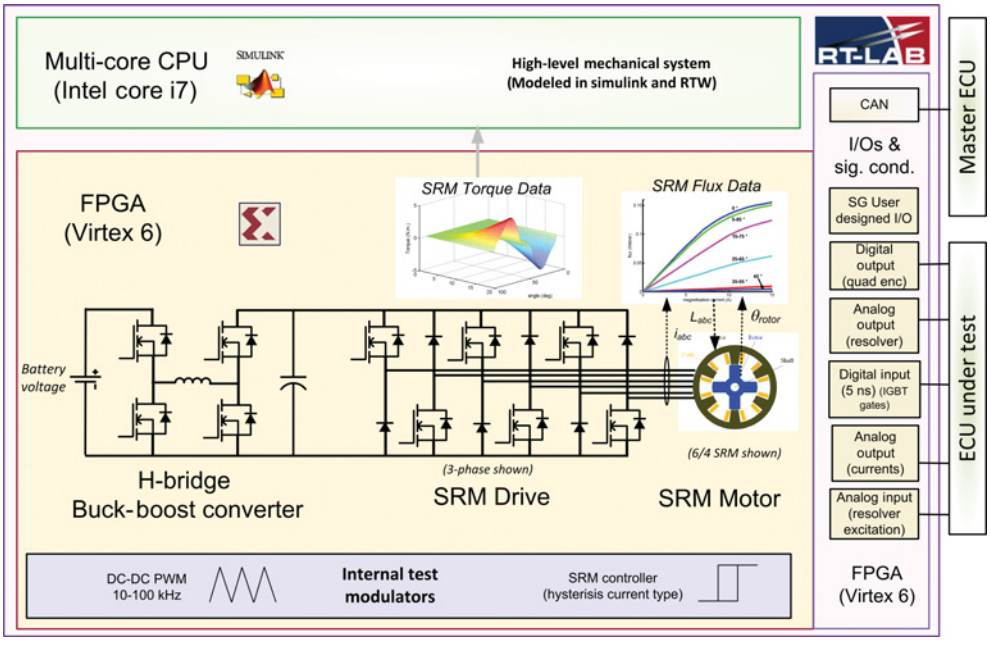

Figure 4.18 FPGA-based SRM Drive HIL simulator with DC-DC converter.

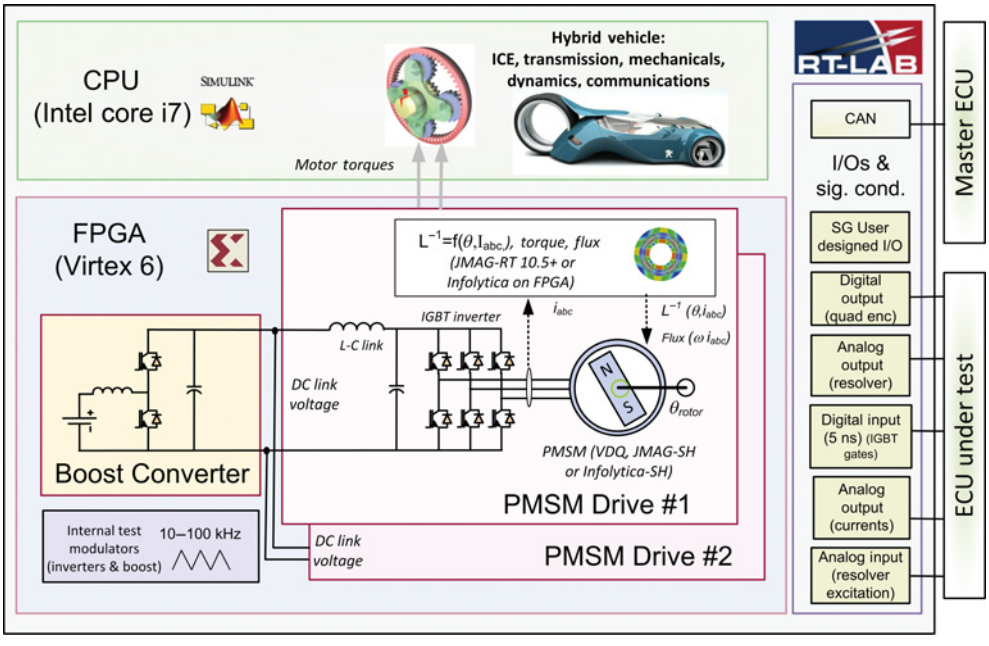

Figure 4.19 Dual-PMSM drive with boost converter of FPGA.

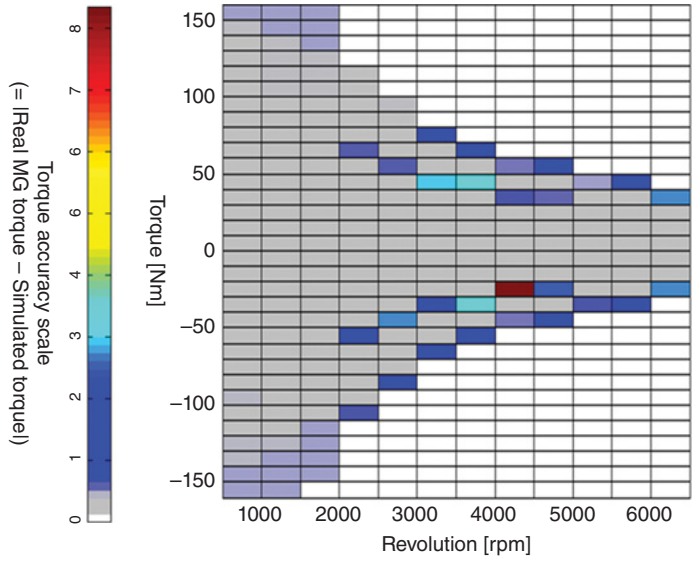

Figure 4.20 FEA model accuracy check with real driveline.

4.9 Educational System: RPC-Based Study of DFIM Wind Turbine

Working with fully virtual systems may not be advised at the undergraduate level. The fear of smoke certainly still has some educational value. In this case, it is possible to combine a real-time simulator, used as an RPC device, in conjunction with a medium-level power device. An example of such a product is produced by OPAL-RT and Lab-Volt, in which a student can learn about wind turbine controls and make various experiments with it. Two power levels are available: 200 W and 2 kW.

The system, shown in Figure 4.21, has been specially designed to be simple and robust for use in educational laboratories, but is sufficiently open to allow professors or students to expand the system to meet their unique requirements, and to develop new control strategies and test them on the platform.

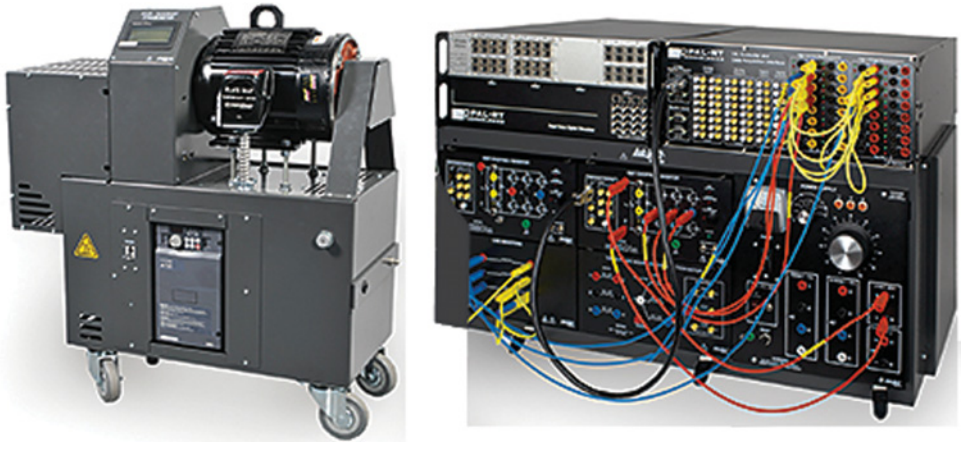

Figure 4.21 DFIM training kit OPAL-RT/Lab-volt.

4.10 Mechatronic Real-Time Simulation Applications

4.10.1 Aircraft Flight Training Simulator

Aircraft manufacturer Empresa Brasileira de Aeronáutica (Embraer) is using the RT-LAB real-time simulation software platform as the core component of a real-time simulator executing a high-fidelity aircraft model of a fighter plane [29]. In this application, the RT-LAB system runs in closed loop with the real onboard aircraft computer and the real aircraft cockpit. RT-LAB also provides control of force feedback (e.g. flight control joystick), visual display and sound generator.

The RT-LAB simulator is composed of more than 200 digital I/O points, more than 64 analogue I/Os (force feedback and pot reading), two MIL1553s and two Arinc 429 boards (for communication with onboard computer and aircraft components). TCP/IP communication handles sending data to the visual display and sound generator. Custom-made I/O developed by OPAL-RT reads the aircraft rotary variable differential transformer (RVDT) throttle position sensor (high speed analogue I/O). This type of I/O was designed using the Xilinx system generator blockset, supported by the RT-LAB system. The whole simulation is controlled by training software designed by Embraer. This software uses the RT-LAB API to control the entire simulation.

4.10.2 Aircraft Flight Parameter Identification

The development of the Embraer 170 Jet [30] has benefitted from an expanded modelling and simulation capability at Embraer. Development of a highly accurate aerodynamic model became an important part of the design development phase. This modelling was primarily conducted using Simulink. To obtain an accurate model, parameter identification needed to be done using actual flight data. This was performed using a software suite called RT-LAB/Dinamo 0. A real-time simulator is necessary for handling this task since multiple batch runs are required to fit the model parameters to actual flight data using the Nelder–Mead simplex and Levenberg–Marquardt optimization algorithms. The latter algorithm is used to fit model coefficients using manoeuvre time history – a particularly computation-intensive task. These fittings are made using captured flight data of actual aircraft manoeuvres such as take-off, jet Dutch roll and jet stall.

The final aircraft model includes all aspects of the plane, including motion and aerodynamic equations, engine, hydraulic systems and sensors. The different teams involved in the development of the jet use the resulting model. Control engineers use it to develop the control laws, the autopilot team uses it to make sure that their design meets specifications, and the systems team uses it to verify all possible contingencies and faults.

4.10.3 International Space Station Robotic Arm Testing

As a partner in the International Space Station (ISS), Canada is responsible for the verification of all tasks involving the special purpose dextrous manipulator (SPDM), depicted in Figure 4.22.

Testing the SPDM before deployment on the ISS represented a unique challenge, since it could not support its own weight when subjected to Earth's gravity! Therefore, the best way to test the robot controls was through HIL simulation [31].

One of the main technical challenges is to verify the feasibility of the insertion/extraction tasks by the robot hand self adaptive robotic auxiliary hand (SARAH) [32]. The forces involved are the result of complex frictional contact between the payload and the work site. Good contact models are being developed for non-real-time simulation but their real-time equivalents are still lacking precision. Moreover, the evaluation of different parameters is still mostly a trial and error process. Therefore, while most of the verification can rely on pure simulation, the contact part needs to be verified using a real robotic hand.

In the HIL test system, based on RT-LAB, a ground robot is driven by the output of the remote-operated space robot simulation. The system is shown in Figure 4.23. It is a HIL simulator consisting of

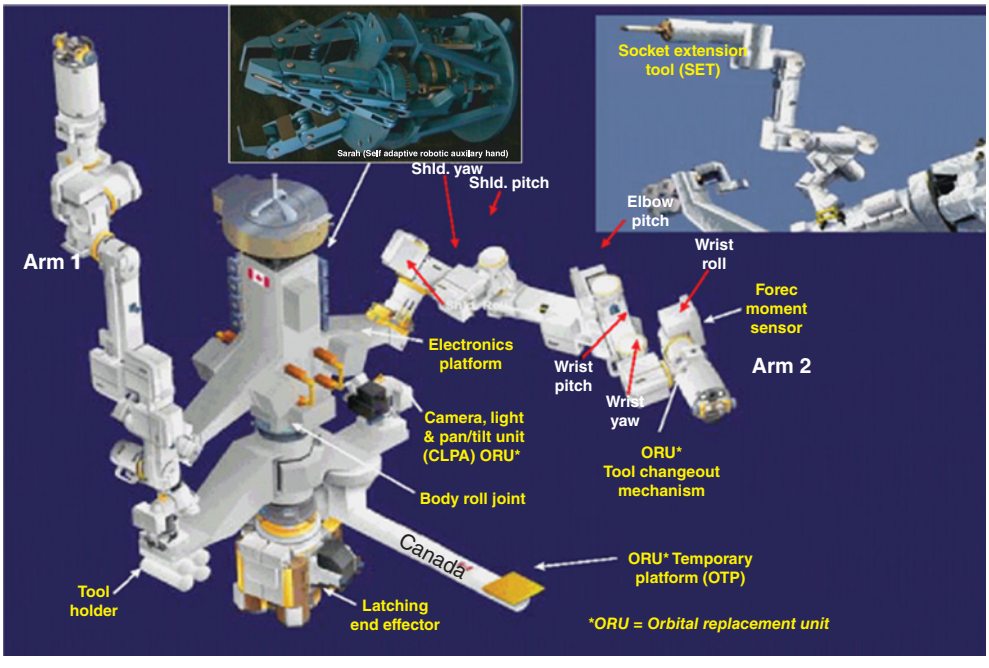

Figure 4.22 The Special Purpose Dextrous Manipulator of ISS.

Figure 4.23 SPDM Hardware-in-the-Loop testing system.

a rigid robot with its control, a simulation of SPDM dynamics and a visualization engine. An operator controls the motion of the SPDM through the simulation engine that generates the endpoint motion of the SPDM. It is then used as a set-point for the robot controller that ensures that the robot endpoint follows the same trajectory as the SPDM model running in real-time. The contact forces are measured using force/moment sensors and fed back into the simulator to allow the dynamic simulation engine to react to external contact forces. This concept is very flexible since it can accommodate vibration of the space robot base and other phenomena. It can also be used to represent different space robots.

The control laws of the SARAH were also developed and tested using RT-LAB prior to integration on the SPDM.

4.11 Conclusion

This chapter has briefly presented various industrial applications of real-time simulation in the fields of power systems, motor drives, avionics and robotics. A brief description of the model-based design methodology was also presented, together with a discussion of the main challenges encountered in the design of real-time simulators. It was demonstrated that the most complex applications found during the integration of very complex grids can now be simulated in real-time to test actual control equipment using simulators based on standard computer systems.

As modern engineering projects become more complex, often with tight budgets and shortened development times, simulation technologies are becoming increasingly crucial to their success. We believe that modern engineering curricula would benefit from the inclusion of real-time simulation technology courses because of the widespread use of simulation technology, both by industry and by researchers.

References

[1] Kuffel, R., Geisbrecht, J., Maguire, T. *et al.* (1995) RTDS – a fully digital power system simulator operating in real time. WESCANEX – IEEE Conf. on Communications, Power, and Computing, Winnipeg, MA, Canada, 15–16 May 1995.

[2] Gagnon, R., Fecteau, M., Prud'Homme, P. *et al.* (2013) Hydro-Québec strategy to evaluate electrical transients following wind power plant integration in the Gaspésie transmission system. *IEEE Transactions on Sustainable Energy*, **3**(4), 880–889.

[3] Dufour, C., Mahseredjian, J., Bélanger, J. and Naredo, J.L. (2010) An advanced real-time electromagnetic simulator for power systems with a simultaneous state-space nodal solver. IEEE/PES T&D – Latin America, São Paulo, Brazil, November 8–10, 2010.

[4] Devaux, O., Levacher, L. and Huet, O. (1998) An advanced and powerful real-time digital transient network analyser. *IEEE Transactions on Power Delivery*, **13**(2), 421–426.

[5] Dufour, C., Ould Bachir, T., Grégoire, L.-A. and Bélanger, J. (2012) Real-time Simulation of Power Electronic Systems and Devices, Chapter 15, in *Dynamics and control of switched electronic systems: advanced perspectives for modeling, simulation and control of power converters* (eds F. Vasca and L. Iannelli), Springer Series on Advances in Industrial Control, Springer. ISBN 978-1-4471-2885-4.

[6] Dufour, C., Cense, S., Ould Bachir, T. *et al.* (2012) General-purpose reconfigurable low-latency electric circuit and drive solver on FPGA. 38th IEEE Industrial Electronics Society (IECON), Montreal, QC, Canada, 25–28 October 2012.

[7] Wang, C., Li, W. and Bélanger, J. (2013) Real-time and faster-than-real-time simulation of modular multilevel converters using standard multi-core CPU and FPGA chips. 39th IEEE Industrial Electronics Society (IECON), Vienna, Austria, 10–13 November 2013.

[8] Dufour, C., Mahseredjian, J. and Bélanger, J. (2011) A combined state-space nodal method for the simulation of power system transients. *IEEE Transactions on Power Delivery*, **26**(2), 928–935.

[9] Dufour, C. and Bélanger, J. On the use of real-time simulation technology in smart grid research and development. to be published in *IEEE Transactions on Industry Applications*.

[10] Tremblay, O., Fecteau, M. and Prud'homme, P. (2013) Precise algorithm for nonlinear elements in large-scale real-time simulator. CIGRE conference, Montreal, QC, Canada, 24–26 September 2013.

[11] Dufour, C. and Tremblay, O. (2014) Iterative algorithms of surge arrester for real-time simulators. 18th Power Systems Computation Conference (PSCC), Wroclaw, Poland, 18–22 August 2014.

[12] Anderson, P.M. and Fouad, A.A. (1994) *Power System Control and Stability*, IEEE Press.

[13] Jalili-Marandi, V., Robert, E., Lapointe, V. and Bélanger, J. (2012) A real-time transient stability simulation tool for large-scale power systems. IEEE PES General Meeting, San Diego, CA, USA, July 2012.

[14] Hogan, E., Cotilla-Sanchez, E., Halappanavar, M. *et al.* (2013) Towards effective clustering techniques for the analysis of electric power grids. 3rd International Workshop on High Performance Computing, Networking and Analytics for the Power Grid (HiPCNA-PG), Denver, CO, USA, 22 November 2013.

[15] Pruvost, F., Cadeau, T., Laurent, P. *et al.* (2011) Numerical accelerations for power systems transient stability simulations. 17th Power System Computation Conference (PSCC), Stockholm, Sweden, 22–26 August 2011.

[16] Viehweider, A., Lauss, G. and Lehfuss, F. (2011) Stabilization of power hardware-in-the-loop simulations of electric energy systems. *Simulation Modelling Practice and Theory*, **19**(7), 1699–1708.

[17] Hong, M., Miura, Y., Ise, T. *et al.* (2010) Stability and accuracy analysis of power hardware-in-the-loop simulation of inductor coupled systems. *IEEJ Transactions on Industry Applications*, **130**(7), 902–912.

[18] Ren, W., Steurer, M. and Baldwin, T.L. (2008) Improve the stability and the accuracy of power hardware-in-the-loop simulation by selecting appropriate interface algorithm. *IEEE Transactions on Industry Applications*, **44**(4), 1286–1294.

[19] Ocnasu, D., Bacha, S., Munteanu, I. and Dufour, C. (2009) Real-time power-hardware-in-the-loop facility for shunt and serial power electronics benchmarking. 13th European Conference on Power Electronics and Applications (EPE), Barcelona, Spain, 8–10 September 2009.

[20] Vahidi, B., Ghorat, M. and Goudarzi, E. (2007) Overvoltage calculation on Bam substation by Monte Carlo method with accurate substation components modeling. IEEE PowerTech Conference, Lausanne, Switzerland, 1–5 July 2007.

[21] Paquin, J.N., Bélanger, J., Snider, L.A. *et al.* (2009) Monte-Carlo study on a large-scale power system model in real-time using eMEGAsim. IEEE Energy Conversion Congress and Exposition (ECCE), San Jose, CA, USA, 20–24 September 2009.

[22] Lesnicar, A. and Marquardt, R. (2003) An innovative modular multilevel converter topology suitable for a wide power range. IEEE Power Tech Conference, Bologna, Italy, June 2003.

[23] Grégoire, L.-A., Li, W., Bélanger, J. and Snider, L. (2011) Validation of a 60-level modular multilevel converter model – Overview of offline and real-time HIL testing and results. International Power Systems Transients (IPST), Delft, The Netherlands, July 2011.

[24] Saad, H., Dufour, C., Mahseredjian, J. *et al.* (2013) Real time simulation of MMCs using the state-space nodal approach. International Power Systems Transients (IPST), Vancouver, BC, Canada, 18–20 July 2013.

[25] Li, X., Liu, Y., Zhu, Y. *et al.* (2011) Real-time simulation of dynamic performance of multiinfeed UHVDC transmission system to be connected to North China power grid before 2015. *Power System Technology*, 2011-08.

[26] Harakawa, M., Yamasaki, H., Nagano, T. *et al.* (2005) Real-time simulation of a complete PMSM drive at 10 μs time-step. International Power Electronics Conf. (IPEC), Niigata, Japan, 4–8 April 2005.

[27] Dufour, C., Cense, S. and Bélanger, J. (2013) FPGA-based switched reluctance motor drive and DC-DC converter models for high-bandwidth HIL real-time simulator. 15th European Conference on Power Electronics and Applications (EPE-ECCE Europe), Lille, France, 3–5 September 2013.

[28] Dufour, C., Cense, S., Yamada, T. *et al.* (2012) FPGA permanent magnet synchronous motor floating-point models with variable-dq and spatial harmonic finite-element analysis solvers. 15th Int. Power Electronics and Motion Control Conference (EPE-PEMC), Novi Sad, Serbia, 4–6 September 2012.

[29] (2008) BANDEIRANTE: Information from Embraer to Brazil and abroad. *Embraer Journal*, **Ano 38**(730), 13–15.

[30] Cavalcanti, S. and Papini, M. (2004) Preliminary model matching of the Embraer 170 Jet: flight vehicle system ID-Part 1. *Journal of Aircraft*, **41**(4), 703–710.

[31] Piedboeuf, J.C., Aghili, F., Doyon, M. *et al.* (2001) Emulation of space robot through hardware-in-the-loop simulation. 6th Int. Symposium on Artificial Intelligence and Robotics & Automation in Space (i-SAIRAS), Canadian Space Agency, St-Hubert, QC, Canada, 18–22 June 2001.

[32] Martin, É., Lussier-Desbiens, A., Laliberté, T. and Gosselin, C.M. (2004) SARAH hand used for space operations on STVF robot. International Conference on Intelligent Manipulation and Grasping, Genoa, Italy, 1–2 July 2004.

5

Calculation of Power System Overvoltages

Juan A. Martinez-Velasco and Francisco González-Molina

5.1 Introduction

An overvoltage is a voltage – between one phase and ground or between two phases – having a crest value exceeding the corresponding crest of the maximum system voltage. Standards distinguish several classes and shapes of overvoltages [1–4]:

1. *Temporary overvoltages*: These are undamped or weakly damped oscillatory phase-to-ground or phase-to-phase overvoltages of relatively long duration (seconds, even minutes). Temporary overvoltages are originated by faults, load rejection, resonance and ferroresonance conditions or by a combination of these factors.
2. *Slow-front overvoltages*: These are unidirectional or oscillatory highly damped overvoltages, with a slow front and a short duration. They are caused by switching operations, fault initiation or remote lightning strokes.
3. *Fast-front overvoltages*: These are caused primarily by lightning strokes, although they can also be caused by some switching operations or fault initiation.
4. *Very-fast-front overvoltages*: In general, these are the result of switching operations or faults. They are usually associated with high-voltage disconnect switch operation in gas insulated substations (GISs), and with cable-connected motors.

Standards also include continuous power-frequency voltages, which are originated when the system is under normal operating conditions [1]. For systems whose maximum voltage exceeds that given in the standards, the actual maximum system operating voltage should be used.

A short description of the main causes and methods for limitation of overvoltages is presented in the Section 5.2 [1–11]. Sections 5.3–5.6 detail the analysis and calculation of typical overvoltages. Each section provides the modelling guidelines to be used with any class of overvoltage, a description of the phenomena that cause overvoltages and some illustrative cases. Due to space limitations only some of the main causes are analysed. For more details, readers are referred to the specialized literature on overvoltage calculation and insulation coordination studies in [5–11].

Transient Analysis of Power Systems: Solution Techniques, Tools and Applications, First Edition.
Edited by Juan A. Martinez-Velasco.

5.2 Power System Overvoltages

5.2.1 Temporary Overvoltages

The representative temporary overvoltage (TOV) is characterized by a standard short duration (1 min) power-frequency waveshape. The causes that lead to temporary overvoltages are many; the most frequent are summarized below.

Fault overvoltages: Phase-to-ground faults produce power frequency, phase-to-ground overvoltages on the unfaulted phases. The overvoltage magnitude depends on the system grounding and on the fault location. In effectively grounded systems, the temporary overvoltage is about 1.3 p.u. and the duration of the overvoltage, including fault clearing, is generally less than 1 s. In resonant grounded systems, the temporary overvoltage is about 1.73 p.u. or greater and, with fault clearing, the duration is generally less than 10 s. Depending on the system configuration, separated portions of the system may become ungrounded during fault clearing, and high overvoltages can be produced in the separated part.

Load rejection overvoltages: Overvoltages caused by load rejection are a function of the rejected load, the system topology after disconnection and the characteristics of the sources (e.g. speed and voltage regulators of generators). In a symmetrical three-phase power system the same relative overvoltages occur phase-to-ground and phase-to-phase. The longitudinal temporary overvoltages depend on whether phase opposition is possible; such phase opposition can occur when the voltages on each side of the open switching device are not synchronized. A distinction should be made between various system configurations when large loads are rejected. A system with relatively short lines and high short-circuit power at terminal stations will have low overvoltages. A system with long lines and low short-circuit power at generating sites will have high overvoltages.

Resonance and ferroresonance overvoltages: Temporary overvoltages may arise from the interaction of capacitive elements (lines, cables, series capacitors) and inductive elements (transformers, shunt reactors). The resonant overvoltage is initiated by a sudden change in the system configuration (e.g. load rejection, single-phase switching of a transformer terminated line or the isolation of a bus potential transformer through breaker capacitance). Resonant and ferroresonant overvoltages can have magnitudes greater than 3.0 p.u. and last until the condition is cleared.

Transformer energization: Resonance overvoltages can occur when a line and an unloaded or lightly loaded transformer are energized together. The transformer can cause inrush currents due to the nonlinear behaviour of its core. The inrush currents, which can have a high magnitude with a significant harmonic content, will interact with the power system, whose frequency response may exhibit a resonance at a frequency included in the transformer inrush current. The consequence may be a long-duration resonant TOV [12].

Longitudinal overvoltages may occur during *synchronization* due to phase opposition on both sides of the switch. The representative longitudinal TOVs are derived from the expected overvoltage, which has amplitude equal to twice the phase-to-ground operating voltage and a duration that can vary from several seconds to some minutes. When synchronization is frequent, the probability of occurrence of a ground fault and consequent overvoltage must be considered; in such cases the representative overvoltage amplitudes are the sum of the assumed maximum ground-fault overvoltage on one terminal and the continuous operating voltage in phase opposition on the other [1, 2].

Other causes of temporary overvoltages are electromagnetic induction or open conductors.

Temporary overvoltages are used to select surge arresters; that is, arresters are selected to withstand these overvoltages, which are not limited. Resonant and ferroresonant overvoltages are an exception, and they should not be used for arrester selection, but should be limited by detuning the system from the resonant frequency by changing the system configuration or by installing damping resistors.

The combination of TOVs of different origin may lead to higher arrester ratings and consequently to higher protection and insulation levels. The combination *ground fault with load rejection* is an example that can occur when, during a fault on the line, the load side breaker opens first and the disconnected load causes a load rejection overvoltage in the faulted part of the system before the supply side circuit-breaker

opens [2]. This combination can also exist when a large load is switched off and the subsequent TOV causes a ground fault on the remaining system.

5.2.2 Slow-Front Overvoltages

Slow-front overvoltages are generally caused by switching operations (line and cable energization, faults and fault clearing, load rejections, switching of capacitive or inductive currents). They may have time to crest of about 20–5000 μs and time to half value of up to 20 ms. The representative slow-front overvoltage is characterized by a standard switching impulse, and a peak voltage or a probability distribution of overvoltage amplitudes. The most frequent causes of slow-front overvoltage are discussed below.

Line/cable energization and reclosing overvoltages: A three-phase energization or reclosing of a line/cable may produce switching overvoltages on all three phases. The overvoltage generation depends on the circuit breaker, and its calculation has to consider trapped charges left on the phases in case of high-speed reclosing. In the worst case, each switching operation produces three-phase-to-ground and three-phase-to-phase overvoltages. Two methods are in use for characterizing the overvoltage probability distribution function: the case-peak method (each switching operation contributes one value to the overvoltage distribution) and the phase-peak method (each operation contributes three crest values to the probability distribution). The longitudinal insulation between non-synchronous systems can be subject to energization overvoltages of one polarity at one terminal and the crest of the operating voltage of the other polarity at the other terminal; consequently, the longitudinal insulation is exposed to significantly higher overvoltages than the phase-to-ground insulation. In synchronized systems, the highest switching overvoltage and the operating voltage have the same polarity, and the longitudinal insulation is exposed to a lower overvoltage than the phase-to-ground insulation.

Fault overvoltages: Slow-front overvoltages can be produced during phase-to-ground fault initiation and clearing. These overvoltages are only between phase and ground. If the switching overvoltages for energizing and reclosing are controlled to below 2.0 p.u., fault and fault clearing may produce higher overvoltages. A conservative estimate may assume that the maximum overvoltage during fault clearing is about 2.0 p.u., and the maximum value caused by a fault initiation is about $(2k - 1)$ p.u., where k is the ground fault factor in per unit of the peak line-to-ground system voltage.

Load rejection overvoltages: Load rejection may increase longitudinal voltage stresses across switching devices, the phase-to-ground insulator stress and the energy discharged through the arresters. If the arresters are used to limit energization and reclosing overvoltages to below 2 p.u., the energy dissipation in the arresters should be studied, especially when generators, transformers, long transmission lines or series capacitors are present.

Inductive and capacitive current switching overvoltages: The switching of inductive or capacitive currents may produce overvoltages. Capacitor bank energizing produces overvoltages at the capacitor location, line terminations, transformers, remote capacitor banks and cables. The energizing transient at the switched capacitor location should be less than 2.0 p.u. phase-to-ground and 3.0 p.u. phase-to-phase. The phase-to-phase transients at line terminations can be 4.0 p.u. or higher, due to travelling wave reflections. The higher phase-to-phase overvoltages are most commonly associated with energizing ungrounded capacitor banks. Restrikes or reignitions during the interruption of capacitive currents (switching off unloaded lines, cables or capacitor banks) can produce extremely high overvoltages. The chopping of inductive current may also produce high overvoltages due to the transformation of magnetic energy to capacitive energy.

5.2.3 Fast-Front Overvoltages

They are generally produced by lightning discharges, although switching of nearby equipment may also produce fast-front waveshapes. Their time to peak value may vary between 0.1 and 20 μs.

Fast-front lightning overvoltages can be caused by strokes to phase conductors (shielding failure), strokes to line shield wires which flashover to phase conductors (backflash), or by nearby strokes to ground. Induced voltages by nearby strokes are generally below 400 kV and are important only for lower (distribution) voltage systems. Either cause will generate surge voltages that impinge on the substation equipment, those surges caused by the backflash being more severe than those caused by shielding failures. As these surges travel from the stroke terminating point to the station, corona decreases both the front steepness and the crest magnitude.

Fast-front switching overvoltages: The connection or disconnection of nearby equipment can produce oscillatory short-duration fast-rising surges with similar waveshapes to lightning. The insulation strength for this waveshape is closer to that of the standard lightning impulse than to that of the standard switching impulse. However, as their magnitudes are usually smaller than those caused by lightning, their importance is restricted to special cases. Their maximum value is approximately 3.0 p.u. with restrike and 2.0 p.u. without restrike.

5.2.4 Very-Fast-Front Overvoltages

Very-fast-front transients belong to the highest frequency range of transients in power systems (100 kHz to 50 MHz). Their shape is usually unidirectional, with time to peak below 0.1 μs, total duration below 3 ms and with superimposed oscillations at frequencies of up to 50 MHz. Causes of these very fast transient overvoltages (VFTOs) are disconnector operations and faults within gas insulated substations (GIS), switching of motors and transformers with short connections to the switchgear and certain lightning conditions.

5.3 Temporary Overvoltages

5.3.1 Introduction

The most frequent causes of temporary overvoltages are faults, load rejection, resonance and ferroresonance. Except for some types of resonance and ferroresonance, these causes also lead to slow-front overvoltages. For instance, a phase-to-ground fault can cause a slow-front overvoltage during fault initiation and clearing, and a temporary overvoltage when the during-fault steady-state condition is reached. Therefore, modelling guidelines for these causes might also be those recommended for analysis and simulation of slow-front (switching) overvoltages. The following subsection summarizes the modelling guidelines that can be applied to calculating temporary overvoltages, except ferroresonance. The rest of the section is dedicated to the analysis and simulation of the most frequent causes of TOVs in power systems. An introduction to the origin and the mitigation of these overvoltages is given in [13].

5.3.2 Modelling Guidelines for Temporary Overvoltages

Temporary overvoltages arise with frequencies close to the power frequency – usually below 1 kHz – so the models required for their analysis are power-frequency models, for which the frequency dependence of parameters does not have to be considered.

A methodology for analysis of temporary overvoltages is presented in IEC TR 60071-4 [14], which provides guidelines for representing components and for determining the study zone, and a discussion about the required input data. The IEC report does not cover ferroresonance.

The guidelines proposed in [14] and other references such as [15, 16] can be summarized as follows:

- The power supply model will depend on the case study. It can be represented as an ideal voltage source in series with a three-phase impedance (specified by its positive- and zero-sequence impedances), as a synchronous generator or as a network equivalent whose impedance has been fitted in a frequency

range typically below 1 kHz. If a synchronous generator model is required, then it has to include saturation, control units and the mechanical part.

- Lines and cables will be represented by a pi-equivalent with parameters calculated at power frequency, although in some cases zero-sequence parameters must be fitted in a frequency range of up 1 kHz. The number of pi-sections required for representing a line/cable will depend on the length and the frequency range of the transients to be analysed. Line transpositions and cable crossbonding will also affect the number of pi-sections.
- Corona effect is required only when the overvoltage can exceed the ionization threshold.
- Line towers and insulators are not required. Grounding impedances of a line may be required in some fault calculations, in which case a low-frequency low-current model will suffice.
- Models for transformers, shunt reactors and capacitor banks will usually be required. Transformer models should be implemented with caution, mainly in ferroresonant studies. It is important to properly model the transformer core and its saturation characteristics. Note that a saturable reactance can be a source of harmonics which may cause resonance problems.
- Models for loads and power electronic converters can also be required. As a rule of thumb, a no-load condition will usually represent the most conservative scenario, since load adds damping. However, in some cases a load model may be required to limit the conditions under which overvoltages can arise. Different approaches for representing loads were presented in [17]; see also the next section of this chapter.
- Models of power electronic converters are usually required, mainly when the converter can be the source of harmonics that can cause resonance overvoltages. In such cases, including filter models is mandatory.
- Substation busbar models are not required because it can be assumed that the voltage is the same in the whole substation. However, some substation equipment and the substation ground grid may be required. For instance, the model of a voltage transformer can be critical in some ferroresonance studies.
- Temporary overvoltages are used to select arresters, and the arrester model is not usually required, although there can be some exceptions for which including the arrester model can be important.

5.3.3 Faults to Grounds

5.3.3.1 Introduction

The magnitude of overvoltages due to ground faults depends on the method of system grounding (solidly grounded, resistance grounded, high resistance grounded or ungrounded systems), the equivalent sequence impedances seen from the fault location and the fault impedance. Their duration depends on the fault clearance times, and therefore on the design of the protection system. An estimation of the duration and magnitude of these overvoltages is crucial for selection of surge arresters in most power systems.

The grounding system determines the overvoltages that can occur during a fault to ground. A single-phase-to-ground fault shifts the ground potential at the fault location, depending on the severity of this shift on the grounding configuration – see Figure 5.1. On a solidly grounded system with a good return path to the grounding source, the shift is usually negligible. On an ungrounded system, a full offset may occur and the phase-to-ground voltage on the unfaulted phases approaches the phase-to-phase voltage. On a multigrounded distribution system with a solidly grounded station transformer, fault overvoltages very rarely exceed 1.3 p.u. [18].

5.3.3.2 Calculation of Ground Fault Overvoltages

The single-phase-to-ground fault is one of the most important causes of TOVs in power systems, and in most system configurations this type of fault produces the maximum fault voltages.

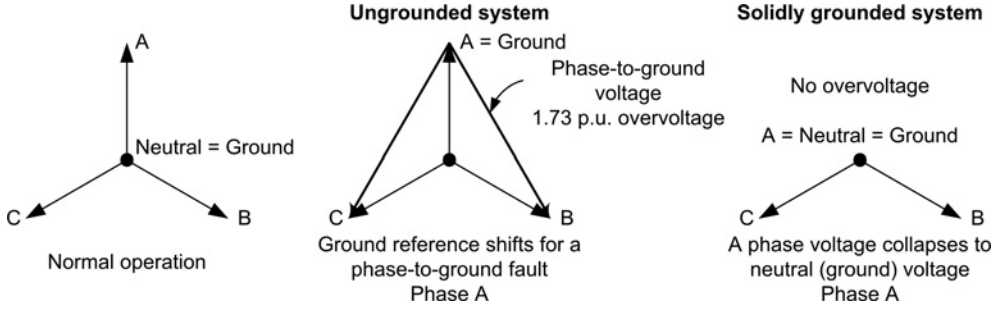

Figure 5.1 Voltage shifts as a function of the grounding configuration.

Two factors may be used to measure the magnitude of this type of overvoltage [18–20]:

- coefficient of grounding (COG)

$$\text{COG} = \frac{V'_{LN}}{V_{LL}} \tag{5.1}$$

- earth fault factor (EFF)

$$\text{EFF} = \frac{V'_{LN}}{V_{LN}} \tag{5.2}$$

where V'_{LN} is the maximum phase-to-ground voltage on the unfaulted phases during a fault, and V_{LN}, V_{LL} are the nominal phase-to-neutral and phase-to-phase voltages, respectively.

Obviously:

$$\text{EFF} = \sqrt{3} \cdot \text{COG} \tag{5.3}$$

Consider the diagrams shown in Figure 5.2. The equivalent circuit from the fault location is reduced to a three-phase symmetrical voltage source in series with the sequence impedances seen from this location. For a single-phase-to-ground fault on phase A, the voltages on the unfaulted phases are [8, 21]

$$\underline{V}_B^F = \frac{3\underline{a}^2\underline{Z}_f - j\sqrt{3}\cdot\left(\underline{Z}_2 - \underline{a}\underline{Z}_0\right)}{\underline{Z}_1 + \underline{Z}_2 + \underline{Z}_0 + 3\underline{Z}_f} \cdot \underline{E} \tag{5.4a}$$

$$\underline{V}_C^F = \frac{3\underline{a}\underline{Z}_f + j\sqrt{3}\cdot\left(\underline{Z}_2 - \underline{a}^2\underline{Z}_0\right)}{\underline{Z}_1 + \underline{Z}_2 + \underline{Z}_0 + 3\underline{Z}_f} \cdot \underline{E}, \tag{5.4b}$$

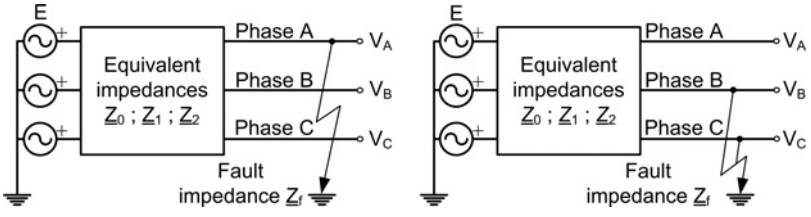

Figure 5.2 Equivalent circuit for calculation of ground fault overvoltages.

where $\underline{Z}_1$, $\underline{Z}_2$ and $\underline{Z}_0$ are the positive-, negative- and zero-sequence impedances respectively, seen from the fault location. $\underline{Z}_f$ is the fault impedance and $\underline{E}$ is the phase-to-neutral voltage magnitude prior to the fault.

From the above results it follows that for $\underline{Z}_0 = 0$, the voltages of the unfaulted phases have the same magnitude, and when $\underline{Z}_0 \to \infty$, the magnitude of both voltages tends to the phase-to-phase voltage. Very high voltages occur when the difference between the phase angles of $\underline{Z}_1$ and $\underline{Z}_0$ is greater than 90°. In practice, this is only possible in power systems with isolated neutral and a capacitive zero-sequence impedance. In general, the positive and negative sequence impedances have an inductive character.

When $\underline{Z}_1 = \underline{Z}_2$, the voltages at the unfaulted phases during a single-phase-to-ground fault are [8, 18, 21]

$$\underline{V}_B^F = \left(\underline{a}^2 + \frac{\underline{Z}_1 - \underline{Z}_0}{2\underline{Z}_1 + \underline{Z}_0 + 3\underline{Z}_f} \right) \cdot \underline{E} \tag{5.5a}$$

$$\underline{V}_C^F = \left(\underline{a} + \frac{\underline{Z}_1 - \underline{Z}_0}{2\underline{Z}_1 + \underline{Z}_0 + 3\underline{Z}_f} \right) \cdot \underline{E}. \tag{5.5b}$$

For a double-phase-to-ground fault on phases B and C, the voltage on the unfaulted phase is

$$\underline{V}_A^F = \left(\frac{3\underline{Z}_0 + 6\underline{Z}_f}{\underline{Z}_1 + 2\underline{Z}_0 + 6\underline{Z}_f} \right) \cdot \underline{E}. \tag{5.6}$$

In some special cases, the double-phase-to-ground fault causes overvoltages that are slightly higher than the single-phase-to-ground fault.

The COG for the unfaulted phases can be calculated by the following equations [8, 21]:

- single-phase-to-ground fault:

$$\text{COG} = \left| -\frac{1}{2} \left(\frac{\sqrt{3}\underline{k}}{2 + \underline{k}} \pm j1 \right) \right| \tag{5.7}$$

- Double-phase-to-ground fault:

$$\text{COG} = \left| \frac{\sqrt{3}\underline{k}}{1 + 2\underline{k}} \right| \tag{5.8}$$

where $\underline{k}$ is given by

$$\underline{k} = \frac{\underline{Z}_0}{\underline{Z}_1}. \tag{5.9}$$

When the fault impedance is just a resistance, $\underline{k}$ can be modified as follows to take into account the fault resistance [21]:

$$\underline{k} = \frac{R_0 + R_f + jX_0}{R_1 + R_f + jX_1} \quad \text{single-phase-to-ground fault} \tag{5.10a}$$

$$\underline{k} = \frac{R_0 + 2R_f + jX_0}{R_1 + 2R_f + jX_1} \quad \text{double-phase-to-ground fault} \tag{5.10b}$$

If resistances are neglected, then the above equations reduce to

$$\text{COG} = \frac{\sqrt{1+k+k^2}}{2+k} \quad \text{single-phase-to-ground fault} \tag{5.11a}$$

$$\text{COG} = \frac{\sqrt{3k}}{1+2k} \quad \text{double-phase-to-ground fault,} \tag{5.11b}$$

where

$$k = \frac{X_0}{X_1}. \tag{5.12}$$

Figure 5.3 shows the EFF as a function of sequence impedances, namely the ratios R_1/X_1, X_0/X_1 and R_0/X_1, assuming that $X_1 = X_2$ [2, 18]. The numbers on the curves indicate the EFF for the area bounded by the curve and the axes. All impedances must be on the same MVA base. In general, fault resistance

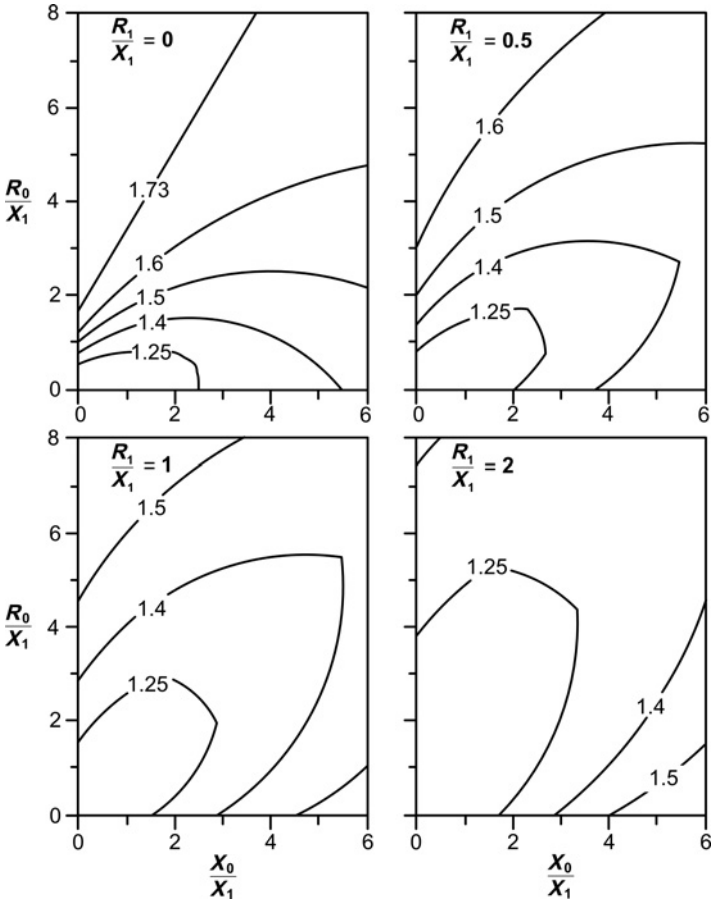

Figure 5.3 Earth fault factor in per unit for phase-to-ground faults (the contours mark the threshold of voltage).

Table 5.1 Typical values for the coefficient of grounding – faults to ground.

System grounding	COG (p.u.)
Grounded systems	
• High short-circuit capacity	0.69–0.80
• Low short-circuit capacity	0.69–0.87
• Low impedance	0.80–1.0
Resonant grounded systems	
• Meshed network	1.0
• Radial lines	1.0–1.15
Isolated systems	
• Distribution	1.0–1.04

will reduce EFF, except in low-resistance systems. In extended resonant-grounded networks, the earth fault factor may be higher at other locations than the fault. The range of high values for X_0/X_1 positive and/or negative, apply to resonant grounded or isolated neutral systems; low values of positive X_0/X_1 apply to grounded neutral systems, whereas low values of negative X_0/X_1 are not suitable for practical application due to resonant conditions [2].

A system is *effectively grounded* if the coefficient of grounding is less than or equal to 80% (so the earth fault factor is less than 138%) [18]. This situation is approximately met when $X_0/X_1 < 3$ and $R_0/X_1 < 3$.

Solidly grounded systems (i.e. systems where no intentional impedance is introduced between system neutral and ground) generally meet the definition of effectively grounded, since the ratio X_0/X_1 is positive and less than 3.0 and the ratio R_0/X_1 is positive and less than 1.0, where X_1, X_0, and R_0 are the positive-sequence reactance, zero-sequence reactance and zero-sequence resistance, respectively. These systems are generally characterized by a COG of about 0.8.

It is difficult to assign X_0/X_1 and R_0/X_0 values for ungrounded systems (i.e. systems with no intentional connection to ground except through potential transformers, metering devices of high impedance or distributed phase capacitances), since the ratio X_0/X_1 is negative and may vary from low to high values. The COG may approach 1.2 p.u. For values of X_0/X_1 between 0 and -40, the possibility of resonance with consequent generation of high voltages exists.

Table 5.1 provides some typical values of the coefficient of grounding for different grounding systems [6, 19, 20].

5.3.3.3 Case Study 1: Ground Fault Overvoltages in a Transmission System

Figure 5.4 shows the diagram of the test system, in which a 110 kV subtransmission line is fed from a step-down transformer. The transformer is Y-Y connected the neutral at the 220 kV side being ungrounded, while the neutral at the 110 kV side is connected to ground with a reactor of variable impedance. The subsequent plots depict the initial transient overvoltage and the TOVs that result when provoking both single-phase-to-ground and double-phase-to-ground faults at the sending end of the line with two different combinations of positive- and zero-sequence impedances. All simulation results were derived from the assumption of bolted fault; that is $\underline{Z}_f = 0$. From the formulas presented above the following coefficients are obtained:

- For $\underline{Z}_1 = \underline{Z}_2 = 23.5\angle 79°$, $\underline{Z}_0 = 20350\angle 90°$, $\underline{Z}_f = 0\ \Omega$: $\underline{k} \approx 866\angle 11°$, EFF for single-phase-to-ground fault ≈ 1.73, EFF for double-phase-to-ground fault ≈ 1.50.

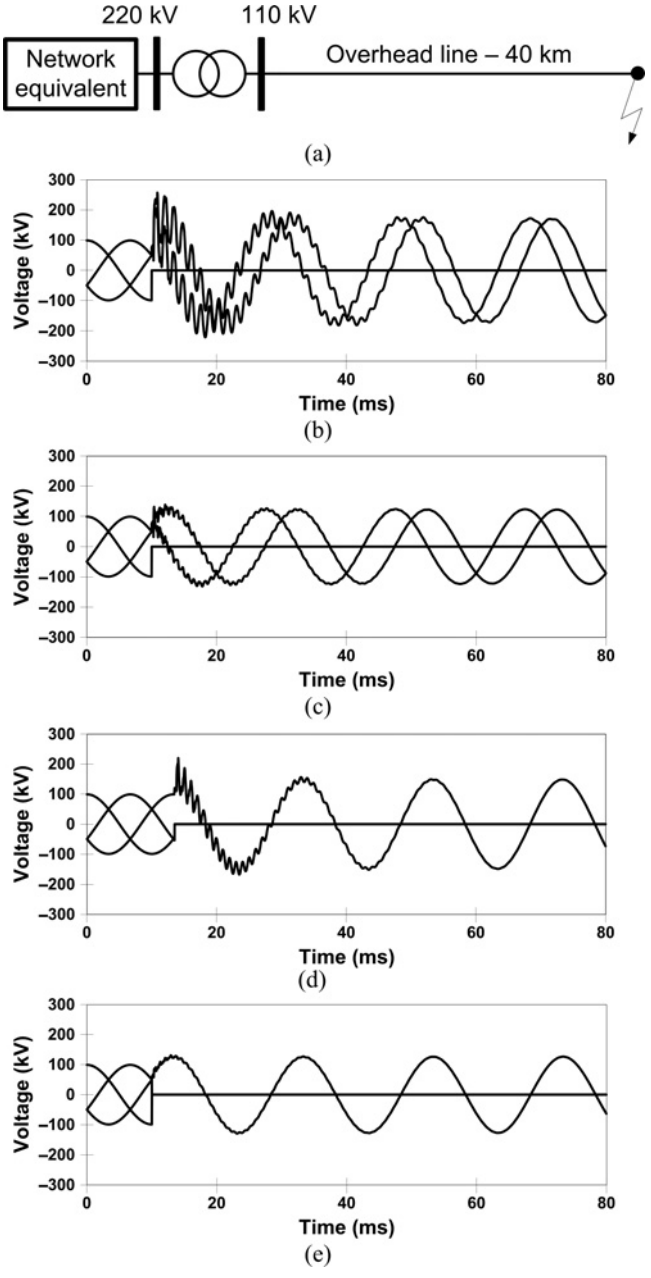

Figure 5.4 Case Study 1: Fault overvoltage study. (a) diagram of the test system, simulation results: (b) single-phase-to-ground fault – $\underline{Z}_1 = \underline{Z}_2 = 23.5\angle 79°$, $\underline{Z}_0 = 20350\angle 90°$, $\underline{Z}_f = 0\ \Omega$. (c) double-phase-to-ground fault – $\underline{Z}_1 = \underline{Z}_2 = 23.5\angle 79°$, $\underline{Z}_0 = 20350\angle 90°$, $\underline{Z}_f = 0\ \Omega$. (d) single-phase-to-ground fault – $\underline{Z}_1 = \underline{Z}_2 = 23.5\angle 79°$, $\underline{Z}_0 = 68.5\angle 80°$, $\underline{Z}_f = 0\ \Omega$. (e) double-phase-to-ground fault – $\underline{Z}_1 = \underline{Z}_2 = 23.5\angle 79°$, $\underline{Z}_0 = 68.5\angle 80°$, $\underline{Z}_f = 0\ \Omega$.

- For $\underline{Z}_1 = \underline{Z}_2 = 23.5\angle 79°$, $\underline{Z}_0 = 68.5\angle 80°$, $\underline{Z}_f = 0\ \Omega$: $\underline{k} \approx 2.91\angle 1°$, EFF for single-phase-to-ground fault ≈ 1.24, EFF for double-phase-to-ground fault ≈ 1.28.

Since the peak voltage in all phases prior to the fault is 99 kV, it is easy to check that the peak voltage of the resulting steady-state voltage in the unfaulted phases is in all cases very close to the voltage that results from using the above factors. Take into account that a value of 99 kV is 10% below the rated peak voltage of a 110 kV system.

For ungrounded systems (i.e. an ineffectively grounded system), the peak voltage that results during the initial transient reaches very high values, namely about 2.5 p.u. in the case of single-phase-to-ground fault, and a little more than 2 p.u. in the case of a double-phase-to-ground fault.

5.3.4 Load Rejection

5.3.4.1 Introduction

Load rejection is a sudden three-pole switching system that causes three similar phase-to-ground voltage rises; therefore, the same relative overvoltages occur phase-to-ground and phase-to-phase. The voltage rises depend on the rejected load, and they may be especially important in the case of load rejection at the remote end of a long line due to the Ferranti effect.

5.3.4.2 Calculation of Load Rejection Overvoltages

Power flow across an impedance causes a voltage difference between the sending and receiving ends when the load has an inductive component. If the load is suddenly disconnected, a power-frequency voltage increase may result at the point of load.

Consider the system depicted in Figure 5.5. It is a very general configuration for load rejection analysis that consists of a generator, a step-up transformer and a transmission line (although it may also be a cable). Note that the generator is represented by its internal emf behind its subtransient reactance, the transformer model includes its short-circuit impedance referred to its secondary side, and the line is represented by its pi-equivalent model with constant parameters calculated at power frequency. Assume that the transformation ratio of the transformer can be variable. The model is single-phase since the transient process is assumed symmetrical.

Under steady-state conditions, the excitation of the generator and the regulation of the step-up transformer are controlled in such a way that the operating voltages do not exceed the highest permissible voltage of the system. Due to the loading, the internal voltage of the generator will be higher or much higher than 1 p.u. After a sudden load shedding, an overexcited generator will remain supplying the transformer and the open-circuited transmission line. The phenomena that occur after load rejection in the three main components are as follows:

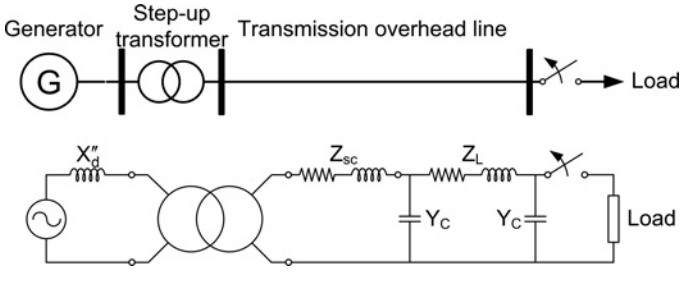

Figure 5.5 Diagram and equivalent circuit of the test system for load rejection analysis.

- *Generator*: If the current change is assumed to be sudden, the subtransient voltage that appears at the terminal voltage depends on both the initial steady state voltage and the subtransient reactance. Without a voltage regulator, the terminal voltage of the generator rises, the process being governed by the no-load time constants. Since such a voltage stress may not be acceptable, a fast voltage regulation is needed. In the moment of load rejection the exciting voltage may even reverse, and after a few hundred milliseconds it is set to the no-load exciting voltage.
- *Transformer*: The load current under normal operating conditions produces a voltage drop over the short-circuit impedance of a transformer. This voltage drop can be compensated by the voltage regulator of the transformer. In any case, the secondary voltage will not exceed the maximum permissible voltage. However, after load rejection the secondary voltage goes up and may exceed the maximum voltage; that is, the magnitude of the secondary voltage rises to the no-load voltage condition, which, due to the transformation ratio of the transformer prior to the switching event, can exceed the rated voltage.
- *Transmission line/cable*: After a load rejection at the receiving end of long transmission lines or cables the voltage at that end will raise because of the capacitive charge current, which leads to a negative voltage drop over the series impedances of the pi-equivalent circuit of the line or cable. Due to the Ferranti effect, the voltage at the open end of the line/cable will usually exceed the voltage at the sending end after load rejection.

Table 5.2 shows the steady-state equations and the approximated voltage rise that occurs in each component after load rejection. These equations were derived by assuming that the load is disconnected at the terminals of the respective component. This is not the case of the system shown in Figure 5.5 because after load rejection at the receiving end of the transmission line, the no-load condition is strictly correct for the transmission line, but not for the transformer and the generator. After load rejection, the line remains under voltage and generating capacitive power, so the currents at the secondary side of the transformer and the generator terminals are not zero; in fact, the currents for these two components can be large and capacitive, which will produce the Ferranti effect and voltage rises that are larger than those obtained from the expressions given in the table. In this condition, the voltage rise at the generator and transformer terminals can be more accurately obtained by increasing the reactive power of the load with the capacitive power generated by the transmission line under no-load condition. That is:

$$\Delta V \approx \frac{X_d''(Q_G + Q_\ell)}{V_G} \quad \text{for the generator} \tag{5.13a}$$

$$\Delta V \approx \frac{R_{sc}P_S + X_{sc}(Q_S + Q_\ell)}{V_S} \quad \text{for the transformer,} \tag{5.13b}$$

where the reactive power generated by the line at its sending end when it is unloaded can be approximated by

$$Q_\ell \approx V_S^2 \frac{\tan \gamma \ell}{Z_s}. \tag{5.14}$$

The value of the voltage at the sending end of the transmission line may significantly increase after load rejection since there can be a voltage rise at the secondary side of the transformer.

5.3.4.3 Case Study 2: Load Rejection Overvoltages in a Transmission System

Figure 5.6 shows a 110 kV, 40 km line fed from a step-up transformer. The transformer is delta-wye connected with grounded neutral at the line side. The load at the end of the transmission line is 120 MVA,

Table 5.2 Voltage rise at the power system components after load rejection.

Component	Steady-state equations	Voltage rise
Generator	$\underline{E'} \approx \underline{V}_G + jX'_d\underline{I}$ E' is the internal emf V_G is the terminal voltage X''_d is the d-axis subtransient reactance	$\Delta V = \left\lvert\underline{V}_{G(o)}\right\rvert - \left\lvert\underline{V}_G\right\rvert \approx \dfrac{X''_d Q_G}{V_G}$ $\left\lvert\underline{V}_{G(o)}\right\rvert = \lvert\underline{E'}\rvert$ $V_{G(o)}$ is the voltage at the terminal after load rejection (i.e. with $I = 0$) Q_G is the reactive power supplied by the generator before load rejection
Transformer	$\underline{V}_P = t\left(\underline{V}_S + \underline{Z}_{sc}\underline{I}_S\right)$ $\underline{I}_P = \underline{I}_S / t$ V_P, V_S are the voltages at the primary and secondary side, respectively I_P, I_S are the currents at the primary and secondary side, respectively t is the transformation ratio, which is controlled by the transformer regulator Z_{sc} is the short-circuit impedance referred to the secondary side	$\Delta V = \left\lvert\underline{V}_{S(o)}\right\rvert - \left\lvert\underline{V}_S\right\rvert \approx \dfrac{R_{sc}P_S + X_{sc}Q_S}{V_S}$ $\left\lvert\underline{V}_{S(o)}\right\rvert = \left\lvert\dfrac{\underline{V}_P}{t}\right\rvert$ $V_{s(o)}$ is the voltage at the secondary side after load rejection (i.e. with $I_S = 0$) R_{sc}, X_{sc} are the short-circuit resistance and reactance, respectively P_S, Q_S are the active and reactive power at the secondary side before load rejection
Transmission line	$\begin{bmatrix}\underline{V}_S \\ \underline{I}_S\end{bmatrix} = \begin{bmatrix}\cosh\underline{\gamma}\ell & \underline{Z}_s\sinh\underline{\gamma}\ell \\ \underline{Y}_s\sinh\underline{\gamma}\ell & \cosh\underline{\gamma}\ell\end{bmatrix} \cdot \begin{bmatrix}\underline{V}_R \\ \underline{I}_R\end{bmatrix}$ $\underline{\gamma} = \sqrt{(R + j\omega L)(G + j\omega C)}$ $\underline{Z}_s = \sqrt{\dfrac{(R + j\omega L)}{(G + j\omega C)}} \quad \dfrac{1}{\underline{Z}_s} = \underline{Y}_s \quad \omega = 2\pi\mathrm{f}$ V_S, V_R are the voltages at the sending and receiving end, respectively I_S, I_R are the currents at the sending and receiving end, respectively γ is the propagation constant Z_s is the surge impedance R, L, G, C are the parameters per unit length f is the power frequency ℓ is the line length	$\Delta V = \left\lvert\underline{V}_{R(o)}\right\rvert - \left\lvert\underline{V}_R\right\rvert$ $\left\lvert\underline{V}_{R(o)}\right\rvert = \left\lvert\dfrac{\underline{V}_S}{\cosh\underline{\gamma}\ell}\right\rvert$ $V_{R(o)}$ is the voltage at the receiving end after load rejection (i.e. with $I_R = 0$)

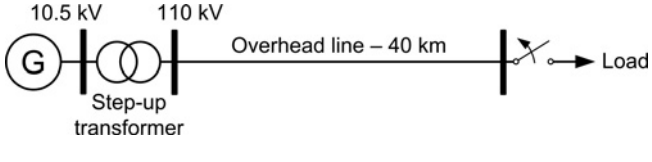

Figure 5.6 Case Study 2: Diagram of the test system.

with a power factor of 0.87 (lagging). The entire load is suddenly disconnected by opening a switch at the receiving end of the line.

Since the line is not too long and the voltage not too high, the Ferranti effect will not take place, so it should be assumed that there will not be a voltage rise at the receiving end of the line with respect to its sending end. Plots of Figure 5.7 show the simulation results obtained when the generator exciter is included in the model.

These results may be justified as follows. Since the generator exciter is included, the generator voltage comes back to its nominal value, and since the Ferranti effect is negligible, voltages at the transformer secondary and the receiving end of the line are basically the same once the load has been disconnected. In this case, the voltage rise at the remote end of the line is the result of several effects: the internal voltage drop in the transformer, which is almost negligible after load rejection; the voltage increase caused by the transformer ratio, which is working with a tap that produces a secondary voltage above the rated voltage (i.e. 110 kV) to compensate for the internal voltage drop; and the voltage drop along the line, which can be also assumed to be negligible. Note, however, that although the steady-state voltage rise at the remote end of the line above the rated voltage is not too high (about 7%), the initial transient overvoltage reaches a value of 1.5 p.u. It is also interesting to observe that the voltage rise, as a percentage of the initial voltage, is more than 20%, since this initial voltage is less than 90% of the rated voltage as a consequence of the voltage drops in the transformer and the line.

Without the exciter model, there would be voltage rises at the generator terminals, at the secondary side of the transformer and at the remote end line terminals; consequently, the rise would be even higher and rather unrealistic.

5.3.4.4 Mitigation of Load Rejection Overvoltages

Overvoltages caused by load rejection can be controlled by shunt reactors, series capacitors or static compensators.

Shunt reactors are placed at the ends of the line sections and their effect is to increase the effective shunt reactance of the line, and consequently to reduce the TOV. They reduce transient overvoltages in the same way as TOVs. They can also provide the draining of trapped charges on isolated line sections, which avoids excessive transient voltages when reclosing the line.

Shunt compensation may also be seen as a reduction of the surge impedance, which can be a desirable condition in the initial phase of the system; that is, when it operates with a light load. When the system is later operated at higher loads, the increased reactive demand of a line will cause an elevated excitation in the generators; this can have, on the one hand, the favourable effect that the system becomes stiffer and exhibits a better performance with respect to stability, but, on the other hand, an unfavourable effect on both temporary and transient overvoltages, which will be higher.

The application of shunt compensation may take advantage of shunt reactors with a variable magnetizing characteristic (i.e. when the saturation point is exceeded, the reactor consumes a larger fundamental component current which effectively means augmented shunt compensation) [13]. Reactors of this type produce harmonics which may act in an unfavourable way and even cause TOVs. These reactors can be successfully applied to line lengths beyond 300 km. Below 300 km the third harmonic voltage is superimposed in an unfavourable way, producing TOVs with a frequency of oscillation higher than the power frequency. Load rejection overvoltages can be reduced from a level of 1.5 p.u. for linear reactors to a level of about 1.3 p.u. for gapped-core reactors.

When employing permanently connected reactors, reactive current has to be supplied during normal operation causing increased losses and an elevated excitation in the generators. This can be avoided by switching the reactors, connecting them when energizing the line and when shedding load. This can only be made to a limited extent because the switching operation during load shedding cannot be carried out fast enough. This may justify the use of reactors with an extreme magnetizing characteristic – a negligible magnetizing current in the normal operating region and a rather flat characteristic above the

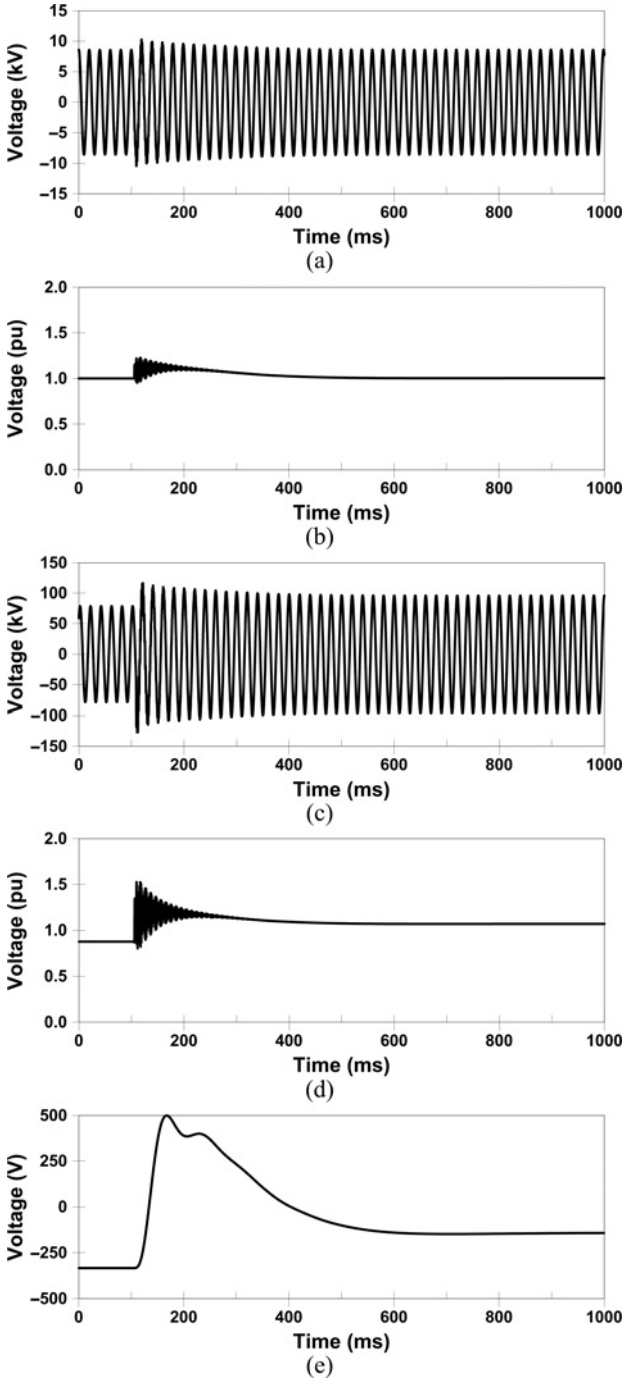

Figure 5.7 Case Study 2: Simulation results with control of generator excitation: (a) voltage at generator terminal, (b) rms voltage at generator terminal (in p.u.), (c) voltage at the receiving end of the transmission line, (d) rms voltage at the receiving end of the transmission line, (e) generator exciter voltage.

rated flux [13]. These reactors require special design to compensate the harmonics, which makes the equipment relatively expensive.

A more flexible compensation can be achieved by means of a static VAr compensator (SVC), in which thyristors are used to control the reactive current through the inductance. The control range goes from zero to a maximum power of V^2/X, where V is the line voltage and X is the reactance, the response of this compensation scheme being rather fast. To take full advantage of the potential of reactive-power control, the compensator is usually complemented by capacitor banks to allow the supply of reactive power at a leading power factor to the system. For reduction of TOVs, the decisive parameter is the inductance of the compensator. This compensation scheme can reduce reactive power during normal operation and quickly restore compensation in the case of load rejection.

5.3.5 Harmonic Resonance

5.3.5.1 Introduction

Resonance is a condition that occurs when the input frequency of a circuit coincides with one of the natural frequencies of the circuit. As a first approach, power system models may be seen as composed of different combinations of series and parallel circuits consisting of RLC elements. After a change of the system configuration that may result from some switching operations or short-circuits, a match between a natural oscillation of the power system and the frequency of an external sinusoidal source can occur. This resonance phenomenon leads to increased voltages and/or currents.

Different types of the resonance phenomenon can be distinguished: (1) natural resonance, when a natural oscillation frequency is equal to the source frequency; (2) ultra-harmonic resonance, when a natural oscillation frequency is equal to a harmonic frequency of the source; (3) subharmonic resonance, when a natural oscillation frequency is equal to a subharmonic frequency of the source.

Typical harmonic voltage sources are synchronous generators and asynchronous machines (slope-ripple harmonics), and transformers (current harmonics that cannot spread in the magnetization current in transformers with isolated neutral and without a delta winding). Typical harmonic current sources are corona, static converters or rectifiers, and transformers (e.g. non-sinusoidal no-load current due to the nonlinear magnetization curve).

The resonance phenomenon in nonlinear circuits, known as ferroresonance, basically caused by the nonlinear saturation characteristics of inductances with an iron core, is analysed in Section 5.3.7. The rest of this section is dedicated to introducing resonance in linear circuits and resonance overvoltages caused by harmonic currents in the presence of capacitor banks.

For a thorough analysis of both phenomena, resonance and ferroresonance, including several actual case studies, see the CIGRE Brochure 569 [22].

5.3.5.2 Resonance in Linear Circuits

Figure 5.8 shows the two simplified linear circuits used to explain the generation of resonance overvoltages. For the sake of simplicity the circuits are lossless. Note that the supplying source is a voltage source

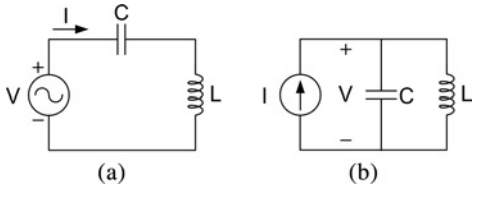

Figure 5.8 Linear *LC* circuits: (a) series LC circuit, (b) parallel LC circuit.

Table 5.3 Equations of linear LC circuits.

Series LC circuit	Parallel LC circuit
$\underline{V} = \underline{V}_L + \underline{V}_C = j\omega L\underline{I} + \frac{\underline{I}}{j\omega C}$	$\underline{I} = \underline{I}_L + \underline{I}_C = \frac{\underline{V}}{j\omega L} + \frac{\underline{V}}{1/j\omega C}$
$\underline{I} = \frac{\underline{V}}{j\omega L + \frac{1}{j\omega C}} = j\frac{\omega C}{1-\omega^2 LC}\underline{V}$	$\underline{V} = \frac{\underline{I}}{\frac{1}{j\omega L} + j\omega C} = j\frac{\omega L}{1-\omega^2 LC}\underline{I}$
$\underline{V}_L = j\omega L\underline{I} = \frac{\omega^2 LC}{\omega^2 LC - 1}\underline{V}$	$\underline{I}_L = \frac{\underline{V}}{j\omega L} = \frac{1}{1-\omega^2 LC}\underline{I}$
$\underline{V}_C = \frac{\underline{I}}{j\omega C} = -\frac{1}{\omega^2 LC - 1}\underline{V}$	$\underline{I}_C = j\omega C\underline{I} = -\frac{\omega^2 LC}{1-\omega^2 LC}\underline{I}$

for the series LC circuit, and a current source for the parallel LC circuit. Table 5.3 shows the equations of the two circuits. The main conclusions can be summarized as follows:

- By modulating the frequency of the voltage source that supplies the series circuit, a high current will flow through the circuit when the quantity $\omega^2 LC - 1$ is small, since for this condition the circuit impedance is very small; consequently, high voltages may occur across both the inductance and the capacitance. This may be seen as a magnification of the voltage.
- By modulating the frequency of the current source that supplies the parallel circuit, a high voltage will occur across both circuit components when the quantity $\omega^2 LC - 1$ is small, since for this condition the circuit impedance is very large; consequently, high currents may flow through both the inductance and the capacitance. This may be seen as a magnification of the current.

Note that in both cases the resonant frequency is given by the same expression:

$$\omega_r = \sqrt{\frac{1}{LC}} \quad \rightarrow \quad f_r = \frac{1}{2\pi}\sqrt{\frac{1}{LC}} \tag{5.15}$$

TOVs due to resonance can occur in special network configurations. A possible network configuration where resonance overvoltages may occur is a system feeding a transformer and an unloaded transmission line. The magnetizing inductance of the transformer changes periodically with double frequency due to the modulation of the saturation characteristic by the voltage source. If the natural frequency of the resulting circuit is equal to the frequency of magnetizing inductance, even ultra-harmonic resonance is possible. This phenomenon is called parametric resonance. Similar overvoltages can be originated when an unloaded transformer is switched on – see the following subsection.

TOVs due to resonance can be reduced or avoided by detuning the resonance frequency of the system, by changing the system configuration or by introducing or increasing the damping of the system. In general, system configurations prone to resonance overvoltages have to be detected from field measurements or by means of detailed studies.

5.3.5.3 Parallel Harmonic Resonance

Harmonic resonance can occur when shunt capacitors banks are installed for reactive power compensation in distribution systems that have nonlinear loads (e.g. power electronic converters) – see Figure 5.9.

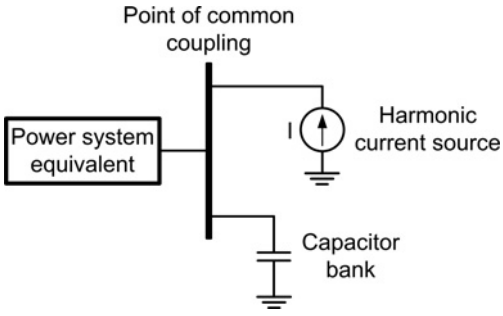

Figure 5.9 Power system configuration for harmonic resonance.

Ignoring resistance, the impedance seen from the point of application of the capacitor bank may be approximated by an LC parallel combination:

$$\frac{j\omega L \cdot \dfrac{1}{j\omega C}}{j\omega L + \dfrac{1}{j\omega C}} \tag{5.16}$$

where L is the equivalent inductance of the system prior to the installation of the capacitor and C is the capacitance of the capacitor bank.

If L and C remain invariant with frequency, resonance will occur when the inductive and capacitive inductance of the denominator in (5.16) are equal, and the denominator is zero; that is, when the impedance of the combination is infinite for a lossless system. At the resonant frequency f_r, the condition given by equation (5.15) is satisfied.

Without the presence of the capacitor bank, the natural resonant frequency of the power system is usually high. When frequency increases, the capacitive reactance decreases and the inductive reactance increases, and it may happen that, after installing the capacitor bank, the condition $\omega^2 LC = 1$ is satisfied at the frequency of a load-generated harmonic. The capacitor bank and the rest of the system act like the parallel branches of a tuned circuit. Such a circuit, when excited at the resonant frequency, will result in the magnification of the harmonic current, which may even exceed the fundamental frequency current. This will overload the capacitor and all the system components with damaging results.

The condition (5.15) can be rewritten as

$$h = \frac{f_r}{f} = \sqrt{\frac{\text{kVA}_{sys}}{\text{kvar}_{cap}}}, \tag{5.17}$$

where h is the order of the harmonic, f_r is the resonant frequency, f is the supply system frequency, kVA_{sys} is the short-circuit kVA at the point of application of the capacitor, and kvar_{cap} is the shunt capacitor rating. This type of resonance is a major concern in power systems, and must be avoided in any application of power capacitors.

This simple analysis can be used to size capacitor banks for a given distribution system to avoid resonance. A capacitor bank size has to be selected so that the resonant frequency does not coincide with any load-generated harmonic. However, the short-circuit level in a power system is not a constant parameter, and it will vary with the switching conditions: for example, a generator or a tie-line circuit may be out of service or part of the motor loads may have been shut down, which will lower the

short-circuit level. Therefore, the resonant frequency will vary, depending on the switching conditions, and a reorganization of the system may bring about a resonant condition where none existed before.

A method of predicting the resonant frequency of the system in the presence of capacitors is to run a frequency scan. A current source of variable frequency is applied at the point of common coupling (PCC) for the range of harmonics to be studied. For a unit current injection, the calculated voltages give the driving point and transfer impedances, both in modulus and phase angle. That is, plots of modulus and phase angle impedance are obtained at varying frequency, which provides the loci of resonant frequencies. The procedure is valid regardless of the number of harmonic-producing loads, as long as the principle of superimposition is valid; that is, when the system contains only linear elements for the range of frequencies. System component (e.g. transformers, generators, reactors and motors) must be adequately represented as a function of the frequency [14, 15, 23].

Resonance phenomena caused by the installation of capacitor banks can be propagated and can impact remotely. A study aimed at detecting the possibility of resonance is therefore important to prevent this situation and to apply a solution technique. A harmonic source can be considered as a harmonic generator. Apart from the overloading of capacitors, the harmonic currents can seriously de-rate transformers, produce additional losses in conductors, result in negative sequence overloading of generators, give rise to transient torques and torsional oscillations in rotating machinery or negatively affect protective relays.

5.3.5.4 Case Study 3: Harmonic Resonance

A very common means for preventing resonance is either to use passive or active harmonic filters, or to apply modern power electronics technologies that limit the harmonics at the source. Figure 5.10 shows the diagram of the test case: a linear load, paralleled by a diode rectifier, is being fed from the lowest voltage side of a step-down transformer. To improve the load power factor, a 9 Mvar capacitor bank will be installed at the PCC. After installing the capacitor bank, a resonance problem may occur due to the presence of harmonic currents injected by the diode rectifier. This problem can be predicted by performing a frequency scan of the system once the capacitor bank has been placed. Figure 5.11 shows the waveshape of the AC-side rectifier current and its harmonic spectrum.

A frequency scan of the system from the PCC after installing the capacitor bank is performed to detect resonance problems. The plot in Figure 5.12 confirm that a resonance will occur at a frequency close to the fifth harmonic. The harmonic currents going to the rectifier can be seen as harmonic currents injected into the PCC; they will flow to the HV system through the transformer and divide into other components connected to the PCC, depending upon their harmonic impedances.

Figure 5.13 shows some simulation results corresponding to the system that results after installing the capacitor bank. It is evident, as predicted from the frequency scan, that a resonance phenomenon occurs, and the capacitor bank can be damaged as a consequence of the large current. This is a characteristic of a parallel-tuned circuit: while the exciting current (i.e. the harmonic currents from the rectifier) can be small, the capacitor forms a resonant tank circuit with the source impedance, resulting in magnification of the injected current.

This problem can be solved by installing a filter tuned to the fifth harmonic; that is, the capacitor bank is replaced by a shunt filter, whose tuned frequency is five times the fundamental. The new frequency

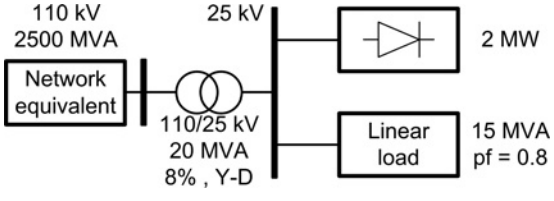

Figure 5.10 Case Study 3: Diagram of the test system.

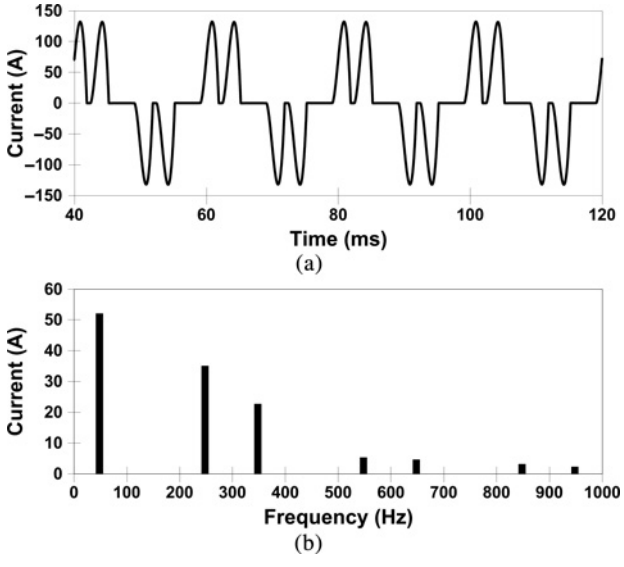

Figure 5.11 Case Study 3: AC-side rectifier current: (a) current waveshape, (b) harmonic spectrum.

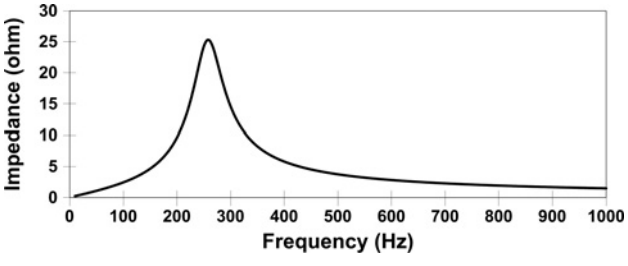

Figure 5.12 Case Study 3: Frequency scan with capacitor bank.

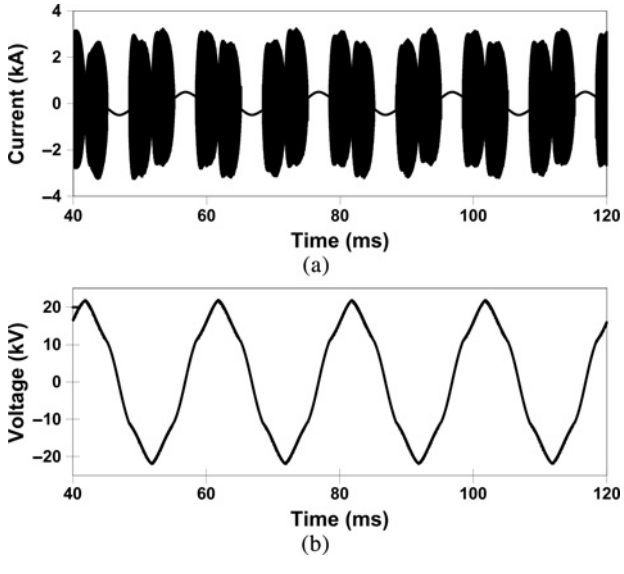

Figure 5.13 Case Study 3: Installation of a capacitor bank: (a) capacitor bank current, (b) voltage at point of common coupling.

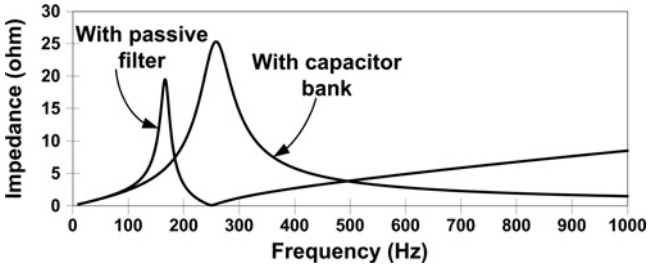

Figure 5.14 Case Study 3: Frequency scan with capacitor bank and with filter.

scan is shown in Figure 5.14, and compared to the frequency response obtained with the capacitor bank. The application of a band-pass filter has not eliminated resonances, but now they occur at frequencies below the tuned frequency and correspond to points that are away from the load-generated harmonics. For a practical filter design, it is important to account for some variations in the tuned and resonant frequency with various system switching conditions. Figure 5.15 shows some results with the applied filter; they can be compared with Figure 5.13.

5.3.6 Energization of Unloaded Transformers

5.3.6.1 Introduction

Switching off a loaded transformer is not usually a problem, and no overvoltage is usually created in the system or within the transformer. However, re-energizing the transformer can cause high inrush currents due to the nonlinear behaviour of its core. Transformer inrush currents can have a high magnitude with a

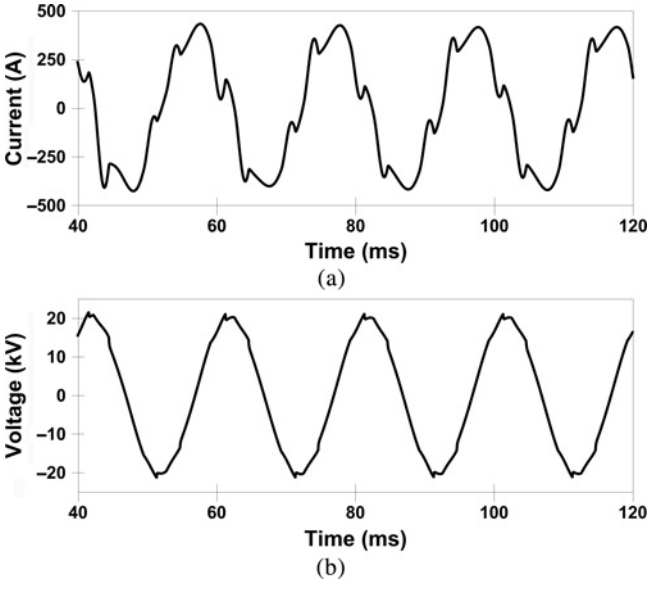

Figure 5.15 Case Study 3: Installation of a passive filter: (a) capacitor bank current, (b) voltage at point of common coupling.

significant harmonic content (note that the inrush current contains both odd and even harmonics), so when a line and a transformer are energized together, resonance overvoltages can occur. The inrush currents interact with the power system, whose resonant frequencies are a function of the series inductance (associated with the short-circuit strength of the system) and the shunt capacitances of lines and cables. This may result in long-duration resonant TOVs.

A transmission system will generally be weak during the first steps of a system restoration following a blackout. The equivalent system inductances are then relatively high because relatively few generators are on line and the grid tends to be sparse. Therefore, the first system resonant frequency can be much lower than during normal system operation. Large capacitances also contribute to the low resonant frequencies. One of the major concerns during the early stages of a power system restoration is the occurrence of resonance overvoltages as a result of switching procedures [24]. During a restoration phase, the capacitive voltage rise due to charging currents can be sufficient to overexcite transformers and generate significant harmonics. If the combination of the system impedance and the line capacitance is adverse, then a harmonic resonance will result. Harmonic distortions produced by transformer saturation will excite these resonances, which can cause damaging overvoltages that result from several factors that are characteristic of networks during restoration [24]: (1) the natural frequency of the series circuit formed by the source inductance and line charging capacitance may, under normal operating conditions, be a low multiple of the power frequency; (2) the magnetizing inrush caused by energizing a transformer produces many harmonics; (3) during early stages of restoration, the lines are lightly loaded while transients are lightly damped, which means that the resulting resonance voltages may be very high. If transformers become overexcited due to power frequency overvoltage, harmonic resonance voltage will be sustained or even grow. Energizing equipment during black-start conditions can result in overvoltages higher than during normal operation, and they can cause arrester failures and system faults, and prolong system restoration [24].

The trapped charge that remains in the line/cable after a switching operation caused by a fault condition that initially opened the circuit may also generate substantial overvoltages when energizing an unloaded transformer through a line or cable. When closing the transformer, a path for the discharge of the current trapped along the line/cable is established through the magnetizing impedance of the transformer and as long as the core of the transformer is not saturated it represents a high impedance. However, as the transformer comes into saturation its impedance drops rather quickly, resulting in an increase in current and in a rapid discharge of the cable. As the core comes out of saturation the process reverses and the interchange of stored energies will continue to repeat it. The voltage will oscillate with a square wave and, with each oscillation, a certain amount of the original energy will be dissipated until the oscillation dies out.

Temporary resonant harmonic overvoltages may also develop when transformers are switched in high voltage cable systems and HVDC stations [25]. The AC filter circuits connected at the HVDC stations produce several parallel resonance points in the impedance–frequency characteristic of the system, so high saturation overvoltages may occur if the system also has a low degree of damping.

The energizing of an unloaded transformer through a line/cable can also bring up a situation where extremely high voltages can be generated within the transformer and lead to a transformer failure. These internal overvoltages develop whenever the resonant frequencies of the feeder and of the transformer match themselves. Since the length of the line/cable determines the travel time and the resonant frequency of the line/cable and the transformer, a simple alternative to decrease or mitigate the effects of these switching transients is to change the length of the feeder. Another option is connecting capacitors at the secondary terminals of the transformer.

For more details on transformer energization studies, including some actual case studies, see the CIGRE Brochure 568 [26].

5.3.6.2 Transformer Inrush Current

The magnetizing current necessary to maintain the magnetic flux in the core of an unloaded transformer is in general only a small percentage of the rated current. However, the magnetizing current of an unloaded transformer during energization may become extremely high when the transformer core

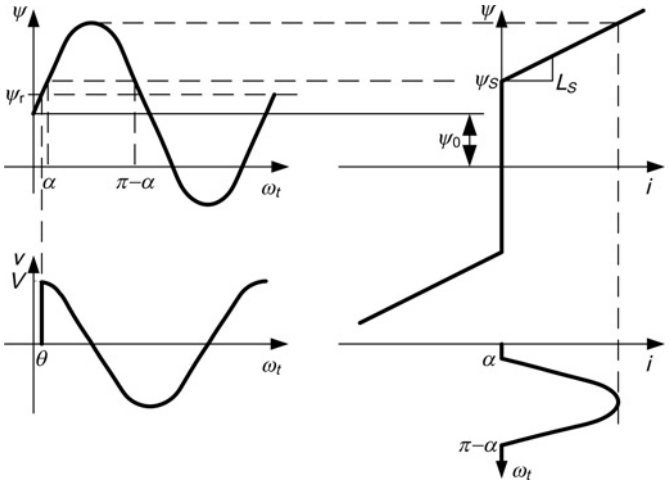

Figure 5.16 Simplified transformer magnetization characteristic for inrush current analysis.

comes into saturation, see Figure 5.16. Since saturation is a highly nonlinear phenomenon, the inrush current contains a DC component and harmonics besides its fundamental. When a power transformer has been switched off from the system, the transformer core is left with residual flux. When the power transformer is connected to the network again at an instant when the polarity of the system voltage is the same as the polarity of the residual flux, then at maximum voltage the total flux density in the core would have increased. The core is forced into saturation and the transformer draws a large current from the supplying network. When the voltage reverses its polarity in the next half cycle, then the maximum flux in the core is less than the maximum flux density in the no-load situation. The transformer inrush current is therefore asymmetrical and also contains a DC component, and may need seconds to disappear.

5.3.6.3 Overvoltages During Transformer Energization

A harmonic analysis can be carried out by representing an inrush current as a harmonic current source $I(h)$ connected to the transformer bus. The relation between nodal voltages, network impedance matrix and current injections can be then analysed by means of impedance equations [27]:

$$\mathbf{V}(h) = \mathbf{Z}(h)\mathbf{I}(h), \tag{5.18}$$

where h represents the harmonic frequencies (multiples of the fundamental frequency), and $\mathbf{Z}(h)$ is a symmetrical matrix with as many rows and columns as the harmonic currents. $\mathbf{V}(h)$ and $\mathbf{I}(h)$ are the vectors of harmonic voltages and currents, respectively.

The harmonic current components of the same frequency that the system resonance frequencies are amplified in the case of parallel resonance, thereby creating high voltages at the transformer terminals, as seen in the previous section. This leads to a higher level of saturation resulting in higher harmonic components of the inrush current, which again results in increased voltages. This can happen particularly in lightly damped systems, common at the beginning of a restoration procedure when a path from a black-start source to a large power plant is being established and only a few loads have been restored [24, 28].

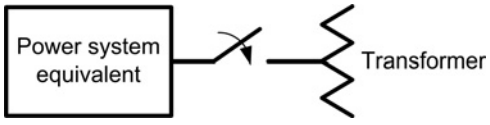

Figure 5.17 Diagram of the test system.

Figure 5.17 illustrates a condition that can lead to harmonic resonance overvoltages. It is a very simplified representation of a power system at the early stages of a restoration procedure in which the analysis is concentrated on the energization of a transformer that is assumed to be unloaded. Figure 5.18 shows some simulation results. One conclusion from a frequency scan from the point of connection of the transformer is that the impedance seen from this bus shows a parallel resonance peak at the second harmonic. When the transformer is energized, this resonance condition results in the overvoltage depicted in Figure 5.18(e).

5.3.6.4 Methods for Preventing Harmonic Overvoltages During Transformer Energization

Equipment is usually designed to withstand a power frequency overvoltage of about 1.6 p.u. for 1 minute [29]. The equipment can withstand higher overvoltages if the duration of the overvoltage is shorter, but the magnitude of resonance overvoltages may exceed 1.6 p.u. for a longer time if the phenomenon is poorly damped. In general, surge arresters will normally be activated before the resonance overvoltage reaches the equipment's overvoltage withstand limits. However, the withstand capability of equipment may deteriorate due to aging or other internal defects; therefore, sustained resonance overvoltages may damage the system equipment, even if they are below the specified overvoltage withstand capability. This situation is not desirable, and the risk of resonance overvoltage should be minimized.

The key factors for analysis of harmonic overvoltages include: the resonance frequency of the network; the system damping (including the network losses and the load connected to the network); the voltage level at the transformer terminals; the saturation characteristic and the remanent flux in the core of the transformer; and the closing time of the circuit breaker pole. Factors that contribute to a higher level of resonance overvoltage are [29]: (1) higher rating of the transformer to be energized; (2) lower value of source fault level; (3) longer circuit length; (4) smaller amount of load in the system; (5) higher system voltage profile; (6) higher working flux density of the transformer; and (7) transformer energized at the point near the maximum voltage.

Harmonic TOVs during transformer energization are sensitive to several parameters: circuit breaker closing times, switching angles, transformer saturation curve, residual flux in transformers, source impedances and system capacitances. The methods that have been proposed to prevent harmonic resonance overvoltages are:

- adding as much load as possible before energizing a transformer: This leads to a decrease in the magnitude of the impedance and, consequently, to a reduced amplification of the injected harmonic currents. To ensure that resonance is damped, sufficient load should be connected to the underlying system. Analysis for a 500 kV line has shown that a load of about 3 MW per mile is adequate [24].
- selecting a low impedance path for energization of a transformer: A high source impedance can be reduced by bringing additional generators on-line since a higher number of generators results in a lower overall inductance and, consequently, in a higher resonance frequency. This means that if generators are added, the resonance peak is shifted to higher frequencies and if generators are omitted, it is shifted to lower frequencies.

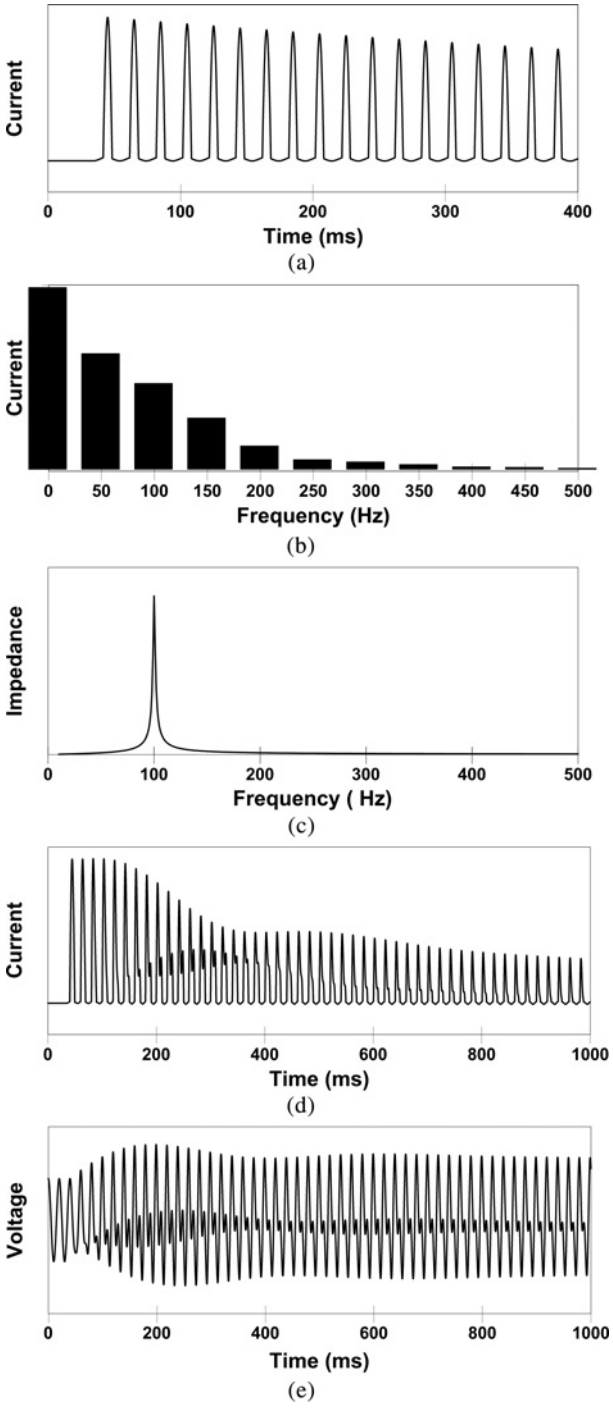

Figure 5.18 Energization of an unloaded transformer: (a) transformer inrush current, (b) harmonic content of the inrush current, (c) impedance at transformer bus, (d) transformer current during energization, (e) transformer terminal voltage.

- reducing the system voltage before energizing a transformer: The reactive power of a lightly loaded system can be reduced by minimizing the number of unloaded lines to be energized and setting the sending-end transformers at the lowest tap position. Sustained harmonic overvoltages caused by over-excitation of transformers can be controlled by selecting a transformer tap which equals or exceeds the power-frequency voltage applied (or lowering system voltage to at or below the tap) before energizing. Decreasing the generators' scheduled voltage leads to a proportional decrease of the preswitching steady-state voltages. This effect results in a change of the transformer inrush current.
- controlling the switching time: Controlled switching is a reliable method of reducing overvoltages during energization of transformers. This method is based on the measurement of the residual flux, which can significantly affect inrush currents. This technique is the most effective method for the limitation of the switching transients, since the magnitudes of the created transients are strongly dependent on the closing instants of the switch. The determination of the optimal switching time aimed at reducing harmonic overvoltages caused by transformer energization during power system restoration has been analysed in [30]. Up to three different strategies (*rapid*, *delayed* and *simultaneous* closing) were proposed in [31, 32] for controlled energization of multiphase transformers.

5.3.7 Ferroresonance

5.3.7.1 Introduction

Ferroresonance in power systems can involve large substation transformers, distribution transformers or instrument transformers. The general requirements for ferroresonance are an (applied or induced) source voltage, a saturable magnetizing inductance of a transformer, a capacitance and low damping [22, 33, 34]. The capacitance can be in the form of the capacitance of underground cables or transmission lines, capacitor banks, coupling capacitances between double circuit lines or in a temporarily ungrounded system, and voltage grading capacitors in HV circuit breakers. Other possibilities are generator surge capacitors and SVCs in long transmission lines. In fact, ferroresonance may also arise solely due to transformer winding capacitance.

System events that may initiate ferroresonance include single-phase switching or fusing, or loss of system grounding.

5.3.7.2 Ferroresonance in a Single-Phase Transformer

Figure 5.19 shows an illustrative example. A very small excitation current flows when the rated voltage is applied to an unloaded single-phase transformer. This current consists of two components: the magnetizing current and the core loss current. The magnetizing current, which flows through the nonlinear magnetizing inductance L_m, is required to induce a voltage in the secondary winding of the transformer. The core loss current, flowing through R_c, is made up of the eddy current losses and the hysteresis losses in the transformer's steel core. Although usually assumed linear, R_c is dependent on voltage and frequency. The excitation current contains high-order odd harmonics, due to transformer core saturation, see Figure 5.19(a).

R_{w1}/R_{w2} and L_{w1}/L_{w2} are the winding resistances and winding leakage inductances, respectively. They are assumed to be linear, with magnitudes relatively small compared to R_c and L_m, so they are usually ignored in no-load situations [33].

If a capacitor is placed between the voltage source and the unloaded transformer, ferroresonance may occur, see Figure 5.19(b). An extremely large exciting current is drawn, while the voltage induced on the secondary may be larger than the rated one. The high current here is due to resonance between the series capacitor and L_m. Due to nonlinearity, two other ferroresonant operating modes are possible, depending on the magnitudes of source voltage and series capacitance. In general, gradual changes in source voltage or capacitance will cause state transitions.

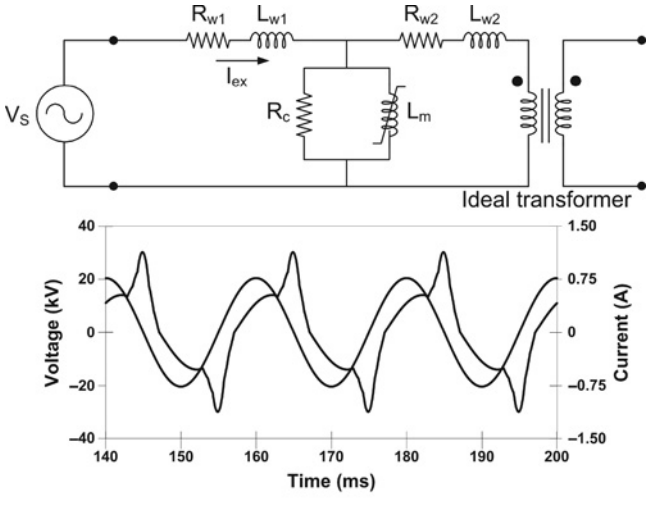

(a)

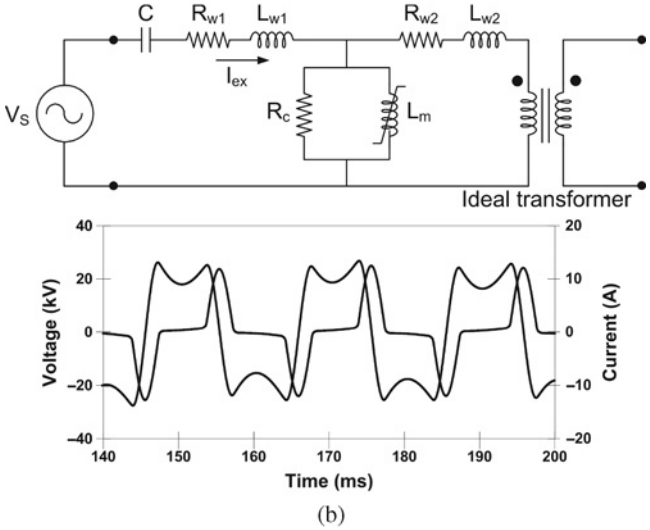

(b)

Figure 5.19 Ferroresonance in an unloaded single-phase transformer with rated voltage applied: (a) unloaded single-phase transformer, (b) unloaded single-phase transformer with series capacitor.

Damping added to the circuit will attenuate the ferroresonant voltage and current. Although some damping is always present in the form of resistive source impedance, transformer losses and even corona losses in high-voltage systems, most damping is due to the load applied to the secondary of the transformer. A lightly loaded or unloaded transformer fed through capacitive source impedance is the most frequent scenario for ferroresonance.

5.3.7.3 Ferroresonance in Three-Phase Systems

Ferroresonance is rarely seen, provided all three source phases are energized, but it may occur when one or two of the source phases are lost while the transformer is unloaded or lightly loaded. The loss of one

or two phases can happen due to clearing of single-phase fusing, operation of single-phase reclosers or sectionalizers, or when energizing or de-energizing using single-phase switching procedures. If one or two poles of the switch are open and if either the capacitor bank or the transformer have grounded neutrals, then a series path through capacitance(s) and magnetizing reactance(s) exists, and ferroresonance is possible. If both neutrals are simultaneously grounded or ungrounded, then no series path exists and there is no clear possibility of ferroresonance [16, 33]. In all of these cases, the voltage source is the applied system voltage.

Ferroresonance is possible for any transformer core configuration. Three-phase core types provide direct magnetic coupling between phases, where voltages can be *induced* in the open phase(s) of the transformer.

Whether ferroresonance occurs depends on the type of switching and interrupting devices, the type of transformer, the load on the secondary of the transformer and the length and type of line/cable. However, due to nonlinearities, increased capacitance does not necessarily mean an increased likelihood of ferroresonance.

Figure 5.20 shows three examples of ferroresonance occurring in a network where single-phase switching is used. A wye-connected capacitance is paralleled with an unloaded wye-connected transformer. The capacitance could be a capacitor bank or the shunt capacitance of the lines or cables

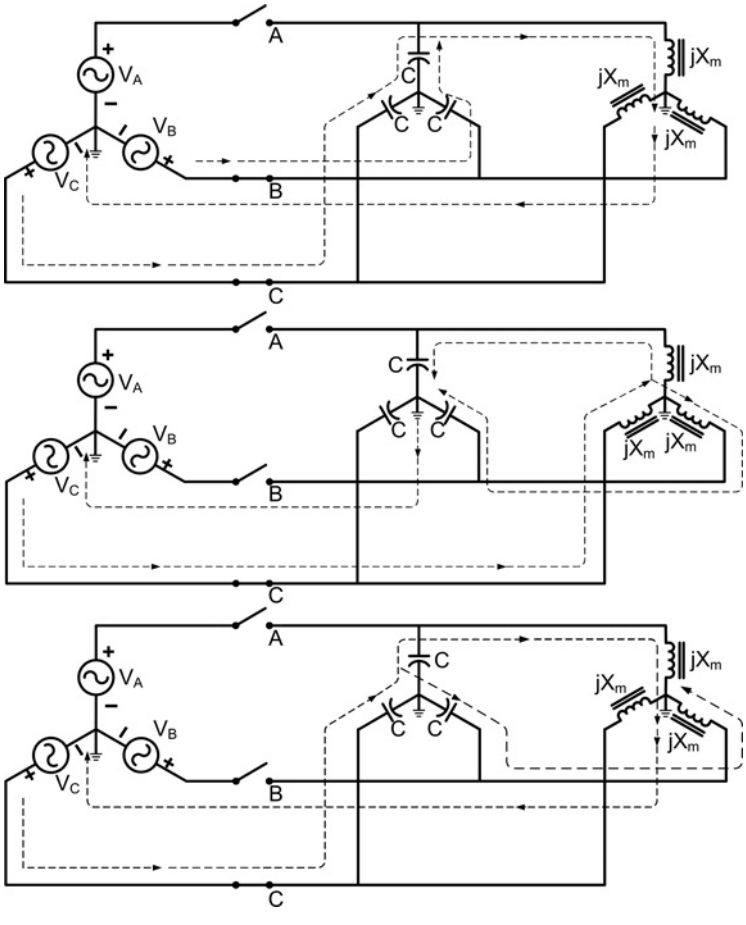

Figure 5.20 Examples of ferroresonance in three-phase systems [16, 33].

connecting the transformer to the source. Each phase of the transformer is represented only by the magnetizing reactance jX_m [16, 33].

If one of the three switches of Figure 5.20 were open, only two phases of the transformer would be energized. If the transformer is of the triplex design or is a bank of single-phase transformers, the open phase is simply de-energized, and the energized phases draw normal exciting current. However, if the transformer is of the multilegged core type, a voltage is *induced* in the 'open' phase. This induced voltage will 'backfeed' the distribution line back to the open switch. If the shunt capacitance is significant, ferroresonance may occur. The ferroresonance that occurs involves the nonlinear magnetizing reactance of the transformer's open phase and the shunt capacitance of the distribution line and/or transformer winding capacitance. Single-phase loads connected along this backfeed phase will continue to be supplied with poor power quality.

The use of single-phase interruption and switching practices in systems containing multilegged core transformers is a common condition for initiating ferroresonance. Replacement of all single-phase switching and interrupting devices with three-phase devices would eliminate this problem. An alternative solution would be to replace multilegged core transformers with single-phase banks or triplex designs wherever there is a small load factor.

5.3.7.4 Nonlinear Dynamics Applied to Ferroresonance

Even though ferroresonance involves a capacitance and an inductance, there is no definite resonant frequency, and more than one response is possible for the same set of parameters, and gradual drifts or transients may cause the response to jump from one steady-state response to another.

Ferroresonant circuits can be analysed as damped nonlinear systems driven by sinusoidal forcing function(s) [35]. The nonlinear behaviour of ferroresonance falls into two main categories. In the first, the response is a distorted periodic waveform, containing the fundamental and higher-order odd harmonics of the fundamental frequency. The second type is characterized by a non-periodic response. In both cases the response contains fundamental and odd-harmonic frequency components. In the non-periodic response, however, there are also distributed frequency harmonics and subharmonics.

'Lower energy modes' occur more typically for very large capacitance values and produce periodic voltages. Some of the periodic modes of ferroresonance may contain subharmonics, but still have strong power frequency components, and take longer than one fundamental cycle to repeat [36]. The 'higher energy modes' of ferroresonance involve relatively large capacitances and can produce non-periodic voltages [36]. Transitions between periodic and non-periodic modes occur due to gradual changes in circuit parameters or to transients. Initial conditions determine the mode in which the operation settles down after the transients die down.

Techniques developed for analysis of nonlinear dynamical systems and chaos (phase plane projections and Poincaré sections) can be applied to analysing ferroresonance [35, 37].

5.3.7.5 Modelling for Ferroresonance

Simulation can be used to avoid ferroresonance when designing a system. However, simulation results have a great sensitivity to the model used and errors in nonlinear model parameters. Although much effort has been made on refining equivalent circuit models for transformers, and performing simulations using transient circuit analysis programs such as EMTP, determining nonlinear parameters is still a difficult task. A different model is required and also a different means of determining the model parameters for each type of core.

The transformer model is probably the most critical part of any ferroresonance study. Another critical part is the system zone that must be represented in the model. Both aspects are discussed in the following paragraphs.

The study zone: Parts of the system that must be simulated are the source impedance, the transmission or distribution line(s)/cable(s), the transformer and any capacitance not already included. Source representation is not generally critical; unless the source contains nonlinearities, it is sufficient to use the steady-state Thevenin impedance and open-circuit voltage. Lines and cables may be represented as RLC coupled pi-equivalents, cascaded for longer lines/cables. Shunt or series capacitors may be represented as a standard capacitance, paralleled with the appropriate resistance. Stray capacitance may also be incorporated, either at the corners of open-circuited delta transformer winding or midway along each winding. Other capacitance sources are transformer bushings, interwinding capacitances and busbar capacitances.

Single-phase transformers: They are typically modelled as shown in Figure 5.19. This model is topologically correct only for the case where the primary and secondary windings are not concentrically wound. L_{w2} is essentially zero for concentric coils. Errors in leakage representation are not significant unless the core saturates. Obtaining the linear parameters for this two-winding transformer may not be easy. Short-circuit tests give total impedance; that is, $(R_{w1} + R_{w2}) + j(X_{w1} + X_{w2})$. A judgement must be made as to how it is divided between the primary and secondary windings.

Model performance depends mainly on the representation of the nonlinear elements R_c and L_m. R_c is modelled as a linear resistance. Such a core-loss model represents the average losses at the level of excitation being simulated, and may yield reasonable results. Since eddy current losses and hysteresis losses are nonlinear, the calculation of the loss resistance R_c gives a different value for each level of excitation. Using the value of R_c closest to the rated voltage may be a good enough estimate. Past research has shown low sensitivities to fairly large changes in R_c for single-phase transformers, but a high sensitivity for three-phase cores [38]. L_m is typically represented as a piecewise linear λ–i characteristic or as a hysteretic inductance [39–41]. The linear value of L_m (below the knee of the curve) does not much affect the simulation results [42], although great sensitivities are seen for the shape of the knee and the final slope in saturation.

Factory test data provided by the transformer manufacturer may be insufficient to obtain the core parameters. It is important that open circuit tests be performed for voltages as high as the conditions being simulated, otherwise the final λ–i slope of L_m must be guessed. Open circuit tests should therefore be made for 0.2 to 1.3 (or higher) p.u.

The SATURATION supporting routine, available in some EMTP-like tools [43], is often used to convert the rms V–I open circuit characteristic to the instantaneous λ–i characteristic of L_m. To successfully use this method, the first (lowest) level of excitation must result in sinusoidal current, or errors will result in the form of an S-shaped λ–i curve. Also, the V–I characteristic must extend as high as the highest voltage that will be encountered in the simulation. An extension to this method has been proposed to obtain a nonlinear representation of R_c [44], but the resulting flux-linked versus excitation current (I_{EX}) loop does not seem to correctly represent the core losses.

Modern low-loss transformers have comparatively large interwinding capacitances, which can affect the shape of the excitation curve [45]. This can cause significant errors when the above method is being used to obtain core parameters. In these cases, factory tests must be performed to get the V–I curve before the coils are placed on the core. A means of removing the capacitive component of the exciting current has also been developed [38].

For three-winding transformers, a star-connected short-circuit equivalent may be obtained from binary short-circuit tests (shorting two windings at a time while leaving all others open). Although the terminal-to-terminal transfer impedances are always positive, one of the reactances in this mathematical representation may be negative. Such short-circuit models do not correctly account for mutual coupling between all windings and may cause problems in time-domain transient simulation [46, 47]. Another weakness of this short-circuit representation is that the core equivalent cannot be correctly incorporated. Although a solution to these problems has been presented in [48], some difficulties still remain since no standard nonlinear model is available in any simulation package.

Three-phase transformer models: A simplified model is possible for triplex core configuration by connecting together three of the above single-phase models. However, including the zero-sequence

effects for three-phase single-core transformers is not obvious, and some of the proposed approaches are questionable.

A complete transformer representation can be obtained by using a coupled inductance matrix (to model the winding characteristics) [49], to which the core equivalent is attached. The inductance matrix is obtained from standard short-circuit tests involving all windings. Problems can arise for rms short-circuit data involving windings on different phases, since the current may be non-sinusoidal. The hybrid model presented in [50, 51] is based on this approach.

A method of obtaining topologically correct models is based on the duality between magnetic and electrical circuits [52, 53]. The method uses duality transformations, and so equivalent circuit derivations reduce to exercises in topology. This approach results in models that include saturation in each individual leg of the core, interphase magnetic coupling and leakage effects.

Several topology transformer models based on the principle of duality have been presented in the literature [40, 41, 54–57]. However, since no standard model is available in any simulation package, tests suggested in the literature cannot always be performed, and no standard test have been developed for determining the parameters specified in some models [40], the use of some models is presently limited.

Factory excitation test reports will not provide the information needed to get the magnetizing inductances for this model. Standards assume that the exciting current is the 'average' value of the rms exciting currents of the three phases, which is not correct except for triplex cores, since the currents are not sinusoidal and they are not the same for every phase. Therefore, the waveforms of the applied voltage and exciting currents in all three phases should be given by the manufacturer for all levels of applied voltage.

5.3.7.6 Case Study 4: Distribution Transformer Ferroresonance

Figure 5.21 shows the diagram of the test system. The objective of the study is to estimate the cable length that can initiate ferroresonance when one or two poles of a circuit breaker are open and the load at the LV side of the distribution transformer is very low. As discussed above, the system configuration exhibits the prerequisites for ferroresonance: capacitance provided by the insulated cable, saturable inductance provided the distribution transformer, and low damping (i.e. unloaded or lightly loaded transformer).

The main parameters of the components that are of concern for a ferroresonance study are detailed below:

1. HV network: 110 kV, 1500 MVA, $X/R = 10$, $X_0/X_1 = 1.1$.
2. Substation transformer: Triplex core, 110/25 kV, 35 MVA, 12%, Yd11, grounded through a zigzag reactance with 75 Ω per phase.
   - No-load test (positive sequence, MV side): $V_0 = 100\%$; $I_0 = 0.296\%$; $W_0 = 18.112$ kW.
   - Short-circuit test (positive sequence, HV side): $V_{sh} = 12\%$; $I_{sh} = 83.34\%$; $W_{sh} = 348.263$ kW.
3. Cable: Al RHV, $3 \times (1 \times 240\ \text{mm}^2)$, 18/30 kV (see Figure 5.22).

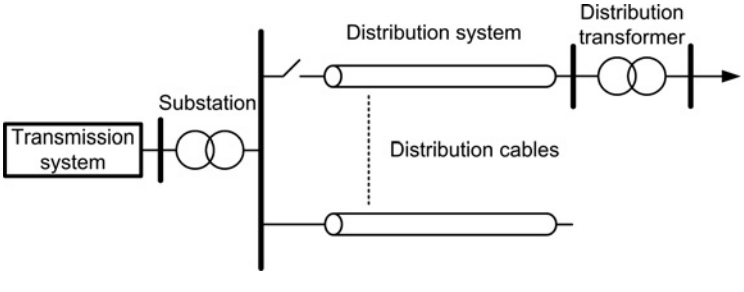

Figure 5.21 Case Study 4: Diagram of the test system.

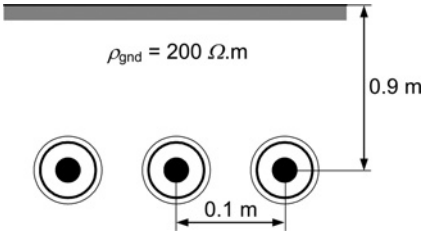

Figure 5.22 Case Study 4: Configuration of the distribution cable system.

4. Distribution transformer: Three-legged stacked core, 25/0.4 kV, 1 MVA, 6%, Dyn11.
   - Short-circuit test (positive sequence, MV side): $V_{sh} = 6\%$; $I_{sh} = 100\%$; $W_{sh} = 12$ kW.
   - No-load test (homopolar sequence, LV side): $V_h = 100\%$; $I_h = 0.5\%$; $W_h = 1.8$ kW.
   - Saturation curves are shown in Figure 5.23.

Observe that the configuration of the system zone to be analysed is very similar to the system shown in Figure 5.20. Therefore the scenarios to be analysed can be those depicted in that figure.

The models selected for each component (HV network, cable, transformers) have the following features:

- The HV transmission network is represented as an ideal balanced and constant three-phase voltage source in series with a three-phase impedance specified by its symmetrical impedances Z_1 and Z_0.
- The cable is represented by its pi-equivalent, whose parameters are obtained at power frequency.
- A different approach has been used for representing the substation and the distribution transformers. In fact, neither the model nor the parameters of the substation transformer are critical, and it can

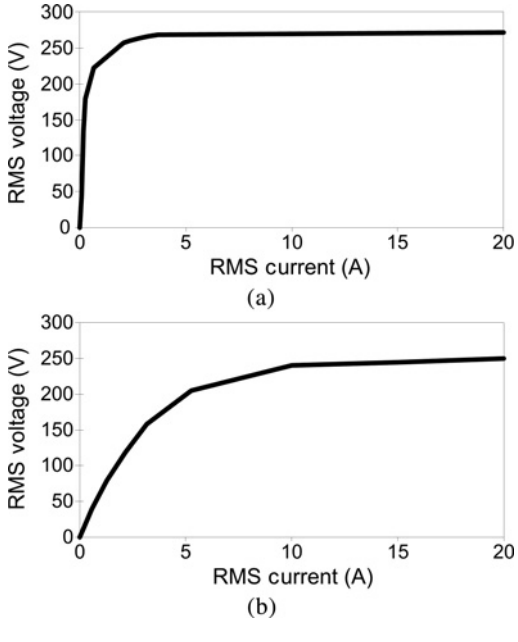

Figure 5.23 Case Study 4: Saturation curves of the distribution transformer: (a) legs, (b) yokes.

be represented by using any of the standard models implemented in most transients programs (e.g. XFORMER or BCTRAN), or even a simpler model without including nonlinearities. The model implemented for the distribution transformer is that described in reference [40].

- The switch needed to open the phases that can originate ferroresonance has an ideal behaviour.

The scenarios analysed always consider a lightly loaded transformer. In all cases the load power was assumed to be purely active, represented by means of constant resistors.

An important conclusion from the study is that ferroresonance does not originate when the cable length is shorter than 50 m, but it can appear with any length above 10 km.

As for the effect of the number of poles that are open, plots of Figures 5.24 and 5.25 show that less damping is required when two poles are open, to avoid ferroresonance. We can also see that the pattern of the oscillations is different for any of the cases presented in these figures.

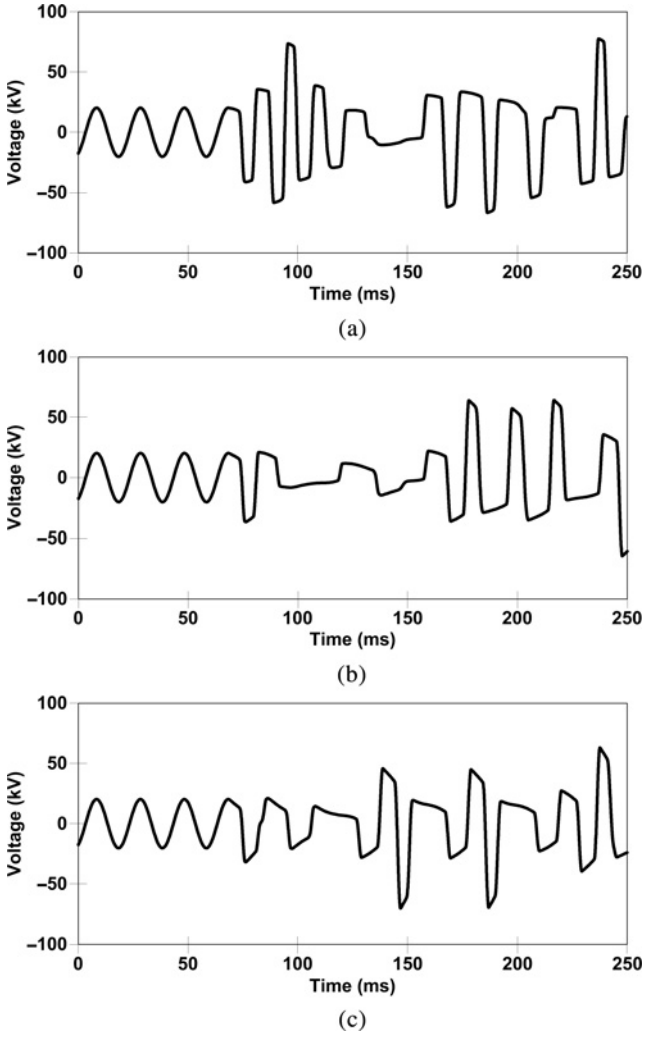

Figure 5.24 Case Study 4: MV side, one pole open (cable length = 1 km): (a) unloaded distribution transformer, (b) transformer load: 5 kW, (c) transformer load: 10 kW.

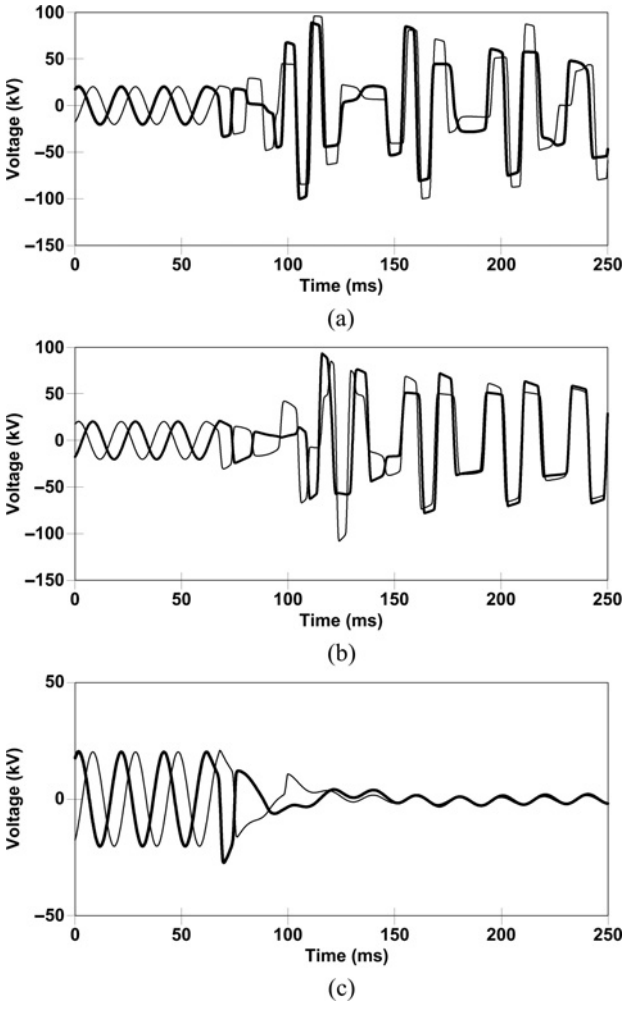

Figure 5.25 Case Study 4: MV side., two poles open (cable length = 1 km): (a) unloaded distribution transformer, (b) transformer load: 5 kW, (c) transformer load: 10 kW.

The effect of transformer capacitances was not considered in any of the simulations. Although these parameters can have some influence on the conditions that can originate ferroresonance, we should not expect to see large differences from the results presented here since the cable capacitances are much larger than the transformer capacitances.

The simulation results presented in Figures 5.24 and 5.25 correspond to a cable length of 1 km. According to these results the overvoltages at the MV side of the distribution transformer can reach values higher than 3 p.u. when one or two poles are open. As expected, a light load favours ferroresonance, which can be avoided by increasing the damping, in this case the transformer load.

5.3.8 Conclusions

Temporary overvoltages (TOVs) are difficult to prevent during the normal operation of a power system. Their voltage levels and probability of occurrence depend mostly on the design of the power system.

System planning and operational procedures may have an important effect on the appearance of these overvoltages.

TOVs in linear systems can be analysed in a rather easy manner, and the countermeasures are essentially confined to reactive compensation. Nonlinear components can cause a variety of TOVs, and not all of them can be mitigated in the same way. Only the category of subharmonic and even-harmonic modes allows the possibility of damping; in other cases reactive compensation is still the main countermeasure to limit the amplitudes of TOVs. Although there is a significant experience in ferroresonance studies [22, 58–61], and some validation work has been presented [62], more effort is still required. Present research is focused in improving transformer models and studying ferroresonance at the system level. Theories and experimental techniques of nonlinear dynamics and chaotic systems can be applied to better understand ferroresonance and the limitations inherent in modelling a nonlinear system. Because of nonlinearities, solution of the ferroresonant circuit must be obtained using time-domain methods; that is, computer-based numerical integration methods using time-domain simulation programs such as EMTP.

Typical values as a function of the overvoltage origin are given below [1, 18]:

- Overvoltages caused by faults to ground will have typical magnitudes of 1.2/1.3 p.u., the worst case being in the order of 1.5 p.u. Their duration will vary between 0.1 and 2 seconds, although they can last for 10 seconds or more.
- Ferroresonance overvoltage will exhibit magnitudes of 1.5–2 p.u., the worst case being in the order of 3 p.u. They can last from several seconds to several minutes.
- Overvoltages caused by load rejection can reach amplitudes of up to 1.2 p.u. in moderately extended systems and 1.5 p.u. or even more (due to Ferranti or resonance effects) in extended systems. Their duration depends on the operation of voltage-control equipment and may vary from some seconds, in extended systems, to several minutes, in moderately extended systems. If only static loads are on the rejected side, the longitudinal TOV is normally equal to the phase-to-ground overvoltage. In systems with motors or generators on the rejected side, a network separation can give rise to a longitudinal TOV composed of two phase-to-ground overvoltage components in phase opposition, whose maximum amplitude is normally below 2.5 p.u. (greater values can be observed for exceptional cases such as very extended high-voltage systems).

Mitigation methods depend mostly on the cause of the overvoltage:

- *Ground-fault overvoltages*: Ground-fault overvoltages depend on the system parameters and can only be controlled by selecting these parameters during the system design. The overvoltage amplitudes are normally less severe in grounded neutral systems. An exception exists in grounded neutral systems, a part of which in unusual situations can become separated with ungrounded transformer neutrals. In such situations, the duration of the high overvoltages due to ground faults in the separated part can be controlled by fast grounding at these neutrals, by switches or by specially selected neutral surge arresters, which will short-circuit the neutral after failing [2].
- *Load rejection overvoltages*: TOVs in systems with a linear behaviour can be affected by a change in system parameters or a change in source voltage only. Reactive compensation, either in the form of straight shunt compensation or controllable compensation, supplemented by appropriately structuring the system and by fast-acting voltage regulators, is the means to reduce TOVs caused by load rejection.
- *Resonance and ferroresonance*: These overvoltages should be limited by detuning the system from the resonance frequency, by changing the system configuration, or by using damping resistors.
- *Overvoltages caused by transformer energization*: Methods proposed to prevent harmonic resonance overvoltages caused during transformer energization include adding as much load as possible by the source before energizing a transformer, selecting a low impedance path for energization of a transformer, reducing the system voltage before transformer energization, or controlling the closing time.

5.4 Switching Overvoltages

5.4.1 Introduction

Switching transients in power systems are caused by the operation of breakers and switches. The switching operations can be classified into two categories: energization and de-energization. The former category includes energization of lines, cables, transformers, reactors and capacitor banks. The latter category includes current interruption under faulted or unfaulted conditions.

The results from the study of switching transients are useful to: (1) determine voltage stresses on equipment; (2) select arrester characteristics; (3) calculate the transient recovery voltage across circuit breakers; and (4) analyse the effectiveness of mitigating devices (e.g. pre-insertion resistors or inductors).

The level of detail required in the model varies with the study. For example, a line may be represented by a pi-section equivalent in some line energization studies; in other situations, a distributed-parameter model with frequency dependence may be necessary. In addition, the results are highly sensitive to the value of certain parameters; for example, the maximum overvoltage for a line energization depends on the exact point on the wave at which the switch contacts close. Thus a number of runs for the same system have to be made with the time of energization being different in each run either in a predictable manner (for determining the peak overvoltage) or statistically (for obtaining an overvoltage probability distribution).

5.4.2 Modelling Guidelines

A discussion of the extent of the system to be modelled and details about equipment models typically used for switching transient simulation are presented in the following subsections [17].

5.4.2.1 Lines and Cables

The most accurate line/cable representations are based on distributed-parameter models. Lumped-parameter models (pi-circuits) are less accurate and computationally more expensive, because a number of cascaded short-sections are needed to approximate the distributed nature of the physical line/cable.

The frequency dependence of the line parameters may be an important consideration, particularly when the (zero sequence) ground return mode is involved (e.g. during a line-to-ground fault). In these cases, a frequency-dependent distributed-parameter line model gives a very accurate representation for a wide range of frequencies in transient phenomena. The parameters for the selected model (with either frequency-dependent or constant parameters) are obtained from geometrical and physical information (line/cable geometry, conductor and soil characteristics) by using line/cable constants supporting routines, embedded in most EMTP-like tools.

The use of nominal pi-circuits is usually restricted to the case of very short lines when the travelling time τ is smaller than the integration step Δt of the simulation [43, 63]. However, cascaded pi-sections can be used without excessive loss of accuracy for some studies, such as line energization [15, 64]. The number of pi-circuits will usually depend on the desired accuracy.

The parameters for the pi-section of an overhead line can be obtained from positive- and zero-sequence fundamental frequency impedance values that are used in load flow studies. Typical positive and zero-sequence parameters of overhead lines are presented in Table 5.4 [17].

The self and mutual impedances to be used in the pi-representation can be deduced using the following expressions:

$$\begin{aligned} X_s &= \frac{1}{3}(X_0 + 2X_1) \quad X_m = \frac{1}{3}(X_0 - X_1) \\ C_s &= \frac{1}{3}(C_0 + 2C_1) \quad C_m = \frac{1}{3}(C_0 - C_1) \end{aligned} \tag{5.19}$$

Table 5.4 Typical transmission line parameters at 60 Hz ($\rho = 100$ Ω.m) [17].

	Voltage level			
	230 kV	345 kV	500 kV	765 kV
Number of circuits	2	1	1	1
Conductors/phase	1	2	3	4
Ground wires	1	2	2	2
X_1 (Ω/km)	0.5000	0.3800	0.3800	0.3400
R_1 (Ω/km)	0.0520	0.0320	0.0180	0.0170
X_0 (Ω/km)	2.5000	1.3000	1.2000	1.0090
R_0 (Ω/km)	0.4900	0.3410	0.3300	0.3300
C_1 (μF/km)	0.0088	0.0120	0.0130	0.0130
C_0 (μF/km)	0.0041	0.0083	0.0075	0.0093

In many cable studies in which the frequencies span a large bandwidth and the cable parameters significantly vary within this range, the constant-parameter assumption can be too limiting, so a frequency-dependent parameter model must be used. However, for solid dielectric cables, the constant parameter model is often adequate. The estimation of the maximum allowable pi-section length and the associated errors are discussed in [17].

5.4.2.2 Transformers

For switching transient studies, a lumped-parameter coupled-winding model with a sufficient number of RLC elements that fit the impedance characteristics at the terminal within the frequency range of interest will suffice. The nonlinear characteristic of the core should usually be included, although the frequency characteristic of the core is often ignored. This may be an oversimplification because the eddy current effect prevents the flux from entering the core steel at high frequencies, thereby making the transformer appear to be air-cored. This effect begins to be significant even at frequencies of the order of 3–5 kHz.

For switching surge studies, the following approaches may be used:

- a model developed from the transformer nameplate – most standard EMTP models fall into this category [43, 49, 65]
- a model synthesized from the measured impedance vs. frequency response of the transformer, as described in [66–69]
- a very detailed model obtained from the transformer geometry and material characteristics. The model is then reduced to one that is usable in the time-domain solution [70, 71].

When possible, validation of the model should be made. A frequency response obtained by simulation can be compared within the desired bandwidth with the actual characteristic if available. Determining the fundamental frequency response in the form of open and short-circuit impedances is a standard check, and should be done for all possible open and short-circuit conditions on the windings. Induced winding voltages at fundamental frequency are of interest. Comparison with factory tests if available also validates the model. If terminal capacitance measurements are available, a comparison between measured and computed responses is useful.

5.4.2.3 Switchgear

In switching transient studies, the switch is often modelled as an ideal conductor (zero impedance) when closed, and an open circuit (infinite impedance) when open. Transients packages allow various options to

vary the closing time, ranging from one-shot deterministic closings to multishot statistical or systematic closings [43].

Opening: Transient studies are based on an ideal switch model that opens at a current zero. The dynamic characteristic of the arc is usually not important and is not modelled in most cases, although it can be useful in some cases [72–75].

In certain instances where small inductive currents are being interrupted, the current in the switch can extinguish prior to its natural zero crossing. Severe voltage oscillations can result due to this current-chopping that can stress the circuit breaker. For a detailed description of this phenomenon see [76].

Statistical switching: Transient voltage and current magnitudes depend upon the instant on the voltage waveform at which the circuit breaker contacts close electrically. A statistical switching case typically consists of several hundred separate simulations, each using a different set of circuit breaker closing times. Statistical methods can be used to post-process the peak overvoltages from each simulation. Circuit breakers can close at any time (angle) on the power frequency wave. For a single-phase circuit, the set of circuit breaker closing times can be represented as a uniform distribution from 0 to 360 degrees, with reference to the power frequency.

A three-phase (pole) circuit breaker can be modelled as three single-phase circuit breakers, each with an independent uniform distribution covering 360 degrees. However, an alternative (dependent) model can be used if the three poles are mechanically linked and adjusted so that each pole attempts to close at the same instant. In reality, there will be a finite time, or pole span, between the closing instants of the three poles. The pole span can be modelled with an additional statistical parameter, typically a normal (Gaussian) distribution. For a mechanically linked three-pole circuit breaker, the closing times use both uniform distribution parameters and Gaussian distribution parameters. All three dependent poles use the same parameter from the uniform distribution, which varies from 0 to 360 degrees. Each pole uses a unique parameter from the Gaussian distribution. The standard deviation of the maximum pole span is typically 17–25% of the maximum pole span.

Statistical cases with pre-insertion resistors or reactors require a second set of three-phase switches. The first set is modelled as described above. The closing times of the second set (which shorts the resistors or reactors) depend upon the first set plus a fixed time delay, which is typically one-half to one cycle for pre-insertion resistors used with circuit breakers, and 7 to 12 cycles (depending on application voltage class) for pre-insertion reactors used with circuit-switchers closing in air through high-speed disconnect blades.

Prestriking: The withstand strength of the contacts decreases as the contacts come closer. When the field stress across the contacts exceeds this withstand strength, prestrike occurs. If this is taken into account, the distribution of closing angles is confined to the rising and peak portions of the voltage waveshapes [77]. Some modern devices can control the closing angle of the poles to close at or near the voltage zero between the contacts [78–80]. Such devices can reduce overvoltages and inrush currents. For such devices, the maximum angle in the tolerance of the voltage zero closing control should be used. Alternatively, a statistical switching method can be applied to the breaker poles over the time span around the voltage zero, within the tolerance of the closing time [77].

Faults: Faults are usually modelled as ideal switches in series with other elements if necessary. The switch can be closed during the steady state solution or closed at a specific time or voltage. Several runs with variations in the closing instant should be carried out as the point on wave of switching can affect the transient. Faults may also be modelled with flashover controlled switches to represent a gap; the switch is operated when the gap voltage exceeds a fixed value.

More sophisticated models include a volt–time characteristic. Faults generally involve arcs, which can be modelled by various approximations: (1) ideal switch ($V = 0$, $R = 0$); (2) constant voltage V or linear resistance R; (3) constant V and series R; (4) series V and R that vary according to some assumed function; (5) V and/or R that vary according to some differential equation [81]. The most commonly used option is the first one since the arc voltage is usually small compared with voltage drops elsewhere (i.e. along the transmission line). Arc modelling can be important when studying secondary arc phenomena, such as single-phase reclosing. For a discussion on the modelling of this phenomenon see [82].

5.4.2.4 Capacitors and Reactors

Capacitor banks are usually modelled as a single-lumped element. However, some switching transient simulations require the modelling of secondary parameters such as series inductance and loss resistance. The inductance of the buswork is sometimes important when studying the back-to-back switching of capacitor banks, or in the study of faults on the capacitance bus. The damping resistance of this inductance should be estimated for the natural frequency of oscillations.

Reactors are usually modelled by a simple lumped inductor with a series resistance. A parallel resistance may be added for realistic high-frequency damping. The core saturation characteristic may also have to be modelled. A parallel capacitance across the reactor should be included for reactor opening studies (chopping of small currents). The total capacitance includes the bushing capacitance and the equivalent winding-to-ground capacitance. For series reactors, there is a capacitance from the terminal to ground and from terminal to terminal. More sophisticated models may be developed for determining internal stresses [83].

5.4.2.5 Surge Arresters

Gapless metal oxide surge arresters can be modelled as a nonlinear resistance. The preferred representation is a true nonlinear element which iterates at each time-step to a convergent solution and is thus numerically robust [84–86]. The *V–I* characteristic should be modelled with 5–10 (preferably exponential as opposed to linear) segments. Waveshape-dependent characteristics are usually not required for most slow-front switching transient simulations. The surge arrester lead lengths and separation effects can also be ignored for such studies [14].

5.4.2.6 Loads

In general, the power system load is represented using an equivalent circuit with parallel-connected resistive and inductive elements. The power factor of the load determines the relative impedance of the resistive and inductive elements. Shunt capacitance is represented with the resistive and inductive elements of the load if power factor correction capacitors are used. Whenever loads are lumped at a load bus, the effects of lines, cables and any transformers downstream from the load bus need to be considered [14].

This is particularly important for the simulation of high-frequency transient phenomena. In such cases, an impedance Z_s in series with the parallel RLC load equivalent circuit is appropriate, as shown in Figure 5.26. The series impedance, combined with the equivalent source impedance at the load bus, is typically in the range of 10–20% of the load impedance.

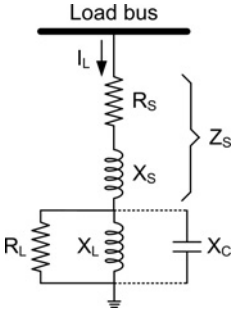

Figure 5.26 Equivalent circuit representation of power system loads for simulating switching transients.

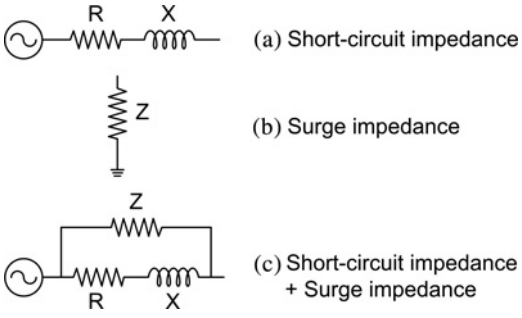

Figure 5.27 Conventional network equivalents [17].

Certain types of load may require specific representation of some components (e.g. induction motors, adjustable-speed drives or fluorescent lighting loads). The need for such detailed representation is determined by the phenomenon being investigated.

A load model will be included in the study only when it can add crucial information; otherwise, the load is not considered and the most conservative results are derived.

5.4.2.7 Power Supply

As for other components, the power supply model depends on the phenomenon being investigated. In some transient studies, a generator can be modelled as a voltage behind the subtransient impedance. If the zone under study is fed from a power system, the supply system can be modelled as an ideal sinewave source in series with its equivalent impedance.

Often a network equivalent is used in order to simplify the representation of the portion of the power network not under study. Figure 5.27 shows some simple network equivalents [17]. The first type (a) represents the short-circuit impedance (Thevenin equivalent) of the connected system, being the *X*/*R* ratio selected to adequately represent the damping (the damping angle is usually in the range 75–85°). The second type (b) represents the surge impedance of connected lines; this equivalent may be used to reduce connected lines to a simple equivalent surge impedance and where the lines are long enough so that reflections are not of concern in the system under study. If the connected system consists of a known Thevenin equivalent and additional transmission lines, the two impedances may be combined in parallel as in Figure 5.27(c). However, it should be noted that this approach may yield an incorrect steady-state solution if the equivalent impedance of the parallel connected lines is of comparable magnitude to the source impedance. If so, it may not be possible to lump the source and the lines into a single equivalent impedance.

More complex equivalents which properly represent the frequency response characteristic (as opposed to the ones above, which are most accurate near to the fundamental frequency) may be required [87, 88]. An update of the work performed on network equivalents has been presented in [89].

5.4.3 Switching Overvoltages

Typical case studies are analysed for a practical demonstration of the modelling guidelines [5, 17, 75]. Several different examples are considered: energization of lines and cables, transient recovery voltage determination for line and transformer faults and switching of shunt and series capacitor banks.

5.4.3.1 Energization of Lines and Cables

The energization of lines and cables by closing the circuit breaker may cause significant transient overvoltages. It is important to distinguish between energization and reclosing. In the former case, there

is no trapped charge. In case of reclosing, the line/cable may have been left with a trapped charge after the initial breaker opening. Under such circumstances, the transient overvoltages can reach values of up to 4.0 p.u. The aim of these studies is to determine the overvoltage stresses and choose the insulation strength in order to achieve an outage rate criterion [6, 90] – see the case studies in Section 5.4.4.

The source, transformer, overhead lines, insulated cables, circuit breaker and the trapped charges (if any) are to be modelled in order to study energization transients. A variety of line and cable models can be used in these studies, including pi-circuit and distributed-parameter models. As shown in [17], either a constant distributed-parameter model or a pi-circuit model can be used to represent a cable in statistical energizations, being results very similar. However, for pipe-type cables a frequency-dependent distributed-parameter model is recommended, since eddy current losses in the iron pipe can have a considerable effect on switching transients, especially if the frequency content is above 1 kHz.

5.4.3.2 Transient Recovery Voltage

A transient voltage is developed across the contacts of a switch when they start to open. This voltage, known as transient recovery voltage (TRV), is present immediately after the current zero, and in actual systems its duration is in the order of milliseconds. The recovery voltage will consist of two components: a transient component, which occurs immediately after a current zero, and a steady-state component, which is the voltage that remains after the transient dies out. The actual waveform of the voltage oscillation is determined by the parameters of the power system. Its rate of rise and amplitude are of vital importance for a successful operation of the interrupting device. If the rate of recovery of the contact gap at the instant of current zero is faster than the rate of rise of the recovery voltage (RRRV), the interruption is successful in the thermal region. It may be followed by a successful recovery voltage withstand in the dielectric region and then by a full dielectric withstand of the recovery voltage. If, however, the RRRV is faster than the recovery of the gap, then failure will occur either in the thermal region or in the dielectric region. A good understanding of the transient phenomena associated with circuit breaker operations in power systems has led to improved testing practice and resulted in more reliable switchgear. Recommended characteristic values for simulation of the TRV are fixed in standards [91–93]. Some important cases of current interruption are analysed in this section [17, 75].

Single-line fed bus fault: Consider the circuit in Figure 5.28, which shows a fault fed from a single line, which in turn is fed by a bus with substantial capacity and several connected long transmission lines. When a fault at the remote end of a transmission line is cleared, the receiving end voltage at the remote end oscillates with a half period equal to the travel time of the line. The peak magnitude in the lossless case can be up to twice the sending end voltage at the instant of fault clearing. This voltage now appears as the TRV across the open breaker. In the actual case, the slope and magnitude of the TRV is dependent on the damping present in the system.

Figure 5.28(b) shows the equivalent circuit that could be used to analyse this case. The network equivalent may be of the types (a) and (c) shown in Figure 5.27. The inductance value is obtained from the short-circuit current at the bus. If a type (c) network equivalent is chosen, the parallel resistance results from a parallel combination of the surge impedance of the unfaulted lines. This representation is appropriate when the lines are long and no reflections affect the protective device during the transient period under consideration. If the fundamental frequency impedance of the source is much smaller than the equivalent parallel impedance of the transmission lines, the warning sentence of the previous subsection does not apply. If the lines are not so long, then each one is represented by its travelling time and surge impedance, as in Figure 5.27(b). When considering unbalanced faults, a full model may be necessary. The faulted line may be also represented as a low-frequency lossless line with lumped resistance at the midpoint and at the end of the line. Lumped capacitances represent the bus capacitances of the supply station and the station at the end of the line. The transient recovery voltage across the circuit breaker will exhibit a waveform that will depend on the distance of the fault location to the bus, the surge impedance of the lines and the number of lines – see Figure 5.28(c).

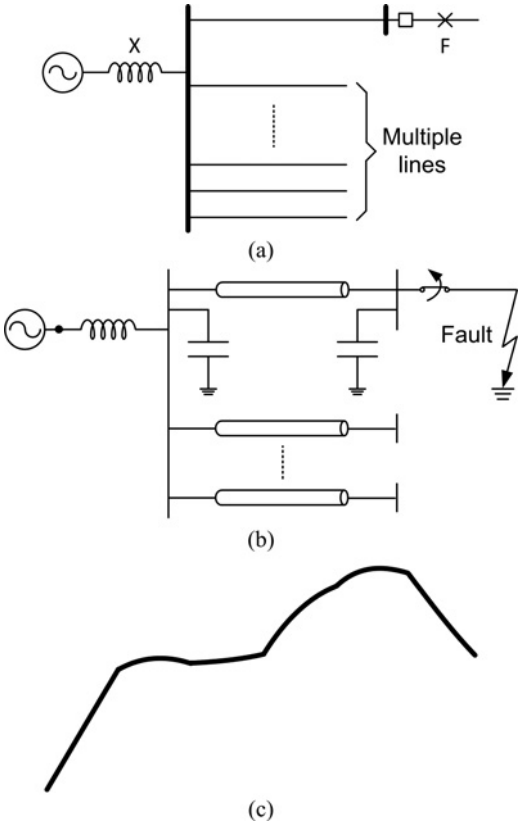

Figure 5.28 Single-line fed bus fault: (a) diagram of the test system, (b) equivalent circuit, (c) typical waveform.

Transformer Secondary-Fault: The aim is to find the TRV on the circuit breaker on the primary side of a transformer after it clears a secondary-side fault, see Figure 5.29. When a fault occurs on the secondary side of a transformer, the relatively large leakage inductance of the transformer will limit the magnitude of the fault current through the primary-side protective device. In addition, the source-side bus voltage drops to a level determined by the leakage inductance of the transformer and the effective source impedance. At the same time, the transformer secondary-side voltage collapses to zero, dropping the bus voltage (reduced from its pre-fault value due to the fault) across the leakage inductance of the transformer. When the fault is cleared, the source-side bus voltage recovers in an oscillatory fashion with a frequency determined by the source inductance and its equivalent capacitance. If the transformer is located at the end of a line, the source-side bus voltage will attempt to recover to the pre-fault voltage level through a ramp, and overshoot. This sets up a damped 'oscillation' on the source side of the protective device with a period determined by the positive- and zero-sequence travel times of the line. For short lines, the source inductance dominates, reducing the magnitude of oscillations that occur at a higher frequency. The voltage on the transformer side of the switch collapses to zero in an oscillatory fashion with a frequency determined by the leakage reactance of the transformer and its equivalent terminal capacitance. The resulting switch transient recovery voltage rate of rise is very steep, with a substantial peak value – see Figure 5.29(c).

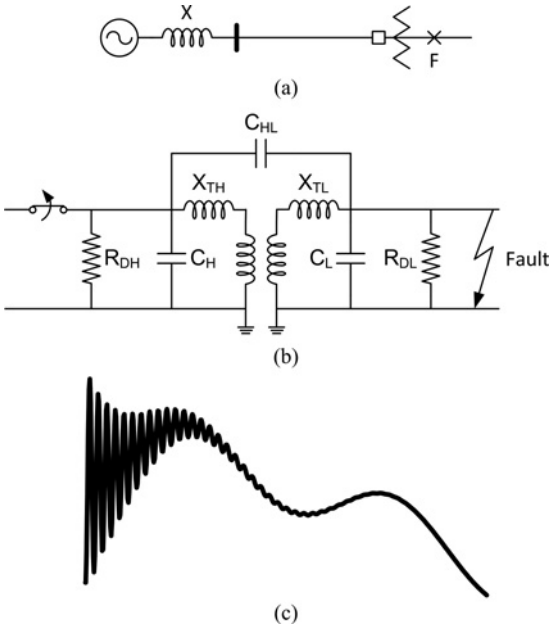

Figure 5.29 Transformer secondary fault: (a) diagram of the test system, (b) equivalent circuit of the transformer, (c) typical waveform.

The transformer can be represented as shown in Figure 5.29(b). Transformer terminal capacitances are included when a fault on one side of the transformer is cleared from the other side. The capacitive coupling ratio, $C_{HL}/(C_{HL} + C_L)$, is generally lower than 0.4. The capacitance is calculated from the known winding frequencies. Representative frequencies for power transformers are reported in [94]. The effective terminal capacitances can be determined based on the frequency of oscillation of each winding by using

$$C = \frac{1}{(2\pi f)^2 L_T}, \tag{5.20}$$

where f is the frequency of oscillation of each of the windings in Hz, L_T (henries) is the transformer leakage inductance (referred to the winding of interest) and C (farads) is the effective capacitance, where

$$C = C_H + C_{HL} \quad \text{for the high-voltage winding,} \tag{5.21a}$$

$$C = C_L + C_{HL} \quad \text{for the low-voltage winding.} \tag{5.21b}$$

Due to high-frequency winding resistance and eddy current losses, the oscillations are damped. This damping is represented by the resistance to ground in the equivalent circuit. For most transformers the damping is usually such that the damping factor (i.e. the ratio of successive peaks of opposite polarity in the oscillation) is of the order of 0.6 to 0.8.

Short-line fault: A fault on a transmission line close to the terminals of a high-voltage circuit breaker is known as a *short-line fault* – see Figure 5.30(a). The clearing of a short-line fault puts a high thermal stress on the arc channel in the first few microseconds after current interruption due to the electromagnetic waves reflecting from the short-circuit back to the terminals of the circuit breaker which can result in a TRV with a rate of rise of 5–10 kV/μs [95, 96]. Figure 5.30(c) shows the typical saw-tooth shape of the

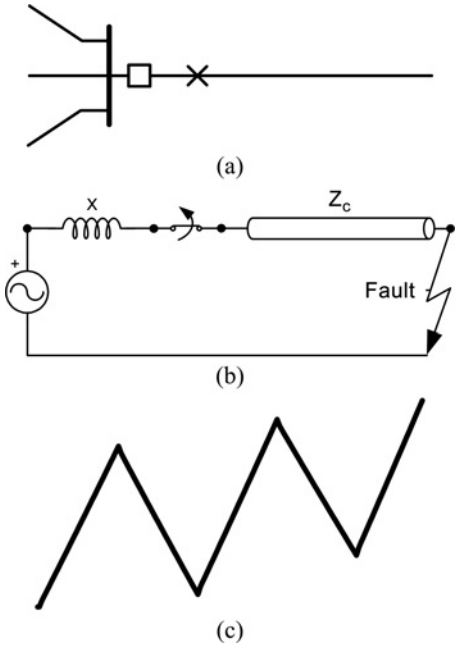

Figure 5.30 Short-line fault: (a) diagram of the test system, (b) equivalent circuit, (c) typical waveform.

recovery voltage during a short-line fault clearing. For some kinds of circuit breakers, the initial TRV is the most critical period, and the stress caused by a short-line fault may be the most severe. The value of the rate of rise at the line side depends on the interrupted short-circuit current and the characteristic impedance of the overhead transmission line. The parameter of concern is not the maximum TRV but its initial rate of rise. For the system represented in Figure 5.30(b), this value may be approached by [75, 95]

$$RRRV \approx \sqrt{2}V\omega\frac{S_{sh}}{SIL} \quad (\omega = 2\pi f), \tag{5.22}$$

where S_{sh} is the short-circuit capacity at the circuit breaker location and *SIL* is the surge impedance load of the transmission line.

Interruption of small inductive currents: The interruption of small inductive currents can lead to situations that are known as *current chopping* and *virtual chopping* [76, 96]. If the current is interrupted at current zero, the interruption is normal and the transient recovery voltages are usually within the specified values. However, if premature interruption occurs, due to current chopping, the interruption will be abnormal and it can cause high-frequency reignitions and overvoltages. When the breaker chops the peak current, the voltage increases almost instantaneously, if this overvoltage exceeds the specified dielectric strength of the circuit breaker, reignition takes place. When this process is repeated several times, due to high-frequency reignitions, the voltage increase continues with rapid escalation. The high-frequency oscillations are governed by the electrical parameters of the concerned circuit, the circuit configuration and the interrupter design, and result in a zero crossing before the actual power-frequency current zero.

Figure 5.31 compares the transient recovery voltages that are generated when arc interruption takes place at current zero, and before current zero (current chopping), respectively. It is obvious from this example that the second case is more severe.

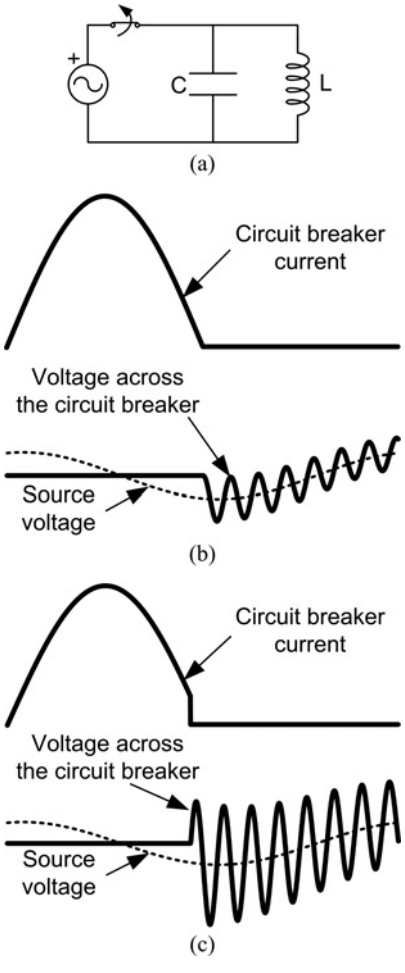

Figure 5.31 Interruption of small inductive currents: (a) equivalent circuit, (b) interruption at current zero, (c) interruption before current zero.

Since the frequency of the oscillations, $1/(2\pi\sqrt{LC})$, will usually be much higher than the power frequency, the above value should be added to the peak voltage of the source to obtain the TRV across the circuit breaker.

In the case of *current chopping*, the instability of the arc around current zero causes a high-frequency transient current to flow in the neighbouring network elements. This high-frequency current superimposes on the power-frequency current whose amplitude is small and which is actually *chopped* to zero. In the case of *virtual chopping*, the arc is made unstable through a superimposed high-frequency current caused by oscillations with the neighbouring phases in which current chopping took place. Virtual chopping has been observed for gaseous arcs in air, SF_6 and oil. Vacuum arcs are also very sensitive to current chopping.

The circuit shown in Figure 5.31(a) was used to illustrate the problems related to current chopping; more accurate models are usually required, mainly when reignitions/restrikes need to be analysed, see for instance [75, 97, 96].

5.4.3.3 Capacitor Switching

Capacitor switching can cause significant transients at both the switched capacitor and remote locations. The most common problems when switching capacitors are [17]: (1) overvoltages at the switched capacitor during energization, (2) voltage magnification at lower voltage capacitors during capacitor energization, (3) transformer phase-to-phase overvoltages at a line termination during capacitor energization, (4) breaker current due to inrush from capacitors at the same bus while a capacitor is being energized, (5) breaker current due to outrush from a capacitor into a nearby fault, and (6) capacitor breaker restrike. Although all of these phenomena can be initiated by capacitor switching or fault initiation near a capacitor, they each produce different types of transients that can adversely affect different power system apparatus. These phenomena and their modelling requirements are briefly discussed below. Several practical cases have been presented in the literature, for example [98–101].

Capacitor energization: Energizing a shunt capacitor from a predominantly inductive source results in an oscillatory transient voltage at the capacitor bus with a magnitude that can approach twice the peak bus voltage prior to energization. The characteristic frequency of the energization transient is

$$f = \frac{1}{2\pi\sqrt{L_S C}}, \tag{5.23}$$

where L_S is the source inductance and C is the capacitor bank capacitance.

This energization transient can excite system resonances or cause high frequency overvoltages at transformer terminations. The magnitude and duration of the energizing voltage transient is dependent upon a number of factors including system strength, local transmission lines, system capacitances and switching device characteristics. Voltage transient magnitudes increase as system strength is reduced, relative to capacitor size. In addition to reducing system surge impedance and increasing system strength, transmission lines provide damping. These three characteristics of transmission lines help reduce capacitor energizing transients. Other capacitors in the vicinity of a switched bank help reduce capacitor energizing transients because they reduce system surge impedance.

Switching devices can be designed to reduce transients by using closing control, pre-insertion resistors, or pre-insertion inductors. The closer to zero voltage a capacitor is energized, the lower the resulting transients. The optimum closing resistor size is approximately equal to the surge impedance calculated as

$$R_{optimum} = \sqrt{\frac{L_S}{C}}, \tag{5.24}$$

where L_S is the source inductance and C is the capacitor bank capacitance.

Voltage magnification: Normal capacitor bank energizing transients, which are limited to twice the preswitch capacitor bus voltage, are not a concern at the switched capacitor location. Significant transient voltages can occur at remote capacitors or cables when magnification of the capacitor energizing transient occurs. The simple circuit in Figure 5.32 illustrates the voltage magnification phenomena.

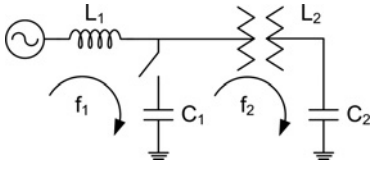

Figure 5.32 Voltage magnification.

The highest transient voltages, on a per unit basis, occur at the lower voltage capacitance (C_2) during capacitor C_1 energization when (1) the capacitive Mvar rating of C_1 is significantly greater than that of C_2 and (2) the natural frequencies f_1 and f_2 (as defined below) are nearly equal:

$$f_1 = \frac{1}{2\pi\sqrt{L_1 C_1}} \quad f_2 = \frac{1}{2\pi\sqrt{L_2 C_2}} \tag{5.25}$$

The magnitude of the voltage magnification transient at C_2 is dependent on switched capacitor size, source impedance, the impedance between the two capacitances, system loading and the existence of other nearby low-voltage capacitors. Moderate increases in distribution system loading can significantly reduce voltage magnification transients. Because transformer losses increase significantly at higher frequencies, modelling the frequency dependence of transformer losses, or simply modelling the transformer *X*/*R* ratio at the capacitor's natural frequency, can improve model accuracy and reduce the severity of the voltage magnification simulated. Controlled breaker closing, pre-insertion resistors or pre-insertion inductors can be used to reduce voltage magnification related transients. Voltage magnification can also cause excessive energy duty at arresters protecting distribution capacitors. High-energy arresters may be necessary if other methods of reducing voltage magnification are not implemented.

Transformer termination phase-to-phase overvoltages: Capacitor energization can initiate travelling waves that will increase in magnitude when reflected at transformer terminations. These reflected surges will be limited to approximately 2 p.u. by the transformer line-to-ground arresters. Phase-to-phase voltage transients of 4 p.u. can be caused by 2 p.u. surges of opposite polarity appearing simultaneously on different phases. This 4 p.u. switching transient may exceed a transformer's switching surge withstand capability.

System short-circuit capacity and the number of lines at the switched capacitor location do not significantly affect this phenomenon. Switched capacitor size affects the frequency of oscillation that occurs when a capacitor is energized. Higher phase-to-phase transients often occur on longer lines because the travelling wave oscillation peak begins to match up with the natural frequency of the capacitor energization transient. Oscillations that occur on very short lines may also be important, as they have the potential for exciting transformer internal resonances.

As with other capacitor switching related transients, these transients can be reduced by the use of synchronous closing control, pre-insertion resistors or pre-insertion inductors.

Back-to-back capacitor switching: The inrush currents associated with back-to-back capacitor switching must be evaluated with respect to the capacitor switch capabilities. Standards specify inrush current magnitude and frequency limits for general and definite-purpose breakers [102]. A circuit illustrating back-to-back switching is shown in Figure 5.33.

The equations for calculating current magnitude and frequency are

$$I = \frac{V_{C1}}{Z} \quad f = \frac{1}{2\pi\sqrt{L_{eq} C_{eq}}} \quad I \times f = \frac{V_{C1}}{2\pi L_{eq}}, \tag{5.26}$$

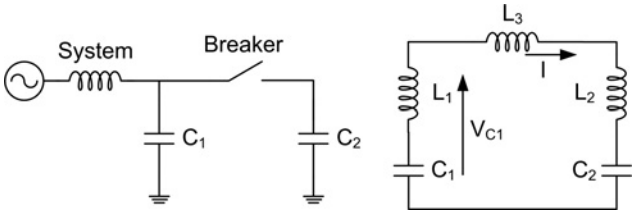

Figure 5.33 Back-to-back switching.

where

$$Z = \sqrt{\frac{L_{eq}}{C_{eq}}} \quad L_{eq} = L_1 + L_2 + L_3 \quad C_{eq} = \frac{C_1 \cdot C_2}{C_1 + C_2}, \tag{5.27}$$

V_{C1} is the voltage across C_1 as switch closes, L_1, L_2 are the self-inductances of the capacitor banks and L_3 is the inductance between capacitor banks.

A simple model that includes all impedances between the energized and switched capacitors will suffice to simulate back-to-back switching inrush currents. If the calculated inrush currents are excessive, current-limiting reactors can be used to bring them within acceptable limits. The size of the current-limiting reactor necessary to limit the inrush current to an acceptable level can be estimated by rearranging the equation for $I \times f$ above, as shown below, and using peak preswitch current and voltage values:

$$L_{eq} = \frac{V_{C1}}{2\pi(I \times f)} \tag{5.28}$$

Current outrush into a nearby fault: Current outrush from a capacitor can be a concern when a breaker closes into a fault. For general-purpose breakers, ANSI standards indicate that the product of the outrush current peak magnitude and the frequency is limited to less than 2×10^7 [102]. The limitation for definite purpose breakers is less severe, generally 6.8×10^7.

Figure 5.34 illustrates the capacitor current outrush phenomenon. The equations necessary to calculate current magnitude and frequency are

$$I = \frac{V_{C1}}{Z} \quad f = \frac{1}{2\pi\sqrt{L_{eq}C_{eq}}} \quad I \times f = \frac{V_{C1}}{2\pi L_{eq}}, \tag{5.29}$$

where

$$Z = \sqrt{\frac{L_{eq}}{C_{eq}}} \quad L_{eq} = L_1 + L_3 \quad C_{eq} = C_1, \tag{5.30}$$

V_{C1} is the voltage across C_1 as the switch closes, L_1 is the self-inductance of the capacitor bank and L_3 is the inductance between the capacitor banks and the fault.

If outrush currents are a concern, they can be limited by the use of reactors. The reactor size can be quite accurately determined by the following equation when peak preswitch voltage and current values are used [17]:

$$L_{eq} = \frac{V_{C1}}{2\pi(I \times f)} \tag{5.31}$$

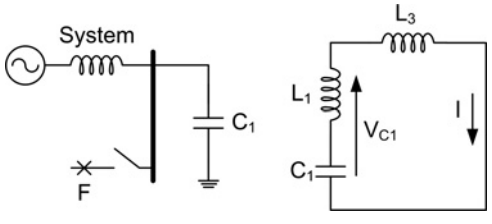

Figure 5.34 Outrush switching.

Arrester energy duty during capacitor breaker restrike: If the circuit breaker restrikes during the interruption of a capacitive current, there will be an inrush current flow which will force the voltage in the capacitor to oscillate with respect to the instantaneous system voltage to a peak value that is approximately equal to the initial value at which it started but with a reversed polarity. If the restrike happens at the peak of the system voltage, then the capacitor voltage will reach a value of 3.0 p.u. Under these conditions, if the high-frequency inrush current is interrupted at the zero crossing, then the capacitor will be left with a charge corresponding to a voltage of 3.0 p.u. and half a cycle later there will be a voltage of 4.0 p.u. applied across the circuit breaker contacts. If the sequence is repeated, the capacitor voltage will reach 5.0 p.u. [5, 75]. If damping is ignored, there could be a theoretical unlimited voltage escalation across the capacitor.

Arresters applied at large shunt capacitors should be evaluated for their energy duty during breaker restrike, even when the capacitor breakers are designed to be 'restrike free'.

There are several methods of determining arrester energy requirements during the first capacitor breaker restrike. The energy during subsequent restrikes can be much higher, but is usually not considered when sizing arresters.

An accurate method of determining arrester energy requirements during capacitor breaker restrike is to simulate the restrike event using a detailed transient model. The model should represent the system in detail for at least two busses in each direction from the capacitor.

The arrester energy requirement during restrike of a grounded capacitor can be calculated by [103]

$$E = \frac{C \times V_p}{2(V_p - V_s)} \cdot \left[4V_s^2 - (V_p - V_s)^2\right], \tag{5.32}$$

where C is the capacitor capacitance, V_p is the arrester protective level and V_s is the peak line-to-ground voltage.

Because the effects of system losses, loads or transmission lines are not included, the resulting arrester energy requirements will be conservatively but not excessively high. Derating of the arrester energy may be required because of the high magnitude currents associated with capacitor restrike transients.

Series capacitor switching: Series capacitors are usually installed on transmission lines to increase power transfer capability. Transient studies may be required to determine the impact of the series compensation on the existing system to ensure safe and reliable operation. The aspects to be evaluated may include the following [17]:

- surge arrester sizing: Establish surge arrester duty and related protection settings for the capacitor bank.
- line breaker TRV: Determine the transient recovery voltage for the transmission line breakers.
- line energization: Investigate system behaviour when the compensated line is energized.
- bank insertion and bypass: Investigate system behaviour when the series capacitor is bypassed or inserted.
- single-phase reclosing: Determine line end arrester duty for single-phase reclosing operation.
- line protection: Investigate relay requirements.

Simulated events may consider varying size and location of the series capacitor, although these are generally determined by steady-state, transient stability and subsynchronous resonance studies, and by relaying requirements.

The system model typically includes lines and transformers at least one bus back from the switching locations of interest. Transmission lines are represented as distributed-parameter models. Transformers are modelled using a saturable transformer component model. Equivalent sources can be modelled as mutually coupled elements considering their positive and zero sequence characteristics. Series capacitors and other system components are modelled as lumped-parameter elements, including quality factor. The model should also include the bypass breaker with its series reactor, and the surge arrester connected across the series capacitor.

The worst-case fault conditions that keep the capacitor bank inserted determine the maximum surge arrester energy requirements. The case list includes three-phase, double-phase and single-phase faults. Single-phase reclosing events under fault conditions must be also considered: the line end breakers open on the faulted phase only to clear the fault, and then one end recloses.

The maximum TRV of line breakers may be evaluated by applying three-phase and single-phase faults at various locations along the line and at the series capacitor. In some cases, arresters or pre-insertion devices may be required to reduce the TRV to acceptable levels. The effect of energizing the series-compensated line with and without the capacitor bypassed can be evaluated. The impact of capacitor bank insertion and bypass should be simulated under varying power flow and other operating conditions. The bypass switch TRV is evaluated from the simulation of capacitor bank insertion. The simulation of capacitor bypass determines the inrush currents. Results should then be compared to the withstand ratings at the breaker and its series reactor.

An illustrative example of series capacitor switching was presented in [17].

5.4.4 Case Studies

5.4.4.1 Case Study 5: Transmission Line Energization

Figure 5.35 shows the tower design of the test line, a 50 Hz, 400 kV transmission line. Characteristics of phase conductors and shield wires are provided in Table 5.5. The objective is to determine the probability distribution of switching overvoltages, assuming the line length is 200 km. To perform the calculations, the source side will be represented by a network equivalent with a short-circuit capacity of 10 000 MVA and considering the following ratios: $Z_1 = Z_2$, $X_1/R_1 = 12.0$, $X_1/X_0 = 1.3$, $X_0/R_0 = 8.0$.

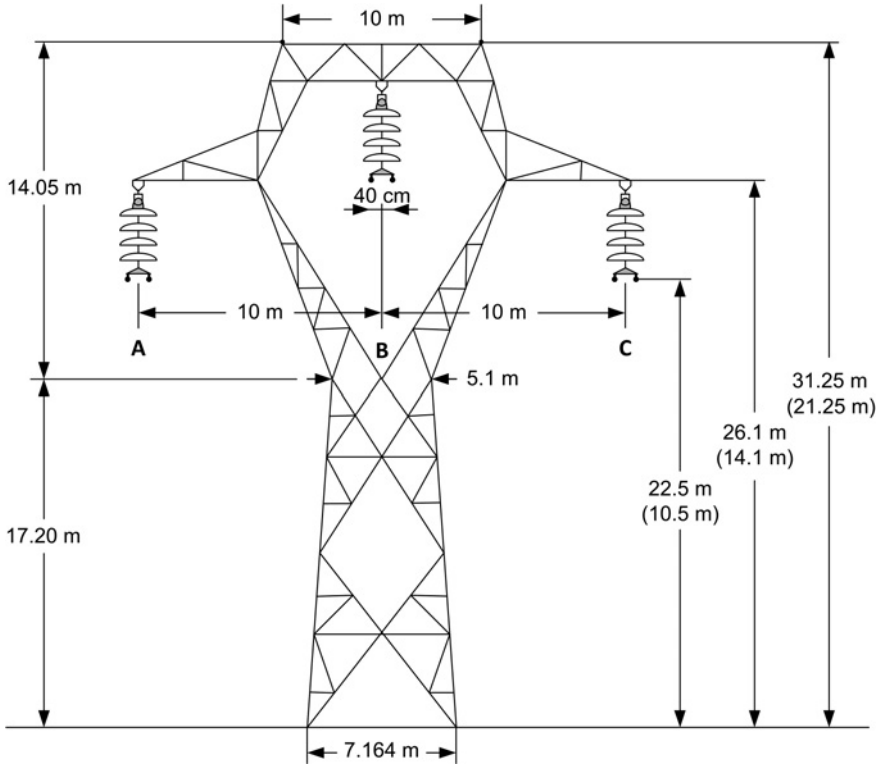

Figure 5.35 Case Study 5: Transmission line energization – test line configuration.

Table 5.5 Case Study 5: Characteristics of wires and conductors.

	Conductor type	Diameter (mm)	DC resistance (Ω/km)
Phase conductors	Curlew	31.63	0.05501
Shield wires	94S	12.60	0.64200

The transmission line is represented by means of a non-transposed, constant and distributed-parameter model, with parameters calculated at power frequency. Although a more rigorous approach should be based on a frequency-dependent distributed-parameter line model [14, 17], the model used in this study will provide conservative values, since parameter dependence with respect to the frequency increases the conductor resistance and damping.

As a consequence of multimodal wave propagation, the overvoltages that can occur at the open end of an overhead transmission line during energization may be greater than 2 p.u. However, the most onerous scenario corresponds to a reclosing operation (i.e. a line energization with trapped charge), since in this situation the magnitude of the resulting voltages at the open end may be above 3 p.u.

Figure 5.36 shows some simulation results obtained when energizing and reclosing the test line. Note that the peak voltages can exceed 2 p.u. with a simple energization and 3 p.u. when reclosing (in the case of Figure 5.36(b) there was a 1 p.u. trapped charge in all line phases).

Reclosing overvoltages can be reduced by pre-inserting resistors. First, the auxiliary contacts of the pre-insertion resistors close; after a time interval of about half a cycle of the power frequency the main contacts close and pre-insertion resistors are short-circuited.

The three scenarios (energizing, reclosing, pre-insertion of resistors) are analysed. The simulations in these scenarios were made with the following common features:

- It is assumed that only phase-to-ground overvoltages are of concern, and only the highest peak value of the three overvoltages is collected from each run.
- The energizations are performed over the entire range of a cycle, and assuming that the three poles are independent. The closing time of each pole is randomly varied according to a normal (Gaussian) probability distribution, with a standard deviation of 2.5 ms.

Table 5.6 shows the characteristic parameters that result for the scenarios analysed in this chapter. The aiming time was chosen following the method presented in [75]. Reclosing is analysed by assuming that a 1 p.u. voltage is trapped on each phase, and a pre-insertion resistance of 400 Ω is used. Figure 5.37 depicts the peak voltage distributions.

5.4.4.2 Case Study 6: Shunt Capacitor Switching

Figure 5.38 shows a diagram of the 60 Hz power system that will be used to illustrate some of the overvoltages that can be caused by capacitor switching. The system zone included in the system model has up to three voltage levels. The goal is to estimate some of the overvoltages that can be originated at nodes L1 and L2 when switching the capacitor bank installed at the MV side of the substation transformer.

The main parameters of the system components are indicated in the figure. The 115 kV network equivalent is represented by its symmetrical impedances ($\underline{Z}_1 = \underline{Z}_2 = 0.715 + j4.370$ Ω, $\underline{Z}_0 = 0.557 + j5.041$ Ω). The feeders that supply the two load nodes of interest, L1 and L2, have the same characteristics and are also represented by their symmetrical impedances ($\underline{Z}_1 = \underline{Z}_2 = 1.822 + j2.195$ Ω, $\underline{Z}_0 = 3.688 + j6.404$ Ω). The transformers are modelled without including the saturation characteristics and assuming

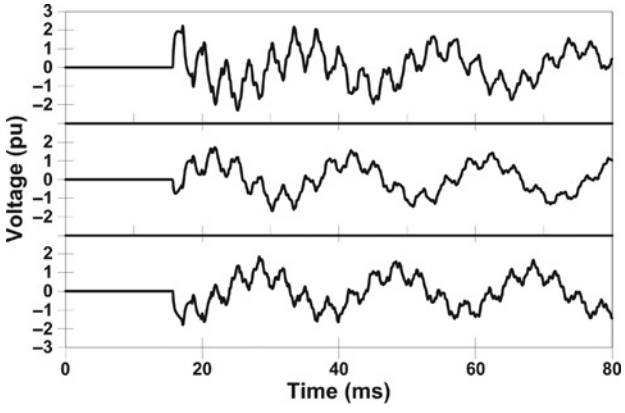

(a)

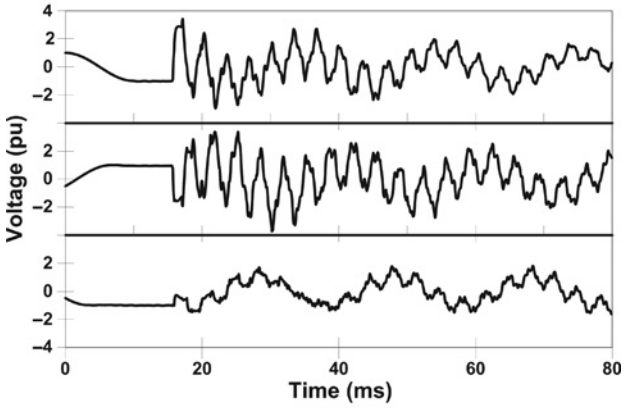

(b)

Figure 5.36 Case Study 5: Transmission line energization – simulation results: (a) open terminal voltages – line energization, (b) open terminal voltages – line reclosing.

triplex core, which may be unrealistic. The other components (surge arresters, capacitor banks and loads) are represented by means of the models presented in Section 5.4.2.

The transients analysed in this example are the voltage magnification that can occur at the lowest voltage load nodes when connecting the capacitor bank and the overvoltages that can arise at the same nodes as a consequence of a capacitor breaker restrike. The energy duty of the arresters installed in parallel with the capacitor bank is also of concern in this second case.

Table 5.6 Case Study 5: Statistical distribution of phase-to-ground voltages.

Case	Mean value (p.u.)	Standard deviation (p.u.)
Energizing	2.301	0.268
Reclosing	3.190	0.666
Pre-insertion resistors – 400 Ω	1.541	0.032

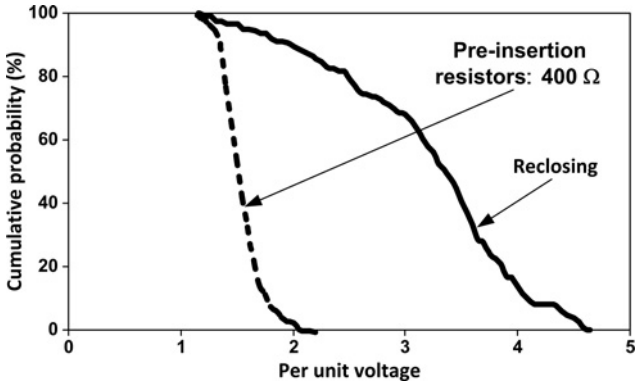

Figure 5.37 Case Study 5: Transmission line energization – peak voltage distribution.

Figure 5.39 compares the switching overvoltages caused at nodes L1 and L2 after switching a 4 Mvar shunt capacitor bank. The oscillograms show that the peak overvoltage is much higher at the LV node L1, where a compensating capacitor has been installed, although the load is higher (i.e. the equivalent parallel RL model has lower parameter values) than at the other load node, L2, where the peak voltage is less than twice the rated peak value. This confirms the prerequisite of a lower voltage capacitance for voltage magnification. On the other hand, a more moderate peak overvoltage value should be expected with a more accurate transformer model.

Figure 5.40 compares again the overvoltages caused at the same load nodes when a restrike occurs during the interruption of the capacitor current. The restrike occurs a few milliseconds before the peak of the transient recovery voltage for the first open pole is reached. The simulation results show that the peak overvoltage is again higher at the LV node, where a remote capacitor bank was installed, and that the value is even higher than for the previous case.

The simulations were performed with a Y-connected ungrounded capacitor bank, so the TRV across the breaker poles are very different from those that would be derived with a grounded capacitor bank. In

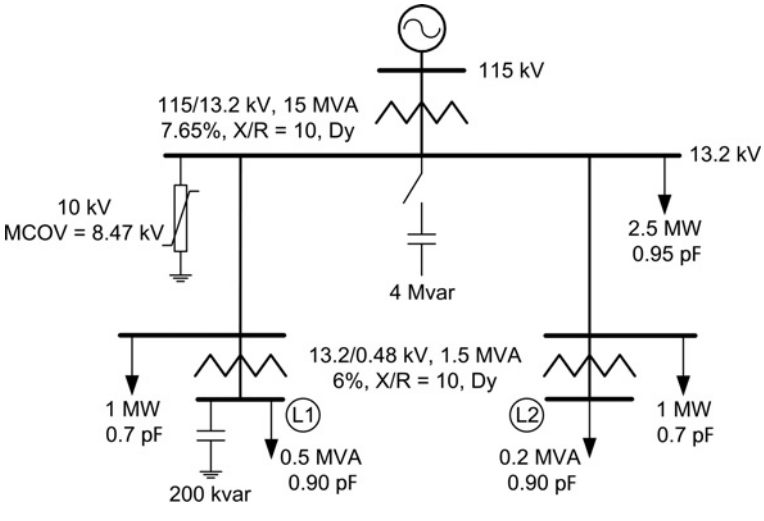

Figure 5.38 Case Study 6: Capacitor bank switching – diagram of the test system.

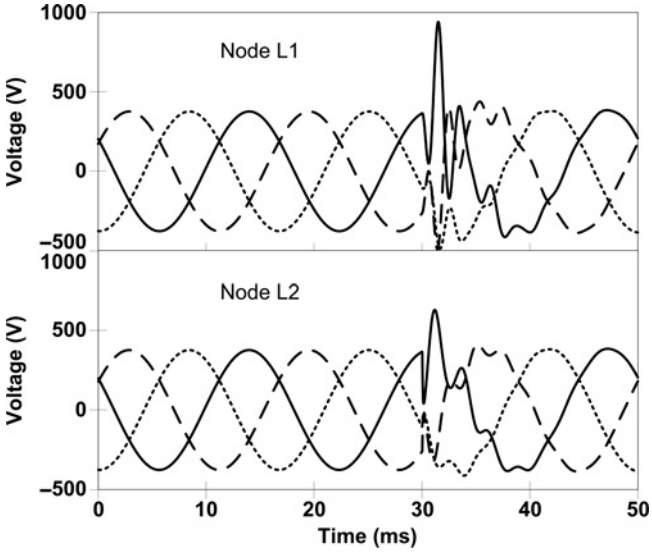

Figure 5.39 Case Study 6: Voltage magnification – low voltage side.

fact, the TRV across the other poles can reach much higher values than for the first pole after this one restrikes; consequently a second restrike should be expected.

Figure 5.41 shows that the maximum energy discharged by the MV surge arrester in parallel with the capacitor bank is well below a dangerous value. This seems to be due to the highly damped oscillation originated at the capacitor bank.

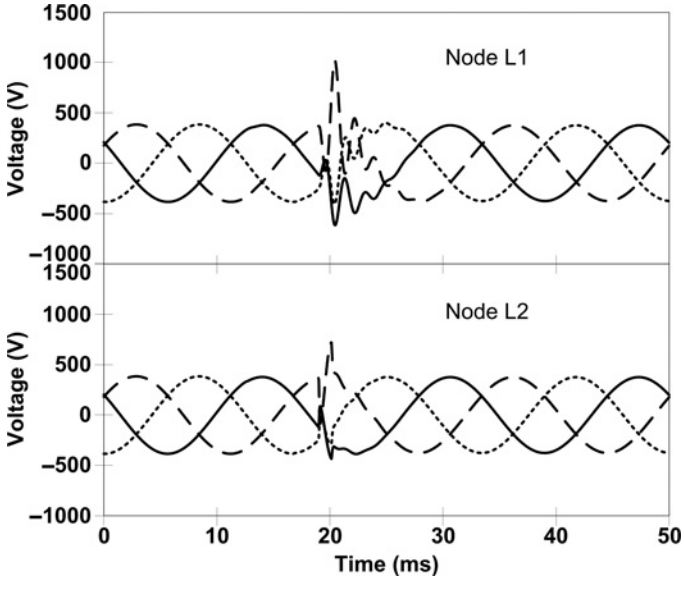

Figure 5.40 Case Study 6: Capacitor restrike – low voltage side.

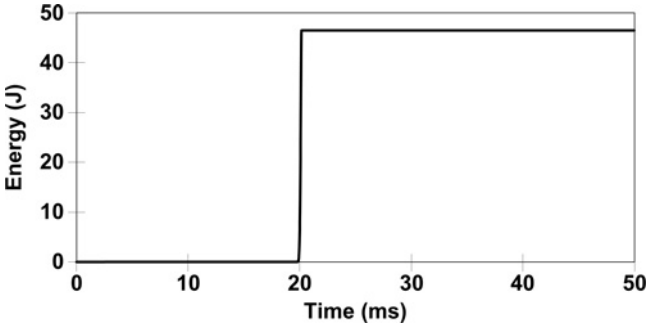

Figure 5.41 Case Study 6: Capacitor restrike – Arrester energy.

5.4.5 Validation

The validation of transients caused by switching operations is perhaps the most affordable one, due to the range of frequencies associated to most switching transients and to the fact that the initiation of the transient is previously scheduled; that is, there is no randomness involved in the origin of the transient. Several field measurements have been presented to date for validation of computer models. Reference [104] presents some cases, including ferroresonance, with a good agreement between simulation results obtained with an EMTP-like tool and either field measurements or TNA results.

5.5 Lightning Overvoltages

5.5.1 Introduction

Lightning strokes are one of the primary causes of fast-front transients in power systems. Lightning studies are performed to design lines and substations, and for the protection of power system equipment [6, 105]. Some of the objectives of these studies are to characterize the magnitude of the lightning overvoltages for insulation requirements, and to find the critical lightning stroke current that causes insulation flashover.

Specific study objectives for transmission lines are to determine lightning flashover rate (LFOR) and to select line arresters. For substations the objectives may be to calculate mean time between failures (MTBF), to determine surge arrester ratings, to find optimum location for surge arresters for lightning surge protection, or to estimate minimum phase-to-ground and phase-to-phase clearances.

Fast-front overvoltages are caused by the impact of a lightning stroke to a transmission line, to a phase conductor (shielding failure), or to a tower or a shield wire (backflashover). Direct strokes to substations are generally ignored, since it is commonly assumed that the substation is perfectly shielded, via shield wires or lightning masts; that is, only strokes with a peak current magnitude below the critical value will hit substation equipment.

Direct strokes to phase conductors: Direct strokes to the phase conductors of a shielded transmission line occur typically when lightning strokes of low magnitude (a few kA) bypass the overhead shield wires (shielding failure). Traditionally, the electrogeometric model based upon strike distance has been used to determine the maximum prospective peak lightning current that can bypass the shielding and hit phase conductors. A detailed description of this model can be found in the literature [6]. The usual approach has been to design the transmission line insulation to withstand the maximum shielding failure current predicted by the electrogeometric model without an outage to the line.

Backflashovers: The event of greater concern is backflashover, which occurs when the lightning discharge strikes the tower or the shield wire, and the resultant tower top voltage is large enough to cause

flashover of the line insulation from the tower to the phase conductor. When backflashover occurs, a part of the surge current will be transferred to the phase conductors through the arc across insulator strings. By default, it is assumed that the backflashover causes a line-to-ground fault that will be cleared by a circuit breaker, causing a line outage until the circuit breaker is reclosed.

The voltage surge as a result of the backflashover is very steep, and generally dictates the modelling requirements of the study, since direct strokes to the phase conductors will create relatively less steep voltage waveforms. The steepness and the magnitude of the voltage decrease as the surge propagates along the line, depending upon the line parameters. Corona is another important factor that reduces the steepness of the incoming voltage surge.

The lightning performance of the transmission lines is characterized by the outage rate, which may dictate the insulation requirements of the line. In the design studies, the minimum lightning stroke current (i.e. critical current) that causes insulator backflashover is determined. The probability of occurrence of a lightning current is described by a log-normal distribution [106, 107]. The number of strokes to the line per year depends on the keraunic level of the region and the exposed area of the shield wires. The LFOR for the line can be calculated by multiplying the probability of the flashover and the number of strokes to the shield wire.

For substation design studies, lightning is assumed to hit a nearby tower or shield wire of the incoming line causing a backflashover. The resultant lightning surge enters the substation and propagates inside. A discontinuity exists at junction points where a change in height or cross-section of the busbar takes place, and at equipment terminals. The discontinuity points inside the substation, the status of circuit breakers/switches (open/closed) and the location of the lightning arresters are especially important for the overvoltage characterization at the substation. These overvoltages will provide the data required for detailed arrester specifications. Then, the insulation levels (i.e. basic lightning impulse insulation level, (BIL)) of the substation equipment can be coordinated with the protective level of the arresters.

5.5.2 Modelling Guidelines

This section describes the models of power system components to be used in lightning studies. For each component, model parameters are justified, and typical values are provided. General trends and rules of thumb that should be followed in the model development are also discussed. A critical question is the extent to which the power system has to be represented. Since lightning-related surge voltages and currents cannot be easily measured or verified, the models presented should be treated as the recommended approach in representing the behaviour of the power system components within the specified frequency range [108, 109].

5.5.2.1 Overhead Transmission Lines

The model of an overhead line in lightning studies must include the representation of phase conductors and wires, towers and footing/grounding impedances. Phase conductors and shield wires are explicitly modelled between towers, and only a few spans are normally considered. Tower models include the effects of tower geometry and tower grounding impedance, with special emphasis on its lightning-dependent characteristics due to soil ionization. Insulators are also modelled with their flashover characteristics. Figure 5.42 shows the model for lightning studies.

Phase conductors and shield wires: The overhead line is represented by multiphase untransposed distributed-parameter line sections for each span. Bundled phase conductors can be represented by one equivalent conductor. The line parameters are usually calculated by means of a Line Constants routine [43], using the tower structure geometry and conductor data as input. The parameters are generally calculated at 400/500 kHz, including skin effect. Comparative EMTP studies for single-circuit transmission lines have shown that computer simulation results with frequency-dependent line models are very

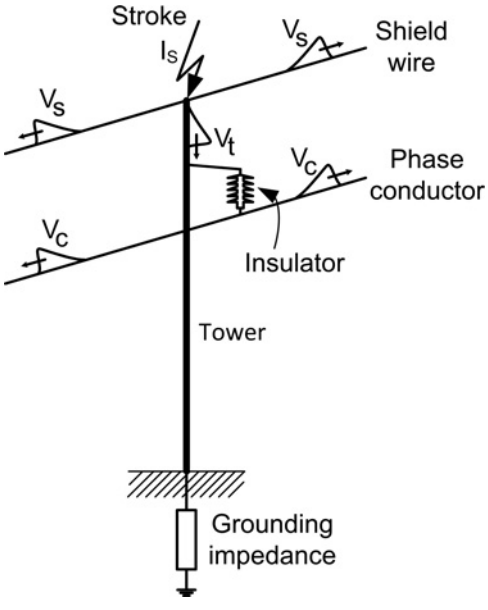

Figure 5.42 Overhead transmission line representation.

similar to those obtained with constant-parameter line models. Typical values for surge impedances are 250–500 Ω for line modes, while the ground mode surge impedance is higher, generally around 700 Ω. The velocity of propagation for aerial modes is close to the speed of light, being much slower for the ground mode.

Line length and termination: In transmission line design studies, the peak voltage at the struck tower may be influenced by reflections from the adjacent towers. A sufficient number of adjacent towers at both sides of the struck tower should be modelled to determine the overvoltages accurately. This can be achieved by selecting the number of line spans modelled, such that the travel time between the struck tower and the farthest tower is more than one-half of the lightning surge front time. The number of line spans modelled must be increased when the effects due to the tail of the lightning surge are considered, especially when evaluating the insulator flashovers with the leader propagation method or the energy discharged by arresters. In substation design studies, a similar approach can be followed, provided that all the line spans and towers between the struck tower and the substation are modelled in detail. Furthermore, it may be desirable to determine the first reflections of overvoltages accurately at any point inside the substation. This criterion may require detailed modelling of additional towers further away from the substation, depending upon the distance from the struck tower and the substation layout. In both transmission line and substation design studies, the line extended beyond the last tower can be represented with a matrix of self and mutual resistances equal to the corresponding line surge impedances. This matrix can be determined by a Line Constants routine [43]. Another simpler option is to add a line section long enough to avoid reflections from the open point reaching the last tower included in the model.

Towers: The representation of a tower is usually made in circuit terms. The simplest model represents a tower as a single-phase distributed-parameter lossless line, whose surge impedance depends on the structure details [105]. Typical values are 100–300 Ω, and the velocity of propagation can be assumed to be equal to the speed of light. Since the surge impedance of the tower varies as the wave travels from top to ground, more complex models have been developed that represent a tower by means of several

line sections and circuit elements that are assembled, taking into account its structure. These models are based on non-uniform transmission lines, or on a combination of lumped- and distributed-parameter circuit elements [110,111]. This approach is also motivated by the fact that, in many cases, it is important to obtain the lightning overvoltages across insulators located at different heights above ground; this is particularly important when two or more transmission lines with different voltage levels are sharing the same tower.

Grounding impedance: The peak overvoltage on the tower depends on the grounding impedance, whose influence on the tower top voltage is determined by its response time and current dependence. The response time is usually only important in cases where counterpoises with distances greater than 30 m from the tower base are installed. In that case, a frequency-dependent distributed-parameter model should be considered [6, 111, 112]. Within 30 m of the tower base, the time response can generally be neglected, and the tower grounding impedance is determined by using the current dependence of the grounding resistance using [106, 113]

$$R_T = \frac{R_o}{\sqrt{1 + I/I_g}}, \tag{5.33}$$

where R_T is the tower grounding resistance, R_o is the tower grounding resistance at low current and low frequency, I_g is the limiting current to initiate sufficient soil ionization and I is the lightning current through the grounding impedance.

The limiting current is a function of soil ionization and is given by

$$I_g = \frac{1}{2\pi} \frac{E_o \rho}{R_o^2}, \tag{5.34}$$

where ρ is the soil resistivity (Ω-m), and E_o is the soil ionization gradient (about 300–400 kV/m [114]).

In most studies, it is recommended to consider the waveshape dependence of tower foundation and counterpoise grounding. Lumped grounding resistance may not be adequate as compared to more detailed models of counterpoise grounding. The counterpoise can be represented as a nonlinear resistance with values calculated by (5.33), or as distributed-parameter lines at ground level with dispersed conductive connections to earth [111]. The typical tower grounding resistance is 10–100 Ω.

Insulators: The insulators may be represented by voltage-dependent flashover switches in parallel with capacitors connected between the respective phases and the tower. The capacitors simulate the coupling effects of conductors to the tower structure. Typical capacitance values for suspension insulators are of the order of 'some 10 pF' [115, 116], while for pin insulators, the capacitance is around 100 pF/unit. Capacitance values for non-ceramic insulators are an order of magnitude lower than for comparable ceramic insulators.

For a simplified analysis, a detailed arcing model for flashover is not necessary, and an idealized representation can be adequate. In this case, the flashover mechanism of the insulators is represented by voltage–time curves, whose characteristics are a function of insulator length and are applicable only within the range of parameters covered experimentally [105, 108, 109, 117, 118]. The insulator flashover voltage for the standard voltage–time curves can be calculated using

$$V_{v-t} = K_1 + \frac{K_2}{t^{0.75}}, \tag{5.35}$$

where V_{v-t} is the flashover voltage in kV, $K_1 = 400 \times \ell$, $K_2 = 710 \times \ell$, ℓ is the insulator length in m and t is the elapsed time after lightning stroke in μs.

The insulator is represented as a voltage-controlled switch across a capacitor which is closed when the insulator voltage exceeds the flashover voltage calculated from voltage–time curve, simulating a flashover. The front time for the arcing can be quite steep (around 20 ns) and is determined by the

physics of air gap breakdown. The startup time for the voltage–time characteristics must be synchronized to the instant at which the lightning stroke hits the shield wire or the tower top.

Multiple flashovers at consecutive towers are also possible, which are likely to reduce the peak overvoltages. It is recommended to represent all the insulators that are on the path of the lightning surge with their voltage–time characteristics for accurate calculation of the overvoltages.

The behaviour of insulation under the stress of the standard impulse cannot accurately predict its performance when exposed to any non-standard lightning impulse. Furthermore, it is inaccurate to assume that flashover will occur when a voltage wave just exceeds the voltage–time curve at any time. The experimental voltage–time characteristic is only be adequate for relating the peak of the standard impulse voltage to the time of flashover. In order to obtain correct results, further modifications to voltage–time curve would be required.

Accurate representation of air gap (insulator strings and spark gaps) breakdown, subject to standard and non-standard lightning impulses, is necessary for insulation coordination studies. Analytical procedures to predict the performance of insulation as a function of the impulse voltage waveform, the time to flashover, the gap configuration and others, have been developed and validated by tests performed in the high voltage laboratories. The most widely used procedures are the integration method and the leader progression model (LPM) [106, 111, 119]. A description of these methods is presented in [111].

Corona: Corona has a significant effect on overvoltage surges associated with lightning strokes to overhead lines [120–124]. The work carried out by Wagner, Cross and Lloyd [125] resulted in the following conclusions:

- For high magnitude positive surges, the corona effect is independent of the conductor size and geometry. The same applies for negative polarity surges except for one conductor size (24 mm diameter).
- For low voltages, the effect differs due to the different corona inception voltages.
- Weather conditions have no significant impact on corona distortion.
- The coupling factor between phases increases with increasing surge voltage.
- The tail of the surge is not influenced by corona.

Corona introduces a time delay to the front of the impulse corresponding to the loss of energy necessary to form the corona space charge around the conductor. This time delay takes effect above the corona inception voltage (V_i) and varies with surge magnitude. This variation with voltage can be expressed as a voltage-dependent capacitance (C_k) which is added to the geometrical capacitance of the transmission line.

The corona inception voltage (V_i) for a single conductor above earth is given by [105]

$$V_i = 23 \cdot \left(1 + \frac{1.22}{r^{0.37}}\right) \cdot r \cdot \ln \frac{2h}{r}, \tag{5.36}$$

where r is the conductor radius in cm, and h is the conductor height in cm.

The modelling details of corona can be expressed by curves of charge (q) versus impulse voltage (V). These q–V curves can be divided into three parts:

1. Below corona inception voltage V_i, the curve is a straight line determined by the geometrical capacitance.
2. Above corona inception voltage V_i, the curve shows an initial capacitance jump (C_i) plus an increase in capacitance, which is voltage dependent as long as the voltage is increasing.
3. For decreasing voltages, the curve again is practically determined by the geometrical capacitance.

The excess capacitance (C_k) to be added during the second stage of the q–V curve is given by [106]

$$C_k = C_i + K\left(V - V_i\right), \tag{5.37}$$

where C_i is the initial capacitance jump, K is a corona constant, V_i is the corona inception voltage and V is the instantaneous impulse voltage.

The sum of the excess capacitance (C_k) and the geometric capacitance (C_g) is the dynamic capacitance (C_{dyn}):

$$C_{dyn} = C_k + C_g \tag{5.38}$$

The constant K varies with conductor diameter and the number of subconductors, as well as the polarity of the applied surge voltage. For example, for conductors with 31 mm diameter, K varies from 4.8×10^{-3} pF/kVm for a single conductor and positive polarity surges to 2.4×10^{-3} pF/kVm for eight subconductors and positive polarity surges. For negative polarity surges, the constant is approximately half of these values.

The coupling factor between phases increases due to corona and is given by

$$K_c/K_g = 1 + C_k/C_g, \tag{5.39}$$

where K_c is the coupling factor in the corona, and K_g is the geometric coupling factor [106]. K_g is calculated using the method proposed in [105].

Several corona models can be used to represent the dynamic capacitance region of the q–V curve in a piecewise linear fashion [111, 123]. The approach proposed in [122] can be used to estimate the variation of the steepness of lightning overvoltages impacting on substations with travel length. This approach relies upon the observation that for voltages substantially higher than the corona inception level, the time delay as a function of travel distance becomes linear; that is, in this region, the steepness of the overvoltage is independent of the voltage value. This yields the relationship [2, 4]

$$S = \frac{1}{\frac{1}{S_o} + A \cdot d}, \tag{5.40}$$

where S_o is the original steepness of the overvoltage, S is the new steepness after the waveform travels for a distance d and A is a constant. The constant A is a function of the line geometry only and is also dependent on the surge polarity. Typical values are given in [2, 4, 122]. See the Case Study at the end of this section.

Although corona effects may reduce the peak of lightning-related overvoltages more than 20% [123], in some studies corona is neglected to obtain conservative results.

5.5.2.2 Substations

The overall substation model can be derived from the substation layout, and must include buswork, insulators and other substation equipment [109].

Buswork and conductors: The buswork and conductors between the discontinuity points inside the substation, and connections between the substation equipment, are explicitly represented by line sections. These line sections are modelled by untransposed distributed-parameter sections if they are longer than 3 m; otherwise, a lumped-parameter inductance of 1.0 μH/m can be used. The line parameters can be calculated using a Line Constants routine [43]. Note that the minimum conductor length with distributed-parameter representation dictates the simulation time-step.

Substation equipment: The substation equipment, such as circuit breakers, substation transformers and instrument transformers are generally represented by their stray capacitances to ground. Figure 5.43 shows some circuit breaker representations, while Table 5.7 provides minimum capacitance values used in lightning studies for different types of substation equipment, when the actual data is not available.

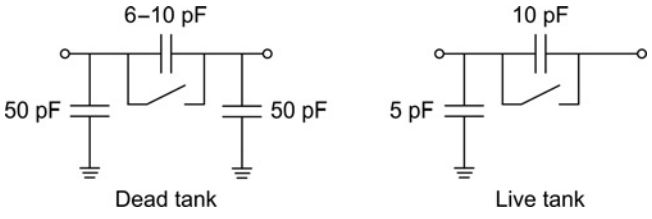

Figure 5.43 Circuit breaker representations [108, 109].

If the disconnect switches or breakers have more than one support, appropriate capacitances should be added to the model. Furthermore, if some of the substation equipment is close to each other (i.e. less than 3–5 m), their capacitances can be grouped together for simplification. The open/closed status of circuit breakers/switches should be considered.

In lightning studies conducted to design transformer protection against fast-front overvoltages, a conservative approach is to represent the transformer as an open circuit. To increase the level of accuracy, it is recommended to account for the capacitance of the winding. A resistance equal to the surge impedance of the winding can be placed across the capacitance. The model can be enhanced by adding the inductive transformer model and relevant capacitances between windings, windings to core and windings to ground, as well as bushing capacitances. Such a model can also be used to calculate the surge transfer from winding to winding as in the case of generator (or motor) protection studies. Capacitances can be determined from the geometry of the coil and core structure, from manufacturers' data and from tables available in the literature. Values of the winding capacitance together with capacitance values for outdoor bushings are presented in [5].

Some transformer models can accurately determine how a voltage applied to one set of terminals is transferred to another set of terminals [41, 66, 69, 126, 127]. These models duplicate the transformer behaviour over a wide range of frequencies, and act like a filter, suppressing some frequencies and passing others. The use of a frequency-dependent transformer model is important when determining the surge that appears on a generator bus when a steep-fronted surge impinges on the high-voltage terminals of the generator step-up transformer. Some models allow the simulation of any type of multiphase, multiwinding transformer as long as its frequency characteristics are known, either from measurements or from calculations based on the physical layout of the transformer.

Insulators and bus support structures: The bus support structures are represented by a distributed-parameter model with surge impedances calculated from the structure geometry, and with velocity of

Table 5.7 Minimum capacitance-to-ground values for substation equipment [108, 109].

	Capacitance-to-ground		
Equipment	115 kV	400 kV	785 kV
Disconnector switch	100 pF	200 pF	160 pF
Circuit breaker (dead tank)	100 pF	150 pF	600 pF
Bus support insulator	80 pF	120 pF	150 pF
Capacitive potential transformer	8000 pF	5000 pF	4000 pF
Magnetic potential transformer	500 pF	550 pF	600 pF
Current transformer	250 pF	680 pF	600 pF
Autotransformer[a]	3500 pF	2700 pF	5000 pF

[a]Capacitance also depends on MVA.

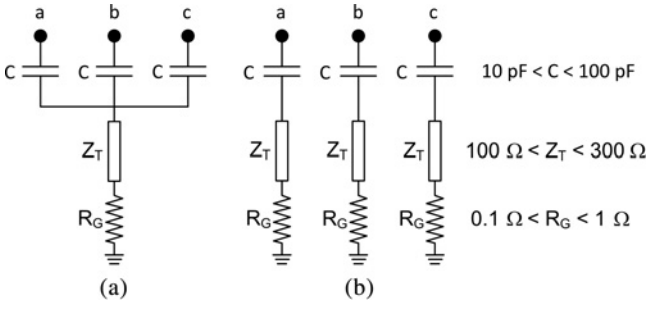

Figure 5.44 Insulator and bus support structure models. Bus support structure: (a) common to all phases, (b) individual for each phase [109].

propagation equal to the speed of light, similar to the transmission line bus tower models [108, 109]. Models for typical bus support configurations are shown in Figure 5.44. The representative grounding resistance inside the substations is usually 0.1–1 Ω. Comparative simulations have shown that the support structures do not have much impact on the simulation results, and can be neglected [109].

The capacitance to ground of all insulators should be represented, since the substation capacitance is one of the critical parameters that modify lightning surge waveshapes.

5.5.2.3 Surge Arresters

The voltage–current characteristics of metal-oxide surge arresters are a function of the incoming surge steepness. Protective characteristics for surge arresters showing crest discharge voltage versus time-to-crest of discharge voltages are available from manufacturers. Since arrester terminal voltage and current do not reach their peak values at the same time, the frequency-dependent characteristics of arresters may be of significant importance when excited by fast-front transient surges [85, 86].

The arresters can be modelled as nonlinear resistors with 8×20 μs maximum voltage–current characteristics. Several frequency-dependent surge arrester models have been developed [84–86, 128–133]. These models can reproduce metal-oxide surge arrester characteristics over a wide range of frequencies such as lightning, switching and temporary overvoltages.

The nonlinear arrester characteristics need to be modelled up to at least 20–40 kA, since high current surges initiated by close backflashovers can result in arrester discharge currents above 10 kA. The arrester lead lengths at the top and at bottom must be considered to account for the effects of additional voltage rise across the lead inductance. A lumped element representation with an inductance of 1.0 μH/m will be sufficient.

In all studies, the energy through the arresters must be monitored, and verified that the maximum allowed energy dissipation is not exceeded.

5.5.2.4 Sources

Two types of inputs must be considered in lightning studies: the instantaneous phase voltage at the time the stroke hits the line and the lightning stroke current. The insulator stress is a combination of the voltage due to the lightning current and the power-frequency voltage.

Initial conditions: The instant of lightning stroke with respect to the instantaneous steady-state AC voltage must be coordinated to maximize its impact for worst case conditions. This can be achieved by properly selecting the magnitude and phasing of the three-phase sinusoidal voltage sources at the terminating point of the transmission lines.

In transmission line design studies, one of the objectives is to determine the highest line outage rate which is generally maximized by finding the minimum critical lightning current that causes insulator backflashovers. If the lightning hits the tower when the contribution of AC power-frequency voltage to the insulation stress is maximum, the backflashover can occur with a smaller lightning current.

In substation design studies, it is desirable to maximize the steepness and magnitude of the line-to-ground voltage surges towards the substation [6]. The steepness is directly related to the arcing mechanism across the flashing insulator, while the magnitude jumps up to the tower top voltage after the backflashover. Thus, if the tower voltage has sufficient time to build up before the backflashover, the worst case overvoltages can be observed. Setting the magnitude of the power-frequency voltage to +0.5 p.u. for a negative polarity lightning stroke will minimize the insulator stress and delay the backflashover, which will maximize the voltage surge. Other power-frequency voltages will cause earlier backflashovers on the other phases. Note that under these conditions, two of the phases may backflashover at the same time, due to similar voltages across the insulators, and give the impression of reduced current and/or energy at the substation arresters due to current sharing which may not be the case in reality [109].

Lightning stroke: The lightning stroke is represented by a current source. Its parameters, such as crest, front time, maximum current steepness, duration and polarity are determined by using a statistical approach, since they all are statistical in nature, generally characterized by log-normal distributions [106, 107]. In addition, the peak current can be statistically correlated to the steepness and the time to crest of the current wave form. Both the steepness and the front time increase as the peak current increases. The detailed calculation procedure for these parameters is shown in the CIGRE Guide [106], and see also [6].

A rigorous approach requires the front of the lightning current source to be upwardly concave, although for practical purposes a linearly rising front at the selected maximum current steepness can be sufficient. In this case, a negative triangular waveshape for the lightning current source can be selected. The double exponential impulse model should be used with caution since this model does not accurately reflect the concave waveshape of the wave front [108, 109]. Typical lightning current values for backflashovers and direct strokes are as follows:

- *Backflashover*: Lightning strokes of high magnitude, in the range of 20 kA up to values rarely exceeding 200 kA, cause the backflashovers. In this current range, median front times (30–90%) range from about 3 μs at 20 kA to about 8 μs at 200 kA. Maximum current steepness ranges from about 20 kA/μs at 20 kA to about 48 kA/μs at 200 kA [106, 134].
- *Shielding failure*: Lightning strokes of amplitude below the critical shielding current, generally less than 20 kA, can bypass the overhead shield wires and strike directly on the phase conductors. The maximum lightning current that can strike the phase conductors of any given overhead transmission line can be predicted by using the method recommended in [117, 135, 136].

Here are some other issues that should also be considered [109]:

- Regardless of the mechanism by which a lightning overvoltage is generated, the maximum amplitude of the surge may be taken equal to 1.2 × CFO, where CFO is the critical flashover voltage of the insulation [6]. The 1.2 multiplier accounts for two effects: (1) the CFO (U_{50} in IEC standards) is a median value and hence the insulation can carry higher voltages 50% of the time, and (2) the CFO is based on the standard 1.2 × 50 μs impulse waveform. The withstand voltage is higher for steeper fronts and may also be higher for some non-standard waveforms – see [111].
- In determining the maximum stroke current that can cause shielding failure, several references use a model in which the striking distance to ground is taken equal to βS (see for instance [6, 105, 136]), where S is the striking distance to the wires and β is a factor which is a function of either the voltage or the height of the phase wires. As noted in the discussion by Mousa [117], varying β (with voltage or height of the conductors) produces results which are inconsistent with the physics of the problem. Reference [137] presents a revised electrogeometric model in which the striking distance to ground is kept constant. This approach is more consistent with the physics of the problem.

5.5.3 Case Studies

The modelling guidelines presented previously are applied in two case studies. The first is aimed at obtaining the lightning performance of an overhead transmission line, and includes a sensitivity study of lightning-caused overvoltages. The second case presents the calculation of lightning overvoltages within a substation for which the surge arresters must be selected, assuming that the characteristics of the incoming surge are already known.

5.5.3.1 Case Study 7: Lightning Performance of a Transmission Line

Test system: Consider the tower design shown in Figure 5.35. It corresponds to a 400 kV transmission line with two conductors per phase and two shield wires, whose characteristics are presented in Table 5.5. The average span length is 400 m and the striking distance of insulator strings is 3.212 m. The calculations will be made by assuming that the line is located at sea level. The goal of this example is to estimate the lightning performance of this line.

Modelling guidelines: The models used to represent the different parts of the line are [14, 15, 108, 109] as follows:

1. The line is modelled by means of four spans at each side of the point of impact. Each span is represented as a multiphase untransposed frequency-dependent and distributed-parameter line section. Corona effect is not included.
2. A line termination at each side of the above model is needed, to avoid reflections that could affect the simulated overvoltages caused around the point of impact. Each termination is represented by means of a long enough section whose parameters are also calculated as for line spans.
3. A tower is represented as an ideal single-phase distributed-parameter line. The approach used in this example is the twisted model recommended by CIGRE [106]. This model can suffice for single circuits with towers shorter than 50 m [6].
4. The grounding impedance is represented as a nonlinear resistance whose value is approximated by the equation (5.33), recommended in standards [2, 4]. The soil ionization gradient E_0 is 400 kV/m [114].
5. This analysis will be performed by using two different approaches for representing insulator strings. In the first model insulator strings are represented as voltage-controlled switches. The CFO/U_{50} is calculated according to the expression proposed by IEC 60071-2 for negative polarity strokes [2]

$$U_{50}^{-} = 700S \tag{5.41}$$

where S is the striking distance of the insulator strings. With this model, a flashover occurs if the overvoltage exceeds the lightning insulation withstand voltage.

In the second model, the representation of insulator strings relies on the application of the leader progression model (LPM), being the leader propagation obtained by means of [106, 119, 138, 139].

$$\frac{d\ell}{dt} = k_l V(t) \left[\frac{V(t)}{g - \ell} - E_{l0} \right], \tag{5.42}$$

where $V(t)$ is the voltage across the gap, g is the gap length, ℓ is the leader length, E_{l0} is the critical leader inception gradient and k_l is a leader coefficient.
6. Phase voltages at the instant at which the lightning stroke hits the line are included. For statistical calculations, phase voltage magnitudes are deduced by randomly determining the phase voltage reference angle and considering a uniform distribution between 0 and 360°.

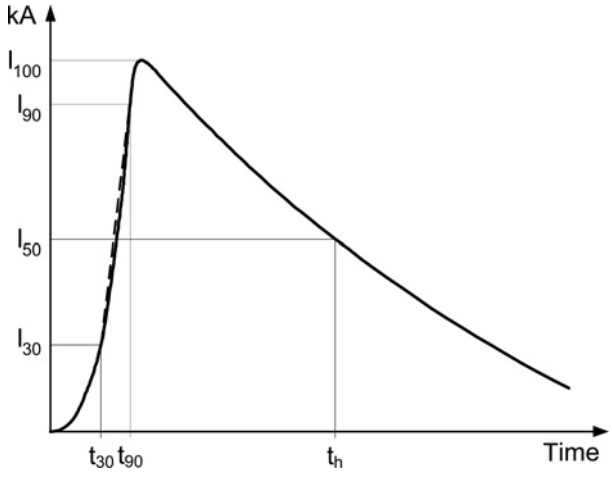

Figure 5.45 Stroke current concave waveform.

7. A lightning stroke is represented as an ideal current source (infinite parallel impedance) of negative polarity and a concave waveform, with no discontinuity at $t = 0$ – see Figure 5.45. The mathematical expression used in this example is the so-called Heidler model, which is given by [140]:

$$i(t) = \frac{I_p}{\eta} \frac{k^n}{1 + k^n} e^{-t/\tau_2}, \tag{5.43}$$

where I_p is the peak current, η is a correction factor of the peak current, n is the current steepness factor, $k = t/\tau_1$ and τ_1, τ_2 are time constants determining current rise and decay time, respectively. The value selected for parameter n is 5 in all simulations performed for this example. In statistical calculations, stroke parameters are randomly determined according to the distribution density functions recommended in the literature [106, 107]. See below for more details.

The study of this example has been divided into two parts. The first part summarizes the main results of a sensitivity study aimed at analysing the influence that some line parameters have on the overvoltages originated across insulator strings. The second part presents the application of the Monte Carlo method to assess the lightning performance of this line.

Sensitivity study: The goal is to simulate overvoltages caused by strokes to towers and phase conductors, and determine the influence that some parameters have on the peak voltages. All the calculations presented in this example have been performed by representing insulator strings as open switches and grounding impedances as constant resistances:

- *Strokes to a tower*: Figure 5.46 depicts the relationships with respect to some parameters. These results were derived without including power-frequency voltages. One can easily deduce that both parameters have a strong influence: the greater the grounding resistance value and the shorter the rise time, the higher the overvoltages.
- *Strokes to a phase conductor*: For the same stroke peak current, overvoltages originated by strokes to phase conductors will be much higher than those originated by strokes to towers or shield wires. A new parametric study was carried out to deduce the influence of the stroke peak current and the voltage angle, using the phase angle of the outer phase (phase A) to which the lightning stroke impacts

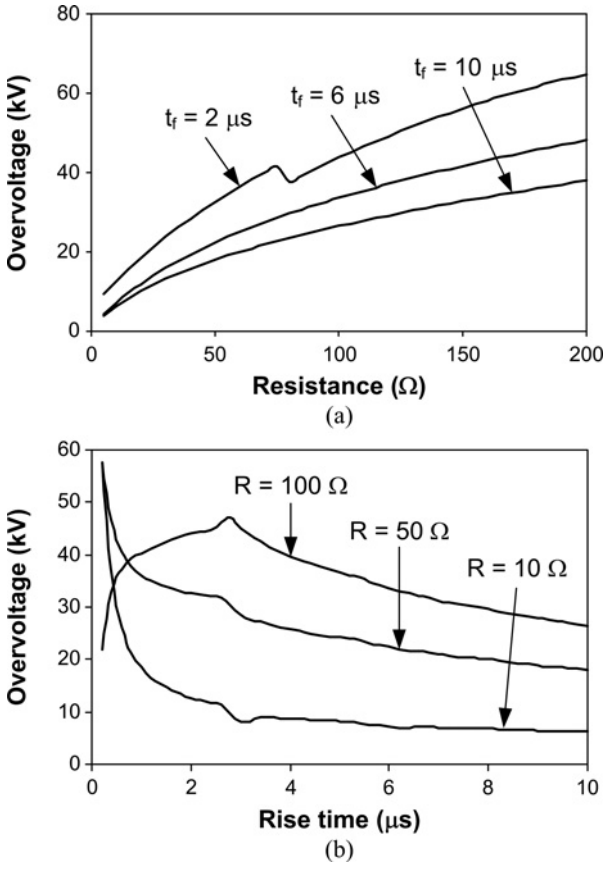

Figure 5.46 Case Study 7: Overvoltages caused by strokes to a tower: (a) insulator string overvoltage vs grounding resistance (I_p = 1 kA), (b) insulator string overvoltage vs rise time of the lightning stroke (I_p = 1 kA).

as a reference. Figure 5.47 presents the results obtained by considering the worst case from each simulation. The plots show very high voltages, but it is worth noting that shield wires will prevent strokes with a peak current higher than 20 kA from reaching phase conductors, as shown in the subsequent section. The influence of the grounding resistance when the lightning stroke hits a phase conductor is negligible. The voltage caused by a lightning stroke to a phase conductor increases linearly with the peak current magnitude and depends on the phase angle at the moment it hits the conductor.

Statistical calculation of lightning overvoltages: The main aspects of the Monte Carlo procedure used in this example are [141]:

- The values of the random parameters are generated at every run, according to the probability distribution function assumed for each one. The calculation of random values includes the parameters of the lightning stroke (peak current, rise time, tail time, location of the vertical channel), the phase conductor voltages, the grounding resistance and the insulator strength.

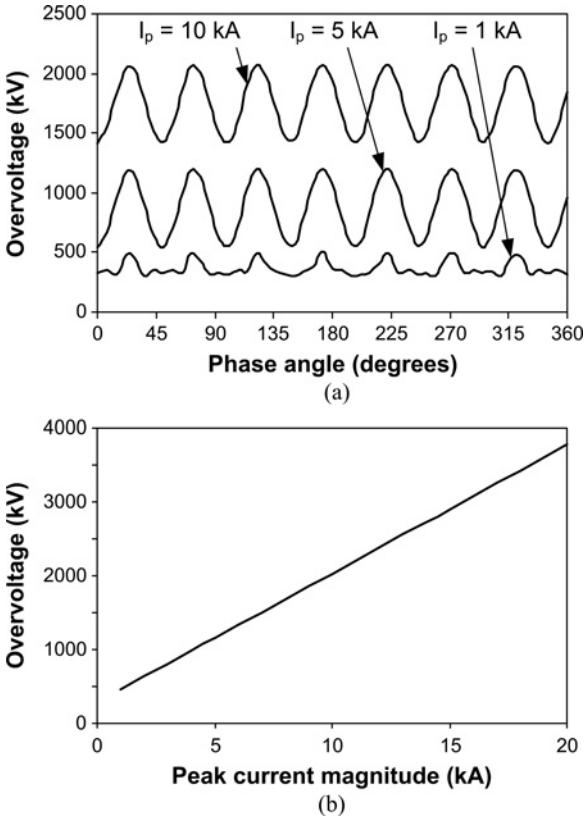

Figure 5.47 Case Study 7: Overvoltages caused by strokes to phase conductors: (a) insulator string overvoltage vs reference phase angle, (b) insulator string overvoltage vs the peak current magnitude.

- The determination of the point of impact requires a method for discriminating strokes to line conductors from those to ground. In addition, it is important to distinguish return strokes to shield wires from those to phase conductors. This step will be based on the application of the electrogeometric model recommended by Brown–Whitehead [142]:

$$r_c = 7.1I^{0.75} \quad r_g = 6.4I^{0.75}, \tag{5.44}$$

  where r_c is the striking distance to both phase conductors and shield wires, r_g is the striking distance to earth and I is the peak current magnitude of the lighting return stroke current. With this model, only return strokes with a peak current magnitude below 20 kA will reach phase conductors.
- The overvoltage calculations can be performed once the point of impact of the randomly generated stroke has been determined. Overvoltages originated by nearby strokes to ground are neglected.
- Voltages across insulator strings are continuously monitored. Since the goal of the procedure is to obtain the lightning flashover rate, every time a flashover is produced the run is stopped, the counter is increased and the flashover rate is updated.
- The entire simulation is stopped when the convergence of the Monte Carlo method is achieved or the specified maximum number of iterations is reached. The convergence is checked by comparing the probability density function of all variables to their theoretical functions, so the procedure is stopped when they match within the maximum error or the maximum number of runs is reached.

Lightning stroke waveform and parameters: Only single-stroke negative polarity flashes are considered in this study. The stroke waveform is that shown in Figure 5.45. The main parameters used in statistical calculations to define the waveform of a lightning stroke are the peak current magnitude, I_p (or I_{100}), the front time, t_f (= 1.67 ($t_{90} - t_{30}$)) and the tail time, t_h – see Figure 5.45. Since these values cannot be directly defined in the Heidler model, a conversion procedure [143] is performed to derive the parameters to be specified in (5.43) from the stroke parameters, which are randomly calculated, as detailed below.

The statistical variation of the lightning stroke parameters is usually approximated by a log-normal distribution, with the probability density function [107]

$$p(x) = \frac{1}{\sqrt{2\pi}x\sigma_{\ln x}} \exp\left[-0.5\left(\frac{\ln x - \ln x_m}{\sigma_{\ln x}}\right)^2\right], \tag{5.45}$$

where $\sigma_{\ln x}$ is the standard deviation of $\ln x$, and x_m is the median value of x. In addition, it is assumed that stroke parameters are independently distributed.

Random parameters: The following probability distributions have been assumed:

- Insulator string parameters are determined according to a Weibull distribution. The mean value and the standard deviation of E_{l0} are 570 kV/m and 5%, respectively. The value of the leader coefficient is k_l = 1.3E−6 m^2/(V^{2}s) [106]. The value of the average gradient at the critical flashover voltage is assumed to be the same as E_{l0}.
- The phase conductor reference angle has a uniform distribution, between 0 and 360°.
- The grounding impedance has a normal distribution with a mean value R_m = 50 Ω and a standard deviation σ = 5 Ω. Remember that the grounding resistance model accounts for soil ionization effects, so parameter R_m is the mean value of the low-current and low-frequency resistance, R_o. The value of the soil resistivity is 200 Ω-m.
- Stroke parameters are determined assuming a log-normal distribution for all of them. Table 5.8 shows the values used for each parameter.
- The stroke location, before the application of the electrogeometric model, is estimated by assuming a vertical path and a uniform ground distribution of the leader.

The line model has been implemented considering that only flashovers across insulator strings can occur.

Simulation results: All the studies have been performed by executing 40 000 runs [141]. Figures 5.48 and 5.49 show the results obtained with each of the scenarios considered in this example. Note that the range of peak current magnitudes that cause backflashover (stroke to a shield wire or to a tower) are different from the range of values that cause shielding failure flashover (strokes to phase conductors). After 40 000 runs the statistical distribution is well defined for backflashovers, but not for shielding failures, indicating that even more runs are needed to obtain an accurate enough distribution of this type of overvoltages.

Table 5.8 Case Study 7: Statistical parameters of the return stroke [107].

Parameter	x	$\sigma_{\ln x}$
I_{100}, kA	34.0	0.740
t_f, μs	2.0	0.494
t_h, μs	77.5	0.577

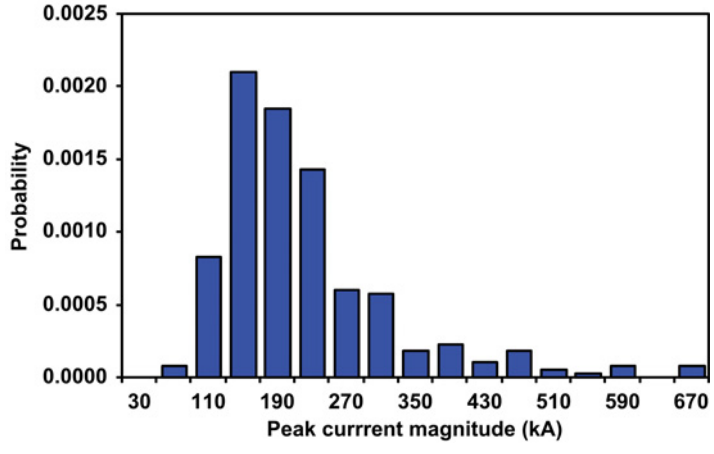

(a)

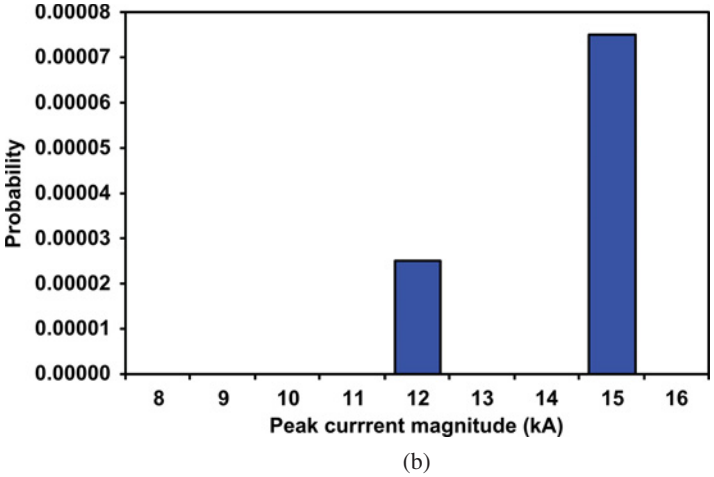

(b)

Figure 5.48 Case Study 7: Distribution of stroke currents that caused flashovers. Voltage-controlled switch model: (a) strokes to shield wires, (b) strokes to phase conductors.

The lightning flashover rate of the test line, assuming a ground flash density $N_g = 1$ fl/km^2-year, is 0.845 per 100 km-year when the insulator strings are modelled as voltage-controlled switches, and 0.347 per km-year when they are represented by means of the LPM. Although the parameters used in both approaches are those recommended by IEC [2] and CIGRE [106], the difference between rates is significant. Note that the range of values that cause flashover with each insulation representation is different, and each modelling approach exhibits a different trend: when the LPM is used, the range of values that cause flashover is narrower than when the insulation is modelled as a voltage-controlled switch, while the trend is opposite in the case of shielding failure flashover. This latter performance means that, when the LPM is used, there can be flashovers caused by lightning strokes with lower peak current magnitudes. Remember that with the LPM a flashover can occur during the tail of the lightning current; that is, the insulation can flash over after passing the peak value of the lightning overvoltage, which is not possible with the other modelling approach.

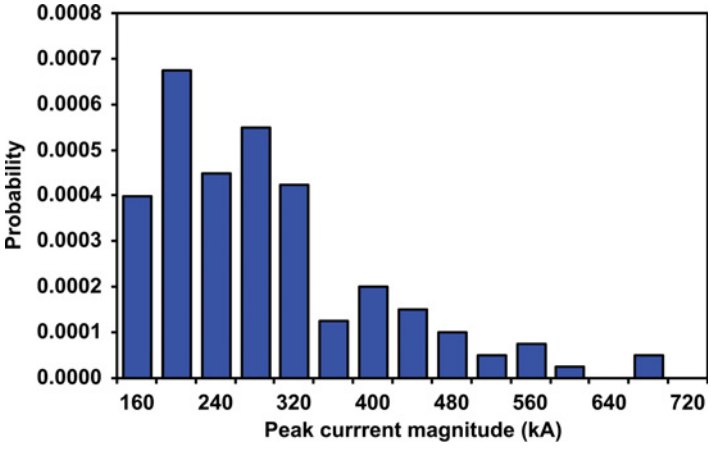

(a)

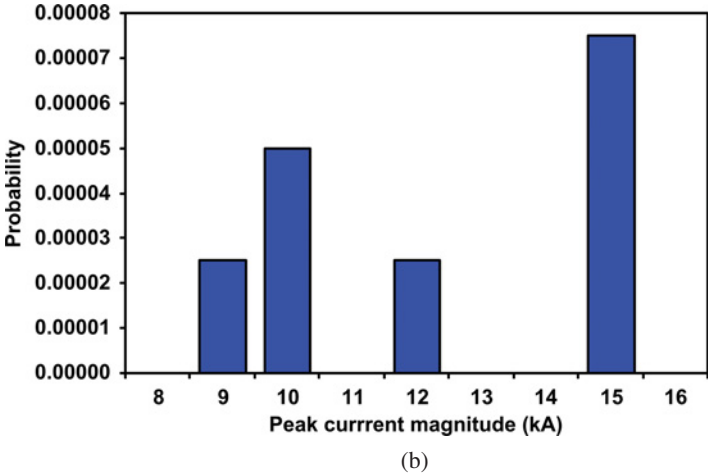

(b)

Figure 5.49 Case Study 7: Distribution of stroke currents that caused flashovers. Leader progression model (LPM): (a) strokes to shield wires, (b) strokes to phase conductors.

5.5.3.2 Case Study 8: Substation Overvoltages

Test system: Figure 5.50 shows the diagram of a 50 Hz, 220 kV single-line substation. The objective of this study is to calculate the lightning overvoltages that will be produced inside the substation when the surge arresters are selected to obtain a specified MTBF for the substation. The results derived for this study can be later used for selecting the insulation level of substation equipment [86]. The information required for this study is as follows:

- *Power system*:
  Frequency = 50 Hz
  Rated voltage = 220 kV
  Grounding = Low impedance system, EFF = 1.4
  Duration of temporary overvoltage = 1 second

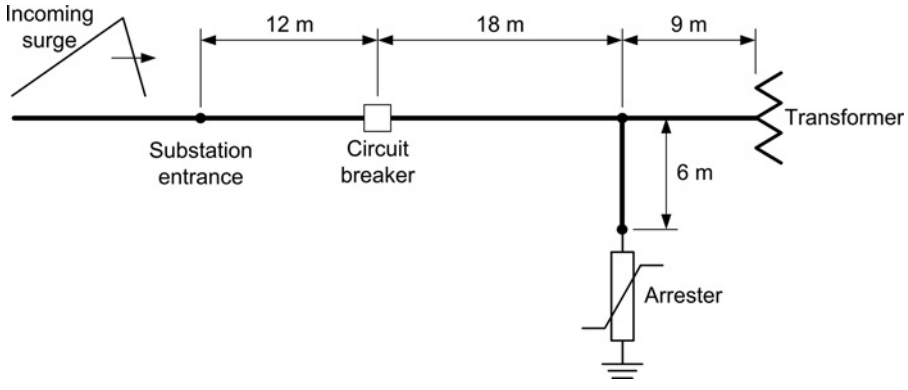

Figure 5.50 Case Study 8: Diagram of a 220 kV substation.

- *Line*:
  Length = 80 km
  Span length = 250 m
  Insulator string strike distance = 2.0 m
  Positive polarity CFO/U_{50} = 1400 kV
  Conductor configuration = one conductor per phase
  Capacitance per unit length = 10.5 nF/km
  Backflashover rate (BFR) = 2.0 flashovers/100km-years
  Ground wire surge impedance = 438 Ω
  High current grounding resistance = 25 Ω
  Peak voltage at the remote end = 520 kV
- *Substation*:
  Single-line substation in an area of high lightning activity
  MTBF = 200 years
  Transformer capacitance = 2–4 nF.

Assume the surge impedance of each substation section is the same as the surge impedance of the line, 400 Ω. The substation is located at sea level, and calculations are performed assuming standard atmospheric conditions.

Arrester selection: In IEC the rated voltage is the TOV capability at 10 seconds with prior energy, TOV_{10}, whose value can be obtained from [144]

$$TOV_{10} = TOV_C \cdot \left(\frac{t}{10}\right)^m, \tag{5.46}$$

where TOV_C is the representative TOV, t is the duration of this overvoltage and m is a factor for which the recommended value is 0.02.

The standard maximum system voltage for 220 kV is U_m = 245 kV in IEC. Taking into account that there is a low impedance grounding system (EFF = 1.4) and the duration of the temporary overvoltage is 1 second, using the IEC expression, the following values are obtained:

- *MCOV – COV*

$$COV = \frac{245}{\sqrt{3}} = 141.45 \text{ kV}$$

- TOV_C

$$TOV_C = 1.4 \cdot \frac{245}{\sqrt{3}} = 198.0 \text{ kV}$$

- TOV_{10}

$$TOV_{10} = 1.4 \cdot \frac{245}{\sqrt{3}} \cdot \left(\frac{1}{10}\right)^{0.02} = 189.1 \text{ kV}$$

The ratings of the selected arrester are:

- rated voltage (rms): $U_r = 210$ kV.
- MCOV (rms): $U_c = 156$ kV (170 kV according to IEEE).
- TOV capability at 10 seconds: $TOV_{10} = 231$ kV.
- nominal discharge current (peak): $I = 20$ kA (15 kA according to IEEE).
- line discharge class: Class 4.

From the manufacturer's data sheets, the height and the creepage distance of the selected arrester are respectively 2.105 m and 7.250 m.

The procedure to calculate parameters of the fast-front model will be applied to a one-column arrester, with an overall height of 2.105 m, being $V_{10} = 478$ kV and $V_{ss} = 435$ kV for a 3 kA, 30/60 μs current waveshape.

- Initial values: The parameters that result from using the procedure recommended in [130] are $R_0 = 210.5\ \Omega$, $L_0 = 0.421$ μH, $R_1 = 136.85\ \Omega$, $L_1 = 31.575$ μH, $C = 47.51$ pF.
- Adjustment of A_0 and A_1 to match switching surge discharge voltage: The arrester model was tested to adjust the nonlinear resistances A_0 and A_1. A 3 kA, 30/60 μs double-ramp current was injected into the initial model. The result was a 436.1 kV voltage peak that matches the manufacturer's value within an error of less than 1%.
- Adjustment of L_1 to match lightning surge discharge voltage: Next, the model was tested to match the discharge voltages for an 8/20 μs current. This is now made by modifying the value of L_1 until a good agreement between the simulation result and the manufacturer's value is achieved. The resulting procedure is shown in Table 5.9.

Incoming surge: A conservative estimate of the crest voltage for the incoming surge is to assume that it is 20% above U_{50} [4]. For the line under study, the crest voltage is $1.2 \times 1400 = 1680$ kV. The distance to flashover is obtained by using

$$d_m = \frac{1}{n \cdot (MTBF) \cdot BFR}, \tag{5.47}$$

Table 5.9 Case Study 8: Adjustment of surge arrester model parameters.

Run	L_1 (mH)	Simulated V_{10} (kV)	Difference (%)	Next value of L_1
1	31.57	496.7	3.76	15.78
2	15.78	480.0	0.42	14.20
3	14.20	478.2	0.04	—

Table 5.10 Corona constant [2, 4].

Conductor	K_S (kV.km)/μs
Single conductor	700
Two conductor bundle	1000
Three/four conductor bundle	1700
Six/eight conductor bundle	2500

where n is the number of lines arriving at the substation, *MTBF* is the mean time between failures of the substation, and *BFR* is the backflashover rate of the line.

The desired MTBF for the substation is 200 years. Since the BFR of the line is 2.0 flashovers/100 km-years, the span length is 250 m, and it is a single-line substation ($n = 1$), the distance to flashover is 0.25 km. This distance coincides with a tower location, so it does not have to be modified. That is, $d = d_m$. The steepness, S, and tail time, t_h, of the incoming surge are calculated by using [2, 4]

$$S = \frac{K_S}{d} \quad t_h = \frac{Z_g}{R_i} t_s, \tag{5.48}$$

where K_S is the corona constant, obtained from Table 5.10, d is the backflashover location, Z_g is the shield (ground) wire surge impedance, R_i is the high current resistance and t_s is the travel time of one line span.

For a single-conductor line $K_S = 700$ (kV-km)/μs. The other values to be used in the above expressions are: $Z_g = 438\ \Omega$, $R_i = 25\ \Omega$ and $t_s = 0.833$ μs. The incoming surge will have the following characteristic values: $S = 2800$ kV/μs, $t_f = 0.60$ μs, where t_f is the front time. The tail time is $t_h = 14.6$ μs.

Simulation results: The voltage at the different equipment locations (station entrance, circuit breaker, arrester-bus junction and transformer) must be calculated taking into account the power-frequency voltage at the time the incoming surge arrives to the substation. IEEE Std 1313.2 recommends a voltage of opposite polarity to the surge, equal to 83% of the crest line-to-neutral power-frequency voltage [4]. In the case under study, the value of this voltage is 149 kV. Figure 5.51 and Table 5.11 show some results obtained with two values of the transformer capacitance.

These results can be used to select the lightning insulation level of substation equipment by following the procedures recommended in standards [4]. If the resulting values were above the standardized values, then arresters with lower protective characteristics should be selected.

5.5.4 Validation

The validation of lightning simulations is very difficult due to the random nature of lightning and the fact that no two lightning strokes have the same characteristics. The analysis of transient surges generated during the backflashover of a transmission line in close proximity to a substation was the main goal of an EPRI investigation [145]. A full-scale mock-up of a 115 kV rated substation was constructed to investigate the behaviour of substation insulation in front of non-standard voltage impulses. The substation clearances and insulation were reproduced according to standard design procedures. The substation contained a combination of aluminium rigid bus with various types of insulators, cap-and-pin switches, station post insulators, and standard suspension insulators on strain bus dead-ends. The switches were installed to provide reflections under different operating modes as well as realistic substation equipment gap configurations. Other typical substation air gaps (rod-rod, ring-ring, and conductor-structure) were also incorporated. Flashover tests were conducted by applying phase-to-ground and phase-to-phase impulses. The impulses were generated by discharging a bank of capacitors into the tertiary winding of a

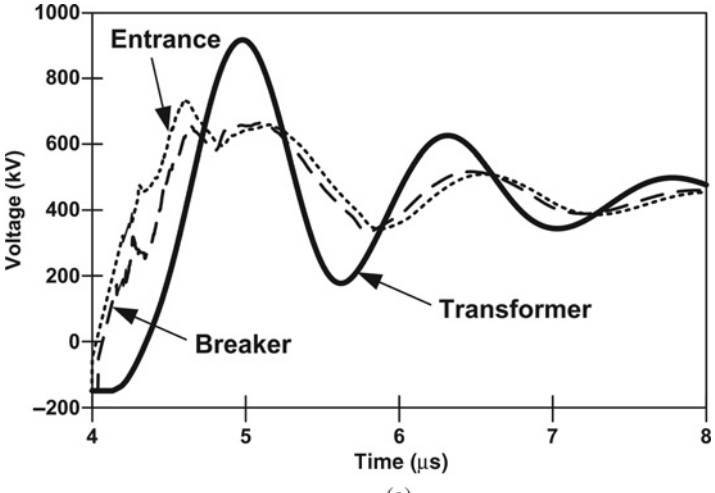

(a)

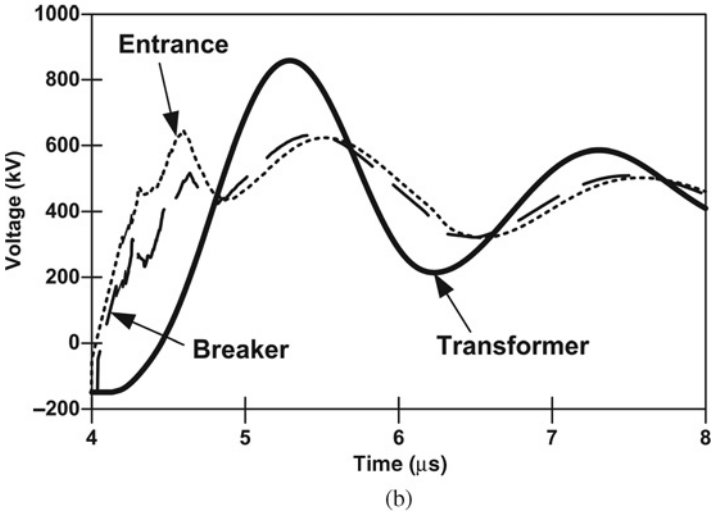

(b)

Figure 5.51 Case Study 8: Simulation results: (a) transformer capacitance = 2 nF, (b) transformer capacitance = 4 nF.

Table 5.11 Case Study 8: Voltages at substation equipment.

	Transformer capacitance	
Voltage	2 nF	4 nF
Transformer	752 kV	785 kV
Station entrance	737 kV	645 kV
Circuit breaker	669 kV	632 kV
Arrester – bus junction	684 kV	657 kV
Transformer	917 kV	858 kV

single-phase autotransformer and then through a peaking gap and capacitor, which resulted in an impulse having a shape of 0.2/200 μs.

Computer simulations of several flashover tests were performed for benchmarking the substation model. The substation mock-up and test circuit were modelled based on guidelines similar to those described above. The phase conductors were represented using a frequency-dependent distributed-parameter line model. The insulators were represented by capacitances, with different values for each type of insulator (cap-and-pin, station post, and suspension). The grounding copper-conductor cable that connected insulators to the support structure was represented by distributed-parameter line segments. The grounding conductors that connected the towers to the grounding cable were represented with lumped linear elements.

The substation stress was caused by a surge impinging on the substation from an incoming line, being the steep voltage entering the substation the result of a backflashover of the line insulation in close proximity to the substation. The magnitude of the voltage was limited by surge arresters installed at the substation entrance. Good agreement was found between the calculated voltage waveforms and the oscillograms obtained by direct measurements, so it was concluded that the benchmarking was satisfactory. More detailed information concerning measurements and calculations is available in [145].

5.6 Very Fast Transient Overvoltages in Gas Insulated Substations

5.6.1 Introduction

Very fast transients (VFT), also known as very fast-front transients, can be caused by disconnector operations and faults within gas insulated substations (GISs), switching of motors and transformers with short connections to the switchgear, or certain lightning conditions [2].

VFTs in GISs can arise any time there is an instantaneous change in voltage. This change can be caused by disconnector/breaker operations, the closing of a grounding switch or the occurrence of a fault. These transients have a rise time in the range of 4–100 ns, and are normally followed by oscillations having frequencies in the range of 1–50 MHz. Their magnitude is in the range of 1.5–2.0 p.u. of the line-to-neutral voltage crest. These values are generally below the insulation level of the GIS and connected equipment of lower voltage classes. VFTOs in GISs are of greater concern at the highest voltages, for which the ratio of the insulation level to system voltage is lower [146].

The generation and propagation of VFTs from their original location throughout a GIS can produce internal and external overvoltages. This section discusses the origin and propagation of VFTs in GISs, proposes modelling guidelines of GIS components for the study of internal VFTOs and includes a case study of internal transients in a 765 kV GIS.

5.6.2 Origin of VFTO in GIS

VFTOs are generated in a GIS during disconnector or breaker operations, or by line-to-ground faults. During a disconnector operation a number of pre- or restrikes occur due to the relatively slow speed of the moving contact [147]. Figure 5.52 shows the simplified configuration used to explain the general switching behaviour and the pattern of voltages on closing and opening of a disconnector at a capacitive load [147–150].

During closing, as the contacts approach, the electric field between them will rise until sparking occurs. The first strike will usually occur at the crest of the power-frequency voltage. Thereafter current will flow through the spark and charge the capacitive load to the source voltage. As it does so, the potential difference across the contacts falls and the spark will eventually extinguish. The behaviour on opening is very nearly a complete reversal of the above description.

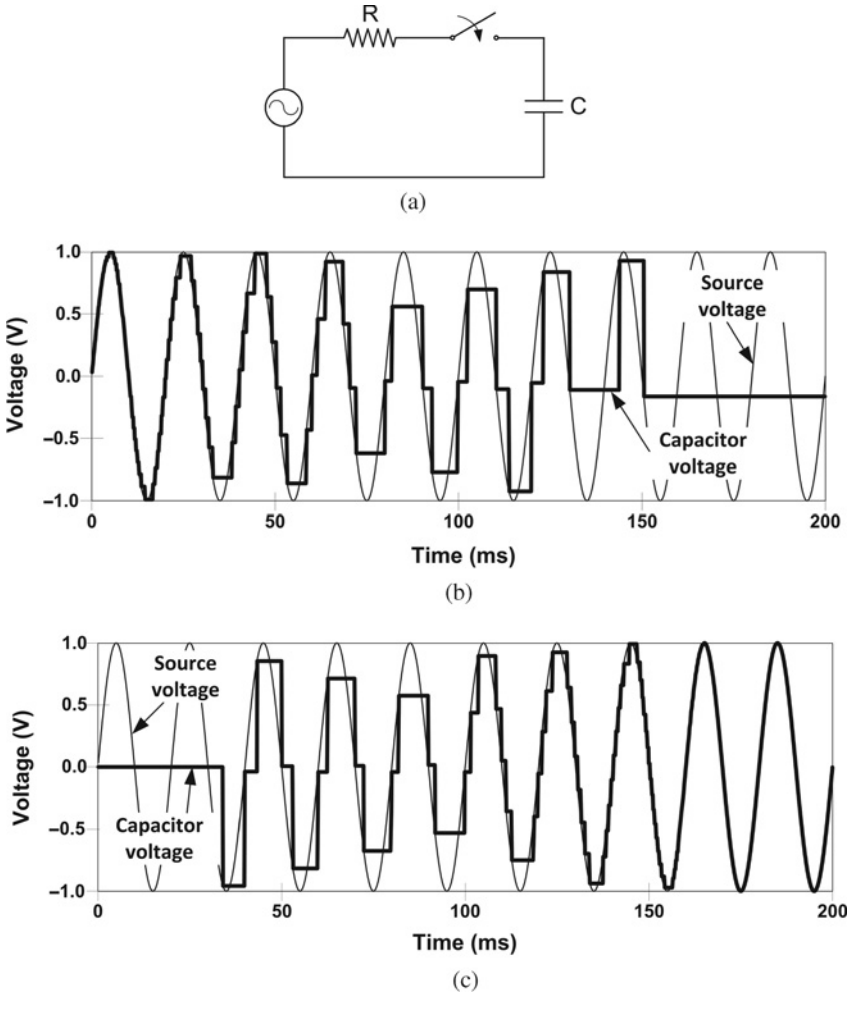

Figure 5.52 Variation of load and source side voltages during disconnector switching: (a) diagram of the capacitive circuit, (b) opening operation, (c) closing operation.

In case of a line-to-ground fault, the voltage collapse at the fault location occurs in a similar way as in the disconnector gap during striking. Step-shaped travelling surges are generated and injected into the GIS lines connected to the collapse location. The rise time of these surges depend on the voltage preceding the collapse.

Figure 5.53 illustrates the generation of a VFT due to a disconnector operation. The breakdown of a disconnector during closing originates two surges V_L and V_S whose magnitude is given by

$$V_L = \frac{Z_L}{Z_S + Z_L}(V_1 - V_2) \quad V_S = -V_L, \tag{5.49}$$

where Z_S and Z_L are the surge impedance on the source and on the load side, respectively, V_1 is the intercontact spark voltage and V_2 is the trapped charge voltage at the load side.

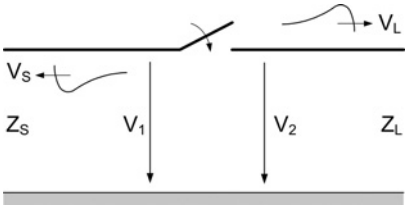

Figure 5.53 Generation of VFT in GIS.

5.6.3 Propagation of VFTs in GISs

VFTs in GISs can be divided into internal and external. Internal transients can produce overvoltages between inner conductors and the encapsulation, external transients can cause stress on secondary and adjacent equipment. A summary of the propagation and main characteristics of both types of phenomena is presented below [151, 152].

Internal transients: Breakdown phenomena across the contacts of a disconnector generate very short rise time travelling waves which propagate in either direction from the breakdown location. As a result of the fast rise time of the wave front, the propagation throughout a substation must be analysed by representing GIS sections as low-loss distributed-parameter lines, each section being characterized by a surge impedance and a transit time. Travelling waves are reflected and refracted at every point where they encounter a change in the surge impedance. The transients depend on the GIS configuration and the superposition of the surges reflected and refracted on discontinuities such as breakers, T-junctions or bushings. Due to multiple reflections and refractions, travelling voltages can increase above the original values, and very high frequency oscillations can occur.

The internal damping of the VFT influencing the highest frequency components is determined by the spark resistance. Skin effects due to the aluminium enclosure can be generally neglected. The main portion of the damping of the VFT occurs at the transition to the overhead line. Due to the travelling wave behaviour of the VFT, the overvoltages caused by disconnector switches show a spatial distribution. Normally the highest overvoltage stress is reached at the open end of the load side.

Overvoltages are dependent on the voltage drop at the disconnector just before striking, and on the trapped charge that remains on the load side of the disconnector. For a normal disconnector with a slow speed, the maximum trapped charge reaches 0.5 p.u., resulting in a most unfavourable voltage collapse of 1.5 p.u. For these cases, the resulting overvoltages are in the range of 1.7 p.u. and reach 2 p.u. in very specific cases. For a high-speed disconnector, the maximum trapped charge could be 1 p.u. and the highest overvoltages reach values up to 2.5 p.u. Although values larger than 3 p.u. have been reported, they have been derived by calculation, using unrealistic simplified simulation models. The main frequencies depend on the length of the GIS sections affected by the disconnector operation and are in the range of 1–50 MHz.

Figures 5.54 and 5.55 present two very simple cases, a single-bus duct and a T-junction with GIS components modelled as lossless distributed-parameter lines. These examples will illustrate the influence of some parameters on the frequency and magnitude of VFT in GIS. The source side is represented in both cases as a step-shaped source in series with a resistance. This is a simplified model of an infinite-length bus duct. The surge impedance of all bus sections is 50 Ω. For the simplest configuration, the reflections of the travelling waves at both terminals of the duct will produce, when the source resistance is neglected, a pulse-shaped transient of constant magnitude – 2 p.u. – and constant frequency at the open terminal. The frequency of this pulse can be calculated using

$$f = \frac{1}{4\tau}, \tag{5.50}$$

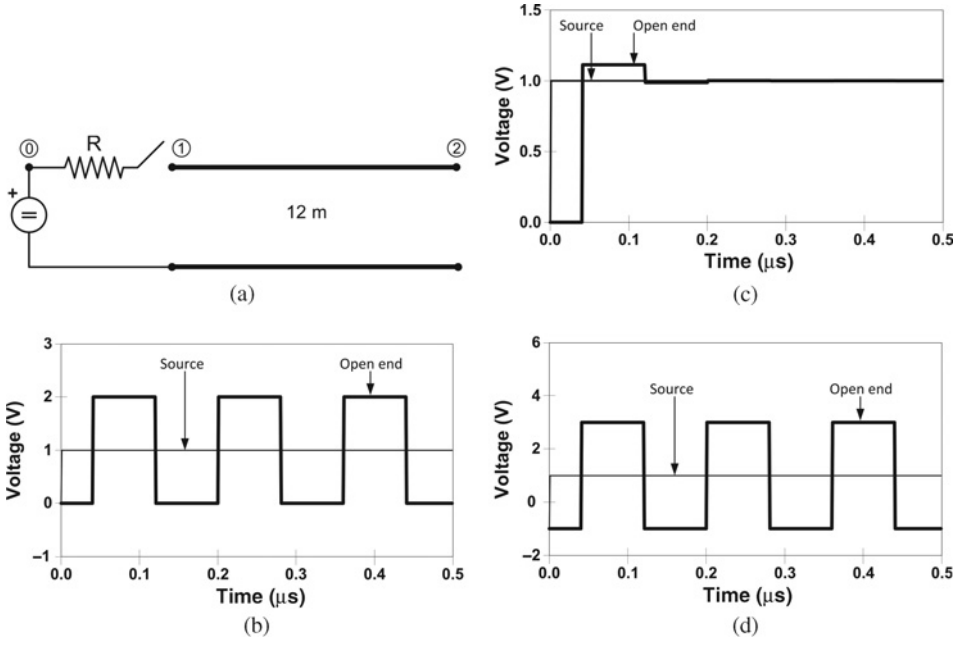

Figure 5.54 Generation of VFTO in a GIS bus duct: (a) scheme of the network, (b) $R = 0$, $V_1 = 1$ p.u., $V_2 = 0$ p.u., (c) $R = 40\ \Omega$, $V_1 = 1$ p.u., $V_2 = 0$ p.u., (d) $R = 0$, $V_1 = 1$ p.u., $V_2 = -1$ p.u. [151].

where τ is the transit time of the line. If the propagation velocity is close to that of light, the frequency, in MHz, of the voltage generated at the open terminal will be

$$f = \frac{75}{d} \tag{5.51}$$

where d is the duct length, in meters. When a more realistic representation of the source is used, (e.g. $R = 40\ \Omega$), the maximum overvoltage at the open terminal will depend on the voltage at the disconnector just before striking, and on the trapped charge that remains on the load side.

Overvoltages can reach higher values in more complex GIS configurations. The simulations performed for the T-configuration gave the highest values, being node 4, the location where the highest overvoltages were originated.

External transients: An internally generated VFT propagates throughout the GIS and reaches the bushing where it causes a transient enclosure voltage and a travelling wave that propagates along the overhead transmission line. The external transients include transient voltages between the enclosure and ground at GIS–air interfaces, voltages across insulating spacers in the vicinity of GIS current transformers (CTs) when they do not have a metallic screen on the outside surface, voltages on the secondary terminals of GIS instrument transformers and radiated electromagnetic fields, which can be dangerous to adjacent control or relay equipment:

- *Transient enclosure voltages*: Transient enclosure voltages (TEVs) are short-duration high-voltage transients that appear at the enclosure of the GIS through the coupling of internal transients to enclosure at enclosure discontinuities. The usual location for these voltages is the transition between the GIS and the overhead line at an air bushing, although they can also emerge at other points, such as visual inspection ports, insulated spacers for CTs or insulated flanges at GIS/cable interfaces. The simplified circuit shown in Figure 5.56 will be used to explain the generation of TEV [150].

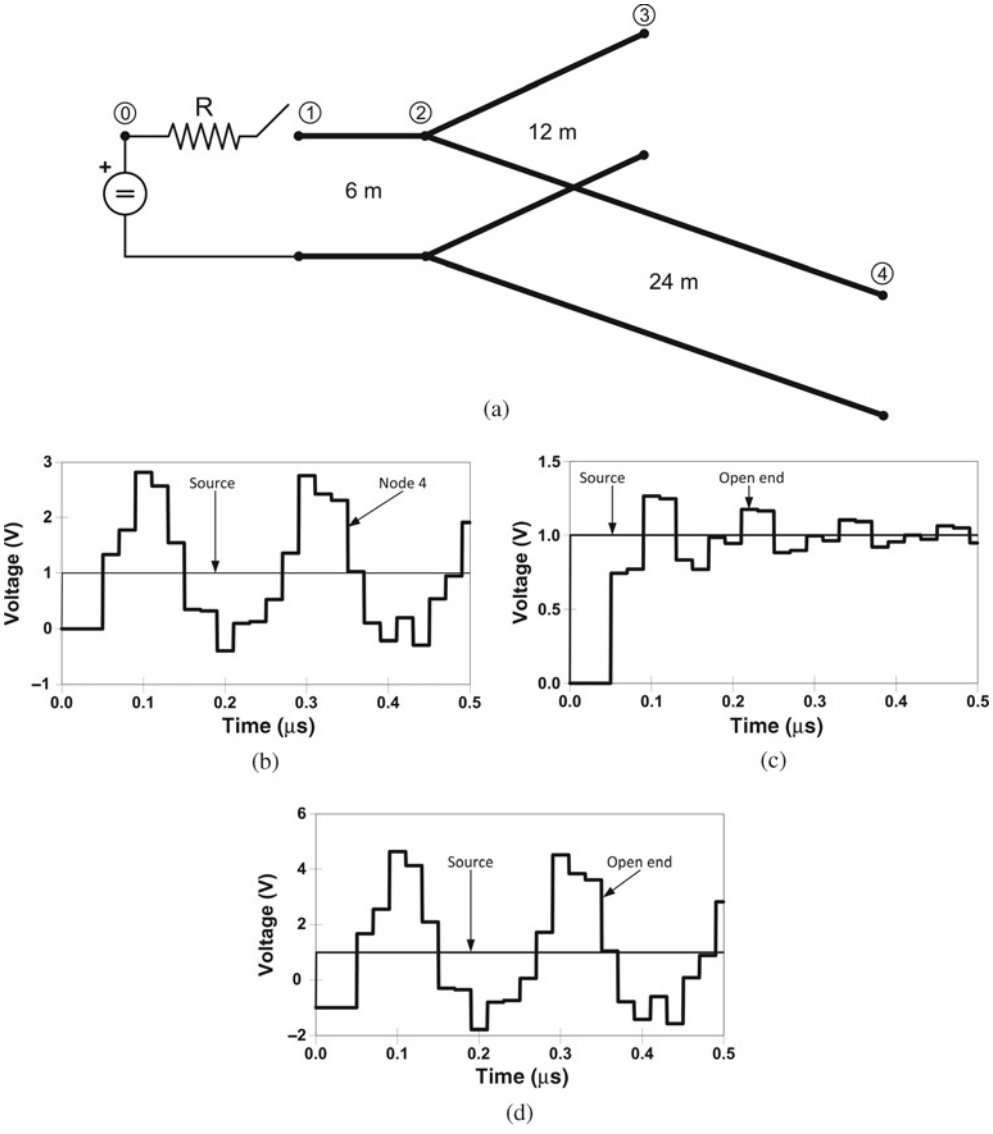

Figure 5.55 Generation of VFTO in a GIS with a bifurcation point: (a) scheme of the network, (b) $R = 0$, $V_1 = 1$ p.u., $V_2 = 0$ p.u., (c) $R = 40\,\Omega$, $V_1 = 1$ p.u., $V_2 = 0$ p.u., (d) $R = 0$, $V_1 = 1$ p.u., $V_2 = -1$ p.u. [151].

At the GIS–air interface, three transmission lines can be distinguished: the coaxial GIS transmission line, the transmission line formed by the bushing conductor and the overhead line, and the GIS enclosure-to-ground transmission line. Each of them has a different surge impedance. When an internal wave propagates to the gas-to-air bushing, a portion of the transient is coupled onto the overhead line-to-ground transmission line, and a portion is coupled onto the GIS enclosure-to-ground transmission line. The latter constitutes the TEV.

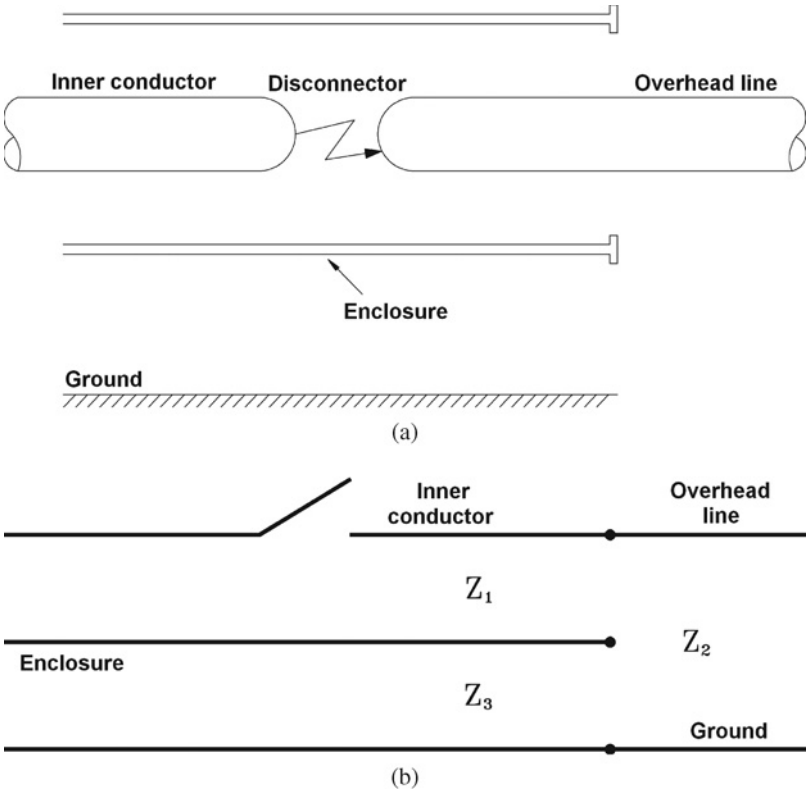

Figure 5.56 Generation of transient enclosure voltages (TEV): (a) GIS–air transition, (b) single-line diagram [151].

In general, TEV waveforms have at least two components: the first one has a short initial rise time, followed by high frequency oscillations determined by the lengths of various sections of the GIS, and concentrated in the range of 5–10 MHz; the second component is of lower frequency – hundreds of kHz – and is often associated with the discharge of capacitive devices with the grounding system. Both components are damped quickly as a result of the lossy nature of the enclosure-to-ground plane transmission mode. TEV generally persists for a few microseconds. The magnitude varies along the enclosure; it can be in the range of 0.1– 0.3 p.u. of the system voltage, and reaches the highest magnitude near the GIS–air interface.

The TEV wave, which couples onto the enclosure, encounters grounding connections that form transmission line discontinuities and attenuate the TEV. Mitigation methods include grounding using low surge impedance short-length leads and the installation of metal-oxide surge arresters across any insulating spacers.

Transients on overhead connections: A portion of the VFT travelling wave incident at a gas–air transition is coupled onto the overhead connection and propagates to other components. This propagation is lossy, and results in some increase of the waveform rise time, although transients can have rise times in the range of 10–20 ns if the air connection is relatively short. In general, external waveforms have two different characteristics: (a) the overall waveshape, dictated by lumped-circuit parameters (e.g. the capacitance of voltage transformers or line and grounding inductances) with a rise time of a few hundred nanoseconds; (b) a fast-front portion, dictated by transmission line effects, with a rise time in the range of 20 ns and usually reduced in magnitude, due to discontinuities in the

transmission path. The fast rise time of the initial portion is possible because capacitive components, such as bushings, are physically long and distributed, and they cannot be treated as lumped elements.

The magnitude of the rise time portion of external transients is generally lower than that of internal VFT, while the voltage rate-of-rise can be in the range of 10–30 kV/μs. However, since each disconnector operation can generate tens to hundreds of individual transients, possible ageing on the insulation of external components has to be considered. These overvoltages can cause stress to adjacent equipment, and resonance phenomena in exposed transformers.

- *Transient electromagnetic fields*: These are radiated from the enclosure and can cause some stress on secondary equipment, mainly on computer-related equipment. Their frequency depends on the GIS arrangement, but it is typically in the range of 10–20 MHz.

5.6.4 Modelling Guidelines

Due to the travelling nature of VFTs, modelling of GIS components makes use of electrical equivalent circuits composed of lumped elements and distributed-parameter lines. At very high frequencies, the skin losses can produce a noticeable attenuation. Due to the geometrical structure of GISs and the enclosure material, skin losses are usually neglected, which gives conservative results. Only the dielectric losses in some components (e.g. capacitive-graded bushing) need be taken into account.

Modelling guidelines for representing GIS equipment in computation of internal transients are discussed in the following paragraphs [14, 15, 151–156]. The models are based on single-phase representations, but depending on the substation layout and the study to be performed, three-phase models for inner conductors should be considered [157]. More advanced guidelines were analysed and proposed in [158]. For the calculation of internal transients all the distributed-parameter lines take into account the internal mode (conductor–enclosure) only, assuming that the external enclosure is perfectly grounded. If TEV is of concern, then a second mode (enclosure–ground) has to be considered.

Here is a short description of most important GIS component models [151, 152, 156]:

- *Bus ducts*: For a range of frequencies lower than 100 MHz, a bus duct can be represented as a lossless transmission line. The inductance and the capacitance per unit length of a horizontal single-phase coaxial cylinder configuration, as shown in Figure 5.57, are given by

$$L = \frac{\mu_o}{2\pi} \ln \frac{R}{r} \tag{5.52a}$$

$$C = \frac{2\pi\varepsilon}{\ln \frac{R}{r}} \quad \left(\varepsilon \approx \varepsilon_0\right), \tag{5.52b}$$

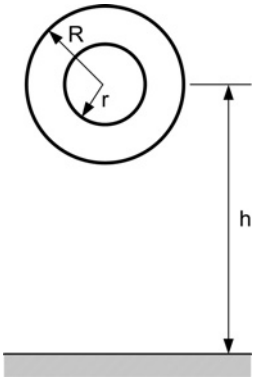

Figure 5.57 Coaxial bus duct cross section.

from where the following form for the surge impedance is derived:

$$Z = \sqrt{\frac{L}{C}} \approx \frac{\sqrt{\mu_o/\varepsilon_o}}{2\pi} \ln \frac{R}{r} = 60 \ln \frac{R}{r} \tag{5.53}$$

A different approach should be used for vertical bus sections. As for the propagation velocity, empirical corrections are usually required to adjust its value. Experimental results show that the propagation velocity in GIS ducts is close to 0.95–0.96 of the speed of light [153]. The error committed by ignoring skin effect losses is usually negligible.

Other devices, such as elbows, can also be modelled as lossless transmission lines.

- *Surge arresters*: Experimental results have shown that switching operations in GISs do not usually produce voltages high enough to cause metal-oxide surge arresters to conduct, so the arrester can be modelled as a capacitance-to-ground. However, when the arrester conducts, the model should take into account the steep-front wave effect, since the voltage developed across the arrester for a given discharge current increases as the time to crest of the current increases, but reaches a crest prior to the crest of the current. A detailed model must represent each internal shield and block individually, and include the travel times along shield sections, as well as the capacitances between these sections, capacitances between blocks and shields and the blocks themselves.
- *Circuit breakers*: A closed breaker can be represented as a lossless transmission line, whose electrical length is equal to the physical length, the propagation velocity being reduced to 0.95–0.96 of the speed of light. The representation of an open circuit breaker is more complicated due to internal irregularities. In addition, circuit breakers with several chambers contain grading capacitors, which are not arranged symmetrically. The electrical length must be increased above the physical length, due to the effect of a longer path through the grading capacitors, while the speed of progression must be decreased due to the effects of the higher dielectric constant of these capacitors.
- *Gas-to-air bushings*: A bushing gradually changes the surge impedance from that of the GIS to that of the line. A detailed model of the bushing must consider the coupling between the conductor and shielding electrodes, and include the representation of the grounding system connected to the bushing. A simplified model consists of several transmission lines in series with a lumped resistor representing losses. The surge impedance of each line section increases as the location goes up the bushing. If the bushing is distant from the point of interest, the resistor can be neglected and a single-line section can be used. A more advanced model for capacitive-graded bushings was proposed in [159].
- *Power transformers*: A common practice is to model a power transformer as a capacitor representing the capacitance of the winding to ground. At very high frequencies, the saturation of the magnetic core can be neglected, as well as leakage impedances. When voltage transfer has to be calculated, interwinding capacitances and secondary capacitance-to-ground must also be represented. At very high frequencies a winding of a transformer behaves like a capacitive network consisting of series capacitances between turns and coils, and shunt capacitances between turns and coils to the grounded core and transformer tank. The terminal capacitance to ground, which mostly comes from the capacitance of the terminal bushing to ground, must be added to obtain the total capacitance of the winding. If voltage transfer is not of concern, an accurate representation can be obtained by developing a circuit that matches the frequency response of the transformer at its terminals. The modelling of transformers for analysis very fast-front transients has been the subject of several works; see [126, 127, 160–165].
- *Current transformers*: Insulating gaps are usually installed in the vicinity of current transformers. During high-voltage switching operations, these gaps flash over, establishing a continuous path. Travelling waves propagate with little distortion. Current transformers can often be neglected. In any case several approaches have been proposed to represent these transformers – see for instance [155].
- *Spark dynamics*: The behaviour of the spark in disconnector operations can be represented by a dynamically variable resistance, with a controllable collapse time. In general, this representation does not affect the magnitude of the maximum VFTO, but it can introduce a significant damping on internal transients [166].

5.6.5 Case Study 9: VFT in a 765 kV GIS

The collapsing electric field during a breakdown produces travelling waves which propagate in both directions from the disturbance location. This propagation can be analysed, assuming that propagation losses are negligible. Due to the very high frequencies generated by a dielectric breakdown, a simulation is restricted to calculations during the VFT waveform period, usually 1–2 μs. If the simulation is performed with an EMTP-like tool, which uses a constant time-step size, then the value of this step size will depend on the shorter transit time in the GIS, and must be equal to or smaller than one-half of the shorter transit time.

For normal studies, the transient may be originated by any of the following three causes:

- a ramp voltage with a magnitude determined by the voltage across the switch
- two ramp currents on opposite sides of the switch, such that the voltage across the switch is equal to zero at the crest of the inputs
- a switch-closing operation after charging both sides of the switch to the desired value.

Low voltage tests are a very useful tool for development and validation of GIS models. The case analysed in this section presents the simulation of internal transients during low-voltage tests of a 765 kV GIS. Figures 5.58 and 5.59 show the one-line and the connectivity diagram of a 765 kV GIS bay [151]. Detailed data is given in Table 5.12. Models used to represent components of this case are those discussed above. These models were developed by using the following procedure [151]:

1. Low-voltage tests on individual components were performed using waves with fronts of 4 and 20 ns.
2. Models based on physical dimensions were developed, assuming a propagation velocity equal to that of light.
3. Digital models were adjusted so that simulation results were matched to measurements. The main adjustment was to decrease the propagation velocity to 0.96 that of light.

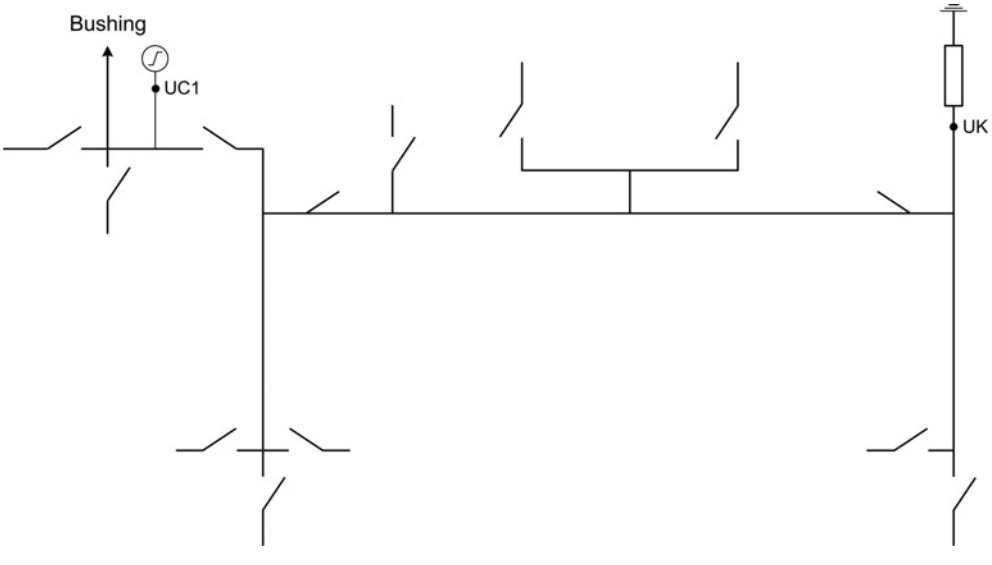

Figure 5.58 Case Study 9: One-line diagram of the test system [151].

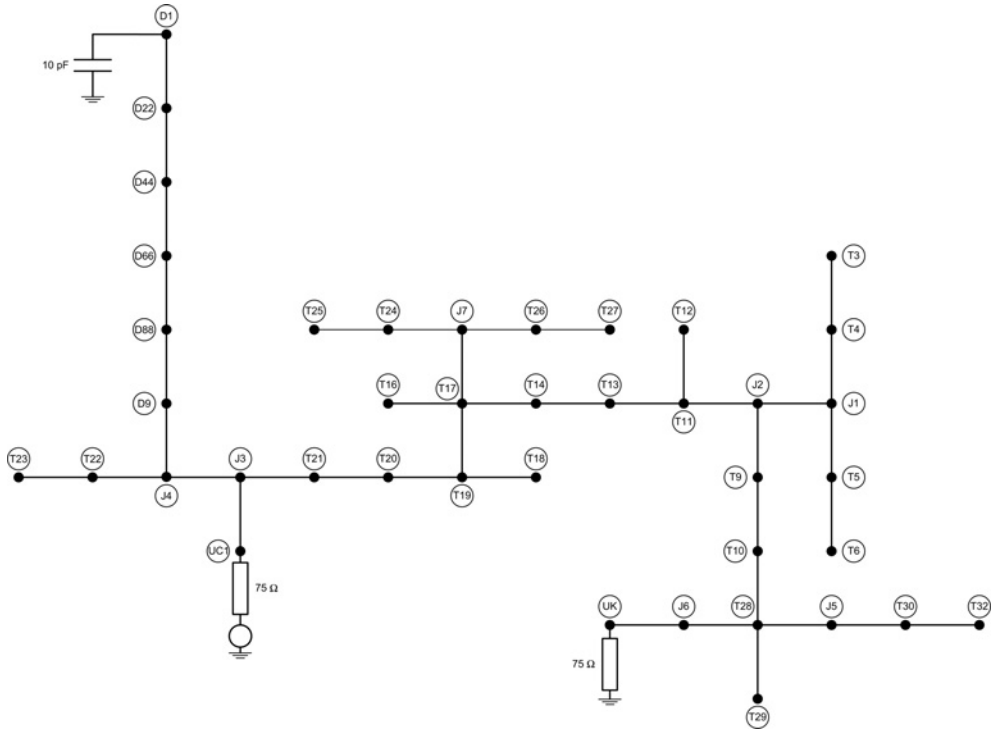

Figure 5.59 Case Study 9: Connectivity diagram of the test system [151].

Two transients have been reproduced: (1) a ramp voltage is applied at $t = 0$; (2) the ramp voltage source is also used but the transient starts after closing a switch at the instant the ramp reaches its maximum value. Waveforms obtained for each case at two nodes are shown in Figures 5.60 and 5.61. It can be observed that waveforms for both cases are essentially the same, except for the first nanoseconds in the vicinity of the input node UC1. These simulation results were validated by comparison with low-voltage measurements.

5.6.6 Statistical Calculation

The level reached by VFTO is random by nature. The maximum overvoltage produced by a disconnector breakdown depends on the geometry of the GIS, the measuring point, the voltage prior to the transient at the load side (trapped charge) and the intercontact voltage at the time of the breakdown [148, 166–168].

The transient overvoltages as a function of time t and position s may be derived from

$$V(t, s) = V_b \cdot K(t, s) + V_q, \tag{5.54}$$

where $K(t, s)$ is the normalized response of the GIS, V_b is the intercontact spark voltage and V_q the voltage prior to the transient at the point of interest. Since V_b and V_q are random variables, $V(t, s)$ is also random. This equation can be used to estimate worst case values [168].

For slow switches the probability of a re-/prestrike with the greatest breakdown voltage (in the range 1.8–2 p.u.) is very small; however, due to the large number of re-/prestrikes that are produced with one

Table 5.12 Case Study 9: Data of the 765 kV GIS [151].

Branch	Z (Ω)	Travel time (ns)
UC1 – J3	75	6.40
J3 – J4	75	48.0
J4 – T22	75	2.20
T22 – T23	51	1.90
J4 – D9	78	2.20
D9 – D88	68	1.80
D88 – D66	59	4.20
D44 – D22	33	5.80
D22 – D1	330	9.10
J3 – T21	75	2.20
T21 – T20	51	1.90
T20 – T19	160	0.67
T19 – T18	65	1.70
T19 – T17	75	6.80
T17 – T16	65	1.70
T17 – J7	75	8.50
J7 – T24	75	2.20
T24 – T25	51	1.90
J7 – T26	75	2.20
T26 – T27	51	1.90
T17 – T14	160	0.67
T14 – T13	51	1.90
T13 – T11	75	9.90
T11 – T12	65	1.70
T11 – J2	75	7.50
J2 – T9	75	2.20
T9 – T10	51	1.90
T10 – T28	160	0.67
T28 – J6	75	7.10
J6 – UK	75	6.40
T28 – T29	65	1.70
T28 – J5	75	8.80
J5 – T30	75	2.20
T30 – T32	51	1.90
J2 – J1	75	6.70
J1 – T4	75	2.20
T4 – T3	51	1.90
J1 – T5	75	2.20
T5 – T6	51	1.90

operation, this probability should not always be neglected. The value of the trapped charge is mainly dependent on the disconnect switch characteristics: the faster the switch, the greater the mean value that the trapped charge voltage can reach.

Consider that the performance of a disconnector during an opening operation is characterized by the pattern shown in Figure 5.53. A difference in breakdown voltages for the two polarities indicates a

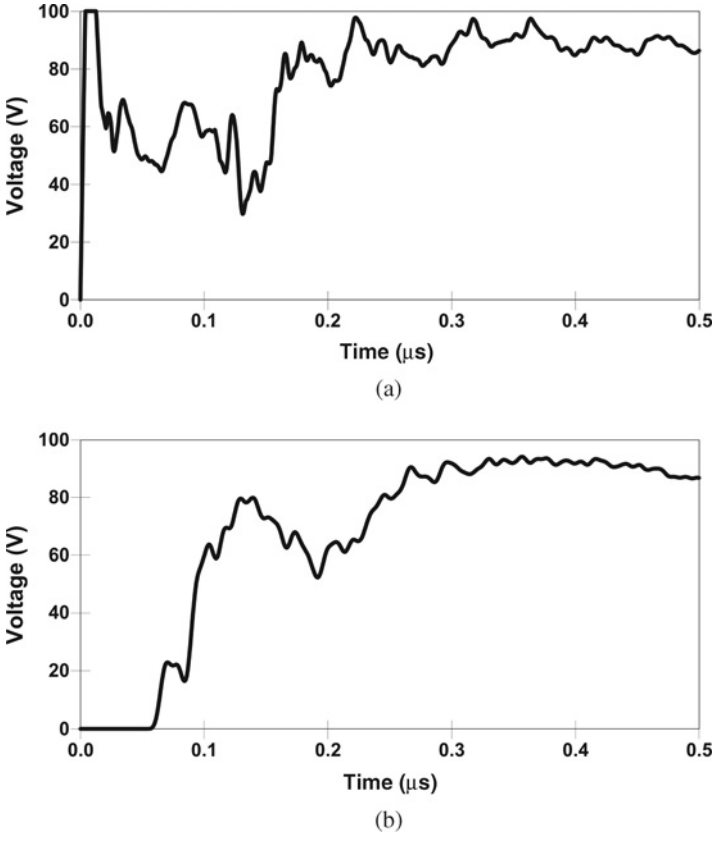

Figure 5.60 Case Study 9: Simulation results with 4 ns ramp: (a) voltage at location UC1, (b) voltage at location UK [151].

dielectric asymmetry. The final trapped charge voltage has a distribution which is very dependent on the asymmetry in the intercontact breakdown voltage. The dielectric asymmetry of a disconnector is usually a function of contact separation. A disconnector may show different performances at different operating voltages. Consequently, very different stresses will be originated as a result of different operational characteristics.

5.6.7 Validation

The plot presented in Figure 5.62 illustrates the accuracy with which VFT can be simulated. This plot compares a computer simulation with a direct measurement of a transient waveform in an actual GIS. The computer model neglects the presence of propagation losses, which result in somewhat less damping of the high frequency part of the waveform, but includes the effects of spacers, flanges, elbows, corona shields and other connection hardware [151].

The characterization and quantification of VFTs in GISs, as well as the electromagnetic fields radiated during switching operations have been the subject of several works that also validated the approaches proposed for representing GIS equipment, see [169–171]. See also [155, 156].

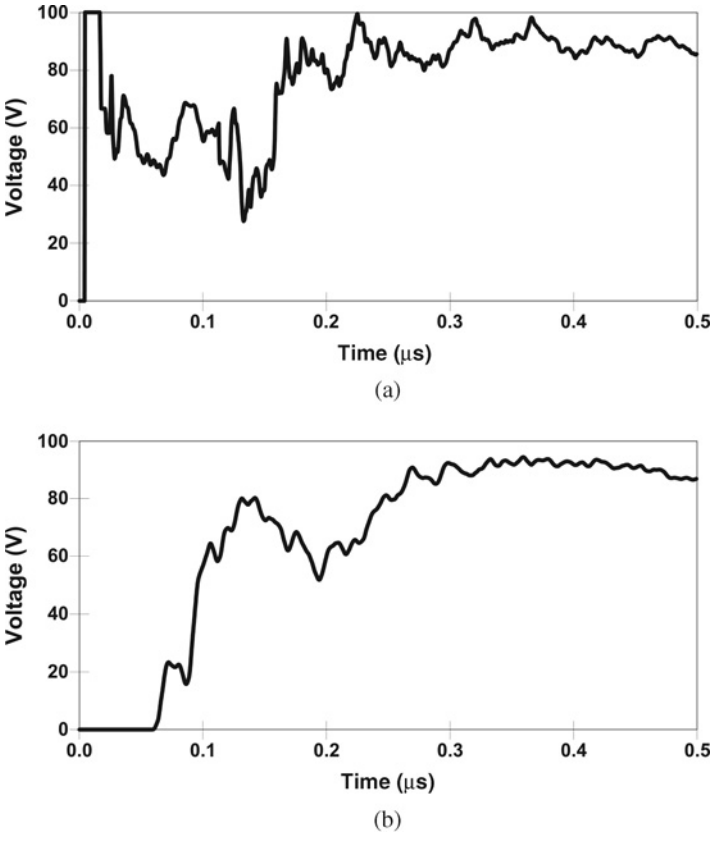

Figure 5.61 Case Study 9: Simulation results from closing a switch: (a) voltage at location UC1, (b) voltage at location UK [151].

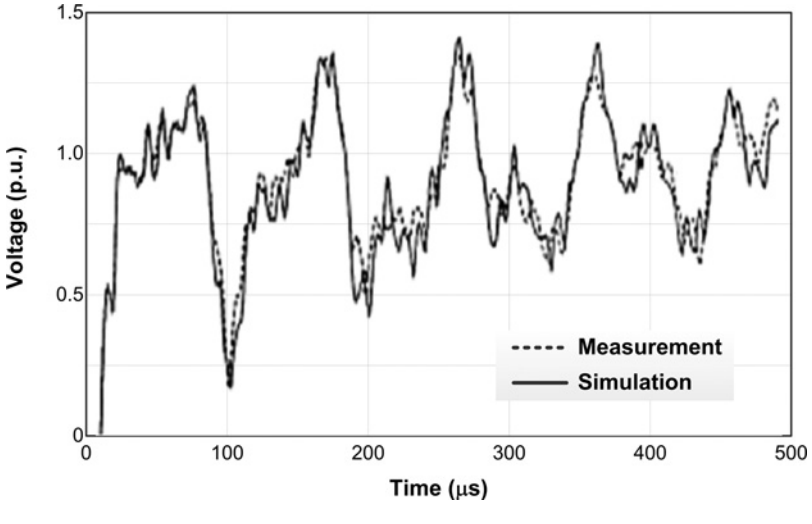

Figure 5.62 Comparison of measurement and simulation of disconnect switch induced overvoltages in a 420 kV GIS (© 1998 IEEE) [151].

5.7 Conclusions

This chapter has provided an introduction to the causes of overvoltages in power systems and given the general rules for their study using electromagnetic transient tools. The main concerns are related to modelling and to the extent of the system to be modelled. These aspects have been addressed through several test studies that have covered the full range of transient overvoltages.

The model of the system zone to be represented in the data input file depends on the frequency range of the transients. Irrespective of the class of overvoltage to be analysed, the rule of thumb is that the higher the range of frequencies, the smaller the zone modelled. In general, the user should try to optimize (i.e. minimize) the part of the system represented in the data input file. The more components represented in the file, the higher the probability of insufficient or wrong modelling. In addition, a very detailed representation of a system will require very long simulation times. In general, some experience will be needed to decide how detailed the system should be and to choose the model for the most important components.

EMTP-like tools are based on the trapezoidal rule and use a time-domain solution technique with a fixed time-step; that is, it must be chosen by the user. A few rules must be applied for this selection: (1) the time-step should be small enough to properly represent the smallest time constant in the modelled system; (2) it should also be significantly smaller (typically 1/20th) than the period of the highest frequency oscillatory component; (3) when distributed-parameter line models are included in the model, the time-step should be smaller than one half of the shortest transit time. Additional factors that affect the time-step are the presence of nonlinearities (e.g. arrester characteristics) and switching models of power electronic converters.

Time-steps in the range of 5–50 ms are used in typical switching transients, ranging the simulation time from 20–200 ms [17]. In lightning studies, the time-step depends upon the steepness of the surge, the minimum length of travelling wave models, plus the use of flashover gaps and surge arresters with significant lead lengths. As a general rule, it will be in the range of 1–20 ns, with a simulation length of 20–50 ms. However, there can be some studies for which much longer simulation time can be necessary, such as arrester energy stresses.

The validation of a transient model can be a crucial aspect and is always a difficult task, mainly when the cause of the transient is random (e.g. lightning) or the system is very nonlinear (e.g. ferroresonance). There is, however, a significant experience in validating transients caused by switching operations for which the starting time of the transient is previously scheduled.

Acknowledgement

Some sections of this chapter are based on material used in the publication *Modeling and Analysis of System Transients Using Digital Programs* [23]. The first author, who was a co-editor of the publication, wants to express his gratitude to the IEEE WG members who contributed to that publication.

References

[1] IEC 60071 (2010) Insulation co-ordination – Part 1: Definitions, principles and rules. Part 1.
[2] IEC 60071–2 (1996) Insulation co-ordination, Part 2: Application guide.
[3] IEEE Std 1313.1 (1996) IEEE Standard for Insulation Coordination – Definitions, Principles and Rules.
[4] IEEE Std 1313.2 (1999) IEEE Guide for the Application of Insulation Coordination.
[5] Greenwood, A. (1991) *Electrical Transients in Power Systems*, 2nd edn, John Wiley & Sons, Ltd.
[6] Hileman, A.R. (1999) *Insulation Coordination for Power Systems*, Marcel Dekker.
[7] Chowdhuri, P. (2003) *Electromagnetic Transients in Power Systems*, 2nd edn, RS Press-John John Wiley & Sons, Ltd, Taunton, UK.

[8] Das, J.C. (2010) *Transients in Electrical Systems. Analysis, Recognition, and Mitigation*, McGraw-Hill, New York, NY.
[9] Fulchiron, D. (1995) Overvoltages and Insulation Coordination in MV and HV, Cahier Technique Schneider 151.
[10] Ragaller, K. (ed.) (1980) *Surges in High-Voltage Networks*, Plenum Press, New York, NY-USA.
[11] Martinez-Velasco, J.A. (ed.) (2009) *Power System Transients. Parameter Determination*, CRC Press.
[12] Durbak, D. (2006) Temporary overvoltages following transformer energizing. *Siemens PTI Newsletter*, No. 99, pp. 1–3.
[13] Glavitsch, H. (1980) Temporary overvoltages, Chapter 7, in *Surges in High-Voltage Networks* (ed. K. Ragaller), Plenum Press, pp. 115–129.
[14] IEC TR 60071-4 (2004) Insulation Co-ordination – Part 4: Computational Guide to Insulation Co-ordination and Modeling of Electrical Networks.
[15] CIGRE WG 33.02 (1990) Guidelines for Representation of Network Elements when Calculating Transients. CIGRE Brochure 39.
[16] Iravani, R., Chaudhary, A.K.S., Hassan, I.D. *et al.* (1998) Modeling guidelines for low frequency transients, Chapter 3, *Modeling and Analysis of System Transients Using Digital Programs* (eds A. Gole, J.A. Martinez-Velasco, and A. Keri), IEEE Special Publication TP-133–0, IEEE Catalog No. 99TP133–0.
[17] Durbak, D.W., Gole, A.M., Camm, E.H., *et al.* (1998) Modeling guidelines for switching transients, Chapter 4, *Modelling and Analysis of System Transients using Digital Systems* (eds A. Gole, J.A. Martinez-Velasco and A.J.F. Keri), IEEE Special Publication, TP-133-0.
[18] EPRI Report (2005). Effects of Temporary Overvoltage on Residential Products: System Compatibility Research Project, Report 1008540, Palo Alto, CA.
[19] IEEE Std C62.22 (1997). IEEE guide for the application of metal-oxide surge arresters for alternating-current systems.
[20] IEC 60099–5 (2000). Surge arresters – Part 5: Selection and application recommendations, Edition 1.1.
[21] Das, J.C. (2002) *Power System Analysis. Short-Circuit, Load Flow and Harmonics*, Marcel Dekker, New York, NY.
[22] CIGRE WG C4.307 (2014) Resonance and Ferroresonance in Power Networks, CIGRE Brochure 569.
[23] Gole, A., Martinez-Velasco, J.A., and Keri, A. (eds) (1998) *Modeling and Analysis of Power System Transients Using Digital Programs*, IEEE Special Publication TP-133–0, IEEE Catalog No. 99TP133-0.
[24] Adibi, M.M., Alexander, R.W., and Avramovic, B. (1992) Overvoltage control during restoration. *IEEE Transactions on Power Systems*, **7**(4), 1464–1470.
[25] Povh, D. and Schultz, W. (1978) Analysis of overvoltages caused by transformer magnetizing inrush current. *IEEE Transactions on Power Apparatus and Systems*, **97**(4), 1355–1365.
[26] CIGRE WG C4.307 (2014) Transformer Energization in Power Systems: A Study Guide, CIGRE Brochure 568.
[27] Lindenmeyer, D., Dommel, H.W., Moshref, A. and Kundur, P. (1999) Analysis and control of harmonic overvoltages during system restoration. International Conference on Power Systems Transients (IPST), Budapest, 20–24 June 1999.
[28] Morin, G. (1987) Service restoration following a major failure on the Hydro-Quebec power system. *IEEE Transactions on Power Delivery*, **2**(2), 454–463.
[29] Cheng, C.P. and Chen, S. (2006) Simulation of resonance over-voltage during energization of high voltage power network. *Electric Power Systems Research*, **76**, 650–654.
[30] Ketabi, A., Ranjbar, A.M. and Feuillet, R. (2002) Analysis and control of temporary overvoltages for automated restoration planning. *IEEE Transactions on Power Delivery*, **17**(4), 1121–1127.
[31] Brunke, J.H. and Fröhlich, K.J. (2001) Elimination of transformer inrush currents by controlled switching – Part I: Theoretical considerations. *IEEE Transactions on Power Delivery*, **16**(2), 276–280.
[32] Brunke, J.H. and Fröhlich, K.J. (2001) Elimination of transformer inrush currents by controlled switching – Part II: Application and performance considerations. *IEEE Transactions on Power Delivery*, **16**(2), 281–285.
[33] Iravani, M.R., Chaudhary, A.K.S., Giewbrecht, W.J. *et al.* (2000) Modelling and analysis guidelines for slow transients: Part III: The study of ferroresonance. *IEEE Transactions on Power Delivery*, **15**(1), 255–265.
[34] Rudenberg, R. (1950) *Transient Performance of Electric Power Systems*, McGraw-Hill, New York.
[35] Mork, B.A. and Stuehm, D.L. (1994) Application of nonlinear dynamics and chaos to ferroresonance in distribution systems. *IEEE Transactions on Power Systems*, **9**(2), 1009–1017.

[36] Andrei, R.G. and Halley, B.R. (1989) Voltage transformer ferroresonance from an energy standpoint. *IEEE Transactions on Power Delivery*, **4**(3), 1773–1778.
[37] Kieny, C. (1991) Application of the bifurcation theory in studying and understanding the global behaviour of a ferroresonant electric power circuit. *IEEE Transactions on Power Delivery*, **6**(2), 866–872.
[38] Mork, B.A. (1992) Ferroresonance and chaos – Observation and simulation of ferroresonance in a five-legged core distribution transformer. North Dakota State University, Ph.D. dissertation, Publication no. 9227588, UMI Publishing Services, Ann Arbor, MI 48106, (800) 521–0600, May 1992.
[39] Martinez, J.A. and Mork, B. (2005) Transformer modelling for low- and mid-frequency transients – A review. *IEEE Transactions on Power Delivery*, **20**(2), 1625–1632.
[40] Martinez, J.A., Walling, R., Mork, B. *et al.* (2005) Parameter determination for modeling systems transients. Part III: Transformers. *IEEE Transactions on Power Delivery*, **20**(3), 2051–2062.
[41] de León, F., Gómez, P., Martinez-Velasco, J.A. and Rioual, M. (2009) Transformers, Chapter 4, *Power System Transients. Parameter Determination* (ed. J.A. Martinez-Velasco), CRC Press.
[42] Brenner, E. (1956) Subharmonic response of the ferroresonance circuit with coil hysteresis. *AIEE Transactions*, **75**, 450–456.
[43] Dommel, H.W. (1986) *ElectroMagnetic Transients Program Reference Manual (EMTP Theory Book)*, Bonneville Power Administration, Portland, OR, USA.
[44] Neves, W.L.A. and Dommel, H.W. (1993) On modelling iron core nonlinearities. *IEEE Transactions on Power Systems*, **8**(2), 417–425.
[45] Walling, R.A., Barker, K.D., Compton, T.M. and Zimmerman, I.E. (1993) Ferroresonant overvoltages in grounded padmount transformers with low-loss silicon-steel cores. *IEEE Transactions on Power Delivery*, **8**(3), 1647–1660.
[46] Chen, X. (2000) Negative inductance and numerical instability of the saturable transformer component in EMTP. *IEEE Transactions on Power Delivery*, **15**(4), 1199–1204.
[47] Henriksen, T. (2002) How to avoid unstable time domain responses caused by transformer models. *IEEE Transactions on Power Delivery*, **17**(2), 516–522.
[48] de León, F. and Martinez, J.A. (2009) Dual three-winding transformer equivalent circuit matching leakage measurements. *IEEE Transactions on Power Delivery*, **24**(1), 160–168.
[49] Brandwajn, V., Dommel, H.W. and Dommel, I.I. (1982) Matrix representation of three-phase n-winding transformers for steady-state and transient studies. *IEEE Transactions on Power Apparatus and Systems*, **101**(6), 1369–1378.
[50] Mork, B.A., González, F., Ishchenko, D. *et al.* (2007) Hybrid transformer model for transient simulation: Part I: Development and parameters. *IEEE Transactions on Power Delivery*, **22**(1), 248–255.
[51] Mork, B.A., Ishchenko, D., González, F. and Cho, S.D. (2008) Parameter estimation methods for five-limb magnetic core model. *IEEE Transactions on Power Delivery*, **23**(4), 2025–2032.
[52] Cherry, E.C. (1949) The duality between interlinked electric and magnetic circuits and the formation of transformer equivalent circuits. *Proceedings of the Physical Society, pt. B*, **62**, 101–111.
[53] Slemon, G.R. (1953) Equivalent circuits for transformers and machines including nonlinear effects. *Proceedings of IEE*, **100**(Part IV), 129–143.
[54] Arturi, C.M. (1991) Transient simulation and analysis of a three-phase five-limb step-up transformer following an out-of-phase synchronization. *IEEE Transactions on Power Delivery*, **6**(1), 196–209, 207.
[55] Narang, A. and Brierley, R.H. (1994) Topology based magnetic model for steady-state and transient studies for three-phase core type transformers. *IEEE Transactions on Power Systems*, **9**(3), 1337–1349.
[56] Mork, B.A. (1989) Five-legged core transformer equivalent circuit. *IEEE Transactions on Power Delivery*, **4**(3), 1786–1793.
[57] Mork, B.A. (1999) Five-legged wound-core transformer model: Derivation, parameters, implementation and evaluation. *IEEE Transactions on Power Delivery*, **14**(4), 1519–1526.
[58] Hopkinson, R.H. (1965) Ferroresonance during single-phase switching of three phase distribution transformer banks. *IEEE Transactions on Power Apparatus and Systems*, **84**(4), 289–293.
[59] Dollan, E.J., Gillies, D.A. and Kimbark, E.W. (1972) Ferroresonance in a transformer switched with an EHV line. *IEEE Transactions on Power Apparatus and Systems*, **91**(3), 1273–1280.
[60] Jacobson, D.A.N., Swatek, D. and Mazur, R. (1996) Mitigating potential transformer ferroresonance in a 230 kV converter station. IEEE T&D Conference, Los Angeles, 15 Sept. 1996.
[61] Van Craenenbroeck, T., Van Dommelen, D. and Janssens, N. (2000) Damping circuit design for ferroresonance in floating power systems. *European Transactions on Electrical Power (ETEP)*, **10**(3), 155–159.

[62] Germay, N., Mastero, S. and Vroman, J. (1978) Single phase ferroresonance on a $150/\sqrt{3}$ kV voltage transformer: Comparison of measured and computer results. *Proceedings of IEEE*, **125**(6), 533–535.
[63] Dommel, H.W. (1985) Overhead line parameters from handbook formulas and computer programs. *IEEE Transactions on Power Apparatus and Systems*, **104**(2), 366–372.
[64] Truax, C.J., Brown, J.D. and Neugebauer, W. (1978) The study of reclosing transients on a 765 kV shunt compensated transmission line. *IEEE Transactions on Power Apparatus and Systems*, **97**(4), 1447–1457.
[65] Degeneff, R.C. (1978) A method for constructing terminal models for single phase N-winding transformers. IEEE PES Summer Power Meeting, Los Angeles, July 1978, Paper A78 539–9.
[66] Morched, A., Martí, L. and Ottevangers, J. (1993) A high frequency transformer model for the EMTP. *IEEE Transactions on Power Delivery*, **8**(3), 1615–1626.
[67] Galarza, R.J., Chow, J.H. and Degeneff, R.C. (1995) Transformer model reduction using time and frequency domain sensitivity techniques. *IEEE Transactions on Power Delivery*, **10**(2), 1052–1058.
[68] Gustavsen, B. and Semlyen, A. (1998) Application of vector fitting to the state equation representation of transformers for simulation of electromagnetic transients. *IEEE Transactions on Power Delivery*, **13**(3), 834–842.
[69] Gustavsen, B. (2004) Wide band modeling of power transformers. *IEEE Transactions on Power Delivery*, **19**(1), 414–422.
[70] de León, F. and Semlyen, A. (1992) Reduced order model for transformer transients. *IEEE Transactions on Power Delivery*, **7**(1), 376–383.
[71] de León, F. and Semlyen, A. (1994) Complete transformer model for electromagnetic transients. *IEEE Transactions on Power Delivery*, **9**(1), 231–239.
[72] CIGRE Working Group 13.01 (1988) Practical application of arc physics in circuit breakers. Survey of calculation methods and application guide. *Electra* (118), 64–79.
[73] CIGRE Working Group 13.01 (1993) Applications of black box modelling to circuit breakers. *Electra* (149), 40–71.
[74] Martinez, J.A., Mahseredjian, J. and Khodabakhchian, B. (2005) Parameter determination for modeling systems transients. Part VI: Circuit breakers. *IEEE Transactions on Power Delivery*, **20**(3), 2079–2085.
[75] Martinez-Velasco, J.A. and Popov, M. (2009) Circuit breakers, Chapter 7, *Power System Transients. Parameter Determination* (ed. J.A. Martinez-Velasco), CRC Press.
[76] CIGRE WG 13.02 (1995) Interruption of Small Inductive Currents (ed. S. Berneryd), CIGRE Brochure 50.
[77] Woodford, D.A. and Wedepohl, L.M. (1997) Impact of circuit breaker pre-strike on transmission line energization transients. International Conference on Power Systems Transients, Seattle, June 22–26, 1997.
[78] Fröhlich, K. *et al.* (1997) Controlled closing on shunt reactor compensated transmission lines. Part I: Closing control device development. *IEEE Transactions on Power Delivery*, **12**(2), 734–740.
[79] Fröhlich, K. *et al.* (1997) Controlled closing on shunt reactor compensated transmission lines. Part II: Application of closing control device for high speed autoreclosing on BC Hydro 500 kV transmission line. *IEEE Transactions on Power Delivery*, **12**(2), 741–746.
[80] CIGRE WG A3.07 (2004) Controlled Switching of HVAC Circuit Breakers. CIGRE Brochure 262, December 2004.
[81] Sousa, J., Santos, D. and Correia de Barros, M.T. (1995) Fault arc modeling in EMTP. International Conference on Power Systems Transients, Lisbon, September 3–7, 1995.
[82] Goldberg, S., Horton, W. and Tziouvaras, D. (1989) A computer model of the secondary arc in single-phase operation of transmission lines. *IEEE Transactions on Power Delivery*, **4**(1), 586–595.
[83] Prikler, L., Ban, G. and Banfai, G. (1997) EMTP models for simulation of shunt reactor switching transients. *Electrical Power and Energy Systems*, **19**(4), 235–240.
[84] Durbak, D.W. (1987) The choice of EMTP surge arrester models. *EMTP Newsletter*, **7**(3), 14–18.
[85] Martinez, J.A. and Durbak, D. (2005) Parameter determination for modeling systems transients. Part V: Surge arresters. *IEEE Transactions on Power Delivery*, **20**(3), 2073–2078.
[86] Martinez-Velasco, J.A. and Castro-Aranda, F. (2009) Surge arresters, Chapter 6, *Power System Transients. Parameter Determination* (J.A. Martinez-Velasco), CRC Press.
[87] Morched, A.S. and Brandwajn, V. (1983) Transmission network equivalents for electromagnetic transients studies. *IEEE Transactions on Power Apparatus and Systems*, **102**(9), 2984–2994.
[88] Morched, A.S., Ottevangers, J.H. and Martí, L. (1993) Multiport frequency dependent network equivalents for the EMTP. *IEEE Transactions on Power Delivery*, **8**(3), 1402–1412.

[89] Annakkage, U.D., Nair, N.K.C., Liang, Y. *et al.* (2012) Dynamic system equivalents: A survey of available techniques. *IEEE Transactions on Power Delivery*, **27**(1), 411–420.
[90] CIGRE WG 13.02 (1973) Switching overvoltages in EHV and UHV systems with special reference to closing and reclosing of transmission lines. *Electra* (30), 70–122.
[91] IEC 60694 (2002) IEC standard with common specifications for high-voltage switchgear and controlgear standards.
[92] IEEE Std C37.09-1999 IEEE Standard Test Procedure for AC High-Voltage Circuit Breakers Rated on a Symmetrical Current Basis.
[93] IEEE Std C37.011-2005 IEEE Application Guide for Transient Recovery Voltage for AC High-Voltage Circuit Breakers.
[94] Harner, R.H. and Rodriguez, J. (1972) Transient recovery voltages associated with power-system three-phase transformer secondary faults. *IEEE Transactions on Power Apparatus and Systems*, **91**(5), 1887–1896.
[95] Ragaller, K. (ed.) (1978) *Current Interruption in High-Voltage Networks*, Plenum Press, New York.
[96] van der Sluis, L. (2001) *Transients in Power Systems*, John Wiley & Sons, Ltd.
[97] Popov, M., van der Sluis, L. and Paap, G.C. (2001) Investigation of the circuit breaker reignition overvoltages caused by no-load transformer switching surges. *European Transactions of Electrical Power (ETEP)*, **11**(6), 413–422.
[98] Bhasavanich, D. *et al.* (1985) Digital simulation and field measurements of transients associated with large capacitor bank switching on distribution systems. *IEEE Transactions on Power Apparatus and Systems*, **104**(8), 2274–2282.
[99] Bayless, R.S. *et al.* (1988) Capacitor switching and transformer transients. *IEEE Transactions on Power Delivery*, **3**(1), 349–357.
[100] McGranaghan, M.F. *et al.* (1992) Impact of utility switched capacitors on customer systems – Magnification at low voltage capacitors. *IEEE Transactions on Power Delivery*, **7**(2), 862–868.
[101] Bhargava, B. *et al.* (1993) Effectiveness of pre-insertion inductors for mitigating remote overvoltages due to shunt capacitor energization. *IEEE Transactions on Power Delivery*, **8**(3), 1226–1238.
[102] ANSI C37.06-2000 High-Voltage Circuit Breakers Rated on a Symmetrical Current Basis-Preferred Ratings and Related Required Capabilities.
[103] Reid, W.E., McGranaghan, M.F., Law, S.W. and Gresham, D.W. (1984) Overvoltage protection of shunt capacitor banks using MOV arresters. *IEEE Transactions on Power Apparatus and Systems*, **103**(8), 2326–2333.
[104] Dommel, H.W., Yan, A., Ortiz de Marcano, R.J. and Miliani, A.B. (1993) *Case Studies for Electromagnetic Transients*, 2nd edn, University of British Columbia, Vancouver.
[105] *Transmission Line Reference Book, 345 kV and Above*, 2nd edn, Electric Power Research Institute, Palo Alto, California, 1982.
[106] CIGRE WG 33.01 (1991) Guide to Procedures for Estimating the Lightning Performance of Transmission Lines. CIGRE Brochure 63.
[107] IEEE TF on Parameters of Lightning Strokes (2005) Parameters of lightning strokes: A review. *IEEE Transactions on Power Delivery*, **20**(1), 346–358.
[108] IEEE TF on Fast Front Transients (1996) Modeling guidelines for fast transients. *IEEE Transactions on Power Delivery*, **11**(1), 493–506.
[109] Imece, A.F., Durbak, D.W., Elahi, H. *et al.* (1998) Modeling guidelines for fast front transients, Chapter 5, *Modeling and Analysis of System Transients using Digital Systems* (eds A. Gole, J.A. Martinez-Velasco and A.J.F. Keri), IEEE Special Publication, TP-133-0.
[110] Martinez, J.A. and Castro-Aranda, F. (2005) Tower modeling for lightning analysis of overhead transmission lines. IEEE PES General Meeting, San Francisco, June 2005.
[111] Martinez-Velasco, J.A., Ramirez, A.I. and Dávila, M. (2009) Overhead lines, Chapter 2, *Power System Transients. Parameter Determination* (ed. J.A. Martinez-Velasco), CRC Press.
[112] Grcev, L. and Popov, M. (2005) On high-frequency circuit equivalents of a vertical ground rod. *IEEE Transactions on Power Delivery*, **20**(2), 1598–1603.
[113] Weck, K.H. (1988) Remarks to the current dependence of tower footing resistances. CIGRE Session, Paper 33-85, Paris.
[114] Mousa, A.M. (1994) The soil ionization gradient associated with discharge of high currents into concentrated electrodes. *IEEE Transactions on Power Delivery*, **9**(3), 1669–1677.
[115] Kuffel, E. and Zaengl, W.S. (1984) *High Voltage Engineering Fundamentals*, Pergamon Press.
[116] Looms, J.S.T. (1988) *Insulators for High Voltages*, Peter Peregrinus Ltd.

[117] IEEE WG on Lightning Performance of Transmission Lines (1985) A simplified method for estimating lightning performance of transmission lines. *IEEE Transactions on Power Apparatus and Systems*, **104**(4), 919–932.
[118] IEC 60060-1 (1989) High-voltage test techniques – Part 1: General definitions and test requirements.
[119] CIGRE WG 33.01 (1992) Guide for the evaluation of the dielectric strength of external insulation. CIGRE Brochure 72.
[120] Suliciu, M.M. and Suliciu, I. (1981) A rate type constitutive equation for the description of the corona effect. *IEEE Transactions on Power Apparatus and Systems*, **100**(8), 3681–3685.
[121] Lee, K.C. (1983) Non-linear corona models in an electromagnetic transients program (EMTP). *IEEE Transactions on Power Apparatus and Systems*, **102**(9), 2936–2942.
[122] Eriksson, A.J. and Weck, K.H. (1988) Simplified procedures for determining representative substation impinging lightning overvoltages. CIGRE Session, Paper 33–16, Paris.
[123] Elahi, H., Sublich, M., Anderson, M.E. and Nelson, B.D. (1990) Lightning overvoltage protection of the Paddock 362–145 kV gas insulated substation. *IEEE Transactions on Power Delivery*, **5**(1), 144–149.
[124] Gallagher, T.J. and Dudurych, I.M. (2004) Model of corona for an EMTP study of surge propagation along HV transmission lines. *IEE Proceedings – Generation Transmission and Distribution*, **151**(1), 61–66.
[125] Wagner, C.F., Gross, I.W. and Lloyd, B.L. (1954) High-voltage impulse test on transmission lines. *AIEE Transactions*, **73**(pt. III-A), 196–210.
[126] Martinez-Velasco, J.A. (2012) Basic methods for analysis of high frequency transients in power apparatus windings, Chapter 2, *Electromagnetic Transients in Transformer and Rotating Machine Windings* (ed. C.Q. Su), IGI Global.
[127] Popov, M., Gustavsen, B. and Martinez-Velasco, J.A. (2012) Transformer modelling for impulse voltage distribution and terminal transient analysis, Chapter 6, in *Electromagnetic Transients in Transformer and Rotating Machine Windings* (ed. C.Q. Su), IGI Global.
[128] Schmidt, W. *et al.* (1989) Behaviour of MO-surge-arrester blocks to fast transients. *IEEE Transactions on Power Delivery*, **4**(1), 292–300.
[129] Hileman, A.R., Roguin, J. and Weck, K.H. (1990) Metal oxide surge arresters in AC systems. Part V: Protection performance of metal oxide surge arresters. *Electra* (133), 132–144.
[130] IEEE Working Group on Surge Arrester Modeling (1992) Modeling of metal oxide surge arresters. *IEEE Transactions on Power Delivery*, **7**(1), 302–309.
[131] Kim, I. *et al.* (1996) Study of ZnO arrester model for steep front wave. *IEEE Transactions on Power Delivery*, **11**(2), 834–841.
[132] Pinceti, P. and Giannettoni, M. (1999) A simplified model for zinc oxide surge arresters. *IEEE Transactions on Power Delivery*, **14**(2), 393–398.
[133] Caserza Magro, M., Giannettoni, M. and Pinceti, P. (2004) Validation of ZnO surge arresters model for overvoltage studies. *IEEE Transactions on Power Delivery*, **19**(4), 1692–1695.
[134] Anderson, R.B. and Eriksson, A.J. (1980) Lightning parameters for engineering application. *Electra* (69), 65–102.
[135] Anderson, J.G. (1981) Chapter 12, *Transmission Line Reference Book, 345 kV and Above*, 2nd edn, EPRI, Palo Alto.
[136] IEEE WG on Lightning Performance of Transmission Lines (1993) Estimating lightning performance of transmission lines II: Updates to analytical models. *IEEE Transactions on Power Delivery*, **8**(3), 1254–1267.
[137] Mousa, A.M. and Srivastava, K.D. (1988) A revised electrogeometric model for the termination of lightning strokes on ground objects. International Aerospace and Ground Conference on Lightning and Static Electricity, Oklahoma City, Oklahoma, pp. 342–352.
[138] Pigini, A. *et al.* (1989) Performance of large air gaps under lightning overvoltages: Experimental study and analysis of accuracy of predetermination methods. *IEEE Transactions on Power Delivery*, **4**(2), 1379–1392.
[139] Weck, K.H. (1981) Lightning performance of substations. CIGRE Conference, SC 33, Rio de Janeiro, 1981.
[140] Heidler, F., Cvetic, J.M. and Stanic, B.V. (1999) Calculation of lightning current parameters. *IEEE Transactions on Power Delivery*, **14**(2), 399–404.
[141] Martinez, J.A. and Castro-Aranda, F. (2005) Lightning performance analysis of overhead transmission lines using the EMTP. *IEEE Transactions on Power Delivery*, **20**(3), 2200–2210.

[142] Brown, G.W. and Whitehead, E.R. (1969) Field and analytical studies of transmission line shielding: Part II. *IEEE Transactions on Power Apparatus and Systems*, **88**(3), 617–626.
[143] Martinez, J.A., Castro-Aranda, F. and Hevia, O.P. (2003) Generación aleatoria de los parámetros del rayo en el cálculo de sobretensiones atmosféricas, (in Spanish). ALTAE 2003, San José (Costa Rica), August 18–23, 2003.
[144] IEC Std 60099-5 (2000) Surge arresters – Part 5: Selection and application recommendations, Edition 1.1.
[145] EPRI Substation Voltage Uprating, Volumes I and II, EPRI EL-6474, April 1992.
[146] Yamagata, Y. *et al.* (1996) Suppression of VFT in 1100 kV GIS by adopting resistor-fitted disconnector. *IEEE Transactions on Power Delivery*, **11**(2), 872–880.
[147] Ecklin, A., Schlicht, D. and Plessl, A. (1980) Overvoltages in GIS caused by the operation of isolators, Chapter 6, in *Surges in High-Voltage Networks* (ed. K. Ragaller), Plenum Press, pp. 115–129.
[148] Boggs, S.A. *et al.* (1982) Disconnect switch induced transients and trapped charge in gas-insulated substations. *IEEE Transactions on Power Apparatus and Systems*, **101**(6), 3593–3602.
[149] CIGRE Working Group 33/13.09 (1988) Very fast transient phenomena associated with gas insulated substations. CIGRE Session, Paper No. 33-13, Paris, 1988.
[150] Meppelink, J., Diederich, K., Feser, K. and Pfaff, D.W. (1989) Very fast transients in GIS. *IEEE Transactions on Power Delivery*, **4**(1), 223–233.
[151] Martinez, J.A., Povh, D., Chowdhuri, P. *et al.* (1998) Modeling guidelines for very fast transients in gas insulated substations, Chapter 6, *Modeling and Analysis of System Transients using Digital Systems* (eds A. Gole, J.A. Martinez-Velasco and A.J.F. Keri), IEEE Special Publication, TP-133-0.
[152] Martinez-Velasco, J.A. (2012) Very fast transients, Chapter 10, in *Power Systems*, 3rd edn (ed. L.L. Grigsby), CRC Press.
[153] Fujimoto, N., Stuckless, H.A. and Boggs, S.A. (1986) Calculation of disconnector induced overvoltages in gas-insulated substations, in *Gaseous Dielectrics IV*, Pergamon Press.
[154] Ogawa, S. *et al.* (1986) Estimation of restriking transient overvoltage on disconnecting switch for GIS. *IEEE Transactions on Power Delivery*, **1**(2), 95–102.
[155] CIGRE WG 33/13-09 (1988) Monograph on GIS Very Fast Transients.
[156] IEEE TF on Very Fast Transients (D. Povh, Chairman) (1996) Modelling and analysis guidelines for very fast transients. *IEEE Transactions on Power Delivery*, **11**(4).
[157] Miri, A.M. and Stojkovic, Z. (2001) Transient electromagnetic phenomena in the secondary circuits of voltage- and current transformers in GIS (measurements and calculations). *IEEE Transactions on Power Delivery*, **16**(4), 571–575.
[158] Haznadar, Z., Carsimamovic, C. and Mahmutcehajic, R. (1992) More accurate modeling of gas insulated substation components in digital simulations of very fast electromagnetic transients. *IEEE Transactions on Power Delivery*, **7**(1), 434–441.
[159] Ardito, A. *et al.* (1992) Accurate modeling of capacitively graded bushings for calculation of fast transient overvoltages in GIS. *IEEE Transactions on Power Delivery*, **7**(3), 1316–1327.
[160] Shibuya, Y., Fujita, S. and Tamaki, E. (2001) Analysis of very fast transients in transformers. *IEE Proceedings – Generation Transmission and Distribution*, **148**(5), 377–383.
[161] Popov, M., van der Sluis, L., Paap, G.C. and De Herdt, H. (2003) Computation of very fast transient overvoltages in transformer windings. *IEEE Transactions on Power Delivery*, **18**(4), 1268–1274.
[162] Zhongyuan, Z., Fangcheng, L. and Guishu, L. (2003) A high-frequency circuit model of a potential transformer for the very fast transient simulation in GIS. *IEEE Transactions on Power Delivery*, **23**(4), 1995–1999.
[163] Liang, G., Sun, H., Zhang, X. and Cui, X. (2006) Modeling of transformer windings under very fast transient overvoltages. *IEEE Transactions on Electromagnetic Compatibility*, **48**(4), 621–627.
[164] Fujita, S., Shibuya, Y. and Ishii, M. (2007) Influence of VFT on shell-type transformer. *IEEE Transactions on Power Delivery*, **22**(1), 217–222.
[165] Popov, M., van der Sluis, L., Smeets, R.P.P. and Lopez-Roldan, J. (2007) Analysis of very fast transients in layer-type transformer windings. *IEEE Transactions on Power Delivery*, **22**(1), 1268–1274.
[166] Yanabu, S. *et al.* (1990) Estimation of fast transient overvoltage in gas-insulated substation. *IEEE Transactions on Power Delivery*, **5**(4), 1875–1882.
[167] Boggs, S.A., Fujimoto, N., Collod, M. and Thuries, E. (1984) The modeling of statistical operating parameters and the computation of operation-induced surge waveforms for GIS disconnectors. CIGRE Session, Paper No. 13-15, Paris.
[168] Fujimoto, N., Chu, F.Y., Harvey, S.M. *et al.* (1988) Developments in improved reliability for gas-insulated substations. CIGRE Session, Paper No. 23-11, Paris.

[169] Vinod Kumar, V., Thomas, M.J. and Naidu, M.S. (2001) Influence of switching conditions on the VFTO magnitudes in a GIS. *IEEE Transactions on Power Delivery*, **16**(4), 539–544.

[170] Rao, M.M., Thomas, M.J. and Singh, B.P. (2005) Frequency characteristics of very fast transient currents in a 245-kV GIS. *IEEE Transactions on Power Delivery*, **20**(4), 2450–2457.

[171] Rao, M.M., Thomas, M.J. and Singh, B.P. (2007) Electromagnetic field emission from gas-to-air bushing in a GIS during switching operations. *IEEE Transactions on Electromagnetic Compatibility*, **49**(2), 313–321.

6

Analysis of FACTS Controllers and their Transient Modelling Techniques

Kalyan K. Sen

6.1 Introduction

Electrical energy is transported from the generating stations to the points of use through interconnected transmission lines as shown in Figure 6.1. The flow of electricity takes place freely through the path of least impedance. This natural or uncompensated flow of electricity is, in general, not economically optimal and may cause certain transmission lines to be overloaded or underloaded. The flow of electricity in a particular line of a transmission system can be controlled with the use of a power flow controller (PFC), as shown in Figure 6.2 [1, 2].

The transmission of power in a single line with a sending-end voltage, $\mathbf{V_s}$ (of magnitude, V_s, and angle, δ_s), and a receiving-end voltage, $\mathbf{V_r}$ (of magnitude, V_r, and angle, δ_r), connected by a line reactance (X) and the related phasor diagrams are shown in Figure 6.3. Ignoring the line resistance, the natural voltage, $\mathbf{V_{Xn}}$ (i.e. $\mathbf{V_s} - \mathbf{V_r}$), across the line reactance (X) is the difference between the sending- and receiving-end voltages. The resulting line current ($\mathbf{I}$) lags the voltage ($\mathbf{V_{Xn}}$) by 90°. The natural active and reactive power flows (P_{sn} and Q_{sn}) at the sending end and (P_{rn} and Q_{rn}) at the receiving end are

$$P_{sn} = P_{rn} = A_n \sin\delta \tag{6.1}$$

$$Q_{sn} = A_n \left[\left(V_s/V_r\right) - \cos\delta\right] \tag{6.2a}$$

$$Q_{rn} = A_n \left[\cos\delta - \left(V_r/V_s\right)\right], \tag{6.2b}$$

where $A_n = V_s V_r/X$ and $\delta = \delta_s - \delta_r$.

The definition of FACTS (flexible alternating current transmission systems) is 'alternating current transmission systems incorporating power electronic based and other static controllers to enhance controllability and increased power transfer capability.'

Transient Analysis of Power Systems: Solution Techniques, Tools and Applications, First Edition.
Edited by Juan A. Martinez-Velasco.

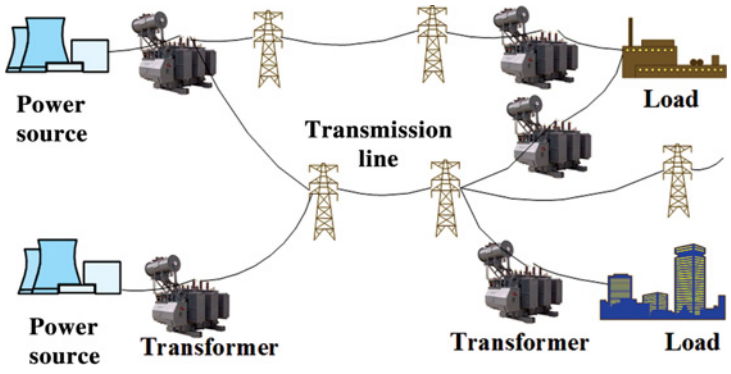

Figure 6.1 Part of a large interconnected transmission system supplying electric power from the generating point to the loads.

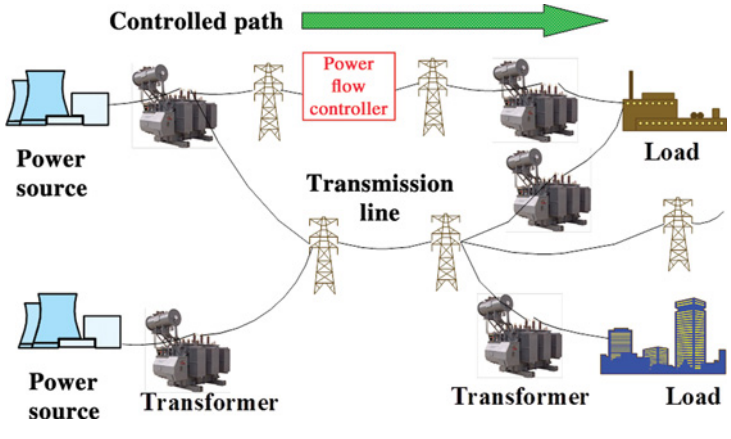

Figure 6.2 Power flow along a controlled path.

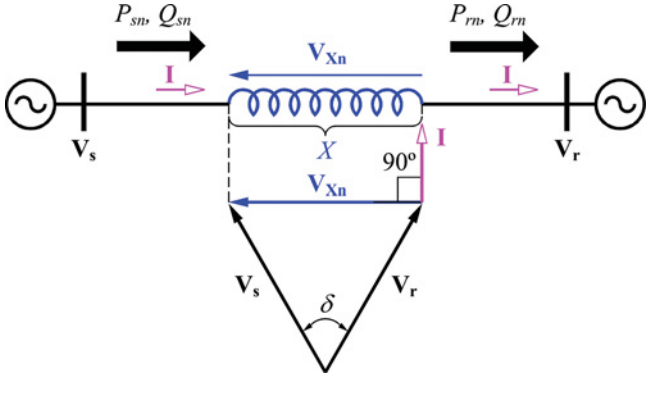

Figure 6.3 Simple power transmission system and the related phasor diagrams.

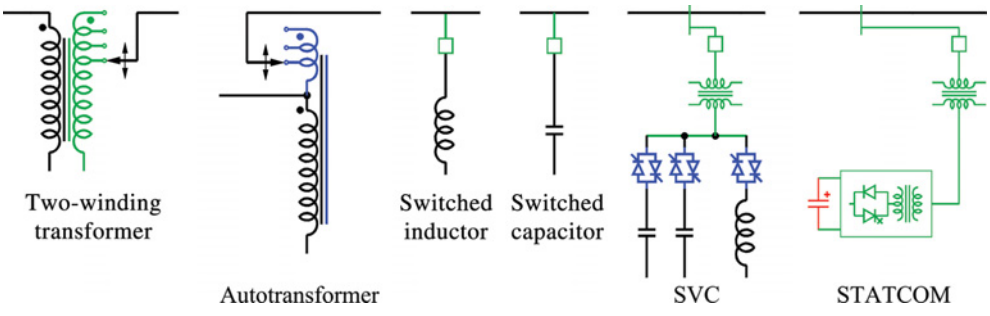

Figure 6.4 Transmission line voltage regulators.

The power flow control parameters are voltage magnitudes, their phase angles and line reactance. Any of these parameters can be controlled individually with the use of the following, now considered conventional, equipment:

- voltage regulating transformer (VRT), shunt-connected switched inductor/capacitor, static VAr compensator (SVC) or static synchronous compensator (STATCOM) for voltage regulation, as shown in Figure 6.4
- phase angle regulator (PAR) or phase shifting transformer (PST) for phase angle regulation, as shown in Figure 6.5
- thyristor-controlled series capacitor (TCSC) for series reactance regulation, as shown in Figure 6.6.

The VRT is in the form of a two-winding transformer with isolated windings, and an autotransformer with electrical connection between the windings. In both transformers, the line voltage is applied to the primary windings. In the two-winding transformer, the full line voltage is induced in the secondary windings, whereas in the autotransformer only a fraction of the line voltage is induced in the secondary windings that are connected to the primary windings to produce the full line voltage. In both cases, the magnitude of the line voltage is regulated. The secondary voltage is varied with the use of load tap changers (LTCs) [3]. An LTC can step up/down the voltage without interruption of the load current.

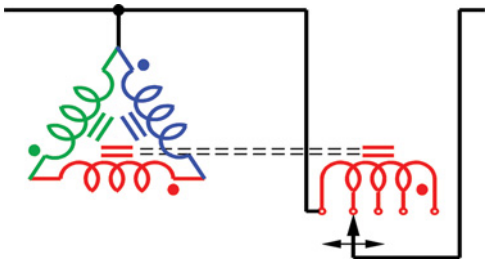

Figure 6.5 Transmission line voltage phase angle regulator.

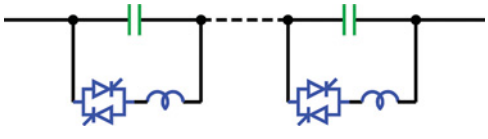

Figure 6.6 Thyristor-controlled series capacitor for transmission line reactance regulation.

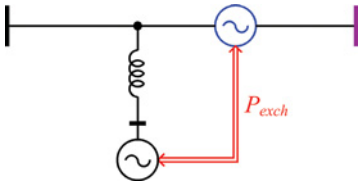

Figure 6.7 Independent active and reactive power flow controller using a shunt-series power converter.

Both primary and secondary windings in the two-winding transformer carry the full transmitted power. Both primary and secondary windings in the autotransformer carry only a fraction of the full transmitted power. This is a useful feature to consider when designing a power flow controller for the smallest power rating. The indirect way to regulate the line voltage is to connect an inductor or a capacitor in shunt with the transmission line. A shunt-connected inductor absorbs reactive power from the line and lowers the line voltage, whereas a shunt-connected capacitor raises the line voltage with its generated reactive power. The SVC connects fixed capacitors in a step-like manner in shunt with the line through thyristor switches and also connects an inductor in shunt with the line through thyristor switches whose duty cycle can be varied, thereby making it function as a variable inductor. The indirect way to regulate the shunt-connected inductor or capacitor is to use a voltage-sourced converter (VSC)-based STATCOM that connects an electronically generated sinusoidal voltage (with some harmonic components) in shunt with the transmission line through a tie inductor. The same concept has been practised with the use of a synchronous condenser. The power flow in a transmission line has also been regulated with the use of the PAR. The line voltage is applied to the primary windings and the induced secondary voltage that is varied with the use of LTCs is connected in series with the line. Through the use of the TCSC, a series-connected variable capacitor or a variable inductor can be implemented.

By changing any one of the power flow control parameters (voltage, its phase angle or line reactance) using a PFC, both active and reactive power flows in a transmission line can be affected simultaneously. The independent control of active and reactive power flows in a transmission line can maximize the flow of active power while minimizing the flow of reactive power, thus generating the most revenue from an AC transmission system.

An ideal PFC controls the above-mentioned three power flow control parameters simultaneously, to regulate the magnitude and the phase angle of the line voltage independently by adding a series-connected compensating voltage to the original voltage with the use of a shunt-series power converter, as shown in Figure 6.7. As a result, the flows of active and reactive powers in the line can be controlled independently. This concept was implemented in transmission line applications using a unified power flow controller (UPFC) as shown in Figure 6.8. The series-connected VSC that is rated for a fraction of the line voltage carries the full line current. The shunt-connected VSC that is rated for the full line voltage carries only a fraction of the line current. Therefore, each VSC carries only a fraction of the full transmitted power.

The compensating voltage in an autotransformer is in phase (0°) or out of phase (180°) with the line voltage and therefore regulates the magnitude of the transmission line voltage. The compensating voltage in the PAR is in quadrature (+90° or –90°) with the line voltage and therefore regulates the phase

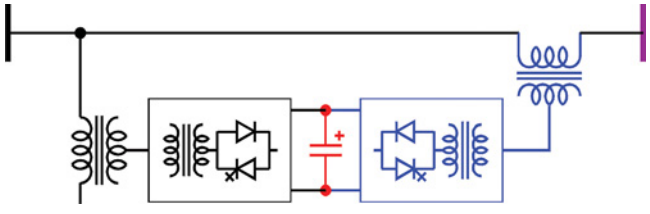

Figure 6.8 Realization of Figure 6.7 by a shunt-series power converter (unified power flow controller).

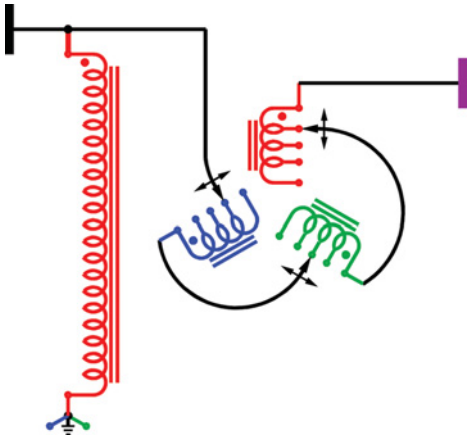

Figure 6.9 Realization of Figure 6.7 by a tap-changer transformer (Sen transformer).

angle of the transmission line voltage. The Sen transformer (ST), as shown in Figure 6.9, creates a series compensating voltage that is variable in magnitude and phase angle and can control the transmission line voltage in both magnitude and phase angle in order to achieve independent control of active and reactive power flows in the line. This compensating voltage may be thought of as two orthogonal compensating voltages of a separate autotransformer and a PAR. Therefore in the ST, the functions of the autotransformer and the PAR are combined in a single unit that results in a reduced amount of hardware compared with what is required for a separate autotransformer and a PAR.

The objective of this chapter is to present transient modelling techniques of FACTS controllers with various levels of details. To verify the steady-state results from the simulation, some simple formulae are derived.

The modelling techniques used in this chapter refer to an EMTP-type simulation package, although any circuit simulation package can be employed for this purpose. The EMTP models and accompanying descriptions are powerful tools that provide the sequence of the way a VSC is commissioned step by step and used as a FACTS controller. The models include all the necessary components: a VSC with a DC link capacitor, a magnetic circuit and a realizable controller. The same techniques can be employed to model other power electronics based systems, such as an adjustable speed drive, an arc furnace compensator or an HVDC transmission system.

6.2 Theory of Power Flow Control

The basic principle of electric power flow enhancement in an AC transmission line is explained in Figures 6.10–6.14. The power flow is a function of the line impedance (R, X), the magnitudes of the sending-end voltage ($\mathbf{V_s}$) and the receiving-end voltage ($\mathbf{V_r}$) and the phase angle (δ) between these voltages.

Consider a simple power transmission system of Figure 6.3 with a series-connected compensating voltage, $\mathbf{V_{s's}}$, (of magnitude, $V_{s's}$, and angle, $\delta_s + \beta$) as shown in Figure 6.10(a). For simplicity, V_s and V_r are considered to be 1 p.u. each, the phase angle, δ ($= \delta_s - \delta_r$), between these voltages to be 30° and X to be 0.5 p.u. When uncompensated (i.e. $\mathbf{V_{s's}} = 0$), the natural voltage, ($\mathbf{V_{Xn}} = \mathbf{V_s} - \mathbf{V_r}$) across the transmission line is the difference between the sending-end and receiving-end voltages, the magnitude of which is 0.5176 p.u.

Consider that the point of compensation in a transmission line is at its sending end. Assuming that there are no changes in the transmission line's impedance and the voltage at the receiving end, a power flow controller can control the flows of active and reactive powers (P and Q) to be a particular pair

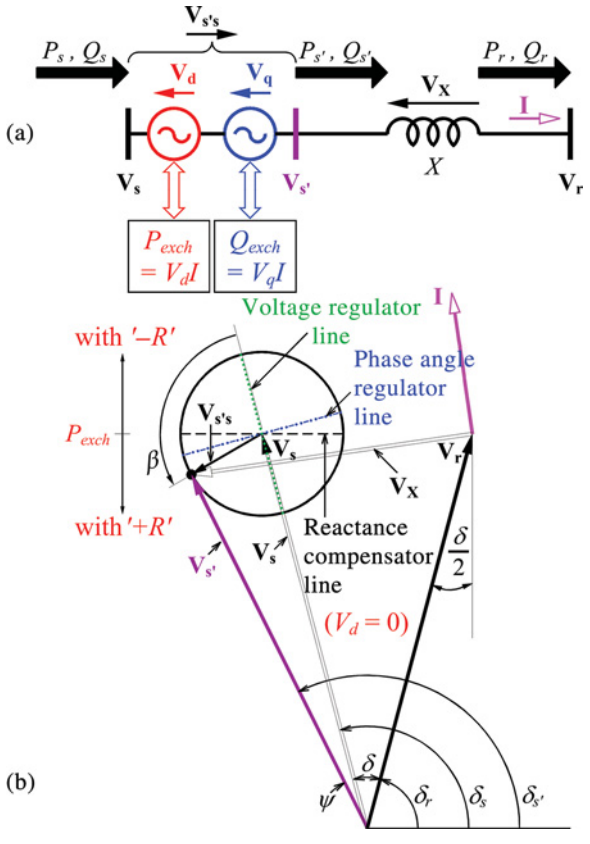

Figure 6.10 (a) Power transmission system with a series-connected compensating voltage ($\mathbf{V}_{s's}$), (b) phasor diagram.

of values by modifying the transmission line's sending-end voltage to be of one particular magnitude and at a specific angle. Successful injection of a compensating voltage in series with the transmission line modifies the line voltage so that the active and reactive power flows in the line are independently controlled. For a desired amount of active and reactive power flows in the line, the compensating voltage has to be of one particular magnitude and at a specific angle with respect to the line voltage.

When a compensating voltage ($\mathbf{V}_{s's}$) is added in series with the transmission line, the *effective* sending-end voltage becomes $\mathbf{V}_{s'}$ (i.e. $\mathbf{V}_s + \mathbf{V}_{s's}$). Figure 6.10(b) shows the phasor diagram related to a series-connected compensating voltage with a fixed magnitude of 0.2 p.u. and its entire controllable range of $0° \leq \beta \leq 360°$. The difference ($\mathbf{V}_{s'} - \mathbf{V}_r$) provides the *compensated* voltage ($\mathbf{V}_X$) across the line reactance (X). As the angle (β) is varied over its full 360° range, the end of phasor ($\mathbf{V}_{s's}$) moves along a circle with its centre located at the end of phasor ($\mathbf{V}_s$). The rotation of phasor ($\mathbf{V}_{s's}$) with an angle (β) modulates both the magnitude and the angle of phasor ($\mathbf{V}_X$). The flows of active and reactive powers (P_s and Q_s) at the sending end in a compensated line are calculated as

$$P_s = P_{sn} + A_s \sin\beta \tag{6.3a}$$

$$Q_s = Q_{sn} + A_s \cos\beta, \tag{6.3b}$$

where $A_s = V_s V_{s's}/X$.

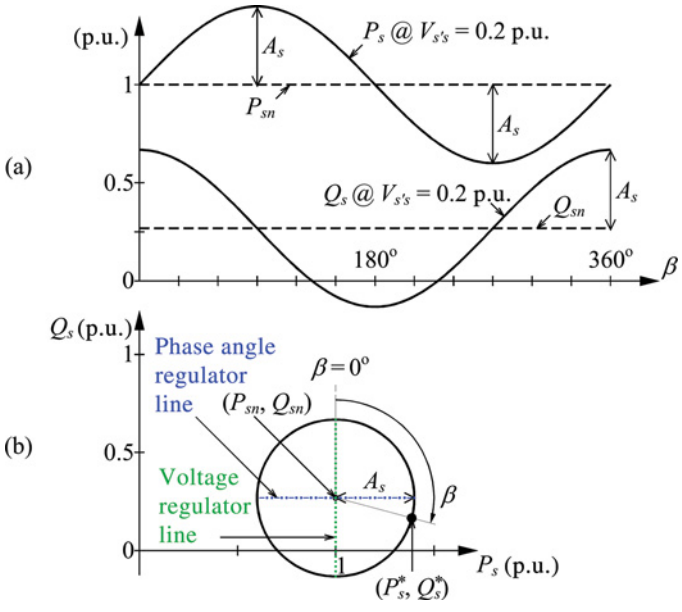

Figure 6.11 (a) Variation of the sending-end active and reactive power flows (P_s and Q_s) as a function of the relative phase angle (β) of the compensating voltage ($\mathbf{V_{s's}}$) with a fixed magnitude of 0.2 p.u. (b) sending-end Q_s versus P_s.

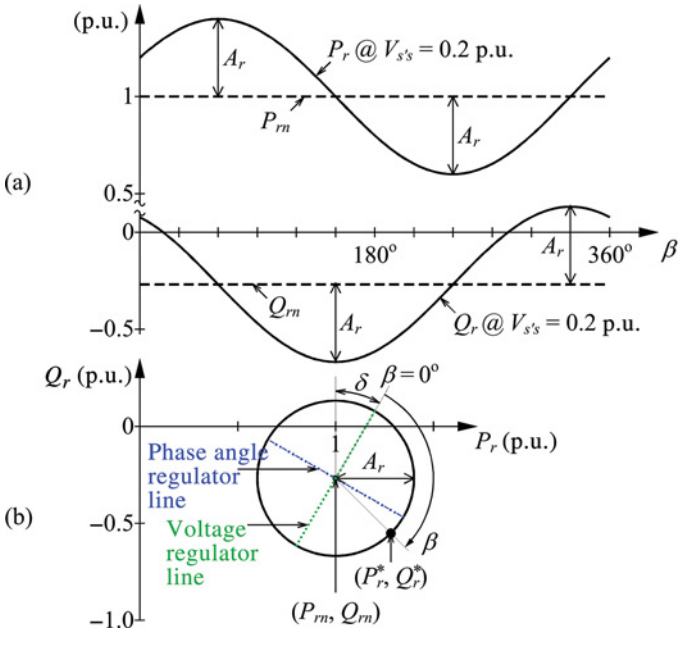

Figure 6.12 (a) Variation of the receiving-end active and reactive power flows (P_r and Q_r) as a function of the relative phase angle (β) of the compensating voltage ($\mathbf{V_{s's}}$) with a fixed magnitude of 0.2 p.u. (b) receiving-end Q_r versus P_r.

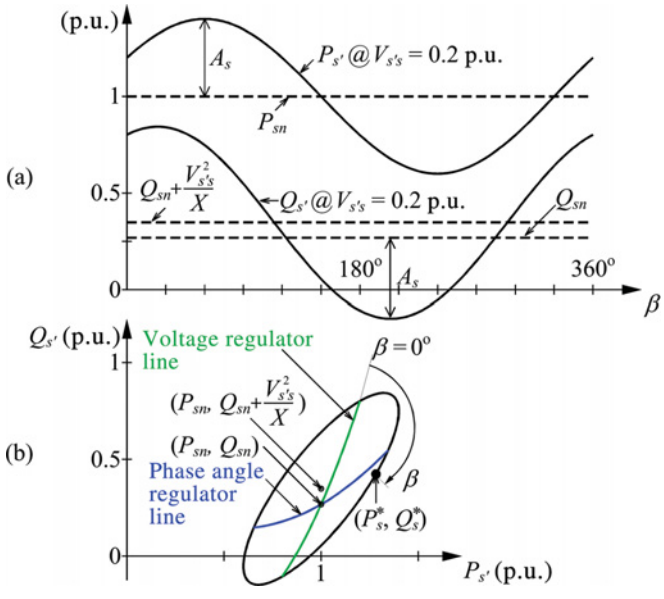

Figure 6.13 (a) Variation of the modified sending-end active and reactive power flows ($P_{s'}$ and $Q_{s'}$) as a function of the relative phase angle (β) of the compensating voltage ($\mathbf{V_{s's}}$) with a fixed magnitude of 0.2 p.u. (b) modified sending-end $Q_{s'}$ versus $P_{s'}$.

The flows of active and reactive powers (P_s and Q_s) at the sending end as functions of the angle (β) are plotted in Figure 6.11(a). The relationship between Q_s and P_s is described as

$$(P_s - P_{sn})^2 + (Q_s - Q_{sn})^2 = A_s^2, \tag{6.4}$$

which is a circle centred at (P_{sn}, Q_{sn}) with a radius of A_s. The active and reactive power flows at the sending end of the line can be regulated within the range defined by the P–Q plot in Figure 6.11(b) by controlling the magnitude ($V_{s's}$) of the compensating voltage ($\mathbf{V_{s's}}$) within its rated value and the angle

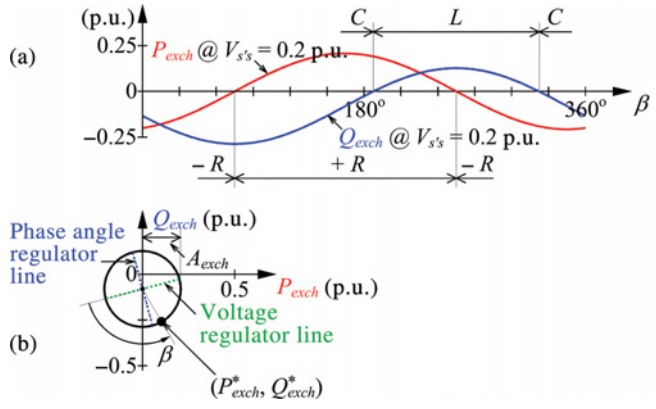

Figure 6.14 (a) Variation of the exchanged active and reactive powers (P_{exch} and Q_{exch}) as a function of the relative phase angle (β) of the compensating voltage ($\mathbf{V_{s's}}$) with a fixed magnitude of 0.2 p.u. (b) exchanged reactive power (Q_{exch}) versus active power (P_{exch}).

(β) between 0° and 360°, respectively. For desired power flows (P_s^* and Q_s^*) at the sending end, the required magnitude ($V_{s's}$) and the angle (β) of the compensating voltage are calculated from equations (6.3) and (6.4) as

$$V_{s's} = (X/V_s)\sqrt{(P_s^* - P_{sn})^2 + (Q_s^* - Q_{sn})^2} \tag{6.5a}$$

$$\beta = \tan^{-1}\left\{(P_s^* - P_{sn})/(Q_s^* - Q_{sn})\right\}. \tag{6.5b}$$

For a VRT, $\beta = 0°$ or 180°; therefore, P_s and Q_s are related as

$$P_s = P_{sn} \tag{6.6a}$$

$$Q_s = Q_{sn} \pm A_s. \tag{6.6b}$$

For a PAR, $\beta = \pm 90°$; therefore, P_s and Q_s are related as

$$P_s = P_{sn} \pm A_s \tag{6.7a}$$

$$Q_s = Q_{sn}. \tag{6.7b}$$

Therefore, for a VRT, only the reactive power (Q_s) and for a PAR, only the active power (P_s) at the sending end varies with the magnitude ($V_{s's}$) of the compensating voltage ($\mathbf{V_{s's}}$) as shown in equations (6.6b) and (6.7a).

The flows of active and reactive powers (P_r and Q_r) at the receiving end in a compensated line are calculated as

$$P_r = P_{rn} + A_r \sin(\delta + \beta) \tag{6.8a}$$

$$Q_r = Q_{rn} + A_r \cos(\delta + \beta), \tag{6.8b}$$

where $A_r = V_r V_{s's}/X$.

The flows of active and reactive powers (P_r and Q_r) at the receiving end as functions of the angle (β) are plotted in Figure 6.12(a). The relationship between Q_r and P_r is described as

$$(P_r - P_{rn})^2 + (Q_r - Q_{rn})^2 = A_r^2, \tag{6.9}$$

which is a circle centred at (P_{rn}, Q_{rn}) with a radius of A_r. The active and reactive power flows at the receiving end of the line can be regulated within the range defined by the *P–Q* plot in Figure 6.12(b) by controlling the magnitude ($V_{s's}$) of the compensating voltage ($\mathbf{V_{s's}}$) within its rated value and the angle (β) between 0° and 360°, respectively. For the desired active and reactive power flows (P_r^*, Q_r^*) at the receiving end, the required magnitude ($V_{s's}$) and the relative phase angle (β) of the compensating voltage are calculated from the equations (6.8) and (6.9) as

$$V_{s's} = (X/V_r)\sqrt{(P_r^* - P_{rn})^2 + (Q_r^* - Q_{rn})^2} \tag{6.10a}$$

$$\beta = \tan^{-1}\left[(P_r^* - P_{rn})/(Q_r^* - Q_{rn})\right] - \delta. \tag{6.10b}$$

For a VRT, $\beta = 0°$ or 180°; therefore, P_r and Q_r are related as

$$Q_r = (Q_{rn} + V_r^2/X)(P_r/P_{rn}) - V_r^2/X. \tag{6.11}$$

For a PAR, $\beta = \pm 90°$; therefore, P_r and Q_r are related as

$$Q_r = (-P_{rn}P_r + P_{rn}^2)/(Q_{rn} + V_r^2/X) + Q_{rn}. \tag{6.12}$$

Therefore, for a VRT or a PAR, both the active and reactive power flows (P_r and Q_r) at the receiving end vary with the magnitude ($V_{s's}$) of the compensating voltage ($\mathbf{V_{s's}}$) as shown in equations (6.8). For a

given $V_{s's}$ and $\beta = 0°$, 180° or ± 90°, first calculate P_r from equation (6.8a) and then use equation (6.11) for $\beta = 0°$, 180° and equation (6.12) for $\beta = \pm 90°$ to calculate Q_r.

The flows of active and reactive powers ($P_{s'}$ and $Q_{s'}$) at the modified sending end are calculated as

$$P_{s'} = P_{sn} + A_r \sin(\delta + \beta) \tag{6.13a}$$

$$Q_{s'} = Q_{sn} + V_{s's}^2/X + 2A_s \cos\beta - A_r \cos(\delta + \beta). \tag{6.13b}$$

The flows of active and reactive powers ($P_{s'}$ and $Q_{s'}$) at the modified sending end as functions of the angle (β) are plotted in Figure 6.13(a). The relationship between $Q_{s'}$ and $P_{s'}$ is described as

$$(P_{s'} - P_{sn})^2 + (Q_{s'} - Q_{sn} - V_{s's}^2/X)^2 = A_r^2 + 4A_s^2 \cos^2\beta - 4A_sA_r \cos\beta \cos(\delta + \beta), \tag{6.14}$$

which is an ellipse centred at (P_{sn}, $Q_{sn} + V_{s's}^2/X$). The active and reactive power flows at the modified sending end of the line can be regulated within the range defined by the *P–Q* plot in Figure 6.13(b) by controlling the magnitude ($V_{s's}$) of the compensating voltage ($\mathbf{V_{s's}}$) within its rated value and the angle (β) between 0° and 360°, respectively. For desired power flows ($P_{s'}^*$ and $Q_{s'}^*$) at the modified sending end, the required magnitude ($V_{s's}$) and the angle (β) of the compensating voltage can be calculated from equations (6.13) and (6.14), following the steps shown before, though this is cumbersome. A simpler method is presented later in this section.

For a VRT, $\beta = 0°$ or 180°; therefore, $P_{s'}$ and $Q_{s'}$ are related as

$$Q_{s'} = (Q_{sn} - V_s^2/X)P_{s'}/P_{sn} + (V_s \pm V_{s's})^2/X. \tag{6.15}$$

Note that the + sign is applicable to $\beta = 0°$ and the − sign is applicable for $\beta = 180°$.

For a PAR, $\beta = \pm 90°$; therefore, $P_{s'}$ and $Q_{s'}$ are related as

$$Q_{s'} = (-P_{sn}P_{s'} + P_{sn}^2)/(Q_{sn} - V_s^2/X) + Q_{sn} + V_{s's}^2/X. \tag{6.16}$$

Therefore, for a VRT or a PAR, both active and reactive power flows ($P_{s'}$ and $Q_{s'}$) at the modified sending end vary with the magnitude ($V_{s's}$) of the compensating voltage ($\mathbf{V_{s's}}$) as shown in equations (6.13). For a given $V_{s's}$ and $\beta = 0°$, 180° or ± 90°, first calculate $P_{s'}$ from equation (6.13a) and then use equation (6.15) for $\beta = 0°$, 180° and equation (6.16) for $\beta = \pm 90°$ to calculate $Q_{s'}$.

In all of the above cases, if the magnitude ($V_{s's}$) of the compensating voltage is increased, the controllable range of the power flow in the *P–Q* plane is also increased. When the controllable range extends to all four quadrants, a bidirectional and independent active and reactive power flow control is achieved.

The compensating voltage ($\mathbf{V_{s's}}$) is at any phase angle with the prevailing line current ($\mathbf{I}$) and therefore, it exchanges with the line both active and reactive powers (P_{exch} and Q_{exch}) which are defined as

$$P_{exch} = -\mathbf{V_{s's}} \bullet \mathbf{I} = V_d I \tag{6.17}$$

$$Q_{exch} = \left|-\mathbf{V_{s's}} \times \mathbf{I}\right| = V_q I, \tag{6.18}$$

where $\mathbf{V_d}$ and $\mathbf{V_q}$ are the respective active or direct and reactive or quadrature components of the compensating voltage with load convention as shown in Figure 6.10.

The exchanged active and reactive power (P_{exch} and Q_{exch}) by the compensating voltage with the transmission line can also be derived as

$$P_{exch} = P_s - P_{s'} = A_{exch} \sin\left\{\beta - \tan^{-1}(P_{sn}/Q_{sn})\right\} \tag{6.19a}$$

$$Q_{exch} = Q_s - Q_{s'} = -V_{s's}^2/X - A_{exch} \cos\left\{\beta - \tan^{-1}(P_{sn}/Q_{sn})\right\}, \tag{6.19b}$$

where $A_{exch} = V_{Xn}V_{s's}/X$.

Note that the natural voltage (V_{Xn}) across the transmission line is $V_{Xn} = \sqrt{V_s^2 + V_r^2 - 2V_sV_r\cos\delta}$. The exchanged active and reactive powers (P_{exch} and Q_{exch}) as functions of the relative phase angle (β) are plotted in Figure 6.14(a). For a given magnitude of the compensating voltage, the exchanged capacitive power (Q_{exch}) is larger than its inductive counterpart due to the fact that the capacitive compensation produces a larger line current. The compensating voltage, being at any angle with the prevailing line current, emulates in series with the line a capacitor (C) or an inductor (L) and a positive resistor ($+R$) or a negative resistor ($-R$). The relationship between Q_{exch} and P_{exch} is described as

$$P_{exch}^2 + (Q_{exch} + V_{s's}^2/X)^2 = A_{exch}^2, \tag{6.20}$$

which is a circle centred at $(0, -V_{s's}{}^2/X)$ with a radius of A_{exch}. Note that as $V_{s's}$ decreases, the centre of the circle moves toward the origin (0, 0). The exchanged active and reactive powers can be controlled within the range defined by the P–Q plot in Figure 6.14(b) by choosing the magnitude ($V_{s's}$) of the compensating voltage ($\mathbf{V_{s's}}$) within its rated value and the relative phase angle (β) between 0° and 360°, respectively. For a desired exchanged power (P_{exch}^* and Q_{exch}^*), the required magnitude ($V_{s's}$) and the angle (β) of the compensating voltage are calculated from the equations (6.19) and (6.20) as

$$V_{s's} = \sqrt{\left(V_{Xn}^2/2 - Q_{exch}^*X\right) - \sqrt{\left(V_{Xn}^2/2 - Q_{exch}^*X\right)^2 - \left(P_{exch}^{*2} + Q_{exch}^{*2}\right)X^2}} \tag{6.21a}$$

$$\beta = \tan^{-1}\left\{P_{sn}/Q_{sn}\right\} - \tan^{-1}\left\{P_{exch}^*/\left(Q_{exch}^* + V_{s's}^2/X\right)\right\}. \tag{6.21b}$$

For a VRT, $\beta = 0°$ or 180°; therefore, P_{exch} and Q_{exch} are related as

$$Q_{exch} = (Q_{sn}/P_{sn})P_{exch} - V_{s's}^2/X \tag{6.22}$$

For a PAR, $\beta = \pm 90°$; therefore, P_{exch} and Q_{exch} are related as

$$Q_{exch} = -(P_{sn}/Q_{sn})P_{exch} - V_{s's}^2/X \tag{6.23}$$

Therefore, for a VRT or a PAR, the exchanged active and reactive powers (P_{exch} and Q_{exch}) vary with the magnitude ($V_{s's}$) of the compensating voltage ($\mathbf{V_{s's}}$) as shown in equations (6.19). For a given $V_{s's}$ and $\beta = 0°$, 180°, or ±90°, first calculate P_{exch} from equation (6.19a) and then use equation (6.22) for $\beta = 0°$, 180° and equation (6.23) for $\beta = \pm 90°$ to calculate Q_{exch}.

In an alternative method to regulate the modified sending-end active and reactive power flows independently, the active and the reactive power flows (P_s and Q_s) at the sending end are measured. Knowing the desired active and reactive power flows ($P_{s'}^*$ and $Q_{s'}^*$) at the modified sending end, the required exchanged active and reactive powers (P_{exch}^* and Q_{exch}^*) are calculated as

$$P_{exch}^* = P_s - P_{s'}^* \tag{6.24a}$$

$$Q_{exch}^* = Q_s - Q_{s'}^*. \tag{6.24b}$$

Then, using equations (6.21), the required magnitude ($V_{s's}$) and the angle (β) of the compensating voltage ($\mathbf{V_{s's}}$) can be calculated. This is an open-loop control scheme, which requires the knowledge of the line reactance (X). The active and the reactive power flows at any point in the transmission line can also be controlled independently by using a closed-loop control scheme. One such scheme is implemented at the world's first UPFC installation. The automatic power flow control mode of operation of a UPFC for achieving independent control of active and reactive power flows at the modified sending end has been simulated in a mathematical model, and the simulation results are compared with the field results from the ±160 MVA-rated UPFC. This UPFC demonstrated for the first time that the active and

the reactive power flows in a transmission line could be regulated independently, while maintaining a fixed line voltage at the point of common coupling [1, 2].

It is demonstrated that a series-connected compensating voltage of variable magnitude and variable phase angle modifies the magnitude and the phase angle of the transmission line voltage and, in turn, provides independent control of active and reactive power flows in the line. For desired active and reactive power flows at various locations in a transmission line, such as the sending end, the receiving end and the modified sending end, the magnitude and phase angle of the series-connected compensating voltage are given in equations (6.5), (6.10) and (6.21), respectively.

6.3 Modelling Guidelines

General guidelines for modelling power electronics in electrical power engineering applications have been presented in [4–34]. The common practices for a successful simulation are presented in this section.

6.3.1 Representation of a Power System

A power system can easily extend to a large electrical and geographic radius, consisting of hundreds and thousands of miles of transmission lines and hundreds of power plants. The model of this entire network is a subject of load flow study. For transient study, however, this model of large network can be reduced to a simple network that is sufficient to generate the answers that the designers seek at the beginning of a new project. Although the consideration of a larger network would resemble closer to reality, the fact is that the transient effects become less in a line further away from equipment under study. Therefore, it is highly recommended to define the issues first before deciding how large or small a network must be to conduct a study. The proper level of system reduction depends on the objectives of the study. For example, if the purpose is to characterize the harmonics generated by a particular type of power electronics application, the power system model can be reduced to just a few lines around the application. When a pre-existing voltage distortion level at a power electronics-interfacing bus is low, the rest of the power system can be satisfactorily represented by one or a set of first order equivalents connected to the bus at a higher system voltage level. If the power electronics application interfaces with the system at the low voltage bus of a step-down transformer, the equivalent of the system can be placed on the high voltage bus of the transformer. When a pre-existing voltage distortion level is greater than 2%, one needs an adequate harmonic source to properly represent the background distortion.

If the objective is to evaluate the effects of the power electronics in an interconnected utility system, the model will be extended to cover all sensitive loads (i.e. rotating machines and all other major power electronics equipment) within a given electrical radius. Special attention is needed if an unbalanced system condition is involved.

For a harmonic propagation and resonant study, an extensive power system model is required. In this case, the main system components and the dominant topology need to be kept in the power system model. Filter banks, nonlinear passive circuit components and all other harmonic injection sources should be represented. Frequency-dependent characteristics of the system components might need to be considered.

6.3.2 Representation of System Control

The system control is one of the most important aspects of a power electronics simulation. As illustrated in this section, a switching device is greatly simplified. The proper switching performance of a device is realized via appropriate gating signals coupled with detailed modelling of the device characteristics and distributed resistance, inductance and capacitance around the device. Modelling of power electronics control consists of three steps:

1. monitoring and sampling
2. signal processing and control reference derivation
3. device gating signal generation.

Most simulation tools provide some means to implement system control. They may be in the form of control block diagrams and flow-chart structures. Using these tools, a user can define the specified control in a simulated system with great flexibility. Some key issues that ensure a correct control modelling is briefly mentioned below. These issues are more thoroughly treated in the guideline [4] with illustration examples.

- For a time-domain simulation, the highest resolution for a signal sampling is determined by a selected time-step. In general, this is no problem for analogue control. However, for digital control simulation, if the selected time-step is too large, and if the simulated sampling resolution is significantly different from the real system sampling resolution, significant errors can be introduced, which may even lead to instability.
- For a time-domain simulation, the computation time does not reflect the simulated control logic response time. Users should always remember to introduce a reasonable time delay to match with the limitations of the control hardware and software.
- When modelling a control response, it is important to understand the program-introduced time delay between the primary system and the control interface. For example, the control model may introduce one or greater time-step delay because of the structure and solution method used in the program. This may not cause any problem in some simulations. However, if the modelled control logic makes an error that can accumulate over a period of time, it can eventually result in the solution divergence. This problem can be corrected in most cases by reducing the size of the time-step or avoiding the possible accumulation mechanism in the control model.
- Different methods may be used to synchronize the power electronics gating signals with the required system references. In many cases, a real phase-locked-loop (PLL) can be greatly simplified to reduce the complexity of the system modelling. However, when the system contains significant waveform distortions – either from harmonics or transient disturbances – a practical PLL with all signal filters should be carefully implemented in the control model in order to accurately predict the control response. This is particularly important when the objective of the simulation is to verify a control design and to evaluate the response of a power electronics application to the system dynamics.
- All power electronics devices have their limits in switching frequencies. When a load commutation and a standard pulse width modulation (PWM) type scheme are simulated, the highest switching frequency in the simulation is controlled by the system frequency and by the carrier frequency, respectively. Even considering a variable carrier frequency, the number of switching events per fundamental frequency cycle is known and the highest switching frequency can be made under a physical limit of the simulated device. However, if the device gating is determined by a simple comparison between the system control reference and the system output, a device switching may take place in simulation whenever a comparison difference is detected. Therefore, the switching frequency becomes highly dependent on the time-step size, and the average switching frequency becomes unpredictable. When using this type of gating logic, users should always take extra measures, such as introducing a hysteresis loop, to ensure that the modelled device is working under its physical switching capability.

The PLL angle is referenced to a cosine wave, meaning that during a complete cycle of a cosine wave, the phase angle (θ) linearly increases from 0 to 2π. The three-phase *a-b-c* to two-phase *d-q* transformation in stationary frame is written as

$$v_{ds} = v_a = V_1 \cos\theta \tag{6.25}$$

$$\begin{aligned} v_{qs} &= -\frac{1}{\sqrt{3}}\left(v_a + 2v_c\right) = -\frac{V_1}{\sqrt{3}}\left(\cos\theta + 2\cos(\theta + 120^\circ)\right) \\ &= -\frac{V_1}{\sqrt{3}}\left(\cos\theta - \cos\theta - \sqrt{3}\sin\theta\right) = V_1 \sin\theta. \end{aligned} \tag{6.26}$$

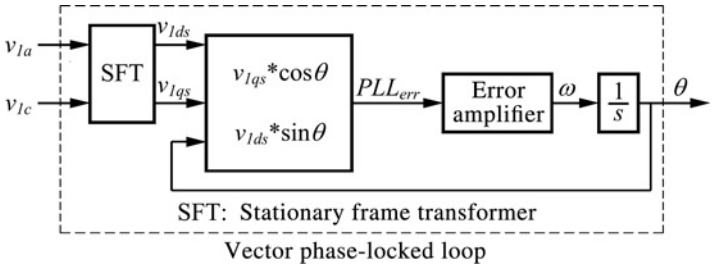

Figure 6.15 Block diagram of a vector PLL.

Therefore

$$\theta = \tan^{-1}\left(\frac{\sin\theta}{\cos\theta}\right) = \tan^{-1}\left(\frac{v_{qs}}{v_{ds}}\right) \tag{6.27}$$

The ordinary PLL (OPLL) signal obtained from equation (6.27) does not preserve the phase angle during a line fault as shown in Figure 6.16. This necessitates the use of a vector PLL (VPLL).

Figure 6.15 shows the commonly used block diagram of the VPLL. The stationary frame components (v^s_{1d} and v^s_{1q}) of the line voltage (v_1) at BUS01 in the simple two-bus power system network model shown in Section 6.4 are calculated and converted to rotating frame components v_{1d} and v_{1q}. The quadrature component (v_{1q}) is regulated to be zero by the use of an error amplifier, the output of which is the synchronously rotating angular speed (ω) that produces the PLL angle (θ) after passing through an integrator. With this approach, the direct component (v_{1d}) is maintained to be the amplitude (V_1) of the line voltage (v_1) at BUS01 under steady-state condition.

Figure 6.16 shows that the VPLL is able to track the near original phase for a phase-to-ground fault. During a fault, the current through the line inductor changes rapidly, causing numerical instability in the simulation. To minimize this problem, a numerical snubber in the form of a resistor across each line inductor is used. The value of the snubber resistor should be high enough so that it does not cause spurious results in the simulation but facilitates the decaying of an oscillating current during a disturbance.

Note that this example of PLL implementation is based on the three-phase to *d-q* transformation on a three-phase balanced system. The synchronously rotating reference variables appear as a DC component. In an unbalanced system, these variables become a DC component superimposed with AC components

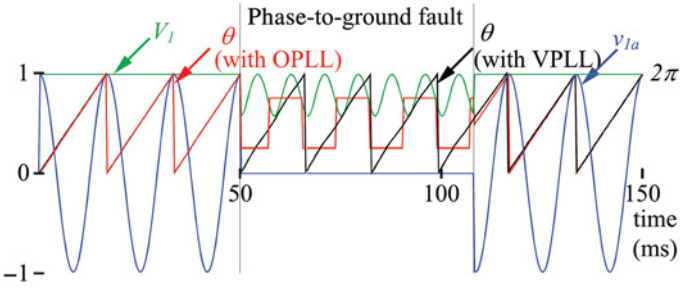

Figure 6.16 Phase a of line voltage (v_{1a}) at BUS01, its magnitude (V_1) and the PLL angle (θ) with and without a phase-to-ground fault.

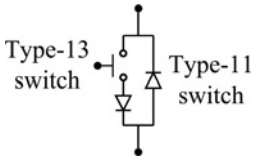

Figure 6.17 Representation of a controlled turn-off device in EMTP.

that correspond to the unbalance amount. The gain parameters need to be adjusted to minimize the effect of unbalanced input signals on the PLL's output signal.

6.3.3 Representation of a Controlled Switch

The heart of a power electronics based VSC is a controlled turn-off switch, such as a GTO, IGBT or IGCT. Figure 6.17 shows the representation of a controlled turn-off device in EMTP. A device module is built with a controlled bidirectional current-flowing switch (type-13 switch) in series with a built-in diode device (type-11 switch). Considering that the module is often utilized in applications with a reactive power carrying capability, a reversal diode (freewheeling diode) is included.

Figure 6.18 shows the actual implementation of the controlled turn-off device module in EMTP. The switch and diode use a RC snubber circuit across it. Some small resistors are used to introduce intermediate nodes between EMTP switches and snubber elements that are used in the controlled turn-off device module. The finite nature of the simulation time-step that the EMTP-type simulation packages use poses a problem for power electronics circuit simulation, which necessitates the use of snubber circuits across fast-acting power electronics switches. Note that in some situations the snubber R and C

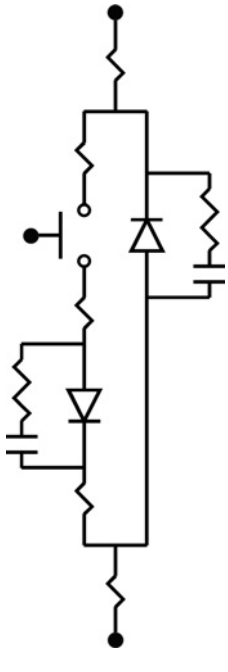

Figure 6.18 Representation of a controlled turn-off device in EMTP with snubber circuits.

values of the actual system may or may not work in simulations using some programs. In this case, the R and C values of the snubbers needed for stable simulation are primarily dependent on the time-step and secondarily on system configuration (capacitors and inductors in the system) and the load current level. Programs using special features such as variable time-steps (very short time-steps during switching) or interpolate switching (simulate the switching very close to the required instant using linear interpolation between time-steps) do not require fictitious snubber circuits. Therefore one of the following measures, or their combinations, can be taken to prevent numerical instability in the simulation:

- selection of smaller time-step
- use of artificial snubber circuits
- introduction of a small smoothing reactor for DC links
- introduction of proper stray capacitances in the system model
- implementation of parallel damping for a lumped system

A model for a general, unidirectional-conducting, three-terminal, controllable power electronics device with snubber connections is shown in Figure 6.18. The actual snubber configuration can be different from one application to another. However, if the purpose of a simulation is not to design the snubber, a sample snubber configuration shown in this figure can often provide satisfactory results. The actual analysis of a VSC pole, consisting of a DC capacitor, switches and snubber circuits is discussed later in the chapter.

6.3.4 Simulation Errors and Control

Errors in a power electronics simulation can come through the following sources:

1. switching device approximation and system reduction
2. added circuit elements for numerical oscillation control
3. control system simplification
4. time-step related truncation
5. program structure and solution method-introduced interfacing time delay
6. incorrect system initial conditions

For application simulations, some errors resulting from the system simplification and measures of numerical oscillation control are acceptable. Items 4 and 5 in the list can be controlled by reducing the time-step size. The time-step size is recommended not to be greater than 1/5 to 1/20 of the period of the highest concerned frequency cycle. For example, for an IGBT VSC simulation with 5 kHz PWM switching, a selected time-step could be 10 μs. However, if the objective of the simulation is to see the detailed transient at the terminal of the induction motor which is fed by the VSC through a section of cable with a 1.0 μs travel time, an adequate time-step would be 0.2 μs or smaller.

Errors caused by incorrect system initial conditions can be reduced by just letting the simulation run for a period of time to reach a corrected initial condition. This may take more computing time, but time is saved in model construction, especially if the program can be restarted. Some methods, such as initial phasor calculation, are developed to accelerate the system into the correct initial condition quickly.

The above-mentioned modelling techniques are successfully applied in modelling FACTS controllers as presented in the next section.

6.4 Modelling of FACTS Controllers

Figure 6.19 shows the block diagram of the modelling structure in EMTP. First, some general constants are defined. Next, the control or the transient analysis of control systems (TACS) section receives its

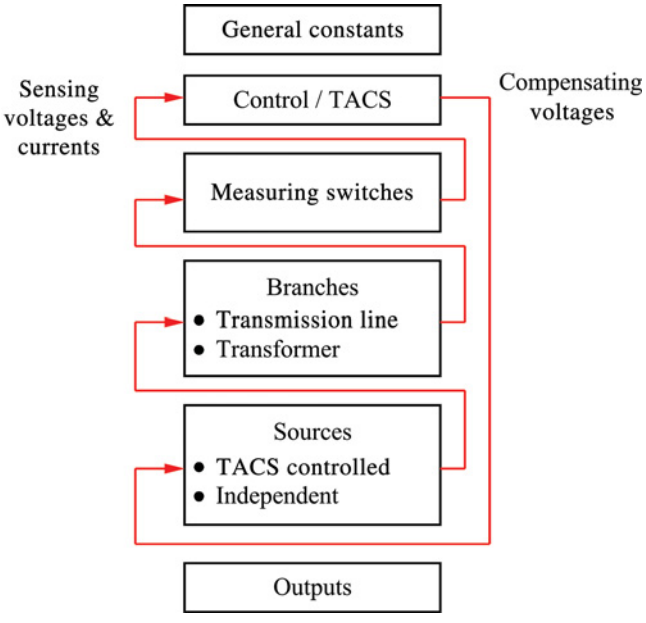

Figure 6.19 EMTP modelling structure.

input signals from the sensors or measuring switches. The TACS section generates the free-running PLL angle. The control operations and calculations are performed in this section.

The compensating voltages that are created in the TACS section are fed to a magnetic circuit, which is located in the branch section. The effects of a non-ideal magnetic circuit, which includes leakage reactance, magnetic saturation and so on, can be studied. The source section contains some independent voltage sources, which establish the power flow in a transmission line. The controlled and the independent sources are fed to the branch section, which contains the transmission line and the coupling transformer. The line voltage and the current through the compensating voltage are measured by the measuring switches. Finally, the output section is defined.

A simple two-bus power system network model, shown in the single line diagram of Figure 6.20, is used for verifying the operation of various FACTS controllers. In the natural or uncompensated network, no PFC is connected. Later, the network is studied with various PFCs connected to it. The simplified two-bus network reveals most of the controller's performance under both dynamic and steady-state conditions.

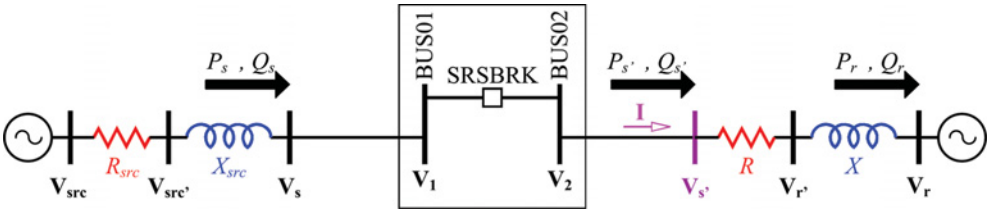

Figure 6.20 Two-bus network model in EMTP.

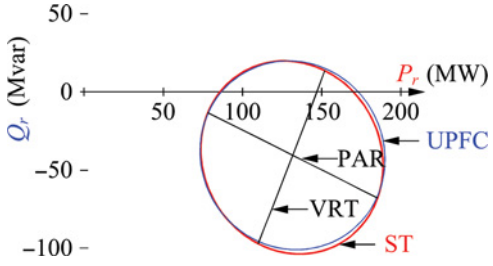

Figure 6.21 Comparison of active and reactive power flows at the receiving end of the transmission line with the operation of the VRT, PAR, UPFC and ST.

6.4.1 Simulation of an Independent PFC in a Single Line Application

An independent PFC regulates the active and reactive power flows in the transmission line independently by connecting a compensating voltage in series with the line. The compensating voltage exchanges active and reactive power with the transmission line. In the case of the ST, both the active and reactive power exchanged by the series compensating voltage appear at the transmission line through the shunt-connected exciter unit. However, for the UPFC, only the exchanged active power passes through the shunt unit. Both the shunt and series units exchange reactive power at their AC terminals independently.

The controllable range of active and reactive power flows with the operation of the ST and UPFC are presented in Figure 6.21. The ST and UPFC offer controllable areas that are almost identical. The radius of the controllable area increases with larger series compensating voltages. With proper series compensating voltage, the controllable area covers all four quadrants, resulting in a reversal of power flow from its natural direction. Special operations of the ST with $\beta = 0°$ and $\beta = 90°$ show the functionalities of the VRT and PAR. Whereas the ST offers a controllable area, the PAR and the VRT offer linear control range. For every 2 MW increase in active power, a PAR increases reactive power by 1 Mvar. Note also that a PAR increases the active power flow by 7% less than can be achieved using an ST.

Figure 6.22 shows the active, reactive and apparent powers (P_{exch}, Q_{exch} and S_{exch}) exchanged by the series compensating voltages of the ST and UPFC with the line. The maximum exchanged active, reactive and apparent powers, in this example, are 21 MW, 29 Mvar and 30 MVA, respectively. In the case of the ST, both the active and reactive powers flow bidirectionally through the exciting shunt unit. In the case of the UPFC, only the active power flows bidirectionally through the STATCOM.

The summary of the study results are as follows:

- The variation of phase-to-phase voltage at the point of compensation is between 132.8 and 139.8 kV for the ST, and between 133.3 and 140.1 kV for the UPFC, whereas the uncompensated or natural voltage is 136.7 kV.
- Line active power flow changes from the natural flow of 132 MW by +57 and –58 MW for the ST, and by ±58 MW for the UPFC.
- Line reactive power flow changes from the natural flow of −41 Mvar by +60 and −63 Mvar for the ST, and by ±60 Mvar for the UPFC.
- Rating of the ST is 30 MVA.
- Rating of the UPFC is a series unit of 30 MVA and a shunt unit of 21 MVA.

6.4.2 Simulation of a Voltage Regulating Transformer

The VRT model is shown in Figure 6.23. The primary winding with n_1 turns is excited by the input voltage, and the secondary winding with n_2 turns is induced with a voltage. The secondary voltage is

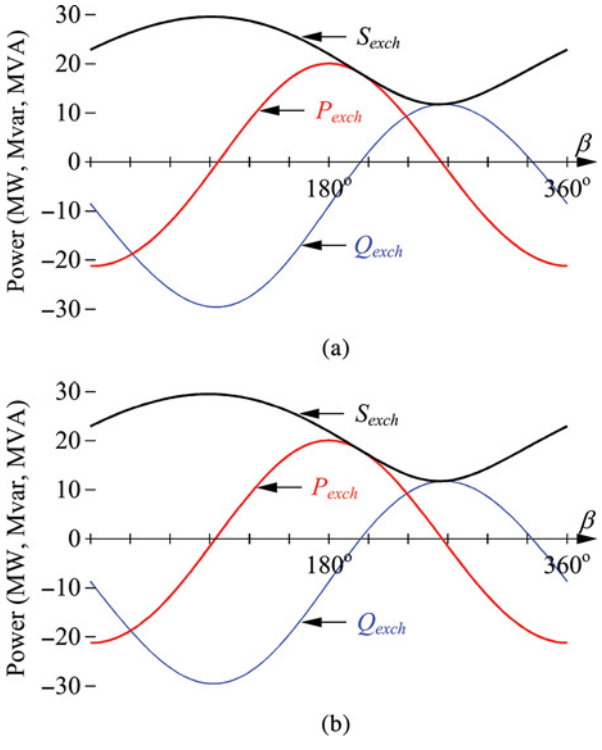

Figure 6.22 Variations of exchanged powers between the transmission line and the series unit of the (a) ST and (b) UPFC.

usually a fraction of the input voltage and the output voltage is the phasor sum of the primary and secondary voltages. The compensating secondary voltage is connected in series with the transmission line. There is no electric isolation between the input and output voltages. The active number of turns in the secondary winding is varied by the use of load tap changers (LTCs) to vary the compensating voltage.

Figure 6.24 shows that a compensating voltage of $\mp 15\%$ of the voltage ($\mathbf{V_s}$) at the sending end results in a voltage ($\mathbf{V_{s'}}$) at the modified sending end in the range 0.87–1.09 p.u. In the process, the voltage

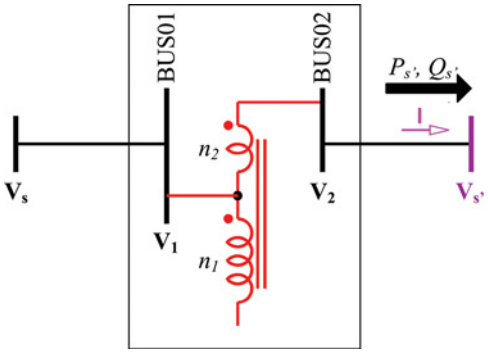

Figure 6.23 Voltage regulating transformer.

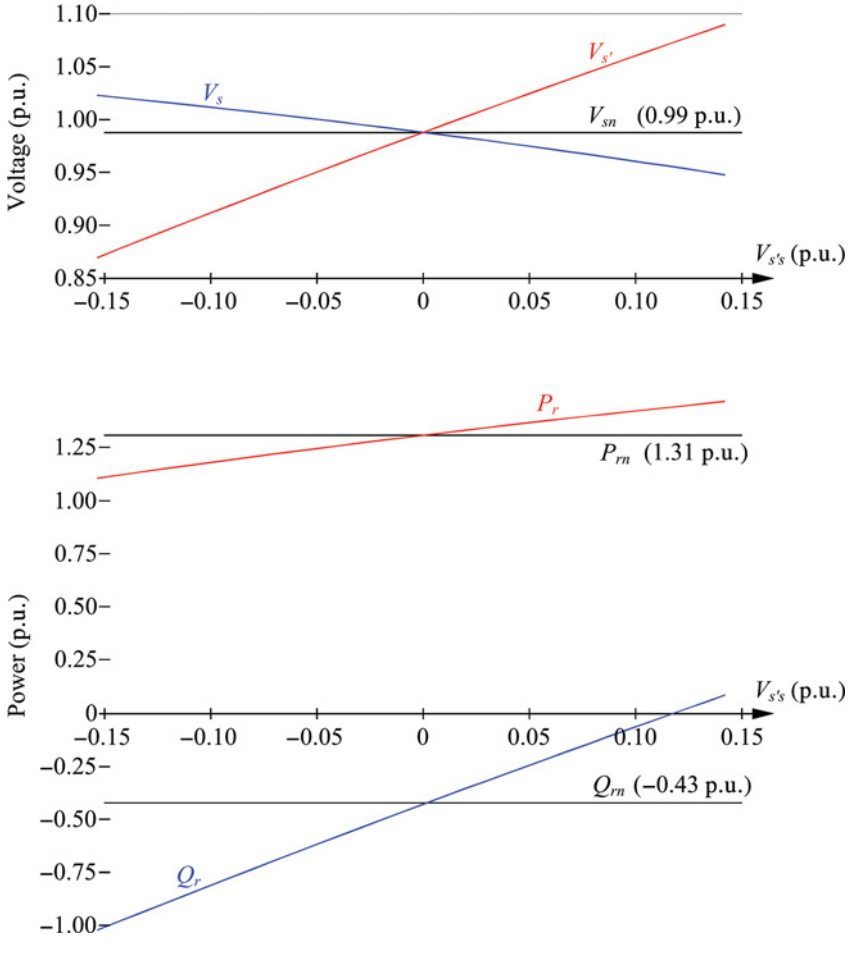

Figure 6.24 Ranges of voltages at the sending and modified sending ends and active and reactive power flows at the receiving end with a VRT.

($\mathbf{V_s}$) at the sending end varies in the range 1.02–0.95 p.u. The reactive power flow at the receiving end changes from −1.02 to +0.09 p.u. during the range of compensating voltage from –0.15 to +0.15 p.u. However, the active power flow at the receiving end changes in the range 1.10–1.47 p.u. for the same range of variation in the compensating voltage. Therefore, a $\mp$0.15 p.u. change in line voltage changes the reactive power flow by 1.11 p.u. and the active power flow by 0.37 p.u.

6.4.3 Simulation of a Phase Angle Regulator

The one-transformer phase angle regulator (PAR) configuration and the corresponding phasor diagram are shown in Figure 6.25(a) and (b). The input voltage ($\mathbf{V_1}$) at BUS01 is applied to a Δ-connected, three-phase primary winding and a secondary voltage ($\mathbf{V_{21}}$) that is in quadrature with the primary voltage is connected in series with the transmission line. With proper polarities of the series-connected windings, the compensating secondary voltage is connected in series with the transmission line at 90° or –90° to the primary voltage. The resulting effect is that the phase angle of the line voltage is regulated.

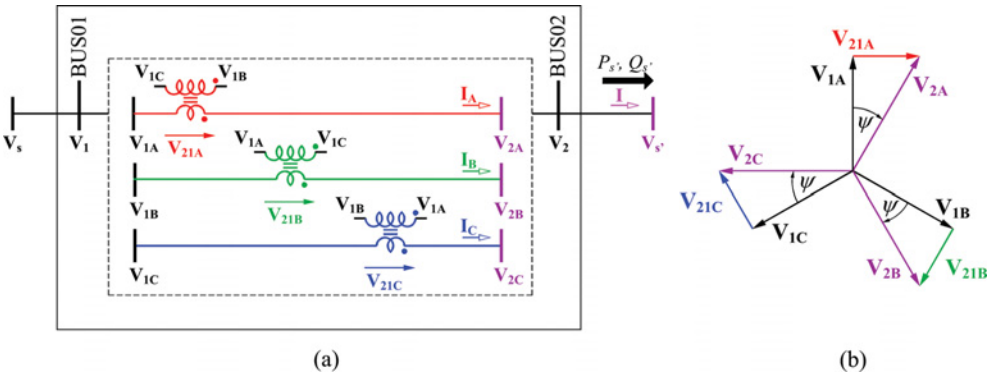

Figure 6.25 (a) Phase angle regulator, (b) phasor diagram.

Figure 6.26 shows that a compensating voltage of ∓15% of the voltage ($\mathbf{V}_s$) at the sending end results in a voltage ($\mathbf{V}_{s'}$) at the modified sending end in the range 1.005–0.986 p.u. In the process, the voltage ($\mathbf{V}_s$) at the sending end varies in the range 0.993–0.973 p.u. The reactive power flow at the receiving end changes from −0.15 p.u. to −0.7 p.u. during the range of compensating voltage from −0.15 p.u. to +0.15 p.u. However, the active power flow at the receiving end changes in the range 0.78–1.82 p.u. for the same range of variation in the compensating voltage. Therefore, a ∓15% compensating voltage in quadrature with line voltage changes the reactive power flow by −0.55 p.u. and the active power flow by 1.04 p.u.

6.4.4 Simulation of a Unified Power Flow Controller

Figure 6.27 shows the schematic diagram of the UPFC. The UPFC consists of two harmonic neutralized (HN)-VSCs (VSC1 and VSC2), two magnetic circuits (MC1 and MC2), a shunt coupling transformer (SHNTR), a series coupling transformer (SRSTR), a shunt breaker (SHNBRK), a series disconnect switch (SRSDS), an electronic bypass switch (ES), a DC link switch (DCLS), a series bypass breaker (SRSBRK), current and voltage sensors and a control and protection unit. Each VSC is coupled with a transformer at its output. Both VSCs generate almost sinusoidal voltages.

When the DCLS is closed, the VSCs share the DC link. The series-connected, variable magnitude, compensating voltage that is at any phase angle with respect to the line current, exchanges an active power as well as a reactive power with the line. This exchanged active power at the AC terminal of the series-connected VSC flows bidirectionally to the AC terminal of the shunt-connected VSC through the shared DC link. Both shunt and series-connected VSCs can also provide independent reactive power compensation at their respective AC terminals. When the DCLS is open, the two VSCs can be operated as standalone, independent, reactive compensators, such as a shunt-connected compensator (STATCOM) and a series-connected compensator (SSSC) and, in turn, exchange almost exclusively reactive power with the line at their respective terminals.

The heart of a power electronics based FACTS controller is a VSC. Figure 6.28 shows the block diagram of a DC-to-AC VSC that generates a three-phase AC voltage. A three-phase AC voltage set generated from an ideal VSC is also shown. In the TACS/control section, a free-running PLL angle (θ) is generated from the power system frequency. The free-running phase angle (θ) is reset at every 2π radians to produce a saw-tooth-like angle (θ_1) in the range of 0 to 2π radians.

Although it is desirable to generate a fundamental frequency AC voltage using a VSC, the quality of the AC voltage, meaning that the associated level of harmonic components in it depends on the topology of the VSC. The choice of the topology is very much influenced by the guidelines set by the IEEE 519

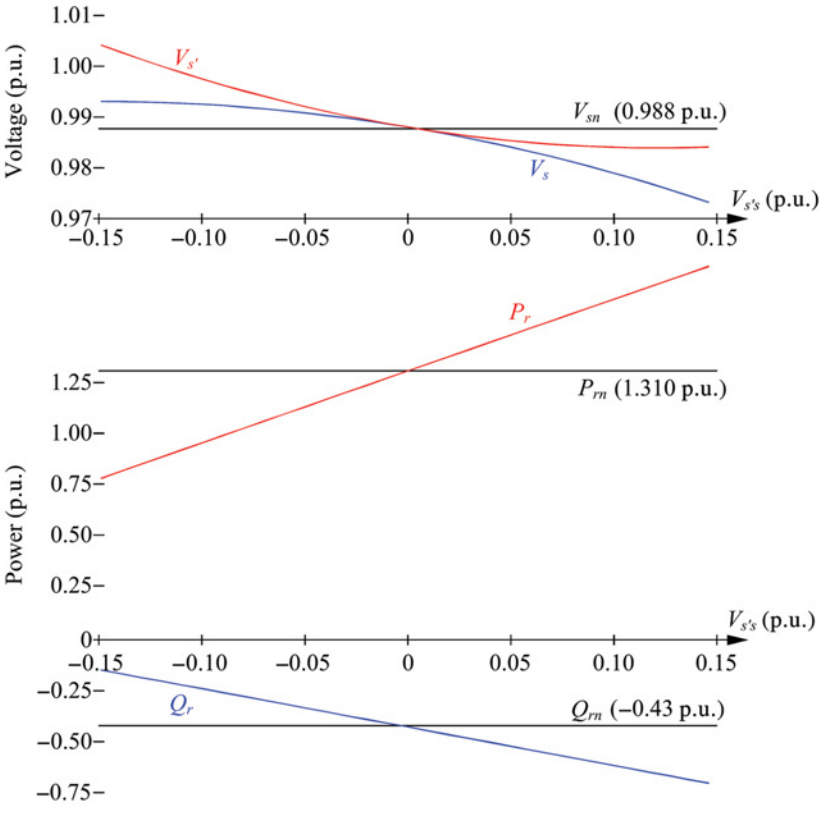

Figure 6.26 Ranges of voltages at the sending and modified sending ends and active and reactive power flows at the receiving end with a phase angle regulator.

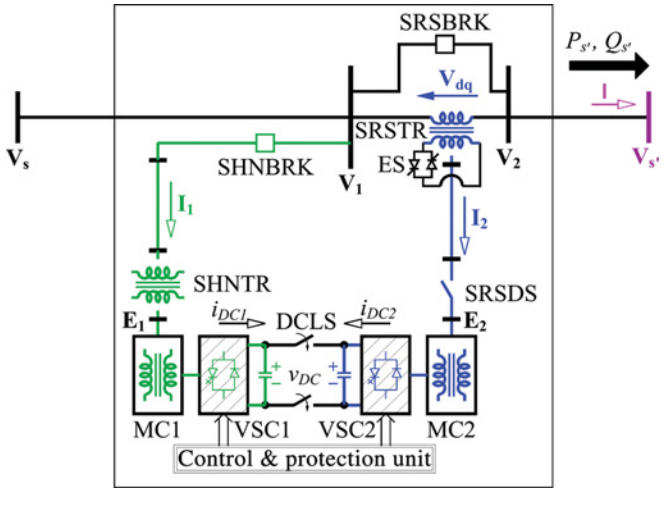

Figure 6.27 Unified power flow controller.

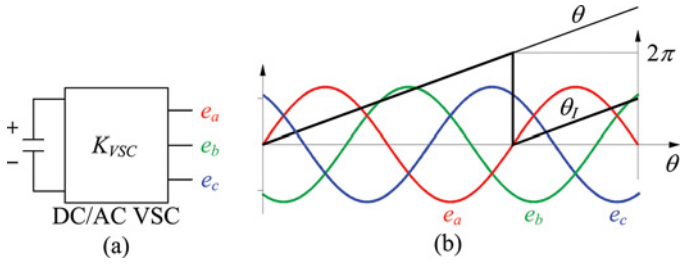

Figure 6.28 Generation of a three-phase ideal VSC voltage.

standard that calls for limits on individual voltage and current distortions and total voltage and current harmonic distortions at the point of compensation for various line voltage levels.

A VSC that produces voltages that are independent in each phase is operated with the PWM technique. Figure 6.29 shows one such configuration. A DC capacitor is connected to one side of the VSC that generates a three-phase AC voltage at its output. The VSC is made up of a set of semiconductor switches, such as IGBTs. The semiconductor switches in the VSC are grouped into three poles: A, B and C. Each pole consists of an upper switch and a lower switch. Each switch has an antiparallel diode across it. The operation of the PWM-VSC is described below.

As shown in Figure 6.30, a fundamental frequency reference signal is compared with a high-frequency triangular carrier signal (v_{tri}). When the reference signal is higher than the carrier signal, the upper switch, A+, is turned on; otherwise, the lower switch, A−, is turned on. The generated PWM square wave voltage contains a fundamental component, the amplitude of which is the same as that of the fundamental frequency reference signal and harmonic components with the largest amplitude at the carrier frequency. Therefore, the amplitude of the fundamental component in the generated voltage can be varied by varying the amplitude of the fundamental frequency reference signal.

The frequency of the dominant harmonic component in the generated voltage can be varied by varying the carrier frequency and, thereby, the switching frequency of the semiconductor devices. It is desirable to increase the frequency of the dominant harmonic component in the PWM voltage. By increasing the switching frequency, the dominant harmonic component can be moved outside the range of concern. For example, if each switch is operated at 25 times the reference signal frequency, the output voltage contains a reference signal frequency and a first dominant harmonic component of 25th order. Increasing the switching frequency is not an attractive option because it increases the switching loss. The compromise is to use a combination of high switching frequency and a harmonic trapping filter as shown in Figure 6.29.

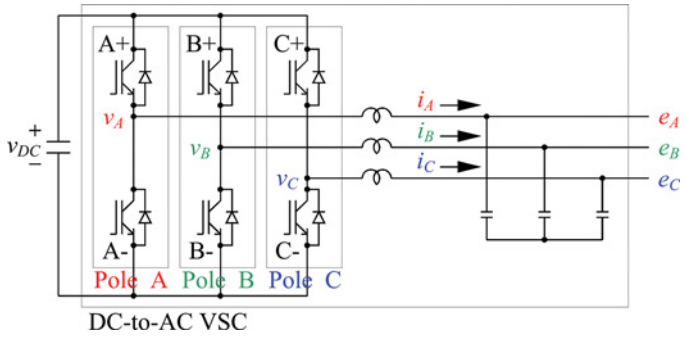

Figure 6.29 DC-to-AC VSC operated with the PWM technique.

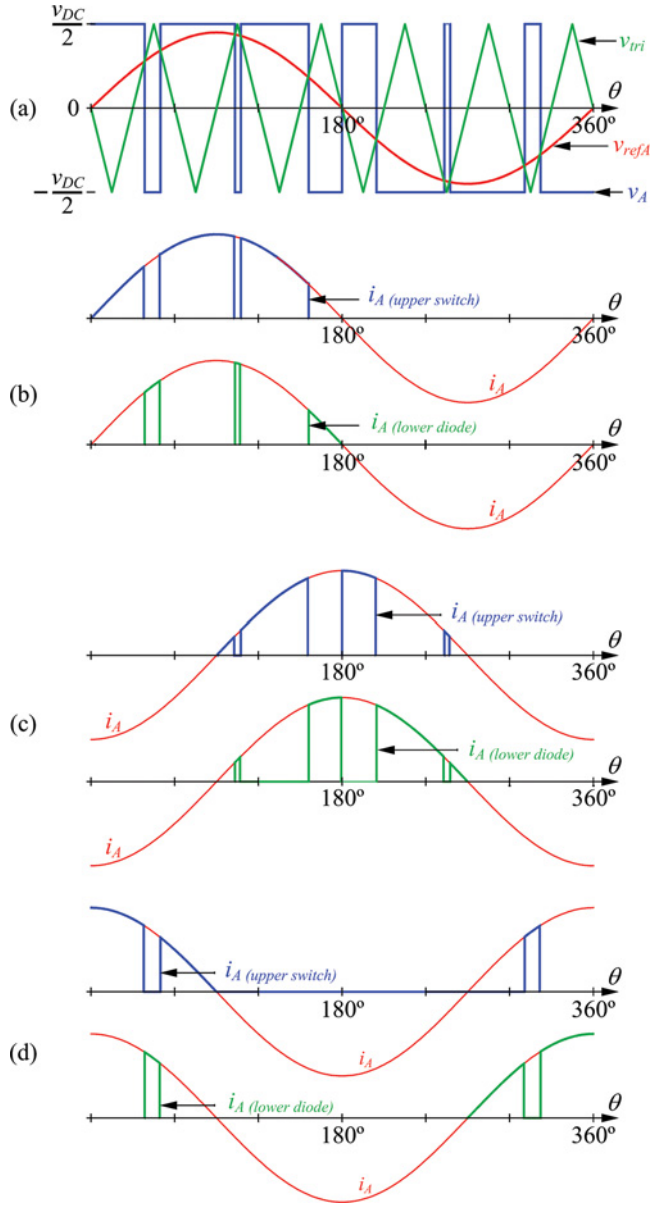

Figure 6.30 (a) Carrier voltage, pole A reference voltage and pole A output voltage, (b) currents through upper switch, lower diode and pole A for unity power factor, (c) currents through upper switch, lower diode and pole A for zero power factor lagging, (d) currents through upper switch, lower diode and pole A for zero power factor leading.

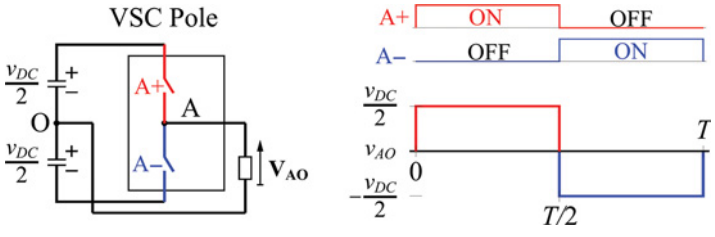

Figure 6.31 VSC pole and its output voltage.

If every individual power electronics switching device is represented, a system model containing power electronics applications can easily reach a complication level that is difficult to implement. A UPFC contains many tens of series-connected GTO devices in one converter leg for high voltage and MVA ratings. Obviously, to represent each individual GTO device in this UPFC system model, will mean building a very large model.

Fortunately, except for some failure mode analyses, for the purposes of most application simulations it is not necessary to represent all the individual devices. Usually, what needs to be simulated is the terminal characteristics of a power electronics subsystem and how it interfaces with the connected system. Thus, the following procedures can be used to reduce the modelling complexity:

- use of one or a few equivalent devices to represent series and parallel combination of a group of devices
- representation of power electronics loads with similar characteristics by an equivalent load
- use of the simplest device model which is appropriate for the application
- representation of a power electronics subsystem by equivalent source injection whenever acceptable
- representation of only the front end of the drive system when the major concern is utility interfacing
- inclusion of the system dynamic and control only when necessary
- use of modular approach for large scale model development

With these general guidelines, a VSC model for a system dynamic evaluation can be built as shown in Figure 6.31. Irrespective of how many series and parallel GTO devices are used in an actual application, only two GTO devices are used in each phase of the model to form a converter leg. In this example, the just-discussed GTO module is used as a building block to construct the converter module.

The UPFCs were built with the most efficient VSC topologies: HN-VSCs. A HN-VSC consists of a set of poles (comprising GTOs, diodes and snubbers), a DC capacitor, a magnetic circuit and a control and protection unit. In order to produce a sinewave-like voltage using a HN-VSC, there are three required stages: (1) the control unit must produce a set of gate pulses, (2) the gate pulses operate a set of poles, which produce a set of square wave voltages, (3) the square wave voltages are combined with a magnetic circuit to produce a sinusoidal voltage. A HN-VSC with a finite pulse number produces a high-quality sinusoidal voltage with acceptable harmonic content. If a VSC produces a pure sine voltage of fundamental frequency, it can be thought of as a VSC of infinite pulse number. These topologies can be modelled step by step in the following ways.

6.4.4.1 Generation of a Square Wave Voltage with a Two-Level Pole

The fundamental building block of an HN-VSC pole is a pair of DC capacitors and a set of switches, which can be used to generate a square wave voltage. Figure 6.31 shows a single-phase VSC circuit, referred to as a pole, which consists of a positive switch (A+) and a negative switch (A−). The pole is connected across a pair of capacitors that are charged with a total DC voltage of v_{DC}. When the switch

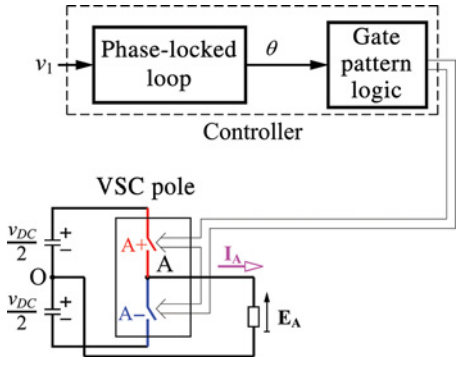

Figure 6.32 Model of a VSC pole.

A+ is on, the midpoint of the pole is tied to the positive DC terminal; when the switch A− is on, the midpoint of the pole is tied to the negative DC terminal. When the switches are closed and opened alternately, the pole output voltage (v_{AO}) at the midpoint of the pole A with respect to the midpoint (O) of the DC link capacitors is a square wave with two levels ($+v_{DC}/2$ and $-v_{DC}/2$). Therefore, this pole circuit is referred to as a two-level pole. The time period, T (i.e. $1/f$), is equally divided between the positive and the negative half cycles, where f is the fundamental frequency of the square wave voltage.

A controller, as shown in Figure 6.32, can be implemented in EMTP TACS to generate a PLL angle and the gating signals to operate the switches of a two-level pole. Figure 6.33 shows the pole voltages and currents generated by the operation of the pole.

6.4.4.2 Six-Pulse VSC with Two-Level Poles

A six-pulse VSC requires the generation of three square wave voltages using the three poles A, B and C. Figure 6.34 shows the three square wave voltages (v_{AO}, v_{BO} and v_{CO}) and the corresponding fundamental components ($v_{AO,1}$, $v_{BO,1}$ and $v_{CO,1}$). The fundamental pole voltage phasors ($\mathbf{V_{AO,1}}$, $\mathbf{V_{BO,1}}$ and $\mathbf{V_{CO,1}}$) are at 0° (reference), −120°, −240°, respectively. The A-B-C set of square wave voltages are said to be placed at 0°.

Figure 6.35 shows three poles A, B and C that are connected across a shared DC link with a pair of capacitors and the related voltages. Note that the pole outputs are connected to a three-phase load whose neutral point (N) is not connected to the midpoint of the DC link capacitor.

The square wave voltages generated by the six-pulse VSCs can be combined using HN techniques to generate a high-quality sinusoidal voltage with acceptable harmonic content. The two key points in the design of a multipulse VSC are that

- the displacement angle between two consecutive six-pulse VSCs in an m six-pulse VSC configuration is $2\pi/6m$

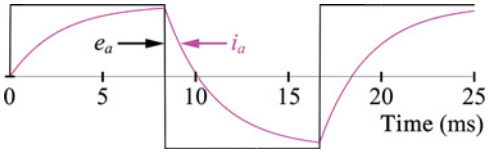

Figure 6.33 Voltages and currents from the simulation of a VSC pole.

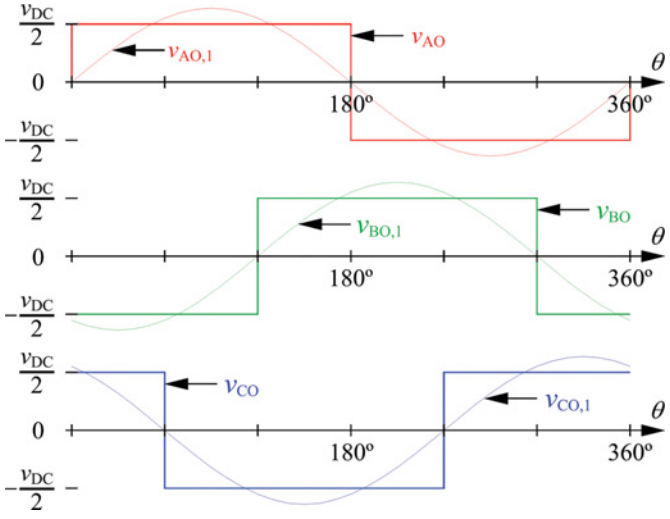

Figure 6.34 Pole voltages and three 120° phase-shifted, fundamental voltage phasors in a six-pulse VSC configuration.

- the configuration of the magnetic circuit is such that if a VSC pole voltage is time-shifted by an equivalent fundamental angle of $-\theta$, the fundamental component of the pole voltage gets a phase shift by an angle of $+\theta$ and vice versa.

6.4.4.3 Twelve-Pulse HN-VSC with Two-Level Poles

A 12-pulse HN-VSC requires the generation of two three-phase sets (A-B-C and D-E-F) of square wave voltage. The displacement angle between two consecutive six-pulse VSCs in a multipulse VSC configuration is $2\pi/6m$ (i.e. 30°), where m (i.e. 2) is the total number of six-pulse VSCs that are used.

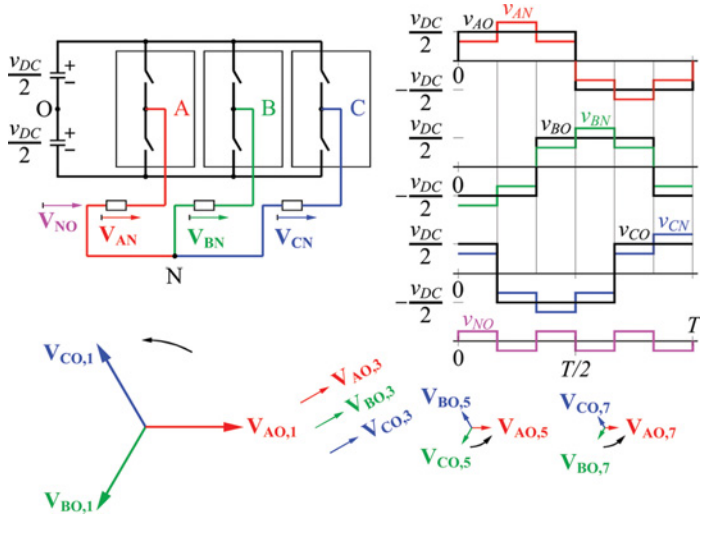

Figure 6.35 Six-pulse VSC and its output voltages.

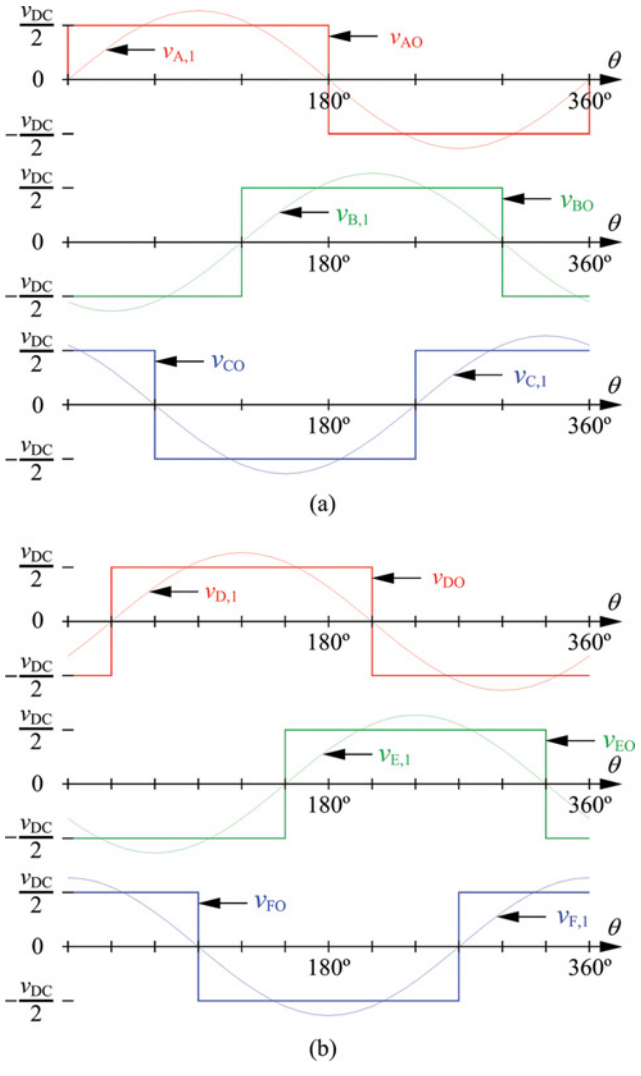

Figure 6.36 Pole voltages and fundamental voltage phasors in a 12-pulse HN-VSC configuration: (a) three 120° phase-shifted fundamental pole voltages and the corresponding square wave voltages at 0°, (b) three 120° phase-shifted fundamental pole voltages and the corresponding square wave voltages at −30°.

Figure 6.36(a) and (b), show the two sets of three square wave voltages (v_{AO}, v_{BO} and v_{CO} and v_{DO}, v_{EO} and v_{FO}) and the corresponding fundamental components ($v_{A,1}$, $v_{B,1}$ and $v_{C,1}$ and $v_{D,1}$, $v_{E,1}$ and $v_{F,1}$). The fundamental pole voltage phasors ($\mathbf{V_{A,1}}$, $\mathbf{V_{B,1}}$ and $\mathbf{V_{C,1}}$) are at 0° (reference), −120°, −240°, respectively. The A-B-C set of square wave voltages are said to be placed at 0°. The fundamental pole voltage phasors ($\mathbf{V_{D,1}}$, $\mathbf{V_{E,1}}$ and $\mathbf{V_{F,1}}$) are at −30°, −150°, 90°, respectively. The D-E-F set of square wave voltages are said to be placed at −30°.

Figure 6.37 shows two six-pulse VSCs (A-B-C and D-E-F) that are connected across a shared DC link with a pair of capacitors and the related fundamental voltage phasors. The pole voltages are combined

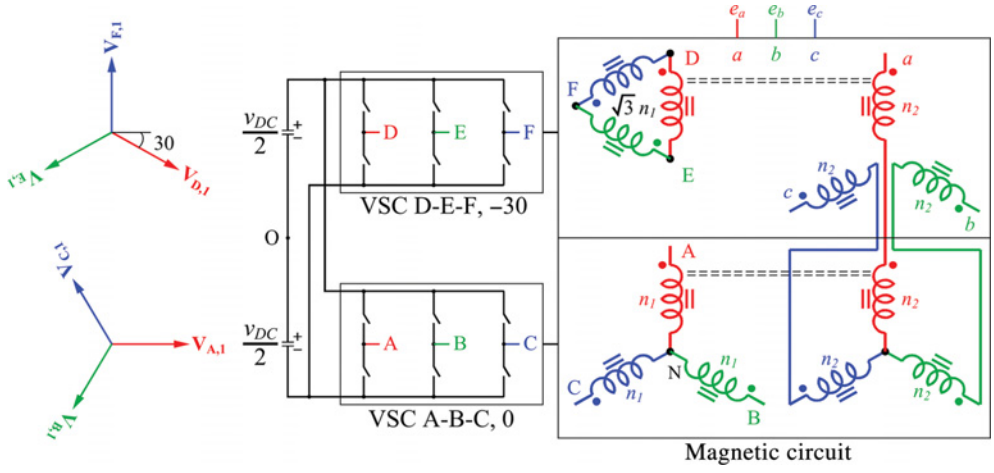

Figure 6.37 Twelve-pulse HN-VSC configuration (all angles are in degrees).

by a magnetic circuit to form a three-phase (*a*-*b*-*c*) voltage. The poles A, B, C, D, E and F are operated in such a way that the pole voltages (v_{AO}, v_{BO} and v_{CO}) of the A-B-C VSC are time-shifted from one another by one-third of the time period (T) of the pole voltage. The pole voltages (v_{DO}, v_{EO} and v_{FO}) of the D-E-F VSC are time-shifted with respect to the corresponding A, B and C pole voltages by a twelfth of the time period, equivalent to a fundamental angle of −30°. Therefore, the fundamental phasors in a group ($\mathbf{V_{A,1}}$, $\mathbf{V_{B,1}}$ and $\mathbf{V_{C,1}}$ of the A-B-C VSC; and $\mathbf{V_{D,1}}$, $\mathbf{V_{E,1}}$ and $\mathbf{V_{F,1}}$ of the D-E-F VSC) are 120° apart, and the fundamental voltage phasor set of the D-E-F VSC lags the fundamental voltage phasor set of the A-B-C VSC by 30°. Note that the fundamental components in the square wave voltages ($\mathbf{V_{DO,1}}$, $\mathbf{V_{EO,1}}$ and $\mathbf{V_{FO,1}}$) of the D-E-F VSC with respect to the midpoint of the DC link capacitor are referred to as $\mathbf{V_{D,1}}$, $\mathbf{V_{E,1}}$ and $\mathbf{V_{F,1}}$.

The configuration of the magnetic circuit is such that if a VSC pole voltage is time-shifted by an equivalent fundamental angle of −30°, the fundamental component of the pole voltage gets phase-shifted by an angle of +30°. The simplest way to give the fundamental components in the D-E-F pole voltages a +30° phase shift is to apply these voltages to the terminals of a Δ winding. The square wave voltages from the A-B-C VSC are fed to the primary windings of a Y-Y transformer, and those from the D-E-F VSC are fed to the primary windings of a Δ-Y transformer. In order to keep the same volts per turn in both Y and Δ windings, the Δ-connected primary windings have $\sqrt{3}$ times the number of turns (n_1) of the Y-connected primary windings. Both sets of secondary Y windings are connected in series in the respective phases, and the final output voltage is connected to a three-phase load (*a*-*b*-*c*).

The presence of 12-pulse harmonic components in the VSC output voltage may not be acceptable in many applications. As a result, a VSC with a higher pulse output voltage is considered. A true p-pulse HN-VSC generates the first dominant harmonic in the spectrum as $p - 1$. The magnetic circuit for a VSC with 24-pulse and higher is quite cumbersome. Its non-standard features make it unattractive because of its higher cost. Therefore, an alternate solution is to use a magnetic circuit for a quasiharmonic neutralized (QHN) VSC.

6.4.4.4 Twenty-Four-Pulse QHN-VSC with Two-Level Poles

A 24-pulse QHN-VSC, shown in Figure 6.38, requires the generation of four three-phase sets (A1-B1-C1, A2-B2-C2, D1-E1-F1 and D2-E2-F2) of square wave voltages. The displacement angle between two consecutive six-pulse VSCs in a multipulse VSC configuration is $2\pi/6m$ (i.e. 15°), where m (i.e. 4)

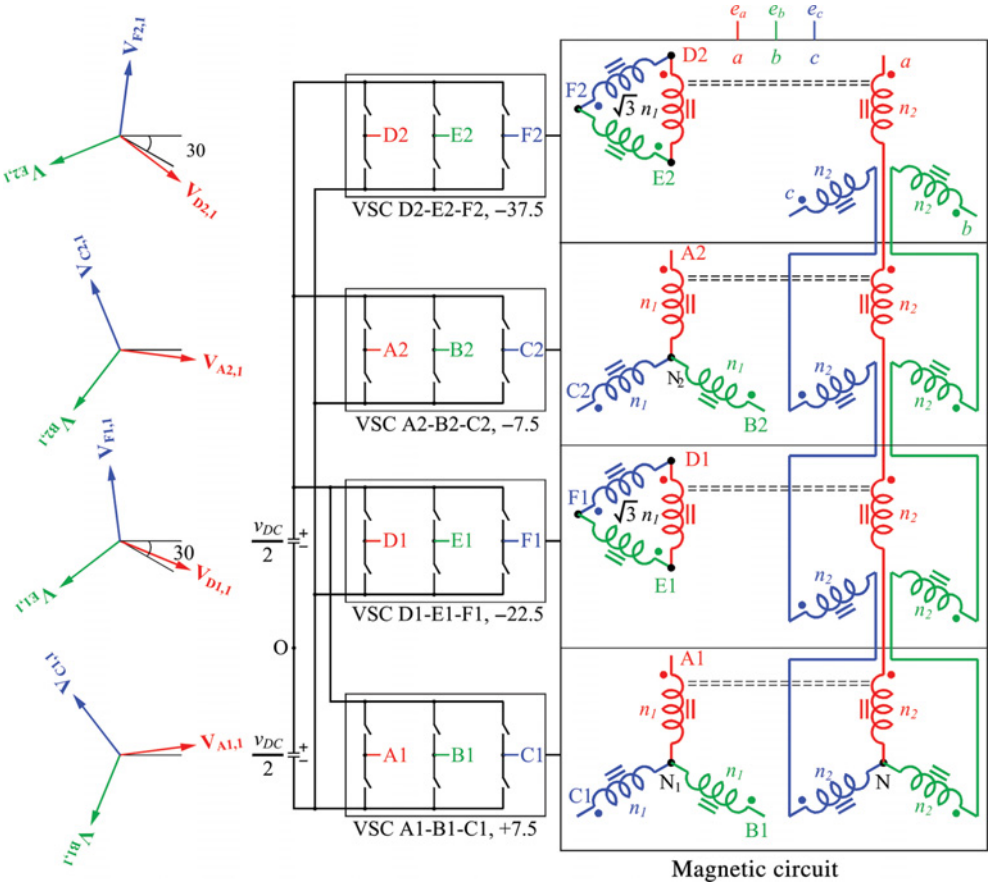

Figure 6.38 Twenty-four-pulse QHN-VSC configuration (all angles are in degrees).

is the total number of six-pulse VSCs that are used. The two phasors in the A-B-C three-phase groups (A1-A2, B1-B2 and C1-C2) are centred on 0°, −120° and −240°, respectively, with a displacement angle ($\theta_{displacement}$) of ±7.5°. The two phasors in the D-E-F three-phase groups (D1-D2, E1-E2 and F1-F2) are centred on −30°, −150° and +90°, respectively, with a displacement angle ($\theta_{displacement}$) of ±7.5°. The fundamental pole voltage phasors ($\mathbf{V_{A1,1}}$, $\mathbf{V_{B1,1}}$ and $\mathbf{V_{C1,1}}$ and $\mathbf{V_{A2,1}}$, $\mathbf{V_{B2,1}}$ and $\mathbf{V_{C2,1}}$), shown in Figure 6.38, are at 7.5°, 7.5°−120° (i.e. −112.5°) and 7.5°−240° (i.e. −232.5°); and −7.5°, −7.5°−120° (i.e. −127.5°) and −7.5°−240° (i.e. −247.5°), respectively. The fundamental pole voltage phasors ($\mathbf{V_{D1,1}}$, $\mathbf{V_{E1,1}}$ and $\mathbf{V_{F1,1}}$ and $\mathbf{V_{D2,1}}$, $\mathbf{V_{E2,1}}$ and $\mathbf{V_{F2,1}}$), shown in Figure 6.38, are at 7.5°−30° (i.e. −22.5°), 7.5°−30°−120° (i.e. −142.5°) and 7.5°−30°−240° (i.e. −262.5°); and −7.5°−30° (i.e. −37.5°), −7.5°−30°−120° (i.e. −157.5°) and −7.5°−30°−240° (i.e. −277.5°), respectively.

When the pole voltages from the VSCs A1-B1-C1 and D1-E1-F1 are magnetically combined, as shown in Figure 6.38, the output voltage exhibits a 12-pulse HN waveform with harmonic components $n = 12k \pm 1$ for $k = 1, 2, 3$ and so on. In the 12-pulse HN-VSC of Figure 6.37, there are two sets of square wave voltages: one set from the A-B-C VSC is at 0° and the other set from the D-E-F VSC is at −30°; the *a-b-c* 12-pulse voltage set is at 0°. In the 24-pulse QHN-VSC of Figure 6.38, there are two sets of square wave voltages: one set from the A1-B1-C1 VSC is at 7.5° and the other set from the D1-E1-F1 VSC is at −22.5°; therefore, the *a1-b1-c1* 12-pulse voltage set is at 7.5°. There are additional two sets of square

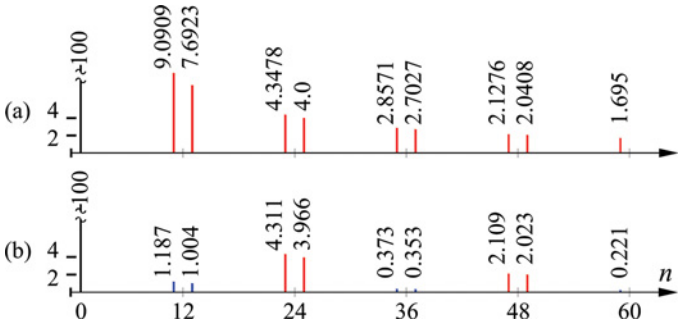

Figure 6.39 Normalized harmonic components of output voltages from (a) a 12-pulse HN-VSC and (b) a 24-pulse QHN-VSC as a function of harmonic order (n).

wave voltages: one set from the A2-B2-C2 VSC is at −7.5° and the other set from the D1-E1-F1 VSC is at −37.5°; therefore, the *a2-b2-c2* 12-pulse voltage set is at −7.5°. Each 12-pulse waveform contains the same magnitudes of fundamental and harmonic components ($n = 12k \pm 1$ for $k = 1, 2, 3$, etc.). When all the output voltages from each six-pulse VSC are combined by connecting the corresponding phases in series as shown in Figure 6.38, the resulting output voltages contain fundamental components and harmonic components $n = 12k \pm 1$ for $k = 1, 2, 3$ and so on, and exhibit a 24-pulse QHN waveform. Figure 6.39 shows the normalized harmonic components of the output voltages from a 12- and 24-pulse HN/QHN-VSCs as a function of harmonic order (n). A 24-pulse or higher order VSC is more than adequate in most applications to meet the power quality standard.

The QHN-VSC circuits that have been discussed so far are made out of two-level poles, which produce a square wave voltage with two levels: a positive level and a negative level. The magnitude of the AC voltage is related to the magnitude of the DC voltage by the gain of the VSC. In certain applications, more than one VSC may operate from a shared DC link capacitor and one VSC is required to produce a variable magnitude AC voltage from zero to the maximum value within the design limit. One way to generate a variable AC voltage from a fixed DC voltage is to use a three-level pole. A three-level pole produces a variable width square wave voltage. As a special case, a three-level pole produces a square wave voltage when used as a two-level pole. Next, a QHN-VSC with three-level poles is described.

6.4.4.5 Generation of a Quasi-Square Wave Voltage with a Three-Level Pole

Figure 6.40 shows the single phase VSC circuit, referred to as a three-level 'pole', which consists of a positive switch, A+, a negative switch, A− and an AC switch, A_{AC}. Each switch may be made out of several controllable semiconductor switches, such as GTOs, that are connected in a series or parallel combination to achieve the desired voltage and current ratings of the switch. The pole is connected across

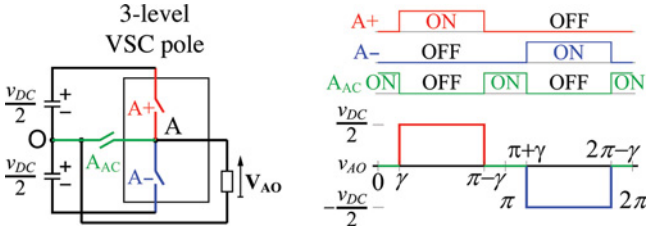

Figure 6.40 Three-level VSC 'pole' and its output voltage (all angles are in radians).

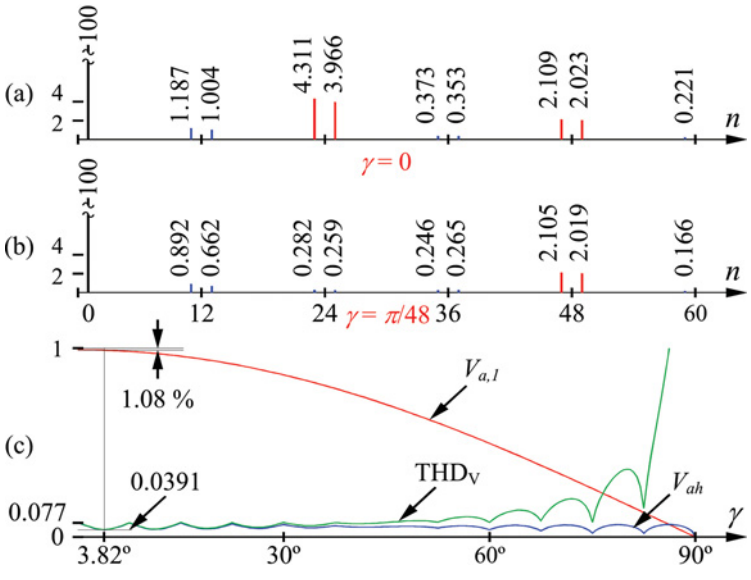

Figure 6.41 Normalized harmonic components of output voltages from (a) a 24-pulse QHN-VSC and (b) a 48-pulse QHN-VSC as a function of harmonic order, (c) variations of amplitude of fundamental component, harmonic content and THD as a function of γ, which is the dead angle of a three-level pole.

a pair of capacitors that are charged with a total DC voltage of v_{DC}. When the switch A+ is on, the midpoint of the pole is tied to the positive DC terminal; when the switch A_{AC} is on, the midpoint of the pole is tied to the midpoint of the DC link capacitor; and when the switch A− is on, the midpoint of the pole is tied to the negative DC terminal. When the switches are closed and opened alternately, the pole output voltage (v_{AO}) at the midpoint of the pole A with respect to the midpoint (O) of the DC link capacitor is a quasi-square wave, which has three levels ($+v_{DC}/2$, 0 and $-v_{DC}/2$). Therefore, this pole circuit is referred to as a three-level pole. The time period, T (i.e. $1/f$), is equally divided between the positive and the negative half cycles where f is the fundamental frequency of the quasi-square wave.

Note that the output voltage of a 24-pulse QHN-VSC with three-level poles is referred to as a 24-pulse QHN waveform when the poles are operated with dead angle $\gamma = 0°$. If a 24-pulse QHN-VSC with three-level poles is operated with $\gamma = \pi/48$, the resulting output voltage is the same as that obtained from a 48-pulse QHN-VSC. In conclusion, a QHN-VSC produces, in addition to the first dominant harmonic in the spectrum, the same as the pulse number of the VSC, a residual harmonic content of $12k \pm 1$ components for $k = 1, 2, 3$ and so on, plus, of course, a fundamental voltage.

Figure 6.41 (a) and (b), show the normalized harmonic components of the output voltages from a 24-pulse QHN-VSC and a 48-pulse QHN-VSC as a function of harmonic order (n). The variations of fundamental component, harmonic content and total harmonic distortion factor of a 24-pulse QHN-VSC with three-level poles as a function of γ is shown in Figure 6.41(c). At $\gamma_{optimum} = 3.82°$, the fundamental amplitude decreases by 1.08%, compared to what is obtained from a two-level operation of the poles, but the harmonic content is reduced from 7.7% to 3.91%, obtained from a two-level operation of the poles in a 24-pulse VSC, resulting in the smallest THD_V.

6.4.4.6 Analysis of a Two-Level Pole

Each of the two switches in a pole (for example, A+ and A− in pole A) can be composed of a GTO and an antiparallel diode, as shown in Figure 6.42. During the positive output voltage, the positive current

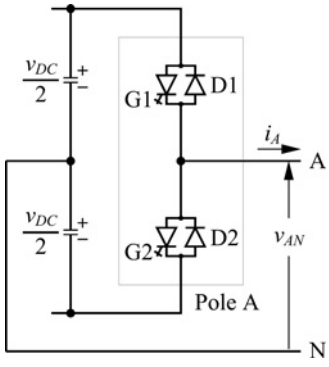

Figure 6.42 Realization of a two-level pole A with GTOs and antiparallel diodes.

flows through the GTO (G1) and the negative current flows through the diode (D1). During the negative output voltage, the positive current flows through the diode (D2) and the negative current flows through the GTO (G2).

When the pole output voltage transitions from negative to positive, the positive current transitions from diode (D2) to GTO (G1), and the negative current transitions from GTO (G2) to diode (D1). When the pole output voltage transitions from positive to negative, the positive current transitions from GTO (G1) to diode (D2), and the negative current transitions from diode (D1) to GTO (G2).

Therefore, the current transitions from a diode to a GTO that is turned on with a gate signal. Also, the current transitions from a GTO to a diode and then to its antiparallel GTO, such as GTO (G1) to diode (D2) to GTO (G2). The question is when the GTO (G2) should be turned on. If it is turned on at the time that the GTO (G1) is turned off, there may be a period of a time when the GTO (G1) is not quite turned off and the GTO (G2) is on its way to being turned on. During this time period, both GTOs may be in between on and off states, which may cause a short-circuit at the DC link capacitor, resulting in a destructive shoot-through current in the capacitor and the GTOs. Therefore, it is necessary to delay the turn-on of GTO (G2) following the turn-off of GTO (G1) by a certain delay time (t_{delay}). The effect of this delay time is investigated.

It is sufficient to study the transition processes from a GTO to a diode and from a diode to a GTO at peak current. It is true that a pole operating at other than zero power factor transitions at other than peak current. However, a designer should study the worst operating point at zero power factor. For the following analysis, two operating conditions – commutating peak current from diode (D2) to GTO (G1) and from GTO (G1) to diode (D2) – are considered.

The details of a pole circuit are shown in Figure 6.43. The reference directions of currents and polarities of voltage for computation purposes are also shown. The two halves (upper and lower) of the pole are symmetric. Each of the two switches (upper and lower) consists of a single GTO (G1 or G2) with an antiparallel diode (D1 or D2) across the GTO. The line stray inductances are *LS1* and *LS4*. The turn-on snubber circuits include *di*/*dt* limiting inductors *L1* and *L2*. These inductors have shunt loops, each consisting of a freewheeling diode (DS1 or DS3), a stray inductance (*LS2* or *LS5*) and a series resistor (*R1* or *R4*). The turn-off snubber circuits include *dv*/*dt* limiting capacitors (*C1* and *C3*), diodes (DS2 and DS4) and the snubber capacitor discharge resistors (*R2* and *R5*). The snubber capacitor leakage inductors are *LS3* and *LS6*. The snubber circuits of the snubber diodes (DS2 and DS4) are *R3-C2* and *R6-C4*, respectively. The pole circuit is analysed by freezing the instantaneous DC link voltage (v_{DC}) to V_{DC} and output current (i_O) to I_O that is equal to the peak current (I_p) at the output of the pole.

The switching characteristics of the diodes (D1 and D2) in this model are shown in Figure 6.44. When the diode conducts, a current (i_D) flows in the forward direction, and the voltage (v_D) across the diode is zero. When the diode current reverses at $t = t_x$, the voltage continues to remain at zero value until the

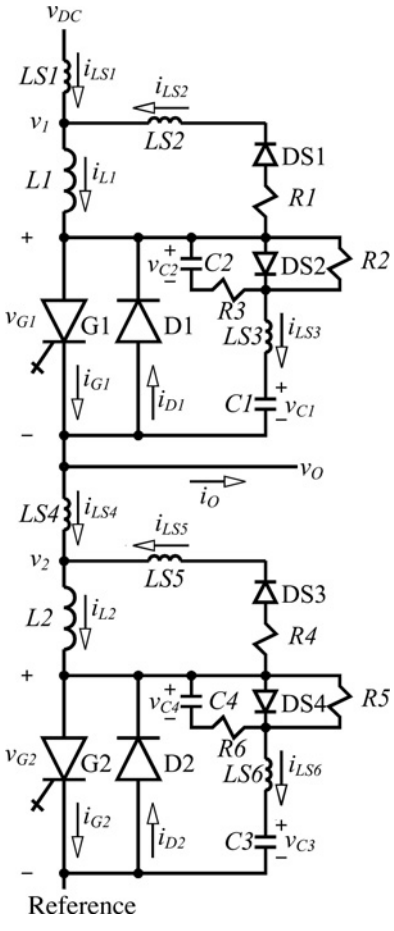

Figure 6.43 Details of a two-level pole circuit.

reverse recovery charge (Q_a) is swept away during $t_x \leq t \leq t_y$. The reverse current through the diode is determined by the dynamics of the circuit. For $t > t_y$, the reverse current (i_D) of the diode rises to zero in a nonlinear fashion.

The maximum slope (y_m) of i_D at $t_y + T$ is considered to be four times the average slope of i_D between t_x and t_y. The diode starts to develop the reverse voltage (v_D) at time t_y. During turn-on, the GTO acts as a variable voltage source (v_G) that falls linearly from the forward blocking voltage (v_B) to zero. During turn-off, the GTO acts as a variable current source (i_G) that falls nonlinearly from the forward conducting current (I_O) to a low value at the end of the fall time (T_{fall}); then the current tapers off at a much slower rate until the end of the tail time (T_{tail}).

To analyse the pole circuit model, two modes of operation need to be studied: commutating output current (I_O) from the antiparallel diode (D2) to the GTO (G1) and commutating output current (I_O) from the GTO (G1) to the GTO (G2) to the antiparallel diode (D2). In the latter mode of operation, three different conditions are studied when the GTO (G2) is turned on after the GTO (G1) is turned off with various delay times (t_{delay}), such as 2 μs, 0 and 20 μs, respectively. With a large delay time, such as $t_{delay} = 20$ μs, the output current (I_O) at full load commutates naturally from the GTO (G1) to the antiparallel diode (D2).

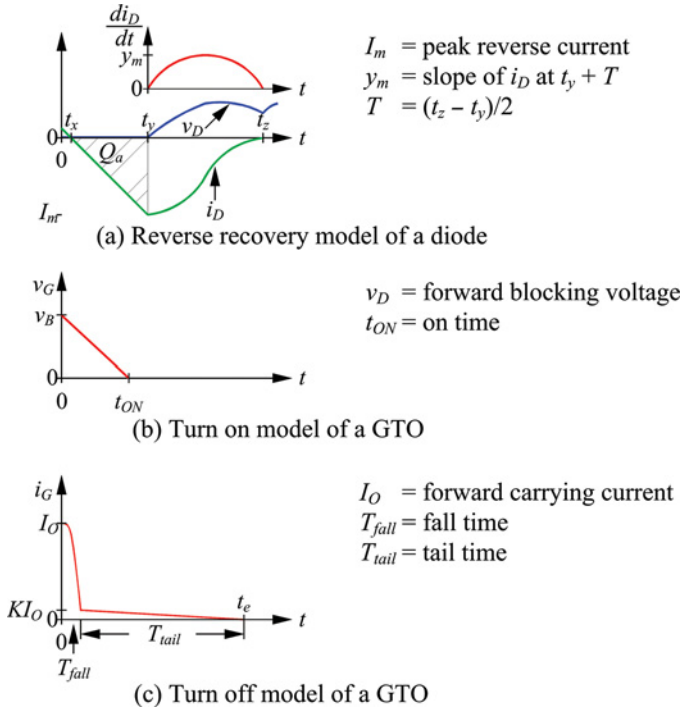

Figure 6.44 Switching characteristics of a diode and a GTO.

Figure 6.45 shows the steady-state operation of the circuit before and after the commutation of output current (I_O) from the antiparallel diode (D2) to the GTO (G1). The transient waveforms in this mode of operation are shown in Figure 6.46.

Figure 6.47 shows the steady-state operation of the circuit before and after the commutation of output current (I_O) from the GTO (G1) to the GTO (G2) to the antiparallel diode (D2). The transient waveforms in this mode of operation are shown in Figure 6.48.

To examine the situation when the worst voltage stress across and current stress through a GTO occur, both types of commutation processes – from the diode (D2) to the GTO (G1) and from the GTO (G1) to the GTO (G2) to the diode (D2) – are studied with various delay times (t_{delay}). The results are given in Table 6.1.

The worst overvoltage of 1.88 p.u. occurs across the GTO (G1) when the output current (I_O) commutates from the GTO (G1) to the GTO (G2) to the diode (D2) under full load condition with $t_{delay} = 0$. The worst overcurrent of 1.75 p.u. occurs through the GTO (G1) when the output current (I_O) commutates from the diode (D2) to the GTO (G1) under full load condition. Therefore, in the pole circuit under consideration, the GTO must be derated at least by a factor of two in terms of its voltage and current ratings. In real-world applications, each switch consists of a number of GTOs that are connected in series. Considering the need for continuous operation of the VSC with an allowable number of failed GTOs, each GTO is further derated in terms of its voltage rating.

Since the voltage across and the current through each element of the circuit is calculated in the simulation, the total loss in the pole circuit can be calculated for trade-off analyses of components selection, heat sink sizing and determining the overall efficiency of the pole circuit. The single GTO switch model can serve as the basis for extending the simulation of the circuit, shown in Figure 6.43,

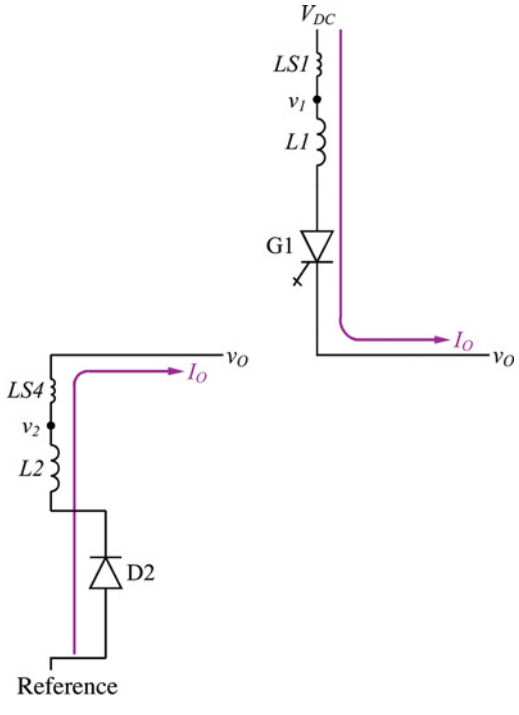

Figure 6.45 Commutation from D2 to G1.

to represent a higher power switch built with a stack of GTO modules that are connected in series, although there may be only one *di/dt* limiting inductor serving all the GTO modules. Each GTO module has its own antiparallel diode and turn-off snubber circuit, as shown in Figure 6.43. Failure of any one GTO in the stack will make the upper and lower halves of the VSC pole asymmetric. Circuit behaviour under this asymmetric condition can be examined as well as the variations caused by differences in the dynamic switching characteristics of the individual GTOs in the stack. The acceptable dynamic sharing of each GTO may be obtained by proper selection of GTOs with similar characteristics. Since the leakage resistance of each GTO is different, static sharing is ensured by connecting a high resistance (of the order of 100 kΩ) across each GTO.

6.5 Simulation Results of a UPFC

Figure 6.49(a) shows a single-line diagram of a simple transmission line with an inductive reactance (X) and a compensating voltage ($\mathbf{V}_{\mathbf{s's}}$) connecting a sending-end voltage source ($\mathbf{V}_{\mathbf{s}}$) and a receiving-end voltage source ($\mathbf{V}_{\mathbf{r}}$). The voltage across the transmission line reactance (X) is $\mathbf{V}_{\mathbf{X}}$ and $\mathbf{I}$ is the prevailing current in the transmission line.

The voltage ($\mathbf{V}_{\mathbf{X}}$) across the transmission line can be controlled by controlling the compensating voltage ($\mathbf{V}_{\mathbf{s's}}$) in series with the transmission line; consequently, the line current and the power flow in the line are regulated. Consider the case where $\mathbf{V}_{\mathbf{s's}} = 0$ as shown in Figure 6.49(b). The transmission line's sending-end voltage ($\mathbf{V}_{\mathbf{s}}$) leads the receiving-end voltage ($\mathbf{V}_{\mathbf{r}}$) by a phase angle (δ). The resulting current in the line is $\mathbf{I}$ and the active and reactive power flows at the receiving end are P_r and Q_r, respectively. With a compensating voltage ($\mathbf{V}_{\mathbf{s's}}$) in series with the transmission line, the transmission line's modified sending-end voltage ($\mathbf{V}_{\mathbf{s}'}$) still leads the receiving-end voltage ($\mathbf{V}_{\mathbf{r}}$), but by a different phase angle (δ') as

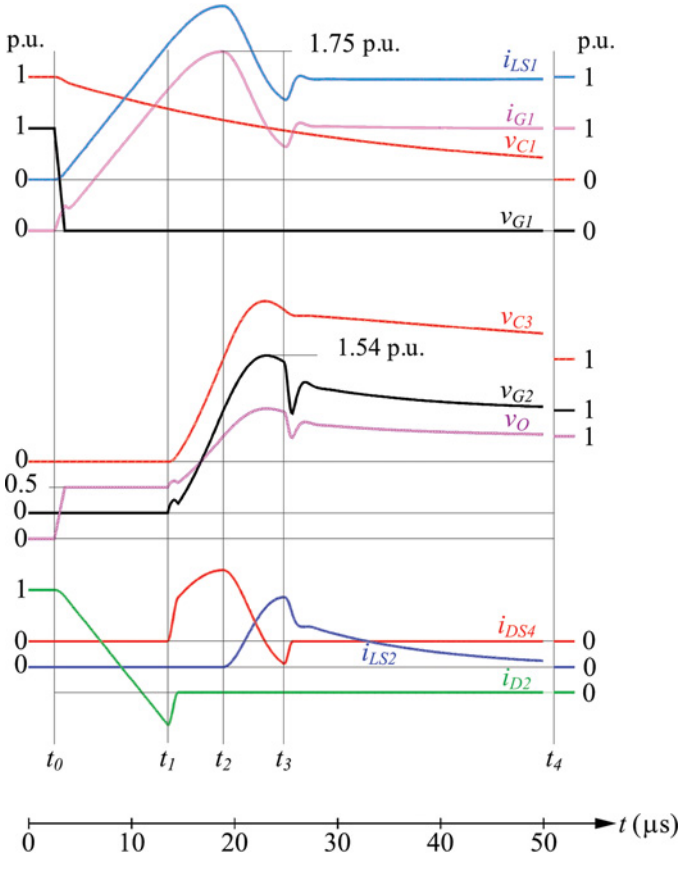

Figure 6.46 Transient waveforms from commutation from D2 to G1.

shown in Figure 6.49(c). The resulting line current and the amount of power flow change. With a larger amount of compensating voltage ($\mathbf{V}_{s's}$) in series with the transmission line, the sending-end voltage ($\mathbf{V}_{s'}$) now lags the receiving-end voltage ($\mathbf{V}_{\mathbf{r}}$) by a different phase angle (δ') as shown in Figure 6.49(d). The resulting line current and the power flow now reverse.

The phase angle (ϕ) between the negative compensating voltage (i.e. $-\mathbf{V}_{s's} = +\mathbf{V}_{\mathbf{dq}}$) and the line current ($\mathbf{I}$), as shown in Figure 6.49(c) and (d), can be between 0 and 2π. The component of the negative compensating voltage that is in or out of phase with the line current emulates a positive or a negative resistance in series with the transmission line. The remaining component that is in quadrature with the line current emulates an inductive or a capacitive reactance in series with the transmission line.

The active power is absorbed from or delivered to the line through the STATCOM, which injects a current at the point of compensation. The current injected by the STATCOM has an active or direct component (I_d), which is in phase with or in opposite phase to the line voltage. The current injected by the STATCOM also has a reactive or quadrature component (I_q), which is in quadrature with the line voltage, thereby emulating an inductive or a capacitive reactance at the point of compensation. This reactive current can be independently controlled, which in turn regulates the line voltage at the point of compensation.

The UPFC model in EMTP is shown Figure 6.50. The UPFC consists of two VSCs that are connected through a shared DC link. The configurations of the two VSCs used are identical for practical reasons,

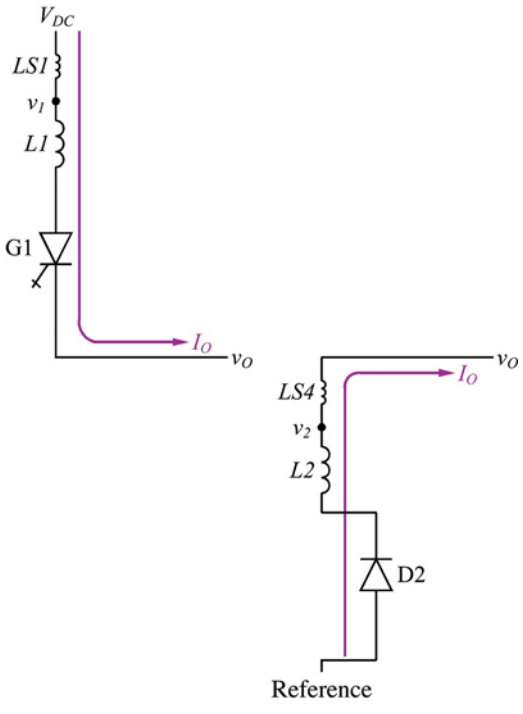

Figure 6.47 Commutation from G1 to G2 to D2.

such as storing spare parts, maintenance and so on. Each VSC is coupled with a transformer at its output. The first VSC, known as the STATCOM, injects an almost sinusoidal current of variable magnitude at the point of compensation in shunt with the line. The second VSC, known as the SSSC, injects an almost sinusoidal voltage of variable magnitude at the point of compensation in series with the line.

The control of the UPFC can be divided into two parts: the control of the STATCOM and the control of the SSSC. When the STATCOM and the SSSC operate as standalone FACTS controllers, they exchange almost exclusively reactive power at their terminals. During the standalone operations, the SSSC injects a voltage in quadrature with the line current, thereby emulating an inductive or a capacitive reactance at the point of compensation in series with the line, and the STATCOM injects a reactive current, thereby also emulating a reactance at the point of compensation in shunt with the line.

While operating both the VSCs together as the UPFC, the series-connected compensating voltage can be at any phase angle with respect to the prevailing line current. Therefore, the exchanged power at the terminal of each VSC can be reactive as well as active. The exchanged active power at the terminal of one VSC with the line flows to the terminal of the other VSC through the shared DC link. The exchanged reactive powers at both the AC terminals of the UPFC are independent of each other.

The SSSC can be operated in many different modes such as voltage injection, phase angle regulation, line impedance emulation or automatic power flow control. In each mode of operation, the final outcome is such that the SSSC injects a voltage in series with the transmission line. The control block diagram of the SSSC in an open loop voltage injection mode of operation is shown in Figure 6.51.

The desired peak fundamental voltage ($V^*_{s's}$) at the output of the VSC and its relative phase angle (β) with respect to the reference PLL angle (θ) are specified. The absolute phase angle (θ_2) of the VSC output voltage is calculated by adding the relative phase angle (β) of the VSC output voltage and the PLL angle (θ). The dead angle (γ) of each pole is calculated.

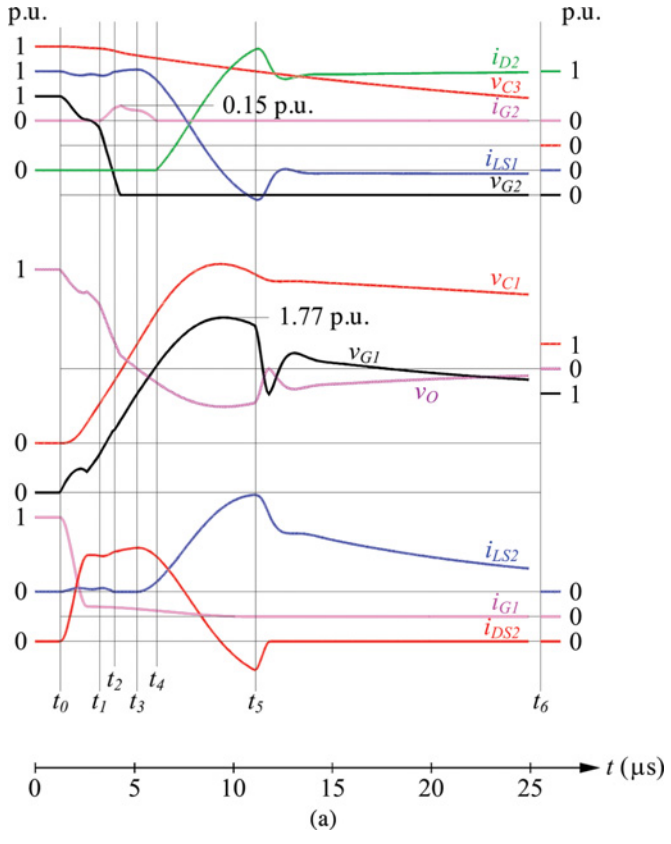

Figure 6.48 Transient waveforms from commutation from G1 to G2 to D2 with (a) t_{delay} = 2 μs, (b) with t_{delay} = 0 (c) t_{delay} = 20 μs. (*continued*)

The controller of the STATCOM is used to operate the VSC in such a way that the phase angle between the VSC output voltage and the line voltage is dynamically adjusted, so that the STATCOM generates or absorbs the desired VARs at the point of compensation. Figure 6.52(a) shows the reactive current control block diagram of the STATCOM.

An instantaneous three-phase set of line voltages (v_1) at BUS01 is used to calculate the PLL angle (θ), which is phase locked to the phase a of the line voltage (v_{1a}). An instantaneous three-phase set of measured currents (i_1) through the VSC is decomposed into its active or direct component (I_{1d}) and reactive or quadrature component (I_{1q}). The quadrature component is compared with the desired reference value (I^*_{1q}), and the error is passed through an error amplifier, which produces a relative phase angle (α) of the compensating voltage ($\mathbf{E_1}$) with respect to the line voltage ($\mathbf{V_1}$). The absolute phase angle (θ_1) of the compensating voltage is calculated by adding the relative phase angle of the compensating voltage with respect to the PLL angle (θ).

The reference quadrature component (I^*_{1q}) of the current through the VSC is defined to be either positive if the STATCOM is emulating a capacitive reactance or negative if it is emulating an inductive reactance. The DC link capacitor voltage (v_{DC}) is dynamically adjusted in relationship with the compensating voltage. The control scheme described above shows the implementation of the inner current control loop, which regulates the reactive current flow through the VSC, regardless of the line voltage. However, if it is desired to regulate the line voltage, an outer voltage control loop must be implemented. The outer

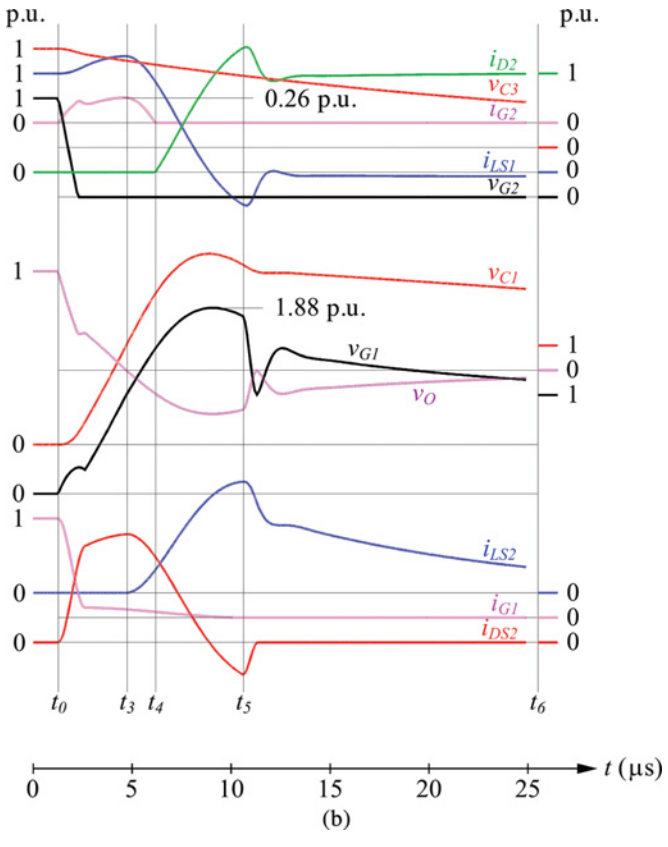

Figure 6.48 (*Continued*)

voltage control loop automatically determines the reference reactive current for the inner current control loop, which in turn regulates the line voltage.

Figure 6.52(b) shows the voltage control block diagram of the STATCOM. Using the reference PLL angle (θ), the instantaneous three-phase set of measured line voltage (v_1) at BUS01 is decomposed into its active or direct component (V_{1d}) and reactive or quadrature component (V_{1q}). The magnitude of the BUS01 voltage (V_{1dq}) is calculated, which is compared with the desired reference value, V_1^* (adjusted by the droop factor, K_{droop}), and the error is passed through an error amplifier, which produces the reference current (I_{1q}^*) for the inner current control loop. The droop factor (K_{droop}) is defined as the allowable voltage error at the rated reactive current flow through the STATCOM.

Figure 6.53 shows the digital simulation results from the open loop voltage injection mode of operation of the SSSC while the STATCOM is operated to deliver no reactive current. At the beginning of the operation, the series bypass breaker (SRSBRK) and the series disconnect switch (SRSDS) are open and the ground switch (GNDSW) is closed. The HN-VSC (VSC2) generates no compensating voltage. The voltage (v_{12a}) at the terminal of the series coupling transformer (SRSTR) is the voltage across its leakage reactance. The active and reactive compensating powers ($P_{c\text{-}se}$ and $Q_{c\text{-}se}$) exchanged at the terminal of the series coupling transformer (SRSTR) are mostly reactive due to the high quality factor of the leakage reactance. The shunt breaker (SHNBRK) is open. The DC link capacitor is precharged.

At 50 ms, the SHNBRK closes and the quadrature current demand (I_{1q}^*) of the VSC1 is set to zero. At 100 ms, a series compensating voltage at the VSC2 side is set at 0.2 p.u. with a relative phase angle

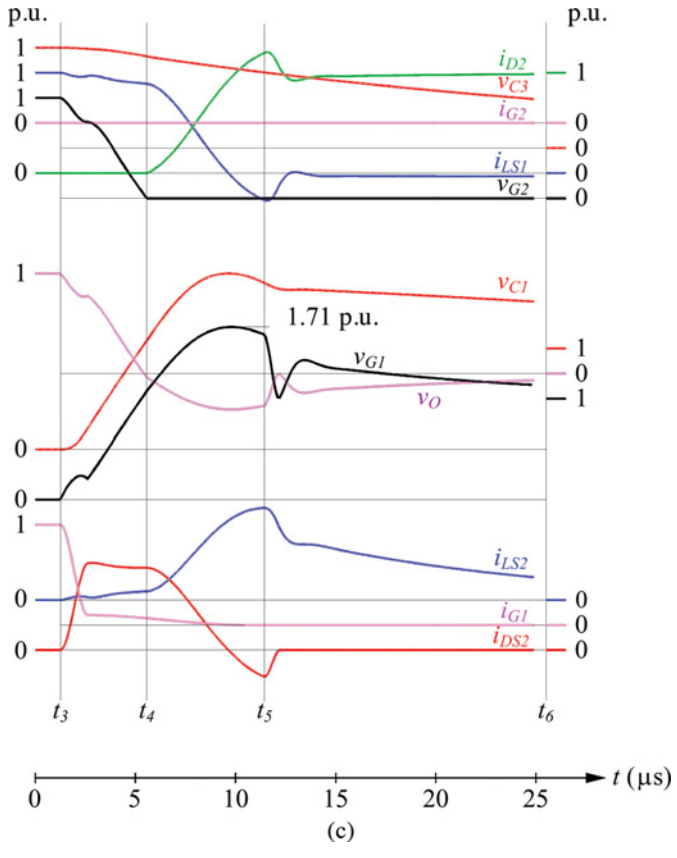

Figure 6.48 (*Continued*)

$\beta = 300°$ leading the reference PLL angle (θ). The series VSC2 output voltage (e_{2a}) of phase a leads the line current (i_a) by a phase angle (ϕ). Since $\phi > 90°$, the SSSC emulates a negative resistance in addition to an inductive reactance in series with the transmission line. The active power that is delivered to the line by the series VSC2 flows from BUS01 through the STATCOM. The shunt VSC1 output voltage (e_{1a}) of phase a is almost in phase with the current (i_{1a}) flowing through it. The voltage (v_{2a}) of phase a at BUS02 leads the voltage (v_{ra}) of phase a at the receiving end. The active power (P_r) delivered at the receiving end decreases. The reactive power (Q_r) delivered at the receiving end becomes inductive. At 200 ms, the series-connected compensating voltage is maintained at 0.2 p.u. while the relative phase angle (β) is changed to 240°. The active power that is absorbed from the line by the series VSC2 flows to BUS01 through the STATCOM. The shunt VSC1 output voltage (e_{1a}) of phase a is almost 180° out of phase with the current (i_{1a}) flowing through it. The reactive power (Q_r) delivered at the receiving end becomes capacitive. At 300 ms, the series-connected compensating voltage is increased to 0.4 p.u. while the relative phase angle (β) stays at 240°. The voltage (v_{2a}) of phase a at BUS02 lags the voltage (v_{ra}) of phase a and the active power flow (P_r) at the receiving end reverses. The series VSC2 output voltage (e_{2a}) of phase a lags the line current (i_a) by a phase angle (ϕ). The reactive compensating power ($Q_{c\text{-}se}$) exchanged at the terminal of the series coupling transformer (SRSTR) becomes capacitive. Figure 6.54 shows the expanded view of two sections of Figure 6.53. The VSC2 voltage and current show the presence of only fundamental components.

Table 6.1 Voltage and current stresses when a GTO turns on and off.

		Peak voltage across the GTO, G1 (p.u.)	Peak voltage across the GTO, G2 (p.u.)	Peak current through the GTO, G1 (p.u.)	Peak current through the GTO, G2 (p.u.)
GTO (G1) turn-on	Full load		1.54	1.75	
	No load		1.46	0.66	
GTO (G1) turn-off and GTO (G2) turn-on with $t_{delay} = 2$ μs	Full load	1.77			0.15
GTO (G1) turn-off and GTO (G2) turn-on with $t_{delay} = 0$	Full load	1.88			0.26
	No load	1.46			0.66
GTO (G1) turn-off and GTO (G2) turn-on with $t_{delay} = 20$ μs	Full load	1.71			0

The results are indicated in p.u. with one p.u. current as the nominal output current ($I_O = 4000$ A) and the one p.u. voltage as the nominal DC link voltage ($V_{DC} = 1900$ V).

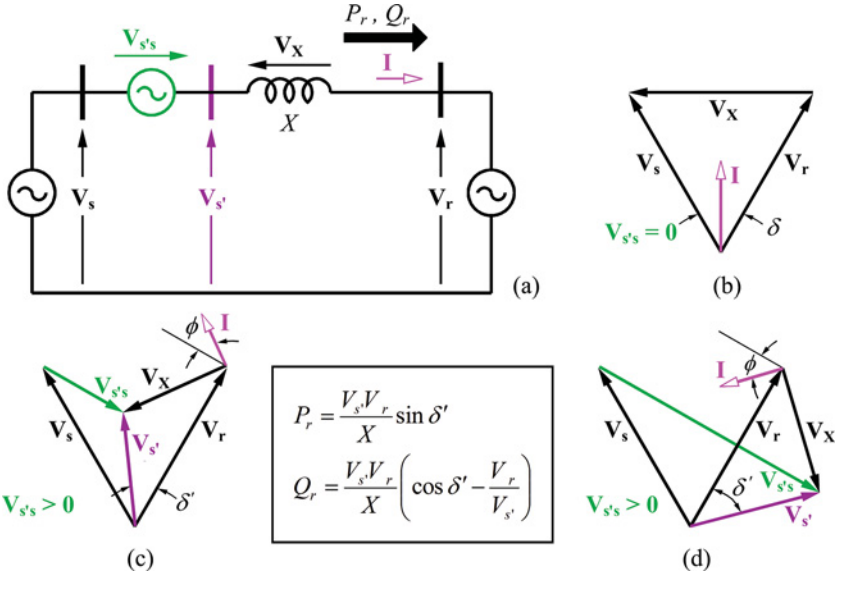

Figure 6.49 UPFC operating with an open loop compensating voltage and the related phasor diagrams.

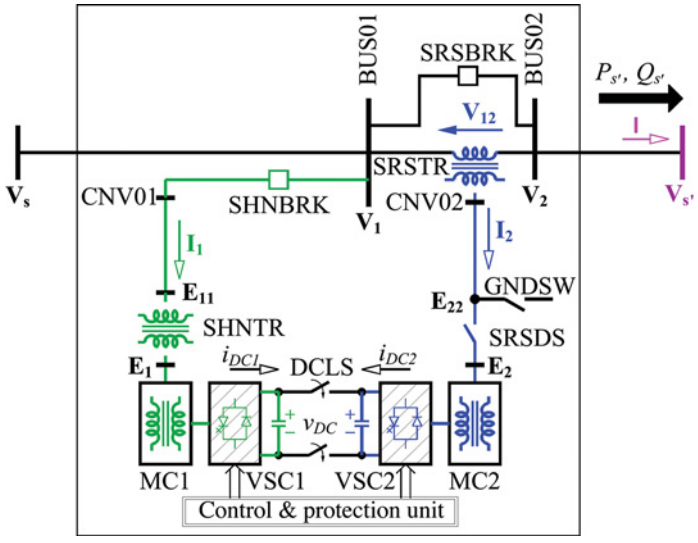

Figure 6.50 UPFC model in EMTP.

The previous test case was rerun for the UPFC with two 24-pulse QHN-VSCs with three-level poles: one operating as the STATCOM with a fixed dead angle (γ) to produce a 48-pulse waveform and the other operating as the SSSC to produce a variable output voltage. The results are shown in Figures 6.55 and 6.56, respectively. The VSC2 voltage and current show the presence of harmonic components.

In the above test cases, the STATCOM was operated in a reactive current control mode with the reactive current through the STATCOM set to zero. The only current that passed through the STATCOM was either in phase or out of phase with the BUS01 voltage, depending on whether the SSSC was delivering or absorbing active power to or from the line. The BUS01 voltage was not regulated. However, the remaining current carrying capability of the STATCOM can be utilized to inject reactive current to the line at the point of compensation and, in the process, the line voltage can be regulated. Figure 6.57 shows the previous test case with the voltage control mode of operation of the STATCOM. The STATCOM carries additional reactive current, and regulates the line voltage at the point of compensation (BUS01).

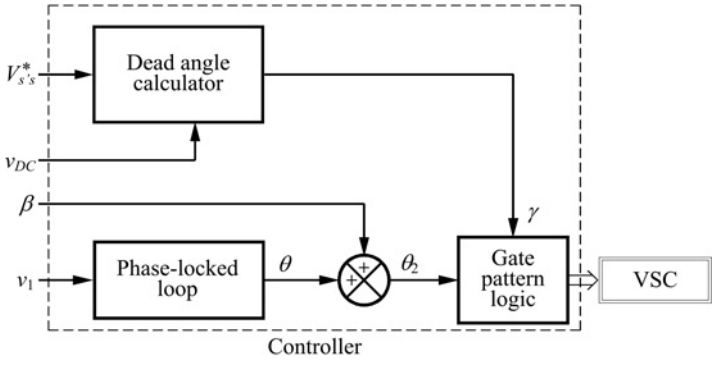

Figure 6.51 Control block diagram of the SSSC in an open loop voltage injection mode of operation of the UPFC.

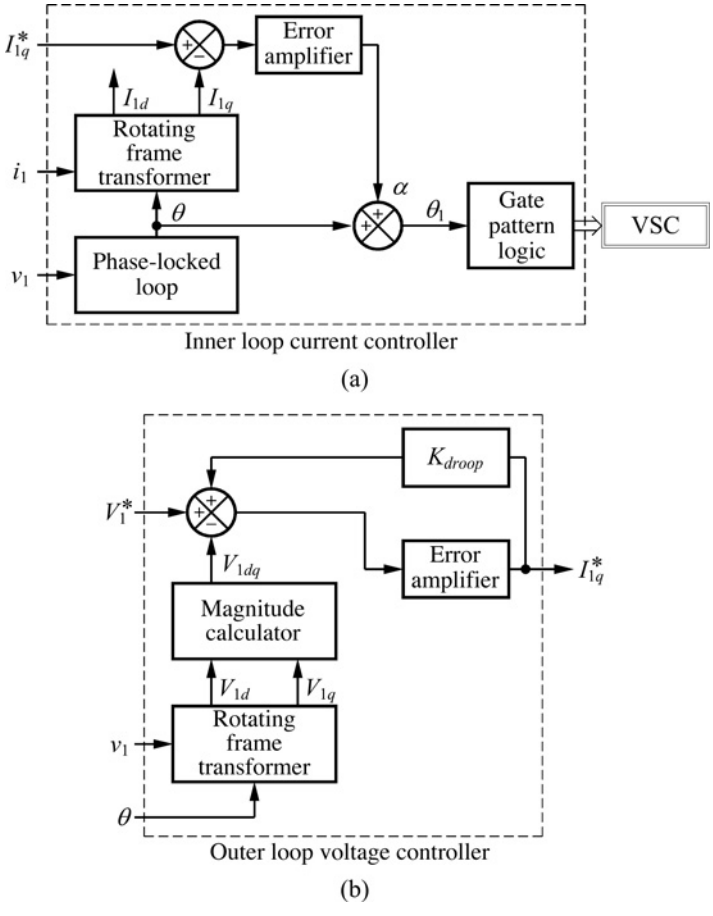

Figure 6.52 (a) Reactive current control block diagram of the STATCOM, (b) voltage control block diagram of the STATCOM.

6.6 Simulation Results of an ST

The ST shown in Figure 6.58(a) has two main units: exciter unit and compensating voltage unit. The exciter unit consists of Y-connected shunt primary windings (A, B and C), and the compensating voltage unit consists of nine secondary windings, three of which are placed on each limb of the core: a_1, a_2 and a_3 on the first limb, b_1, b_2 and b_3 on the second limb and c_1, c_2 and c_3 on the third limb. The three-phase transmission line voltages ($\mathbf{V_{sa}}$, $\mathbf{V_{sb}}$ and $\mathbf{V_{sc}}$) at the sending end are applied in shunt to the exciter unit. By choosing the number of turns from each of the three windings and therefore the magnitudes of the components of the three 120° phase-shifted induced voltages, the compensating voltage ($\mathbf{V_{s's}}$) in any phase is derived from the phasor sum of the voltages induced in a three-phase winding set (a_1, b_1 and c_1 for compensation in the A phase; a_2, b_2 and c_2 for compensation in the B phase; and a_3, b_3 and c_3 for compensation in the C phase). The compensating voltage is also at any phase angle with respect to the prevailing line current. The active or direct component of the compensating voltage provides the series resistance emulation, which can be a positive resistor that absorbs active power from the line or a negative resistor that delivers active power to the line. The reactive or quadrature component of the

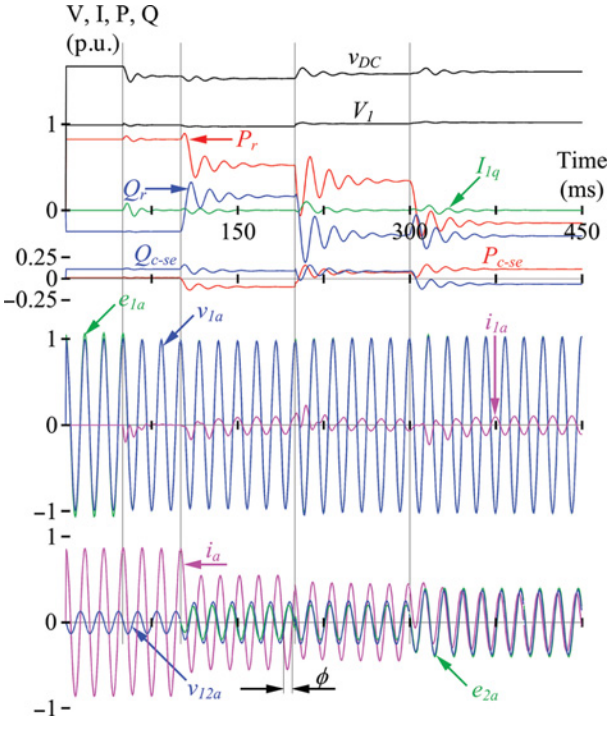

Figure 6.53 Performance of the UPFC with an infinite pulse VSC2 operating in an open loop voltage injection mode while regulating a zero reactive current through an infinite pulse VSC1.

compensating voltage provides the series reactance emulation, which can be a capacitor that delivers reactive power to the line and, in the process, increases the power flow of the line, or an inductor that absorbs reactive power from the line and decreases the power flow of the line. Therefore, the desired compensating voltage is actually an impedance emulator. The effect of impedance emulation is such that the active and reactive power flows in a transmission line can be regulated independently. The power

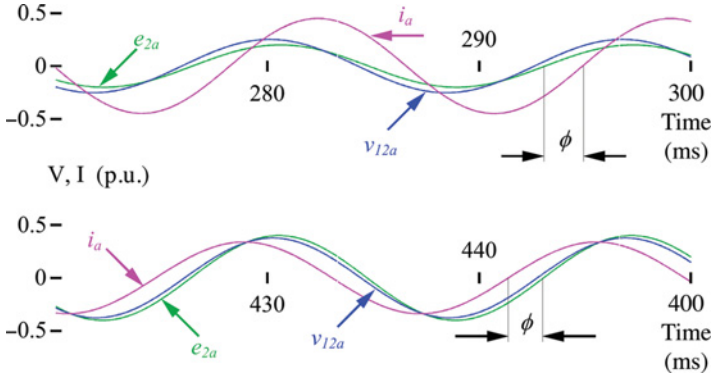

Figure 6.54 Waveforms from the UPFC with an infinite pulse VSC2 operating in an open loop voltage injection mode.

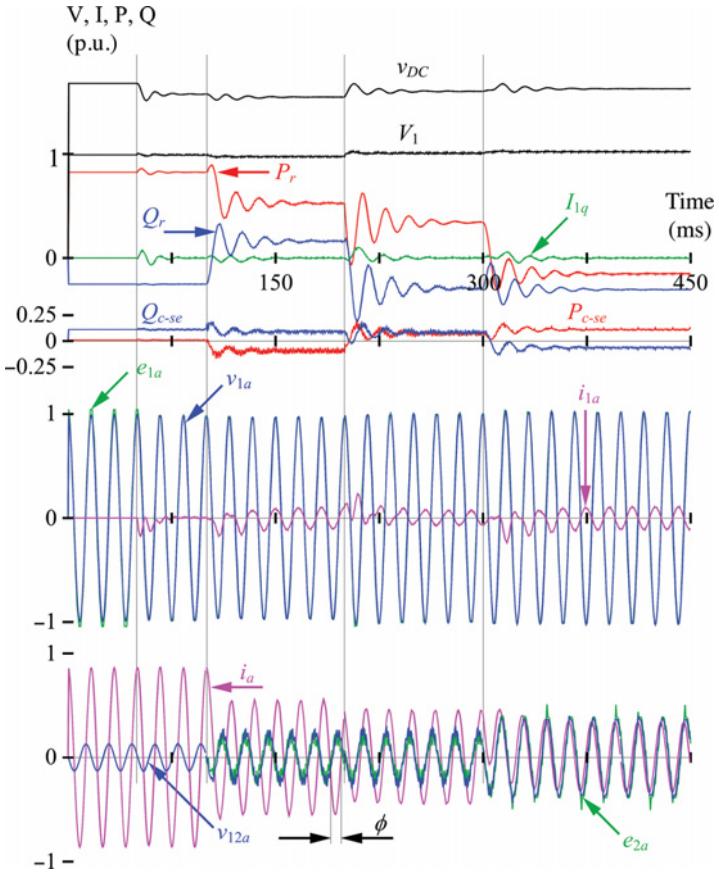

Figure 6.55 Performance of the UPFC with a 24-pulse QHN-VSC2 with three-level poles operating in an open loop voltage injection mode while regulating a zero reactive current through a 24-pulse QHN-VSC1 with three-level poles operating at a fixed dead angle to act as a 48-pulse QHN.

Figure 6.56 Waveforms from the UPFC with a 24-pulse QHN-VSC2 with three-level poles operating in an open loop voltage injection mode.

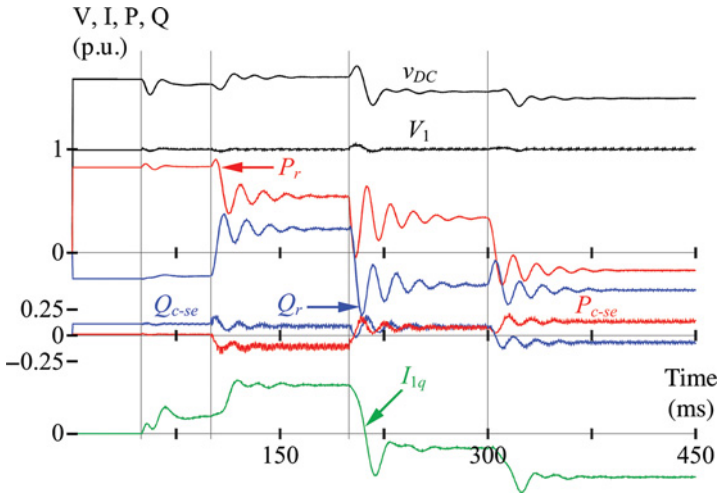

Figure 6.57 Performance of the UPFC with a 24-pulse QHN-VSC2 with three-level poles operating in an open loop voltage injection mode while regulating the BUS01 voltage with a 24-pulse QHN-VSC1 with three-level poles operating at a fixed dead angle to act as a 48-pulse QHN.

circuit is identical for both the voltage regulator and the impedance regulator. Both functions of voltage regulation and independent control of active and reactive power flows can be implemented in just one unit by proper programming of the tap control unit. Figure 6.58(b) shows the related phasor diagram.

It should be noted that each of a_1, b_2 and c_3 is tapped at the same number of turns; each of b_1, c_2 and a_3 is tapped at the same number of turns; and each of c_1, a_2 and b_3 is tapped at the same number

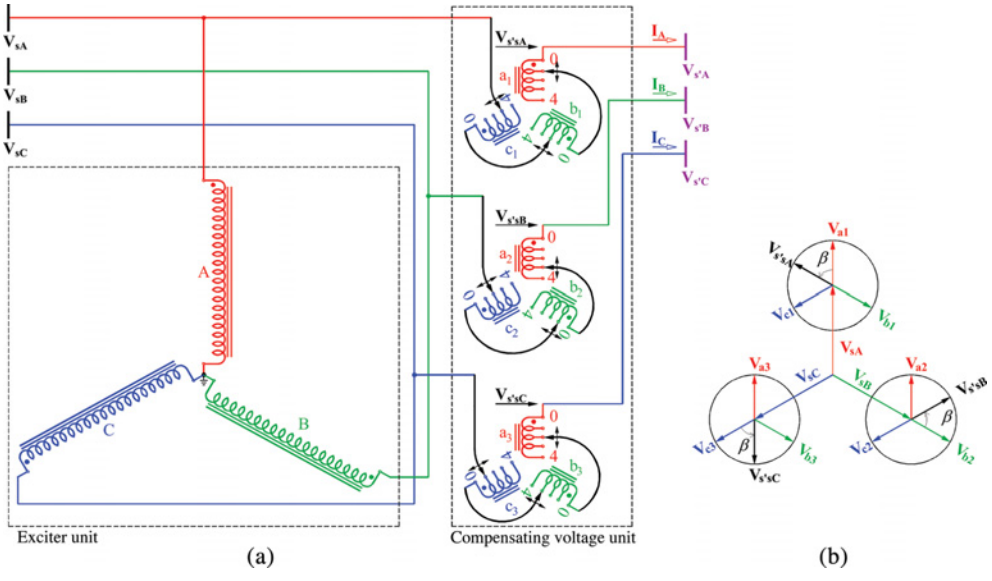

Figure 6.58 (a) ST for voltage compensation in the entire control range of 0° through 360°, (b) phasor diagram.

of turns. However, the number of turns in the a_1-b_2-c_3 set, b_1-c_2-a_3 set and c_1-a_2-b_3 set can be different from each other with one exception: when the ST is used as a voltage regulator to decrease the modified sending-end voltage, there are the same number of turns in two windings that are connected to each phase for the case when the relative phase angle (β) is 180°.

Since the LTCs that are used in the ST change their positions in steps, the compensating points in the ST are discrete in the allowable control range. If the allowable magnitude ($V_{s's}$) of the compensating voltage ($\mathbf{V}_{s's}$) is assumed to be 0.2 p.u. and the change of voltage in each step of an LTC is 0.05 pu, there are $N = 4$ steps associated with each secondary winding. A comprehensive study of the power system network integrated with the PFC can only show how many steps is the right number of steps. Figure 6.59

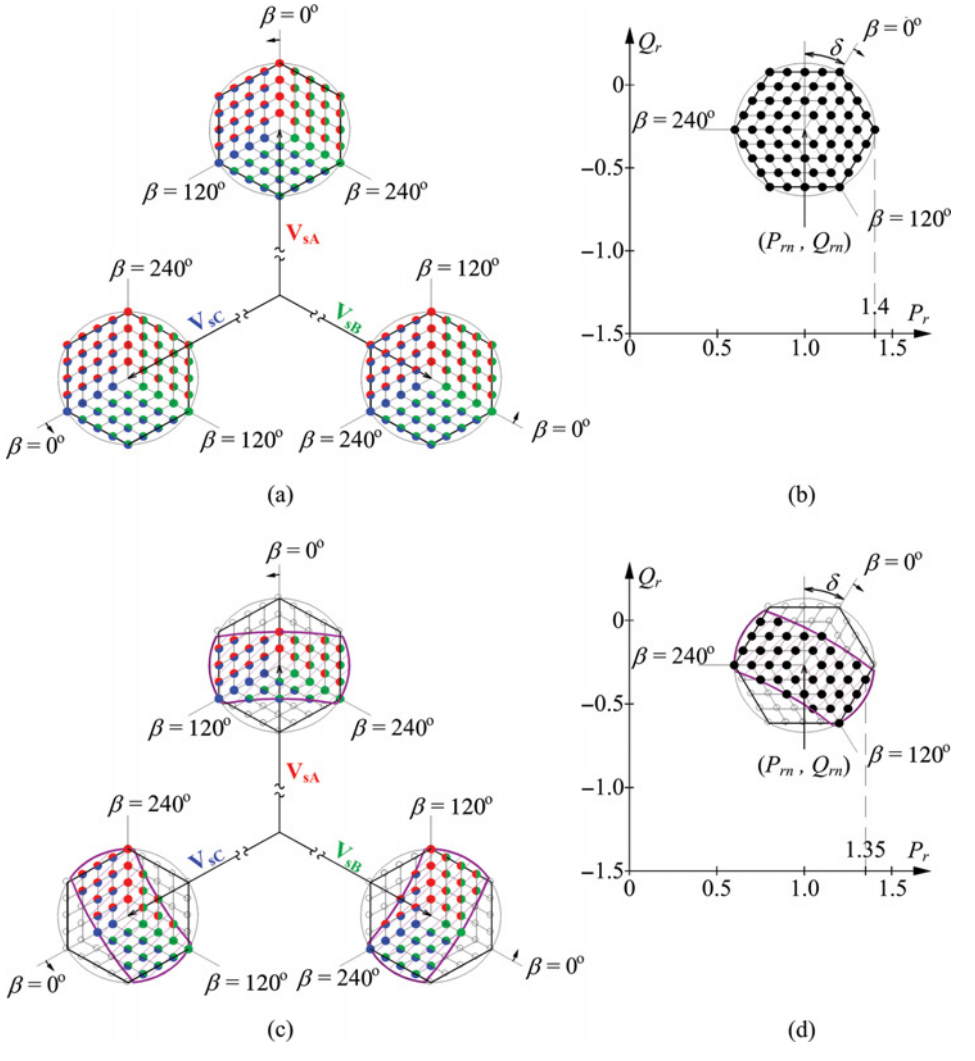

Figure 6.59 Compensating points with the use of the Sen transformer within the entire control range of 0° and 360°. Theoretically possible (a) modified sending-end voltage and (b) active and reactive power flows at the receiving end. Practically possible (c) modified sending-end voltage and (d) active and reactive power flows at the receiving end.

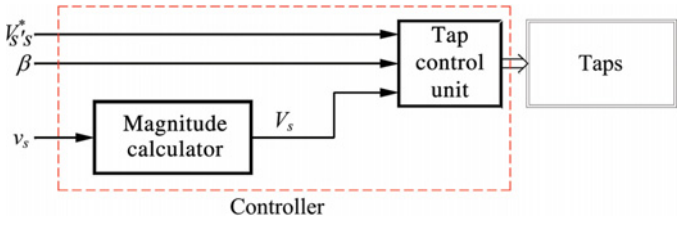

Figure 6.60 Open loop compensating voltage unit control block diagram of the ST.

shows that the theoretical circular control area is actually a hexagon. Shorter steps in the LTCs make the compensating points closer to each other and vice versa. Figure 6.59(a) shows the theoretically possible compensating points of the modified sending-end voltage with the use of the ST and Figure 6.59(b) the corresponding active and reactive power flows at the receiving end within the control range of 0° and 360°. Figure 6.59(c) and (d) show the practical control range of the ST. The filled dots, within the allowable voltage range in Figure 6.59(c), show a total of 36 compensating points of the ST lie within the 10% range of the nominal voltage. Figure 6.59(d) shows that the maximum active power flow enhancement at the receiving end, within the allowable voltage range, is actually 0.35 p.u. instead of the theoretically possible 0.40 p.u., as shown in Figure 6.59(b).

The controllable range of the active and reactive power flows can easily be determined with an open loop control by specifying to the tap control unit the rated compensating voltage ($V^*_{s's}$) and varying the relative phase angle (β) within its entire 360° range, as shown in Figure 6.60.

Consider the power system network of Figure 6.20. An ST was connected between BUS01 and BUS02. The ST consists of three primary windings and nine secondary windings (three for series connection in each of the three phases). Each primary and secondary winding is considered to have 1.0 p.u. and 0.2 p.u. voltage ratings, respectively. Considering an LTC contact located at every 5% mark, each secondary winding consists of four LTC taps. The leakage reactance of the ST was set to zero to eliminate its secondary effect. The natural flows of active and reactive powers (P_{rn} and Q_{rn}) at the receiving end are 209.12 MW (1.31 p.u.) and −68.54 Mvar (−0.43 p.u.), respectively.

The control was implemented in an open loop voltage injection mode travelling from one operating point to the next in one particular hexagon in the entire control range of 0° to 360°. The actual magnitude of the compensating voltage ($V_{s's}$) in p.u. (considering the primary voltage to be one p.u.) and its relative phase angle (β) are shown in Figure 6.61.

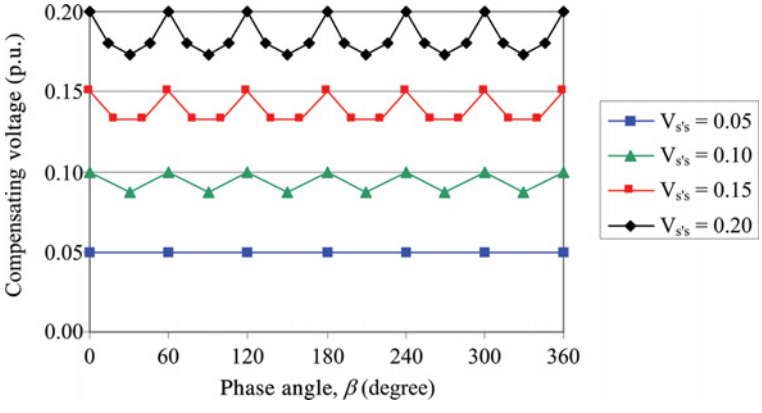

Figure 6.61 Magnitude of the series-connected compensating voltage ($V_{s's}$) in p.u. during the entire control range of its relative phase angle (β) from 0° and 360°.

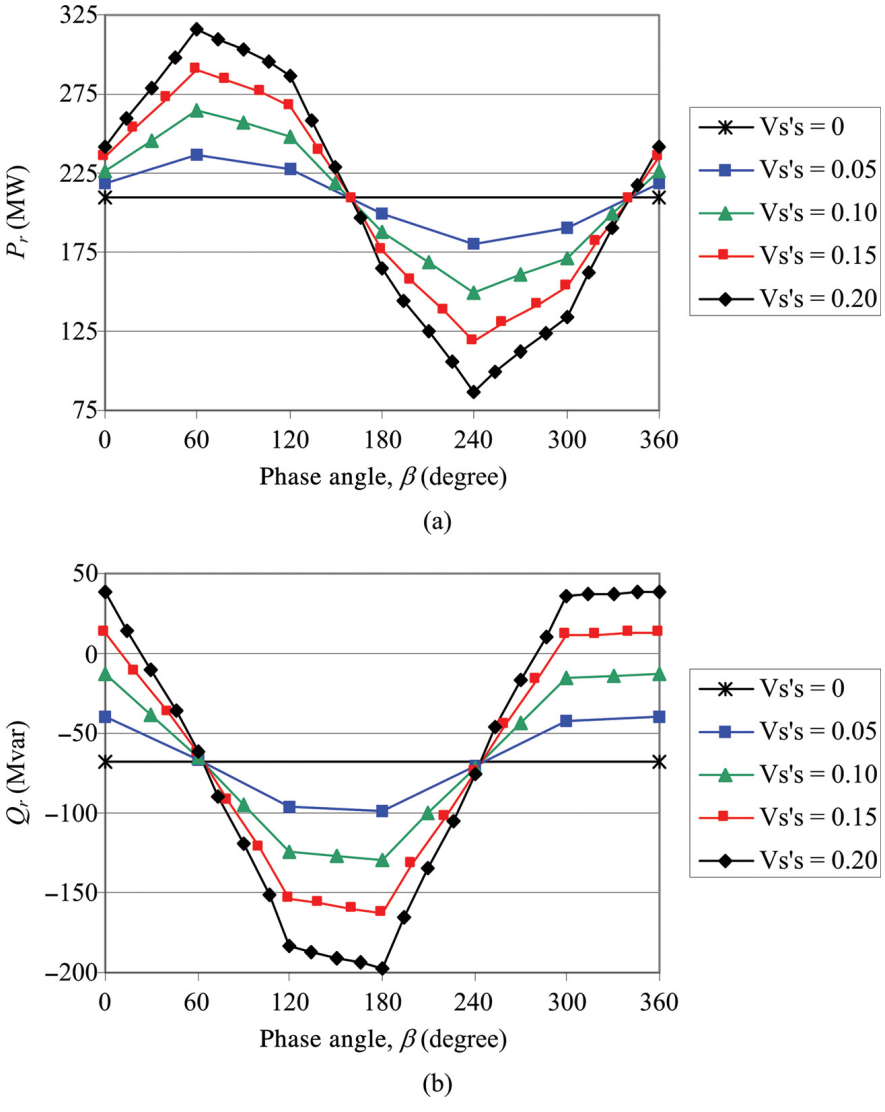

Figure 6.62 (a) Active power (P_r) and (b) reactive power (Q_r) flows at the receiving end during the entire control range of the relative phase angle (β) from 0° and 360°.

Figure 6.62 shows the active and reactive power flows (P_r and Q_r) at the receiving end during the entire stepped control range of the relative phase angle (β) from 0° and 360°. Figure 6.63 shows the active power (P_r) versus reactive power (Q_r) flow at the receiving end during the entire control range of the relative phase angle (β) from 0° and 360°. The *P*–*Q* plot is somewhat different from an ideal hexagon because the primary voltage ($\mathbf{V}_s$) keeps moving from its original (uncompensated) location due to the change of load in the line during compensation and the amount of Thevenin impedance at the point of compensation and the shunt loading due to the exciter unit of the ST. A more hexagon-like characteristic results if the point of compensation is closer to a stiff bus.

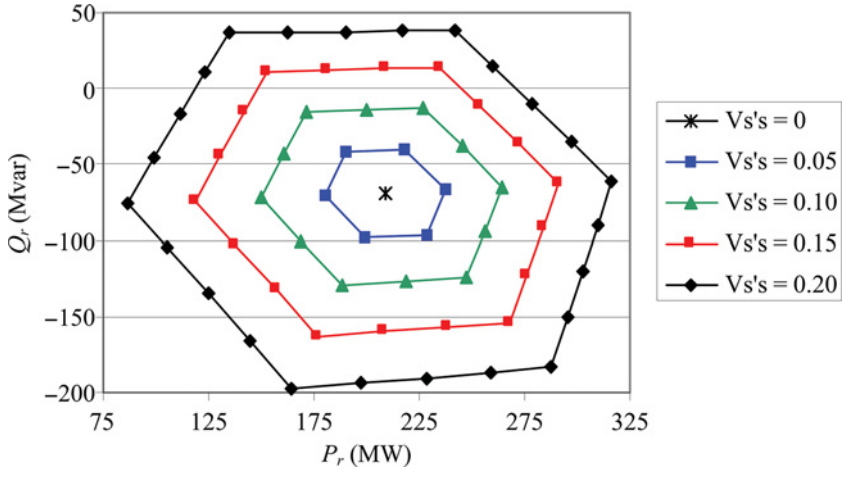

Figure 6.63 Active power (P_r) versus reactive power (Q_r) flows at the receiving end during the entire control range of the relative phase angle (β) from 0° and 360°.

6.7 Conclusion

Various tools for analysing flexible alternating current transmission Systems (FACTS) controllers have been presented. For calculation of the first-order magnitude of the benefits of FACTS controllers, simple formulas have been derived. FACTS controllers with various levels of details have been presented using an EMTP-type simulation package, which can be easily substituted by another circuit simulation package.

The models of a VSC-based FACTS controller include all the necessary components: a VSC with a DC link capacitor, a magnetic circuit and a realizable controller. The same techniques can be employed to model other power electronics based system, such as an adjustable speed drive, an arc furnace compensator or an HVDC transmission system.

The operation of the FACTS controllers is verified by the models connected to a simple two-bus network and the response of the controller is verified following a step change in the reference of the control inputs. These models demonstrate the performance of a FACTS controller that can be used to accurately predict the behaviour of the controller at an installation site. The FACTS controller models can be quite beneficial for utility system planners and they can easily be incorporated into a larger network to obtain validation of the simulation results and the field measurements.

Acknowledgement

A part of this chapter is taken from reference [4].

References

[1] Hingorani, N.G. and Gyugyi, L. (2000) *Understanding FACTS – Concept and Technology of Flexible AC Transmission Systems*, IEEE Press, New York.

[2] Sen, K.K. and Sen, M.L. (2009) *Introduction to FACTS Controller: Theory, Modeling, and Applications*, IEEE Press and John Wiley & Sons, Inc., New York.

[3] Faruque, M.O. and Dinavahi, V. (2007) A tap-changing algorithm for the implementation of Sen transformer. *IEEE Trans. on Power Delivery*, **22**(3), 1750–1757.

[4] Sen, K.K., Tang, L. (Chairmen), Dommel, H.W., *et al.* (1999) Guidelines for modelling power electronics in electric power engineering applications, Chapter 2, in *Modeling and Analysis of System Transients Using Digital Programs* (eds A. Gole, J.A. Martinez-Velasco and A. Keri), IEEE Special Publication TP-133-0, IEEE Catalog No. 99TP133-0.
[5] (1990) *ATP Rule Book*, Leuven EMTP Center (Ed.).
[6] *EMTP Rule Book*, EPRI/DCG Version 1.0.
[7] Dommel, H.W. (1986) *EMTP Reference-Manual (EMTP Theory Book)*, BPA.
[8] CIGRE Working Group 02 (SC 33) (1990) Guidelines for Representation of Network Elements when Calculating Transients. CIGRE Brochure 39.
[9] Ribeiro, P.F. (1998) Distribution system and other elements modeling, in Chapter 3 of *Tutorial on Harmonics Modeling and Simulation*, IEEE Special Publication TP-125-0.
[10] IEEE Joint Working Group (Dandeno, P.L. Chair) (1983) Symposium on Synchronous Machines Modelling for Power System Studies. *IEEE Power Engineering Society*, Publication 83THO101-6-PWR.
[11] IEEE Std. 115. (1983) IEEE Guide: Test Procedures for Synchronous Machines.
[12] Canay, I.M. (1993) Modelling of alternating-current machines having multiple rotor circuits. *IEEE Transactions on Energy Conversion*, **8**(2), 280–296.
[13] Rogers, G.J. and Shirmohammadi, D. (1987) Induction machine modelling for electromagnetic transient program. *IEEE Transactions on Energy Conversion*, **2**(4), 622–628.
[14] Dubé, L. and Dommel, H.W. (1977) Simulation of control system in an Electromagnetic Transient Program with TACS. Proceedings of IEEE PICA, pp. 266–271.
[15] Goldsworthy, D. and Vithayathil, J.J. (1986) EMTP model of an HVDC transmission system. Proceedings of the IEEE Montech '86 Conference on HVDC Power Transmission, pp. 39–46, September 26–October 1, 1986.
[16] Bui, L.X., Casoria, S. and Morin, G. (1989) Modeling of digital controls with EMTP. CEA Meeting, Montreal (Canada), March 25–29, 1989.
[17] Reeve, J. and Chen, S.P. (1984) Versatile interactive digital simulator based on EMTP for AC/DC power system transient studies. *IEEE Transactions on Power Apparatus and Systems*, **103**(12), 3625–3633.
[18] Fehrle, K.G. and Lasseter, R.H. (1981) Simulation of control systems and application to HVDC converters. IEEE Tutorial Course 81 EHO173-PWR on Digital Simulation of Electrical Transient Phenomena.
[19] Bui, L.X., Casoria, S., Morin, G. and Reeve, J. (1992) EMTP TACS-FORTRAN interface development for digital controls modeling. *IEEE Transactions on Power Systems*, **7**(1), 314–319.
[20] Morin, G., Bui, L.X., Casoria, S. and Reeve, J. (1993) Modeling of the Hydro-Quebec – New England HVDC system and digital controls with EMTP. *IEEE Transactions on Power Delivery*, **8**(2), 559–566.
[21] Lee, S.Y., Bhattacharya, S., Lejonberg, T., *et al.* (1992) Detailed modeling of static VAr compensators using the Electromagnetic Transients Program (EMTP). *IEEE Transactions on Power Delivery*, **7**(2), 836–847.
[22] Lefebvre, S. and Gérin-Lajoie, L. (1991) A static compensator model for the EMTP. Proceedings of IEEE PES Summer Meeting, Paper 91 SM 461–4 PWRS, San Diego (CA), 28 July–1 August 1991.
[23] Dubé, L. and Bonfanti, I. (1992) MODELS: a new simulation tool in the EMTP. *European Transactions on Electrical Power Engineering*, **2**(1), 45–50.
[24] Martinez, J.A. (1994) Simulation of power electronics using the EMTP, Part I: Power converters. a survey. Proceedings of UPEC'94, Galway (Ireland), 14–16 September 1994.
[25] Capolino, G.A. and Henao, H. (1988) ATP simulation for power electronics and AC drives. Proceedings of 15th European EMTP Users Group Meeting, Paper 88R-027, Leuven (Belgium), 17–18 October 1988.
[26] Capolino, G.A. and Henao, H. (1990) Simulation of electrical machine drives with EMTP. Proceedings of 18th European EMTP Users Group Meeting, Paper M7, Marseille (France), 28–29 May 1990.
[27] Martinez, J.A. and Capolino, G.A. (1991) TACS and MODELS: Drive simulation languages in a general purpose program. Proceedings of MCED'91, pp. R1–R13, Marseille (France), 1–2 July 1991.
[28] Capolino, G.A. and Henao, H. (1993) ATP advanced use for electrical drives. *EMTP Summer Course*, Leuven (Belgium), 5–8 July 1993.
[29] Daboussi, Z. and Mohan, N. (1988) Digital simulation of field-oriented control of induction motor drives using EMTP. *IEEE Transactions on Energy Conversion*, **3**(3), 667–673.
[30] Meng, X.Z., Sloot, J.G.J. and Rijanto, H. (1995) Modelling of semiconductor fuses in EMTP. Proceedings of First International Conference on Power Systems Transients (IPST'95), Lisbon (Portugal), 3–7 September 1995, pp. 481–486.
[31] Martinez-Velasco, J.A., Abdo, R. and Capolino, G.A. (1995) Advanced representation of power semiconductors using the EMTP. Proceedings of First International Conference on Power Systems Transients (IPST'95), Lisbon (Portugal), 3–7 September 1995, pp. 505–510.

[32] Lefebvre, S. and Rangel, R.D. (1995) Modeling of power electronics devices in EMTP-TACS. Proceedings of First International Conference on Power Systems Transients (IPST'95), Lisbon (Portugal), 3–7 September 1995, pp. 511–516.

[33] Martinez, J.A. and Capolino, G.A. (1992) EMTP simulation of power electronics and drives using data modularization. Proceedings of First International Aegean Conference on Electrical Machines and Power Electronics, Kucadasi (Turkey), 27–29 May 1992.

[34] Szechtman, M., Wess, T. and Thio, C.V. (1991) First benchmark model for HVDC control studies. *Electra*, (135), 55–73.

7

Applications of Power Electronic Devices in Distribution Systems

Arindam Ghosh and Farhad Shahnia

7.1 Introduction

One of the main concerns in any electric power distribution system is the reliability of the supply. Usually the supply reliability pertains to maintaining the continuity of power supply. Indices such as system average interruption frequency index (SAIFI), customer average interruption frequency index (CAIFI), system average interruption duration index (SAIDI) and customer average interruption duration index (CAIDI) are used for quantifying the system reliability [1, 2]. By calculating these indices, distribution systems engineers can determine whether yearly interruptions affect one group of customers more than the others so that corrective measures can be taken. Generally, the organizational ability of a particular distributor can be determined by these indices and sometimes system regulators can ask the company to improve their scheduled maintenance process for better reliability.

However, reliability is not the only major concern these days – power quality is equally important. Power quality is defined as having a supply voltage that is a pure sinewave of rated magnitude and frequency (50 or 60 Hz), even though $\pm$ 5% variation in these quantities are often acceptable. The quality of power is said to have deteriorated when the supply voltage fails to attain the ideal specifications mentioned above. Unfortunately, the actual AC line supply that we receive every day departs from the ideal specifications. The causes of power quality problems are complex and not always easy to detect. Table 7.1 lists various power quality problems, their characterization methods and possible causes [3].

There are different adverse effects of power quality problems. An impulsive transient can cause equipment damage at its point of inception, while transient overvoltage resulting from oscillatory transient can damage power line insulators. Undervoltages can cause motor or equipment tripping or stalling, whereas overvoltages can cause equipment damage. Voltage unbalance can cause temperature rise in motors and can even cause a large motor to trip. Harmonics, DC offset and notching cause waveform distortions. Unwanted harmonic currents flowing through the distribution network can causes needless losses. Harmonics can also cause malfunction of ripple control or traffic control systems, losses and heating in transformers, electromagnetic interference (EMI) and interference with communications systems. DC offsets can cause saturation in the power transformer magnetic circuits. A notch is a periodic transient that rides on the supply voltage. It can damage capacitive components connected in

Transient Analysis of Power Systems: Solution Techniques, Tools and Applications, First Edition.
Edited by Juan A. Martinez-Velasco.

Table 7.1 Power quality problems and their causes.

Specific categories	Methods of characterization	Typical causes
Impulsive transient	Peak magnitude, rise time and duration	Lightning strike, transformer energization, capacitor switching
Oscillatory transient	Peak magnitude, frequency components	Line or capacitor or load switching
Voltage sag	Magnitude, duration	Ferroresonant transformers, single line-to-ground faults
Voltage swell	Magnitude, duration	Ferroresonant transformers, single line-to-ground faults
Temporary interruption	Duration	Temporary (self-clearing) faults
Undervoltage	Magnitude, duration	Switching on loads, capacitor de-energization
Overvoltage	Magnitude, duration	Switching off loads, capacitor energization
Sustained interruptions	Duration	Faults
Unbalance	Symmetrical components	Single-phase loads, single-phasing condition
Harmonics	THD, harmonic spectrum	Adjustable speed drives and other nonlinear loads
Notching	THD, harmonic spectrum	Power electronic converters
DC offset	volts, amps	Geo-magnetic disturbance, half-wave rectification
Voltage flicker	Frequency of occurrence	Arc furnace, arc lamps

shunt due to the high rate of voltage rise at the notches. Voltage flickers can have adverse effects on human health as the high frequency flickering of light bulbs, fluorescent tubes or television screens can cause strain on the eyes, resulting in headaches or migraines. Voltage flicker can also reduce the lifespan of electronic equipment.

The term custom power (CP) pertains to the use of power electronic controllers for distribution systems such that almost uninterrupted high-quality power can be supplied to the customers. Some of the CP devices (CPDs) are used for network reconfiguration (such as static transfer switch, static circuit breaker and current limiter). The others are used for load and supply compensation. We shall restrict our attention to this latter group. The devices belonging to this group are [3]:

- distribution static compensator (DSTATCOM) – a shunt-connected device that can perform both load compensation (power factor correction, active harmonic filtering and current balancing) and voltage compensation by balancing the voltage at the point of common coupling (PCC)
- dynamic voltage restorer (DVR) – a series-connected device that can protect downstream critical loads from voltage sag, swell and even harmonics
- unified power quality conditioner (UPQC) – this has both shunt and series connection and can perform a multitude of tasks by combining the effects of DSTATCOM and DVR.

Recently, there has been a growing interest by residential customers in installing single-phase grid-connected rooftop photovoltaic (PV) cells due to renewable energy incentive polices in several countries. The output power of these PVs is not controlled and is dependent on the instantaneous power from the sun. This causes several technical problems such as harmonics, voltage rise and unbalance and power loss. Furthermore, rooftop PVs are usually distributed randomly among the residential loads, depending on

the preference and financial capability of customers. Their ratings can also vary widely. This randomness in the location and rating of the PVs installed by the customers will increase the voltage unbalance (VU) in the network [4]. Another major concern is the voltage rise due to the increasing penetration of PVs, especially since they generate maximum power during the day, when the demand for domestic load is low.

The sales of electric vehicles (EVs) are on the rise and it is expected that the annual sales will exceed a million cars in the next few years. They will cause a significant increase in residential loads when operated in grid-to-vehicle (G2V) mode, especially when the use of EVs is concentrated in a particular area. They can be charged in two general locations: individual charging points (in residential and small business places) and charging stations. Rapid charging (in less than one hour) is expected in charging stations which are being fed from three-phase networks. However, normal charging (in 6–8 hours) from single-phase low voltage (LV) outlets is expected in individual charging points. EV characteristics can impose technical problems on the network and require an expansion or modification to the network structure, policies, control and protection. On the other hand, when operated in vehicle-to-grid (V2G) mode, the EVs can act as single-phase power sources that can cause voltage rise and unbalance problems [5].

This chapter begins with a discussion of different CPDs and their use in alleviating some of the power quality problems. Later, the use of these devices to dynamically improve voltage profile and unbalance that are arising due to the growth of DERs is presented.

7.2 Modelling of Converter and Filter Structures for CPDs

The custom power devices that will be discussed below utilize power electronic based voltage source converters (VSCs). There are a large variety of VSCs that can be used for this purpose. The normal practice is to use full bridge converters with three or four legs. However, depending on the power levels, multilevel converters, such as diode clamped converters or flying capacitor converters, can also be used. We will give a brief description of the converter requirements below. Also note that each converter requires passive filters on the output to eliminate high frequency switching harmonics. A brief description of the filter structures is also given. The choice of filter parameters depends on the bandwidth requirements of these devices and will not be discussed here. Furthermore, several methods can be used for converter modulation and control, such as PWM, hysteretic band control, space vector modulation, current control and voltage control. These will also not be discussed here.

7.2.1 Three-Phase Converter Structures

The schematic diagram of a three-phase full bridge converter is shown in Figure 7.1. This is the most common form of three-phase converter used in various applications. The converter DC side (often called the DC bus) is supplied by a voltage source V_{dc}. The converter contains six switches S_1 to S_6. Each switch consists of a power semiconductor device (e.g. IGBT, MOSFET) and an antiparallel diode that

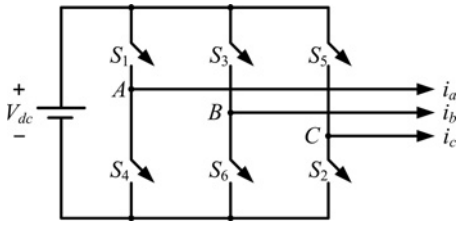

Figure 7.1 A three-phase VSC.

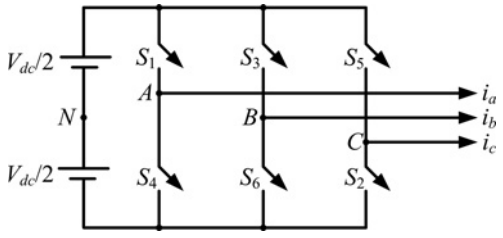

Figure 7.2 A neutral-clamped three-phase VSC.

maintains the continuity of the current once the switch turns off. To prevent the switches of a leg from short-circuiting the DC bus, the switches in each leg are complementary, that is, when S_1 is on, S_4 is off and vice versa. This converter, however, has the disadvantage that the algebraic sum of the three output currents must be zero, that is, $i_a + i_b + i_c = 0$. This is a limitation if the converter is required to supply unbalanced loads. In that case, only two phases can be controlled independently. Therefore this type of converter is not usually used in CPDs – only those converters whose phases can be controlled independently are used.

The converter structure shown in Figure 7.2 is essentially the same as that shown in Figure 7.1, except that the DC bus is split into two, with a centre point at N. The DC bus voltage is still equal to V_{dc}. But it now contains two DC sources, each equal to $V_{dc}/2$. The centre point N, when connected to the load neutral, provides a path for the zero-sequence current to flow. Hence, the three legs of the converter can be treated separately and we can control each leg independent of the other two legs [3].

The four-leg VSC topology was first proposed in [6] and was subsequently used and analysed in [7, 8]. This is shown in Figure 7.3, in which the centre point of the fourth leg (n') is connected to the load neutral (n) through a resistor and an inductor. The current though this path (i_0) is used to cancel the zero-sequence component of the load current. In this case also, we can treat each individual phase separately.

Alternatively, for high-power applications, the VSC shown in Figure 7.4 can be used. It contains three H-bridge converters that are connected to a common DC source [9]. The outputs of the VSCs are connected to three single-phase transformers. The secondary sides of the transformers are connected in wye, with the neutral point being connected to the load neutral n. The transformers provide voltage boosting and isolation and prevent the converter switches from shorting the DC bus. In this case also, we can treat each of the phases independently.

7.2.2 *Filter Structures*

As was mentioned in the previous section, each phase of the converters needs to be controlled independently. Therefore a separate passive filter is needed on the output of each phase. Two types of filters are

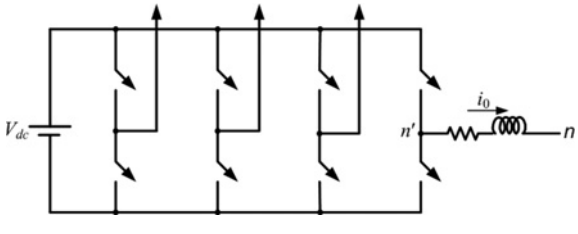

Figure 7.3 A four-leg VSC.

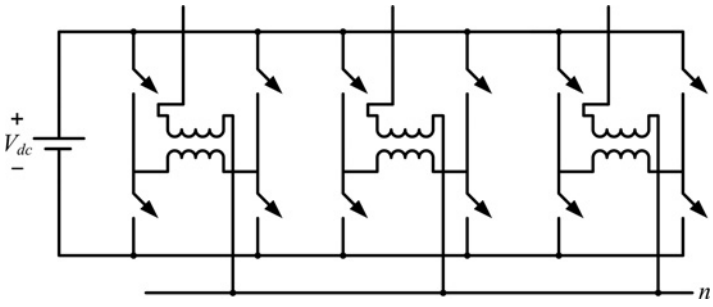

Figure 7.4 VSC structure with three h-bridges and transformers.

commonly used – inductance–capacitance (LC) and inductance–capacitance–inductance (LCL) filters. The single-phase equivalent circuit of a converter, with its associated filter, is shown in Figure 7.5, where the inductors are denoted by L_1 and L_2, while the capacitor is denoted by C. The voltage across the capacitor is denoted by v_c. The resistances R_1 and R_2 are associated with the inductances L_1 and L_2 respectively, arising due to their finite quality factor. When transformers are used (as in Figure 7.4), their leakage inductances and resistances can be used in the filters.

It is interesting to note that these passive filters can be used for voltage or current tracking. For example, consider a CPD that needs to regulate a PCC voltage. Then a converter with an LC filter can be connected in shunt with the PCC. The converter regulates the voltage v_c across the filter capacitor shown in Figure 7.5(a), which is essentially the PCC voltage. On the other hand, if a CPD needs to inject current, an LCL filter can be connected at the output of the converter. The converter then tracks the reference for the current through the inductor i_2 in Figure 7.5(b). The stability of converter operation and the filter bandwidth are discussed in [10].

7.2.3 Dynamic Simulation of CPDs

CPDs can be built in laboratory setups, where only their limited functionalities can be tested. Usually they are connected to large power distribution systems. Therefore they need to be tested thoroughly

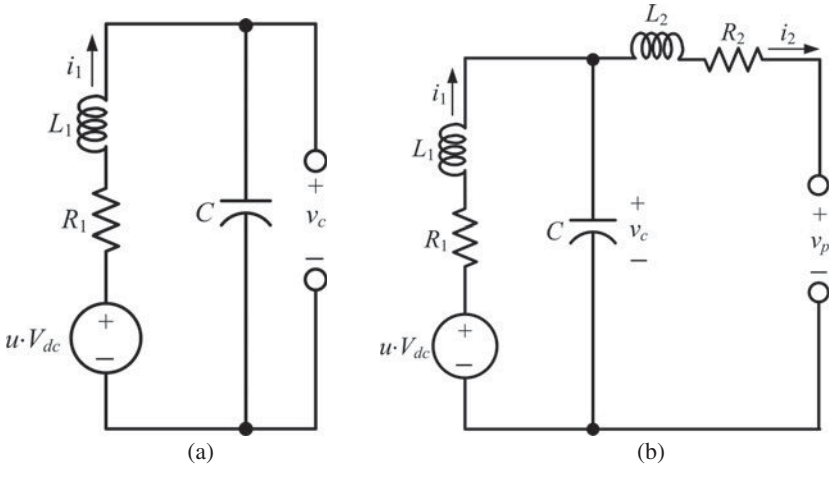

Figure 7.5 Single-phase VSC equivalent circuit with (a) LC and (b) LCL filter.

before they can be successfully deployed in the field. For dynamic modelling of these devices, software like Matlab/Simulink or PSCAD can be used. Matlab is an excellent tool that can be used for converter controller design. For this, the converter plus filter equivalent circuits (e.g. those shown in Figure 7.5) are first expressed in the state-space or input-output forms. Suitable feedback control laws are then obtained through Matlab. Note that the control design must take into consideration the employed modulation technique, such as PWM or hysteretic. All the simulation studies presented in this chapter have been prepared in PSCAD with the control parameters obtained from Matlab. The output simulation results from PSCAD are captured and exported to Matlab for plotting, as these plots give better clarity.

As mentioned earlier, each switch in Figures 7.1–7.4 contains a power semiconductor device with an antiparallel diode and proper snubber circuits. Even though ideal switches (without snubbers) or transformers can be used, this is not advisable as it can give over-optimistic output data. PSCAD is a discrete-time simulation tool, even though it has the capability of data interpolation. The simulation time has to be chosen very carefully. A general rule of thumb is to use a simulation time-step that gives more accurate results, even though this might cause the simulation time to increase. However, a very small time-step can also cause numerical instability. In this chapter, a time-step of 10 μs has been chosen for PSCAD simulations.

7.3 Distribution Static Compensator (DSTATCOM)

As mentioned, a DSTATCOM is a shunt-connected device. It can perform both current and voltage control separately. In this section, we will discuss them briefly.

7.3.1 Current Control Using DSTATCOM

The schematic diagram of a distribution system compensated by a DSTATCOM is shown in Figure 7.6, in which the DSTATCOM is represented by an ideal current source that injects the current i_f into the system. It is assumed that the load is reactive, nonlinear and unbalanced. In the absence of the DSTATCOM, the current i_s flowing from the source through the feeder will also be unbalanced and distorted and, due to the feeder and transformer impedances, so will be the voltages of buses 1 and 2. Therefore the loads connected to these buses will be affected.

In the analysis presented here, instantaneous quantities will be denoted in lowercase, while the rms quantities will be given as uppercase letters. Also, the phases a, b and c will be denoted by the subscripts a, b and c, respectively. Applying Kirchhoff's current law at the PCC, we have

$$i_s + i_f = i_l, \tag{7.1}$$

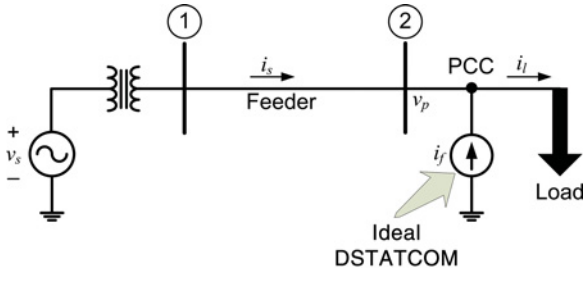

Figure 7.6 Schematic diagram of load compensation.

where i_l is the load current. Let the reference for the output current of the ideal DSTATCOM current be generated based on the following three objectives:

1. The source currents are balanced, that is, $i_{sa} + i_{sb} + i_{sc} = 0$.
2. The source currents are (near) unity power factor, that is, $\angle V_{pk} \approx \angle I_{sk}$, $k = a,b,c$.
3. The DSTATCOM only supplies the load reactive power and no real power so that the entire load power requirement is supplied by the source.

Let us define the load current flowing through a phase as

$$i_l = i_{lp} + i_{lq} + i_{lh}, \tag{7.2}$$

where i_{lp} is the active power component of the load current, i_{lq} is its reactive power component and i_{lh} is the harmonic component of the load current. Then from (7.1) and objectives 2 and 3 above, the DSTATCOM current must be equal to

$$i_f = i_{lq} + i_{lh}. \tag{7.3}$$

Furthermore, to satisfy objective 1, the DSTATCOM must supply the negative and zero sequence components of the load current. This is called the operation of the DSTATCOM in a current control mode.

The distribution system shown in Figure 7.6 is redrawn in Figure 7.7 where the DSTATCOM includes a VSC and three identical LCL filters. The neutral points N, n and n' are isolated for a three-phase, three-wire (3p3w) system and are connected together through the neutral wire for a three-phase, four-wire (3p4w) system. In a 3p3w system, the zero-sequence current has no path to flow and is hence forced to zero, whereas it circulates through the neutral wire in a 3p4w system.

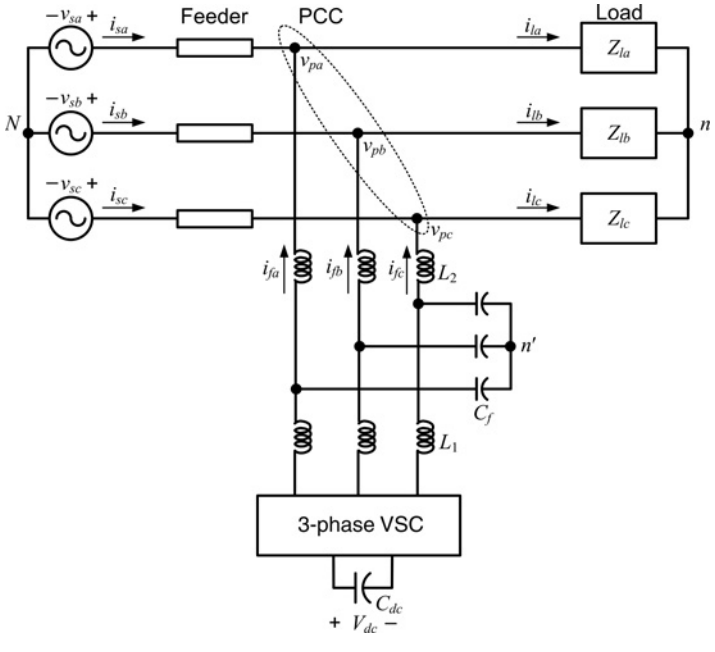

Figure 7.7 Schematic diagram of a DSTATCOM connection for load compensation.

The DC side of the DSTATCOM is supplied from the DC capacitor C_{dc}, as shown in Figure 7.7. This capacitor voltage needs to be maintained above a certain pre-specified value for proper tracking of the output current to occur. If the voltage is below this value, the current tracking degrades. When this voltage gradually decreases, the current tracking gradually degrades, leading to further decrease in the voltage and therefore to a system collapse. Ideally, as given in objective 3 above, the DSTATCOM should not consume or supply any real power. Theoretically therefore, once the capacitor C_{DC} is precharged, it will keep on maintaining its charge (and hence voltage) since no real power transfer occurs between the capacitor and the AC system through the DSTATCOM. Practically, however, the VSC will have switching losses, the passive components will have losses since they are not ideal and the transformers will have core losses. If these losses are to be supplied by the precharged DC capacitor, then its voltage will collapse.

Therefore the condition of objective 3 needs to be relaxed, such that the DSTATCOM can draw enough power to replenish these losses. If the exact amount of power is drawn from the AC system, then the capacitor voltage will neither rise nor fall. From this perspective, a proportional plus integral (PI) controller can be used for the DC capacitor voltage regulation. First the DC capacitor voltage is averaged by a low-pass filter (LPF) to obtain V_{dc}^{av}. This is then compared to its reference V_{dc}^{ref} and the error is passed through a PI controller. The output of the controller gives the power loss p_{loss} that needs to be drawn from the system, as per

$$p_{loss} = K_P \left(V_{dc}^{ref} - V_{dc}^{av} \right) + K_I \int \left(V_{dc}^{ref} - V_{dc}^{av} \right) dt \tag{7.4}$$

One of the most important and challenging aspects of DSTATCOM operation in current control mode is the calculation of the reference currents based on the measurements of the load and source currents and PCC voltage. This is called the reference current generation scheme. Several methods have been proposed for accomplishing this task [9, 11–16]. It is beyond the scope of this chapter to discuss these methods. Below we simply summarize the method presented in reference [9], which has been generalized in reference [17].

The reference currents that the DSTATCOM has to inject are computed based on the three objectives mentioned earlier. The instantaneous values of these currents, computed based on instantaneous measurements, are given by

$$\left.\begin{aligned} i_{fa}^{*} &= i_{la} - \frac{v_{ta}}{\Delta} p_{PCC} \\ i_{fb}^{*} &= i_{lb} - \frac{v_{tb}}{\Delta} p_{PCC} \\ i_{fc}^{*} &= i_{lc} - \frac{v_{tc}}{\Delta} p_{PCC} \end{aligned}\right\}, \tag{7.5}$$

where $\Delta = v_{ta}^2 + v_{tb}^2 + v_{tc}^2$ and p_{PCC} is the power supplied by the source. This is the summation of p_{loss}, obtained from DC capacitor voltage control of (7.4), and the average of the load power p_{lavs}, that is,

$$p_{PCC} = p_{lavs} + p_{loss}. \tag{7.6}$$

The average of the load power p_{lavs} can be computed by passing the three-phase power measurement through an LPF.

Ordinarily v_t should be equal to v_p. However, when the load currents are distorted and unbalanced, the PCC voltages are also distorted and unbalanced. If then these instantaneous values are used in (7.5), some amount of distortion and unbalance will remain in the source currents. To avoid this, the fundamental positive sequence components of v_p are obtained, and they are substituted as v_t [6]. We will now demonstrate the operation of the current-controlled DSTATCOM through an example. In this

Table 7.2 Example 7.1: System parameters.

Source voltage		11 kV (L-L, rms), 50 Hz
Feeder impedance		$6.05 + j36.29\ \Omega$
Load	Linear part	$Z_{la} = 24.2 + j60.51\ \Omega$
		$Z_{lb} = 12.2 + j31.42\ \Omega$
		$Z_{lc} = 48.2 + j94.23\ \Omega$
	Nonlinear part	Full-bridge diode rectifier that supplies 100 Ω and 100 mH
DSTATCOM losses (R_f)		12.125 Ω referred to the AC side
Transformers		Single-phase, 3 kV/11 kV, 1 MVA, 10% leakage reactance
DC bus capacitor		5000 μF

and all the other subsequent plots, phases a, b and c will be denoted by solid, dashed and dotted lines, respectively.

Example 7.1 Let us consider an example to show the behaviour of the DSTATCOM with the above-mentioned reference generation and DC capacitor control law. The system parameters used in this study are given in Table 7.2. The uncompensated load (and hence source) currents and PCC voltages are shown in Figure 7.8. It can be seen that they are unbalanced and distorted. Now let us consider the case in which the DSTATCOM is connected and the system is in steady state when the load of phase-a is disconnected at 0.5 s. The three-phase load currents are shown in Figure 7.9(a). The PCC voltages and source currents are shown in Figure 7.8(b) and (c), respectively. It can be seen that they are sinusoidal and balanced due to the DSTATCOM action. Also, once one of the phases is disconnected, the source currents drop, causing a rise in the PCC voltages.

7.3.2 Voltage Control Using DSTATCOM

From the results of the previous subsection, it is clear that a DSTATCOM can balance the upstream source side currents. As a consequence, if the supply voltage is balanced, the PCC voltages also get

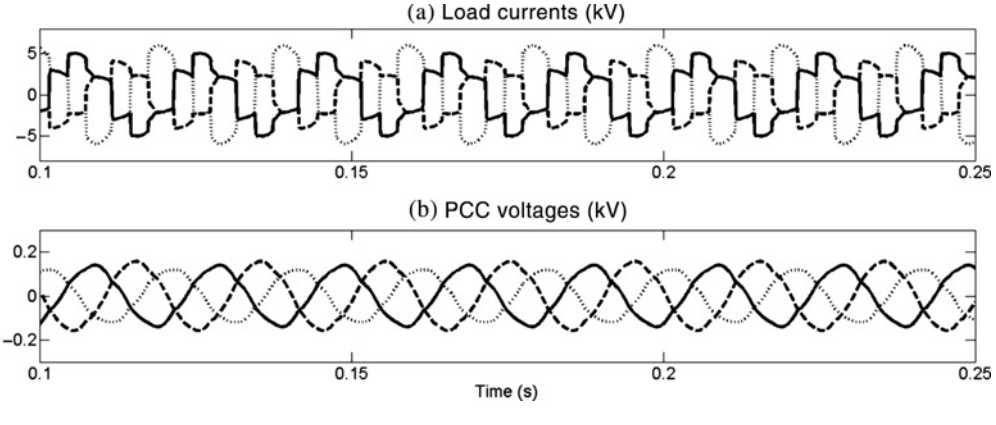

Figure 7.8 Example 7.1: Load currents and PCC voltages before DSTATCOM connection.

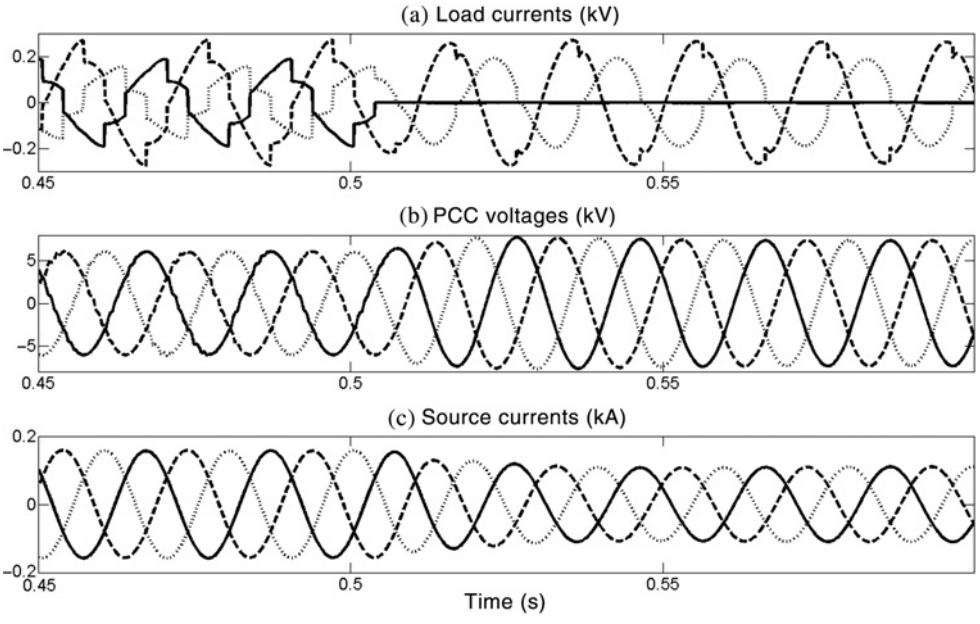

Figure 7.9 Example 7.1: Load currents, PCC voltages and source currents with DSTATCOM connection.

balanced. However, in this scheme, the DSTATCOM cannot regulate the PCC voltages, that is, these voltages are dictated by the line loss that depends on the load level. Given below is a method in which a DSTATCOM can be used only for controlling the voltage of the PCC bus, irrespective of any unbalance and/or distortion in the load currents or source voltages [18].

Consider the distribution system structure with DSTATCOM of Figure 7.7. Let us assume that the inductor L_2 is removed and only an LC filter is connected to the output of the VSC. Therefore, it can be surmised that the PCC voltage is the voltage across the filter capacitor C_f. Hence, if we can set a prespecified reference for this voltage and track the reference voltage through switching the VSC, we can regulate the PCC voltage tightly. This is called the operation of the DSTATCOM in a voltage-control mode.

In the voltage-control mode, the PCC voltage magnitude can be chosen arbitrarily. However, its angle has to be chosen carefully. As mentioned above, the DSTATCOM losses must come from the supply side. This means that the power that reaches the PCC terminal must flow in two directions – towards the load to meet the load requirement and towards the DSTATCOM to supply the losses in the circuit. Note also that the power flow between two AC buses that are separated by an inductance mainly depends on the relative angle difference. Therefore, the angle of the PCC voltage must be chosen such that the required amount of power flows from the upstream source. Again, this is accomplished by the DC bus voltage control as per

$$\delta = K_P \left(V_{dc}^{ref} - V_{dc}^{av} \right) + K_I \int \left(V_{dc}^{ref} - V_{dc}^{av} \right) dt. \tag{7.7}$$

This means that the voltage angle has been made a function of any deviation of the average DC voltage from its reference.

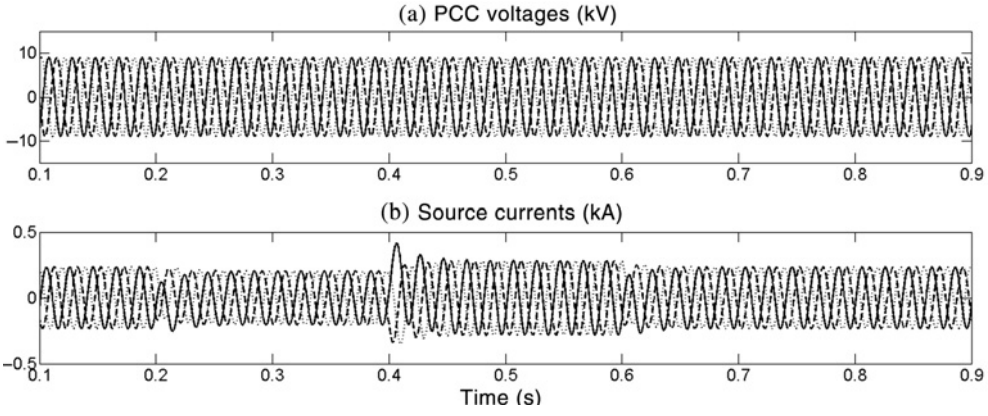

Figure 7.10 Example 7.2: PCC voltages and source currents with a voltage controlled DSTATCOM under voltage sag/swell.

Example 7.2 We consider the same systems as given in Example 7.1. The DSTATCOM has an LC filter and is supplied by a DC source instead of a DC capacitor. Initially, the source voltage is 9 kV peak (i.e. 11 kV L-L rms) and the desired PCC voltage is also chosen as 9 kV peak, while its angle is chosen as -1 rad. The source voltage drops to 5 kV at 0.2 s and rises to 12 kV at 0.4 s. Subsequently at 0.6 s, the peak voltage returns to 9 kV. Furthermore, at 0.8 s, the load of phase-a is disconnected. The PCC voltages are shown in Figure 7.10(a). It can be seen that they remain balanced sinusoidal and at the desired level despite the voltage sag/swell, nonlinear unbalanced load and load disconnection. The source currents are shown in Figure 7.10(b). It can be seen that they vary with the change in the source voltages. In this case, however, the DSTATCOM can exchange both active and reactive power.

Let us now connect a 10 mF DC capacitor instead of the DC source. The reference DC voltage is chosen as 3.5 kV and only a proportional gain (K_P) with a value of -0.75 is chosen. Note that, if V_{dc}^{av} falls below V_{dc}^{ref}, δ must be advanced to draw more power from the system. This is why the value of K_P is chosen to be negative. The peak of the PCC voltage is chosen as 9.0 kV. The DC capacitor voltage is shown in Figure 7.11. It can be seen that the DC voltage settles around 2.6 kV while the angle δ settles around $-37°$ in about six cycles (0.12 s). The PCC voltages are also shown in Figure 7.11. They become balanced and attain their peak value around four cycles. However, they cannot settle until the angle and the DC capacitor voltage settle.

7.4 Dynamic Voltage Restorer (DVR)

A DVR is a series-connected device that is installed to protect sensitive loads from unbalance, sag/swell and/or distortion in the supply voltage. The basic principle of a series compensator is simple: by adding a voltage with required magnitude and frequency, the series compensator can restore the load side voltage to the desired amplitude and waveform, even when the source voltage is unbalanced or distorted. Since the main purpose of a series compensator is to dynamically restore the bus voltage of any critical load to its nominal operating waveform, it is called the dynamic voltage restorer [19].

A typical DVR connection is shown in Figure 7.12. It is connected in series with the distribution feeder that supplies a sensitive load. If, for a fault or line switching at any point of the network, the incoming feeder voltage drops suddenly then the DVR can insert a voltage to offset the voltage drop such that the load bus voltage remains free of transients. Without the presence of the DVR, the voltage sag may trip the sensitive load, causing a loss of production. Note, however, that the rating of a DVR is not unlimited. Thus a DVR can only partially restore the load voltage during very large sags in the source voltage.

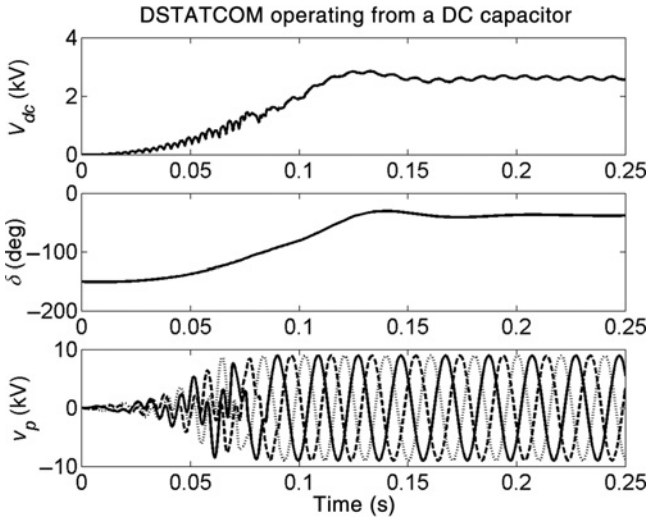

Figure 7.11 Example 7.2: DC capacitor voltage, its angle and PCC Voltages under closed-loop control.

The structure of a DVR-connected distribution system is shown in Figure 7.13. Since the DVR has to add voltage in series with the distribution system, the filter capacitors are placed in series with the lines. Often, the DVR protects a very sensitive load that requires tightly regulated voltage. For example, the voltage magnitude can be 1 p.u. Then the DVR makes the load voltage v_{L1} equal to 1 p.u., irrespective to any sag/swell, unbalance or harmonics in the source side voltage. From Figure 7.13, KVL at the PCC gives

$$v_p + v_d = v_{L1} \quad \Rightarrow \quad v_d = v_{L1} - v_p, \tag{7.8}$$

where v_d is the voltage added by the DVR. Now let us assume that the desired magnitude and the angle of the load voltage are given. Then, the time waveform of the desired load voltage v^*_{L1} can be computed. From this, the desired voltage waveform to be added by the DVR is given by

$$v^*_d = v^*_{L1} - v_p. \tag{7.9}$$

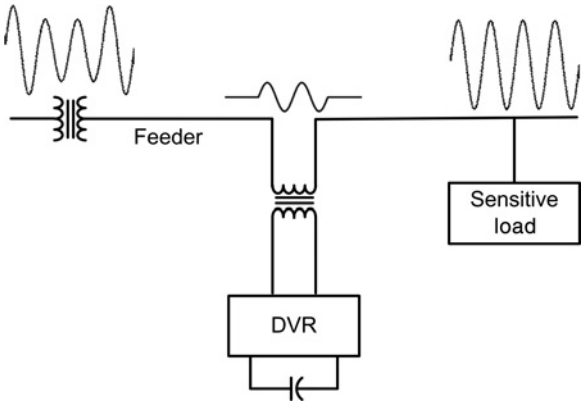

Figure 7.12 DVR inserting voltage to protect a sensitive load.

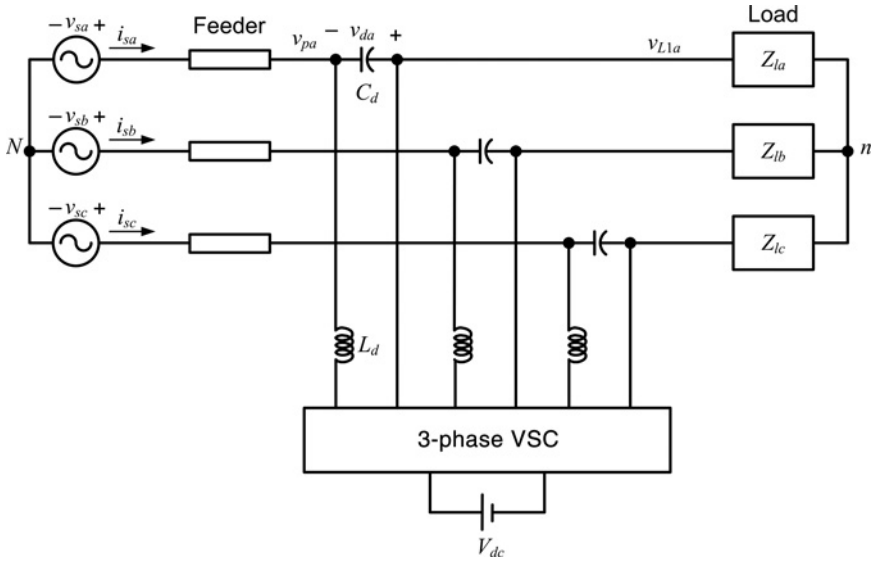

Figure 7.13 Schematic diagram of a DVR compensated distribution system.

The DC bus of the DVR is shown to be a DC source in Figure 7.13. It can however, be a DC source, a DC capacitor or a rectifier. The DC source can be in the form of a battery, fuel cell and so on. The DC capacitor (unlike a DSTATCOM) has the disadvantage that it has a limited range of operation. It can hold the load voltage for a sag of about 15–20%, after which the DC capacitor starts discharging. However, when the DC capacitor is connected to the upstream side through a rectifier such that real power exchange can take place through this path, the DVR can compensate for much deeper sags. This configuration is called a rectifier-supported DVR.

The schematic diagram of the rectifier supported DVR is shown in Figure 7.14. An uncontrolled rectifier supplies the DC bus capacitor C_{dc}. A smoothing inductor L_{DC} is also connected to the DC side of the rectifier. The rectifier is supplied by the AC system through a converter transformer. To bypass the

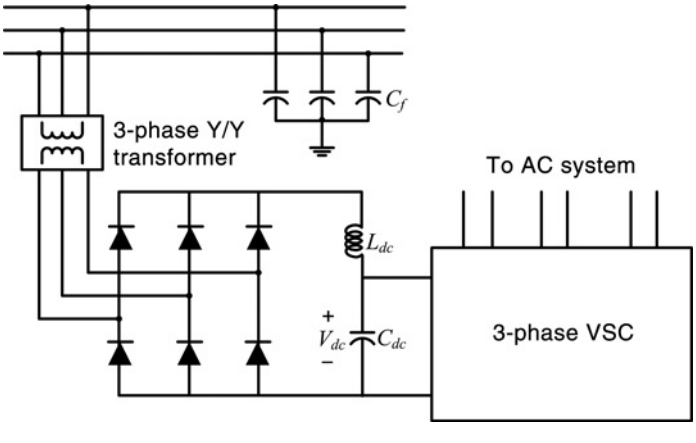

Figure 7.14 Schematic diagram of a rectifier supported DVR.

harmonics generated by the rectifier, filter capacitor C_f is connected in shunt to each of the three phases. Even though the uncontrolled rectifier provides a path for the active power to flow, the DC capacitor voltage V_{DC} still needs to be regulated for faster and better output voltage tracking response.

As with a DSTATCOM, the voltage across the DC capacitor must be maintained by drawing power from the AC circuit to replenish the DVR circuit losses. To accomplish this, we use a proportional controller of the form

$$p_{loss} = K_P \left(V_{dc}^{ref} - V_{dc}^{av} \right), \tag{7.10}$$

where V_{dc}^{av} is the average of the DC capacitor voltage over a cycle and V_{dc}^{ref} is the chosen reference value. Note that a drop/rise in the DC capacitor voltage indicates a real power supply/absorption by the capacitor. Therefore, p_{loss} in (7.10) defines the power losses in the inverter circuit, which must be replenished by the AC circuit.

Let us denote the desired phasor load voltage as $\boldsymbol{V_{L1}^*} = |V_{L1}^*| \angle \theta$, where $|V_{L1}^*|$ is a prespecified magnitude and θ is an unknown angle to be computed. Note that, since the load voltage is strictly positive sequence, the average load power is also positive sequence, even though its instantaneous component p_L might oscillate, depending on the nature of the load. We then get

$$p_{lavs} = \left|V_{L1}^*\right| \left|I_L\right| \cos\left(\theta - \phi\right), \tag{7.11}$$

where $|I_L| \angle \phi$ is the phasor positive sequence component of the load current.

Note from Figure 7.13 that the average power supplied to the load p_{lavs} is equal to the difference between the average active power injected to the PCC by the source (p_{pav}) and the power consumed by the DVR, which is p_{loss}. Therefore from (7.11), we get

$$p_{lavs} = p_{pav} - p_{loss} = \left|V_{L1}^*\right| \left|I_L\right| \cos\left(\theta - \phi\right). \tag{7.12}$$

From (7.12), the desired load voltage angle θ is computed as

$$\theta = \cos^{-1}\left(\frac{p_{pav} - p_{loss}}{\left|V_{L1}^*\right| \left|I_L\right|} \right) + \phi. \tag{7.13}$$

Example 7.3 Consider the distribution system of Figure 7.13 with rectifier structure of Figure 7.14. The system parameters are given in Table 7.3. The DC reference voltage is taken as 1 kV and the proportional gain K_P is chosen as 0.75. The steady-state PCC voltages and L-1 bus voltages are shown in Figure 7.15, where all the voltages are given in kV. It can be seen that the PCC voltages are unbalanced

Table 7.3 Example 7.3: System parameters for DVR example.

Source voltage	11 kV (L-L, rms), 50 Hz
Feeder impedance	$R + j\omega L = 0.605 + j4.84\ \Omega$
Load (L-1)	Balanced with impedance of $72.6 + j54.44\ \Omega$
Filter capacitor (C_d)	30 μF
DVR losses (R_f)	3 Ω
VSC transformer	500 kVA, 440 V/11 kV transformers (5% leakage reactance)
DC bus capacitor	20 mF
Rectifier filters	Smoothing inductor (L_{dc}) = 1 mH Filter capacitor (C_f) = 75 μF

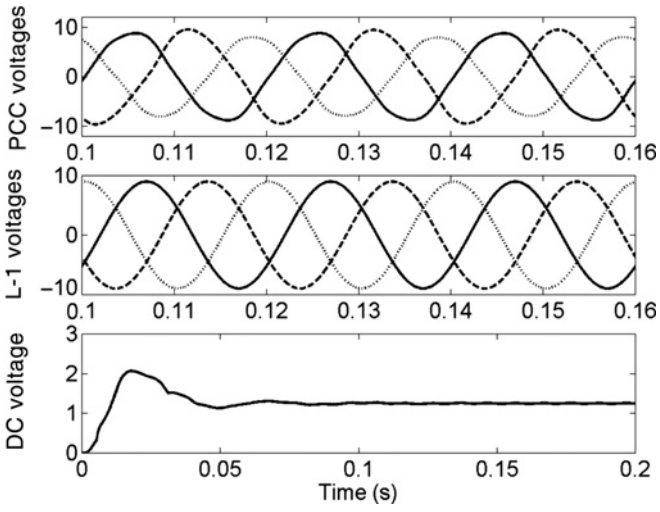

Figure 7.15 Example 7.3: Nominal system operation with a rectifier supported DVR.

due to an unbalanced load upstream, and are distorted due to the presence of the rectifier. However, the load bus voltages are balanced sinusoids. The DC bus voltage (in kV) is also shown in this figure. The DC capacitor is uncharged at the beginning and it gets charged and attains a steady level within 0.05 s.

With the system operating in the steady state, the impedance of phase-a of L-1 is suddenly doubled with the impedances of the other two phases remaining constant. L-1 voltages (in kV), L-1 currents (in A) and the DC voltages (in kV) are shown in Figure 7.16. From this figure, it can be seen that the change and unbalance of the critical load has no impact on the L-1 voltages, as they remain balanced and sinusoidal throughout. However, with the unbalance of the load, the DC capacitor voltage oscillates around a steady-state value at 100 Hz (twice the fundamental frequency).

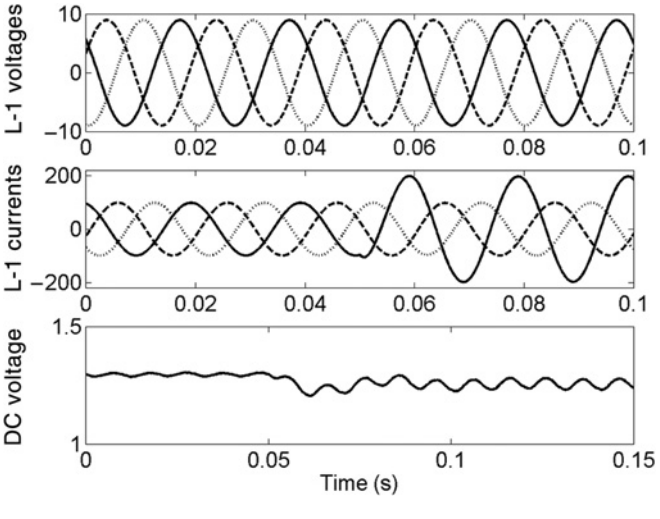

Figure 7.16 Performance of a rectifier supported DVR during a sudden load change.

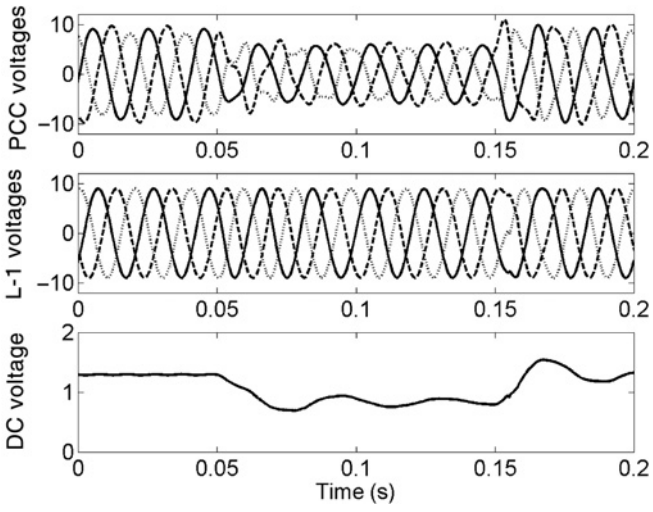

Figure 7.17 Performance of a rectifier supported DVR during sudden voltage sag.

The system response to voltage sag in which the peak of the source voltage drops to 5.75 kV is shown in Figure 7.17, where all the voltages are given in kV. The sag occurs at 0.05 and lasts for five cycles. It can be seen that the sag has very little impact on the load voltage.

7.5 Unified Power Quality Conditioner (UPQC)

A unified power quality conditioner (UPQC) consists of two VSCs that are connected to a common DC storage. One of the VSCs is connected in series with a distribution feeder, while the other is connected in shunt with the same feeder. The two VSCs have a common DC link capacitor (C_{dc}). The schematic diagram of a UPQC is shown in Figure 7.18. The UPQC connection in this figure is called the left-shunt structure as the shunt VSC is connected on the left-hand side of the series VSC. It is also possible to have a right-shunt connection in which the shunt VSC is placed on the right-hand side of the series VSC. Two filter capacitors C_f and C_d are also connected to bypass the switching frequency harmonics.

A UPQC is a versatile device that can perform multiple tasks, but it requires two VSCs and is hence more expensive. Therefore its application has to be chosen carefully. Consider the distribution system

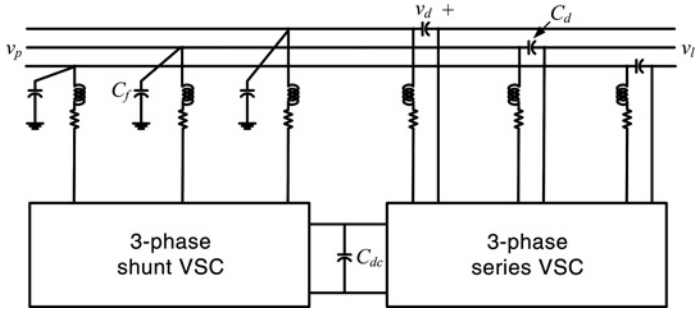

Figure 7.18 Schematic diagram of a UPQC.

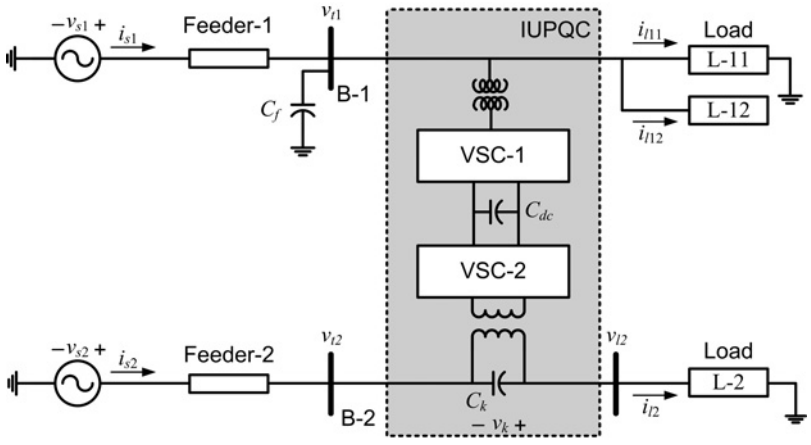

Figure 7.19 Single line diagram of an IUPQC connected distribution system.

of Figure 7.13. As mentioned in Example 7.3, the PCC voltages can get unbalanced and distorted due to the presence of unbalanced and nonlinear upstream loads. We can use the UPQC to alleviate some of the problems associated with the DVR. We stipulate that the UPQC should perform the following functions:

- The series VSC must inject a voltage such that the voltage v_{L1} at the critical load bus L-1 remains balanced and sinusoidal, with a prespecified magnitude and phase angle.
- The shunt VSC must eliminate unbalance and harmonics from the PCC voltage v_p.

The advantage of this scheme is that all loads to the left of the UPQC can then get a balanced supply voltage. This dual voltage-control operation of the UPQC is achieved through a suitable feedback control strategy.

An interesting application of UPQC is presented in [20], in which the UPQC is connected between two adjacent feeders. Since the device is connected between two lines, it is called an interline UPQC (IUPQC). The single-line diagram of an IUPQC-connected distribution system is shown in Figure 7.19. Two feeders, feeder-1 and feeder-2, which are connected to two different substations, supply the system loads L-1 and L-2. The supply voltages are denoted by v_{s1} and v_{s2}. It is assumed that the IUPQC is connected to the two buses B-1 and B-2, the voltages of which are denoted by v_{t1} and v_{t2}, respectively. The two feeder currents are denoted by i_{s1} and i_{s2}, while the load currents are denoted by i_{l1} and i_{l2}. The load L-2 voltage is denoted by v_{l2}.

The purpose of the IUPQC is to hold the voltages v_{t1} and v_{l2} constant against voltage sag/swell or temporary interruption in either of the two feeders. In this configuration, the IUPQC can absorb power from one feeder (say feeder-1) to hold v_{l2} constant if voltage v_{s2} sags. This can be accomplished through the common DC capacitor. In this study, the load L-2 is assumed to be a critical load that requires an uninterrupted, balanced voltage supply, while the load L-1 is both unbalanced and distorted. The aim of the IUPQC is twofold:

- to protect the sensitive load L-2 from the disturbances occurring in the system by regulating the voltage v_{l2}
- to regulate the bus B-1 voltage v_{t1} against sag/swell and or disturbances in the system.

In order to achieve these aims, the shunt VSC-1 is operated as a voltage controller, while the series VSC-2 regulates the voltage v_{l2} across the sensitive load.

The control of the IUPQC is then the combination of the voltage-control principle of the DSTATCOM and the DVR control discussed in the previous two sections. For the control of shunt VSC-1, we assume that its peak of the instantaneous voltage is prespecified and its phase angle (δ_1) is adjusted to maintain the power balance in the system. As before, the DC capacitor (C_{dc}) must be able to supply VSC-1 while maintaining its DC bus voltage constant by drawing power from the AC system. This is accomplished through a proportional controller, given by

$$\delta_1 = K_P \left(V_{dc}^{ref} - V_{dc}^{av} \right) \tag{7.14}$$

where V_{dc}^{av} is the average voltage across the DC capacitor over a cycle, V_{dc}^{ref} is its set reference value and K_P is the proportional gain. Let us denote the reference load L-2 voltage as v_{l2}^*. Then the reference of the voltage to be injected by series VSC-2 v_k^* is computed from

$$v_k^* = v_{l2}^* - v_{t2}. \tag{7.15}$$

Example 7.4 The system parameters used in this study are given in Table 7.4. The peak of the reference voltages for both v_1 and v_{l2} are chosen as 9.0 kV and its angle is computed from the angle controller (7.14) with $K_P = -0.25$. The simulation results are shown in Figures 7.20 and 7.21. It is assumed that the DC capacitor is initially uncharged and both the feeders along with the IUPQC are connected at the beginning. It can be seen from Figure 7.20(a), that the three-phase B-1 voltages, v_{t1}, are perfectly balanced with a peak of 9 kV. Once these voltages become balanced, the currents drawn by feeder-1, i_{s1}, also become balanced. The load L-2 bus voltages, v_{l2}, shown in Figure 7.20(c), are also perfectly sinusoidal with the desired peak of 9 kV as VSC-2 injects the required voltages in the system. The bus B-2 voltages, v_{t2}, can be seen to have a much smaller magnitude (about 7.75 kV peak). The DC capacitor voltage V_{DC} is shown in Figure 7.21(a). It can be observed that it has a settling time of about four cycles (0.08 s) and it attains a steady-state value of about 4.1 kV. The phase angle δ_1, shown in Figure 7.21(b), settles at $-33.88°$.

With the system operating in the steady state, a five-cycle (100 ms) voltage sag occurs at 0.14 s in which the peak of the supply voltage, v_{s1}, reduces to 6.5 kV from their nominal value of 9 kV. The various waveforms of only one phase (phase-a) are shown in Figure 7.22. The trends in the other two phases are similar. It can be seen that the DC capacitor voltage, V_{dc}, drops as soon as the sag occurs. If the bus voltage remains constant, the load power also remains constant. However, since the source voltage, v_{s1}, has dropped, the power coming out of the source has reduced. In order to supply the balance power

Table 7.4 Example 7.4: System parameters for IUPQC study.

Voltage source v_{s1}	11 kV (L-L, rms), phase angle 0°, 50 Hz
Voltage source v_{s2}	11 kV (L-L, rms), phase angle 0°, 50 Hz
Feeder-1 ($R_{s1} + j2\pi fL_{s1}$)	Impedance: $6.05 + j36.28\ \Omega$
Feeder-2 ($R_{s2} + j2\pi fL_{s2}$)	Impedance: $3.05 + j18.14\ \Omega$
Load L-11	Phase-a $24.2 + j60.50\ \Omega$
Unbalanced RL component	Phase-b $36.2 + j78.54\ \Omega$
	Phase-c $48.2 + j94.25\ \Omega$
Load L-12	A three-phase diode rectifier that
Nonlinear component	supplies a load of $250 + j31.42\ \Omega$
Balanced load L-2 impedance	$72.6 + j54.44\ \Omega$
Filter capacitor (C_f)	50 μF
Filter capacitor (C_k)	30 μF
DC capacitor (C_{dc})	3000 μF

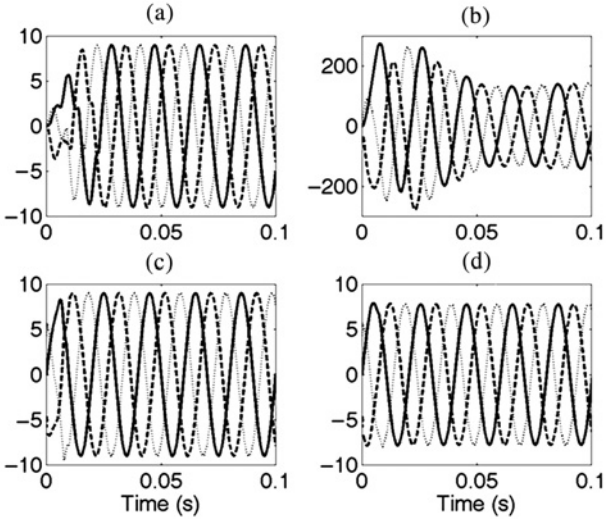

Figure 7.20 Example 7.4: System performance with an IUPQC (a) B-1 bus voltages (v_{t1}), kV, (b) feeder-1 currents (i_{s1}), A, (c) L-2 load voltages (v_{l2}), kV, (d) B-2 bus voltages (v_{t2}), kV.

requirement of the load, V_{DC} drops. To offset this, the angle, δ_1, retards such that the power supplied by the source increases. As the sag is removed, both V_{DC} and δ_1 return to their steady-state values. The current through feeder-1 is also shown in Figure 7.22. It can be seen that in order to supply the same load power at a reduced source voltage, the feeder current increases. Also, the transients in this current occur at the inception and the removal of the sag, due to the change in the source voltage. However, the critical bus voltage remains undisturbed.

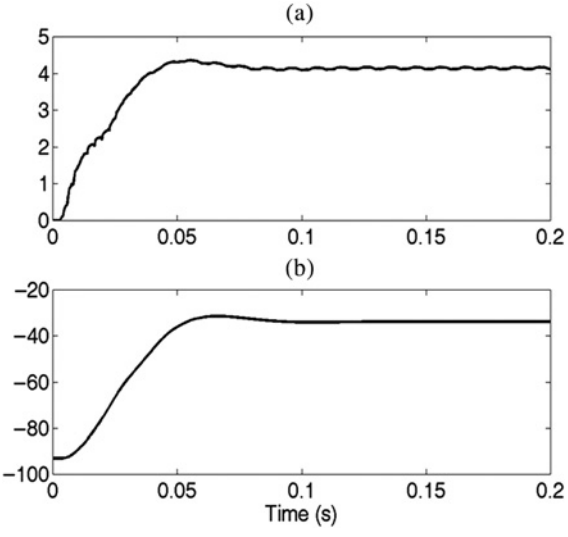

Figure 7.21 Example 7.4: (a) DC capacitor voltage (V_{dc}), kV, (b) phase angle of B-1 bus voltage (δ_1), deg.

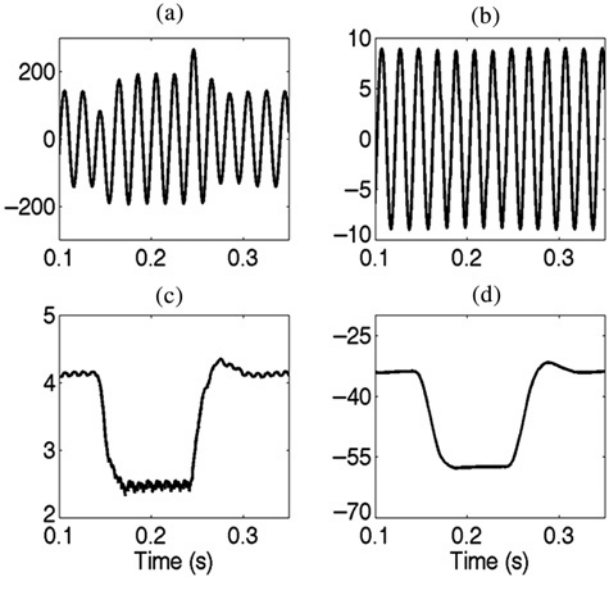

Figure 7.22 Example 7.4: System response during voltage sag in feeder-1 (a) phase-a feeder-1 current, A; (b) phase-a B-1 bus voltage, kV, (c) DC capacitor voltage (V_{dc}), kV, (d) phase angle of B-1 bus voltage (δ_1), deg.

Several other examples are presented in reference [20], including the limits of the performance of the IUPQC. These are not discussed here. This limit on the performance depends on the feeder impedance Z_{s1} ($=R_{s1} + j\omega L_{s1}$). A larger impedance causes a significant voltage drop in the feeder that cannot be compensated by controlling the voltage angle only. However, as will be shown later, if the DC capacitor is replaced by a DC source, this limitation can easily be overcome.

So far we have discussed various CPDs. We will now discuss their application in the power distribution system in the presence of DERs.

7.6 Voltage Balancing Using DSTATCOM and DVR

As mentioned before, VU and voltage drop/rise in LV distribution feeders are the power quality problems that can cause equipment malfunction and damage. Usually, the electric utilities try to distribute the residential loads equally among the three phases of distribution feeders. Although voltages are well balanced at the supply side level, the voltages at the customer side can become unbalanced due to the unequal system impedances, single-phase loads or a large number of single-phase transformers. This problem becomes more severe in the presence of single-phase, grid-connected, rooftop PV. The output power of these PVs is not controlled, and it depends on the meteorological conditions. Moreover, these are usually customer-owned and therefore can be randomly distributed in a distribution feeder. This randomness in their location and in the rating of the customers' PVs may increase VU in the network.

VU in three-phase systems is a condition in which the three-phase voltages differ in magnitude and/or do not have 120° phase difference. We define the VU based on IEEE's recommended practice for monitoring electric power quality [21] as

$$VU\% = \left|\frac{V_-}{V_+}\right| \times 100, \tag{7.16}$$

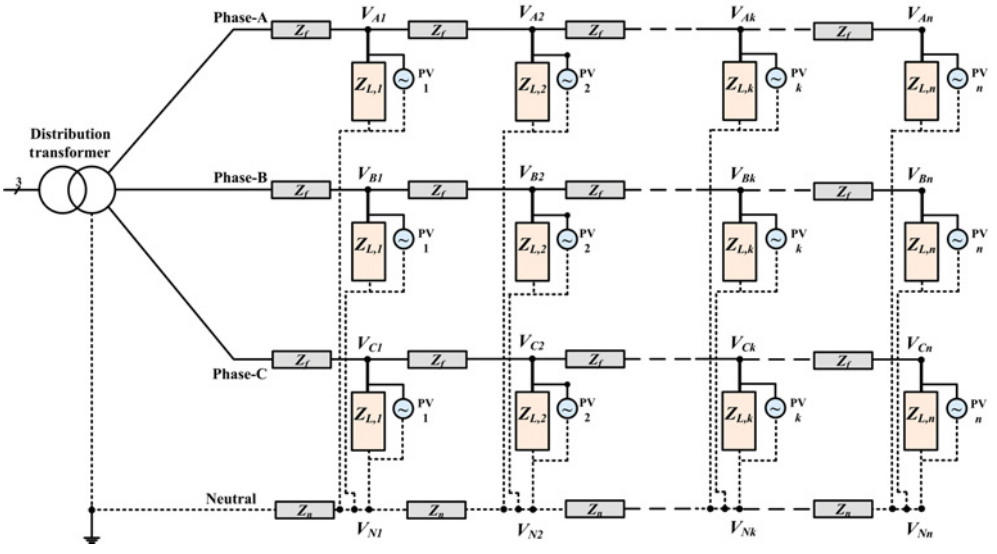

Figure 7.23 Example 7.5: Schematic diagram of an LV distribution system with PVs.

where V_- and V_+ are respectively the negative and positive sequences of the network line voltage. According to IEEE standards 1159, IEC 61000 and EN 50160 [21–23], the allowable limit for VU is 2% in LV networks for 95% of the data measured over a 7-day period in 10-minute rms values. Engineering Recommendation P29 in the UK not only limits VU of the network to 2%, but also limits the VU to 1.3% at the load point [24]. In this chapter, the VU standard limit is assumed to be 2%.

Example 7.5 The schematic diagram of a 400 m long LV distribution network that contains single-phase rooftop PVs is shown in Figure 7.23. It contains 10 buses, two 1 kW PVs, nine 2 kW PVs and eight 3 kW PVs, all distributed randomly. The system data is given in Table 7.5. The VU profile without

Table 7.5 Example 7.5: Data of the distribution system of Figure 7.23.

Distribution transformer	11 kV/ 415 V, 250 kVA, 50 Hz, Δ/ Y_{grounded}, $Z_I = 4\%$
Feeders	$3 \times 70 + 35$ mm^{2}AAC, 400 m overhead line for LV feeder, $Z_f = 0.452 + j \times 0.270$ [Ω/km]
	3×50 mm^2 ACSR, 2 km overhead line for high voltage line, $Z_f = 0.910 + j \times 0.285$ [Ω/km]
Residential loads	1 kW, $\cos\phi = 0.95$, $z = 51.9840 + j \times 17.0863\ \Omega$
	2 kW, $\cos\phi = 0.95$, $z = 25.9920 + j \times 8.5432\ \Omega$
	3 kW, $\cos\phi = 0.95$, $z = 17.3280 + j \times 5.6954\ \Omega$
Rooftop PV	1–5 kW, unity power factor, $L = 5$mH with the PV cell and single-phase inverter data as modelled in [26]
Distribution of PV locations and ratings	1 kW PV at node 7 of phase-a and node 9 of phase-c
	2 kW PV at nodes 1 (2 PVs), 6 (2 PVs), 9 (2 PVs), 10 (2 PVs) of phase-a and node 1 of phase-b
	3 kW PV at nodes 2 (2 PVs), 3 (2 PVs), 5 (2 PVs), 8 of phase-a and node 4 of phase-b

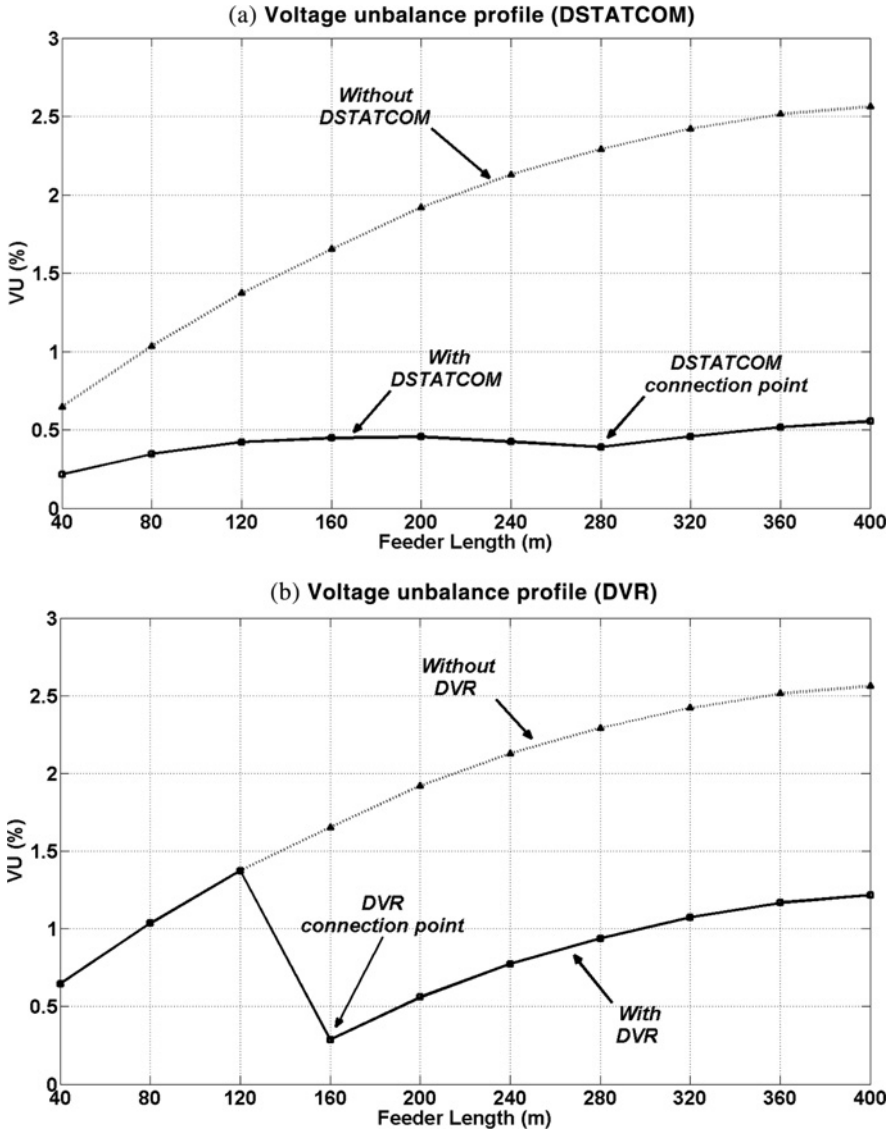

Figure 7.24 Example 7.5: VU profiles with (a) DSTATCOM and (b) DVR.

any compensation (without DSTATCOM or DVR) is shown in Figures 7.24(a) and (b). It can be seen that the VU at the end of the feeder is above 2.5%. It can also be seen that the VU is above the limit of 2% in about the last 45% of the feeder segment.

Now a DSTATCOM is connected at the 2/3 point of the feeder. This is operated in voltage-control mode to balance the voltages at the PCC. The VU profile is shown in Figure 7.24(a). Ideally the VU at the PCC should be zero. However, due to a small voltage tracking error, the DSTATCOM cannot force it to be zero. Nevertheless the VU all along the feeder is kept below 0.6%. Note that the connection point of the 2/3 point is found to be the optimum as reported in reference [25].

Now instead of a DSTATCOM, a DVR is connected at the 1/3 point of the feeder. The VU profile is then as shown in Figure 7.24(b). As opposed to a DSTATCOM, which reduces the VU all along the feeder, a DVR can only reduce the VU on the downstream side. However, the VU at the end of the line is below 2%, which is acceptable. Note that for a longer feeder, a single DVR may not be able to correct the VU profile all along the feeder. In that case, more than one DVR may be required [25]. Note, however, that the DVR only needs to add a small amount of voltage and hence its rating is much less than that of a DSTATCOM.

We will now present some dynamic simulation results. At the beginning, the system is operating in the steady state and the DSTATCOM is connected at the 2/3 point of the feeder. Then subsequently the following changes in system occur:

- At 0.05 s, the PV generation is increased by 13 kW and 1 kW in phase-a and -b, respectively.
- At 0.35 s, a total 4 kW load is reduced from phase-a, 8 kW is increased in phase-b and 12 kW is increased in phase-c.
- At 0.55 s, a total 8 kW of PV output is reduced from phase-a, while 2 kW and 6 kW PV outputs are increased in phase-b and -c, respectively. At the same time, the load in phase-a in increased by 2 kW, while the loads in phase-b and -c are decreased by 4 kW and 6 kW, respectively.

With these transients, the variation in VU at the end of the feeder, with and without the DSTATCOM installation, is shown in Figure 7.25(a). It can be seen that DSTATCOM restricts the VU to below 1% even during the transients.

Now instead of the DSTATCOM, a DVR is connected at the 1/3 point of the same network with the same transients. The variation in VU at the end of the feeder, with and without the DVR installation, is shown in Figure 7.25(b). Even though the DVR restricts the VU to below 1.4%, it is less effective in VU reduction than the DSTATCOM.

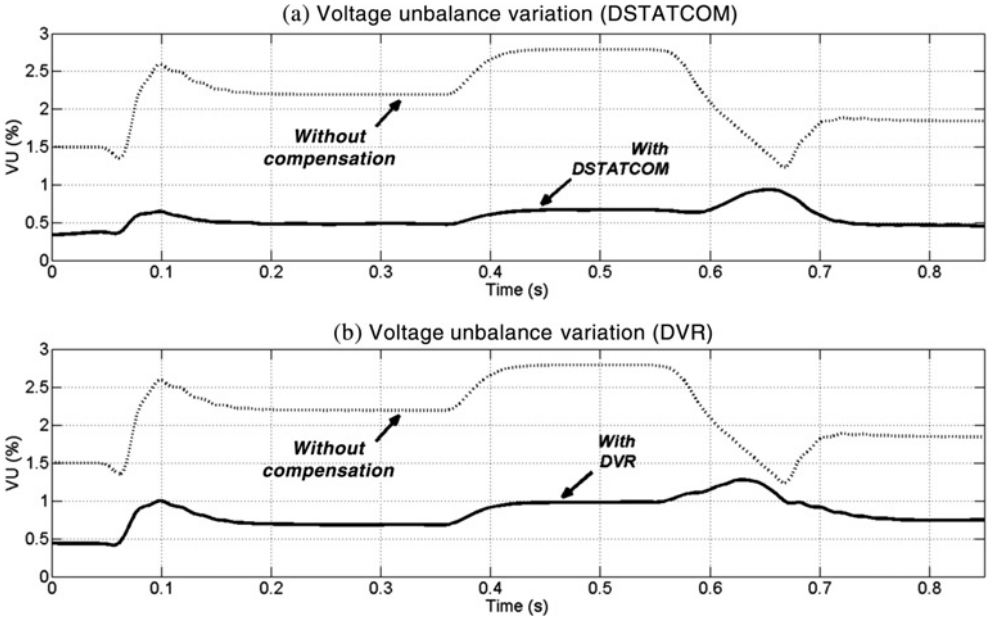

Figure 7.25 Example 7.5: VU at the end of the feeder with (a) DSTATCOM and (b) DVR.

7.7 Excess Power Circulation Using CPDs

As seen in the previous section, DERs are placed randomly in an LV distribution network. In general, the PV generation is at its maximum during the afternoons when the domestic load demand is minimal, especially during the weekdays. If the PV penetration and/or PV ratings are high, it might happen that the generation in a particular phase exceeds the load demand in that phase. In such an event the excess power generated in that particular phase will be fed back to the substation. Severe current unbalance can occur if the other two phases draw power from the substation. This may affect the upstream transmission network badly. Assuming that the source is balanced, the source currents can be made balanced only if the PCC voltages are balanced. As we have seen earlier, this can be achieved through a DSTATCOM, whether it is operating in current or voltage-control modes. Both these approaches are discussed in this section.

7.7.1 Current-Controlled DSTATCOM Application

The current-controlled technique, given by (7.5), depends only on the net average load side power. These equations are valid for both negative and positive power flow, and hence the presence of the DERs will not have any effect on the algorithm. Therefore, the source side currents can be made balanced, irrespective of the power flow direction from the source to the PCC [27].

Example 7.6 Consider the system of Figure 7.26. This has two load buses – each load bus has several y-connected loads and single-phase DERs. The aggregated values of the load and generation are given in Table 7.6. A DSTATCOM, operating in the current control mode using (7.5), is connected

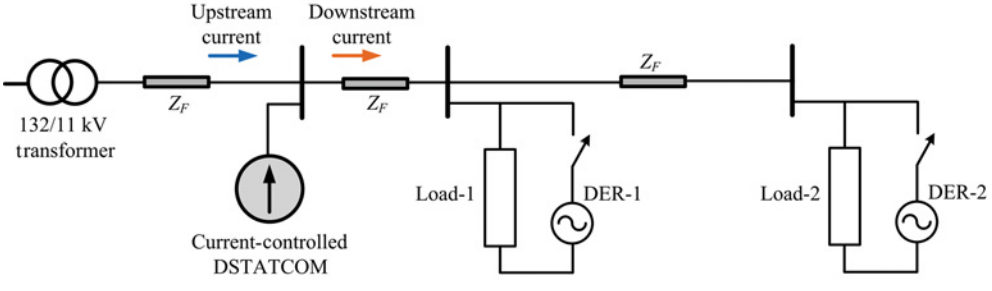

Figure 7.26 Example 7.6: Schematic diagram of a distribution network with current-controlled DSTATCOM.

Table 7.6 Example 7.6: Data for the system of Figure 7.26.

Source voltage	11 kV (L-L, rms), 50 Hz
Feeder impedance	$R_s = 3.025\ \Omega$, $L_s = 57.8$ mH
Load impedance at Bus-1	Phase-a: $100 + j157.1\ \Omega$
	Phase-b: $150 + j235.62\ \Omega$
	Phase-c: $200 + j157.1\ \Omega$
Load impedance at Bus-2	Phase-a: $150 + j235.62\ \Omega$
	Phase-b: $200 + j157.1\ \Omega$
	Phase-c: $100 + j157.1\ \Omega$
DER generation	DER-1: 300 kW connected to phase-a
	DER-2: 150 kW connected to phase-b
	250 kW connected to phase-c

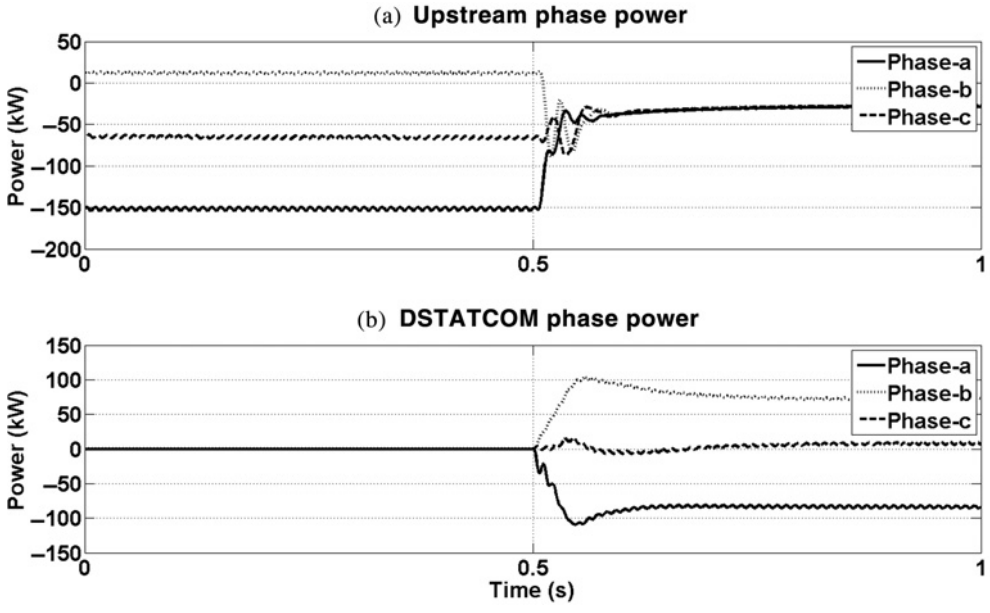

Figure 7.27 Example 7.6: Active power flowing through the system with current-controlled DSTATCOM.

to circulate the excess power. With the system operating in steady state, the DSTATCOM is connected at 0.5 s. The power drawn from the source is shown in Figure 7.27(a). It can be seen that, before the DSTATCOM connection, they are unequal, with two phases feeding power back to the substation (since they are negative). However, all of them become (nearly) equal once the DSTATCOM is connected. The powers flowing in the phases of the DSTATCOM are shown in Figure 7.27(b). It can be seen that these are unequal, since the DSTATCOM is circulating power between the phases to balance the supply side power.

The upstream currents and their unbalance percentages are shown in Figure 7.28. It can be seen that large unbalanced currents flow before the DSTATCOM connection since a large amount of reverse power was flowing into the upstream substation from the two phases, while the third phase was drawing power. However, the magnitude of the currents reduces significantly after the DSTATCOM connection since the upstream network only supplies the power that is required after the power generated by the DERs are utilized. As a consequence, the current unbalance in the upstream network reduces from 25% to below 1%.

7.7.2 Voltage-Controlled DSTATCOM Application

Since the DC bus of the DSTATCOM is connected to a DC source (batteries) rather than a DC capacitor, the DSTATCOM can work like an uninterrupted power supply (UPS). The DC source can supply power if needed or absorb power as well. Of course, these will depend on the state of charge of the batteries. In this case, even if the distribution network gets disconnected from the utility, the DSTATCOM will be able to supply the power shortfall or absorb the excess power. The main drawback of current-controlled DSTATCOM in this application is that it will fail to circulate power between the phases when an islanding occurs. Since a 3p4w configuration has been assumed, the current through each phase of the DSTATCOM must be equal to the load current of the respective phase to prevent a system-wide collapse. This implies that a power circulation will not occur in the islanded situation. To overcome this problem, the DSTATCOM is now operated in the voltage-control mode in which it holds the PCC voltage constant

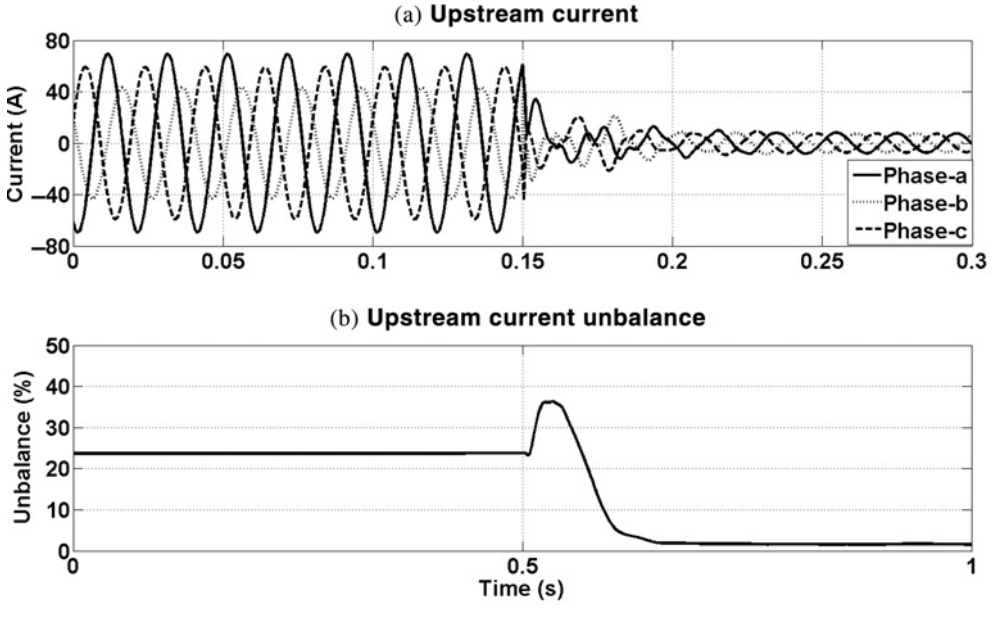

Figure 7.28 Example 7.6: Source currents and their unbalance with current-controlled DSTATCOM.

[28]. The schematic diagram of the configuration is shown in Figure 7.29, in which the circuit breaker *CB* is used for islanding.

For voltage control, the magnitude of the PCC voltage (V_{PCC}) is chosen as 1 p.u., while its angle is controlled by the output power of DSTATCOM (P_D). For example, if the desired output power of the DSTATCOM is P_D^*, then the angle of the PCC voltage is obtained through a PI controller, given by

$$\delta = K_P \left(P_D^* - P_D\right) + K_I \int \left(P_D^* - P_D\right)\, dt. \tag{7.17}$$

Ordinarily, in the grid connected mode, P_D^* will be a small negative value such that the DSTATCOM can absorb power to replenish the losses in its circuit. Otherwise, the batteries will get discharged. Once the islanding occurs, the reference value will be chosen as

$$P_D^* = P_L, \tag{7.18}$$

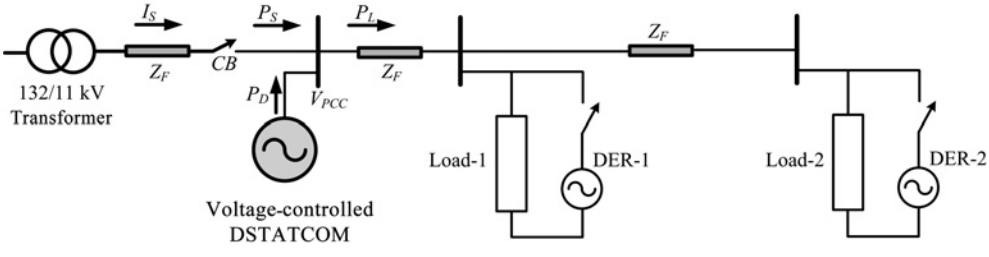

Figure 7.29 Schematic diagram of a distribution network with voltage-controlled DSTATCOM.

Table 7.7 Example 7.7: System data.

Source voltage	11 kV (L-L, rms), 50 Hz
Feeder impedance	$2.4200 + j4.8381$
Line impedance between buses	$0.6712 + j0.2887$
DER rating (in unity power factor and low load condition)	Bus 1 = 50 kW Bus 2 = 100 kW Bus 3 = 150 kW Bus 4 = 200 kW

where P_L is the net load power, that is, the difference between the sum of the powers generated by the DERs and the total power consumed by the loads.

Example 7.7 For this example, a four-bus distribution system is considered instead of the two-bus system shown in Figure 7.29. The system data is given in Table 7.7. All the DERs are connected to phase-a. First the system is operating in steady state with all the DERs and loads connected. The results are shown in Figure 7.30. The DSTATCOM is connected at 0.45 s. It can be seen from Figure 7.30(a) that before the DSTATCOM gets connected, phase-a is feeding back about 350 kW power to the source, while the two other phases are drawing power from the source. All these powers become balanced once the DSTATCOM is connected. The three-phase real and reactive powers supplied by the source are shown in Figure 7.30(b). From Figure 7.30(a) and (b) it is obvious that the total DER generation is slightly more than the total load demand. Hence a small amount of three-phase active power gets fed back to the source. The DSTATCOM must absorb this amount of power when the islanding occurs (at 0.4 s in this example). The three-phase DSTATCOM real and reactive power outputs are shown in Figure 7.30(c). Before the islanding, P_D^* is chosen as -5 kW. Once the islanding occurs, the DSTATCOM absorbs the balance amount of active power. Also, if the balance of power before the islanding was positive, the DSTATCOM

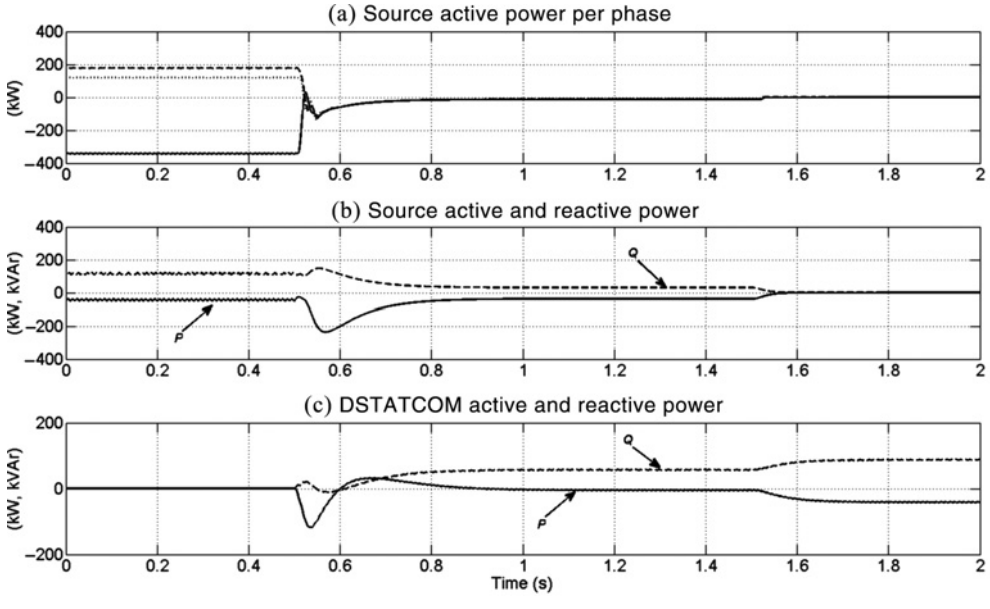

Figure 7.30 Example 7.7: Power flow through the different parts of the test system.

would have been able to supply the required amount of power to the loads. If the DSTATCOM were to be operated from a DC capacitor, it would not have the capacity to absorb or supply power. Hence shedding of some of the loads (during power short fall) or switching auxiliary loads (for excess power generation) would have been required.

In the example discussed above, the magnitude of the PCC voltage is chosen as 6.35 kV L-n, rms (i.e. 9 kV peak). This, however, can cause a large amount of reactive power to flow between the source and the PCC that can cause a large amount of current to flow through the feeder, resulting in severe line drop and heating. The following example illustrates this.

Example 7.8 For this example, we again consider the sample four-bus distribution system of Example 7.7, except that the loads are now higher than the previous case. Also, the DERs inject 200 kW, 250 kW, 300 kW and 350 kW respectively to the four buses (1 to 4). The DSTATCOM is connected at 0.5 s. The results are shown in Figure 7.31, where the total three-phase power drawn from the source is positive. The DSTATCOM raises the PCC voltage. Since the loads are assumed to be constant impedance type, this causes an increase in the active power drawn from the system once the DSTATCOM is connected. The amount of reactive power required to hold the PCC voltage is more than that required by the load. Therefore, as can be seen from Figure 7.31, 60% of the reactive power injected by the DSTATCOM gets fed back to the grid.

Consider the system of Figure 7.29. It is desirable to operate the DSTATCOM in such a way such that the reactive power from the source (Q_S) is zero. Let us assume that the rms supply voltage is equal to $|V|\angle 0°$ and the PCC voltage is $V_{PCC} = |V_P|\angle -\delta$. Then the current flowing from the source to the PCC is

$$I_s = \frac{|V| - |V_P|\angle -\delta}{R_F + jX_F}, \tag{7.19}$$

where $Z_F = R_F + jX_F$. Therefore, the complex power injected into the PCC by the source is

$$P_s + jQ_s = \left(|V_P|\angle -\delta\right) \times I_s^*. \tag{7.20}$$

It can be shown that $Q_s = 0$ when

$$|V_P| = |V| \left[\cos\delta - \frac{R_F}{X_F}\sin\delta\right]. \tag{7.21}$$

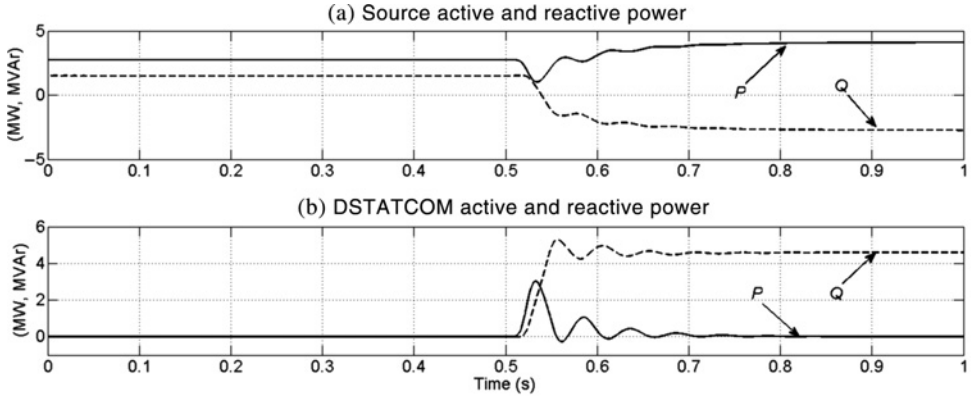

Figure 7.31 Example 7.8: Active and reactive power flow through the different parts of the test system.

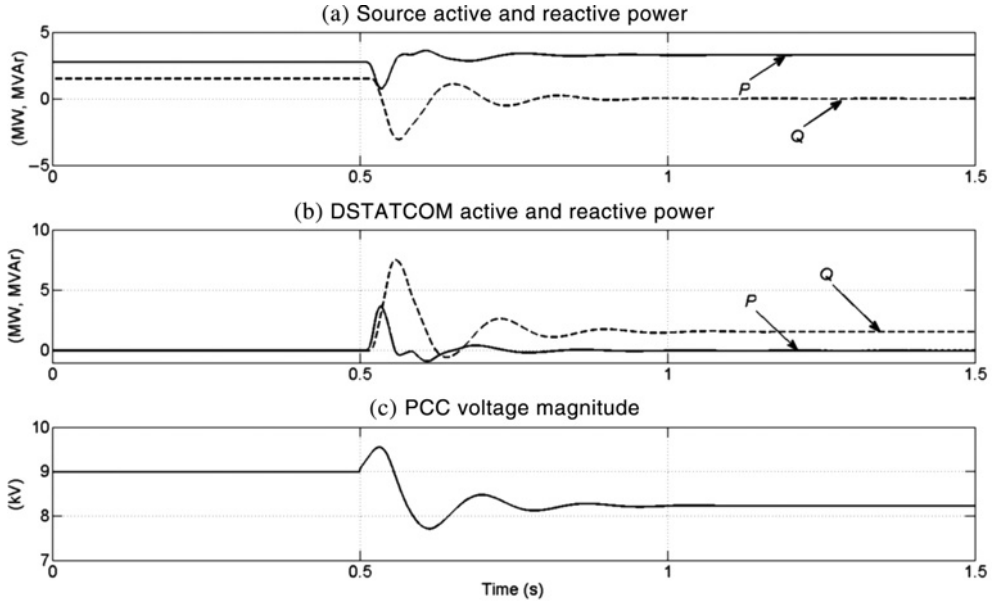

Figure 7.32 Example 7.9: Active and reactive powers and PCC voltage magnitude for upf operation.

Let us assume that $|V|$ is 1 p.u. (i.e. $11/\sqrt{3}$ kV). Now the angle difference δ is expected to be less than 45°. This implies that $\cos\delta > \sin\delta$. Therefore, the term in the square brackets of (7.21) can only be positive and less than 1. Therefore, the reactive power $Q_s = 0$ only when $|V_p|$ is less than 1 p.u. Hence, it is not possible to regulate the PCC voltage close to 1 p.u. without sending reactive power back to the source. In order to ensure unity power factor (upf) injection from the source, the reference for the PCC voltage magnitude can be set through another PI controller of the form

$$\left|V_p^*\right| = K_P\left(0 - Q_s\right) + K_I \int \left(0 - Q_s\right)\, dt, \tag{7.22}$$

where $|V_p^*|$ is the reference voltage magnitude. We now control the DSTATCOM with reference voltage magnitude and angle generated from (7.22) and (7.17), respectively.

Example 7.9 Let us consider the same system as considered in Example 7.8. The DSTATCOM, with its voltage magnitude and angle controllers, is connected at 0.5 s. The results are shown in Figure 7.32. It can be seen that the reactive power injected to the PCC by the source becomes zero after the DSTATCOM connection. As a consequence, the DSTATCOM needs only to supply the reactive power requirement of the load and hence it is much less than that supplied by it in Example 7.8. The PCC voltage magnitude is shown in Figure 7.32(c). It can be seen that it reduces from 9 kV to about 8.2 kV to guarantee the upf operation.

7.7.3 UPQC Application

The examples in the previous subsection show that if the PCC voltage magnitude is held at 1 p.u., a large amount of reactive power is fed back to the source. To compensate for this we have used a voltage

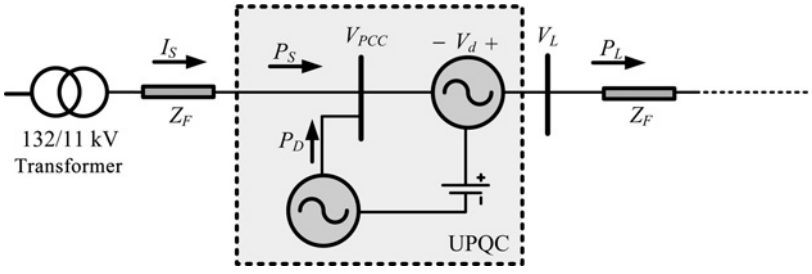

Figure 7.33 UPQC configuration for excess power circulation.

controller that causes the PCC voltage to drop. This, however, will result in further drop along the buses that is not desirable. The solution of this problem is to isolate the load voltage V_L from the PCC voltage V_{PCC}. These two voltages can be controlled independently of each other using a UPQC, the schematic diagram of which is shown in Figure 7.33. Here the UPQC contains a shunt element and a series element, both connected to a common DC bus containing battery stack [29].

The shunt VSC holds the PCC voltage to

$$V_{PCC} = \left|V_p^*\right| \angle -\delta, \tag{7.23}$$

where $|V_p^*|$ is obtained from (7.22) and δ is obtained from (7.17). The series VSC adds a voltage V_d such that the load voltage is given by

$$V_L = V_{PCC} + V_d. \tag{7.24}$$

To restrict the voltage addition by the series VSC to a minimum, its reference is chosen as

$$V_d^* = \left|V_L^* - V_p^*\right| \angle -\phi, \tag{7.25}$$

where $|V_L^*|$ is the desired magnitude of the load voltage and ϕ is calculated such that the power loss in the series VSC, $P_{loss} = P_L - P_S - P_D$, is zero. This guarantees that the power loss in the series VSC is compensated by the shunt VSC, such that it does not cause the battery to discharge. This is accomplished through another PI controller of the form

$$\phi = \delta + K_P\left(0 - P_{loss}\right) + K_I \int \left(0 - P_{loss}\right)\, dt. \tag{7.26}$$

Example 7.10 Let us consider the same system as considered in Example 7.9. At the beginning, the system is operating in the steady state with all the DERs being connected. The shunt VSC, with its voltage magnitude and angle controllers, is connected at 0.2 s. Subsequently, at 0.9 s, the series VSC is connected. The results are shown in Figure 7.34, where (a) shows the rms load voltage. When the shunt VSC is connected at 0.2 s, this voltage magnitude is kept at 5.8 kV. Once the series VSC is connected at 0.9 s, it rises to the desired level of 6.35 kV (i.e. 1 p.u.). The power losses in the two VSCs of the UPQC are shown in Figure 7.34(b). It can be seen that they are nearly zero at steady state. As a consequence, the source and load power are nearly equal in the steady state, as evident from Figure 7.34(c). The converter output voltage angles are shown in Figure 7.34(d). Before the shunt VSC is connected, both of them are zero. Once the shunt VSC is connected, δ and ϕ are equal. Once the series VSC is connected, ϕ deviates from δ. These variations are required to hold the charge in the batteries.

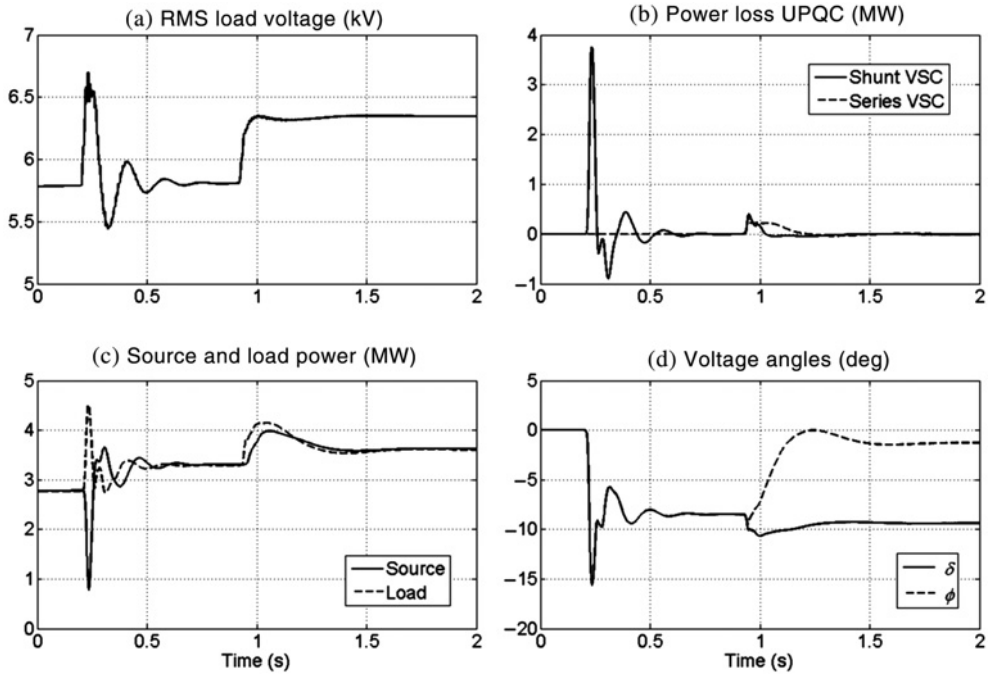

Figure 7.34 Example 7.10: UPQC simulation results.

7.8 Conclusions

This chapter presents the custom power devices and their application to power distribution systems. Some or all the CPDs discussed in this chapter have been in use for several years now. However, their importance is constantly increasing due to the rapid introduction of single-phase DERs in LV networks. As has been highlighted in this chapter, the CPDs can dynamically improve the power quality, even when a large number of DERs are connected. Note, however, that the research in this area is in its infancy. The grid codes need to be adapted regarding the connection of DERs. Only then will the CPDs be more effective in solving the power quality problems arising from the increased use of DERs.

References

[1] Lewis, H.L. (1997) *Power Distribution Planning Reference Book*, Marcel Dekker, New York.

[2] Billinton, R. and Billinton, J.E. (1989) Distribution system reliability indices. *IEEE Transactions on Power Delivery*, **4**(1), 561–568.

[3] Ghosh, A. and Ledwich, G. (2002) *Power Quality Enhancement using Custom Power Devices*, Kluwer Academic Publishers, Norwell, MA.

[4] Shahnia, F., Majumder, R., Ghosh, A., *et al.* (2011) Voltage imbalance analysis in residential low voltage distribution networks with rooftop PVs. *Electric Power Systems Research*, **81**(9), 1805–1814.

[5] Shahnia, F., Ghosh, A., Ledwich, G. and Zare, F. (2013) Predicting voltage unbalance impacts of plug-in electric vehicles penetration in residential LV distribution networks. *Electric Power Components and Systems*, **41**(16), 1594–1616.

[6] Quinn, C.A., Mohan, N. and Mehta, H. (1992) Active filtering of harmonic currents in three-phase, four-wire systems with three-phase and single-phase non-linear loads. Applied Power Electronics Conference, APEC'92, Boston, MA, USA, Feb. 1992, pp. 829–836.

[7] Aredes, M., Hafner, J. and Heumann, K. (1997) Three-phase four-wire shunt active filter control strategies. *IEEE Transactions on Power Electronics*, **12**(2), 311–318.
[8] Kim, J.-H. and Sul, S.-K. (2004) A carrier-based PWM method for three-phase four-leg VSC. *IEEE Transactions on Power Electronics*, **19**(1), 67–75.
[9] Ghosh, A. and Joshi, A. (2000) A new approach to load balancing and power factor correction in power distribution system. *IEEE Transactions on Power Delivery*, **15**(1), 417–422.
[10] Ghosh, A. and Ledwich, G. (2010) High bandwidth voltage and current control design for voltage source converters. 20th Australasian Universities Power Engineering Conference AUPEC 2010, Christchurch, New Zealand, Dec. 2010.
[11] Akagi, H., Kanazawa, Y., Fujita, K. and Nabae, A. (1983) Generalized theory of the instantaneous reactive power and its application. *Electrical Engineering in Japan*, **103**(4), 58–65.
[12] Akagi, H., Kanazawa, Y. and Nabae, A. (1984) Instantaneous reactive power compensators comprising switching devices without energy storage components. *IEEE Transactions on Industry Applications*, **20**(3), 625–630.
[13] Akagi, H., Nabae, A. and Atoh, S. (1986) Control strategy of active power filters using multiple voltage-source PWM converters. *IEEE Transactions on Industry Applications*, **22**(3), 460–465.
[14] Furuhashi, T., Okuma, S. and Uchikawa, Y. (1990) A study on the theory of instantaneous reactive power. *IEEE Transactions on Industrial Electronics*, **37**(1), 86–90.
[15] Watanabe, E.D., Stephan, R.M. and Aredes, M. (1993) New concepts of instantaneous active and reactive powers in electrical systems with generic load. *IEEE Transactions on Power Delivery*, **8**(2), 697–703.
[16] Peng, F.Z. and Lai, J.S. (1996) Generalized instantaneous reactive power theory for three-phase power systems. *IEEE Transactions on Instrumentation & Measurements*, **45**(1), 293–297.
[17] Ghosh, A. and Ledwich, G. (2003) Load compensating DSTATCOM is weak AC systems. *IEEE Transactions on Power Delivery*, **18**(4), 1302–1309.
[18] Mishra, M.K., Ghosh, A. and Joshi, A. (2003) Operation of a DSTATCOM in voltage control mode. *IEEE Transactions on Power Delivery*, **18**(1), 258–264.
[19] Woodley, N.H., Morgan, L. and Sundaram, A. (1999) Experience with an inverter-base dynamic voltage restorer. *IEEE Transactions on Power Delivery*, **14**(3), 1181–1185.
[20] Jindal, A.K., Ghosh, A. and Joshi, A. (2007) Interline unified power quality conditioner. *IEEE Transactions on Power Delivery*, **22**(1), 364–372.
[21] IEEE Standard 1159-1995 Recommended practice for monitoring electric power quality, 1995.
[22] IEC Standard 61000-2-2 Voltages, Electromagnetic Compatibility (EMC), Part 2: Environment-compatibility levels for low-frequency conducted disturbances and signalling in public low-voltage power supply systems, 2002.
[23] EN 50160, Voltage characteristics of electricity supplied by public distribution systems, 1999.
[24] The Electricity Council, Engineering recommendation P29. Planning Limits for voltage unbalance in the United Kingdom, 1990.
[25] Shahnia, F., Ghosh, A., Ledwich, G. and Zare, F. (2014) Voltage unbalance improvement in low voltage residential feeders with rooftop PVs using custom power devices. *International Journal of Electrical Power and Energy Systems*, **55**, 362–377.
[26] Shahnia, F., Majumder, R., Ghosh, A., *et al.* (2011) Operation and control of a hybrid microgrid containing unbalanced and nonlinear loads. *Electric Power Systems Research*, **80**(10), 954–965.
[27] Mazumder, S., Ghosh, A., Shahnia, F., *et al.* (2012) Excess power circulation in distribution networks containing distributed energy resources. IEEE Power and Energy Society General Meeting, San Diego, CA, USA, Jul. 2012.
[28] Mazumder, S., Ghosh, A. and Zare, F. (2013) Improving power quality in low voltage networks containing distributed energy resources. *International Journal of Emerging Electric Power Systems*, **14**(1), 67–78. doi:10.1515/ijeeps-2013-0022
[29] Mazumder, S., Ghosh, A. and Zare, F. (2013) Voltage quality improvement in distribution networks containing DERs using UPQC. IEEE Power and Energy Society General Meeting, Vancouver, BC, Canada, Jul. 2013.

8

Modelling of Electronically Interfaced DER Systems for Transient Analysis

Amirnaser Yazdani and Omid Alizadeh

8.1 Introduction

For a variety of technical, economical and environmental reasons, the electric power system is receiving small-scale distributed generation (DG) and distributed storage (DS) systems at its low- and medium-voltage levels of operation. Consequently, DG and DS systems, which are collectively referred to as *distributed energy resource* (DER) systems, are expected to affect the power system transients, especially as their aggregate installed capacity continues to grow. This expectation indicates the need for modelling, simulation and analysis techniques to reveal the steady-state and transient impacts of DER systems on the power system.

Broadly speaking, DER systems can be classified as rotating-machine-based DER systems or electronically interfaced DER systems. A rotating-machine-based DER system employs a synchronous or asynchronous (induction) generator to convert mechanical energy to electricity. More importantly, the electric machine is directly coupled with the host power system and thus is bound to operate at the power system frequency. Examples include biomass-fuelled generators, diesel-fuelled generators, generators driven by gas-fuelled internal combustion engines, small hydroelectric generators and fixed-speed wind energy systems. By contrast, an electronically interfaced DER system may or may not utilize a rotating machine to generate electricity out of the prime energy resource. However, its electricity generation component is coupled with the power system via a power-electronic interface, and not directly. The main reason is that many energy resources generate either DC power or AC power at a different or even variable frequency with respect to the power system frequency. The best-known examples of electronically interfaced DER systems are photovoltaic (PV) solar energy systems, fuel-cell systems, variable-speed wind energy systems, battery energy storage systems, supercapacitor energy storage systems and flywheel energy storage systems. Note that the boundary between the two classes is not crisp. For example,

Transient Analysis of Power Systems: Solution Techniques, Tools and Applications, First Edition.
Edited by Juan A. Martinez-Velasco.

a generator driven by an internal combustion engine may be equipped with a power-electronic interface, in order to be capable of variable-speed operation and thus running optimally in various operating conditions.

This chapter is concerned with electronically interfaced DER systems. Using a generic model, we first introduce the construction and principles of operation of an electronically interfaced DER system; we will look at how different electronically interfaced DER systems can be considered as special cases of the generic model. Then, important transients pertaining DER systems are introduced. Finally, the procedures to develop circuit-based simulation models and mathematical models will be discussed, using the examples of PV energy systems and wind energy systems.

8.2 Generic Electronically Interfaced DER System

Figure 8.1 illustrates the generic schematic diagram of an electronically interfaced DER system. The DER system consists of an energy resource and a power-electronic interface, which are interconnected from their DC ports. The energy resource, for example, an array of PV modules or batteries, exchanges the power P_{ext} with the power-electronic interface. In turn, the power-electronic interface consists of a DC-AC voltage-sourced converter (VSC) [1], the DC-side capacitor C, an AC-side filter to mitigate harmonic current injection by the converter and a startup/shut-down switchgear. The power-electronic interface exchanges the real and reactive powers P_g and Q_g with the host grid. Although a three-phase configuration is implied in Figure 8.1, the converter (and its filter and switchgear) can be single-phase.

Figure 8.1 also illustrates the control architecture of the power-electronic interface. The converter is switched based on the pulse-width modulation (PWM) strategy, enabling rapid control of the magnitude and phase angle of the converter AC-side terminal voltage, v_t. This process is then employed in a dedicated feedback loop that controls the magnitude and phase angle of the converter AC-side current, i_t, relative to those of the power system voltage, v. This, in turn, enables the regulation of P_g and Q_g at their corresponding set-points (not shown in Figure 8.1). It is also possible to directly control P_g and Q_g by the magnitude and phase angle of v_t. However, the strategy, known as *voltage-mode control*, renders the converter vulnerable to overcurrents (whether in transient or steady-state regimes) as well as to network faults. By contrast, *current-mode control*, described earlier, avoids this vulnerability by

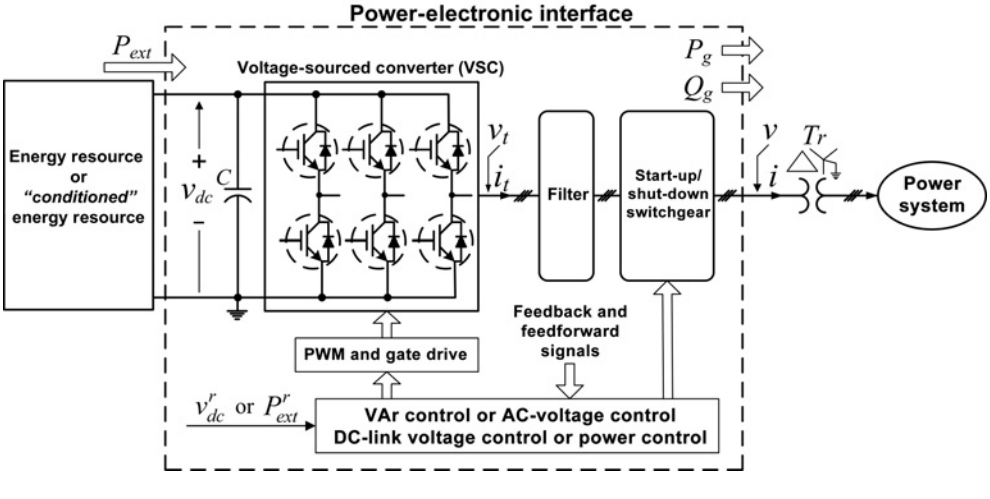

Figure 8.1 Generic schematic diagram of an electronically interfaced DER system.

allowing for the imposition of a safe upper limit to the magnitude of i_t and is therefore widely adopted. The current-control method is assumed for the remainder of our discussion.

The capability of controlling P_g and Q_g permits a number of possible control and operating scenarios for the DER system of Figure 8.1:

- Q_g can be regulated at a pre-specified value, including zero for unity power-factor operation of the DER system. We refer to this control mode as the *VAr control mode*.
- Alternatively, Q_g can be actively controlled by a feedback loop that regulates the magnitude of v. This mode of control is referred in this chapter to as the *AC-voltage control mode*.
- If the energy resource has a current-source nature, P_g can be controlled to regulate the DC-link voltage v_{dc}, at its set-point v_{dc}^r, through a control mode that we refer to as the *DC-link voltage control mode*. Typically, v_{dc}^r is assigned a constant value, towards the goal of a constant v_{dc}. However, in some applications v_{dc}^r, and therefore v_{dc}, are varied. For example, in a so-called *single-stage* PV system, discussed further in Section 8.5.1, the energy resource is a PV array. In a PV array, the terminal current, and therefore the output power, depend on the terminal voltage. Hence, in a single-stage PV system, v_{dc} can be varied to control and maximize the power output, P_{ext}; this process of determining v_{dc}^r for maximizing P_{ext} is better known as the maximum power-point tracking (MPPT).
- Alternatively, if the energy resource is of the voltage-source nature, the DC-link voltage is imposed and cannot be controlled. Rather, the power output P_{ext} is the variable that can be regulated at its set-point P_{ext}^r, by controlling P_g. For example, if the energy resource is a battery bank, P_{ext} is controlled according to the prevailing charging/discharging regime of the battery energy storage system. This control mode is referred in this chapter to as the *power control mode*.

The structure and design of the controllers for each of the aforementioned control modes are extensively discussed in [1]. It should be noted that, irrespective of the control mode, the steady-state values of P_g and P_{ext} are approximately equal (in an average sense) owing to the typically high efficiency of the power-electronic interface.

Figure 8.1 also indicates that the DER system may alternatively employ a *conditioned energy resource*. As illustrated in Figure 8.2, in a conditioned energy resource an intermediate electronic power conditioner precedes the energy resource. In the system of Figure 8.2(a), the energy resource generates DC power and thus a DC-DC electronic power conditioner is utilized, whereas Figure 8.2(b) represents a system in which the energy resource generates single- or three-phase AC power and therefore the electronic power conditioner is of AC-DC type.

In both systems, the output DC terminals of the electronic power conditioner define the DC port of the conditioned energy resource. The electronic power conditioner may be based on a variety of configurations. For example, in some low-power wind energy systems, the AC-DC electronic power conditioner consists of a diode-bridge rectifier followed by a DC-DC boost converter (see Section 8.3.6), whereas in a high-power variable-speed wind energy system, such as that described in Section 8.5.2, the electronic power conditioner is typically an AC-DC VSC (see Section 8.3.6).

Based on the configurations of Figures 8.2(a) and (b), a conditioned energy resource is of the current-source nature. Thus, with reference to our earlier discussion about the control of the DER system of Figure 8.1, we have to use the DC-link voltage control mode. However, since P_{ext} does not depend on v_{dc} in the systems of Figures 8.2(a) and 8.2(b), there is no point in varying v_{dc}. Therefore, v_{dc} is regulated at an optimal fixed value. Consequently, P_{ext} can be controlled, or maximized, only by the control scheme of the electronic power conditioner, as Figure 8.2 illustrates. As discussed in Section 8.5.2, as an example, this is how the output power of large variable-speed wind energy systems is controlled or maximized.

It is worth mentioning that the conditioning of an energy resource, as described above, is usually exercised: (1) to enable the integration of energy resources with low-voltage outputs, as with fuel cells and supercapacitors, (2) to enable output power control or MPPT, as with variable-speed wind energy systems and two-stage PV energy systems or (3) to allow for optimal operation of the power-electronic interface of the DER system, as with two-stage PV systems. The introduction of the electronic power

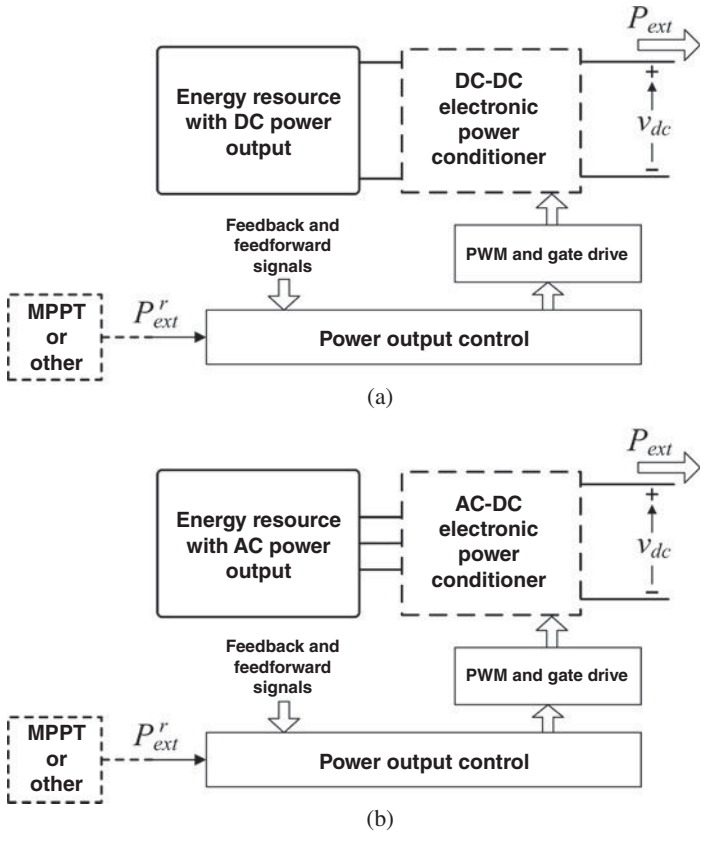

Figure 8.2 Generic schematic diagrams of (a) a conditioned DC energy resource, (b) a conditioned AC energy resource.

conditioner, however, results in a somewhat lower efficiency for the DER system, due to the corresponding power losses.

8.3 Realization of Different DER Systems

This section discusses different DER system realizations based on the generic model of Figure 8.1.

8.3.1 PV Energy Systems

Grid-connected PV energy systems can be classified as single-stage or two-stage systems. A single-stage PV system adheres to the generic model of Section 8.2 if the energy resource in Figure 8.1 is replaced with an array of series- and parallel-connected PV modules. So the control mode is the DC-link voltage control mode (see Section 8.2) and v^r_{dc} is determined by an MPPT scheme. Similarly, a two-stage PV energy system can also be realized based on the architecture of Figure 8.1 in which, as shown in Figure 8.3, the energy resource, that is, the PV array, is conditioned by a DC-DC boost converter that acts as the electronic power conditioner of Figure 8.2(a). To control the two-stage PV system, the set-point v^r_{dc} in

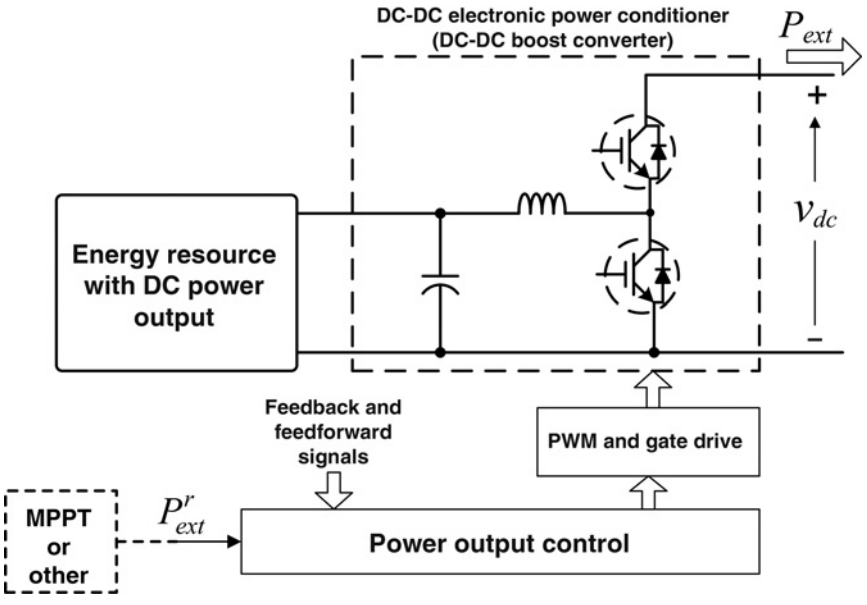

Figure 8.3 Schematic diagram of a conditioned DC energy resource that employs a DC-DC boost converter.

Figure 8.1 is set to a fixed positive value, corresponding to the DC-link voltage control mode, while P^r_{ext} in Figure 8.3 is determined through an MPPT process. In a decentralized two-stage PV system where a multitude of PV arrays are conditioned by corresponding DC-DC converters, multiple conditioned energy resources of the form shown in Figure 8.3 are connected in parallel with the DC port of the power-electronic interface of Figure 8.1.

8.3.2 Fuel-Cell Systems

A fuel-cell system also adheres to the generic model of Figure 8.1 and the conditioned energy resource model of Figure 8.3. Thus, the resultant DER system is controlled such that v^r_{dc} in Figure 8.1 is set to a fixed positive value, corresponding to the DC-link voltage control mode (Section 8.2), while P^r_{ext} in Figure 8.3 is determined based on a desired power dispatch strategy.

8.3.3 Battery Energy Storage Systems

Similar to PV systems, battery energy storage systems can be single-stage or two-stage systems. In a single-stage battery energy storage system, the energy resource, in Figure 8.1, is an array of series- and parallel-connected batteries, and one must exercise the power control mode (see Section 8.2), while P^r_{ext} is determined by the battery charging/discharging requirements and the power deployment strategy. In a two-stage battery energy storage system, however, the battery bank – the energy resource – is conditioned as shown in Figure 8.3. Thus, the DC-link voltage control mode is exercised (see Section 8.2) and the set-point v^r_{dc} in Figure 8.1 is set to a fixed positive value. Moreover, P^r_{ext} is determined by the battery charging/discharging requirements and the power deployment strategy, and is regulated by the DC-DC boost converter (Figure 8.3).

Irrespective of the number of stages, an auxiliary feedback loop may be included to override P^r_{ext} if the battery bank voltage exceeds a maximum permissible value when the batteries are being charged, or if the voltage drops below a minimum threshold when the batteries are being discharged.

8.3.4 Supercapacitor Energy Storage System

For a supercapacitor energy storage system, the energy resource in Figure 8.1 is an array of supercapacitors, conditioned as shown in Figure 8.3. Thus, v^r_{dc} in Figure 8.1 is set to a fixed positive value, corresponding to the DC-link voltage control mode (Section 8.2), while P^r_{ext} in Figure 8.3 is determined by the charging/discharging requirements and the power deployment strategy. Further, an auxiliary feedback loop is needed to override P^r_{ext} if the capacitor bank voltage exceeds a maximum permissible value when the capacitors are being charged.

8.3.5 Superconducting Magnetic Energy Storage System

The energy resource in a superconducting magnetic energy storage (SMES) system is conditioned by, typically, a DC-DC H-bridge converter as the electronic power conditioner, as shown in Figure 8.4. In practice, two of the diagonal transistors of the H-bridge can be omitted, while the corresponding diodes are left in place, since the direction of the coil current does not have to be reversed [2].

For the control, v^r_{dc} in Figure 8.1 is set to a fixed positive value, corresponding to the DC-link voltage control mode (Section 8.2), while P^r_{ext} in Figure 8.4 is determined by the charging/discharging requirements and the power deployment strategy. Also, an auxiliary loop is required to override P^r_{ext} if the coil current exceeds its maximum permissible value when the coil is being charged.

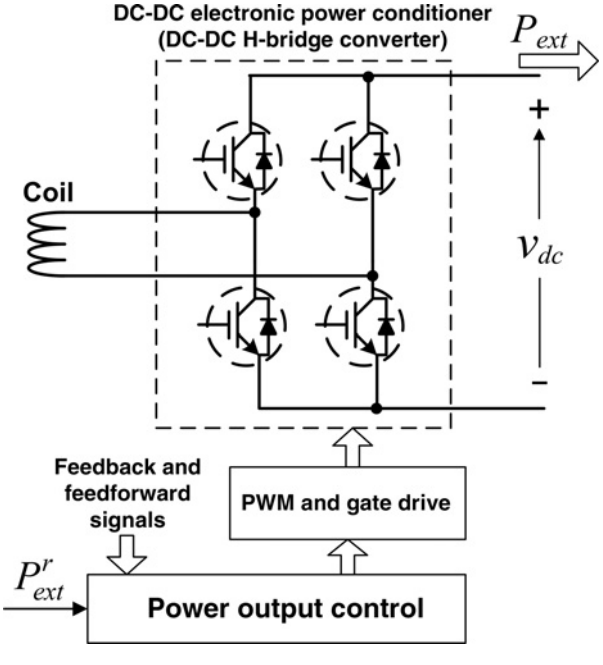

Figure 8.4 Schematic diagram of the conditioned DC energy resource for a SMES system.

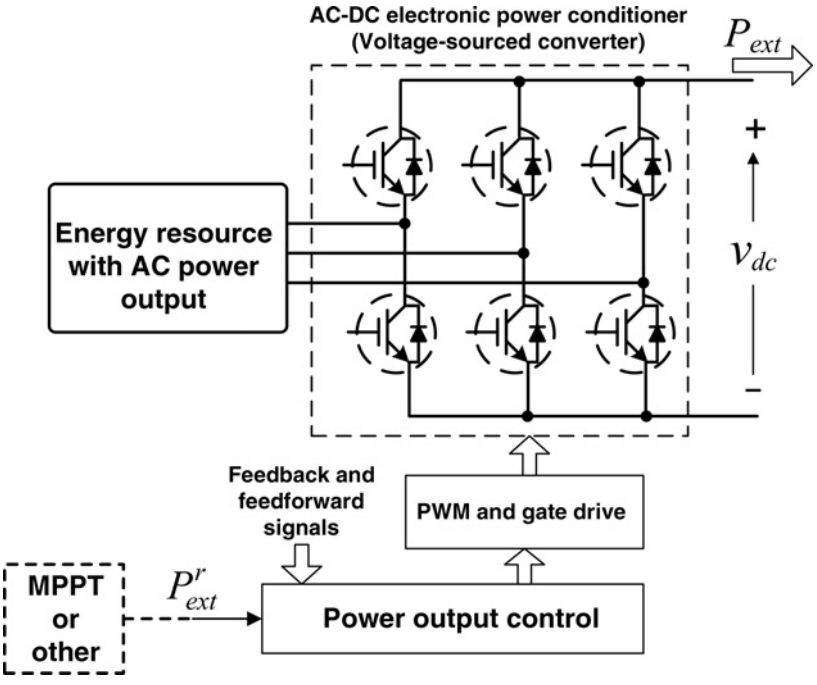

Figure 8.5 Schematic diagram of a conditioned AC energy resource that employs an AC-DC VSC.

8.3.6 Wind Energy Systems

Variable-speed wind energy systems represent another type of electronically interfaced DER system that fits into the model of Figure 8.1, with a conditioned AC energy resource, Figure 8.2(b). Thus, a wind turbine drives a three-phase generator, either directly or through a gearbox, and then, as shown in Figure 8.5, the generator is interfaced with the power-electronic interface (Figure 8.1) through an AC-DC VSC playing the role of the electronic power conditioner.

As discussed in Section 8.2, to control a wind energy system, the DC-link voltage control mode is used (see Section 8.2) and v_{dc} is regulated at a fixed positive value. Thus, the power set-point P^r_{ext} is externally commanded, by a desired power output profile or, alternatively, determined automatically by an MPPT algorithm. Commonly, the MPPT algorithm determines P^r_{ext} by the generator speed and the power-speed characteristic of the turbine. From the standpoint of physics, P_{ext}, which is approximately equal to the electrical power of the generator, is controlled by the electrical torque of the generator, and this, in turn, is controlled by the terminal current of the generator through the generator-side AC-DC VSC.

In a class of small variable-speed wind turbines, the electronic power conditioner consists of the back-to-back connection of a three-phase diode-bridge rectifier and a boost DC-DC converter [3], as shown in Figure 8.6 (the upper transistor of the half-bridge leg can be omitted). Depending on the power rating of the wind energy system, the inductor may be omitted from the rectifier DC side.

Wind energy systems using the doubly fed induction generator (DFIG) represent a special case in relation to the models of Figures 8.1 and 8.2(b). In a DFIG-based wind energy system, P_{ext} equals the power that leaves the rotor terminals of the generator, and the rest of the generator power flows from the stator circuit directly to the power system. The rotor power is, however, a small fraction of the total power, if the generator shaft speed is fairly close to the synchronous speed. Therefore, the power-electronic converters, Figures 8.1 and 8.2(b), can have reduced power ratings.

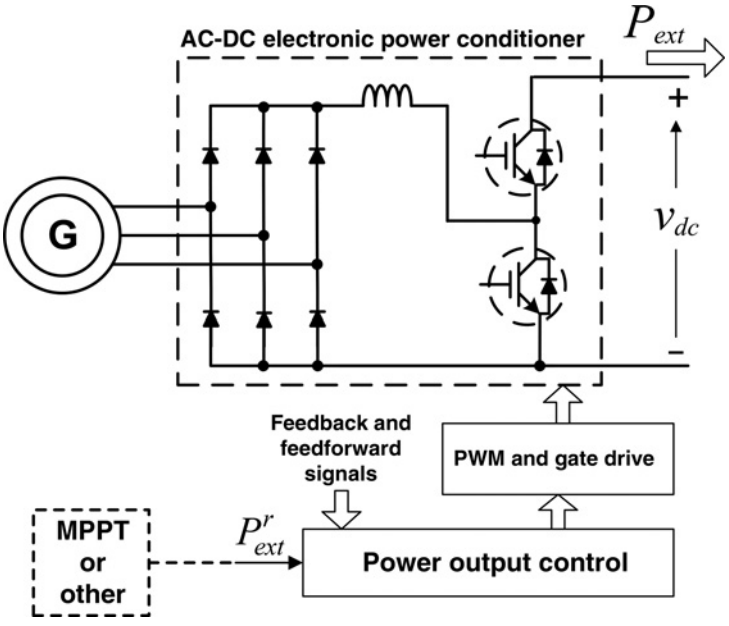

Figure 8.6 Schematic diagram of the conditioned energy resource for a small variable-speed wind energy system.

8.3.7 Flywheel Energy Storage Systems

The model of a flywheel energy storage system is very similar to that of a variable-speed wind energy system described earlier. Thus, the energy resource, a flywheel coupled to a three-phase machine, is conditioned by an AC-DC VSC (Figure 8.5). Again, v^r_{dc} in Figure 8.1 is assigned a fixed positive value, corresponding to the DC-link voltage control mode (Section 8.2), while P^r_{ext} in Figure 8.5 is determined by the charging/discharging requirements and the power dispatch strategy. An auxiliary feedback loop overrides P^r_{ext} to ensure that the flywheel speed remains limited in the charging mode.

8.4 Transient Analysis of Electronically Interfaced DER Systems

Unlike the steady-state characteristic, the transient behaviour of an electronically interfaced DER system is difficult to define accurately at the design stage; the codes often specify limits of important system variables, rather than the forms of response. Thus, depending on the steady-state operating point, control architecture and parameters, disturbance type and host network characteristics, a DER system can exhibit different transient behaviours whose compliance with the codes and standards can, for a variety of practical and economical reasons, be evaluated only through comprehensive simulation studies. This calls for the development of models to study the DER system and its host network.

Depending on the study objectives, different variables in a DER system could be of interest in terms of electromagnetic, electromechanical and thermal transients. For example, the designer of a wind energy system is often interested in transient responses of a wide range of variables, such as drive-train torsion, generator current and flux, converter DC-link voltage and line current and converter semiconductor temperatures. On the other hand, a system integration engineer may only be interested in the transient behaviour of such variables as the point of common coupling (PCC) voltage, DER system real-power output and fault current contribution. Thus, a simulation model should adequately capture the transients

of the variables of interest, while avoiding unnecessary details which increase the simulation runtime but add little relevant information.

In general, simulation studies constitute the first and most important step in evaluation of a design and its impact on the host utility network. Depending on the available simulation platforms or the type of studies to be conducted, electronically interfaced DER systems can be modelled in different ways, for example, using the mathematical relationships and signal processing blocks in the Matlab/Simulink software environment.

However, circuit-based simulation models, developed on specialized software platforms such as PSCAD/EMTDC, PSIM or PSPICE, offer a more tangible perspective on the operation and performance of a DER system and its transients. Moreover, circuit-based simulation models can more conveniently be expanded considerably to models for more complex systems, which may include transmission lines, electric machines, loads of different characteristics, transformers, switching devices and relays. As far as the control schemes are concerned, circuit-based simulation platforms offer libraries of various signal processing building blocks and, in some software packages, such as PSCAD/EMTDC, even the capability to link user-developed control and signal processing codes.

For circuit-based modelling, one major task is the modelling of the power-electronic converter. Effectively, the model of this specific component determines the balance between the accuracy of the overall simulation model and the speed of simulation. While some software packages (e.g. PSPICE) include sophisticated models for transistors and diodes (based on generic mathematical equations whose parameters are specified by device manufacturers) and therefore capture such transient phenomena as diode reverse recovery and transistor tailing current, others represent a diode and/or a transistor by a nonlinear resistor. Again, the type of study and transients to be captured, the size and complexity of the overall simulation model and the tolerable simulation runtime are among the factors that determine the level of complexity required for a valve model. For example, detailed valve models are suitable for studying fast overvoltage transients, device thermal states, switching power losses and so on, but significantly increase the runtime associated with the simulation study. By contrast, simplified valve models do not capture the aforementioned transients, but adequately reveal most transients relevant to power system studies, at a reasonably low runtime. A circuit-based simulation model in which the switching scheme and valves are included is referred to as a *topological model*, a *detailed model* or a *switched model,* and can generally be considered as a close approximation of a hardware prototype.

As the size and complexity of the study system grow, the simulation runtime that is based on switched models can quickly become prohibitively large, even if the crudest models are adopted for the valves, especially if a multitude of DER systems coexist within the study system. For such cases, the switched VSC models can be replaced by equivalent *averaged models* [4], in which no valve or switching scheme is included, but the terminal voltage and current variables of the VSC are approximated by their respective per-switching-cycle moving-average values.

8.5 Examples

This section presents the process of developing circuit-based simulation models and mathematical models, for an electronically interfaced DER system, using the examples of (1) a single-stage PV energy system and (2) a direct-drive variable-speed wind energy system.

8.5.1 Example 1: Single-Stage PV Energy System

In this example, circuit-based simulation models are developed for a single-stage PV energy system. First, two different averaged models are presented. Next, the two averaged models are compared with a detailed (topological) model of the PV system, through a number of study cases, and the limitations of the two averaged models are discussed. The methods discussed, however, are not limited to PV systems,

but can also be applied to other types of electronically interfaced DER systems, in view of the generic model of Section 8.2.

8.5.1.1 Structure of Single-Stage PV System

The schematic diagram of a typical single-stage PV system in Figure 8.7 illustrates that the PV system employs a PV generator [5] connected to the DC side of a three-phase DC-AC VSC [1]. The PV generator consists of an array of series- and parallel-connected PV modules, to be able to offer an adequately large power output at a sufficiently large DC voltage. However, for power system studies, the PV generator can effectively be approximated by an equivalent high-voltage/high-power PV cell [5], unless phenomena specific to the PV generator (e.g. shading effect) are to be studied. In the single-stage PV system, the VSC facilitates MPPT, through the regulation of the DC-link voltage. As Figure 8.7 shows, from the VSC AC side the PV system is interfaced with the grid through a low-pass LC filter and an isolation transformer, *Tr*. Typically, the isolation transformer is an integral part of the PV system, while another transformer (known as the interconnection transformer – not shown in Figure 8.7) may be required by the host utility to ultimately interface the PV system (or a cluster of PV systems) to the grid. To avoid clutter, however, only one transformer is shown in Figure 8.7 and, for simplicity of analysis, considered to be a part of the grid. As such, the real and reactive powers P_g and Q_g, that is, the powers that the PV system delivers at the transformer low-voltage terminals, are defined as the PV system real and reactive power outputs. Moreover, the transformer low-side voltage, v_{abc}, is defined as the *grid voltage*.

Comparing the PV system of Figure 8.7 with the generic model of Figure 8.1, we find that the PV generator and DC cables constitute the energy resource, the components inside the dashed box represent the power-electronic interface, and the power $P_{pv} = i_{pv} v_{dc}$ plays the role of P_{ext}.

Figure 8.8 gives more detailed schematic diagrams of the VSC and low-pass filter, which show that the VSC consists of three legs, each with two semiconductor valves. Each valve consists of a transistor and a diode – Figure 8.8(a). Each leg synthesizes one phase of the VSC AC-side terminal voltage $v_{t,abc}$, through complementary switching of its valves, based on carrier-based PWM or space-vector modulation

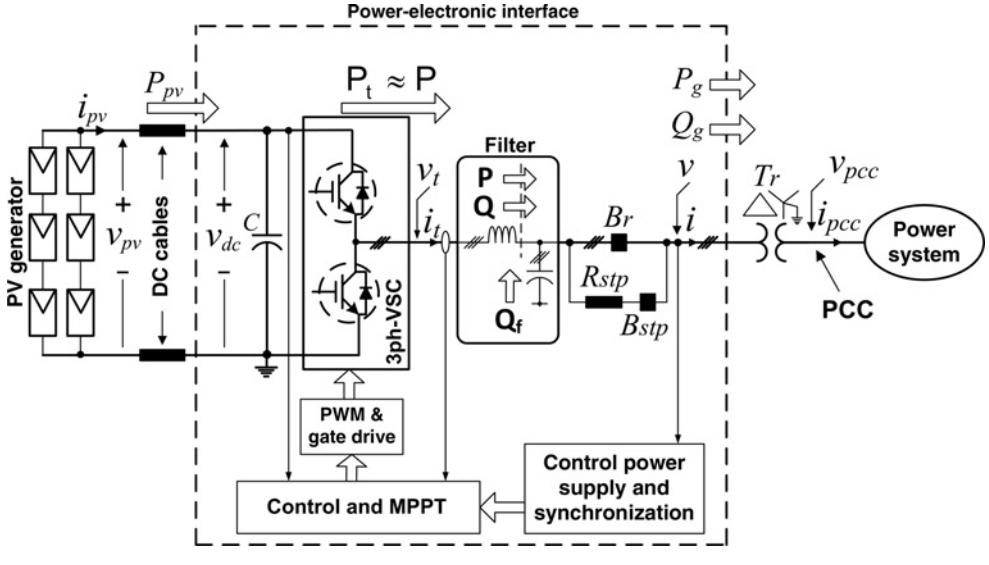

Figure 8.7 Single-line diagram of a single-stage grid-connected PV system (© 2011 IEEE) [5].

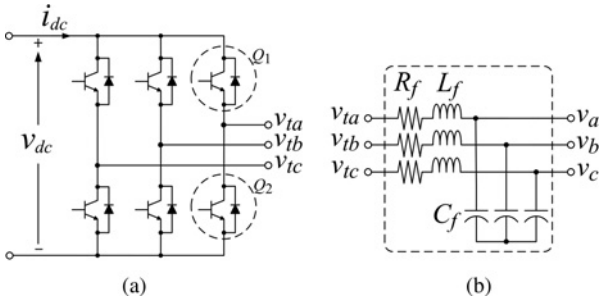

Figure 8.8 More detailed schematic diagrams of (a) VSC, (b) filter (© 2011 IEEE) [5].

(SVM). Figure 8.8(b) shows the filter consisting of a three-phase series reactor and a three-phase bank of shunt capacitors, with the per-phase inductance and capacitance of L_f and C_f, respectively; the resistance R_f represents the per-phase ohmic power loss of the filter reactor.

The function of the filter is to prevent the high-order harmonics of the VSC AC-side terminal voltage from penetrating the host grid and thus to ensure that the grid voltage, v_{abc}, is of low harmonic distortion.

8.5.1.2 Control Scheme of Single-Stage Grid-Connected PV System

Figure 8.9 shows a block representation of the control scheme of the single-stage three-phase PV system of Figure 8.7 [5]. The block diagram of Figure 8.9 assumes a current-mode control strategy, which is exercised in a rotating *dq*-frame whose *d*-axis is aligned with the grid voltage space vector, for example, by means of a phase-locked loop.

As Figure 8.9 illustrates, the current-control scheme of the PV system calculates the signals v_{td}^r and v_{tq}^r, that is, the desired values for the *d*- and *q*-axis components of the fundamental component of the VSC AC-side terminal voltage. The calculation is based on the objective that, if the VSC and its switching strategy can synthesize an AC-side terminal voltage whose fundamental component has *d*- and *q*-axis components equal to v_{td}^r and v_{tq}^r, then the *d*- and *q*-axis components of the VSC AC-side current rapidly and precisely track the two respective set-points, i_{td}^r and i_{tq}^r. This method of control has two distinct features: (1) it ensures that the VSC is protected against network faults, in view of the fact that i_{td}^r and i_{tq}^r (and thus the magnitude of the VSC AC-side current) are limited to pre-specified limits (Figure 8.9), and (2) it enables rapid and almost independent control of the PV system real and reactive power outputs, a feature that is highly desirable for an electronic power processor. The second feature is mathematically

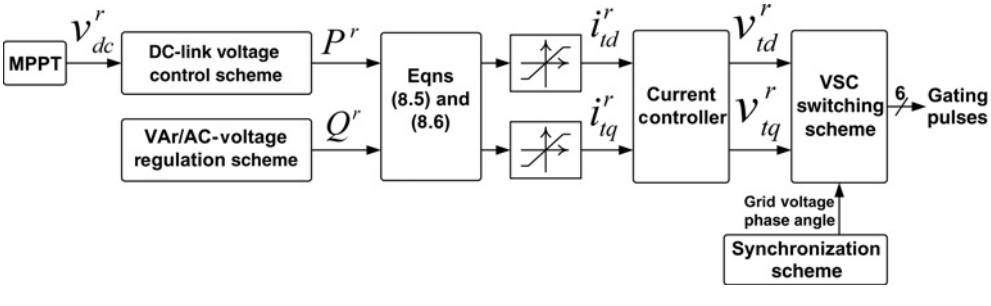

Figure 8.9 Block representation of the overall PV system control architecture (© 2011 IEEE) [5].

represented by the following two equations, which hold if the d-axis of the rotating frame is aligned with the grid voltage vector,

$$P = \frac{3}{2} v_d i_{td} \tag{8.1}$$

$$Q = -\frac{3}{2} v_d i_{tq}, \tag{8.2}$$

where v_d signifies the d-axis component of v_{abc}. Under balanced voltage conditions, v_d is equal to the instantaneous peak value of v_{abc} and, as such, almost constant (the q-axis component of v_{abc}, i.e. v_q, is zero). Therefore, as (8.1) and (8.2) indicate, P and Q are independent of each other and respectively proportional to the current components i_{td} and i_{tq}. The real and reactive powers that the PV system exchanges with the grid are closely related to P and Q, as

$$P_g \approx P \tag{8.3}$$

$$Q_g = Q + Q_f, \tag{8.4}$$

where Q_f is the reactive power that is delivered by the filter capacitor bank (the approximation in (8.3) is due to power losses). Under normal conditions, Q_f is approximately constant since the power system frequency and grid voltage magnitude are almost constant. Therefore, Q_g differs from Q by a constant offset.

Based on (8.1) and (8.2), the real and reactive power set-points P^r and Q^r are used to determine i^r_{td} and i^r_{tq}, as

$$i^r_{td} = \left(\frac{3}{2} V_{dn}\right)^{-1} P^r \tag{8.5}$$

$$i^r_{tq} = -\left(\frac{3}{2} V_{dn}\right)^{-1} Q^r, \tag{8.6}$$

where V_{dn} denotes the nominal value of v_d under a normal operating condition. As explained in reference [5], the set-points P^r and Q^r are obtained, respectively, from the DC-link voltage control scheme (in conjunction with an MPPT scheme) and from the control scheme for AC voltage or VAr.

Once calculated, the set-points v^r_{td} and v^r_{tq} are delivered to a switching scheme that determines the switching instants of the VSC valves. Depending on the adopted strategy, the switching process may involve normalization of v^r_{td} and v^r_{tq} (e.g. to the maximum DC-to-AC voltage gain of the VSC), as well as transformation of the two signals to a three-phase set of modulating signals (e.g. in the carrier-based PWM switching strategy).

8.5.1.3 Circuit-Based Simulation Model

Figure 8.10 illustrates one possible way of realizing an averaged model for the VSC [6], in a circuit-based simulation environment. The averaged model of Figure 8.10 replaces the valves by three dependent voltage sources at the AC side and one dependent current source at the DC side. The positive terminals of the voltage sources correspond to the AC-side terminals of the VSC, while their negative terminals meet at a common node, '0' – to circumvent convergence difficulties, it is sometimes necessary to connect the node '0' to the ground, through a large resistor, as shown in Figure 8.10, if nowhere else in the AC side circuit is connected to the ground. Each voltage source establishes a voltage (with reference to node '0') that is equal in value to the fundamental component of the corresponding phase voltage in the switched model. Thus, the variables v^r_{td} and v^r_{tq} (produced by the PV system current-control scheme, Figure 8.9) are transformed in the averaged model to the waveforms v_{ta}, v_{tb} and v_{tc}, which are then reproduced by

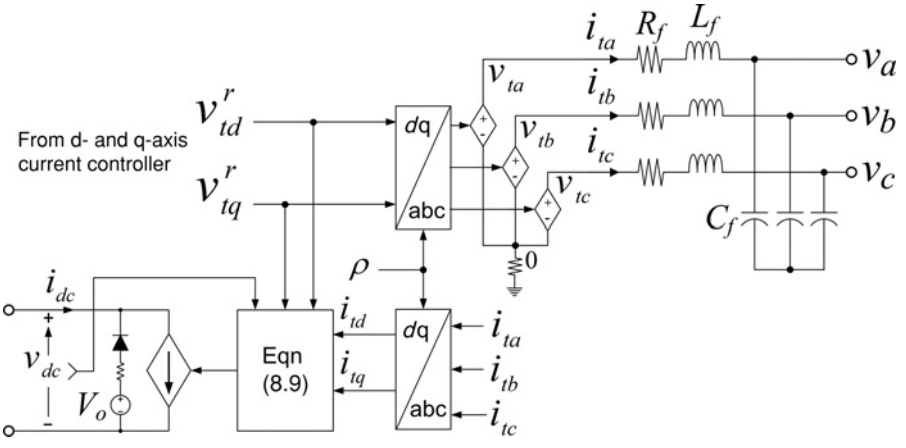

Figure 8.10 Schematic diagram of an averaged model in which the VSC AC side is represented by dependent voltage sources (© 2011 IEEE) [5].

the corresponding voltage sources. The angle for the transformation, ρ, is the phase angle of the grid voltage vector [1]. On the other hand, the current source terminals correspond to the DC-side terminals of the VSC, and the value of the current source is determined based on the principle of power balance, as

$$\underbrace{v_{dc}i_{dc}}_{P_{dc}} = \underbrace{v_{ta}i_{ta} + v_{tb}i_{tb} + v_{tc}i_{tc}}_{P_t \approx P} \tag{8.7}$$

$$i_{dc} = \frac{v_{ta}i_{ta} + v_{tb}i_{tb} + v_{tc}i_{tc}}{v_{dc}}, \tag{8.8}$$

which, assuming a dq-frame control, can be rewritten as

$$i_{dc} = \frac{\frac{3}{2}\left(v_{td}i_{td} + v_{tq}i_{tq}\right)}{v_{dc} + \varepsilon}, \tag{8.9}$$

where the (small) number ε is introduced to prevent division by zero, which would otherwise occur if v_{dc} were zero, for example, at the beginning of the simulation study.

If a switched model is adopted for the VSC in a circuit-based simulation model of the PV system, at the system startup the DC-link capacitor is charged either by the PV generator or by the grid (through the antiparallel diodes of the VSC valves). However, the valves are absent from the averaged model. Therefore, as Figure 8.10 shows, a series branch consisting of a DC voltage source, a resistor and a diode may be connected in parallel with the DC-side terminals of the averaged VSC model, to simulate the aforementioned DC-link precharging process; the DC source voltage should be set to about the peak value of the grid line-to-line voltage (here, the voltage across the low-pass filter capacitors, i.e. v_{abc} in Figure 8.7, is defined as the grid voltage). Subsequent to the startup process and during normal operation, the DC-link voltage becomes larger than (1.15 times) the peak value of the grid line-to-line voltage, due to the boosting property of the VSC, and therefore the diode turns off.

The averaged model of Figure 8.10 does not include the VSC valve models or switching scheme. Therefore, it runs considerably faster than its switched counterpart. However, it does not predict the voltage/current harmonics (generated through the PWM process) and their impact on the grid and control. Moreover, it is valid for frequencies up to about one-third of the VSC switching frequency and only if the VSC in the actual system or in the switched model operates in the linear modulation

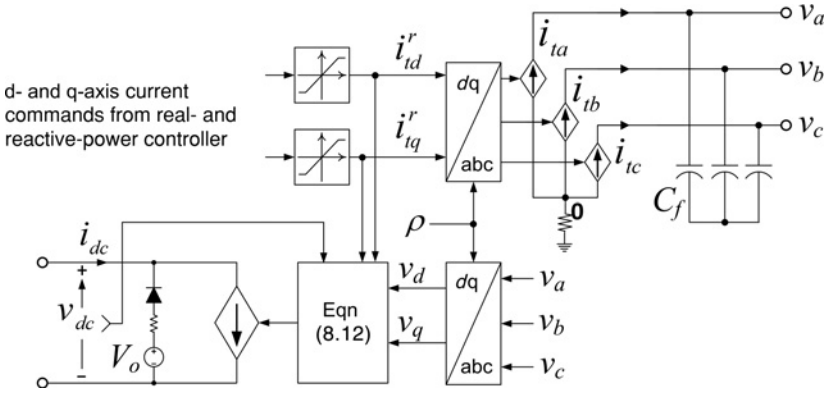

Figure 8.11 Schematic diagram of an averaged model in which the VSC AC side and the filter reactor are replaced by dependent current sources (© 2011 IEEE) [5].

region, that is, if $\sqrt{\left(v^r_{td}\right)^2 + \left(v^r_{tq}\right)^2} \leq 0.5 v_{dc}$(the condition is modified to $\sqrt{\left(v^r_{td}\right)^2 + \left(v^r_{tq}\right)^2} \leq 0.575 v_{dc}$ if the PWM strategy with third-order harmonic injection or the SVM strategy is assumed).

The averaged model of Figure 8.10 can be further simplified to that of Figure 8.11 [6], if one remembers that the VSC and the current-control scheme of the PV system (Figure 8.9) cooperate in such a way that the *d*- and *q*-axis components of the current through the reactor L_f track the set-points i^r_{td} and i^r_{tq}, rapidly and precisely [1]. Thus, as Figure 8.11 shows, in the simplified averaged model, the dependent voltage sources are substituted by three dependent current sources which correspond to the three reactor phase currents, i_{ta}, i_{tb} and i_{tc}, and only the shunt capacitors of the filter are retained; the filter resistance and inductance are omitted from the model, not only because their currents are now dictated by the dependent current sources, but also because the series connection of a series RL branch and a current source can create convergence problems for the simulation software.

In the averaged model of Figure 8.11, the control signals for the current sources are calculated through the *dq*- to *abc*-frame transformation of the signals i^r_{td} and i^r_{tq} which, in turn, are obtained from the real and reactive power control scheme of the PV system (Figure 8.9).

The DC side of the averaged VSC model remains a dependent current source as in the averaged model of Figure 8.10. The control signal for the DC-side current source is again calculated based on the principle of power balance which, for the circuit of Figure 8.11, is formulated as

$$\underbrace{v_{dc} i_{dc}}_{P_{dc}} = \underbrace{v_a i_{ta} + v_b i_{tb} + v_c i_{tc}}_{P} \tag{8.10}$$

$$i_{dc} = \frac{v_a i_{ta} + v_b i_{tb} + v_c i_{tc}}{v_{dc}} \tag{8.11}$$

or alternatively as

$$i_{dc} = \frac{\frac{3}{2}\left(v_d i_{td} + v_q i_{tq}\right)}{v_{dc} + \varepsilon}. \tag{8.12}$$

Note that unlike the switched model, both the switching and current-control schemes are absent from the simplified model of Figure 8.11.

A few remarks about the simplified averaged model of Figure 8.11 may be useful. In the actual PV system or its switched model, the current-control scheme measures, estimates or assumes the grid voltage

components v_d and v_q, and controls the VSC voltage components v_{td} and v_{tq} in such a way that the voltage across the filter reactor is always regulated, in spite of the disturbances. It is the proper implementation of this process that makes the filter reactor act as a three-phase current source with controllable magnitude and phase angle. Depending on the structure, implementation and parameters of the current-control scheme, the assumption of the current-source nature of the VSC and its tie reactor may or may not be valid if the grid voltage is unbalanced, sagged, swelled and so on. Therefore, to correctly interpret the results, we need to be cognizant of the conditions under which the aforementioned composition of components acts as a current source.

Another point is that the averaged model of Figure 8.11 underestimates the power loss of the VSC and its tie reactor, owing to the omission of the filter and VSC valve resistances. However, we could argue that the introduced error is not meaningful, since even the switched model may not be able to accurately predict the power losses if it employs a crude model for the VSC valves.

Finally, it should be noted that, similar to the averaged model of Figure 8.10, the accuracy of the simplified averaged model of Figure 8.11 is compromised if the actual PV system does not satisfy the condition $\sqrt{\left(v_{td}^r\right)^2 + \left(v_{tq}^r\right)^2} \leq 0.5v_{dc}$, for the regular PWM strategy, or $\sqrt{\left(v_{td}^r\right)^2 + \left(v_{tq}^r\right)^2} \leq 0.575v_{dc}$, for the PWM strategy with third-order harmonic injection or for the SVM strategy.

Ignoring certain dynamics, we can further simplify the circuit-based averaged models discussed thus far [6]. For example, assuming a steady-state or quasi steady-state condition, we can assume that the DC-link voltage is tightly regulated at a level that corresponds to the maximum power for the prevailing sunlight and PV cell junction temperature. Thus, the DC-link capacitor, the PV generator, the MPPT scheme and the DC-link voltage control scheme can all be omitted from the model, and the VSC and filter can be represented by the averaged models of Figure 8.12. For this model, the real-power set-point

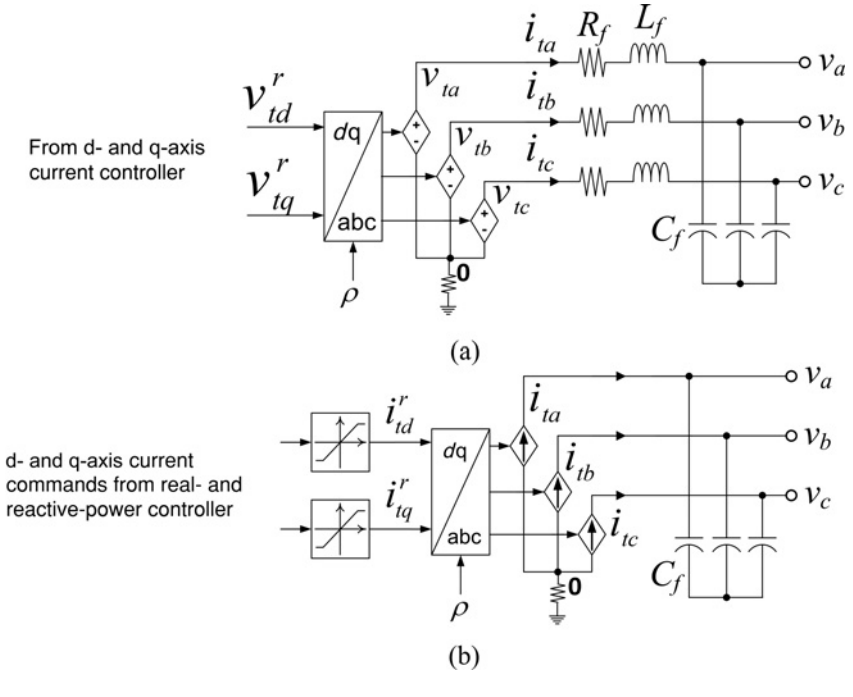

Figure 8.12 Schematic diagram of an averaged model in which the DC-link voltage dynamics are ignored: (a) based on dependent voltage sources, (b) based on dependant current sources (© 2011 IEEE) [5].

P^r can be obtained from a look-up table that specifies the PV generator maximum power for the given sunlight and PV cell junction temperature. As compared to the averaged models of Figures 8.10 and 8.11, the models of Figure 8.12 do not bring about much improvement in terms of the simulation runtime, but obviate the need for modelling the PV generator, MPPT scheme and DC-link voltage control scheme.

8.5.1.4 Test System and Simulation Results

To compare the switched and averaged models, a test 1.4-MW PV system has been simulated (adopting the configuration of Figure 8.7). The PV system is assumed to be interfaced with a typical North American medium-voltage network whose single-line schematic diagram is shown in Figure 8.13 [7]. The PV system is connected to Bus 3 of the network, and the results are obtained from a switched model of the PV system, as well as from the averaged models of Figures 8.10 and 8.11. The details of the switched model and other system data can be found in [5].

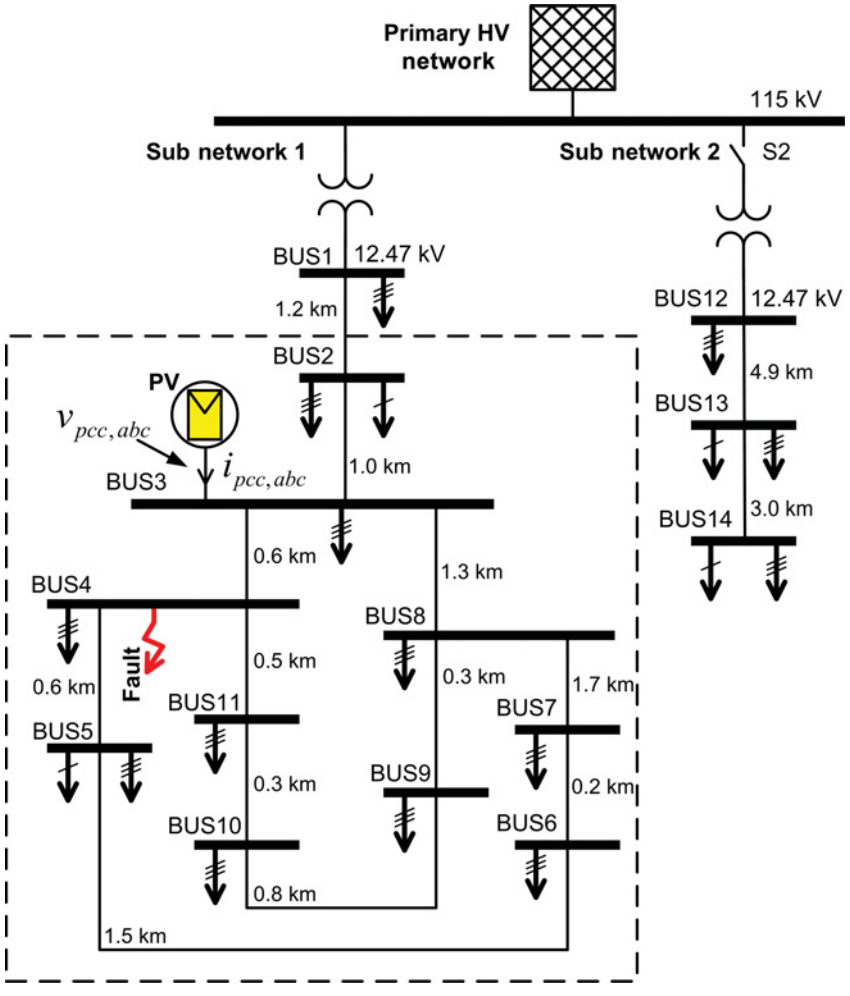

Figure 8.13 Example 1 – Schematic diagram of the test distribution network (© 2011 IEEE) [5].

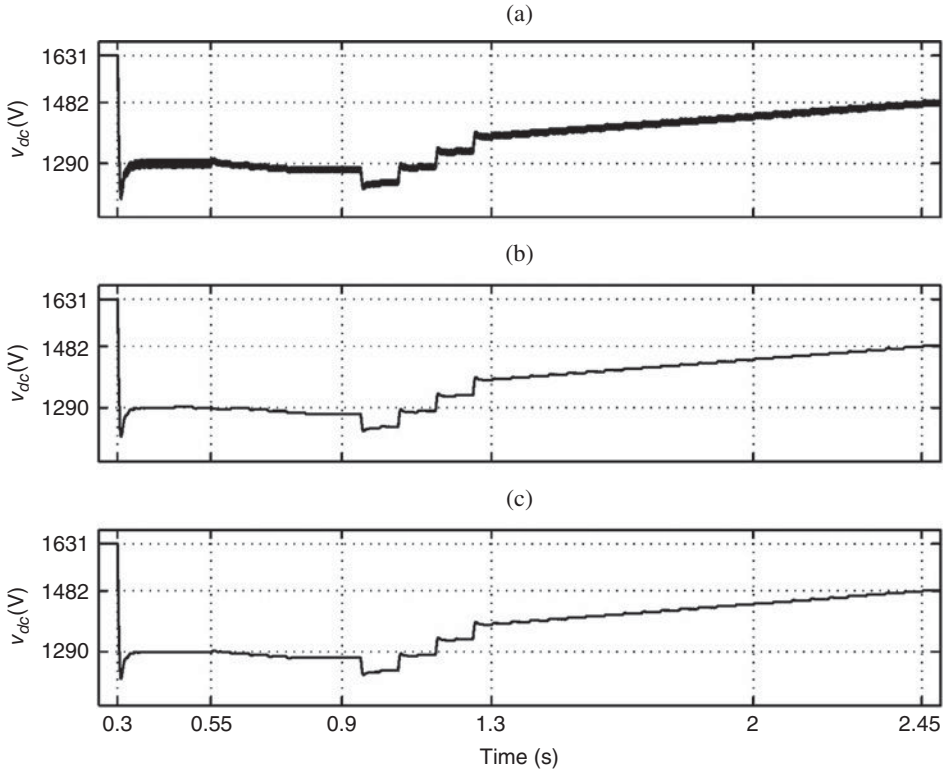

Figure 8.14 Example 1 – Response of the DC-link voltage to the startup process and stepwise changes in solar irradiation and PV cells junction temperature: (a) switched model, (b) averaged model of Figure 8.10, (c) averaged model of Figure 8.11 (© 2011 IEEE) [5].

PV system response to changes in solar irradiation and PV cell junction temperature: Figures 8.14 and 8.15 illustrate the responses of the PV system DC-link voltage and output power when the PV system is subjected to the startup process, a stepwise change in solar irradiation (from 1.0 to 0.6 kW/m^2, at $t = 0.55$ s) and a step change in the PV cell junction temperature (from 40°C to zero, at $t = 0.9$ s). As the figures indicate, the responses predicted by the averaged models closely agree with those obtained from the switched model. Figures 8.15(b) and 8.15(c) indicate that the averaged models predict a slightly larger steady-state power output than that predicted by the switched model. The reason is that the VSC valves, and thus the power loss associated with their on-state resistance, are absent from the averaged models. The PV system response for the aforementioned sequence of events is described and analysed in [5].

Figure 8.16 shows a zoomed view of the VSC AC-side current response to the aforementioned sequence of disturbances, except that for this case the solar irradiation steps from 1.0 to 0.2 kW/m^2; this difference in the irradiance level change has been introduced to subject the PV system to a more severe disturbance. The figure shows that the response predicted by the averaged model of Figure 8.10 closely agrees with the response provided by the switched model. However, the response under the averaged model of Figure 8.11 is slightly different from the two other responses, for a brief period subsequent to the disturbance incident. The reason is that the disturbance results in a sudden drop in the PV generator

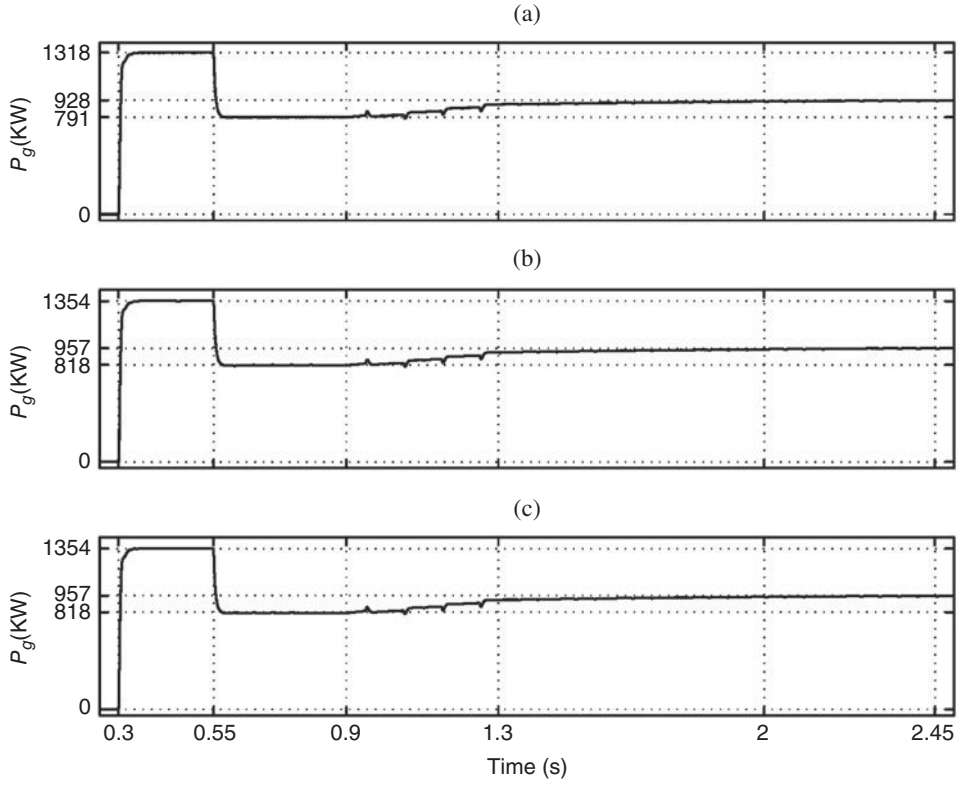

Figure 8.15 Example 1 – Responses of the PV system output power to the startup process and stepwise changes in solar irradiation and PV cells junction temperature: (a) switched model, (b) averaged model of Figure 8.10, (c) averaged model of Figure 8.11 (© 2011 IEEE) [5].

power, which in turn prompts the DC-link voltage controller to rapidly change P^r and i^r_{td}, in an attempt to maintain the DC-link voltage. While in the switched model and the averaged model of Figure 8.10, the response of i_{td} to i^r_{td} is inherently governed by certain dynamics (through the current-control scheme) and thus cannot be instantaneous; in the averaged model of Figure 8.11 the VSC AC-side current is directly calculated from i^r_{td} (and i^r_{tq}) and consequently exhibits an abrupt excursion that does not happen in reality.

Figure 8.16 also highlights the fact that, in contrast to the switched model, the averaged models do not predict the high-frequency harmonic distortions of the VSC AC-side current.

PV system response to three-phase-to-ground faults: In this case, the PV system response to a three-phase to ground network fault is studied using the switched and averaged models. For this case, the solar irradiation and PV cell junction temperature are assumed to be constant at 1.0 kW/m^2 and 40°C, respectively. It is further assumed that two three-phase-to-ground faults strike Bus 4 of the network (Figure 8.13): the first fault is incepted at $t = 0.5$ s and lasts for 0.1 s, whereas the second fault takes place at $t = 0.9$ s and stays.

Figures 8.17–8.19 illustrate the responses of the VSC AC-side current, DC-link voltage and PV system output power, respectively. The figures confirm the close agreement between the averaged models and the switched model. The analysis of the PV system response to the described sequence of disturbances can be found in reference [5].

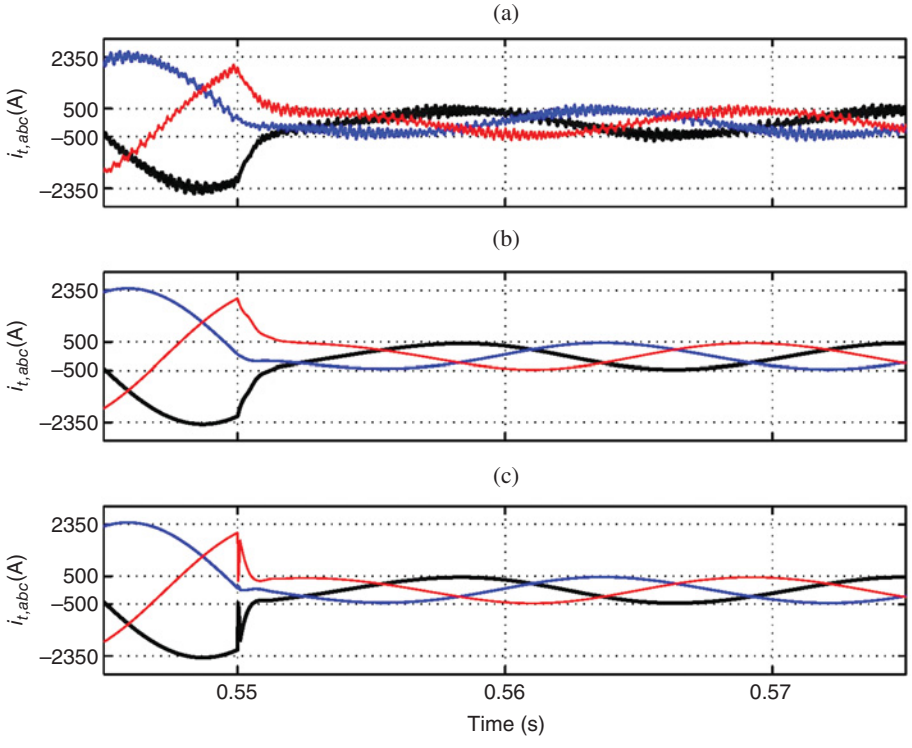

Figure 8.16 Example 1 – Zoomed view of the VSC AC-side current response to an abrupt and large drop in solar irradiation: (a) switched model, (b) averaged model of Figure 8.10, (c) averaged model of Figure 8.11 (© 2011 IEEE) [5].

PV system response to a line-to-line fault: This case demonstrates the response of the PV system to a line-to-line fault striking Bus 4 of the network, as predicted by the switched and averaged models. Prior to the fault incident at $t = 0.5$ s, the PV system is assumed to be in a steady state and under a solar irradiation of 1.0 kW/m^2; the PV cell junction temperature is assumed to be 40°C.

Figures 8.20–8.22 illustrate the responses of the VSC AC-side current, DC-link voltage and PV system output power, respectively. Again, the responses predicted by the averaged models closely agree with those of the switched model. In particular, it is interesting to note the accuracy of the simplified averaged model of Figure 8.11; the accuracy cannot be generalized, but is due to the design and parameters of the current-control and DC-link voltage control schemes of this specific PV system (see [5] for details), which ensure that the PV system controllers and PWM scheme do not become saturated, and therefore the current-control scheme manages to maintain the balance and quality of the VSC AC-side current, Figure 8.20(a), in spite of the severe grid voltage imbalance and sag caused by the fault (not shown in the graphs). An analysis of the PV system response can be found in [5].

8.5.2 *Example 2: Direct-Drive Variable-Speed Wind Energy System*

The objective of the previous example was to illustrate the development and discuss the features of circuit-based simulation models. This example, however, is intended to demonstrate (1) how the generic model presented in Section 8.2 can be used to design the controls of an electronically interfaced DER system; (2)

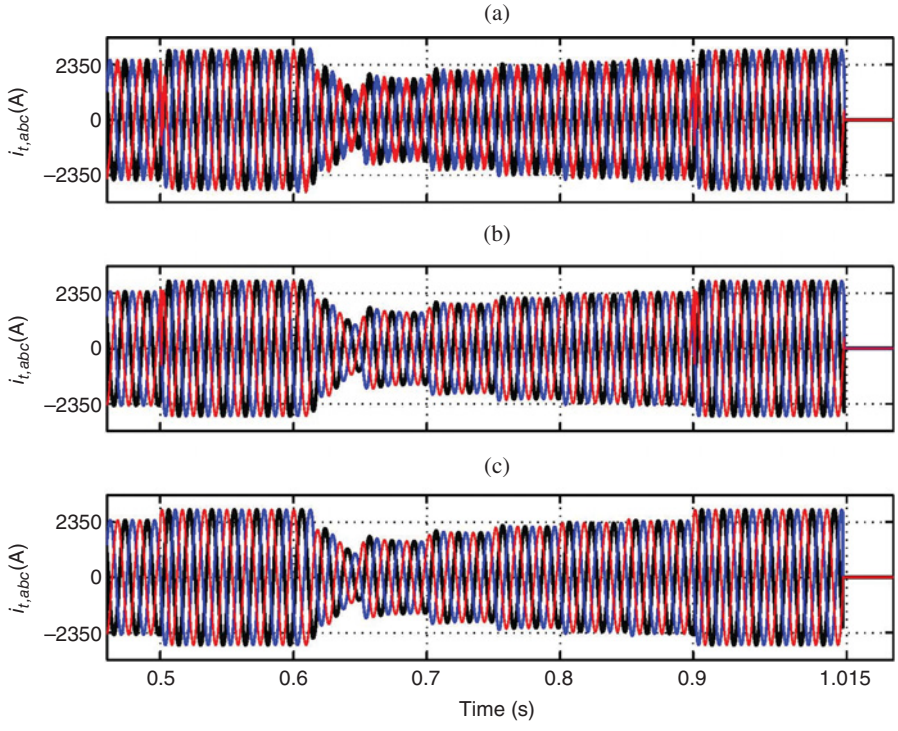

Figure 8.17 Example 1 – Response of the VSC AC-side current to three-phase to ground network faults: (a) switched model, (b) averaged model of Figure 8.10, (c) averaged model of Figure 8.11 (© 2011 IEEE) [5].

how a mathematical model can be developed and used for transient analysis of an electronically interfaced DER system; and (3) how the mathematical model can be validated by comparing its results with those of a circuit-based model. To that end, the section uses the example of a direct-drive variable-speed wind energy system (WES).

8.5.2.1 Structure of the Direct-Drive Variable-Speed Wind Energy System

A simplified schematic diagram of a direct-drive variable-speed WES in Figure 8.23 illustrates that the WES comprises a wind turbine, a high-pole permanent-magnet synchronous generator (PMSG) directly mechanically interfaced with the turbine, a three-phase VSC and the power-electronic interface of Figure 8.1, Section 8.2. The VSC is connected from its DC port in parallel with the DC port of the power-electronic interface. Thus, the collection of the turbine, PMSG and VSC constitute a conditioned AC energy resource, Figure 8.2(b), for the overall DER system.

As discussed in Section 8.3.6, the power-electronic interface is set to operate in the DC voltage control mode, to regulate the DC voltage, v_{dc}, at an optimum constant value. Hence, the VSC controls the PMSG current and therefore torque, in order to either regulate or maximize P_{ext}, the power output of the conditioned energy resource. This, in turn, fulfils the ultimate goal that the power output of the WES, P_g, is also regulated or, alternatively, maximized. In the remainder of this section, we refer to the conditioned AC energy resource as the *wind energy capture subsystem* of the WES, whose mathematical modelling and analysis is the subject of this section. Thus, we assume that the power-electronic interface

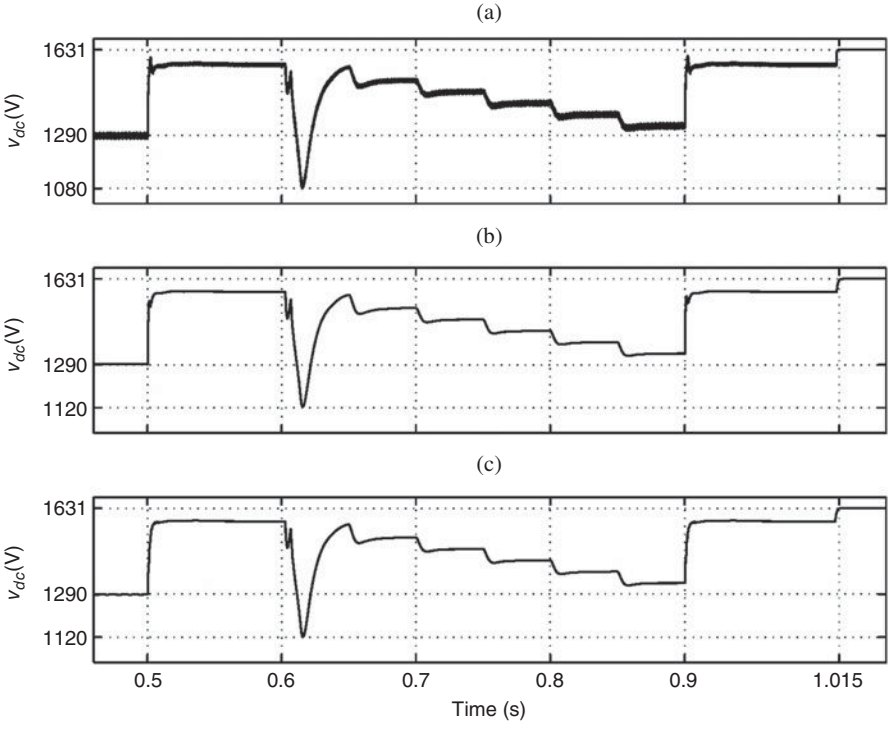

Figure 8.18 Example 1 – Responses of the DC-link voltage to three-phase to ground network faults: (a) switched model, (b) averaged model of Figure 8.10, (c) averaged model of Figure 8.11 (© 2011 IEEE) [5].

tightly regulates v_{dc} at a constant value and therefore imposes negligible transient or steady-state impact on the wind energy capture subsystem. Of course, any such impact, if appreciable, would be captured in a circuit-based simulation of the WES.

8.5.2.2 Basic Control Scheme of the Wind Energy Capture Subsystem

As mentioned in Section 8.5.2.1, the object of the control for the conditioned AC energy resource, that is, the wind energy capture subsystem, is to regulate or maximize P_{ext}. However, assuming a high efficiency for the three-phase VSC, P_{ext} is almost equal to the electrical power output of the PMSG. Consequently, the task boils down to that of regulating or maximizing P_e.

Figure 8.24 shows the block diagram of a control scheme whose objective is to force P_e to track the respective set-point P_e^r, which is determined based on the mode of operation of the WES, as will be explained in Section 8.5.2.4. In turn, P_e is controlled by regulating the PMSG electrical torque, T_e. The PMSG torque control is performed in a rotating dq-frame whose direct axis is aligned with the PMSG rotor flux vector. The control can be tuned such that T_e responds to its set-point, T_e^r, based on the first-order transfer function [1]

$$T_e = \frac{1}{\tau_i s + 1} T_e^r, \tag{8.13}$$

for which the time constant τ_i is a design parameter.

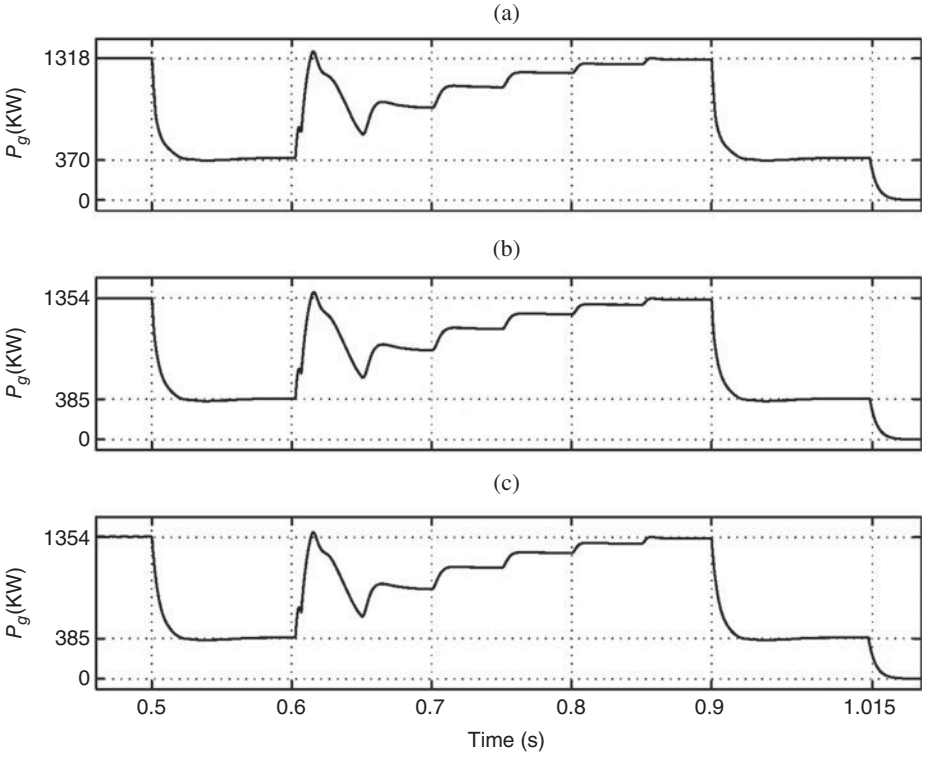

Figure 8.19 Example 1 – Responses of the PV system output power to three-phase to ground network faults: (a) switched model, (b) averaged model of Figure 8.10, (c) averaged model of Figure 8.11 (© 2011 IEEE) [5].

Figure 8.24 also illustrates the pitch-angle control process whose function is to ensure that the rotational speeds of the turbine and PMSG do not exceed a maximum permissible value, $\omega_{r-\max}$. Thus, if the PMSG shaft speed, ω_r, exceeds $\omega_{r-\max}$, a PI compensator increases the pitch angle, β, to decrease the turbine power and regulate ω_r at $\omega_{r-\max}$; if ω_r is smaller than $\omega_{r-\max}$, the compensator output is saturated at its lower limit, $\beta_{\min}$, to maximize the turbine power. Figure 8.24 further shows that the PI compensator output passes through a rate limiter, which represents the limited speed at which the pitch angle can be changed in practice.

8.5.2.3 Mechanical Model of Drive-Train

The mechanical torque of a wind turbine is given by

$$T_{tur} = \frac{P_{tur}}{\omega_t} = \frac{0.5\pi R^2 \rho C_p(\lambda, \beta) v_w^3}{\omega_t}, \tag{8.14}$$

where T_{tur} is the turbine torque (Nm), P_{tur} is the turbine power (W), ω_t is the turbine angular speed (rad/s), R is the turbine radius (m), ρ is the air mass density (kg/m^3), v_w is the wind speed (m/s), $\lambda = R\omega_t / v_w$ is the turbine tip-speed ratio (unitless), β is the pitch angle (degrees) and C_p (unitless), known as the turbine power efficiency, is a nonlinear function of λ and β.

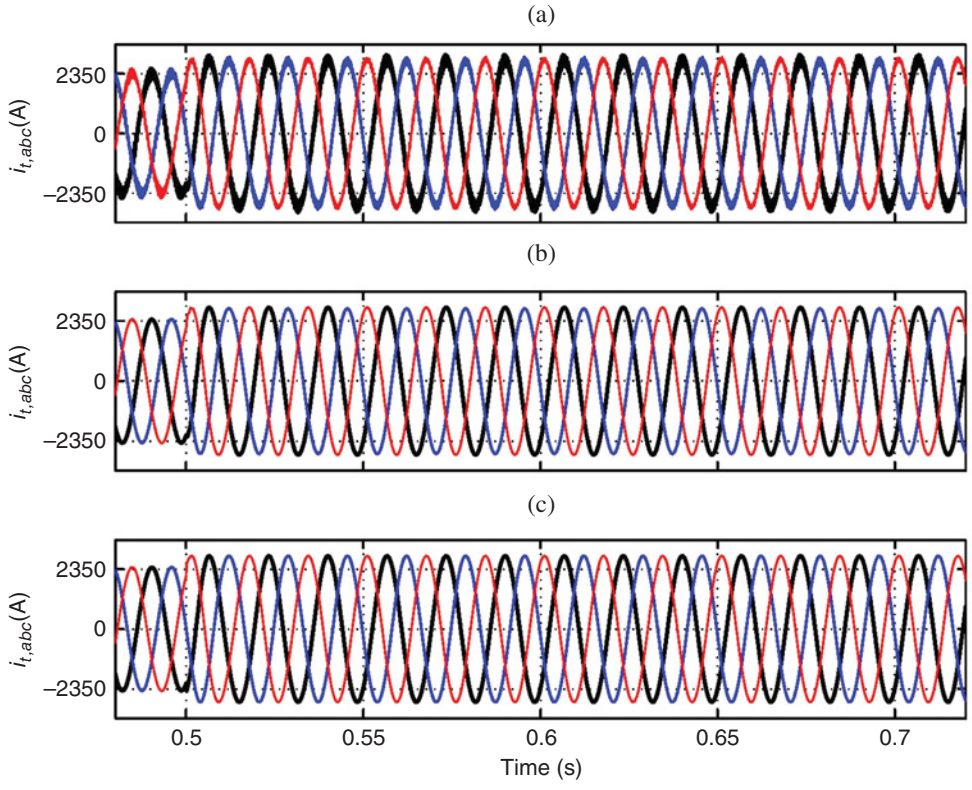

Figure 8.20 Example 1 – Response of the VSC AC-side current to a line-to-line network fault: (a) switched model, (b) averaged model of Figure 8.10, (c) averaged model of Figure 8.11 (© 2011 IEEE) [5].

Drive-train dynamics may be represented by models of different levels of complexity. However, a two-mass model is adequate for capturing the dynamics that affect stability; higher-order models are commonly employed for studying the mechanical fatigue of the drive-train. Therefore, ignoring the mechanical losses, the drive-train is represented by the two-mass model

$$J_t \frac{d\omega_t}{dt} = T_{tur} - k_s \gamma \tag{8.15}$$

$$J_r \frac{d\omega_r}{dt} = k_s \gamma - T_e \tag{8.16}$$

$$\frac{d\gamma}{dt} = \omega_t - \omega_r, \tag{8.17}$$

where J_t and J_r signify the turbine and PMSG moments of inertia (kgm^2), respectively; k_s is the drive-train shaft stiffness (Nm/rad); the variable γ represents the torsional displacement of the drive-train (rad); and T_e denotes the PMSG torque (Nm). The shaft speed of the PMSG, ω_r, is in rad/s. Equations (8.14) through (8.17) constitute a state-space drive-train model for the wind energy capture subsystem.

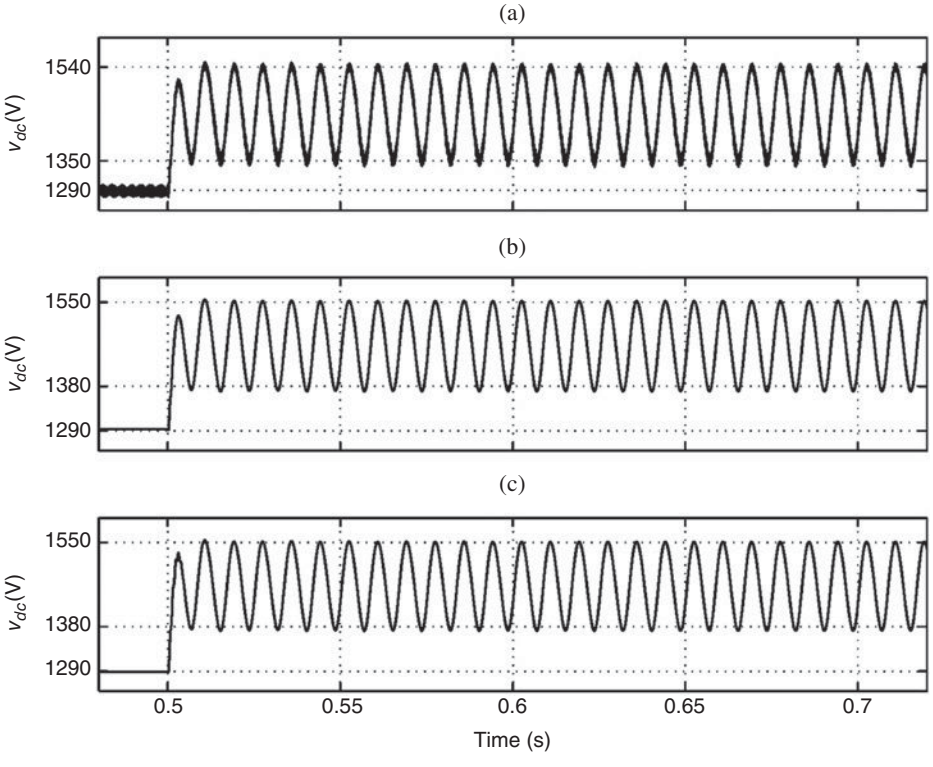

Figure 8.21 Example 1 – Response of the DC-link voltage to a line-to-line network fault: (a) switched model, (b) averaged model of Figure 8.10, (c) averaged model of Figure 8.11 (© 2011 IEEE) [5].

8.5.2.4 Modes of Operation of WES

Two modes of operation are defined for the WES of Figure 8.23: (1) the MPPT mode, whose objective is to maximize P_{ext} and (2) the controlled-power (CP) mode, whose task is to regulate P_{ext} at an externally commanded value, P_{cmd}.

The MPPT mode can be achieved if the turbine mechanical power output is maximized. This, in turn, calls for maximizing C_p. To maximize C_p, the tip-speed ratio, λ, must be kept constant at its optimum value λ_{opt}, regardless of the wind speed. The objective is fulfilled if the PMSG power set-point is determined based on

$$P_e^r = k_{opt}\omega_r^3, \tag{8.18}$$

in which the constant k_{opt} is:

$$k_{opt} = \frac{0.5\pi R^5 \rho}{\lambda_{opt}^3} C_p(\lambda_{opt}, \beta_{\min}). \tag{8.19}$$

The CP mode is exercised if the PMSG power output, P_e, is regulated at the command value P_{cmd}, regardless of the wind speed. Thus, the set-point, P_e^r, Figure 8.24, is given the value P_{cmd}. It can be noted

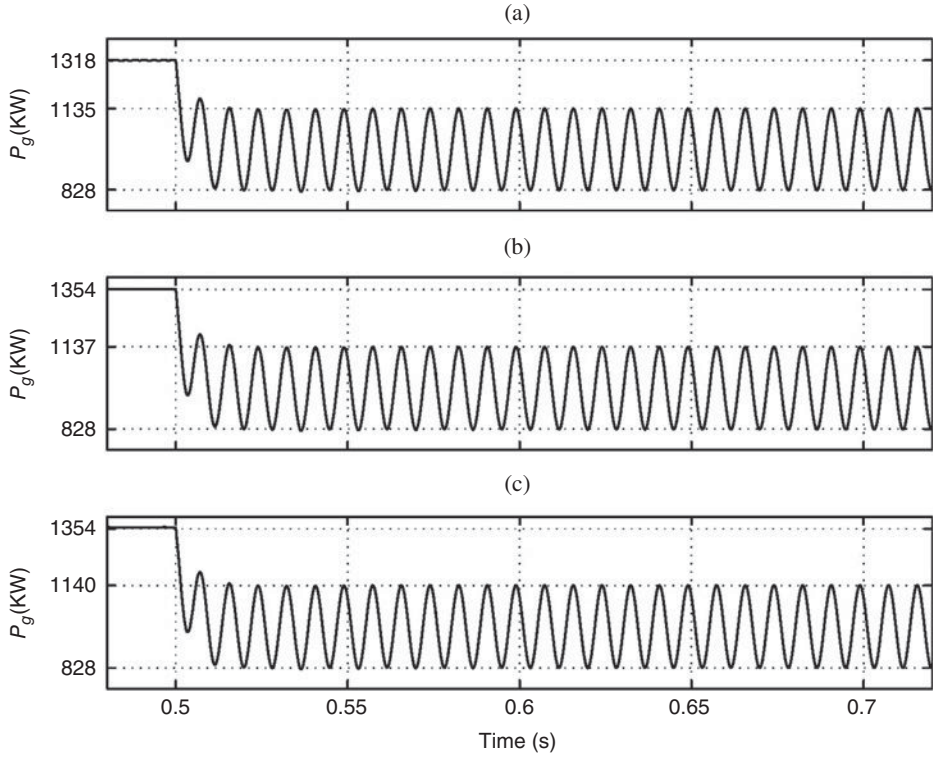

Figure 8.22 Example 1 – Response of the PV system output power to a line-to-line network fault: (a) switched model, (b) averaged model of Figure 8.10, (c) averaged model of Figure 8.11 (© 2011 IEEE) [5].

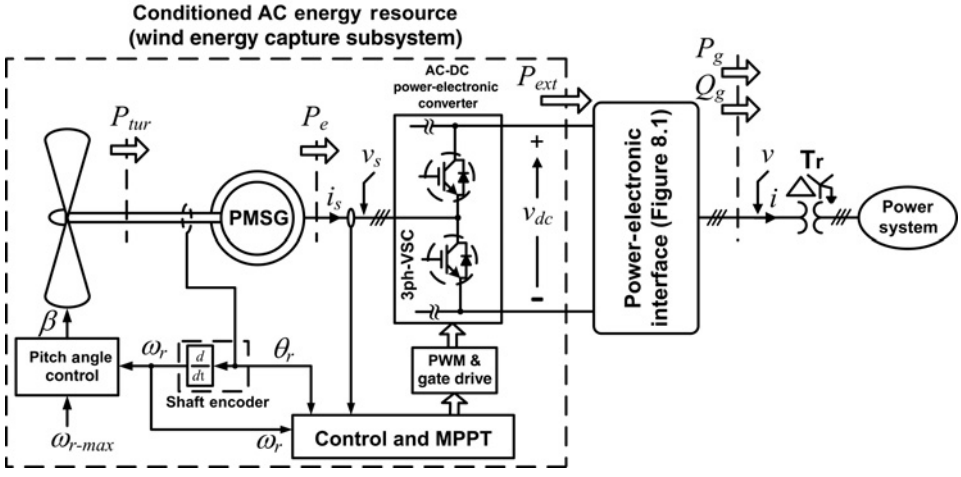

Figure 8.23 Simplified schematic diagram of a direct-drive PMSG-based wind energy system (© 2013 IEEE) [8].

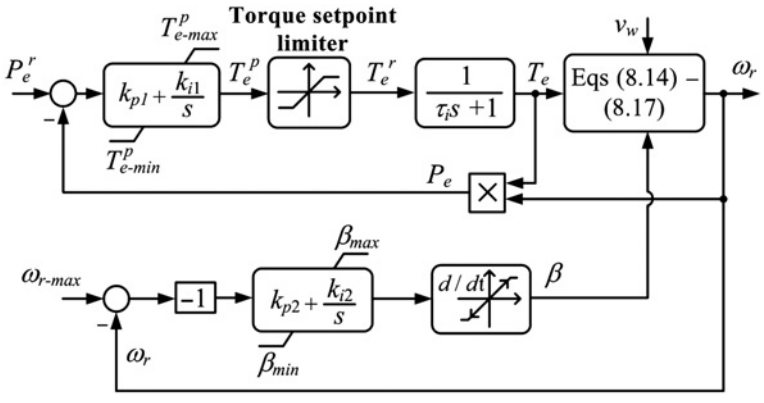

Figure 8.24 Block diagram of the PMSG power control scheme (© 2013 IEEE) [8].

that P_{cmd} should be smaller than the maximum available turbine power at the prevailing wind speed, such that the physics permit P_e to track P_{cmd}.

8.5.2.5 Damping Strategy

The WES drive-train is subject to oscillations in the CP mode of operation, due to its undamped torsional modes, which calls for a damping mechanism. Therefore, a damping scheme shown in Figure 8.25 is added to the basic control system of Figure 8.24. As Figure 8.25 shows, if the saturation is ignored, the PMSG torque set-point, T^r_e, is augmented with a high-pass filtered measure of the rotor speed. First, the AC component of the rotor speed is extracted by passing ω_r through a high-pass filter, $F(s)$. Then, compensator $C(s)$ processes the error between zero and the filter output ω_{rf}, and determines the supplementary component T_{ed} for the PMSG torque set-point T^r_e. As illustrated in Figure 8.26, the damping scheme of Figure 8.25 results in a control loop whose objective is to (rapidly) force the AC component of ω_{rf} to zero.

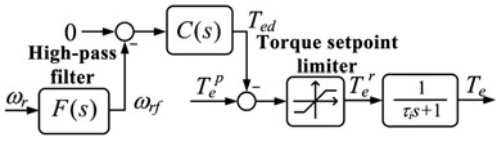

Figure 8.25 Block diagram illustrating the implementation of the damping mechanism (© 2013 IEEE) [8].

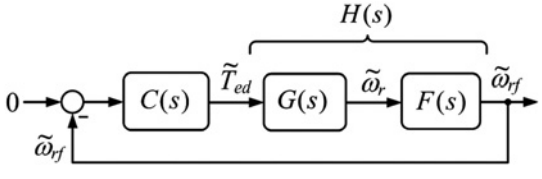

Figure 8.26 Control block diagram of the damping scheme (© 2013 IEEE) [8].

Let $F(s)$ be a second-order high-pass filter of the form

$$F(s) = \frac{\omega_{rf}(s)}{\omega_r(s)} = \frac{s^2}{s^2 + \left(\frac{\omega_c}{Q}\right) s + \omega_c^2}, \tag{8.20}$$

for which ω_c and Q are the corner frequency and quality factor, respectively.

The angular frequency of the unstable mode of the two-mass drive-train varies over a fairly narrow band around its undamped natural frequency, ω_{osc}, which is described as:

$$\omega_{osc} = \sqrt{\frac{k_s(J_t + J_r)}{J_t\, J_r}}. \tag{8.21}$$

Considering this frequency, the parameters ω_c and Q can be chosen such that the AC components of ω_{rf} and ω_r are almost equal in terms of magnitude and phase angle. Moreover, as will be discussed next, a pure gain for $C(s)$ results in stable operation of the WES.

8.5.2.6 Eigenvalue Analysis

If $C(s) = k_d$, where k_d is a pure gain in Nm/(rad/s), as Figure 8.25 indicates, the supplementary component of the PMSG torque set-point is

$$\tilde{T}_{ed} = k_d\, \tilde{\omega}_{rf}, \tag{8.22}$$

where '$\sim$' denotes the small-signal perturbation of a variable.

It then follows from replacing T_e^r by $T_e^p - T_{ed}$ in (8.13) (see Figure 8.25), expressing the result in the small-signal time-domain form and substituting for $\tilde{T}_{ed}$ from (8.22) in the final form, that:

$$\frac{d\tilde{T}_e}{dt} = -\frac{1}{\tau_i}\tilde{T}_e + \frac{1}{\tau_i}\tilde{T}_e^p + \frac{k_d}{\tau_i}\,\tilde{\omega}_{rf}. \tag{8.23}$$

As Figure 8.24 indicates, the compensator of the power control scheme can be described by

$$T_e^p = \left(k_{p1} + \frac{k_{i1}}{s}\right)\,(P_e^r - P_e). \tag{8.24}$$

Replacing P_e with $T_e\omega_r$ in (8.24) and expressing the result in time domain, we find

$$\frac{dT_e^p}{dt} = -k_{p1}\omega_r\frac{dT_e}{dt} - k_{p1}T_e\frac{d\omega_r}{dt} - k_{i1}T_e\omega_r + k_{p1}\frac{dP_e^r}{dt} + k_{i1}P_e^r. \tag{8.25}$$

Eliminating $d\omega_r/dt$ between (8.25) and (8.16), linearizing the result and substituting for $d\tilde{T}_e/dt$ from (8.23) in the final form, we deduce that

$$\begin{aligned}\frac{d\,\tilde{T}_e^p}{d\,t} = {} & (-k_{i1}\,\overline{T}_e)\,\tilde{\omega}_r + \left(-\frac{k_{p1}k_s}{J_r}\overline{T}_e\right)\tilde{\gamma} + \left(\frac{k_{p1}}{J_r}\overline{T}_e + \frac{k_{p1}}{\tau_i}\overline{\omega}_r - k_{i1}\overline{\omega}_r\right)\tilde{T}_e \\ & + \left(-\frac{k_{p1}}{\tau_i}\overline{\omega}_r\right)\tilde{T}_e^p + \left(-\frac{k_{p1}k_d}{\tau_i}\,\overline{\omega}_r\right)\tilde{\omega}_{rf} + k_{p1}\frac{d\tilde{P}_e^r}{dt} + k_{i1}\tilde{P}_e^r.\end{aligned} \tag{8.26}$$

Differentiating (8.16) with respect to time, eliminating $d\gamma/dt$ between the result and (8.17) and expressing the result in the small-signal form, gives

$$\frac{d^2\tilde{\omega}_r}{dt^2} = \frac{k_s}{J_r}\left(\tilde{\omega}_t - \tilde{\omega}_r\right) - \frac{1}{J_r}\frac{d\tilde{T}_e}{dt}. \tag{8.27}$$

Substituting for $d\tilde{T}_e/dt$ from (8.23) in (8.27), we have

$$\frac{d^2\tilde{\omega}_r}{dt^2} = \frac{k_s}{J_r}\left(\tilde{\omega}_t - \tilde{\omega}_r\right) - \frac{1}{J_r}\left(\frac{1}{\tau_i}\tilde{T}_e^p - \frac{1}{\tau_i}\tilde{T}_e + \frac{k_d}{\tau_i}\tilde{\omega}_{rf}\right). \tag{8.28}$$

Eliminating $d^2\tilde{\omega}_r/dt^2$ between (8.28) and the expression of (8.20) in the small-signal time-domain form, we conclude that

$$\frac{d^2\tilde{\omega}_{rf}}{dt^2} = \left(\frac{k_s}{J_r}\right)\tilde{\omega}_t - \left(\frac{k_s}{J_r}\right)\tilde{\omega}_r + \left(\frac{1}{J_r\tau_i}\right)\tilde{T}_e - \left(\frac{1}{J_r\tau_i}\right)\tilde{T}_e^p - \left(\omega_c^2 + \frac{k_d}{J_r\tau_i}\right)\tilde{\omega}_{rf} - \frac{\omega_c}{Q}\frac{d\tilde{\omega}_{rf}}{dt}. \tag{8.29}$$

Equations (8.23), (8.26), (8.29) and the small-signal versions of (8.15)–(8.17) constitute a state-space model for the wind energy capture subsystem augmented with the presented damping scheme.

In the MPPT mode, P_e^r is determined based on (8.18). Taking derivatives with respect to time from both sides of (8.18) and eliminating $d\omega_r/dt$ between the resulting equation and (8.16), we have

$$\frac{dP_e^r}{dt} = 3k_{opt}\omega_r^2\left(\frac{k_s}{J_r}\gamma - \frac{1}{J_r}T_e\right). \tag{8.30}$$

Replacing for $\tilde{P}_e^r$ and $d\tilde{P}_e^r/dt$ from the small-signal forms of (8.18) and (8.30) in the aforementioned state-space model, the following linear state-space model is obtained for the MPPT mode of operation:

$$\frac{d\tilde{X}_d}{dt} = A_1\tilde{X}_d + B_1\tilde{v}_w, \tag{8.31}$$

where $\tilde{X}_d = [\tilde{\omega}_t, \tilde{\omega}_r, \tilde{\gamma}, \tilde{T}_e, \tilde{T}_e^p, \tilde{\omega}_{rf}, d\tilde{\omega}_{rf}/dt]^T$ (superscript T denotes matrix transposition) and the matrices A_1 and B_1 are functions of the steady-state operating point of the subsystem described as

$$A_1 = \begin{bmatrix} \frac{1}{J_t}\frac{\partial T_{tur}}{\partial\omega_t}|\overline{v}_w,\overline{\omega}_t & 0 & -\frac{k_s}{J_t} \\ 0 & 0 & \frac{k_s}{J_r} \\ 1 & -1 & 0 \\ 0 & 0 & 0 \\ 0 & -k_{i1}\overline{T}_e + 3k_{i1}k_{opt}\overline{\omega}_r^2 & -\frac{k_{p1}k_s}{J_r}\overline{T}_e + \frac{3k_{p1}k_{opt}k_s}{J_r}\overline{\omega}_r^2 \\ 0 & 0 & 0 \\ \frac{k_s}{J_r} & -\frac{k_s}{J_r} & 0 \end{bmatrix}$$

$$\begin{bmatrix} 0 & 0 & 0 & 0 \\ -\frac{1}{J_r} & 0 & 0 & 0 \\ 0 & 0 & 0 & 0 \\ -\frac{1}{\tau_i} & \frac{1}{\tau_i} & \frac{k_d}{\tau_i} & 0 \\ \frac{k_{p1}}{J_r}\overline{T}_e + \frac{k_{p1}}{\tau_i}\overline{\omega}_r - k_{i1}\overline{\omega}_r - \frac{3k_{p1}k_{opt}}{J_r}\overline{\omega}_r^2 & -\frac{k_{p1}}{\tau_i}\overline{\omega}_r & \frac{k_{p1}k_d}{\tau_i}\overline{\omega}_r & 0 \\ 0 & 0 & 0 & 1 \\ \frac{1}{J_r\tau_i} & -\frac{1}{J_r\tau_i} & -\omega_c^2 - \frac{k_d}{J_r\tau_i} & -\frac{\omega_c}{Q} \end{bmatrix} \tag{8.32}$$

$$B_1 = \left[\frac{1}{J_t}\frac{\partial T_{tur}}{\partial v_w}|\overline{v}_w, \overline{\omega}_t \quad 0 \quad 0 \quad 0 \quad 0 \quad 0 \quad 0 \right]^T. \tag{8.33}$$

In the CP mode of operation, $P_e^r = P_{cmd}$, and therefore the following linear state-space model is obtained for this mode of operation:

$$\frac{d\tilde{X}_d}{dt} = A_2\tilde{X}_d + B_2\begin{bmatrix} \tilde{v}_w \\ \tilde{P}_{cmd} \\ \frac{d\tilde{P}_{cmd}}{dt} \end{bmatrix}, \tag{8.34}$$

where

$$A_2 = \begin{bmatrix} \frac{1}{J_t}\frac{\partial T_{tur}}{\partial \omega_t}|\overline{v}_w, \overline{\omega}_t & 0 & -\frac{k_s}{J_t} & 0 & 0 & 0 & 0 \\ 0 & 0 & \frac{k_s}{J_r} & -\frac{1}{J_r} & 0 & 0 & 0 \\ 1 & -1 & 0 & 0 & 0 & 0 & 0 \\ 0 & 0 & 0 & -\frac{1}{\tau_i} & \frac{1}{\tau_i} & \frac{k_d}{\tau_i} & 0 \\ 0 & -k_{i1}\overline{T}_e & -\frac{k_{p1}k_s}{J_r}\overline{T}_e & \frac{k_{p1}}{J_r}\overline{T}_e + \frac{k_{p1}}{\tau_i}\overline{\omega}_r - k_{i1}\overline{\omega}_r & -\frac{k_{p1}}{\tau_i}\overline{\omega}_r & \frac{k_{p1}k_d}{\tau_i}\overline{\omega}_r & 0 \\ 0 & 0 & 0 & 0 & 0 & 0 & 1 \\ \frac{k_s}{J_r} & -\frac{k_s}{J_r} & 0 & \frac{1}{J_r\tau_i} & -\frac{1}{J_r\tau_i} & -\omega_c^2 - \frac{k_d}{J_r\tau_i} & -\frac{\omega_c}{Q} \end{bmatrix} \tag{8.35}$$

$$B_2 = \begin{bmatrix} \frac{1}{J_t}\frac{\partial T_{tur}}{\partial v_w}|\overline{v}_w, \overline{\omega}_t & 0 & 0 & 0 & 0 & 0 & 0 \\ 0 & 0 & 0 & 0 & k_{i1} & 0 & 0 \\ 0 & 0 & 0 & 0 & k_{p1} & 0 & 0 \end{bmatrix}^T. \tag{8.36}$$

For a test WES whose parameters are reported in Tables 8.1–8.3, Figure 8.27 plots the migration of the (initially) unstable complex-conjugate eigenvalues in the CP mode, when the damping mechanism is enabled and k_d is varied from zero to 30×10^6. The migration plot is sketched for the operating point

Table 8.1 Example 2 – Wind turbine parameters (© 2013 IEEE) [8].

Parameter	Value	Comment
Rated power	5 MW	
Rated angular speed	12.9 rpm	
Rated wind speed	12 m/s	
Radius	60.5 m	R
k_{opt}	2 023 251 $\text{Nms}^2/(\text{rad})^2$	
Pitch angle range	1–90 deg.	
Moment of inertia	12 892 100 kgm^2	J_t

Table 8.2 Example 2 – PMSG parameters (© 2013 IEEE) [8].

Parameter	Value	Comment
Rated power	5 MW	
Rated voltage	2.2 kV rms	$l-l$
Rated current	1.3 kA rms	
Rated angular speed	12.9 rpm	
Number of pole pairs	60	p
Maximum rotor flux	22.25 Wb	λ_m
d- and q-axis inductance	4.0 mH	L_d, L_q
Stator resistance	5.35 mΩ	R_s
Moment of inertia	1 371 500 kgm^2	J_r

that corresponds to $v_w = 9.0$ m/s and $P_e^r = P_{cmd} = 1.5$ MW. It is observed that the eigenvalues, which are unstable for $k_d = 0$, migrate toward the left-half plane as k_d is increased, but move back toward the imaginary axis once k_d surpasses a certain value. This behaviour indicates the existence of an optimum value for k_d. The optimum value is computed such that the complex-conjugate eigenvalues possesses the maximum damping ratio. This, for the test WES, corresponds to the selection of $k_d = 14 \times 10^6$, which results in the smallest angle between the real axis and the tangent to the migration plot.

Table 8.4 also reports the eigenvalues of the wind energy capture subsystem under the MPPT and CP modes of operation, for $v_w = 9.0$ m/s, $k_d = 14 \times 10^6$ and in the CP mode $P_e^r = P_{cmd} = 1.5$ MW. The table indicates that the damping scheme has stabilized the system in the CP mode, as the entire eigenvalues lie in the left-half plane.

For the test WES, Figure 8.28 plots the migration of the dominant eigenvalues for $k_d = 14 \times 10^6$ and two different values of the ratio P_{cmd}/P_{opt}, when the wind speed is varied from 6.0 to 12 m/s, in steps of 1.0 m/s. It is observed that some eigenvalues approach the imaginary axis as the wind speed increases.

Table 8.3 Example 2 – Compensators and other parameters (© 2013 IEEE) [8].

Parameters	Value	Comments
k_{p1}, k_{i1}	1.0, 2.4	
k_{p2}, k_{i2}	3.0, 6.0	
Air mass density	1.225 kg/m^3	ρ
Drive-train shaft stiffness	21 264 367 Nm/rad	k_s
Switching frequency	1500 Hz	
ω_c, Q	0.7 rad/s, 0.5	

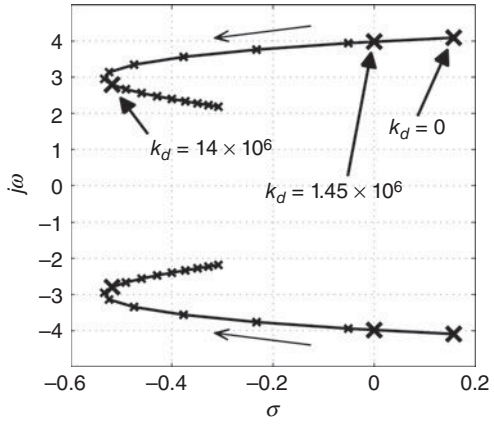

Figure 8.27 Example 2 – Migration plot of the (initially) unstable eigenvalues in the CP mode for different values of k_d (© 2013 IEEE) [8].

Table 8.4 Example 2 – Eigenvalues of the wind energy capture subsystem with the damping mechanism (© 2013 IEEE) [8].

MPPT mode	CP mode
-95.92	-110
-2.68	-5.34
-0.51	-0.19
$-1.19 \pm 3.43\,j$	$-0.45 \pm 0.31\,j$
$-0.50 \pm 0.39\,j$	$-0.52 \pm 2.80\,j$

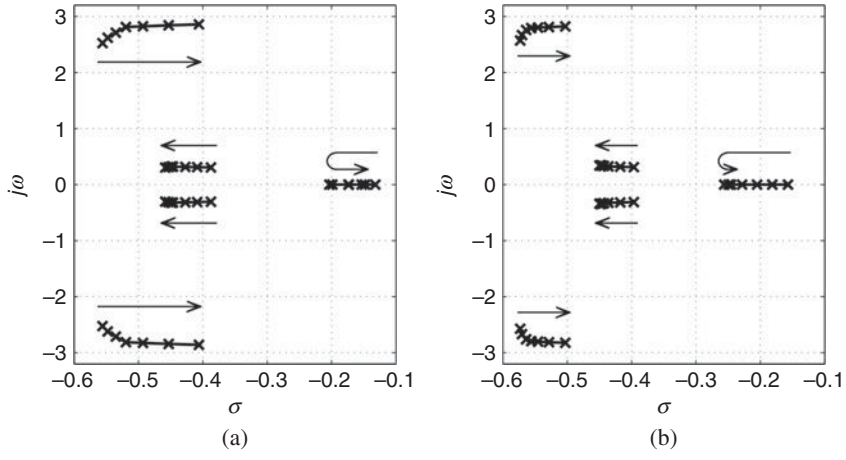

Figure 8.28 Example 2 – Migration plot of the dominant eigenvalues: (a) $P_{cmd} = 0.7P_{opt}$, (b) $P_{cmd} = 0.4P_{opt}$ (© 2013 IEEE) [8].

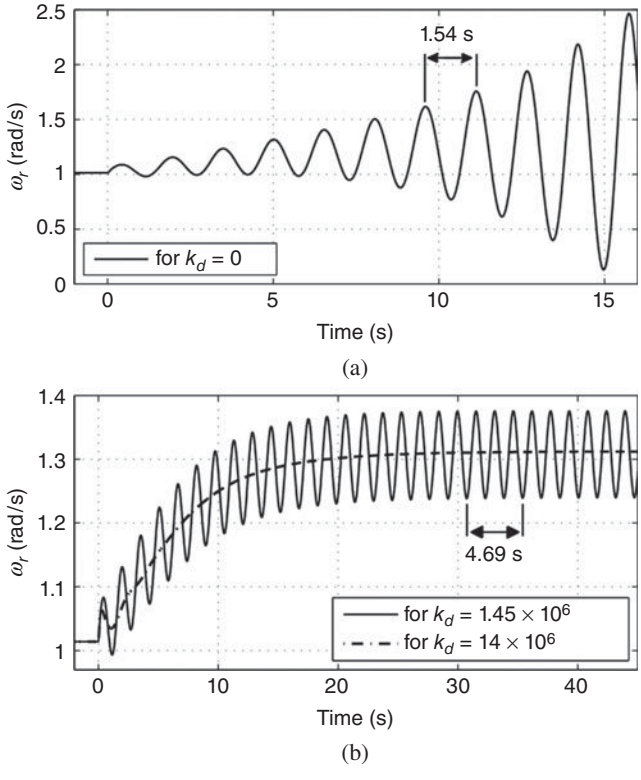

Figure 8.29 Example 2 – Response to the operation mode change from MPPT to CP (© 2013 IEEE) [8].

Nonetheless, the system remains stable over the entire wind speed range, and the eigenmodes are well damped.

To verify the accuracy of the developed mathematical model, the response of ω_r to an abrupt switching from the MPPT mode to the CP mode is depicted in Figure 8.29. The response is obtained from a detailed switched model of the test WES, developed in the PSCAD/EMTDC environment, for the gains $k_d = 0$, $k_d = 1.45 \times 10^6$ and $k_d = 14 \times 10^6$. As Figure 8.29 shows, for $k_d = 0$, the response is oscillatory and unstable, while $k_d = 1.45 \times 10^6$ results in sustained oscillations. However, as expected, $k_d = 14 \times 10^6$ results in a damped response. Figure 8.29 further indicates that the frequency of oscillations closely match those predicted by the eigenvalue analysis. For example, Figure 8.29(b) indicates that the period of oscillations for $k_d = 1.45 \times 10^6$ is about 1.56 (4.69/3) s, which corresponds to an angular frequency of about 4.03 rad/s. This frequency is very close to that indicated by Figure 8.27 for $k_d = 1.45 \times 10^6$.

8.5.2.7 Test System and Simulation Results

The switched model of the test WES has been subjected to various operating conditions. In the graphs to follow, the angular velocities are expressed in rad/s, the torques in MNm, the powers in MW, the DC-link voltage in kV, the wind speed in m/s and the pitch angle in degrees.

Startup process and operation in the MPPT mode: Figure 8.30 illustrates the performance of the test WES in the MPPT mode of operation, subsequent to a startup process. For this case, the wind speed is

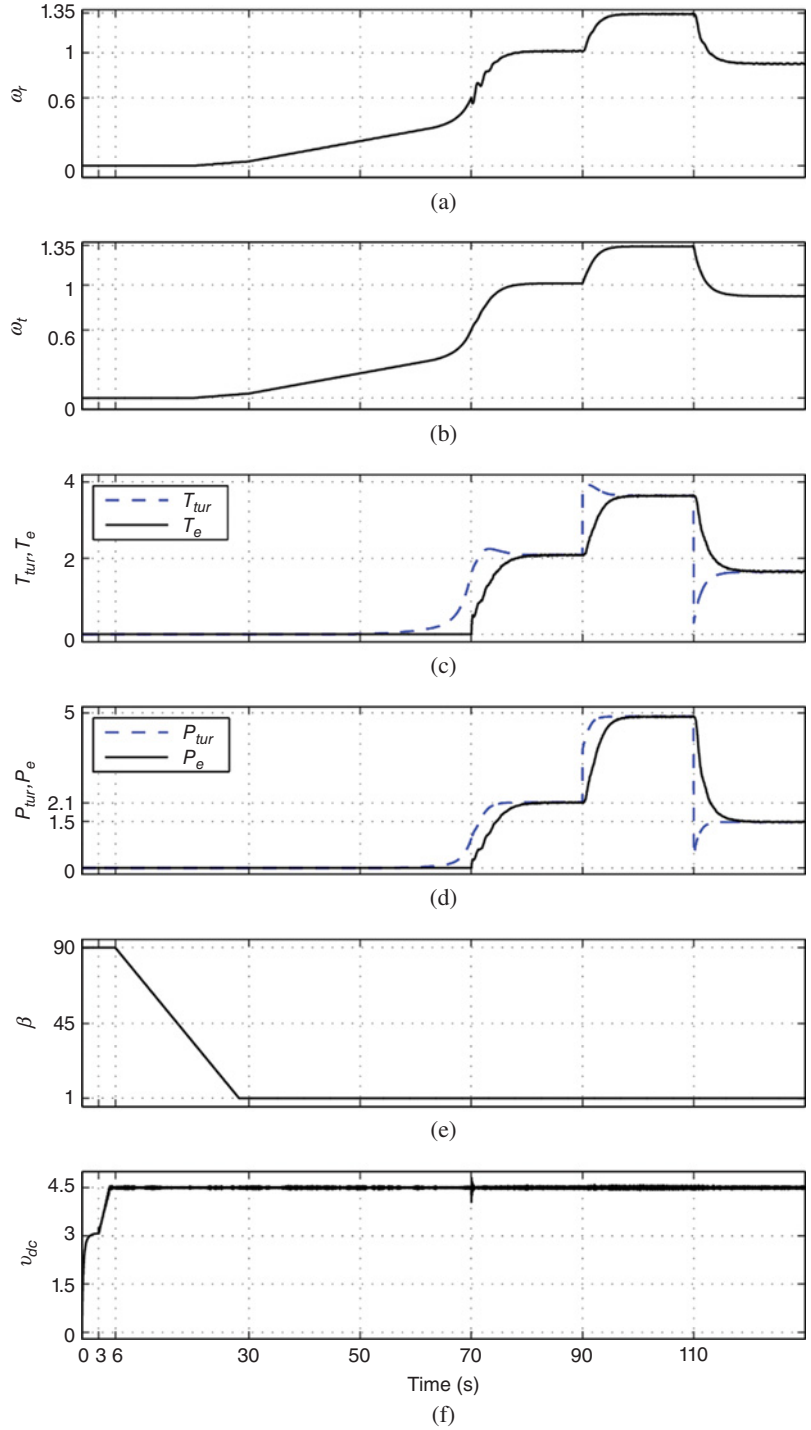

Figure 8.30 Example 2 – Startup process and operation of the WES in the MPPT mode (© 2013 IEEE) [8].

assumed to be 9.0 m/s from the startup moment to $t = 40$ s, 12 m/s from $t = 40$ to 70 s and 8.0 m/s from $t = 70$ s onwards.

Initially, the turbine-generator set is in a standstill mode in which the mechanical brakes are engaged, the blade pitch angle is at the maximum value of 90°, to reduce the aerodynamic torque of the turbine to almost zero and the gating pulses of the two VSCs – that of the wind energy capture subsystem (Figure 8.23) and that of the power-electronic interface (Figure 8.1) – are blocked. Once it is recognized that the wind speed is sufficient for startup, that is, $t = 0$ s in Figure 8.30, the WES is connected to the grid via the startup resistors and therefore the DC-link capacitor is charged by the antiparallel diodes of the VSC in the power-electronic interface to a voltage of about 3.1 kV. At $t = 3.0$ s, the startup resistors are bypassed, and the gating pulses of the VSC in the power-electronic interface are released and thus the power-electronic interface starts to function. The DC-link voltage, v_{dc}, is raised gradually towards its final set-point of 4.5 kV and is settled at $t = 5.0$ s. At $t = 6.0$ s, the mechanical brakes are released and the pitch angle of the blades is reduced from 90° to the minimum pitch of 1.0° to achieve sufficient aerodynamic torque of the turbine to enable the rotor to accelerate from rest. Once the rotor reaches an angular velocity of about 0.6 rad/s, the gating pulses of the VSC in the wind energy capture subsystem, Figure 8.23, are also released and thus the subsystem starts to function. Therefore, the PMSG torque is permitted to rise to the value that is stipulated by the power control scheme (Figures 8.24 and 8.25). Thereafter, the WES starts to generate power and its output settles at the maximum power for $v_w =$ 9.0 m/s, that is, about 2.1 MW.

Figure 8.30 also shows that, subsequent to each step change in the wind speed, the output power smoothly approaches the corresponding steady-state value. The steady-state value at each wind speed is equal to the maximum turbine power for that wind speed. For example, the wind speed of 12 m/s yields an output power of about 5.0 MW, at the rotor angular speed of about 1.35 rad/s; these values agree with the specifications mentioned in Table 8.1, for the test WES.

Response to operation mode and wind speed changes: Figures 8.31 and 8.32 illustrate the WES response to changes in the operating mode and wind speed. Before $t = 0$ s, the wind speed is assumed to be 9.0 m/s, and the WES is operating in the MPPT mode and the turbine yields the maximum power (equal to 2.1 MW). The test WES then experiences the following sequence of events: (1) at $t = 0$ s, the operation mode is changed from the MPPT mode to the CP mode, where $P_{cmd} = 1.582$ MW ($0.75P_{opt}$); (2) at $t = 40$ s, the wind speed assumes a step change from 9.0 m/s to 12 m/s and the WES remains in the CP mode; (3) at $t = 80$ s, P_{cmd} is stepped further down to 0.5 MW and the WES continues to operate in the CP mode; (4) at $t = 110$ s, the wind speed changes stepwise from 12 m/s to 9.0 m/s. However, because the maximum power corresponding to $v_w = 9.0$ m/s is larger than $P_{cmd} = 0.5$ MW, the WES retains its CP operating mode; (5) at $t = 150$ s, P_{cmd} is stepped up to 3.5 MW. This command is larger than the maximum power for $v_w = 9.0$ m/s, that is, 2.1 MW. Therefore, the WES operation mode is changed from the CP mode to the MPPT mode and so its output power settles at 2.1 MW; and (6) at $t =$ 190 s, the wind speed again rises stepwise from 9.0 m/s to 12 m/s and, because the maximum power corresponding to $v_w = 12$ m/s (about 5.0 MW) is larger than $P_{cmd} = 3.5$ MW, the operating mode can be reverted back to the CP mode and the output power settles at 3.5 MW. It should be noted that real wind speed variations do not happen very fast, and sharp variations of the WES output real power may not be required. However, in this section, the objective is to evaluate the performance of the test WES in response to sharp wind speed and output real power variations for the sake of analytical studies to assess the stability of the WES.

Figure 8.31 shows that the output power rapidly tracks P_{cmd} during the periods when the WES operates in the CP mode, that is, from $t = 0$ to 150 s and from $t = 190$ s onwards. The figure also indicates that the rise and fall in the wind speed, respectively at $t = 40$ s and 110 s, when the system is in the CP mode, result in transient excursions in the output power, but have no effect on the steady-state command following. It is interesting to note that at $t = 150$ s when P_{cmd} is changed from 0.5 to 3.5 MW, the output power transiently overshoots, but reverts to its steady state value of 2.1 MW (that is, the maximum available power for the wind speed of 9.0 m/s). The reason for the overshoot is the stored kinetic energy of the rotor inertia, which is momentarily released.

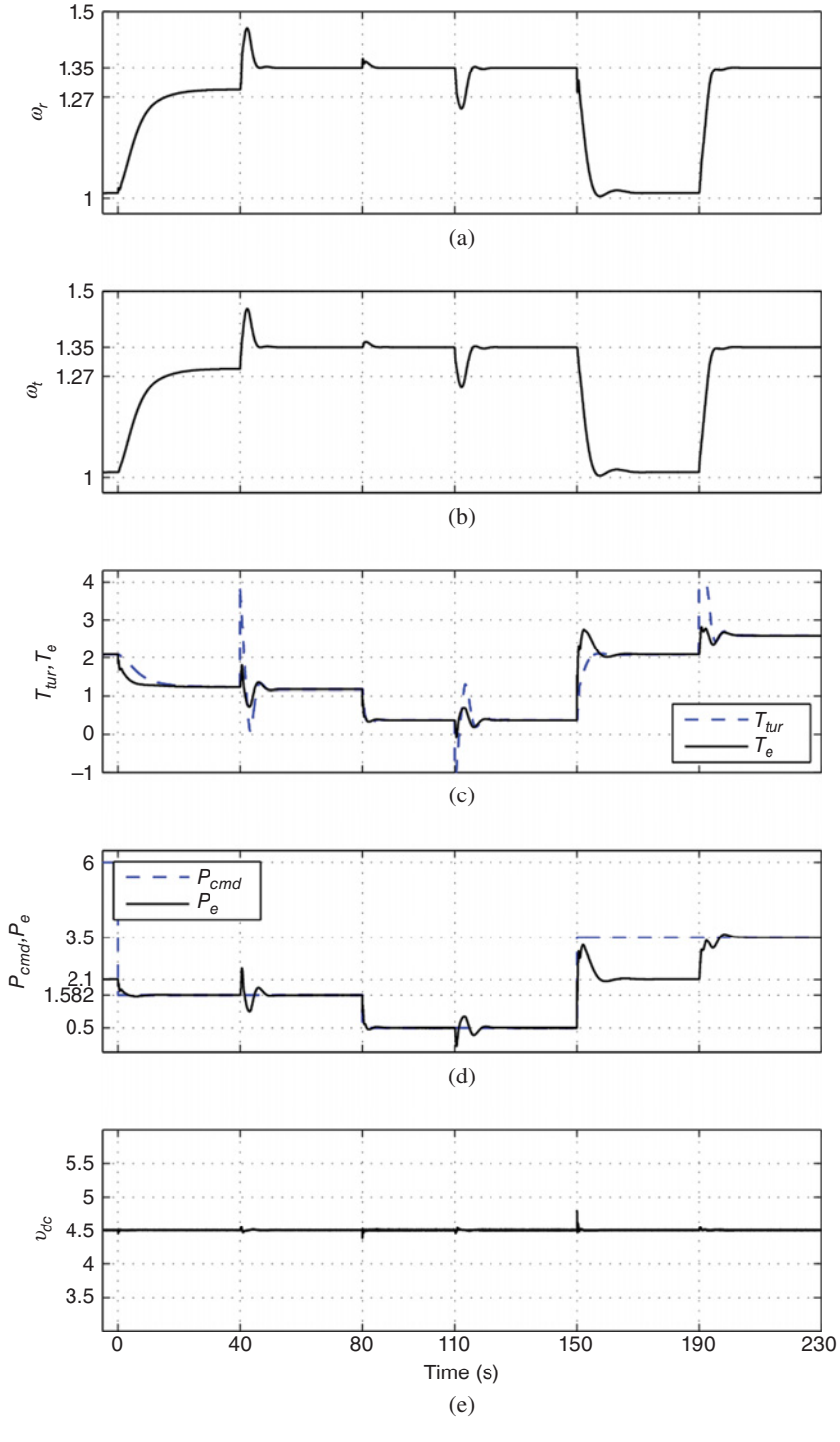

Figure 8.31 Example 2 – Response to changes in the operation mode and wind speed (© 2013 IEEE) [8].

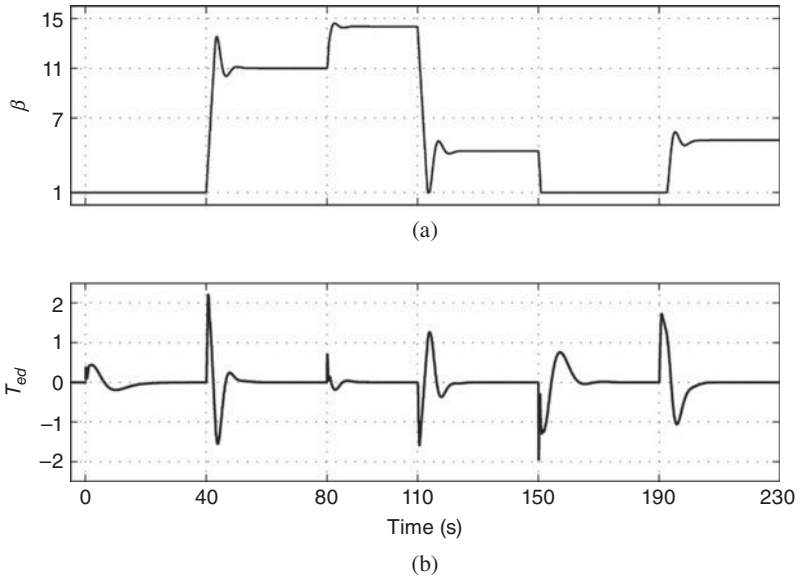

Figure 8.32 Example 2 – Response to changes in the operation mode and wind speed (cont.) (© 2013 IEEE) [8].

Figure 8.32 shows (a) the pitch angle waveform, β and (b) the waveform of the supplementary component of PMSG torque set-point, T_{ed}. It is observed that T_{ed} transiently responds to each disturbance, but settles down at zero. By contrast, the pitch angle only responds to those disturbances that cause the drive-train speed to exceed (and to be in need of regulation at) the maximum permissible value of 1.35 rad/s – see Figures 8.31(a) and (b).

8.6 Conclusion

The proliferation of electronically interfaced DER systems has necessitated impact assessment studies by the manufacturers, system integrators and utility companies. Such studies can be conveniently conducted by means of circuit-based simulation models, which are expandable to larger system models. As discussed in this chapter, as far as power system transients are concerned, most electronically interfaced DER systems can be modelled by a generic circuit/control configuration. Then, depending on the required accuracy and types of transients to capture, a developed model can be simplified to different extents, in order to avoid prohibitively large simulation runtimes, especially in large models. The chapter presented a few such simplification strategies and discussed that their impacts must be understood and considered, to avoid erroneous conclusions in regards to the performance and transients of the system under study.

The chapter also presented the way that the aforementioned generic model can be used to design the controls of an electronically interfaced DER system, how a mathematical model can be developed and used for transient analysis of an electronically interfaced DER system and how the mathematical model can be validated by comparing its results with those of a circuit-based simulation model.

References

[1] Yazdani, A. and Iravani, R. (2010) *Voltage-Sourced Converters: Modeling, Control and Applications*, John Wiley & Sons, Inc., Hoboken (NJ).

[2] Ise, T., Kita, M. and Taguchi, A. (2005) A hybrid energy storage with a SMES and secondary battery. *IEEE Transactions on Applied Superconductivity*, **15**(2), 1915–1918.
[3] Carrasco, J.M., Franquelo, L.G., Bialasiewicz, J.T. *et al.* (2006) Power-electronic systems for the grid integration of renewable energy sources: a survey. *IEEE Transactions on Industrial Electronics*, **53**(4), 1002–1016.
[4] Chiniforoosh, S., Jatskevich, J., Yazdani, A. *et al.* (2010) Definitions and applications of dynamic average models for analysis of power systems. *IEEE Transactions on Power Delivery*, **25**(4), 2655–2669.
[5] Yazdani, A., Di Fazio, A.R., Ghoddami, H. *et al.* (2011) Modeling guidelines and a benchmark for power system simulation studies of three-phase single-stage photovoltaic systems. *IEEE Transactions on Power Delivery*, **26**(2), 1247–1264.
[6] Yazdani, A. (2011) Electromagnetic transients of grid-tied photovoltaic systems based on detailed and averaged models of the voltage-sourced converter. IEEE Power and Energy Society General Meeting, Detroit (MI, USA), July 2011.
[7] CIGRE Task Force C6.04 (2014) Benchmark systems for network integration of renewable and distributed energy resources. CIGRE Technical Brochure 575.
[8] Alizadeh, O. and Yazdani, A. (2013) A strategy for real-power control in a direct-drive PMSG-based wind energy conversion system. *IEEE Transactions on Power Delivery*, **28**(3), 1297–1305.

9

Simulation of Transients for VSC-HVDC Transmission Systems Based on Modular Multilevel Converters

Hani Saad, Sébastien Dennetière, Jean Mahseredjian, Tarek Ould-Bachir and Jean-Pierre David

9.1 Introduction

The development of controllable semiconductor switches and voltage source converter (VSC) technologies is rapidly expanding the fields of applications of HVDC and FACTS in power systems. VSC-based HVDC systems present several advantages in comparison with traditional line-commutated converter (LCC) based HVDC transmission [1]. VSC-HVDC technology combines IGBT-based VSC with DC transmission lines to transfer power up to 1000 MW [2]. The potential applications of VSC-HVDC systems include interconnections of asynchronous systems, grid integration of offshore wind farms, electrification of remote islands and multiterminal DC grids [3, 4]. VSC-HVDC systems can independently control both active and reactive powers by maintaining stable voltage and frequency [5], which enables the supply of very weak grids and even passive networks [6].

Various VSC topologies, including the conventional two-level, multilevel diode-clamped and floating capacitor multilevel converters, have been proposed and reported in [7]. However, due to the complexity of controls and practical limitations, the VSC-HVDC system installations have been limited to the two-level and three-level diode-clamped converters. Recently, the development of the modular multilevel converter (MMC) technology with series-connected half-bridge modules, has allowed overcoming the limitations of other multilevel converter topologies for HVDC applications [8]. Switching frequency and transient peak voltages on IGBT devices are normally lower in MMCs, and converter losses are reduced. In addition, filter requirements are eliminated by using a significant number of levels per phase. Scalability to higher voltages is easily achieved, and reliability is improved by increasing the number of submodules (SMs) per arm [9]. The typical configuration of an MMC station is presented in Figure 9.1.

Transient Analysis of Power Systems: Solution Techniques, Tools and Applications, First Edition.
Edited by Juan A. Martinez-Velasco.

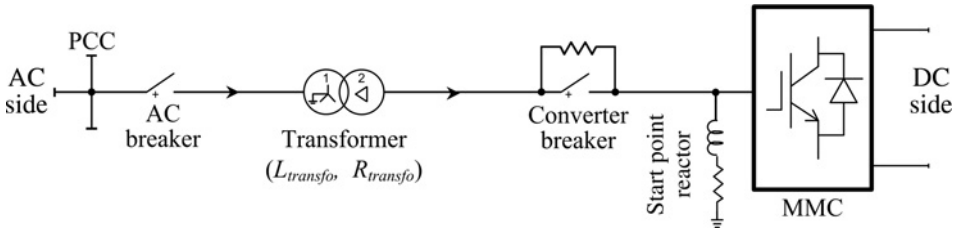

Figure 9.1 Typical monopole configuration of a MMC station.

The large number of IGBTs in MMCs creates complicated computation problems in electromagnetic transient type (EMT-type) simulation tools. Detailed MMC models include the representation of thousands of IGBT switches and must use small numerical integration time-steps to accurately represent fast and multiple simultaneous switching events. The computational burden introduced by such models highlights the need to develop more efficient models. This becomes particularly complex for performing real-time simulations. In real-time simulations, modelling a highly detailed switching device is currently out of reach, and simplifications are required to achieve hardware-in-the-loop (HIL) simulations. A current trend is based on simplified and average value models (AVM) [10, 11] capable of delivering sufficient accuracy [12] in dynamic simulations. AVMs and other simplified modelling approaches for MMCs have been presented in [13–16].

The objective of this chapter is to present an overview of modelling of MMC-based HVDC transmission systems in EMT-type programs for off-line and real-time simulations. The presented models, studies and references will be useful to researchers and practising engineers who are using transient simulation tools for modelling and analysis of power systems with MMCs.

Section 9.2 introduces the MMC topology. Section 9.3 derives the four different MMC modelling approaches that are used in EMT-type programs [17]. The complete control system used for MMC-HVDC transmission is developed in Section 9.4. Comparisons between different types of MMC models are presented in Section 9.5 for deriving their advantages and limitations according to simulation needs, and the section also provides guidelines for the dynamic behaviour and computational performance for a practical MMC-based HVDC transmission system. Section 9.6 presents the MMC model implementation using both CPU and FPGA technologies for real-time simulations [18].

9.2 MMC Topology

Figure 9.2(a) shows the three-phase configuration of the MMC topology. The MMC is composed of N SMs per arm, which results in a line-to-neutral voltage waveform of $(N+1)$ levels [19]. The inductor L_{arm} is added on each arm to limit arm-current harmonics and fault currents. Each SM is a half-bridge converter as depicted in Figure 9.2(b) and includes mainly a capacitor C and two IGBTs with antiparallel diodes (S_1 and S_2).

Since the IGBT device is controllable (see gate signals g_{1_i} and g_{2_i}), the SM can have three different states. In the ON state: g_{1_i} is on, g_{2_i} is off and the SM voltage v_{SM_i} is equal to the capacitor voltage v_{C_i}. In the OFF state: g_{1_i} is off, g_{2_i} is on and $v_{SM_i} = 0$. In the blocked state: g_{1_i} is off, g_{2_i} is off and v_{SM_i} depends on the arm current (i_{arm}) direction. The capacitor may charge through S_1 and cannot discharge.

Other SM circuit configurations exist, such as full-bridge and double-clamp-SM [20], but this chapter will focus only on the half-bridge configuration since it is the most widely used.

Since the MMC topology is of VSC type [21], it uses an upper-level control. However, the MMC topology requires additional controllers in order to stabilize internal variables [22] (lower-level control): SM capacitor voltages, currents in each arm and modulation technique. The lower-level control may

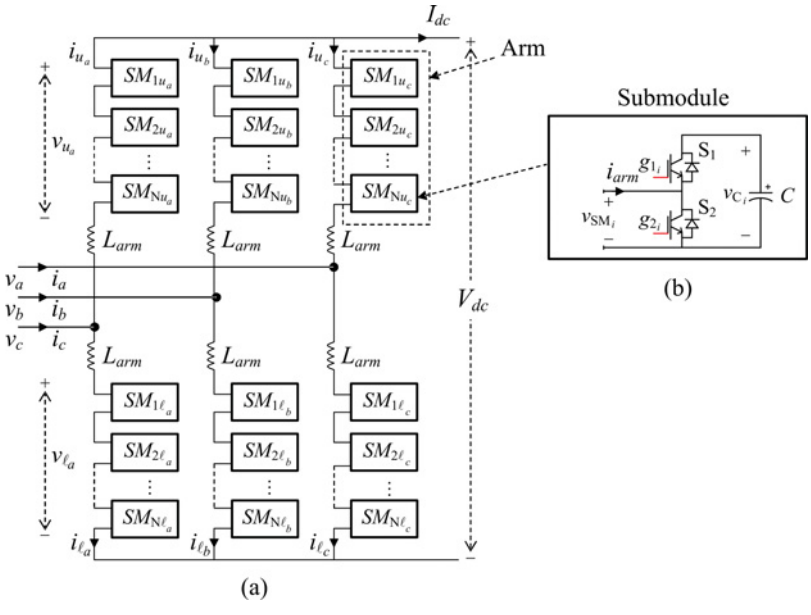

Figure 9.2 (a) MMC topology, (b) half-bridge converter for the *i*th SM.

change according to converter manufacturers. A top-level view of the control structure is presented in Figure 9.3.

Several control methods are available for upper-level control. Among them, the power-angle and vector-current controls are the mostly widely used. The principle of power-angle control is simple. The active power is controlled by the phase-angle shift between the VSC and the AC system, while the reactive power is controlled by varying the VSC voltage magnitude [23]. Power-angle control (or V/F control) is used when the VSC is connected to an AC system with passive load or weak grid, or for wind-turbine

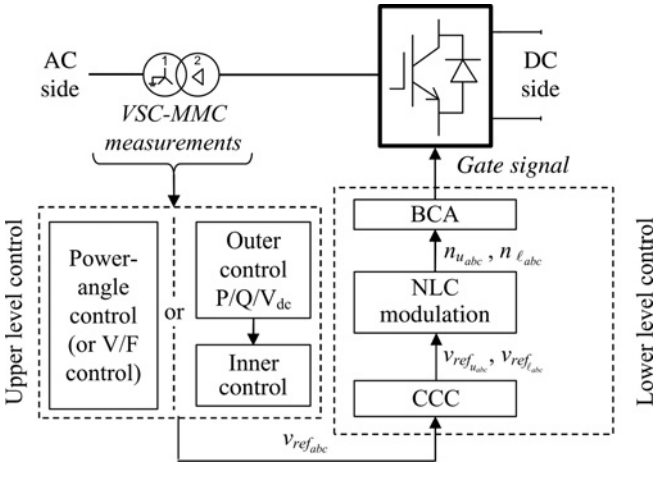

Figure 9.3 Control hierarchy for the MMC station.

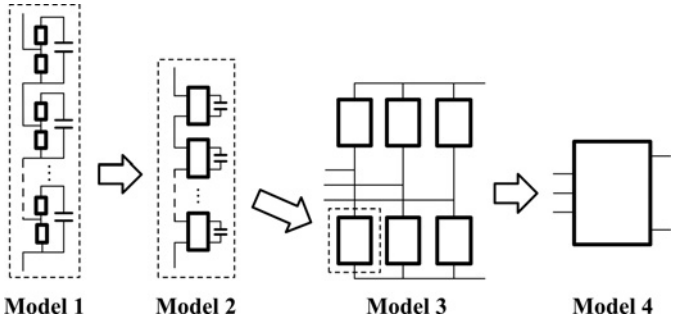

Figure 9.4 MMC model evolution in decreasing complexity order.

applications. Vector-current control [5] is a current-control-based technology. Thus, it can naturally limit the current flowing into the converter during disturbances. The basic principle of vector-current control is to regulate the instantaneous active and reactive powers independently through a fast inner current control loop. By using a *dq* decomposition technique with the grid voltage as phase reference, the inner current control loop decouples the current into *d* and *q* components, where outer loops can use the *d* component to control active power or DC voltage, and the *q* component to control reactive power or AC voltage.

9.3 MMC Models

Four types of MMC models can be derived. These models can be used according to the type of study and required accuracy. MMC model evolution in decreasing complexity is depicted in Figure 9.4. Black boxes represent simplifications for each model. It is expected that computational performance can be increased by decreasing model complexity. The model descriptions and details are presented below. Model 1 is the most detailed. Model 2 uses a simplified power switch circuit model. Model 3 makes a simplified arm circuit equivalent. In Model 4, the complete MMC structure is reduced to an equivalent system.

9.3.1 Model 1 – Full Detailed

This model is based on nonlinear IGBT/diode representation. The IGBT/diode circuit shown in Figure 9.5 is modelled using an ideal controlled switch, two non-ideal (series and antiparallel) diodes and a snubber circuit. The non-ideal diodes are modelled with nonlinear resistances using the classical V–I curve of a

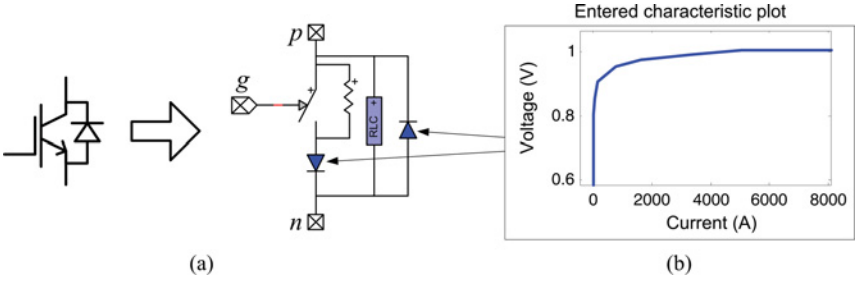

Figure 9.5 Model 1: (a) representation of a nonlinear IGBT valve, (b) diode V–I characteristic.

diode. The nonlinear characteristic can be adjusted according to the manufacturer's data. It is the most accurate model for EMT-type programs and can account for every conduction mode of the MMC.

This model type [16] offers several advantages, due to its increased accuracy in the modelling of IGBTs. It replicates the nonlinear behaviour of switching events (through diodes) allowing us to account for conduction losses. It also allows us to simulate specific conditions, such as blocked states, SM details, converter startup procedures, internal converter faults and different SM circuit topologies.

The introduction of thousands of components (e.g. for a 401-level MMC we have 4800 ideal switches and 9600 non-ideal diodes) involves a high computational effort and therefore, except for specific cases mentioned above, this modelling approach should be mainly used as an accuracy reference for validating and tuning simplified MMC models.

9.3.2 Model 2 – Detailed Equivalent

In this model the SM power switches are replaced by ON/OFF resistors: R_{ON} (small value in mΩ) and R_{OFF} (large value in MΩ). This approach allows us to perform an arm circuit reduction for eliminating internal electrical nodes and to create a Norton equivalent for each MMC arm. Figure 9.6 shows the representation of each SM. R_{1_i} and R_{2_i} are controlled and used for replacing the two IGTB/diode combinations. With the trapezoidal integration rule, each SM capacitor is replaced by an equivalent current history source $i^h_{C_i}(t-\Delta t)$ in parallel with a resistance $R_C = \Delta t/(2C)$ (Figure 9.6), where Δt is the numerical integration time-step.

By simplifying each SM as in Figure 9.6, an equivalent Norton equivalent circuit can be derived for each MMC arm as shown in Figure 9.7.

The equations used for deriving the Norton equivalent circuit of each MMC arm are summarized in Table 9.1. In Table 9.1(b) it can be seen that the computation of ON/OFF states is based only on gate signal values. However, when the blocked state is set, only the freewheeling diodes can conduct. Hence, the diode conduction states depend on current and voltage variables – Table 9.1(b). These variables are known only from the previous iteration ($v_{SM_i}(t-\Delta t)$ and $v_{C_i}(t-\Delta t)$). The zero-crossing of the arm current will cause numerical oscillations. To avoid this problem, an iterative process is proposed in [17].

When the blocked state is set for one of the SMs and a change in conduction state of one of the diodes is detected, an iterative process is activated in the current time-step in order to find the correct conduction states and the trapezoidal integration rule is switched to the backward Euler method for the next two half time-steps (see Figure 9.8). The latter is for eliminating numerical oscillations [24] caused by discontinuities in the trapezoidal integration.

As can be seen from Figure 9.7, the main advantage of Model 2 is the significant reduction in the number of electrical nodes in the main system of network equations. The algorithm still considers each SM separately and maintains a record for individual capacitor voltages and currents. It is applicable to any number of the SMs per arm.

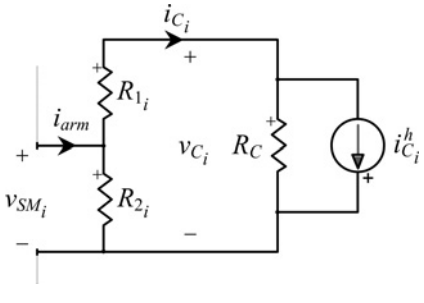

Figure 9.6 Discretized SM with simplified IGBT/diode models.

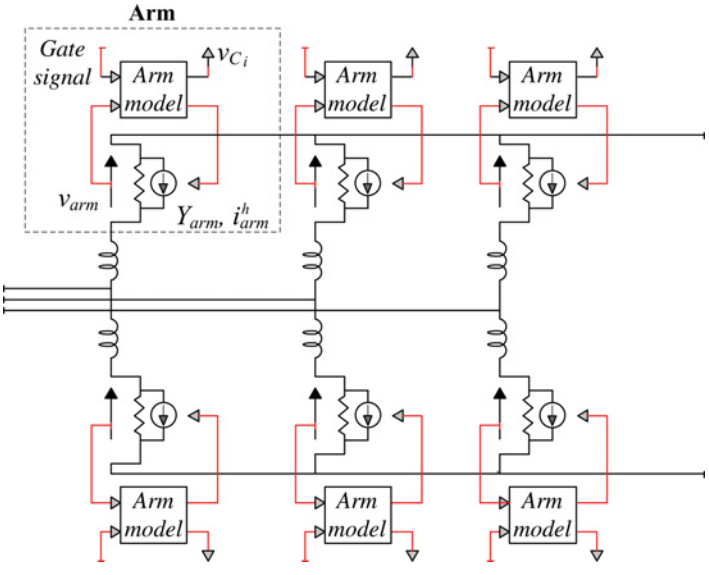

Figure 9.7 Model 2 main circuit diagram.

9.3.3 *Model 3 – Switching Function of MMC Arm*

In this model, each MMC arm is averaged using the switching function concept of a half-bridge converter. Let S_i be the switching function which takes the value 0 when the state of SM is OFF, and 1 when it is ON. For each SM

$$\begin{aligned} v_{SM_i} &= S_i\, v_{C_i} \\ i_{C_i} &= S_i\, i_{arm}. \end{aligned} \tag{9.1}$$

Assuming that capacitor voltages of each arm are balanced, the average values of capacitor voltage are equal. In addition, by neglecting the voltage differences between capacitors, the following assumption can be made:

$$v_{C_1} = v_{C_2} = \ldots = v_{C_i} = \frac{v_{C_{tot}}}{N}, \tag{9.2}$$

where $v_{C_{tot}}$ represents the sum of all capacitor voltages of an arm. The accuracy of assumption (9.2) increases when the number of SMs per arm is increased and/or when the fluctuation amplitudes of capacitor voltages are decreased. This assumption allows us to deduce an equivalent capacitance $C_{arm} = C/N$ for each arm.

By defining the switching functions of an arm as

$$\frac{1}{N}\sum_{i=1}^{N} S_i = s_n, \tag{9.3}$$

and including the linear conduction losses (R_{ON}) for each SM, the following switching functions can be derived for each arm when the SMs are in ON/OFF states [15]:

$$\begin{aligned} v_{arm} &= s_n\, v_{C_{tot}} + \left(NR_{ON}\right) i_{arm} \\ i_{C_{tot}} &= s_n\, i_{arm}. \end{aligned} \tag{9.4}$$

where v_{arm} and i_{arm} are the arm voltage and current, respectively.

Table 9.1 Model 2 – MMC arm algorithm.

(a) Retrieve arm voltage from the network solution and compute arm current:

$$i_{arm}(t) = v_{arm}(t).Y_{arm}(t - \Delta t) + i^h_{arm}(t - \Delta t) \text{ (see Figure 9.7)}$$

(b) For each SM, set R_{1_i} and R_{2_i} values depending on gating signals, current arm direction, previous SM voltage and previous capacitor voltage:

if(SM$_i$==ON_state)
$\left\{R_{1_i} = R_{ON}; R_{2_i} = R_{OFF}\right\}$
elseif(SM$_i$==OFF_state)
$\left\{R_{1_i} = R_{OFF}; R_{2_i} = R_{ON}\right\}$
elseif(SM$_i$==BLOCKED_state) {
if $\left(\left(i_{arm}(t) > 0\right)$ && $\left(v_{SM_i}(t - \Delta t) > v_{C_i}(t - \Delta t)\right)\right)$
$\left\{R_{1_i} = R_{ON}; R_{2_i} = R_{OFF}\right\}$
if $\left(\left(i_{arm}(t) < 0\right)$ && $\left(v_{SM_i}(t - \Delta t) < 0\right)\right)$
$\left\{R_{1_i} = R_{OFF}; R_{2_i} = R_{ON}\right\}$
else %High impedance mode
$\left\{R_{1_i} = R_{OFF}; R_{2_i} = R_{OFF}\right\}\}$

(c) Compute capacitor voltages and currents for each SM:

$$i_{C_i}(t) = i_{arm}(t) - \frac{v_{R_{2_i}}}{R_{2_i}}; \quad v_{C_i}(t) = \left(i_{C_i}(t) - i^h_{C_i}(t)\right) R_C$$

(d) Compute Thevenin equivalent for each SM:

$$R_{SM_i}(t) = \frac{R_{2_i}\left(R_{1_i} + R_C\right)}{R_{2_i} + R_{1_i} + R_C}$$

$$v^h_{SM_i}(t - \Delta t) = R_{SM_i}(t)\left(\frac{R_C}{R_C + R_{1_i}}\right) i^h_{C_i}(t - \Delta t)$$

(e) Compute voltages of each SM:

$$v_{SM_i}(t) = i_{arm}(t) R_{SM_i}(t) + v^h_{SM_i}(t - \Delta t)$$

(f) Compute and send Norton equivalent variables (Figure 9.7):

$$Y_{arm}(t) = 1/\left(\sum_{i=1}^{N} R_{SM_i}(t)\right)$$

$$v^h_{arm}(t - \Delta t) = \sum_{i=1}^{N} v^h_{SM_i}(t - \Delta t)$$

$$i^h_{arm}(t - \Delta t) = -v^h_{arm}(t - \Delta t).Y_{arm}(t)$$

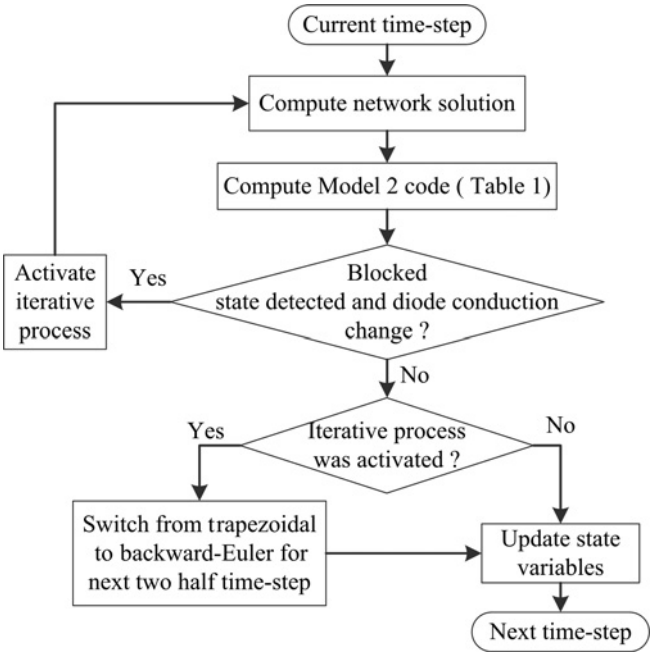

Figure 9.8 Model 2 – Block diagram of MMC arm.

Half-bridge converters are non-reversible in voltage. In order to avoid negative voltages, a diode D is added in parallel with the equivalent capacitor – Figure 9.9(a).

When all SMs are in the blocked state, each MMC arm can be simply represented by an equivalent half-bridge diode connected to the equivalent capacitor – Figure 9.9(b).

By reducing each arm to an equivalent switching function model, the SMs are no longer represented. This means that the balancing controls of the capacitor voltages in each arm cannot be studied using this approach. However, circulating currents and the linear conduction losses can be represented. Moreover,

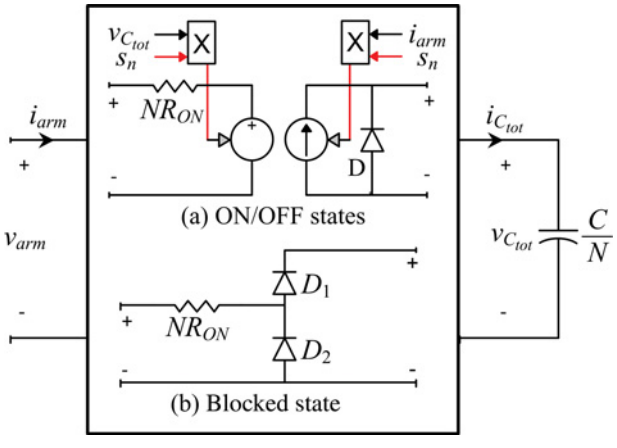

Figure 9.9 Model 3: (a) ON/OFF states model, (b) blocked state model.

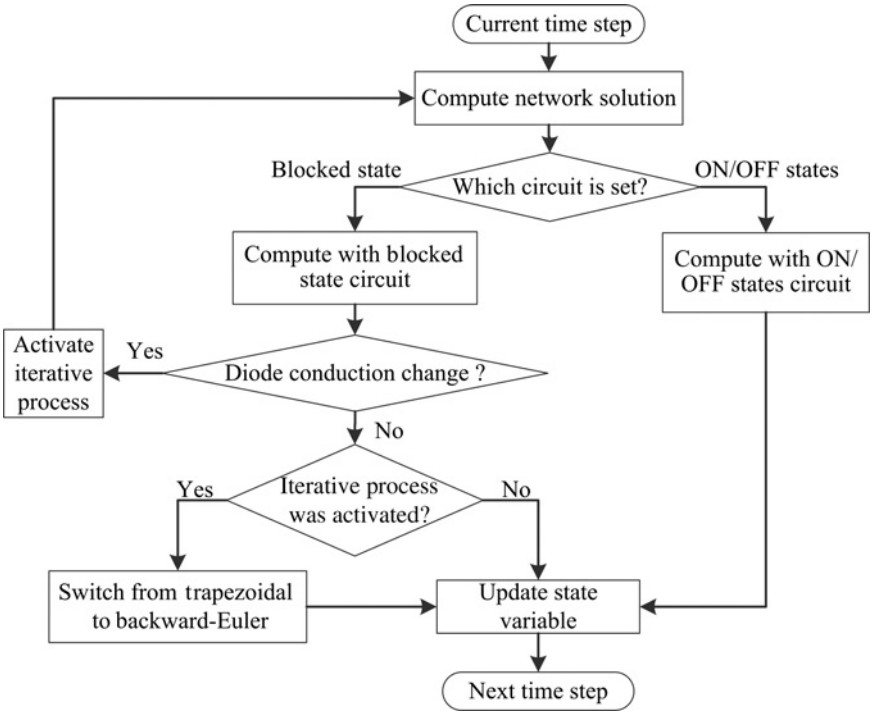

Figure 9.10 Model 3 – block diagram of MMC arm.

the energy transferred from AC and DC sides into each arm of the MMC is taken into account, which is useful for control system strategies based on internal MMC energy equilibrium [22, 25].

Since this model includes two circuit models (Figure 9.9), its implementation in EMT-type programs is hard-coded to increase computational performance. Depending on the states of each arm, the appropriate circuit is interfaced with the main network. The block diagram of the algorithm is shown in Figure 9.10.

Note that this model type can be implemented using a single electrical circuit with controllable switches to change from ON/OFF states and blocked state circuits. The development of this approach can be found in [26, 27].

9.3.4 Model 4 – AVM Based on Power Frequency

In the average value model (AVM) [28], the IGBTs and their diodes are not explicitly represented and the MMC behaviour is modelled using controlled voltage and current sources. The classical AVM approach developed for two- and three-level VSCs in [29] is extended to MMCs in [16]. It is used by assuming that the internal variables of the MMC are perfectly controlled, that is, all SM capacitor voltages are perfectly balanced, and second harmonic circulating currents in each phase are suppressed. The following equation can be derived from Figure 9.2 for each phase $j = a, b, c$:

$$\frac{V_{dc}}{2} = v_{u_j} + L_{arm}\frac{di_{u_j}}{dt} + v_j \tag{9.5}$$

$$\frac{V_{dc}}{2} = v_{\ell_j} + L_{arm}\frac{di_{\ell_j}}{dt} - v_j \tag{9.6}$$

The following variable is defined:

$$v_{conv_j}^{ac} = \frac{v_{\ell_j} - v_{u_j}}{2} \tag{9.7}$$

Using (9.7) and subtracting (9.6) and (9.5), we get

$$v_{conv_j}^{ac} = \frac{L_{arm}}{2}\frac{di_j}{dt} - v_j. \tag{9.8}$$

Assuming that the total number of inserted SMs in each phase is constant, and since the circulating current is assumed to be zero, then

$$v_{u_j} + v_{\ell_j} = V_{dc}. \tag{9.9}$$

From equations (9.8) and (9.9), the MMC can be represented as a classical VSC (two- and three-level topologies). Thus, using an approach similar to [29], the controlled voltage sources become

$$v_{conv_j}^{ac} = v_{ref_j}\frac{V_{dc}}{2}, \tag{9.10}$$

where v_{ref_j} are the voltage references generated from the inner controller. The AC-side representation of this model is shown in Figure 9.11(a).

The DC-side model in Figure 9.11(b) is derived using the principle of power balance, thus it assumes that no energy is stored inside the MMC:

$$V_{dc}I_{dc} = \sum_{j=a,b,c} v_{conv_j}^{ac}\, i_j \tag{9.11}$$

The DC current function is derived from (9.11) and (9.10):

$$I_{dc} = \frac{1}{2}\sum_{j=a,b,c} v_{ref_j} i_j \tag{9.12}$$

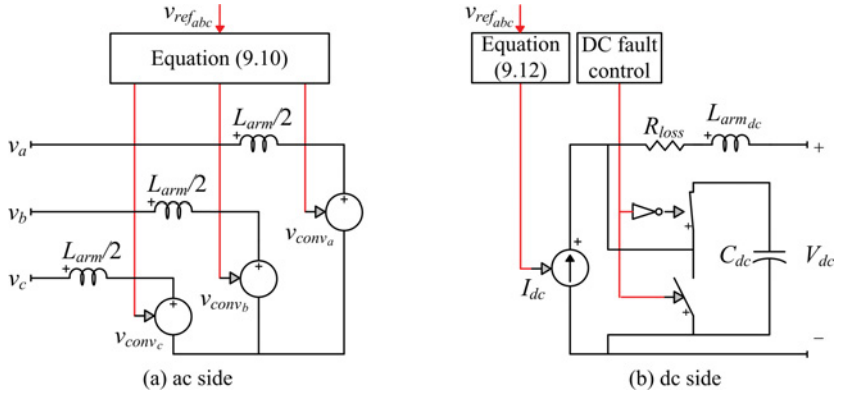

Figure 9.11 Model 4: (a) AC side and (b) DC side.

The equivalent capacitor C_{dc} is calculated using the energy conservation principle and neglecting the energy stored in arm inductances:

$$E_{MMC} = 6\sum_{i=1}^{N}\left(\frac{1}{2}C\cdot v_{C_i}^2\right) \simeq 6\left(N\frac{1}{2}C\cdot v_C^2\right) = 6\left(\frac{1}{2}\frac{C}{N}\cdot V_{dc}^2\right) \tag{9.13}$$

$$C_{dc} = \frac{6C}{N} \tag{9.14}$$

Unlike the classical VSC model, an inductance is included in each arm of the MMC, thus an equivalent inductance should also be added on the DC side. Since one-third of the DC current flows in each arm and the same DC current flows in the upper and lower arms of each phase, the equivalent inductance is given by $L_{arm_{dc}} = (2/3)L_{arm}$. The total conduction losses of the MMC can be found using $R_{loss} = (2/3)N\,R_{ON}$.

During a DC fault, all SMs in the MMC are blocked, thus transforming the MMC into a six-pulse bridge diode converter (see Figure 9.2). However, since only the equivalent tree-phase MMC is represented, the blocked state behaviour cannot be accurately modelled. In order to mimic this behaviour, the equivalent capacitor C_{dc} is disconnected and the current source control is short-circuited.

9.4 Control System

This section develops the control system for the MMC topology. Since the MMC topology is of VSC type [21], it uses an upper-level control similar to the previous VSC technology (e.g. two-level, multilevel diode-clamped, etc.) and lower-level control specific to MMC technology. Each variable is regulated through a PI control loop. All PI controllers are equipped with anti-windup functions [30] to prevent the integral part of accumulating errors when the output value reaches the limit set by the user. In this section the PI control function is defined as $C_X(s) = k_p + k_i/s$ in the Laplace domain and the subscript X refers to the related control loop.

9.4.1 Operation Principle

In order to understand the principle of the VSC-MMC control system, let us first consider the two-bus system (Figure 9.12), where V_S is the AC voltage source, V_{conv} is the AC voltage of the converter and X is the equivalent inductance between the AC source and converter (i.e. transformer leakage inductance, equivalent arm inductance, etc.). The losses are neglected for simplification purposes. The transferred active and reactive powers from the source to the converter are given by

$$\begin{aligned} P_R &= \frac{V_S V_{conv}}{X}\sin(\delta) \\ Q_R &= \frac{V_S V_{conv}\cos(\delta) - V_{conv}^2}{X}, \end{aligned} \tag{9.15}$$

where δ is the angle difference between the two bus voltages.

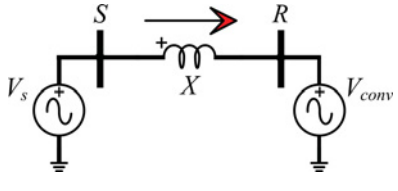

Figure 9.12 Two-bus system for representing the functionality of the VSC-MMC control system.

Assuming that the angle δ is small, the power equations (9.15) can be linearized as

$$\begin{aligned} P_R &\simeq \frac{V_S V_{conv}}{X}\delta \\ Q_R &\simeq \frac{V_{conv}\left(V_S - V_{conv}\right)}{X}. \end{aligned} \tag{9.16}$$

From (9.16), we can see that by controlling the voltage amplitude and phase angle of the converter, it is possible to regulate the active and reactive powers at a desired set-point.

9.4.2 Upper-Level Control

Two main structures of upper-level controls exist (Figure 9.3): V/F control and vector-current control represented by the outer/inner control.

9.4.2.1 dq0 Reference Frame

The use of a rotating *dq0*-frame simplifies the control analysis of three-phase circuits. A set of three-phase voltages in the *abc*-frame can be transformed into two-dimensional $\alpha\beta$ complex frame by the Clark transformation:

$$\begin{bmatrix} v_\alpha \\ v_\beta \end{bmatrix} = \frac{3}{2}\begin{bmatrix} 1 & -1/2 & -1/2 \\ 0 & \sqrt{3}/2 & -\sqrt{3}/2 \end{bmatrix}\begin{bmatrix} v_a \\ v_b \\ v_c \end{bmatrix}, \tag{9.17}$$

where v_a, v_b and v_c are the three-phase voltages in the *abc* frame, v_α and v_β are the corresponding voltages in the $\alpha\beta$ frame (Figure 9.13(a)). The $\alpha\beta$-*dq* transformation is given by the Park transformation using the reference frame of Figure 9.13(b):

$$\begin{bmatrix} v_d \\ v_q \end{bmatrix} = \begin{bmatrix} \cos(\theta) & \sin(\theta) \\ -\sin(\theta) & \cos(\theta) \end{bmatrix}\begin{bmatrix} v_\alpha \\ v_\beta \end{bmatrix}, \tag{9.18}$$

where θ is the transformation angle being equal to ωt, with ω being the angular velocity in rad/s of the AC system under consideration. The direct (**T**) and the inverse ($\mathbf{T}^{-1}$) *abc-dq* transformation matrices are

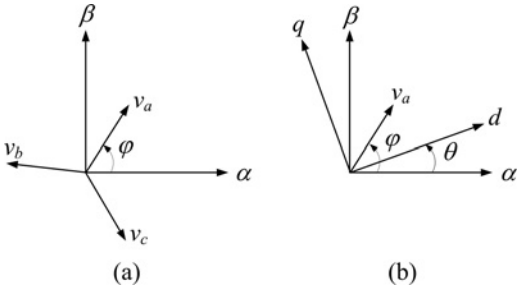

Figure 9.13 Reference frames: (a) stationary, (b) rotating dq.

defined as

$$\begin{bmatrix} v_d \\ v_q \end{bmatrix} = \mathbf{T}\begin{bmatrix} v_a \\ v_b \\ v_c \end{bmatrix} = \sqrt{(2/3)}\begin{bmatrix} \cos(\theta) & \cos(\theta - 2\pi/3) & \cos(\theta + 2\pi/3t) \\ -\sin(\theta) & -\sin(\theta - 2\pi/3) & -\sin(\theta + 2\pi/3) \\ 1/2 & 1/2 & 1/2 \end{bmatrix}\begin{bmatrix} v_a \\ v_b \\ v_c \end{bmatrix} \tag{9.19}$$

$$\begin{bmatrix} v_a \\ v_b \\ v_c \end{bmatrix} = \mathbf{T}^{-1}\begin{bmatrix} v_d \\ v_q \end{bmatrix} = \begin{bmatrix} \cos(\theta) & -\sin(\theta) \\ \cos(\theta - 2\pi/3) & -\sin(\theta - 2\pi/3) \\ \cos(\theta + 2\pi/3t) & -\sin(\theta + 2\pi/3) \end{bmatrix}\begin{bmatrix} v_d \\ v_q \end{bmatrix}. \tag{9.20}$$

The same transformations can be applied on current variables:

$$\begin{bmatrix} i_d \\ i_q \end{bmatrix} = \mathbf{T}\begin{bmatrix} i_a \\ i_b \\ i_c \end{bmatrix} \tag{9.21}$$

$$\begin{bmatrix} i_a \\ i_b \\ i_c \end{bmatrix} = \mathbf{T}^{-1}\begin{bmatrix} i_d \\ i_q \end{bmatrix} \tag{9.22}$$

The active and reactive powers and the AC grid voltage are calculated in the *dq* reference frame as

$$P = v_d i_d + v_q i_q \tag{9.23}$$

$$Q = -v_d i_q + v_q i_d \tag{9.24}$$

$$v = \sqrt{v_d^2 + v_q^2}. \tag{9.25}$$

9.4.2.2 Phase-Locked Loop (PLL)

When a VSC terminal is connected to an AC grid, the frequency and phase must be detected at a predefined reference point in order to synchronize the converter and control system accordingly. This action is performed by the PLL system which synchronizes with the AC grid voltage. For HVDC transmission, the grid voltage vector is chosen to align with the *d*-axis reference. Several PLL techniques can be used and can be found in [31]. The PLL will produce the phase angle that will be used to transform *abc* to *dq* reference frame.

9.4.2.3 Vector Control (Outer/Inner Control)

The basic principle of vector-current control is to regulate the instantaneous active and reactive powers independently through a fast inner current control loop. Using a *dq* decomposition, the inner current control loop decouples the current into *d* and *q* components, where outer loops can use the *d* component to control active power (*P*-control) or DC voltage (V_{dc}-control) or droop control (P/V_{dc}-control), and the *q* component to control reactive power (*Q*-control) or ac voltage (V_{ac}-control) at point of common coupling (PCC). One of the main advantages of this control system is its ability to limit the current flowing into the converter during disturbances. Due to its successful application in HVDC transmission systems, vector-current control has become the dominant control method for grid-connected VSCs in almost all modern applications [32].

Inner control – Using the current sign convention from Figures 9.1 and 9.2 (current entering into the MMC) and neglecting the star point reactor, the following equations can be written for each phase $j = a, b, c$:

$$\frac{V_{dc}}{2} = v_{u_j} + L_{arm}\frac{di_{u_j}}{dt} + R_{arm}i_{u_j} - L_{transfo}\frac{di_j}{dt} - R_{transfo}i_j + v_{PCC_j} \tag{9.26}$$

$$\frac{V_{dc}}{2} = v_{\ell_j} + L_{arm}\frac{di_{\ell_j}}{dt} + R_{arm}i_{\ell_j} + L_{transfo}\frac{di_j}{dt} + R_{transfo}i_j - v_{PCC_j} \tag{9.27}$$

The following variable is defined:

$$v^{ac}_{conv_j} = \frac{v_{\ell_j} - v_{u_j}}{2} \tag{9.28}$$

Using (9.28) and subtracting (9.26) and (9.27) gives

$$v_{PCC_j} - v^{ac}_{conv_j} = \left(\frac{L_{arm}}{2} + L_{transfo}\right)\frac{di_j}{dt} + \left(\frac{R_{arm}}{2} + R_{transfo}\right)i_j. \tag{9.29}$$

Park transformation allows (9.29) to be rewritten as

$$\begin{aligned} v_{PCC_d} - v^{ac}_{conv_d} &= \left(\frac{L_{arm}}{2} + L_{transfo}\right)\frac{di_d}{dt} + \left(\frac{R_{arm}}{2} + R_{transfo}\right)i_d - \omega\left(\frac{L_{arm}}{2} + L_{transfo}\right)i_q \\ v_{PCC_q} - v^{ac}_{conv_q} &= \left(\frac{L_{arm}}{2} + L_{transfo}\right)\frac{di_q}{dt} + \left(\frac{R_{arm}}{2} + R_{transfo}\right)i_q + \omega\left(\frac{L_{arm}}{2} + L_{transfo}\right)i_d. \end{aligned} \tag{9.30}$$

The control loop is applied to (9.30) to give

$$\begin{aligned} v^{ac}_{conv_{d_{ref}}} &= -\left(i_{ref_d} - i_d\right)C_i(s) + v_{PCC_d} + \left(\frac{L_{arm}}{2} + L_{transfo}\right)\omega\, i_q \\ v^{ac}_{conv_{q_{ref}}} &= -\left(i_{ref_q} - i_q\right)C_i(s) + v_{PCC_q} - \left(\frac{L_{arm}}{2} + L_{transfo}\right)\omega\, i_d, \end{aligned} \tag{9.31}$$

where $C_i(s)$ is current control transfer function.

The inner controller is presented in Figure 9.14 and permits the controlling of the reference voltages ($v^{ac}_{conv_{d_{ref}}}$ and $v^{ac}_{conv_{q_{ref}}}$) that will be used for lower-level control. In order to decouple the d- and q-axes, a feed-forward technique is used to compensate the cross-coupling terms.

Active power control (P-control) – As the grid voltage vector is aligned with the d-axis, the q component of the grid voltage is equal to zero and the d component is equal to the voltage magnitude. Equation (9.23) becomes

$$P = v_{PCC_d}i_d. \tag{9.32}$$

An integral control is sufficient to produce the desired d current reference ($i_{d_{ref}}$). The control law of P-control is defined by

$$i_{d_{ref}} = \frac{1}{v_{PCC_d}}\left(\frac{k_i}{s}\right)\left(P_{ref} - P\right). \tag{9.33}$$

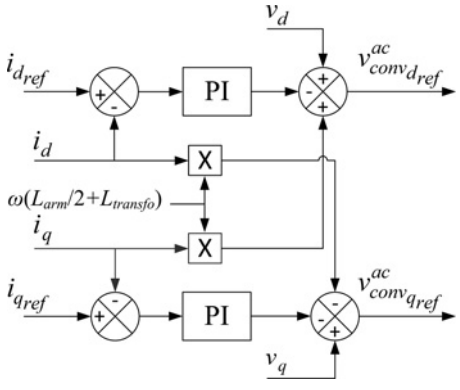

Figure 9.14 Inner control.

DC voltage control (V_{dc}-control) – From the linearized model (Model 4 in Section 9.3.4) it can be found that SM capacitors can be represented as an equivalent capacitor C_{dc}. Since the energy in the equivalent inductance is small, it can be neglected. The following equation results in the *dq* reference frame:

$$C_{dc}\frac{dV_{dc}}{dt} = i_d - I_{dc} \tag{9.34}$$

After neglecting the feed-forward component I_{dc}, a simple PI control ($C_{V_{dc}}(s)$) can be applied to regulate the DC voltage:

$$i_{d_{ref}} = C_{V_{dc}}(s)\left(V_{dc_{ref}} - V_{dc}\right), \tag{9.35}$$

where $C_{V_{dc}}(s)$ is the DC voltage control transfer function.

P/V_{dc}-droop control – The functionality of droop control in the DC grid is similar to that in the AC grid. In the AC grid the relationship is between frequency and active power, but in the DC grid the DC voltage is a function of active power. The droop coefficient is given by

$$k_{droop} = \frac{\Delta V_{dc}}{\Delta P_{ref}}. \tag{9.36}$$

The active power delta reference is added over the active power reference (P_{ref}) as shown in Figure 9.15.

Reactive power control (Q-control) – As the grid voltage vector is aligned with the *d*-axis, the *q* component of the grid voltage is equal to zero and the *d* component is equal to the voltage magnitude. Equation (9.24) becomes

$$Q = -v_{PCC_d} i_q. \tag{9.37}$$

An integral control is sufficient to produce the desired *q* current reference ($i_{q_{ref}}$). The control law of *Q*-control is defined as (see Figure 9.15)

$$i_{q_{ref}} = -\frac{1}{v_{PCC_d}}\left(\frac{k_i}{s}\right)\left(Q_{ref} - Q\right) \tag{9.38}$$

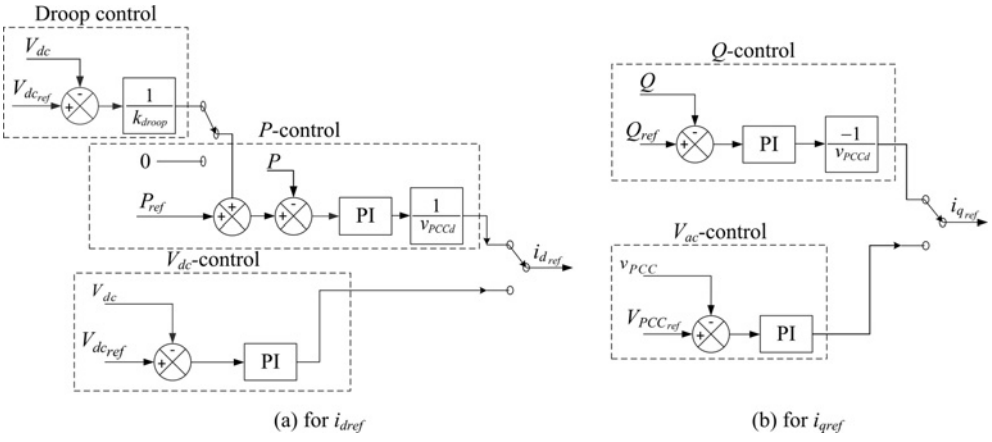

Figure 9.15 Outer control block: (a) block for i_{dref}, (b) block for i_{qref}.

AC voltage control (V_{ac}-control) – As in (9.16), the voltage drop Δv_{PCC} over the reactance (X_{PCC}) of the AC grid at PCC can be approximated as

$$\Delta v_{PCC} = v_{conv} - v_{PCC} \approx \frac{X_{PCC} Q}{v_{PCC}}. \tag{9.39}$$

Since the grid voltage vector is aligned with the d-axis and using (9.37), (9.39) becomes

$$\Delta v_{PCC} \approx X_{PCC} i_q. \tag{9.40}$$

An integral control is sufficient to produce the desired q current reference ($i_{q_{ref}}$):

$$i_{q_{ref}} = \left(\frac{k_i}{s}\right)\left(V_{PCCref} - v_{PCC}\right) \tag{9.41}$$

Current reference limiter – Since the VSC type does not have any overload capability, a large transient current due to disturbances may stress or damage its semiconductors. Therefore, a current limiter must be implemented in the control system of Figure 9.16 [33]. The current limit $i_{\lim}$ is compared with the current magnitude computed from $i_{d_{ref}}$ and $i_{q_{ref}}$. When the current limit is exceeded, both $i_{d_{ref}}$ and $i_{q_{ref}}$ have to be limited. The choice of how to limit both reference currents will depend on the application. For instance, if the converter is connected to a strong grid, the $i_{d_{ref}}$ will be given high priority (i.e. P-priority) to produce more active power when the current limit is exceeded. If the converter is connected to a weak grid or used to supply an industrial plant, the VSC will give high priority to $i_{q_{ref}}$ (i.e. Q-priority) to keep up the AC voltage when the current limit is exceeded. The remaining capability is then available for active power production. The following equations are used:

$$\text{For } P\text{-priority:} \quad i_{\lim} \geq \sqrt{i^2_{d_{ref_{\lim}}} + i^2_{q_{ref}}} \tag{9.42}$$

$$\text{For } Q\text{-priority:} \quad i_{\lim} \geq \sqrt{i^2_{d_{ref}} + i^2_{q_{ref_{\lim}}}} \tag{9.43}$$

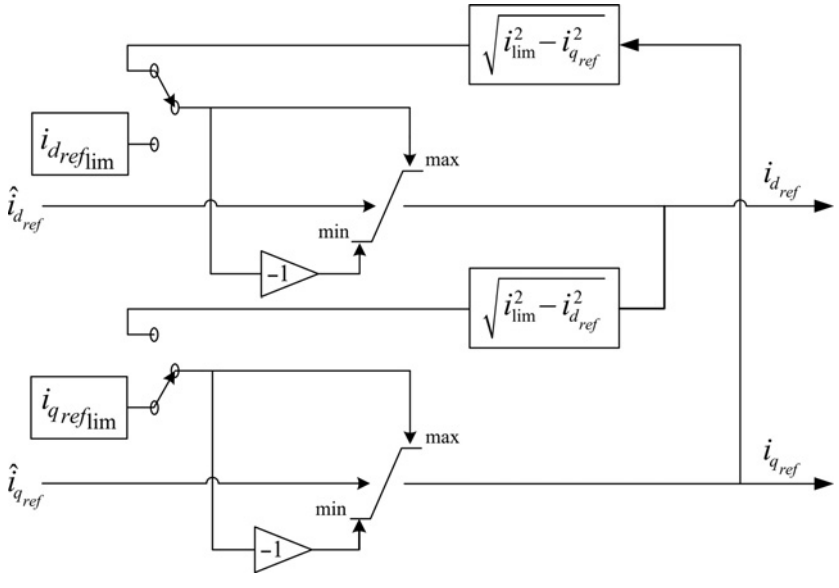

Figure 9.16 Current reference limiter.

9.4.2.4 V/F-Control

To produce three-phase AC voltages, the converter needs three variables: magnitude, phase angle and frequency. In V/F control, the phase angle and frequency are generated from an internal oscillator. However the AC voltage magnitude is regulated by means of a PI control. The control law is

$$\Delta v_{PCC} = C_{V_{ac}}(s)\left(V_{PCC_{ref}} - v_{PCC}\right), \tag{9.44}$$

where $C_{V_{ac}}(s)$ is the DC voltage control transfer function.

As the grid voltage vector (v_{PCC}) is aligned with the d-axis, the following equation can be found [33]:

$$v_{conv_d} = \left(V_0 + \Delta v_{PCC}\right) + H_{HP}(s)\, i_d \tag{9.45}$$

$$v_{conv_q} = 0, \tag{9.46}$$

where V_0 is the nominal voltage, $H_{HP}(s)$ is a high-pass filter and the term $H_{HP}(s)i_d$ is a feed-forward loop used to improve the damping [33]. The V/F control block is shown in Figure 9.17.

V/F control is usually used when the VSC is connected to an AC system with passive load or for wind-power applications.

9.4.3 Lower-Level Control

Unlike standard VSC technology, the MMC topology requires additional controllers in order to stabilize internal variables. The top-level view of the control structure is presented in Figure 9.3. Lower-level control may change, depending on manufacturers and SM circuit configuration (half-bridge, full-bridge, etc.). The following sections describe the key points in this type of control and present a survey of the different techniques.

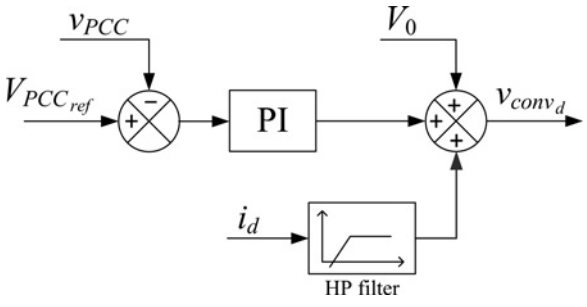

Figure 9.17 V/F control block.

Lower-level control is essentially composed of circulating current control, modulation and control for balancing the capacitor voltage of each SM.

9.4.3.1 Circulating Current Control

Voltage unbalances between the arm phases of the MMC introduce circulating currents containing a second-harmonic component which not only distorts the arm currents, but also increases the ripple on SM capacitor voltages. Circulating currents can be eliminated by adding a parallel capacitor (resonant filter) between the midpoints of the upper and lower arm inductances on each phase [34] or using an active control over the AC voltage reference $v_{conv_{abc}}$ [35]. The latter is presented below.

The differential current i_{diff_j} for each phase is defined as

$$i_{diff_j} = \frac{i_{u_j} + i_{\ell_j}}{2}. \tag{9.47}$$

In [36], it was shown that the circulating currents in the MMC are generated by the inner voltage differences between phases, and that they are composed of a negative sequence component with twice the fundamental frequency. Thus, the three-phase differential currents are given by

$$\begin{aligned} i_{diff_a} &= \frac{I_{dc}}{3} + I_{2f_a}(2\omega t + \phi) \\ i_{diff_b} &= \frac{I_{dc}}{3} + I_{2f_b}\left(2\omega t + \phi + \frac{2\pi}{3}\right) \\ i_{diff_c} &= \frac{I_{dc}}{3} + I_{2f_c}\left(2\omega t + \phi - \frac{2\pi}{3}\right). \end{aligned} \tag{9.48}$$

First define the voltage across arm inductance and resistance as

$$v_{diff_j} = L_{arm}\frac{di_{diff_j}}{dt} + R_{arm}\, i_{diff_j}, \tag{9.49}$$

and then apply Park transformation,

$$\begin{aligned} v_{diff_d} &= L_{arm}\frac{di_{2f_d}}{dt} - 2\omega L_{arm} i_{2f_q} + R_{arm} i_{2f_d} \\ v_{diff_q} &= L_{arm}\frac{di_{2f_q}}{dt} + 2\omega L_{arm} i_{2f_d} + R_{arm} i_{2f_q}. \end{aligned} \tag{9.50}$$

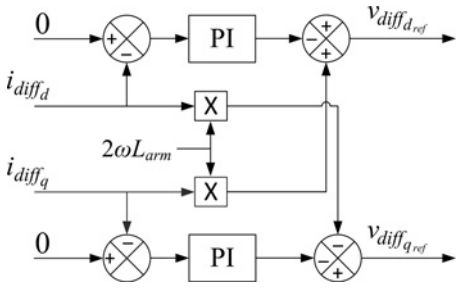

Figure 9.18 Circulating current control.

To eliminate the circulating current, two PI controls are applied to the *dq* differential currents:

$$\begin{aligned} v_{diff_d} &= \left(0 - i_{2f_d}\right)\left(k_p + \frac{k_i}{s}\right) - 2\omega L_{arm} i_{2f_q} \\ v_{diff_q} &= \left(0 - i_{2f_q}\right)\left(k_p + \frac{k_i}{s}\right) + 2\omega L_{arm} i_{2fd} \end{aligned} \tag{9.51}$$

The circulating current control structure is presented in Figure 9.18.

9.4.3.2 Coupling Equations

Adding (9.26) to (9.27) and using the definition of (9.49) gives

$$V_{dc} - v_{conv_j}^{dc} = 2v_{diff_j} = 2L_{arm}\frac{di_{diff_j}}{dt} + 2R_{arm}\, i_{diff_j}, \tag{9.52}$$

where

$$v_{conv_j}^{dc} = v_{u_j} + v_{\ell_j}. \tag{9.53}$$

Using (9.28), (9.29), (9.52) and (9.53) the voltage coupling equations become

$$\begin{aligned} v_{u_j} &= \frac{V_{dc}}{2} - v_{diff_j} - v_{conv_j}^{ac} \\ v_{\ell_j} &= \frac{V_{dc}}{2} - v_{diff_j} + v_{conv_j}^{ac}. \end{aligned} \tag{9.54}$$

9.4.3.3 NLC Modulation

Traditional modulation techniques proposed to date for MMCs include phase-disposition modulation (PD-PWM) [37], phase-shift modulation (PS-PWM) [38], space-vector modulation (SV-PWM) [8] and the improved selective harmonic elimination method (SHE) [39]. As the number of MMC levels increases, the PWM and SHE techniques become cumbersome. Therefore, more efficient staircase-type methods, such as the nearest level control (NLC) technique, can be used. NLC modulation uses the round function [35] to transform the reference variables to a staircase waveform with the total number of steps equal to

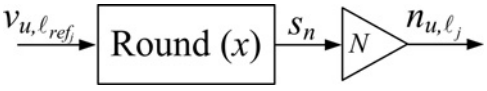

Figure 9.19 NLC modulation.

the number of MMC levels. In Figure 9.19, the output n_{u,ℓ_j} represents the number of SMs to be inserted in each arm.

9.4.3.4 Capacitor Balancing Control

The capacitor voltage at all SMs must be balanced and kept in an acceptable voltage range during normal operation. Two main approaches exist for balancing the capacitor voltages: by controlling each SM capacitor voltage by a PI controller [19] or by means of an algorithm that handles all SM capacitors of each arm. The latter is more suitable for a large number of MMC levels. To achieve this, capacitor voltages must be monitored and switched on and off, based on a balancing control algorithm (BCA) [37] (Figure 9.20). The BCA measures the capacitor voltages at each SM at any instant and sorts them before selecting the upper and lower SM to switch ON. The number of SMs to be inserted is determined by n_{u,ℓ_j}. To improve the efficiency of the algorithm, the model includes a trigger control that activates the BCA only when a new (ON/OFF) state in the n_{u,ℓ_j} functions is reached. This will avoid switching the SMs at each time-point.

9.4.4 Control Structure Requirement Depending on MMC Model Type

All of the above controllers are included when MMC Model 1 (Full detailed) and Model 2 (Detailed equivalent) are used. However, if Model 3 (Switching function of MMC arm) is used, the BCA is excluded from the lower-level control and if the Model 4 (AVM) is used, the Lower Level Control system is excluded and only the upper level control can be taken into account.

9.5 Model Comparisons

This section provides a comparison between the MMC models presented in the previous section: Models 1, 2, 3 and 4. The dynamic behaviour comparison is conducted for step change of active power reference, three-phase AC fault, pole-to-pole DC fault and startup sequence.

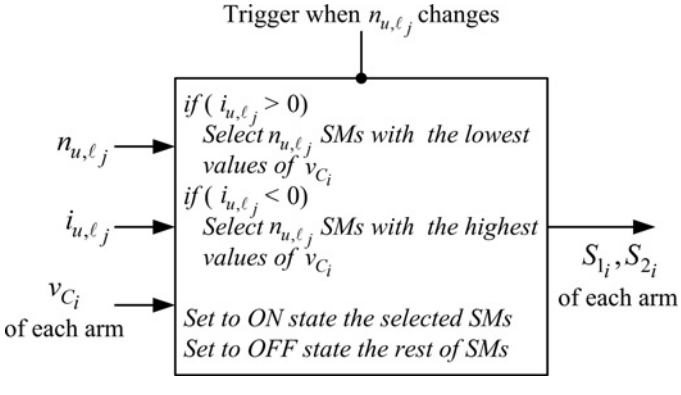

Figure 9.20 Balancing control algorithm (BCA).

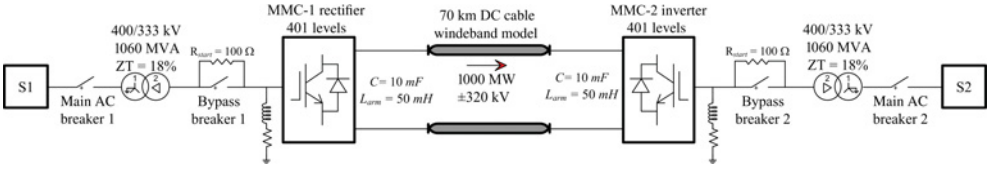

Figure 9.21 MMC-HVDC transmission test system.

The studied system is presented in Figure 9.21. The control strategy considers a *P/Q*-control on the sending end (MMC-1) and a V_{DC}/*Q*-control on the receiving end (MMC-2). The AC grids are represented as equivalent sources with a short-circuit level of 10 000 MVA each. The transmission capacity of the system is 1000 MW from S1 to S2. The DC cable is modelled using a wideband line model [40]. Each MMC station considers a 401-level MMC (400 SMs/arm). The Model 1 (Full Detailed) constitutes the reference model. Accuracy verification is based on a time-step of 1 μs for all model types. All model developments and simulations are performed using the EMTP-RV software [41].

9.5.1 Step Change on Active Power Reference

A step change in the active power reference of MMC-1 is applied at 0.5 s of the simulation. The active power reference (P_{ref}) is reduced from 1 to 0.5 p.u. In Figure 9.22 all four models deliver identical results. Figure 9.23 presents internal variables related to the studied MMC topology: the difference current in phase A (i_{diff_a}) and the sum of all capacitor voltages of each arm of phase A, $v_{C_{tot_{ua}}}$ and $v_{C_{tot_{la}}}$ (see Figure 9.9), respectively. Since arm details are not represented in Model 4 (Figure 9.11), only Models 1, 2 and 3 are compared here. As it can be seen, the three models give similar accurate results.

9.5.2 Three-Phase AC Fault

A 200 ms three-phase-to-ground fault is applied on the AC side of MMC-2 at 1 s of simulation time. Figure 9.24 compares the dynamic responses. The results from Models 2 and 3 are similar to Model 1, and Model 4 remains sufficiently accurate. Figure 9.24(d) shows an attenuated oscillation around 413 Hz during the fault, which has slightly higher amplitude (peak-to-peak mean value 0.008 p.u.) in Models 1 and 2 than in Model 3 (peak-to-peak mean value 0.001 p.u.). This oscillation is related to the interaction between the MMC and the DC cable. The current increases rapidly during the AC fault. The capacitor voltage fluctuations of each SM will also increase, and the assumption in equation (9.2) will become less accurate. This transient generates harmonics in the MMC that interact with the DC cable.

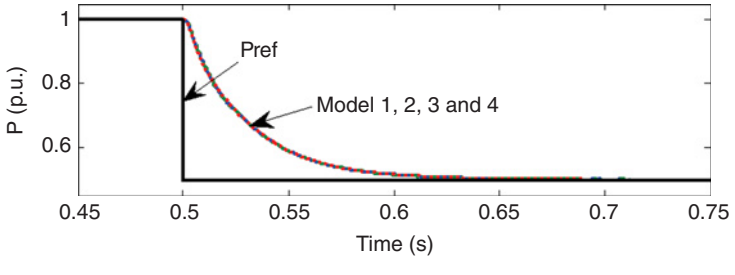

Figure 9.22 Active power responses, power flowing into MMC-1.

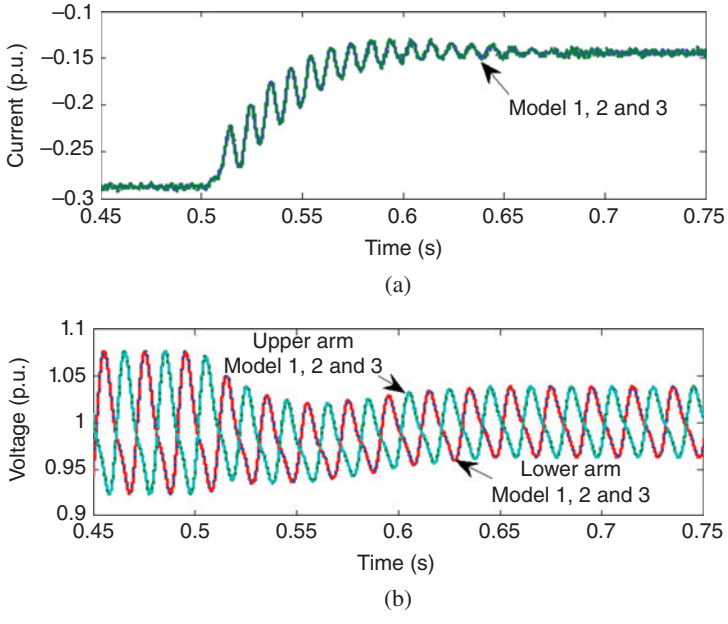

Figure 9.23 Step change in active power reference for MMC-1: (a) MMC-1 phase A, difference current i_{diff_a}, (b) MMC-1 phase A upper and lower arms, $v_{C_{tot}}$.

9.5.3 Influence of MMC Levels

The number of MMC levels can vary, depending on the application and the manufacturer. In order to evaluate the effect of MMC levels, the 401-level MMC in the test case of Figure 9.21 is replaced by a 51-level MMC. SM capacitors are scaled to $C * 50/400$. All the other parameters are kept the same.

The results on the AC side are similar to those found in Figure 9.24. However, the DC-side behaviour (Figure 9.25) is not the same, due to the reduced number of levels.

Note that during the AC fault the DC voltage oscillation frequency found in Figure 9.24(d) appears in Figure 9.25(b). However, this oscillation has a higher amplitude and does not attenuate in Models 1 and 2 in contrast with Model 3. In the fault interval, the DC voltage peak-to-peak mean value of Model 2 is close to Model 1 at around 0.063 p.u., but the peak-to-peak mean value of Model 3 is 0.010 p.u. Moreover, this oscillation has a repercussion on the DC current shown in Figure 9.25(a). Indeed, there are noticeable differences between the waveforms from Models 1 to 2 and Model 3.

For an MMC of 101 levels, differences can still be found between Models 1, 2 and 3. The DC voltage peak-to-peak mean value for Models 1 and 2 are 0.031 p.u., and Model 3 is estimated at around 0.006 p.u. However, it may be considered as a precision trade-off, since the oscillations are attenuated and the differences between current waveforms are less apparent.

This section and the previous one, Section 9.5.2, confirm that assumption (9.2) in Model 3 depends on the number of MMC levels and capacitor voltage fluctuations.

9.5.4 Pole-to-Pole DC Fault

The models are tested for a permanent DC fault between the positive and negative poles in the middle of the DC cable. The fault is applied at 1.9 s. Since the protection system is activated, the AC breaker is opened and the MMCs are blocked after fault occurrence. The DC and AC currents in MMC-1 are

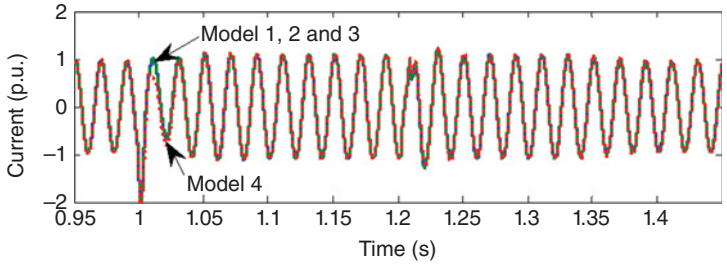

(a)

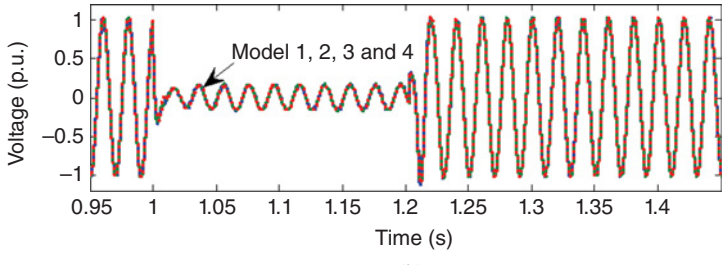

(b)

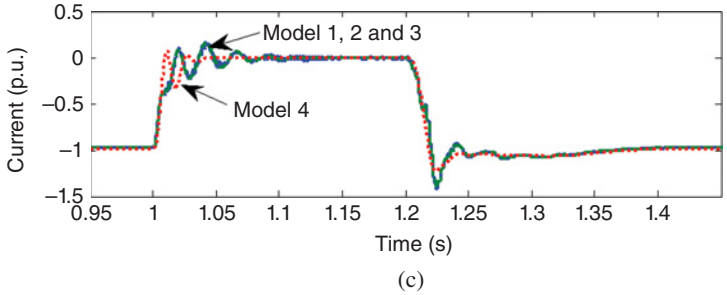

(c)

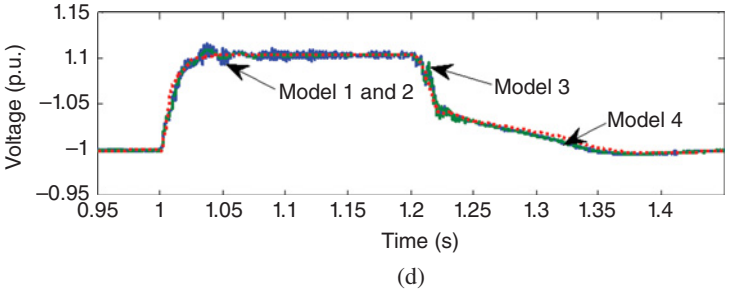

(d)

Figure 9.24 Three-phase fault, 401 levels: (a) MMC-2 phase A current i_a, (b) MMC-2 phase A voltage v_a, (c) MMC-2 DC current I_{dc}, (d) MMC-2 DC voltage V_{dc}.

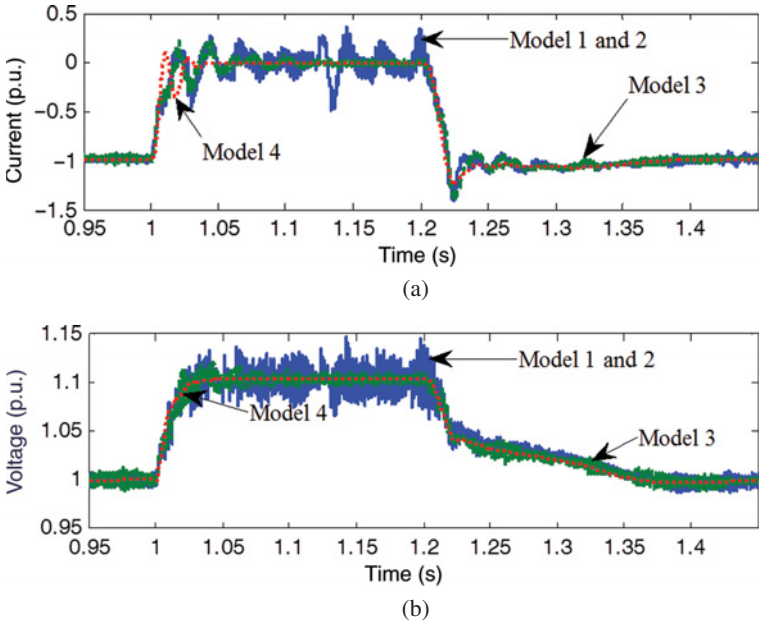

Figure 9.25 Three-phase fault, 51 levels: (a) MMC-2 DC current I_{dc}, (b) MMC-2 DC voltage V_{dc}.

compared in Figure 9.26 for different models. The DC current peak during a pole-to-pole fault reaches a value of approximately 8.2 p.u. for Models 1–3. A peak value of 6.2 p.u. is reached with Model 4.

From the zoomed waveform of Figure 9.27, it can be seen that just after the DC fault occurs, Model 4 accurately mimics the slope and peak values of I_{dc}. However, after around 1 ms, the behaviour becomes different due to the inaccurate representation of the MMC blocked state in Model 4.

9.5.5 *Startup Sequence*

This test examines the startup procedure of the converter, where all capacitor voltages are initially set to zero and all SMs are in blocked state. The breakers, Bypass Breaker 1 and Bypass Breaker 2 (Figure 9.21), are kept open for this test. A resistance R_{start} is connected between the converter and its transformer in order to limit the inrush current. Since arm details are not represented in Model 4, this model cannot be used to study startup. Only Models 1, 2 and 3 are compared in the following figures.

Since in Figure 9.28 both Models 2 and 3 are able to match the results from Model 1, it is concluded that these two simplified models can be used to study converter startup.

The zoomed waveforms of Figure 9.29 are used to highlight the detailed modelling effect of power switches in Model 1. It is observed that Model 1 mimics the reverse recovery behaviour of diodes [42], whereas in Models 2 and 3 this behaviour cannot be represented due to the linear representation of power switches.

9.5.6 *Computational Performance*

Computing times were measured for a 1 s simulation period for the system of Figure 9.21. The simulations were performed on a computer with a 2.80 GHz Intel Core i7–2640M processor and 8 GB of RAM.

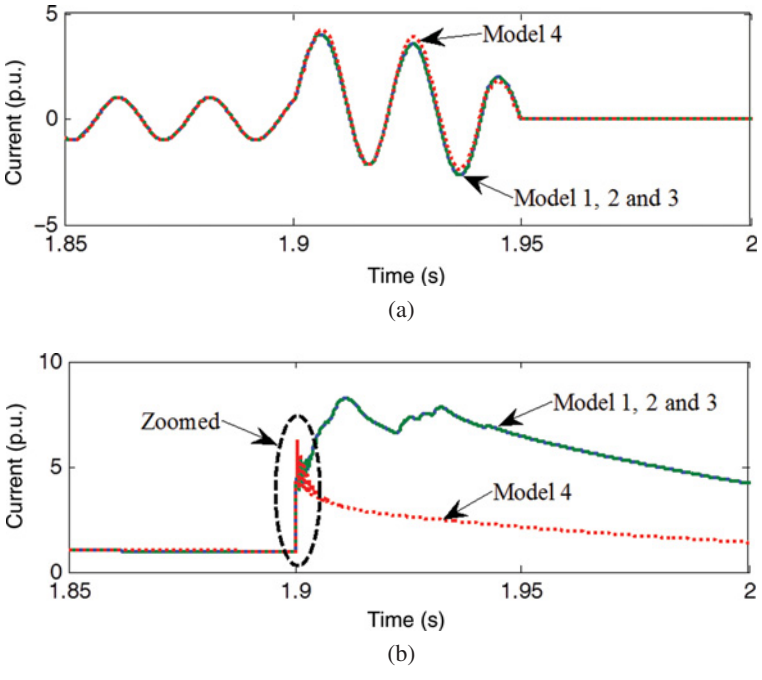

Figure 9.26 DC fault results: (a) MMC-1 AC current: i_a, (b) MMC-1, DC current: I_{dc}.

In order to study the impact of the number of MMC levels on computing time, four different levels are tested: 20, 50, 100 and 400 SMs/arm. The computing times are compared for all models using time-steps of 10 μs and 100 μs (only for Model 4). The results presented in Table 9.2 show that the best computing speed is understandably achieved by Model 4. Its time-step and computing speed can be further increased without significantly affecting its accuracy. Nevertheless, the computational speed of Model 3 is very close to Model 4 when the same time-step is used. Computing times for Models 1 and 2 are related to the number of MMC levels.

From Table 9.2, we can see that linear behaviour can be achieved with the implementation used in this chapter. The computing time function for Model 1 is slightly exponential, owing to its iterations with nonlinear functions, which increase when the number of nonlinear devices increases.

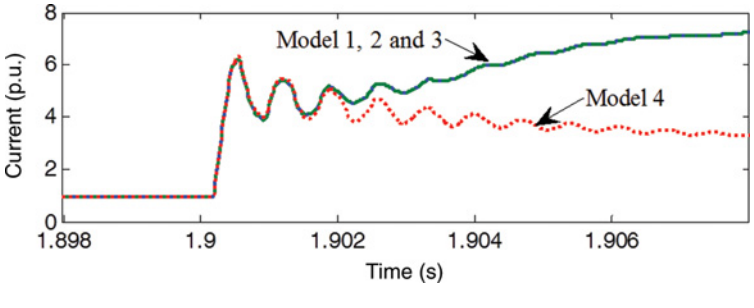

Figure 9.27 Zoomed waveform, MMC-1, I_{dc} in Figure 9.26.

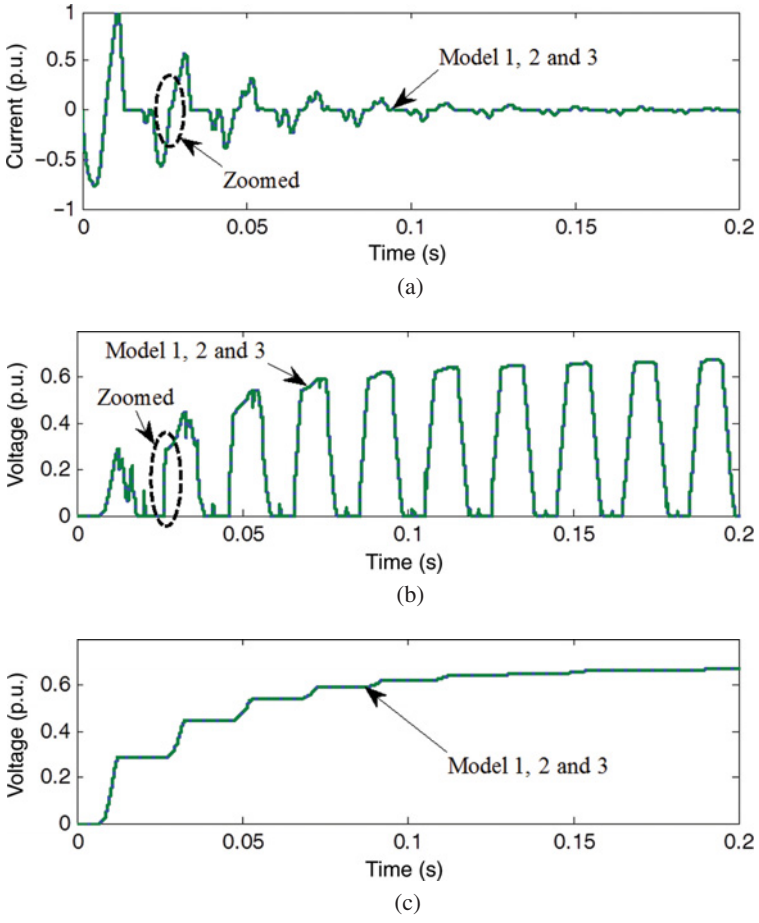

Figure 9.28 MMC-1 phase A variables, startup sequence, 401 levels: (a) MMC-1 phase A; upper arm current i_{u_a}, (b) MMC-1 phase A; upper arm voltage v_{u_a}, (c) MMC-1 phase A; upper arm $v_{C_{tot_{ua}}}$.

When the number of SMs in each arm increases, the gain in simulation speed for Models 3 and 4 as compared to Models 1 and 2, also increases; that is, for 20 SMs per arm the ratios are 2 and 15 when compared to Models 2 and 1, respectively. However, for 400 SMs per arm the same ratios become 26 and 791.

9.6 Real-Time Simulation of MMC Using CPU and FPGA

Real-time modelling of power electronics can be implemented mainly through CPUs and field programmable gate arrays (FPGAs). CPU-based execution times for each time-point remain in the range of tens of microseconds and constitute a limiting factor for simulation accuracy. FPGA technology offers a better alternative and reduces computation times to the range of hundreds of nanoseconds. However, important concerns remain for the broad adoption of this technology owing to the significant efforts needed to implement complex solvers.

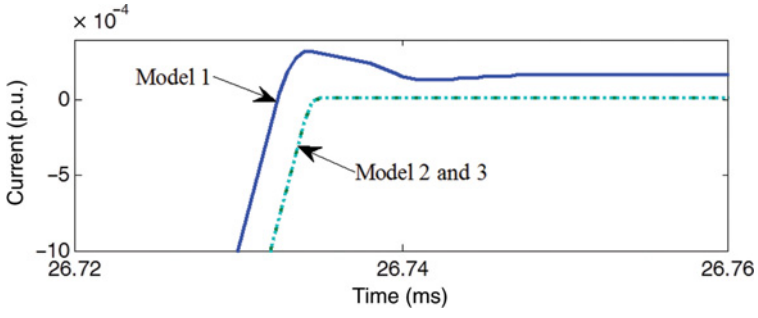

(a)

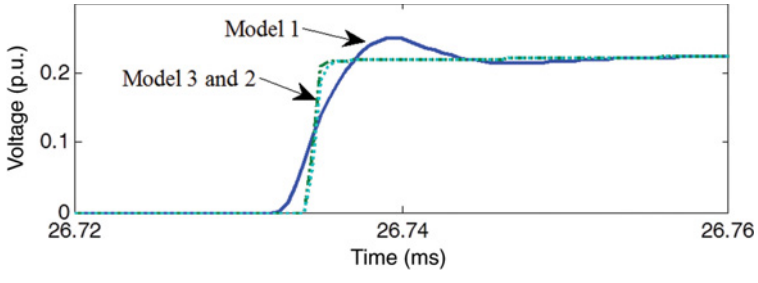

(b)

Figure 9.29 Zoomed waveform MMC-1, phase A variables for startup sequence: (a) zoomed waveform MMC-1 phase A, upper arm current i_{u_a}, (b) zoomed waveform MMC-1 phase A, upper arm voltage v_{u_a}.

In real-time simulations, modelling the MMC full detailed type (i.e. Model 1) is currently out of reach due to the excessive computing times shown in the previous section (Table 9.2). Considering current real-time simulator technologies, the most detailed model that can be achieved is Model 2. Table 9.2 showed that computation time of Model 2 increases with the number of MMC levels. For real-time simulation, the computation time should always be lower than the real-time time-step, in order to prevent overruns and miss-operation of system loops. This requirement constitutes the main boundary for which a model can be simulated on a real-time platform.

This section presents the MMC model implementation on CPU and FPGA. Note that Models 3 and 4 are not studied in this section since their computing times (Table 9.2) are sufficiently low and do not create any complexity for performing real-time simulations.

Table 9.2 Computing times, simulation of 1 s, MMC-HVDC system of Figure 9.21.

		Computing times as function of SMs/arm (s)			
Model	Time-step (μs)	20 SMs/arm	50 SMs/arm	100 SMs/arm	400 SMs/arm
1	10	253	792	2006	13 159
2	10	42	65	114	441
3	10	18	18	18	18
4	10	15	15	15	15
4	100	2	2	2	2

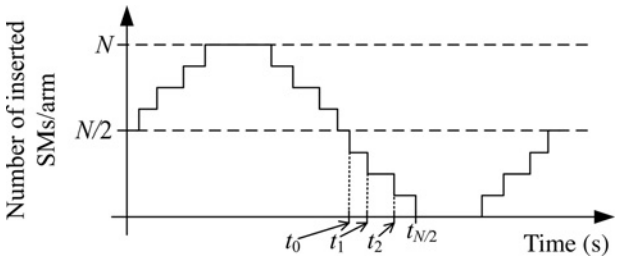

Figure 9.30 Typical NLC output waveform for a MMC-9-level ($N = 8$).

9.6.1 Relation between Sampling Time and N

The main objective of this study is to evaluate the feasibility and performance of the MMC model in real-time simulation. The sampling time of the control system plays an important role in determining the dynamic performance of the system. This sampling time is mainly affected by the modulation technique used. As mentioned previously, when N increases, the PWM types become less efficient. The NLC modulation presented in Section 9.4.3.3 is used for this study. In order to guarantee the transition through each level, the sampling time must maintain a given criterion. A typical waveform produced by the NLC modulation for MMC-9-level ($N = 8$) is shown in Figure 9.30. The equation of this staircase waveform is given by

$$s_n = \frac{N}{2} \sin\left(2\pi f\ t_n\right) + \frac{N}{2}, \tag{9.55}$$

where $t_n = t_0, t_1, \ldots, t_{N/2}$, s_n is the number of SMs to be inserted in each arm and f is the network frequency.

The smallest time interval between two different levels is found where the slope of the desired sinewave is the highest, that is between t_0 and t_1. Therefore, the controller sampling time-step Δt should obey the following inequality in order to guarantee the replication of each MMC level

$$\Delta t \leq \frac{1}{2\pi f} \arcsin\left(\frac{2}{N}\right) \tag{9.56}$$

Note that equation (9.56) does not account for variations produced by the control system. The amplitude related to *N/2* and *f* may vary owing to reference voltage variations. These parameters depend essentially on the MMC application. For HVDC and FACTS applications, these parameters can be bounded, since frequency and amplitude of an AC grid cannot exceed practical limits. If we set a 1.2 p.u. upper limit for frequency and a 1.4 p.u. limit for amplitude, equation (9.56) yields

$$\Delta t \leq \frac{1}{1.2\,(2\pi f)} \arcsin\left(\frac{2}{1.4N}\right). \tag{9.57}$$

Equation (9.57) is shown in Figure 9.31. The coloured area under the curve represents the admissible zone in which Δt will guarantee the replication of each MMC level. As expected, when N increases, the Δt limit decreases.

In order to analyse the impact of Δt, a NLC modulation for an MMC-191-level ($N = 190$) is simulated with three different Δt values highlighted with a cross in Figure 9.31 ($\Delta t = 10$, 20 and 30 μs). Figure 9.32 shows the modulated waveforms and resulting harmonics for different values of Δt. For sampling times that respect (9.57) ($\Delta t = 10$ and 20 μs) the transition through each MMC level is guaranteed and the harmonic contents are sufficiently close. With $\Delta t = 30$ μs, it is not possible to reproduce all levels, and

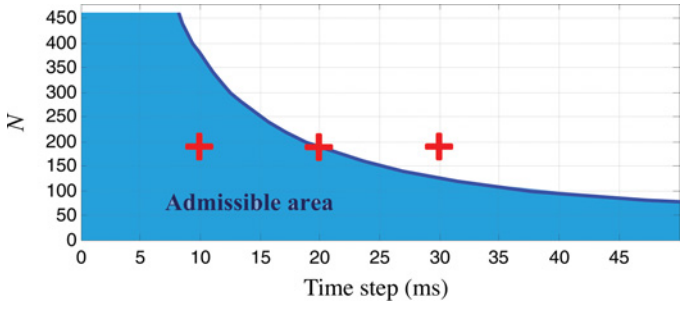

Figure 9.31 *N* as a function of sampling time-step limit.

the harmonic content is significantly affected. The resulting level jumps will also impact the switching frequency of each SM and the BCA.

Equation (9.57) is valid for the NLC modulation, and different formulas must be derived for other modulation techniques.

9.6.2 *Optimization of Model 2 for Real-Time Simulation*

From Table 9.1(b), the ON/OFF states can be computed directly (without iterations) according to the gate signals. However, the blocked state is defined depending on state and non-state variables. Thus, the

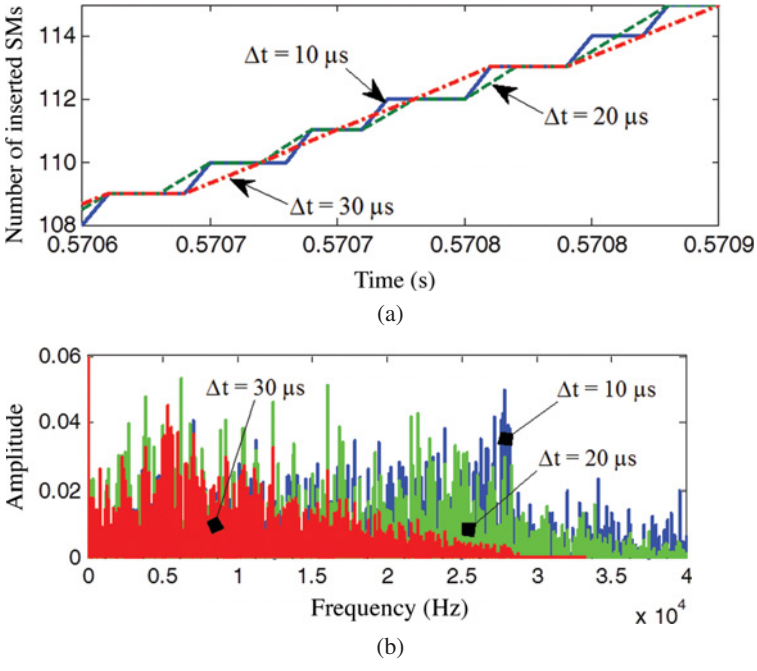

Figure 9.32 Impact of Δt on the modulated waveform: (a) accuracy of modulated waveform for different Δt cases, (b) FFT of modulated waveform for different Δt cases.

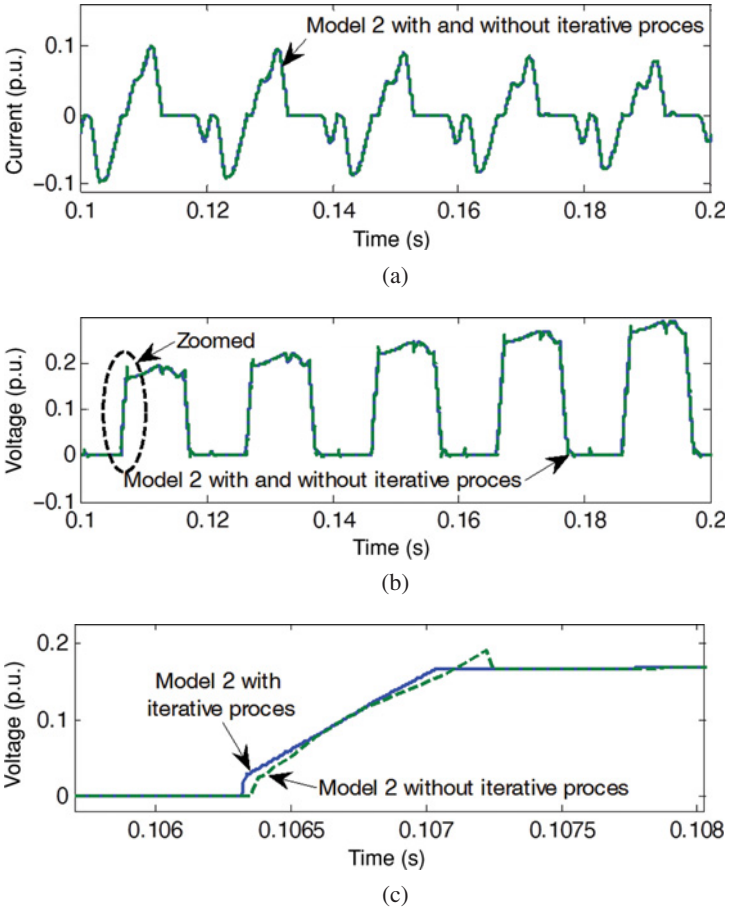

Figure 9.33 Model 2 comparisons with and without iterative process, startup sequence of MMC-1: (a) MMC-1 phase A; upper arm current i_{u_a}, (b) MMC-1 phase A; upper arm voltage v_{u_a}, (c) zoomed waveforms, MMC-1 phase A; upper arm voltage v_{u_a}.

zero-crossing of the arm current variable will cause numerical oscillations. To avoid this problem, an iterative process was implemented for off-line simulation (Section 9.3.2). However, this approach will require more computing time, which is problematic for real-time performance. In order to overcome this issue and avoid iterations, a trigger is added to detect and maintain the 'high impedance mode' (Table 9.1(b)) for one more time-step. This approach is slightly less precise than the iterative approach, but it is sufficiently accurate for real-time simulation as depicted in Figure 9.33 (where the startup sequence test presented in Section 9.5.5 is considered). Further accuracy verification can be found in [43].

9.6.3 Real-Time Simulation Setup

The studied case is presented in Figure 9.34. The control strategy considers a *P/Q*-control. The AC grid is represented by an equivalent voltage source with a short-circuit level of 10 000 MVA. The transmission capacity of the system is 1000 MW. The DC side is represented with a DC cable modelled using the

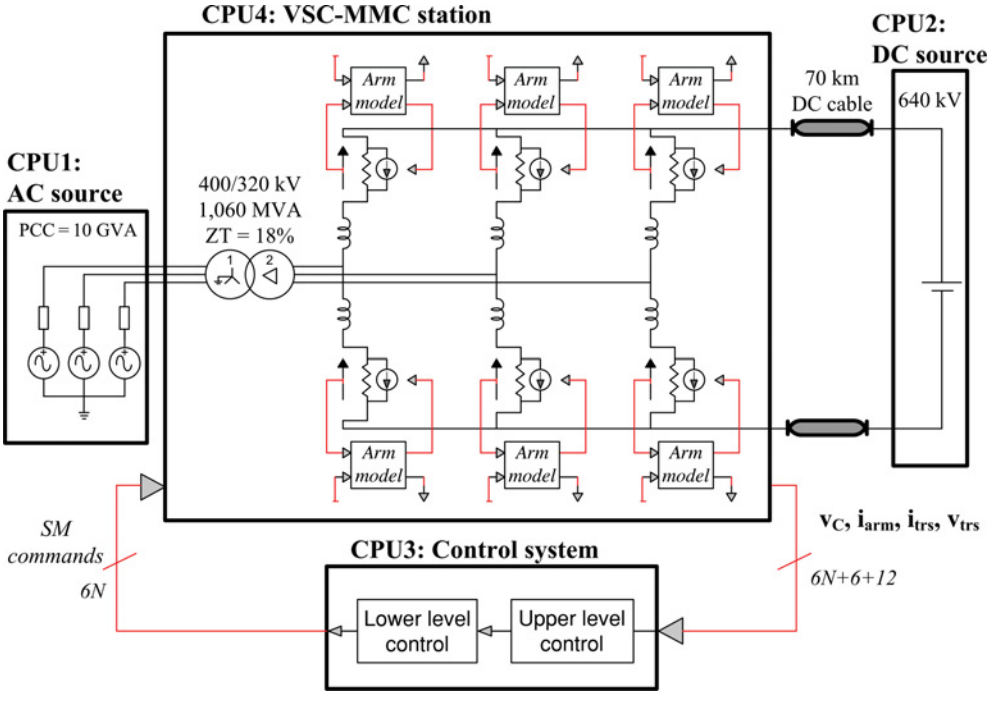

Figure 9.34 MMC circuit and one-CPU MMC model structure.

distributed parameter cable (DPC) model (constant parameters) and a DC voltage source of 640 kV. The simulations were performed on the OP5600 real-time simulator from Opal-RT. The OP5600 simulator has three quad-core processors (for a total of 12 Intel Xeon CPUs) that communicate through a shared memory of 8 GB, and that are able to communicate with the FPGA board through a second-generation PCIe link.

9.6.4 CPU-Based Model

This section presents a feasibility analysis using CPU technology. To simulate an electrical network in real time, it is necessary to decouple the network on a multiprocessor system in order to parallelize and accelerate computations.

9.6.4.1 One-CPU MMC

A logical separation is presented in Figure 9.34: CPU1 for the equivalent network, CPU2 for the DC voltage source, CPU3 for the control system and CPU4 for the MMC station.

A large amount of data is exchanged between CPU3 and CPU4:

- all SM commands (6*N* variables) sent from CPU3 to CPU4
- the capacitor voltages vector $\mathbf{v_C}$ of all SMs (6*N* variables)
- the arm currents $\mathbf{i_{arm}}$ (six variables)
- transformer primary and secondary currents $\mathbf{i_{trs}}$ and voltages $\mathbf{v_{trs}}$ (12 variables) transmitted from CPU4 to CPU3.

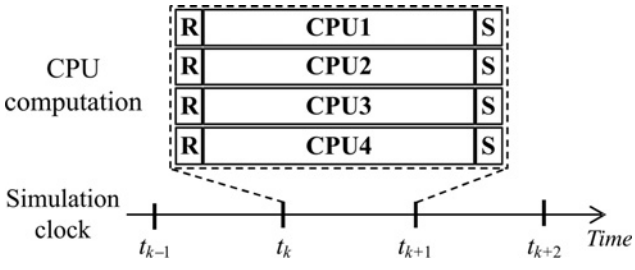

Figure 9.35 Real-time computations for one-CPU MMC model.

Stub line blocks are used between CPU1 and CPU4 to decouple the processed equations. The DPC model decouples CPU4 and CPU2. Further details about these decoupling techniques can be found in [44].

The complete circuit is parallelized as shown in Figure 9.35. The R and S blocks represent receiving and sending data functions, respectively.

Real-time simulation verification for this MMC model is presented in [43]. Comparison with the full detailed MMC model (i.e. Model 1) shows a close match with a relative error of less than 5%. Thus, in this section, the one-CPU MMC model is taken as the reference model to verify all other configurations presented in the following subsections.

9.6.4.2 MultiCPU MMC

In order to improve computational performance, each arm model is solved on its own CPU (Figure 9.36). In this structure, CPU4 contains only the Norton equivalent circuits. Parallelization now requires the

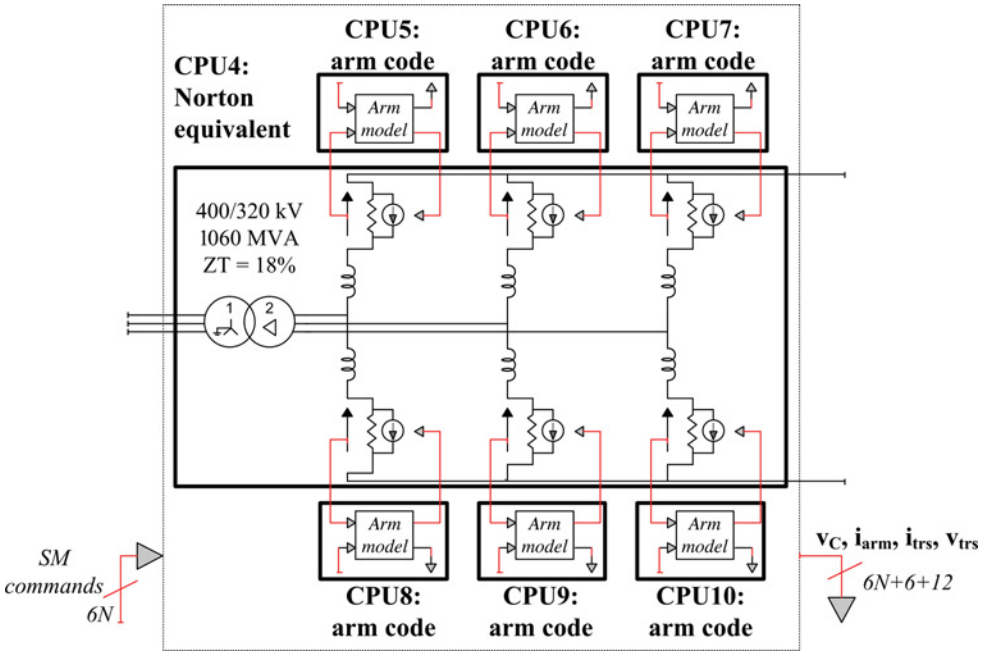

Figure 9.36 Structure of the multi-CPU MMC model.

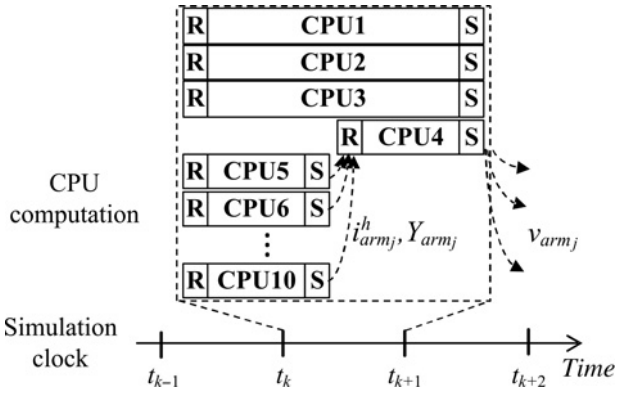

Figure 9.37 Real-time computation for multi-CPU MMC model.

introduction of an artificial one-time-step delay, which is not acceptable since the Norton equivalent circuit should be computed within the same time-step [45]. The artificial delay is avoided by computing the arm models and the Norton equivalent circuit in series. Nevertheless, since each arm code is computed independently, parallelization between arms is still possible. Thus, the MMC model uses the series/parallel computation scheme depicted in Figure 9.37.

9.6.4.3 Real-Time CPU-Based Model Verification

An evaluation of the multi-CPU model performance in real-time simulation is performed here, and compared against the one-CPU model (considered the *reference* model in this Section 9.6). In all figures, a solid line is used for the reference model, and a dotted line for the multi-CPU MMC model. An MMC-101-level is considered with a time-step of 30 μs. A 150 ms three-phase-to-ground fault is applied on the AC side (between CPU1 and CPU4) at 10 s of simulation time.

Figure 9.38 and Figure 9.39 compare the dynamic responses of several MMC variables. It is apparent that a close match is achieved between the two CPU configurations. The relative errors in compared variables vary between 0.1 to 2%. Similar results are obtained for all other test cases simulated in Section 9.5.

9.6.4.4 Real-Time Performance of CPU-Based Models

The real-time performance of one-CPU and multi-CPU configurations are analysed by varying N from 60 to 400. For both configurations, the execution times of CPU1 and CPU2 are not affected by N and remain very low (1 μs and 2.1 μs, respectively). On the other hand, the control system CPU3 is affected by the increase in N and this is mainly due to the presence of the BCA. The execution time ratio between CPU3 and MMC circuit CPUs (i.e. CPU5 to CPU10 of Figure 9.36) is less than 0.5, which proves that the MMC circuit CPUs constitute the main bottleneck for real-time simulation.

Figure 9.40 presents N as a function of execution time for CPU4 in Figure 9.34 (one-CPU setup). As depicted in reference [43], the execution time increases linearly with the number of SMs and crosses the NLC sampling time limit for real-time simulation at $N = 120$. Figure 9.40 also shows the execution time results for the multi-CPU MMC configuration. Parallelization between arm models reduces execution time, but the gain is not 6 times, since the CPU4 in Figure 9.36 is in series with CPUs 5 to 10 (Figure 9.37). For 100 SMs per arm the mean execution time for the multi-CPU MMC setup is ≈ 12.3 μs, whereas the one-CPU MMC version uses 26.4 μs, which gives a ratio of 2.15. This ratio increases with the number

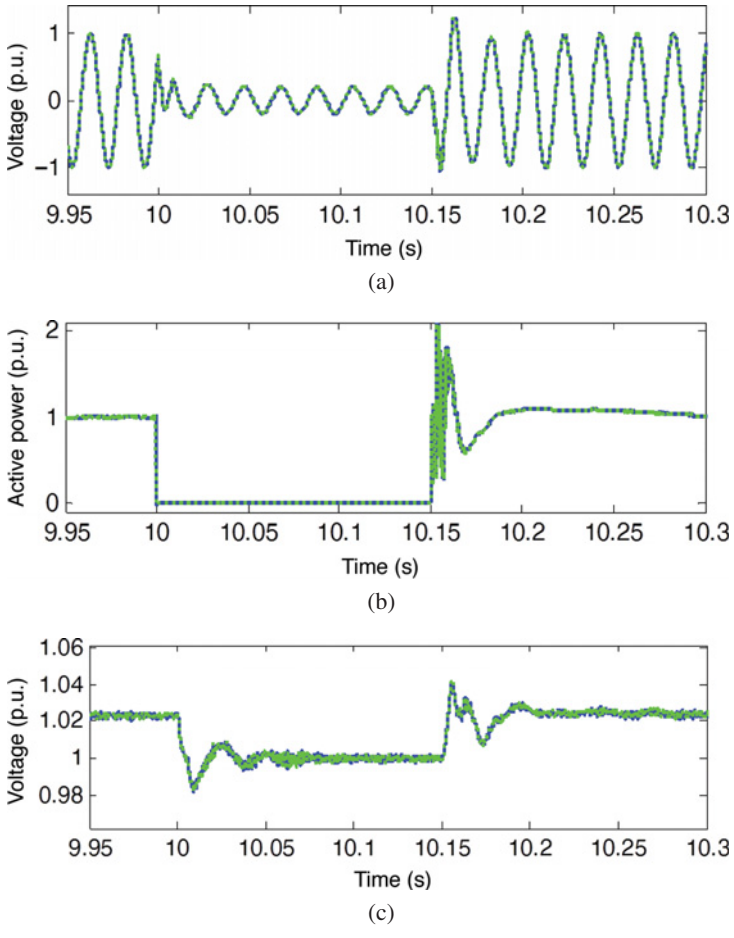

Figure 9.38 MMC external variables, reference and multi-CPU MMC models: (a) phase voltage: v_a, (b) active power: P, (c) DC voltage: V_{dc}.

of SMs. The maximum number of SMs/arm that can be simulated in real time with the multi-CPU MMC setup is about 230.

If the CPU-based models are to be used in an HIL configuration, where a real control system is interfaced with the numerical simulator, the latency produced by communication overhead and I/O management is estimated to reach 9 μs. The curves in Figure 9.40 must be shifted to the right to account for this time delay, and the maximum number of SMs/arm for real-time CPU-based simulations now reduces to 160.

9.6.5 FPGA-Based Model

In recent years FPGA devices have become an integral part of HIL simulators, where they are used to provide access to digital and analogue I/Os as well as to fulfil various computing purposes [46]. The density of modern FPGAs is sufficient to handle tens to hundreds of floating point operators, which enables them to offer tens of GFLOPS of computing power. The FPGA used for these current tests is

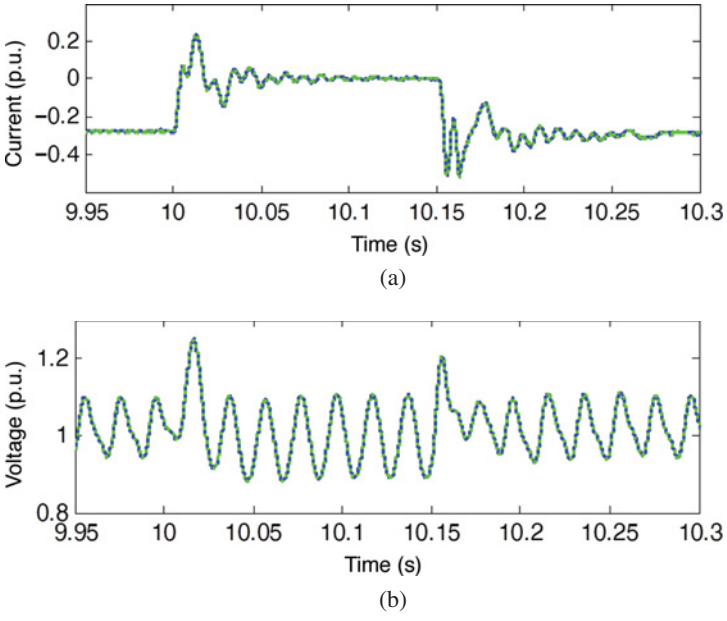

Figure 9.39 MMC internal variables, reference and multi-CPU MMC models: (a) differential current: i_{diff_a}, (b) sum of all capacitor voltages: $v_{Ctot_{u_a}}$.

the Virtex 6 LX240T [47] that comes with the ML605 board, and the board is provided along with the OP5600.

Unlike other technologies (CPU, DSP or GPU), FPGA programming requires a complete design of a so-called application-specific processor (ASP) to handle all the computations.

9.6.5.1 FPGA-Based MMC Model Implementation

The same arm model (Table 9.1) algorithm implemented on CPU is used here on FPGA, except for the SM blocked state code. The structure of the MMC model implemented on the FPGA is presented in Figure 9.41. CPU4 contains the Norton equivalent circuit. At each simulation time-point, CPU5

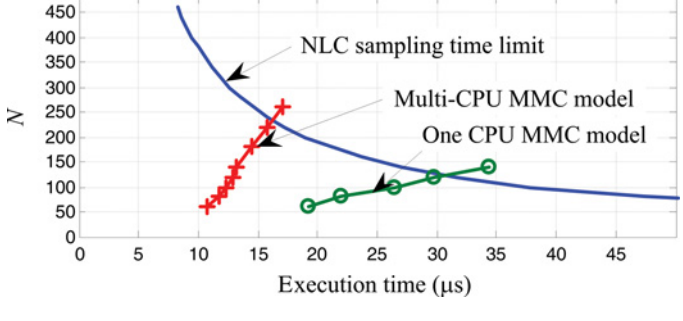

Figure 9.40 N as a function of execution time for CPU-based models.

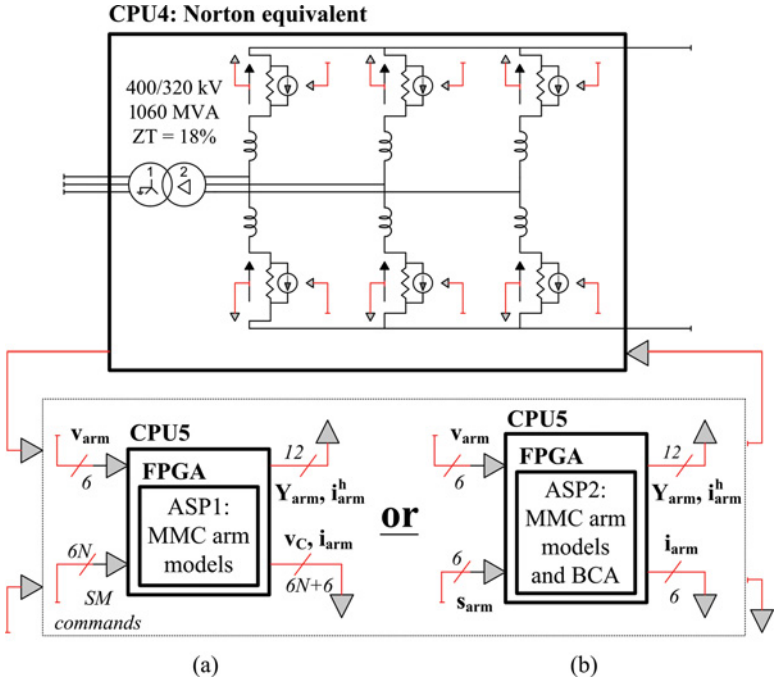

Figure 9.41 Structure of the FPGA-based MMC model with (a) ASP1 and (b) ASP2.

exchanges data with the FPGA through the PCIe protocol (Figure 9.42). Two versions of the ASP are implemented. ASP1 includes only six arm models. It receives from CPU5 $\mathbf{v}_{\mathbf{arm}}$ and the SM commands, and sends back $\mathbf{i}^{\mathbf{h}}_{\mathbf{arm}}$, $\mathbf{R}_{\mathbf{arm}}$, $\mathbf{v}_{\mathbf{C}}$ and $\mathbf{i}_{\mathbf{arm}}$ through the PCIe. ASP2 includes the six-arm models and a simplified version of the BCA system. The communication burden is considerably reduced since $\mathbf{v}_{\mathbf{C}}$ is not sent from the FPGA to CPU5, and the SM commands are not received from CPU5. Only $\mathbf{i}_{\mathbf{arm}}$ and the number of SMs to be inserted ($\mathbf{s}_{\mathbf{arm}}$) in each arm are exchanged between CPU3 and CPU5. Both ASPs are responsible for computing the Thevenin equivalent of the arm, which will be converted to a Norton

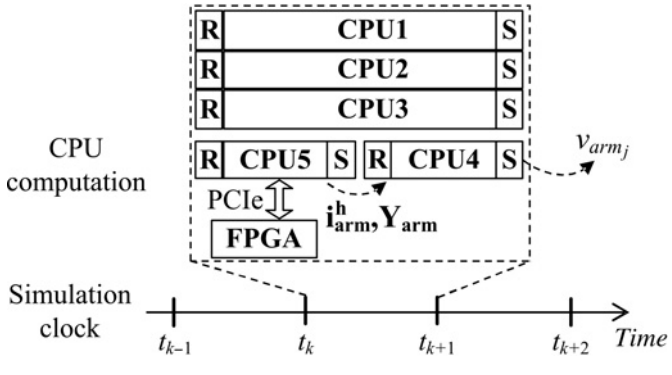

Figure 9.42 Real-time computation for FPGA-based MMC model.

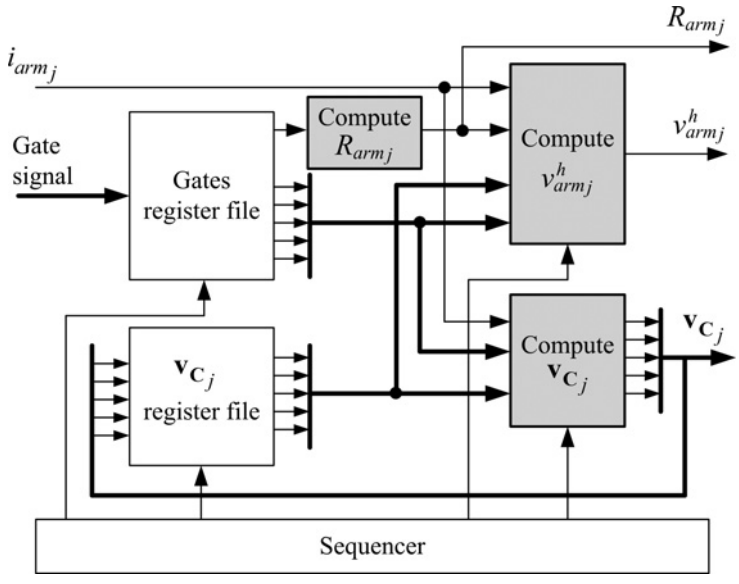

Figure 9.43 ASP arm model implemented on FPGA.

equivalent on CPU5. ASP2 is closer to a real HIL prototyping environment since the BCA acts like an HIL through low latency FPGA I/O.

Figure 9.43 illustrates the complete architecture of the ASP-based arm model. It is designed to handle up to 400 SMs/arm and to be easily configurable for other values of N. It consists of a sequencer for controlling the ASP, register files and processing elements. Register files are memory elements for storing $\mathbf{v_C}$ and SM commands. Each register file is able to read/write up to five values at the same time (parallel processing), leading to a maximum of 80 clock cycles for all values. The processing elements compute the components shown in Figure 9.43 and require about 20 additional clock cycles once the reading task is completed.

The ASPs are able to handle up to six arm models by treating each arm model sequentially. This leads to a minimal time-step of 480 clock cycles (6 times 80), that is 2.4 μs, for the three-phase MMC (the system clock frequency is 200 MHz). The latency of processing elements is not taken into account because the resulting $\mathbf{v_C}$ elements are rewritten to the register file, while new values are being processed for the other arms. When the ASPs handle less than 400 SMs/arm, the processing elements are either idle or unused during the remaining clock cycles. The choices of treating arm models serially and reading five values at a time from the register files, constitute a design trade-off motivated by the fact that 2.4 μs is sufficient to correctly conduct a real-time simulation with 400 SMs/arm.

Figure 9.44 presents the three processing elements that are identified by greyed out boxes in Figure 9.43. An MMC may contain tens to hundreds of SMs/arm, thus all numerical values are represented with floating-point formats in order to allow a large dynamic range. A non-standard floating-point format is used with intermediate precision (between simple and double), while all the additions (including accumulation) are carried out using an internal floating-point format called self-alignment format (SAF). The SAF methodology was introduced in [48] and is thoroughly discussed in [49]. The SAF provides higher numerical accuracy while allowing the implementation of complex operators with very low latencies. More specifically, all the variables use a 35-bit signed mantissa, all the constants use a 44-bit

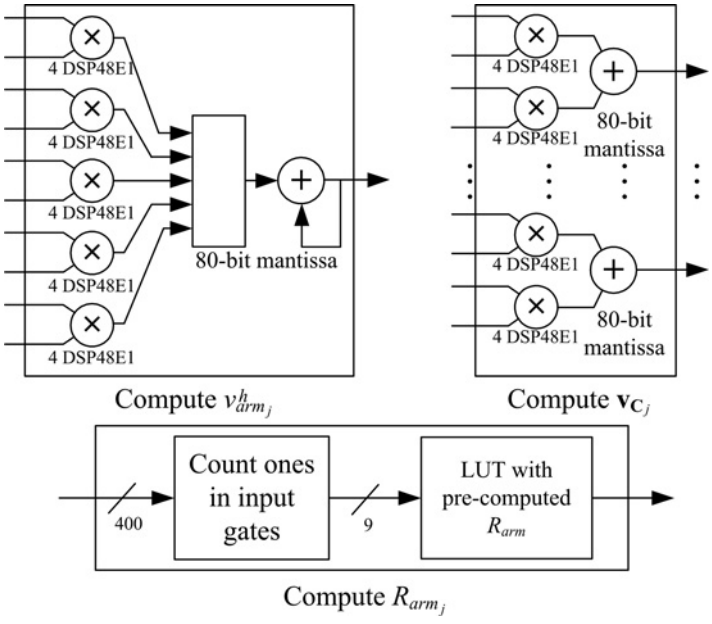

Figure 9.44 Detailed view of the FPGA computing blocks.

signed mantissa and all the additions are computed using an 80-bit extended mantissa [49]. Hence, each multiplication needs three clock cycles and four DSP blocks.

Table 9.3 presents the synthesis estimates of the ASPs for the Virtex 6 LX240T. The two designs meet the timing constraint of 5 ns imposed by the 200 MHz system clock frequency. As can be seen, ASP2 uses more resources than ASP1 because it also implements the BCA system. In the context where a physical controller is involved in the real-time simulation, the performance of ASP1 is similar to the real-time performance of ASP2.

9.6.5.2 Real-Time FPGA-Based Model Accuracy Verification

Before evaluating the real-time performance of the FPGA-MMC model,we need to verify its accuracy. Only FPGA-ASP2 results are presented here, since it allows us to verify both arm models and the BCA system simultaneously. The same three-phase-to-ground fault is reproduced. An MMC-401-level is simulated with a time-step of 9 μs. The FPGA-ASP2 results (dotted line) are in real-time simulation, whereas the reference model (one-CPU MMC model) is simulated in off-line mode (solid line), since it cannot compute with this many SMs in real time (Figure 9.40).

Table 9.3 Design results for the Virtex 6 LX240T [47].

	ASP1	ASP2
Registers	33 302 (11%)	72 957 (24%)
LUTs	23 266 (15%)	39 702 (26%)
BRAM	92 (22%)	146 (35%)
DSP48E1	60 (7%)	84 (10%)

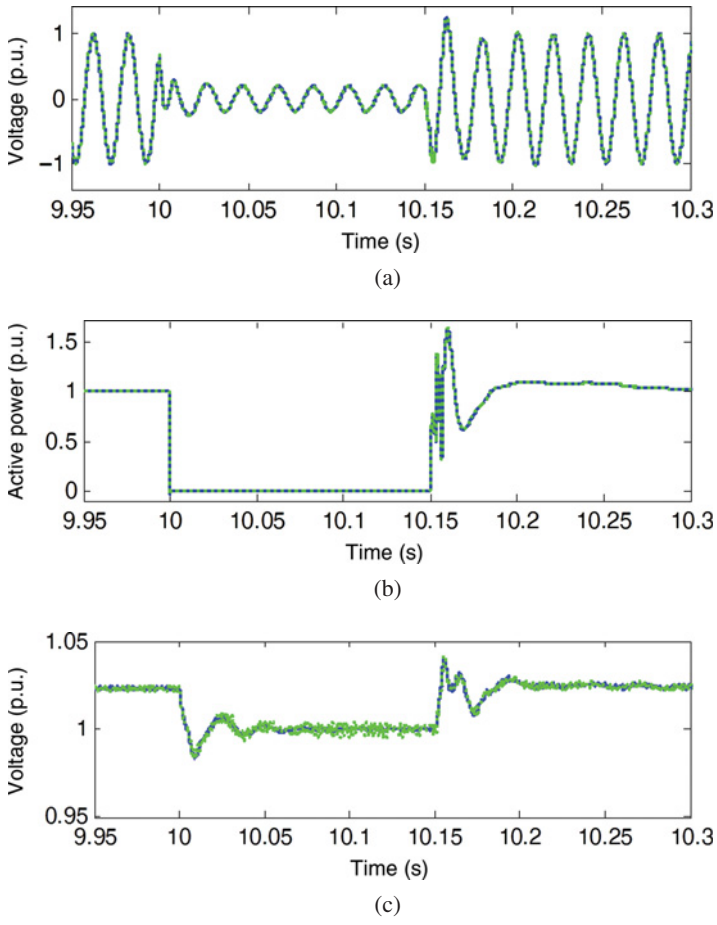

Figure 9.45 MMC external variables, reference and FPGA-SPA2 model: (a) phase voltage: v_a, (b) active power: $\boldsymbol{P}$, (c) DC voltage: V_{dc}.

Figures 9.45 and 9.46 present the simulation results. The differences between the model implementations are negligible, and the relative errors vary between 0.3 to 3%. This is confirmed by other simulation cases.

9.6.5.3 Real-Time Performance of the FPGA-Based Model

Real-time performances are evaluated in Figure 9.47. For both ASPs, the FPGA runs at 2.4 µs, but the execution times depicted in Figure 9.47 include CPU4 and CPU5, since they are in series (Figure 9.42). The results indicate that the FPGA-ASP1 MMC model has a poor performance in comparison with the CPU-based model. This is explained by the important amount of data that has to be exchanged between the FPGA and CPU5 of Figure 9.41(a), connected through the PCIe link ($2 \times 6N + 6$ variables). This link has a latency that is higher than that of shared-memory-based communication. However, this situation is less realistic in regard of the HIL simulation context where the real controller is physically connected to the simulator by means of the FPGA.

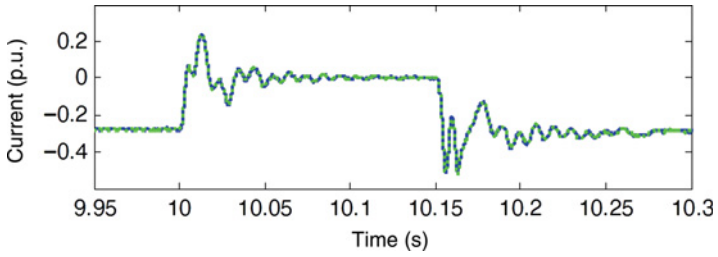

(a)

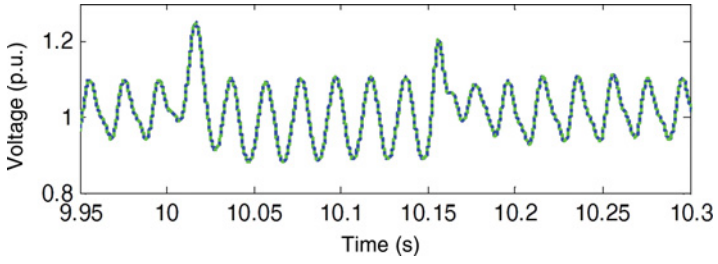

(b)

Figure 9.46 MMC internal variables, reference and FPGA-SPA2 model: (a) differential current: i_{diff_a}, (b) sum of all capacitor voltages: $v_{Ctot_{u_a}}$.

The real-time performance of the FPGA-ASP2 model is the best of those reported in this chapter. It is able to achieve an execution time of 9 μs for MMC with up to 400 SM/arm. Moreover, the time-step is not dependent upon the number of SMs (see the setup in Figure 9.41(b)).

9.7 Conclusions

This chapter has presented and compared various EMT-type models for MMCs used in the simulation of MMC-HVDC transmission systems. Practical test cases, including faults, power reference change and converter startup, have been used to study these models:

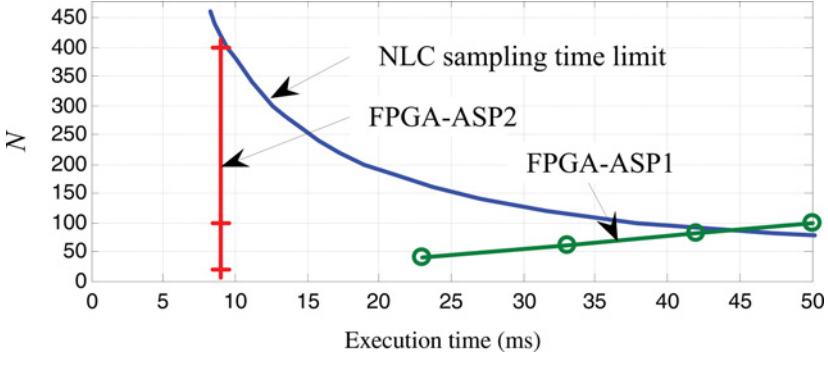

Figure 9.47 N as a function of execution time for FPGA configurations.

- Model 1 is currently the most detailed model, but requires very high computing times with available numerical methods. It can currently be used as a highly accurate reference model and for calibrating simplified models.
- Model 2 avoids the detailed modelling of power switches, and reduces the converter circuit for achieving much higher computing speeds. This model provides accurate results and can be used when redundant SMs are included in the MMC and/or when the balancing control of each capacitor has to be analysed.
- Model 3 delivers further improvements in computational performance. Sufficiently accurate results can be achieved when the number of MMC levels is higher than 101. It should be used with caution when the number of levels decreases. This model can account for startup sequence, circulating currents and energy storage in each arm, but not for the balancing control algorithm of SM capacitors.
- Model 4 allows us to increase the time-step, to speed up computing times. In this model, AC system dynamics can be accurately represented, but DC side modelling remains less accurate.

This chapter also presented studies on real-time simulations with Model 2. It has been shown that the CPU-based MMC model is limited to 231 levels. This limit is reduced to 161 levels for HIL simulations due to latencies in communications and I/Os.

Two different FPGA-based MMC model setups were presented. In the first setup (ASP1) the large amount of data exchanged between arm models and the control system does not produce acceptable performance. In the second setup (ASP2) the BCA is implemented on the FPGA, and the lowest execution time of 9 μs is achieved. However, the FPGA-based MMC arm models run at 2.4 μs. These execution times do not depend on the number of MMC levels. No additional latency is expected for HIL simulation, since the arm models are coded on the FPGA.

For an MMC having more than 400 SMs/arm, the presented FPGA setup has enough resources in reserve to handle more powerful ASPs. The computing power of such ASPs is a design trade-off that depends on the number of SMs per arm and the targeted simulation time-step. In fact, the actual bottleneck lies in the communication time between the FPGA and the remaining CPU-based network model.

References

[1] Flourentzou, N., Agelidis, V.G., and Demetriades, G.D. (2009) VSC-based HVDC power transmission systems: an overview. *IEEE Transactions on Power Electronics*, **24**(3), 592–602.

[2] It is time to connect, Technical description of HVDC Light technology. ABB, Sweden, March 2008.

[3] Karaagac, U., Mahseredjian, J., Saad, H. *et al.* (2013) Examination of fault-ride-through methods for offshore wind farms connected to the grid through VSC-based multiterminal HVDC transmission. IPST 2013, International Conference on Power Systems Transients, Vancouver, BC, Canada, 18–20 July 2013.

[4] Lu, W. and Ooi, B.T. (2003) Optimal acquisition and aggregation of offshore wind power by multiterminal voltage-source HVDC. *IEEE Transactions on Power Delivery*, **18**(1), 201–206.

[5] Lindberg, A. (1995) PWM and control of two- and three-level high power voltage source converters. Licentiate Thesis, Royal Institute of Technology, Stockholm, Sweden.

[6] Du, C. (2007) VSC-HVDC for industrial power systems. Ph.D. Thesis, Chalmers Univ. of Technology, Göteborg, Sweden.

[7] Andersen, B.R., Xu, L. and Wong, K.T.G. (2001) Topologies for VSC transmission. 7th International Conference on AC-DC Power Transmission, London, Nov. 2001, pp. 298–304.

[8] Lesnicar, A. and Marquardt, R. (2003) An innovative modular multilevel converter topology suitable for a wide power range. IEEE Power Tech. Conference, vol. 3, Bologna, June 2003.

[9] Gemmell, B., Dorn, J., Retzmann, D. and Soerangr, D. (2008) Prospects of multilevel VSC technologies for power transmission. IEEE Transmission and Distribution Conf. Exp., Milpitas, CA, April 2008, pp. 1–16.

[10] Middlebrook, R.D. and Cuk, S. (1976) A general unified approach to modelling switching power converter stages. IEEE PESC., Cleveland, OH, USA, June 8–10, 1976, pp. 18–34.

[11] Krein, P.T., Bentsman, J., Bass, R.M. and Lesieutre, B.L. (1990) On the use of averaging for the analysis of power electronic systems. *IEEE Transactions on Power Electronics*, **5**(2), 182–190.

[12] Jin, H. (1997) Behavior-mode simulation of power electronic circuits. *IEEE Transactions on Power Electronics*, **12**(3), 443–452.
[13] Teeuwsen, S.P. (2009) Simplified dynamic model of a voltage-sourced converter with modular multilevel converter design. IEEE PES Power System Conference and Exp., Seattle, WA, USA, Mar. 2009, pp. 1–6.
[14] Gnanarathna, U.N., Gole, A.M. and Jayasinghe, R.P. (2011) Efficient modeling of modular multilevel HVDC converters (MMC) on electromagnetic transient simulation programs. *IEEE Transactions on Power Delivery*, **26**(1), 316–324.
[15] Norrga, S., Angquist, L., Ilves, K. *et al.* (2012) Frequency-domain modeling of modular multilevel converters. IECON 2012–38th Annual Conference on IEEE Industrial Electronics Society, 25–28 Oct. 2012, pp. 4967–4972.
[16] Peralta, J., Saad, H., Dennetière, S. *et al.* (2012) Detailed and averaged models for a 401-level MMC-HVDC system. *IEEE Transactions on Power Delivery*, **27**(3), 1501–1508.
[17] Saad, H., Dennetière, S., Mahseredjian, J. *et al.* Modular multilevel converter models for electromagnetic transients. *IEEE Transactions on Power Delivery*. doi:10.1109/TPWRD.2013.2285633
[18] Saad, H., Ould-Bachir, T., Mahseredjian, J. *et al.* Real-time simulation of MMCs using CPU and FPGA. *IEEE Transactions on Power Electronics*. doi:10.1109/TPEL.2013.2282600
[19] Hagiwara, M. and Akagi, H. (2008) PWM Control and experiment of modular multilevel converter. IEEE Power Electronics Specialists Conference, Tokyo, June 2008, pp. 154–161.
[20] Marquardt, R. (2011) Modular multilevel converter topologies with DC-short circuit current limitation. 2011 IEEE 8th International Conference on Power Electronics and ECCE Asia (ICPE & ECCE), May 30–June 3, 2011, pp. 1425–1431.
[21] Franquelo, L.G., Rodriguez, J., Léon, J.I. *et al.* (2008) The age of multilevel converters arrives. *IEEE Industrial Electronics Magazine*, **2**(2), 28–39.
[22] Antonopoulos, A., Angquist, L. and Nee, H.P. (2009) On dynamics and voltage control of the modular multilevel converter. 13th European Conf. on Power Electronics and Applications, Barcelona, Oct. 2009.
[23] Ooi, B.T. and Wang, X. (1990) Voltage angle lock loop control of the boosted type PWM converter for HVDC application. *IEEE Transactions on Power Electronics*, **5**(2), 229–235.
[24] Mahseredjian, J., Lefebvre, S. and Mukhedkar, D. (1991) Power converter simulation module connected to the EMTP. *IEEE Transactions on Power Systems*, **6**(2), 501–510.
[25] Munch, P., Gorges, D., Izak, M. and Liu, S. (2010) Integrated current control, energy control and energy balancing of modular multilevel converters. IECON 2010–36th Annual Conference, IEEE Industrial Electronics Society, 7–10 Nov. 2010, pp. 150–155.
[26] Ahmed, N., Ängquist, L., Norrga, S. and Nee, H.-P. (2012) Validation of the continuous model of the modular multilevel converter with blocking/deblocking capability. 10th IET International Conference on AC and DC Power Transmission (ACDC 2012), 4–5 Dec. 2012, pp. 1–6.
[27] Venjakob, O., Kubera, S., Hibberts-Caswell, R. *et al.* (2013) Setup and performance of the real-time simulator used for hardware-in-loop-tests of a VSC-based HVDC scheme for offshore applications. IPST 2013, International Conf. on Power Systems Transients, Vancouver, BC, Canada, 18–20 July 2013.
[28] Sanders, S.R., Noworolski, J.M., Liu, X.Z. and Verghese, G.C. (1991) Generalized averaging method for power conversion circuits. *IEEE Transactions on Power Electronics*, **6**(2), 251–259.
[29] Ouquelle, H., Dessaint, L.A. and Casoria, S. (2009) An average value model-based design of a deadbeat controller for VSC-HVDC transmission link. IEEE Power Energy Soc. Gen. Meeting, Calgary, AB, Canada, July 2009, pp. 1–6.
[30] Edwards, C. and Postlethwaite, I. (1998) Anti-windup and bumpless-transfer schemes. *Automatica*, **34**(2), 199–210.
[31] Hsieh, G-C. and Hung, J.C. (1996) Phase-locked loop techniques. A survey. *IEEE Transactions on Industrial Electronics*, **43**(6), 609–615.
[32] Kazmierkowski, M.P. and Malesani, L. (1998) Current control techniques for three-phase voltage-source PWM converters: a survey. *IEEE Transactions Industrial Electronics*, **45**(5), 691–703.
[33] Zhang, L. (2010) Modeling and control of VSC-HVDC links connected to weak AC systems. Ph.D. Thesis, Royal Institute of Technology, Stockholm, Sweden.
[34] Jacobson, B., Karlsson, P., Asplund, G. *et al.* (2010) VSC-HVDC transmission with cascaded two-level converters. CIGRE Conference, Paris, Aug. 2010.
[35] Tu, Q., Xu, Z. and Xu, L. (2011) Reduced switching-frequency modulation and circulating current suppression for modular multilevel converters. *IEEE Transactions on Power Delivery*, **23**(3), 2009–2017.
[36] Rohner, S., Bernet, S., Hiller, M. and Sommer, R. (2009) Analysis and simulation of a 6 kV, 6 MVA modular multilevel converter. IECON '09. 35th Annual Conference of IEEE, 3–5 Nov. 2009, pp. 225–230.

[37] Saeedifard, M. and Iravani, R. (2010) Dynamic performance of a modular multilevel back-to-back HVDC system. *IEEE Transactions on Power Delivery*, **25**(4), 2903–2912.
[38] Solas, E., Abad, G., Barrena, J.A. *et al.* (2010) Modulation of modular multilevel converter for HVDC application. 14th International Power Electronic and Motion Control Conference, Mondragon, Sep. 2010, pp. 84–89.
[39] Ding, G., Tang, G., He, Z. and Ding, M. (2008) New technologies of voltage source converter (VSC) for HVDC transmission system based on VSC. IEEE Power Eng. Soc. Gen. Meeting, Beijing, June 2008, pp. 1–8.
[40] Morched, A., Gustavsen, B. and Tartibi, M. (1999) A universal model for accurate calculation of electromagnetic transients on overhead lines and underground cables. *IEEE Transactions on Power Delivery*, **14**(3), 1032–1038.
[41] Mahseredjian, J., Dennetière, S., Dubé, L. *et al.* (2007) On a new approach for the simulation of transients in power systems. *Electric Power Systems Research*, **77**(11), 1514–1520.
[42] Gong, X. (2012) A 3.3 kV IGBT module and application in modular multilevel converter for HVDC. 2012 IEEE International Symposium on Industrial Electronics (ISIE), 28–31 May 2012, pp. 1944–1949.
[43] Saad, H., Dufour, C., Mahseredjian, J. *et al.* (2013) Real time simulation of MMCs using the state-space nodal approach. IPST 2013, International Conf. on Power Systems Transients, Vancouver, Canada, 18–20 July 2013.
[44] eMEGAsim http://www.opal-rt.com/product/emegasim.
[45] Dufour, C., Mahseredjian, J. and Bélanger, J. (2011) A combined state-space nodal method for the simulation of power system transients. *IEEE Transactions on Power Delivery*, **26**(2), 928–935.
[46] Ould-Bachir, T., Dufour, C., Bélanger, J. *et al.* (2012) Effective floating-point calculation engines intended for the FPGA-based HIL simulation. IEEE International Symposium on Industrial Electronics (ISIE), May 2012, pp. 1363–1368.
[47] Xilinx Data sheet DS150 v2.4. Virtex 6 family overview, January 2012.
[48] Ould-Bachir, T., Dufour, C., Bélanger, J. *et al.* (2013) A fully automated reconfigurable calculation engine dedicated to the real-time simulation of high switching frequency power electronic circuits. *Mathematics and Computers in Simulation*, **91**, 167–177.
[49] Ould-Bachir, T. and David, J.P. (2013) Self-alignment schemes for the implementation of addition-related floating-point operators. *ACM Transactions on Reconfigurable Technology and Systems*, **6**(1), Article 1, 1–21.

10

Dynamic Average Modelling of Rectifier Loads and AC-DC Converters for Power System Applications

Sina Chiniforoosh, Juri Jatskevich, Hamid Atighechi and
Juan A. Martinez-Velasco

10.1 Introduction

The most common type of rectifier load is the conventional three-phase (six-pulse) line-commutated rectifier which is typically used as the input stage in low- to medium-power variable frequency drives and motor loads common in industrial and commercial applications [1–7]. Such loads are often referred to as front-end rectifier loads [8, 9], and may appear in large numbers in distribution systems, industrial facilities [10], distributed generation [11], transportation [12], and arc furnaces [13, 14]. A typical configuration considered in this chapter is shown in Figure 10.1. Depending on the application, the source may be a distribution feeder (or transformer) as in Case I, or a rotating machine (generator) as in Case II. The AC filter network may take various configurations depending on application and cost constraints, among which phase shifting transformers, passive or active filters may be considered to reduce the harmonics. Commonly used passive filters include series choke inductors and shunt filters that are tuned to lower harmonics (typically 5th and 7th) [15, 16].

Modelling of the above rectifier systems has been of particular interest to the power engineering community for a long time [18,19]. Detailed models, where the switching of all diodes is fully represented, can be readily carried out using available digital time-domain simulation packages [20–26]. The resulting models have been investigated quite extensively and are shown to be sufficiently accurate for various applications. The main challenge in using the detailed models, however, is the increased computational complexity which arises due to the inherent repeated switching. Such models are computationally intensive, and can become the bottleneck for system-level studies, leading to longer simulation times when the overall system contains many rectifiers, switching modules and controllers. Moreover, due to the

Transient Analysis of Power Systems: Solution Techniques, Tools and Applications, First Edition.
Edited by Juan A. Martinez-Velasco.

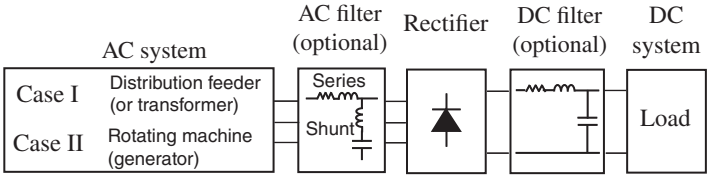

Figure 10.1 Typical configuration of a front-end rectifier load system (© 2012 IEEE) [17].

inherent switching, detailed switching models are discontinuous and cannot be efficiently linearized and used for small-signal analysis. Therefore, extracting the small-signal frequency-domain characteristics of the system from the detailed models is often a challenging and time-consuming procedure.

These challenges have led to the development of the so-called average-value models (AVMs), in which the effects of fast switching are neglected (or averaged) within a typical switching interval [27]. In the AVMs, unlike detailed models, there are no switching events to demand smaller time-steps and/or interpolation (or iterations) for accurately locating the opening or closing of the switches in the circuit. The resulting AVMs are therefore computationally efficient and could run orders of magnitudes faster than the original switching models. The AVMs can therefore be effectively utilized to remove the high-frequency switching from the model while preserving the lower-frequency dynamics of the system [17]. Such AVMs can particularly be used for simulations of system transients where the switching harmonics (i.e. the harmonics due to converter switching injected into the AC grid or the DC link) are neglected. Also, since AVMs are time-invariant, they can be conveniently linearized about any desired operating point for small-signal analysis, that is, obtaining local transfer functions.

Construction of AVMs for line-commutated converters requires averaging of current/voltage waveforms over a typical switching interval, and can generally be carried out using analytical or numerical approaches. For example, in simplified cases where only certain operating modes are considered, such averaging may be done analytically [28, 29]. However, as the number of pulses increases, the complexity of switching pattern and the number of possible operational modes increases as well. The possibility of multiple operating modes makes the analytical derivations quite challenging [30–34]. These challenges may be overcome using the parametric approach in which the final AVM is assumed to have a well-defined structure, and the key model parameters are numerically extracted using the detailed simulations.

This chapter begins with an introduction to the practical variations of front-end diode rectifier loads (Figure 10.1) that lead to discontinuous conduction modes (DCM) and continuous conduction modes (CCM). The detailed analysis is then presented with an overview of all possible modes of operation from open-circuit to short-circuit conditions. The basic approaches for developing the AVMs are then discussed. Three selected AVMs are utilized in extracting steady-state operational characteristics of the rectifier system, followed by a comparative analysis of the AVM dynamic orders. The small-signal input/output impedance characteristics predicted by different models are also compared. The transient performance of the AVMs is then investigated for various operating conditions including light and heavy loading conditions, discontinuous and continuous modes, as well as balanced and unbalanced AC side. Finally, generalization of the analyses is considered for high-pulse-count converters using an example six-phase (12-pulse) topology. The studies demonstrate that all critical characteristics and impedances are accurately predicted by the considered dynamic average models [35]. This is an extremely desirable property of AVMs making them suitable for investigating a wide range of steady-state and transient conditions caused by balanced or unbalanced faults.

10.2 Front-End Diode Rectifier System Configurations

Topological variations of the system depicted in Figure 10.1, such as including/excluding the series and/or shunt filters on the AC side, significantly affect rectifier operation, leading to DCMs and CCMs

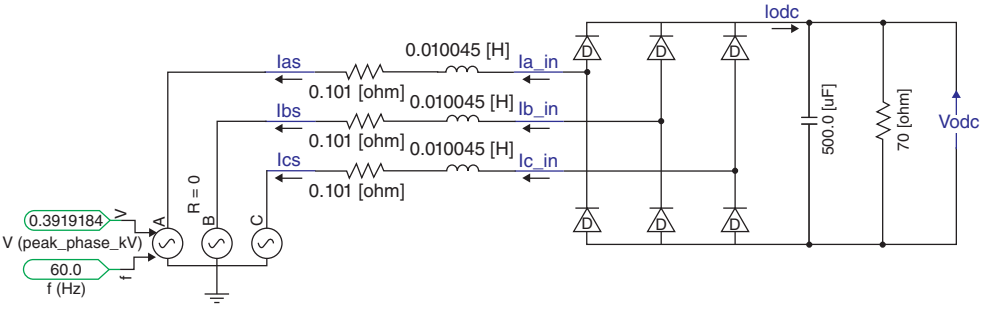

(a)

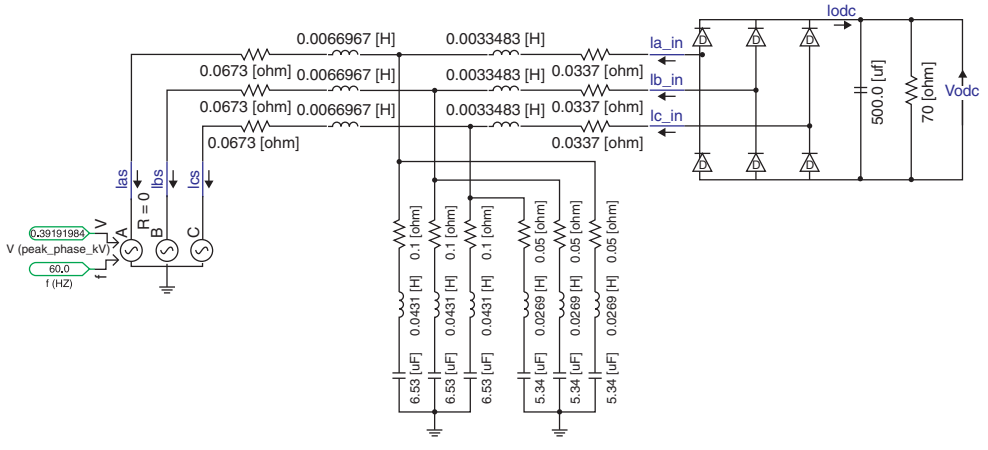

(b)

Figure 10.2 The AC side in a typical three-phase front-end rectifier load system represented in PSCAD: (a) equivalent series impedance (b) general network with shunt filters (© 2013 IEEE) [35].

commonly encountered in practical applications. The difference between these modes primarily lies in the DC bus current, which remains continuous within the CCM operation unlike the DCM operation.

To compare the system performance with different AC power networks, two possible configurations of the system, with and without the shunt filters, are considered. Figure 10.2 shows the corresponding diagrams of the detailed models implemented in PSCAD. In Figure 10.2(a), the AC side consists only of series RL components, which represent the Thevenin equivalent impedance of the AC power network, combined with the optional series choke inductor. If present, the choke inductor typically has the dominant value. In Figure 10.2(b), a more general AC network is composed of two series RL branches on both sides of the parallel RLC shunt filter that is tuned to specific harmonics (in this case 5th and 7th). As seen in this figure, when both series and shunt filters are included, the series inductor is typically split into two unequal parts, for example, 67% and 33%, and placed on both sides of the shunt filter [16]. The parameters of the considered system correspond to a typical medium-power front-end rectifier operating at 480 V level and are given in Appendix.

For a given load, the rectifier mode of operation is predominantly determined by the value of the equivalent series inductance present on the AC side, due to the large impedance of the shunt filter at the fundamental frequency. If the additional series choke is excluded from both diagrams, the resulting inductance value will be small enough to force the system into the DCM under normal loading conditions

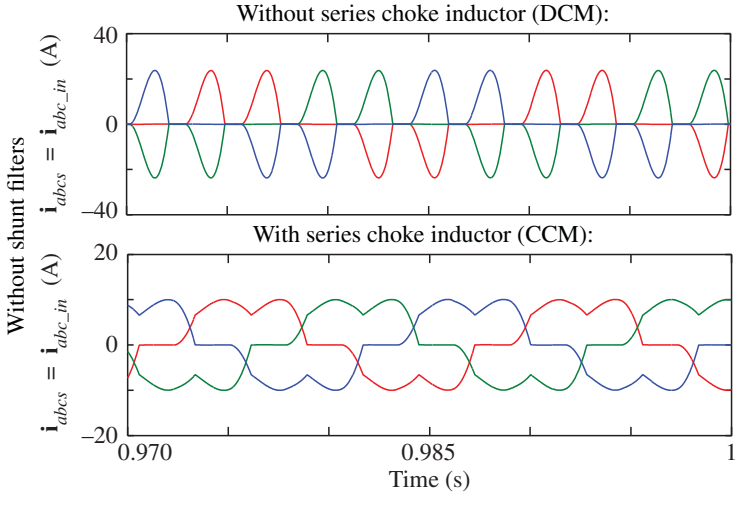

(a)

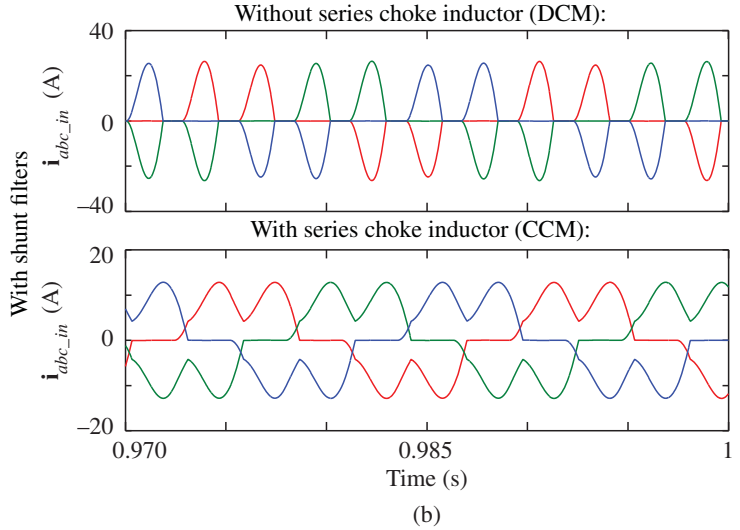

(b)

Figure 10.3 Typical three-phase currents at the rectifier bridge terminals without and with series choke inductor (DCM and CCM): (a) without shunt filters, (b) with shunt filters (© 2013 IEEE) [35].

[17]. For example, the three-phase AC currents in DCM corresponding to $R_L = 70\ \Omega$ are shown for both configurations in the top subplots of Figures 10.3(a) and 10.3(b), respectively. The DC bus current in this mode is also illustrated in Figure 10.4 (top plot). It is evident that the DC bus current is discontinuous, hence the name DCM.

The currents at the source and bridge terminals, denoted by $\mathbf{i}_{abcs}$ and $\mathbf{i}_{abc\_in}$, are identical in the absence of shunt filters – Figure 10.2(a). In this case, the high-harmonic-content currents of Figure 10.4(a) (top plot) are directly fed to the AC network. In the presence of shunt filters (Figure 10.3(b)), the resulting AC source currents are those depicted in Figure 10.5 (top plot). These waveforms show that a much

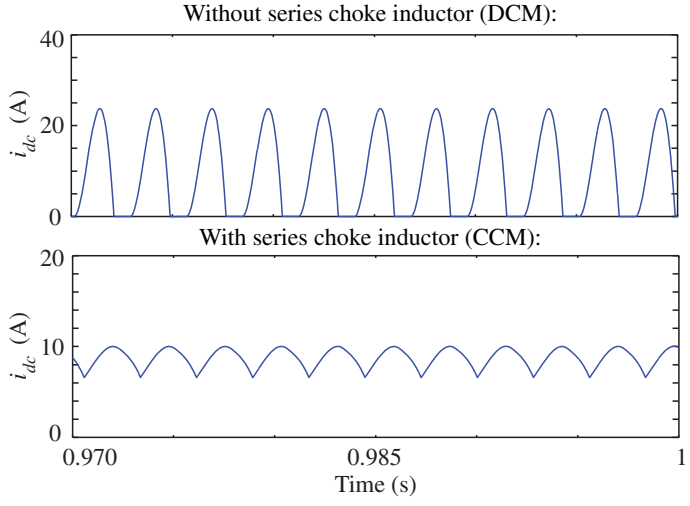

Figure 10.4 DC bus current in the absence of shunt filters for DCM and CCM operations (© 2013 IEEE) [35].

lower harmonic content is achieved due to the shunt filters. Since these filters are essentially tuned to the 5th and 7th harmonics [16], their effect on the system operation is intended to be minimal, except for ensuring that the corresponding harmonic content flows through the shunt path instead of into the AC network. The mode of operation and other characteristics of the system are then expected to remain essentially intact as long as the DC load and the equivalent series inductive component on the AC side do not vary significantly. The bridge currents are then expected to be very similar in the presence and absence of the shunt filters. This is indeed observed in the top plots in Figures 10.3(a) and 10.3(b), which have been obtained in the absence and presence of the shunt filters, respectively.

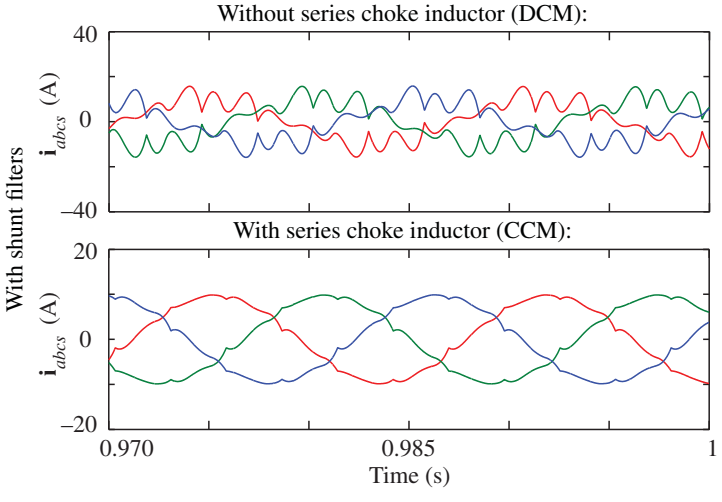

Figure 10.5 Three-phase AC currents of the system at the input source terminals in the presence of shunt filters for DCM and CCM operations (© 2013 IEEE) [35].

The DCM operation is frequently encountered in the front-end rectifiers of low- to medium-power variable-frequency drives [36–38] where the series AC filter is often not used (or is very small) but there is a large capacitor on the DC bus. This mode is associated with the needle-shape AC current waveforms that have high harmonic content that is generally expensive to filter out. As observed in Figure 10.5 (top plot), even in presence of the shunt filters of Figure 10.2(b), the source AC currents have visibly high harmonic content. This problem, of course, can be alleviated using additional shunt filters tuned to the next present harmonics until the desired total harmonic distortion (THD) criteria are satisfied. It should be noted, however, that this would further increase the size, cost and complexity of the filter network.

With the series choke inductors in both configurations, the DC bus current becomes continuous, which results in CCM operation [17]. Alternatively, omitting the DC filter capacitor from the system would also prevent DCM operation and force the current drawn at the bridge terminals to remain continuous within the switching interval, as observed in Figure 10.4 (bottom plot). As the load increases, three distinct types of CCM operation can be observed, as introduced in the previous section. The bridge three-phase AC currents for the most common type of CCM operation (CCM-1) corresponding to the same operating point defined by $R_L = 70\ \Omega$, are illustrated in Figures 10.3(a) and 10.3(b) (bottom plots) in the absence and presence of the shunt filters, respectively. Comparing these plots to the respective top plots, it is observed that, in both cases, the harmonic contents of the bridge currents are reduced when the system enters the CCM. Also, comparing the two bottom plots of Figures 10.3(a) and 10.3(b), it is seen that the bridge currents are essentially similar in the absence and presence of the shunt filter, except for a minor difference in the ripple. In the absence of shunt filters, the bridge currents of Figure 10.3(a) (bottom plot) are directly fed into the AC source. However, as depicted in Figure 10.5 (bottom plot), the source currents are significantly improved in the presence of the shunt filters, especially compared to those in the DCM operation (top plot).

The above studies demonstrate, on the one hand, that the value of the AC-side equivalent series inductance essentially determines the mode of operation at a given DC load. On the other hand, the effect of shunt filters is mainly confined to the currents drawn from the source network, which are important in system-level studies concerning the overall performance of the power system.

For dynamic average modelling, it is important to relate the AC currents at the bridge terminals to the current injected into the DC bus. This step relies on the knowledge of the mode of operation which determines the shape and waveforms of the currents, as well as their respective averages. Therefore, for the purpose of dynamic average modelling, the currents injected into the bridge terminals are of most interest. From this point of view, the series component of the AC inductance has the dominant impact. The system performance may then be typically investigated for two cases – without and with the series AC inductor filter – whereas the details of the shunt filter branches appear to be less important. However, it should be noted that if the shunt filters are included, the currents drawn from the AC network are smoother than the bridge currents since some harmonics flow through the filters branches.

10.3 Detailed Analysis and Modes of Operation

To set the stage for discussing the system operation and modelling, a simplified circuit diagram for the front-end rectifier load system considered in this chapter is depicted in Figure 10.6. Since the presence of shunt filters does not generally change the development of dynamic average models, only series filters are considered here. The AC network is represented by its Thevenin equivalent voltages $\mathbf{e}_{abcs}$ with series resistance r_{th} and inductance L_{th}. The impedance of the optional series AC filter is represented by r_{ac} and L_{ac}. The combined equivalent impedance of the AC subsystem is denoted by r_s and L_s, respectively. The DC filter represented by r_{dc}, L_{dc} and C is also optional and may be partially present in the system.

If the system is fed from a synchronous generator (Figure 10.1 Case II), the machine can be represented using the voltage-behind-reactance formulation, which results in a circuit similar to Figure 10.6 (but possibly with coupled and/or variable equivalent inductances) [39–41]. In many cases, such as battery charging [42, 43] and variable speed drive applications [8, 9], the DC filter inductor may be omitted,

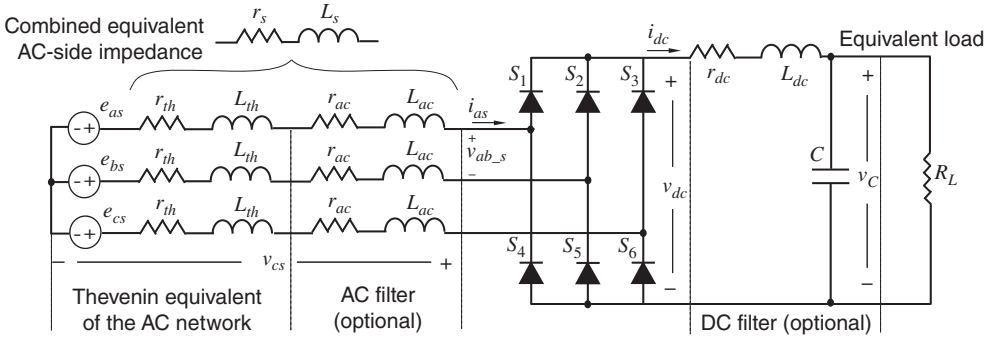

Figure 10.6 Simplified circuit diagram of a typical three phase front-end rectifier load system (© 2012 IEEE) [17].

whereas the capacitor is included to smooth the DC bus voltage. The AC filter inductor often must be included in order to reduce the AC-side current harmonics.

To represent an equivalent energy-dissipating load on the DC side in Figure 10.6, a simple resistor, R_L, is connected to the DC bus [36, 37, 42]. Although such an assumption ignores the interharmonics [38], it is deemed acceptable in low-power applications [44, 45], and is considered sufficient for the purpose of this chapter.

In this system, a DCM operation is typically observed at light load. This mode is frequently encountered in the front-end rectifiers of low- to medium-power variable-frequency drives [36, 38], where the AC filter is often not used (or is very small) but there is a significant capacitor on the DC bus. The corresponding waveforms are illustrated in Figure 10.7(a). There are six equal switching intervals within a single electrical cycle. In DCM, each switching interval is divided into two subintervals. During the conduction subinterval, t_{cond}, two diodes are conducting and two of the phases carry the DC bus current in opposite directions. At some point, the line-to-line voltage in these two phases becomes smaller than the DC bus voltage, and the current reaches zero and remains zero for the rest of the interval – hence discontinuous mode. This subinterval is denoted by t_{dcm} in Figure 10.7(a). During t_{dcm}, all diodes are off. The DC load is, in the meanwhile, being fed from the DC capacitor, as observed in the DC bus voltage waveform v_{dc}. The switching pattern in the DCM is therefore 2–0.

If the combined value of the source and AC filter inductances becomes sufficiently large [36, 46], or the load on the DC bus is sufficiently increased, the DC bus current becomes continuous – hence continuous mode. In this case, as the load varies from a light load to a short-circuit, three different switching patterns can be observed, resulting in three distinct CCMs of operation [47]. The typical waveforms of the phase currents and the corresponding DC bus voltage are shown in Figure 10.7(b). The operational modes are summarized in Table 10.1, together with the conduction pattern and the commutation angle.

Within CCM-1 (see Figure 10.7(b), top plot), each switching interval is divided into two subintervals referred to as commutation and conduction [28]. During the conduction subinterval, t_{cond}, only two diodes conduct, whereas during the commutation subinterval, t_{com}, corresponding to the commutation angle $\mu = \omega_e \cdot t_{com}$, the current is being switched from one phase to another and three diodes conduct. Therefore, a conduction pattern of 2–3 diodes is observed within each 60 electrical degrees, and $0° < \mu < 60°$.

The mode CCM-2 (Figure 10.7(b), middle plot) may be achieved by further increasing the load current. In this mode, the commutation angle μ increases and reaches 60°, resulting in the disappearance of the conduction subinterval. Consequently, there will be three diodes carrying current throughout the switching intervals. Hence, the conduction pattern becomes just 3 (or 3–3).

If the load current is further increased, the commutation angle μ starts to increase, resulting in the third mode, CCM-3 (Figure 10.7(b), bottom plot). This changes the switching pattern to 3–4 conducting

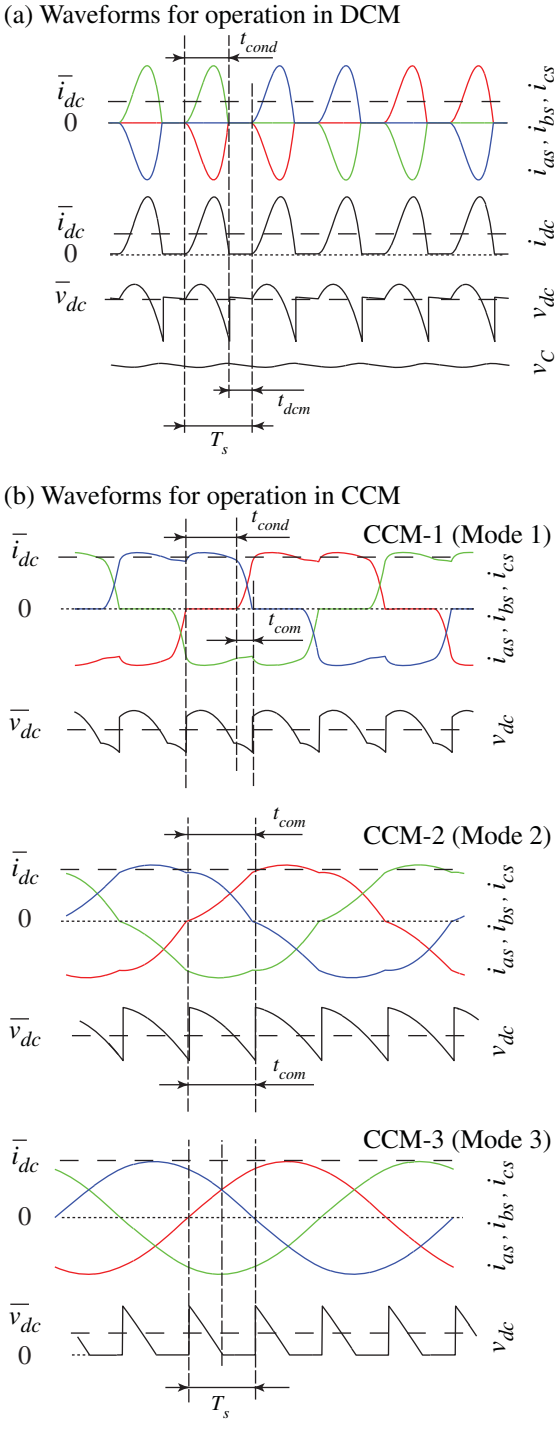

Figure 10.7 Typical current and voltage waveforms of the six-pulse rectifier: (a) operation in DCM, (b) operation in CCM (© 2012 IEEE) [17].

Table 10.1 Operational modes of the conventional three-phase (six-pulse) rectifier (© 2012 IEEE) [17].

Operational modes	Conduction pattern	Commutation angle
DCM	2–0	$\mu = 0°$
CCM-1	2–3	$0° < \mu < 60°$
CCM-2	3	$\mu = 60°$
CCM-3	3–4	$60° < \mu < 120°$

diodes. Note that this mode contains a topology with four simultaneously conducting diodes, which short-circuits the output as observed in Figure 10.7(b) (bottom plot). This last mode rarely occurs in practical systems, but it is possible in rotating machines and brushless exciters with very large inductances [48].

Certain variations in topology of the system of Figure 10.6 may prevent the occurrence of some of the operational modes. For instance, without the DC filter inductor, the CCM-3 mode cannot occur, and the system could only operate in DCM, CCM-1 or CCM-2. Comparing the phase currents in DCM shown in Figure 10.7(a), it can also be concluded that such currents will inject significant harmonics into the network. To avoid operation in DCM, medium and large drives with front-end rectifiers often install additional AC filters (series inductors and shunt filters) to shift the operation to CCM-1 or CCM-2.

10.4 Dynamic Average Modelling

The dynamic average models for six-pulse converters can be generally developed using two main approaches: analytical [28, 29, 34, 49–51] and parametric [30, 31]. Using the first approach, the system variables are analytically averaged over a typical switching interval [28], and the system state and algebraic equations are derived. The fast averaging over a typical switching interval T_s is defined as:

$$\bar{f}(t) = \frac{1}{T_s}\int_{t-T_s}^{t} f(\tau)\, d\tau, \tag{10.1}$$

where f is a network variable – for example, voltage or current – and $\bar{f}$ is the so-called fast average of f. While the definition (10.1) may be directly applied to the DC variables, the AC variables first have to be transformed into an appropriate synchronously rotating reference frame [28]. Here, we adopt the qd-reference frame convention where the q-axis is leading the d-axis by 90° [28]. In such reference frame, the resulting qd variables in steady-state are composed of a constant (DC) component and a ripple. The averaging of these variables using (10.1) removes the switching ripple but preserves the slower (DC) variations of the transformed variables. The converter reference frame is typically chosen wherein the d-axis component of voltage is zero as depicted in Figure 10.8.

The relationship between the voltages in the converter and arbitrary reference frames may be written as

$$\begin{bmatrix} v_{qs}^{c} \\ v_{ds}^{c} = 0 \end{bmatrix} = \begin{bmatrix} \cos(\phi_c) & \sin(\phi_c) \\ -\sin(\phi_c) & \cos(\phi_c) \end{bmatrix} \begin{bmatrix} v_{qs}^{a} \\ v_{ds}^{a} \end{bmatrix}, \tag{10.2}$$

while the angle between the respective components of the voltage in converter and arbitrary reference frame may be obtained from

$$\phi_c = \tan^{-1}\left(\frac{v_{ds}^{a}}{v_{qs}^{a}}\right). \tag{10.3}$$

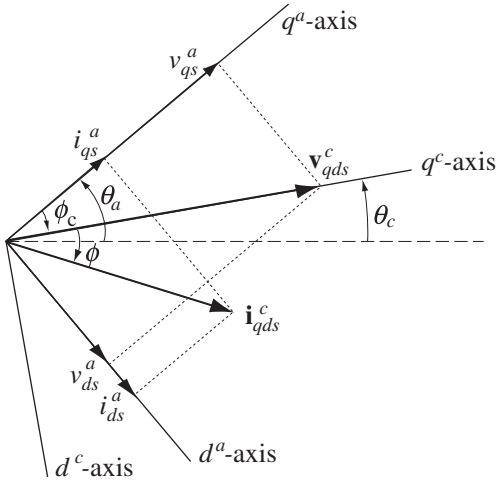

Figure 10.8 Relationship between the AC variables expressed in the converter and the arbitrary reference frames.

Table 10.2 lists various dynamic average models present in the literature for the six-pulse system, together with the list of features included in each model. The first challenge in deriving the AVMs analytically is the existence of various operational modes discussed previously. The AVM is typically considered for the most common mode of operation, CCM-1. In order to extend such models to all modes, the corresponding equations for each mode must be derived and averaged using a similar procedure. Moreover, the boundary conditions for each of the modes should be established. Therefore there will be an AVM valid for each operational mode that is in the range of interest. Such models can then be 'switched' as the system changes modes, which makes this approach additionally challenging. Other challenges of the analytical approach include the difficulty of establishing closed-form explicit equations describing the system in more complicated configurations, for example, machine-fed converter systems (Case II in Figure 10.1) [29, 50, 51]. In many cases, the final model will be implicit and would

Table 10.2 Average models of the three-phase rectifier systems (© 2012 IEEE) [17].

Models	Steady-state/ dynamic	Dynamic order (full/reduced)	DCM, CCMs (1, 2, 3)	AC filter (r_{ac}, L_{ac})	DC filter (r_{dc}, L_{dc}, C)	Variable AC inductance (yes/no)
[28]	Dynamic	Reduced	CCM 1	L_{ac}	r_{dc}, L_{dc}, C	No
[52]	Dynamic	Reduced	CCM 2	r_{ac}, L_{ac}	C	No
[53]	Dynamic	Reduced	CCM 2	L_{ac}	C	No
[34, 49]	Dynamic	Reduced	CCM 1	r_{ac}, L_{ac}	r_{dc}, L_{dc}, C	No
[50]	Steady-state	N/A	CCM 1	—	r_{dc}, L_{dc}, C	Yes
[29]	Dynamic	Reduced	CCM 1	—	r_{dc}, L_{dc}, C	Yes
[51]	Dynamic	Reduced	CCM 1	—	C	Yes
[30]	Dynamic	Full	CCM 1	—	C	Yes
[48]	Dynamic	Reduced	CCMs 1, 2, 3	—	r_{dc}, L_{dc}, C	Yes
[31]	Dynamic	Full	CCMs 1, 2, 3	—	r_{dc}, L_{dc}, C	Yes

require an iterative solution. Analytically derived AVMs have been formulated in [28, 29, 34, 49–51] for voltage-source and machine-fed converters. For example, the model presented in [28], in addition to only being valid in CCM-1 mode, also neglects the resistance on the AC side, r_s in Figure 10.6. Subsequent improvements have been made in [36], to include the AC-side resistance and improve the model dynamics. The particular case of three-phase rectifier feeding constant-voltage loads has been addressed in [52,53]. The parametric approach has been considered in [30,31]. Extension of this method to more general cases and topologies is rather straightforward. Average modelling of power electronic systems on a polynomial chaos basis was presented in [54].

10.4.1 Selected Dynamic AVMs

The AVM models listed in the previous section are selected for further comparisons and discussions. Two models (denoted AVM-1 and AVM-2) are based on the analytical approach, while the third model (PAVM) is based on the parametric approach. These models are briefly reviewed below.

Classical reduced-order model (AVM-1): The classical model requires the state equation that describes the DC bus current dynamics as [28]:

$$\frac{d\bar{i}_{dc}}{dt} = \frac{\frac{3\sqrt{3}}{\pi}\sqrt{2}E - \left(\frac{3}{\pi}\omega_e L_s + r_{dc}\right)\bar{i}_{dc} - v_C}{2L_s + L_{dc}}, \tag{10.4}$$

where E is the rms value of the phase voltage and v_C is the DC bus voltage on the filter capacitor.

To establish the average q- and d-axis components of the phase currents, the DC current is assumed constant and equal to its average value during the switching interval. The current dynamics disappear, resulting in a reduced-order model. The phase currents are then expressed during conduction and commutation subintervals and are averaged, respectively. The result of this procedure yields the following equations:

$$\bar{i}^c_{qs,com} = \frac{-2\sqrt{3}}{\pi}\bar{i}_{dc}\left[\sin\left(\mu - \frac{5\pi}{6}\right) + \sin\left(\frac{5\pi}{6}\right)\right] - \frac{3}{\pi}\frac{\sqrt{2}E}{\omega_e L_s}(\cos\mu - 1) + \frac{3}{4\pi}\frac{\sqrt{2}E}{\omega_e L_s}(\cos(2\mu) - 1) \tag{10.5}$$

$$\bar{i}^c_{ds,com} = \frac{-2\sqrt{3}}{\pi}\bar{i}_{dc}\left[\cos\left(\frac{5\pi}{6}\right) - \cos\left(\mu - \frac{5\pi}{6}\right)\right] - \frac{3}{\pi}\frac{\sqrt{2}E}{\omega_e L_s}\sin\mu + \frac{3}{4\pi}\frac{\sqrt{2}E}{\omega_e L_s}(\sin(2\mu) + 2\mu) \tag{10.6}$$

$$\bar{i}^c_{qs,cond} = \frac{-2\sqrt{3}}{\pi}\bar{i}_{dc}\left[\sin\left(\frac{7\pi}{6}\right) - \sin\left(\mu + \frac{5\pi}{6}\right)\right] \tag{10.7}$$

$$\bar{i}^c_{ds,cond} = \frac{-2\sqrt{3}}{\pi}\bar{i}_{dc}\left[\cos\left(\mu + \frac{5\pi}{6}\right) - \cos\left(\frac{7\pi}{6}\right)\right] \tag{10.8}$$

The final averaged AC side currents are obtained as

$$\bar{i}^c_{qs} = \bar{i}^c_{qs,com} + \bar{i}^c_{qs,cond} \tag{10.9}$$

$$\bar{i}^c_{ds} = \bar{i}^c_{ds,com} + \bar{i}^c_{ds,cond}. \tag{10.10}$$

The model defined by (10.4)–(10.10) is referred to as AVM-1.

Improved reduced-order model (AVM-2): A similar model has been derived in [49], where instead of assuming a constant value for the DC current during the switching interval, this current is assumed to change as

$$i_{dc}(\theta) = i_{dc0} + k \cdot \left(\theta - \frac{\mu}{2}\right), \tag{10.11}$$

where i_{dc0} is the average value of i_{dc} during the commutation period, and k is the derivative $di_{dc}/d\theta_e$ during this period of time. The effect of the AC-side resistance has also been partly taken into account. The resulting model has the following form:

$$\left[\frac{\frac{\pi}{3} - \mu + \frac{3\mu^2}{4\pi}}{\omega_e} r_s + \frac{4\pi - 3\mu}{2\pi} L_s + \frac{\frac{\pi}{3} - \mu}{2\omega_e} r_{dc} + L_{dc}\right] \frac{di_{dc}}{dt}$$

$$= \frac{3\sqrt{3}}{\pi}\sqrt{2}E \left(1 - \frac{r_s}{\omega_e L_s} \frac{\mu - \sin\mu}{2}\right) - \left(\frac{2\pi - 3\mu}{\pi} r_s + \frac{3}{\pi}\omega_e L_s + r_{dc}\right) i_{dc0} - v_C, \tag{10.12}$$

$$\bar{i}^c_{qs} = -\frac{2\sqrt{3}}{\pi} i_{dc0} \cos\mu + \frac{\sqrt{3}}{\pi} k \left(-\sin\mu + \frac{\pi}{3}\right) + \frac{3}{\pi} \frac{\sqrt{2}E}{\omega_e L_s} \left(\cos\mu - \frac{\cos(2\mu)}{4} - \frac{3}{4}\right), \tag{10.13}$$

$$\bar{i}^c_{ds} = -\frac{2\sqrt{3}}{\pi} i_{dc0} \sin\mu + \frac{\sqrt{3}}{\pi} k \left(\cos\mu + 1 - \frac{\sqrt{3}\pi}{3}\right) + \frac{3}{\pi} \frac{\sqrt{2}E}{\omega_e L_s} \left(\sin\mu - \frac{\sin(2\mu)}{4} - \frac{\mu}{2}\right). \tag{10.14}$$

The model defined by (10.12)–(10.14) is referred to as AVM-2. Both AVM-1 and AVM-2 utilize the same commutation angle,

$$\mu = \cos^{-1}\left(1 - \frac{\sqrt{2}\omega_e L_s}{\sqrt{3}E} \bar{i}_{dc}\right). \tag{10.15}$$

Parametric average-value model (PAVM): In the parametric approach [31], the rectifier switching cell is considered as an algebraic block that relates the DC voltage and current $\bar{v}_{dc}$, $\bar{i}_{dc}$ to the AC voltages and currents $\bar{\mathbf{v}}^c_{qds}$ and $\bar{\mathbf{i}}^c_{qds}$ through the respective parametric functions as

$$\left\|\bar{\mathbf{v}}^c_{qds}\right\| = \alpha(.)\ \bar{v}_{dc} \tag{10.16}$$

$$\bar{i}_{dc} = \beta(.) \left\|\bar{\mathbf{i}}^c_{qds}\right\|, \tag{10.17}$$

where $\alpha(.)$ and $\beta(.)$ are algebraic functions of the loading conditions. To complete this model, the angle between the vectors $\bar{\mathbf{v}}^c_{qds}$ and $\bar{\mathbf{i}}^c_{qds}$ is calculated based on Figure 10.8 as

$$\phi(.) = \tan^{-1}\left(\frac{\bar{i}^a_{ds}}{\bar{i}^a_{qs}}\right) - \tan^{-1}\left(\frac{\bar{v}^a_{ds}}{\bar{v}^a_{qs}}\right). \tag{10.18}$$

Deriving closed-form analytical expressions for $\alpha(.)$, $\beta(.)$ and $\phi(.)$ is impractical. Instead, these functions may be extracted using simulation and expressed in terms of dynamic impedance of the switching cell defined as [31]

$$z = \frac{\bar{v}_{dc}}{\left\| \bar{\mathbf{i}}^{c}_{qds} \right\|}. \tag{10.19}$$

10.4.2 Computer Implementation

PSCAD/EMTDC, EMTP-RV and Matlab/Simulink have been used to implement the considered models. The results predicted by all packages are essentially identical, provided that the time-step and solver properties are chosen appropriately. The test system parameters are summarized in the Appendix.

The PAVM implementation in PSCAD is shown in Figure 10.9. The block shown in Figure 10.9(a) contains (10.16)–(10.19) and the transformations between *qd* and *abc* coordinates. To interface the AVM with the external AC network, three controllable voltage sources are used whose values are determined by (10.16) transformed into *abc* coordinates. The DC side is interfaced using a controllable current source whose value is determined by (10.17). The values of the AC currents and the DC voltage are read from the network solution and taken as the inputs into the algebraic block, wherein the AC currents are transformed into *qd* coordinates for the use in (10.17). The subsystem of Figure 10.9(a) is encapsulated into a single module-block that is then interconnected using its nodes with the external network, as shown in Figure 10.9(b). This AVM block can then replace the detailed switching rectifier module within a larger AC and DC network (which may include AC filters, e.g. shunt harmonic filters). Figure 10.9(b) also depicts the timed breaker blocks that are used to implement the system changes.

10.5 Verification and Comparison of the AVMs

10.5.1 Steady-State Characteristics

The steady-state regulation characteristic provides a suitable measure for comparing the performance of various models under a wide range of loading conditions. Such regulation characteristics may be obtained by varying the load from open-circuit to short-circuit and recording the average values of the DC bus voltage $\bar{v}_{dc}$ and current $\bar{i}_{dc}$. For plotting purposes, the voltages and currents are typically normalized by their corresponding maximum values, that is, open-circuit and short-circuit, as predicted by the detailed model. In order to investigate the performance of various models in DCM and CCM, the considered rectifier system is assumed without and with the series AC inductor filter, respectively. The dynamic AVMs considered in this section are those detailed in the previous section and proposed in [28, 31, 49].

10.5.1.1 Operation in DCM

Figure 10.10 shows the regulation characteristics obtained from the detailed and average-value models in the absence of series AC inductor filter and the presence of the DC bus capacitor. The calculated values of the short-circuit currents and open-circuit voltages are summarized in Table 10.3. It should be noticed that without the AC filter inductor and only the network Thevenin impedance, the short-circuit current would be extremely high at 1982.3 A. In practice, the system with such configuration and parameters typically operates at lighter loads (mostly in the DCM or CCM-1), whereas the operation under heavy load current may occur only during abnormal faults. A magnified view of the practical lighter-load region is provided in Figure 10.11. As seen in this figure, the DCM extends up to the 34.5 A of the average DC current. The characteristics predicted by the analytical models, AVM-1 and AVM-2, give a lower voltage and deviate from that predicted by the detailed model, which is the reference. Observing the results in

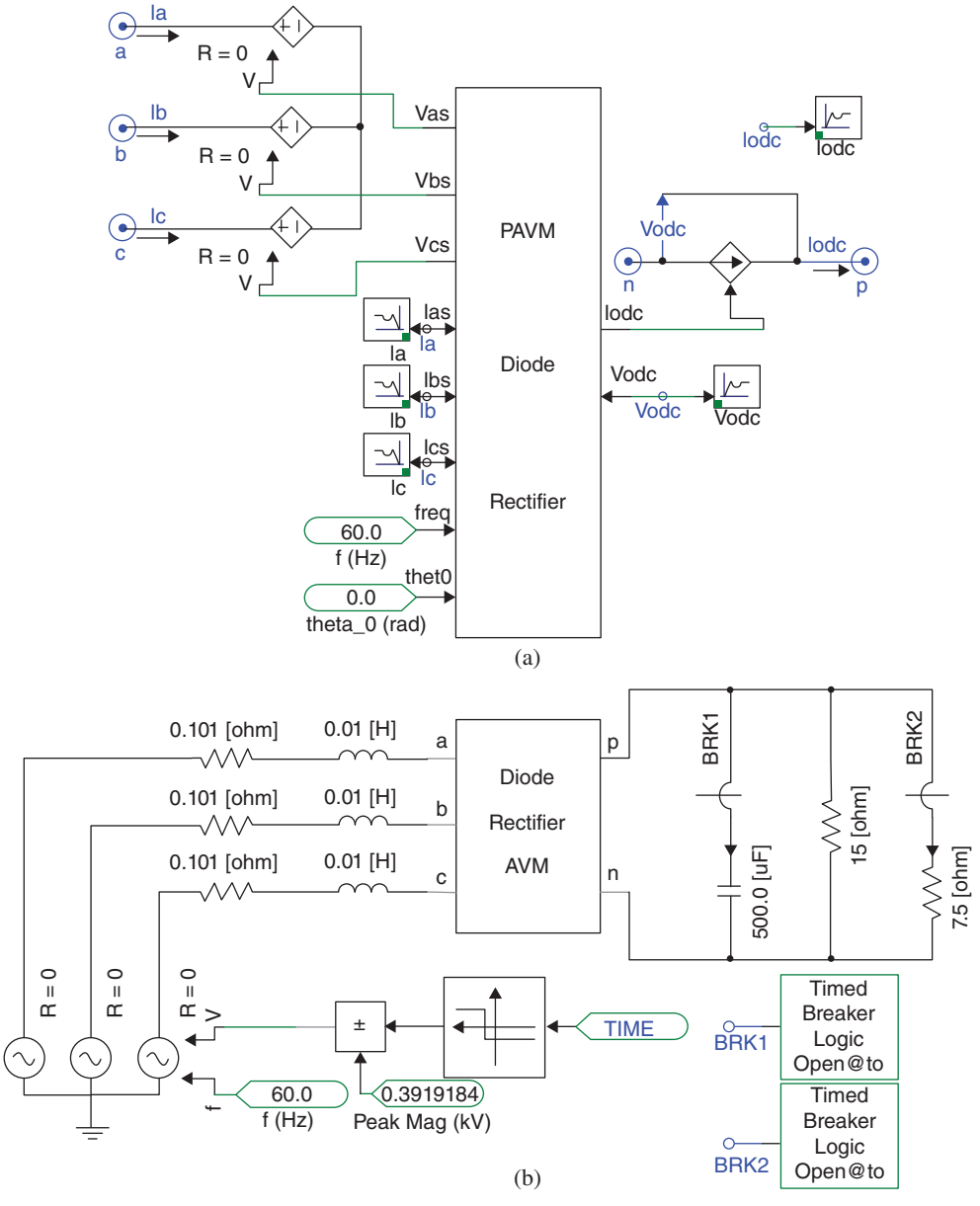

Figure 10.9 Example of parametric average-value model implemented in PSCAD: (a) PAVM block together with controllable sources and interfacing ports, (b) AVM module interfaced with external AC and DC subsystems (© 2012 IEEE) [17].

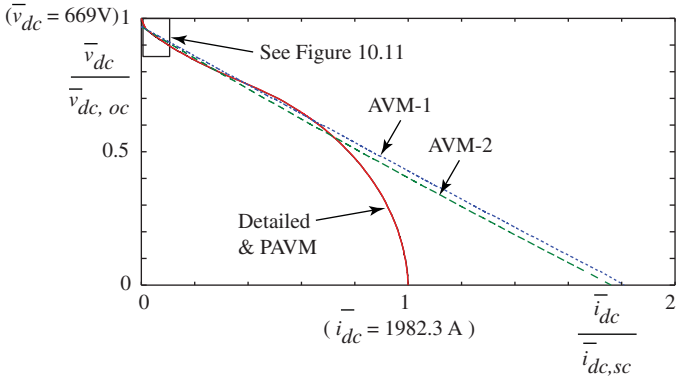

Figure 10.10 Regulation characteristic of the six-pulse rectifier system without AC input filter but with DC capacitor predicted by detailed and average models (© 2013 IEEE) [35].

Table 10.3 Maximum values of the DC bus voltage and current for different topologies of the 6-pulse rectifier system (© 2013 IEEE) [35].

Configuration	Open-circuit voltage, $\bar{v}_{dc,oc}$	Short-circuit current, $\bar{i}_{dc,sc}$
Without r_{ac}, L_{ac}	669 V	1982.3 A
With r_{ac}, L_{ac}	648.2 V	98.8 A

Figure 10.10, it is also evident that the short-circuit current is incorrectly predicted by the analytical models, because these models are not valid for heavy loading conditions in CCM-2 and below. At the same time, the PAVM predicts the same characteristic as the detailed model over the entire region from open- to short-circuit.

To better compare the accuracy attained by the average models, the steady-state values of the DC bus voltage and currents calculated by these models are summarized in Table 10.4, for two operating points in DCM. The values computed by the detailed model are assumed as reference. As can be seen in this table,

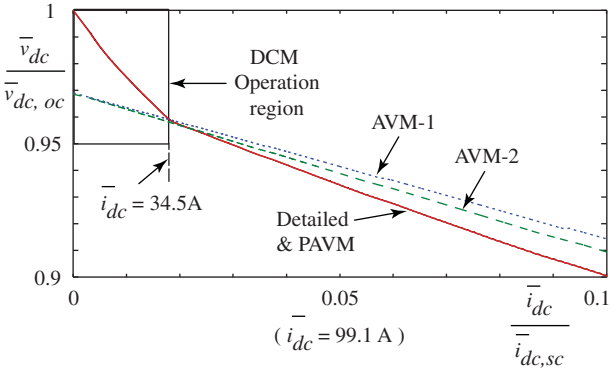

Figure 10.11 Magnified view of the regulation characteristic showing performance of models in DCM region (© 2013 IEEE) [35].

Table 10.4 Steady-state values of the DC bus voltage and current predicted by different models in DCM operation (© 2013 IEEE) [35].

Models	$R_L = 35\ \Omega$	$R_L = 70\ \Omega$
Detailed model (reference)	$\bar{i}_{dc} = 18.6625$ A; $\bar{v}_{dc} = 653.1879$ V	$\bar{i}_{dc} = 9.4354$ A; $\bar{v}_{dc} = 660.4708$ **V**
AVM-1	$\bar{i}_{dc} = 18.4260$ A; $\bar{v}_{dc} = 644.9111$ **V** $error = 1.2672\%$	$\bar{i}_{dc} = 9.2366$ A; $\bar{v}_{dc} = 646.5652$ V $error = 2.1070\%$
AVM-2	$\bar{i}_{dc} = 18.4160$ A; $\bar{v}_{dc} = 644.5613$ V $error = 1.3208\%$	$\bar{i}_{dc} = 9.2341$ A; $\bar{v}_{dc} = 646.3869$ V $error = 2.1335\%$
PAVM	$\bar{i}_{dc} = 18.6618$ A; $\bar{v}_{dc} = 653.1625$ V $error = 0.0038\%$	$\bar{i}_{dc} = 9.4353$ A; $\bar{v}_{dc} = 660.4708$ V $error = 0.0011\%$

under heavier load, $R_L = 35\ \Omega$, closer to the CCM (but still in DCM), both analytical models AVM-1 and AVM-2 underestimate the DC voltage and current by about 1.3%. Under a lighter load in DCM, $R_L = 70\ \Omega$, the error increases to above 2%. Such errors may still be reasonable for some studies. Note that the error in DC voltage and current is the same since all models assume the same load resistance. At the same time, the PAVM predicts the steady-state DC voltages and current in DCM with great accuracy (up to the third digit).

10.5.1.2 Operation in CCM

When the additional series choke inductor is added to the AC side, the value of the short-circuit current decreases to 98.8A, as shown in Table 10.3 and Figure 10.12. Moreover, the DCM operation will be limited to a very small region at extremely light load, close to an open circuit at the DC bus. This will also improve the AC current waveforms making them similar to the bottom plots of Figure 10.3, while

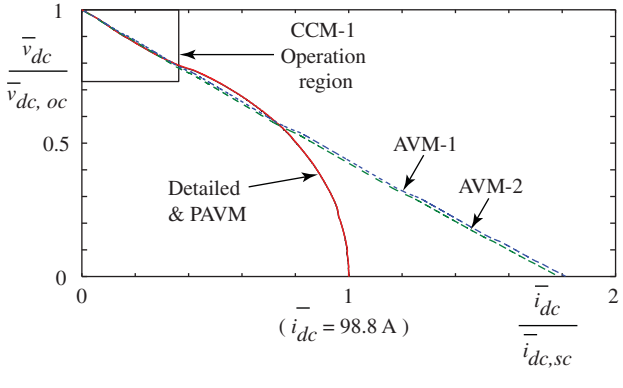

Figure 10.12 Regulation characteristic of the six-pulse rectifier system as predicted by the detailed and average models for CCM operation (© 2013 IEEE) [35].

Table 10.5 Steady-state values of the DC bus voltage and current predicted by different models in CCM-1 operation (© 2013 IEEE) [35].

Models	$R_L = 35\ \Omega$	$R_L = 70\ \Omega$
Detailed model (reference)	$\bar{i}_{dc} = 16.6247$ A; $\bar{v}_{dc} = 581.8654$ V	$\bar{i}_{dc} = 8.7308$ A; $\bar{v}_{dc} = 611.1575$ V
AVM-1	$\bar{i}_{dc} = 16.7864$ A; $\bar{v}_{dc} = 587.5247$ V $error = 0.9726\%$	$\bar{i}_{dc} = 8.8055$ A; $\bar{v}_{dc} = 616.3853$ V $error = 0.8556\%$
AVM-2	$\bar{i}_{dc} = 16.7161$ A; $\bar{v}_{dc} = 585.0649$ V $error = 0.5498\%$	$\bar{i}_{dc} = 8.7848$ A; $\bar{v}_{dc} = 614.9369$ V $error = 0.6185\%$
PAVM	$\bar{i}_{dc} = 16.6442$ A; $\bar{v}_{dc} = 582.5479$ V $error = 0.1173\%$	$\bar{i}_{dc} = 8.7864$ A; $\bar{v}_{dc} = 615.0515$ V $error = 0.6368\%$

reducing the harmonic content. Figure 10.12 illustrates the regulation characteristic for this case, in which the CCM-1 extends to about 35% of the short-circuit DC current and 72% of the open-circuit voltage. In this range of CCM-1 – which is the most practical range – the characteristics predicted by the analytical models AVM-1 and AVM-2 match very closely the characteristic predicted by the detailed model. As expected, the characteristics predicted by analytical models then start to deviate when the system enters CCM-2 and finally significantly overestimate the average DC current all the way to the short-circuit current which is higher by 180%. The PAVM remains valid for these modes, and its corresponding characteristic matches the detailed model over the entire region. In general, however, it is also possible to include these modes of operation in the analytical models whereby their performance would be improved [48].

The steady-state values of the DC bus voltage and currents calculated by these models are summarized in Table 10.5 for two operating points in CCM-1. The values computed by the detailed model are assumed as reference. As seen in this table, under heavier load, $R_L = 35\ \Omega$, closer to the CCM-2 (but still in CCM-1), the AVM-1 and AVM-2 overestimate the DC voltage and current by 0.97% and 0.55%, respectively. Under a lighter load in CCM-1, $R_L = 70\ \Omega$, these errors are still below 1% which is deemed acceptable. The PAVM also predicts the steady-state DC voltages and currents in CCM-1 with great accuracy.

10.5.2 Model Dynamic Order and Eigenvalue Analysis

In order to compare the transient responses of the models and see the effects of the model dynamic order, the system configuration is considered with the series inductor filter but without the DC capacitor. The system is assumed to operate initially under a very light load, close to open circuit condition. Then, at $t = 0.3$ s, the load resistance is stepped to $R_L = 13.1\ \Omega$, which forces the DC bus current to increase. The corresponding transient responses predicted by the detailed and average models are shown in Figure 10.13. As seen in this figure, the new operating point is achieved in CCM-1, and all models predict the new steady state with reasonable accuracy, that is, the average responses go through the ripple of the waveforms predicted by the detailed model as shown in Figure 10.13. This result is expected and agrees with the steady-state characteristics presented in the previous subsection.

A close look at Figure 10.13 also shows that the observed responses predicted by the detailed model and PAVM include an overshoot. This overshoot in response is possible because these two models accurately

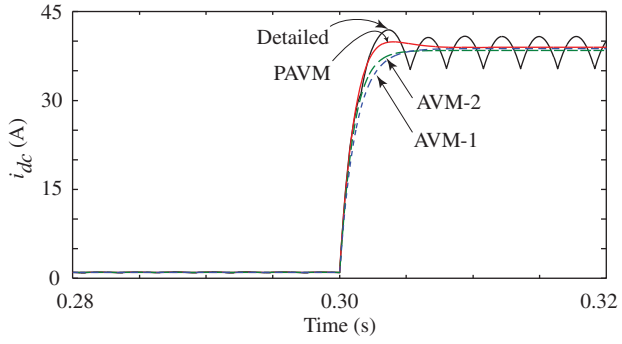

Figure 10.13 Transient response of the rectifier system with AC filter and without the DC capacitor (© 2013 IEEE) [35].

represent the second-order dynamic nature of the underlying physical system (without the DC capacitor) [28]. The AVM-1 and AVM-2, however, are both first-order (reduced-order) models and hence incapable of predicting this effect. These properties are evident from the eigenvalues of the system that have been extracted using numerical linearization. This linearization may be performed almost instantaneously for the AVMs using the LINMOD command in Matlab/Simulink [21]. For example, the eigenvalues of the system in DCM and CCM are summarized in Table 10.6. In the right column, corresponding to the same operating point as the study of Figure 10.13, it is observed that the AVM-1 and AVM-2 each have the first order, corresponding to a real eigenvalue. The PAVM, however, has a pair of complex conjugate eigenvalues corresponding to an oscillatory transient response. The oscillations are not easy to see in Figure 10.13 due to the high damping dictated by the large real part of these eigenvalues. The left column in Table 10.6 corresponds to the DCM operation with the DC filter capacitor that increases the system order by one, making AVM-1 and AVM-2 of the second and PAVM of the third order.

10.5.3 Dynamic Performance Under Balanced and Unbalanced Conditions

10.5.3.1 Balanced Conditions

Operation in DCM: The rectifier system is assumed to operate without the AC filter but with the DC capacitor so as to enable the DCM. In the following study, the system initially operates in steady state in DCM with load $R_L = 35\ \Omega$. At $t = 0.3$ s, the load resistance is stepped to $R_L = 70\ \Omega$, which forces the system deeper into the DCM operation at a lighter load. The transient responses obtained by the considered detailed and average models are shown in Figure 10.14. The analytical models AVM-1 and AVM-2 predict the DC and AC currents with reasonable accuracy, including the change in operating

Table 10.6 Eigenvalues of the rectifier system in DCM and CCM (© 2013 IEEE) [35].

Model	DCM (w/o AC filter, with dc capacitor) $R_L = 35\ \Omega$	CCM-1 (with AC filter, w/o DC capacitor) $R_L = 13.1\ \Omega$
PAVM	-35580 $-463.54 \pm 1408.9j$	$-737.8 \pm 529.3j$
AVM-1	$-118.6 \pm 1412.9j$	-1081.8
AVM-2	$-128.9 \pm 1419.6j$	-832.1

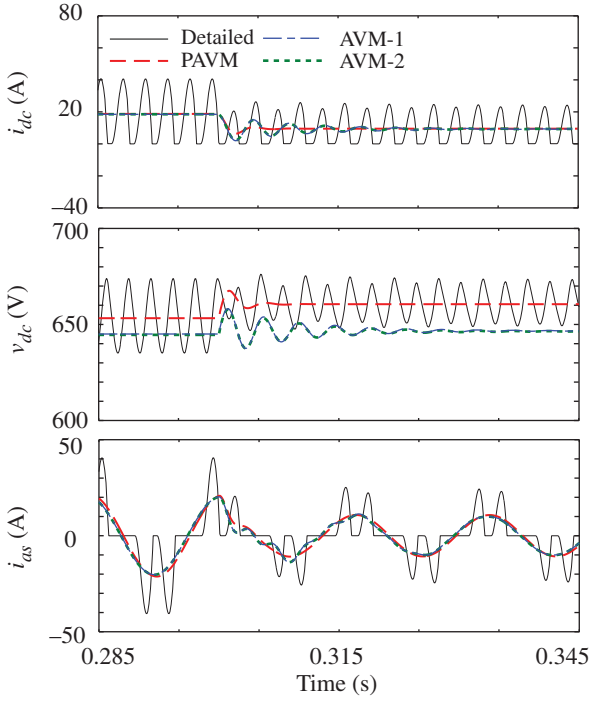

Figure 10.14 Transient response of the six-pulse rectifier system in DCM (© 2012 IEEE) [17].

conditions. The PAVM shows a somewhat higher damping than the other models but a superior prediction of the DC voltage.

Operation in CCM: To investigate the performance in CCM, the AC series filter is added. In the following study, the system is assumed to start from zero initial conditions in CCM-1 with the load $R_L = 11.9\ \Omega$. At $t = 0.05$ s, the load is stepped to $R_L = 2\ \Omega$, forcing the system into the CCM-2 – see Figure 10.7(b). The resulting transient response predicted by various models is shown in Figure 10.15. This figure clearly shows that although AVM-1 and AVM-2 have been derived for CCM-1, their transient response does not exactly follow the dynamic response of the detailed model. The improved model AVM-2 predicts the transient slightly better than the classical model AVM-1. The PAVM perfectly follows the initialization transient including the overshoot oscillations. At $t = 0.05$ s, the rectifier system undergoes another transient, and transitions into CCM-2. Both AVM-1 and AVM-2 clearly do not follow this transition very well and predict higher DC voltage and current. However, the response of the full-order PAVM model is very much consistent with the transient and new steady state predicted by the detailed model.

10.5.3.2 Unbalanced Conditions

Unbalanced operation in DCM: For implementing the DCM operation, the AC input filter is removed, and the DC capacitor is added to the rectifier system. In the following study, the rectifier system initially operates under a balanced condition with resistive load of $R_L = 20\ \Omega$. This operating point is close to the boundary between DCM and CCM-1. At $t = 0.08$ s, a phase shift of 45° in the phase c voltage, e_{cs}, is introduced, making the three phases asymmetric. This change in input voltage throws the rectifier

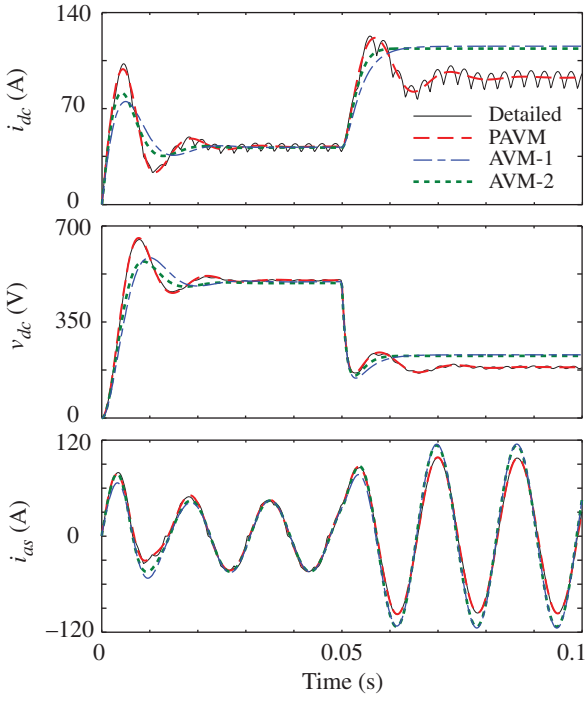

Figure 10.15 Transient response of the six-pulse rectifier system with DC capacitor (© 2012 IEEE) [17].

system into unbalanced operation in DCM. Next, at $t = 0.11$ s, the load is stepped to $R_L = 50\ \Omega$, making the DCM operation even lighter. The corresponding transient responses are shown in Figures 10.16 and 10.17. As can be seen in Figure 10.16, the heavy asymmetry of the input AC voltages leads to a pronounced change in the conduction pattern of the rectifier diodes, making the AC currents particularly spiky and uneven among the phases. The resulting DC current and voltage are shown in Figure 10.17. It can also be seen that the models AVM-1 and AVM-2 do not predict this condition well by producing larger ripple in DC voltage and current. At the same time, PAVM appears to predict the DC variables with much greater accuracy, closely resembling the peaks and fluctuation produced by the detailed simulation of the rectifier system.

Unbalanced operation in CCM: To implement the CCM, the input AC filter is added to the system, and the DC capacitor is removed. In the following study, the rectifier is assumed to start in CCM-1 with a balanced three-phase source and a resistive load $R_L = 15\ \Omega$. At $t = 0.03$ s, the magnitude of e_{cs} is reduced by half, leading to unbalanced operation among the rectifier phases. Then, at $t = 0.06$ s, the load is stepped to $R_L = 5\ \Omega$, which changes the mode to CCM-2. The resulting AC phase currents predicted by all the models are illustrated in Figure 10.18. The corresponding DC bus current and voltage are shown in Figure 10.19. The results of PAVM obtained using PSCAD, EMTP-RV and Simulink are all superimposed and are essentially identical. The PAVM predicts the unbalanced operation of DC and AC variables quite well.

The number of time-steps required by the considered models is summarized in Table 10.7. In PSCAD, the detailed model is run using a time-step of 50 μs. In Simulink, a variable-step solver ODE15s, has been used, which dynamically adjusts the time-step size and may therefore require fewer time-steps – see Table 10.7. Here, the maximum allowable time-step is 1 ms, and both absolute and relative tolerances of

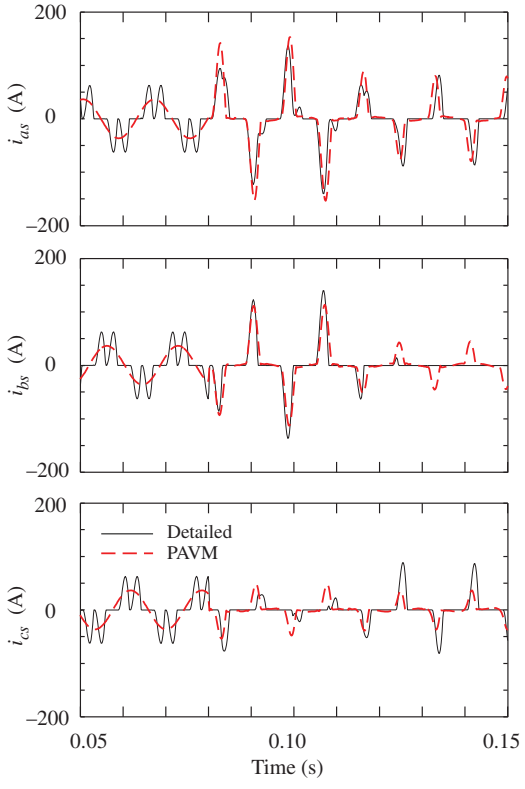

Figure 10.16 Transient response of the rectifier system AC phase currents to change in AC voltages leading to unbalanced operation in DCM (© 2012 IEEE) [17].

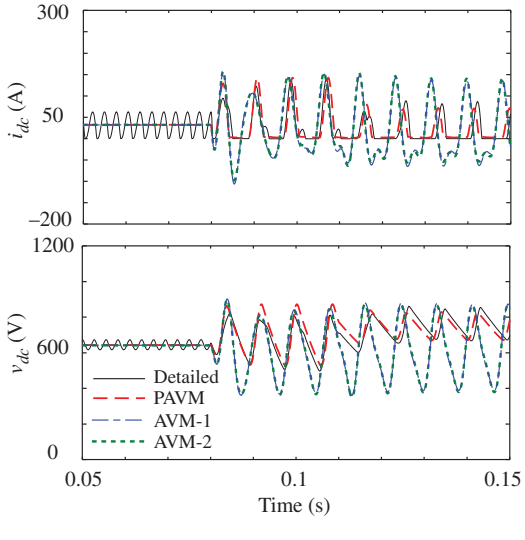

Figure 10.17 Transient response of the rectifier system DC current and voltage to change in AC voltages leading to unbalanced operation in DCM (© 2012 IEEE) [17].

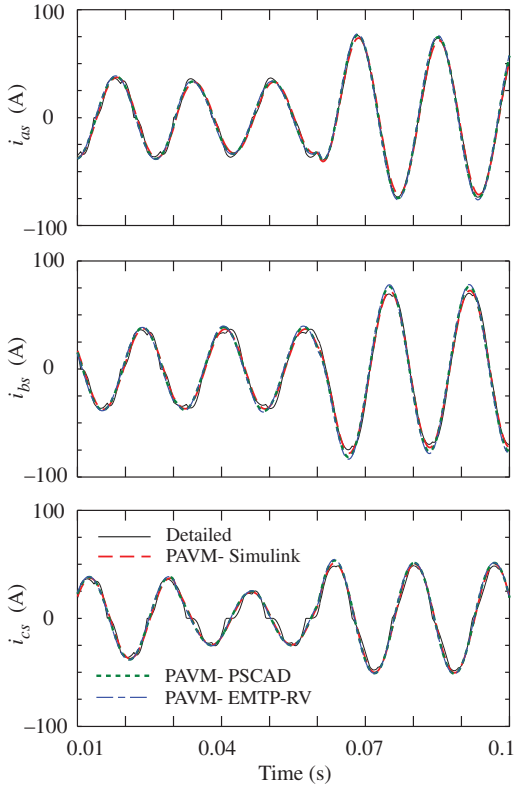

Figure 10.18 Transient response of the rectifier system AC phase currents in CCM under unbalanced AC input voltages (© 2012 IEEE) [17].

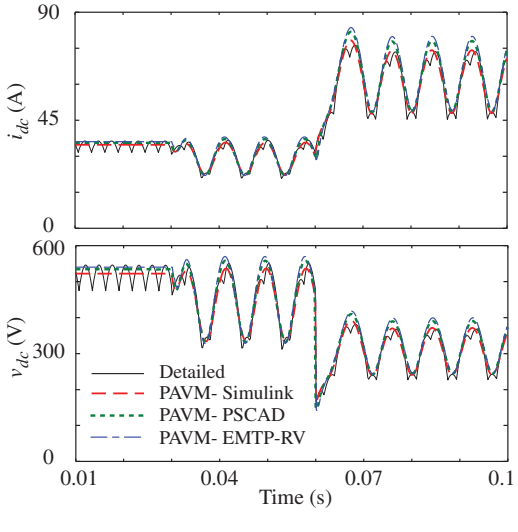

Figure 10.19 Transient response of the DC current and voltage of the rectifier system in CCM under unbalanced AC input voltages (© 2012 IEEE) [17].

Table 10.7 Comparison of models (© 2012 IEEE) [17].

Model	Step size, Δt	# Time-steps
Detailed – PSCAD	50 μs	2001
Detailed – Simulink	1 ms (max)	1042
PAVM – PSCAD	200 μs	501
PAVM – EMTP-RV	300 μs	334
PAVM – Simulink	1 ms (max)	247

1E−4 have been used. As seen in Table 10.7, the PAVMs require far fewer time-steps, and are therefore significantly faster than the respective detailed models. For consistency, the PAVM-Simulink model was run with the same solver, ODE15s, step-size limits and tolerances as the corresponding detailed model. To obtain a similar result, the PAVM in PSCAD and EMTP-RV had to use a time-step of 200 μs and 300 μs, respectively.

10.5.4 Input Sequence Impedances under Unbalanced Conditions

The three-phase rectifier currents and their harmonics depend on the rectifier operating mode and the overall equivalent inductance at the AC side. Performing a Fourier analysis on these currents and obtaining the fundamental component, the AC input impedance of the system, Z_{ac}, as seen from the input terminals, may be readily established.

To investigate the case of unbalanced operation, it is assumed that the magnitude of phase *c* source voltage, e_{cs}, is reduced by half, leading to asymmetry among the rectifier phases. In practice, such a condition may occur due to a partial fault on the AC side. The phasor diagrams for the input voltages in this case are depicted in Figure 10.20(a). Since the input voltages are known, the respective positive, negative and zero sequence components may be readily obtained, applying the appropriate transformation [55]. The phasor diagrams corresponding to the resulting symmetric components are also depicted in Figure 10.20 (b)–(d). It is evident from Figures 10.1 and 10.17 that the AC source neutral point is floating with respect to the rectifier (which actually sees only the line voltages). Hence, the zero sequence currents will not exist in the system, even though the zero sequence is present in the input phase voltages of Figure 10.20. Under these conditions, the input currents are asymmetric (as shown in

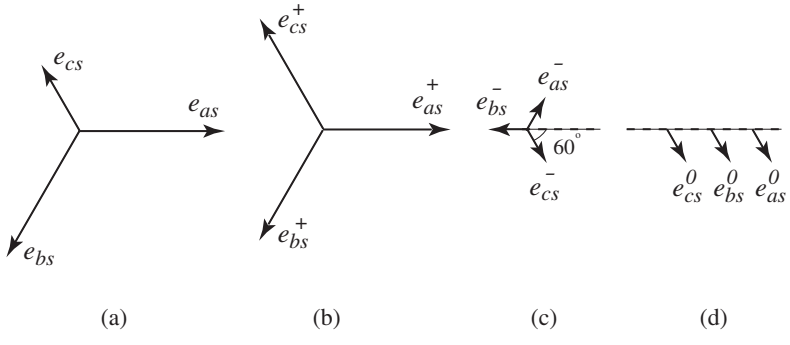

Figure 10.20 Phasor diagrams representing unbalanced operation: (a) asymmetric input voltages, (b) positive sequence components, (c) negative sequence components, (d) zero sequence components. (© 2013 IEEE) [35].

Table 10.8 Sequence impedances for unbalanced operation in different modes (© 2013 IEEE) [35].

		DCM	CCM-1 (with DC cap)	CCM-1 (w/o DC cap)
$R_L = 70\ \Omega$	Z_{ac}	$36.4\ \angle 10.2°\ \Omega$	$40.8\ \angle 18.9°\ \Omega$	$40.5\ \angle 16.9°\ \Omega$
	Z_{ac}^{+}	$30.4\ \angle 5.3°\ \Omega$	$40\ \angle 28.2°\ \Omega$	$40.5\ \angle 16.3°\ \Omega$
	Z_{ac}^{-}	$6.1\ \angle 5.3°\ \Omega$	$8.9\ \angle 34.7°\ \Omega$	$34.1\ \angle 3.5°\ \Omega$
$R_L = 35\ \Omega$	Z_{ac}	$18.4\ \angle 12.1°\ \Omega$	$21.6\ \angle 24.3°\ \Omega$	$21.5\ \angle 24.1°\ \Omega$
	Z_{ac}^{+}	$15.4\ \angle 1.1°\ \Omega$	$21.9\ \angle 30.1°\ \Omega$	$21.5\ \angle 23.2°\ \Omega$
	Z_{ac}^{-}	$3.1\ \angle 1.1°\ \Omega$	$5.8\ \angle 40.9°\ \Omega$	$16.8\ \angle 7.1°\ \Omega$

[28]) consisting of the positive and negative sequences. The symmetric components of the fundamental currents may be obtained numerically by performing the Fourier analysis. The input impedances of the system corresponding to the positive and negative sequences may then be established from the respective phasors as

$$\left|Z_{ac}^{\pm}\right| = \frac{\left|e_{as}^{\pm}\right|}{\left|i_{as}^{\pm}\right|}, \quad \angle Z_{ac}^{\pm} = \angle e_{as}^{\pm} - \angle i_{as}^{\pm}. \tag{10.20}$$

The values of the input impedance for the balanced input AC voltages and the sequence impedances for the considered unbalanced input voltages have been extracted using the AVM and detailed simulation, wherein both models predicted very close and consistent results. Owing to limited space, only the AVM results are summarized in Table 10.8, for DCM and CCM operation. For DCM operation, the series AC filter inductor is removed from the system but the DC capacitor is included. For CCM operation with the series AC filter inductor, two separate cases (with and without the DC capacitor) are considered.

10.5.5 Small-Signal Input/Output Impedances

Next, the small-signal output and input impedances as predicted by the average models under balanced conditions are compared to the reference (the detailed model). For this purpose, the rectifier system is first assumed to work at the steady-state operating point defined by the equivalent load R_L. The small-signal impedance of the system looking into the DC bus can then be expressed as

$$Z_{dc} = \frac{\hat{v}_{dc}}{-\hat{i}_{dc}}, \tag{10.21}$$

where $\hat{v}_{dc}$ is the small-signal perturbation in the DC bus average voltage about its quiescent value, $\overline{V}_{dc}$. Similarly, $\hat{i}_{dc}$ is the small-signal perturbation in the DC bus average current about its quiescent value, $\overline{i}_{dc}$. Note that this impedance is in fact the impedance of the three-phase AC network and input filter as mapped through the switching converter cell to the DC side. This impedance therefore depends not only on the dynamics of the AC network but also on the operational mode of the rectifier.

To extract this impedance from the detailed model of the rectifier system, a small-signal current perturbation $\hat{i}_{dc}$ (that is significantly smaller than the operating current $\overline{i}_{dc}$) can be injected into the DC bus, while the response of the system is obtained for the calculated value of $\hat{v}_{dc}$. This procedure is equivalent to linearization of the system in the small-signal sense, and it is carried out by calculating the data points for the magnitude and phase, and sweeping the desired range of frequencies (typically below the switching frequency, e.g. 360 Hz). An equivalent result can be obtained for the average models using the numerical linearization by LINMOD, which is a very efficient and almost instantaneous procedure in Matlab/Simulink [21]. The resulting impedances calculated using different models are shown in

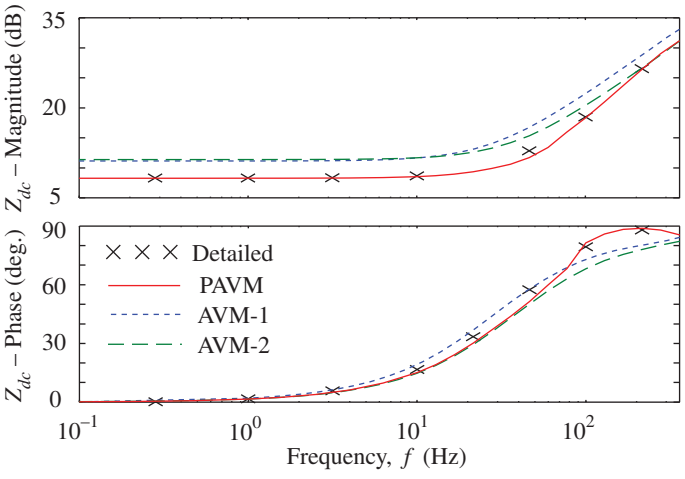

Figure 10.21 DC-side impedance Z_{dc} of the rectifier system in CCM-1 with input AC filter but without the DC capacitor (© 2013 IEEE) [35].

Figure 10.21 for operation in CCM (with the AC inductor filter but without the DC capacitor) defined by $R_L = 13.1\ \Omega$. As expected, all models predict inductive-type impedance, with the analytically derived reduced-order models AVM-1 and AVM-2 being less accurate than the full-order PAVM.

Evaluating the small-signal input impedance looking into the AC terminals of the rectifier system requires special consideration because, in the actual switching rectifier, the AC variables (currents and voltages) are inherently time-variant and contain harmonics even in the steady state. Deriving analytical expressions for the positive and negative sequence impedances and mapping the impedances for various harmonics can be extremely useful for analysing the impact of the rectifier loads on the AC network, the system stability and power quality [56–60].

To extend the impedance approach of (10.21) to the AC side of the rectifier system, the AC variables have to be viewed in a synchronous reference frame [56]. Considering the AC-side impedance in this sense is required for analysing the dynamic stability of the AC systems [56] for which special experimental procedures have also been developed. Therefore, the AC-side physical variables $\mathbf{v}_{abcs}$ and $\mathbf{i}_{abcs}$ are transferred using a synchronous reference frame into $\mathbf{v}_{qd}$ and $\mathbf{i}_{qd}$, respectively. The zero sequence is again omitted as dictated by the system topology. The final impedance four-by-four transfer matrix is defined as [27]

$$\mathbf{Z}_{qd} = \begin{bmatrix} Z_{qq} & Z_{qd} \\ Z_{dq} & Z_{dd} \end{bmatrix} = \begin{bmatrix} \left.\dfrac{\hat{v}_q(s)}{\hat{i}_q(s)}\right|_{\hat{i}_d=0} & \left.\dfrac{\hat{v}_q(s)}{\hat{i}_d(s)}\right|_{\hat{i}_d=0} \\ \left.\dfrac{\hat{v}_d(s)}{\hat{i}_q(s)}\right|_{\hat{i}_q=0} & \left.\dfrac{\hat{v}_d(s)}{\hat{i}_d(s)}\right|_{\hat{i}_q=0} \end{bmatrix}. \tag{10.22}$$

Here, the small-signal perturbations are injected in both q- and d-axes and the appropriate responses are also seen in each of the q- and d-axes, respectively.

To give an example, for the same configuration and operating point as in the previous study, the (1,1) element of the transfer matrix (10.22), the impedance Z_{qq}, has been calculated for all considered models, and the result is shown in Figure 10.22. As seen in this figure, overall, the system has an inductive-type response, with the detailed model and the PAVM clearly showing a higher-order response and a closer agreement as compared to AVM-1 and AVM-2, which are reduced-order models. Figure 10.23 also shows

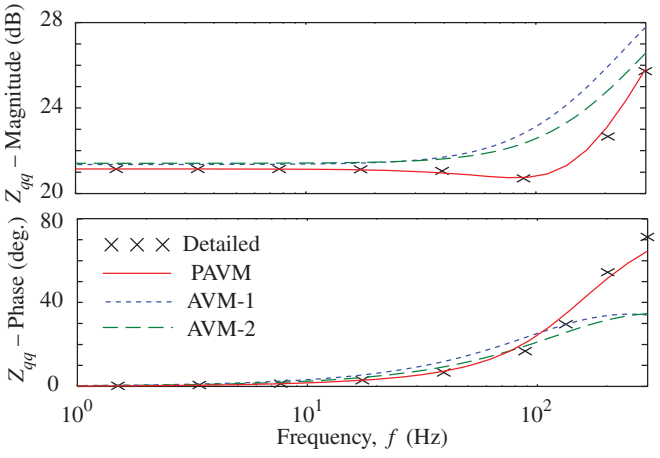

Figure 10.22 AC-side impedance Z_{qq} of the rectifier system in CCM-1 with input AC filter but without the DC capacitor (© 2013 IEEE) [35].

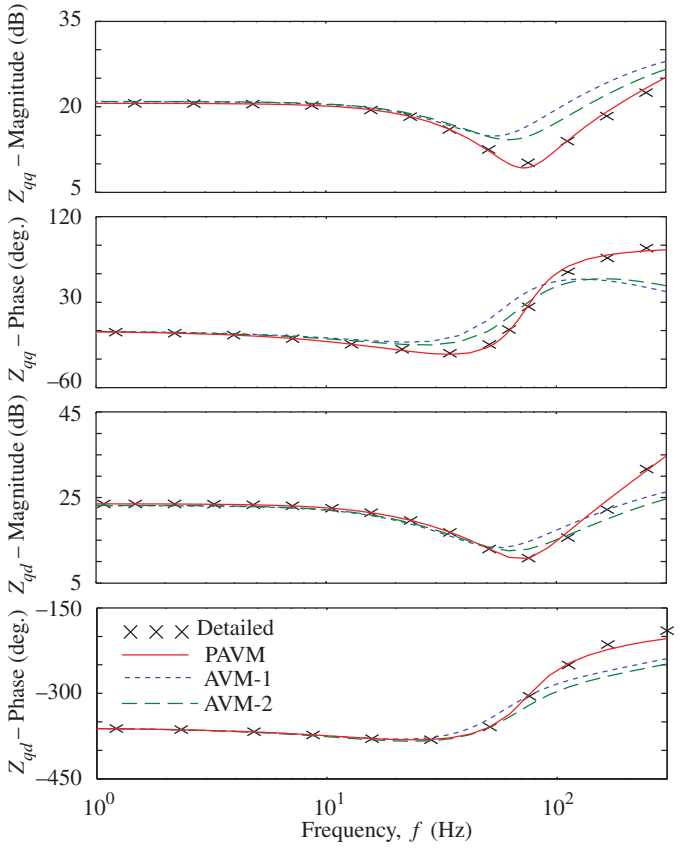

Figure 10.23 AC-side impedance Z_{qq} (top) and Z_{qd} (bottom) of the rectifier system in CCM-1 with the input AC filter and the DC capacitor (© 2013 IEEE) [35].

that the AVM-2 exhibits an improvement over the classical model AVM-1, especially in predicting the magnitude in the high-frequency range.

Note that the impedance seen from the AC side, in addition to including the AC input filter, also maps the DC-side load impedance as appeared through the rectifier switching cell. This impedance therefore depends not only on the dynamics of the load and filters, but also on the operational mode of the rectifier.

To demonstrate the effects of the DC side on the AC-side impedance, the DC capacitor is added to the rectifier system and the AC-side impedances are calculated using the detailed and average models. Due to limited space, only the impedances Z_{qq} and Z_{qd}, that is, the first row of the impedance matrix (10.22), are shown in Figure 10.23. The effects of the DC capacitor can be clearly seen in all plots of this figure. This effect is particularly pronounced at higher frequency. The results presented in Figure 10.23 prove that the full-order PAVM predicts the magnitude and phase of both impedances with great accuracy.

10.6 Generalization to High-Pulse-Count Converters

Converters with higher pulse-count include 12-, 18- and 24-pulse configurations, which are generally considered to improve the quality of DC voltage and current at the output terminals as well as of the input AC current. To demonstrate the generalization of the analyses presented above for the conventional three-phase six-pulse converter, an example six-phase twelve-pulse rectifier shown in Figure 10.24 is considered. A similar configuration may be achieved by utilizing two sets of wye/delta windings of a conventional three-phase system (transformer and/or synchronous generator). Without loss of generality, the two six-pulse bridges form a parallel connection. The displacement angle between the two three-phase sets is commonly chosen to be 30 electrical degrees, but in certain applications the displacement angle may be 60 electrical degrees [59]. The configuration of the 12-pulse rectifier may also be varied by either including or excluding the interphase transformer (IPT) and by connecting/disconnecting the

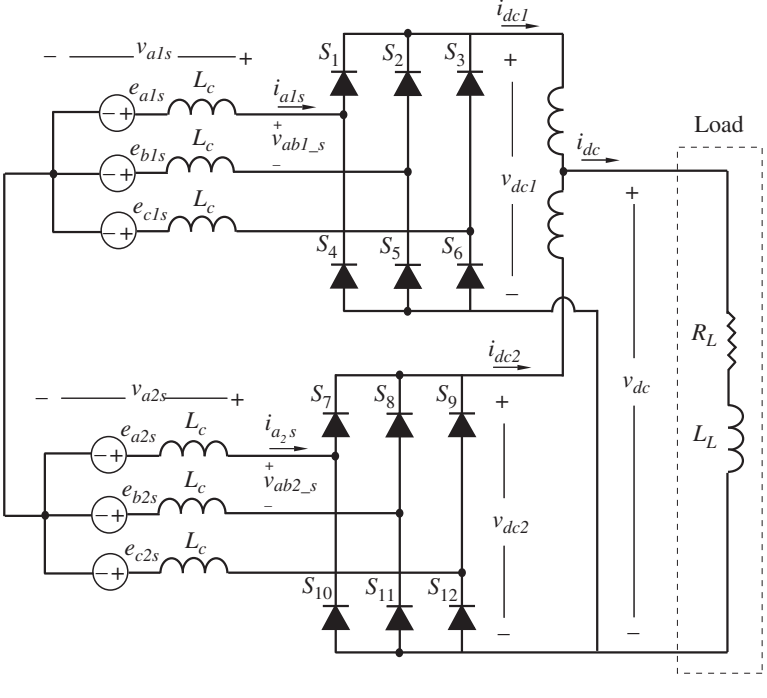

Figure 10.24 Typical six-phase twelve-pulse bridge rectifier system.

Table 10.9 Operational modes of the 12-pulse rectifier.

Operational modes	Conduction pattern
1	4–2
2	5–4–2–4
3	5–4
4	6–5–4–5
5	6–5
6	6
7	7–6

neutral points of the two sets of three-phase voltage sources. These configurations result in a more complicated switching pattern and a large number of operational modes which are more difficult to establish analytically [59, 60].

10.6.1 Detailed Analysis

Modes of operation for the case of 30° displacement angle, disconnected neutrals and without the interphase transformer have been analytically established in [33], where a simplified case of constant DC bus current is assumed. These modes are summarized in Table 10.9, and the regulation characteristic for this case is shown in Figure 10.25. Reference [33] also assumes a case with an ideal interphase

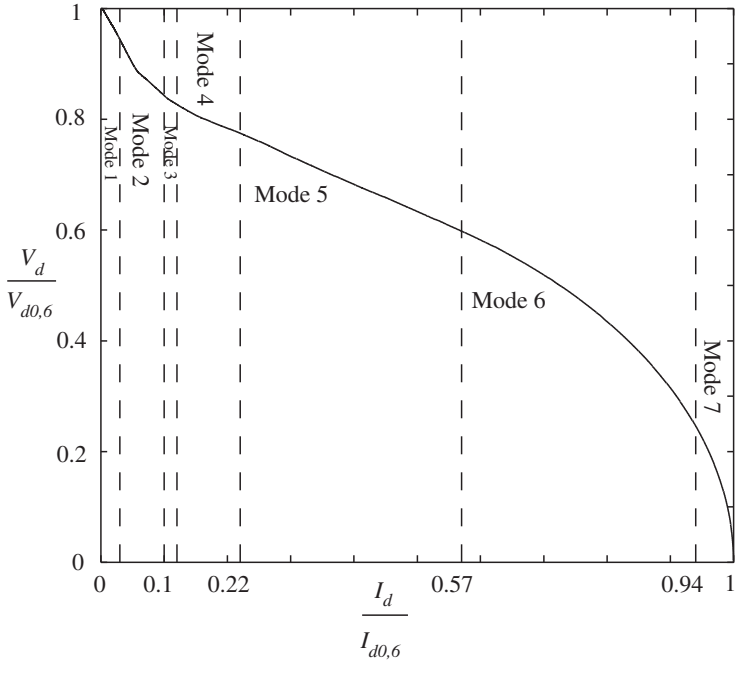

Figure 10.25 Steady-state regulation characteristic for the six-phase twelve-pulse bridge converter with the neutral points disconnected.

Table 10.10 Operational modes of the 12-pulse rectifier with ideal IPT.

Operational modes	Conduction pattern
1	4–2
2	5–4–2–4
3	5–4

transformer, that is, the magnetizing reactance of the IPT is assumed to be infinite. Thus the load current will be equally shared between the two bridges, which operate independently. Under these assumptions, the operational modes may be derived by analysing one of the bridges with one-half of the load current [33]. Three modes of operation are then recognized, which are summarized in Table 10.10. It should be noted that in the case of a non-ideal interphase transformer, the regulation characteristic will lie between these two extreme cases [33].

If the neutral points of the two sets of three-phase voltage sources in Figure 10.24 are connected, a new set of line-to-line voltages is established between the phases. This will allow the phase current waveforms to become asymmetric, resulting in more complicated operational modes. The regulation characteristic for this case is shown in Figure 10.26, with the modes of operation summarized in Table 10.11.

10.6.2 Dynamic Average Modelling

The dynamic AVM for the above 12-pulse rectifier system has been developed using the generalized parametric approach [27]. Simulation studies of the twelve-pulse rectifier have been conducted using the

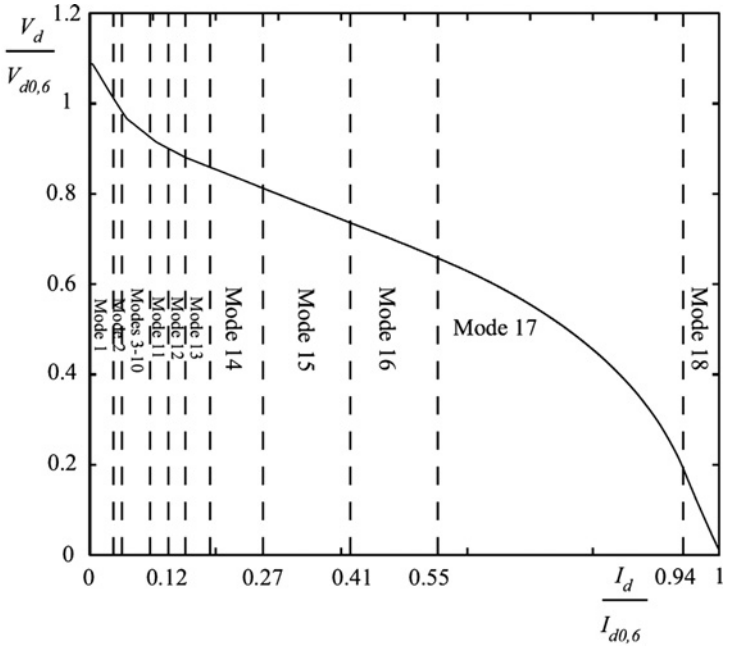

Figure 10.26 Steady-state regulation characteristic for the six-phase twelve-pulse bridge converter with connected neutral points.

Table 10.11 Operational modes of the 12-pulse rectifier with connected neutral points.

Operational modes	Conduction pattern
1	3–4–3–2
2	5–4–3–2–3–4
3	5–4–3–3–2–3–4
4	5–4–3–4–3–3–2–3–4
5	5–4–3–4–3–3–4
6	5–4–3–4–3–4–3–4
7	5–4–3–4–4–3–4
8	5–4–3–4–4
9	5–4–5–4–3–4
10	5–4–5–4–4
11	5–4
12	6–5–4–5–4–5
13	6–5–4–5
14	6–5–5
15	6–5–6–5
16	6–6–5
17	6
18	7–6

detailed model and the parametric AVM only, because the analytically derived models do not capture the intermode transitions. A transient study has been carried out in which the load resistance is stepped from 1 Ω to 0.1 Ω at $t = 0.5$ s. The corresponding responses, for the case of connected neutral points, are superimposed in Figure 10.27. In this case, the operational mode is changing from Mode 13 (i.e. 6–5–4–5 conduction pattern) to Mode 17 (6-valve conduction pattern). As the plots of this Figure 10.27 show, the AVM predicts the transient response very accurately.

To evaluate the effectiveness of the AVMs relative to the switching models, we can compare the time-step size and the total number of time-steps that were required by each of the models to complete the entire transient response. For the purpose of comparison, a transient study duration of 1 s was assumed. For example, in case of six-pulse rectifier the time-steps taken by each of the models implemented in Simulink are summarized in Table 10.12. All Simulink models were executed using a variable time-step solver that can automatically adjust the step size during the transient. The table shows that the switching model required the largest number of time-steps (22 659), which were needed to accurately handle all the switching events (discontinuities). The AVMs could utilize a much larger time-step, because these models are continuous, taking far fewer steps (281, 271 and 309, respectively).

The studies with 12-pulse rectifier were carried out using both PSCAD and Simulink. The summary of the time-steps is also given in Table 10.12. For the considered time interval/study of 1 s, the detailed model again took the largest number of steps (20 001 and 15 366). There is some difference between the PSCAD and Simulink detailed models, which can be attributed to the fact that PSCAD uses fixed time-step to solve the entire transient, whereas Simulink can vary the time- step to accommodate the switching and other transients. The detailed PSCAD model was run with a typical time-step of 50 μs required to properly handle the switching of diodes. However, the PSCAD-AVM and Simulink-AVM could use appreciably larger time-steps, which altogether demonstrates the benefits of the AVM approach, where each model took significantly fewer time-steps (5586 and 194). The PSCAD-AVM could not run at very large time-steps because the time-step was still limited by the relatively fast transient observed during the rapid change in the load.

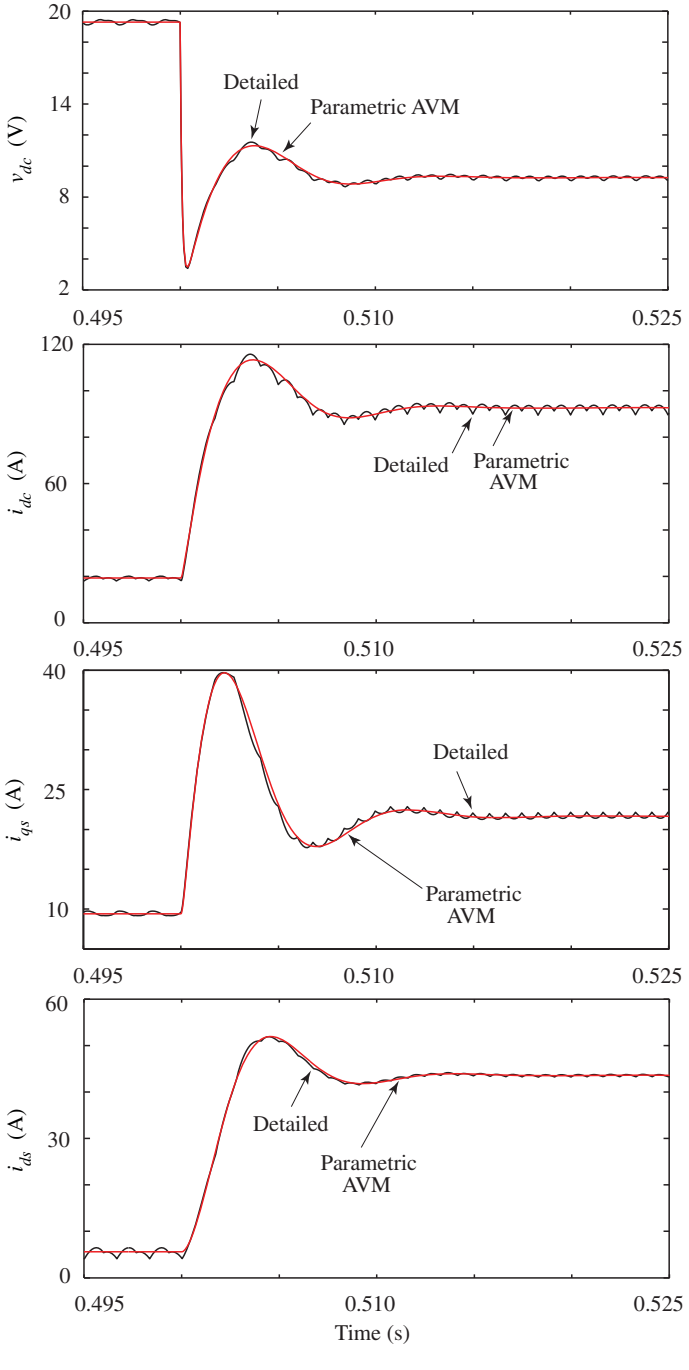

Figure 10.27 Twelve-pulse bridge converter transient response from Mode 13 to Mode 17 as predicted by detailed and averaged models.

Table 10.12 Comparison of model performance.

Rectifier	Model	Time-steps
Six-pulse rectifier	Detailed model	22 659
	AVM-1	281
	AVM-2	271
	Parametric AVM	309
Twelve-pulse rectifier	Detailed – PSCAD	20 001
	Detailed – Simulink	15 366
	AVM – PSCAD	5586
	AVM – Simulink	194

Dynamic average models are extremely advantageous for simulations of system transients where the switching harmonics injected into the AC grid or the DC link are neglected. Including the effect of switching harmonics would require a special consideration and may be pursued in combination with other approaches, such as multiple reference frames and harmonic-domain modelling. Dynamic AVMs neglect (remove) the effect of fast switching but preserve the slower dynamics of the system. As a result, they can be effectively used to improve the simulation efficiency for the system-level transient studies with a large number of such loads and subsystems.

10.7 Generalization to PWM AC-DC Converters

For conversion between DC and AC, a three-phase converter may be realized using the conventional full-bridge topology depicted in Figure 10.28. Depending on whether the upper or the lower switches are conducting, each phase terminal can be connected to either the upper or the lower rail (or left floating if none of the switches are conducting). Hence, the topology of Figure 10.28 is often referred to as a two-level converter.

10.7.1 PWM Voltage-Source Converters

A full-bridge converter depicted in Figure 10.28 requires active switches (transistors) that can be switched at a much higher frequency than the AC-side line frequency. The energy may be converted from a DC source to supply a load such as an AC motor. Alternatively, the converter can also operate as a rectifier taking the energy from AC side (which may be an AC generator) and feeding the DC bus to supply other loads. In general, such converter systems may provide bidirectional energy flow during steady state

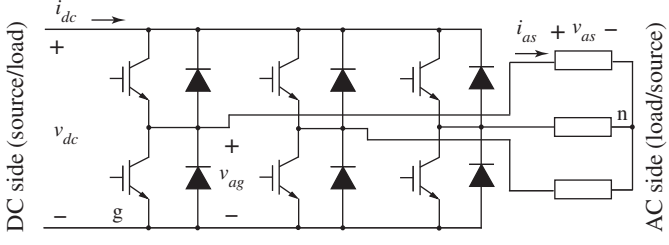

Figure 10.28 Typical two-level three-phase converter topology (© 2010 IEEE) [27].

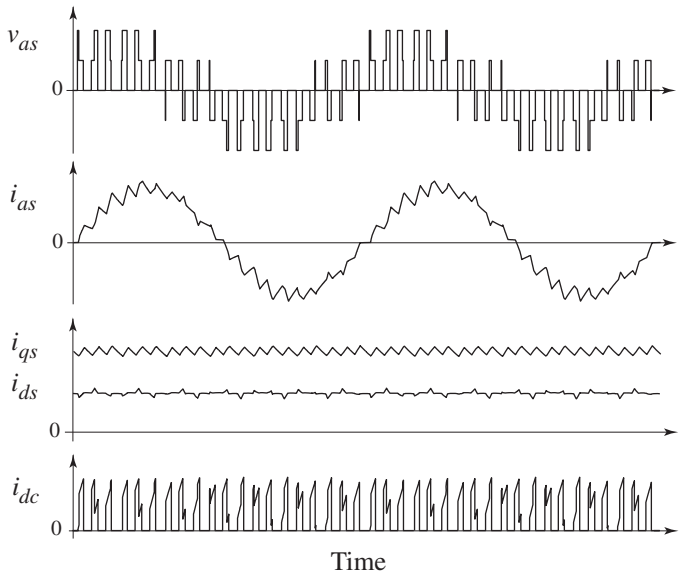

Figure 10.29 Typical voltage and current waveforms corresponding to the two-level VSI feeding an inductive load (© 2010 IEEE) [27].

and/or transients, and are very common in motor drives as well as rectifiers in generator sets. These converters are often used for medium power level and applications requiring grid interfacing.

To keep the switching losses low, the switching frequency of such converters in power applications is typically not very high. For a 50/60 Hz fundamental frequency, the switching frequency f_{sw} may be in the range from several kHz to tens of kHz. Thus the voltages and/or currents on the AC side can be modulated with the desired quality approaching ideal sinusoidal waveforms. For example, the typical waveforms of the PWM VSI supplying an inductive load are shown in Figure 10.29, which shows that the phase current essentially consists of the fundamental sinusoidal component with the superimposed high-frequency switching ripples (relatively low content of low-frequency harmonics). The strength of the low-frequency harmonics in the phase current depends on many factors, including the PWM strategy and the switching frequency. Various PWM voltage or current control strategies can be used here as well [28]. Typical modulation strategies include the sine-triangle PWM (with third-harmonic injection) and space vector modulation. However, for any switching strategy, in a typical operation, each phase terminal is always connected to either the upper or lower rail, which ensures that the current is always continuous.

10.7.2 Dynamic Average-Value Modelling of PWM Voltage-Source Converters

To demonstrate dynamic average modelling of AC-DC converters, let us first consider the PWM VSC based on the topology depicted in Figure 10.28. In many power applications, the efficiency of converters is quite high, and therefore the conduction losses are often neglected in the analysis of transients. The averaging over a typical switching interval $T_s = 1/f_{sw}$ is carried out on the transformed AC variables as well as on the DC variables. The relationship between the converter and arbitrary reference frames is the same as for the rectifier system of Figure 10.8. Moreover, the voltages on the AC side and DC

link can be related using algebraic functions (10.16–19). Similar to the line-commutated converters, $\alpha(\cdot)$ and $\beta(\cdot)$ depend on the type of inverter and its operating/loading conditions. However, for the PWM converters the functions (10.16–19) can be established by applying the energy conservation principle to the converter cell. In particular, looking at the AC side, the three-phase power can be written as

$$P = \frac{3}{2} \left\| \bar{\mathbf{v}}_{qds} \right\| \left\| \bar{\mathbf{i}}_{qds} \right\| \cos \phi, \tag{10.23}$$

where ϕ is the power factor angle. Assuming an ideal (lossless) converter, the power calculated using (10.23) is equal to the power on the DC link. Therefore, the DC bus current can be written as

$$\bar{i}_{dc} = \frac{P}{\bar{v}_{dc}} = \left(\frac{3}{2} \alpha(\cdot) \cos \phi \right) \left\| \bar{\mathbf{i}}_{qds} \right\|. \tag{10.24}$$

Finally, comparing (10.23) and (10.24), $\beta(\cdot)$ is obtained as

$$\beta(\cdot) = \frac{3}{2} \alpha(\cdot) \cos \phi. \tag{10.25}$$

Since the angle ϕ depends on the load, the value of $\beta(\cdot)$ also depends on the loading conditions. Based on Figure 10.8, the angle ϕ may be expressed in terms of the qd components of the voltage and current as

$$\phi(\cdot) = \tan^{-1} \left(\frac{\bar{i}^a_{ds}}{\bar{i}^a_{qs}} \right) - \tan^{-1} \left(\frac{\bar{v}^a_{ds}}{\bar{v}^a_{qs}} \right). \tag{10.26}$$

The values of parametric functions $\alpha(\cdot)$ and $\beta(\cdot)$ for several commonly used modulation strategies (basic six-step, PWM, sine-triangle and space-vector) [28] are summarized in Table 10.13. The corresponding average-value model is shown in Figure 10.30, which assumes that the DC-link voltage is available (which is typically the case due to a large capacitor in the DC link) and that the AC side is connected to an inductive network (e.g. electric machine). If the state-variable approach is used, the inductive network typically requires input voltages $\bar{\mathbf{v}}_{qds}$. Therefore, the AC-side voltages become the output of the converter AVM and are calculated in terms of the DC bus voltage using (10.16) and the function $\alpha(\cdot)$. A coordinate transformation may be used to recalculate these voltages from the converter reference frame to the physical variables for interfacing with the external inductive network [28]. The AC side currents $\bar{\mathbf{i}}_{qds}$ are calculated by the external network and become the input for the converter AVM. Finally, the current $\bar{i}_{dc}$, that is injected into the DC bus, is calculated using (10.17) and the function $\beta(\cdot)$.

Table 10.13 Algebraic functions for common voltage-source inverters (© 2010 IEEE) [27].

Function	Six-step inverter	Six-step PWM	PWM sine-triangle/ space-vector modulation
α	$\frac{2}{\pi}$	$\frac{2}{\pi} d$	$\frac{1}{2} d$
β	$\frac{3}{\pi} \cos \phi$	$\frac{3}{\pi} d \cos \phi$	$\frac{3}{4} d \cos \phi$

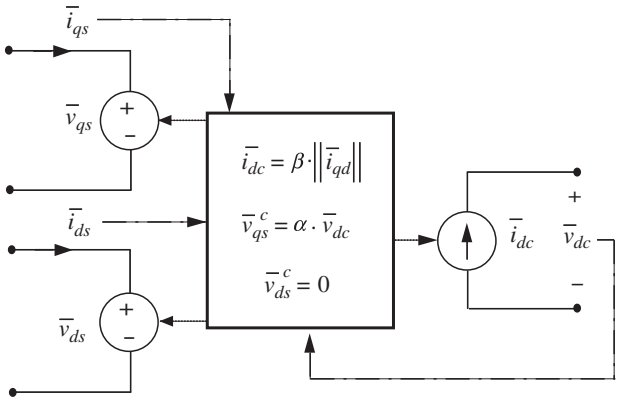

Figure 10.30 Dynamic average-value model for the voltage source inverter using algebraic-parametric functions relating the AC and DC variables (© 2010 IEEE) [27].

10.8 Conclusions

This chapter provided an overview of dynamic average-modelling of front-end rectifier loads and PWM AC-DC converter systems. The typical configurations of the three-phase front-end rectifier with and without the smoothing AC choke inductor and variations of the DC filter, were discussed and shown to result in the two distinct types of operating modes: DCM and CCM. The analytical and parametric approaches for developing AVMs were reviewed, followed by a comprehensive comparison of three selected AVMs. Although the analytically derived models (AVM-1 and AVM-2) possess reduced dynamic order, they can be effectively used for the steady-state and transient analysis limited to the CCM-1 operation under balanced as well as unbalanced conditions among the AC phases. The PAVM model is shown to have good accuracy over a wider range, covering both DCM and all submodes of CCM, under balanced and unbalanced input AC voltages. The studies demonstrated the effects of the commonly used filters on the rectifier operation, the steady-state operational characteristics, the input sequence impedances under unbalanced excitation and the small-signal input/output impedance characteristics. The generalization to high-pulse-count converters was demonstrated through an example six-phase twelve-pulse rectifier system.

Finally, the dynamic average-value modelling methodology was extended to the PWM VSCs, which are also commonly used in power applications. Since for such converters, the phase current is typically continuous, it becomes possible to derive the explicit algebraic relationships between the currents and voltages on the AC and DC terminals of the converter switching cell.

Appendix

1. Parameters for the rectifier circuits:

$$\sqrt{2}E = 13.2 \text{ V}, \omega_e = 2\pi 100, \; L_c = 0.37 \text{ mH}, \; C = 1 \text{ mF}.$$

2. Front-end rectifier system parameters:

$$V_{line} = \sqrt{3}E = 480 \text{ V}, f_e = 60 \text{ Hz}, \; r_{th} = 0.01 \; \Omega, \; L_{th} = 500 \; \mu\text{H},$$
$$r_{ac} = 0.091 \; \Omega, \; L_{ac} = 9.545 \text{ mH}, \; r_{dc} = L_{dc} = 0, \; C = 500 \; \mu\text{F},$$
$$r_{f5} = 0.1 \; \Omega, \; L_{f5} = 43.1 \text{ mH}, \; C_{f5} = 6.53 \; \mu\text{F},$$
$$r_{f7} = 0.05 \; \Omega, \; L_{f7} = 26.9 \text{ mH}, \; C_{f7} = 5.34 \; \mu\text{F}.$$

References

[1] Wu, B. (2006) *High-Power Converters and AC Drives*, IEEE Press/John Wiley & Sons, Inc., Piscataway, NJ.

[2] Lee, K., Blasko, V., Jahns, T.M. and Lipo, T.A. (2010) Input harmonic estimation and control methods in active filters. *IEEE Transactions on Power Delivery*, **25**(2), 953–960.

[3] Villablanca, M.E. and Nadal, J.I. (2008) Current distortion reduction in six-phase parallel-connected AC/DC rectifiers. *IEEE Transactions on Power Delivery*, **23**(2), 953–959.

[4] Lee, K., Venkataramanan, G. and Jahns, T.M. (2006) Source current harmonic analysis of adjustable speed drives under input voltage unbalance and sag conditions. *IEEE Transactions on Power Delivery*, **21**(2), 567–576.

[5] Singh, B., Bhuvaneswari, G. and Garg, V. (2006) Power-quality improvements in vector-controlled induction motor drive employing pulse multiplication in AC-DC converters. *IEEE Transactions on Power Delivery*, **21**(3), 1578–1586.

[6] Chang, G.W. and Chen, S.K. (2005) An analytical approach for characterizing harmonic and interharmonic currents generated by VSI-fed adjustable speed drives. *IEEE Transactions on Power Delivery*, **20**(4), 2585–2593.

[7] Rifai, M.B., Ortmeyer, T.H. and McQuillan, W.J. (2000) Evaluation of current interharmonics from AC drives. *IEEE Transactions on Power Delivery*, **15**(3), 1094–1098.

[8] Jiang, J. and Holtz, J. (2001) An efficient braking method for controlled AC drives with a diode rectifier front end. *IEEE Transactions on Industry Applications*, **37**(5), 1299–1305.

[9] Wang, F., Chen, G., Boroyevich, D. *et al.* (2008) Analysis and design optimization of diode front-end rectifier passive components for voltage source inverters. *IEEE Transactions on Power Electronics*, **23**(5), 2278–2289.

[10] Hwang, J.G., Lehn, P.W. and Winkelnkemper, M. (2010) A generalized class of stationary frame-current controllers for grid-connected AC-DC converters. *IEEE Transactions on Power Delivery*, **25**(4), 2742–2751.

[11] Haque, M.E., Negnevitsky, M. and Muttagi, K.M. (2010) A novel control strategy for a variable-speed wind turbine with a permanent-magnet synchronous generator. *IEEE Transactions on Industry Applications*, **46**(1), 331–339.

[12] Bhide, R.S., Kulkarni, S.V. and Bhandarkar, P.B. (2011) Analysis of five-legged transformer used for parallel operation of rectifiers by coupled circuit field approach. *IEEE Transactions on Power Delivery*, **26**(2), 607–616.

[13] Ladoux, P., Postiglione, G., Foch, H. and Nuns, J. (2005) A comparative study of AC/DC converters for high-power DC arc furnace. *IEEE Transactions on Industrial Electronics*, **52**(3), 747–757.

[14] Suh, Y., Park, H., Lee, Y. and Steimer, P.K. (2010) A power conversion system for AC furnace with enhanced arc stability. *IEEE Transactions on Industry Applications*, **46**(6), 2526–2535.

[15] Chang, G.W., Wang, H., Chuang, G. and Chu, S. (2009) Passive harmonic filter planning in a power system with considering probabilistic constraints. *IEEE Transactions on Power Delivery*, **24**(1), 208–218.

[16] Zubi, H.M., Dunn, R.W. and Robinson, F.V.P. (2010) Comparison of different common passive filter topologies for harmonic mitigation. University Power Engineering Conference, Cardiff, Wales, UK, Aug.–Sep. 2010.

[17] Chiniforoosh, S., Atighechi, H., Davoudi, A. *et al.* (2012) Dynamic average modeling of front-end diode rectifier loads considering discontinuous conduction mode and unbalanced operation. *IEEE Transactions on Power Delivery*, **27**(1), 421–429.

[18] Krause, P.C. and Asipo, T.A. (1969) Analysis and simplified representations of rectifier-inverter reluctance-synchronous motor drives. *IEEE Transactions on Power Apparatus and Systems*, **88**(6), 962–970.

[19] Eyman, E.D. and Kolchev, Y.V. (1976) Universal analog computer model for three-phase controlled rectifier bridges. *IEEE Transactions on Power Apparatus and Systems*, **95**(4), 1136–1144.

[20] *PSCAD/EMTDC V4.0 On-Line Help,* Manitoba HVDC Research Centre and RTDS Technologies Inc., 2005.

[21] Simulink Dynamic System Simulation Software, Users Manual, The MathWorks Inc., 2008. www.mathworks.com.

[22] *SimPowerSystems: Model and simulate electrical power systems – User's Guide*, The MathWorks Inc., 2008. www.mathworks.com.

[23] *Piecewise Linear Electrical Circuit Simulation (PLECS) – User Manual*, Ver. 1.4, Plexim GmbH (www.plexim.com).

[24] Automated State Model Generator (ASMG) – Reference Manual, Version 2, P C Krause & Associates, Inc. 2003 (www.pcka.com).

[25] Alternative Transients Programs, ATP-EMTP, ATP User Group, 2007. http://www.emtp.org.

[26] *Electromagnetic Transient Program,* EMTP-RV, CEA Technologies, Inc., 2007. http://www.emtp.com.

[27] Chiniforoosh, S., Jatskevich, J., Yazdani, A. *et al.* (2010) Definitions and applications of dynamic average models for analysis of power systems. *IEEE Transactions on Power Delivery*, **25**(4), 2655–2669.

[28] Krause, P.C., Wasynczuk, O. and Sudhoff, S.D. (2002) *Analysis of Electric Machinery and Drive Systems*, IEEE Press, Piscataway, NJ.
[29] Sudhoff, S.D., Corzine, K.A., Hegner, H.J. and Delisle, D.E. (1996) Transient and dynamic average-value modeling of synchronous machine fed load-commutated converters. *IEEE Transactions on Energy Conversion*, **11**(3), 508–514.
[30] Jadric, I., Borojevic, D. and Jadric, M. (2000) Modeling and control of a synchronous generator with an active DC load. *IEEE Transactions on Power Electronics*, **15**(2), 303–311.
[31] Jatskevich, J., Pekarek, S.D. and Davoudi, A. (2006) Parametric average-value model of synchronous machine-rectifier systems. *IEEE Transactions on Energy Conversion*, **21**(1), 9–18.
[32] Zhang, B. and Pekarek, S.D. (2004) Analysis and average value model of a source-commutated 5-phase rectifier. IEEE PESC 2004, Aachen, Germany, Jun. 2004.
[33] Tzeng, Y., Chen, N. and Wu, R. (1997) Modes of operation in parallel-connected 12-pulse uncontrolled bridge rectifiers without an interphase transformer. *IEEE Transactions on Industrial Electronics*, **44**(3), 344–355.
[34] Zhu, H., Burgos, R.P., Lacaux, F. *et al.* (2005) Average modeling of three-phase and nine-phase diode rectifiers with improved AC current and DC voltage dynamics. IECON 2005, Raleigh, NC, USA, 2005.
[35] Chiniforoosh, S., Atighechi, H., Davoudi, A. *et al.* (2013) Steady-state and dynamic performance of front-end diode rectifier loads as predicted by dynamic average-value models. *IEEE Transactions on Power Delivery*, **28**(3), 1533–1541.
[36] Lian, K.L., Perkins, B.K. and Lehn, P.W. (2008) Harmonic analysis of a three-phase diode bridge rectifier based on sampled-data model. *IEEE Transactions on Power Delivery*, **23**(2), 1088–1096.
[37] Grotzbach, M. and Reiner, R. (2000) Line current harmonics of VSI-fed adjustable-speed drives. *IEEE Transactions on Industry Applications*, **36**(2), 683–690.
[38] Carpinelli, G., Iacovone, F., Russo, A. *et al.* (2004) Analytical modeling for harmonic analysis of line current of VSI-fed drives. *IEEE Transactions on Power Delivery*, **19**(3), 1212–1224.
[39] Pekarek, S.D., Wasynczuk, O. and Hegner, H.J. (1998) An efficient and accurate model for the simulation and analysis of synchronous machine/converter systems. *IEEE Transactions on Energy Conversion*, **13**(1), 42–48.
[40] Pekarek, S.D. and Walters, E.A. (1999) An accurate method of neglecting dynamic saliency of synchronous machines in power electronic based systems. *IEEE Transactions on Energy Conversion*, **14**(4), 1177–1183.
[41] Wang, L. and Jatskevich, J. (2006) A voltage-behind-reactance synchronous machine model for the EMTP-type solution. *IEEE Transactions on Power Systems*, **21**(4), 1539–1549.
[42] Mohan, N., Undeland, T.M. and Robbins, W.P. (1995) *Power Electronics: Converters, Applications and Design*, 2nd edn, John Wiley & Sons, Inc., New York.
[43] De Broe, A.M., Drouilhet, S. and Gevorgian, V. (1999) A peak power tracker for small wind turbines in battery charging applications. *IEEE Transactions on Energy Conversion*, **14**(4), 1630–1635.
[44] Prasad, A.R., Ziogas, P.D. and Manias, S. (1992) Passive input current waveshaping method for three-phase diode rectifiers. *IEE Proceedings – Part B, Electric Power Applications*, **139**(6), 512–520.
[45] Barbi, I., Fangundes, J.C. and Cruz, C.M.T. (1994) A low cost high power factor three-phase diode rectifier with capacitive load. Appl. Power Electron. Conference Expo., Orlando, FL, USA, Feb. 1994.
[46] Pilvelait, B., Ortmeyer, T. and Grizer, M. (1992) Harmonic evaluation of inductor location in a variable speed drive. International Conference on Harmon. Power Syst., Atlanta, GA, USA, Sep. 1992.
[47] Davis, R.M. (1971) *Power Diode and Thyristor Circuits*, Cambridge University Press, Cambridge.
[48] Aliprantis, D., Sudhoff, S.D. and Kuhn, B.T. (2006) A brushless exciter model incorporating multiple rectifier modes and Preisach's hysteresis theory. *IEEE Transactions on Energy Conversion*, **21**(1), 136–147.
[49] Zhu, H. (2005) New multipulse diode rectifier average models for AC and DC power systems studies. PhD Dissertation, Virginia Polytechnic Inst. State Univ., Blacksburg, VA.
[50] Sudhoff, S.D. and Wasynczuk, O. (1993) Analysis and average-value modeling of line-commutated converter-synchronous machine systems. *IEEE Transactions on Energy Conversion*, **8**(1), 92–99.
[51] Alt, J.T., Sudhoff, S.D. and Ladd, B.E. (1999) Analysis and average-value modeling of an inductorless synchronous machine load commutated converter system. *IEEE Transactions on Energy Conversion*, **14**(1), 37–43.
[52] Caliskan, V., Perreault, D.J., Jahns, T.M. and Kassakian, J.G. (2003) Analysis of three-phase rectifiers with constant-voltage loads. *IEEE Transactions on Circuits and Systems I: Fundamental Theory and Applications*, **50**(9), 1220–1226.
[53] Pejović, P. and Kolar, J.W. (2008) Exact analysis of three-phase rectifiers with constant voltage loads. *IEEE Transactions on Circuits and Systems II: Express*, **55**(8), 743–747.
[54] Su, Q. and Strunz, K. (2011) Stochastic polynomial-chaos-based average modeling of power electronic systems. *IEEE Transactions on Power Electronics*, **26**(4), 1167–1171.

[55] Grainger, J.J. and Stevenson, W.D. Jr. (1994) *Power System Analysis*, McGraw-Hill.
[56] Sun, J. and Karimi, K. (2008) Small-signal input impedance modeling of line-frequency rectifiers. *IEEE Transactions on Aerospace and Electronic Systems*, **44**(4), 1489–1497.
[57] Bing, Z., Karimi, K.J. and Sun, J. (2009) Input impedance modeling and analysis of line-commutated rectifiers. *IEEE Transactions on Power Electronics*, **24**(10), 2338–2346.
[58] Huang, J., Corzine, K.A. and Belkhayat, M. (2009) Small-signal impedance measurement of power-electronics-based AC power systems using line-to-line current injection. *IEEE Transactions on Power Electronics*, **24**(2), 445–455.
[59] Jatskevich, J. and Pekarek, S.D. (2005) Six-phase synchronous generator-rectifier parametric average value modeling considering operational modes. *HAIT Journal of Science and Engineering B*, **2**(3–4), 365–385.
[60] Jatskevich, J., Wasynczuk, O., Walters, E.A. *et al.* (2000) Automated identification of the operational modes of switched electric circuits. *SAE Transactions, Journal of Aerospace*, Sect. 1, Set 3, 955–961.

11

Protection Systems

Juan A. Martinez-Velasco

11.1 Introduction

Protection systems are a critical part of the power system and their behaviour is an important aspect of the power system response to a transient event. A detailed model of a protection system is complex and will usually consist of three major parts: instrument transformers, protective relays and circuit breakers – see Figure 11.1 [1–7]. The instrument transformers lower the power system voltages to safe working levels. The protective relays receive information about the operating conditions of the high-voltage power system via the instrument transformers. The relays make decisions whether the power system is in a healthy state or an unhealthy state. In the latter case, the relays send signals to circuit breakers which will interrupt the large currents.

Actual power systems and their protection systems operate in a closed-loop manner. The power system influences the protection system through the instrument transformers. The protection system can modify the topology of the power system by opening and closing circuit breakers. Modern software tools allow users to represent a closed-loop interaction, which is an accurate approach to analysing the performance of the power system under transient conditions [8–12].

Early modelling activities were aimed at representing the characteristics of some relay types, evaluating the performance of relay algorithms, implementing relay models in software tools or using models in teaching power system protection. A summary of early works on relay modelling has been provided in various tutorial publications [10–12].

Relay models are now being used at the design stage, to analyse system performance or to study the impact of relay operation on system security. These models can reproduce relay characteristics, relay input pre-processing, measurement processes and the outputs provided by relays [12]. Some of the first relay models were developed by manufacturers in an attempt to better understand the (electromechanical and electromagnetic) processes involved in their response, and to optimize relay design. Nowadays the use of computer programs that mimic relay performance may be used to replace the practice of building relay prototypes.

This chapter provides general modelling guidelines and summarizes the work done to date in modelling protection systems for use in digital simulation tools. It lists some of the uses, advantages, disadvantages and limitations of protection system models, and discusses the modelling of the various relay technologies (electromechanical, static/electronic and microprocessor-based) and instrument transformers. The

Transient Analysis of Power Systems: Solution Techniques, Tools and Applications, First Edition.
Edited by Juan A. Martinez-Velasco.

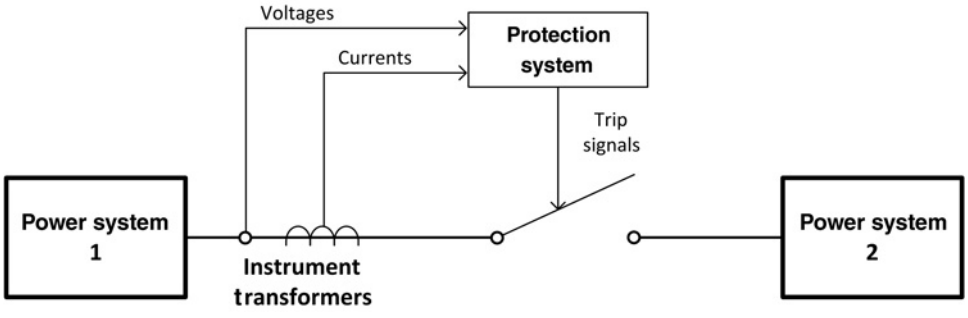

Figure 11.1 Scheme of a protection system for implementation in a digital simulation tool.

modelling guidelines provided here are sufficiently general and applicable to any time-domain simulation tool; for example, EMTP-like tools [10, 11, 13]. The term EMTP stands for Electromagnetic Transients Program and is employed in this chapter as a generic term that refers to a specific family of software tools.

To ensure that a protection system model will perform as expected, it must be tested under realistic power system conditions. This generally means that models of instrument transformers and relays must be tested with data obtained from a transient simulation tool. The power system model that generates the data must be represented with sufficient detail and accuracy. Therefore, it is desirable that the simulation environment be capable of simulating any fault scenario and system configuration.

Sections 11.2–4 review guidelines for representing respectively power system components, instrument transformers and relays, in protection studies using a transient simulation tool. For a successful model, the actual relay and the implemented model must produce the same outputs for the same inputs under transient and steady-state conditions; however, it is important to keep in mind that a relay model that reproduces relay performance may have no direct correspondence to the code within the relay.

Relay models have to be interfaced with the power-system model. Section 11.5 discusses implementation of relay models, interfacing issues and the use of models in open loop and closed loop. An alternative approach to evaluating relay model performance is to use the data recorded in the actual power system for testing the performance of a relay. Instead of testing the relays, the data can be used with relay models repeatedly, so reasons for inappropriate operation of the relay can be thoroughly investigated. The section offers a direction in which sources of information for building relay models are identified and a summary of the most common software tools used in relaying modelling and analysis. An analysis of the different applications of protection system models, the use and advantages of these models as well as their limits is provided in Section 11.5.

Before any model is used in system analysis or for designing relays, it must be validated, so the issue of model validation is addressed in Section 11.6. Different methods of validation, relay-testing procedures and assessing accuracy of models are discussed as well.

Two case studies, aimed at illustrating the present state of the art, are presented in Section 11.7, where different relay models and their behaviour are analysed.

Most of this chapter is dedicated to protective devices for transmission level systems; the design of the protection systems for distribution systems follows a different methodology. Modelling of distribution system protective devices and their coordination is discussed in Section 11.8, which also covers the study of distribution systems with distributed energy resources (DERs).

Section 11.9 summarizes the main conclusions of the chapter.

This chapter is not aimed at introducing the principles on which the devices installed to protect power systems (e.g. protective relays) are based, nor how they are coordinated. Readers interested in these aspects should consult the specialized literature [1–7]. See also [12–23].

11.2 Modelling Guidelines for Power System Components

Protection studies may be performed using either a steady-state program or a time-domain tool (e.g. EMTP-like tools). When using a time-domain simulation tool, the representation of power system components is usually made taking into account guidelines recommended for low-frequency and switching transients [24]. This section provides a summary of modelling guidelines for those power system components that can be affected by a fault and whose behaviour is critical for the behaviour of the protection system [10, 11, 25].

11.2.1 Line Models

Transmission line parameters are evenly distributed along the line length, and some of them are also functions of frequency. For steady-state studies, such as short-circuit calculations, positive- and zero-sequence parameters calculated at the power frequency from tables and simple handbook formulas may suffice. For electromagnetic transient studies, line parameters are generally computed using auxiliary subroutines available in most EMTP-like tools [13]. These tools contain two major categories of transmission line models: constant- and frequency-dependent models. In both cases, the models may use either a lumped- or a distributed-parameter representation. In the constant-parameter category, there are a variety of options such as positive- and zero-sequence lumped-parameter representation, pi-section representation, or distributed-parameter transposed and untransposed line representation. In the frequency-dependent category, the distributed-parameter approach may be considered for either transposed or untransposed lines.

Line models for steady-state studies: There are steady-state studies for which modelling transmission lines at only one particular frequency may suffice. Software tools have a number of models that could be used for this purpose:

- *Exact-pi circuit model*: This lumped-parameter model can represent the line accurately at one specific frequency. This model is based on hyperbolic equations, may take into account skin effect and ground return corrections and may be multiphase in the phase domain with constant parameters. The model is correct for steady-state solutions and frequency scans, but is not adequate for transient studies.
- *Nominal-pi circuit model*: This model is derived from the exact-pi model and used when the frequency of transients is low. The line is generally assumed untransposed and can be used to model particular transposition schemes in great detail by cascaded connection of pi sections. This model has the same limitations as the exact-pi model in addition to being limited for short lines. It cannot represent frequency-dependent parameter lines and should not be used for 'electrically long' lines.

Line models for transient studies: Distributed- and frequency-dependent parameter models are the most adequate for transient studies. They use travelling wave solutions, and can be valid over a very wide frequency range:

- *Constant distributed-parameter line model*: This model assumes that the line parameters are constant. The line inductance and capacitance are distributed, and losses are lumped. The above conditions are met for positive-sequence parameters to approximately 1–2 kHz, but not for zero-sequence parameters, so the model is good only where the zero-sequence currents are very small, or oscillate with a frequency close that at which the parameters were calculated. This frequency should not be very high, to meet the condition $R_l \ll Z_{surge}$, otherwise the line must be split into smaller sections.
- *Frequency-dependent distributed-parameter line model*: The line parameters are not constant but a function of frequency. Most frequency-dependent models are based on the modal theory where multiphase line equations are decoupled through modal transformation matrices, so that each mode can be studied separately as a single-phase line. The transformation matrices for untransposed, or

unbalanced lines are complex and frequency-dependent. However, it is possible to obtain good accuracy by using real and constant transformation matrices. Some programs may provide the option of using frequency-dependent transformation matrix. Recent frequency-dependent line models are based on a frequency-dependent phase-domain model, which does not use the modal transformation matrix.

The exact pi-model can be used when a steady-state analysis suffices. For transient analysis the frequency-dependent distributed-parameter model should be used for the lines of main interest, and the constant distributed-parameter model used for lines of secondary interest. Although the pi-circuit model is not a good choice for transient studies, it has been used for transient studies by cascading a number of nominal-pi sections.

11.2.2 Insulated Cables

The application of insulated cable models for protection studies follows the same guidelines as for overhead lines. Cable models may also use either a lumped- or a distributed-parameter representation, and their parameters can also be computed using auxiliary subroutines available in most EMTP-like tools [13].

11.2.3 Source Models

Source models used in protection studies are represented by means of detailed machine models or as ideal sinusoidal sources behind subtransient reactances or the equivalent Thevenin impedances of the system [24]. The choice of a specific model depends on system configuration, the location of the fault and the objectives of the study:

- *Model 1*: A detailed model of the machines involved in a disturbance is mostly used for representing small generating stations in non-integrated systems where the system disturbance is likely to cause change in frequency and the relays are slow in responding to that disturbance. The model requires complete machine data, including the mechanical part and the control systems, depending upon the time frame of study and their response time.
- *Model 2*: A representation based on an ideal source with subtransient reactance is used for representing large generating stations. The assumption is that the system inertia is infinite and the disturbance under study does not cause the system frequency to change. The time frame of interest is small (approximately 10 cycles) and the machine controls, such as excitation system and governor, will not respond to the disturbance. Large systems can be divided into subsystems, and each subsystem can be then reduced to an ideal three-phase source in series with equivalent positive- and zero-sequence Thevenin impedances. The main advantage of this model is that the computation requirements are significantly reduced; its main disadvantage is that the Thevenin impedance represents the system equivalence at power frequency only, so the transient response is not as accurate as when the complete system is represented.

11.2.4 Transformer Models

Transformer modelling over a wide frequency range still presents substantial difficulties: the transformer inductances are nonlinear and frequency dependent, the distributed capacitances between turns, between winding segments and between windings and ground produce resonances that can affect the terminal and internal transformer voltages. Models of varying complexity can be developed for power transformers using supporting routines or built-in models available in EMTP-like tools. Although none of the existing models can portray the physical layout of the transformer, or the high-frequency characteristics introduced by interwinding capacitance effects, most EMTP-like tools have capabilities that can be used to model any transformer type over a particular frequency range.

Here is a summary of built-in capabilities available in EMTP-like tools for representing power transformers [24, 25]:

- *Ideal transformer model*: It ignores all leakages, by assuming that all the flux is confined in the magnetic core, and neglects magnetization currents by assuming no reluctance in the magnetic material. This capability can be used together with other linear and nonlinear components to represent more complex transformer models not available in EMTP-like tools.
- *Saturable transformer model*: It considers that around each individual coil there is a magnetic leakage path and a magnetic reluctance path. This model uses a star-circuit representation for single-phase transformers with multiple windings. This model requires, as a minimum, the following information: (1) the voltage rating of each winding; (2) the leakage impedance of each winding, (3) the core saturation characteristic; (4) the transformer connectivity information. The leakage impedances are fixed inductances and resistances, separated into individual elements for each winding. The representation of the magnetizing branch is optional. This model is good for low-frequency transients. Since the winding resistances are frequency dependent, they need to be modified to reflect proper behaviour at higher frequencies. In general, the turns ratio cannot be dynamically changed during the simulation to reflect tap changer operation, although some tools include this option.
- *Matrix model*: In a transformer bank of single-phase units, the individual phases are not magnetically coupled, and their modelling is balanced, assuming that all three phases have equal parameters. In three-phase core transformers, there is magnetic coupling between windings. In addition, they may have asymmetry of magnetic path lengths, which results in asymmetrical flux densities in the individual legs of the transformer core. The core asymmetry effects are more noticeable for unbalanced operation. An accurate representation requires the use of a model that takes into consideration the coupling of every phase winding with all other phase windings. Models based on matrices of mutually coupled coils can represent quite complex coil arrangements. The matrix elements for transformers with any number of windings can be derived from the short-circuit impedances between pairs of windings. The calculations are rather complex. Support routines available in some EMTP-like tools can be used to produce the branch matrices from the positive- and zero-sequence short-circuit and excitation test data. The resulting models are good up to 2 kHz. They can take into account excitation losses, but nonlinear behaviour is not represented and must be added externally. Two matrix representations are possible for transformer modelling: the admittance and impedance matrix representations. The impedance matrix representation is only possible if the exciting current is non-zero; otherwise the matrix is singular.

Transformer saturation should be modelled if the flux will exceed the linear region. In the saturated region, it may make a difference where it is placed. EMTP-like tools have auxiliary routines to calculate the magnetization branch saturation parameters. The supporting saturation routine generates the data for the piecewise linear inductance by converting the rms voltage–current data into peak flux–peak current data. The resulting curve is single-valued (without hysteresis). Although the nonlinear inductor model works well for a number of cases, it also exhibits several limitations: it is frequency independent and does not represent hysteresis effects, which means that remanent flux in the core cannot be represented. EMTP-like tools also provide a pseudo-nonlinear hysteretic reactor, which could overcome some of the above limitations. Data for this model can be obtained using another supporting routine. The user needs to supply the scaling – that is the location of the positive saturation point (the point of the first quadrant where the hysteresis loop changes from being multivalued to being single-valued). Hysteretic models have some limitations and numerical problems [25].

Low-frequency transformer models: They can be based on the built-in capabilities summarized above. Supporting routines may be used for modelling transformer windings as mutually coupled branches. When matrix models are used, the magnetic core of the transformer is typically represented with a nonlinear or a hysteretic reactance branch, connected externally to the terminals of the windings. The built-in saturable transformer component is simpler to use than the matrix models, but if zero-sequence behaviour of three-phase core-type transformers needs to be modelled, then the matrix approach must

be used. The transformer models discussed here are valid only at moderate frequencies. In general, these models are accurate enough for overcurrent protection studies. Eddy currents in the transformer core introduce losses and they delay flux penetration into the core. Modelling of eddy currents is not an easy task since data is not usually available. No-load losses include hysteresis and eddy current losses and can be represented by a resistor in parallel with the magnetizing inductance branch.

High-frequency transformer models: The above models are used in studies at frequencies below 2 kHz. At frequencies above 2 kHz, capacitances and capacitive coupling between windings can be important or very important. For frequencies of up to 30 kHz, the simple addition of total capacitances of windings to ground and between windings is sufficient for many purposes. For frequencies above 30 kHz, a more detailed representation of the internal winding arrangement is required, and capacitances between winding and among winding segments must be modelled. The values of terminal-to-ground capacitance including bushing capacitance vary considerably, with typical values in the range of 1–10 nF. This is due mainly to the physical arrangement of the transformer windings and the overall transformer design. High-frequency transformer models may be derived from its terminal behaviour. In relaying studies, the interest may be in internal faults [26]. If explicit representation of transformers is not required, the user can model transformer effects without modelling the transformer itself; for example, a Thevenin equivalent representation in the sequence domain can be used in these situations. New high-frequency transformer models have been developed in recent years [27, 28].

11.2.5 Circuit Breaker Models

Circuit breakers are usually represented as ideal switches; that is, the switch opens at a current zero and there is no representation of arc dynamics and losses. Custom-made circuit breaker models can be employed for detailed arc modelling [29, 30]. The types of switches that are applicable for protection studies are presented below [13, 25].

- *Time-controlled switch*: In this type of switch both the time at which it is to close and the time at which it is to open are specified. The actual switch opening time will occur at the next current zero after the time at which it is required to open. To simulate current chopping, a current margin is also specified and the switch actually opens at the instant the current magnitude falls below the current margin and the time is greater than the time at which it is to open.
- *Statistical switch*: This type of switch is used to open or close the circuit breaker randomly with predetermined distribution functions, such as Gaussian or uniform. The user needs to specify the mean time and the standard deviation, in addition to the type of distribution, and the switch performs the same close or open operation repetitively according to the specified distribution characteristics. This switch can be employed to determine the maximum peak currents that can flow through a relay when closing into a fault. Usually a few hundred simulations are run to determine the statistical distribution of interest such as the maximum relay currents.
- *Controlled switch*: Most EMTP-like tools have a module that can provide the control signal to open or close a switch following a given strategy. In such cases, the switch would behave similarly to the time-controlled switch.

11.3 Models of Instrument Transformers

11.3.1 Introduction

To achieve the proper performance of the protection system model during transient phenomena, an accurate representation of instrument transformers is needed. Since instrument transformer transients considerably influence the performance of the relays, the models must be as realistic as possible [10, 11, 31]. The transient performance of current transformers (CTs) is influenced by a number of factors; for instance, the build-up of the core flux is likely to cause saturation and subsequently substantial errors in

the magnitude and phase angle of the generated signals. The CT core may also retain an unknown amount of flux because of the ferromagnetic character, which can contribute to saturation in fault conditions. The transient response of magnetic voltage transformers (VTs) and coupling capacitor voltage transformers (CCVTs) depends on several phenomena taking place in the primary network, such as sudden decrease of voltage at the transformer terminals due to a fault, or sudden overvoltages on the sound phases caused by the line-to-ground faults in the network. These phenomena can generate high-frequency (VT) or low-frequency aperiodic (CCVT) oscillations on the secondary side and saturation of the magnetic core.

Studies related to the performance of instrument transformers under transient conditions have shown the following areas of concern [10, 11, 31]:

- CT saturation reduces the magnitude of the secondary current. The consequence for electromechanical relays is a reduction of the operating force or torque; a reduced torque increases the operation time and reduces the reach of the relay.
- CT saturation affects the zero-crossings of the current wave, and hence will affect schemes that depend on the zero crossings, such as phase comparators.
- The relaxation current in the CT secondary is the current that flows when the primary circuit is de-energized. This current is more pronounced in the case of CTs with an anti-remanent air gap. The relaxation current can delay the resetting of low-set overcurrent relays and also cause the false operation of breaker failure relays.
- VTs and CCVTs can be subjected to ferroresonance. This phenomenon leads to overvoltages, which can lead to misoperation and (thermal and dielectric) failure.
- The reduction of the primary voltage to zero creates a subsidence transient on the CCVT secondary, because of the stored energy in the capacitive and inductive elements. This transient affects the speed of the protection scheme and can cause relay misoperation for reverse faults.

This section presents a summary of the models proposed to represent instrument transformers in power system transient analysis. For more details readers are referred to the specialized literature [10, 11, 31–52].

11.3.2 Current Transformers

Figure 11.2 shows the conventional equivalent circuit of a CT [10, 11, 31]. One of the main concerns in this model is the representation of the nonlinear magnetization characteristic. The CT iron-core saturates whenever flux inside the CT core exceeds the saturation level, resulting in a distorted and reduced secondary current that may cause relay misoperation. Under normal operating conditions, a CT operates below the saturation flux density (the knee) and the exciting current drawn is small. Under heavy fault conditions, saturation may be reached. However, CTs cannot saturate immediately upon the fault inception. The time that it takes to begin the CT saturation is called time-to-saturation. An accurate representation of the magnetization characteristic should include the hysteresis loop and should simulate minor loops. Interwinding capacitance can be neglected at the frequencies of interest in protection studies.

To study the impact of saturation, the CT equivalent circuit may be represented as shown in Figure 11.3. The CT primary wire resistance and inductance can usually be neglected. The CT secondary wire inductance may also be neglected, although in some cases it may be taken into consideration. The magnetizing branch L_m can be modelled on either the primary or the secondary side. Modelling on the secondary is preferred because *V–I* curve measurements are regularly performed from the CT secondary. The magnetizing branch is represented by a nonlinear inductor whose nonlinear characteristic is specified in piecewise linear form by the user.

Since the flux-current data points are not readily available, some tools provide a routine to convert the rms *V–I* characteristic into an equivalent flux-current set. Some routine version extrapolates the λ–*I* curve using the slope defined by the last two points of the λ–*I* data set. If *V–I* curve data is such that the slope is

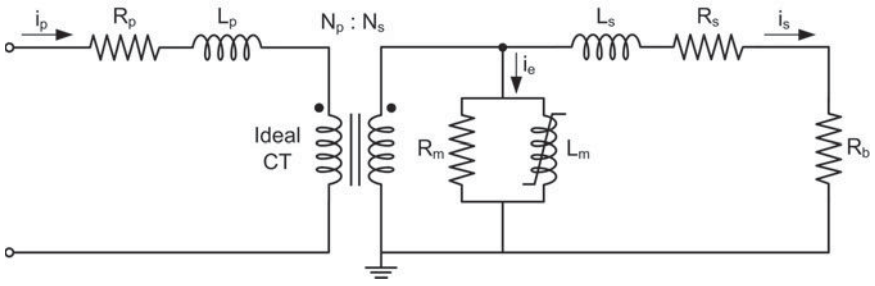

i_p	Primary current
i_s	Secondary current
i_e	Exciting current
R_p, L_p	Primary winding resistance and leakage inductance
R_s, L_s	Secondary winding resistance and leakage inductance
L_m	Magnetizing inductance
R_m	Core loss resistance
R_b	CT burden resistance, including lead resistance

Figure 11.2 Equivalent circuit of a current transformer.

not monotonically decreasing, then the λ–I curve may get extrapolated at a higher slope. This may result in incorrect response. The problem may be solved by adding an additional point to the V–I curve to ensure that the λ–I curve slope appropriately represents deep saturation region. When using branches external to the transformer model to represent L_m, the CT secondary winding resistance must be connected on the burden side of L_m. This means that it is necessary to set the winding resistance in the transformer model to near zero (e.g. 1 μΩ) and include the correct winding resistance in the connected burden.

Hysteresis representation is important if the study is intended to include the effects of remanence on CT performance. If the model cannot represent the hysteresis, it still may allow the specification of a steady-state flux level at the beginning of a study. Specification of an initial value of flux will simulate the presence of remanent flux as if the model had included hysteresis. Models that do not allow specification of initial value of flux and do not represent hysteresis are valid and produce satisfactory results for studies where remanent flux is not a concern.

Modern microprocessor-based protection devices have very low impedance that may be neglected when considering the saturation. The impedance of the CT wire and the leads that interconnect CTs and

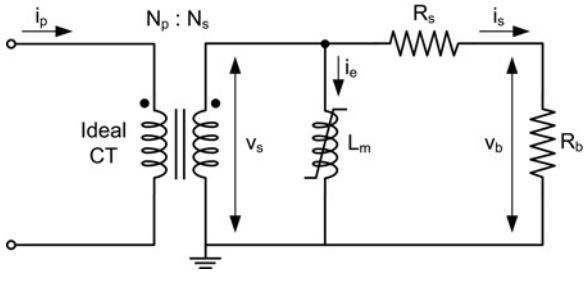

Figure 11.3 Current transformer model for relay protection applications.

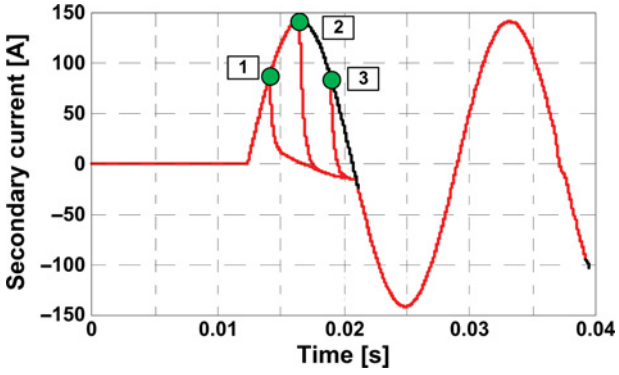

Figure 11.4 Impact of remanence for symmetrical fault currents: (1) 80% remanent flux, (2) 0% remanent flux, (3) −80% remanent flux.

protective relays should be represented when studying the CT saturation. The R_b value is usually provided, and it may represent a combined CT secondary winding resistance, lead resistance and CT burden.

CT saturation can be caused by any or a combination of the following events:

- symmetrical short-circuit currents, which can cause CT saturation if the CT secondary voltage exceeds the saturation level
- asymmetrical short-circuit currents, which can cause CT saturation at smaller current magnitudes compared to symmetrical short-circuit currents due to the DC component
- remanent flux in the CT core, which reduces the margin for flux increase in one direction and leads to earlier saturation (i.e. reduces time-to-saturation) if the fault current creates flux in the same direction as the remanent flux (positive remanence) – however, if the fault current creates flux in the opposite direction of the remanent flux (negative remanence) this will extend the time to saturation.

A remanent flux will only be marginally reduced by a load current. The load current will only require a flux that is a small fraction of the saturation flux. Therefore, the remanent flux may remain practically unchanged for a long period. To remove the remanent flux, one method is to saturate the CT core by applying the voltage at the CT secondary winding while having the primary winding open. The voltage is increased until the CT saturates and then is slowly reduced to zero.

Figure 11.4 shows the impact of remanence on a CT without an air gap for symmetrical and asymmetrical 60 Hz fault current 20 times the CT-rated current and at rated resistive load. The secondary current is shown for a remanent flux (remanence) of +80%, 0% and −80% of the saturation flux. This figure shows how a +80% positive remanence reduces time-to-saturation to about 2 ms, while time-to-saturation for 0% remanence is about 5 ms. For −80% remanence nearly no saturation occurs in the first half-cycle.

Validation of the V–I curve model: Validation tests have shown that the CT model shown in Figure 11.2 can reproduce with good accuracy the rise of the flux in the core during a fault with maximum DC offset, the behaviour of the flux-current loops under transient conditions, the actual secondary current (which can differ severely from the ideal one) and the effect of the remanence on the onset of saturation [39, 42]. The CT *V–I* curve of a 1200/5 A CT was represented using different number of linear segments. The influence of the *V–I* curve slope in the nonlinear region was also investigated. To obtain a reference waveform of saturated CT, one 1200/5 A CT was tested in a high-power laboratory. Primary and secondary CT currents, referred to the primary, are shown in Figure 11.5. The CT saturation was considerable in the first three cycles. Computer simulations did not produce accurate results when *V–I* curve modelling was

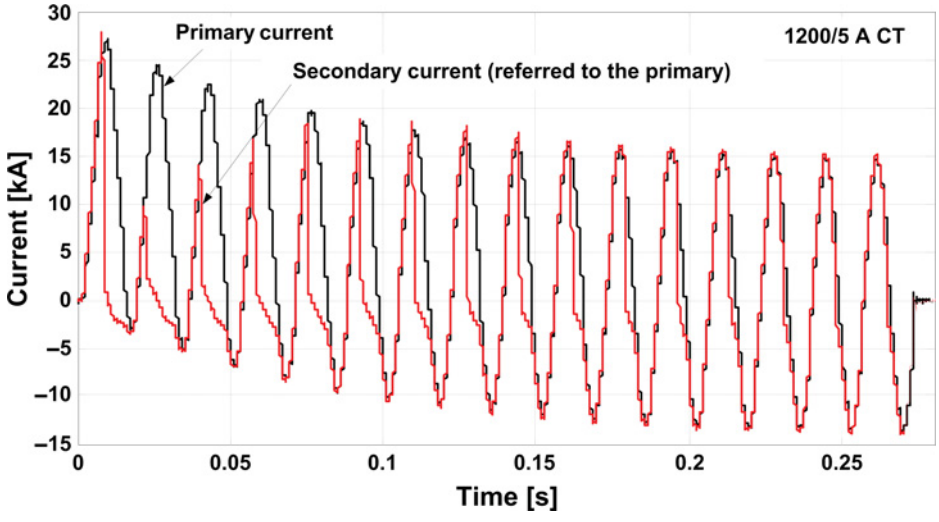

Figure 11.5 1200/5 A CT primary and secondary currents (laboratory test).

based on published *V–I* curves, since this is a region where CTs do not saturate. The number of *V–I* curve segments used for modelling was not relevant. Figure 11.5 shows a flux-current curve modelled using eight segments. Figure 11.6 confirms that modelling did not accurately replicate the laboratory test results. The same conclusion applies when a flux-current curve was modelled using two segments. Figure 11.7 shows a flux–current curve modelled using two segments. For proper CT modelling it is important to extend the last segment of the *V–I* curve to the deep CT saturation region by extending the *V–I* curve with the same slope. The second segment was extended with the same slope by multiplying current 10 times. The simulation results shown in Figure 11.8 demonstrate that the extension of the nonlinear region of the CT *V–I* curve can be more important than the number of flux–current segments. As a conclusion, to obtain realistic results, it is enough to represent the CT *V–I* characteristic with only two slopes but with an extended segment.

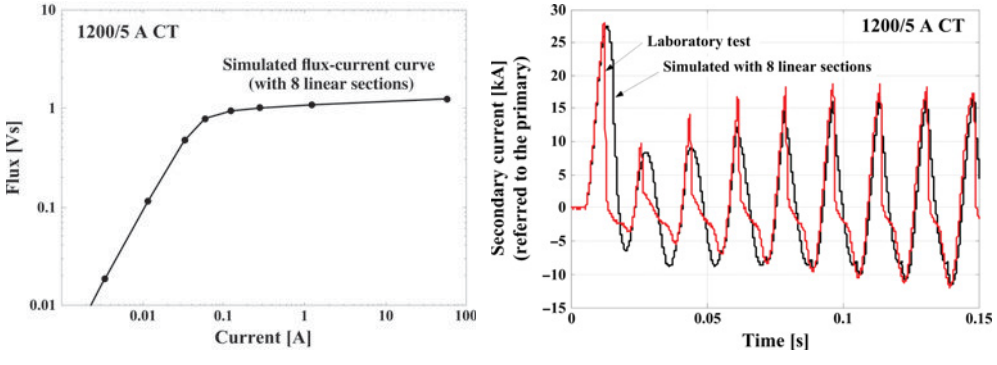

Figure 11.6 Simulated CT response with eight linear segments: (a) flux-current curve, (b) CT response.

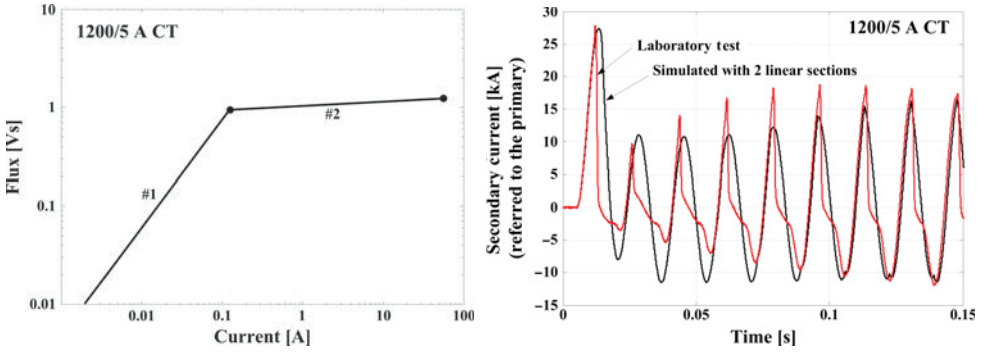

Figure 11.7 Simulated CT response with two linear segments: (a) flux-current curve, (b) CT response.

11.3.3 Rogowski Coils

Rogowski coils consist of a wire wound on a non-magnetic core. The coil is placed around the conductor whose current is to be measured, as shown in Figure 11.9 [52]. If the core has a constant cross-section S and the wire is wound perpendicular on the core centre line with constant density n, then the coil output voltage is defined by the following equation:

$$v(t) = -\mu_0 nS\frac{di(t)}{dt} = -M\frac{di(t)}{dt} \tag{11.1}$$

For an ideal Rogowski coil, mutual inductance M is independent of the conductor location inside the coil loop. The Rogowski coil equivalent circuit and vector diagram are shown in Figure 11.10 [52]. A Rogowski coil signal is a scaled-time derivative di/dt of the primary current. To use such signals with phasor-based protective relays, signal processing is required to extract the power frequency signal. This may be achieved by using one of two methods: (a) integrate the Rogowski coil output signal, or (b) use the non-integrated Rogowski coil output signal and then perform signal processing to adjust the magnitude and shift the phase signal by 90°.

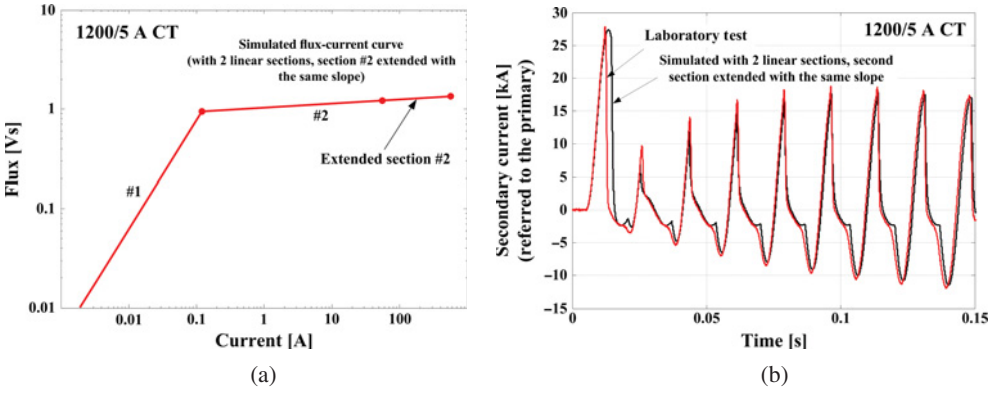

Figure 11.8 Simulated CT response with two linear segments (second segment extended): (a) flux-current curve, (b) CT response.

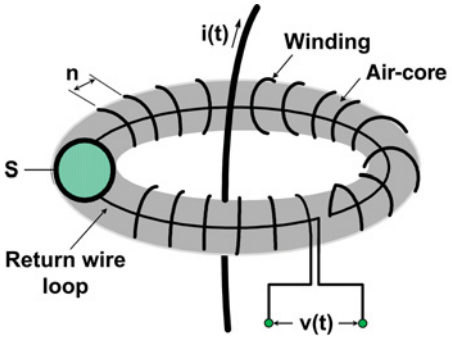

Figure 11.9 Principle of the Rogowski coil design.

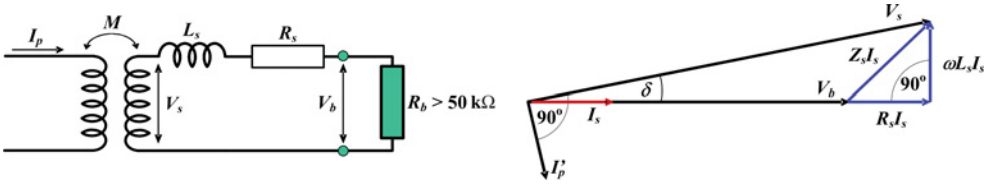

Figure 11.10 Rogowski coil equivalent circuit and vector diagram.

The non-integrated Rogowski coil signal is shifted 90° with respect to the primary current, as shown in Figure 11.10. Figure 11.11 shows a Rogowski coil signals for both symmetrical and asymmetrical fault currents.

To prevent the influence of nearby conductors that are carrying high currents, Rogowski coils are designed with two wire loops connected in electrically opposite direction. This cancels electromagnetic fields coming from outside the coil loop. This other loop can be formed by returning the wire through the winding or near the winding. Another solution is to add an additional winding wound in the opposite direction over the existing one or placing the second winding near the first winding.

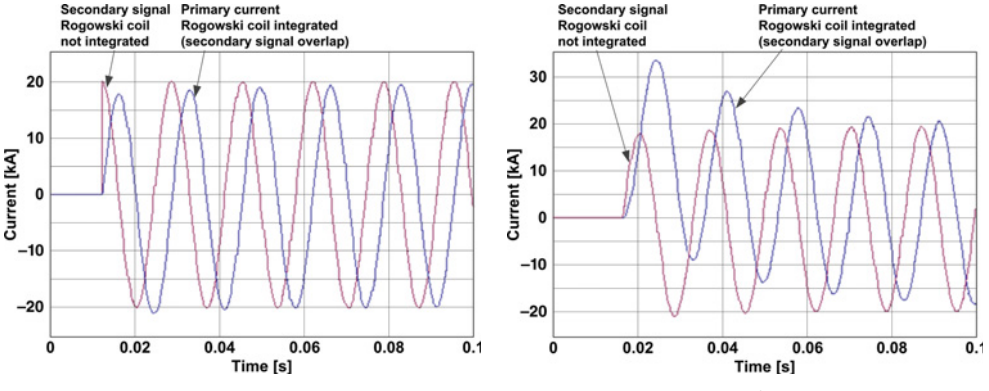

Figure 11.11 Rogowski coil signal for fault currents: (a) symmetrical fault currents, (b) asymmetrical fault currents.

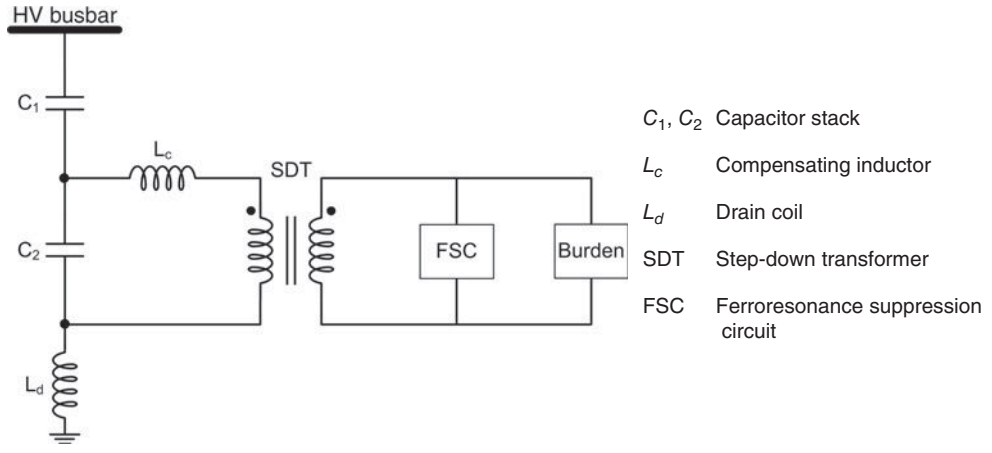

Figure 11.12 A CCVT circuit connection.

11.3.4 Coupling Capacitor Voltage Transformers

Coupling capacitor voltage transformers (CCVTs) are widely used in high-voltage power systems to obtain standard low-voltage signals for protective relaying and for measuring instruments. They are usually designed as standalone single-phase units. A CCVT transforms the line voltage to low voltage through a sequence of capacitive potential dividers and an electromagnetic voltage transformer (VT). A typical circuit connection is shown in Figure 11.12 [10,11, 31]. A relatively heavy current may be drawn from the protective device when the burden is an electromechanical relay; in such a situation a large error can result. To avoid this problem, the loading effect on the capacitive divider is tuned by a compensating reactor on the primary side of the VT. An additional circuit, designed to suppress ferroresonance, is added on the secondary side. All these components make circuitry quite complex and influence its transient response.

The CCVT equivalent circuit can be represented as shown in Figure 11.13. The main components are coupling capacitors (C_1 and C_2), compensating inductor (R_c, L_c, C_c), step-down transformer (R_p, L_p, C_p, C_{ps}, R_s, L_s, C_s, L_m, R_m) and ferroresonance suppression circuit [10, 11, 31].

Ferroresonance may occur in a circuit containing capacitors and iron-core inductors. It is usually characterized by overvoltages and distorted waveforms of currents and voltages. Ferroresonance suppression circuits (FSCs) are incorporated in CCVTs [44] and designed to attenuate ferroresonance quickly after it occurs. The FSC may have considerable effect on the transient response of the CCVT. There are several FSC designs. A very common FSC design includes capacitors and iron core inductors connected in

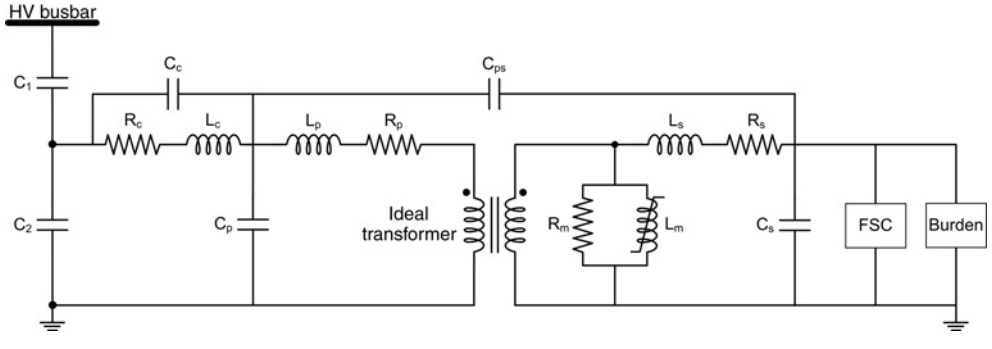

Figure 11.13 CCVT detailed equivalent circuit.

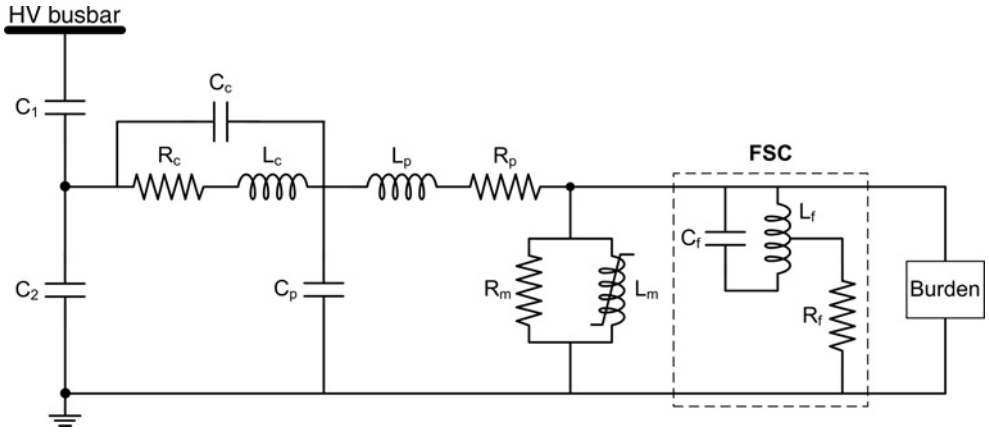

Figure 11.14 Reduced CCVT model with ferroresonant suppression circuit.

parallel and tuned to the fundamental frequency. They are permanently connected on the secondary side and affect the CCVT's transient behaviour (Figure 11.14). Capacitor C_f is connected in parallel with an iron core inductor L_f, tuned to the fundamental frequency. Resistor R_f is a damping resistor designed to damp ferroresonance oscillations within one cycle. The circuit is tuned with a high Q factor in order to attenuate ferroresonance oscillations at any harmonic except the fundamental. A second design includes a resistor connected on the step-down transformer secondary side. Another option is to have a gap or an electronic circuit connected in series with the resistor, which is activated whenever an overvoltage occurs. FSCs do not affect transient response unless an overvoltage occurs.

The FSC can be modelled using the non-saturable transformer. The calculated L_f value must be incorporated in the transformer model as a self-inductance. Primary and secondary windings are connected in such a way that parallel resonance occurs only at the fundamental frequency. At other frequencies, only the leakage inductance is involved, so the damping resistor is the one that attenuates ferroresonance oscillations. Comparison between the FSC frequency response obtained by measurement and performing a transient simulation of a CCVT is shown in Figure 11.15.

Validation tests performed without stray capacitances have shown that the CCVT model can reproduce the subsidence transients and the ferroresonance behaviour – see, for instance, [38,39]. Simulation results

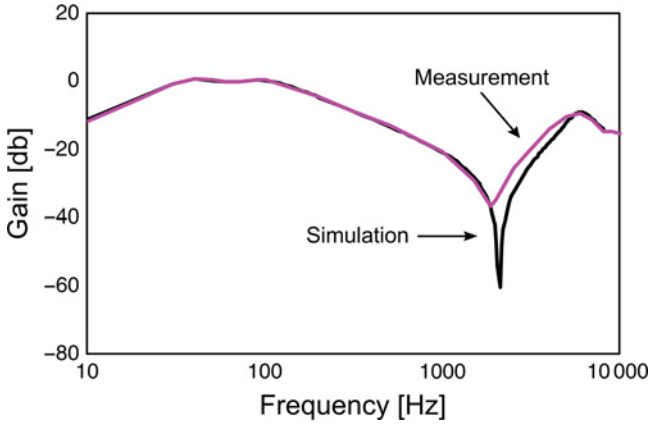

Figure 11.15 CCVT frequency response (measured vs. computer simulation).

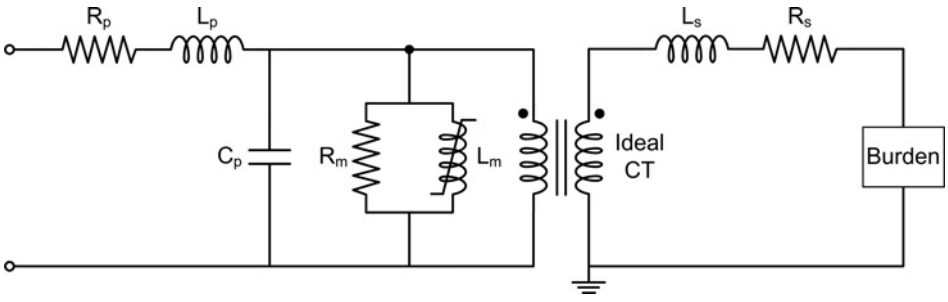

Figure 11.16 Voltage transformer model.

show that (1) the magnetization inductance has a negligible effect on the subsidence transients, (2) the magnitude of the subsidence transient increases with an increased burden and when the values of the divider capacitances are decreased, and (3) the subsidence transient has the largest magnitude and lasts the longest time when the fault occurs at a primary voltage zero.

11.3.5 Voltage Transformers

Modelling of magnetic voltage transformers is similar to modelling any other power transformer. Figure 11.16 shows one model that can be used to accurately simulate the transient response of VTs [10, 11, 31].

11.4 Relay Modelling

11.4.1 Introduction

To develop a relay model it is necessary to have a general knowledge of all the parts involved in its design and operation. The accuracy of a model could depend on many factors, such as the aim of the simulation (concept verification, performance evaluation, education), the simulation tool in which the model is to be implemented, the relay technology or economic considerations.

The development of a relay model for use in transient simulation will usually follow an iterative process. The first step is to identify and implement the components of the relay to be modelled, depending on the studies to be done. Once a model has been developed, it should be validated to confirm that it can represent the behaviour of the original relay under the conditions to be studied. If the developed model meets the requirements, the modelling process is complete. If it does not, the components that need to be remodelled or additional components that need to be added should be identified and a revised model should be developed. This revised model should again be validated. The process is continued until a suitable model is achieved.

The rest of this section is dedicated to classifying the various relay models developed to date and summarizing the models proposed, taking into account the relay technology. Some illustrative examples are included.

11.4.2 Classification of Relay Models

Different types of relay models have been developed and used. The classification may be based on the source of input waveforms, relaying system structure, modelling details and relay technology [12].

- *Input waveforms*: Two different types of relay models can be defined based on the source of the input waveforms [53]: (1) steady-state models, (2) transient models. *Steady-state models* use mathematical

equations to represent a relay characteristic that is valid for stationary voltages and currents, without any consideration of transients. The models should reflect all the relations between phasors in the original relays (e.g. relations between voltage and current phasors). These models can be used to: (1) evaluate the relay design concept and its main characteristics, (2) make general decisions regarding the selection of the protection type, (3) calculate the relay parameters (or settings), (4) evaluate the relay settings which determine the relay actions (pickup or tripping signals) initiated by network calculation results, or (5) establish relay coordination margins. Some slow dynamics, such as power swings, may also be evaluated using static phasor-based models. Although these relay models are included in some commercial software packages, they cannot provide all the information that is required in transient studies. *Transient models* use instantaneous samples obtained from a transient simulation tool, from sampled data recorded by digital fault recorders (DFRs) or from numerical relays during actual power system disturbances. They are more sophisticated models and include the time behaviour and the dynamics of the relay. A transient model is needed when the relay behaviour is evaluated under actual fault conditions. This type of model can be used to investigate the behaviour of the relay models in front of critical transients or during network disturbances (e.g. time sequence of tripping commands or pickup signals) or analyse the influence of parameter changing on the protection behaviour.

- *Relaying system structure*: From this point of view, the models can be divided into two categories: structural and black-box models. *Structural models* mimic the actual relay by adequately representing its internal structure; they are applicable when a detailed relay description is available and imitate relay performance on the basis of mathematical models of the physical phenomena. *Black-box models* reflect the relay performance by mapping input signals to the output, without taking into consideration the internal logical or physical structure of the relay.
- *Model details*: The models can be divided into two categories: detailed and generic [53]. A *detailed model* reproduces the characteristics, algorithms and behaviour of the actual relay in detail. This approach models every component of the relay, as well as interactions between components. These models can be very complex and may require long simulation times. Obviously, they can be developed only when there is a full knowledge of the relay structure and parameters. Practically, only manufacturers can develop such models. A *generic model* is based on the relay performance and characteristics. It is a simplified model that behaves in a similar manner to the relay, within specified and clearly understood bounds. Such a model does not represent all performance specifications of a relay, since in many situations there is no reason to use a detailed model. In addition, the required information may not be available. In general, a generic model reproduces frequency and dynamic features of the original relay. Although generic models are rather easy to develop, and give considerable insight into the operation of the relay type, they may not be adequate for some marginal cases and for precise timing.
- *Relay technology*: The relay models reflect the technology used in relay construction. The following three groups of relays should be considered [10,11]: electromechanical, static (electronic) and numerical (microprocessor-based). To model *electromechanical relays,* relay dynamics must be adequately represented [54–56]. In the case of *static electronic relays,* the representation of electronic elements is the most critical issue [57–59]. Detailed models of the *numerical relays* represent measurement and decision-making algorithms in the same or similar form as in the physical relay [7, 15, 18–20, 60,61]. The relay protection function can be modelled by simply transferring the corresponding relay firmware module to the simulation environment [62]. Numerical relays also have analogue circuitry that can be adequately included and represented in the protection scheme model [16].

11.4.3 Relay Models

11.4.3.1 Electromechanical Relays

Electromechanical relays are difficult to model because they involve complex combination of mechanical, electrical and magnetic phenomena. A schematic representation is shown in Figure 11.17.

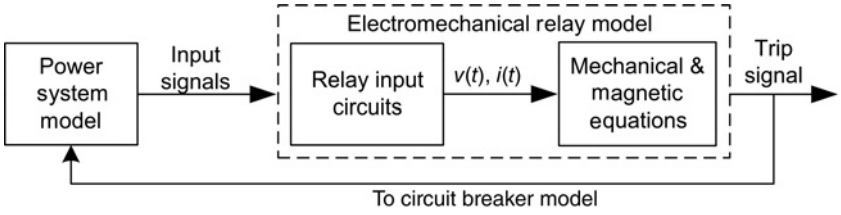

Figure 11.17 Schematic diagram of an electromechanical relay model.

References [55, 56] present the modelling of electromechanical type-50 overcurrent relays as three subsystems: electrical, magnetic and mechanical. This approach offers some advantages: for example, the three subsystems can be developed separately and combined as desired. The electrical subsystem represents the relay burden impedance as a function of frequency and magnitude of the input current, see Figure 11.18. Because the relay can saturate at high current levels, the nonlinearity of the burden has to be represented. In [55, 56] this nonlinearity was modelled as one lumped nonlinear inductance. The linear part of the electrical equivalent circuit was synthesized from frequency scan tests at very low current levels to avoid saturation. The mechanical action of the relay was simplified to a second-order system involving mass, spring and dashpot. A free-body diagram was drawn and the mechanical forces, together with the magnetic force due to the current flowing in the relay coil, were summed up to zero. The mass, spring constraint and friction constant were estimated from direct measurements of the relay components. The magnetic force acting on the armature or plunger of the device was calculated from the magnetic subsystem of the model. The current through the coil was considered as an input. With known number of turns, the magnetomotive force (MMF) was determined. The reluctance of the magnetic structure was calculated for the dimensions of the device and known magnetic properties of the material. The analytical expression of the reluctance included the time-varying air gap of the device when the armature (or the plunger) was in motion.

An example of the mechanical and magnetic parts of the relay model is shown in Figure 11.19 as a block diagram. The complete model was implemented using a combination of electrical circuit modelling for the electrical subsystem (Figure 11.18) and a control section for mechanical and magnetic subsystems (Figure 11.19). The model was verified extensively against experimental results for a variety of transient fault conditions. The agreement between the operating times of the model and the actual device was typically within 2–3 ms.

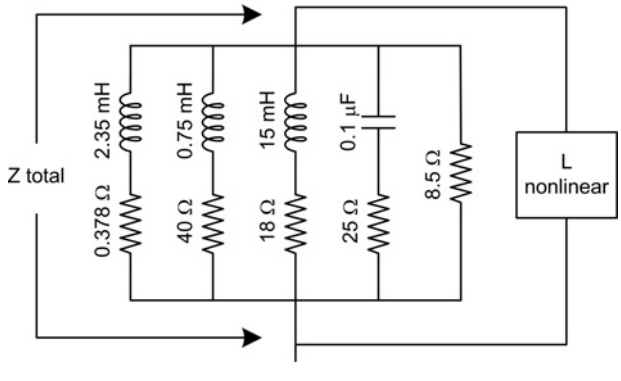

Figure 11.18 Equivalent circuit of armature relay impedance (© 1996 IEEE) [55].

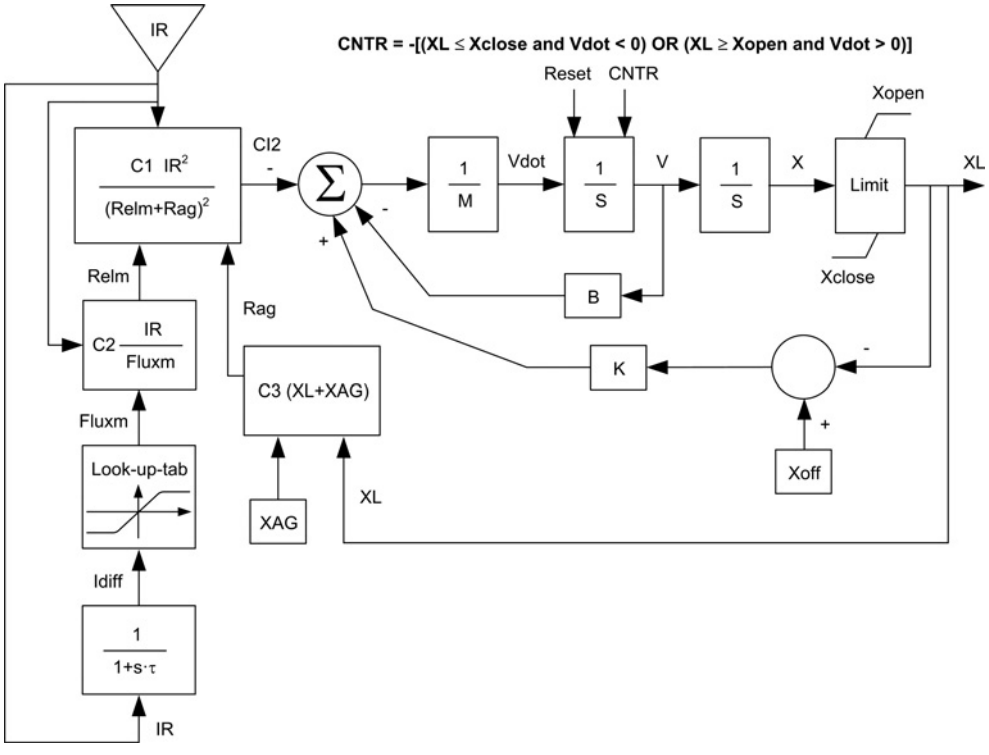

Figure 11.19 Block diagram of an armature relay model (© 1996 IEEE) [55].

11.4.3.2 Electronic Relays

Static electronic relays use solid state components such as transistors, diodes, gates, flip-flops, comparators, counters, level detectors and integrators. They were mainly developed from the late 1960s until the early 1990s. In distance relays, this technology offered higher speed and greater accuracy than electromechanical relays.

Several computational tools have been used to simulate static relays. One of the earliest static relay models, a distance relay for phase-phase fault detection, was presented in [57]. The general approach was to develop a separate standalone FORTRAN subroutine for each major relay component, such as a transactor, a block-average phase comparator or a series RLC filter.

A static mho phase distance relay intended for the protection of transmission lines was modelled using an EMTP-like tool [58, 59]. The relay model had a tendency to overreach during the verification of the steady-state testing of the mho characteristic. One reason for this overreach could be the initialization of control variables for the fault at $t = 0.0-$. Those results proved the importance of the filter circuits in the development of the exact relay model and the necessity of an accurate prefault simulation.

11.4.3.3 Microprocessor-Based Relays

Modern numerical microprocessor-based relays include frequency tracking algorithms to make relays insensitive to frequency excursions. They may also include additional protection functions such as directional elements, detection of power-swing, computation of sequence quantities and phase selection logic [60–62].

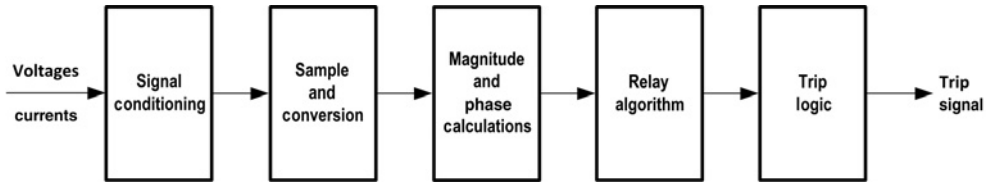

Figure 11.20 Schematic diagram of a microprocessor-based relay.

Some protection algorithms are based on voltage and current phasors. Since a time-domain simulation tools calculate voltage and current waveforms as functions of time, it may be necessary to convert the sequences of the values of voltages and currents to their equivalent phasors as functions of time. This conversion can be done by using signal-processing techniques such as the *discrete Fourier transform algorithm* [7] and the *least squares algorithm* [63].

Currents and voltages during faults contain components of high frequencies. To obtain phasor values of voltages and currents, many digital relays first have to sample (digitize) the input voltages and currents, then recover the estimates of the phasor values. To prevent aliasing, digital relays must have an input anti-aliasing (low-pass) filter [64].

Microprocessor-based relays convert the analogue information to numerical form using sampler and analogue-to-digital converters (ADCs). The A/D conversion process can be considered as a two-stage process, consisting of a sampler and a quantizer. The first stage creates the sequence $s(n)$ by sampling the analogue signal $s(t)$ at regular intervals of Δt seconds. This part of the process is usually considered accurate and without any addition of errors. The second stage expresses each sample of the sequence $s(n)$ by a finite number of bits giving the sequence $s_q(n)$. The difference between the elements of the sequence $s_q(n)$ and $s(n)$ is the quantization noise (also called A/D conversion noise). The quantizing process can either truncate the signal (as it converts the analogue information to numerical form) or round it. The quantizer stage may be skipped for some cases. Depending on the accuracy requirements of the relay model, the values obtained from the sampler may be directly used for phasor calculations and for modelling relay algorithm and/or relay dynamics.

The general organization of a numerical microprocessor-based relay can consist of several sections or submodels, as shown in Figure 11.20 [60–62]: (1) the first section may include input auxiliary transformers and anti-aliasing low-pass filters, (2) the second section may be the ADC, (3) the third section is the detector that estimates fundamental frequency information, (4) the relay measuring principles are next, (5) finally, a section that represents the trip logic.

The main limitation of relay models may be the level of approximation used to represent an actual relay. The existing practice in the industry is to make available only limited information regarding relay design and its behaviour. This is particularly true with microprocessor-based design. Most of the information provided in relay manuals is given in a form of operating characteristics and related phasor equations. In general, this description is not sufficient for a full description of the relay behaviour under transient conditions.

It is important to recognize that the limitations of relay models are relative, depending on their application. If the purpose is to provide general education about relay designs and behaviour, phasor-based models may suffice. If the purpose is to determine actual behaviour of a relay under fault condition, phasor-based models can be quite limited and very often inaccurate.

Example The general organization of the distance relay model presented in [60] is shown in Figure 11.21. According to the diagram the model is divided into four sections or submodels whose roles within the model are analysed below.

1. *Low-pass filter model*: The first section consists of the input analogue anti-aliasing low-pass filter. The model uses a third-order Butterworth design and has a 3 dB roll-off frequency of 235 Hz. The

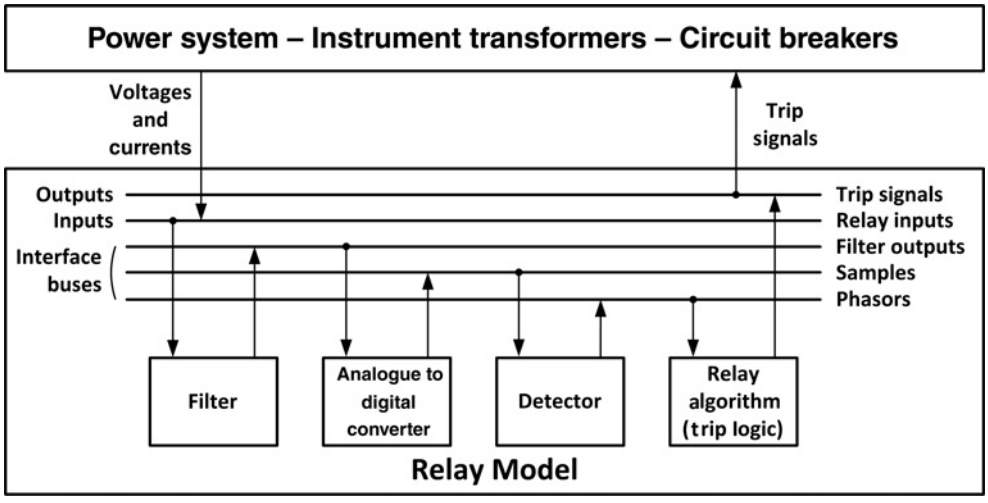

Figure 11.21 Diagram of a distance relay model and interface to the power system model.

frequency, order and design were listed in the manufacturer's instruction book for the actual physical relay. The Butterworth filter with a roll-off frequency of 1 radian/second has poles equally spaced along a unit circle in the complex plane and located at: (1) $p_1 = -1.0 + \text{j}0$; (2) $p_2 = -0.5 + \text{j}0.866$; (3) $p_3 = -0.5 - \text{j}0.866$. The transfer function is:

$$H(s) = \frac{1}{(s - p_1)(s - p_2)(s - p_3)}. \tag{11.2}$$

For a filter with a roll-off frequency of 235 Hz, a simple frequency scaling results in: (1) $p_1 = -1476.5 + \text{j}0$; (2) $p_2 = -738.3 + \text{j}1278$; (3) $p_3 = -738.3 - \text{j}1278$. The denominator polynomial becomes: $s^3 + 4.3604 \times 10^6 s + 3.219 \times 10^9$.

2. *Analogue-to-digital converter model*: An ADC model was implemented to sample the 60 Hz fundamental eight times per cycle (480 Hz). The model receives a vector of dimension four as input, and produces an output vector of dimension one greater than the number of samples per cycle. This model produces four vector outputs of dimension nine. The first and the last entries in the output vector correspond to samples of the input signal one cycle apart.
3. *Detector model*: The relay uses a Fourier notch filter. The Fourier detector recovers fundamental frequency (phasor) information. The purpose of the detector is to estimate the real and imaginary components of the fundamental frequency phasor. The implemented detector is a recursive-realization of a discrete Fourier transform; it is a three-phase (plus zero sequence) Fourier detector that recovers Fourier coefficients from a single-phase input signal. Both inputs to and outputs from this model are vectorial. Four different phase-specific vectors are the inputs. For the inputs, the vector components correspond to different samples in time. There are two output vectors of the real and imaginary Fourier components.
4. *Distance measuring unit model*: The relay uses the mho relay measuring principle and makes decisions whether to open the circuit breaker. The circular mho relay characteristic was developed from comparisons made between two different inputs. The inputs are called S1 and S2. The equations for the two inputs to the comparator are all that needs to be known for steady-state modelling. In this study the S1 signal is called the operating signal and S2 the polarizing signal. The trip decision can be made with an amplitude or phase angle comparison criteria.

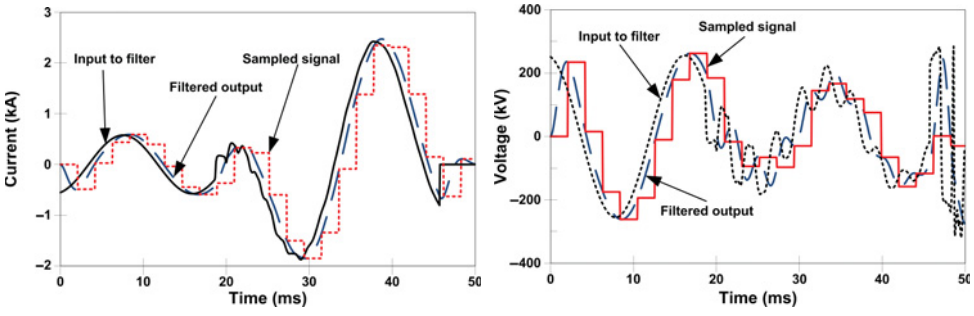

Figure 11.22 Filtered and sampled signals from a single-phase-to-ground fault: (a) current, (b) voltage.

Models of the uncompensated, self-polarized and zero-sequence compensated, quadrature-voltage polarized mho measuring units were implemented:

- For a phase A, self-polarized mho characteristic, the two inputs are:

$$S_1 = I_a Z_{cg} - V_{fa} \qquad S_2 = V_{fa}. \tag{11.3}$$

- For a phase A zero-sequence compensated quadrature-voltage polarized mho characteristic, the two inputs are:.

$$S_1 = \left(I_a - kI_0\right) Z_{cg} - V_{fa} \qquad S_2 = V_{fbc}, \tag{11.4}$$

where I is the secondary current, k is the zero-sequence compensation factor ($= (Z_0 - Z_1)/3Z_1$), Z_0 is the zero-sequence transmission line impedance, Z_1 is the positive-sequence line impedance, Z_r is the relay replica impedance and V_f is the voltage at the relay location.

The relay model can be enhanced by including zones of protection and the ability to vary setting parameters according to the specific application. Communications between relay macromodels at each end of the line can also be simulated; that is, the model can simulate the time interval required to transmit a digital signal from one end of the line to the other. A time delay of 8 ms, commonly used in laboratory relay testing, was used for the simulations. See [10, 65] for more details.

Figure 11.22 shows some simulation results corresponding to a single-phase-to-ground fault; they illustrate the way in which voltages and currents inputted to the relay model are filtered and sampled for further manipulation.

11.5 Implementation of Relay Models

11.5.1 Introduction

A relay model is composed of modules representing its various parts, and can be developed using either a single tool or a combination of different software and hardware platforms [66, 67].

The behaviour of a relay model can be simulated and checked by interfacing the relay model to the power system model. Instrument transformers are the physical interface between relays and power systems. To make sure that the relay inputs are properly specified during the simulation of a given event, the representation of instrument transformers is very important [31]. One important issue is the influence of the relay burden on the transformer response. An equally important part of the interface is the effect of relay operation on the circuit breaker operation during a fault clearing sequence. The operation of circuit breaker contacts may need detailed investigation to determine how the switching

that takes place during the fault clearing affects the power system behaviour. An adequate model for the communication system is also fundamental to analysing relaying systems with communication. For detailed modelling of the communication system, the following basic features of the physical system should be represented: (1) signal form (analogue or digital), (2) signal transmission media (wire pilot protection, power line carrier pilot protection, microwave pilot protection, fibre optic communication), (3) pilot protection scheme (unit or non-unit scheme). A combined simulation of the protection system and the communication system requires coordination in different substations concerning synchronized or non-synchronized sampling.

A crucial aspect is to properly reflect dynamic interactions between the power system and relays during fault events as well as during normal operations that cause disturbances that may be misinterpreted as faults. A relay model evaluated with *playback* waveforms in an *open-loop* simulation has no influence on the power system from which the input signals are derived. Input signals can be delivered in a form of a file containing the recorded data or directly from EMTP-like tools via a suitable interface [68, 69]. Output and intermediate signals are stored for further analysis, and the model can represent the complete relay or only a separate unit. In a *closed-loop* evaluation, the relay model is included in the general protective system model, so the transient simulator must be able to accept the output information from the relay model and use this information in ongoing simulation. In this case, the model should represent the behaviour of the complete relay.

The various computational procedures can be implemented, by taking advantage of capabilities available in general-purpose circuit-based tools, such as the EMTP [59, 70, 71], or using generic programming platforms, such as Matlab/Simulink. This section provides a discussion of the sources of information and software tools for building relay models, implementation options and interface of relay models to recorded data.

11.5.2 Sources of Information for Building Relay Models

To develop a reliable relay model, it is necessary to know the details of the design and the operation characteristics of the relay. This knowledge can be obtained from technical design characteristics and operation data of all relay elements (transducers, filters, A/D converters, etc.), tests results carried out on the relays and information on the algorithms that govern the relay operation. The development of a model may be relatively simple for digital relays, provided that sufficient information about the algorithms is available. For static and electromechanical relays, as well as for the analogue sections of digital relays, a detailed modelling is a non-trivial task.

Manufacturers: A relay engineer using the manufacturer's instruction book and some discussion with the manufacturer can create a relay model. Manufacturers usually release a certain amount of information. The available sources of information may include service, instruction or technical manuals, application or relay setting notes, type testing and approval documentation and technical description of the components. With some exceptions, relay circuit diagrams and algorithm source codes are usually not available for confidentiality reasons. The electronic component description is usually available in the form of technical data specifications or catalogues, which allows a mathematical model of such components to be built. If the available data is not sufficient for building a complete model, at least it can be used to calibrate generic simulation models. Moreover, some technical data sheets include a ready-to-use simulation model for the specific simulation software, which can be used to capture the dynamic behaviour of the specific components. Items described in the manufacturer's data sheet include the nature and cut-off frequency of the anti-aliasing low-pass filter, the primary sampling rate and the relay's sampling rate.

The information provided by the manufacturer gives some appreciation of the relay's operating principle. The most fundamental source of information is always the instruction manual, but the full documentation is very rarely available. Often the model that is created on the basis of manufacturer's description of operation does not fully correspond to the actual dynamic behaviour of the relay. Therefore, it is important to perform an extensive validation procedure in order to assess the accuracy of the simulation results under varyious power system fault conditions and, if possible, introduce additional corrections to the relay model.

Published literature: This includes books, papers, special reports, courses and patents. Most relaying principles are in the public domain, and in many industrial products, the proprietary information is minimal. Reference [72] presents a technique for implementing the sample-and-hold algorithm, while [73] describes the development of a computer-aided design tool for developing digital controllers and relays, including ADC modelling. Patents taken out by the manufacturer are very often a source of detailed information.

Relay test data information: Relay test data can be used to evaluate relay characteristics and support model development. This information includes some additional test data (apart from the standard tests performed by the manufacturers). In the past, it has been difficult to construct an accurate model because of insufficient availability of test facilities, which would allow the actual relay and the software model to be fed with exactly the same transients test waveforms. However, currently manufacturers carry out thousands of tests during product development using digital and analogue power systems simulators.

Test methods are evolving and are taking advantage of the advances in both test equipment and computers to allow more accurate modelling and testing of instrument transformers and protection relays. Digital simulators have been utilized for relay testing by providing an interface between simulation computers and relays to be tested. Several open- and closed-loop real-time simulators have been developed which provide an advanced relay testing capability. References [74–85] discuss some developments in digital simulators and relay testing methodologies. Many utilities have DFRs distributed across the whole power system, so waveforms of actual faults recorded in DFR files are becoming a valuable source of information to achieve more realistic protection system models. However, the dynamic range of the DFR measurements can limit accuracy of the information. Often a conversion to COMTRADE format is necessary before this information can be used for relay testing purposes [86]. Proper settings of protection relays are a prerequisite for a reliable operation. In the determination of the setting values, it is necessary to determine the fault values at various places at the time of fault occurrence. Also, it is necessary to consider the coordination task for the adjustment of multiple protective relays and different types of protective relays ranging from electromagnetic to digital ones [87–89].

Due to the increased availability of advanced relay testing equipment, it is becoming easier to obtain large volumes of empirical data from actual relays. In some cases, especially when the manufacturer's data is not available or the behaviour of the device or some of its components is particularly complex, empirical data can be used to develop a black box model.

11.5.3 Software Tools

Computer tools for development and implementation of relay models must facilitate a proper interface with the power system model and provide a flexible environment where the relay model can be tested and modified. Nowadays, it is possible to accurately simulate the dynamic behaviour of very large power systems using complex and detailed relay models.

General characteristics of the most common programs used in the development of relay models have been described elsewhere [10–12].

The most common approaches for development and implementation of a relay model are based on the use of general-purpose software tools. Some of them use only one software package while other models combine different software packages. When using an interface method, the power system is usually modelled with an EMTP-like tool, and the relay model is developed with different software.

Relay models have been classified according to the software tools used in the relay modelling:

- *EMTP-like tools*: This is the most common approach. Significant experience is currently available using EMTP-like tools (e.g. ATP, EMTP-RV, PSCAD). For a detailed list of works, see [12]. See also the case studies presented in Section 11.7.
- *Matlab/Simulink*: A modelling package implemented in Matlab for generating software models of any microprocessor-based relay using general-purpose relay is presented in [68].

Several other works have been based on Matlab/Simulink capabilities for modelling power systems and relay components in a unified environment [69, 90–92]. The hardware and software elements of digital relays have been reduced to their generic models and implemented as library blocks. For relay elements, those libraries include data acquisition board, digital filter, discrete Fourier Transform, basic measurement, differential equation-based impedance measurement, universal comparator, zone comparator, triggering element, symmetrical components and bias characteristics. The developed relay models can be tested with the input signal from SimPowerSystems [93], an EMTP-like tool or DFR data. Some works use a link between Matlab and an EMTP-like tool: the power system is represented in EMTP and the protection system models in Matlab [90, 91]; this approach allows the relay model to be implemented in a high-level language, so it can be more flexible and detailed.

Many other works have been based on other software tools and modelling techniques [94–98]. Artificial neural networks (ANNs) applied to protection system modelling eliminate the need to derive complex mathematical formulas for programming purposes, but once trained, the ANN cannot be modified without being retrained [99]. An integrated modelling environment for general modelling of power system protection is presented in [66, 100], in which the power system is simulated using ATP and the protection system is constructed with a hierarchical, object-oriented structure using the C++ programming language.

11.5.4 Implementation of Relay Models

The interface between relay models and the power system model, using either a single software tool or a combination of tools, can be realized by means of either open- or closed-loop interaction [12, 101]. Each method has its advantages and disadvantages and has to be selected depending on the type and purpose of the study.

Open-loop method: The principle is illustrated in Figure 11.23(a). Primary current and voltage waveforms are obtained from the transient response of the power system under fault conditions. Instrument transformer models use the simulated waveforms to calculate the secondary voltages and currents, which may exhibit distortion introduced by the transducers. Finally, the protection scheme model processes the secondary values and produces a protection system response. In many cases the immediate tripping response of the relay gives a sufficient answer for the simulated event, but in more complex scenarios it is impossible to obtain the correct answer.

Closed-loop method: It is particularly suitable for protection schemes involving tripping activity – see Figure 11.23(b). It is the most challenging option, since it requires the interaction between the power system and protection model on a step-by-step basis, regardless of the software tools involved in the

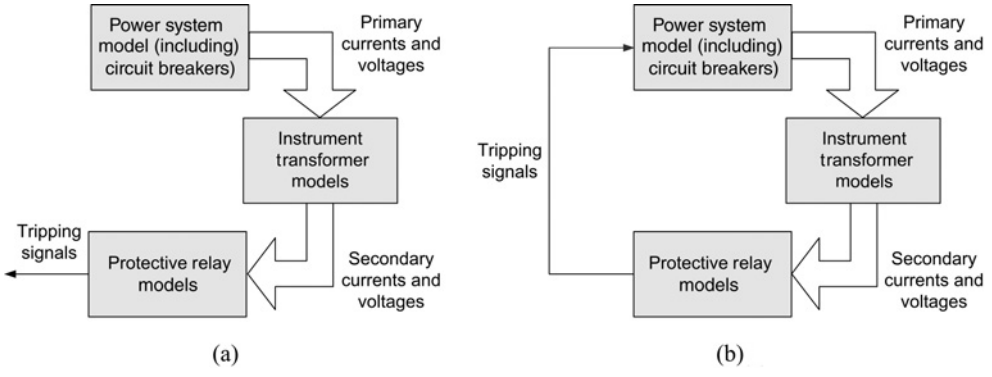

Figure 11.23 Interaction between power system and protection system: (a) open loop interaction, (b) closed-loop interaction.

calculations. Reference [102] gives an example of an interactive study on a double circuit case using Matlab models for the four relays involved, plus the communication link, running interactively inside an EMTP-like tool.

A third approach, known as *semi-closed loop method,* can be considered [12]. When the feedback from the protection scheme is limited to a few tripping/reclosing activities, it is possible to temporarily break the loop and run the whole simulation in a sequence. Knowing the response of the protection scheme to the disturbance gives the correct tripping of the circuit breakers. This involves another loop of simulation, which takes into account the initial response of the protection scheme and produces an amended protection system response. Should the new response differ in any way from the previous one, the simulation loop is repeated. This iteration continues until the same result is obtained from two consecutive protection system responses. This approach can potentially lead to lengthy simulations, especially in complex fault scenarios or in systems containing more than one protection scheme [102].

11.5.5 Interfacing Relay Models to Recorded Data

Sources of recorded data: Relay models can be validated by using recorded signals from the real power system or laboratory tests. The sources of recorded data that are used as input signals for actual relays and relay models are: (1) fault recorders installed in utility and industrial power networks, (2) field and laboratory tests performed to validate and test certain relay functions, (3) fault records available from modern numerical relays that are in service. An advantage of recorded data is that effects of instrument transformers, time-varying fault resistance and nonlinearities of the power system components are already included in the recorded fault data. Recorded data may be used to improve the system model. DFRs record analogue signals by periodically sampling them and converting the measured signals to digital values. Samples of voltage and current waveforms are recorded with a high sampling rate up to 10 kHz. However, a lower sampling rate is usually required by numerical protection relays and relay models. Most of the DFRs support as output file COMTRADE format [86]. The time resolution of fault data acquisition is rather low and lays in the range of 16 to 64 sampled values per system period (50/60 Hz). Fault recordings can be useful to test and improve relay algorithms, particularly in the case of misoperation of the relay in service. These records can be used later as input to relay models for testing purposes. Using relay-recorded signals can require both scaling and resampling of the recorded quantities. See below.

Types of recorded data: Different recording methods are applied depending on the intended use of the data. In general, voltage and current waveforms measured at a certain location are digitized and recorded. Phasor measurement units (PMUs), which generate synchronized phasors of measured voltages and currents marked with global positioning system (GPS) time, may be used to determine the fault location on lines with synchronized measurements at both line ends [103]. Recorded data may belong to a disturbance at normal operating conditions or to a fault condition. It can be important to test the relay model with signals recorded also at normal operation, since they might be misinterpreted by the relays as faults. Foreign recorded data available off-line can only be used for open-loop testing.

Conversion of recorded data: Voltage and current waveforms from a DFR or a PQ monitor are usually captured at a high sampling rate. Protective relays may, however, have lower sampling rate. The sampling rate of relay models is selected by the user, while the sampling rate is fixed for real DFRs or other transient recorders. Therefore, resampling is required before feeding recorded data to relay models [104]. The operation of reducing the sampling rate by an integer factor, including any prefiltering, is called down-sampling. Down-sampling can be performed without aliasing if the bandwidth of the signal is reduced before sampling rate reduction. The sampling rate can be reduced by an integer factor M without the appearance of aliasing effect, if the original sampling rate is at least $2M$ times greater than the *Nyquist* frequency. The principal method of down-sampling, known as decimation, includes a anti-aliasing low-pass filter and a compressor – see Figure 11.24. The cut-off frequency of the filter is calculated from the selected relay sampling rate. Finite impulse response (FIR) filters are suitable for anti-aliasing. There may be situations for which resampling of time-discrete signals by a non-integer

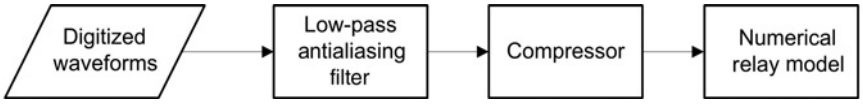

Figure 11.24 Down-sampling to feed relay models with recorded numerical data [12].

factor is necessary. This operation is performed by applying sequentially sampling rate expander and decimator. Sampling rate expansion is also called interpolation [104]. Anti-aliasing low-pass filter needed for up- and down-sampling can be unified in a single filter.

11.5.6 Applications of Relay Models

A relay model can be used to select a measuring principle and/or to check relay settings. With accurate models, different relay measuring principles can be investigated for a particular protection application, and relay settings can be optimized. Since simulations are performed without needing the actual relay and test equipment (i.e. only the simulation software is required), a significant potential cost reduction in testing can be achieved. An important application of computer models is the analysis of protection system misoperations and their causes. This can help to provide insight into the relaying process and for the analysis of power system disturbances and blackouts. In addition, computer modelling can automate the calculation of the response of every relay measuring element to a large number of simulated fault conditions.

The usefulness and applications of relay models can be analysed as follows [12].

- *Manufacturers*: The development and testing of a relay model precedes the building of a prototype relay, because it offers the possibility to evaluate the new design and its applicability prior to building the actual device. This allows developers to test various relaying algorithms and make necessary changes without extensively changing the hardware or software modules of the actual device. Manufacturers may also use closed-loop simulations to evaluate the transient behaviour of the protective relaying algorithms due to network changes and network switching. Several benefits can be derived from the use of relay models; for instance, careful investigation of the protection software (i.e. filter designs, sampling rates, relay algorithms and communication interfaces), fast testing of software changes or testing the ability of a protection device to cooperate with other devices (e.g. remote control systems). Although these possibilities cannot completely replace tests with actual protection devices, they can be realized much more easily, faster and without necessarily using complete set of amplifiers for voltages and currents, circuit breakers and other equipment. Relay models can also be useful for analysing the impact of fast variations of parameters.
- *Utilities*: Relay models can be used to evaluate and select the proper protection according to network conditions. In this evaluation, one can include the power system model and the complete protection system. These models can be used to select a relay measuring principle and to evaluate how different measuring principles perform in a specific power system protection application. Relay models can also be used to optimize relay settings and to determine the security and dependability margins by verifying how close a relay comes to operation as opposed to the trip/no trip results of conventional relay testing. Relay models can be used to predict protection actions under different system conditions and to help identifying power system constraints.
- *Training and education*: Relay models can effectively support the education of students, engineers and researchers, since they can easily demonstrate the general working principles of protection systems. The interaction between the power system and the protection system can be shown easily. It is also possible to show the protection coordination process and how it actually works. Students can learn how to improve relay settings in order to avoid protection failures and maloperations.

11.5.7 Limitations of Relay Models

Several factors must be considered before a relay model can be widely and safely used. On one hand, there will be a lack of detailed information, since relay manufacturers do not divulge sensitive information about their products. On the other hand, a relay model can be very large if all elements of the physical relay are incorporated. A large model will probably require a long computer execution time. Simplifications raise questions of accuracy, and oversimplifications can lead to erroneous conclusions. Microprocessor-based relay models are built as interconnected modules. It is important to first verify the different modules and then verify the accuracy of the assembled set. In the physical relay, there may be interactions between the modules that are not modelled in the assembled larger model. A relay model may not include hardware limitations such as component tolerances, component value change with temperature, or interaction with external hardware devices, such as contact bounce from inputs, outputs, control signals and power supply transients. The oversimplification problem requires a full understanding of relay modelling limitations; however, the main limitation may be the level of approximation used to represent an actual relay, although the limitations are relative depending on the model purpose.

Relay models can be inadequate for evaluating the performance of protection systems because of several limitations, as follows:

Valid operating range: Studies conducted with relay models can be used to identify critical cases for which relay systems should be tested. Relay models can be used for studies in which the range of system operation is limited. In addition, several types of studies cannot be performed using relay models, such as the impact of radio-frequency radiation on relays, seismic disturbances, contact bounce and environmental factors.

Modelling of critical components: Some limitations are due to the fact that, in general, not all relay components are modelled. In many cases, the dynamics of electromechanical relays are complex and difficult to model. The properties of most electronic components change with time, an aspect that is not included in models. Some factors that affect the performance of numerical relays cannot be, or are not, modelled in sufficient details; specific issues include modelling of ADCs, deviation of frequency and accumulation of errors in recursive computations and integrity of components.

Modelling of communication channels: The performance of relay systems is affected by the performance of the communication channels used for intertrip or blocking. In some cases, the communication channels and their delays can be included, but in other cases it is almost an impossible task. For example, if a utility uses the lines of a telephone company for sending messages from one end of the line to the other but no dedicated telephone line is assigned for this purpose, the messages would follow a different route each time they are sent; that is, the delay in the transmission of messages will be different on each occasion and, therefore, impossible to correctly model in a protection system [12].

11.6 Validation of Relay Models

11.6.1 Validation Procedures

A model is an approximation of the actual phenomenon and so requires careful validation to ensure adequate accuracy of the model. The general principle of validation is the comparison of the results produced by the model and those from the actual device under various system fault conditions. The following validation procedures have been used [12]:

1. *Modular validation*: A validation procedure may concern either individual relay components or the whole relay. Validation of the individual components is feasible when the relay has a modular architecture, and each module (component) can be monitored separately. The range of input/output signals should suffice to capture the required operational characteristics of the modelled component. Validated model components may then be utilized to build models of larger structures and/or entire relays. The validation of the components, however, does not eliminate the need for validation of the whole relay.

2. *Use of secondary injection*: Relays can be tested by using specialized injection equipment that reproduces secondary current and voltage waveforms from digital fault recorder data. Records can be obtained from an actual network event or by means of simulation. A common practice for testing relays is to inject only fundamental frequency components of waveforms, without adding frequency components that may exist in the actual recordings. This type of test is based on the assumption that the relay measures only fundamental frequency components. The injection of the real relay and the model with the same signal is an effective validation method, since both the relay and the model are then subjected to the same input signals and both should exhibit the same response. However, when using a phasor-based test method, differences between the model and the real relay may be observed due to the non-realistic nature of this type of test.
3. *Use of published test results and relay technical specification*: It is also possible to validate a relay model using public domain data or the data from manufacturer testing procedures. This approach is particularly practical in the case of phasor-based models, which do not require detailed dynamic behaviour to be taken into account. In such cases, theoretical characteristics may suffice to validate the required scope of operation of the model. When an accurate dynamic behaviour is necessary, it is important to perform the validation procedure under varying system fault conditions.

The application of a given validation method depends on a few factors [12]:

- *Relay type*: In the case of electromechanical relays, validation primarily involves the calibration of model parameters such as resistances and magnetic properties of the relay mechanism. Because of the strong interdependence of all the parts, it is usually not possible to apply the modular approach. However, electronic and numerical relays are suited to a modular validation due to their internal modular architecture.
- *Modelling extent*: Static vector-based relay models do not require a very detailed dynamic verification procedure, and their validation can be constrained to the comparison of the relay theoretical (or measured) static tripping characteristics with the model simulation results. The time factor is not taken into account, since the relay model does not have enough detail in order to respond dynamically to the input signals, although a constant time delay can still be incorporated, especially for evaluating the time response of higher zones. However, dynamic models require more extensive measurement and validation procedures, since not only must the static tripping characteristic be consistent, but also tripping times under various system conditions have to be tested.
- *Data availability*: Different designs of relays require different levels of information; for example, internal recording facilities are very useful for the purposes of individual module validation.

11.6.2 Relay Model Testing Procedures

Testing procedures vary depending on the type of model and on the relay design. A general principle is that tests should include a range of realistic conditions under which the device is expected to operate; that is, faults under which the relay trips as well as those for which the relay remains stable. Due to the limited number and range of recorded network faults, only a restricted test set can generally be formed from fault records. Simulation then becomes an effective way of creating a suitably extensive test set. The tests to be conducted for model validation should contain – depending on the type of relay and the type of model – some or all of the following test categories [12]:

- *Operational tests* (static conditions): These tests are performed to ensure proper steady-state operation. Simulations include marginal conditions for relay operation such as faults on the verge of a zone in the case of distance relays, or high resistance faults and external worst-case scenario faults for unit protection relays. Operational tests may be sufficient for vector-based static relay models, for which input signals are presented in the form of vectors, rather than sampled voltage and current waveforms.

- *Timing tests* (dynamic conditions): These are designed to verify the dynamic response of the relay. A number of simulations are performed, and the tripping times are recorded under various fault conditions. Variable fault parameters may include: (1) the type of protected circuit (overhead line, cable, transformer, etc.), (2) the length of the protected circuit, (3) the position of the fault along the protected circuit, (4) power system fault level, (5) fault connection and resistance, and (6) type of earthing in the grid. This category of tests is necessary for transient relay models. Input signals are sampled current and voltage traces.
- *Transient traces* (dynamic conditions): If possible it is recommended to use the recording of transient signals from inside the relay. In the case of transient models this helps to verify individual sections of the model through comparing model and relay transient responses. This is the most reliable method of validation of the dynamic protection models.

This diversity of the simulation scenarios may lead to a rather large quantity of tests. Therefore, the marginal values of the variables have to be identified carefully and in accordance with the expected conditions under which the relay might operate.

11.6.3 Accuracy Assessment

The proper assessment of a model accuracy is essential for further interpretation of relay simulation results and diagnoses. A suitable method for accuracy evaluation needs to be adopted according to the design and the scope of the relay model operation. It is often difficult to predict or assess the accuracy outside the scope of testing. Maximum as well as average error should be calculated to better indicate the sensitivity of the model to changing fault conditions. Information indicating under which specific conditions the relay model accuracy deteriorates most is useful in assessing the confidence of the results. The maximum possible deviation between the relay and its model is obviously of special interest. The ways of expressing an error depend on the type of model and the extent of validation [12]:

- *Static models*: The error can only be measured in terms of operational characteristics of the relay. For the operation of distance zones, the error may be expressed as a percentage of the length of the protected circuit; for unit protection marginal conditions, under the faults with high resistance, the error may be expressed as a percentage of the marginal fault resistance for which the relay trips.
- *Dynamic models*: Two general categories can be distinguished in terms of time response. For fast-operating relays (tripping within one or two cycles), the error may be characterized as the absolute time difference between the model and the relay (in ms); for slower-operating schemes (operation from a few hundred milliseconds to seconds), the error may be expressed as a percentage of the recorded actual tripping time.

11.6.4 Relay Testing Facilities

There are three main types of transient simulators: analogue simulators (transient network analysers or TNAs), real-time digital simulators and playback digital simulators. The TNA consists of scaled analogue models that represent the transient behaviour of the actual power system components up to a few kHz. The models can include magnetic nonlinearities of the transformers and reactors. The TNA output is amplified and fed to the relays under test. The actual relay characteristics can be tested with various currents and voltages, including the effects of DC offset. Since identical currents and voltages are supplied to the relay model, the time-to-operation and no-operation can be analysed and compared. TNA studies are limited to the available parameters of lines and transformers, so not all configurations can be tested.

Development of real-time digital simulators for relay testing has enabled a flexible and accurate environment for relay models or actual relays [75, 105–107], since these platforms can test actual relays

by converting sampled waveforms into analogue signals and amplifying them to the levels required by the relays. This is accomplished with digital-to-analogue converters and power amplifier interfaces.

Data simulation files useful for testing both actual relays or relay models can be obtained by simulation or from field measurements. Waveforms can then be passed to instrument transformers by amplifiers. A real-time playback simulator uses restored waveforms and plays the data back to the relay (actual or model) in real time.

A detailed analysis of some validation examples is presented in the CIGRE brochure [12].

11.7 Case Studies

11.7.1 Introduction

This section presents two examples that illustrate the scope of models and case studies that can be carried out with the most common tools presently used in protection studies. The first example deals with an electromechanical distance relay, while the second is based on a detailed model of a numerical distance relay. The study is carried out in both cases with a complete system model, including instrument transformers.

Distance relays compute the ratio of voltage/current (i.e. the apparent impedance) on a transmission line and operate when the value is less than a preset value. These relays are applied universally on transmission lines. The terms 'impedance relay' and 'distance relay' are often used interchangeably. 'Distance' is actually the more general term; the impedance-type relay is merely one of many distance relays.

The operation characteristic is often plotted on the impedance plane. Figure 11.25(a) shows the mho characteristic for phase and ground fault protection, which is considered the classic distance characteristic. Distance relays can have multiple protection zones (forward and reverse). Zones may be enabled or disabled. Figure 11.25(b) shows a typical case with three forward and one reverse zone. General aspects of phase and ground distance settings may be as follows:

- *Zone 1*. This section provides high-speed protection for any type of fault within most of the line segment. Experience suggests setting this zone to reach less than 100% of the line, since it could risk overreaching for close-in faults just beyond the remote end substation. For example, to account for errors in line data and measurement errors in the instrument transformers and relay, the Zone 1 reach can be set to 85% of the line. Zone 2, with communications assist, protects the remaining 15%.

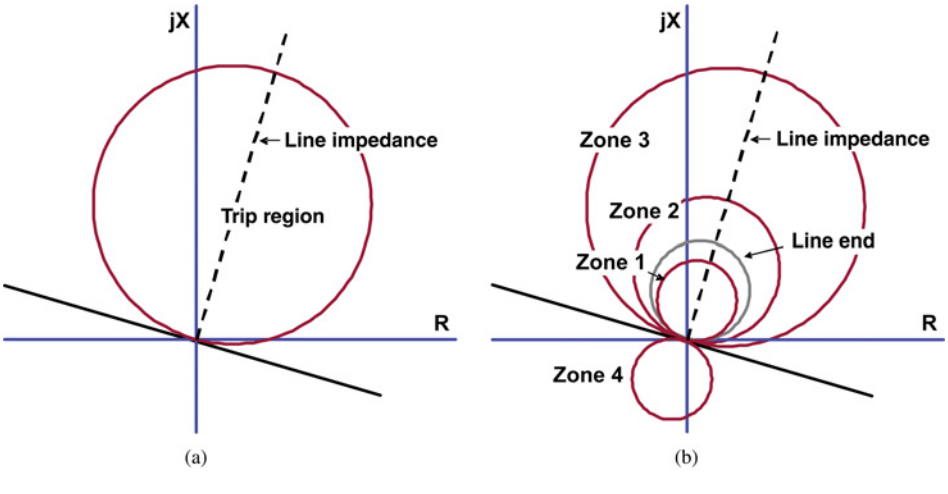

Figure 11.25 Mho characteristic: (a) typical mho characteristic, (b) mho characteristic zones.

- *Zone 2*. This section is set to protect the remainder of the line plus a safety margin, typically greater than 20%. Zone 2 delay time is coordinated with instantaneous fault clearing at the remote bus, typically 15–30 cycles.
- *Zone 3*. This section is set with progressively longer time delays and provides extended backup protection.
- *Zone 4*. This may be set as a reverse-looking section with the reach exceeding the remote end Zone 2 reach, plus a safety margin.

11.7.2 Case Study 1: Simulation of an Electromechanical Distance Relay

This test case presents a methodology for representing electromechanical relays in an EMTP-like tool. The model is applied to the protection study of a power network. Although the test system is a real one, the studies are theoretical; that is, no validation has been performed. The main goals of the test case are to present how to represent the protection system in a transients program and what type of studies can be carried out [108, 109].

A dynamic state-space model of the electromechanical distance relay model used in this study was presented in [110]. The EMTP/ATP representation of that model using TACS capabilities was detailed in [54]. The approach used in this chapter to represent the relay uses MODELS code [70].

A diagram of a typical mho distance relay is shown in Figure 11.26. The relay has two coils: a polarizing coil and an operating coil. The polarizing coil is connected to a potential transformer through a memory circuit consisting of a variable inductor and a capacitor. The operating coil is connected to a current transformer through a transactor.

The electromagnetic torque is developed by the interaction of currents through the two coils; if the torque is of the correct direction, magnitude and duration, the relay will trip. The magnitude of the impedance setting can be adjusted by a potentiometer or transactor and autotransformer taps. The angle of maximum torque can be adjusted by using the variable inductor.

From this diagram a state-space model can be obtained. A ninth-order state-space model was presented in [110] with the following form:

$$\frac{d}{dt}[X] = [A][X] + [B][Y], \tag{11.5}$$

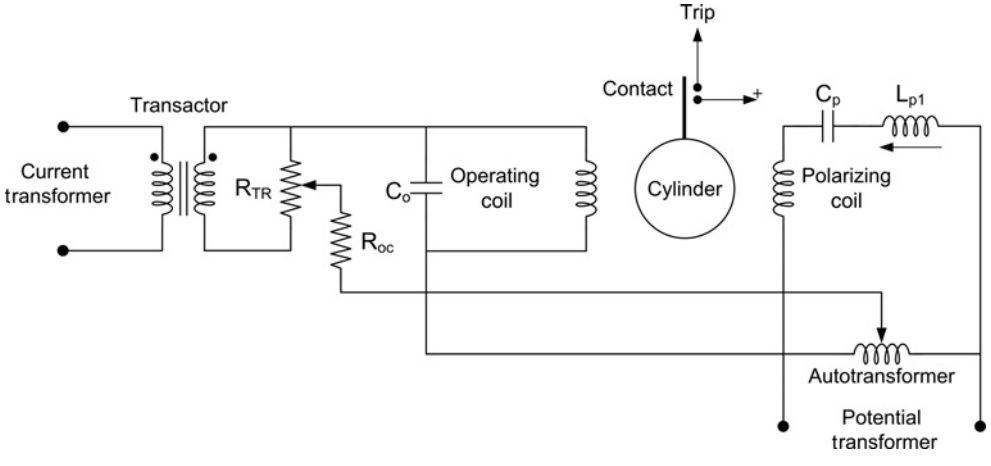

Figure 11.26 Case Study 1: Diagram of a mho distance relay (© 1990 IEEE) [54].

where

$$[X] = [\, x_1 \quad x_2 \quad x_3 \quad x_4 \quad x_5 \quad x_6 \quad x_7 \quad x_8 \quad x_9 \,]^T \tag{11.6a}$$

$$[Y] = [\, y_1 \quad y_2 \quad y_3 \,]^T. \tag{11.6b}$$

x_1 current through the transactor secondary
x_2 current through the operating coil
x_3 voltage across the operating coil
x_4 voltage across the memory circuit capacitor
x_5 current through the polarizing coil
x_6 maximum density of induced current by the polarizing coil
x_7 maximum density of induced current by the operating coil
x_8 angular displacement of the cylinder
x_9 angular velocity of the cylinder
y_1 input voltage from the potential transformer
y_2 derivative of the input current from the current transformer
y_3 electromagnetic torque.

Details of matrices [A, B], the calculation of their elements, as well as the electromagnetic torque, were presented in [110]. It is important to note that the torque acts as an input, but its value is calculated from values of some state-variables (i.e. x_2, x_5, x_6, x_7).

A hybrid approach is used in this chapter for simulating this state-space relay model [108, 109]. The relay model is split up into two parts and different ATP capabilities are used to represent each part in a data file: circuits of the operating and polarizing coils are represented in the BRANCH section, and cylinder dynamics are represented by means of a MODELS section – see Figure 11.27.

The relay parameters were those presented in [54, 110]. The relay model does not incorporate the representation of protection zones; that is, the user cannot specify protection zones as depicted in Figure 11.25.

Figure 11.28 shows the diagram of the power network studied in this case, a 60 Hz 115 kV actual transmission line. The protection system model developed for this study includes instrument transformer models.

A more detailed representation of this network is depicted in Figure 11.29. The transmission line to be protected is represented by a frequency-dependent model; network equivalents at both ends of the line are modelled as linear lumped-parameter impedances.

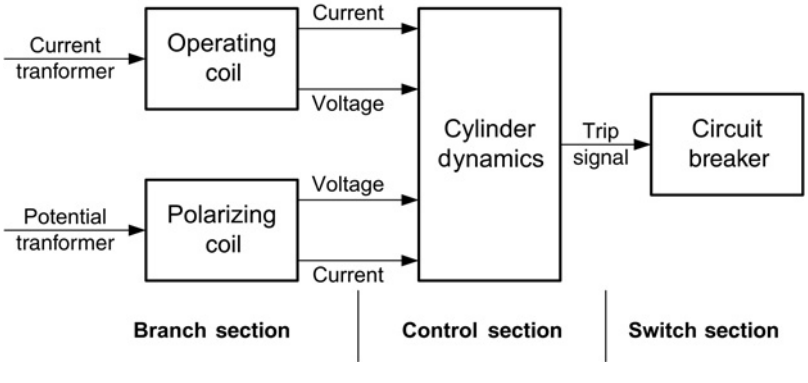

Figure 11.27 Case Study 1: Schematic representation of the electromechanical relay in EMTP/ATP.

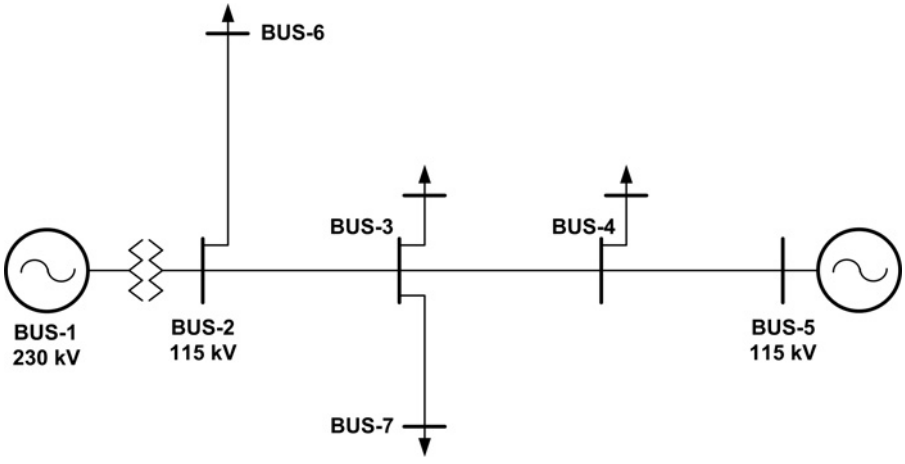

Figure 11.28 Case Study 1: Diagram of the test power system.

The models used to represent instrument transformers are similar to those presented in the literature; see Section 11.3 and Figures 11.2 and 11.13. The CCVT model incorporates some stray capacitances, which can have an appreciable influence, although validation tests performed without considering stray capacitances have shown that the model can accurately reproduce the subsidence transients and the ferroresonance behaviour. The subsidence transients have a major effect on CCVT behaviour. According to simulation results, these transients have the largest magnitude and the longest time duration when the fault occurs at a primary voltage zero, and their magnitude increases with increased burden. The magnetization inductance has a negligible effect on the subsidence transients.

To test the distance relay model under transient conditions, the following cases were run:

1. Asymmetrical single-phase-to-ground fault at location NODE2A
2. Asymmetrical single-phase-to-ground fault at location NODE1A
3. Symmetrical single-phase-to-ground fault at location NODE1A
4. Asymmetrical single-phase-to-ground fault at location BUS-2A
5. Symmetrical single-phase-to-ground fault at location BUS-2A.

An asymmetrical fault is obtained by closing the switch that creates the fault at voltage zero, while symmetrical faults were caused by closing the switch at peak voltage.

Figures 11.30–11.34 show simulation results corresponding to the tests mentioned above. We can see that the closer the fault is to the location of the protection relay, the higher the probability of causing CT saturation: at node BUS-2A both types of fault cause saturation, at node NODE1A saturation was caused by only the asymmetrical fault, while at node NODE2A CT saturation was not reached, even with the asymmetrical fault. Voltages at the CCVT location, after the fault is caused, should be zero for the last two test cases. However, we can see that an oscillatory voltage, the subsidence transient, does appear on both sides of the potential transformer. As expected, faster relay operations are caused by faults that are closer to the relay location. In addition, we can see that for faults caused at the same location, the asymmetrical one causes faster operation.

11.7.3 Case Study 2: Simulation of a Numerical Distance Relay

Numerical distance relays are digital realizations of proven electromechanical distance relay designs. Voltage and current signals from the CCVT and CT secondary are input for a low-pass filter that removes

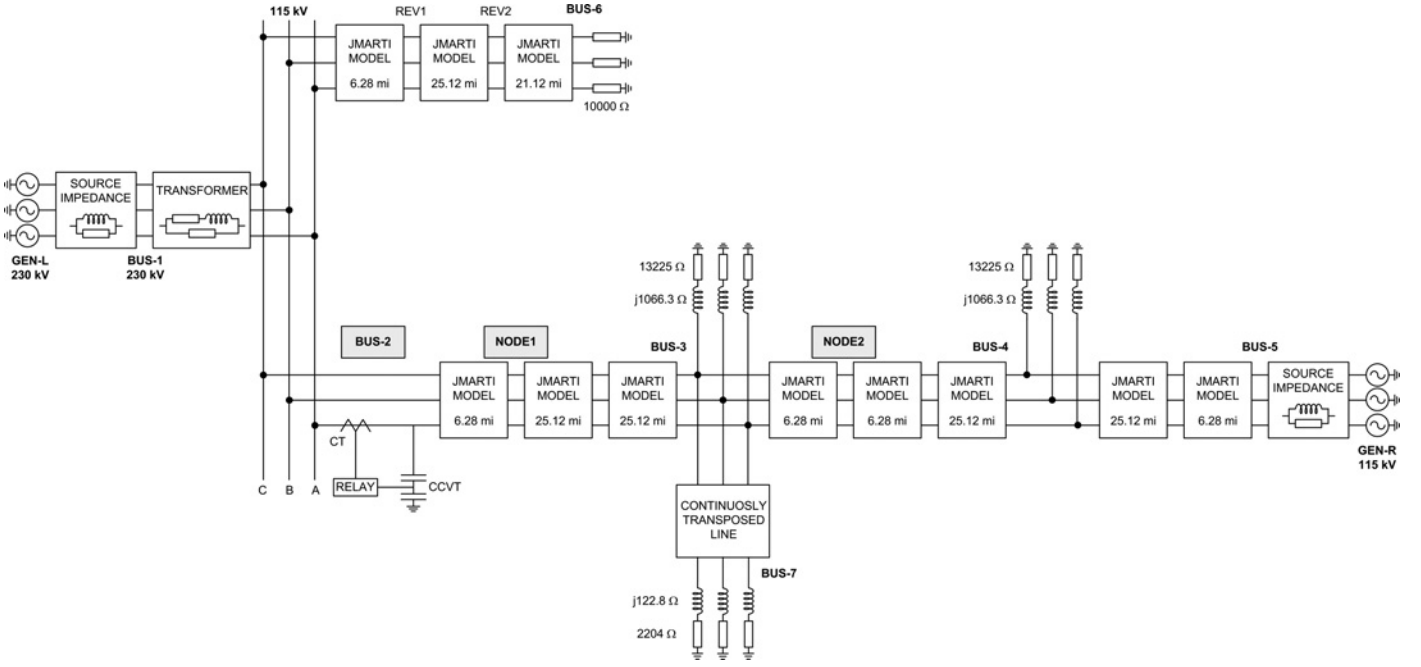

Figure 11.29 Case Study 1: Detailed representation of the test system.

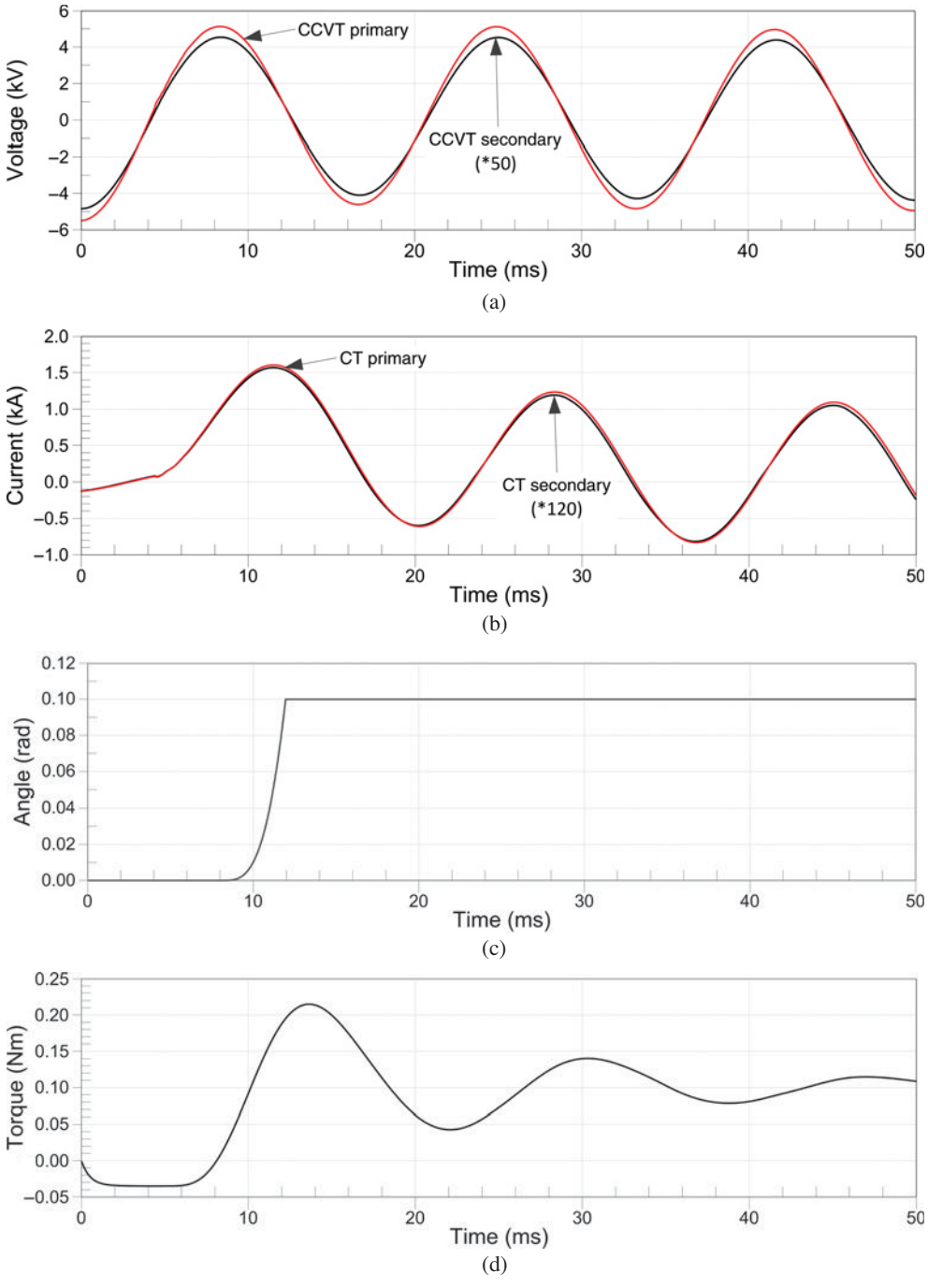

Figure 11.30 Case Study 1: Asymmetrical fault at NODE2A: (a) CCVT primary and secondary voltages, (b) CT primary and secondary currents, (c) relay angular displacement, (d) relay electromagnetic torque.

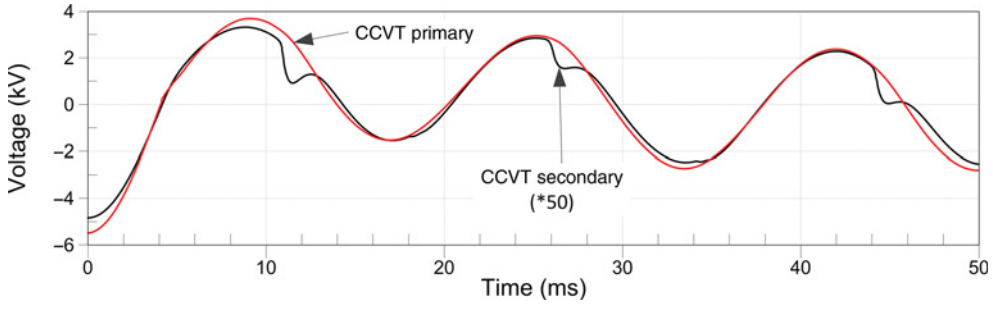

(a)

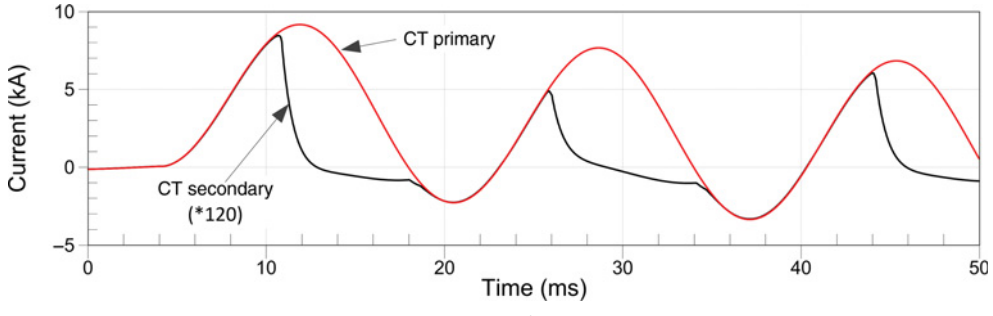

(b)

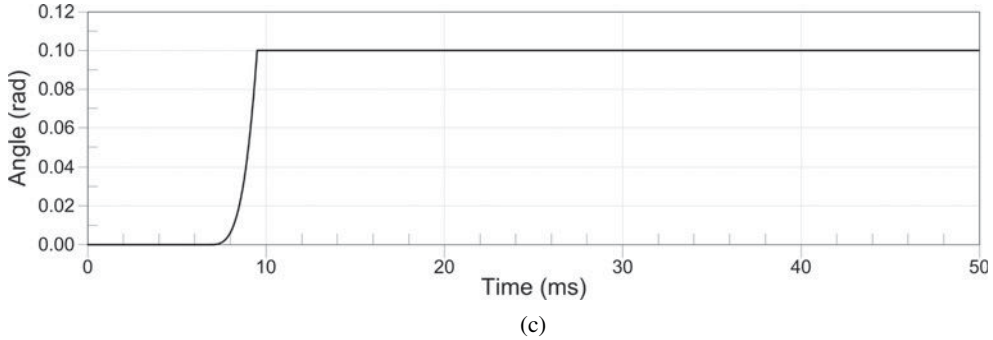

(c)

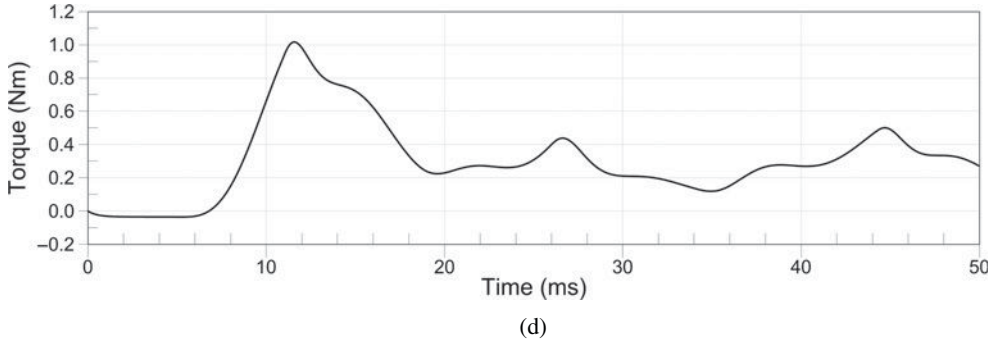

(d)

Figure 11.31 Case Study 1: Asymmetrical fault at NODE1A: (a) CCVT primary and secondary voltages, (b) CT primary and secondary currents, (c) relay angular displacement, (d) relay electromagnetic torque.

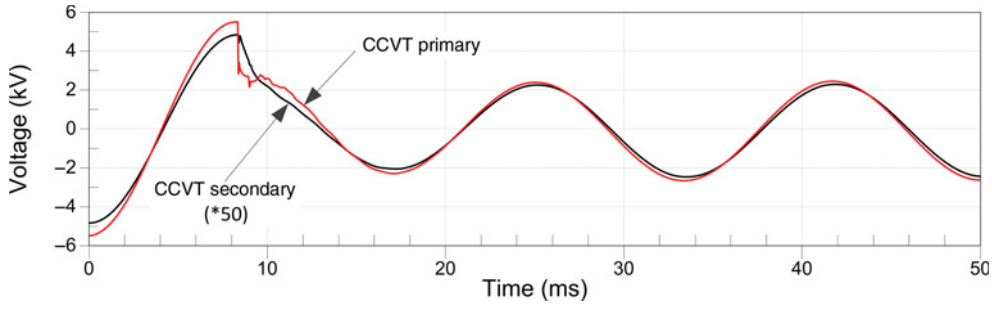

(a)

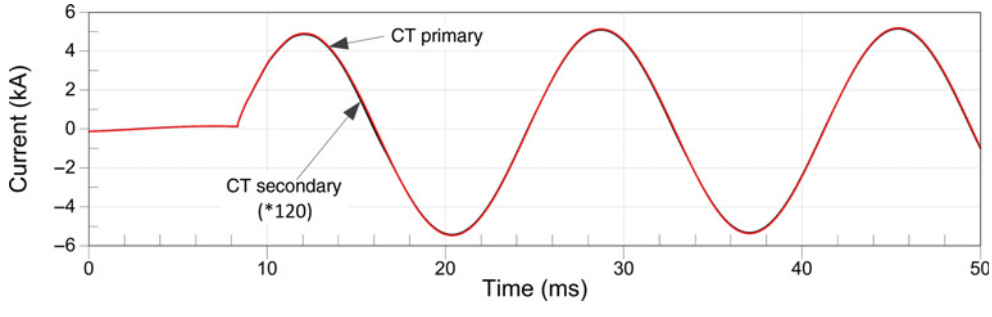

(b)

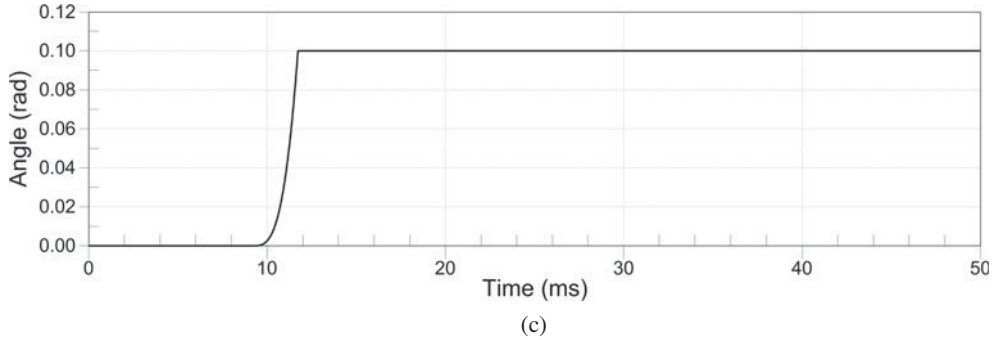

(c)

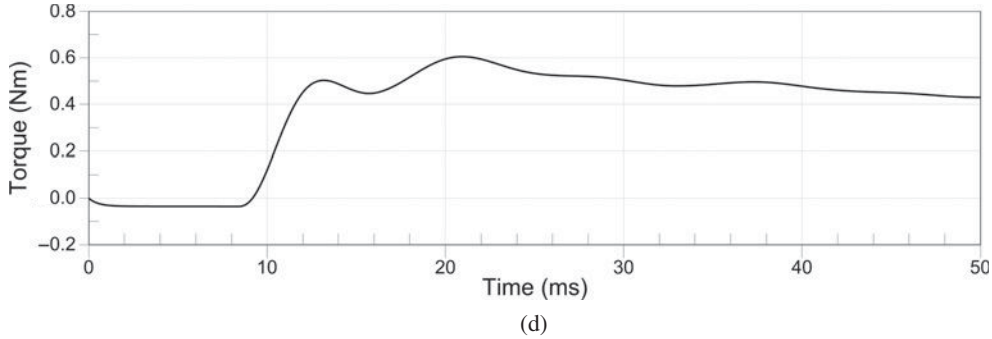

(d)

Figure 11.32 Case Study 1: Symmetrical fault at NODE1A: (a) CCVT primary and secondary voltages, (b) CT primary and secondary currents, (c) relay angular displacement, (d) relay electromagnetic torque.

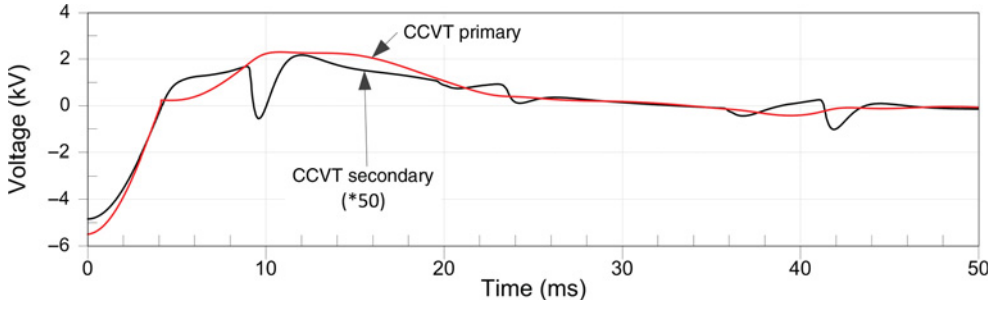

(a)

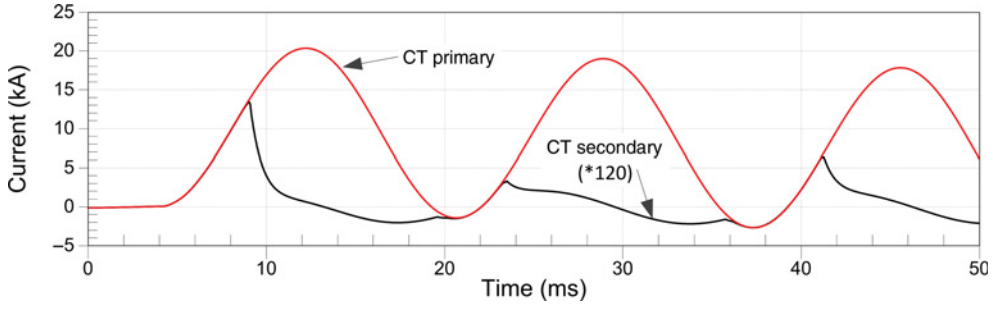

(b)

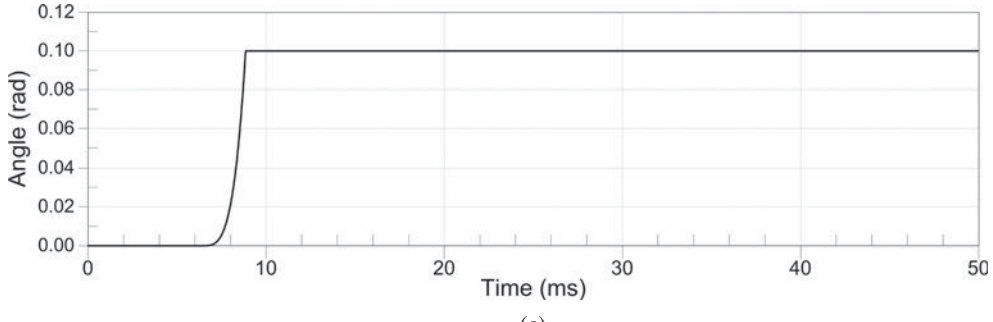

(c)

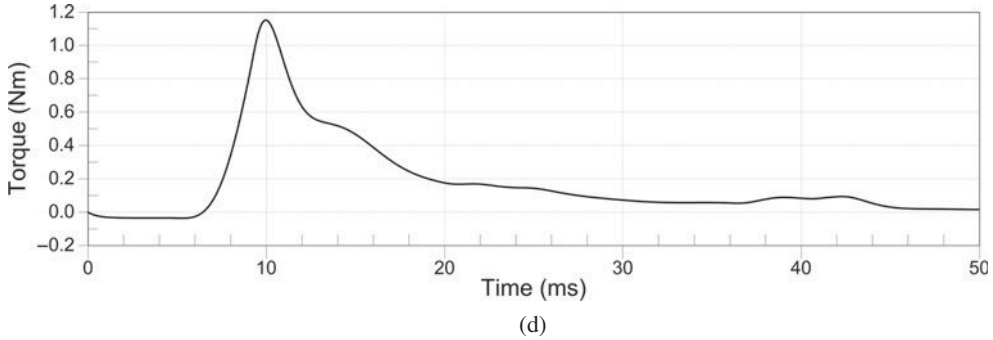

(d)

Figure 11.33 Case Study 1: Asymmetrical fault at BUS-2A: (a) CCVT primary and secondary voltages, (b) CT primary and secondary currents, (c) relay angular displacement, (d) relay electromagnetic torque.

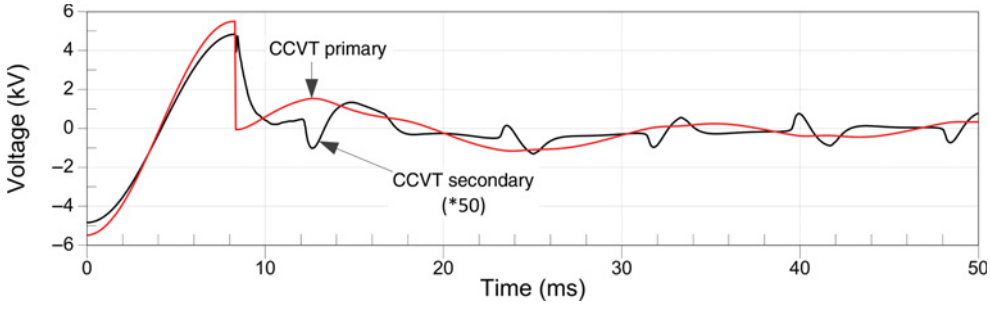

(a)

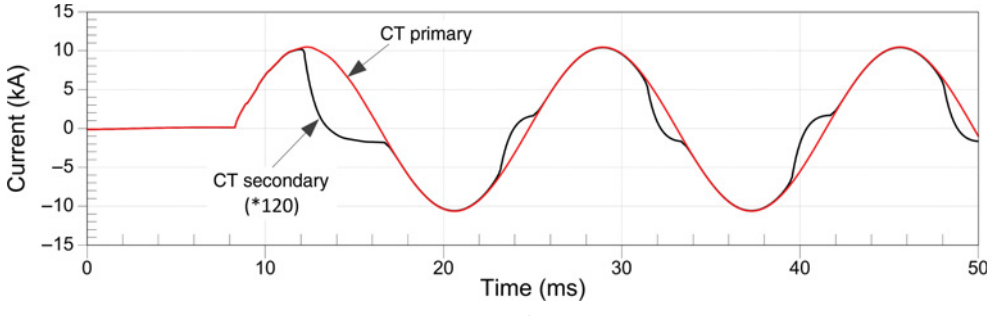

(b)

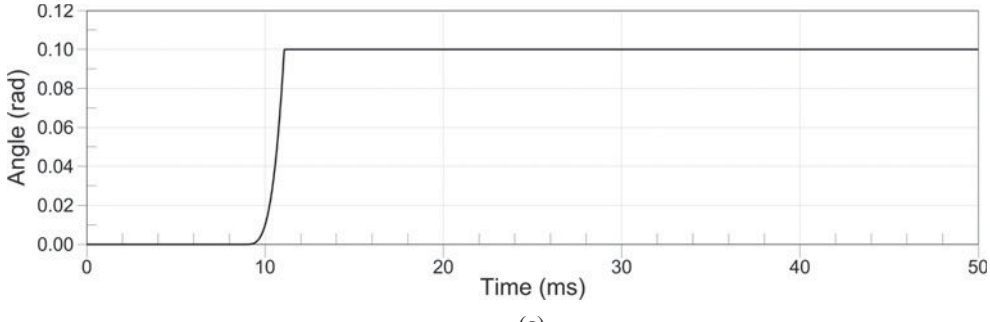

(c)

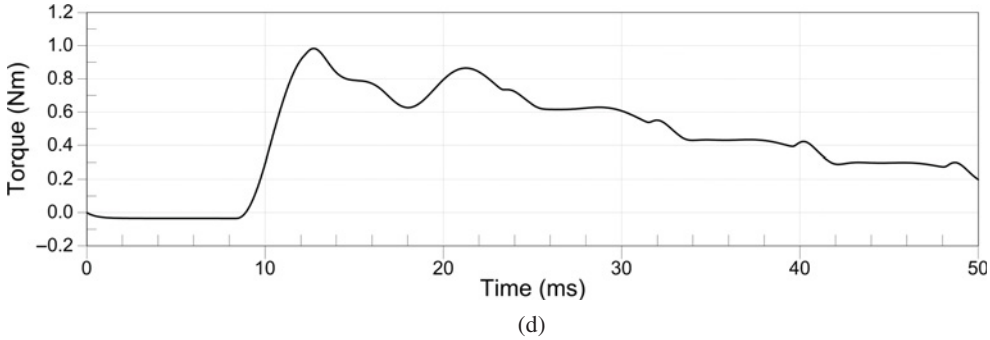

(d)

Figure 11.34 Case Study 1: Symmetrical fault at BUS-2A: (a) CCVT primary and secondary voltages, (b) CT primary and secondary currents, (c) relay angular displacement, (d) relay electromagnetic torque.

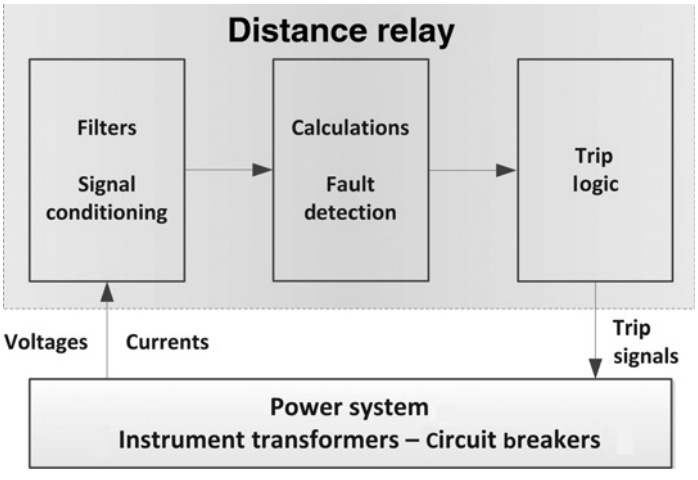

Figure 11.35 Case Study 2: Schematic representation of the distance relay and its interaction with the power system.

frequency content above 1/3 of the sampling frequency. The signal is then sampled by the ADC at a rate (which varies with the relay) of about 16–64 samples per power system cycle. The sampled data is then passed through a low-pass filter that removes the frequency content that is above the fundamental frequency. Most digital relays estimate amplitudes and phase angles of phasors using digital filters. This information is then used to detect abnormal operating conditions.

Numerical distance relays may be divided into three categories [12]:

1. generic relays that emulate their electromechanical or solid-state counterparts. – these relays implement the amplitude or phase comparator equations after computing the voltage and current phasors.
2. relays that compute voltage and current phasors from the sampled and quantized data, and calculate the impedance from the voltage and current phasors and then use appropriate logic to arrive at a trip decision. The impedances as seen from the relay terminal are calculated from appropriate phasors.
3. relays that use voltage and current samples to estimate the impedance by fitting the parameters of the fault loop in the form of first-order differential equation – a number of numerical techniques can be used to replace the continuous-time differential equations at various instants into algebraic equations. A set of these equations is then solved to estimate the impedance. These relays also use appropriate logic to make a trip decision.

The relays in the second and third categories generally use mho or quadrilateral type characteristics.

The relay model used in this study is based on a model originally developed by Institut de Recherche d'Hydro-Québec (IREQ) using a library of modules for protection studies [111]. The relay model organization is that presented in Figure 11.35: (1) the initial section filters input voltage and current signals, (2) the intermediate section detects fault conditions, and (3) the last section decides whether to trip or not the associated circuit breaker and when to reclose it. Users have to specify line parameters, protection zones and relay settings (i.e. opening and reclosing delays). For details on the implementation of mho distance relays in an EMTP-like tool, see [112].

Figure 11.36 shows the transmission system studied in this case. The study zone includes the 60 Hz 230 kV system equivalent, a power plant represented by a synchronous generator and its step-up transformer, and the transmission line that delivers the energy generated by the power plant to the power

Figure 11.36 Case Study 2: Diagram of the test system.

system. The test system parameters are taken from the benchmark proposed by the IEEE PSRC Working Group [25].

The overall system model has been implemented in EMTP-RV as follows:

- The two source sides (i.e. the left-side 230 kV equivalent system and the right-side power plant) are modelled using EMTP-RV capabilities; the equivalent system is represented by means an ideal three-phase voltage source plus its series impedance.
- The transmission line is represented by a frequency-dependent distributed-parameter model and is divided into several sections to analyse the relay response against faults at internal nodes.
- The transmission line is protected by two admittance mho-type distance relays located at its terminals. There is no pilot communication between the two relays, which operate independently.

The main parameters are summarized below. For more details, see [25].

1. Left-side power system: It is a 60 Hz 230 kV transmission system in series with its equivalent impedance with the following parameters:

$$R_0 = 2.70 \qquad X_0 = 8.37\,\Omega$$

$$R_1 = R_2 = 6.1 \qquad X_1 = X_2 = 16.7\,\Omega$$

2. Transmission line: The overall length is 65 miles. The line is divided into three sections with respective lengths of 30, 20 and 15 miles. The per unit length parameters (to be specified in the distance relay model) are:

$$R_0 = 0.3627 \qquad X_0 = 2.4379\,\Omega/\text{mile}$$

$$R_1 = 0.0955 \qquad X_1 = 0.7599\,\Omega/\text{mile}$$

3. Power plant: It is represented by a synchronous generator and its step-up transformer. Ratings and parameters of both machines are:
   - synchronous generator: 24 kV, 830 MVA, two poles, solidly grounded
   - step-up transformer: 22.8/229.893 kV, 725 MVA, ΔYn.
4. Numerical distance relay: The selected settings of each relay are different. Figure 11.37 shows these settings:
   - left-side mho distance relay: Zone 2 covers the left-side 30 mile line section; Zone 1 reaches 50% of this line section, while Zone 3 covers the entire line.
   - right-side mho distance relay: Zone 2 covers the right-side 15 mile line section; Zone 1 also reaches 50% of this line section, while Zone 3 covers again the entire line.

     Note that each relay has a reverse section that reaches the same percentage of the corresponding Zone 3.

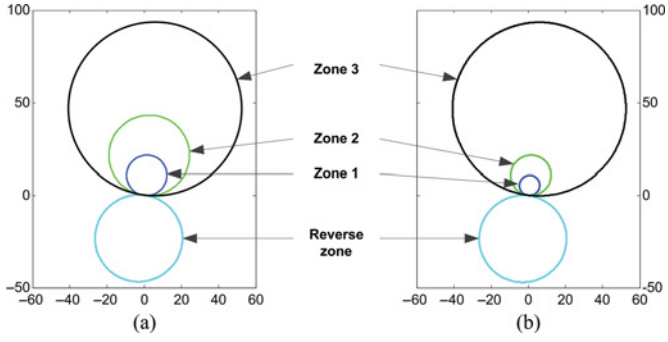

Figure 11.37 Case Study 2: Protection zones of the test distance relays: (a) left-side mho relay, (b) right-side mho relay.

The operating times for faults located within the different zone are 0.001 s for Zone 1, 0.4 s for Zone 2 and 1.5 s for Zone 3. In case of a fault located at the reverse section, the selected time is 2.5 s. The relays will reclose 1.5 s after the opening action.

5. Instrument transformers: The ratios selected for CTs and CCVTs are:
   - current transformer (Figure 11.3): 2000/5 A.
   - coupling capacitor voltage transformer (Figure 11.13): 230 000/115 V.

All the simulation cases presented in this section correspond to a three-phase fault located within the transmission line. The operating conditions at the fault instant are also the same: the synchronous generator is injecting 500 MW, being the voltage at the machine terminals 24 kV.

Simulation results have been obtained following a gradual approach. In order to understand the relay responses to faults located close to each terminal of the transmission line, a first model was implemented without instrument transformers and circuit breakers; that is, the model will present the transient caused by a three-phase fault and the response of each distance relay. The second model includes instrument transformers and circuit breakers; the instant of the trip signal from each relay will depend on the fault location. A reclosing operation from each relay will take place 1.5 s after the first trip. The instant at which the fault starts, 0.5 s, the duration of the fault, 2 s and the time during which the system is simulated, 3 s, are the same in all studies. The variables plotted for each case are also the same.

A. *System model without instrument transformers and circuit breakers* – Figures 11.38 and 11.39 show some of the results when the fault is located 30 mile from the left line terminal and 15 miles from the right line terminal, respectively. Considering these two locations, the first fault is within Zone 1 of the left-side relay and Zone 2 of the right-side relay, while the second fault is within Zone 1 of the right-side relay and Zone 2 of the left-side relay.

From the plots shown in the two figures it is evident that the shape of the fault current at the line terminals are different. This is due to the different characteristic of the source impedances; at the left side, the 230 kV power system is represented by its 60 Hz equivalent impedance, while the impedance characteristic at the right side is that of a synchronous generator. Note also that the fault current level seen by each relay is different, being higher at the right side.

The relay responses shown in plots (c) and (g) are correct; that is for a fault located 30 miles from the left terminal the relay located at this terminal reacts first (Figure 11.38(c)), while for a fault located 15 miles from the right terminal, the first trip signal is sent by the relay located at this terminal – see Figure 11.39(g).

An interesting result from this study is the variation of the admittance seen by each relay phase during the simulation of both faults. Remember that before the fault the power is flowing from the power plant

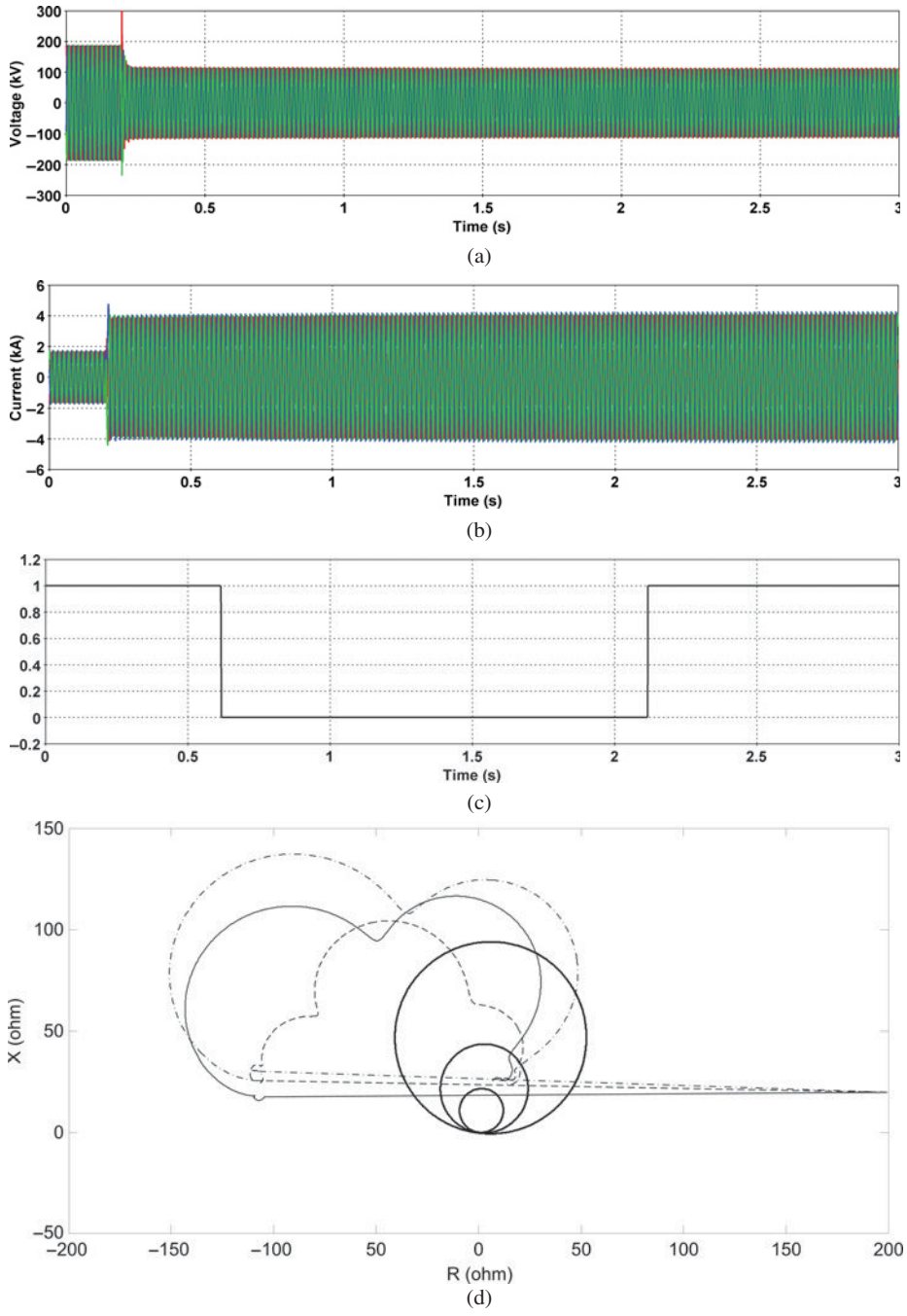

Figure 11.38 Case Study 2: Simulation results with a three-phase fault at 30 miles from the left line terminal – Without instrument transformers and circuit breakers: (a) left-side line terminal voltages, (b) left-side line terminal currents, (c) left-side mho relay trip and reclosing signals, (d) impedance path measured by the left-side mho relay, (e) right-side line terminal voltages, (f) right-side line terminal currents, (g) right-side mho relay trip and reclosing signals, (h) impedance path measured by the right-side mho relay.

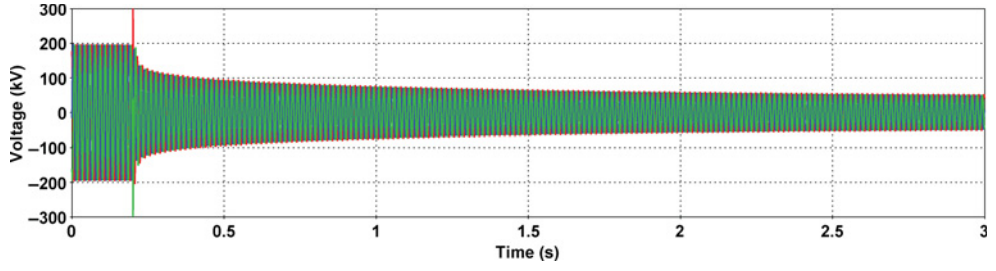

(e)

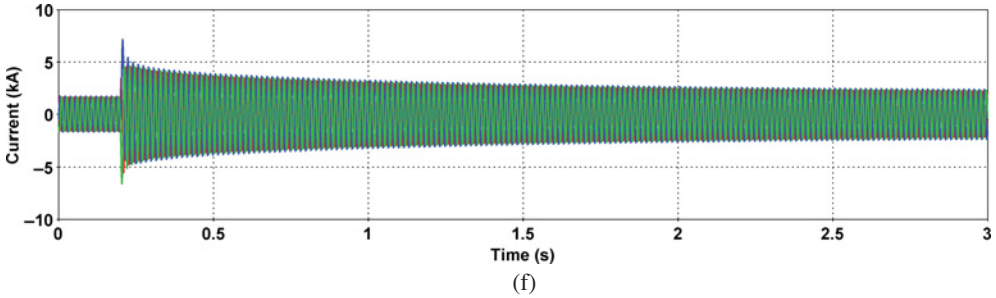

(f)

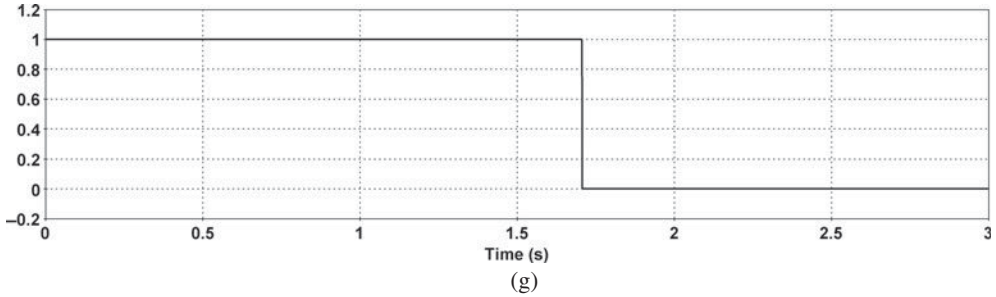

(g)

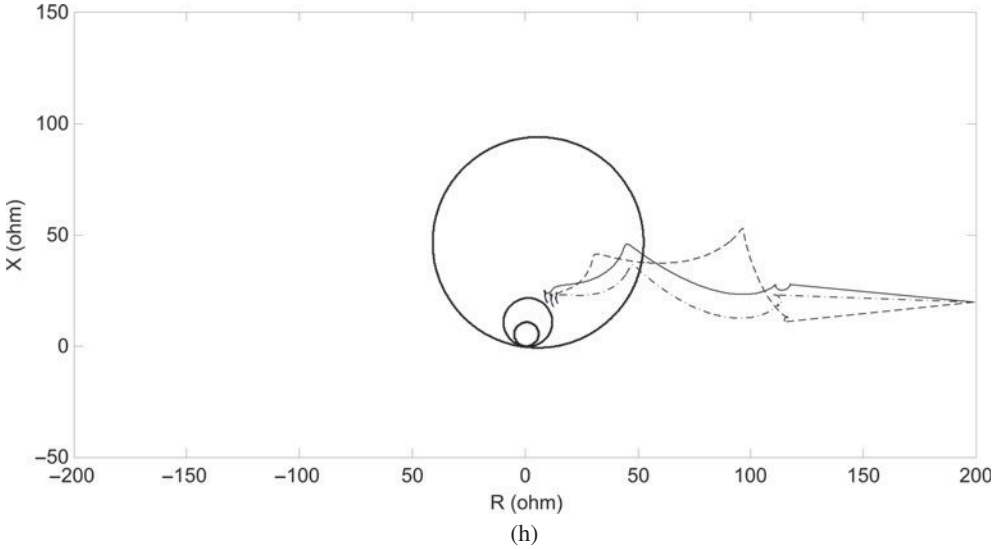

(h)

Figure 11.38 (*Continued*)

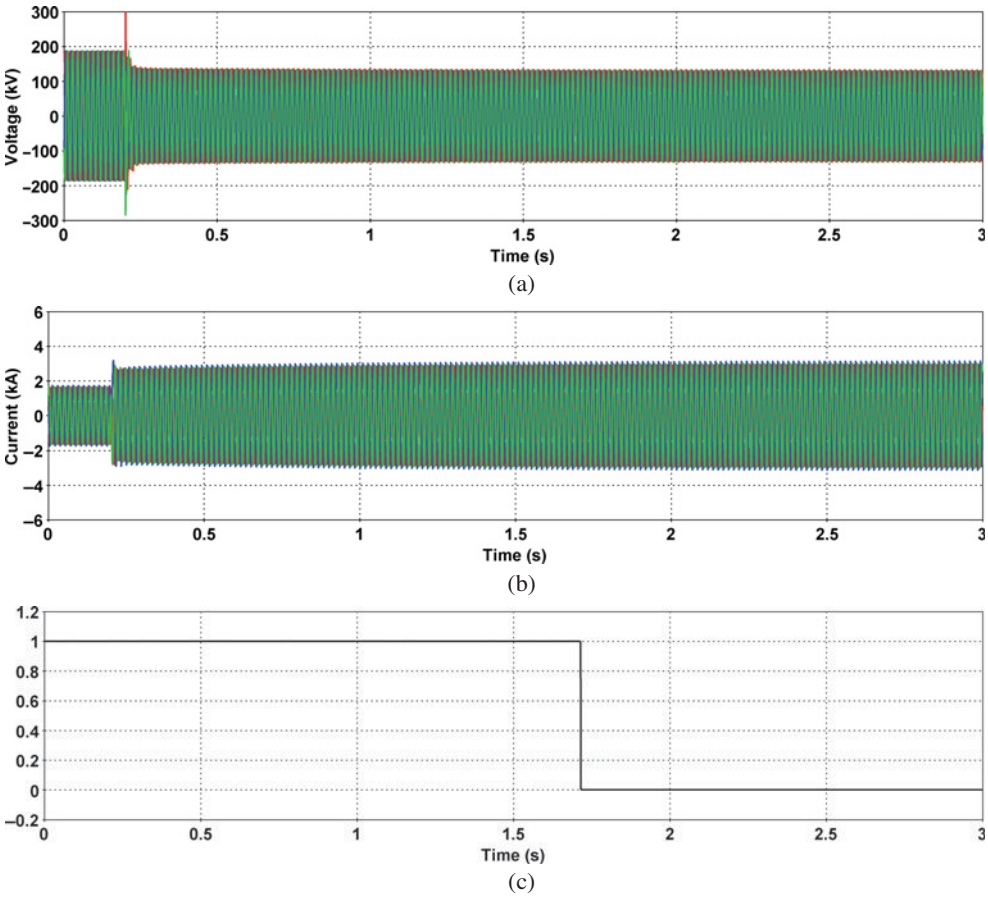

Figure 11.39 Case Study 2: Simulation results with a three-phase fault at 15 miles from the right line terminal – Without instrument transformers and circuit breakers: (a) left-side line terminal voltages, (b) left-side line terminal currents, (c) left-side mho relay trip and reclosing signals, (d) impedance path measured by the left-side mho relay, (e) right-side line terminal voltages, (f) right-side line terminal currents, (g) right-side mho relay trip and reclosing signals, (h) impedance path measured by the right-side mho relay.

(right side) to the power system (left side), so the direction of the current measured by each relay will be different: positive at the right side, negative at the left side. However, during the fault condition, the direction of the fault current measured by each relay is positive. After an initial interval, the admittances seen by the left relay pass to the left side of the circles and move to within the circle corresponding to Zone 2 and Zone 3, respectively, during the fault condition. The admittances seen by the right relay remain always at the right side of the circles and move to within the circle of Zone 3 and Zone 2, respectively, during the fault condition.

B. *System model with instrument transformers and circuit breakers* – With this model the trip signals will cause the opening of the circuit breakers and their reclosing after the corresponding reclose intervals. Figures 11.40 and 11.41 show some of the results derived for the same fault locations.

We can see that for a fault closer to the left line terminal, the left-side circuit breaker opens first; the opening of the right-side breaker caused by the trip signal of the right-side relay comes after. When

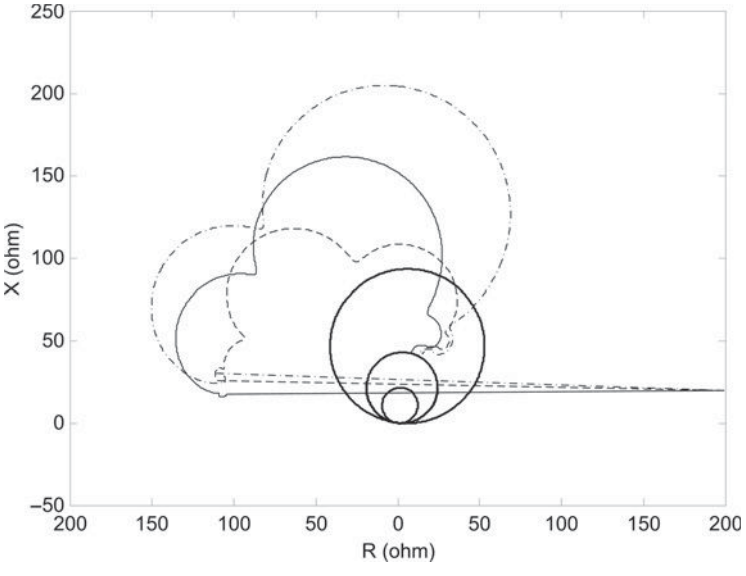

(d)

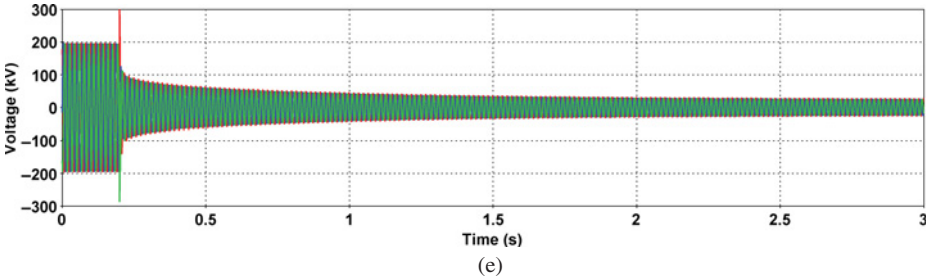

(e)

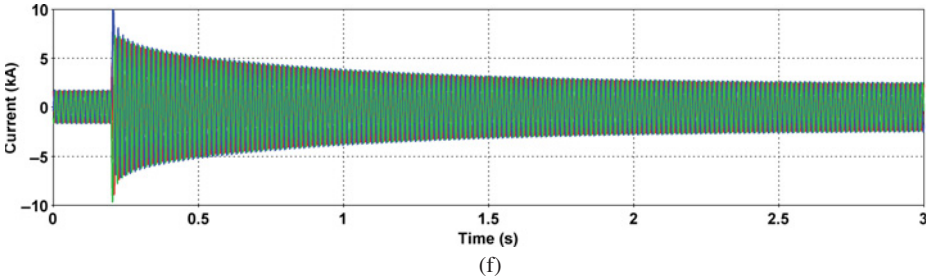

(f)

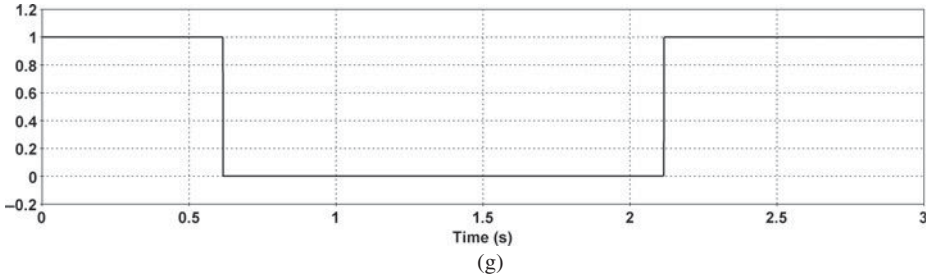

(g)

Figure 11.39 (*Continued*)

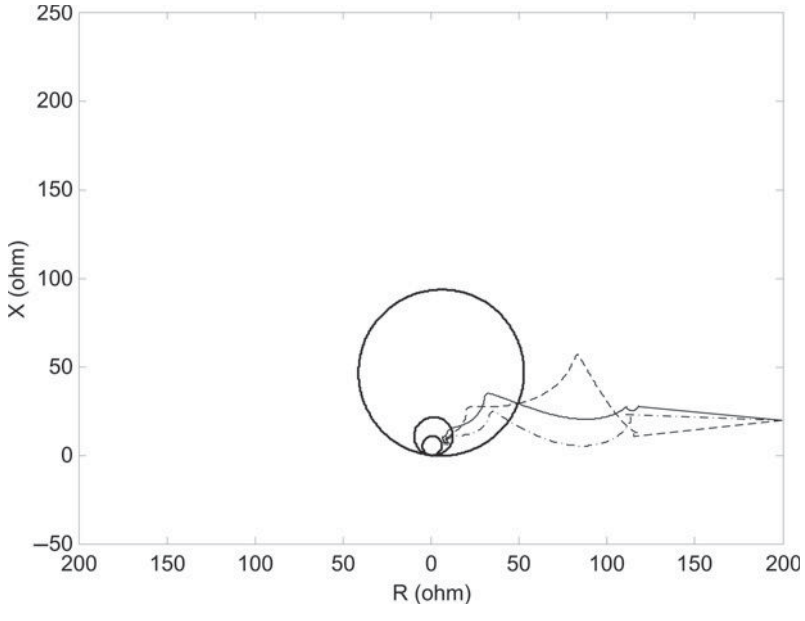

(h)

Figure 11.39 (*Continued*)

the left-side circuit breaker recloses, the fault condition has disappeared. This sequence of events is supported by the trip signals shown in Figures 11.40(c) and 11.40(g).

For a fault closer to the right line terminal, the right-side circuit breaker opens first, and it is followed by the opening of the right-side breaker. In this case, the right-side circuit breaker also recloses first. As for the previous case, the sequence of events is supported by the trip signals shown in Figures 11.41(c) and 11.41(g).

The plots showing the variation of the admittances seen by each relay exhibit some differences with respect to the same plots derived from the previous study. This is due to the fact that this time there is a closed-loop interaction between the relays and the system: the trip signals generated by the relays open the corresponding circuit breakers; therefore, the currents seen by each relay drop to zero and then reclose, so the currents recover their values. In fact, the variation of the admittances depicted by each plot is similar to those in the previous case until the corresponding circuit breaker opens.

The relay response depends on the inputs from the instrument transformers. Aspects to be considered are the waveform of the voltage and current inputs (e.g. peak values or decay), and the distortion introduced by CTs and CCVTs. Among the parameters that can affect this performance we need to consider the selected instrument transformers, relay burdens and the point-of-wave with which the fault transient is initiated. Some examples were presented in the first case study. For the case simulated here, the distortion introduced by instrument transformers is very small and only takes place during a few cycles of the fault currents seen by the right-side relay when the fault location is close to the right line terminal.

From the previous simulation results, it is evident that for an internal transmission line fault the highest peak current values are seen by the instrument transformers located at the right side terminal of the line. On the other hand, given that only three-phase faults are being simulated, at least one asymmetrical fault current should be expected.

Two parameters have been varied to further investigate the performance of the protection model implemented for this case study: the fault resistance, which will affect the peak value of the fault

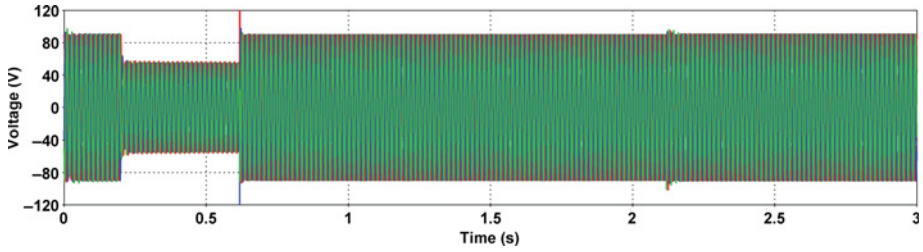

(a)

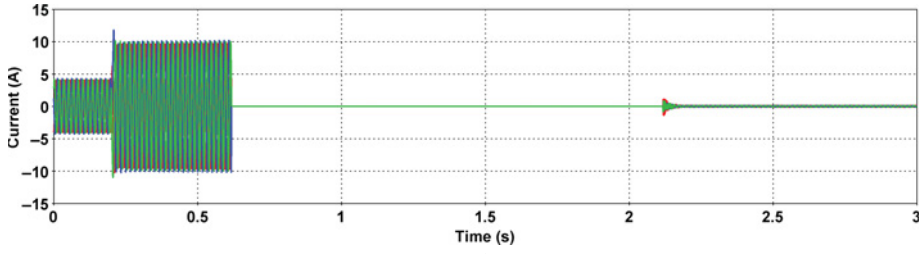

(b)

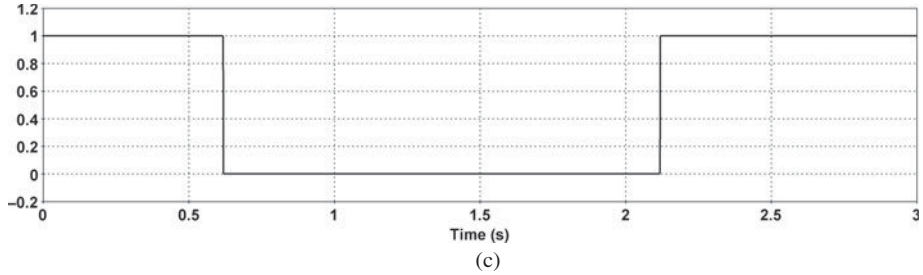

(c)

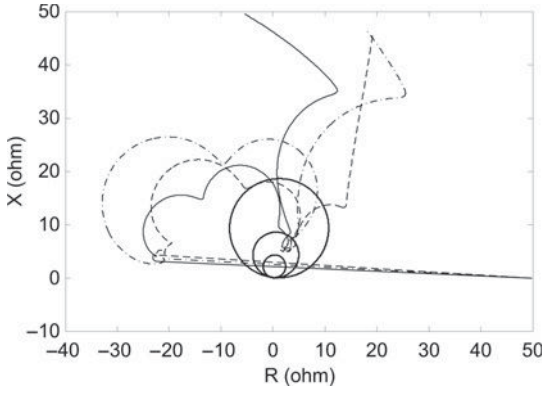

(d)

Figure 11.40 Case Study 2: Simulation results with a three-phase fault at 30 miles from the left line terminal – With instrument transformers and circuit breakers: (a) left-side line terminal voltages, (b) left-side line terminal currents, (c) left-side mho relay trip and reclosing signals, (d) impedance path measured by the left-side mho relay (voltages and currents measured at the secondary of instrument transformers), (e) right-side line terminal voltages, (f) right-side line terminal currents, (g) right-side mho relay trip and reclosing signals, (h) impedance path measured by the right-side mho relay (voltages and currents measured at the secondary of instrument transformers).

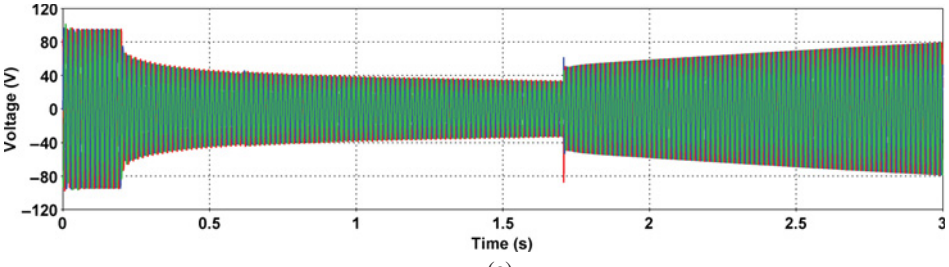

(e)

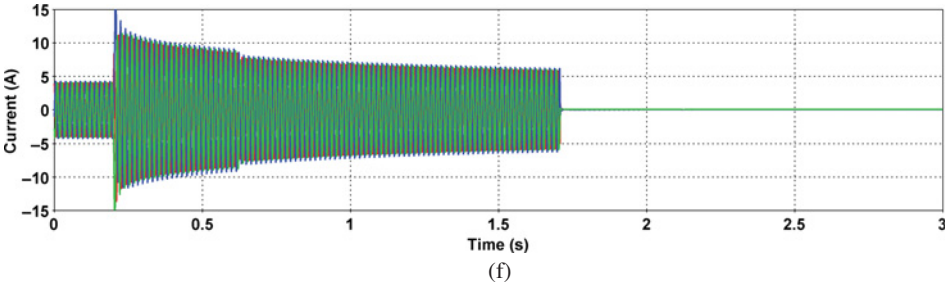

(f)

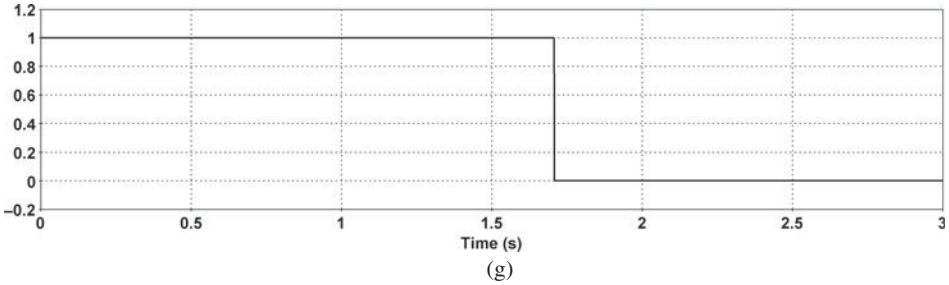

(g)

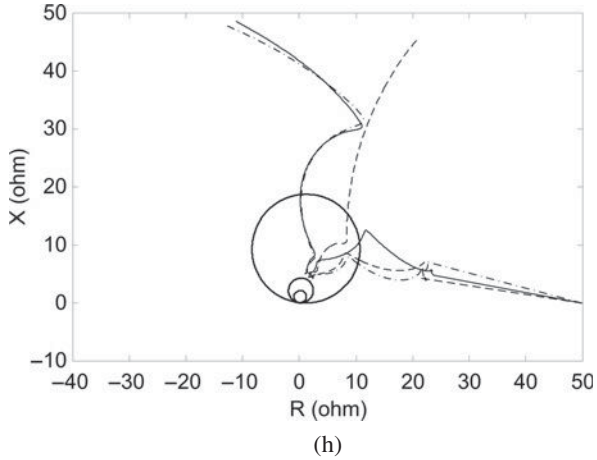

(h)

Figure 11.40 (*Continued*)

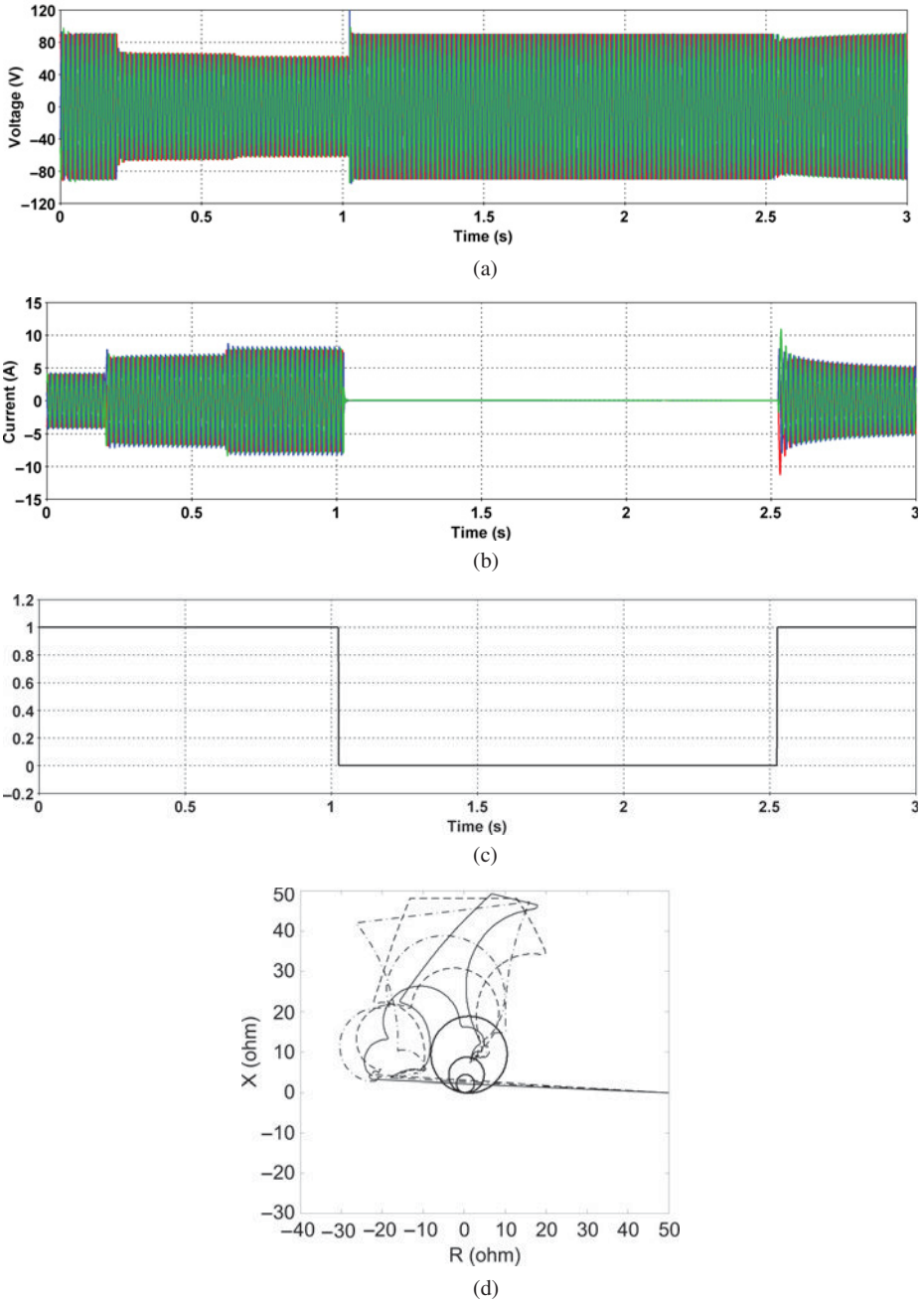

Figure 11.41 Case Study 2: Simulation results with a three-phase fault at 15 miles from the right line terminal – With instrument transformers and circuit breakers: (a) left-side line terminal voltages, (b) left-side line terminal currents, (c) left-side mho relay trip and reclosing signals, (d) impedance path measured by the left-side mho relay (voltages and currents measured at the secondary of instrument transformers), (e) right-side line terminal voltages, (f) right-side line terminal currents, (g) right-side mho relay trip and reclosing signals, (h) impedance path measured by the right-side mho relay (voltages and currents measured at the secondary of instrument transformers).

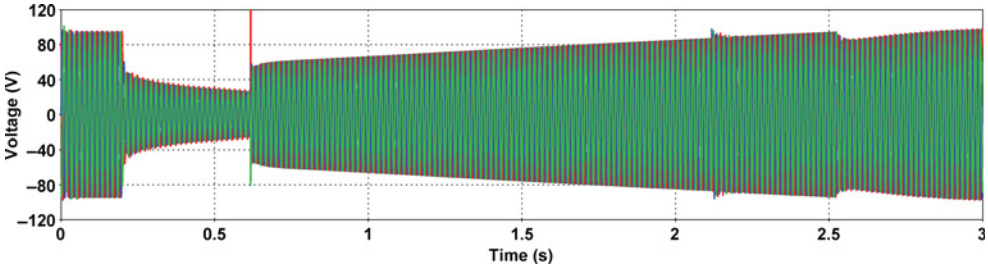

(e)

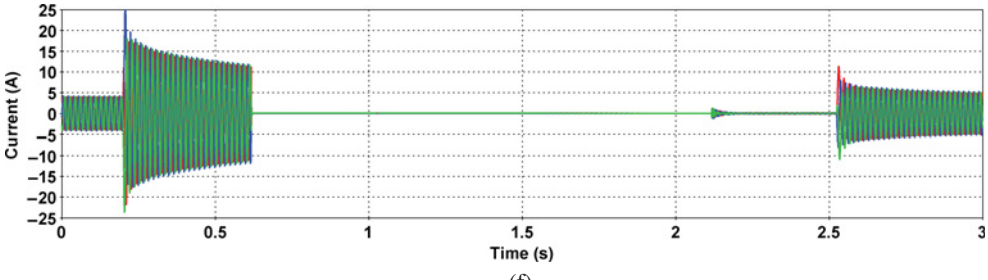

(f)

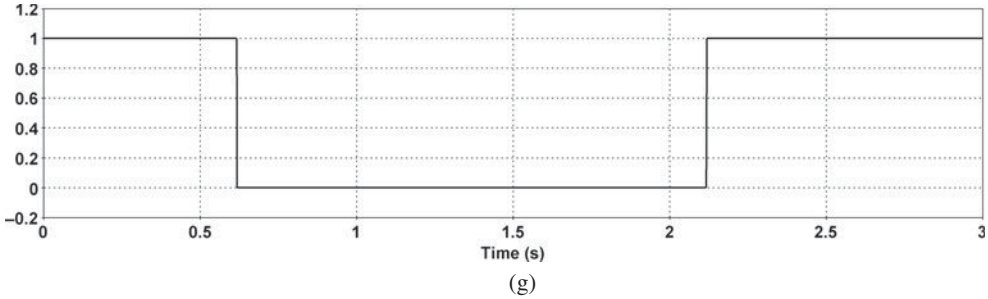

(g)

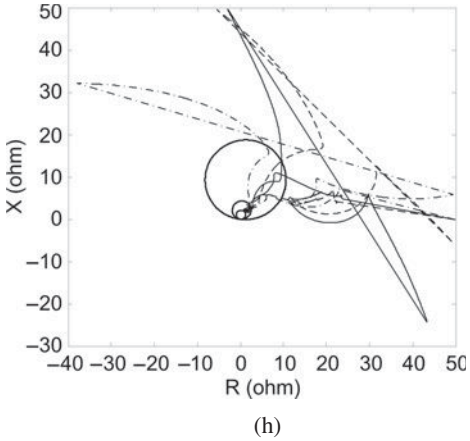

(h)

Figure 11.41 (*Continued*)

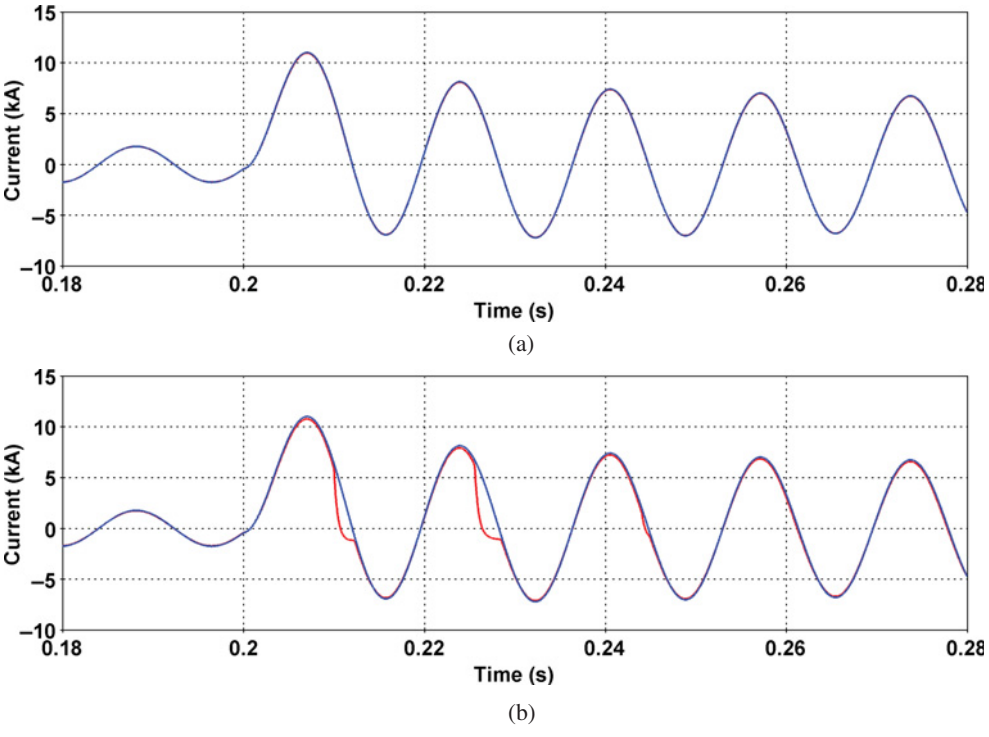

Figure 11.42 Case Study 2: CT currents seen by the right-side distance relay with a three-phase fault at 15 miles from the right line terminal – The secondary current of the CT has been reduced to the primary side. Fault resistance = 5 Ω. (a) CT burden = 4 Ω, (b) CT burden = 20 Ω.

currents, and the CT burden, which can affect the CT performance. Figures 11.42 and 11.43 show some of the simulation results.

Figure 11.42 shows some results obtained with the same fault resistance value that in the previous cases (i.e. 5 Ω) and two different CT burdens: 4 and 20 Ω. The peak values are the same in both cases and some distortion is introduced by the CT saturation into the secondary current; in both cases the relay response is correct and the trip signals are sent to the circuit breaker at the correct instant.

Figure 11.43 shows some results obtained with a lower fault resistance value (i.e. 1 Ω) and the same CT burdens (i.e. 4 and 20 Ω). We can see that the peak values are the same in both cases, and a significant distortion is introduced by the CT saturation into the secondary current. As expected, the peak current values are higher than in the previous example. In both cases the relay response is advanced and the trip signals are sent to the circuit breaker rather quickly. The simulation results presented in the figure were obtained by decreasing the relay setting for Zone 1 in order to obtain the same relay response as in the previous example.

For a single-phase-to-ground fault, the waveforms of transient currents on the faulted phase are similar to those derived with a three-phase fault, but the peak values are not very affected by the fault resistance. That is, the distortion introduced by the CT increases with its burden resistance, but the peak value of the transient current is basically the same with fault resistance of both 5 Ω and 1 Ω. Consequently, the relay response was always correct and was not affected by the fault resistance or the CT burden.

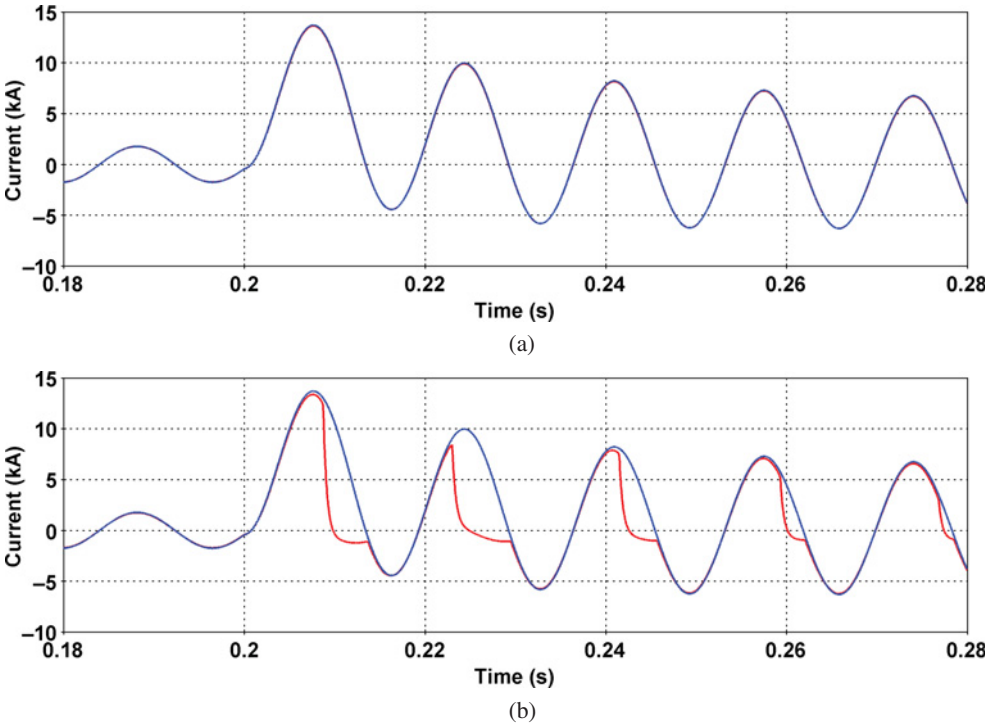

Figure 11.43 Case Study 2: CT currents seen by the right-side distance relay with a three-phase fault at 15 miles from the right line terminal – The secondary current of the CT has been reduced to the primary side. Fault resistance = 1 Ω. (a) CT burden = 4 Ω, (b) CT burden = 20 Ω.

11.8 Protection of Distribution Systems

11.8.1 Introduction

Distribution-level protection is based on a time-overcurrent design. One of the main priorities of protective devices is to prevent further damage to utility equipment. Secondary goals are reliability and power quality. Distribution protection is not designed to have backup, although there must be overlap between protective devices: an upstream device should operate for a fault if the downstream protector fails. In general, distribution protection is based on standardized settings, equipment and procedures [113–115].

Although it is commonly accepted that the installation of small distributed generation (DG) units at distribution levels has many advantages, utilities are generally concerned that the installation of small DG units may result in damage to their equipment or to the equipment of their customers. The connection of DG units raises new challenges [116, 117], one of the main concerns being islanding [117–122]. The impact of DG on the power quality of a distribution system is significantly affected by the design of the distribution system protection and the protection of DG interconnection.

This section summarizes the main features of the devices commonly used to protect radial distribution systems with or without DG and discussed the models that can be used in any of these scenarios. Two case studies will illustrate the modelling of distribution-level protective devices and some of the problems that can be encountered in distribution system protection.

11.8.2 Protection of Distribution Systems with Distributed Generation

11.8.2.1 Distribution Feeder Protection

The distribution system is in general radial in design, and distribution protection is basically overcurrent protection. Highly reliable performance of a distribution system can be achieved by installing different types of protective devices. The coordination between protective devices is another important aspect, and this is particularly difficult in distribution networks, given the number of different protective devices (breaker-relay sets, reclosers, fuses, sectionalizers). This coordination is not easy and, indeed, not always possible. In addition, it can be altered by the presence of distributed generators [116, 117, 123].

11.8.2.2 Interconnection Protection

Small DG units that are interconnected with the utility distribution system can be classified into three groups: synchronous generators (recuperating engines, combustion turbines, small hydro), induction generators (wind generators) and non-traditional asynchronous generators [119–121].

Generator protection is typically connected at the terminals of the generator and provides detection for internal short circuits and abnormal operating conditions (loss-of-field, reverse power, overexcitation and unbalanced currents). For smaller generating units, utilities usually leave to the DG owners the responsibility of selecting the protection level that they believe is appropriate. However, utilities have become very involved in specifying interconnect protection. Typically, the following interconnection areas are specified by utilities: winding configuration of the interconnection transformer, general requirements of 'utility-grade' interconnection relays, CT and VT requirements, functional protection requirements, settings of some interconnection functions, and the speed of operation required to disconnect the DG prior to utility system automatic reclosing.

Interconnection protection provides the protection that allows DG units to operate in parallel with the utility grid. Small DG units (5 MW or smaller) are usually connected to distribution systems, which are designed to supply radial load. Protection requirements to connect a small DG unit to the distribution utility grid are established by each individual utility. Large generators are reviewed on a case-by-case basis; they are usually connected to the utility's transmission system and do not employ specific interconnection protection, because they are integrated into the utility protection system itself. Properly designed interconnection protection should address the concerns of both the DG owner and the utility. Interconnection protection for small generators is established at the point of common coupling (PCC) between the utility and the DG. This point can be at the primary of the interconnection transformer, as illustrated in Figure 11.44(a), or at the secondary of the transformer – Figure 11.44(b) – depending on ownership and utility interconnect requirements. Interconnection protection satisfies the utility's requirements to allow the DG to be connected to the grid. Its function is threefold [119–121]:

1. disconnect the DG when it is no longer operating in parallel with the utility system
2. protect the utility system from damage caused by connection of the DG, including the fault current supplied by the DG for utility system faults and transient overvoltages
3. protect the generator from damage from the utility system, especially through automatic reclosing.

11.8.3 Modelling of Distribution Feeder Protective Devices

This subsection presents a summary of the main characteristics of protective devices presently used by utilities to protect radial distribution systems and the modelling approaches to be considered for each one. Readers are referred to textbooks and standards for more details [113–115, 124, 125].

11.8.3.1 Circuit Breakers – Overcurrent Relays

The performance of a breaker during an opening operation is governed by the characteristics of the overcurrent relay. There are two types of relays: instantaneous and time-delay. The time–current

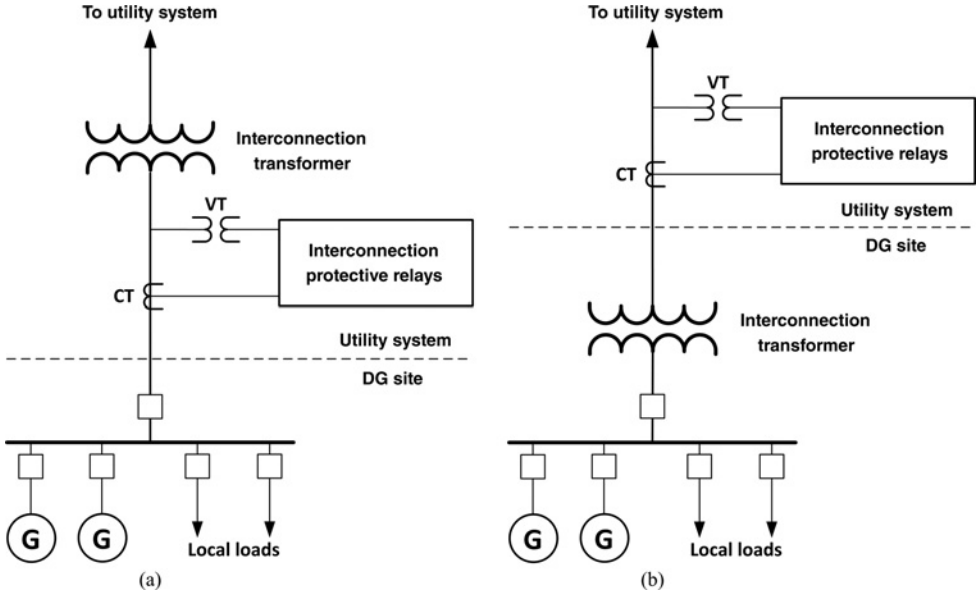

Figure 11.44 Interconnection protection: (a) protection at the transformer primary, (b) protection at the transformer secondary.

characteristic of an overcurrent relay can consist of two sections, the first being independent of the current, the second having an operating time that varies inversely with current. Depending on the rate with which the operating time and current are related, the time–overcurrent characteristic can be classified as inverse, very inverse and extremely inverse – see Figure 11.45. Typical values of these parameters can be found in the literature for each type of characteristic [125–128].

Circuit breaker models for protection studies do not include dynamic arc representation, and by default all opening operations are successful; that is, no reignitions and dielectric breakdowns can be

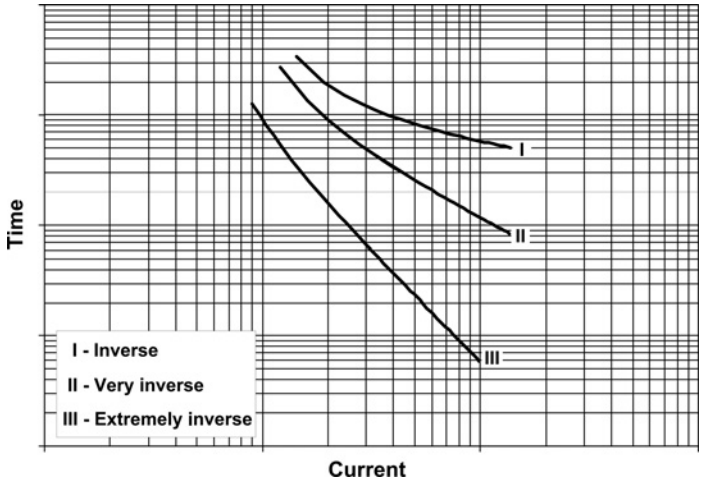

Figure 11.45 Time–current characteristics of overcurrent relays (© 2006 IEEE) [128].

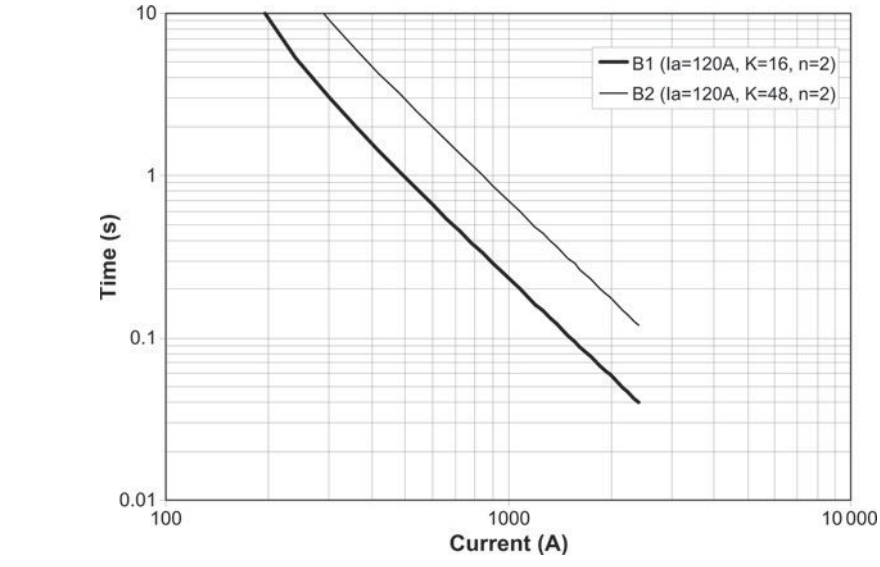

(a)

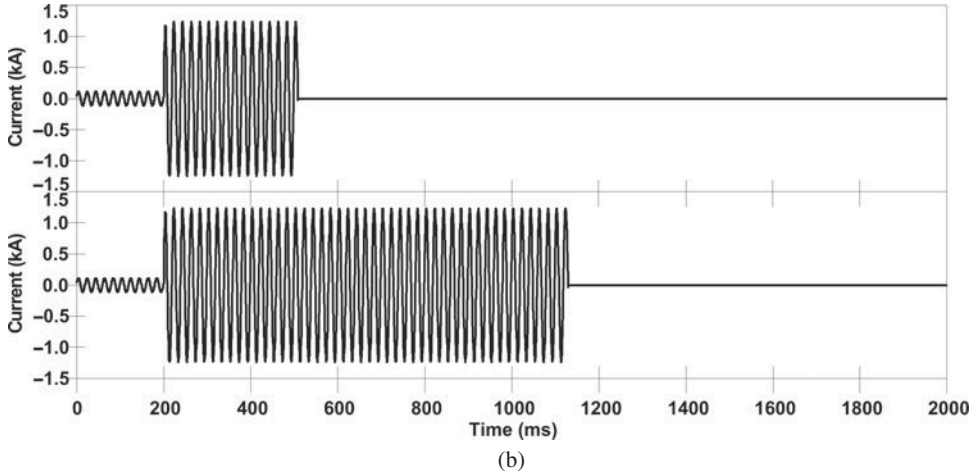

(b)

Figure 11.46 Circuit breaker operation, Three-phase fault: (a) time-current characteristics, (b) circuit breaker currents (© 2006 IEEE) [128].

duplicated by means of simulations. A breaker module is usually based on an ideal switch, controlled by an overcurrent relay whose time–current curve parameters have to be specified by users. Figure 11.46 shows the performance of the circuit breaker model during a three-phase fault with the two different time–current curves of the overcurrent relay.

11.8.3.2 Reclosers

A recloser is an overcurrent protection device that can sense and interrupt fault currents as well as automatically reclose a feeder a predefined number of times. Its operation is similar to that of a breaker

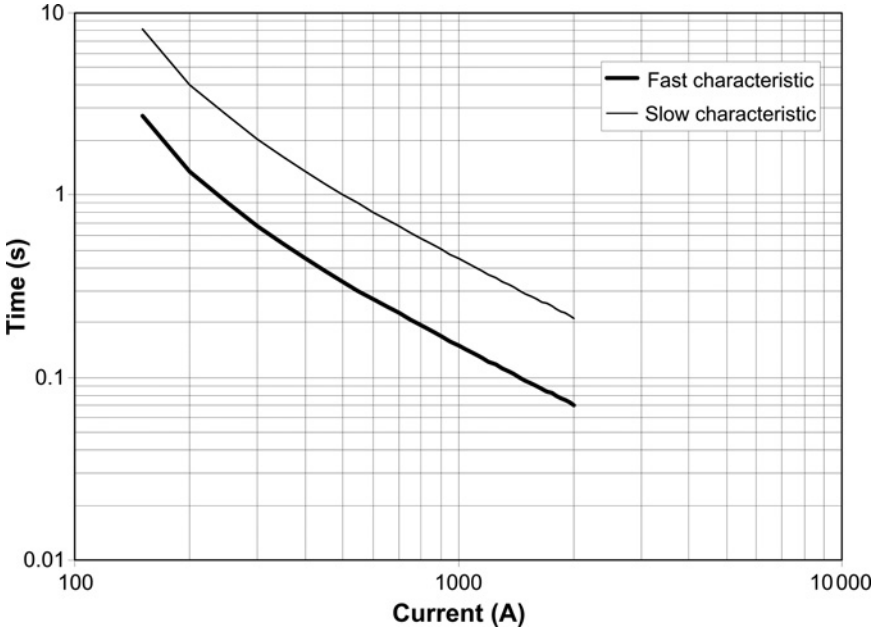

Figure 11.47 Recloser tripping characteristics (© 2006 IEEE) [128].

with a reclosing relay. In general, reclosers have less interrupting capability and cost less than breakers [113–115]. Recloser operation uses two time–current curves, see Figure 11.47. The first – known as fast or instantaneous – is mainly used to save lateral fuses under temporary fault conditions. The second curve is known as slow or time-delay, and its main purpose is to delay recloser tripping and allow fuses to blow under permanent fault conditions. A recloser can be set for a number of different operations, although a very common reclosing sequence has two fast operations followed by two time-delay trips.

The recloser model can also be based on an ideal controlled switch and it must allow users to include two tripping curves (fast and slow), select the type of time–current characteristic (inverse, very inverse, extremely inverse) and specify the number of reclosing operations for each characteristic, as well as the duration of each reclosing interval. Figure 11.48 shows one case in which the fault condition remains after two reclosing operations, and the recloser is opened after the third opening action. Only the fast characteristic was used in the three operations, but the reclosing periods are different.

11.8.3.3 Fuses

Several types of fuses are currently available in the market to protect distribution networks. In this chapter only current-limiting and expulsion fuses are considered. Fuses of the first group limit the magnitude as well as the duration of the current; the second group limits only the duration of the fault, allowing the flow of overcurrents, which will be interrupted after one zero pass. These differences can significantly affect power quality.

A fuse model has to duplicate the following stages [124]: current sensing, arc initiation, arc interruption and current interruption. The melting period, during which temperature rises, begins with the fault and finishes when the fuse melts; during this stage the current flows without limitation. The melting mechanism of a fuse depends on the magnitude and the duration of the current, as well as on the electrical properties of the fuse. This characteristic is shown in the so-called time–current curve provided

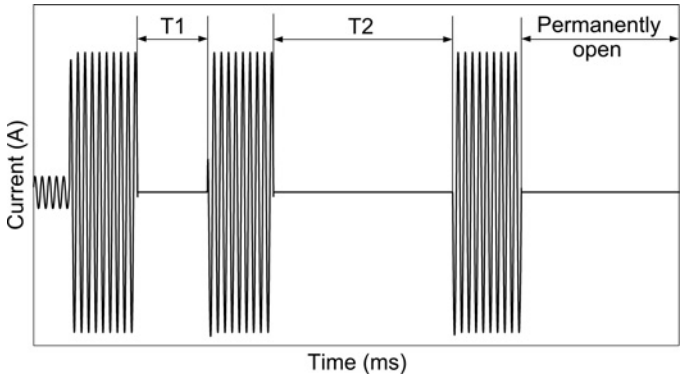

Figure 11.48 Recloser performance (© 2006 IEEE) [128].

by manufacturers. The performance of a fuse is depicted by means of the minimum melting and the total clearing curves: a fuse has an arcing time, which is the time needed to interrupt the current after the fuse melts, so the total clearing time curve results from adding the arcing time to the melting time – see Figure 11.49.

Expulsion fuses typically interrupt fault currents at the first current zero (Figure 11.50). In some cases, expulsion fuses may not be successful in interrupting current at the first current zero, but succeed in interrupting current at the second current zero. If a fuse fails to interrupt current at the second current zero, usually it will be destroyed, and the current will be interrupted by a backup device.

Figure 11.51 shows the operation of a current-limiting fuse (CLF), from the instant at which the fault is caused until the instant at which the fuse melts and the current is interrupted. The operating time of a CLF can be shorter than half a cycle, but this high speed has a cost, since an overvoltage is usually

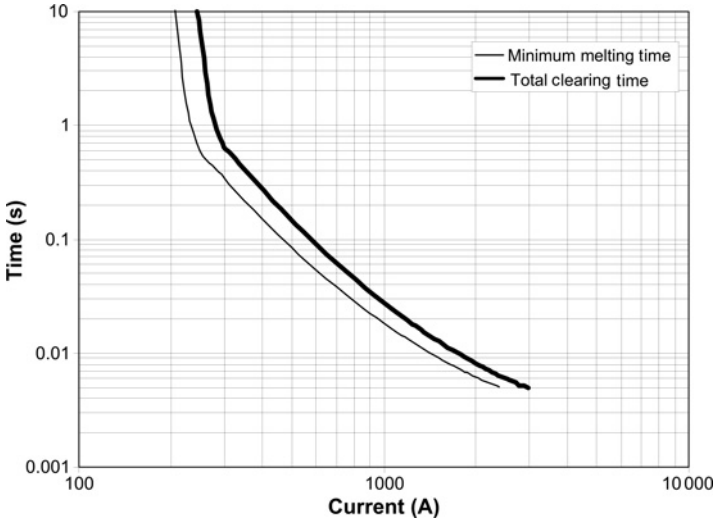

Figure 11.49 Extreme time–current characteristics of a fuse (© 2006 IEEE) [128].

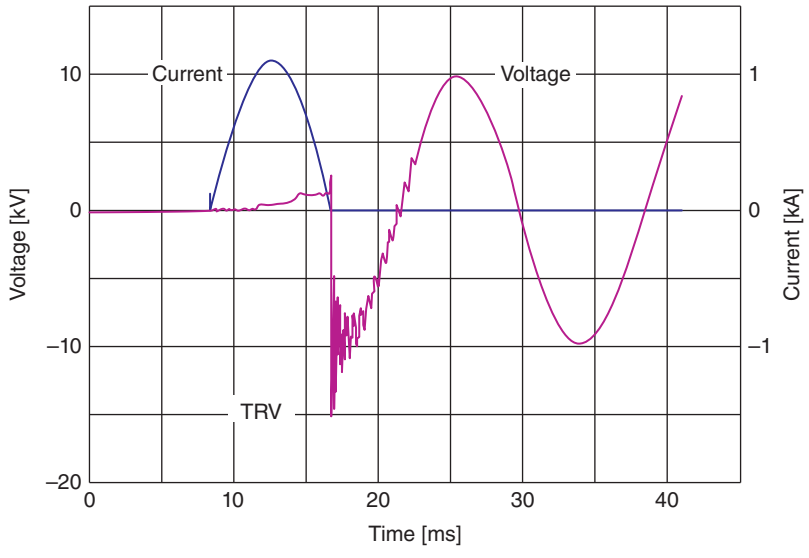

Figure 11.50 Expulsion fuse operation (interrupts current at the first current zero).

obtained. The fuse limits the let-thru energy to a fraction of the energy available from the system. The performance of a CLF can be deduced from the let-thru charts, which are very useful for obtaining the current during a fuse operation. The two main parameters in the CLF operation are the melt I^2t and the nonlinear resistance characteristic after melting. CLF let-thru current waveforms for different fault current levels are shown in Figure 11.52.

An expulsion fuse interrupts a fault current at current zero; a CLF interrupts a fault current by forcing a current zero. Upon interruption, the operation of a CLF results in the insertion of additional impedance and the development of an arc voltage; when this voltage exceeds the system voltage, the arc is extinguished and the action is accomplished [124]. An expulsion fuse heats to its melting point when the fault occurs; the current continues to flow in the form of an arc; at zero current the arc is

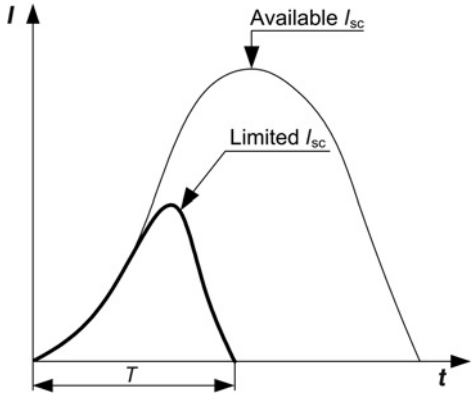

Figure 11.51 Effect of a current-limiting fuse (© 2006 IEEE) [128].

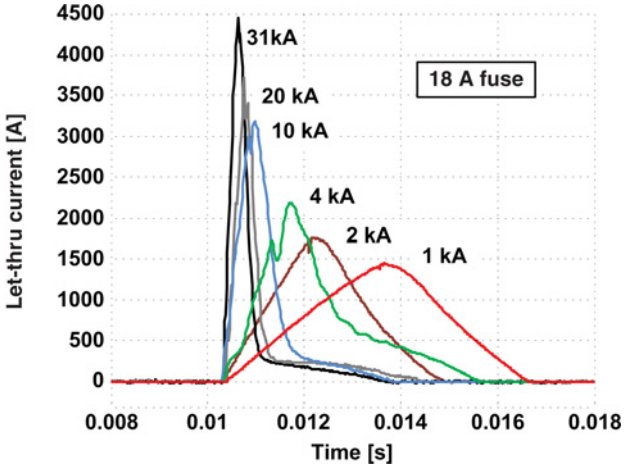

Figure 11.52 Current-limiting fuse let-thru current waveforms for different fault current levels.

extinguished, the fuse being subjected to a transient recovery voltage (TRV), whose magnitude depends on the operating conditions [129]. One or several arc reignitions can be caused by the TRV; the process stops only when the dielectric strength build-up is greater than the TRV.

Although minimum melting curves are similar for both types of fuses, the approach chosen for representing every type has been different. Since the action of a CLF results in the sudden insertion of a high value resistance, this type of fuse has been modelled as a variable resistance controlled from a TACS section in EMTP-like tools, in which users can specify the parameters that govern the fuse resistance [128]. The input of the minimum melting time–current curve is made by means of a regression equation that matches the characteristic provided by the manufacturer. This means that different equation coefficients have to be considered for each manufacturer.

An expulsion fuse can be represented as a switch that opens at the first zero-current. Therefore, these fuses have been modelled as controlled switches. The module required for this type of fuse is basically the same developed for representation of CLFs, but without including any post-melting resistance. For more details, see [127–131].

The temperature of a fuse increases towards its melting value during a fault. When coordinated with a recloser, the time–current characteristic of a fuse is affected by the heating–cooling cycle: if the recloser operates faster than the fuse, this will heat during the fault and cool during the reclosing time interval. An adjustment of the fuse time–current characteristic is therefore needed. A more advanced model can be implemented to account for the thermal response of a fuse during multiple reclosing operations using the coordination principles between fuses and reclosers presented in [132]. The features of this fuse model are detailed in [128].

Figure 11.53 shows the *R*–*t* characteristic of an 8.3 kV, 20 A CLF. A successful model for representing this CLF was implemented in EMTP/ATP. Figure 11.54 compares field tests and computer simulations.

11.8.3.4 Sectionalizers

A sectionalizer is an automatic circuit opening device that has no capacity to break fault current, and it is usually installed downstream of a breaker or a recloser. After a circuit has been de-energized by a backup protective device, such as a recloser or a reclosing breaker, a sectionalizer isolates the faulted portion of a distribution network [113, 115], after which the rest of the circuit is returned to service upon reclosure

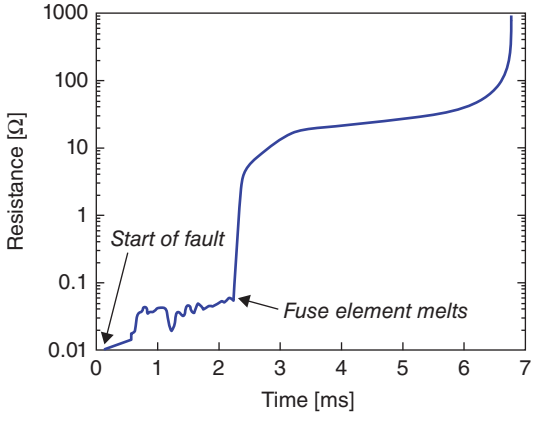

Figure 11.53 8.3 kV, 20 A current-limiting fuse – *R–t* characteristic.

of the backup device. A sectionalizer counts the interruptions of the backup device; it can be set to open after one, two or three counts have been registered within a predetermined time span – see Figure 11.55. A sectionalizer opens during the open interval of the backup device. Although it cannot interrupt faults, it can be closed into them. Sectionalizers are built in single- and three-phase arrangements.

Sectionalizers can be used in place of fuses or between a reclosing device and a fuse. They only detect current interruptions above a predetermined level and have no time–current characteristics, permitting easy coordination with other protective devices on the system. Their advantages over fuse cut-outs are many: they offer safety and do not open accidentally under load; after a permanent fault, the fault-closing capability of the sectionalizer greatly simplifies circuit testing; if a fault is still present, interruption takes place safely at the backup recloser; replacement of fuse links is not required; and the possibility of error in the selection of the correct size is eliminated.

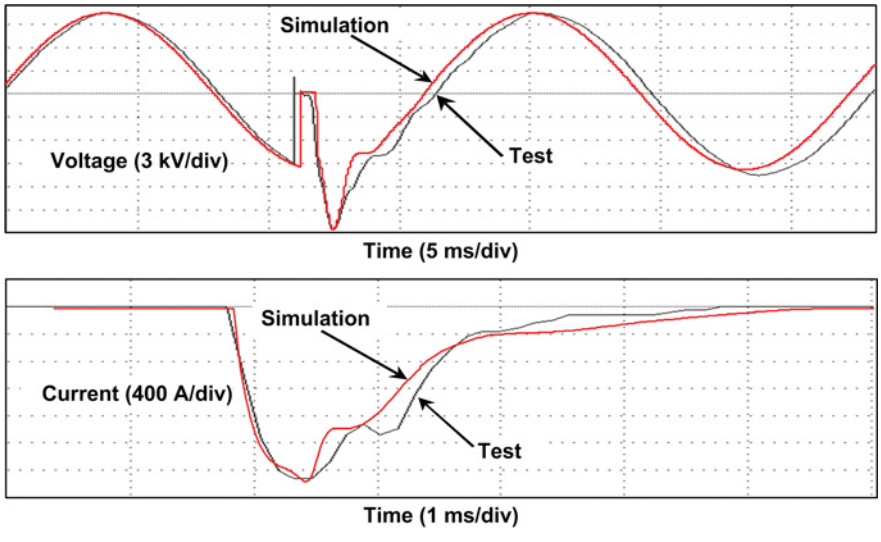

Figure 11.54 8.3 kV, 20 A current-limiting fuse – Voltage and current during a field test.

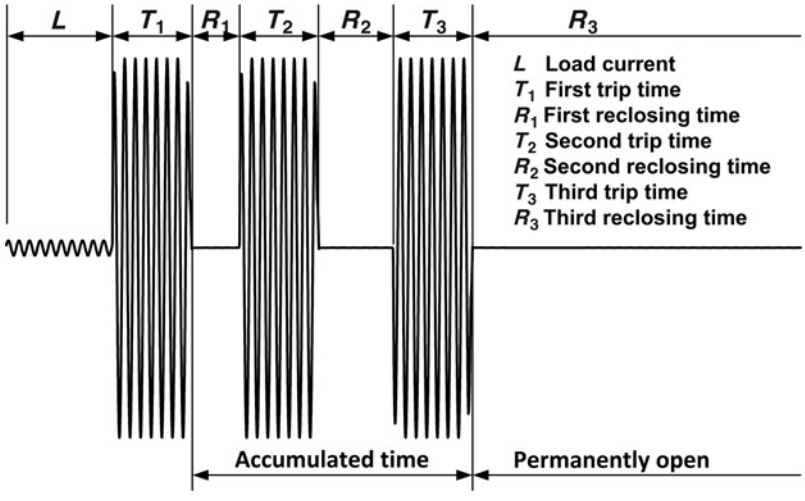

Figure 11.55 Sectionalizer performance.

The sectionalizer model must also be based on an ideal controlled switch. The user has to specify the number of interruptions of the backup device and the minimum time during which the current is interrupted in each operation. Figure 11.56 shows a case in which the sectionalizer opens after detecting the third interruption. Note that the recloser recovers the current of those loads that are not in the path of the fault location situated downstream the sectionalizer.

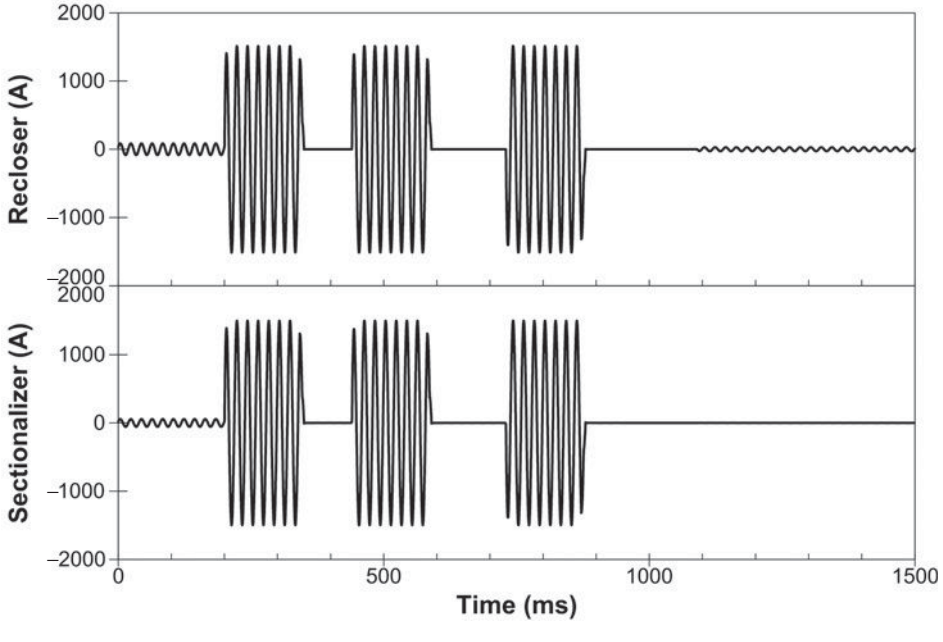

Figure 11.56 Sectionalizer operation when coordinated with a recloser.

11.8.4 Protection of the Interconnection of Distributed Generators

Interconnection protection design depends on factors such as generator size, point of interconnection, type of generator and interconnection transformer connection. The winding connection of the interconnection transformer plays an important role in how DG units will interact with the utility system under faulted conditions. All connections have advantages and disadvantages which need to be addressed by the utility in their guidelines, since the choice of a transformer connection has a deep impact on interconnection protection requirements [119–121]. Transformer connections used to interconnect DGs to distribution systems can be classified into two groups, depending on the primary winding grounding:

- *Ungrounded primary transformer winding*: The major concern with this connection is that after the substation breaker is tripped for a permanent ground fault, the system is ungrounded. This subjects line-to-neutral equipment on the unfaulted phases to an overvoltage that will approach line-to-line voltage. This occurs if the DG is near the capacity of the load on the feeder when the substation breaker trips. Some utilities use ungrounded interconnection transformers only if an overload (200% or more) on the DG occurs when the breaker trips. During ground faults, this overload level will not allow the voltage on the unfaulted phases to rise higher than the normal line-to-neutral voltage. Ungrounded primary windings should generally be reserved for smaller DGs where high overloads are expected on islanding.
- *Grounded primary transformer winding*: This connection provides an unwanted ground fault current for supply circuit faults and reduces the current from the substation breaker at the utility substation, which can result in a loss of relay coordination. When the DG is off-line (i.e. the generator breaker is open), the ground fault current will still be provided to the utility system if the DG interconnect transformer remains connected. This would be the case when interconnect protection trips the generator breaker. The transformer at the DG site acts as a grounding transformer with zero-sequence current circulating in the delta secondary windings. An interconnection transformer with both primary and secondary windings grounded also provides a source of unwanted ground current for utility feeder faults similar to that described above, as it also allows ground relays at the substation to respond to ground faults on the secondary of the DG transformer. This can require the utility to increase ground relay pickup and/or delay tripping to provide coordination, which reduces the sensitivity and speed of operation for feeder faults and can increase wire damage.

Table 11.1 lists specific objectives of an interconnection protection system, as well as the relay requirements to accomplish each objective [118, 132].

11.8.5 Case Study 3

The aim of this example is to illustrate the impact that CT saturation can have on overcurrent protection behaviour. A fast time–current characteristic curve shown in Figure 11.57 was selected to study the impact

Table 11.1 Interconnection protection objectives.

Objective	Protection function
Detection of loss of parallel operation	81O/U, 27, 59, 59I
Fault backfeed detection	Phase faults: 51V, 67, 21 Ground faults: 51N, 67N, 59N, 27N
Detection of damaging system conditions	Negative sequence: 46, 47 Loss of synchronism: 27
Reverse power flow detection	32
Restoration	25

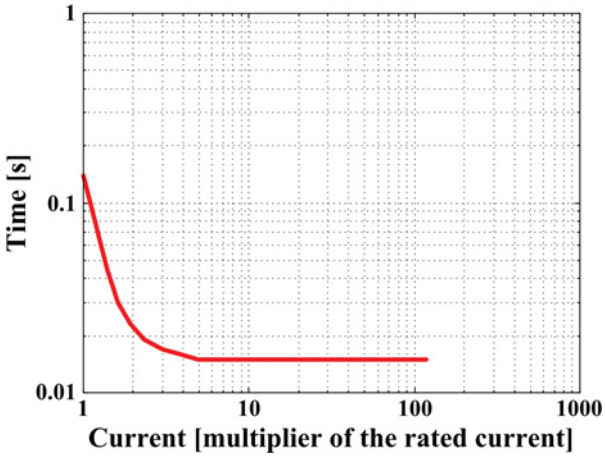

Figure 11.57 Case Study 3: Overcurrent relay characteristic time–current curve.

of CT saturation on microprocessor-based overcurrent protection device operation. Distribution system parameters in this example are as follows: symmetrical short-circuit current = 12 kA, *X*/*R* ratio = 15. Simulations included symmetrical and full asymmetrical fault currents.

12 kA symmetrical fault currents. Figure 11.58 shows the current waveforms. CT secondary currents are referred to the primary. The CT saturation is pronounced only in the first half-cycle. Figure 11.59 shows CT secondary currents and rms values calculated by the protection device for non-saturated and saturated CT. The rms value of the saturated CT is reduced only during the CT saturation when compared to the non-saturated CT. The fault current was maintained at 12 kA_{rms} while the device minimum pickup/trip setting was changed from 500 A to 1200 A. Since the CT only slightly saturated, simulated overcurrent protection device response times were the same for both saturated and non-saturated CTs.

12 kA asymmetrical fault currents without CT remanence. Figure 11.60 shows waveforms for primary and secondary currents. CT secondary currents are referred to the primary. CT saturation was considerable in the first five cycles, resulting in significant reduction of the rms current value. Figure 11.61 shows CT secondary currents and rms values calculated by the protection device for non-saturated and saturated CT. The fault current was again maintained at the same level while the minimum pickup/trip setting changed from 500 A to 1200 A. The device response times were again the same for both saturated and non-saturated CTs. The reason that the device response time for saturated CT was not increased was the fast TCC curve where protection operating point remained on the horizontal part of the TCC curve.

12 kA asymmetrical fault currents with CT remanence. To study the extreme case, simulations were performed representing 80% remanence in the CT core. The CT saturation was considerable in the first five cycles and the rms value of the current significantly reduced. Figure 11.62 shows waveforms for primary and secondary currents, with secondary currents referred to the primary. Figure 11.63 shows the CT secondary currents and rms values calculated by the protection device for non-saturated and saturated CT. In this case, the fault current was again maintained at the same level while the minimum trip setting changed from 500 A to 10 kA. The response times of the overcurrent protection device were not impacted for minimum trip settings up to 1200 A. The response time delay was noticeable for settings between 2000 A and 7000 A. The device did not respond to the fault when minimum trip was set at 10 kA. In practice, the load current has been used to determine minimum pickup/trip for phase and ground time overcurrent elements for relays and reclosers. Normally, when calculating the phase minimum pickup/trip, a factor of 2.0–2.5 times normal load current is included, to account for load growth, contingency operating conditions and cold-load inrush currents. This suggests that in most cases there is no need to set minimum pickup over 2000 A.

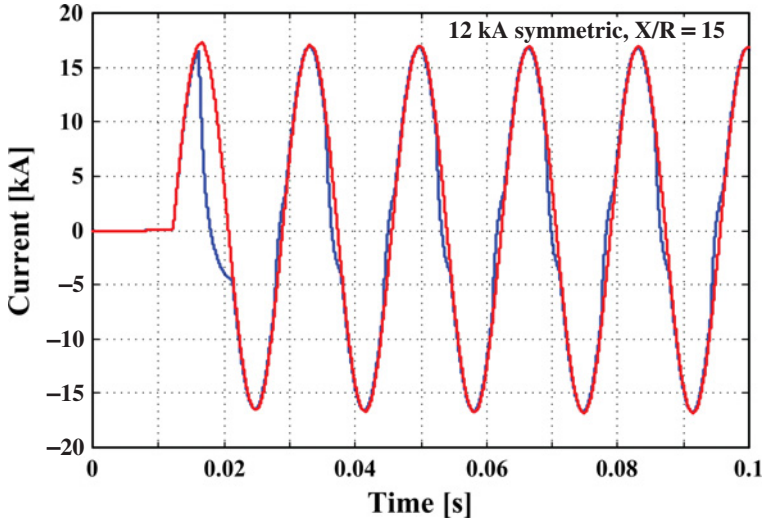

Figure 11.58 Case Study 3: Simulated primary and secondary currents for a 12 kA symmetrical fault with $X/R = 15$.

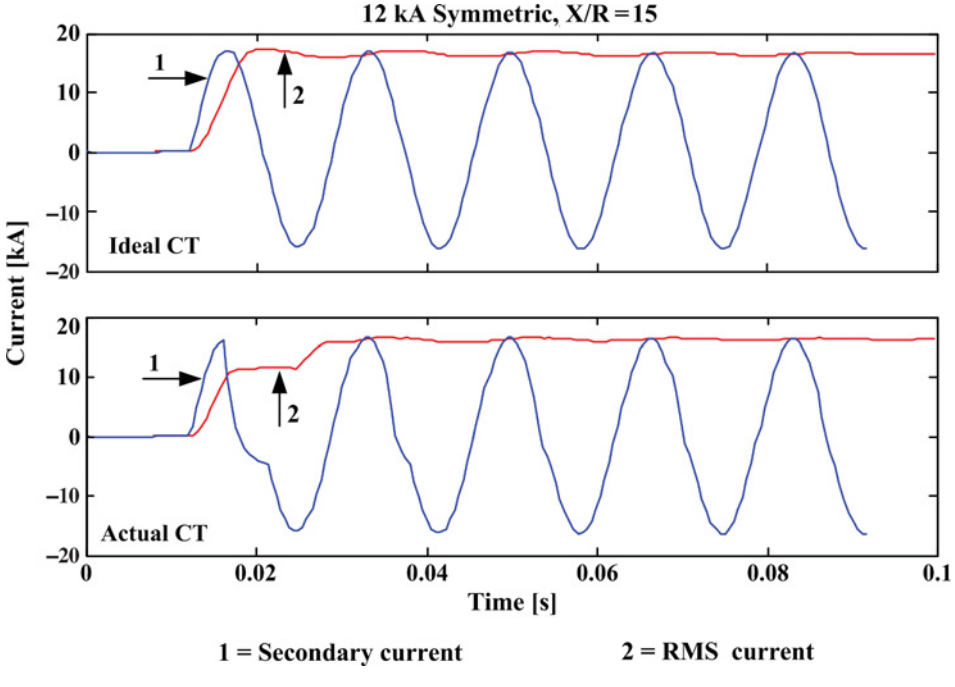

Figure 11.59 Case Study 3: Protection device response for non-saturated and saturated CTs (12 kA symmetrical fault with $X/R = 15$, no remanence).

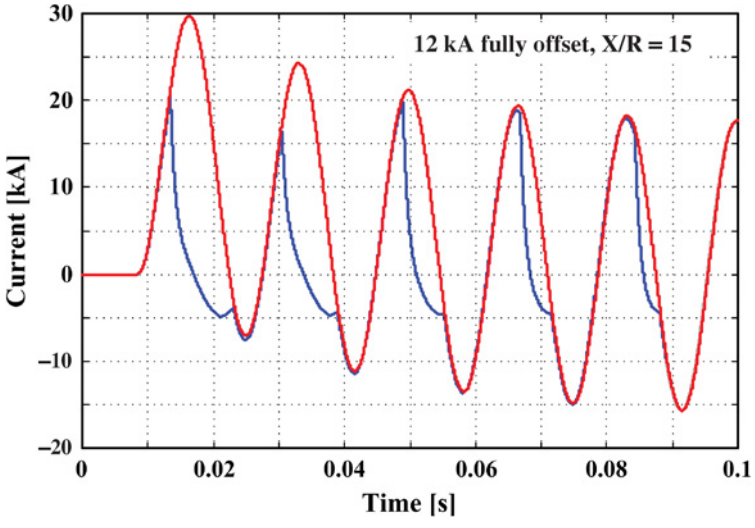

Figure 11.60 Case Study 3: Simulated primary and secondary currents for a 12 kA asymmetrical fault with $X/R = 15$, no remanence.

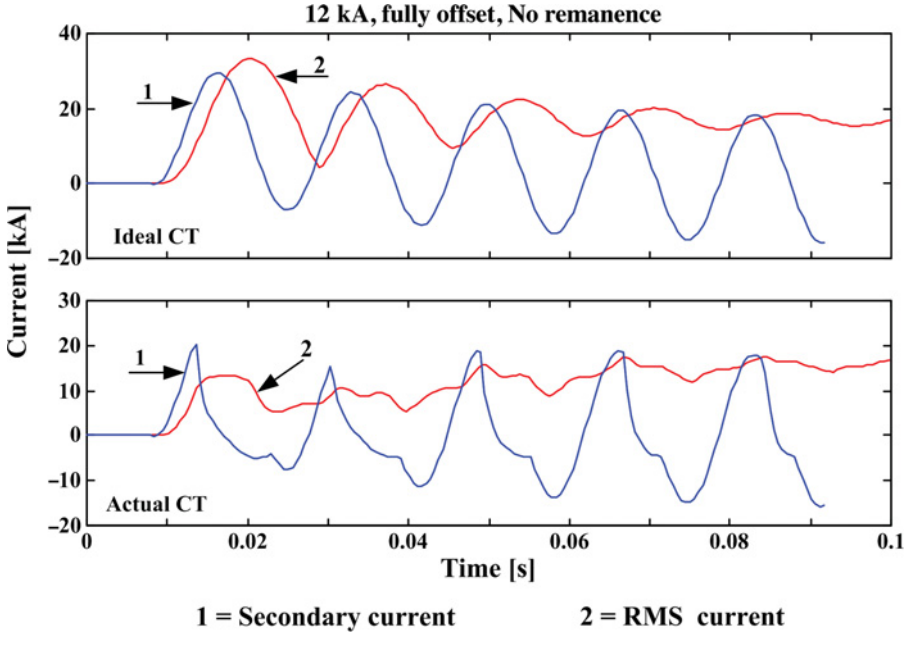

Figure 11.61 Case Study 3: Simulated secondary currents and protection device response for ideal and actual CTs (12 kA asymmetrical fault with $X/R = 15$, no remanence.

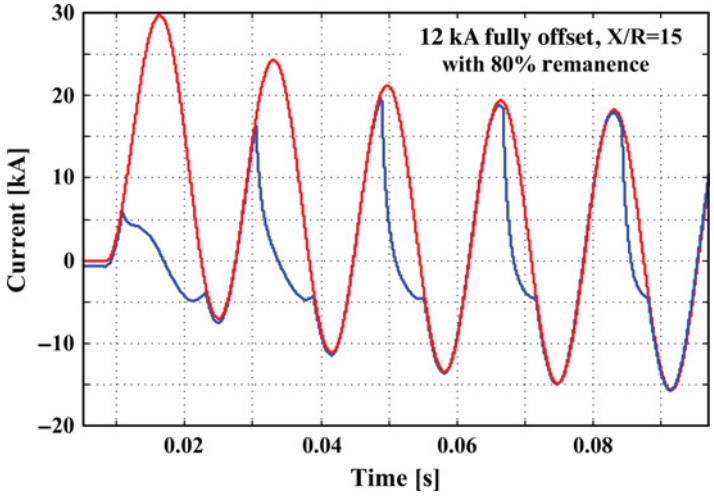

Figure 11.62 Case Study 3: Simulated primary and secondary currents for a 12 kA asymmetrical fault with $X/R = 15$, 80% remanence.

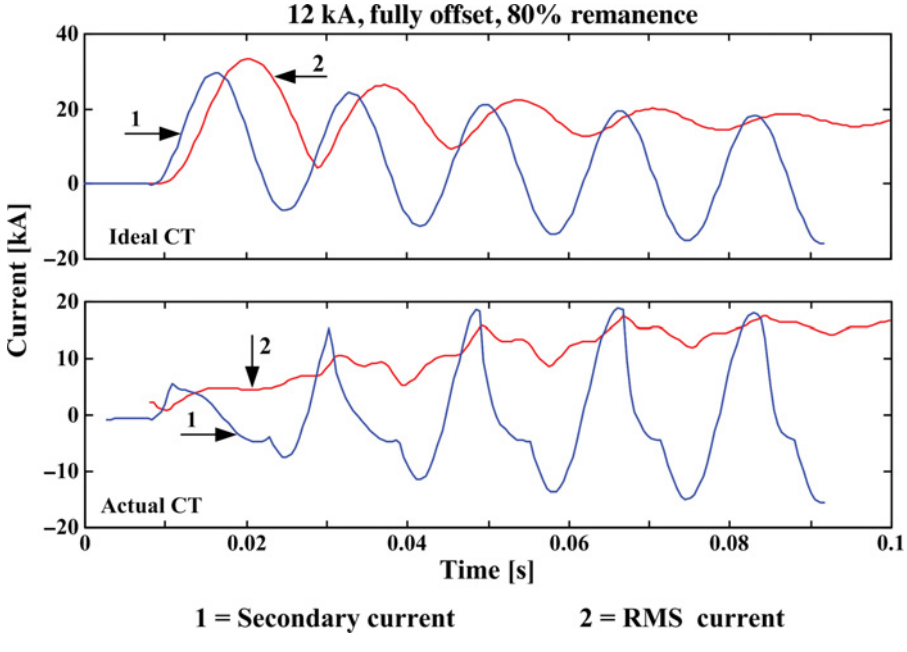

Figure 11.63 Case Study 3: Simulated secondary currents and protection device current calculation for ideal and actual CTs (12 kA asymmetrical fault with $X/R = 15$, 80% remanence).

11.8.6 Case Study 4

Figure 11.64 shows the configuration of the system analysed in this work and the parameters of some components. The lower voltage side of the substation transformer is grounded by means of a zigzag reactor of 75 Ω per phase. The diagram shows the location of some faults that will be used to analyse the performance of the protective device models and the coordination between them. The examples analysed in this work correspond to the following scenarios [133–135]:

- Example 1: There is a fault at node A, which is sensed by overcurrent relays at B1 and B2. Due to the time–current characteristics of the relays, breaker B2 opens first. The example analyses the performance of the relay models and discusses some solutions for this case.
- Example 2: As a consequence of the operation of breaker B2 (e.g. a miscoordination as in the previous example), G2 starts operating in islanding mode. This is not allowed in the interconnection contract with the utility, so the loss of parallel operation must be detected and the generator must be disconnected.
- Example 3: There is a fault at node B, which is sensed by the fuse F1 and the recloser R1. Since fuse-saving is implemented, R1 must open first. So, even if the fault is permanent, fuse F1 should not open before one or several reclosing operations of R1. However, the presence of generator G1 may cause miscoordination between R1 and F1 and consequently F1 will open first. A solution is proposed by installing a sectionalizer instead of fuse F1.

All the examples are based on a system with the configuration shown in Figure 11.64, but the operating conditions and device settings are different for each study.

This case study is aimed at illustrating how the presence of small generation units embedded into the distribution grid can alter the coordination between protective devices and lead to their misoperation and analysing the response of relays installed for protection of DG interconnection.

The simulations were carried out using a library of models implemented in ATP [133–135] and with a few limitations:

- The interconnect protection for DG units is always at the primary side of interconnection transformers.
- The representation of substation and distribution transformers, as well as interconnection transformers, is linear; that is, saturation effects are not included in transformer models. If so, the simulation of some transients (e.g. transformer inrush) makes no sense.

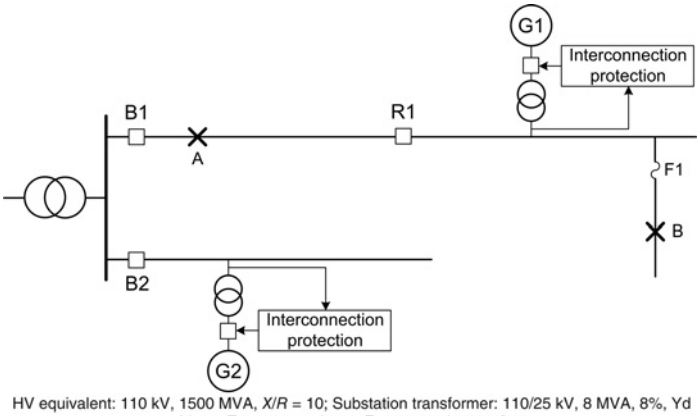

Figure 11.64 Case Study 4: Test system (© 2010 IEEE) [133].

- It is assumed that the input to relays is not modified/altered by instrument transformers. Therefore, CT and VT models are not included in simulations and relay inputs are directly from phase currents and phase-to-ground voltages.

Only simulation results corresponding to three-phase faults are analysed. For a simplified analysis of the impact that the connection of embedded generators can have on the coordination of distribution protective devices, see [134].

11.8.6.1 Example 1: Overcurrent Relay Miscoordination

Figure 11.65 shows the characteristics of the overcurrent relays that control circuit breakers B1 and B2. Although the fault is on the upper feeder, the resulting current flow due to the presence of DG may result in an undesirable tripping of the unfaulted feeder breaker. Simulation results are shown in Figure 11.66. The fault current flowing through the unfaulted feeder is much smaller than the fault current flowing through the breaker installed on the faulted feeder, but for a fault at node A circuit breaker B2 opens first. However, after reclosing both B1 and B2, B1 opens faster and B2 remains closed. Note that although B2 recloses first, and although the fault is isolated because B1 is still opened, the current through B2 is very high; this is due to the opposite phase on the two sides of B2 at the time it recloses. By the time B2 recloses, the generation unit should have been disconnected from the feeder – see the two following examples. Note the different shapes of the overcurrent sensed by each circuit breaker – the current through B2 exhibits the typical waveshape of short-circuit current caused by a fault not far from a synchronous generator.

Several solutions have been proposed for this case [133]. Since this can be seen as a miscoordination between overcurrent relays, one solution is to select faster time–current characteristics for the overcurrent relay of the faulted feeder – see Figure 11.67.

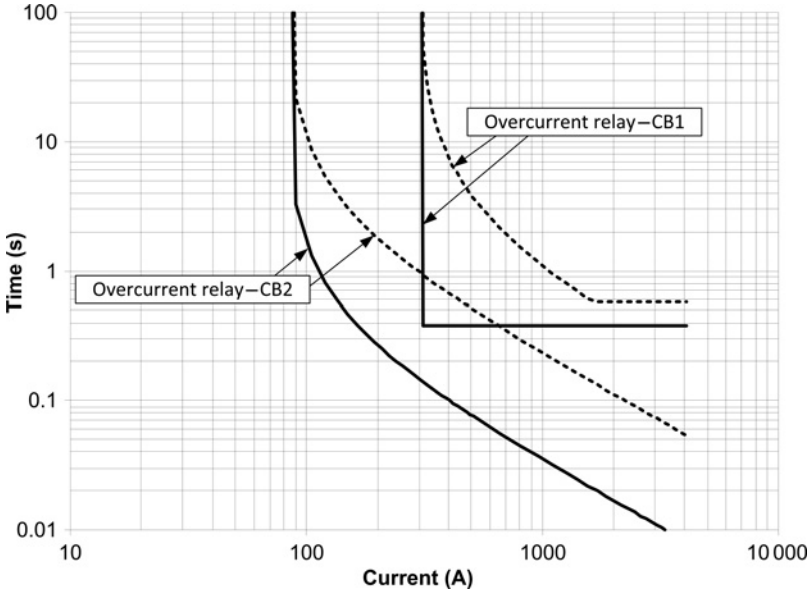

Figure 11.65 Case Study 4 – Example 1: Time–current characteristics of overcurrent relays (© 2010 IEEE) [133].

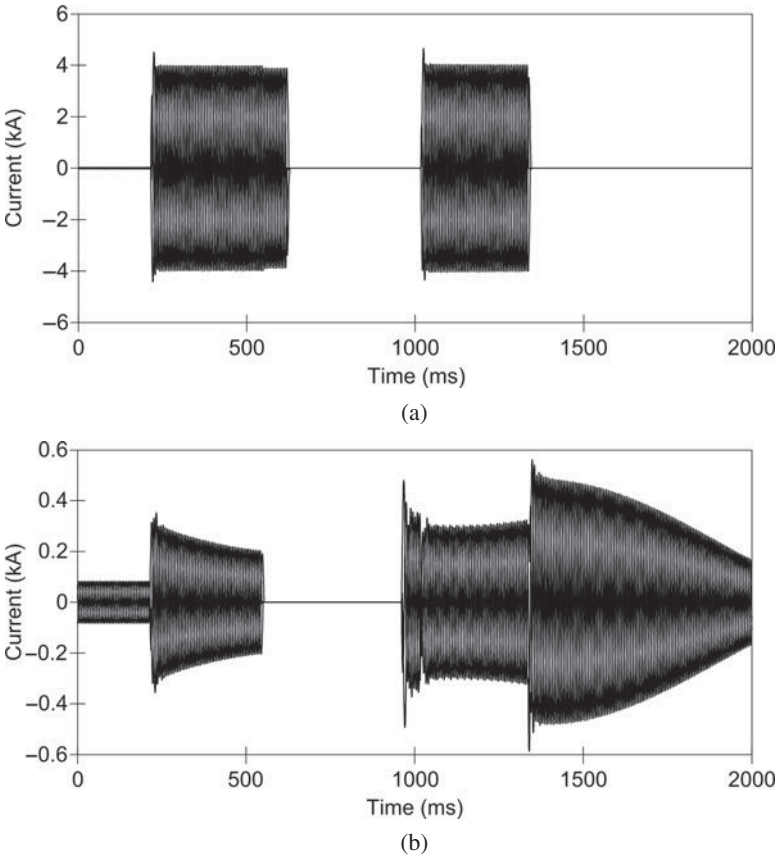

Figure 11.66 Case Study 4 – Example 1 – Simulation results: (a) faulted feeder – current through circuit breaker B1, (b) unfaulted feeder – current through circuit breaker B2 (© 2010 IEEE) [133].

Figure 11.68 shows the results with the new time–current curves. This solution should be chosen with caution because the new characteristic must also be coordinated with protective devices located downstream of B1. Another solution is to directionalize the overcurrent relays of substation breakers; this will avoid future miscoordination with other protective devices.

11.8.6.2 Example 2: Detection of Loss of Parallel

The miscoordination between protective relays in the previous case may create a generation island: after breaker B2 opens, the bottom generation unit is separated from the feeder if the breaker-relay set does not reclose. Several options for detecting the loss of parallel and separating the generation unit from the utility system may be used. Assume that breaker B2 opens and that the feeder demand exceeds the rated power of the generator G2. The unbalance between load and generation can be detected in several ways. Figure 11.69 shows how the current supplied by the generator increased after breaker B2 opens. If the control of the prime mover is disabled, the overcurrent protection will be able to separate the unit from the feeder after more than 4 s.

As mentioned above, detecting the island mode can also be based on measuring the voltage and the frequency at the generator terminals. Unless the exciter control was disabled, a similar performance to

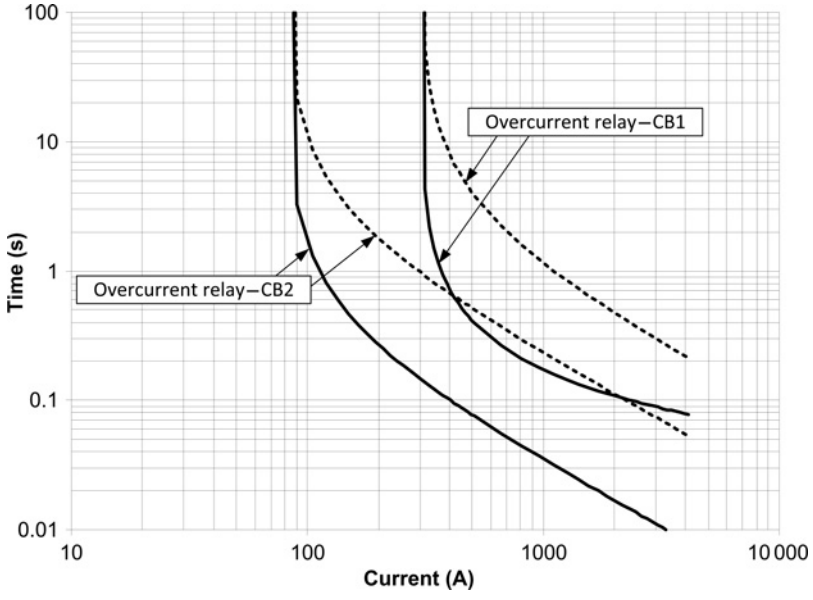

Figure 11.67 Case Study 4 – Example 1: New relay characteristics (© 2010 IEEE) [133].

that shown in Figure 11.69 could be expected from sensing the voltage. An alternative option could be based on the measurement of the frequency.

Figure 11.70 shows the characteristics of the over- and under-frequency relays tested for this case. The frequency measured after breaker B2 opens is shown in Figure 11.71. As expected, the generator frequency decreases, and the relay sends its signal after the frequency value is below 99% of the rated value (50 Hz in this example). Taking into account the operating conditions and the generator parameters (e.g. rotor inertia), the separation takes place more than 3.5 seconds after the opening of breaker B2.

The results from this study can be useful for adjusting the different protective relays and devices involved in the test system. For instance, it is obvious from the above results that the reclosing of breaker B2 should not be made in less than 3.5 s; if this period is too long, then the frequency relays must be readjusted.

For newer and more sophisticated anti-islanding algorithms see [136–138].

11.8.6.3 Example 3: Miscoordination between Protective Devices

The first example presented a case in which miscoordination between overcurrent relays that control circuit breakers may occur. The present example details a case in which a miscoordination between a recloser and a fuse may be caused by the presence of an embedded generator [135]. Since most faults in overhead distribution networks are temporary, utilities use fuse-saving to prevent unnecessary lateral fuse operations. This practice is implemented with an instantaneous relay on a breaker or the fast curve on a recloser.

Assume that there is a temporary fault on the node B (Figure 11.64) and the fault current is sensed by the fuse F1 and the recloser R1. Figure 11.72 shows the fast and the slow characteristics of the recloser R1, the characteristic of the fuse F1, for which the minimum melting time curve is used, and the fault current value sensed by both devices. If no generator is connected to the network, the fault current through both devices is basically the same.

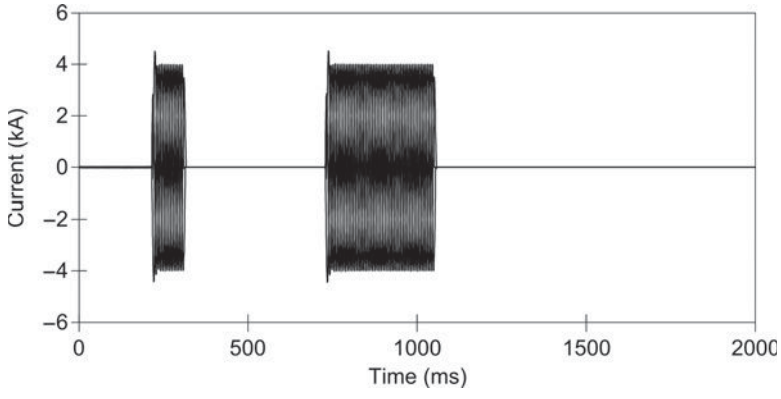

(a)

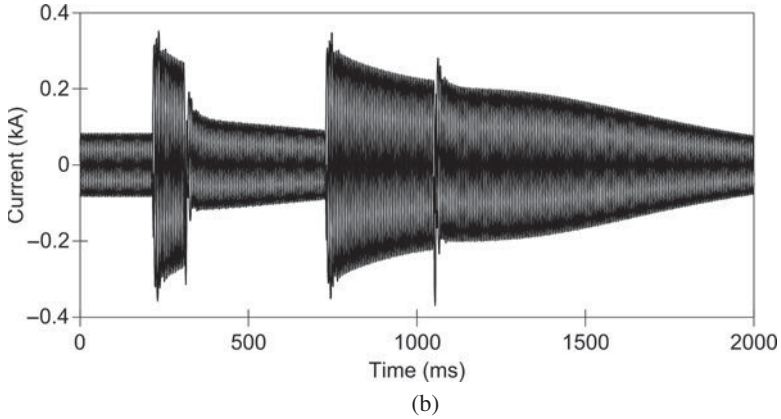

(b)

Figure 11.68 Case Study 4 – Example 1 – Simulation results with new relays: (a) faulted feeder – current through circuit breaker B1, (b) unfaulted feeder – current through circuit breaker B2 (© 2010 IEEE) [133].

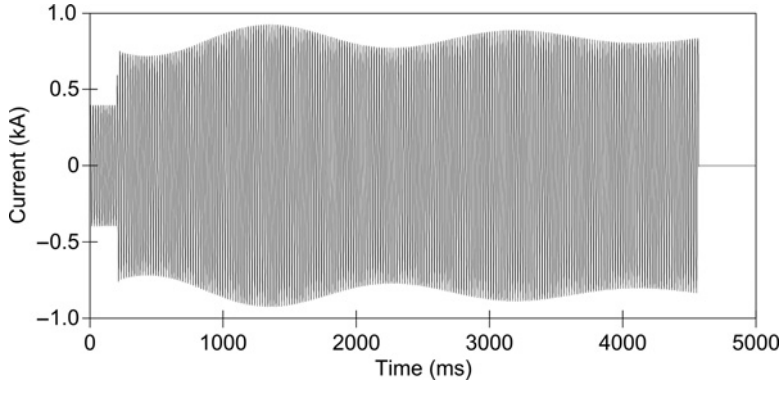

Figure 11.69 Case Study 4 – Example 2: Transient current at the interconnection (© 2010 IEEE) [133].

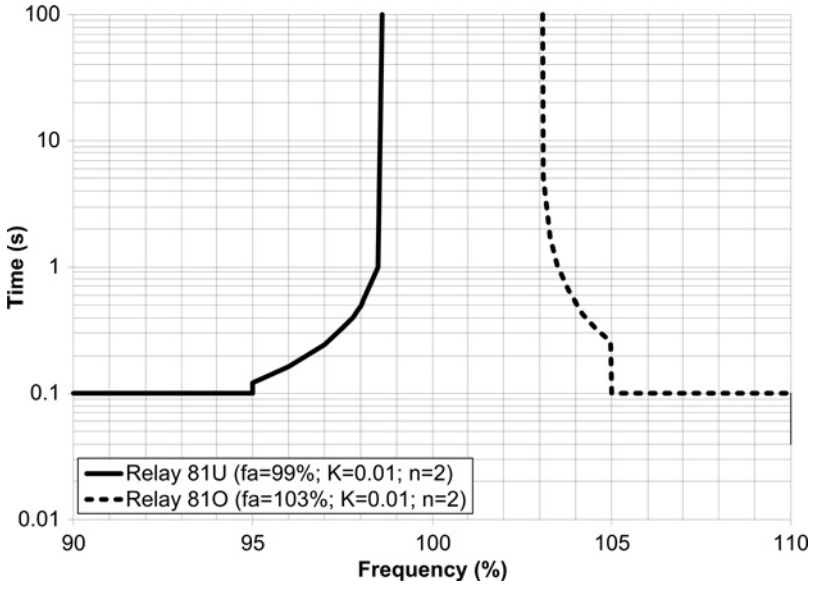

Figure 11.70 Case Study 4 – Example 2: Over-/under-frequency relay characteristics for G2 (© 2010 IEEE) [133].

The sequence of operations implemented in this example under such conditions will be: (1) the recloser operates with its fast curve and opens first, (2) the recloser closes the circuit after the selected reclosing time, (3) if the fault is gone, no other action is necessary, otherwise, the operation is repeated. However, this time the slow characteristic of the recloser is used and then (according to Figure 11.72) the fuse opens. Figure 11.73 shows the results obtained with this case when there is no distributed generation.

When a generator is connected to the system and the point of common coupling is between the recloser and the fuse, as in Figure 11.64, the current through both devices in front of a fault located at point B will be different, since the current through the recloser will decrease and the current through the fuse

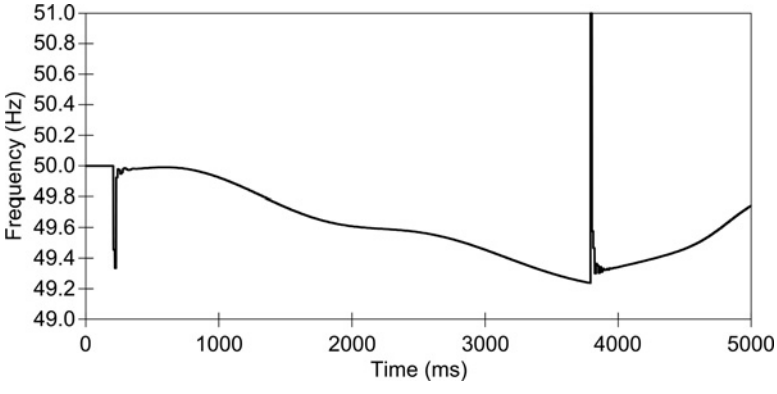

Figure 11.71 Case Study 4 – Example 2: Simulation results with frequency relays (© 2010 IEEE) [133].

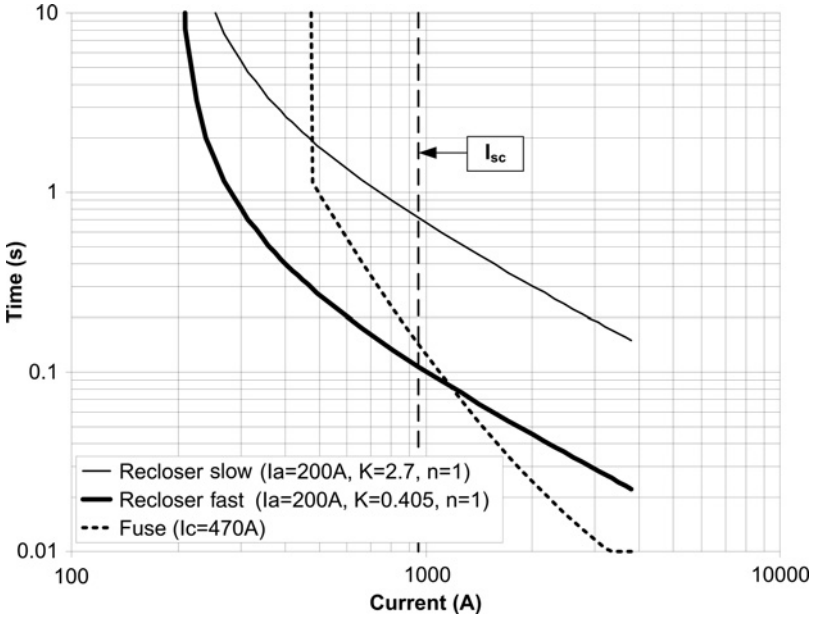

Figure 11.72 Case Study 4 – Example 3: Time–current characteristics of the recloser and the fuse.

will increase with respect to the values without generation [134]. This may cause a miscoordination between the two devices, and the fuse could open first, even if the fault is temporary. Figure 11.74 shows the new fault currents that result after connecting the generator. Note that the fuse opens first, so neither the recloser nor the interconnection protection of the generator act in front of this fault. We can also deduce from the comparison of the plots of Figures 11.73 and 11.74 that, as expected, the fault current through R1 has decreased, and the fault current through F1 has increased when the generator is connected.

This problem may be solved by replacing the fuse with a sectionalizer, coordinated with the recloser. In this case, the sectionalizer will open after the first reclosing and before the second operation of the recloser, as in the previous case, when fuse-saving was working properly and the fuse did not open before the first reclosing operation. Figure 11.75 shows the simulation results when the sectionalizer is installed instead of the fuse F1. It is important to mention that in this case the interconnection protection of the generator decouples the machine from the network before the first reclosing operation, so when the first reclosing of R1 takes place the generator has been already decoupled from the feeder.

11.9 Conclusions

During the first few cycles following a power system fault, the protection system is expected to make a correct decision (by opening and/or closing circuit breakers) to minimize the extent of equipment damage. Protective systems are a critical part of the power system, since an incorrect operation can have detrimental consequences for the power equipment and in terms of power system behaviour.

The performance of protective relays depends on their design principle, which involves aspects such as selectivity, sensitivity, security and dependability. The dynamic performance of protective relays depends to a large extent on the signals received from instrument transformers, and these signals depend not only on the overall transient response of the instrument transformers, but on the type of transients generated by the power system [31].

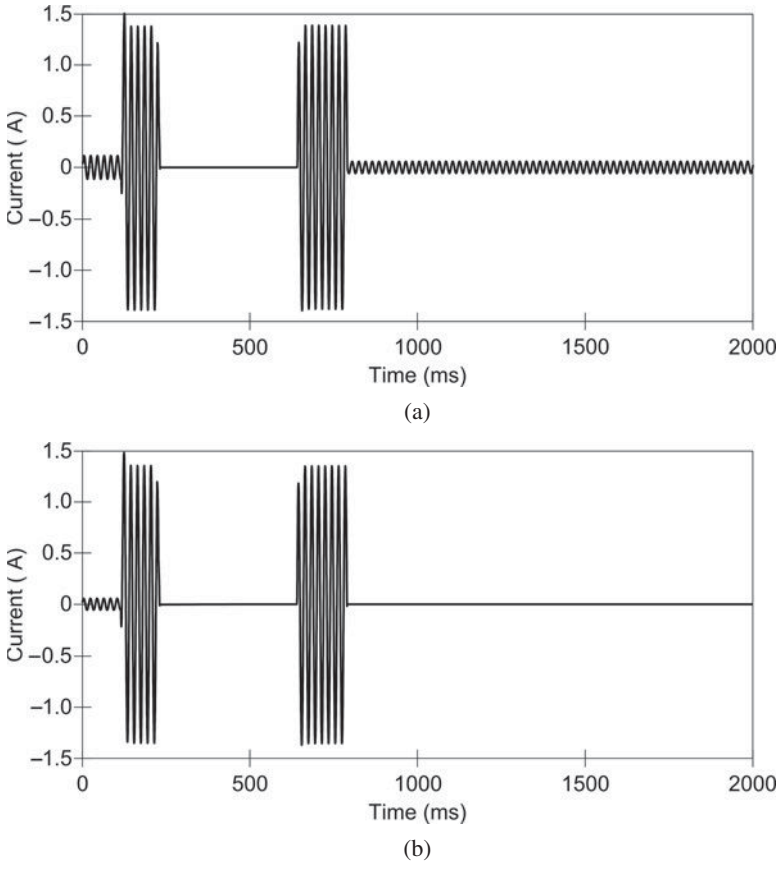

Figure 11.73 Case Study 4 – Example 3 – Simulation results without distributed generation: (a) current through the recloser R1, (b) current through the fuse F1.

Although computer models of major power system components have been used in software packages for many years, relay system modelling has been applied to a lesser degree. The development of new tools, and the implementation of new capabilities in traditional packages, have promoted protective relay modelling. Protection system models are now used to: (1) investigate and improve the protection designs and algorithms, (2) select the relay types suited for a particular application, (3) verify, test and properly adjust the relay settings, (4) investigate the relay behaviour during system disturbances, (5) make relay design easier and less costly and (6) enable off-line closed loop relay testing.

Traditional relay studies have considered fault conditions to be temporary steady-state conditions that can be studied by means of fundamental-frequency steady-state studies. However, some power system effects should not be investigated by any means other than a transient software tool. Conventional short-circuit studies will often exclude some important phenomena; in addition, the dynamic response of the power system to faults and automatic reclosing can have an important effect on relay performance. Time-domain simulation tools, such as EMTP-like tools, provide a convenient way to generate test signals to physically test relay responses to faults. Such generated signals are essential for application, testing and settings of relays.

Protective relays are designed to operate in a shorter time period than that of the transient disturbance during a system fault. Time-domain simulation of instrument transformer transients can be used to study their effect on the performance of relay elements.

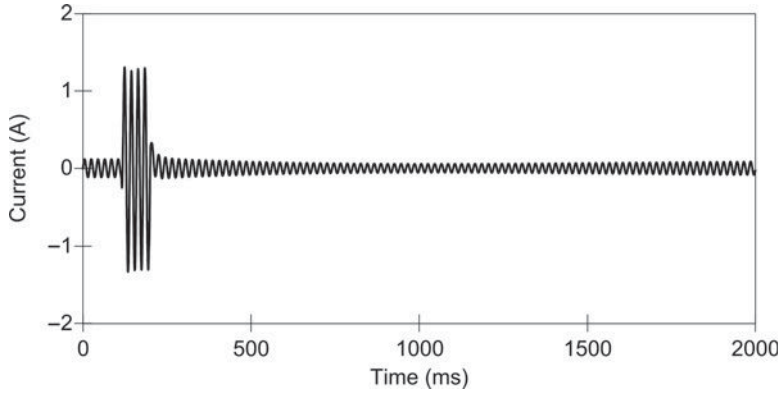

(a)

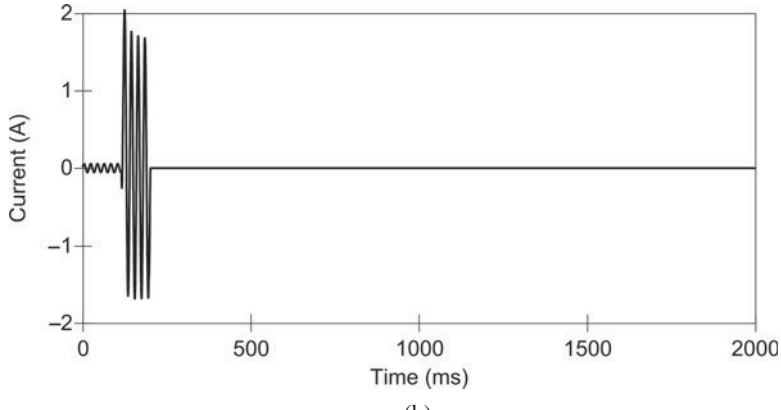

(b)

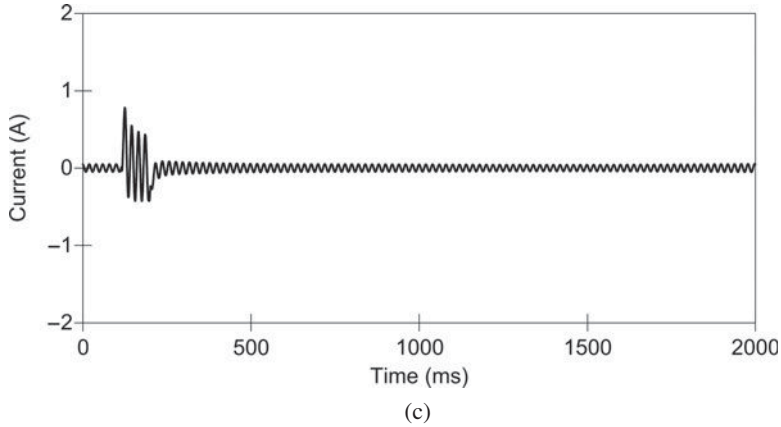

(c)

Figure 11.74 Case Study 4 – Example 3 – Simulation results with distributed generation: (a) current through the recloser R1, (b) current through the fuse F1, (c) current supplied by the generator G1.

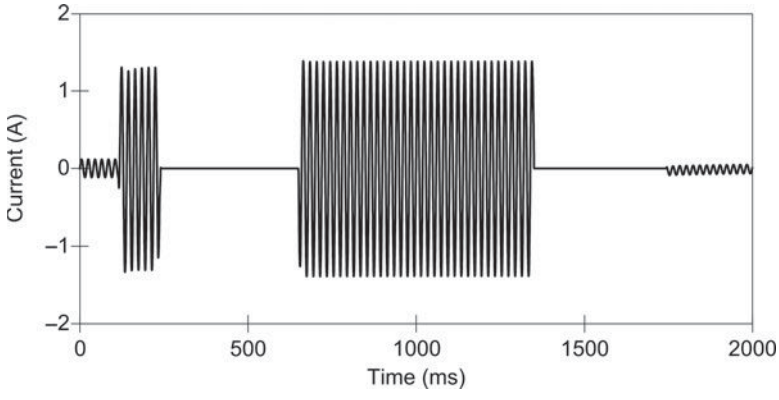

(a)

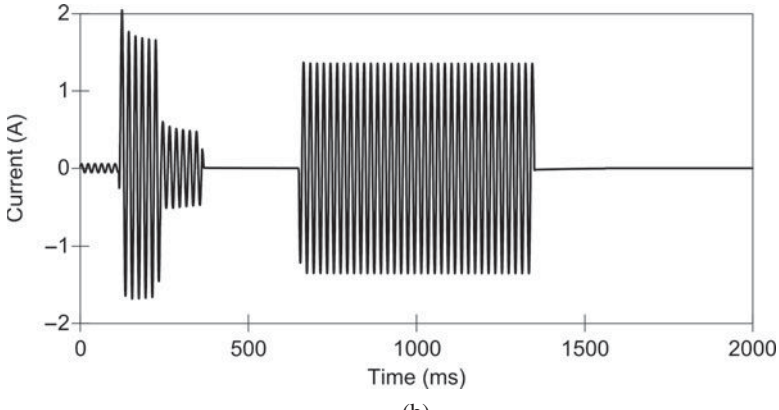

(b)

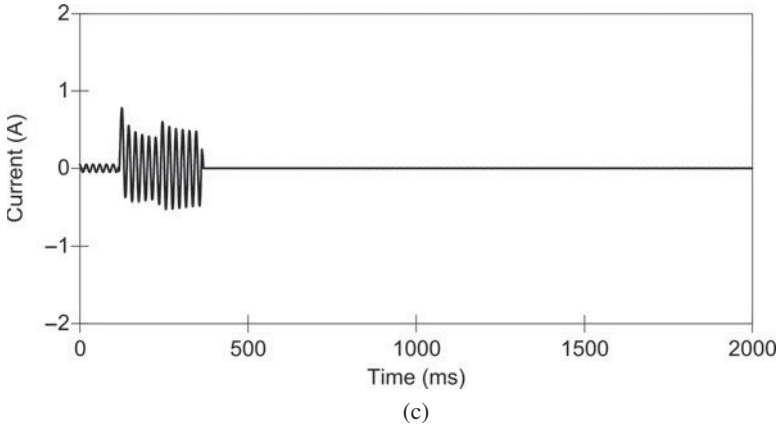

(c)

Figure 11.75 Case Study 4 – Example 3 – Simulation results with the sectionalizer: (a) current through the recloser R1, (b) current through the sectionalizer, (c) current supplied by the generator G1.

The status of protection system modelling presented in this chapter has shown the following:

- The power system network can be modelled very accurately by using a software package capable of simulating electromagnetic transients.
- The behaviour of instrument transformers is very important for relay evaluation, and detailed models of instrument transformers need to be used.
- Current software packages can accurately and effectively represent the behaviour of physical relays if all of the information about the original relay, including algorithms, is available. Many protective relay models, with varying accuracy, are presently available for application in transients tools (e.g. EMTP-like tools). Relay models may be implemented using a variety of options. The final decision may be driven by the convenience of interfacing with the simulation programs or recorded data files.
- It is possible to create more or less sophisticated relay models for different purposes. Simple models need only mathematical equations to describe the pickup and tripping characteristics of the relays, and they can be used to make general decisions for the selection of relay types; together with network calculation programs they can be used to derive relay settings. More sophisticated relay models process transient waveforms from simulations, actual fault waveforms captured by numerical relays or digital fault recorders. Field recorded waveforms reflect the impact of the instrument transformer response.
- The communication system representation is important for the comprehensive assessment of the power system protection performance.

Two basic relay models are used: steady-state (phasor-based) models and transient models. Steady-state models have been in use for several decades; transient models, generic or detailed, are increasingly being used.

Models for power and protection system components may be validated with data obtained from DFRs installed in the actual system being modelled. A validation procedure is a very important part of a model development. Although it cannot guarantee a high level of accuracy under all possible conditions, it can indicate the constraints and the scope of application of the model. When the tests of marginal conditions are carefully chosen, the majority of actual network incidents will remain within the scope of the testing procedures. With a properly selected scope of testing procedures, the validation exercise can also be used to establish the model application limits. This task may require an iterative approach, where the modification of test conditions and re-application of tests is required after the completion of the initial test program. Another limiting factor is the accuracy of the hardware used for testing. In fact, the hardware cost may be a barrier, which may prevent high accuracy results from being achieved. Most models that are based on public domain information (e.g. manufacturers' manuals) require more extensive testing procedures than models supplied by manufacturers, which are usually more reliable.

Relay models may be useful for relay manufacturers, utilities and customers, and for educational purposes. Relay modelling is not meant to replace laboratory or field testing; instead it can complement design and testing of the physical device.

Acknowledgement

The author wants to express his gratitude to those who contributed to the CIGRE Brochure, *Relay software models for use with electromagnetic transient analysis program*; some subsections of this chapter related to relay modelling were based on the material presented in that publication. Thanks are given to Ljubomir Kojovic and Jacinto Martí-Arnedo who provided some figures and protection models used in this chapter. Some parts of this chapter are based on the previous work by L. Kojovic, [139]. The author is also grateful to IREQ for the development of the protective device models implemented in EMTP-RV and used in the second case study presented in this chapter. It is also worth mentioning that some parts of this chapter were inspired by a chapter on protection modelling [10], prepared by an IEEE TF in which the author was involved. Finally, thanks are due to Dmitry Ishchenko, who carefully revised the chapter, but obviously he is not responsible of any errors or omissions.

References

[1] Horowitz, S.H. and Phadke, A.G. (2008) *Power System Relaying*, 3rd edn, John Wiley & Sons, Inc.

[2] Lewis Blackburn, J. and Domin, T.J. (eds) (2007) *Protective Relaying. Principles and Applications*, 3rd edn, CRC Press.

[3] Elmore, W.A. (2003) *Protective Relaying: Theory and Applications*, 2nd edn, CRC Press.

[4] Christopoulos, C. and Wright, A. (1999) *Electrical Power System Protection*, 2nd edn, Springer.

[5] Anderson, P.M. (1998) *Power System Protection*, Mc-Graw Hill – IEEE Press.

[6] Electricity Training Association (1995) *Power System Protection: Principles and Components*, vol. 1: Principles and components, vol. 2: Systems and Methods, vol. 3: Applications, vol. 4: Digital Protection and Signalling, Institution of Engineering and Technology, Revised Version.

[7] Phadke, A.G. and Thorp, J.S. (2009) *Computer Relaying for Power Systems*, 2nd edn, John Wiley & Sons, Inc.

[8] Wright, A. and Charalambous, C.C. (1972) Modeling of power system protective equipment on analogue computers. *Proceedings of IEE*, **121**(6), 689–699.

[9] Garrett, B.W., Dommel, H.W. and Engelhardt, K.H. (1987) Digital simulation of protection systems under transient conditions. Ninth Power Systems Computation Conference, Cascais, Portugal, September 1987.

[10] Chaudhary, A.K.S., Wilson, R.E., Glinkowski, M.T. *et al.* (1998) Modeling and analysis of transient performance of protection systems using digital programs, Chapter 7, in *Modeling and Analysis of System Transients using Digital Systems* (eds A. Gole, J.A. Martinez-Velasco and A.J.F. Keri), IEEE Special Publication, TP-133-0.

[11] IEEE Tutorial Course (D.A. Tziouvaras, Coordinator) (1999) Electromagnetic Transient Program Applications to Power Systems Protection, IEEE.

[12] CIGRE Working Group B 5.17 (2006) Relay Software Models for Use with Electromagnetic Transient Analysis Program. CIGRE Brochure 295.

[13] Dommel, H.W. (1986) *Electromagnetic Transients Program Reference Manual (EMTP Theory Book)*, Bonneville Power Administration, Portland, OR, USA.

[14] Cook, V. (1985) *Analysis of Distance Protection*, Research Study Press Ltd, John Wiley & Sons, Inc.

[15] IEEE Tutorial Course, Microprocessor Relays and Protection Systems, Publication No 88EHO269-1-PWR, 1988.

[16] IEEE Tutorial Course, Advancements in Microprocessor Based Protection and Communication, Publication No. 97TP120-0, 1997.

[17] Horowitz, S.H. (ed.) (1981) *Protective Relaying for Power Systems*, IEEE Press, Selected Reprint Series.

[18] Horowitz, S.H. (ed.) (1992) *Protective Relaying for Power Systems II*, IEEE Press, Selected Reprint Series.

[19] Ziegler, G. (2011) *Numerical Distance Protection. Principles and Applications*, 4th edn, Siemens.

[20] Ziegler, G. (2012) *Numerical Differential Protection. Principles and Applications*, 2nd edn, Siemens.

[21] Paithankar, Y.G. (1997) *Transmission Network Protection: Theory and Practice*, Marcel Dekker.

[22] Johns, A.T. and Salman, S.K. (1997) *Digital Protection for Power Systems*, Peter Peregrinus Ltd, IEE Series 15.

[23] Reimert, D. (2005) *Protective Relaying for Power Generation Systems*, CRC Press.

[24] Durbak, D.W., Gole, A.M., Camm, E.H. *et al.* (1998) Modeling guidelines for switching transients, Chapter 4, *Modeling and Analysis of System Transients using Digital Systems* (eds A. Gole, J.A. Martinez-Velasco and A.J.F. Keri), IEEE Special Publication, TP-133-0.

[25] IEEE Power System Relaying Committee (2005) EMTP Reference Models for Transmission Line Relay Testing, Available at www.pes-psrc.org.

[26] Bastard, P., Bertrand, P. and Meunier, M. (1994) A transformer model for winding fault studies. *IEEE Transactions on Power Delivery*, **9**(2), 690–699.

[27] Martinez-Velasco, J.A. (2012) Basic methods for analysis of high frequency transients in power apparatus windings, Chapter 2, *Electromagnetic Transients in Transformer and Rotating Machine Windings* (ed. C.Q. Su), IGI Global.

[28] Popov, M., Gustavsen, B. and Martinez-Velasco, J.A. (2012) Transformer modelling for impulse voltage distribution and terminal transient analysis, Chapter 6, *Electromagnetic Transients in Transformer and Rotating Machine Windings* (ed. C.Q. Su), IGI Global.

[29] CIGRE Working Group 13.01 (1993) Applications of black box modelling to circuit breakers. *Electra* (149), 40–71.

[30] Martinez-Velasco, J.A. and Popov, M. (2009) Circuit breakers, Chapter 7, *Power System Transients. Parameter Determination* (ed. J.A. Martinez-Velasco), CRC Press.

[31] Tziouvaras, D., McLaren, P., Alexander, C. *et al.* (2000) Mathematical models for current, voltage and coupling capacitor voltage transformers. *IEEE Transactions on Power Delivery*, **15**(1), 62–72.
[32] IEEE Special Publication, Power System Relaying Committee "Transient Response of Current Transformers." Report 76-Ch1130-4 PWR.
[33] IEEE Power System Relaying Committee (1977) Transient response of current transformers. *IEEE Transactions on Power Apparatus and Systems*, **96**(6), 1809–1814.
[34] IEEE Committee Report (1981) Transient response of coupling capacitor voltage transformer. *IEEE Transactions on Power Apparatus and Systems*, **100**(12), 4811–4814.
[35] Poljak, M. and Koliba, N. (1988) Computation of current transformer transient performance. *IEEE Transactions on Power Delivery*, **3**(4), 1816–1822.
[36] Zocholl, S.E., Kotheimer, W.C. and Tajaddodi, F.Y. (1988) An analytic approach to the application of current transformers for protective relaying. 15th Annual Western Protective Relay Conference, Spokane, Washington (USA), October 1988.
[37] Zocholl, S.E. and Kotheimer, W.C. (1990) CT performance in critical relay application. 17th Annual Western Protective Relay Conference, Spokane, Washington (USA), October 1990.
[38] Chaudhary, A.K.S., Anich, J.B. and Wisniewski, J.B. (1992) Influence of transient response of instrument transformers on protection systems. Sargent & Lundy 12th Biennial Transmission & Substation Conf., November 1992.
[39] Lucas, J.R., McLaren, P.G., Keerthipala, W.W.L. and Jayasinghe, R.P. (1992) Improved simulation models for current and voltage transformers in relay studies. *IEEE Transactions on Power Delivery*, **7**(1), 152–159.
[40] Kezunovic, M., Kojovic, Lj., Skendzic, V. *et al.* (1992) Digital models of coupling capacitor voltage transformers for protective relay transient studies. *IEEE Transactions on Power Delivery*, **7**(4), 1927–1935.
[41] IEEE Committee Report (1993) Relay performance considerations with low ratio CTs and high fault currents. *IEEE Transactions on Power Delivery*, **8**(3), 884–897.
[42] M. Kezunovic, Kojovic, Lj., Abur, A. *et al.* (1994) Experimental evaluation of EMTP-based current transformer models for protective relay transient study. *IEEE Transactions on Power Delivery*, **9**(1), 405–413.
[43] Kojovic, L., Kezunovic, M. and Fromen, C.W. (1994) A new method for the CCVT performance analysis using field measurements, signal processing and EMTP modelling. *IEEE Transactions on Power Delivery*, **9**(4), 1907–1915.
[44] Iravani, M.R., Wang, X., Polishchuk, I. *et al.* (1998) Digital time-domain investigation of transient behavior of coupling capacitor voltage transformer. *IEEE Transactions on Power Delivery*, **13**(2), 622–629.
[45] ABB (2009) Instrument Transformers. Application Guide.
[46] IEEE Std. C57.13-2008 IEEE Standard Requirements for Instrument Transformers.
[47] IEEE Std. C37.110-2007, IEEE Guide for the Application of Current Transformers Used for Protective Relaying Purposes.
[48] IEC 61869-1, Instrument transformers – Part 1: General requirements, Edition 1.0, 2007.
[49] IEC 61869-2, Instrument transformers – Part 2: Additional requirements for current transformers, Edition 1.0, 2012.
[50] IEC 61869-3, Instrument transformers – Part 3: Additional requirements for inductive voltage transformers, Edition 1.0, 2011.
[51] IEC 61869-5, Instrument transformers – Part 5: Additional requirements for capacitor voltage transformers, Edition 1.0, 2011.
[52] IEEE Working Group (Lj. Kojovic, Chair) (2010) Practical Aspects of Rogowski Coil Applications to Relaying, IEEE PSRC Special Report.
[53] McLaren, P.G., Benmouyal, G., Chano, S. *et al.* (2001) Software models for relays. *IEEE Transactions on Power Delivery*, **16**(2), 238–245.
[54] Domijan, A. and Emami, M.V. (1990) State space relay modeling and simulation using the electromagnetic transient program and its transient analysis of control system capability. *IEEE Transactions on Energy Conversion*, **5**(4), 697–702.
[55] Glinkowski, M.T. and Esztergalyos, J. (1996) Transient modeling of electromechanical relays. Part I: Armature type relay. *IEEE Transactions on Power Delivery*, **11**(2), 763–770.
[56] Glinkowski, M.T. and Esztergalyos, J. (1996) Transient modeling of electromechanical relays, Part II: Plunger type 50 relays. *IEEE Transactions on Power Delivery*, **11**(2), 771–782.
[57] Garrett, B.W. (1987) Digital Simulation of Power System Protection under Transient Conditions. Ph.D. Thesis, University of British Columbia.

[58] Chaudhary, A.K.S. (1991) Protection System Representation in the Electromagnetic Transients Program. Ph.D. Thesis, Virginia Tech.
[59] Chaudhary, A.K.S., Tam, K.S. and Phadke, A.G. (1994) Protection system representation in the Electromagnetic Transients Program. *IEEE Transactions on Power Delivery*, **9**(2), 700–711.
[60] Wilson, R.E. and Nordstrom, J.M. (1993) EMTP transient modeling of a distance relay and a comparison with EMTP laboratory testing. *IEEE Transactions on Power Delivery*, **5**(3), 984–990.
[61] EPRI (2004) Protective Relays. Numerical Protective Relays. EPRI Report 1009704, December 2004.
[62] Kezunovic, M. and Chen, Q. (1997) A novel approach for interactive protection system simulation. *IEEE Transactions on Power Delivery*, **12**(2), 668–674.
[63] Sachdev, M.S. and Baribeau, M.A. (1979) A new algorithm for digital impedance relays. *IEEE Transactions on Power Apparatus and Systems*, **98**(6), 2232–40.
[64] Huelsman, L.P. (1970) *Active Filters: Lumped, Distributed, Integrated, Digital, and Parametric*, McGraw-Hill Book Company, New York.
[65] Wilson, R.E. (1992) A new method using relay macromodels for simulation of the transient response of distance relays. Ph. D. Thesis. University of Idaho.
[66] Dysko, A., McDonald, J.R., Burt, G.M. *et al.* (1999) Integrated modeling environment: A platform for dynamic protection modeling and advanced functionality. IEEE PES Transmission & Distribution Conference, April 1999.
[67] Peterson, J.N. and Wall, R.W. (1991) Interactive relay controlled power system modelling. *IEEE Transactions on Power Delivery*, **6**(1), 96–102.
[68] Sidhu, T.S., Hfuda, M. and Sachdev, M.S. (1998) Generating relay models for protection studies. *IEEE Computer Applications in Power*, **11**(4), 33–38.
[69] Kezunovic, M. and Kasztenny, B. (1999) New Simulink libraries for modeling digital protective relays and evaluating their performance under fault transients. International Conference on Power Systems Transients (IPST), Budapest, June 1999.
[70] Dubé, L. and Bonfanti, I. (1992) MODELS: A new simulation tool in the EMTP. *European Transactions on Electrical Power Engineering*, **2**(1), 45–50.
[71] Wall, R.W. and Johnson, B.K. (1997) Using TACS functions within EMTP to teach protective relaying fundamentals. *IEEE Transactions on Power Delivery*, **12**(1), 3–8.
[72] Wall, R. and Johnson, B. (1994) Digital filtering and relaying. *EMTP Tech Notes*, EMTP User's Group, Issue 94-4, pp. 3–21.
[73] Sidhu, T.S., Sachdev, M.S. and Wood, H.C. (1992) A computer-aided design tool for developing digital controllers and relays. *IEEE Transactions on Industry Applications*, **28**(6), 1376–1383.
[74] Kennedy, W.O., Gruell, B.J., Shih, C.H. and Yee, L. (1988) Five years experience with a new method of testing cross and quadrature polarized relays. Part I: Results and observations. Part II: Three case studies. *IEEE Transactions on Power Delivery*, **3**(3), 880–893.
[75] Nimmersjö, G., Hillström, B., Werner-Erichsen, O. and Rockefeller, G.D. (1988) A digitally-controlled, real-time, analog power system simulator for closed-loop protective relaying testing. *IEEE Transactions on Power Delivery*, **3**(1), 138–15.
[76] McLaren, P.G., Kuffel, R., Weirckx, R. *et al.* (1992) A real time digital simulator for testing relays. *IEEE Transactions on Power Delivery*, **7**(1), 207–213.
[77] Montmeat, A., Giard, A. and Roguin, J. (1995) MORGAT for testing MV and EHV protective relays. International Conference on Power Systems Transients (IPST), Lisbon, Portugal, 1995.
[78] Kezunovic, M., Domaszewicz, J., Skendzic, V. *et al.* (1996) Design, implementation and validation of a real time digital simulator for protection relay testing. *IEEE Transactions on Power Delivery*, **11**(1), 158–164.
[79] Friedland, R., Pannhorst, H.D. and Kulicke, B. (1996) Digital network model for tests of different equipment in electric power systems. *Electric Power Systems Research*, **36**, 197–202.
[80] Dierks, A. and McElray, J. (1996) Analyzing polarization of impedance relays. Georgia Tech Protective Relaying Conference, Atlanta, USA, May 1996.
[81] McLaren, P.G., Swift, G.W., Dirks, E. *et al.* (1997) Comparisons of relay transient test results using various testing technologies. 2nd Int. Conf. on Digital Power Systems Simulators (ICDS), Varennes, Canada, 1997.
[82] Sidhu, T.S., Sachdev, M.S. and Das, R. (1997) Modern relays: Research and teaching using PCs. *IEEE Computer Applications in Power*, **10**(2), 50–55.
[83] IEEE Committee Report (1996) Relay performance testing, IEEE Special Publication, No. 96 TP 115-0.
[84] Kezunovic, M., Pickett, B.A., Adamiak, M.G. *et al.* (1998) Digital simulator performance requirements for relay testing. *IEEE Transactions on Power Delivery*, **13**(1), 78–84.

[85] CIGRE WG 34-10 (2000) Analysis and guidelines for testing numerical protection schemes. CIGRE Brochure 159.
[86] IEEE Std. C37, 111-1999 (1999) IEEE Standard Common Format for Transient Data Exchange (COMTRADE) for Power Systems, October 1999.
[87] Fugita, N., Ichie, R., Ogawa, S. *et al.* (1995) Computer-aided protective relay settings for large power networks. *Electrical Engineering in Japan*, **115**(5), 22–37.
[88] Baumann, U. and Wellssow, W.H. (1996) Computer aided analysis of protection relay settings with respect to starting conditions. 12th Power System Computation Conference, Zurich, Switzerland, 1996.
[89] De Sa Pinto, J., Afonso, J. and Rodrigues, R. (1997) A probabilistic approach to setting distance relays in transmission networks. *IEEE Transactions on Power Delivery*, **12**(2), 681–686.
[90] Saengsuwan, T. and Crossley, P.A. (1995) Simulation of distance relays for protection performance evaluation. IEEE Power Tech Conference, Stockholm, Sweden, 1995.
[91] Kezunovic, M., Kasztenny, B. and Galijasevic, Z. (1999) Modeling, developing and testing protective relays using Matlab, programmable relays and digital simulators. 3rd Int. Conf. on Digital Power Systems Simulators (ICDS), Vasteras, Sweden, May 1999.
[92] Kezunovic, M. and Guo, Y. (2000) Modeling and simulation of the power transformer faults and related protective relay behaviour. *IEEE Transactions on Power Delivery*, **15**(1), 44–50.
[93] SimPowerSystems User's Guide – R2012b, The MathWorks, Inc., 2012.
[94] Dobraca, F., Pai, M. and Sauer, P.W. (1990) Relay margins as a tool for dynamic security analysis. *Electrical Power and Energy Systems*, **12**(4), 226–234.
[95] Perez, L.G., Flechsig, A.J. and Venkatasubramanian, V. (1994) Modeling the protective system for power system dynamic analysis. *IEEE Transactions on Power Systems*, **9**(4), 1963–1973.
[96] Tumay, M., Smith, J.R., McDonald, J.R. and Burt, G. (2000) The dynamic representation of protection systems. *International Journal of Electrical Power and Energy Systems*, **22**(7), 487–496.
[97] Wang, F. and Tang, J. (1998) Modeling of a transmission network protection system using Petri Nets. *Electric Power Systems Research*, **44**, 175–181.
[98] Tang, J. and Wang, F. (1997) Modeling of a transmission line protection relaying scheme using Petri Nets. *IEEE Transactions on Power Delivery*, **12**(3), 1055–1063.
[99] Dolling, R.M., Dysko, A., McDonald, J.R. and Burt, G.M. (1997) Novel relay modeling techniques for model based diagnosis. 32nd Universities Power Engineering Conference (UPEC), Manchester, UK, September 1997.
[100] Dysko, A., McDonald, J.R., Burt, G.M. *et al.* (1997) Dynamic modeling of protection system performance. 6th International Conference DPSP, Nottingham, UK, March 1997.
[101] Bell, S.C., McArthur, S.D.J., McDonald, J.R. *et al.* (1998) Model based analysis of protection system performance. *IEE Proceedings – Generation, Transmission and Distribution*, **145**(5), 547–552.
[102] Li, H. (1999) A New Adaptive Distance Relay. Ph.D Thesis, University of Manitoba.
[103] Jiang, J.A., Liu, C.W. and Chen, C.S. (2002) A novel adaptive PMU-based transmission line relay – design and EMTP simulation results. *IEEE Transactions on Power Delivery*, **17**(4), 930–937.
[104] Oppenheim, A.V. and Schafer, R.W. (2009) *Discrete-Time Signal Processing*, 3rd edn, Prentice Hall.
[105] McLaren, P.G., Dirks, R.N., Jayasinghe, R.P. *et al.* (1995) Using a real time digital simulator to develop an accurate model of a digital relay. 1st Int. Conf. on Digital Power Systems Simulators (ICDS), Texas, USA, April 1995.
[106] Kezunovic, M., Domaszewicz, J., Skendzic, V. *et al.* (1996) Design, implementation and validation of a real-time digital simulator for protective relay testing. *IEEE Transactions on Power Delivery*, **11**(1), 158–164.
[107] Kezunovic, M. and McKenna, S.M. (1994) Real-time digital simulator for protective relay testing. *IEEE Computer Applications in Power*, **7**(3), 30–35.
[108] Martinez-Velasco, J.A. and Kojovic, Lj.A. (1997) Modeling of electromechanical distance relays using the ATP. 32nd Universities Power Engineering Conference (UPEC), Manchester, UK, September 1997.
[109] Martinez-Velasco, J.A. and Kojovic, Lj.A. (1997) ATP modeling of electromechanical distance relays. International Conference on Power Systems Transients (IPST), Seattle, Washington, June 1997.
[110] Peng, Z., Li, M.S., Wu, C.Y. *et al.* (1985) A dynamic state space model of a MHO distance relay. *IEEE Transactions on Power Apparatus and Systems*, **104**(12), 3558–3564.
[111] Bouchet, R., Saad, O. and Xémard, A. (2007) Module de protection générique sous EMTP-RV. Hydro-Québec, Juillet 2007.
[112] Gérin-Lajoie, L. (2009) A MHO distance relay device in EMTPWorks. *Electric Power Systems Research*, **79**(3), 484–491.

[113] Gers, J.M. and Holmes, E.H. (2004) *Protection of Distribution Networks*, 2nd edn, IEE Power and Energy Series.
[114] Short, T.A. (2004) *Electric Power Distribution Handbook*, CRC Press.
[115] Gönen, T. (2008) *Electric Power Distribution System Engineering*, CRC Press.
[116] Walling, R.A., Saint, R., Dugan, R.C. *et al.* (2008) Summary of distributed resources impact on power delivery systems. *IEEE Transactions on Power Delivery*, **23**(3), 1636–1644.
[117] IEEE Power System Relay Committee (2004) Impact of distributed resources on distribution relay protection. August 2004.
[118] IEEE Std. 1547-2003, IEEE Standard for Interconnecting Distributed Resources with Electric Power Systems.
[119] Mozina, C.J. (2006) Distributed generator interconnect protection practices. IEEE PES T&D Conference, 2006, pp. 1164–1170.
[120] Mozina, C.J. (2001) Interconnect protection of dispersed generators. IEEE PES T&D Conference, 2001, pp. 707–723.
[121] Mozina, C.J. (2001) Interconnection protection of IPP generators at commercial/industrial facilities. *IEEE Transactions on Industry Applications*, **37**(3), 681–688.
[122] IEEE IAS WG Report (2006) Application of islanding protection for industrial and commercial generators. 59th Annual Conference for Protective Relay Eng., 2006.
[123] Girgis, A. and Brahma, S. (2001) Effect of distributed generation on protective device coordination in distribution networks. Large Eng. Syst. Conference, 2001, pp. 115–119.
[124] IEEE Std C37.48.1-2002 IEEE Guide for the Operation, Classification, Application and Coordination of Current-Limiting Fuses with rated Voltages 1–38 kV.
[125] IEEE Std C37.112-1996 IEEE Standard Inverse-Time Characteristic Equations for Overcurrent Relays.
[126] Computer Representation of Overcurrent Relays Characteristics Working Group of the PSRC (1989) Computer representation of overcurrent relay characteristics. *IEEE Transactions on Power Delivery*, **4**(3), 1659–1667.
[127] Martinez, J.A. and Martin-Arnedo, J. (2004) Modeling of protective devices for voltage dip studies in distribution systems. IEEE PES General Meeting, Denver, USA, June 2004.
[128] Martinez, J.A. and Martin-Arnedo, J. (2006) Voltage sag studies in distribution networks. Part I: System modeling. *IEEE Transactions on Power Delivery*, **21**(3), 1670–1678.
[129] Leix, K.L., Kojovic, Lj.A., Marz, M. and Lampley, G.C. (1999) Applying current-limiting fuses to improve power quality and safety. IEEE PES T&D Conference, April 1999, pp. 636–641.
[130] Kojovic, Lj.A., Hassler, S.P., Leix, K.L. *et al.* (1998) Comparative analysis of expulsion and current-limiting fuse operation in distribution systems for improved power quality and protection. *IEEE Transactions on Power Delivery*, **13**(3), 863–869.
[131] Kojovic, Lj.A. and Hassler, S.P. (1997) Application of current-limiting fuses in distribution systems for improved power quality and protection. *IEEE Transactions on Power Delivery*, **12**(2), 791–800.
[132] Cook, C.J. and Myers, D.A. (2004) The use of cooling-factor curves for coordinating fuses and reclosers. IEEE PES General Meeting, Denver, USA, 6–10 June 2004.
[133] Martinez, J.A. and Martin Arnedo, J. (2010) EMTP modeling of protective devices for distribution systems with distributed generation. IEEE PES General Meeting, Minneapolis, USA, July 2010.
[134] Martinez, J.A. and Martin Arnedo, J. (2009) Impact of distributed generation on distribution protection and power quality. IEEE PES General Meeting, Calgary, Canada, July 2009.
[135] Martinez-Velasco, J.A., Martin-Arnedo, J. and Castro-Aranda, F. (2010) Modeling protective devices for distribution systems with distributed generation using an EMTP-type tool. *Ingeniare*, **18**(2), 258–273.
[136] El-Arroudi, K., Joós, G., Kamwa, I. and McGillis, D.T. (2007) Intelligent-based approach to islanding detection in distributed generation. *IEEE Transactions on Power Delivery*, **22**(2), 828–835.
[137] Funabashi, T., Koyanagi, K. and Yokoyama, R. (2003) A review of islanding detection methods for distributed resources. IEEE Power Tech Conference, Bologna, Italy, June 2003.
[138] Affonso, C.M., Freitas, W., Xu, W. and da Silva, L.C.P. (2005) Performance of ROCOF relays for embedded generation applications. *IEE Proceedings – Generation, Transmission and Distribution*, **152**(1), 109–114.
[139] Kojovic, L. (2010) Protection systems, Chapter 10, *Transient Analysis of Power Systems. Solution Techniques, Tools and Applications*, IEEE Catalog Nr. 11TP255E, ISBN 978-1-4577-1501-3.

12

Time-Domain Analysis of the Smart Grid Technologies: Possibilities and Challenges

Francisco de León, Reynaldo Salcedo, Xuanchang Ran
and Juan A. Martinez-Velasco

12.1 Introduction

According to the US Department of Energy, the term smart grid 'refers to a class of technology people are using to bring utility electricity delivery systems into the 21st century, using computer-based remote control and automation. These systems are made possible by two-way communication technology and computer processing that has been used for decades in other industries.' [1].

In terms of vision, the smart grid (SG) is supposed to be [2]:

- intelligent
- efficient
- accommodating
- motivating
- opportunistic
- quality-focused
- resilient
- green.

The smart grid presents an opportunity for the upgrade of electric power systems by optimizing grid operations, enhancing grid security and opening new markets for the utilization of sustainable energy. A few of the examples of the smart gird include the capacity of sensing overloads and rerouting power to prevent or minimize outages. The SG should meet increased consumer demand without adding infrastructure and should accept energy from any alternative source, including solar and wind, and incorporate energy storage technologies. The SG is intended to be free from voltage sags, spikes, disturbances and interruptions.

Transient Analysis of Power Systems: Solution Techniques, Tools and Applications, First Edition.
Edited by Juan A. Martinez-Velasco.

At the time of publishing, the smart grid is not yet a reality. There is a gamut of demonstrations going on all over the world, but no widespread adoption of any particular technology seems to be taking place. It seems that the advanced metering infrastructure (AMI) including phasor measurement units (PMUs) and smart consumer meters are gaining terrain, but not even those technologies (for political, privacy or economic reasons) are being universally adopted.

An important aspect of the smart grid will be the effective use of assets. The control of generation, storage and load demand at the lower levels of the system can help operators regulate the system under normal operating conditions, as well as respond to emergencies. An experiment demonstrating the effectiveness of asset utilization as well as the lessons learned is presented in [3]. Furthermore, studies have suggested that the smart grid would enable the utilization of available end-user reactive-power-capable devices such as the inverters for solar panels or pluggable hybrid electric vehicles to provide voltage support to the grid [4].

The future electrical smarter grid will have more switching operations and will contain substantially more distributed energy resources (DERs) embedded in the system. The switching and interconnection of DER will take place at all voltage levels to reconfigure the system for reliability or economic reasons.

The analytical tools for the design of the smart grid are not necessarily the same as those currently used for traditional power system planning. For example, switching will take place in places where the traditional systems do not have switches [5]. The analysis of the available tools for the study the penetration of DER is given in [6] and some possible issues are described in [7].

In this chapter the use of time-domain analysis for the study of SG technologies is described. The studies particularly include cases of system reconfigurations by large number of switching operations, and discussions of how to exploit the advantage of automation and the self-healing capabilities of a real-life complex network [5]. The chapter also covers the study of DER integration into the system and their possible effects on system voltage violations. Time-domain analysis using electromagnetic transient program (EMTP-type) offers a complete view of the phenomena occurring in the system, where steady-state analytical tools may miss important issues.

Time-domain simulations allow for the study of issues such as power system overvoltages to be analysed in detail, providing a broader understanding of the event. Two of these studies for distribution networks having networked secondary services are discussed in this chapter. Additionally, this chapter presents a discussion of the negative impacts of distributed generation (DG) to distribution system reliability, which is of high importance to utilities. This study would not have been possible without having observed the interaction of the generator, the network switches and the network itself in the time-domain.

The use of electromagnetic transient programs for the study of large power systems is becoming increasingly common and indispensable owing to the requirement of detailed modelling for control systems and nonlinear network elements. A few years ago, time-domain simulations of detailed large power systems were limited or nearly impossible, but because of the continuous progress in computing power and software tools, it is now possible to implement and run such models [8–10].

This chapter also offers some experience of the development of industrial-grade translators for interfacing power-flow programs with EMTP-type programs. This facilitates the simulation of electromagnetic transients to utilities [11] and provides the ability to compute overvoltages, analyse switching of capacitors, ferroresonance or inrush currents and to estimate the impact of DG installations and smart grid technologies that involve switching operations for network reconfiguration.

12.2 Distribution Systems

Configurations of modern distribution systems can be classified into three major types [5], which are depicted schematically in Figure 12.1:

- radial systems
- spot networks
- secondary grid (area) networks

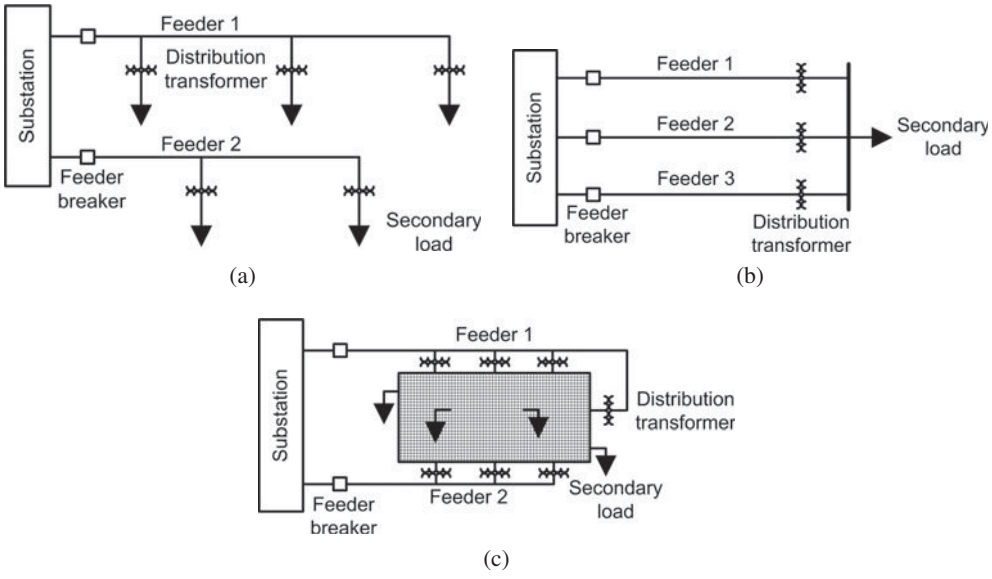

Figure 12.1 Typical configurations of distribution networks (© 2012 IEEE) [5]: (a) radial system, (b) spot network, (c) secondary grid network.

12.2.1 Radial Distribution Systems

Radial systems have found wide application due to their simplicity and relatively low cost. The feeders of the radial system leave a substation and distribute electrical power in the designated area without any additional connections to other points of supply. This configuration is especially popular in rural areas, where long feeders supply isolated loads. The simplicity of radial systems makes them less reliable than the other configurations. To make the radial systems more reliable, damaged parts of the feeders can be isolated, and alternative power supplies can be connected by means of mid-feeder and tie switches installed in more advanced systems. Operation of the switches can be manual or automatic, local operation or a controlled operation from a remote control centre.

The typical configuration of a radial type of distribution system is presented in Figure 12.2. These systems are extensively used to serve the light and medium density load of rural areas, where the primary and secondary circuits are usually carried overhead on poles. Commonly, the medium voltage (MV) level of radial systems is supplied by primary feeders connected by circuit breakers to one or more distribution substations, directly fed by the subtransmission system.

The MV feeders are usually branched into subfeeders and laterals, covering the area to be electrically served. The protection for this type of system is configured such that when a short-circuit occurs, the corresponding breakers open and isolate the faulted section, while partially interrupting service. The feeder branches are tactically divided by sectionalizing switches to minimize service interruptions when unexpected events take place.

Distribution transformers are connected to these branches, mostly through fused cut-outs supplying the radial secondary where the consumer services are connected. Fuses are used to prevent the possible power cut of a considerable portion of the feeder, or even worse, the entire feeder during faults on sections that can be isolated. Similarly, subfeeders and laterals might be fused to prevent the disconnection of circuit breakers at the substation and therefore reduce the expansion of the outage when a fault occurs. Proper coordination must be implemented to feeder breakers, transformer fuses and feeder branch fuses, such that the circuit will be opened fast and at the proper location to minimize outages [12, 13].

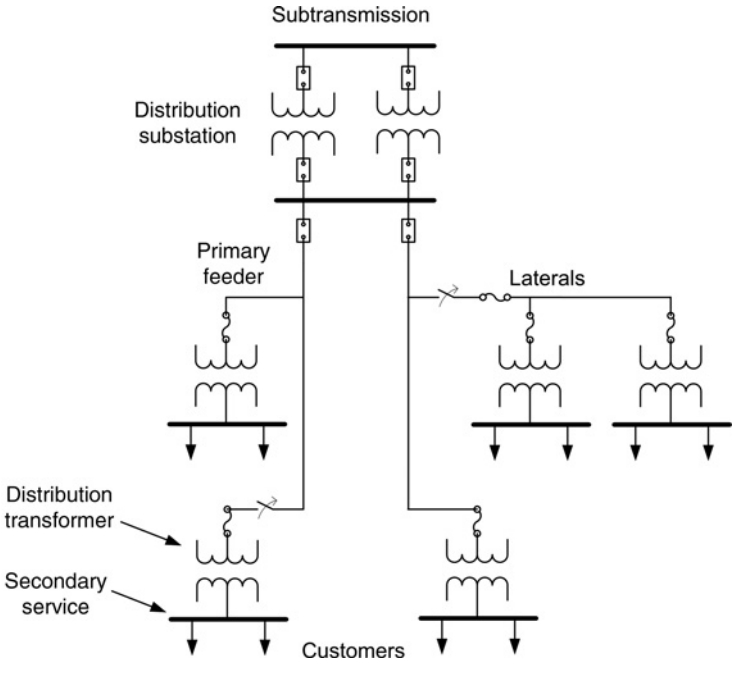

Figure 12.2 Simple configurations of radial distribution networks.

In large cities like New York City, there are several suburban areas having relatively large load density. These types of areas use configurations slightly different from those described above. Although the primary may run as a radial system, for reliability purposes the secondary is mostly networked. Another configuration considers underground feeders at the MV level that energize unit substations connected at midpoint or end-point. These unit substations step down the voltage, say to 4 kV, and from those unit substations the network follows the radial system arrangement.

Because of the smart grid, most electric utilities have expanded their monitoring systems to continuously obtain the network characteristics. This enables a better assessment of the network operation. A series of research and concepts have been (and continue to be) developed, aimed at improving system reliability and operability. Some of these novel ideas and technologies involve system intelligence, system automation and the smart application of DG and renewable resources.

There are many studies analysing the outcomes of integrating DG in radial distribution systems. The push for these studies is strongly supported by the advances in technologies, the reduction of equipment cost and the increasing trends of DG installations. Most published results promote an overall improvement in system reliability, and highlight the positive influence of DGs. Indeed, if properly allocated, DGs can help to sustain system voltages during maximum (peak) load or decrease service interruption during outages [14–16]. However, the smart grid concept is reshaping the power system. The traditional unidirectional power system with distant bulk generation is changing into a decentralized system with localized smaller generation. This system mutation may bring issues that power engineers are not aware of yet. Therefore, careful studies must be performed on the network as the smart grid is implemented.

12.2.2 Networked Distribution Systems

The interconnected configurations such as spot and secondary grid networks are used in cities. A spot network has the secondary terminals of the distribution transformers connected together to a single bus.

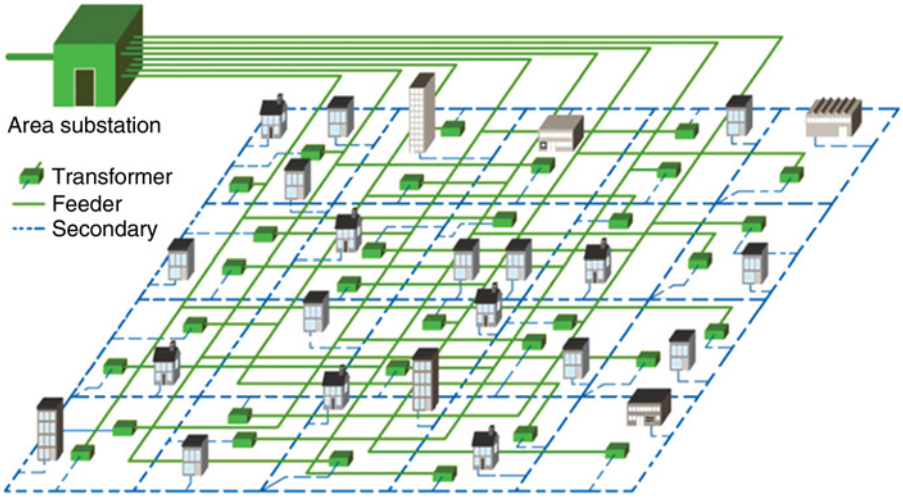

Figure 12.3 Schematic of a LV secondary network. Loads and network transformers are tied together in a highly meshed network (© 2012 IEEE) [7].

At the same time, their primary terminals are supplied from different feeders or power sources. This arrangement is widely used in urban areas, especially when it is needed to ensure reliable delivery of electrical power to some particular facilities, such as hospitals.

Downtown areas of large cities are characterized by high power demands, increased customer density and, at the same time, high prices of real estate and extreme scarcity of free space. In addition, since most of the financial and commercial businesses are located in these areas, the requirements of uninterruptable supply of power and good power quality are especially strict. To comply with these requirements, it is common practice to build meshed networks instead of traditional radial or spot systems. Meshed networks are referred to in the literature as secondary grid networks, area networks or secondary networks. It should be noted that, in North America, the word 'secondary' is often omitted and the term 'network' is used for the secondary grids. In this configuration, distribution transformers are supplied by different feeders from the same area substation. The low-voltage (LV) part of the distribution network is a meshed grid with distributed loads.

An LV secondary network is a distribution system configuration typical of the downtown cores of most cities in North America. An area substation commonly supplies power to two (or more) independent underground networks through a number of MV radial feeders. Each feeder delivers power through several tens of network transformers that reduce the voltage to the utilization level (say 208/120 V). All transformer secondaries and loads are tied together in a highly meshed LV network as shown in Figure 12.3. This arrangement offers the highest levels of reliability of any standard configuration in use today [13]. A detailed oriented network schematic is presented in Figure 12.4, where power system components are presented with their corresponding symbols.

Important components of an LV meshed secondary network are the network protectors [17]. These protective devices are installed on the secondary side of the network transformers, and automatically disconnect them from the secondary grid when the power starts to flow in the reverse direction; that is, from the low-voltage network to the feeders. The network protectors automatically reclose when the conditions for the direct power flow in the system are restored.

An important principle of the smart grid philosophy is the ability of the distribution network to self-heal after disturbance events [18–20]. The implementation of this principle with the existing infrastructure and architecture requires the sectionalizing of the distribution network and the installation of additional

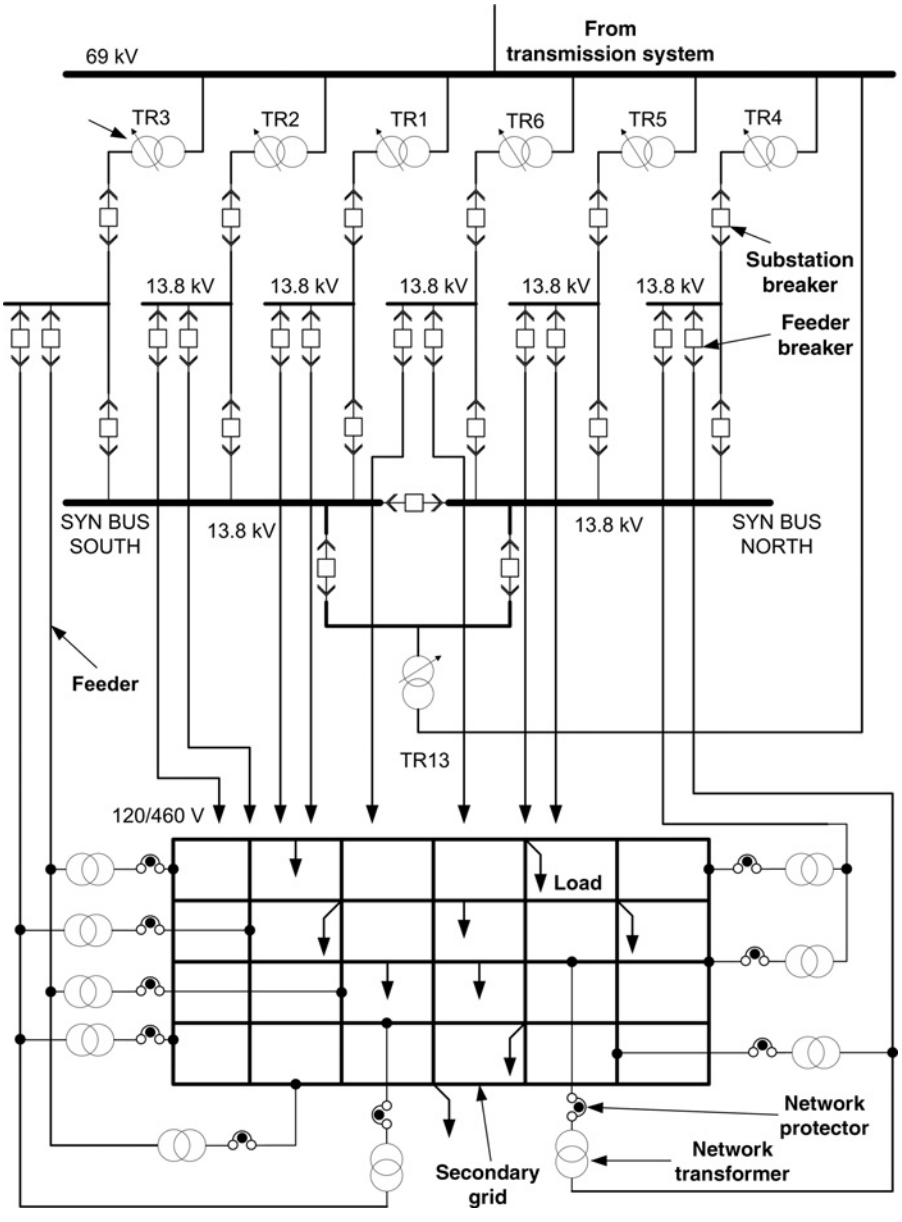

Figure 12.4 Schematic of typical area distribution network highly meshed LV secondary network (© 2012 IEEE) [9].

switching devices and metering equipment. Moreover, the development of two-way communication links and advanced algorithms for fault location detection for automatic switching and control are becoming necessary.

The smart grid also envisions the use of technical advances in the areas of communication and information technology to coordinate the installation of DERs [3]. Allocation algorithms should account

for ageing system constraints (relatively old cables and their ampacity limitations, relevant equipment, limited real state, etc.), newly appearing constraints as changes are implemented and most of all system reliability, power quality and compliance with local, state and federal standards or codes. Proper deployment of DG is expected to provide operational flexibility and a more secure energy infrastructure, of course, in an efficient and economic way.

Following the smart grid concepts and in an attempt to increase the use of distributed generation, standardized interconnection requirements have been revised, expediting the process of installing DG [21]. As part of all the required process, utilities may justify the need for detailed engineering studies for the effects of DG penetration. Recognizing the importance of DG as an energy choice for customers and in order to foresee the future impact of the widespread adoption of DGs, Con Edison Inc. of New York performed probabilistic studies of DG allocation in several of their complex networks [7].

12.3 Restoration and Reconfiguration of the Smart Grid

12.3.1 Introduction

System restoration (or service restoration) can be described as the process of returning the system to normal operation after an interruption or any loss of system components as a result of an outage. Although restoration has always been an important topic for transmission and distribution systems, the last few years have shown a substantial increase in the interest in distribution restoration [22]. This increase is in part due to the significant efforts that have been made in response to the challenges of smart technologies, advances in distribution automation and recent practices related to power deregulation. Considerable attention should be given to the automation of distribution operations which potentially improve the restoration process and reduce the duration of outages as well as the probability of human error. Furthermore, system restoration through automation employs the self-healing principles of the smart grid philosophy, increasing customer satisfaction and service reliability which are of major concern in the power industry.

In a real network, any mistake in the design and/or implementation of new operational techniques may lead to very serious economic and/or social consequences. Therefore, the smart grid concepts must be thoroughly studied, using extensive computer simulations with highly accurate models. In the past, reconfigurable systems were investigated by means of steady-state analyses [23–25]. Nowadays, however, there is a growing understanding that time-domain simulations are to be performed in order to ensure the correct operation of large, complex distribution networks under different fault and switching conditions [26]. A number of power system software programs are capable of performing a transient analysis [27, 28]. Some of their practical applications for electrical distribution networks can be found in [29–34].

System restoration is performed by the switching operation of sectionalizing switches and tie switches. Depending on the restoration method, different switching strategies and configurations must be applied, which may degrade power quality [12]. There are several studies highlighting different approaches to reconfiguration and self-healing in the literature. Some examples are the classic optimization techniques [35, 36], genetic algorithms [37], simulated annealing [38], taboo search [39] and knowledge-based heuristics [40–43] and self-healing by controlled partitioning of power systems into self-sufficient islands using multi-level and multi-objective graph partitioning techniques [44–51]. Furthermore, the smart grid has introduced concepts such as autonomous distribution networks, considering distributed grid intelligence [52], multiagent systems [53–56] and active network management systems [57, 58].

12.3.2 Heavily Meshed Networked Distribution Systems

12.3.2.1 Introduction

As mentioned previously, modern metropolitan distribution networks suffer from a number of problems imposed by their hardwired design. To resolve these problems, Con Edition's 3G System of the Future

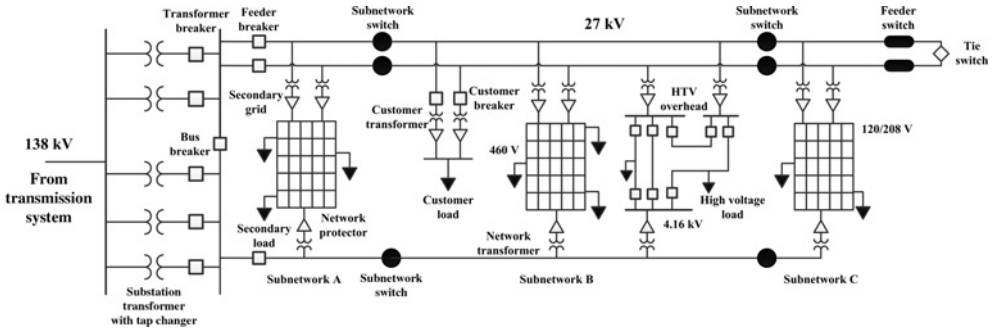

Figure 12.5 Basic interconnection of elements in the Flushing network (© 2012 IEEE) [5].

Department has initiated a pilot project called 'Advanced Distribution Operation with DER Integration'. The main objective of this project is to implement smart grid concepts [18,19] in a very large distribution network. It requires addressing different topics, starting from equipment design and ending at distributed generation allocation, plug-in electric vehicle influence, smart metering, automatic operation and control.

This section is focused only on obtaining reconfigurable system architecture with advanced automation and self-healing capabilities. Currently, practical implementation of the reconfigurable smart grid is taking place in the Flushing network, which supplies electrical power to the northern part of Queens in New York City.

12.3.2.2 Test System

The Flushing network is a large-scale distribution network with a very complex configuration that is hard to visualize in its entirety. Therefore, only its basic interconnections are shown in Figure 12.5. As can be seen in the figure, the secondary side of every distribution transformer in the network is equipped with a network protector [17]. This switching device ensures unidirectional active power flow from the feeders to the secondary grid. The network protector automatically trips when active power flows in the reverse direction and recloses when conditions for forward active power flow are restored. It should be noted that this peculiarity of distribution networks becomes one of the most dominant factors affecting smart grid design where a large number of distributed generators (DGs) and switching events are considered [59].

The Flushing network, at peak loading conditions, supplies over 400 MW through about 10 000 primary feeder sections. It has over 1000 transformers, about 7000 aggregated loads and more than 17 000 secondary grid sections. Detailed information about elements of the Flushing network and a description of its peak and light loading conditions are presented in [9, 60]. According to the operational plan, this network will be subdivided into three subnetworks, as shown in Figure 12.6. Power demands of the subnetworks are given in Table 12.1. The Flushing network has 30 feeders at 27 kV. Ten of them supply power to subnetwork A only (feeders 1–10 according to numeration of their breakers in Figure 12.6). Twenty feeders continue on to subnetwork B (feeders 11–30) and only eight feeders continue to subnetwork C. As can be seen in Figure 12.5, the subdivision of the distribution network into the subnetworks will be implemented by means of especially designed on-load (non-interrupting) subnetwork sectionalizing switches. There are 20 one-way subnetwork switches between subnetworks A and B at the 27 kV level. Separation of subnetworks B and C at 27 kV will be achieved using six one-way subnetwork sectionalizing switches and two multiway switches for increased network reliability.

It should be noted that all the subnetworks are also interconnected at the voltage level of 4 kV. Therefore, to achieve complete isolation of subnetworks B and C, corresponding 4 kV breakers should be opened, together with the 27 kV subnetwork sectionalizing switches.

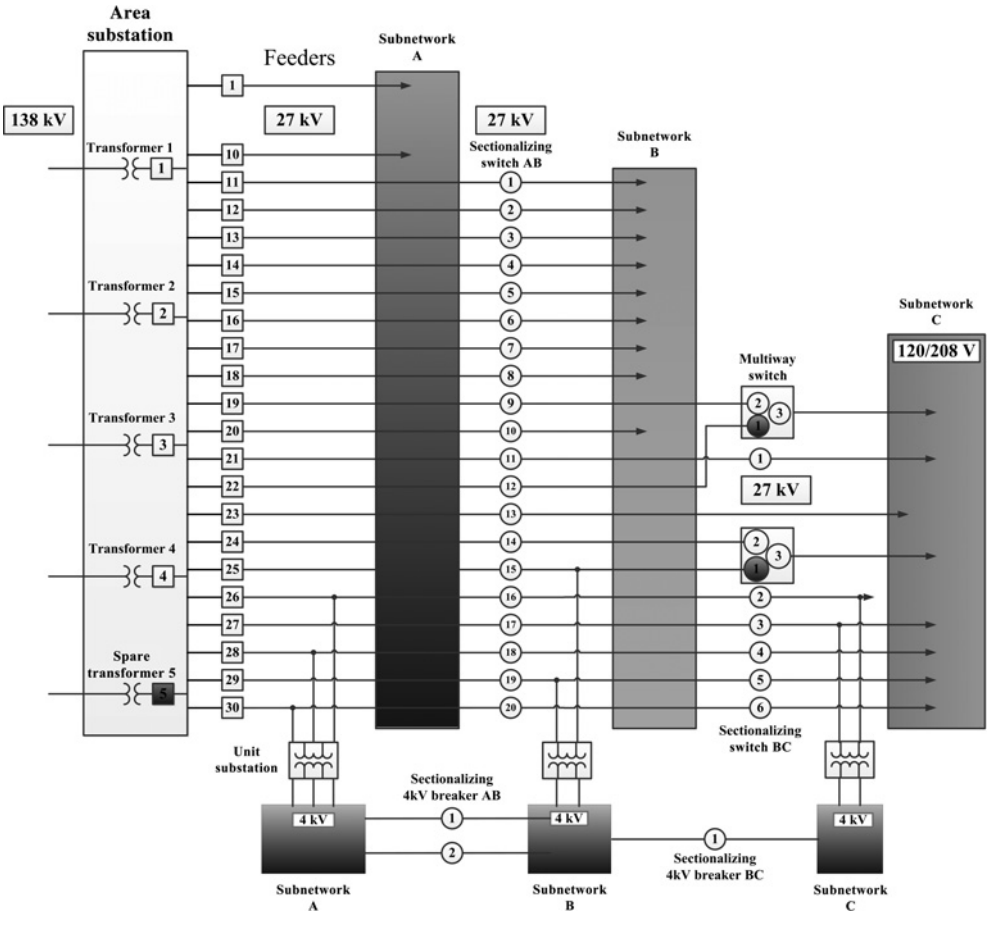

Figure 12.6 Implementation of smart grid concepts in the Flushing network (© 2012 IEEE) [5].

The automatic reconfiguration of the described smart grid is aimed at providing increased reliability of the electrical power supply. Optimal operation and loss minimization criteria are not accounted for in the decision-making process. That is, the system is designed to identify a fault when it occurs, determine its location, isolate the damaged part of the distribution network and reconnect (when possible) the undamaged part through an alternative path. For example, assume that a three-phase short-circuit occurs on feeder 2 in subnetwork A (Figure 12.5). Using current and voltage measurements, this fault is identified and located. Feeder 2 is de-energized when the circuit breaker at its head trips, responding to the short-circuit currents, and all the network protectors along this feeder open due to the reverse power

Table 12.1 Power demands of flushing subnetworks (© 2013 IEEE) [5].

Parameter	Units	Subnetwork A	Subnetwork B	Subnetwork C
Network (grid)	MW	162	90	30
Non-network	MW	42	72	10

flow from the secondary grid. Then, the damaged part of the feeder is isolated by automatic opening of the subnetwork switch on the boundary between subnetworks A and B. Finally, the segments of feeder 2 in subnetworks B and C are re-energized when the normally open tie switch between feeders 1 and 2 closes.

The above-mentioned principle of smart grid reconfiguration seems to be very simple, but its practical implementation may face serious difficulties, especially in the existing distribution networks. This is due to the fact that dozens of the switching and protective devices need to operate in a properly coordinated manner while the network configuration changes. Success can be achieved only if the actual transients of the distribution network can be accurately reproduced with time-domain simulations at the design stage. Otherwise, there is always the possibility that the true behaviour of the network might be overlooked, and the developed switching strategies may not work properly or might even harm the network.

12.3.2.3 Modelling and Validation Approaches

Figure 12.6 shows a simplified diagram of the network under analysis. We will now provide a short review of the simulation approach used to investigate smart grid reconfiguration and some issues related to the required switching are given, focused only on the following topics:

- required speed of switching
- switching failures
- effect of backfeeding
- overcurrents and equipment malfunctioning

Implementation of the smart grid concepts in a real network requires an intensive theoretical analysis and hundreds of transient simulations to be done first. To automate this process, a special software tool based on Matlab [61] and EMTP-RV [62] has been developed. It creates three-phase time-domain models of the network for different operation scenarios, simulates them, performs the analysis of the obtained results and reports overcurrents, overvoltages, undervoltages and the status of every switching device.

The EMTP model for the Flushing network consists of over two million lines of data (network and control signals). Each time-step requires the solution of a matrix equation of order larger than 100 000. Using an integration step of 50 μs, it takes about 16 hours to solve a case with a simulation time of 650 ms in a PC computer with an Intel Core i7 CPU 975 processor operating at 3.33 GHz and installed RAM of 24 GB. A detailed description of the modelling process has been reported in [9, 60].

The obtained EMTP models were validated in the following five ways: (1) comparing steady-state solutions against power flow results calculated by the field-validated poly voltage load (PVL) flow program for peak and light load conditions [63]; differences in node voltages and section currents are very small, (2) simulating some first contingencies; similar good agreement between EMTP and PVL is obtained, (3) evaluating several second contingencies; the results are consistent with PVL, (4) comparing, for many three-phase short-circuits, results obtained with the EMTP with those from the PVL short-circuit computation facility; very small differences occurred in all feeders for all cases, (5) simulating, with the EMTP, a number of actual short-circuit events that had been recorded with PQ Node [64]; the waveshapes of all the three-phase voltages and currents obtained from the simulation matched very well the measurements. These results demonstrate that the EMTP model of the network is correct. The details can be found in [9, 60].

As previously mentioned, during this study hundreds of simulations were performed to analyse the performance of the proposed smart grid concepts. Here, three scenarios are presented to illustrate some of the challenges posed by the implementation of this new technology. The scenarios, corresponding to realistic, but critical situations include: (1) isolation of subnetworks B and C after four contingencies, (2) isolation of subnetworks B and C with one switch stuck, (3) auto-loop operation.

12.3.2.4 Isolation of Subnetworks B and C after Four Contingencies

One of the main features required from the next generation of distribution networks is the ability to be reconfigured and to restore power supply to the maximum number of customers as soon as possible after a major fault. To investigate this issue, the following scenario is studied: Four sequential bolted three-phase short-circuits occur in subnetwork B on feeders 12, 13, 16 and 17. The faults occur within a time interval of six cycles of the fundamental power frequency starting at cycle 2 for feeder 12 and ending six cycles later with feeder 17 (Figures 12.7–12.10). As a result, abnormally high currents flow in the corresponding feeders activating the instantaneous overcurrent protection devices and tripping their breakers (12, 13, 16 and 17) within five or six cycles. Peak values of the fault currents through the feeder breakers and instantaneous current settings of the relay protection are given in Table 12.2.

During the faults, there is reverse power flowing from the secondary grid to the fault locations through the network transformers of the faulted feeders. This phenomenon is called backfeed. A complete backfeed path also includes undamaged feeders and their transformers delivering power to the LV grid in the forward direction. The reverse power flow is sensed by the network protectors installed on the secondary side of the network transformers of the faulted feeders. As a result, these LV network protectors trip on reverse power in about six cycles, completely isolating the faults. It should be noted that, if one opens sectionalizing switches 2, 3, 6 and 7 (of the faulted feeders) between subnetworks A and B after the fault is isolated, feeder breakers 12, 13, 16 and 17 can be reclosed, and a part of subnetwork A supplied by the disconnected feeders will be re-energized. This automatic operation has been simulated in a time interval from the 10th to the 20th cycle.

Finally, in the present switching scenario subnetworks B and C are de-energized. For this purpose, 4 kV breakers between subnetworks A and B are opened first (cycles 22–25 of the fundamental frequency). Then, sectionalizing switches 1, 3–5 and 8–20 between subnetworks A and B are opened as well. In summary, the present case includes 28 intentional switching events which can be produced remotely by an operator or artificial intelligence mechanism as a response to four three-phase short-circuits. Additionally,

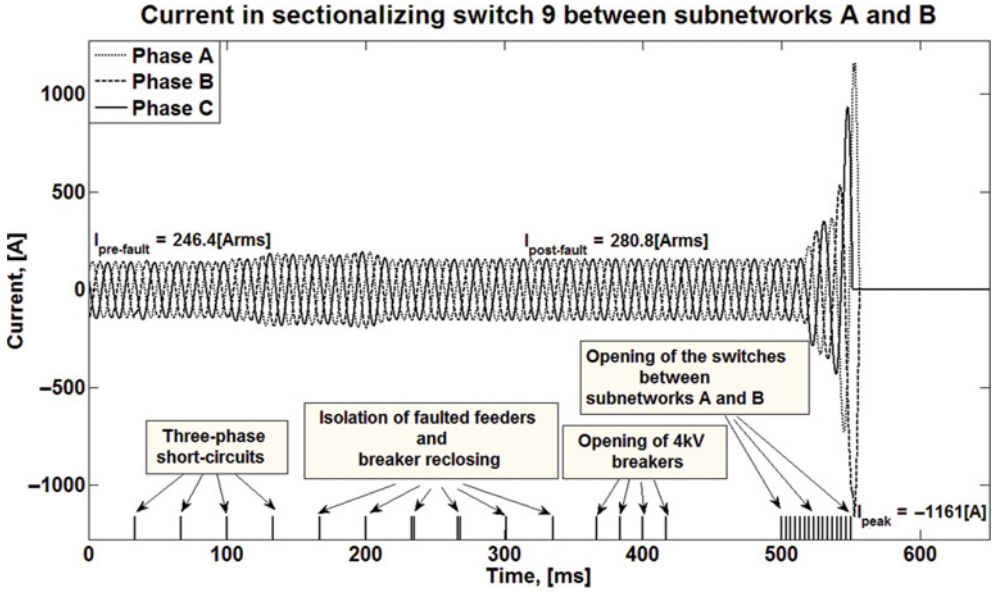

Figure 12.7 Currents in the last opening switch between subnetworks A and B (scenario A) (© 2012 IEEE) [5].

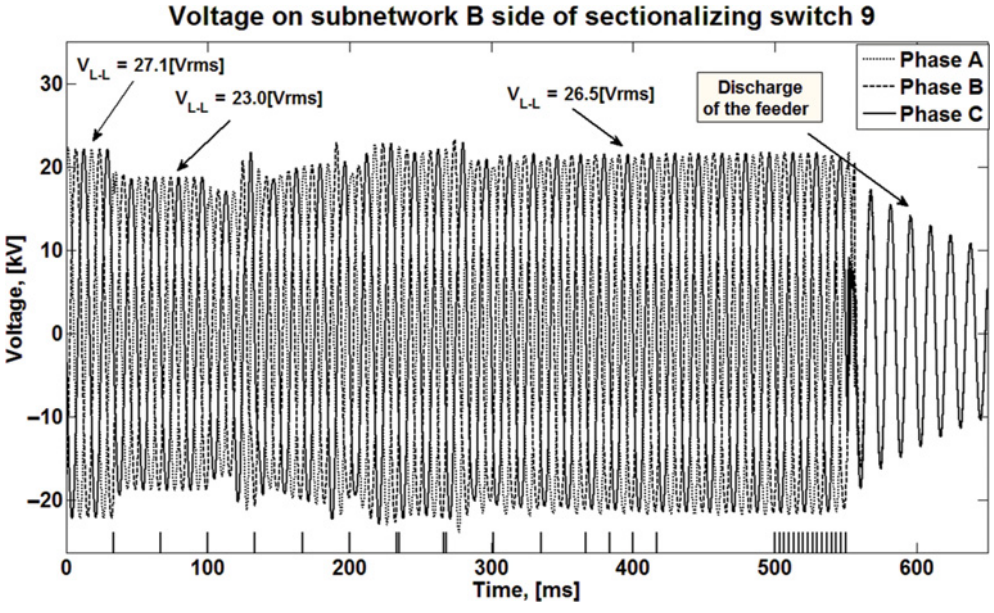

Figure 12.8 Voltage on subnetwork B side of the last opening switch between subnetworks A and B (scenario A) (© 2012 IEEE) [5].

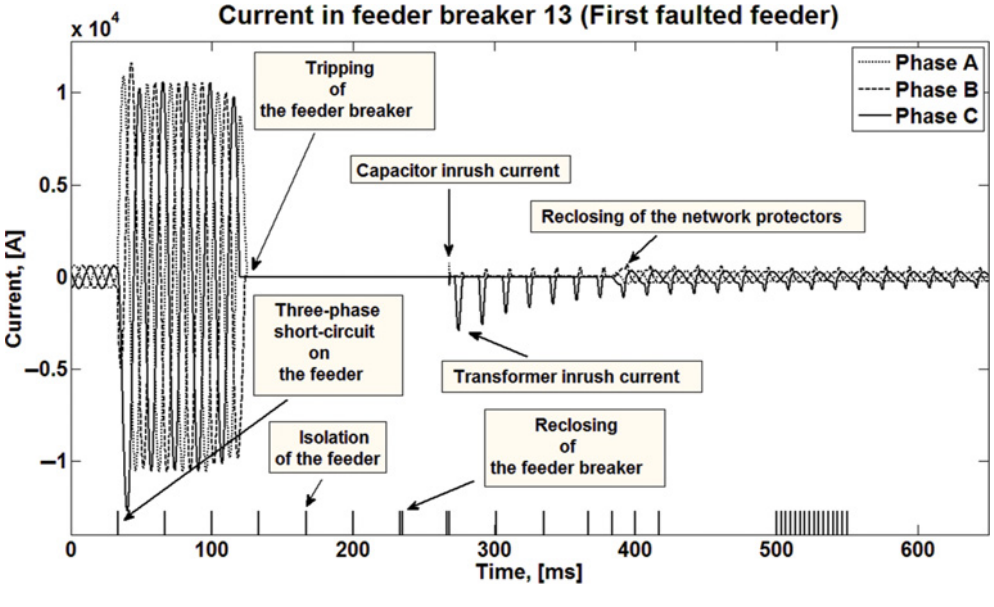

Figure 12.9 Currents in the feeder breaker of the first faulted feeder (scenario A) (© 2012 IEEE) [5].

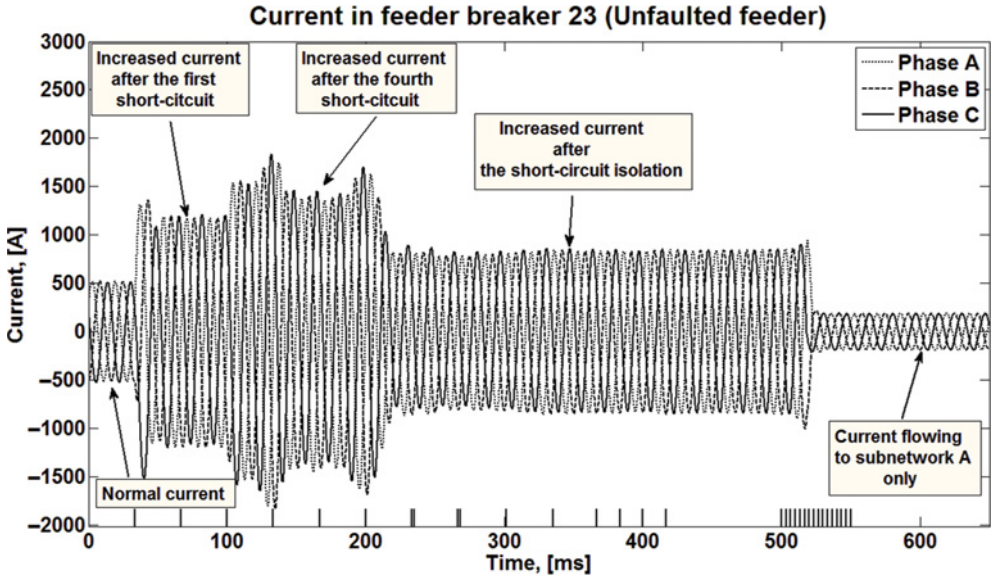

Figure 12.10 Currents in the feeder breaker of one of the unfaulted feeders (scenario A) (© 2012 IEEE) [5].

there are dozens of network protectors and feeder breakers whose dynamics are represented and which operate programmatically as per their settings.

Some of the simulation results are given in Figures 12.7–12.10. The currents flowing in the sectionalizing switch 9 between subnetworks A and B are shown in Figure 12.7. It can be seen that these currents are almost unaffected by the four short-circuits at the beginning of the simulation. However, when the sectionalizing switches start opening to disconnect subnetworks B and C, sectionalizing switch 9 picks up the load usually served by other feeders. As a result, significant currents flow.

Phase voltages on the subnetwork B side of the sectionalizing switch 9 are shown in Figure 12.8. It can be seen that during short-circuit conditions the voltage sags to about 85% of the prefault value. After the isolation of the faulted sections, the voltage is restored to 98% of its initial value. Finally, when subnetworks B and C are completely disconnected, the voltages decay exponentially due to discharge of the energy stored in feeder capacitances and network transformers. Subnetworks B and C are completely discharged in approximately 1.2 seconds.

The currents in the circuit breaker of the first faulted feeder (feeder 13) are given in Figure 12.9. They are equal to 427 A (rms) before the three-phase short-circuit occurred. When the fault occurs the currents increase to about 7.5 kA. The feeder breaker trips at approximately 120 ms. Then it is

Table 12.2 Instantaneous current settings of relay protection (© 2013 IEEE) [5].

Breaker	Instantaneous current setting (A)	Peak current phase A (A)	Peak current phase B (A)	Peak current phase C (A)
Breaker 12	4000	9210	9408	9914
Breaker 13	4000	11 037	11 038	11 055
Breaker 16	4000	11 941	12 712	13 983
Breaker 17	4000	10 899	12 719	1833

intentionally reclosed at 235 ms after the isolation of the fault. A short-duration capacitive inrush current can be observed right after the reclosing. It should be noted that, as a result of the fault, all the network protectors of the transformers connected to feeder 13 trip, disconnecting the secondary grid. Therefore, the reclosing takes place at no-load conditions.

It can be seen in Figure 12.9 that energization of the network transformers under no-load conditions draws inrush currents having a first peak of 2925 A. This inrush current decreases from cycle to cycle. At the same time, the reclosing of the feeder breaker creates the conditions for the network protectors to close (automatically) in the undamaged part of the feeder (subnetwork A). The influence of the network protector reclosing on the currents in the circuit breaker can be observed in Figure 12.9, starting from the time instant of 385 ms.

Finally, phase currents in one of the healthy feeders (feeder 23) are shown in Figure 12.10. These currents are equal to 369 A before the three-phase short-circuits occurred on the adjacent feeders. During the fault, the currents became 2–3 times higher. A peak value of the phase C current reaches 1883 A. When the four short-circuits are isolated, the number of feeders supplying subnetworks B and C reduces. As a result, the individual loading of the healthy feeders increases with respect to the prefault operating conditions. The phase currents in feeder 23 after the isolation of all four short-circuits reach values of almost 600 A. Opening of the subnetwork sectionalizing switches that starts at 500 ms leads to the complete isolation of subnetworks B and C. Thus, the currents through the feeder breaker supply the loads only in the subnetwork A. The phase currents at the final stage of the simulation are 133 A only.

In addition to illustrating the operating logic during the process of the fault isolation and network reconfiguration, the importance of the simulation presented is that it reveals the importance of fast and coordinated switching. For example, one can see that the load redistribution as a result of the sequential opening of the switches produces very high currents in the remaining closed switches. These switches are not designed to interrupt fault currents. Therefore, if the rms values of the currents exceed the rated 600 A (for the investigated network), the operation of the switches is blocked by their protection mechanism. As a result, the energized feeders will become overloaded, perhaps causing tripping of the corresponding feeder breakers at the area substation.

To a great extent, the results of the time-domain analysis of the operation of the 3G smart grid technologies, have allowed us to discover potential dangers that need to be addressed during the practical implementation. In particular, there are important questions related to the reliability of communications, switching coordination and synchronization.

12.3.2.5 Isolation of Subnetworks B and C with One Switch Stuck

Secure operation of the distribution network must be ensured not only under normal operating conditions, but also when equipment fails. The present case consists of disconnecting subnetworks B and C from the area substation when one of the subnetwork sectionalizing switches does not open. This may happen due to electrical or mechanical problems in the switch itself or due to loss of communication. The 4 kV breakers between subnetworks A and B open from cycle 4 to cycle 7 (Figures 12.11 and 12.12). Then the 27 kV subnetwork sectionalizing switches between subnetworks A and B are commanded to open from cycles 10 to 14. It is assumed that switch 4 is stuck; that is, only 19 switches out of 20 open. As a result, subnetworks B and C are not completely disconnected.

The currents in the phases of the stuck sectionalizing switch are given in Figure 12.11. As can be seen, the currents are equal to 308.5 A under normal operating conditions. Then, when the remaining 19 subnetwork sectionalizing switches open, the current in the stuck switch increases significantly, since all the loads in subnetworks B and C are fed through the stuck switch. This is different from the normal operating conditions, where the load is distributed among different feeders. The current of 1907 A in the stuck switch is over three times the rated 600 A. This overloading can also be observed at the head of the feeder with the stuck sectionalizing switch (feeder 14).

The currents in the feeder breaker are presented in Figure 12.12. In this figure, the initial value of the current is 441 A. After opening of 19 switches between subnetworks A and B, the feeder breaker current

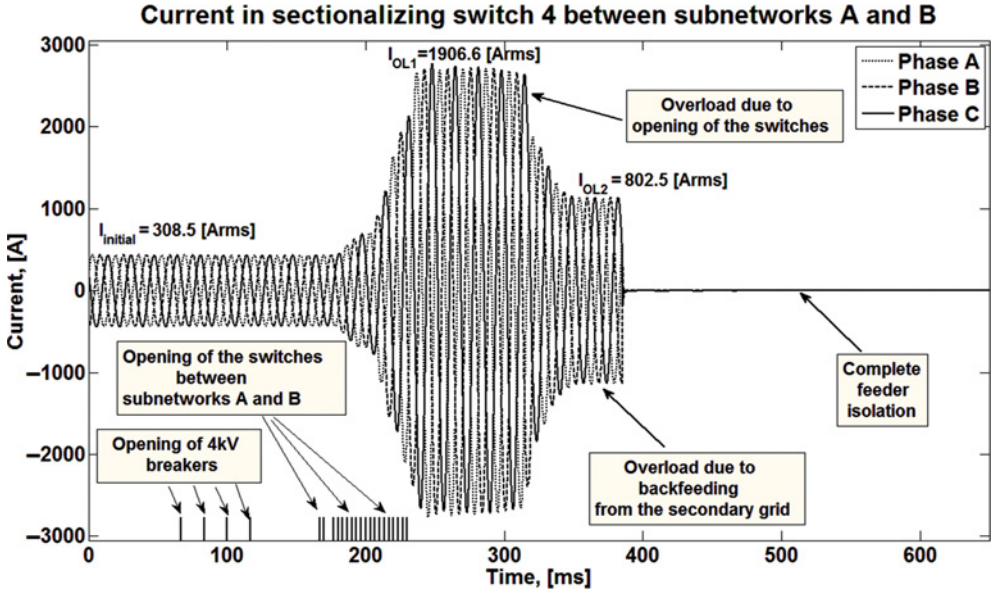

Figure 12.11 Currents in the stuck sectionalizing switch #4 between subnetworks A and B (scenario B) (© 2012 IEEE) [5].

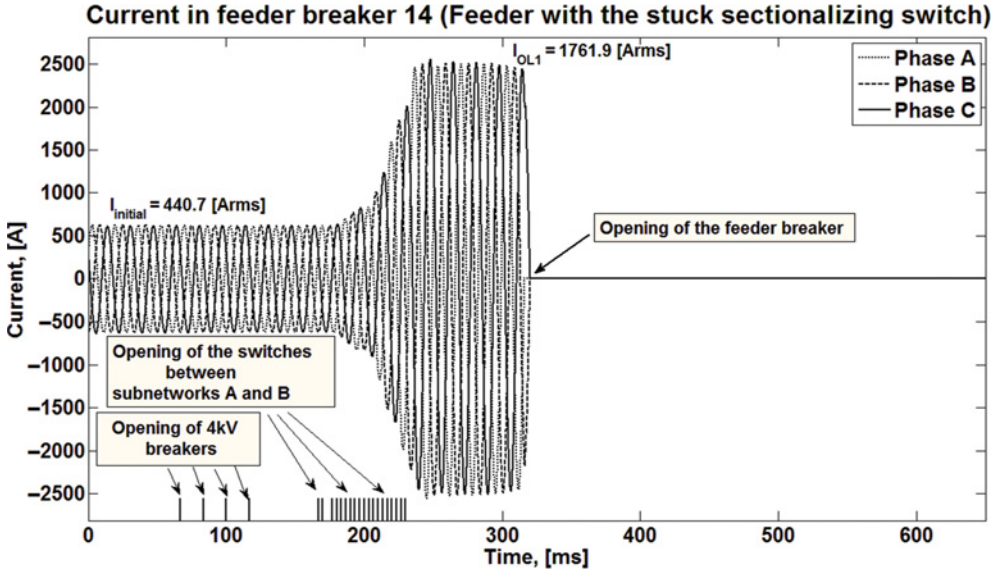

Figure 12.12 Currents in the feeder breaker of the feeder with the stuck sectionalizing switch (scenario B) (© 2012 IEEE) [5].

increases to 1762 A, exceeding the settings of the overcurrent relay protection (1280 A). It is interesting to note that in this case the currents in the sectionalizing switch in the middle of the feeder are higher than the currents in the head of this feeder. This is so because, after the opening of the 19 switches, a part of the current through the stuck switch comes as backfeed from the LV grid of subnetwork A, which is supplied by all the feeders. The power flows from the secondary side to the primary side of the network transformers connected to the feeder with the stuck switch in subnetwork A. When the feeder breaker trips at approximately 320 ms, as shown in Figure 12.12, the backfeeding through the network transformers in subnetwork A does not stop immediately. Tripping of the network protectors is gradual and, as a result, the phase currents in the stuck switch (Figure 12.11) reduce gradually. A current of 802 A flows in the stuck switch for the last three cycles before the last network protector trips. After its tripping, a part of the feeder with the stuck switch supplying subnetwork A is completely isolated from the area substation. Thus, at the end, subnetworks B and C are de-energized and subnetwork A is supplied by 29 feeders instead of 30.

We can conclude that if not all the sectionalizing switches operate, excessive currents can be developed, preventing on-load operation (sectionalized switches are designed to interrupt rated current only). In such cases, the feeders must be disconnected from the area substation by the corresponding breakers to prevent overloading of the equipment such as cables, transformers and switches. The simulation has shown how proper settings of the relay protection prevent extended exposure of the distribution network elements to excessive currents resulting from the malfunction of a sectionalizing switch during the isolation of a subnetwork.

12.3.2.6 Auto-Loop Operation

Figure 12.6 shows that the distribution network under study has two multiway switches that form two auto-loops. In this auto-loop configuration, subnetwork C is supplied by feeders 19 and 24 (nodes 2 and 3 of the second delta-connected multiway switches are closed). It is assumed in the present switching scenario that a three-phase short-circuit occurred in feeder 25 in subnetwork A after four cycles from the beginning of the simulation. As the result, the corresponding feeder breaker trips on instantaneous overcurrent in five cycles, effectively de-energizing the entire feeder.

Due to the installation of the sectionalizing switches, the fault could be isolated in subnetwork A. For this purpose, switch 15 between subnetworks A and B is opened after 10 cycles. After the complete isolation of the short-circuit, a part of feeder 25 in subnetwork B can be re-energized through the second multiway switch. This goal is achieved by connecting nodes 1 and 2 in the switch after 25 cycles. As a result, a part of feeder 25 in subnetwork B is powered from feeder 24.

Phase currents in the feeder breaker 25 are given in Figure 12.13. The initial value is about 95 A and rises to more than 18 kA during the fault. As can be seen in the figure, an attempt to reclose the feeder breaker fails because the three-phase short-circuit in subnetwork A was not cleared.

Currents in feeder breaker 24 are given in Figure 12.14. This feeder is used as a backup to subnetwork B in cases when feeder 25 is de-energized due to a fault in subnetwork A. Initially, the currents in the breaker are equal to 233 A. We can see them rise to 313 A due to the three-phase short-circuit (subnetworks B and C are still connected at both 27 kV and 4 kV levels). When the fault is isolated, the breaker currents reduce to 244 A. Note that they are slightly higher than in the prefault conditions. This is because the increased substation voltages obtained after a part of feeder 25 in subnetwork A is disconnected. When the second section of this feeder, located in subnetwork B, is re-energized there are transformer inrush currents of about 1246 A. Note that these short-duration high-magnitude currents do not cause any problems in the present case. Inrush currents become a concern when their high values are sustained for a long period of time and, as a result, may lead to thermal runaway, overloading or relay misoperation. However, extensive transient analysis performed in these studies did not reveal any abnormal operating conditions resulting from the inrush currents. The final steady-state values of the feeder breaker currents in Figure 12.14 are 283 A.

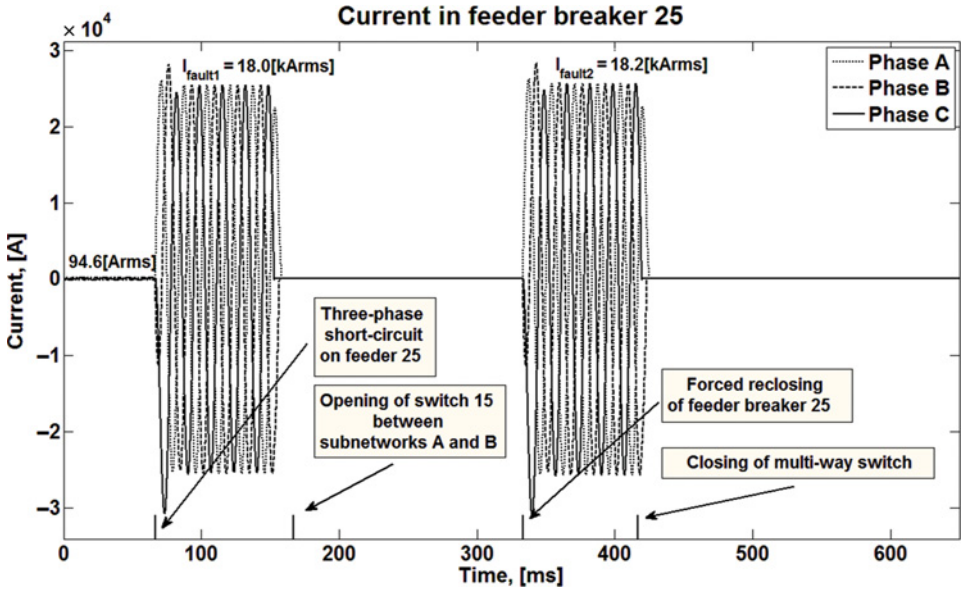

Figure 12.13 Currents in the circuit breaker of the faulted feeder (scenario C) (© 2012 IEEE) [5].

Currents in the sectionalizing switch 15 used to isolate the damaged part of feeder 25 are shown in Figure 12.15. Their values under normal operating conditions are 101 A. Analysing Figure 12.15, we conclude that sectionalizing switch 15 interrupts a portion of the short-circuit current, which exceeds 1000 A. This finding, together with the results obtained in the previous subsections, led to consideration of an enhanced sectionalizing switch design, since the rated current of the existing switches is only 600 A.

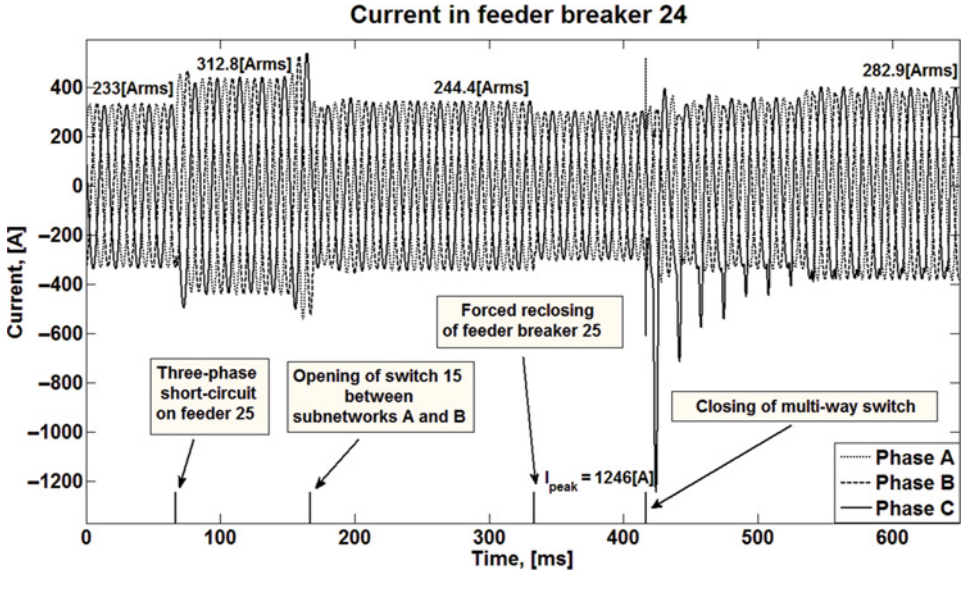

Figure 12.14 Currents in the circuit breaker of the backup feeder (scenario C) (© 2012 IEEE) [5].

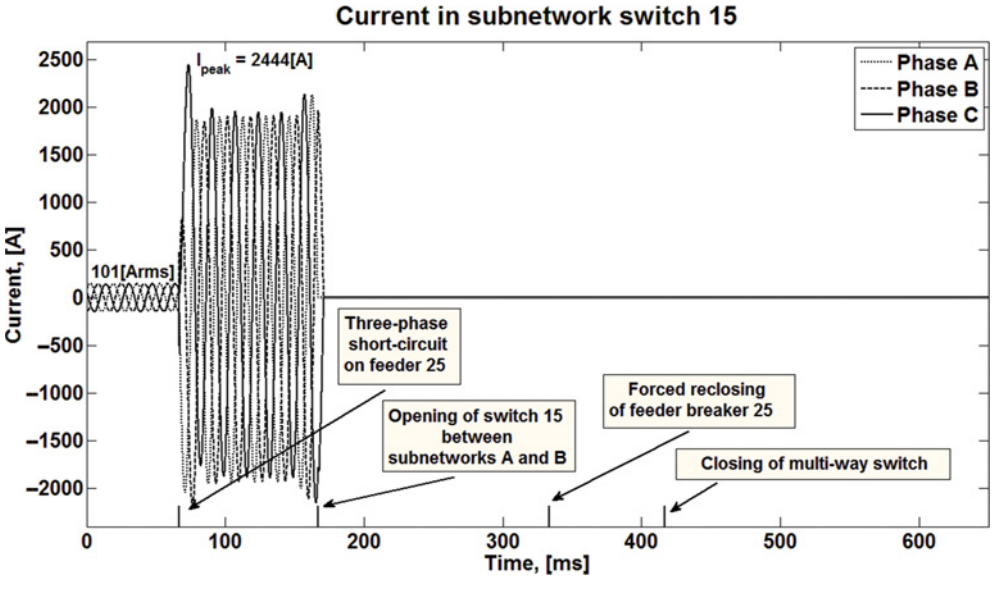

Figure 12.15 Currents in the sectionalizing switch between subnetworks A and B which isolates the three-phase fault (scenario C) (© 2012 IEEE) [5].

It should be noted that another possible solution in this case is a delayed switching of sectionalizing switch 15. Indeed, if its operation is postponed, all the network protectors on feeder 25 would have sufficient time to trip. As a result, the entire feeder could be de-energized by these devices and by the circuit breaker. Then the sectionalizing switch would disconnect subnetworks A and B under zero current conditions.

The restoration of power to a part of feeder 25 is achieved by closing the multiway switch, as shown in Figure 12.16. There is a relatively high first peak (of 1283 A) due to the transformer inrush current. For a time interval of approximately seven cycles of the fundamental power frequency, the secondary grid of subnetwork B is still disconnected from feeder 25 (all the network protectors tripped during and after the fault). Then the network protectors automatically reclose and the feeder picks up a part of the load in subnetwork B.

12.4 Integration of Distributed Generation

12.4.1 Scope

Distributed generation is becoming an increasingly viable option for the future of power systems because of regulations on environmental protection and energy efficiency. Despite its higher price, the installation of DG in distribution systems offers advantages over the traditional unidirectional flow of power from a distant generator. For example, DG reduces the load that needs to be supplied from the substation. This particular advantage gives utilities an economic alternative to building new substations and installing the cables and transformers needed to feed the increasing system load. Although not generalized today, DG could be used to control voltage [65–69] or dampen power oscillations [70]. There are, however, several challenges that DG poses to the safe and reliable operation of a distribution system [71–79].

The analysis of distribution system reliability is of prime importance to the electric utilities. The results of reliability indices allow utilities to track and improve performance in weak parts of the system such that regulations and standards are satisfied. The most commonly used service performance indices

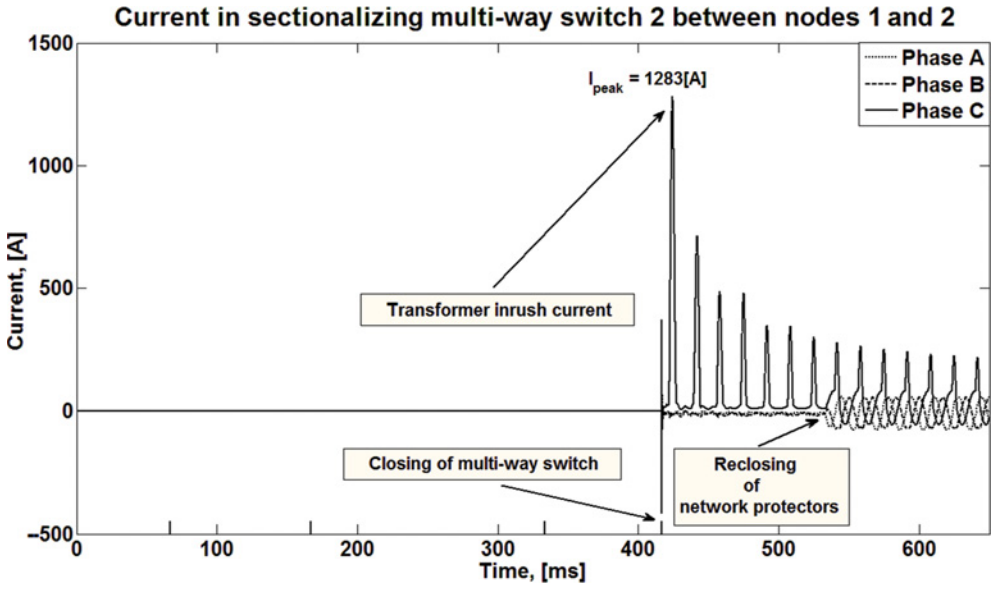

Figure 12.16 Currents in the second multiway switch between nodes 1 and 2 (scenario C) (© 2012 IEEE) [5].

for distribution systems are system average interruption duration index (SAIDI), customer average interruption duration index (CAIDI) and system average interruption frequency index (SAIFI). These indices provide a statistical description of a system's past performance [80].

Depending on the network topology, the increasing trend of DG installations may affect the system reliability indices. It is commonly believed that the overall reliability of a system will be improved because of the installation of DGs. In fact, there are many studies highlighting the beneficial influence of DGs. From maintaining voltage within acceptable limits during heavy loading to partially sustaining customers during feeder outages, DGs promote improvements of the reliability indices by decreasing customer interruptions [15, 81, 16]. However, moving from the traditional unidirectional power system to a decentralized generation distribution system may cause issues not yet considered. Therefore, the possible impacts of DG to the system reliability must be properly assessed to avoid degradation of services.

This section presents two studies of substantial importance to the electricity industry and to academia concerning the integration of DG in the power system. The first study demonstrates possible negative impacts on reliability caused by DGs installations when the system experiences temporary faults [81]. The second analysis focuses on voltage profile problems caused by DG penetration in meshed LV secondary distribution networks. The scenario considers the case in which customers are allowed to freely incorporate DGs on their facilities, making decentralized generation extensive and the maximum DG output coincides with minimum system load conditions (worst case scenario) [7]. These studies were carried out through dynamic simulations using the EMTP.

12.4.2 Radial Distribution Systems

12.4.2.1 Negative Impact on Reliability of DG under Temporary Faults

Reliability in a distribution system is defined as the ability of electrical equipment to supply electricity to customers and utilities over a predefined period of time. Reliability is most vulnerable when distribution systems fail to supply power to their customers, due to outages or interruptions [15].

When a distributed generator is installed in a power system, it is commonly believed that the overall reliability is improved [15, 81, 16]. Previous publications show the effects of various types of DG and also show how to assess the impact of them on the reliability indices [16, 82, 83]. There are also studies based on dynamic analytical solutions aimed at optimizing the positive effects of DG on reliability [84].

Despite the fact that reliability can be generally boosted by adding DG, there are real cases in which the presence of distributed generators may produce negative effects on reliability. The system average interruption frequency index is commonly used as an indicator by electric power utilities of the reliability of the system. This index is computed as:

$$SAIFI = \frac{\text{total number of customer interruptions}}{\text{total number of customers served}} \tag{12.1}$$

The present study shows how SAIFI can be increased, in certain cases, when switching devices clear temporary faults. Only the reliability variation in the steady state is considered in the calculation of SAIFI; utilities exclude from the calculation temporary disturbances lasting for seconds, since they do not cause long-term power loss.

Unlike other analyses in the literature, the presented analysis focuses on time-domain (EMTP) short-circuit simulations of a peculiar, yet currently available in the field, auto-loop distribution system configuration with every power system component modelled in detail [81].

12.4.2.2 Case Analysis

Electromagnetic transient simulations need detailed models of all system components, including: voltage sources, substations, shunt capacitors, transformers, feeder sections and loads. All components are modelled as three-phase. Figure 12.17 shows a commonly used 4 kV city distribution system and Figure 12.18 illustrates the area of focus for the study. This network has approximately 3 MVA of loads and is fed by two 13 kV feeders. Switching devices 01 and 02 are the ones that connect the network to the 13/4 kV substation transformers. Of the eight switching devices, device 06 is the recloser which opens on overcurrent and also carries out reclosing attempts to restore the system after a temporary fault. The time delay between trip and reclose is set to 0.5 s. The DG is a synchronous generator rated at 1.2 MVA

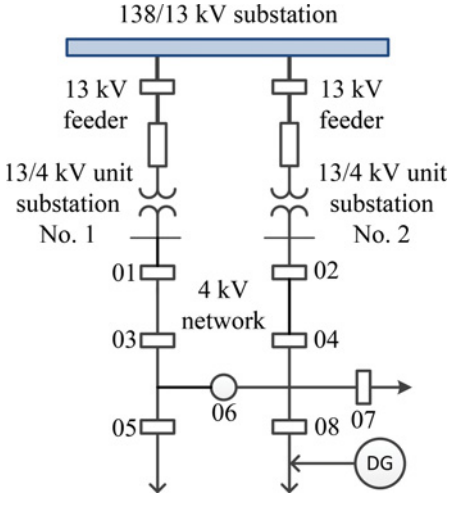

Figure 12.17 Typical 4 kV system configuration.

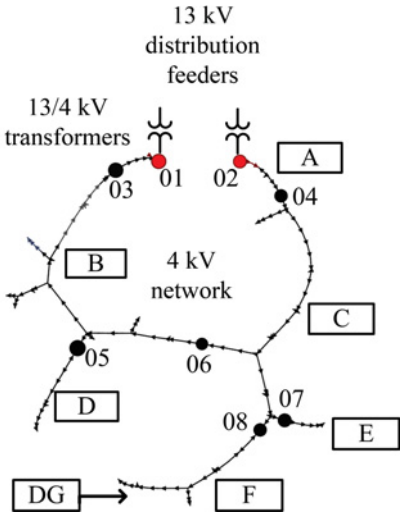

Figure 12.18 Area of focus for the study on the 4 kV system.

and operates at 0.8 power factor (leading). All controllers, such as speed governor and voltage regulator, as well as protective devices, are represented in detail for these simulations.

The characteristic curve of the overcurrent relay is shown in Figure 12.19, which corresponds to the lowest curve time-dial setting of the relay. This is so because nowadays utilities prefer faster-acting relays. The pickup current of each relay is determined by the first contingency. For instance, when device 02 is open because of a contingency, device 01 will be carrying the load of the whole network, and the current it takes is considered the maximum load current. The multiplier factor is chosen to be 1.5, since compared to the normal load current, the fault current is relatively larger in this network [51]. Thus, the pickup current of each switching device is expressed as:

$$I_{pickup} = 1.5 \times I_{maximum\_load} \tag{12.2}$$

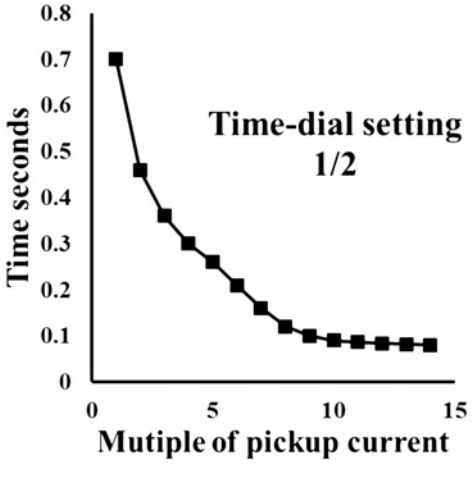

Figure 12.19 Relay operation characteristic curve. Source: [51].

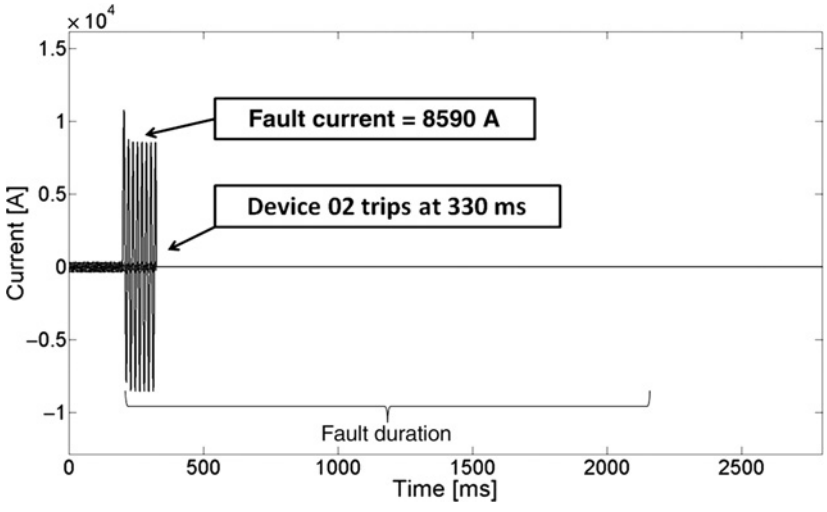

Figure 12.20 Three-phase instantaneous current of device 02.

12.4.2.3 Single-Phase Fault without DG Installed

A line-to-ground fault is simulated on the feeder section between devices 02 and 04 lasting for 2 s; from 200 ms to 2200 ms (Figures 12.20–12.22). The large fault current from the 13 kV distribution system reaches 8.59 kA and trips device 02 at 330 ms, which is about eight cycles after the fault (Figure 12.20).

During the entire event of the fault (occurrence, clearing and reclosing), device 08 remains closed since there is no large current through 08 and the prefault current equals the post-fault current, as shown in Figure 12.21. In the period between the trip and reclosure, there is no current through device 08 since there is no active power source to feed the customers in this area.

For recloser 06, the fault current reaches around 2.0 kA (Figure 12.22). At 400 ms after the fault occurs, the recloser trips. Then it attempts to reclose after another 500 ms. The temporary fault is cleared

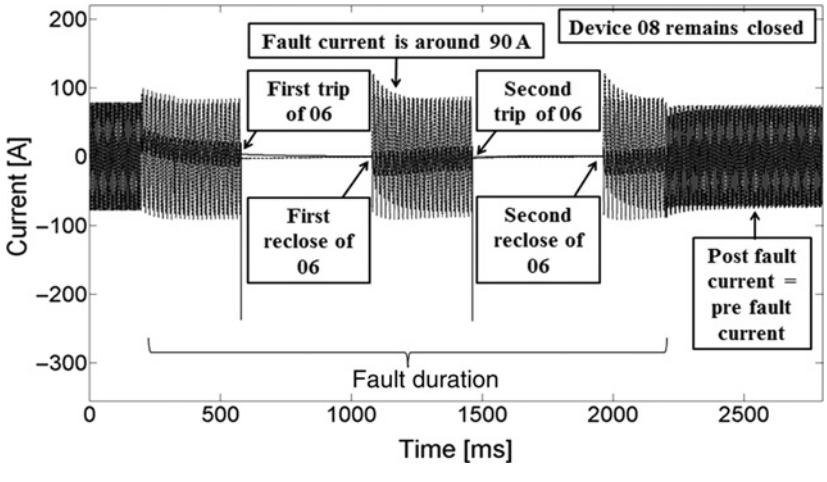

Figure 12.21 Three-phase instantaneous current of device 08.

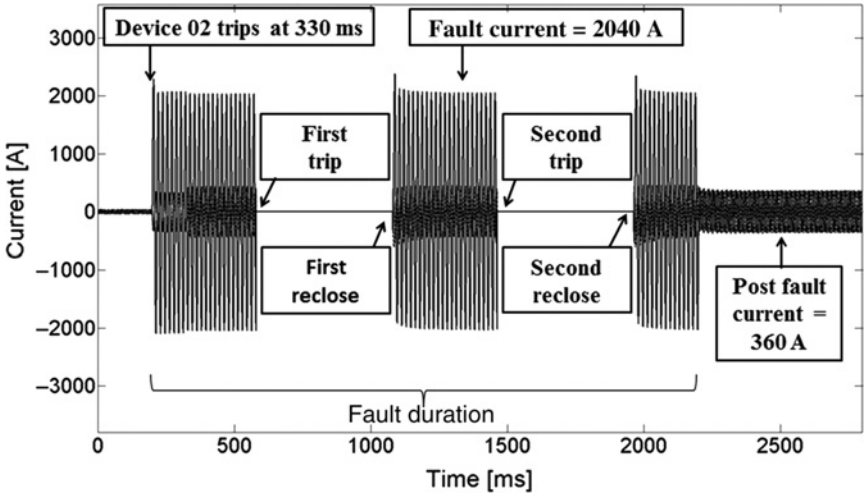

Figure 12.22 Three-phase instantaneous current of device 06.

at 2200 ms and at this time the recloser picks up the loads located downstream of device 02, which is also sectionalized by recloser 06. The post-fault steady state reaches 360 A, as shown in Figure 12.22. In this case no load is lost permanently.

12.4.2.4 Single Phase Fault with DG Installed

In this case, the temporary line-to-ground fault occurs when the DG is installed in the 4 kV network. When the DG is connected, the current flow through each switching device is different, but the operation of the majority of devices remains similar. Device 02 trips on the overcurrent from the 13 kV side and device 06 trips first and then attempts to reclose. While devices 01, 03, 04, 05 and 07 experience different level of overcurrent, they all remain closed. The only device that acts differently is 08. The prefault current through device 08 is 90 A and when the fault happens, the current contribution to the fault from the DG is around 1200 A. Although this current declines due to the dynamic performance of the synchronous DG, it is still high enough to trip device 08, as shown Figure 12.23. In this case, recloser 06 still tries to pick up the loads, but the load located downstream of device 08 cannot be restored because device 08 is open.

As shown in the above case, when the DG is not present, there will actually be no power loss for any customer in this 4 kV system. Every customer is picked up after the fault is cleared. However, if the DG is installed, the customers located downstream of device 08 will lose power, and they would have to wait for the utility to send crews to restore power manually. Therefore, if this temporary fault is considered the sole incident of the year, the total number of customer interruptions changes from none to a positive number, affecting SAIFI. Therefore, the overall reliability of this particular system can be reduced by the presence of the DG.

12.4.3 Heavily Meshed Networked Distribution Systems

12.4.3.1 DG Impact

Modern metropolitan distribution networks, in particular downtown areas of large cities, have strict requirements of electrical power quality and reliability. The introduction of distributed generation forces utilities to change their approach to system protection and operation [85]. A systematic study

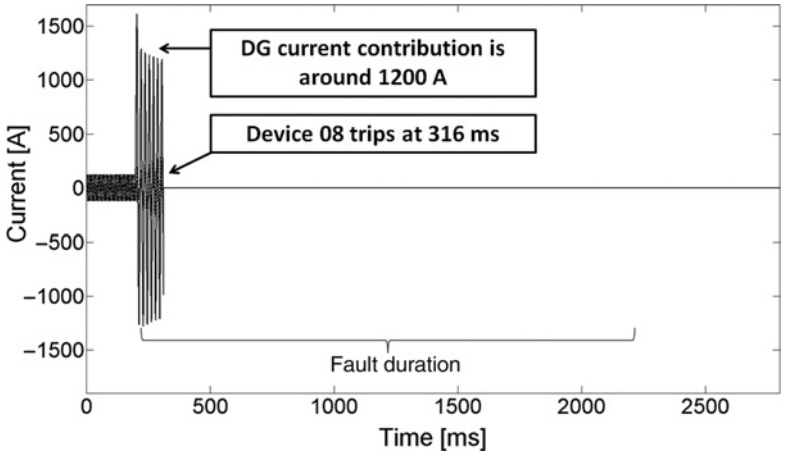

Figure 12.23 Three-phase instantaneous current of device 08 in the presence of DG.

reporting the first attempt to quantify the possible negative impacts on the voltage profile due to different DG penetration levels in a meshed LV secondary distribution system is presented in [7]. There are a considerable number of research papers reporting the advantages and disadvantages of DG for radial distribution systems, such as [13, 69, 86–96]. The operation strategies of radial and networked systems are quite different from each other. For example, radial systems allow for bidirectional power-flow, but may require a different coordination of protections. However, in secondary networks, reverse power from the LV network to the MV feeders is not possible. For safety reasons, all network transformers include network protectors that trip when reverse power is sensed. The requirement for the unidirectional active power flow in the secondary networks imposes additional constraints that are not present in radial systems and vice versa.

This section is intended to elucidate what will happen if customers of meshed LV secondary networks are allowed to freely install DGs on their premises, and DGs become widespread. The analysis focuses on the situation where the maximum DG output coincides with light (minimum) load conditions. This case is recognized in the literature as the worst-case scenario [97, 98].

To simulate possible future scenarios, DG has been probabilistically allocated in increments of 10% of the light load. The study is carried out using a very detailed representation of the system components. Hundreds of time-domain simulations with the EMTP are performed to determine if a given allocation of DGs would produce voltage profile problems.

It was found that even with very small DG penetration, there may be unacceptably low or high voltages at certain loads when DG units are installed at the wrong location. However, very large amounts of DG power (up to 100% of light load) installed with the adequate strategy allow acceptable operating conditions. Under the present operating strategy of secondary networks, no power can be exported from the network to the system.

Intermittent DG technologies such as solar photovoltaic (PV) or wind conversion could also affect secondary voltage profiles due to flicker. Additionally, intermittent DG technologies frequently require optimal management strategies to maximize power delivery since the maximum power output may fluctuate [99].

12.4.3.2 Test System

The selected network for the study is one of the 34 networks that supply the Manhattan service area. It has 12 primary feeders, 1041 feeder cable sections, 1375 secondary cable sections, 27 substation

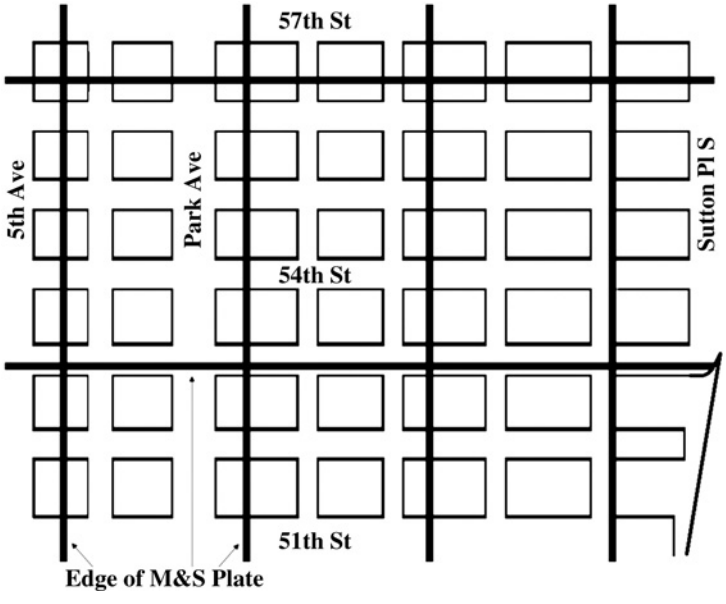

Figure 12.24 Street map of the location of the Sutton. The edges of M&S plates are included as reference (© 2012 IEEE) [7].

breakers, 224 transformers, 224 network protections, 1375 secondary grid sections and 311 aggregated loads. These loads correspond to 284 independent customers, 17 spot networks, mostly at 460 V, and one isolated spot network connected at 208 V. The overall geographical map is shown in Figure 12.24.

The Sutton network is limited by Fifth Avenue, Sutton Place South, 57th Street and 51st Street. For identification purposes, this network has been divided by Consolidated Edison into smaller rectangular areas called mains and services (M&S) plates. A simplified map showing locations of the network loads and transformers in the Sutton network is shown in Figure 12.25. In this figure the lines corresponding to the edges of the M&S plates of Figure 12.24 are used for reference. The typical structure of an isolated spot network is presented in Figure 12.26. The MV network is operated at 13.8 kV from the area substation through the primary feeder sections where the distribution transformers are connected to step down the voltage to 208 V for regular customers and 460 V for larger power consumption customers.

12.4.3.3 Allocation Methods

In this study, DG units will be referred to as deterministic or non-deterministic, depending on whether their location, type and size are known parameters or not. Deterministic DGs are those already installed in the distribution network. The non-deterministic DGs are probabilistically placed at the customer sites to perform analysis of different 'what if' (hypothetical) scenarios, that is, to study the influence of type, size and location of the distributed generators on voltage profile. In this analysis, each scenario corresponds to a different distribution of DGs.

The Gibbs sampler algorithm [100, 101] is used to generate three key parameters for allocation of the non-deterministic DGs: type, size and location. The Gibbs sampler algorithm is one of the Markov chain Monte Carlo methods; it is commonly used for the generation of random variables from a marginal distribution directly, without having to calculate the probability density via integration. An important

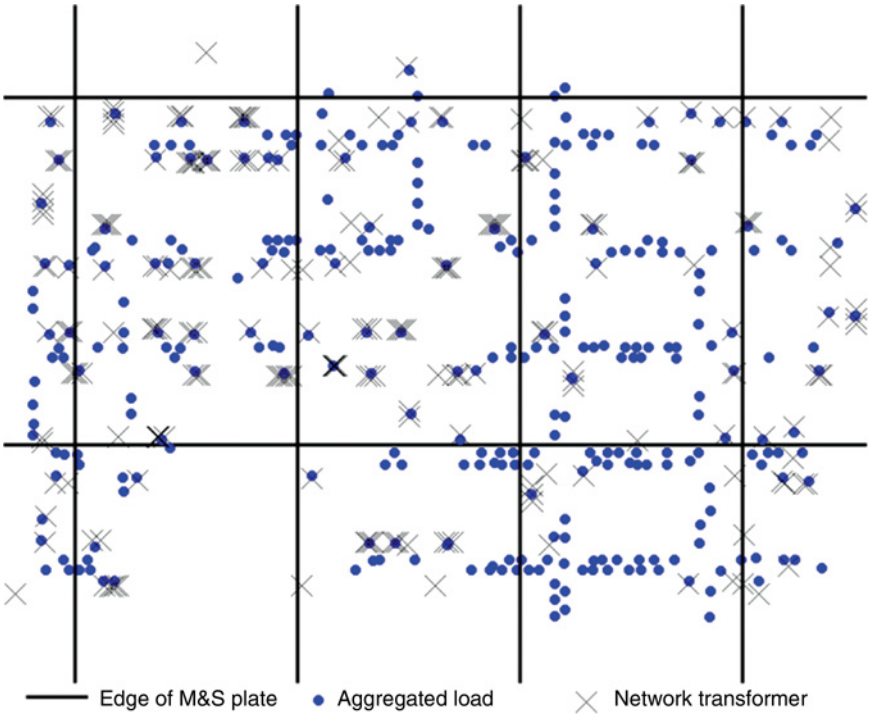

Figure 12.25 Location of loads and transformers in the Sutton network using as reference the edges of the M&S plates (© 2012 IEEE) [7].

advantage of the Gibbs sampler as a tool for the statistical study of DG penetration is that it allows for low-dimensional conditional distributions (avoiding the use of a complicated multivariate distribution). Also, more parameters for DGs can be added easily, for example, the cost of DG.

A brief description of the Gibbs sampler algorithm is given next (see [100] for more details). Suppose that a target distribution $\pi(x)$ corresponds to a joint distribution of several variables $\pi(x_1, x_2,\ldots x_k)$. This joint distribution is assumed to exist and be proper. Each of the x_i terms could represent a block of several random variables grouped together. Let $\pi(x_j)$ represent the marginal distribution of the jth block of variables, x_j and let $\pi(x_j|x_1,\ldots,x_{j-1}, x_{j+1},\ldots, x_k)$ represent the full conditional distribution of the jth block of variables. The Gibbs sampler utilizes a set of full conditional distributions associated with the

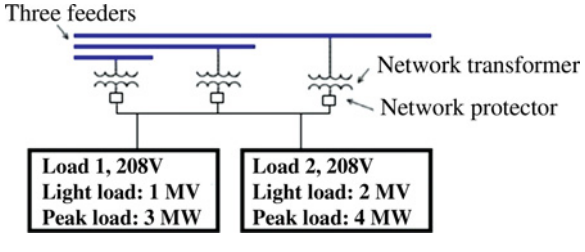

Figure 12.26 Typical configuration of an isolated spot network (© 2012 IEEE) [7].

target distribution of interest in order to define a Markov chain. Gibbs sampler can be implemented with the following iterative sampling scheme:

1. Select initial value $x^{(0)} = (x_1^{(0)}, x_2^{(0)}, \ldots, x_k^{(0)})$.
2. Set the counter index $i = 0$.
3. Simulate the sequence of random draws:

$$\begin{aligned} x_1^{(i+1)} &\sim \pi(x_1 | x_2^{(i)}, x_3^{(i)}, \ldots, x_k^{(i)}) \\ x_2^{(i+1)} &\sim \pi(x_2 | x_1^{(i+1)}, x_3^{(i)}, \ldots, x_k^{(i)}) \\ &\vdots \\ x_k^{(i+1)} &\sim \pi(x_k | x_1^{(i+1)}, x_2^{(i+1)}, \ldots, x_{k-1}^{(i+1)}) \end{aligned} \tag{12.3}$$

and form

$$x^{(i+1)} = (x_1^{(i+1)}, x_2^{(i+1)}, \ldots, x_k^{(i+1)}) \tag{12.4}$$

4. Set $i \leftarrow i + 1$ and return to Step 3 until i is sufficiently large such that each component $x_j^{(i)}$ is very nearly a random draw from the marginal distribution $\pi(x_j)$ – see [100] for details.

Notice that in Step 3, it is required to sample random draws once from each of the full conditional distributions and that the values of the conditioning variables are sequentially updated one by one. This sampling algorithm defines a valid Markov chain Monte Carlo method as described in [100].

The types of distributed generators considered for this study are inverter-based, induction and synchronous. According to local utility regulations, the selection of DG for a particular location has a direct relationship to the output power range of that generator. The output range of inverter-based, induction and synchronous generators are 0.3 kW to 2 MW, 40 kW to 2 MW and 225 kW to 2 MW, respectively.

The probability of choosing a particular DG type and its output power for installation at any customer location depend on the power demand at this location. It is more likely that customers will choose the size of the DGs in accordance with their power consumption. Thus, for a DG unit having a particular large rating, the probability of being installed at locations with large demand is higher. For allocation purposes only, the 311 loads in the network are classified into groups based on the power demand (Table 12.3). The simulations and analyses are based on explicit representation of each one of the 311 loads.

The selected conditional probability functions to allocate non-deterministic DGs were designed in accordance with the IEEE standard for interconnecting distributed resources with electric power systems [102], local utility requirements [103, 104] and physical conditions of the selected distribution network. This implies a basic assumption of this study: large customers are allowed to install larger DG units. On the other hand, larger-size DGs will have higher probability of being installed at customer locations with larger load than at customers with smaller loads.

Table 12.3 Load group classification per size (© 2013 IEEE) [7].

Group location	Power demand range
Very large load	>1 MW
Large load	200 kW–1 MW
Medium load	50–200 kW
Small load	10–50 kW
Very small load	0–10 kW

Table 12.4 Conditional probability functions for choosing a size of the synchronous DG given the size of the customer load (© 2013 IEEE) [7].

	Probability of choosing a size of DG		
Given size of customer load	1–2 MW	500 kW–1 MW	200–500 kW
Larger than 1 MW	3/6	2/6	1/6
200 kW to 1 MW	1/6	3/6	2/6
50–200 kW	1/6	2/6	3/6
10–50 kW	1/6	1/6	4/6
0–10 kW	1/8	1/8	6/8

Table 12.5 Conditional probability functions for choosing a customer in the load group given the size of the synchronous DG (© 2013 IEEE) [7].

	Probability of choosing a customer in the load group				
DG size	>1 MW	200 kW–1 MW	50–200 kW	10–50 kW	0–10 kW
1–2 MW	3/8	2/8	1/8	1/8	1/8
500 kW–1 MW	2/9	3/9	2/9	1/9	1/9
200–500 kW	1/9	2/9	3/9	2/9	1/9

Table 12.6 Individual probability functions of synchronous DG size (© 2013 IEEE) [7].

1–2 MW	500 kW–1 MW	200–500 kW
0.2312	0.3267	0.4421

Table 12.4 provides the specified conditional probability functions for choosing the size of a synchronous DG, given the customer location. For example, for a given customer in the group of 'Larger than 1 MW' the probability that a DG between 1 MW and 2 MW will be chosen is 3/6.

Table 12.5 corresponds to the specified conditional probability functions for choosing customer location given the size of a synchronous DG. For example, if the power of the selected DG is 1–2 MW, then the probability that a customer from the load group 'Larger than 1 MW' will be chosen is 3/8.

Individual probabilities of DG locations and sizes are obtained by applying the Gibbs sampling algorithm with the conditional probability functions described above. These probabilities are shown in Tables 12.6 and 12.7 respectively. For example, the individual probability of selecting a synchronous-type DG of size 1–2 MW is 0.231. It should be noted that Tables 12.6 and 12.7 are the examples for the synchronous type DGs; similar tables can be made for other types of DG.

The following constraints are considered for the allocation of DGs: (1) a DG can only be installed at customer locations, (2) only 'small' DG units are permitted in LV networks – this means that a DG unit

Table 12.7 Individual probability functions of synchronous DG location (© 2013 IEEE) [7].

>1 MW	200 kW–1 MW	50–200 kW	10–50 kW	0–50 kW
0.2084	0.2649	0.2489	0.1634	0.1144

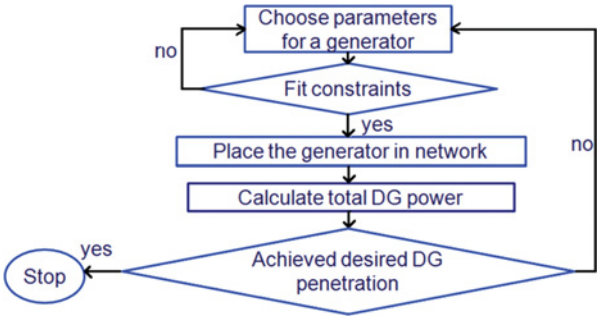

Figure 12.27 Allocation algorithm for non-deterministic DG units (© 2012 IEEE) [7].

cannot exceed 2 MW output power [103, 104], (3) only one type of the DG is allowed per location, (4) each location may have multiple DG units of the same type, (5) the DG units supplying 460 V loads cannot exceed their light load demand for that particular location, (6) the DG units supplying 208 V loads cannot exceed their maximum of the light load demand and 85% of the peak load demand for that particular location, (7) the total DG power in a spot network cannot exceed the total light load demand.

The above-mentioned constraints are based on regulatory requirements and physical limitations of the distribution networks in the metropolitan areas. Operation of these networks under completely deregulated power markets raises concerns of reliability, stability and power quality. Massive reinforcements of the existing urban networks to accommodate new generation units in the LV secondary grid are very time-consuming and require tremendous investments. At the same time, there is a persistently growing requirement to allow for the large-scale penetration of DG. As a result, an approach based on the 'connect and forget' principle becomes more attractive. According to this approach, newly connected DG units should not drive the network beyond its current operation and physical constraints. The constraints must ensure service continuity and reliability. For example, if constraint (6) is applied to the spot network in Figure 12.26 without constraint (7), then the total maximum DG power that can be allocated would be greater than the total light load demand. Therefore, the spot network would be disconnected by the network protectors when sensing backfeed power.

The procedure of allocating non-deterministic DG units is presented in Figure 12.27. The non-deterministic DG units are generated from the conditional and individual probability functions and can be placed at the particular location only when none of the allocation constraints is violated.

Figure 12.28 shows a few examples of the non-deterministic DG allocations obtained by applying the algorithm of Figure 12.27. Figures 12.28(a) and (b) correspond to two different cases of 20% DG penetration applying the same distribution. Similarly, Figures 12.28(c) and (d) correspond to two different cases of 60% DG penetration. The results of non-deterministic DG allocations are not unique, even when applying the same distributions for the same penetration level. Each of the cases corresponds to a different 'what if' scenario. The legend in Figure 12.28 shows the sizes of the distributed generators of all the types allocated at various locations in the network. It should be noted that they are not related to the size groups given in Tables 12.4 and 12.5 for the synchronous generators.

The importance of applying the proposed distributions (Tables 12.4–12.7) is to avoid installing large size DGs at small customer locations. As illustrated below, this can cause voltage profile problems even at low penetration levels.

12.4.3.4 DG Penetration Study

The study was performed with time-domain simulations using the EMTP for the following reasons: (1) commercial power flow programs do not have an adequate model for the network protectors, (2) they also lack the model of all the protective and switching devices needed, in particular under- and overvoltage

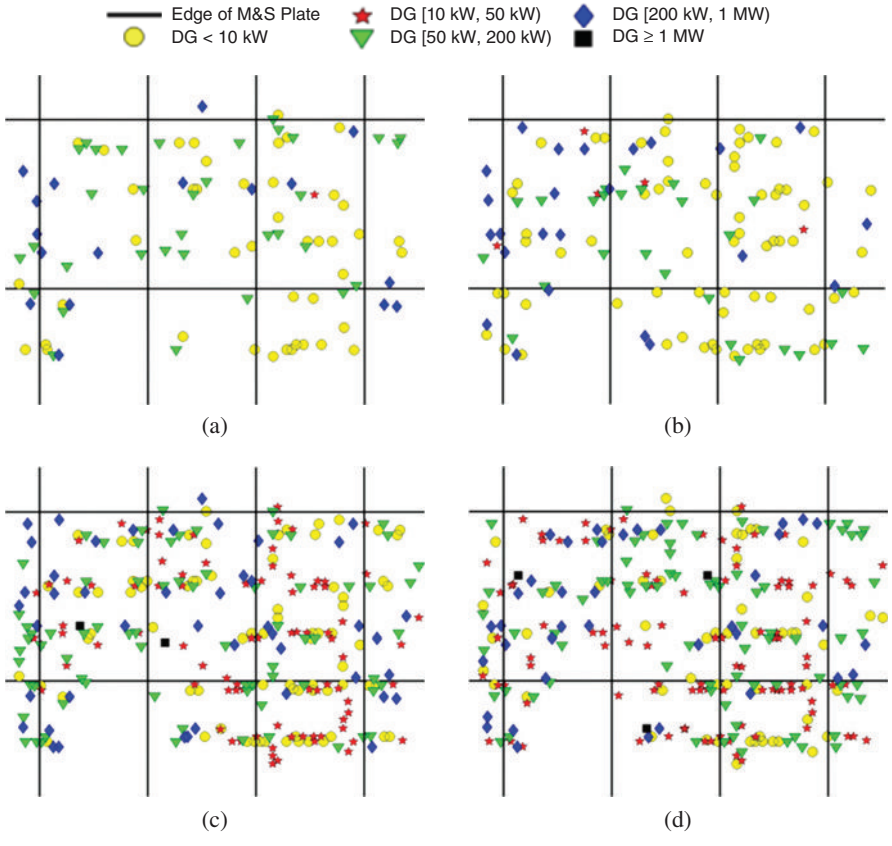

Figure 12.28 Examples of DG allocation for different DG penetrations: (a) case 1 at 20%, (b) case 2 at 20%, (c) case 1 at 60%, (d) case 2 at 60% (© 2012 IEEE) [7].

protection of DGs, (3) the models of DG are not as sophisticated as those in the EMTP, where all kinds of DG (synchronous, induction and inverter-based) can be represented in great detail.

A sufficiently long simulation time was used to reach steady state. For most cases, 800 ms was enough with an integration step of 80 μs (10 000 integration steps in total). However, some cases with high DG penetration, took longer to reach steady state. Each run takes about 40–90 mins using a computer with a processor Intel Core i7 CPU 975 operating at 3.33 GHz and installed RAM memory of 24 GB.

The most important information to be extracted from the experiments is the voltage profile at the loads and transformer primaries, together with the status of the protection devices. The present study does not provide any strategy for preventing voltage violations in the distribution network. The strategies for active network management are reported elsewhere [14].

Prior to the installation of DGs, a review of the light-load network voltage profile was performed, showing that the selected network is stable and suitable for the study. The obtained results confirmed that there are no network protectors open in the base case and that all p.u. voltages on the primary side of the transformers as well as at the load structures remained within 1% deviation from nominal operating voltage. The network transformers voltage profile for all primary feeders have been examined. For all feeders, the slope of lines, containing the voltage profiles at the primary side of the transformers along each feeder, is very close to zero, showing that the system has a very good voltage regulation under light load conditions.

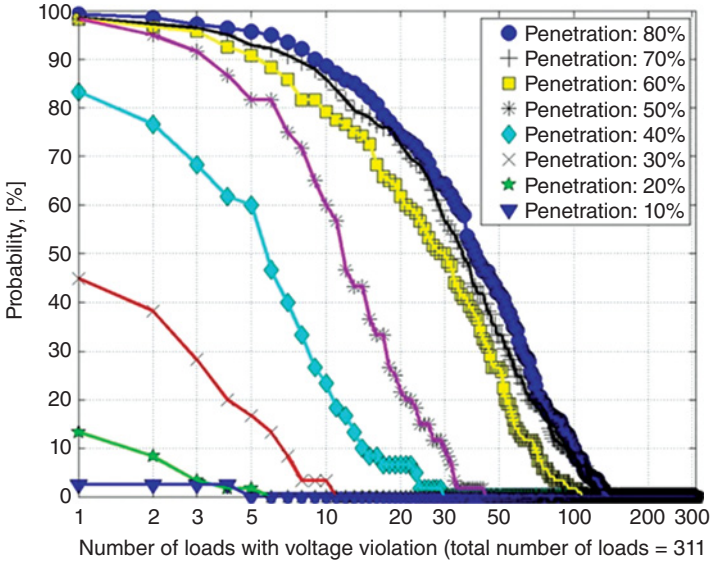

Figure 12.29 Probability of having voltage violations of over ± 5% vs number of loads with violation (© 2012 IEEE) [7].

We can see that, in all the simulations, the input voltage for the transformers is always within the acceptable range. Therefore, the voltage profile analysis presented here is based on the number of loads having voltage violations for different DG power penetration levels. A voltage violation is defined as a load having voltage deviation of larger than ± 5% from its rated voltage for normal operating conditions and ± 10% for emergency conditions as per standards [102, 105].

Figures 12.29 and 12.30 summarize the results of hundreds of simulations aimed at finding potential voltage profile problems. We plot the probability of having voltage violation versus the number of loads with problems for penetration levels of 10–80% of the light load. We can see that as DG penetration increases, the probability of having voltage violations also increases. For example, looking at Figure 12.29, the probability of having at least 10 loads with voltage violation is 90% for a penetration level of 80%. The probability of having at least 10 loads with voltage violations is about 25% if the DG penetration is reduced to 40%.

To determine the number of probabilistic simulations that need to be performed to draw definitive conclusions, we note that loads with voltage violations are independent random variables for each case. Therefore, the weak law of large numbers is applied, which implies that an average convergence to expected values can be reached given a sufficiently large number of experiments [106]. Thus, the number of necessary experiments is determined when the cumulative average number of loads with voltage violation converges as the number of experiments increases.

Figure 12.31 illustrates such convergence properties for the average number of loads having voltage violation versus number of cases at 60% DG penetration. We can see that performing more than 120 simulations, for this case, will not change the conclusions in average. The total number of cases required for the study at different penetration levels is given in Table 12.8. Note that for larger penetrations, not only is a larger number of experiments required, but there are some unstable cases where most of the DGs were disconnected by their overvoltage protection; those unstable cases are excluded from the statistical analysis and are discussed below.

Other important information that can be extracted from each power penetration scenario includes: (1) the average percentage of loads with voltage violations as given in Figure 12.32, (2) the average

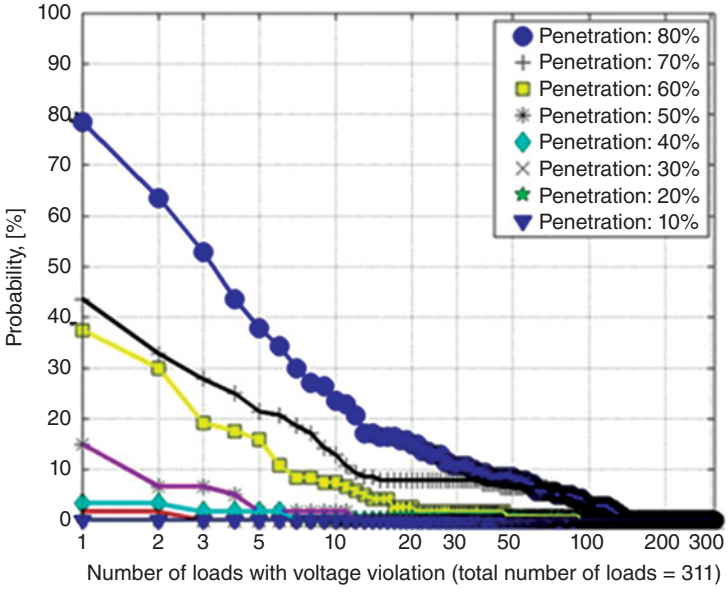

Figure 12.30 Probability of having voltage violations of over ± 10% vs number of loads with violation (© 2012 IEEE) [7].

percentage of open network protectors as shown in Figure 12.33. The obtained standard deviations are given in each plot. A small standard deviation indicates that the data points tend to be close to the average value; in contrast a large standard deviation indicates that data is spread over a wide range of values. One can see that standard deviations in Figure 12.32 increase with DG penetration, meaning that there are cases that have very few (or no) loads with voltage violations at higher DG penetrations. Therefore, it

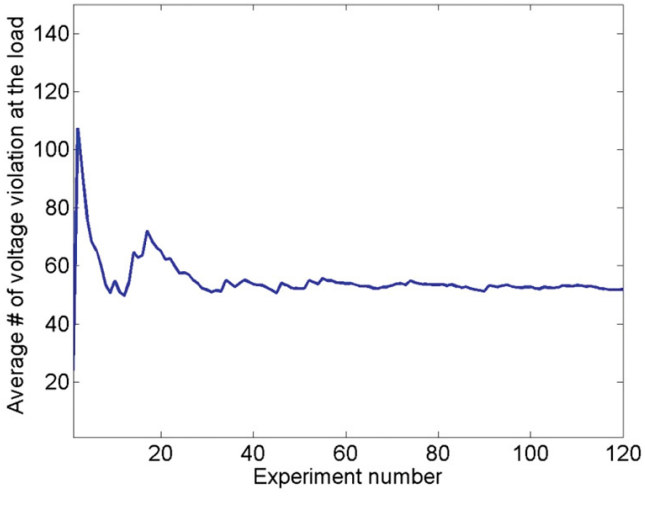

Figure 12.31 Cumulative average of number of loads with voltage violation (5%) as the number of experiments increases (© 2012 IEEE) [7].

Table 12.8 Required cases for different DG penetration levels (© 2013 IEEE) [7].

DG penetration (%)	Number of stable cases	Number of unstable cases
10	40	0
20	60	0
30	60	0
40	60	0
50	60	0
60	120	1
70	140	2
80	140	4

is important to understand how to allocate DGs so that large penetration levels can be achieved without unacceptable voltage profiles. Figure 12.33 shows that average percentage of open network protectors increases as the DG penetration increases.

It is important to compute the number of the open network protectors because owners of DGs would like to operate their units at unity power factor to maximize economic benefits (maximizing generation of active power). Consequently, reactive power needs to be supplied by the utility and a sufficiently large number of network protectors spread out over the network need to be closed for that purpose. As the network protectors trip, there are fewer paths for the reactive power to increasing the possibility of voltage violations.

In this study, DG allocation using uniform distributions was tested and it was found that the output power of the DG connected at some particular node is not related to the electrical load at this node. As a result, it is possible to allocate small DGs to large customers and large DGs to small customers. Therefore, the number of nodes with voltage violations and the amount of open network protectors are

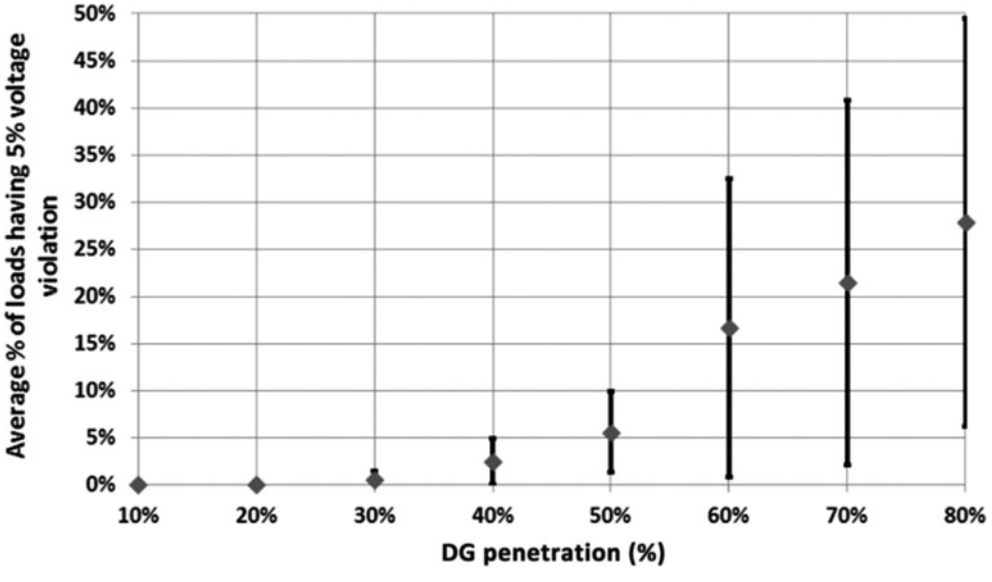

Figure 12.32 Average percentage of loads having voltage violations vs DG penetration level (© 2012 IEEE) [7].

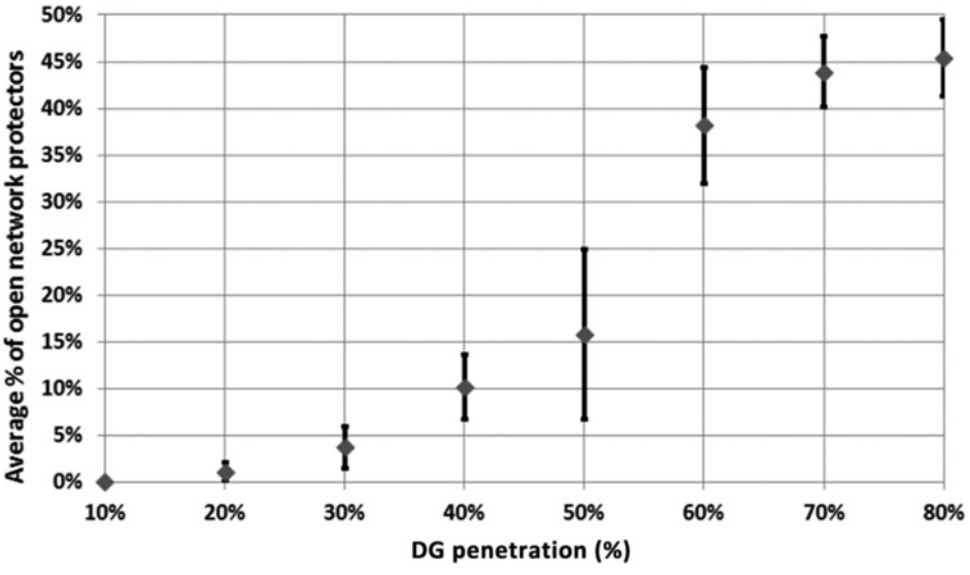

Figure 12.33 Average percentage of open network protectors vs DG penetration level (© 2012 IEEE) [7].

larger than when the load matching approach is used. Moreover, it was determined that the attainable average power of the DG penetration is smaller using uniform distribution functions.

12.4.3.5 An Example of an Unstable Case

During the process of finding the voltage profile we also found a few unstable cases where the automatic protections reconfigure the network. The typical dynamic process of an unstable case is as follows: (1) most of network protectors open on sensing reverse power, (2) many of DG protections open on overvoltage, (3) most of the open network protectors reclose after DGs trip, (4) the voltages at loads return to the acceptable range. The example shown in Table 12.9 initially had 80% DG penetration and after shedding of DG it came to a steady-state condition with only 38% DG penetration.

12.4.3.6 Effects of DG Size

To study the effects of the size of the installed DG on the voltage profile, a set of deterministic tests was performed. Results from these scenarios show that DG penetration could reach 100% of the load when

Table 12.9 Unstable case detail (© 2013 IEEE) [7].

Initial DG penetration (%)	80
Final DG penetration (%)	38
Violation over ±5% (%)	4
Violation over ±10% (%)	1
Max. voltage (p.u.)	1.16
Min. voltage (p.u.)	1.00
Open network protectors (%)	13
Reclosed network protectors (%)	56

Table 12.10 Load voltage violations for deterministic large penetrations (© 2013 IEEE) [7].

DG penetration (%)	Violations over ±5% (%)	Max. voltage (p.u.)	Min. voltage (p.u.)	Open network protectors (%)
90	0	1.048	1.038	0
95	0	1.050	1.040	0
100	1	1.052	1.040	4
101	3	1.052	1.041	21
102	49	1.095	1.047	85

having proper allocation. Conversely, other results show that a small percentage of DG power may cause voltage profile problems depending on the location.

Maximum DG power penetration (best case scenario): To illustrate how large penetrations are possible with no voltage violations, a number of deterministic DG tests were performed. A DG is installed at each customer with penetrations of 90–102% of their light load demand. Simulation results on voltage profile and the number of open network protectors are shown in Table 12.10. For instance, the 90% case means that each load has DG power in the amount of 90% of its light load power. We can see that there are no voltage violations with DG penetrations of up to 95% of the network light load. Note too that the network structure is not modified (no network protectors have opened). When the DG penetration exceeds 100%, the network structure is not reliable anymore (several network protectors open) and voltage violations start occurring.

Minimum DG power penetration (worst case scenario): With deterministic simulations installing DG at certain locations, we are able to produce unacceptably low or high voltages at certain loads. A case with only one DG of 1.2 MW installed at load BC2858 (original demand of 450 kW) serves to illustrate the problem as shown in Table 12.11. The table gives the details of the case, including information of DG and load. Note that there are two loads with voltage violations and four network protectors of the area have opened.

As shown in Table 12.11, the size of this DG is almost three times the light load of load BC2858. This causes the load to have an overvoltage violation. Moreover, a neighbouring load also exceeds the permissible 5% overvoltage.

12.5 Overvoltages in Distribution Networks

12.5.1 Introduction

The analysis of overvoltages in distribution networks is of high importance since they may damage the power system infrastructure and customer equipment. Overvoltages in distribution networks may

Table 12.11 Worst scenario details (© 2013 IEEE) [7].

DG penetration (%)	2.5
Number of voltage violations over ±5%	2
Max. voltage (p.u.)	1.07
Min. voltage (p.u.)	1.00
Number of open network protectors	4
Load voltage (p.u.)	1.07
Light load power (MW)	0.45
Peak load power (MW)	1.68
Size of DG (MW)	1.20

arise due to switching transients, resonance, lightning strikes and ground faults among other causes [13]. Many studies related to overvoltages in electrical distribution systems have been published to date. Some of them consider the overvoltage impact caused by distributed generation [91–93], others address overvoltage phenomena due to lightning, switching operations, harmonic resonances, power system restoration and ground faults [107–114]. And some research has been presented on long duration overvoltages and its effects on the system [115–117]. In [115], a wide range of transient overvoltages and their origins were reviewed. A discussion of temporary overvoltages caused by a ground fault in a large radial medium voltage network is presented in [116]. Finally, [117] provides the analysis and description of field test recordings for cable switching transients in 25 kV underground distribution systems.

The overvoltages discussed in this section arise because of the occurrence of a single-line-to-ground (SLG) fault on the (delta-connected) MV side of the test system. The test systems were designed following the conventional distribution network secondary grid described in [13]. Simulations were performed using the EMTP-RV [62] and considering detailed representation of system components as well as the nonlinear magnetization and losses of transformers.

12.5.2 Ferroresonant Overvoltages

12.5.2.1 Test System

This study will present an investigation of the ferroresonance phenomena occurring in an underground distribution network with secondary grid as a consequence of backfeeding currents. Urban distribution networks located in remote areas are frequently supplied through overhead feeders, although the secondary service may be configured underground. Figure 12.34 shows a schematic diagram of the test system. This case was inspired by the occurrence of ferroresonance due to network protector misoperation resulting in the damage of electrical equipment. There were no field recordings available for the actual event. The system under study is supplied from a substation having four transformers 132/35 kV, two capacitor banks, several bus breakers and feeder breakers. The feeder breakers trip on instantaneous overcurrent of 4000 A-peak in five cycles. Thousands of primary sections are interconnected and energize hundreds of 35/0.460 kV or 35/0.208 kV network transformers. Hundreds of secondary mains are used to feed non-uniformly distributed system loads.

The operation of network protectors prevents the continuous flow of reverse power [5, 9, 17]. There are three modes of operation for the network protectors: sensitive, time delayed and insensitive. In case of a fault, although all of the network protectors sense the fault at the same time, their operation is not simultaneous. Many of them open very quickly with opening times similar to those of the feeder breaker. However, some operate a few cycles later, others take several seconds to open and a few might even fail to operate. Therefore, depending on the settings of the network protectors, faults can last a significantly long time due to backfeeding of current from the LV network into the MV network.

Ferroresonance in distribution systems may cause severe temporary overvoltages. The analysis of this phenomenon in distribution networks with secondary grid is of extreme importance, especially in the case of network protector malfunction. Owing to the typically high capacitances of underground cable system configurations, backfeeding currents might cause large overvoltages [13].

12.5.2.2 Mechanism of Ferroresonance

This case study assumes the common scenario of an SLG fault on an MV feeder, when at least one of the corresponding secondary protection devices of the faulted line fails to trip (Figure 12.34). These network protectors are installed on the secondary side of each network transformer to automatically disconnect when power flows from the secondary grid to the MV side for a predetermined number of cycles (six cycles for this study).

The substation is composed of step-down delta-connected transformers grounded through reactors. During normal operating conditions, breakers remain closed and there is unidirectional power flow from the substation (MV) into the secondary network (LV). On the occurrence of a fault on a feeder, the

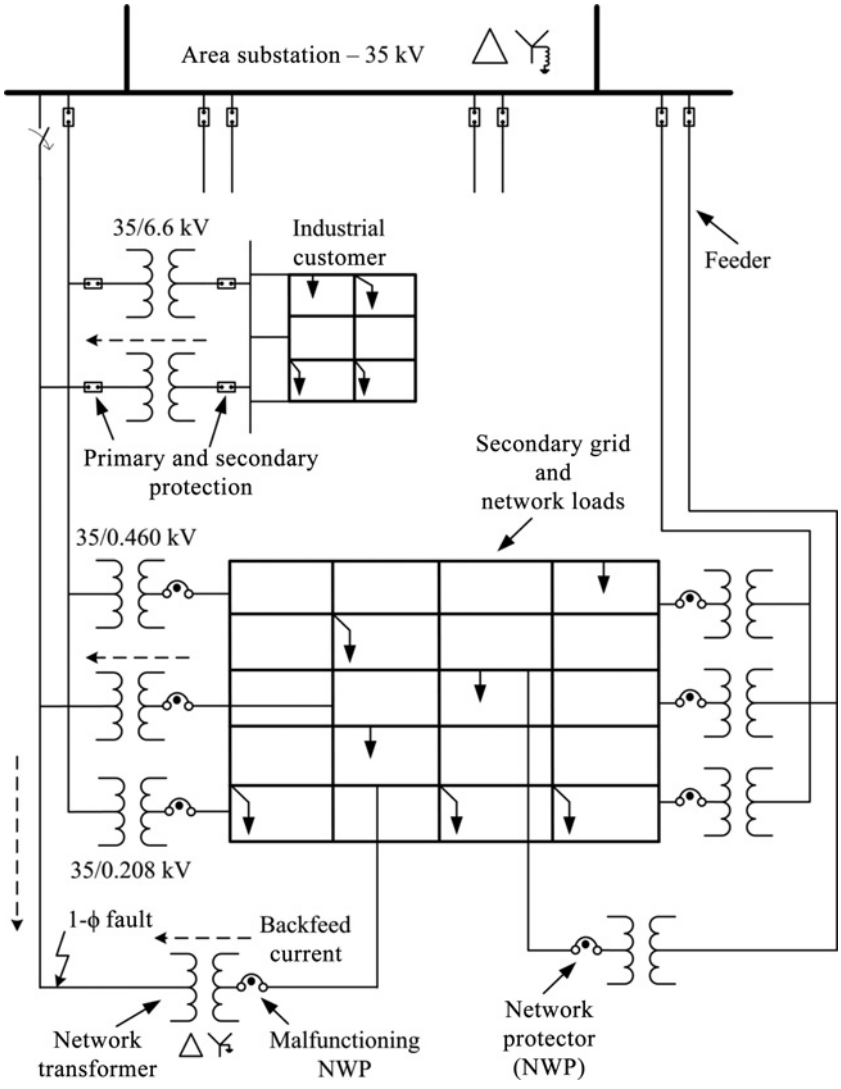

Figure 12.34 Test system for the study of ferroresonance in distribution systems.

circuit breaker is designed to open and isolate the ground fault from the substation. However, the line can remain energized due to the backfeeding current flowing through each of the transformers and network protectors associated with the faulted feeder.

Ideally, each network protector related to the faulted feeder should rapidly disconnect to ensure the successful and fast isolation of the fault. However, it is possible that not all the network protectors operate and the line remains live. Thus, the MV connection of transformers with open secondary side remains energized resulting in the equivalent circuit shown in Figure 12.35. L_m represents the transformer nonlinear magnetizing inductance, L_L is the leakage inductance, L_y is the yoke nonlinear inductance, R_c is the transformer core losses, C_p and C_m are the phase and mutual cable capacitances and V_b and V_c are the resulting overvoltages at healthy phases. Ferroresonance occurs because of the highly nonlinear characteristic of the transformer magnetizing inductance, low core losses and high cable capacitances.

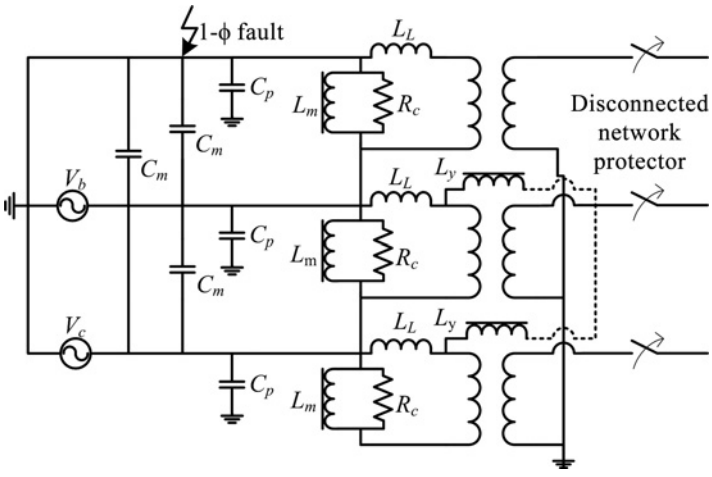

Figure 12.35 Transformer equivalent circuit during single phase fault with open secondary winding.

12.5.2.3 Simulation Results and Discussion

Simulation results of this study show severe ferroresonant overvoltages occurring in an underground distribution network during an SLG fault. The case assumes that the system is operating in steady-state conditions for approximately three cycles of the fundamental frequency (60 Hz) at minimum network load. Thereafter, the short-circuit occurs in phase A on the primary side of a 500 kVA 35/0.208 kV transformer. The network protector corresponding to this transformer remains closed throughout the simulation to represent a malfunctioning unit. The total capacitance of the faulted feeder branches delivers a charging power of 1800 kVAr. An industrial load and a total of 16 distribution transformers connected to the grid are energized by this feeder.

To prevent extreme damages in the interconnection of secondary mains due to operational failure of network protectors, utilities commonly use fuses and cable limiters in the secondary grid. These components are mainly designed to blow on large current magnitudes lasting for several seconds. This time delay is long enough to upset microprocessor-controlled equipment and switching devices in the system with large magnitudes in overvoltages. Fuses and limiters are not modelled because they do not operate within simulation time.

The instantaneous voltage waveforms computed at the fault location are given in Figure 12.36. During prefault conditions, the system is observed at a voltage of 1.0 p.u. The SLG fault occurs at 50 ms, causing the main circuit breaker to open at approximately 146 ms; the feeder remains energized as a result of the reverse power flow. The voltage rises to 1.85 p.u. and exceeds line-to-line level because of the light loading in the secondary grid which continues to be electrically connected to the faulted feeder. This overvoltage is a consequence of Ferranti effect [13]. The network protectors along the line progressively disconnect reducing the feeder loading and increasing the voltage to nearly 2.0 p.u. This overvoltage continues for roughly 47 cycles of the simulation time. In an actual network, the duration of this overvoltage would impose great stresses to electrical equipment. At about 940 ms the industrial customer disconnects, and the majority of the feeder load is dropped, decreasing the line impedance. At this stage, the voltage suffers a sudden increase, reaching 4.0 p.u. on phase B, and then the system drifts into a ferroresonant state. A closer view of the voltage distortion in the network is given in Figure 12.37, where peak values are observed to swing between 3.2 p.u. and 2.3 p.u. on healthy phases. These sustained ferroresonant oscillations are catastrophic to a power system because it deteriorates power quality, imposes heavy stresses on insulation and possibly causes breakdowns and might lead to dielectric or thermal failure of transformers.

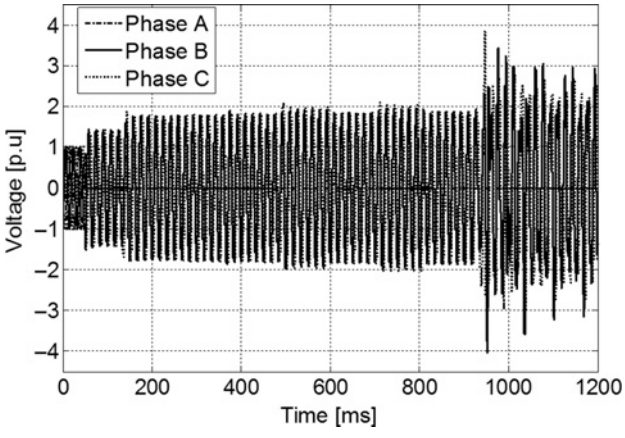

Figure 12.36 Instantaneous voltage on the MV winding of the backfeeding transformer.

In summary, for a system with networked secondary, where backfeeding is possible, the occurrence of ferroresonance may be catastrophic with overvoltages reaching 4.0 p.u. Although the occurrence of ferroresonance is not frequent in the power system, protection schemes should be properly designed and regularly tested to prevent equipment malfunctions.

12.5.3 Long-Duration Overvoltages due to Backfeeding

This study was carried out by dynamically simulating SLG faults with the EMTP on a selected primary section located towards the end of a feeder – see Figure 12.38. The network is studied under different loading conditions to establish a relationship between the overvoltage magnitude, its duration and the network loading.

The analysis of long-lasting overvoltages in networked distribution systems is of high importance, since large voltages sustained for long periods of time would cause degradation in the integrity of the system [90].

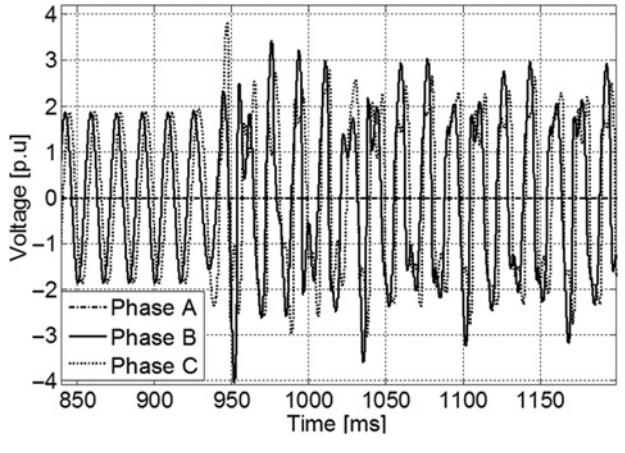

Figure 12.37 Closer view into the ferroresonant oscillations at the backfeeding transformer.

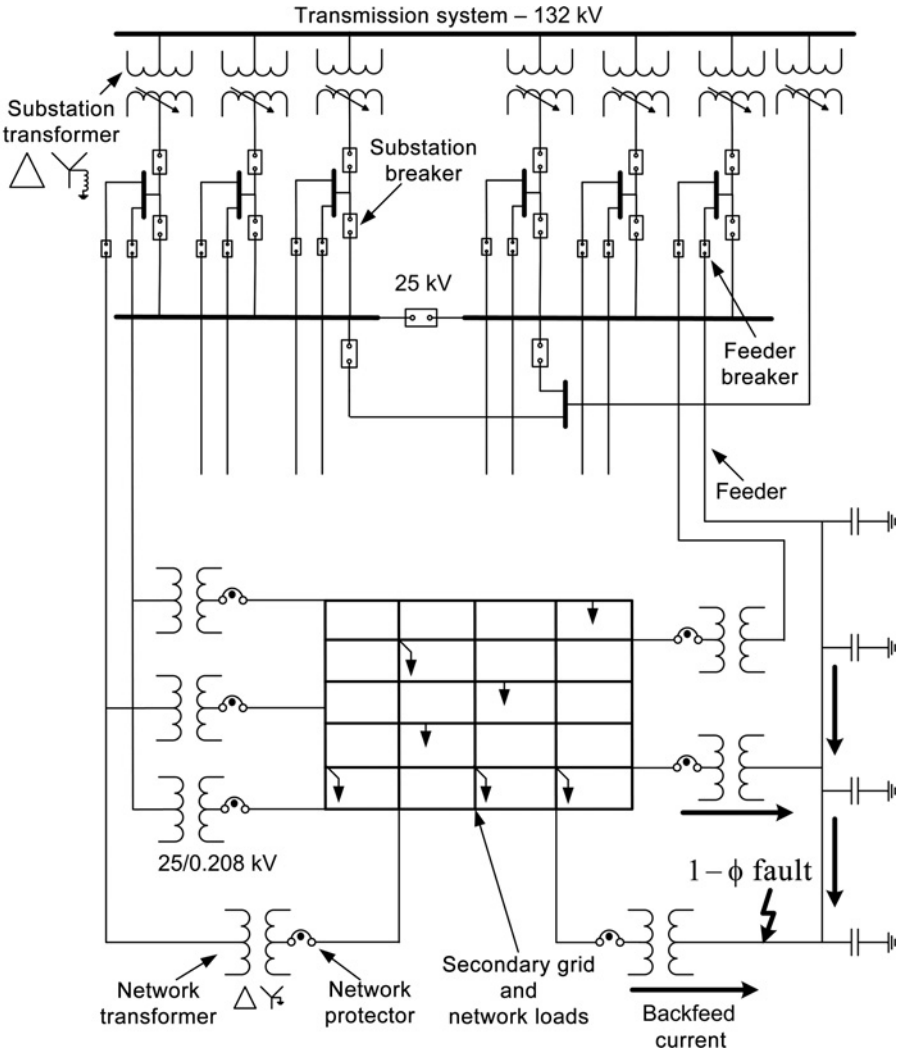

Figure 12.38 Test system for the study of long-duration overvoltages in distribution systems (© 2013 IEEE) [90].

12.5.3.1 Theoretical Considerations

The long-duration transient overvoltages studied in this section are caused by the occurrence of three different phenomena: First, a neutral is displaced as a result of the SLG fault on an MV feeder that is left floating; second, the far-end feeder voltage increases due to the capacitive charging of this feeder during the fault (due to Ferranti effect); and finally, the fault current is chopped by the opening of the last network protector. The individual contributions of each of these phenomena to the compounded long-duration overvoltages are analysed below.

The duration and magnitude of the overvoltages are not very dependent on the size of the network or the number of nodes. Overvoltages exist for as long as there is a meshed secondary network where backfeeding can occur during a fault.

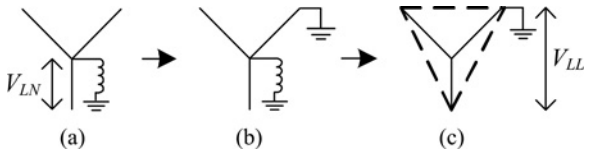

Figure 12.39 Change from wye-grounded to delta due to a single-line-to-ground fault and breaker trip: (a) prefault, (b) fault before breaker opens, (c) fault after breaker opens (© 2013 IEEE) [90].

The network under investigation is supplied from an area substation that has seven transformers 132/25 kV, two capacitor banks, 15 bus breakers and 12 feeder breakers (Figure 12.38). The feeder breakers trip on instantaneous overcurrent of 4000 A-peak, which added to the mechanical time delay results in about five cycles of fundamental frequency in agreement with [118]. There are thousands of primary sections interconnected. These sections energize hundreds of network transformers of voltage 25/0.460 kV or 25/0.208 kV. Nearly 18 000 secondary mains sections are used to feed several thousands of non-uniformly distributed loads.

Neutral displacement during single-line-to-ground faults: overvoltages reaching 1.73 p.u.: As shown in Figure 12.38, the substation is composed of step-down transformers connected delta-wye, grounded by means of reactors. During normal operation, their breakers are closed, and a reference to ground is present on the primary feeder sections as indicated in Figure 12.39(a). When the single-line-to-ground fault occurs, and the circuit breaker of the faulted feeder is still closed, the neutral shifts only a little because the substation transformers are grounded – Figure 12.39(b). However, when this breaker trips to clear the fault, the corresponding feeder becomes isolated from ground (except at the faulted point). Note that the faulted feeder is left floating since the primary of the network transformers are connected in delta. Therefore, the neutral is shifted to the centre of a triangle having the reference on one corner. As a consequence, the line-to-ground voltage of the healthy phases becomes the line-to-line voltage of the system or 1.73 p.u. – Figure 12.39(c).

Mechanism of backfeeding: According to the network architecture design shown in Figure 12.38, when a feeder breaker opens to clear a fault, or due to scheduled operations, the network protectors along the corresponding feeder should also trip to de-energize the feeder. A sequence of electrical transients is initiated at different parts of the network. For the present study, it was assumed that an SLG fault occurs at some point along one of the MV feeders, which is a very common occurrence. Subsequently, the breaker attached to the faulted feeder trips, stopping the fault current contribution from the area substation. After the feeder is isolated from the substation, the fault is solely sustained by reverse current (backfeeding) flowing from the secondary network to the faulted cable section through the network transformers. Because the primaries of the network transformers are connected in delta, the faulted feeder is left floating, and the circulation of backfeeding current is through the capacitance to ground of the MV cables.

Ideally, the backfeeding through each transformer and associated network protector rapidly satisfies operational requirements for network protector tripping. This results in fast isolation of the faulted feeder, which prevents cable sections, joints, fuses and other equipment from being damaged. Furthermore, it allows maintenance crews to fix and re-energize the feeder quickly. As a minimum magnitude of reverse (active) power is needed for the network protectors to trip, feeder length, fault location and power rating of transformers play important roles in determining when these devices open. Upon isolation of the faulted feeder, its corresponding loading redistributes among the remaining energized feeders. For operational reasons, such as to prevent cycling of network protectors, some of them are 'de-sensitized' producing much longer opening times.

Ferranti effect: overvoltages exceeding 1.73 p.u. due to backfeeding current into cable capacitances: In contrast to overhead lines, underground cables have a large capacitance to ground. During backfeeding conditions (current flowing from secondary to primary), these cables behave as capacitive loads.

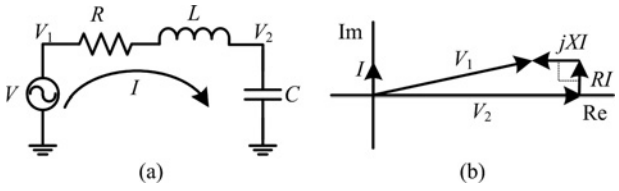

Figure 12.40 Analysis circuit: (a) simplification of the network, (b) phasor diagram.

When an SLG fault occurs in systems similar to Figure 12.38, voltages will increase beyond the line-to-line level due to the Ferranti effect. These overvoltages might reach or even exceed 2 p.u., depending on the capacitive charging power of the feeder and the system loading [119]. These conditions will persist until the last network protector along the faulted feeder trips. For the purpose of analysis, consider the network shown in Figure 12.40(a), where the voltage source, R and L represent the equivalent of the faulted feeder, as seen from the secondary grid, and C represents the cable capacitance. By means of the phasor diagram of Figure 12.40(b) one can see that $|V_2| > |V_1|$ because of the current flowing into the capacitor.

Voltage spike caused by current chopping: As previously discussed, during a single-phase fault in a system such as Figure 12.38, there will be a neutral shift which causes line voltage to be observed on the primary side of the network transformers. Furthermore, as a result of the backfeeding current into the primary cable capacitances, the Ferranti effect might be present in the network depending on how heavily the network is loaded, raising the phase voltages to even higher values. At the instant that the last connected network protector trips, the remaining part of the circuit experiences a large voltage spike, which is produced as a result of the LV circuit breaker interrupting the backfeeding current near its zero crossing. A chopping current level of 0.5 A is assumed for the presented cases [120]. The magnitude of the spike may exceed twice the rated system voltage [120]. This is an outcome of the under-damped behaviour exhibited by the circuit. Its simplified circuit diagram, given in Figure 12.41, corresponds to the equivalent state of the faulted feeder before the opening of the last network protector, represented by the ideal switch in the figure.

12.5.3.2 Simulation Results

Some simulations have been performed to illustrate severe long-duration overvoltages occurring in a typical underground distribution network during SLG faults. These simulations consider three cases of network loading: (1) peak load, (2) light load, (3) no load. In every case, a short-circuit has been applied in phase A on the primary side of a 1000 kVA 25/0.208 kV network transformer which is located at the end of one of the feeders, as shown in Figure 12.38.

It is assumed that the network operates initially in steady-state conditions and the fault occurs after approximately three cycles of the fundamental frequency (60 Hz) from the beginning of every simulation.

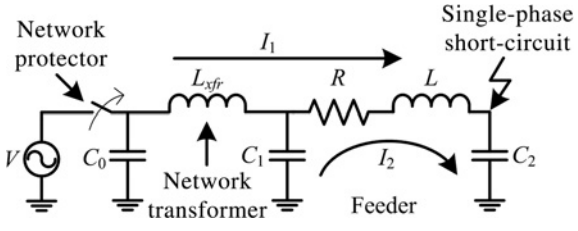

Figure 12.41 Simplification of the network to illustrate current chopping.

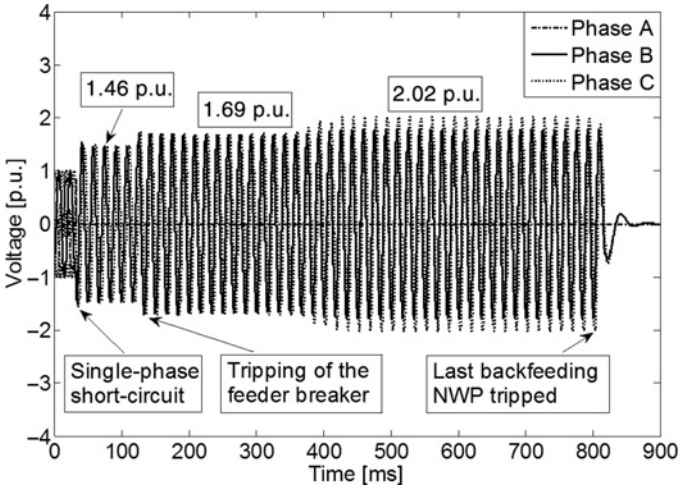

Figure 12.42 Instantaneous voltage at the faulted transformer for peak load case (© 2013 IEEE) [90].

The total length of all branches of the selected feeder is slightly larger than 7.6 km. These branches demand a total charging power of 1624 kVAr. The faulted area has 10 nearby network transformers connected to the grid.

Network at peak load: The voltage waveform computed at the fault location for the peak load conditions is presented in Figure 12.42. When the fault occurs (at 50 ms) the reference to ground is still present in the primary network and the voltages of the unfaulted phases do not exceed 1.46 p.u. After the breaker trips at 136 ms, the feeder remains energized only by reverse power flow and the voltages rise to 1.69 p.u. At this point, the overvoltages do not reach a theoretical value of $\sqrt{3}$ p.u. because of the large loading of the secondary grid which still remains electrically connected to the faulted feeder. As a consequence of the gradual operation of the network protectors, the overvoltage increases. Indeed, the voltages in phases B and phase C reach 1.78 p.u. and 2.02 p.u., respectively. The significant difference in the values of these voltages is due to the high *R/X* ratio of the distribution network as explained above. The total time of the overvoltage extends to approximately 42 cycles. Note that when a large portion of the network protectors disconnect, the feeder loading decreases enough for the Ferranti effect to occur and raise the voltages above the line-to-line level.

Network at light load: The instantaneous voltage waveforms at the fault location for the lightly loaded network are given in Figure 12.43. Analysing these waveforms, we see that for the light network loading the overvoltages are of larger magnitude than those reported for the peak loading. The results illustrate that the voltages of the healthy phases at the fault location reach 1.54 p.u. and remain at this value for five cycles until right before the short-circuit is disconnected from the substation at 136 ms. After the breaker and several network protectors open, the voltage magnitudes rise to 2.48 p.u. due to the Ferranti effect. The Ferranti effect persists for approximately 30 cycles, until the last network protector trips and isolates the feeder at approximately 615 ms. Note that the Ferranti effect is noticeable in this case, right from the tripping of the breaker, because the network loading is relatively small. Furthermore, when the last LV protective device opens, chopping the backfeeding current, the transient voltage rises to 2.76 p.u. as a result of the under-damped network behaviour, which may potentially do damage to electrical equipment.

Network at no load: Simulation results with no load provide an insight into what would be the worst-case scenario regarding magnitudes of transient overvoltages caused by an SLG fault. In the absence of loads in the LV grid, all the current in the nearby secondary area will backfeed to the fault through the

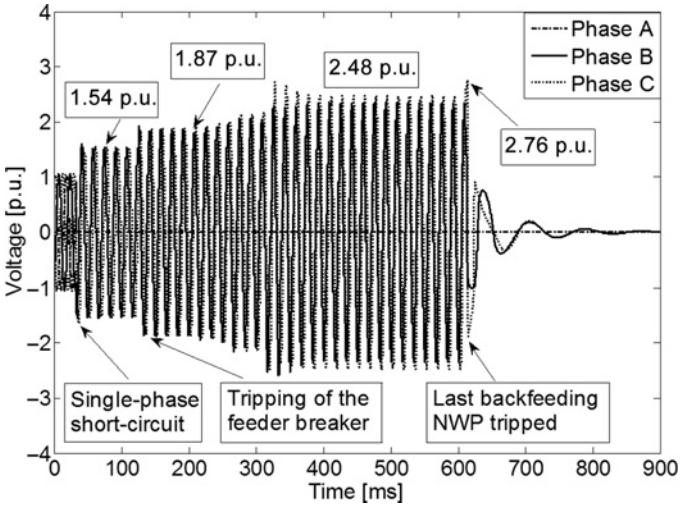

Figure 12.43 Instantaneous voltage at the faulted transformer for light load case (© 2013 IEEE) [90].

network transformers, causing their network protectors to trip at a faster rate than when there is load connected to the network. In the no-load case, the feeder breaker trips at approximately five cycles after the fault occurrence. Figure 12.44 shows voltage waveforms at the fault location. In this figure, voltages of the healthy phases are equal to 1.57 p.u. during the initial phase of the fault. After the breaker opening at 136 ms, there is a voltage rise to 1.98 p.u. The voltages in the healthy phases continue to increase further up to 2.81 p.u. as several network protectors open. Here, voltage rises resulting from the Ferranti effect last for approximately 15 cycles after the breaker opens. After the disconnection of the last network protector, the chopping of the backfeeding current causes a significant transient overvoltage of 3.17 p.u.,

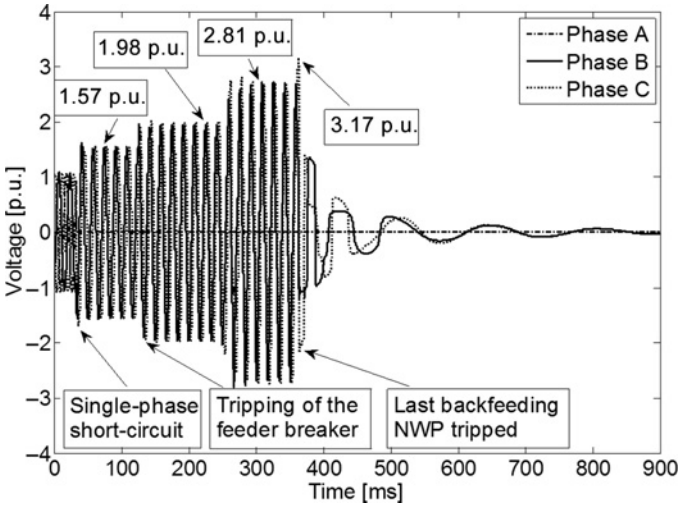

Figure 12.44 Instantaneous voltage at the faulted transformer for no load case (© 2013 IEEE) [90].

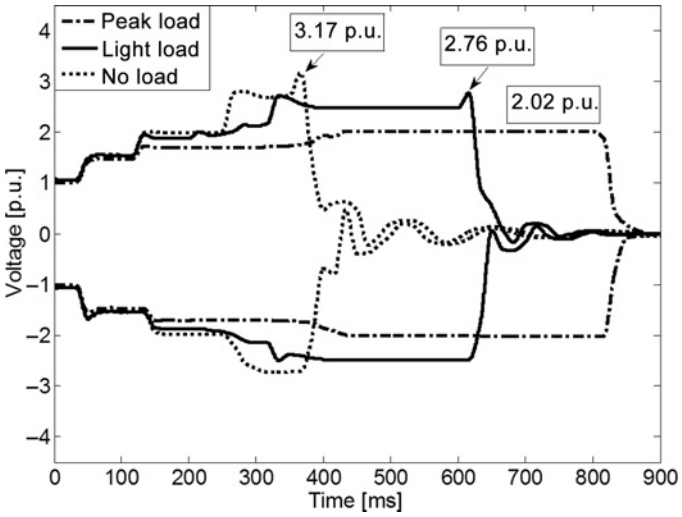

Figure 12.45 Comparison of envelopes for each resulting voltage waveform measured at fault location (© 2013 IEEE) [90].

which appears at the fault location as shown in Figure 12.44. The magnitude of this voltage spike is the largest of the presented simulation cases.

Comparison of simulation results: To facilitate the comparison between simulated cases, the envelopes for the resulting voltage waveforms at the fault location are provided in Figure 12.45. The outcomes of the simulations reveal that the worst-case scenario occurs during no-load conditions with 3.17 p.u. of transient overvoltage at the instant of disconnection of the last network protector. Furthermore, it was observed that, for all cases, after the breaker of the faulted feeder opens, overvoltages exceed the theoretical neutral displacement value of $\sqrt{3}$, owing to the Ferranti effect.

The duration of the overvoltages depends on the system load. There is a direct impact of the network loading on the overvoltage severity. For the unloaded case, network protectors trip relatively fast as the backfeeding conditions are immediately satisfied. As a result, the time interval required for the network to withstand the overvoltages is reduced. However, for loaded cases the network consumption must be supplied, even if there is a fault present on a feeder. This results in smaller backfeeding currents, leading to extended overvoltages.

Table 12.12 summarizes the network voltages for each simulated case during different transient periods. Even though the unloaded case manifests the worst-case scenario, it is unlikely for networks to be unloaded in urban areas (probably during restoration only). Therefore, the more realistic light load conditions are selected to demonstrate two techniques of overvoltage mitigation.

Table 12.12 Comparison of overvoltages due to single-line-to-ground faults (© 2013 IEEE) [90].

Case/period	Fault (p.u.)	Breaker open (p.u.)	Spike (p.u.)
Peak load	1.46	2.02	—
Light load	1.54	2.48	2.76
No load	1.57	2.81	3.17

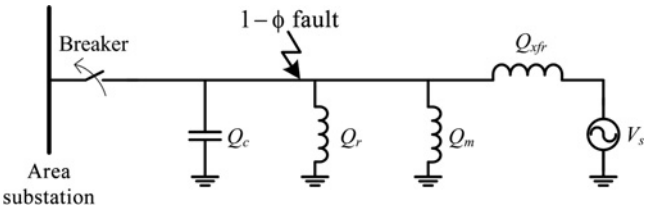

Figure 12.46 Simplification of the network to illustrate overvoltage mitigation using a shunt reactor.

12.5.3.3 Mitigation of Overvoltages

Two methods of overvoltage mitigation are studied. The first method is based on reactive power compensation by means of shunt reactors. The second exploits grounding transformers to provide a reference to the system after circuit breaker tripping in the substation. These solutions are aimed at mitigating the Ferranti effect and to limiting or eliminating completely the spike produced by the under-damped behaviour of the remaining circuit after disconnection of the last network protector. The simulation results demonstrate the following effects: (1) full compensation of the faulted feeder charging power by means of a shunt reactor rated 1624 kVAr connected at the end of the line, near the fault location, and (2) insertion of a grounding transformer (connected in zigzag) with equivalent zero-sequence impedance of 15 Ω selected in accordance with [121].

Single-phase fault mitigated with shunt reactor: One of the most common devices for reducing overvoltages is a shunt reactor. In urban areas where underground cables are installed, it is used for compensating the charging power of long distribution feeders, especially during backfeeding conditions. In underground cable systems there is substantial capacitance to ground, similar to that of a long overhead line. The cables operate below their surge impedance loading and therefore shunt reactors help to maintain a desirable voltage profile. As previously discussed, during an SLG fault the network phase voltage may reach or even exceed the line-to-line value due to displacement of the neutral reference and the Ferranti effect. For the cases presented above, the aim of the shunt reactor is to reduce overvoltages after the substation grounding point is disconnected from the faulted feeder.

To determine the size of the reactor, a theoretical analysis is performed considering the equivalent state of the faulted feeder before the tripping of the last network protector (Figure 12.46). The series impedance of the feeder is significantly smaller than the leakage impedances of the backfeeding network transformers. Therefore, the line impedance can be neglected for this analysis (but it is included in the simulations). At this stage, it can be seen that the location of the shunt reactor along the faulted feeder is irrelevant, provided that a ground reference is established. This is because there is no significant change in voltage between the branches of the MV line. Q_c represents the total charging vars of the feeder, Q_m corresponds to the excitation vars of the disconnected transformers and Q_r is the reactive power of the shunt reactor. Q_m is obtained using individual nonlinear magnetizing curves of the network transformers for 10% voltage rise on the grid side, which is the emergency operating condition as per standards [102, 105]. The value of Q_r has been selected in such a way that, together with Q_m, it compensates for 100% of Q_c in all sequences (positive, negative and zero) during an SLG fault.

The instantaneous voltage waveforms at the fault location are given in Figure 12.47. This result shows that the overvoltages are mitigated during an SLG fault using a shunt reactor that fully compensates capacitive charging power. The voltages before isolation of the substation at 136 ms are 1.54 p.u. After the breaker trips, the voltages rise to 1.77 p.u. due to the Ferranti effect, produced by the current backfeeding. This indicates a significant improvement (28.6% reduction) compared to the case without shunt reactors, where the voltages reached 2.48 p.u. It should be noted that the transient overvoltage spike after the disconnection of the last network protector is not observed when the shunt reactors are connected.

Single-phase fault mitigated with a grounding zigzag transformer: Another commonly used alternative for reducing overvoltages is providing a neutral reference after the substation grounding point is

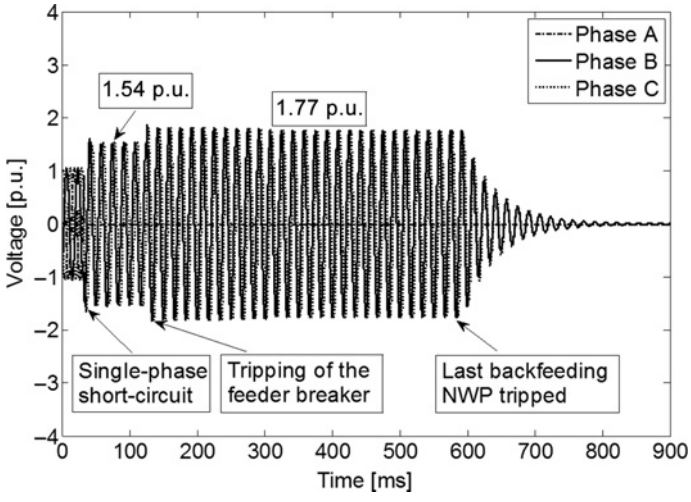

Figure 12.47 Instantaneous voltage at the fault location mitigated using a shunt reactor (© 2013 IEEE) [90].

disconnected from the faulted feeder. For this purpose, a grounding transformer connected in zigzag is used. As opposed to the shunt reactor, the grounding transformer does not affect normal system operation, since it has very high positive and negative-sequence impedances. At the same time, its zero-sequence impedance is low. Thus, the grounding transformer provides a low impedance path to ground only during unbalanced conditions of the network.

The behaviour of voltage at the fault location with a grounding transformer installed in the network is shown in Figure 12.48. It can be seen that the voltages before disconnection of the substation at 136 ms

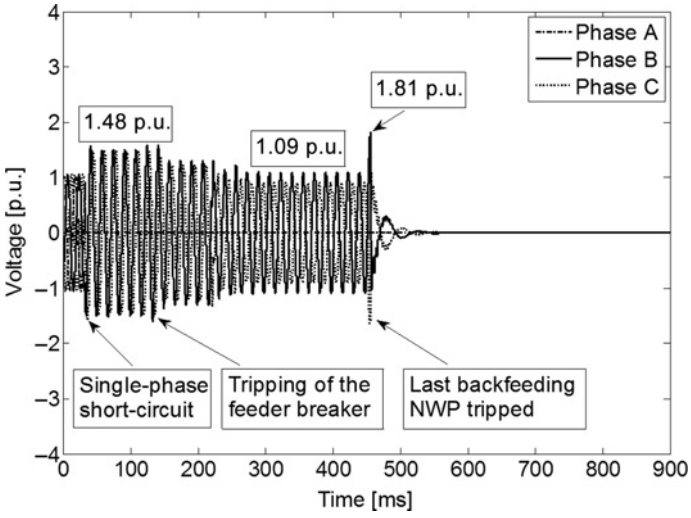

Figure 12.48 Instantaneous voltage at the fault location mitigated using a grounding transformer with zigzag connection (© 2013 IEEE) [90].

Table 12.13 Comparison of overvoltages due to single-line-to-ground faults under different mitigation schemes (© 2013 IEEE) [90].

Case/period	Fault (p.u.)	Breaker open (p.u.)	Spike (p.u.)	Total time (ms)
Base case	1.54	2.48	2.76	615
Shunt reactor	1.54	1.77	1.77	600
Grounding transformer	1.48	1.09	1.81	475

are 1.48 p.u. After the feeder breaker trips and several of the energized transformers are gradually disconnected by their network protectors, voltages in phases B and C reduce to 1.09 p.u. and 0.91 p.u., respectively. Note that without installing the grounding transformer, these voltages would have been significantly higher (1.54 p.u. before the feeder breaker tripping and 2.48 p.u. after).

This greatly reduces the displacement of the neutral and limits the overvoltage to only about 10% of nominal voltage. The simulation results also show that the grounding transformer significantly reduces the transient overvoltage after the opening of the last network protector. Indeed, the magnitude of the voltage spike was 2.76 p.u. without the grounding transformer. However, when such a transformer has been connected, the voltage spike reaches only 1.81 p.u., a reduction of 34.4%.

According to the findings presented above, it is concluded that grounding transformers provide an effective method for overvoltage reduction during SLG faults. Indeed, in comparison with the case without the grounding transformer, its installation has reduced steady-state overvoltages during the fault by 56.1% and transient overvoltages by 34.4%.

Comparison of results for mitigation schemes: It has been determined that grounding transformers have advantages over shunt reactors in mitigation of the overvoltages caused by SLG faults. These transformers successfully eliminate voltage rise due to neutral displacement and the Ferranti effect as well as shortening the duration of overvoltages after isolation of the substation grounding. Furthermore, they greatly reduce the voltage spikes after disconnection of the last network protector on the faulted feeder.

In the case of shunt reactor installation, the Ferranti effect is significantly reduced. The voltages do not rise above 2.0 p.u., though they still exceed 1.73 p.u. This mitigation technique also eliminates the transient overvoltages.

When the grounding transformer is used, the possibility of overvoltages exceeding 1.73 p.u. is greatly reduced since an alternative grounding reference to the system is provided. It was shown by means of the time-domain simulations that grounding transformers can reduce the possible transient overvoltages that occurred after disconnection of the last network protector on the faulted feeder.

Table 12.13 provides a summary of the calculated voltages at different stages of the SLG fault isolation for the light load cases, with and without overvoltage-mitigating devices. A graphical comparison of the instantaneous voltage envelopes obtained at the fault location is given in Figure 12.49.

12.5.3.4 Remarks

This study has presented the analysis of long-duration overvoltages in heavily meshed underground distribution networks. The duration of these overvoltages was found to be longer for peak loading conditions. By means of time-domain simulations, it was proven that backfeeding from the secondary grid to the primary network raises voltages above the theoretical neutral displacement value of $\sqrt{3}$ p.u. due to the Ferranti effect. Also, it was discovered that, during disconnection of the last network protector, a very large voltage spike is produced due to current chopping. The magnitude of this spike exceeds 3 p.u. when the network is lightly loaded.

The observed voltage magnitudes may cause damage to insulation of the distribution network equipment. To prevent their occurrence, a thorough analysis of overvoltages during unbalanced faults is necessary, and the application of grounding transformers or shunt reactors is highly recommended. The

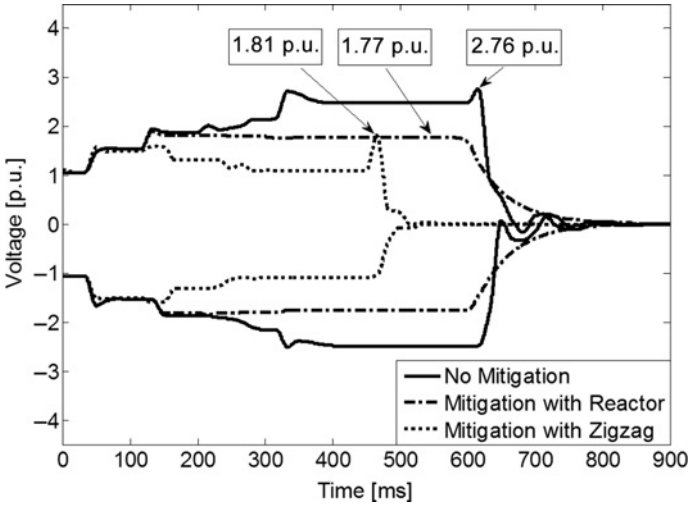

Figure 12.49 Comparison of envelopes for each of resulting voltage under different mitigation schemes (© 2013 IEEE) [90].

comparison of these two overvoltage mitigation methods has shown the grounding transformer to be more effective for mitigating overvoltages during single-line-to-ground faults.

12.6 Development of Data Translators for Interfacing Power-Flow Programs with EMTP-Type Programs

Data needed to perform time-domain studies of smart grid technologies is usually available in the databases of power utilities. The amount of data needed to perform transient studies on large power systems may be massive, and retyping it, in addition to being error prone, is highly inefficient. The techniques presented in this section are intended to establish a bridge between power-flow programs and the EMTP-type programs that will empower utilities to address the growing need to simulate smart grid technologies in the time domain.

12.6.1 Introduction

Time-domain simulations of large power systems using EMTP-type programs are becoming increasingly common. Electromagnetic transients programs are indispensable owing to the requirement of a detailed model of control systems and nonlinear network elements. The push comes from the smart grid technologies that require a large number of switching operations for economical or reliability reasons [5]. The impetus comes from the continuous increase of computing power that has made possible the simulation of electromagnetic transients of large power systems [8, 10, 115].

The objective of the translators is to automatically perform the data conversion between two different databases [122–125]. In many utilities, the available data is in power-flow program formats, such as PSS/E. Therefore, data translators are required to convert the power-flow program files to appropriate formats for EMTP-type programs. Several translators have been developed, intended to convert input data from power-flow (PF) programs into EMTP-type programs [11].

An effective technique for building and maintaining time-domain models of large networks in EMTP-RV was reported in [8]. This technique is based on an automatic translation of text data into a graphical user interface (GUI) model using scripting (JavaScript). It was shown that the resulting model of the network can serve as a unified framework for different types of power system studies. Frequently, transient analyses are required to supplement other studies for the investigation of electrical networks, especially to test smart grid technologies.

In [123], PSCAD/EMTDC is linked to PSS/E through E-Tran. E-Tran is a translator that performs a direct data conversion between phasor-based power flow and stability simulation tools and electromagnetic tools. It can initialize the machines and sources in PSCAD simulations based on the translated data from the power-flow analysis in PSS/E [123, 126–128].

An alternative method applicable to very large distribution networks was presented in [9]. The process of model derivation is fully automated and involves translation of input text files extracted directly from databases into EMTP-RV netlists using a Matlab script. The proposed technique has been successfully applied to various electrical distribution networks, resulting in very accurate three-phase time-domain models. Similar methodologies have been used to translate data from a proprietary power-flow program to EMTP-RV [129], from EMTP-RV to ATP [130, 131] and from ATP/EMTP to OpenDSS.

The data translator allows an electric power utility to perform calculations of overvoltages and other transients, using the power-flow database complemented by additional data. In particular, power distribution utilities can perform EMTP simulations for the calculation of overvoltages due to faults and backfeeding, capacitor switching, ferroresonance, inrush currents and DG penetration, and to corroborate their smart grid technologies on full networks that have many switching operations for network reconfiguration.

12.6.2 Power-Flow to EMTP-RV Translator

EMTP-type programs regularly use a code written in a high-level descriptive language as an input for time-domain simulations. This code is called a netlist. Before the time-domain simulation starts, all models developed with the GUI are converted into the netlist. Although the GUI of the EMTP software has a complex multilayer structure and can be used as a unified framework for different power system studies, development of the models for very large networks cannot rely only on this tool. Indeed, it is impractical to build the entire model having hundreds of thousands of branches and nodes using only mouse-based functions of the GUI. In such a case, a scripting approach should be used. An automatic script can create the network model from the input text files within a relatively short period of time. An alternative is the use of dynamic-link libraries (DLL). It seems possible to link a DLL to custom models. However, this is not efficient when a large variety of the custom models are needed. It was estimated that the development of custom DLLs required more human-hours than developing GUI-based models. Another option would be to have hybrid solutions, that is, GUI combined with ASCII-defined blocks/subnetworks.

Power systems consist of a very large number of similar elements. If a model of some particular element does not already exist among the built-in blocks of an EMTP-type program, it can be built in the GUI. To translate the power-flow data into a netlist, the detailed prototype models for each group of the network elements are developed first, using the GUI. Then each of the prototype models is converted into a short netlist, which textually describes a particular type of the network elements. Applying this technique, the following prototype models are derived:

- area substation transformer with tap changers
- network transformers
- unit substation transformers
- intermittent energy resources
- circuit breakers

- network protectors
- overcurrent protection
- overvoltage protection
- undervoltage protection
- directional power protection
- directional overcurrent protection.

In addition, some of the built-in EMTP models are adopted. They are:

- RLC branches
- PI-sections
- grounding zigzag transformers
- electrical loads
- ideal switches
- synchronous machines
- induction machines.

The netlists of the custom prototype models and those of the relatively complex built-in models (such as the synchronous and induction machines) are placed together in a separate library folder.

The data used by the power-flow to EMTP (PF–EMTP) translator is included in many different types of the text files. These files describe connectivity, ratings, specifications and, in some cases, the geographical location of the network elements. Frequently, the source database of power utilities is very large because it contains more information than is necessary for power-flow studies. Therefore, the information needs to be filtered to extract only the significant data. On the other hand, the source database does not contain all the information needed to perform time-domain simulations. The missing information frequently comes from different databases, datasheets and even from field inspections. Such parameters include

- nonlinear magnetizing curves of different transformers (network, unit substation, high-voltage customers)
- individual relay settings for overcurrent, overvoltage, undervoltage and reverse power
- individual settings of the network protectors.

A PF–EMTP translator has been implemented in Matlab. The software has been chosen because of its built-in capabilities that allow users to deal with different types of variables. Frequently, the translation process involves some calculations, mostly for unit conversion. A flowchart of the translation is shown in Figure 12.50. As shown, the process of model assembly is fully automated and involves translation of input text files extracted directly from the databases into a netlist. As Figure 12.50 shows, the translation starts by reading the power-flow and supplementary files (blocks 2 and 3). Using this data, the parameters of the network elements are calculated in block 4. Block 5 checks whether the prototype model exists in the custom model library. The syntax of the simple built-in models – such as an ideal switch, a PI-section and a constant power load – are not stored in the library but are written directly into the netlist as shown in block 6. For the more complex models, their prototypes are read from the library and copied into the netlist after all the parameters of the particular network element are updated (blocks 7 and 8). The result of the PF–EMTP data translation shown in block 9 is a text file describing the entire power system.

The work reported in this section links two PF programs with two EMTP simulators. At the present stage, only the one-way data conversions shown in Figure 12.51 are considered. In this figure, blocks 1 and 2 correspond to proprietary and commercial software whereas blocks 3 and 4 correspond to royalty-free platforms [132]. The main databases are related to the power-flow program of block 1. Due to the space limitations, discussion here is limited to the PF–EMTP translator.

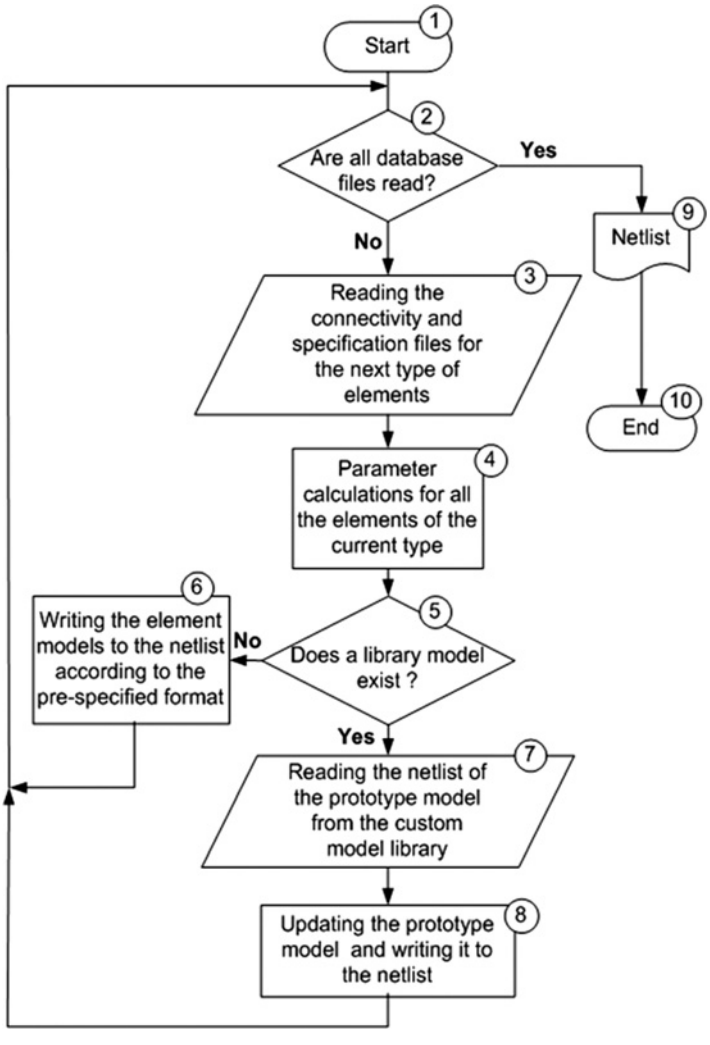

Figure 12.50 A flowchart of the data translation from a power-flow database to EMTP (© 2013 IEEE) [11].

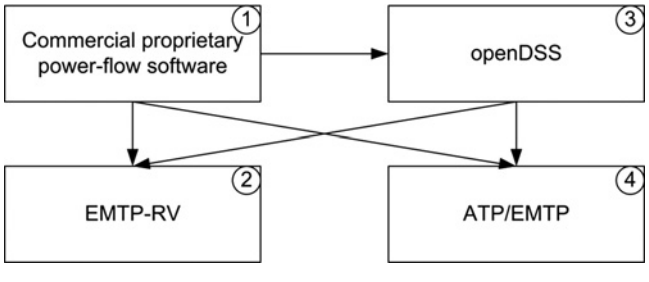

Figure 12.51 Scheme of a one-way power-flow data translation (© 2013 IEEE) [11].

Connectivity File:

From	To	Spec	Length [ft]	Number of Conductors	Normal Rating [A]	Emergency Rating [A]	Under Observation
SW12	M59504	7405XJ	115	2	690	1051	U

Specifications File:

Spec	Nominal Voltage [kV]	Positive Sequence Resistance [mOhm/kft]	Positive Sequence Reactance [mOhm/kft]	Zero Sequence Resistance [mOhm/kft]	Zero Sequence Reactance [mOhm/kft]	Charging Reactive Power [kVA/kft]
7405XJ	13.406	16.2	31.2	203.6	70.9	11.1

EMTP Netlist:

```
_PI;PI1a;6;2;SW12a,M59504a,
3,1Ohm,0,1mH,0,1uF,0,1,1,1,1,1,     } connectivity
_PI;PI1b;6;2;SW12b,M59504b,
_PI;PI1c;6;2;SW12c,M59504c,
0.00904667 0.00718367 0.00718367
0.00718367 0.00904667 0.00718367    } resistance
0.00718367 0.00718367 0.00904667
0.01355425 0.00403679 0.00403679
0.00403679 0.01355425 0.00403679    } inductance
0.00403679 0.00403679 0.01355425
0.01884045 0.00000000 0.00000000
0.00000000 0.01884045 0.00000000    } capacitance
0.00000000 0.00000000 0.01884045
0.00000000 0.00000000 0.00000000
0.00000000 0.00000000 0.00000000    } initial conditions
0.00000000 0.00000000 0.00000000
```

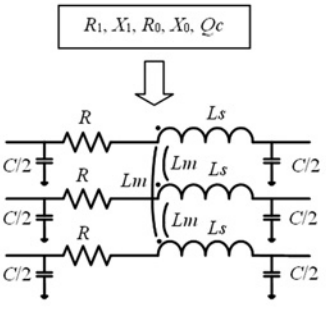

Figure 12.52 Example of the conversion of a transmission line section from the power-flow databases into the EMTP netlist (© 2013 IEEE) [11].

12.6.3 Example of the Translation of a Transmission Line

An example of the translation of transmission line information (feeder sections) from a source databases into an EMTP netlist is presented. The information on connectivity and impedance specifications is contained in separate files. Figure 12.52 shows one data line of the connectivity and the specifications files.

We can see that in the connectivity file, in addition to the information on the 'from' and 'to' nodes and the length of the section, there is also information on conductor rating. In the specifications file, we find the positive- and negative-sequence impedances and the line charging. The translator needs to perform, in addition to operations for unit conversion, calculations to compute phase quantities from sequence quantities. The following formulas are utilized to compute the phase impedance matrix:

$$Z(\Omega) = \frac{Z\,(m\Omega/kft)\ \cdot\ CableLength\ (ft)}{1\,000\,000} \tag{12.5a}$$

$$Z_S = \left(Z_0 + 2X_1\right)/3 \tag{12.5b}$$

$$Z_M = (Z_0 - Z_1)/3 \tag{12.5c}$$

$$\mathbf{Z}^{abc}(\Omega) = \begin{bmatrix} Z_S & Z_M & Z_M \\ Z_M & Z_S & Z_M \\ Z_M & Z_M & Z_S \end{bmatrix} \tag{12.5d}$$

12.6.4 Challenges of Development

The development of reliable data translators for large-scale power systems faces a number of technical and organizational problems, which are discussed in this section.

12.6.4.1 Inconsistencies in the Format of Source Data Files

Currently, the power industry lacks a unified representation of network and device data. Although some standards were suggested in the area [133, 134], they have not been widely adopted in commercial applications. In addition, different stakeholders in the industry design their databases for their particular needs. As a result, serious issues with data exchange arise, even within one organization, when using different software tools or considering the adoption of a new one.

It becomes extremely hard to maintain synchronized and consistent data in numerous databases in different locations. Moreover, data formats of two versions of the same software can be incompatible. For example, E-Tran only generates files compatible with PSCAD version 4.2.1. Users of PSCAD version X4 have some difficulties using the generated data by E-Tran if the substitution library feature of E-Tran is used [128]. The substitution library allows the users to employ detailed models in PSCAD instead of simple power-flow-based models. Therefore, the present approach to the power system data exchange is based on various translators developed per application [27, 135].

12.6.4.2 Data Entry Mistakes and Missing Data

The large databases, containing tremendous amounts of power system elements, are rarely complete. Indeed, they describe systems that constantly change over time. In these databases, human mistakes are not easily identifiable, especially when, instead of halting calculations in case of missing or incorrect data, the software continues execution using various default values. It should be noted that sometimes not all the substitutions are reported. This approach is advantageous in the short term. However, in a long run, it can lead to serious discrepancies between the model and the actual system. Therefore, one of the requirements to the data translators is their capability of verifying the integrity of the input and output data in the original application.

12.6.4.3 Insufficient Data in the Source Databases to Perform Transient Studies

Accurate three-phase time-domain modelling of electrical networks requires much more information than a traditional power-flow program. Details such as sequence impedances, tap-changer scheduling, types of protective relays and their settings and transformer magnetizing curves need to be known. However, this information may not be available. To solve this problem, data exchange between different utilities and between utility and large independent customers is required. In some cases, it implies the necessity of coordinated equipment surveys in the field.

12.6.4.4 High Computational Demands

Three-phase time-domain simulations are considerably more demanding in terms of computational resources than power-flow calculations. This becomes a critical point when extra-large networks are modelled with a very high level of detail. In such a case, the number of subcircuits, stack and necessary memory can be far beyond software and hardware limitations. In addition, a time-domain solution may also fail without accurate prediction of the system matrix sparsity. Therefore, at the early stages of translator development, it is highly desirable to estimate the above-mentioned parameters and adjust the models according to the limitations. Recent versions of EMTP-RV have been significantly enhanced and can handle extra-large power systems with very complex logic [5]. For ATP/EMTP [136], simulations are successful using the available Giga version [137, 138].

12.6.4.5 Validation of Translated Data

Finally, in parallel with the translator, it is very important to develop tools for validation and analysis of the results obtained using the generated EMTP models. These models cannot serve as a reliable source of information until it is proven that they provide results similar to some standard software and/or field

measurements. This is due to the fact that even small modelling errors may result in significant changes in steady-state and dynamic behaviour of large complex systems. Thus, to obtain accurate results, all developed custom models have to be tested individually using time-domain simulations.

The comparison involves hundreds of thousands of different parameters and must be automated. Due to the size of the input and output data, manual processing of system-wide results is impractical. Instead, an automated approach employing custom computer code should be used. Among others, it should include waveform processing, statistical techniques and graphical visualization. According to these guidelines, the developed translator was used in the following fully automated studies: (1) symmetric and asymmetric faults with and without distributed generation, (2) impact of distributed generation on the voltage profile in distribution networks, (3) automatic network reconfiguration and self-healing of the distribution networks – see previous sections. A process of validation is detailed in the next section.

12.6.5 Model Validation

12.6.5.1 Test Systems

Up to three systems of different size have been tested for validating the developed translator. The network architecture for the medium size test system is shown in Figure 12.4. This network is composed of seven station transformer 69/13.8 kV, 15 bus breakers and 12 feeder breakers. Taking feeders into account, there are 1041 primary sections interconnected. These sections energize 224 transformers of voltage 13.8/0.460 kV or 13.8/0.208 kV depending on their location, which use 1375 secondary mains to feed the 311 aggregated loads. To sum up, this network has more than 2500 three-phase branches, considering transformers as well as primary and secondary grid sections, with over 7000 three-phase nodes.

The small size test system has a similar structure to that of the medium size. However, its secondary system is mostly composed of spot networks and has limited residential service with a meshed grid.

Finally, the large size test system is composed of underground as well as overhead services (Figure 12.6) and has nearly 30 000 three-phase branches, accounting for transformers, feeders and secondary sections. This network has several auto-loops for service reliability and a substantial number of MV and LV loads adding up to approximately 400 MW of consumption. Further information on these networks can be found in [9].

12.6.5.2 Validation Stages

Transient analysis is usually carried out to supplement different steady-state techniques that cannot capture complex interaction between different power system components in the time domain. Therefore, the EMTP model should, in addition to providing results similar to those of the power-flow program, accurately reproduce real-life dynamics of the network.

It should be noted that power-flow simulation is a complex linear algebra process based on the fundamental phasor solution. In turn, EMTP-type programs are based on the solution of differential equations. Using the proper integration step, the EMTP solutions are quite accurate at nominal frequency (50 Hz or 60 Hz). The small discrepancies between the steady-state solutions obtained with EMTP-type programs and commercial power-flow programs may be due, among other reasons, to differences in the representation of loads, which are normally considered constant PQ in power-flow programs and become constant impedance in time-domain simulations. Another reason for the discrepancy may be the modelling of nonlinearities, such as transformer saturation in the EMTP, which is not commonly considered in power-flow simulations. Discrepancies can also come from differences in the modelling of electromagnetic unbalances (non-transposed conductors in transmission lines), which are not captured by the use of sequence quantities in power flow programs [139].

To ensure the correctness of the model the following validation steps were taken:

1. comparison of EMTP steady-state solutions against results obtained using a commercial power-flow program for peak, light load conditions, for single and double contingencies. The differences found

in node voltages and section currents were very small. For example, voltage differences of only a few tenths of a per cent were found.
2. comparison of several three-phase short-circuits results obtained with the EMTP and with the short-circuit computation facility of the commercial power-flow software. Very small differences occurred in almost all feeders.
3. experimental validation of the generated EMTP models carried out to compare the simulation results with recordings of several actual transient events that took place in different power systems. The simulation output has been compared with electrical signals recorded at the secondary side of the area substation transformers by the PQ Node hardware [64] and processed in PQ View software [140].

A small sample of the validation stages is presented below.

12.6.5.3 Steady-State Validation

The steady-state validation is an integral part of the translation process. Indeed, once a netlist of an extremely large network is generated according to the steps described in Figure 12.50, it is necessary to verify that the configuration of the network and its parameters did not change and that the results are in line with the power-flow calculations. The validation of the generated EMTP model is carried out automatically as shown in Figure 12.53. After generation of the netlist (block 5), the translator

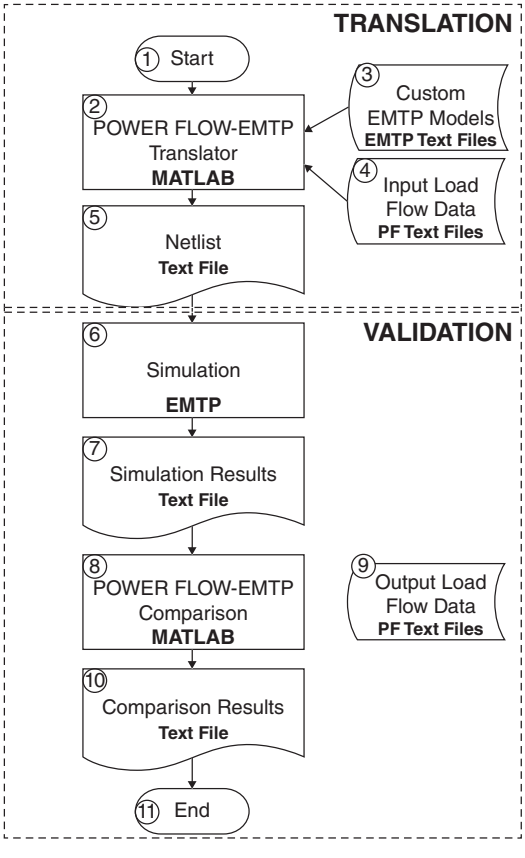

Figure 12.53 A block diagram of the PF-EMTP translator (© 2013 IEEE) [11].

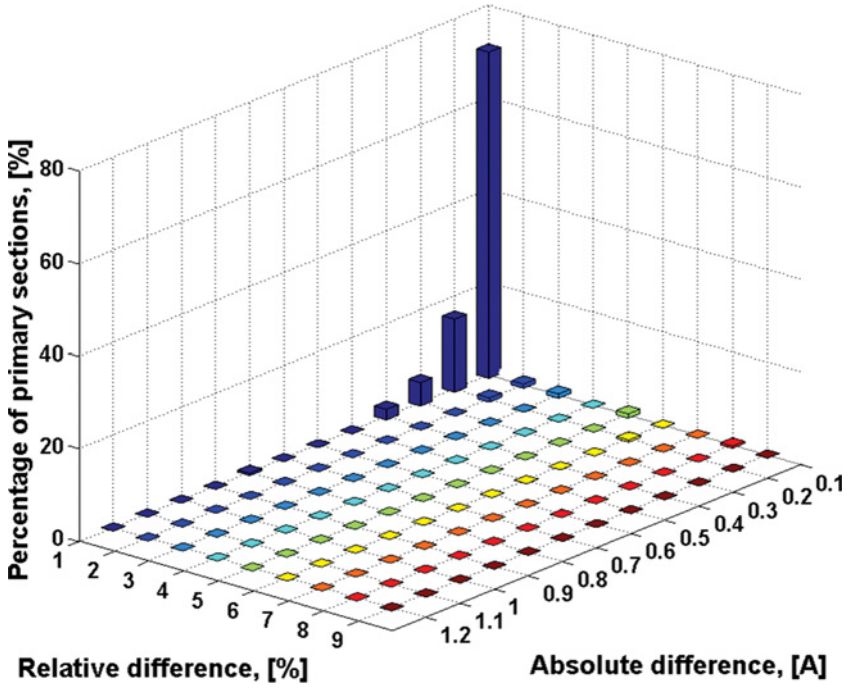

Figure 12.54 Comparison of primary currents in a small-size network calculated using commercial PF program and EMTP time-domain simulator (© 2013 IEEE) [11].

starts a time-domain simulation (block 6). The simulation results are analysed and written into various report files in block 7. Block 8 reads the output data of the power-flow run (block 9) and compares them with those of the EMTP simulation. At this stage, connectivity of the system, branch impedances, currents and node voltages are checked. Finally, the comparison results are written into the text files (block 10).

The results of the steady-state validation for three different power systems of different sizes, and operating at peak loading, are shown in Figures 12.54–12.59. From Figure 12.54, we see that for more than 70% of the primary feeder sections, the results of the power-flow and EMTP calculations differ by less than 0.1 A and less than 1% relatively. The largest absolute error is 1.15 A which is 12.9%. The maximal relative difference of 58.2% corresponds to the negligible current difference of only 0.05 A. As shown in Figure 12.57, more than 40% of the secondary sections have an absolute error below 1 A and the relative error below 1%. The largest absolute error is 1.33 A which corresponds to 3.5%, whereas the largest relative error of 9.2% is equivalent to 0.03 A on the absolute scale. The largest relative difference of all node voltages in the small-size network is negligibly small: 0.005%. Similar information for the other two networks is summarized in Table 12.14. The small differences are attributed to: (1) numeric inaccuracy of the specific database impedances used for the netlist generation, (2) the limited display of significant digits in the results of the commercial power-flow software, and (3) slightly different approaches in modelling. The results obtained for the light loading cases also prove the validity of the derived dynamic model. They are not presented here for sake of brevity.

As mentioned above, there are important differences in the way the loads are modelled in time-domain and power-flow simulations. In power-flow simulations, loads are represented as constant power (PQ), whereas in time-domain (EMTP) simulations loads become constant circuit parameters (RL). In this study, a good match between the two programs has been obtained because, for the time-domain

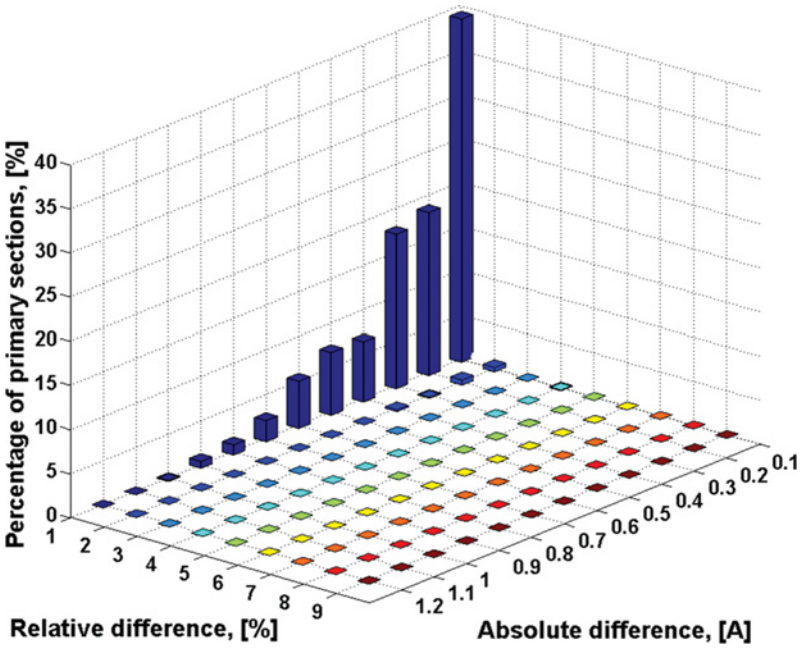

Figure 12.55 Comparison of primary currents in a middle-size network calculated using commercial PF program and EMTP time-domain simulator (© 2013 IEEE) [11].

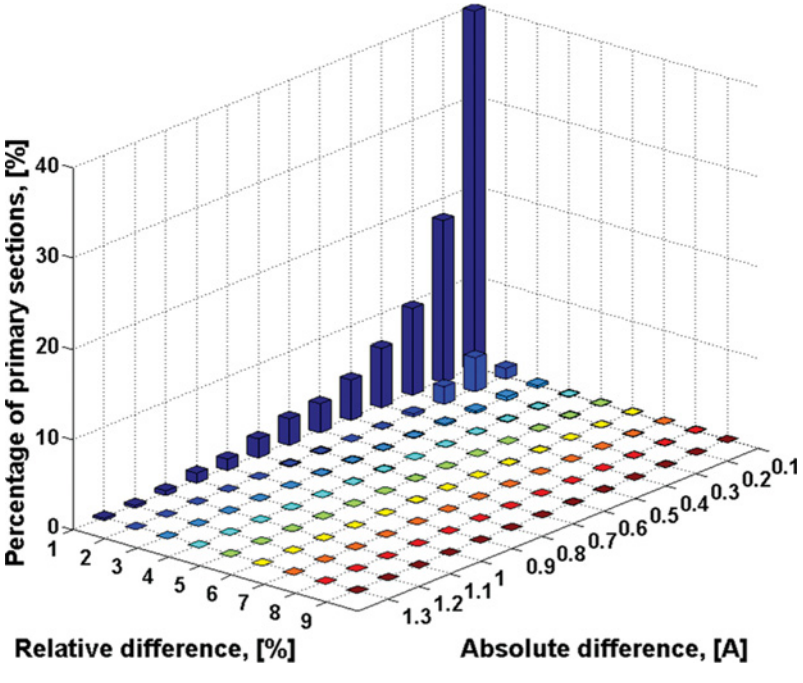

Figure 12.56 Comparison of primary currents of a large-size network calculated using commercial PF program and EMTP time-domain simulator (© 2013 IEEE) [11].

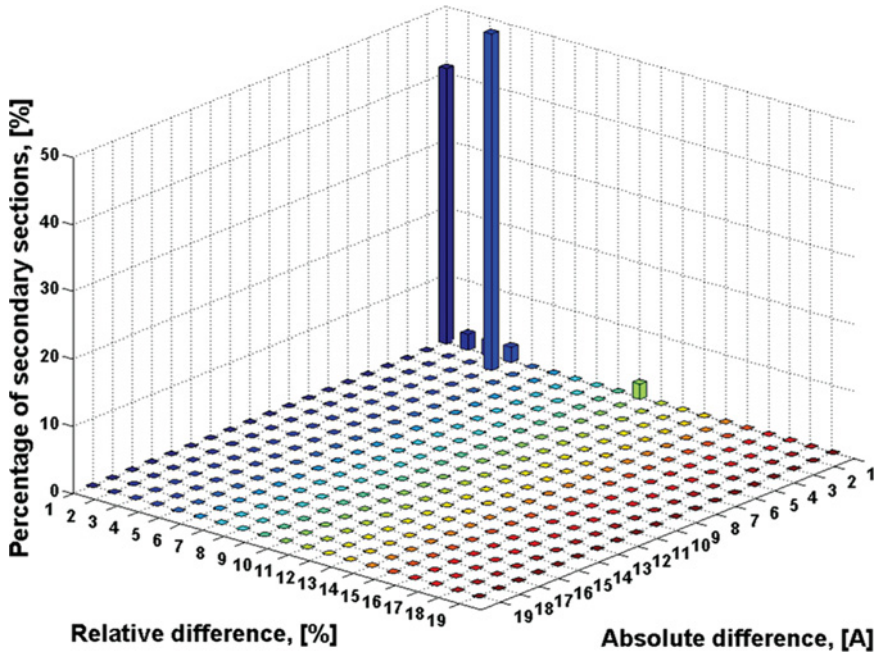

Figure 12.57 Comparison of secondary currents in a small-size network calculated using commercial PF program and EMTP time-domain simulator (© 2013 IEEE) [11].

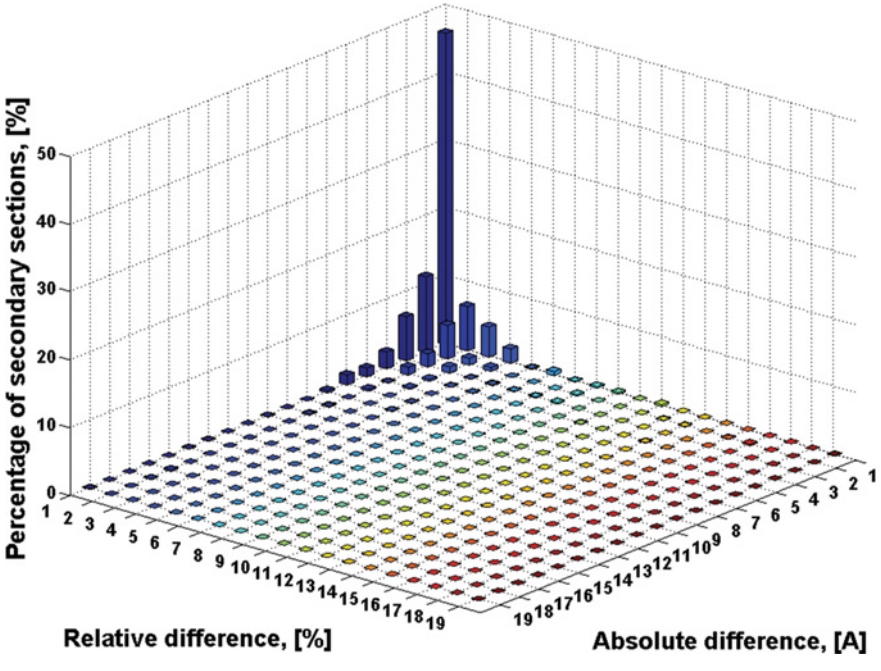

Figure 12.58 Comparison of secondary currents in a middle-size network calculated using commercial PF program and EMTP time-domain simulator (© 2013 IEEE) [11].

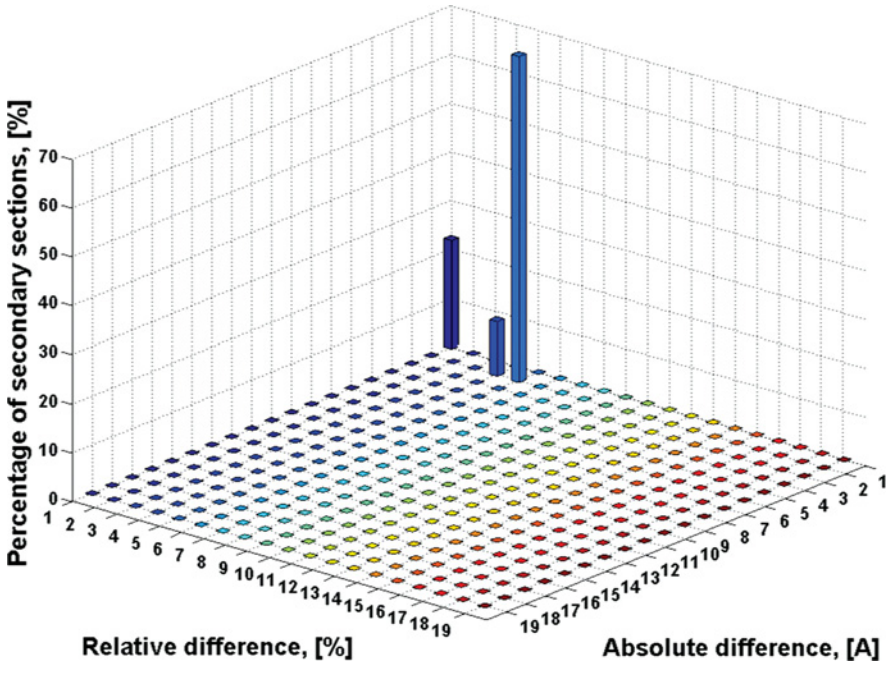

Figure 12.59 Comparison of secondary currents of a large-size network calculated using commercial PF program and EMTP time-domain simulator (© 2013 IEEE) [11].

simulations, the loads were 'adjusted' from the beginning to the known (from the power flow) voltage at their terminals. The development of an efficient constant power load model for the EMTP is of paramount importance because a deviation from the rated voltage may substantially affect the value of the load.

The validation of the EMTP simulation results against the output of the commercial PF program has also been carried out for the case of three-phase short-circuits in the primary and secondary subnetworks.

Table 12.14 Maximal absolute and relative errors (© 2013 IEEE) [11].

		Network		
Parameter	Unit	Small-size	Middle-size	Large-size
Number of the network nodes	—	315	2333	13 523
Maximal relative error in the node voltages	%	0.005	0.029	0.32
Number of the primary sections	—	217	1041	3965
Maximal absolute error	A	1.15	0.92	1.92
Corresponding relative error	%	12.8	0.58	0.28
Maximal relative error	%	58.2	3.45	41.8
Corresponding absolute error	A	0.05	0.06	0.03
Number of the secondary sections	—	44	1375	11 543
Maximal absolute error	A	1.34	18	56.39
Corresponding relative error	%	3.51	0.98	2.46
Maximal relative error	%	9.15	18.13	69.53
Corresponding absolute error	A	0.03	0.64	1.48

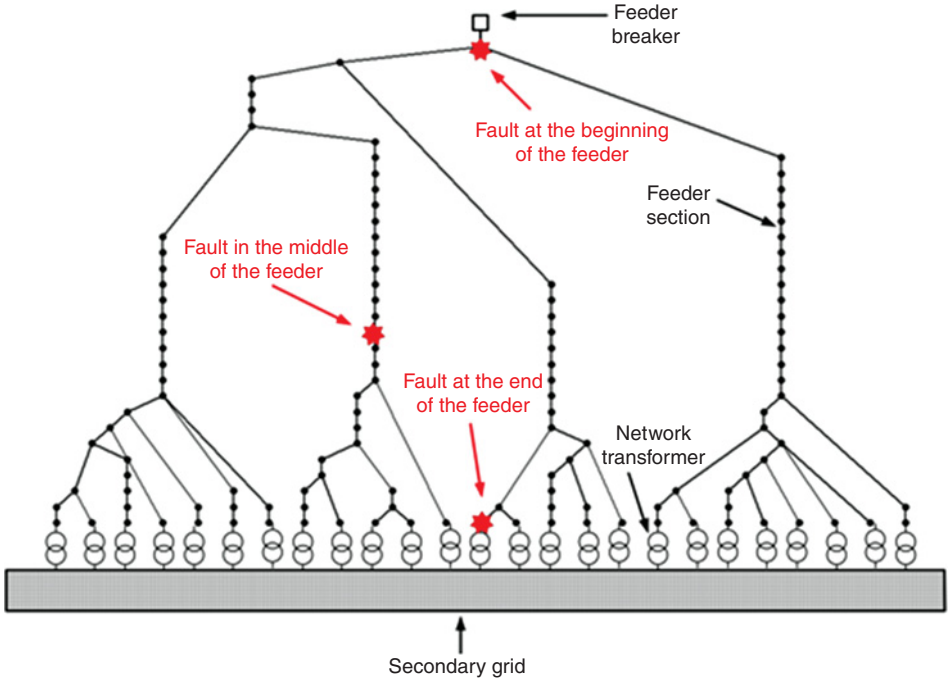

Figure 12.60 Comparison of secondary currents calculated using traditional short-circuit software and EMTP with time-domain simulations (© 2013 IEEE) [11].

For example, three locations shown in Figure 12.60 were chosen to test the fault current levels in one of the primary feeders in the network. The comparison results are given in Table 12.15. Similarly, the fault currents were assessed with the three-phase short-circuits in the secondary subnetwork. The fault locations were chosen at service boxes and transformer vaults. The results for two of them are shown in Table 12.16.

Table 12.15 Comparison of the three-phase short-circuit currents in the middle-size distribution network (faults are in the primary subnetwork) (© 2013 IEEE) [11].

Fault location	PF current (kA)	EMTP current (kA)	Relative difference (%)
Beginning of the feeder	30.5	30.7	0.65
Middle of the feeder branch 2	19.3	19.7	2.07
End of the feeder branch 3	19.8	20.3	2.52

Table 12.16 Comparison of the three-phase short-circuit currents in the middle-size distribution network (faults are in the secondary subnetwork) (© 2013 IEEE) [11].

Fault location	Power flow current (kA)	EMTP current (kA)	Relative difference (%)
Service box	14	14.5	3.57
Vault	81.4	84.6	3.93

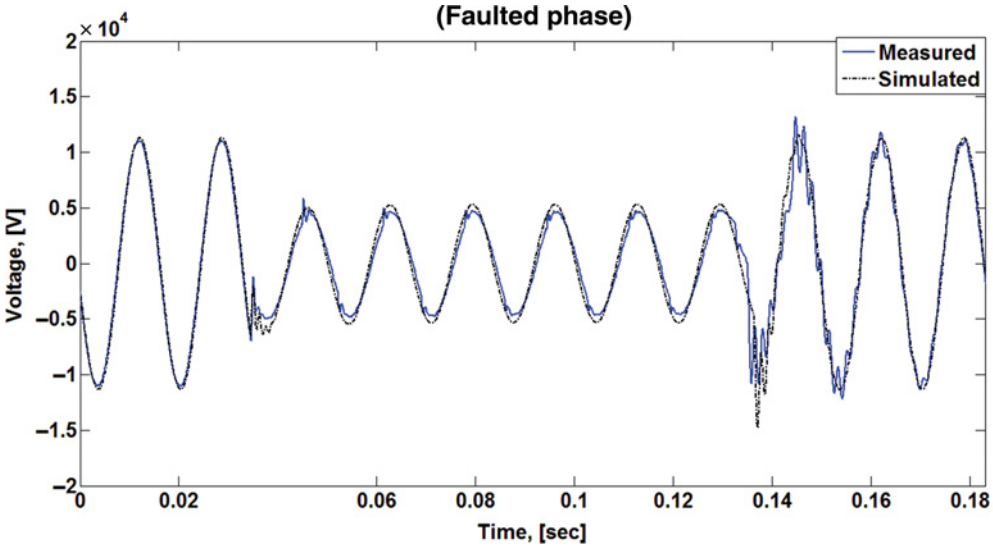

Figure 12.61 Phase A (faulted phase) voltage at the secondary terminals of the area substation transformer (© 2013 IEEE) [11].

12.6.5.4 Transient Validation

The transient validation of the EMTP model has been performed by comparing the numerical results with actual waveform recordings taken in the distribution networks during various faults. One of them is presented below. It consists of a single-line-to-ground fault that occurred at the terminals of a network transformer at the end of a 13.8 kV feeder shown in Figure 12.60. This feeder is one of the 12 primary feeders connected to the 13.8 kV bus. A measurement unit is installed at the secondary side of an area substation transformer and records phase and neutral currents and voltages.

Based on the available measured data, the network loading used in the simulation has been adjusted in order to match the prefault conditions. The simulation starts at steady-state operating conditions. A single-line-to-ground fault occurs in phase A at 34.5 ms. This fault is isolated after approximately six cycles by tripping the breaker of the corresponding feeder and opening all network protectors connected to this feeder. The simulation and measurement results are compared in Figures 12.61–12.66.

From the waveform analysis, it can be concluded that the EMTP simulation has successfully reproduced the prefault, faulted and post-fault behaviour at low frequencies and has captured the higher-frequency oscillations as well. The simulations and the measured overvoltages, undervoltages and short-circuit currents match very well. For example, the first peaks of the simulated and measured fault currents have a difference of only 5.4% (3781.7 A vs 3997.2 A).

12.6.6 Recommendations

12.6.6.1 Data Inventory

Before undertaking the translation task, it is recommended to make a complete inventory of the required data. Depending on the purpose of the time-domain study, some important pieces of information will not be available in the databases used for power-flow simulations. Essential information for transient studies, such as zero-sequence impedances (or line configuration), are not part of a balanced power-flow program and therefore they often do not exist in the source database. A lot of other important data may not be available in the power-flow database, for example, connection of transformers, magnetizing curves,

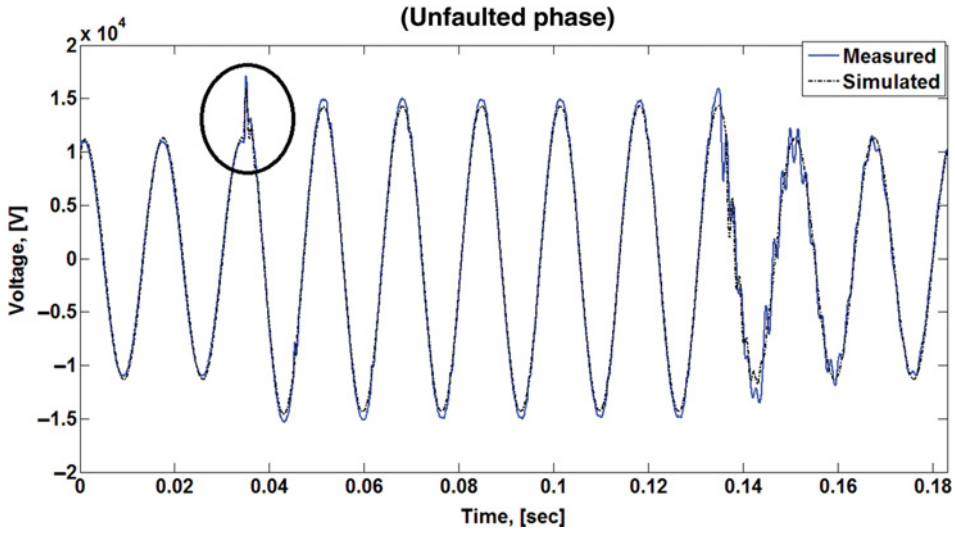

Figure 12.62 Phase B (unfaulted phase) voltage at the secondary terminals of the area substation transformer (© 2013 IEEE) [11].

under-load tap changers, relay protection devices and settings, arcing circuit breakers (with and without restrikes), generator and motor electrical and mechanical data, surge arresters, grounding reactors and so forth.

The biggest efforts and the longest developing times go into the assembly and validation of a complete set of reliable data. Therefore, the more sophisticated the developed tools for data validation the more efficient the overall translation process will become.

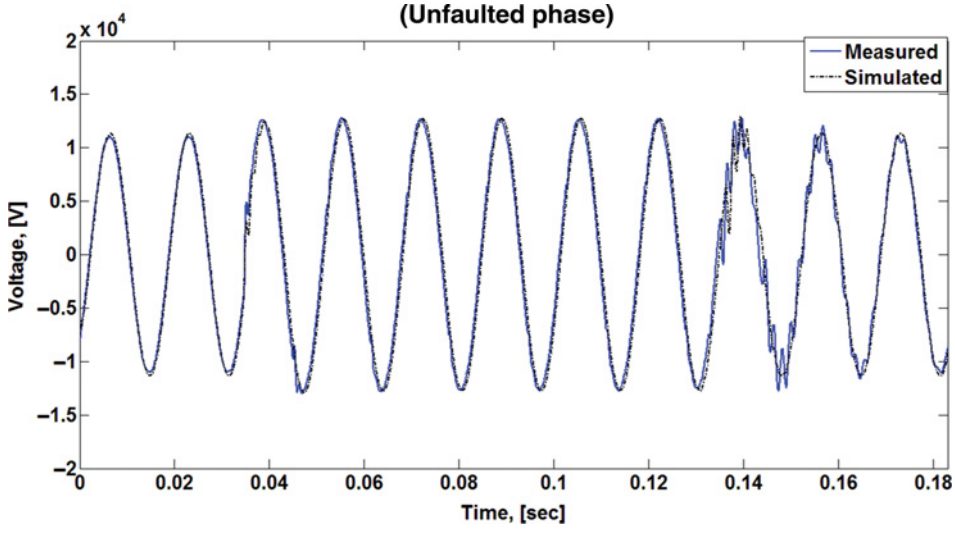

Figure 12.63 Phase C (unfaulted phase) voltage at the secondary terminals of the area substation transformer (© 2013 IEEE) [11].

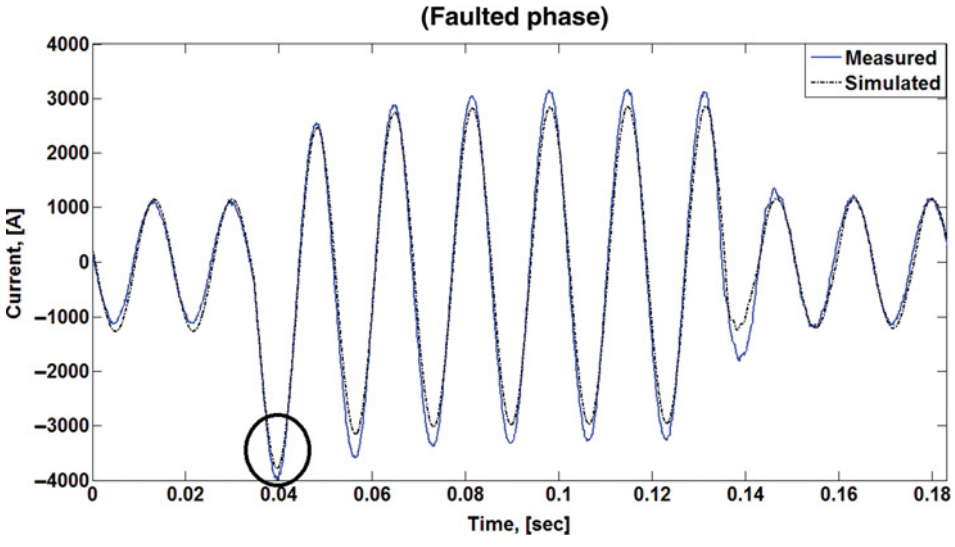

Figure 12.64 Phase A (faulted phase) current at the secondary terminals of the area substation transformer (© 2013 IEEE) [11].

12.6.6.2 Multifile Input – Single-File Output

For the above reasons, it is recommended that the PF-EMTP translator be capable of reading data from several databases. The alternative is to build a unified file from the source databases containing all the necessary information in a common file. Although the former option adds programming complications because the data comes from different files, in the long run, this seems to be a better way to gain access to multiple and varied databases. The latter process, merging all information in one file as input for the

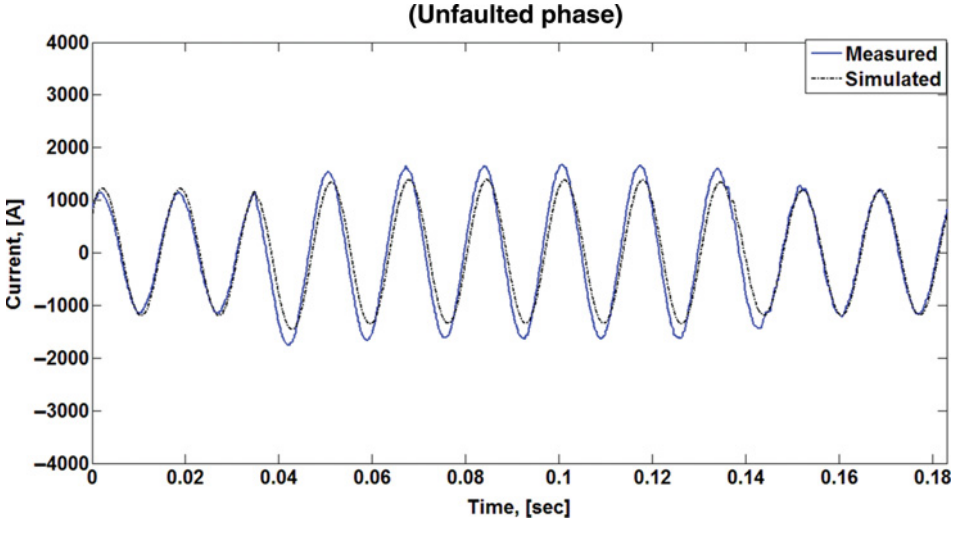

Figure 12.65 Phase B (unfaulted phase) current at the secondary terminals of the area substation transformer (© 2013 IEEE) [11].

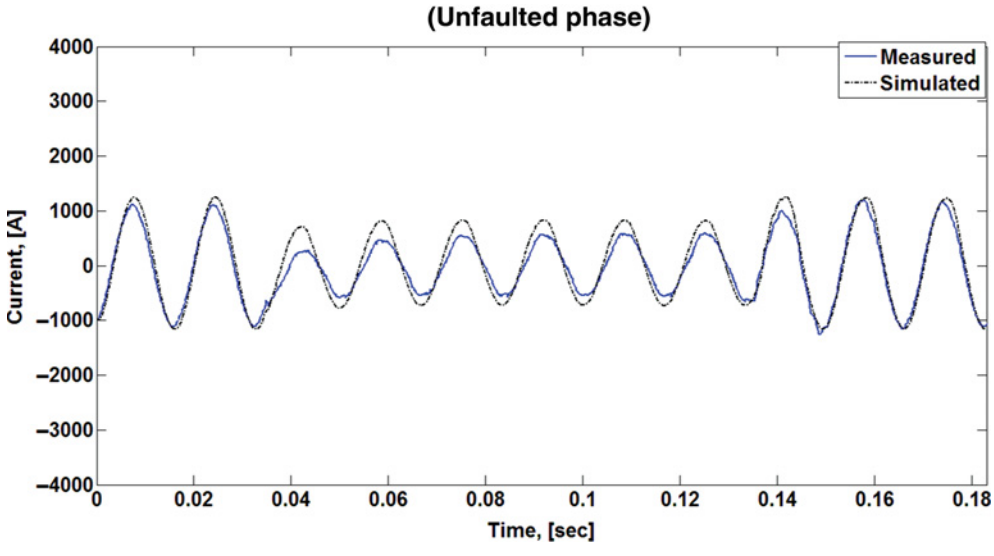

Figure 12.66 Phase C (unfaulted phase) current at the secondary terminals of the area substation transformer (© 2013 IEEE) [11].

translator, was also tried, but it increased the number of human errors and could not be easily generalized to other networks.

12.6.6.3 Data and Model Verification

Validation of each model independently and in the circuit is essential. PF and EMTP-type programs may use different systems of units. To mention a few examples, we have found the following cases: impedances are given in ohms per kilo-feet in the source database while they are needed in ohms in the EMTP (Figure 12.52); magnetizing curves are in p.u. in the source database but they are needed in webers versus amperes in the EMTP.

Frequently, the data archives do not exist in digital form and hand digitalization of the data is required. For these reasons it is recommended to validate each component model (unit testing) separately. This process starts by checking that the performance of each device complies with the specifications. For example, the standardized open circuit and impedance tests on the transformer models should be simulated on a standalone model before interconnection with the network. Similarly, a grounding transformer must deliver the specific positive and zero-sequence reactive powers. Therefore, it is important to connect the model to a positive-sequence (and later to a zero-sequence) source to ensure that the correct amount of reactive power is being demanded in each case.

12.6.6.4 Automated Data Validation

It is also recommended to create a computer code that automatically compares and validates the results obtained from time-domain power-flow (EMTP-type) against the original phasor-based power-flow program. Validation with field recordings offers the ultimate verification of the models. This, however, may not be easy to do in every case since experimentation with a real power system is not commonly done due to the high risks involved.

12.6.6.5 Automatic Post-Processing of Results

An important issue, that can be easily overlooked when translating power-flow data into files for time-domain simulations, is that the required computing resources and tools for the analysis of the results are completely different. Power-flow simulations can be run for very large systems with relatively modest computer resources in a few seconds. Then, the user can analyse the rms voltages and currents (power flow) for hundreds of nodes or branches by inspection of tabulated results. Most commercial PF programs report the exceptions (overcurrent and/or over- and undervoltages) for the convenience of the users. Many programs even produce coloured one-line diagrams to help the user find where the problems are. On the other hand, time-domain simulations are traditionally performed for relatively small networks. Therefore, the computer resources and required effort for analysing graphical (waveshape) results are comparable to those of the power-flow case. However, when converting a large power-flow case into a transient case, the required computer resources increase considerably. Besides taking substantial simulation time to produce the results (seconds become hours), it is impossible to plot and analyse the waveshapes for thousands of signals (voltages, currents, etc.). For the large network presented above, the results data file has 240 million lines! It is, therefore, recommended that an automated software facility be created to analyse the results. We note that the currently available plotting facilities of both EMTP-type tools are not designed to process efficiently this tremendous amount of information.

Acknowledgement

Financial support to Reynaldo Salcedo by the GAANN Fellowship from the US Department of Education is gratefully acknowledged.

References

[1] http://energy.gov/oe/technology-development/smart-grid(October 2012).

[2] The Smart Grid: an introduction. Document prepared for the U.S. Department of Energy by Litos Strategic Communication under contract No. DE-AC26-04NT41817, Subtask 560.01.04. Available on-line at: http://energy.gov/oe/downloads/smart-grid-introduction-0.

[3] Lightner, E.M. and Widergren, S.E. (2010) An orderly transition to a transformed electricity system. *IEEE Transactions on Smart Grid*, **1**(1), 3–8.

[4] Rogers, K.M., Klump, R., Khurana, H. *et al.* (2010) An authenticated control framework for distributed voltage support on the smart grid. *IEEE Transactions on Smart Grid*, **1**(1), 40–47.

[5] Spitsa, V., Ran, X., Salcedo, R. *et al.* (2012) On the transient behavior of large-scale distribution networks during automatic feeder reconfiguration. *IEEE Transactions on Smart Grid*, **3**(2), 887–896.

[6] Martinez, J.A., de León, F., Mehrizi-Sani, A. *et al.* (2011) Tools for analysis and design of distributed resources. Part II: Tools for planning, analysis and design of distribution networks with distributed resources. *IEEE Transactions on Power Delivery*, **26**(3), 1653–1662.

[7] Chen, P., Salcedo, R., Zhu, Q. *et al.* (2012) Analysis of voltage profile problems due to the penetration of distributed generation in low-voltage secondary distribution networks. *IEEE Transactions on Power Delivery*, **27**(4), 2020–2028.

[8] Gérin-Lajoie, L. and Mahseredjian, J. (2009) Simulation of an extra large network in EMTP: From electromagnetic to electromechanical transients. International Conference on Power Systems Transients (IPST), Kyoto, Japan, 2–6 June 2009.

[9] Spitsa, V., Salcedo, R., Ran, X. *et al.* (2012) Three–phase time–domain simulation of very large distribution networks. *IEEE Transactions on Power Delivery*, **27**(2), 677–687.

[10] Mahseredjian, J., Dennetière, S., Dubé, L. *et al.* (2007) On a new approach for the simulation of transients in power systems. *Electric Power System Research*, 1514–1520.

[11] de León, F., Czarkowski, D., Spitsa, V. *et al.* (2013) Development of data translators for interfacing power-flow programs with EMTP-type programs: challenges and lessons learned. *IEEE Transactions on Power Delivery*, **28**(2), 1192–1201.

[12] Zidan, A. and El-Saadany, E.F. (2012) A cooperative multiagent framework for self-healing mechanisms in distribution systems. *IEEE Transactions on Smart Grid*, **3**(3), 1525–1539.
[13] ABB Elect. Syst. Technol. Inst. (1997) *Electrical Transmission and Distribution Reference Book*, 5th edn, ABB Power T&D Company, Raleigh, NC.
[14] Yu, L., Czarkowski, D. and de León, F. (2012) Optimal distributed voltage regulation for secondary networks with DGs. *IEEE Transactions on Smart Grid*, **3**(2), 959–967.
[15] Waseen, I., Pipattanasomporn, M. and Rahman, S. (2009) Reliability benefits of distributed generation as a backup source. IEEE PES General Meeting, Calgary, AB, Canada, 26–30 July 2009.
[16] Hlatshwayo, M., Chowdhury, S., Chowdhury, S.P. and Awodele, K.O. (2010) Impacts of DG penetration in the reliability of distribution systems. International Conference on Power System Technology (POWERCON), Hangzhou, Oct. 2010.
[17] IEEE Standard Requirements for Secondary Network Protectors. IEEE Standard C57.12.44, 2005.
[18] Smart Grid. Washington, DC, Dec. 2007, 110th Congress of United States, Title XIII, Energy Independence and Security Act of 2007.
[19] Heydt, G.T. (2010) The next generation of power distribution systems. *IEEE Transactions on Smart Grid*, **1**(3), 225–235.
[20] Haughton, D. and Heydt, G.T. (2010) Smart distribution system design: Automatic reconfiguration for improved reliability. IEEE PES General Meeting, Minneapolis, MN, USA, July 25–29, 2010.
[21] New York State Public Service Comm., Order modifying standardized interconnection requirements and modifying and approving tariffs. Mar. 2013.
[22] Pérez-Guerrero, R., Heydt, G., Jack, N. *et al.* (2008) Optimal restoration of distribution systems using dynamic programming. *IEEE Transactions on Power Delivery*, **23**(3), 1589–1596.
[23] Jeon, Y.J., Kim, J.C., Kim, J.O. *et al.* (2002) An efficient simulated annealing algorithm for network reconfiguration in large-scale distribution systems. *IEEE Transactions on Power Delivery*, **17**(4), 1070–1078.
[24] Coelho, A. and Da Silva, M.G. (2004) Distribution network reconfiguration with reliability constraints. International Conference on Power System Technology (PowerCon), 21–24 Nov. 2004.
[25] Khodr, H.M., Martinez-Crespo, J., Matos, M.A. and Pereira, J. (2009) Distribution systems reconfiguration based on OPF using benders decomposition. *IEEE Transactions on Power Delivery*, **24**(4), 2166–2176.
[26] Podmore, R. and Robinson, M.R. (2010) The role of simulators for smart grid development. *IEEE Transactions on Smart Grid*, **1**(2), 205–212.
[27] Mahseredjian, J., Dinavahi, V. and Martinez, J.A. (2009) Simulation tools for electromagnetic transients in power systems: overview and challenges. *IEEE Transactions on Power Delivery*, **24**(3), 1657–1669.
[28] Watson, N. and Arrillaga, J. (2003) *Power Systems Electromagnetic Transients Simulation*, IET, London.
[29] Xyngi, I., Ishchenko, A., Popov, M. and van der Sluis, L. (2009) Transient stability analysis of a distributed network with distributed generators. *IEEE Transactions on Power Systems*, **24**(2), 1102–1104.
[30] Thallam, R.S., Suryanarayanan, S., Heydt, G.T. and Ayyanar, R. (2006) Impact of interconnection of distributed generation of electric distribution systems – A dynamic simulation perspective. IEEE PES General Meeting, Montreal, QC, Canada, 18–22 June 2006.
[31] Miao, Z., Choudhry, M.A. and Klein, R.L. (2002) Dynamic simulation and stability control of three-phase power distribution system with distributed generators. IEEE PES Winter Meeting, New York, NY, USA, 19–22 Jan. 2002.
[32] Mak, S.T. (1993) Propagation of transients in a distribution network. *IEEE Transactions on Power Delivery*, **8**(1), 337–343.
[33] Martinez, J.A. and Martin-Arnedo, J. (2004) Voltage sag stochastic prediction using an electromagnetic transients program. *IEEE Transactions on Power Delivery*, **19**(4), 1975–1982.
[34] Lee, B.W. and Rhee, S.B. (2010) Test requirements and performance evaluation for both resistive and inductive superconducting fault current limiters for 22.9 kV electric distribution network in Korea. *IEEE Transactions on Applied Superconductivity*, **20**(3), 1114–1117.
[35] Peponis, G.J., Papadopoulos, M.P. and Hatziargyriou, N.D. (1995) Distribution network reconfiguration to minimize resistive line losses. *IEEE Transactions on Power Delivery*, **10**(3), 1338–1342.
[36] Nagata, T., Sasaki, H. and Kitagawa, M. (1994) A method of determining target configuration for power systems restoration by means of mix integer programming approach. *Transactions IEE Japan*, **114-B**(2), 179–185.
[37] Fukuyama, Y. and Hsaio-Dong, C. (1995) A parallel genetic algorithm for service restoration in electric power distribution systems. IEEE International Conference on Fuzzy Syst., Yokohama, Japan, March 1995.

[38] Mori, H. and Takeda, K. (1994) Parallel simulated annealing for power system decomposition. *IEEE Transactions on Power Systems*, **9**(2), 789–795.
[39] Mori, H. and Ogita, Y. (2002) A parallel tabu search based approach to optimal network reconfigurations for service restoration in distribution systems. IEEE International Conference on Control Applications, Glasgow, UK, 18–20 Sep. 2002.
[40] Popovic, D.S. and Ciric, R.M. (1999) A multi-objective algorithm for distribution networks restoration. *IEEE Transactions on Power Delivery*, **14**(3), 1134–1140.
[41] Goswami, S.K. and Basu, S.K. (1992) A new algorithm for the reconfiguration of distribution feeders for loss minimization. *IEEE Transactions on Power Delivery*, **7**(3), 1484–1491.
[42] Lim, S.I., Lee, S.-J., Choi, M.-S. *et al.* (2006) Service restoration methodology for multiple fault case in distribution systems. *IEEE Transactions on Power Systems*, **21**(4), 1638–1644.
[43] Tsai, L.H. (1993) Network reconfiguration to enhance reliability of electric distribution systems. *Electric Power Systems Research*, **27**, 135–140.
[44] Li, J., Liu, C.C. and Schneider, K.P. (2010) Controlled partitioning of a power network considering real and reactive power balance. *IEEE Transactions on Smart Grid*, **1**(3), 261–269.
[45] You, H., Vittal, V. and Wang, X. (2004) Slow coherency-based islanding. *IEEE Transactions on Power Systems*, **19**(1), 483–491.
[46] Yang, B., Vittal, V. and Heydt, G.T. (2006) Slow coherency based controlled islanding – A demonstration of the approach on the August 14, 2003 blackout scenario. *IEEE Transactions on Power Systems*, **21**(4), 1840–1847.
[47] Sun, K., Zheng, D. and Lu, Q. (2003) Splitting strategies for islanding operation of large-scale power systems using OBDD-based methods. *IEEE Transactions on Power Systems*, **18**(2), 912–923.
[48] Xu, G. and Vittal, V. (2010) Slow coherency based cutset determination algorithm for large power systems. *IEEE Transactions on Power Systems*, **25**(2), 877–884.
[49] Karypis, G. and Kumar, V. (1998) A fast and high quality multilevel scheme for partitioning irregular graphs. *SIAM: SIAM Journal on Scientific Computing*, **20**(1), 359–392.
[50] Schloegel, K., Karypis, G. and Kumar, V. (1999) A new algorithm for multiobjective graph partitioning. Euro-Par, Toulouse, France, 1999.
[51] GE Industrial: Distribution System Feeder Overcurrent Protection, GE Power Management, Ontario, Canada. [Online], 2013. Available: http://www.geindustrial.com/publibrary/checkout/GET-6450?TNR=White%20Papers|GET-6450|generic.
[52] McMillin, B., Akella, R., Ditch, D. *et al.* (2011) Architecture of a smart microgrid distributed operating system. IEEE PES Power Syst. Conf. Expo. (PSCE), Phoenix, AZ, USA, Mar. 2011.
[53] Roche, R., Blunier, B., Miraoui, A. *et al.* (2010) Multiagent systems for grid energy management: a short review. 36th Annual IEEE Conf. Ind. Electron. Soc. (IECON), Glendale, AZ, USA, Nov. 2010.
[54] Colson, C. and Nehrir, M. (2011) Agent-based power management of microgrids including renewable energy power generation. IEEE PES General Meeting, San Diego, CA, USA, July 2011.
[55] Farag, H.E.Z., El-Saadany, E.F. and Seethapathy, R. (2012) A two-way communication-based distributed control for voltage regulation in smart distribution feeders. *IEEE Transactions on Smart Grid*, **3**(1), 271–281.
[56] Nguyen, P., Kling, W., Georgiadis, G. *et al.* (2010) Distributed routing algorithms to manage power flow in agent-based active distribution network. IEEE PES Innovative Smart Grid Tech. Conf. Europe (ISGT Europe), Gothenburg, Sweden, Oct. 2010.
[57] Ochoa, L., Dent, C. and Harrison, G. (2010) Distribution network capacity assessment: Variable DG and active networks. *IEEE Transactions on Power Systems*, **25**(1), 87–95.
[58] Yang, Q., Barria, J. and Green, T. (2011) Communication infrastructures for distributed control of power distribution networks. *IEEE Transactions on Industrial Informatics*, **7**(2), 316–327.
[59] Behnke, M., Erdman, W., Horgan, S. *et al.* (2005) Secondary network distribution systems background and issues related to the interconnection of distributed resources. National Renewable Energy Laboratory, Tech. Rep. NREL/TP-560-38079, Golden, CO, USA, July 2005.
[60] Spitsa, V., Czarkowski, D., de Léon, F. and Zabar, Z. (2011) Final report – Transient and steady-state analysis for the 3G smart grid concepts: Transient analysis for the Flushing network. Consolidated Edison Company, New York, NY, Tech. Rep., Oct. 2011.
[61] Technical Computing Software Matlab, The MathWorks, Inc. [Online]. Available: http://www.mathworks.com.
[62] DCG-EMTP (Development Coordination Group of EMTP) Version EMTP-RV, Electromagnetic Transients Program [Online]. Available: http://www.emtp.com.

[63] Sabin, D.D., Dimitriu, C., Santiago, D. and Baroudi, G. (2009) Overview of an automatic underground distribution fault location system. IEEE PES General Meeting, Calgary, AB, Canada, 26–30 July 2009.
[64] Power Quality Instrumentation, PQNode, Dranetz [Online]. Available: http://dranetz.com
[65] O'Gorman, R. and Redfern, M. (2005) The impact of distributed generation on voltage control in distribution systems. 18th International Conference on Exhibit. Elect. Distrib. (CIRED), Turin, Italy, 6–9 June 2005.
[66] Kanicki, A. (2008) Voltage control in distribution systems, Chapter 3 in *Handbook of Power Quality* (ed. A. Baggini), John Wiley & Sons, Inc., Hoboken, NJ, pp. 59–77.
[67] Bollen, M.H.J. and Sannino, A. (2005) Voltage control with inverter-based distributed generation. *IEEE Transactions on Power Delivery*, **20**(1), 519–520.
[68] Viawan, F.A. and Karlsson, D. (2008) Voltage and reactive power control in systems with synchronous machine-based distributed generation. *IEEE Transactions on Power Delivery*, **23**(2), 1079–1087.
[69] Chiradeja, P. and Ramakumar, R. (2003) Voltage profile improvement with distributed wind turbine generation – a case study. IEEE PES General Meeting, Toronto, ON, Canada, 13–17 July 2003.
[70] de León, F. and Ooi, B.T. (2001) Damping power system oscillations by unidirectional control of alternative power generation plants. IEEE PES Winter Meeting, Columbus, OH, USA, 28 Jan.–1 Feb. 2001.
[71] Bae, I.S. and Kim, J.O. (2007) Reliability evaluation of distributed generation based on operation mode. *IEEE Transactions on Power Systems*, **22**(2), 785–790.
[72] Ayres, H.M., Freitas, W., De Almeida, M.C. and Da Silva, L.C.P. (2010) Method for determining the maximum allowable penetration level of distributed generation without steady-state voltage violations. *IET Generation, Transmission & Distribution*, **4**(4), 495–508.
[73] Dugan, R.C., McDermott, T.E. and Ball, G.J. (2001) Planning for distributed generation. *IEEE Industry Applications Magazine*, **7**(2), 80–88.
[74] Borges, C.L.T. and Falcao, D.M. (2003) Impact of distributed generation allocation and sizing on reliability, losses and voltage profile. IEEE Power Tech Conference, Bologna, Italy 23–26, June.
[75] Ochoa, L.F., Padilha-Feltrin, A. and Harrison, G.P. (2006) Evaluating distributed generation impacts with a multiobjective index. *IEEE Transactions on Power Delivery*, **21**(3), 1452–1458.
[76] Jenkins, N., Allan, R., Crossley, P. *et al.* (2000) *Embedded Generation*, 1st edn, Inst. Elect. Eng., London, UK.
[77] Quezada, V.H.M., Abbad, J.R. and Roman, T.G.S. (2006) Assessment of energy distribution losses for increasing penetration of distributed generation. *IEEE Transactions on Power Systems*, **21**(2), 533–540.
[78] Dugan, R.C. and McDermott, T.E. (2002) Distributed generation. *IEEE Industry Applications Magazine*, **8**(2), 19–25.
[79] Conti, S., Raiti, S. and Tina, G. (2003) Small-scale embedded generation effect on voltage profile: An analytical method. *Proc. Inst. Elect. Eng., Gen., Transm. Distrib.*, **150**(1), 78–86.
[80] Billinton, R. and Wojczynski, E. (1985) Distributional variation of distribution system reliability indices. *IEEE Transactions on Power Apparatus and Systems*, **104**(11), 3151–3160.
[81] Ran, X., Hong, T. and de León, F. Negative impact on reliability of distributed generation under temporary faults. Submitted to *IEEE Transactions on Power Delivery*.
[82] Liu, X., Chowdhury, A.A. and Koval, D.O. (2008) Reliability evaluation of a wind-diesel-battery hybrid power system. IEEE IAS Industrial and Commercial Power Systems Technical Conference (ICPS), Clearwater Beach, FL, USA, 4–8 May 2008.
[83] Abdullah, A.M. (2012) New method for assessment of distributed generation impact on distribution system reliability: Islanded operation. Innovative Smart Grid Technologies – Asia (ISGT Asia), Tianjin, 21–24 May, 2012.
[84] Pozzatti, L.F., Barin, A., Canha, L.N. *et al.* (2007) Simulation of transient state impacts from low power DG aiming at improving power quality and reliability of distribution networks. International Conference on Power Engineering, Energy and Electrical Drives (POWERENG), Setubal, Portugal, 12–14 April, 2007.
[85] Conti, S. (2009) Analysis of distribution network protection issues in presence of dispersed generation. *Electric Power Systems Research*, **79**(1), 49–56.
[86] Wang, D.Y., Jolly, M. and Lee, W.J. (2009) Policy and practice of distributed generation interconnection in the Con Edison distribution system. 8th International Conference on Advances Power Syst. Control, Oper. Manage. (APSCOM), Hong Kong, China, Nov. 8–11, 2009.
[87] Barker, P.P. and De Mello, R.W. (2000) Determining the impact of distributed generation on power systems. I. Radial distribution systems. IEEE PES Summer Meeting, Seattle, WA, USA, July 16–20, 2000.
[88] Falaghi, H. and Haghifam, M.R. (2005) Distributed generation impacts on electric distribution systems reliability: Sensitivity analysis. International Conference on Computer as a Tool (EUROCON), Belgrade, Serbia and Montenegro, Nov. 21–24, 2005.

[89] Fuangfoo, P., Lee, W.J. and Kuo, M.T. (2007) Impact study on intentional islanding of distributed generation connected to a radial subtransmission system in Thailand's electric power system. *IEEE Transactions on Industry Applications*, **43**(6), 1491–1498.

[90] Salcedo, R., Ran, X., de León, F. *et al.* (2013) Long duration overvoltages due to current backfeeding in secondary networks. *IEEE Transactions on Power Delivery*, **28**(4), 2500–2508.

[91] Feero, W.E. and Gish, W.B. (1986) Overvoltages caused by DSG operation: synchronous and induction generators power delivery. *IEEE Transactions on Power Delivery*, **1**(1), 258–264.

[92] Sun, Q., Li, Z. and Zhang, H. (2009) Impact of distributed generation on voltage profile in distribution system. International Joint Conference on Computational Sciences and Optimization (CSO), Sanya, Hainan, Chine, 24–26 April, 2009.

[93] Barker, P. (2002) Overvoltage considerations in applying distributed resources on power systems. IEEE PES Summer Meeting, Chicago, IL, USA.

[94] Chiradeja, P. and Ramakumar, R. (2004) An approach to quantify the technical benefits of distributed generation. *IEEE Transactions on Energy Conversion*, **19**(4), 764–773.

[95] Shayani, R.A. and de Oliveira, M.A.G. (2011) Photovoltaic generation penetration limits in radial distribution systems. *IEEE Transactions on Power Systems*, **26**(3), 1625–1631.

[96] Begovic, M., Pregelj, A., Rohatgi, A. and Novosel, D. (2001) Impact of renewable distributed generation on power systems. Proceedings of 34th Hawaii International Conference on Syst. Sci., Jan. 3–6, 2001, pp. 654–663.

[97] Keane, A., Ochoa, L.F., Vittal, E. *et al.* (2011) Enhanced utilization of voltage control resources with distributed generation. *IEEE Transactions on Power Systems*, **26**(1), 252–260.

[98] Keane, A. and O'Malley, M. (2007) Optimal utilization of distribution networks for energy harvesting. *IEEE Transactions on Power Systems*, **22**(1), 467–475.

[99] She, Y., She, X. and Baran, M.E. (2011) Universal tracking control of wind conversion system for purpose of maximum power acquisition under hierarchical control structure. *IEEE Transactions on Energy Conversion*, **26**(3), 766–775.

[100] Scollnik, D.P.M. (1996) An introduction to Markov Chain Monte Carlo methods and their actuarial applications. *Proc. of Casualty Actuarial Soc.*, **83**, 114–165.

[101] Casella, G. and George, E.I. (1992) Explaining the Gibbs sampler. *The American Statistician*, **46**(3), 167–174.

[102] IEEE Standard for Interconnecting Distributed Resources with Electric Power Systems. IEEE Standard 1547, 2003.

[103] (2006) *Handbook of General Requirements for Electrical Service to Dispersed Generation Customers*, Consolidated Edison Company of New York, Inc., New York.

[104] New York State Public Service Comm., New York State standardized interconnection requirements and application process for new distributed generators 2 MW or less connected in parallel with utility distribution systems. Dec. 2010.

[105] National Electrical Manufacturers Association (NEMA), American National Standards Institute (ANSI) C84.1-2006, Voltage ratings for electric power systems and equipment. Rosslyn, VA, 2006.

[106] Papoulis, A. and Pillai, S.U. (1965) *Probability, Random Variables and Stochastic Processes*, Vol. **196**, McGraw-Hill, New York.

[107] Ali, S.A. (2011) Capacitor banks switching transients in power systems. *Energy Science and Technology*, **2**(2), 62–73.

[108] Silfverskiold, S., Thottappillil, R., Ye, M. *et al.* (1999) Induced voltages in a low-voltage power installation network due to lightning electromagnetic fields: an experimental study. *IEEE Transactions on Electromagnetic Compatibility*, **41**(3), 265–271.

[109] Galvan, A., Cooray, V. and Thottappillil, R. (2001) A technique for the evaluation of lightning-induced voltages in complex low-voltage power installation networks. *IEEE Transactions on Electromagnetic Compatibility*, **43**(3), 402–409.

[110] Borghetti, A., Morched, A., Napolitano, F. *et al.* (2009) Lightning-induced overvoltages transferred through distribution power transformers. *IEEE Transactions on Power Delivery*, **24**(1), 360–372.

[111] Shareef, H., Khalid, S.N., Mustafa, M.W. and Mohamed, A. (2008) Modelling and simulation of overvoltage surges in low voltage systems. Power and Energy Conf. (PECon), Johor Bahru, Malaysia, 1–3 December, 2008.

[112] Orsagova, J. and Toman, P. (2009) Transient overvoltages on distribution underground cable inserted in overhead line. 20th International Conference on Exhibit. Elect. Distrib. (CIRED), Prague, Czech Republic, 8–11 June, 2009.

[113] Adibi, M.M., Alexander, R.W. and Avramovici, B. (1992) Overvoltage control during restoration. *IEEE Transactions on Power Systems*, **7**(4), 1464–1470.
[114] Chen, S. and Yu, H. (2010) A review on overvoltages in microgrid. Power and Energy Eng. Conf. Asia-Pacific (APPEEC), Chengdu, China, 28–31 Mar., 2010.
[115] Bickford, J.P. and Heaton, A.G. (1986) Transient overvoltages on power systems. *IEE Proceedings*, **133**(4), 201–225.
[116] Cerretti, A., Gatta, F.M., Geri, A. *et al.* (2012) Ground fault temporary overvoltages in MV networks: Evaluation and experimental tests. *IEEE Transactions on Power Delivery*, **27**(3), 1592–1600.
[117] Walling, R.A. and Melchior, R.D. (1995) Measurement of cable switching transients in underground distribution systems. *IEEE Transactions on Power Delivery*, **10**(1), 534–539.
[118] IEEE Standard for AC High-Voltage Circuit breakers rated on a Symmetrical Current basis–Preferred Ratings and Related Required Capabilities for Voltages Above 1000 V. IEEE Standard C37.06, 2009.
[119] Das, J.C. (2002) *Power System Analysis-Short-Circuit, Load Flow and Harmonics*, Marcel Dekker, New York.
[120] Greenwood, A. (1991) *Electrical Transients in Power Systems*, 2nd edn, John Wiley & Sons, Inc., New York.
[121] IEEE Guide for the Application of Neutral Grounding in Electrical Utility Systems, Part IV – Distribution. IEEE Standard C62.92.4, 1991.
[122] McMorran, A.W., Ault, G.W., Elders, I.M. *et al.* (2004) Translating CIM XML power system data to a proprietary format for system simulation. *IEEE Transactions on Power Systems*, **19**(1), 229–235.
[123] Irwin, G. and Woodford, D. (2003) E-Tran: Translation of load flow/stability data into electromagnetic transients programs. International Conference on Power Systems Transients (IPST), New Orleans, LA, USA, Sep. 28–Oct. 2, 2003.
[124] Santodomingo, R., Rodriguez-Mondéjar, J.A. and Sanz-Bobi, M.A. (2012) Using semantic web resources to translate existing files between CIM and IEC 61850. *IEEE Transactions on Power Systems*, **27**(4), 2047–2054.
[125] Mahseredjian, J., Saad, O. and Dennetière, S. (2009) Computation of power system transients: Modeling portability. IEEE PES General Meeting, Calgary, AB, Canada, 26–30 July, 2009.
[126] E-Tran User's Manual, [Online]. Available: http://www.electranix.com/E-Tran/E-Tran_Chap9_Theory.pdf.
[127] [Online]. Available: http://pscad.com/products/etran.
[128] [Online]. Available: http://www.electranix.com/E-Tran/index.htm.
[129] Spitsa, V., Czarkowski, D., de León, F. and Zabar, Z. (2012) PVL-EMTP Translator. Project Report, Polytechnic Institute of NYU, Brooklyn, New York, February 2012.
[130] Thiruvedhi, C.P.T. (2012) Modeling of Randall's Network in EMTP. Project Report, Polytechnic Institute of NYU, Brooklyn, New York, December 2012.
[131] Sandraz, J. (2012) ATP Modeling of 2500-Bus Power Grid Network for Transients Studies and Validated Topology. Project Report, Polytechnic Institute of NYU, Brooklyn, New York, December 2012.
[132] Simulation Tool – OpenDSS. [Online]. Available: http://smartgrid.epri.com/SimulationTool.aspx.
[133] IEEE Standard Common Format for Transient Data Exchange (COMTRADE) for Power Systems. IEEE Standard C37.111-1999, 1999.
[134] Common Information Model (CIM). [Online]. Available: http://dmtf.org/standards/cim.
[135] Filizadeh, S., Heidari, M., Mehrizi-Sani, A. *et al.* (2008) Techniques for interfacing electromagnetic transient simulation programs with general mathematical tools. *IEEE Transactions on Power Delivery*, **23**(4), 2610–2622.
[136] ATP –EMTP. [Online]. Available: http://www.emtp.org/
[137] European EMTP-ATP Users Group Association – Giga ATP MinGW. Available: http://www.eeug.org/files/secret/ATP_MingW32/gigmingw.zip
[138] European EMTP-ATP Users Group Association – ATP Rulebook. Available: http://www.eeug.org/files/secret/ATP_RuleBook/
[139] Peralta, J., de León, F. and Mahseredjian, J. (2011) Assessing the errors introduced by common assumptions made in power system studies. IEEE PES General Meeting, Detroit, MI, USA, July 2011.
[140] Power Quality Database Management and Analysis Software. PQView, Elektrotek Concepts.

13

Interfacing Methods for Electromagnetic Transient Simulation: New Possibilities for Analysis and Design

Shaahin Filizadeh

13.1 Introduction

Unprecedented growth in power demand combined with the advancements made in new technologies such as high-power electronics has greatly affected the size and complexity of modern power systems. The advent of power electronics and its dramatic progress in the past few decades, which has led to the realization of concepts such as HVDC and more recently FACTS, has contributed to hitherto unseen complexities. This trend will continue to dominate, as new technologies such as distributed generation and plug-in hybrid vehicles gain further popularity and become more prevalent.

The development of tools and techniques used for the analysis and design of today's sophisticated power systems needs to stay abreast with this rapid pace of change. Advanced computer simulation is a widely accepted approach for analysis and design of power systems. Power flow [1], transient stability [2], small signal stability [3] and electromagnetic transient (EMT) simulation [4] are well-known examples of typical simulation tools for various kinds of power system studies. Among these, EMT simulation offers the highest level of detail in modelling individual systems elements. An EMT simulation model is typically valid for frequencies of up to a few kHz [4], which allows us to representing nonlinear and switching elements [4–8].

While EMT simulators remain standard tools for the analysis of fast, short-term transients, it has recently been shown that interfacing these simulators to other mathematical algorithms is a viable approach for extending their existing capabilities not only for enhanced analysis but also for design of emerging power systems.

Interfacing allows the constituent components – the EMT simulator and the external algorithms/tools – to communicate in a specified manner in order to carry out the overall simulation cooperatively and more

Transient Analysis of Power Systems: Solution Techniques, Tools and Applications, First Edition.
Edited by Juan A. Martinez-Velasco.

efficiently. The level of cooperation between the interfaced tools can range from mere post-processing and visualization of simulation results [9] to relegating an integral part of the simulation to an external tool where specific analyses can be done more effectively than in the original simulation tool [10–12]. Interfacing opens up unprecedented possibilities as the new multiagent simulation platform will benefit from specific strengths of the individual algorithms, and it equips the user with an enhanced set of tools and procedures for detailed scrutiny of the problem at hand.

Interfacing is also an enabling approach to the development of the next generation of EMT simulators with extended capabilities for design. The conventional procedure for design of power systems using an EMT simulation program often requires a human expert to conduct several simulation runs before finalizing the design. These simulation runs are conducted for example to select suitable parameter values for a control system or to study the response of the designed system under different operating conditions. This trial and error approach tends to become overwhelmingly lengthy when dealing with large systems involving several parameters and various modes of operation. There is a growing trend towards developing design-support methods and algorithms to aid the designer when using EMT simulation programs. The conventional multiple-run simulation, which is a feature offered by many EMT simulation programs, is one such method [13,14]. Here a number of simulation runs are conducted automatically with pre-selected sequential or random parameter sets. Although multiple-run simulations relieve the search process to an extent by automating the parameter selection task, they are often excessively time-consuming because the selection of parameters for use in the sequence of simulations is done without taking advantage of the experience accumulated in previous simulations.

Interfacing EMT simulation programs with other mathematical algorithms, which has been proposed recently, can significantly improve the design procedure, not only by offering an extended set of design-support facilities, but also by enabling effective studies with a limited number of computationally expensive EMT simulations [15–17].

In the following sections, the chapter provides an overview of various interfacing methods and procedures for connecting an EMT simulator with an external algorithm. It will be followed by a review of the particular possibilities for using interfacing to create a design-ready EMT simulator. A glance at future developments and directions concludes the chapter.

13.2 Need for Interfacing

Commercially available EMT simulation tools include a fairly comprehensive library of components that allow the user to conveniently assemble a circuit for the purpose of simulation. These so-called library components may represent sources, electric machines, cables and transmission lines, semiconductor and power electronic devices and control and processing functions (e.g. comparators, transfer functions and integrators).

Despite the availability of standard library components, users often find that components for performing specialized computations are not readily available. Therefore, we need to extend the capabilities of EMT simulation programs by incorporating facilities for performing specialized computations. In commercial EMTP-type programs, such facilities are provided through enabling user-defined components and/or interfacing to other simulation software or programming languages [18–23].

Interfacing has been used for simulation of complex protection systems [24], development of advanced digital control systems [25] and simulation of power electronic converters using EMTP-TACS [26]. An interface that uses synchronizing clocks for connecting a simulation program with a real controller hardware is proposed in [27]. Attempts have also been made to develop simulation platforms in which multiple tools interact. Examples of interfaces between PSCAD/EMTDC and Matlab/Simulink are presented in [9, 28, 29]. A different interfacing method, in which an entire simulation is broken into smaller pieces is reported in [30] and is demonstrated using the CIGRE HVDC benchmark model [31]. In [15] a transient simulator is interfaced with a nonlinear simplex optimization algorithm written in Fortran to add optimization features to the simulator. A comprehensive example of interfacing between

a transient simulator and Matlab/Simulink and a comparison between EMTDC and Matlab/Simulink-PSB is presented in [32], in which the CIGRE HVDC benchmark model [31] is considered as the base network.

As well as EMT simulation tools, interfacing [33] has also been used for interconnecting electronic circuit simulators. Reference [34] presents Delight.Spice, which is an integration of Delight interactive optimization-based CAD system and Spice for circuit optimization. Reference [35] interfaces optimization routines written in Matlab with Saber circuit simulator. References [36, 37] show other examples of interfacing circuit simulation programs with optimization algorithms.

13.3 Interfacing Templates

The method used for interfacing EMTP-type tools with other algorithms and the level of complexity involved in doing so depend on the problem that it aims to solve. In the following subsections, a number of interfacing methods will be addressed.

13.3.1 Static Interfacing

Consider, for example, interfacing a transient simulator with an external agent in order to plot traces of simulated variables. Ordinarily, we need to establish a channel between the simulator and the plotting agent to send (in a unidirectional manner) data for the intended variables as they are obtained at each time-step. Note that no buffer is necessary to store past values, as data is sent to the plotting agent as it becomes available. And note that plotting every point on the simulated trace is not necessary, and plotting the waveform sampled at regular intervals (other than every time-step) still produces graphs of acceptable accuracy. Therefore, it is possible to lower the communication burden by calling the plotting algorithm at regular intervals with a width of N samples, thus expediting the task. The time-line in Figure 13.1 shows the procedure graphically for intermittent communication with an external algorithm. Static interfacing may be used for such purposes as plotting or computation of complex functions.

When a simulation case is assembled, the code sections pertaining to the components used are gathered, along with their control rules. Thus at every time-step, the code for each component is run only if its control rule so allows.

Static interfaces have been further categorized as on-line or off-line [9]. In an on-line interface, the transient simulation tool communicates with the external algorithm throughout the simulation, for example, in the visualization of simulated waveforms. In an off-line interface, an external tool is called, after the completion of the simulation, which does further processing on the simulated data. An external agent that performs statistical analysis of the simulation results falls into the category of off-line static interfacing.

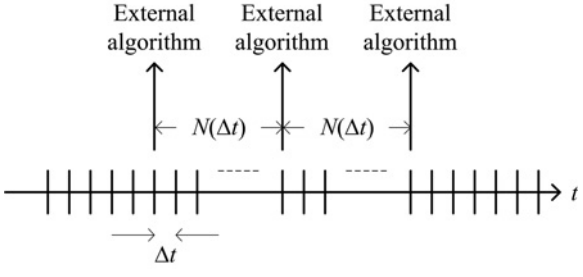

Figure 13.1 Static interface to an external algorithm.

13.3.2 Dynamic Interfacing and Memory Management

Dynamic interfaces are more involved than static ones, as memory management becomes an integral part of the interface. Processes that simulate dynamic elements, such as controllers or filters, come in this category. Unlike static interfaces, in which data only from the current time-step is communicated between the transient simulator and the interfaced algorithm, dynamic interfaces exchange current as well as past data.

As an example of a dynamic interface, consider a peak-detection component. The component is supposed to track a given signal $x(t)$ and find its peak value, and then update its output whenever a higher peak is detected. The peak-detector algorithm is shown below.

Algorithm 1 Peak detection.

```
1  If current simulation time (t)=0
2      PeakValue=x(0)
3      Output=PeakValue
4  Else
5      if x(t)>PeakValue
6          PeakValue=x(t)
7      End
8      Output=PeakValue
9  End
```

The algorithm uses a storage variable (PeakValue) to store the last peak detected. Although the algorithm is quite simple, its implementation requires access to memory location(s) that are kept intact from one time-step to the next. These memory segments are used for storing variables by components that need such storage, and transient simulation tools often provide access to this kind of storage for use in user-defined components.

An important issue when dealing with memory segments is to note that the pointers to memory locations should be updated and maintained in a unified manner. Since in each time-step, the simulation executes the code of individual elements in the order they are placed within the code, it is important to ensure that the stored variables can be retrieved properly. Properly incrementing the pointers guarantees that they always point to the correct memory locations for all components.

13.3.3 Wrapper Interfaces

A wrapper interface is one that does not communicate with the transient simulator on a regular basis throughout the simulation as static and dynamic interfaces do. Instead, it has limited communication at specific points in time, normally at the beginning and end of a simulation. This kind of interface is created when external code actually controls and steers the sequence of simulations. An example of this interface is given later, where optimization and run-control algorithms are discussed.

Note that a wrapper interface is different from an off-line one in that the wrapper interface is often a supervisory algorithm that controls the simulation program and normally performs multiple simulations, whereas an off-line interface is usually meant to perform post-processing of simulation results.

13.4 Interfacing Implementation Options: External vs Internal Interfaces

Once an algorithm is developed or selected for interfacing with a simulation tool, we need to decide where to implement the algorithm. Options for implementation are discussed below.

13.4.1 External Interfaces

For algorithms that are available externally through standalone software, external interfacing is normally the most logical option. Depending on the input/output configuration of the algorithm, external interfacing can potentially eliminate the need for rewriting the external code in the indigenous language of the simulation tool. Physical establishment of the interface requires access to the memory management routines of the transient simulator. An example of an external interface is interfacing an EMTP-type program to Matlab [23], which allows the user to store required variables in predefined locations, call Matlab to execute a standard or user-developed code and retrieve data back to the simulation program for further processing. The interface may allow execution of the external algorithm in each time-step or intermittently; therefore, both dynamic and static interfaces described earlier can be implemented externally.

An important observation about external interfacing is the speed implications involved. Transient simulation tools often use optimized methods for enhancing simulation speed. External programs, however, are not necessarily designed with such provisions. Therefore, a simulation tool that uses an interface with an external program can be drastically slower than the same procedure implemented entirely internally in the EMTP-type tool. Apart from the intrinsic speed differences between the two agents, the overhead of communication between the programs can also significantly affect the overall simulation performance. Unless high-speed, efficient communication methods are deployed, exchange of large amounts of data between the interfaced tools normally results in marked reductions in the speed. The problem will be exacerbated if the interface is used as part of a multirun simulation.

Depending on the facilities present in the externally interfaced tool, this type of interfacing can serve as a powerful means for rapid algorithm development, verification and debugging. It is sometimes easier to make changes to an algorithm developed in a dedicated external agent such as Matlab than one implemented in the rigidity of an EMTP-type program. Modifications can be easily done and tested through the combined interface. If the speed reduction due to external interfacing is severe, one can consider converting the external interface to an internal one (described below).

Another important aspect of external interfacing is the ability of interfacing to multiple platforms. For example, when an EMTP-type tool is interfaced with Matlab, other simulation tools (e.g. Simulink) or mathematical and programming tools (e.g. coding in multiple languages) may become available as well.

13.4.2 Internal Interfaces

A method of alleviating drawbacks associated with external interfaces is to use internal interfacing, where a user-supplied algorithm (unavailable in the transient simulation tool) is implemented within the transient simulator. Internal interfacing is possible when the user has access to the code of the algorithm and is knowledgeable about its inner workings.

Internal interfaces have been used for interfacing nonlinear optimization algorithms with transient simulators (described later). Dynamical models of electric vehicles [38], advanced switching schemes for power converters [39] and specialized motor drives and mechanical models for vehicular power systems [38, 40] have also been interfaced using internal interfacing mechanisms.

Note that internal interfaces are faster than external ones due to the elimination of the communication overhead. However, their implementation is normally more involved.

13.5 Multiple Interfacing

In addition to the main high-power electric circuitry, modern power equipment often contains advanced control blocks, digital processors, nonlinear elements and so on. Proper simulation of these systems must allow uncompromised analysis, and so it is sometimes necessary to interface more than two simulation programs, each with special features for detailed modelling of a certain portion of a complex circuit. In

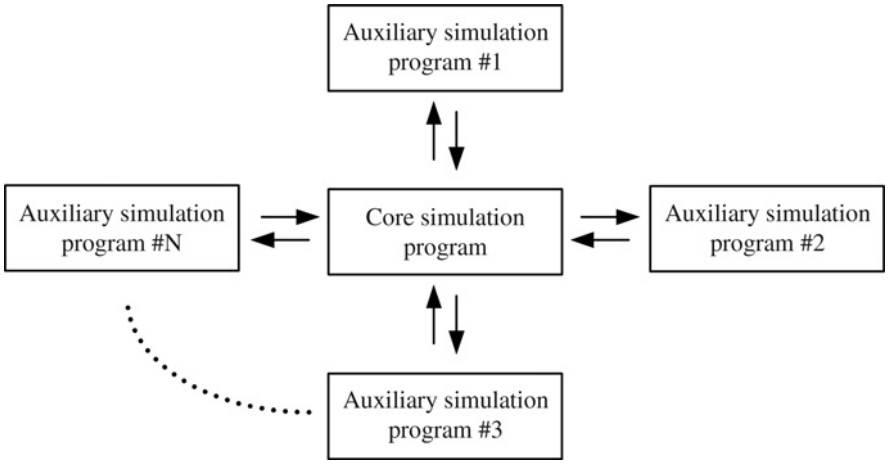

Figure 13.2 Core-type interfacing.

this section, some of the schemes for multiple interfacing of a transient simulation programs with other simulation programs or mathematical tools are explained. Variations of these schemes are obviously possible, although they are not discussed here.

13.5.1 Core-Type Interfacing

In core-type interfacing of simulation programs, one program serves as the core and all the other (auxiliary) programs are connected to the core. Figure 13.2 shows a block diagram of such a structure. The auxiliary programs in this structure can be implemented externally or internally and may manifest static, dynamic or wrapper properties as discussed earlier.

The core-type interfacing structure usually happens when a major portion of the system under study can be modelled in a single simulation program (the core) and the auxiliary programs are assigned minor tasks such as data visualization or other calculations. The firing pulse generation and visualization example shown later in the chapter is a core-type interface, in which generation of firing pulses and visualization tasks are assigned to auxiliary algorithms that communicate with the core simulator in which the main power circuit is simulated.

13.5.2 Chain-Type Interfacing

Unlike a core-type interface where the core program is used as a common node for all other programs, in chain-type interfacing the simulation programs are connected to each other in a row. There are two common templates for chain-type interfacing, as shown in Figure 13.3.

In the first scheme, Figure 13.3(a), chain-type interfacing is used for pre-processing and post-processing of the data. As an example, consider simulation of a network with transmission lines. Prior to simulating the network, an algorithm is often used to calculate the line constants to be used in the actual simulator (pre-processing). Visualization of the simulated data using a graphing program constitutes post-processing, and the entire scheme takes on the form of a chain-type interface.

A second variation of a chain-type interface, Figure 13.3(b), may be used when simulation programs cannot be interfaced directly and readily. An intermediate agent, such as Matlab, can be used to bridge the gap between originally incompatible simulators.

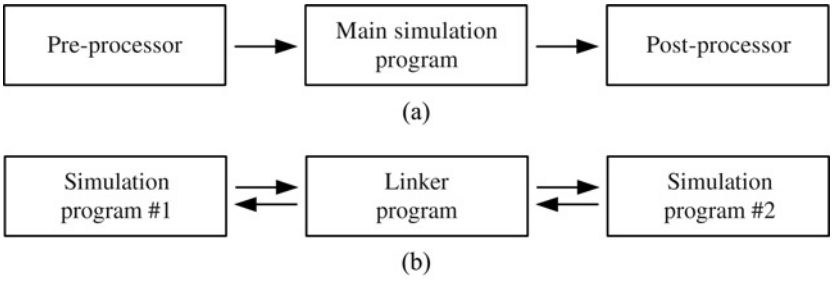

Figure 13.3 Variations of chain-type interfacing: (a) chain-type interfacing for pre- and post-processing, (b) chain-type interfacing for linking non-compatible simulators.

13.5.3 Loop Interfacing

If, in a chain of simulation programs or external hardware, the last program is also connected to the first one, the result will be a loop interfacing scheme – Figure 13.4. Such combinations occur frequently when real-time EMT simulators are connected to several interacting external pieces of equipment, such as relays, controllers, amplifiers and digital signal processors [41]. Since interfacing of real-time simulators is not the focus of this chapter, loop interfacing is not discussed in any further detail.

13.6 Examples of Interfacing

13.6.1 Interfacing to Matlab/Simulink

This section explains an interface made between a transient simulator (PSCAD/EMTDC) and Matlab/Simulink. Similar interfaces have also been made between EMTP and Matlab [23]. These interfaces can be used in a variety of ways, allowing full exploitation of the computational facilities in Matlab and modelling capabilities of Simulink.

The interface between the EMTP-type simulation engine and Matlab is essentially an external interface. The transient simulation engine can communicate with Matlab either in each time-step or intermittently, depending on the nature and requirements of the externally sourced task.

To interface with Matlab, the user needs to perform the tasks of (1) declaring memory requirements, (2) storing input variables to Matlab (transient simulator outputs), (3) calling Matlab and (4) receiving Matlab outputs and feeding them back to the simulator. In EMTDC, the subroutine MLAB_INT, which is

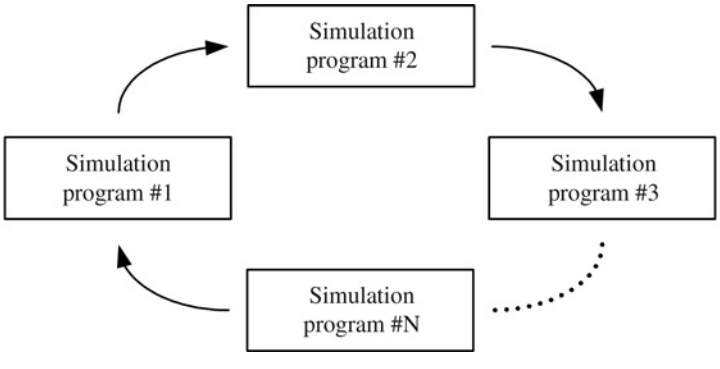

Figure 13.4 Loop interfacing scheme.

Step 1: Declare memory requirements

e.g., Nf floating point variables (Nf1 floating point inputs and Nf2 outputs)

Ni integers variable (Ni1 integer inputs and Ni2 integer outputs)

Step 2: Store inputs in respective storage queues

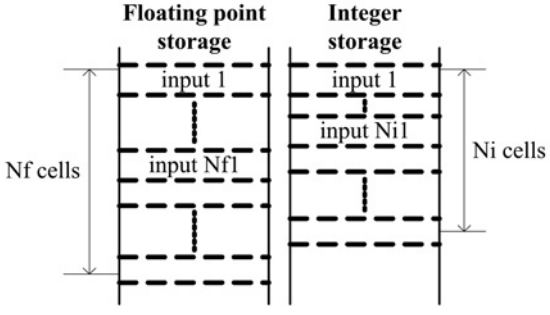

Step 3: Call MLAB_INT subroutine

Inputs: Matlab function name

Matlab function path

Type and size of inputs to the Matlab function

Type and size of outputs from Matlab function

Step 4: Store outputs in respective storage queues

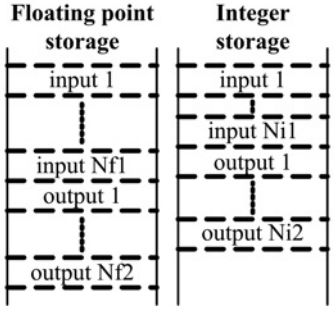

Figure 13.5 Sequence of events in the EMTDC/Matlab interface.

accessible by user-defined components, establishes the connection between the two agents. Exchange of data between the simulator and Matlab is administered through the use of data storage queues for storing floating-point, integer and other data types. Figure 13.5 shows a schematic diagram of the sequence of events that occur within the EMTDC/Matlab interface.

As shown, a number of memory storage locations equal to the total number of inputs and outputs communicated to and from Matlab is first declared. Inputs to the Matlab environment are placed in the respective storage locations, and then the Matlab interface subroutine is called, which reads the data from the memory locations and communicates them with the respective Matlab function.

Upon completion of the tasks in Matlab (this can include some Simulink models as well), the MLAB_INT returns the outputs to the remaining memory locations assigned for output storage. At this point, the transient simulator is able to access and read the outputs.

Note that the respective Matlab function may (1) contain user-developed algorithms, (2) call built-in Matlab functions, or (3) set up and call Simulink. Examples of such possibilities are presented in Section 13.7, where some interfacing cases are discussed.

13.6.2 Wrapper Interfacing: Run-Controllers and Multiple-Runs

Transient simulation tools are sometimes used in studies where multiple simulations are conducted. A number of parameters in the simulated network are varied sequentially or randomly (with a given distribution) and simulations are done in order to assess the impact of such parameter variations on the simulation results. Simulation results for a given set of parameter values are often distilled into a small number of indices that represent a figure-of-merit for the parameters used. For example, severity of a lightning-strike fault as a function of its location can be examined by conducting multiple simulations in which the fault location is varied along a given transmission line and the magnitude of the resulting voltage surge is recorded. EMTP-type tools often provide built-in engines for conducting multiple simulations using specified parameter variations [18].

The so-called multiple-run simulation can be described as in the following algorithm (Algorithm 2). As shown, the multiple-run algorithm is responsible for (1) selecting suitable parameter values according to the specified parameter variation rule, (2) feeding the simulation with the parameters and (3) recording the respective figure of merit for further processing.

Algorithm 2 Multiple-run simulations.

```
1   create a set of parameters Pi (a total of N points
    representing parameter combinations)
2   i=1
3   if i<=N
4       run the simulator with parameter set P(1)
5       record the figure-of-merit for P(1)
6       i=i+1
7   End
```

Note that pre-selection of parameter combinations in a sequential multiple run, or random selection with a given distribution resembles a passive approach to the true potential of the multiple-run algorithm. Through proper interfacing, however, we can design more advanced run-control algorithms to conduct multiple simulations in ways other than the conventional approach, where it is possible to steer future simulations based on the outcome of current and past simulations.

A wide range of opportunities is opened when wrapper interfaces are designed with the capability of steering the sequence of multiple simulations based on the cumulative history of previous simulations. These opportunities are particularly important in the design process using EMT simulators. In the following section, use of EMT simulators for design of complex networks and the role of interfacing in enabling design-ready EMT simulators is described.

13.7 Design Process Using EMT Simulation Tools

In a broad sense, we can identify parameter selection and uncertainty analysis as the major steps involved in a generic power system design problem. Parameter selection is the process in which suitable parameter values or other specifications are obtained for the designed component. The selection chiefly aims to

meet some desired objectives regarding the performance of the system; however, it may also take into account other considerations such as robustness or varying operating conditions.

Having found suitable parameter values, it is often necessary to perform a thorough uncertainty analysis to determine potential deviations in the system performance in the face of perceived tolerances and other sources of uncertainty that have not been directly considered in the initial parameter selection phase. A common source of uncertainty, for example, is the manufacturing tolerance of system components, which may cause deviations from their nominal values. Inevitable changes in the operating conditions of the system may also lead to some loss of performance, particularly for nonlinear systems.

13.7.1 Parameter Selection Techniques

Since EMT simulation programs enable the designer to simulate the system in great detail, they are extensively used in the initial phase of design, where suitable parameters need to be selected. The methods commonly used for parameter selection using EMT simulations are described below, with a view to highlighting the interfacing aspects in their architecture.

13.7.1.1 Trial and Error

Trial and error is the most basic, yet highly creative, approach to the parameter selection problem. Although it is repetitive and clearly not scientifically elegant, it is an approach that relies heavily on the designer's experience and intuition to start and steer the search properly and in a creative manner by scrutinizing the simulated results to assess the degree to which the design objectives are being met.

Note that the trial-and-error method may require a large number of experiments (i.e. EMT simulation runs) before a design can be finalized. It is therefore quite likely to be wasteful in terms of simulation time, and it also requires constant intervention by the designer. There is no need to interface the EMT simulator with any run-control algorithm in a trail-and-error design process.

13.7.1.2 Multiple-Run Simulation

Multiple-run (MR) EMT simulations, discussed previously, and shown in Figure 13.6, can improve this process by reducing human supervision. In each simulation run, system parameters are adjusted to values pre-selected randomly or sequentially. Desired system performance is defined in terms of quantities measurable using the simulated results and is measured for each set of parameter combinations. Following the completion of the entire simulations, the designer examines results and may use the parameter set that yields the closest match to the desired objectives. Development of the so-called objective function (see Figure 13.7) in terms of the desired and simulated behaviour is a creative task that relies on the designer's expertise and may require a few iterations before one that truly encapsulates the desired goals is formed.

It is apparent that the conventional MR method enhances the parameter selection by eliminating the need for designer intervention at every simulation run. However, it is noted that pre-selection of

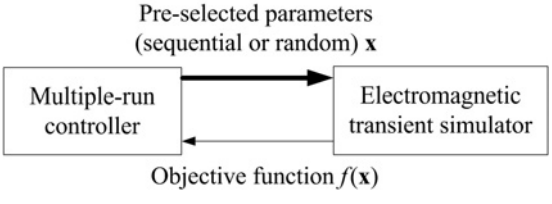

Figure 13.6 Schematic diagram of the multiple-run simulations.

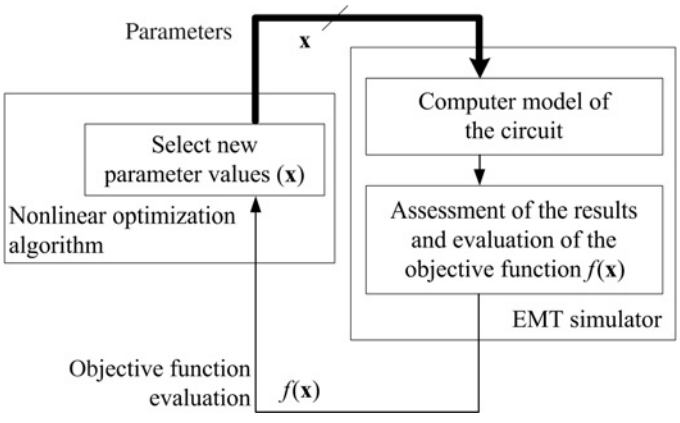

Figure 13.7 Schematic diagram of a simulation-based optimization tool.

parameter values for use in actual simulations is still inefficient because it will involve a large number of simulations in order to ensure that the search space is adequately covered and that the final results are of acceptable accuracy. In other words, the MR method may imply an unnecessarily long search process.

Intelligent algorithms have been proposed for conducting multiple simulations in a more efficient manner by avoiding search in areas that are not likely to yield any improvement. This is done by taking advantage of the cumulative experience of the past simulations in generating parameter sets for use in future simulations. In other words, parameters will not be blindly pre-selected but will rather be selected taking into consideration the closeness of previous simulated results to the desired objectives.

13.7.1.3 Simulation-Based Optimal Design

Nonlinear optimization algorithms can be interfaced with an EMT simulation program to take over the steering of multiple simulations. Schematically shown in Figure 13.7, the algorithm feeds the simulator with parameter values that are selected based on the objective function values calculated by the EMT simulator for the previously selected parameters.

Some aspects of uncertainty, such as robustness, can also be incorporated into the optimization-based parameter selection. Here the optimization is carried out with a view to minimizing an aggregate objective function that includes system performance for a wide range of operating conditions, as shown in Figure 13.8. This ensures a robust design, but does not constitute a formal and comprehensive approach to the sensitivity and uncertainly analysis, as robustness is only a small subclass of uncertainty issues.

13.7.1.4 Additional Considerations

When dealing with optimization in the EMT simulation loop for tuning of system parameters, questions arise as to whether the optimal parameters represent a local or the global optimum.

Since the simulation of the network is used for evaluation of the objective function, this falls within a category of optimization problems commonly referred to as black-box optimization. In general, there is no universal rule for determining whether the underlying optimization problem is unimodal, that is, there is only one global optimum, or multimodal, where multiple local minima exist. As long as desired objectives are met by the parameter set obtained by the optimization algorithm it should not matter whether the set is a local minimum or the global one. However, in cases where objectives such as lowest cost are sought, it is essential that the global minimum be found, which may require specialized

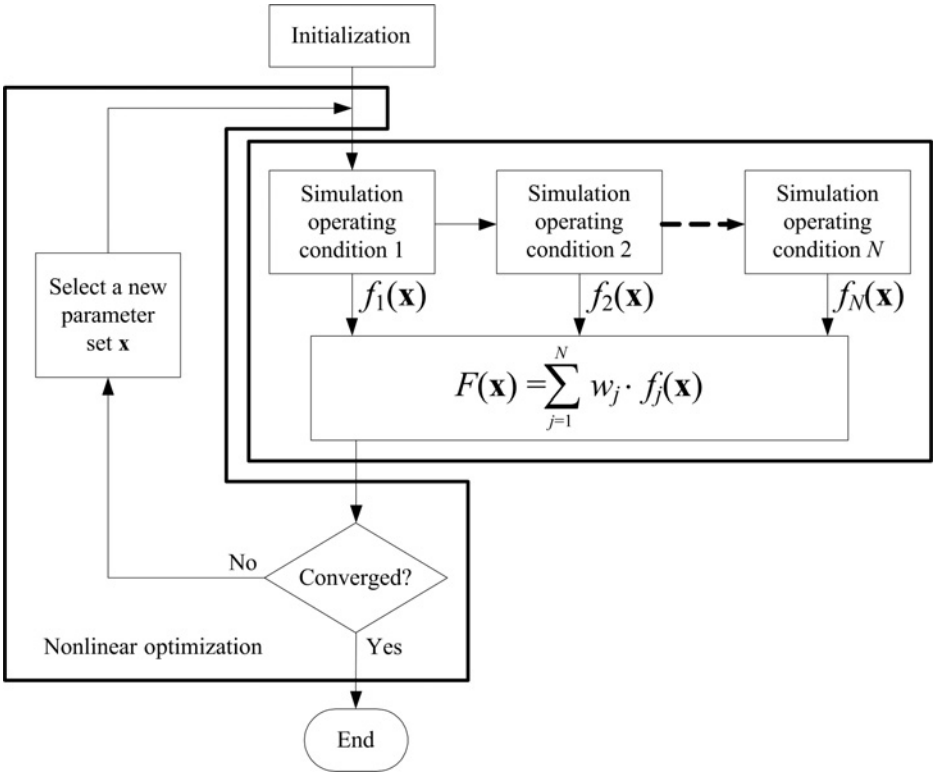

Figure 13.8 Schematic diagram of a robust optimization interface.

optimization algorithms. Regardless of the objectives, however, it seems that the majority of conventional optimization algorithms can be interfaced with an EMT simulator.

A significant benefit of the parameter selection through interfacing with a nonlinear optimization algorithm is the reduction of the number of simulation runs. It is often observed that the design cycle using optimization is orders of magnitude faster than one relying only on primitive multiple-run simulations.

It is sometimes observed that simulation-based optimization for design does not provide an entirely acceptable result merely after the first round of optimization. There are often unforeseen details that arise when optimized results are assessed. This usually leads to subsequent cycles of optimization where the objective function is refined to fittingly capture designer's objective. This is due to the simple fact that the optimization algorithm gives what the designer asks for. It is the designer's responsibility to formulate the objectives correctly and precisely in a mathematically objective function.

13.7.2 Uncertainty Analysis

Uncertainty analysis is the second stage of a design problem, following the initial stage of parameter selection. The purpose of uncertainty analysis is to study the impact of tolerances and uncertainties that have been ignored in the parameter selection phase. Note that parameter selection may itself be done with a view to eliminating or reducing the effects of some certain types of uncertainties. As noted earlier, varying operating conditions are a source of uncertainty that can be taken into account during the parameter selection phase by the process of robust optimization. Addressing other sources of uncertainty, however, may not be straightforward and their impact should be studied following the parameter selection stage.

Component manufacturing tolerances and aging are two common sources of uncertainty that affect the performance of a design, whether or not it is optimized. Digital implementation of control systems improves the accuracy and robustness of optimized control system parameters; however, it introduces concerns about the resolution of signals converted between analogue to digital. Independent of the control system parameters, component values still remain vulnerable to manufacturing tolerances.

EMT simulation programs interfaced with suitable mathematical algorithms provide effective tools for the analysis of uncertainties. Given the fact that complex systems cannot be readily expressed in terms of mathematical equations in enough detail, a simulation-based approach is often the only viable option for uncertainty analysis. In the following subsections, a few types of studies that fall under the umbrella of uncertainty analysis and can be done through interfaced EMT simulators are addressed. Note that there are limited standard definitions for the following studies and they are sometimes treated slightly differently or interchangeably by different researchers.

13.7.2.1 Tolerance Analysis

Tolerance analysis aims to determine the expected range of the variations of a given performance index, given tolerance bands of parameters. It is apparent that we cannot truly remove the statistical information of how parameters change within their tolerance bands from the tolerance analysis. However, in lieu of a formal and usually time-consuming statistical analysis, we can choose to conduct a relatively crude tolerance analysis by removing the statistical variations of the parameters, and by considering the extremities of parameter boundaries only.

Consider a performance index function $f(\mathbf{x})$, where $\mathbf{x} = (x_1, x_2, \dots, x_n)$. If x_i is allowed to vary within $[x_{i\text{-}min}, x_{i\text{-}max}]$, there are n^2 different combinations of extreme values; evaluation of the function for these combinations can be used to find an interval $[f_{min}, f_{max}]$, which specifies the expected range of variation for the performance index when individual parameters are allowed to vary within their tolerance intervals. Note that this is only valid when the performance index function has a quadratic (or generally unimodal) behaviour around its nominal value. While in general there is no guarantee that a given performance index has such behaviour, it holds true for optimized functions, for which a quadratic approximation is often attainable around the optimum and for a small range of parameter variations.

13.7.2.2 Statistical Analysis

Statistical analysis is the formal approach to investigating the variations of a given performance index including the statistical variations of the parameters for both optimized and non-optimized systems.

Monte-Carlo methods are widely used for conducting such analyses. A mathematical algorithm selects random samples of individual parameters within their specified tolerance intervals and according to their probability density function, and it combines the samples into an input vector $\mathbf{x}$, which is then fed into the EMT simulator. A large number of EMT simulations are often required to obtain an acceptable representation of the statistical behaviour for the performance index. Note that since statistical properties are included, and samples are taken from the entire interval, restrictions on unimodality of the function and small variation intervals are removed. The results obtained are highly accurate, but the computational intensity of the algorithm is commensurately high.

13.7.2.3 Tolerance Determination

An important design question is to determine how much tolerance in parameter values is allowed if the designer is willing to accept a certain amount of deviation in the performance index. This is the reverse problem to the tolerance analysis, and its outcome can be used to select components that have a certain amount of tolerance.

13.7.2.4 Additional Considerations

While the use of an EMT simulation tool is inevitable in the design of complex systems, it is desirable to develop methods to lower the computational burden of the process by reducing the number of required EMT simulations. Simulation-based optimization described earlier is a design-support tool with a reduced burden. There has been a growing trend towards making improved design-support tools for the post-optimization task of uncertainty analysis as well.

Since uncertainty analysis is essentially carried out for a small range of parameter variations, it has been suggested that the EMT tool be used to develop a locally acceptable model of the underlying complex system; such a 'surrogate model' will then be used instead of the actual EMT simulation model of the system. Note that the success of the surrogate model in representing the system depends on the complexity of the system around the operating point of interest and also the adequacy of the form of the surrogate model to match the original function.

A method based on using an EMT simulator to form a second-order approximation of a performance index is proposed in [17]; this closed-form mathematical approximation replaces the expensive EMT simulation of the network and allows the designer to assess the tolerance effects without recourse to time-consuming simulations. Figure 13.9 shows a schematic diagram of the interfaced tool that calculates first- and second-order derivatives of the performance index using EMT simulations.

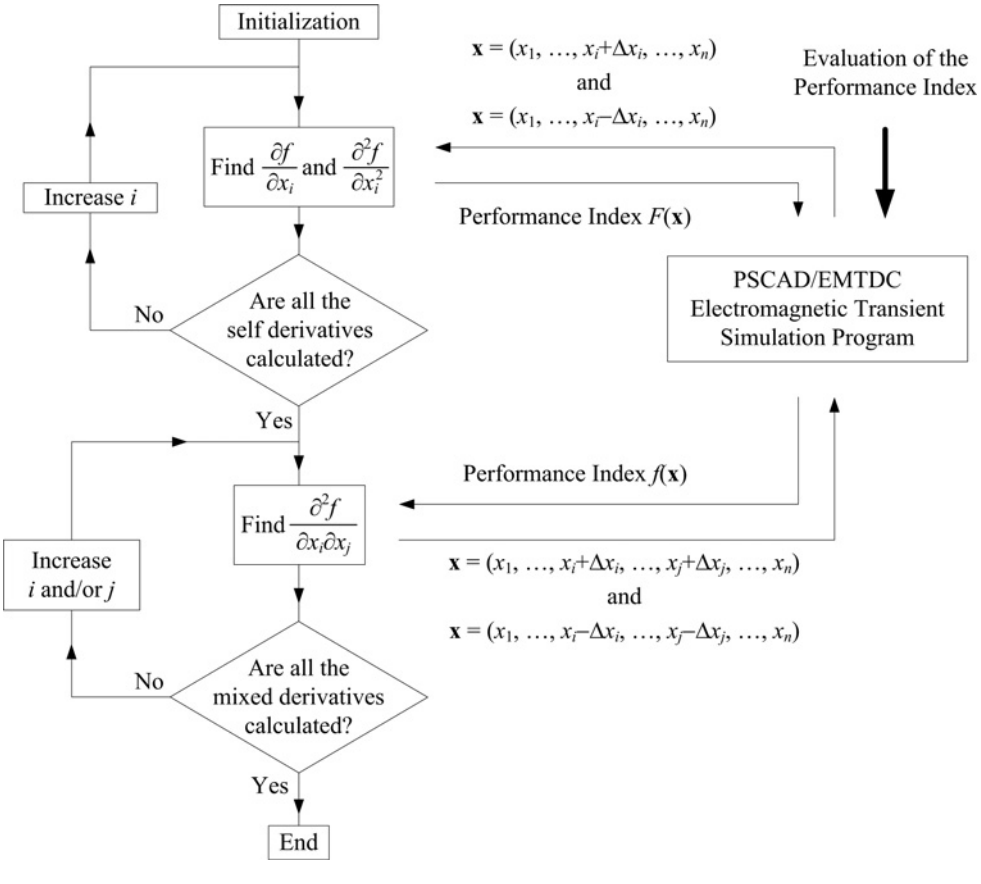

Figure 13.9 Surrogate model formation tool.

13.8 Conclusions

The chapter has described the principles and methods of the analysis and design of complex power systems using electromagnetic transient simulation tools that are interfaced with external mathematical algorithms. A suitably designed algorithm can be employed to intelligently conduct multiple simulations of a system using an EMT tool. The intelligence of the algorithm often reduces the number of simulations required and provides the designer with pre-processed information that will assist in making decisions.

References

[1] Stott, B. (1974) Review of load-flow calculation methods. *Proceedings of IEEE*, **62**(7), 916–929.
[2] Ao, Z., Fleming, R.J. and Sidhu, T.S. (1995) A transient stability simulation package (TSSP) for teaching and research purposes. *IEEE Transactions on Power Systems*, **10**(1), 11–17.
[3] Kundur, P., Rogers, G.J., Wong, D.Y. *et al.* (1990) A comprehensive computer program package for small signal stability analysis of power systems. *IEEE Transactions on Power Systems*, **5**(4), 1076–1083.
[4] Dommel, H.W. (1969) Digital computer solution of electromagnetic transients in single and multiphase networks. *IEEE Transactions on Power Apparatus and Systems*, **88**(4), 388–399.
[5] Sood, V.K. and Gole, A.M. (1990) A static compensator model for use with electromagnetic transients simulation programs. *IEEE Transactions on Power Delivery*, **5**(3), 1398–1407.
[6] Jiang, S., Annakkage, U.D. and Gole, A.M. (2006) A platform for validation of FACTS models. *IEEE Transactions on Power Delivery*, **21**(1), 484–491.
[7] Woodford, D.A., Gole, A.M. and Menzies, R.W. (1983) Digital simulation of DC links and AC machines. *IEEE Transactions on Power Apparatus and Systems*, **102**(6), 1616–1623.
[8] Filizadeh, S. and Gole, A.M. (2005) Harmonic performance analysis of an OPWM-controlled STATCOM in network applications. *IEEE Transactions on Power Delivery*, **20**(2, Part 1), 1001–1008.
[9] Gole, A.M., Demchenko, P., Kell, D. and Irwin, G.D. (1999) Integrating electromagnetic transient simulation with other design tools. Proceedings of International Conference on Power Systems Transients (IPST' 99), Budapest, Hungary, June 1999.
[10] Mahseredjian, J. (2000) Merging, prototyping and hybrid tools for power system transient simulation. Proceedings of Power Engineering Society Summer Meeting, Seattle, WA, July 2000.
[11] Wang, X., Wilson, P.L. and Woodford, D. (2002) Interfacing transient stability program to EMTDC program. Proceedings of International Conference on Power System Technology, Kunming, China, October 2002.
[12] Zavahir, J.M., Arrillaga, J. and Watson, N.R. (1993) Hybrid electromagnetic transient simulation with the state variable representation of HVDC converter plant. *IEEE Transactions on Power Delivery*, **8**(3), 1591–1598.
[13] Gole, A.M. (2006) Electromagnetic transient simulation of power electronic equipment in power systems: Challenges and solutions. Proceedings of Power Engineering Society Summer Meeting, Montreal, Canada, June 2006.
[14] Martinez, J.A. and Martin-Arnedo, J. (2003) Expanding capabilities of EMTP-like tools: From analysis to design. *IEEE Transactions on Power Delivery*, **18**(4), 1569–1571.
[15] Gole, A.M., Filizadeh, S., Menzies, R.W. and Wilson, P.L. (2005) Optimization-enabled electromagnetic transient simulation. *IEEE Transactions on Power Delivery*, **20**(1), 512–518.
[16] Filizadeh, S. and Gole, A.M. (2005) A gradient based approach for power system design using electromagnetic transient simulation programs. Proceedings of International Conference on Power Systems Transients (IPST' 05), Montreal, Canada, June 2005.
[17] Heidari, M., Filizadeh, S. and Gole, A.M. (2008) Support tools for simulation-based optimal design of power networks with embedded power electronics. *IEEE Transactions on Power Delivery*, **23**(3), 1561–1570.
[18] EMTDC Manual, Manitoba HVDC Research Centre, April 2004.
[19] Dessaint, L.A., Al-Haddad, K., Le-Huy, H. *et al.* (1999) A power system simulation tool based on Simulink. *IEEE Transactions on Industrial Electronics*, **46**(9), 1252–1254.
[20] Gole, A.M., Fernando, I.T., Irwin, G.D. and Nayak, O.B. (1997) Modeling of power electronic apparatus: Additional interpolation issues. Proceedings of International Conference on Power Systems Transients (IPST' 97), Seattle, WA, June 1997.
[21] Watson, N. and Arrillaga, J. (2002) *Power Systems Electromagnetic Transients Simulation*, IEE.

[22] Dubé, L. and Dommel, H.W. (1977) Simulation of control systems in an electromagnetic transients program with TACS. Proceedings of IEEE PICA, 1977, pp. 266–271.
[23] Mahseredjian, J., Benmouyal, G., Lombard, X. *et al.* (1998) A link between EMTP and Matlab for user-defined modeling. *IEEE Transactions on Power Delivery*, **13**(2), 667–674.
[24] Kezunovic, M. and Chen, Q. (1997) A novel approach for interactive protection system simulation. *IEEE Transactions on Power Delivery*, **12**(2), 668–674.
[25] Bui, L.X., Casoria, S., Moin, G. and Reeve, J. (1992) EMTP TACS-Fortran interface development for digital controls modeling. *IEEE Transactions on Power Systems*, **7**(1), 314–319.
[26] Mahseredjian, J., Lefebvre, S. and Mukhedkar, D. (1991) Power converter simulation module connected to the EMTP. *IEEE Transactions on Power Systems*, **6**(2), 501–510.
[27] Reeve, J. and Lane-Smith, S.P. (1990) Integration of real-time controls and computer programs for simulation of direct current transmission. *IEEE Transactions on Power Delivery*, **5**(4), 2047–2053.
[28] Wild, G., Messner, H., Moosburger, A. *et al.* (1997) An integrated simulation and control implementation environment. Proceedings of International Conference on Power Systems Transients (IPST 97), Seattle, WA, June 1997.
[29] Gole, A.M. and Daneshpooy, A. (1997) Toward open systems: A PSCAD/EMTDC to Matlab interface. Proceedings of International Conference on Power Systems Transients (IPST 97), Seattle, WA, June 1997.
[30] Strunz, K. and Carlso, E. (2007) Nested fast and simultaneous solution for time-domain simulation of integrative power-electric and electronic systems. *IEEE Transactions on Power Delivery*, **22**(1), 277–287.
[31] Szechtman, M., Wess, T. and Thio, C.V. (1991) First benchmark model for HVDC control studies. *Electra* (135), 54–73.
[32] Faruque, M.O., Zhang, Y. and Dinavahi, V. (2006) Detailed modeling of CIGRE HVDC benchmark system using PSCAD/EMTDC and PSB/Simulink. *IEEE Transactions on Power Delivery*, **21**(1), 378–387.
[33] Filizadeh, S., Heidari, M., Mehrizi-Sani, A. *et al.* (2008) Techniques for interfacing electromagnetic transient simulation programs with general mathematical tools. *IEEE Transactions on Power Delivery*, **23**(4), 2610–2622.
[34] Nye, W., Riley, D.C., Sangiovanni-Vincentelli, A. and Tits, A.L. (1988) Delight.Spice: An optimization-based system for the design of integrated circuits. *IEEE Transactions on Computer-Aided Design Integrated Circuits System*, **7**(4), 501–519.
[35] Kragh, H., Blaabjerg, F. and Pedersen, J.K. (1998) An advanced tool for optimized design of power electronic circuits. Proceedings of IEEE Industry Applications Conference, St. Louis, MO, October 1998.
[36] Rigbers, K., Schroder, S., Durbaum, T. *et al.* (2004) Integrated method for optimization of power electronic circuits. Proceedings of 35th Annual IEEE Power Electronics Specialists Conference (PESC' 2004), Aachen, Germany, June 2004.
[37] Conn, A.R., Coulman, P.K., Haring, R.A. *et al.* (1998) JiffyTune: Circuit optimization using time-domain sensitivities. *IEEE Transactions on Computer-Aided Design Integr. Circuits Syst.*, **17**(12), 1292–1309.
[38] Northcott, D.R. and Filizadeh, S. (2007) Electromagnetic transient simulation of hybrid electric vehicles. Proceedings of IEEE International Symposium on Industrial Electronics (ISIE' 07), Vigo, Spain, June 2007.
[39] Mehrizi-Sani, A., Filizadeh, S. and Wilson, P.L. (2007) Harmonic and loss analysis of space-vector modulated converters. Proceedings of International Conference on Power Systems Transients (IPST 07), Lyon, France, June 2007.
[40] Chevrefils, A. and Filizadeh, S. (2007) Transient simulation of an AC synchronous permanent magnet motor drive for an all-electric all-terrain vehicle. Proceedings of IEEE Vehicle Power and Propulsion Conference, Arlington, TX, September 2007.
[41] Kezunovic, M., Domaszewicz, J., Skendzic, V. *et al.* (1996) Design, implementation and validation of a real-time digital simulator for protection relay testing. *IEEE Transactions on Power Delivery*, **11**(1), 158–164.

Annex A

Techniques and Computer Codes for Rational Modelling of Frequency-Dependent Components and Subnetworks

Bjørn Gustavsen

A.1 Introduction

Several power system components, such as overhead lines, underground cables and power transformers, are characterized by strongly frequency-dependent effects in their behaviour. The accurate simulation of electromagnetic transients [1] requires us to take the frequency dependency into account. One way of modelling such components is by characterizing their behaviour in the frequency domain, followed by a model extraction procedure. The use of rational functions is an essential ingredient in such modelling as it leads to highly efficient time-domain simulations [2].

Since most difficulties in frequency-dependent modelling of overhead lines and underground cables have been overcome these days [3–5], this annex focuses on the modelling of terminal equivalents from tabulated data. Here, significant challenges remain. Typical applications include modelling of subnetworks by frequency-dependent network equivalents [6, 7] and high-frequency transformer modelling [8, 9]. We first list the rational fitting methods that have been traditionally applied within the power systems area, and we describe the basic steps for including a rational model in a circuit simulator. We next describe a very powerful method for 'fitting' a rational function to the data, known as vector fitting [10]. A perturbation method [11] is described, which is capable of enforcing passivity of the model, thereby guaranteeing the stability of time-domain simulations. We next describe a freely available computer implementation of the above methods. Finally, the application of the software is demonstrated for high-frequency modelling of a transformer starting from frequency sweep measurements.

Transient Analysis of Power Systems: Solution Techniques, Tools and Applications, First Edition.
Edited by Juan A. Martinez-Velasco.

A.2 Rational Functions

A rational function can in the frequency domain be expressed in alternative forms, including:

- Polynomial form, see (A.1)
- Pole-zero form, see (A.2)
- Pole-residue form, see (A.3)
- State-space form, see (A.4):

$$f(s) = \frac{a_0 + a_1 s + \cdots a_n s^N}{1 + b_1 s + \cdots b_n s^N} \tag{A.1}$$

$$f(s) = k\frac{\prod_{m=1}^{N}(s - z_m)}{\prod_{m=1}^{N}(s - a_m)} \tag{A.2}$$

$$f(s) = \sum_{m=1}^{N} \frac{r_m}{s - a_m} + r_0 \tag{A.3}$$

$$f(s) = \mathbf{c}^T(s\mathbf{I} - \mathbf{A})^{-1}\mathbf{b} + r_0 \tag{A.4}$$

The problem at hand is to calculate the rational function $f(s)$, such that it approximates a given frequency response $h(s)$ as closely as possible.

$$f(s) \cong h(s) \tag{A.5}$$

This process is often referred to as "fitting".

A.3 Time-Domain Simulation

The motivation for using rational functions is twofold. It allows direct transformation from the frequency domain into the time domain, and it leads to highly efficient simulations in the time domain via recursive convolution [2]. For instance, with the pole-residue form (A.3), each term leads directly to the exponential form (A.5) for the time-domain impulse response, and the convolution between the impulse response and an input can with a fixed time-step be expressed by the *recursive convolution* form (A.6) [12]. The formulation (A.6) can be interfaced to EMTP-type programs via a Norton equivalent, where the current source is updated in each time-step. An alternative procedure is to generate an *equivalent lumped circuit* in an EMTP-type netlist [6, 13]. The latter approach, however, often produces large circuits and is less efficient than the recursive convolution approach:

$$f(s) = \sum_{m=1}^{N} \frac{r_m}{s - a_m} \rightarrow f(t) = \sum_{m=1}^{N} r_m e^{a_m t} \tag{A.6a}$$

$$y(t) = f(t) * u(t) \rightarrow \begin{cases} x_n = \alpha x_{n-1} + u_{n-1} \\ y_n = \beta x_n + \gamma u_n \end{cases} \tag{A.6b}$$

A.4 Fitting Techniques

A.4.1 Polynomial Fitting

Rational fitting (A.5) can in principle be easily done via the polynomial form (A.1) by multiplying with the denominator. This leads to the following linear least-squares (LS) problem:

$$\left(1 + b_1 s + \cdots b_n s^N\right) h(s) \cong a_0 + a_1 s + \cdots a_n s^N \tag{A.7}$$

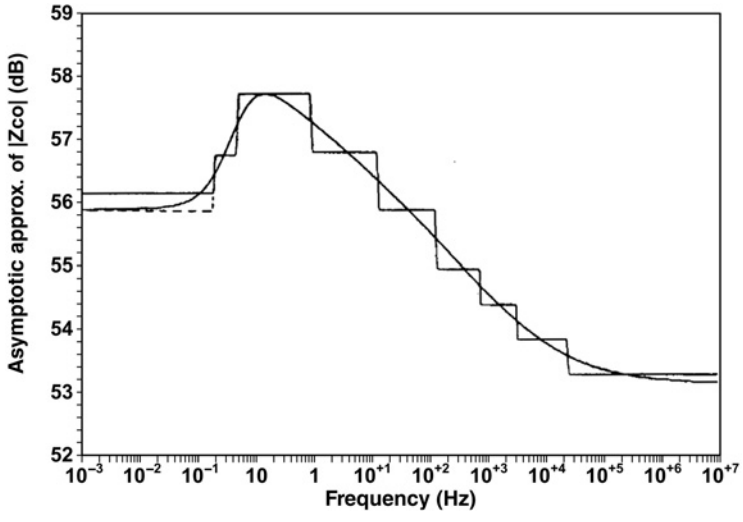

Figure A.1 J Martí fitting of rational function asymptotes to magnitude (Taken from [16]).

Direct solving of (A.7) leads to an approximation which is strongly biased. Although the biasing can be removed via reweighting (Sanathanan–Koerner iteration [14]), the method is troubled with effects of numerical ill-conditioning, which often limits its application to problems of low order and small bandwidths.

A.4.2 Bode's Asymptotic Fitting

In the case of frequency responses that are smooth and of minimum phase shift type, a quite accurate model can be obtained by fitting the magnitude function and using real poles and zeros in the left half-plane. This allows the fitting process to be based on the asymptotes of the rational function on the pole-zero form (A.2) [15]. The fitting process was automated by J.R. Martí [3] in 1982 for application to travelling-wave type transmission line modelling. Starting from a low frequency, a pole/zero is added when the asymptote departs by a positive/negative amount higher than a predefined tolerance – see Figure A.1. Finally, the zero locations are adjusted iteratively to improve the accuracy of the final result. The method has proved to be robust and usually sufficiently accurate. More importantly, it avoids the numerical problems associated with polynomial formulations. It is still in use in several EMTP-type programs for frequency-dependent modelling of transmission lines by the travelling wave method.

A.4.3 Vector Fitting

More general fitting approaches are those based on vector fitting (VF) [10]. These iterative methods are applicable to both smooth and non-smooth data as the fitter will automatically produce real and/or complex poles and residues as needed. VF relocates a set of initial poles to better positions by solving a linear equation (A.8) with known poles, $\{a_m^{(i)}\}$, with i denoting the ith iteration. It can be shown that the zeros of $\sigma(s)$ approach the poles $\{a_m\}$ of $h(s)$, provided that a good approximation of (A.8) exists. The zeros are computed by solving the eigenvalue problem (A.9) with matrices established from the rational model of $\sigma(s)$. By replacing the poles with new poles, a better set of poles is achieved such that

$\{a_m^{(i)}\} \rightarrow \{a_m\}$. Stability of the poles is ensured by flipping any unstable pole into the left half-plane. Finally, the unknown residues are calculated by solving (A.8) with $\sigma(s)$ equal to unity:

$$\overbrace{\left(\sum_{m=1}^{N} \frac{\tilde{r}_m}{s - a_m^{(i)}} + 1\right)}^{\sigma(s)} h(s) \cong \sum_{m=1}^{N} \frac{r_m}{s - a_m^{(i)}} + r_0 \tag{A.8}$$

$$z = eig(\mathbf{A} - \mathbf{bc}^T) \tag{A.9}$$

In the actual implementation, all poles and residues are forced to be real or to come in complex conjugate pairs.

VF can also be applied to a vector of elements (hence its name), which results in all elements in the vector becoming fitted with a common pole set. By stacking the upper (or lower) triangle of a matrix **H** in a single vector and subjecting it to VF, a symmetrical and stable pole-residue model (A.10) is obtained:

$$\mathbf{H}(s) \cong \sum_{m=1}^{N} \frac{\mathbf{R}_m}{s - a_m} + \mathbf{R}_0 \tag{A.10}$$

Several improvements have been made to the original VF formulation in [10], including:

- relaxation of the non-triviality constraint in order to achieve faster convergence and less biasing [17]
- orthonormalization of basis functions in order to reduce sensitivity to initial poles [18]
- fast implementation [19] when applied to vector of elements
- modal formulation, which maintains the relative accuracy of the eigenvalues of a matrix **H**, via inverse weighting [20].

In addition, VF has been extended for use with responses in the time domain [21] and the z-domain [22].

In this annex we apply a variant of VF, which uses a combination of relaxation and fast implementation – the fast relaxed vector fitting (FRVF).

A.5 Passivity

Although a model extracted by VF has stable poles only, the model may still yield unstable results when included in a time-domain simulation. This is because the model may generate power under certain terminal conditions, since VF does not guarantee the *passivity* of the extracted model. Passivity can, however, be enforced by a post-processing step, as described below.

We will assume that the model is formulated in terms of admittance parameters and a pole-residue model, which defines the relation between terminal voltages **v** and terminal currents **i**,

$$\mathbf{i}(s) = \mathbf{Y}(s)\mathbf{v}(s) \tag{A.11}$$

with

$$\mathbf{Y}(s) = \sum_{m=1}^{N} \frac{\mathbf{R}_m}{s - a_m} + \mathbf{R}_0. \tag{A.12}$$

When the extracted model (A.12) is symmetrical, passivity implies the real part of $\mathbf{Y}$ has positive eigenvalues, that is,

$$eig(\mathrm{Re}\{\mathbf{Y}(s)\}) > 0. \tag{A.13}$$

The passivity can be enforced [11] by perturbing the residues of the model while minimizing the change to its behaviour (A.14a), such that the passivity condition (A.14b) is satisfied:

$$\mathbf{\Delta Y} = \sum_{m=1}^{N} \frac{\Delta \mathbf{R}_m}{s - a_m} + \Delta \mathbf{R}_0 \cong \mathbf{0} \tag{A.14a}$$

$$eig\left(\mathrm{Re}\left\{ \mathbf{Y} + \sum_{m=1}^{N} \frac{\Delta \mathbf{R}_m}{s - a_m} + \Delta \mathbf{R}_0 \right\} \right) > 0 \qquad \forall s \tag{A.14b}$$

Equation (A.14a) is cast in the form of a linear problem $\mathbf{A}_{sys}\,\Delta\mathbf{x} \cong 0$, while (A.14b) is formulated as a linear constraint $\mathbf{B}_{sys}\,\Delta\mathbf{x} < \mathbf{c}$ via first-order eigenvalue perturbation [11]. The actual solving of (A.14) [11] can be done using quadratic programming (A.15):

$$\min_{\Delta\mathbf{x}} \frac{1}{2}(\Delta\mathbf{x}^T\,\mathbf{A}_{sys}^T\mathbf{A}_{sys}\,\Delta\mathbf{x}) \tag{A.15a}$$

$$\mathbf{B}_{sys}\,\Delta\mathbf{x} < \mathbf{c} \tag{A.15b}$$

Other passivity enforcement schemes are possible, including perturbation of Hamiltonian matrix eigenvalues with minimization of an energy norm [23]. In this annex we use one version that perturbs the residue matrix eigenvalues (spectral perturbation) in order to reduce the computational effort [24].

A.6 Matrix Fitting Toolbox

A.6.1 General

Some software packages are available that can be used for rational function approximation, such as

- IdEM (Politecnico di Torino, Italy) [25]
- matrix fitting toolbox (SINTEF, Norway) [26].

Many useful tools are also available in the SUMO Lab [27] from the University of Ghent, Belgium.

In this annex we will use routines from the matrix fitting toolbox (MFT). These routines are open-source Matlab functions that can be freely downloaded from the web [26].

A.6.2 Overview

VFdriver.m is a routine for fitting a symmetrical, square matrix $\mathbf{H}$, given at frequencies in array *s*. The performance of the routine is controlled via a structure *opts*, such as the number of iterations, automated initial pole specification, least-squares weighting (error control) and plotting of results. The extracted model is returned in a structure *SER*, in pole-residue form and in state-space form. The user can request the state-space model to have $\mathbf{A}$ being diagonal with a mix of real and complex conjugate elements, or a real-only model (with 2×2 blocks on the diagonal of $\mathbf{A}$). The actual fitting is done by routine *vectfit3.m*, which is an implementation of the FRVF [10, 17, 19] – see Figure A.2.

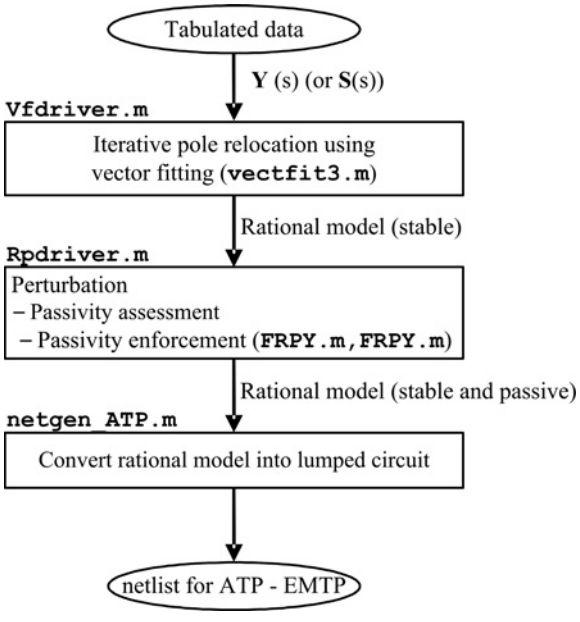

Figure A.2 Computational procedure.

Function call: `[SER,rmserr,Hfit,opts2]=VFdriver(H,s,poles,opts)`

RPdriver.m is a routine for enforcing passivity of a model that has been previously extracted by *VFdriver*. The routine identifies bands of passivity violations and enforces passivity at a set of carefully selected frequencies, so as to enforce passivity while minimizing the change to the original behaviour. The performance of the routine is controlled via a structure *opts*, such as least-squares weighting (error control) and iterations. The passivity assessment is done using a half-size test matrix [28, 29], while the passivity enforcement is done using perturbation of residue matrix eigenvalues [24]. The associated quadratic programming problem (A.15) is solved using the Matlab routine *quadprog.m*, which is part of the Matlab Optimization Toolbox. Note that the routine can be applied to models that represent admittance (or impedance) parameters, as well as scattering (S-) parameters.

Function call: `[SER,Yfit,opts2]=RPdriver(SER,s,opts)`

netgen.m is a routine for converting the model (contained in structure *SER*) into a lumped RLC circuit representation. The RLC network is dumped to a file as an ATP-EMTP netlist.

Function call: `netgen_ATP(SER,NOD,fname)`

A.7 Example A.1: Electrical Circuit

One of the examples included in the MFT is the electrical circuit in Figure A.3. The frequency response is calculated in the range 10 Hz to 100 kHz and is subjected to rational fitting by routine *VFdriver,* using eight pole-residue terms, see (A.10). The fitting error is close to machine precision – see Figure A.4.

The resulting model is exported to a netlist for ATP by routine *netgen_ATP*. A time-domain simulation is carried out where a unit step voltage is applied to terminal 1 in Figure A.3 with terminal 2 grounded – see Figure A.5. The simulated current flowing from ground into terminal 2 is shown in Figure A.6, along with the analytical solution. Clearly, a very accurate result has been achieved.

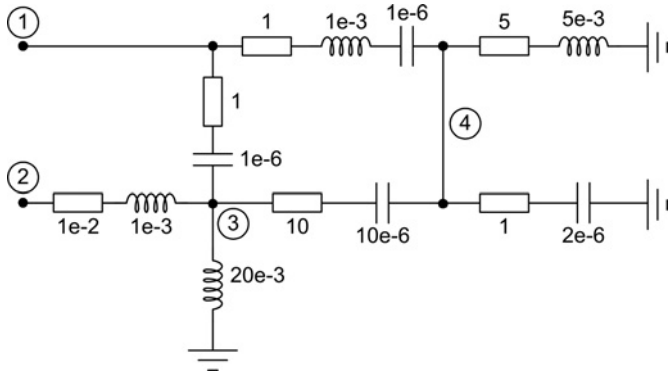

Figure A.3 Lumped circuit. Circuit values in ohms, henries and farada.

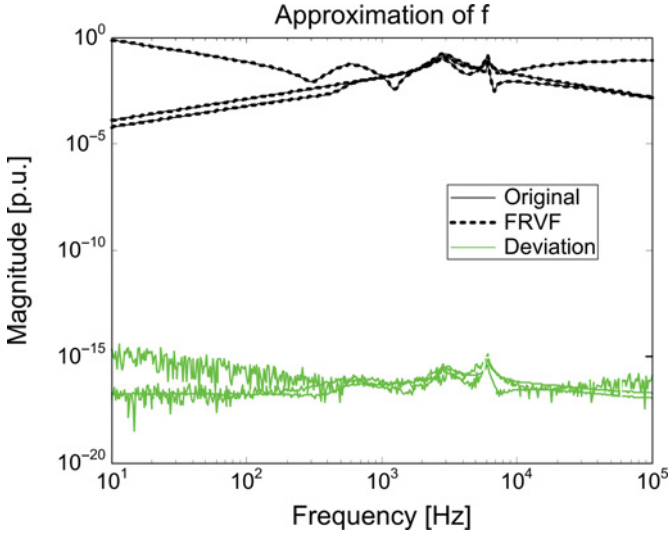

Figure A.4 Rational fitting of **Y**.

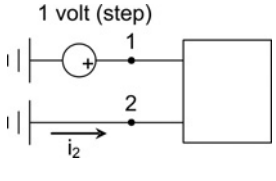

Figure A.5 Step voltage excitation on terminal 1.

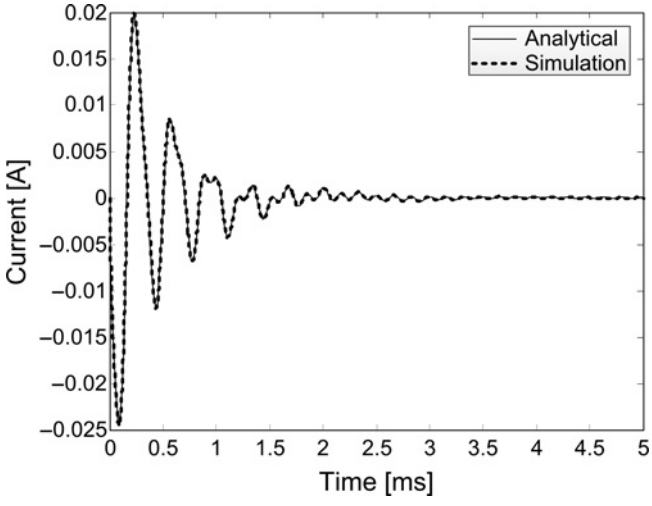

Figure A.6 Current response on terminal 2. ATP simulation vs analytical solution.

A.8 Example 6.2: High-Frequency Transformer Modelling

A.8.1 Measurement

This example is taken from wideband modelling of power transformers from frequency sweep measurements. The transformer is a 300 kVA distribution transformer with 11 kV/230 V voltage ratio – see Figure A.7. Using a measurement setup similar to the one in [9], the 6×6 admittance matrix $\mathbf{Y}$ has been measured in the range 50 Hz to 10 MHz.

A.8.2 Rational Approximation

Using the routine *VFdriver*, a rational model (A.10) with 80 pole-residue terms is extracted. The call requests stable poles only, 10 iterations, and inverse magnitude weighting for achieving relative error control. Total computation time: 9 sec. Figure A.8 shows that a highly accurate fitting result is achieved over the full frequency band.

A.8.3 Passivity Enforcement

The model is passed to routine *RPdriver,* in order to enforce passivity of the model. The function call requests inverse weighting for the least-squares part of the problem (A.15a). Two iterations are used for the inner loop of the iterative procedure. After a total of 13 sec, a passive model is returned. Figure A.9 shows that the passivity enforcement step removes a large passivity violation above 10 MHz; that is, all eigenvalues of $\mathbf{G} = \mathrm{Re}\{\mathbf{Y}\}$ are enforced to be positive.

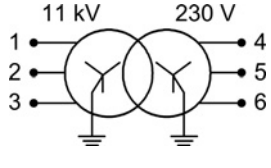

Figure A.7 Distribution transformer.

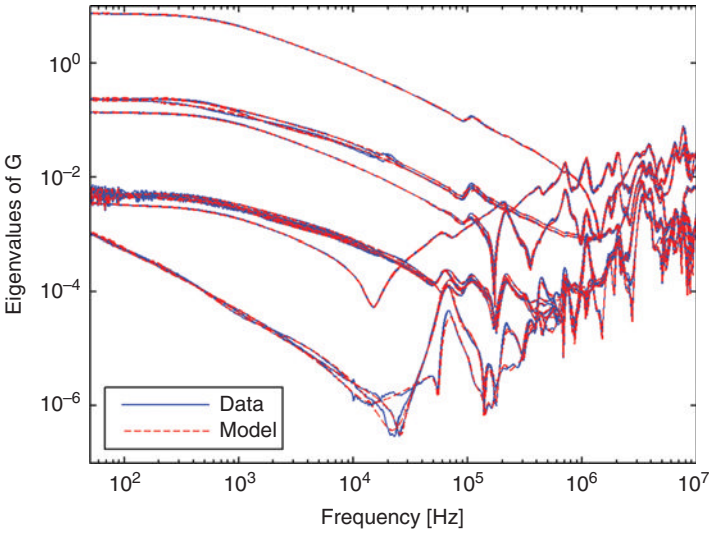

Figure A.8 Rational approximation. Elements of **Y**.

A.8.4 Time-Domain Simulation

Using routine *netgen_ATP*, a lumped circuit equivalent is generated for use with ATP-EMTP. Using ATP, the voltage step response on terminals 4 and 6 is simulated for the terminal conditions in Figure A.10. The voltage waveforms are shown in Figure A.11, together with the simulated response using recursive convolution [2]. The simulation based on recursive convolution was done in a small Matlab program, assuming trapezoidal integration [12, 30]. The two approaches give a nearly identical result. (The difference between the traces is smaller than $1E{-}5$).

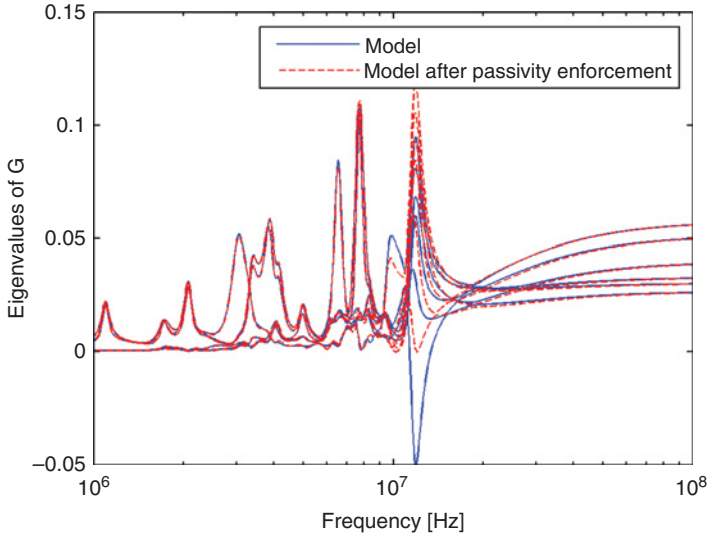

Figure A.9 Passivity enforcement. Eigenvalues of **G**.

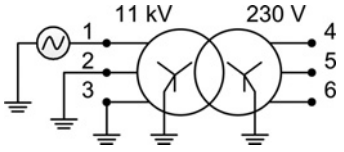

Figure A.10 Step voltage excitation.

A.8.5 Comparison with Time-Domain Measurement

As a validation of the measurement and modelling procedure, we compare measured and simulated time-domain waveforms for the excitation in Figure A.10. The measured step voltage excitation on terminal 1 is realized in the simulation (Matlab program with recursive convolution) as an ideal voltage source, and the voltage response at terminals 4 and 6 are simulated and compared with the measurement. Figure A.12 shows that an excellent agreement is achieved. (The dots represent a fraction of the time-steps).

Figure A.13 shows the same result as in Figure A.12, when the passivity enforcement step has not been carried out. It is seen that the simulation becomes unstable. Thus, passivity enforcement is a mandatory step in the modelling procedure.

In [31], the extracted model was applied in a number of study cases which demonstrated that a transient overvoltage on a feeder cable could lead to excessive overvoltages due to resonance between the cable and the transformer.

Figure A.14 shows the diagram of one case. Two cables of equal length are connected to a busbar that is fed from an overhead line. When switching in the second cable, an oscillating overvoltage results on the cable due to travelling waves which propagate back and forth between the two cables. The dominant frequency component coincides with a peak in the transformer transfer voltage from high to low. This result in an excessive overvoltage on the LV side, – see Figure A.15.

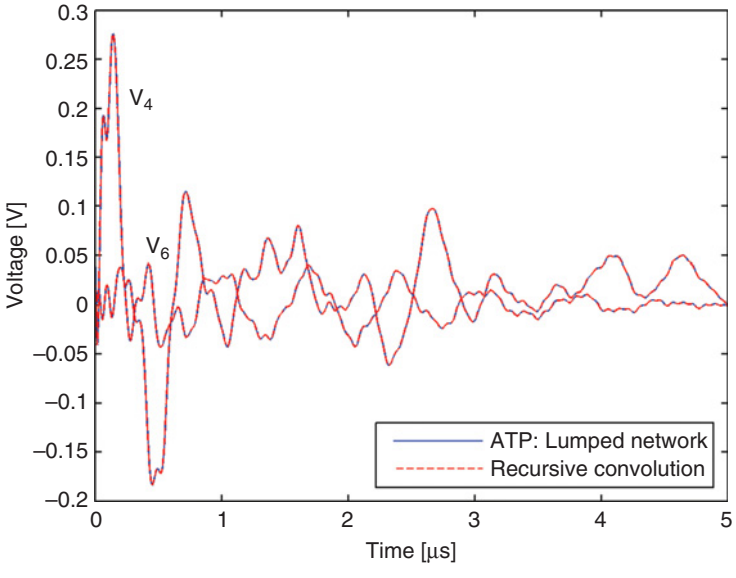

Figure A.11 Step voltage response.

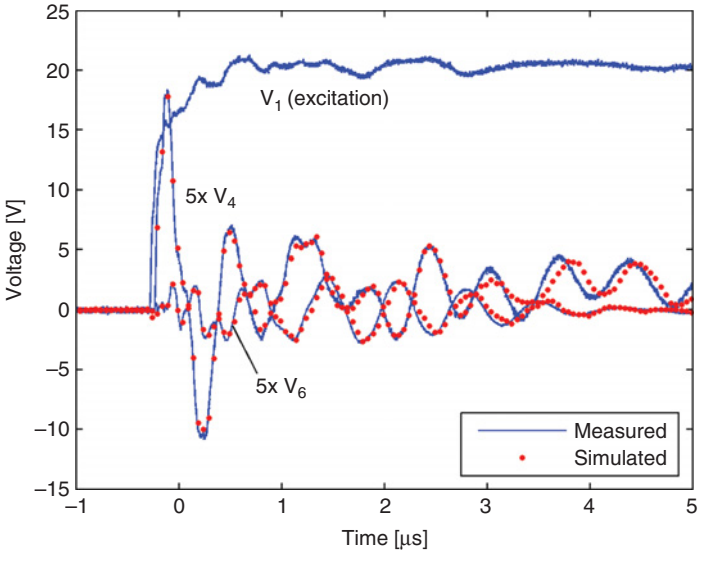

Figure A.12 Simulated vs measured voltage response.

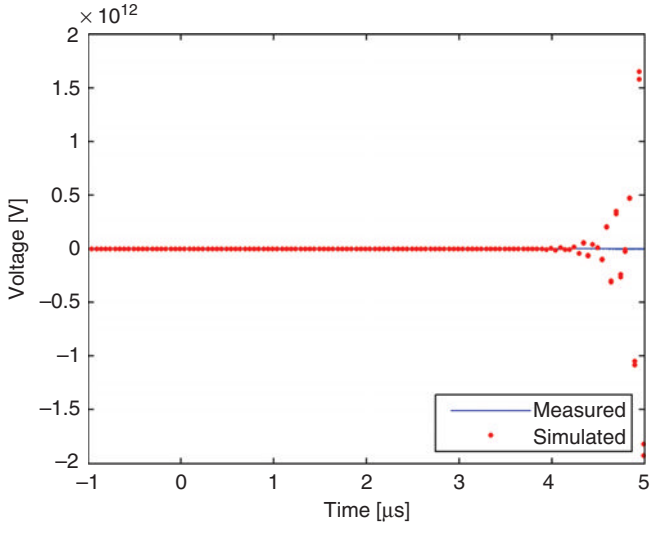

Figure A.13 Simulated vs measured voltage response. No passivity enforcement.

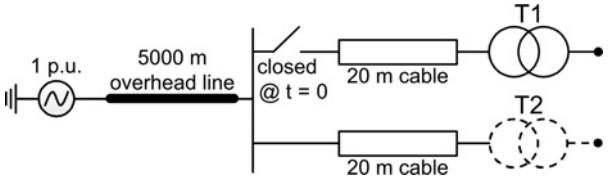

Figure A.14 Transformer energization from three-phase power system. Closing first breaker pole at $t = 0$ [31].

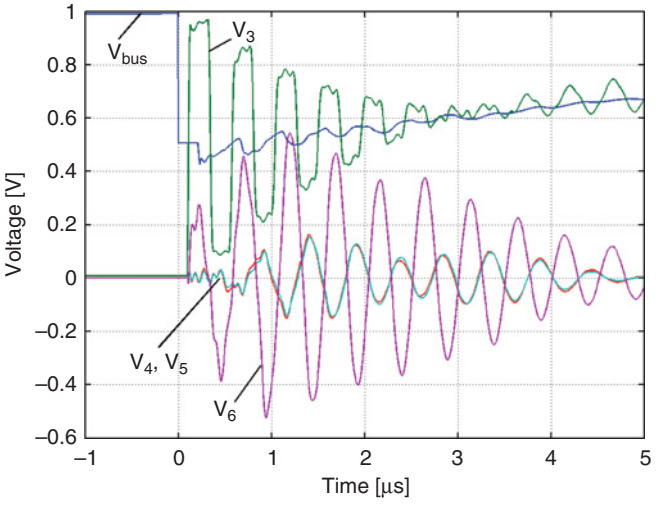

Figure A.15 Transient overvoltages (© 2010 IEEE) [31].

References

[1] Dommel, H.W. (1986) *ElectroMagnetic Transients Program. Reference Manual (EMTP Theory Book)*, Bonneville Power Administration, Portland.

[2] Semlyen, A. and Dabuleanu, A. (1975) Fast and accurate switching transient calculations on transmission lines with ground return using recursive convolutions. *IEEE Transactions on Power Apparatus and Systems*, **94**(2), 561–575.

[3] Martí, J.R. (1982) Accurate modelling of frequency-dependent transmission lines in electromagnetic transient simulations. *IEEE Transactions on Power Apparatus and Systems*, **101**(1), 147–157.

[4] Noda, T., Nagaoka, N., and Ametani, A. (1996) Phase domain modeling of frequency-dependent transmission lines by means of an ARMA model. *IEEE Transactions on Power Delivery*, **11**(1), 401–411.

[5] Morched, A., Gustavsen, B., and Tartibi, M. (1999) A universal model for accurate calculation of electromagnetic transients on overhead lines and underground cables. *IEEE Transactions on Power Delivery*, **14**(3), 1032–1038.

[6] Morched, A., Ottevangers, J., and Martí, L. (1993) Multiport frequency dependent network equivalents for the EMTP. *IEEE Transactions on Power Delivery*, **8**(3), 1402–1412.

[7] Noda, T. (2005) Identification of a multiphase network equivalent for electromagnetic transient calculations using partitioned frequency response. *IEEE Transactions on Power Delivery*, **20**(2), 1134–1142.

[8] Morched, A., Martí, L., and Ottevangers, J. (1993) A high frequency transformer model for the EMTP. *IEEE Transactions on Power Delivery*, **8**(3), 1615–1626.

[9] Gustavsen, B. (2004) Wide band modeling of power transformers. *IEEE Transactions on Power Delivery*, **19**(1), 414–422.

[10] Gustavsen, B. and Semlyen, A. (1999) Rational approximation of frequency domain responses by vector fitting. *IEEE Transactions on Power Delivery*, **14**(3), 1052–1061.

[11] Gustavsen, B. and Semlyen, A. (2001) Enforcing passivity for admittance matrices approximated by rational functions. *IEEE Transactions on Power Systems*, **16**(1), 97–104.

[12] Gustavsen, B. and Mo, O. (2007) Interfacing convolution based linear models to an electromagnetic transients program. International Conference on Power Systems Transients, 4–7 June 2007, Lyon, France.

[13] Gustavsen, B. (2002) Computer code for rational approximation of frequency dependent admittance matrices. *IEEE Transactions on Power Delivery*, **17**(4), 1093–1098.

[14] Sanathanan, C.K. and Koerner, J. (1963) Transfer function synthesis as a ratio of two complex polynomials. *IEEE Transactions on Automatic Control*, **8**(1), 56–58.

[15] Bode, H.W. (1945) *Network Analysis and Feedback Amplifier Design*, D. Van Nostrand, Inc.

[16] Martí, J.R. (1981) The problem of frequency dependence in transmission line modelling. PhD thesis, The University of British Columbia, Canada.
[17] Gustavsen, B. (2006) Improving the pole relocating properties of vector fitting. *IEEE Transactions on Power Delivery*, **21**(3), 1587–1592.
[18] Deschrijver, D., Haegeman, B., and Dhaene, T. (2007) Orthonormal vector fitting: a robust macromodeling tool for rational approximation of frequency domain responses. *IEEE Transactions on Advanced Packaging*, **30**(2), 216–225.
[19] Deschrijver, D., Mrozowski, M., Dhaene, T., and De Zutter, D. (2008) Macromodeling of multiport systems using a fast implementation of the vector fitting method. *IEEE Microwave and Wireless Components Letters*, **18**(6), 383–385.
[20] Gustavsen, B. and Heitz, C. (2009) Fast realization of the modal vector fitting method for rational modeling with accurate representation of small eigenvalues. *IEEE Transactions on Power Delivery*, **24**(3), 1396–1405.
[21] Grivet-Talocia, S. (2003) Package macromodeling via time-domain vector fitting. *IEEE Microwave and Wireless Components Letters*, **13**(11), 472–474.
[22] Mekonnen, Y.S. and Schutt-Aine, J.E. (2007) Broadband macromodeling of sampled frequency data using z-domain vector-fitting method. Proceedings of IEEE Workshop on Signal Propagation on Interconnects, Genova, Italy, 13–16 May 2007, pp. 45–48.
[23] Grivet-Talocia, S. (2004) Passivity enforcement via perturbation of Hamiltonian matrices. *IEEE Transactions on Circuits and Systems I*, **51**(9), 1755–1769.
[24] Gustavsen, B. (2008) Fast passivity enforcement for pole-residue models by perturbation of residue matrix eigenvalues. *IEEE Transactions on Power Delivery*, **23**(4), 2278–2285.
[25] IdEM website, http://www.emc.polito.it/software/IdEM/idem_home.asp.
[26] Vector Fitting website, http://www.sintef.no/Projectweb/VECTFIT/.
[27] SUMO Lab website, http://www.sumo.intec.ugent.be/.
[28] Semlyen, A. and Gustavsen, B. (2009) A half-size singularity test matrix for fast and reliable passivity assessment of rational models. *IEEE Transactions on Power Delivery*, **24**(1), 345–351.
[29] Gustavsen, B. and Semlyen, A. (2009) On passivity tests for unsymmetrical models. *IEEE Transactions on Power Delivery*, **24**(3), 1739–1741.
[30] Gustavsen, B. and De Silva, H.M.J. (2013) Inclusion of rational models in and electromagnetic transients program – Y-parameters, Z-parameters, S-parameters, transfer functions. *IEEE Transactions on Power Delivery*, **28**(2), 1164–1174.
[31] Gustavsen, B. (2010) Study of transformer resonant overvoltages caused by cable-transformer high-frequency interaction. *IEEE Transactions on Power Delivery*, **25**(2), 770–779.

Annex B

Dynamic System Equivalents

Udaya D. Annakkage

B.1 Introduction

There are two commonly used power system simulation models: (1) electromagnetic transient (EMT) models, and (2) transient stability models or 'phasor models'. In EMT programs, power system components are adequately modelled to simulate high-frequency transients in power systems. This makes EMT programs very valuable in studies of lightning and switching overvoltages, and the effects of power-electronic devices on system behaviour. In order to cover the necessary bandwidth, these programs use small integration time-steps of the order of 50 μs or less, making EMT programs much slower than transient stability programs. On the other hand, stability programs, based on 'phasor models' of transmission lines and simplified rotating machine models use a much larger integration time-step (typically half a cycle) enabling such programs to solve large power systems in excess of 50 000 buses. The common practice in dealing with large systems using EMT programs is to divide the system into a *study zone* where transient phenomena occur and an *external system* encompassing the rest of the system, in order to reduce computational burden. The generators in the external system are represented by power frequency voltage sources. This simplification eliminates electromechanical-type low-frequency behaviour from the model, and the resulting model is suitable for the simulation of lightning and switching overvoltages. In situations where power-electronic devices are used to mitigate low-frequency electromechanical oscillation problems in a power system, the high-frequency equivalent network representation for the external system is inadequate. Therefore, there is a need to develop suitable techniques to determine dynamic equivalent models that accurately represent the relevant low-frequency as well as high-frequency behaviour of the external system.

The adequacy of the power system model depends on the transient or dynamic phenomena to be studied. This could be broadly classified into three categories: to investigate (1) high-frequency transients, where the transmission lines must be properly modelled to reflect the frequency-dependent effects, (2) for low-frequency electromechanical oscillation studies, where the transmission lines can be modelled as constant impedances, and the generators can be modelled without stator winding transients, and (3) studies that involve subsynchronous oscillations, where both the turbine-generator dynamics and network transients must be adequately modelled. These three types of studies need three types of equivalents: high-frequency equivalents (HFE), low-frequency equivalents (LFE) and wideband equivalents, respectively. This annex is divided according to this classification. The discussion on the LFE is limited to the methods that are relevant to EMT analysis.

Transient Analysis of Power Systems: Solution Techniques, Tools and Applications, First Edition.
Edited by Juan A. Martinez-Velasco.

B.2 High-Frequency Equivalents

B.2.1 Introduction

The HFEs can be further classified into frequency-dependent network equivalents (FDNE) and two-layer network equivalents (TLNE). Both of these methods attempt to model the frequency-dependent terminal admittance of a network using either a lumped-parameter circuit model or a rational function model.

The modelling – which assumes linearity of the considered subsystem – is normally based on an admittance formulation which defines the relation between voltages $[V]$ and currents $[I]$ on the ports (terminals) of the equivalent

$$[Y][V] = [I] \tag{B.1}$$

where $[Y]$ is the nodal admittance matrix.

B.2.2 Frequency-Dependent Network Equivalent (FDNE)

The known frequency response admittance characteristic of the external system can be estimated by fitting it to a function of the appropriate order,

$$f_{fit}(s) = \frac{p_0 + p_1 s + p_2 s^2 + \cdots + p_N s^N}{1 + q_1 s + q_2 s^2 + \cdots + q_N s^N}, \tag{B.2}$$

or the equivalent form,

$$f(s) = c_0 + \sum_{k=1}^{N} \frac{c_k}{s - a_k}. \tag{B.3}$$

As measured or calculated values of $f(j\omega_p)$ are known at an arbitrarily large number of frequency points, (B.3) (or equivalently (B.2)) can be expressed as an over-determined fitting problem in the $2n + 1$ variables $a_1, a_2 \ldots a_N$, and $c_0, c_1, c_2 \ldots c_N$. However, this is a nonlinear problem that cannot be solved by well-known linear regression methods.

An early work reported in the literature used frequency domain computed data to fit parameters to the model in (B.2) [1].

References [2, 3] overcome ill-conditioning problems of FDNE, by dividing the frequency response into sections. Other techniques, such as column scaling, adaptive weighting and iterations step adjustment are also utilized in these references.

A time-domain approach to obtain the fitted function (B.3) using Prony analysis is presented in [4]. Time-domain approaches have also been applied to identify the external system as a digital filter in [5, 6]. In [7–9], the external system is modelled using lumped parameters.

Recently, a more powerful *vector fitting technique* has been employed [10–14]. Vector fitting converts the problem in (B.2) into a linear problem as will be described. An unknown rational function of the form (B.4) is introduced with an initial pole set $d_1, d_2 \ldots d_N$

$$\sigma(s) = 1 + \sum_{k=1}^{N} \frac{b_k}{s - d_k} \tag{B.4}$$

The function $\sigma(s)$ with yet-to-be-determined residues b_k is required to satisfy the condition (B.5), where the right side has the same poles as $\sigma(s)$. Since the poles in (B.5) are known, the equation is

linear in its unknown residues and can therefore be solved as an over-determined linear problem in the least-squares sense.

$$f(s)\sigma(s) = e_0 + \sum_{k=1}^{N} \frac{e_k}{s - d_k} \tag{B.5}$$

An improved pole set for the approximation of $f(s)$ is calculated as the zeros of $\sigma(s)$, which are obtained by solving an eigenvalue problem (B.6) [10]. In (B.6), A is a diagonal matrix holding the initial poles $\{d_k\}$, b is a column vector of ones and c^T is a row vector holding the residues $\{e_k\}$:

$$a_m = eig\left(A - bc^T\right) \tag{B.6}$$

This procedure is applied in an iterative manner where (B.5) and (B.6) are solved repeatedly with the new poles replacing the previous poles $\{d_k\}$. This pole relocation procedure usually converges in 3–5 iterations. After the poles have been identified, the residues of (B.3) are finally calculated by solving the corresponding least-squares problem with known poles.

The fitting process works better when the arbitrarily assigned poles d_k of $\sigma(s)$ are close to the poles a_k of $f(s)$. Hence, although one pass through the procedure should be sufficient, we can get improved fitting by using the values of a_k determined through an earlier iteration as seed values d_k for the next iteration. Additional care is required to ensure that the fitted function is stable and passive.

Most practical applications involve one or more three-phase buses. In such multiport cases, the same modelling procedure is applicable because vector fitting can be applied to several elements simultaneously. In practice, we stack the elements of Y into a single vector and subject it to vector fitting which produces a rational model with a common pole set, which after rearrangement of fitting parameters gives the pole-residue model (B.7). A symmetrical model is obtained by fitting only the upper (or lower) triangle of Y:

$$Y = R_0 + \sum_{k=1}^{N} \frac{R_k}{s - a_k} \tag{B.7}$$

B.2.3 Examples of High-Frequency FDNE

B.2.3.1 Example 1: Dynamic Network Equivalent of a Distribution System

Modelling: This example taken from [15] demonstrates how to calculate a high-frequency FDNE (HFDNE) for the distribution system in Figure B.1 with respect to the two three-phase buses A and

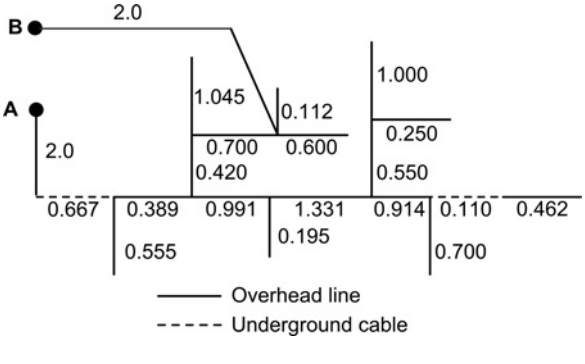

Figure B.1 Example 1: Topology of the distribution test system (lengths in kilometres) (© 2010 IEEE).

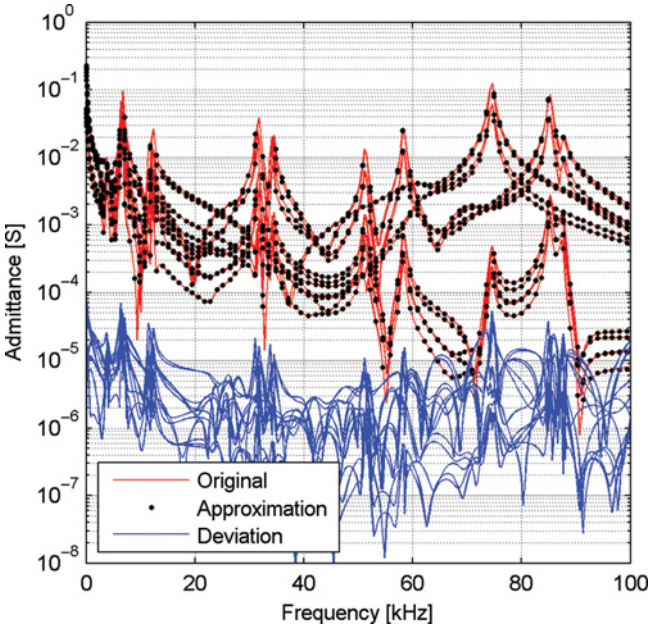

Figure B.2 Example 1: Rational fitting of Y (6×6) (from Ref. [15]).

B. The admittance matrix with respect to these buses is established via the nodal admittance matrix where each branch (line/cable) is represented by its exact PI-equivalent in phase domain coordinates. Using vector fitting and passivity enforcement, a rational model is obtained in the frequency range 10 Hz to 100 kHz – see Figure B.2. The model has 60 pole-residue terms.

Time-domain simulation: The model is included in the PSCAD/EMTDC circuit simulator via a user-defined component. In a time-domain simulation, bus A is energized from a three-phase voltage source with bus B being open. At $t = 20$ ms, a ground fault occurs at A3 – see Figure B.3. The voltage response at B3 is simulated in PSCAD/EMTDC in two alternative ways:

- using HFDNE
- using standard simulation with all lines/cables explicitly represented by the universal line model [16]

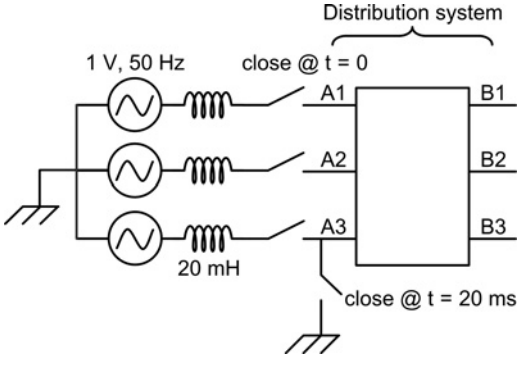

Figure B.3 Example 1: Energization and ground fault initiation (from Ref. [15]).

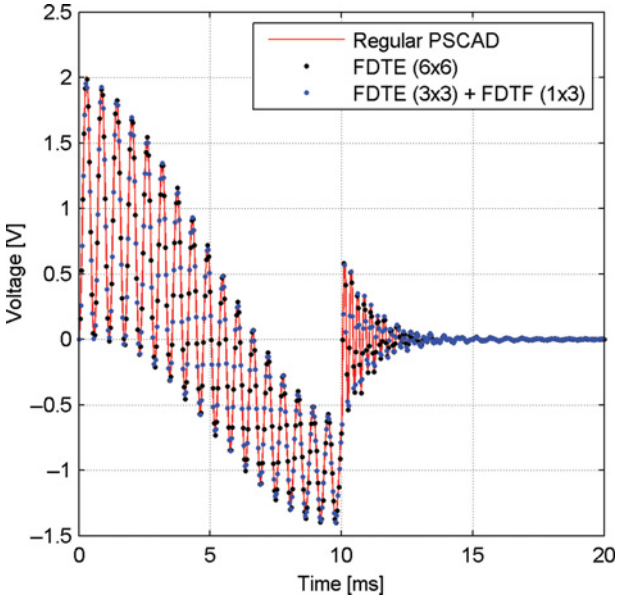

Figure B.4 Example 1: Transient voltage on B3 (from Ref. [15]). FDTF stands for the frequency-dependent transfer function model and FDTE stands for the frequency-dependent terminal equivalent.

Figures B.4 and B.5 show the voltage responses on B3 with two alternative simulation procedures. The responses by the two approaches are seen to match very closely. The computation time by the HFDNE can be made much smaller than that by the full model [15]. With the full model, the time-step must be kept smaller than 0.2 μs due to the presence of small stub lines, since the travelling-wave method requires the time-step to be smaller than the time delay of all lines. With the HFDNE, however, a larger time-step is permissible. This gives large savings in computation time [15].

B.2.3.2 Example 2: Partitioning the Frequency Response

This example was taken from [2] to demonstrate the effectiveness of partitioning the frequency response. The test system shown in Figure B.6 is a three-phase, 500 kV transmission network. Figure B.7(a) shows the equivalent circuit for generators G 1–4. The electromotive forces (emfs) are represented by the three-phase sinusoidal voltage source E and the subtransient impedance by the circuit block consisting of L_1, R_2 and L_2. Figure B.7(b) is the equivalent circuit used to represent the transformers TR 1–4, consisting of the Δ-Y ideal transformer and the L_1–R_2–L_2 circuit block. This circuit block represents the frequency dependence of the leakage impedances of the transformers. The loads LD 1–6 are modelled by the simple R–L circuit in Figure B.7(c). As in Figure B.7(d), the capacitor bank consists of the delta-connected capacitors and the step-down transformer. The step-down transformer is represented in the same way as TR 1–4, and the stray capacitance to the ground is considered by the 1 nF capacitances. See [2] for details of the transmission-line model.

The admittance matrix $\mathbf{Y}(s)$ of the test network's external zone is calculated at 2000 equidistant frequency points between 0 Hz and 10 kHz. The trace of $\mathbf{Y}(s)$ is then calculated and partitioned into ten frequency sections, as shown in Figure B.8. Each partition of the trace is fitted by the rational fitting method described in [2]. Figure B.9 shows the fitted result, where only some elements of the admittance matrix are shown, but the other elements are also fitted with the same degree of accuracy. The responses have many resonance peaks, mainly due to the transmission lines, and all of those peaks are fitted accurately.

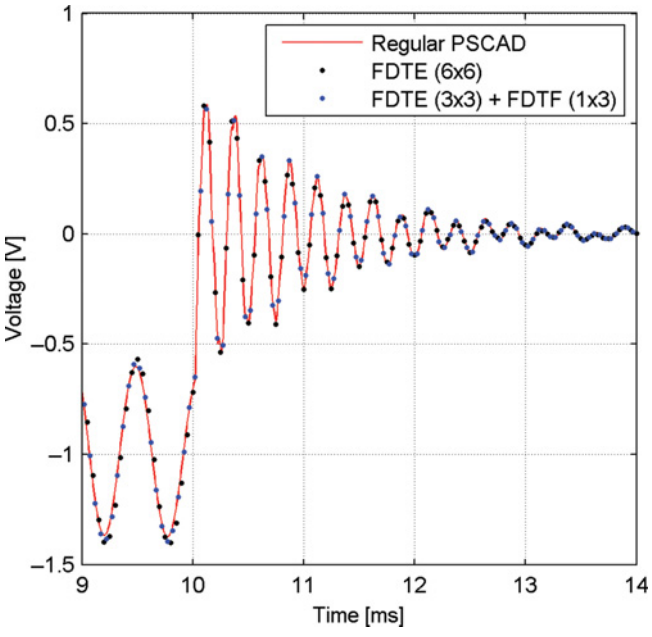

Figure B.5 Example 1: Transient voltage on B3 (expanded view) (from Ref. [15]).

The switching transient due to closing the CB 1 at 7.09 ms is shown in Figure B.10. It compares the calculated voltages at CB 2 obtained by the full system representation and by the identified equivalent, where these results are practically the same.

B.2.4 Two-Layer Network Equivalent (TLNE)

In large systems, the complexities of an external system result in a high-order rational function (matrix), which requires excessive computations in transient simulations. This is not only an obstacle in off-line simulation, but also the main bottleneck in achieving real-time simulation of realistic size power systems. The TLNE [17–19] in which the external system is further partitioned (Figure B.11) into a surface layer composed of low-order frequency-dependent transmission lines and a deep region composed of low-order FDNE model, overcomes this obstacle. The contribution of the surface layer and deep region on the external system input admittance varies with frequency. In particular, the surface layer and deep region have effects on the admittance at low frequency. However, since transients in the study zone do not travel very far in external systems, the deep region mainly contributes to the lower frequency range, while the high-frequency characteristics of the external system are predominantly determined by the surface-layer transmission lines immediately connected to the study zone. Both the surface layer and deep region parameters can be further optimized in terms of their accuracy and efficiency in order to achieve a robust TLNE [19] for real-time simulation. An application of the robust TLNE for real-time transient simulation of large-scale systems on a PC-cluster-based real-time simulator is shown in [20]. The concept similar to this has been applied in [21], where the time delay in a transmission line, which connects the external system and the study zone, is used to perform the necessary calculations to interface the frequency-domain model of the external system to the study zone. The frequency-domain model of the external system is obtained by performing Fourier transform over the time-domain data collected over a period of 2τ, where τ is the wave travel delay in the transmission line.

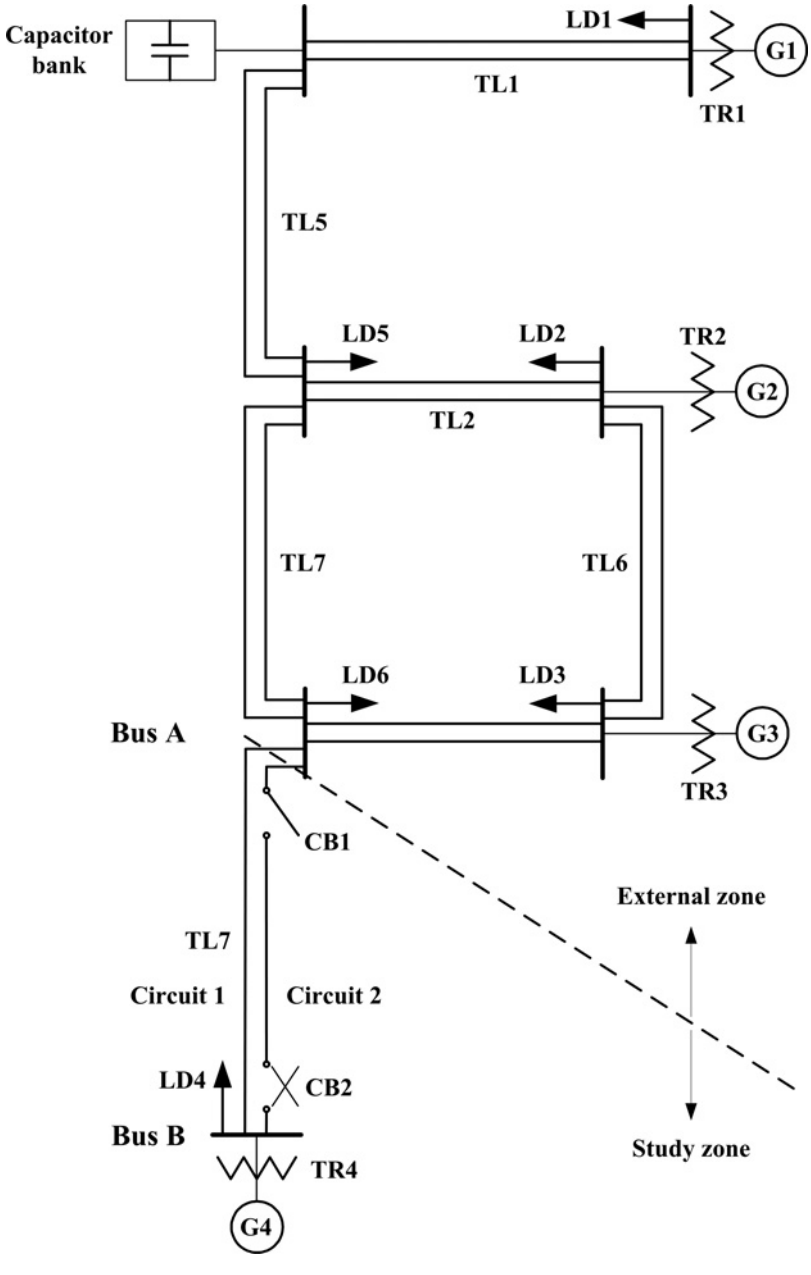

Figure B.6 Example 2: The 500 kV test network (© 2010 IEEE).

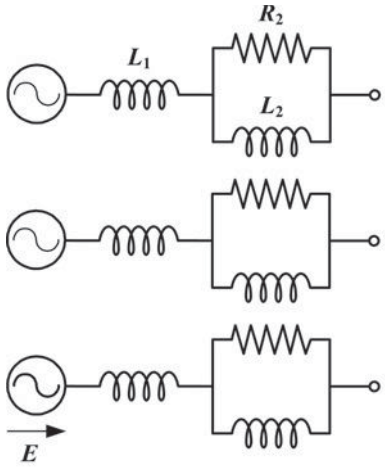

	E (15 kV base)
G1	1.14 ∠37.6°
G2	1.10 ∠12.4°
G3	1.10 ∠10.4°
G4	1.45 ∠24.5°

For all generators, $L_1 = 7.96$ μH, $R_2 = 0.0262$ Ω, $L_2 = 18.1$ μH

(a)

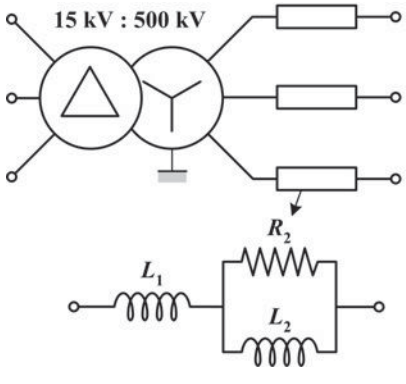

	L_1 (mH)	R_2 (Ω)	L_2 (mH)
TR1	10.0	2.75	0.587
TR2	14.5	3.97	0.847
TR3	14.5	3.97	0.847
TR4	4.89	1.34	0.286

(b)

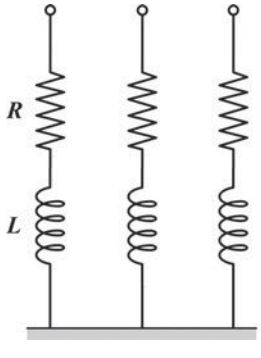

	R (Ω)	L (mH)
LD1	58.0	57.4
LD2	86.6	86.6
LD3	85.1	89.4
LD4	14.8	6.71
LD5	130	3.45
LD6	129	3.41

(c)

Figure B.7 Example 2: Representations of the network components: (a) generator representation; (b) transformer representation; (c) load representation; (d) capacitor bank representation (© 2010 IEEE). (*Continued*)

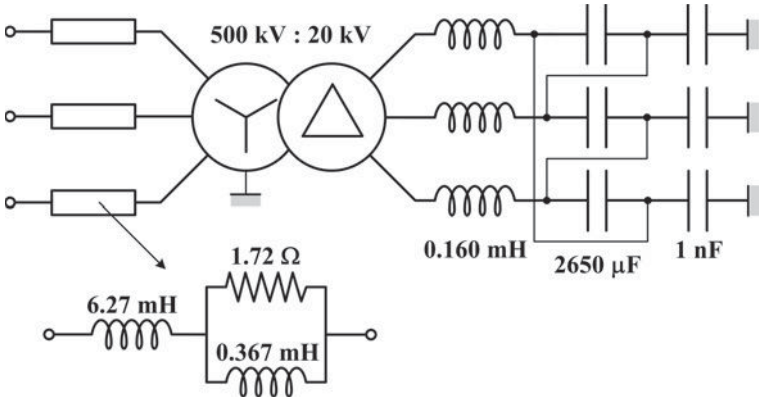

(d)

Figure B.7 (*Continued*).

The passivity criterion has a strong impact on the stability of time-domain simulations; an electric network with passivity violations will result in unstable and erroneous simulations. For a network represented by the nodal (B.1), the passivity criterion requires that the real part of the input admittance **Y** be positive at all frequencies for a single-port network, or all eigenvalues of the real part of the input admittance matrix **Y** be positive in the entire frequency range for a multiport network.

In the TLNE method, the approximations of surface layer admittance $\mathbf{Y}_{surface}(\omega)$ and deep region admittance $\mathbf{Y}_{deep}(\omega)$ are obtained from low-order vector fitting [10]. Then, the input admittance $\mathbf{Y}_{input}(\omega)$ of the external system is obtained by combining $\mathbf{Y}_{surface}(\omega)$ and $\mathbf{Y}_{deep}(\omega)$, as shown in Figure B.12.

In the robust TLNE, genetic algorithms are used to find out the best low-order deep region $\mathbf{Y}_{deep}(\omega)$ approximation which can minimize the deviation of external system input admittance $\mathbf{Y}_{input}(\omega)$ approximation. Further improvement is achieved by the constrained nonlinear least-square optimization with the inclusion of frequency response at DC and the optimal deep region order determination feature:

1. *Surface layer:* The surface layer consists of reduced-order frequency-dependent transmission-line models. In the robust TLNE model, Marti's frequency-dependent line model [22] is employed for real-time implementation. It is based on the well-known line model equations in the frequency domain:

$$V_k(\omega) = \cosh[\gamma(\omega)\ell]\, V_m(\omega) - Z_c(\omega)\sinh[\gamma(\omega)\ell]\, I_m(\omega) \tag{B.8a}$$

$$I_k(\omega) = \frac{\sinh[\gamma(\omega)\ell]}{Z_c(\omega)} V_m(\omega) - \cosh[\gamma(\omega)\ell]\, I_m(\omega), \tag{B.8b}$$

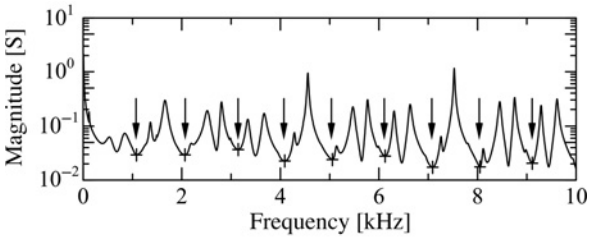

Figure B.8 Example 2: Frequency response (magnitude) of the trace of the test network's admittance matrix and its partitioning. The response is partitioned into ten frequency sections and the boundaries are marked as by the '+' symbols (© 2010 IEEE).

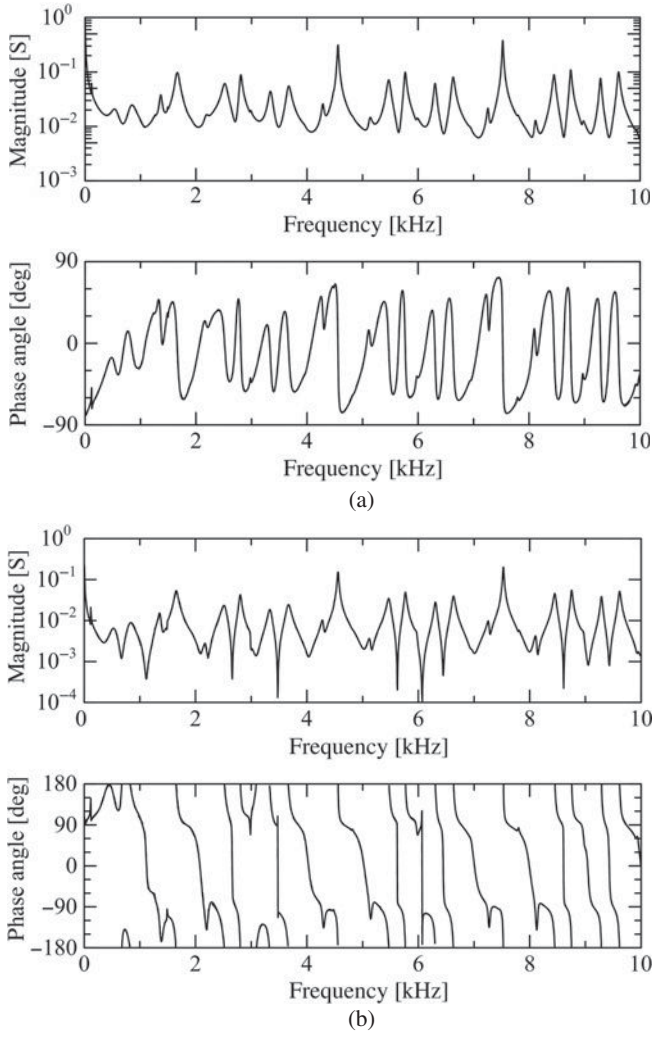

Figure B.9 Example 2: Fitted result for some elements of the admittance matrix: (a) (1, 1) element; (b) (1, 2) element. The given responses are shown by the solid lines. The fitted responses are superimposed with the dashed lines and the difference from the solid lines cannot be observed (© 2010 IEEE).

where $V_k(\omega)$, $V_m(\omega)$, $I_k(\omega)$ and $I_m(\omega)$ are the voltages and currents corresponding to the sending end (k) and receiving end (m), respectively, ℓ is the line length and $Z_c(\omega)$ and $\gamma(\omega)$ are the frequency-dependent characteristic impedance and propagation function, respectively.

From individual lines, which have the nodal equations (B.8a) and (B.8b), the admittance matrix of the reduced-order surface-layer network can be constructed as follows:

$$\tilde{\mathbf{Y}}_{surface}(\omega) = \begin{bmatrix} \tilde{\mathbf{Y}}_{AA}(\omega) & \tilde{\mathbf{Y}}_{AB}(\omega) \\ \tilde{\mathbf{Y}}_{BA}(\omega) & \tilde{\mathbf{Y}}_{BB}(\omega) \end{bmatrix}, \tag{B.9}$$

where subscript A stands for the ports connected to the study zone, subscript B stands for the ports connected to the deep region (Figure B.12) and $\sim$ designates an approximation.

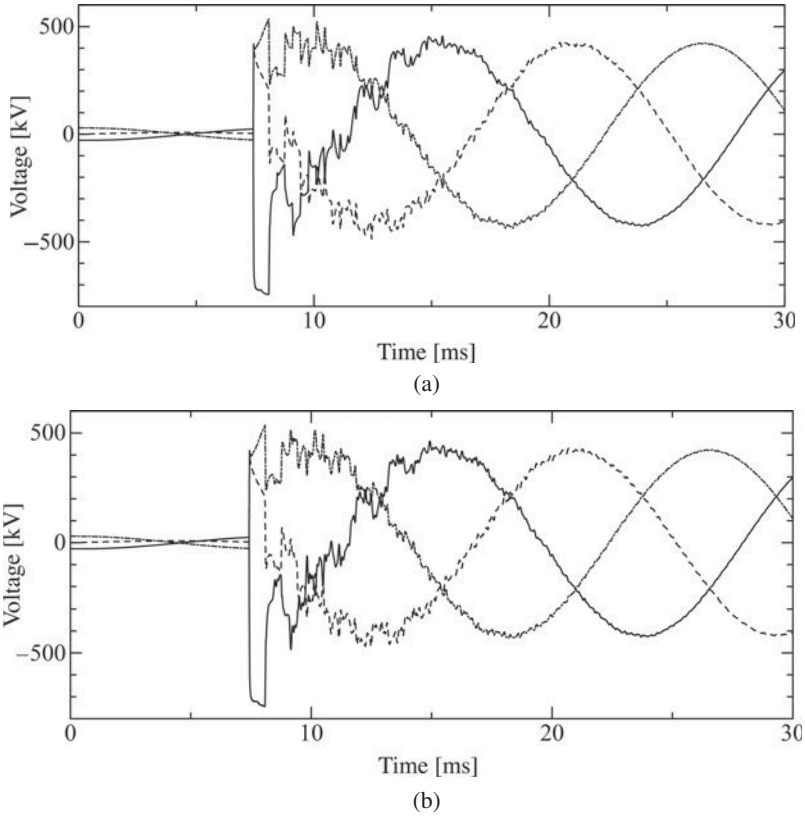

Figure B.10 Example 2: Switching transient simulation results by (a) the full system representation and (b) the identified equivalent. (Solid line: phase *a*, dashed line: phase *b* and dash-dot line: phase *c*) (© 2010 IEEE).

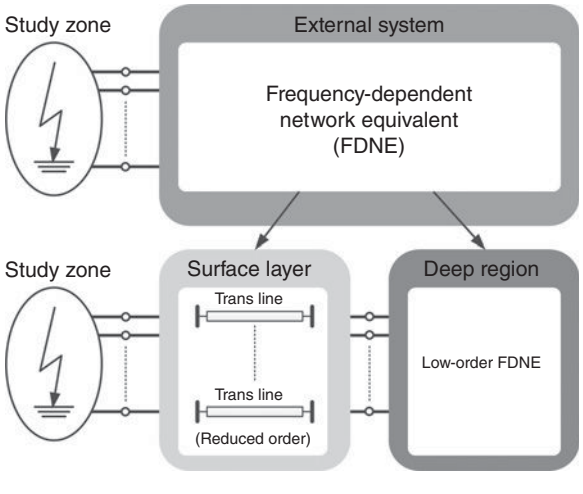

Figure B.11 Two-layer network equivalent concept [19] (© 2010 IEEE).

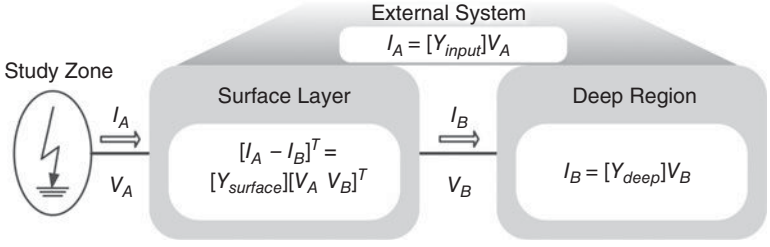

Figure B.12 Admittance matrix construction for the TLNE external system (© 2010 IEEE).

2. *Deep region:* The fitting of the external system by vector fitting is stressed on a relatively lower frequency range since high-frequency transients do not travel very far in the external system. In the TLNE, the deep region is further insulated from the study zone by the surface layer. Thus, the order of the deep region can be significantly reduced.

The first approximation of external system input admittance $\tilde{\mathbf{Y}}^0_{input}(\omega)$ is the initial mathematical combination of admittance matrix $\tilde{\mathbf{Y}}_{surface}(\omega)$ of the surface layer constituting reduced-order line models and $\tilde{\mathbf{Y}}_{deep}(\omega)$ of the deep region comprising low-order FDNE,

$$\tilde{\mathbf{Y}}^0_{input}(\omega) = \tilde{\mathbf{Y}}^0_{AA}(\omega) - \tilde{\mathbf{Y}}^0_{AB}(\omega) * \left[\tilde{\mathbf{Y}}^0_{AB}(\omega) + \tilde{\mathbf{Y}}^0_{deep}(\omega)\right]^{-1} \tilde{\mathbf{Y}}^0_{BA}(\omega), \tag{B.10}$$

where the superscript 0 denotes 'first', since the subsequent optimizations are to be carried out, and $\tilde{\mathbf{Y}}^0_{AA}(\omega)$, $\tilde{\mathbf{Y}}^0_{AB}(\omega)$, $\tilde{\mathbf{Y}}^0_{BA}(\omega)$ and $\tilde{\mathbf{Y}}^0_{BB}(\omega)$ correspond to the blocks of the first approximation of surface layer admittance $\tilde{\mathbf{Y}}^0_{surface}(\omega)$ in (B.9). The ultimate goal of building the robust TLNE is to match $\tilde{\mathbf{Y}}_{input}(\omega)$ with the original external system input admittance $\mathbf{Y}_{input}(\omega)$ as closely as possible, while ensuring stability and passivity of the model and accurate frequency response at DC and power frequency.

Since genetic algorithms try to find out the best low-order deep region $\tilde{\mathbf{Y}}^0_{deep}(\omega)$ that minimizes the difference between $\tilde{\mathbf{Y}}^0_{input}(\omega)$ and $\mathbf{Y}_{input}(\omega)$ while ensuring that $\tilde{\mathbf{Y}}^0_{deep}(\omega)$ is positive-real, the objective function for an m-port external system is defined as

$$f_{obj} = \left\| \mathbf{Y}_{input}(\omega) - \tilde{\mathbf{Y}}^0_{input}(\omega) \right\|^2_F + \mu = \sum_{i,j=1}^{m} \left| Y_{input,ij}(\omega) - \tilde{Y}^0_{input,ij}(\omega) \right|^2 + \mu, \tag{B.11}$$

where $Y_{ij}(\omega)$ is the ijth element of the matrix $\mathbf{Y}(\omega)$; μ denotes a penalty term when the passivity criterion violation occurs in the deep region. If the criterion is violated, μ will be a large positive number, or else $\mu = 0$. This ensures that the outputs from genetic algorithms are the best-fitted deep regions, which are both stable and positive-real.

The complete flowchart of the robust TLNE procedure is given in [19]. This method was employed to derive an accurate frequency-dependent network equivalent of the 240 kV backbone network of the Alberta Interconnected Electric System (AIES), and used in real-time transient simulations which were validated using off-line simulations with full system representation.

B.2.5 Modified Two-Layer Network Equivalent

The modified TLNE (M-TLNE) developed in [23] is an effort to further enhance the computational efficiency of the TLNE. The M-TLNE focuses on the surface region of the TLNE and significantly reduces its order. The model for the transmission lines in the surface layer is further simplified by

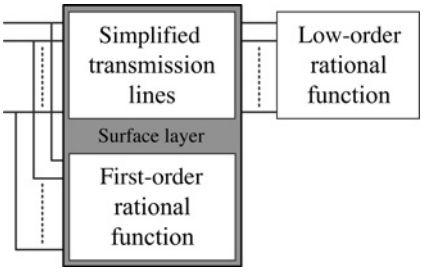

Figure B.13 Conceptual representation of the M-TLNE (© 2010 IEEE).

representing the characteristic impedance as a constant resistance rather than by a frequency-dependent rational function. The adverse impact of this simplification, which mainly shows up in the frequency response of the equivalent, approximately within 0–150 Hz, is overcome by adding a first-order rational function to the input port of the M-TLNE. Thus, in the M-TLNE, the surface layer is approximated with a set of low-order transmission lines and a first-order rational function connected at the interface port of the equivalent, whereas the deep region is approximated with a low-order rational function. Figure B.13 shows a schematic of the proposed M-TLNE equivalent.

Although the schematic of the proposed M-TLNE (Figure B.13) appears more complicated than that of the original TLNE, the transmission-line model used in the M-TLNE is significantly simpler than the one used in the original TLNE.

A transmission line is characterized by two frequency-dependent functions: a propagation function H_p and a characteristic impedance Z_c [22], [24,25]. The propagation function H_p defines the relationship between the reflected wave at one end of the line and the incident wave at the other end,

$$H_p = e^{-\gamma \ell}, \tag{B.12}$$

where γ is the propagation constant and ℓ is the line length. H_p can be decomposed into a delay component H_o and a shaping component H_{sh},

$$H_p = H_o H_{sh}, \tag{B.13}$$

where H_{sh} is extracted from the propagation function through its multiplication by $e^{j\omega\tau}$, and approximated by a low-order rational function (e.g. using vector fitting (VF) [11]). The shaping function is approximated as a strictly proper rational function.

The characteristic impedance is approximated as the sum of partial fractions in the form of

$$Z_c = R_c + \sum_{i=1}^{n} \frac{r_i}{s + p_i}. \tag{B.14}$$

Usually, a fourth- to sixth-order rational function is used to model the frequency dependence of Z_c.

Figure B.14 shows the transmission-line model, including the frequency dependence of the characteristic impedance [22]. The frequency dependence of Z_c can only be neglected if the transmission line is open-ended; otherwise, it results in deviation in the frequency response [22]. The deviation caused by neglecting the frequency dependence of Z_c is mainly in the low-frequency region (i.e. 0–150 Hz). In the M-TLNE, this deviation is effectively compensated by a first-order rational function connected at the input port of the transmission-line model. Thus, in the time-domain model of the proposed M-TLNE, these RC blocks are discarded, and only a fixed resistance is used to represent Z_c at each segment of the line model.

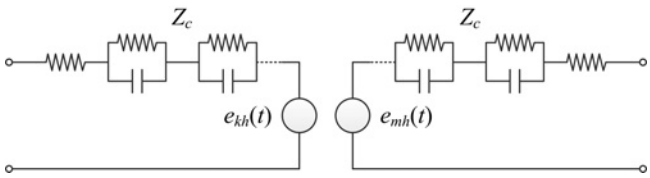

Figure B.14 Frequency-dependent transmission-line model.

The merits of such a simplification are more pronounced when a multiphase multiport system is considered and the surface layer has a number of transmission lines. Thus, elimination of the RC blocks (Figure B.14) significantly reduces the number of equations required for the time-domain simulation model, and thus noticeably reduces the computation time, particularly when the model is intended for real-time simulation.

The first approximation of the M-TLNE is constructed by connecting the approximated surface layer and the approximated deep region together. The input admittance of the first approximation is close to the original input admittance. However, the parameters of the equivalent need to be fine-tuned to minimize deviations between the M-TLNE and the original network input admittance. The initial approximation provides a starting point to initiate the optimization process. The optimization can be achieved based on a least-square process, with the objective function

$$O = \left\| \mathbf{Y}_{input} - \tilde{\mathbf{Y}}_{input} \right\|^2 . \tag{B.15}$$

All of the parameters of the equivalent, either in the surface layer or in the deep region, are subject to optimization.

In comparison with the conventional TLNE, the M-TLNE adopts a simpler surface-layer model, and thus reduces the computation time. This is a salient feature when real-time and statistical time-domain simulation studies are of interest. The generalized methodology for developing the M-TLNE, along with several case studies of single- and multiport systems, is presented in [23]. Reference [26] presents an implementation methodology for the M-TLNE in an FPGA-based real-time power system simulator.

B.2.6 Other Methods

In [27, 28], the time delay in a transmission line is used to interface the EMT model of the study zone with the transient stability model (low-frequency model) of the external system.

Other different approaches have also been proposed that try to find a compromise for the dichotomy between time and frequency analysis. The concept of dynamic phasors has been applied in [29, 30] to allow the use of a larger time-step of integration than that used in EMT simulations. Basically, dynamic phasors provide a dynamic model for the dominant Fourier components of a signal, assuming a sliding window of time. The resulting model is a state-space representation where the state variables are time-variant Fourier components of the signal.

B.2.7 Numerical Issues

1. *Accuracy issues*: When the terminals of the HFE include more than a single three-phase bus, the modelling becomes more challenging because error magnification problems may arise. When applying a voltage source to one bus, the model is required to produce large short-circuit currents with a short circuit applied to the other bus, and small currents if the second bus is open (charging currents). This behaviour is reflected in the admittance matrix Y as large and small eigenvalues, respectively. Direct

fitting of the elements of Y may easily result in corruption of its small eigenvalues, which may lead to error magnification with certain terminal conditions [31]. Some approaches, such as modal vector fitting [31], overcome this problem by assigning high weights to the small eigenvalues of Y in the least-squares fitting process.

2. *Passivity*: One major difficulty with rational function-based models is unstable simulation results due to passivity violations. Loss of passivity implies that the model can generate power under certain terminal conditions. A model is passive iff its nodal admittance matrix satisfies the passivity criterion [32]

$$eig\left(Y + Y^H\right) > 0. \tag{B.16}$$

The passivity of the model can be checked by assessing the eigenvalues in (B.16) over a set of discrete frequency samples. In the case of rational models, the boundary frequencies of passivity violations can be checked by assessing the eigenvalues of a Hamiltonian matrix that is established directly from the models' state-space matrices [33]. In the case of symmetrical models, half-size matrices can be applied. The passivity can then be enforced by perturbing parameters of the model. Most commonly, this is done by perturbing the residues [13, 34, 35].

3. *Transmission-line delay effects*: In many applications, the FDNE contains long transmission lines. The representation of time delays in the FDNE may require an excessively high order with a pure rational model if the fitting has to be done over a wide frequency band. In these cases, the two-layer FDNE is particularly useful since it can greatly reduce the required order of the inner layer.

B.3 Low-Frequency Equivalents

B.3.1 Introduction

These models are used in simulating transient rotor-angle stability of synchronous machines (transient stability analysis). Most of the research efforts in this area were made in the 1970s and 1980s when the computing power was dramatically less than today. The current industry practice is to simulate the full model, owing to the availability of fast computers. Despite the availability of fast computers, the need for LFE is still relevant when the influence of power-electronics devices on low-frequency oscillations is simulated using EMT-type simulations.

A vast amount of research has been done on the topic of LFEs. There is no intention to cover this topic in depth in this annex. Instead, the major branches of research that are relevant to EMT analysis are briefly outlined.

For transient stability simulation, the dynamics of generators and their auxiliary controllers are modelled as nonlinear differential equations. The transients in the network are typically at high frequency and highly damped. Therefore, the voltage and current relationships are modelled by using algebraic equations. This allows the voltages V and currents I to be modelled in rms quantities, and the network to be modelled with the admittance matrix Y calculated at constant frequency. This gives differential and algebraic equations (DAEs) for the kth generator (including auxiliary controllers) in the form

$$\dot{X}_k = f(X_k, V_k, u_k) \tag{B.17}$$

$$I_k = g(X_k, V_k), \tag{B.18}$$

and the network equations in the form of nodal equations (B.1).

The main interest in LFEs is to model the electromechanical oscillation modes, which are typically in the range of 0–2 Hz. These oscillations are relatively less damped. The purpose of equivalencing is to reduce the computing time. This can be achieved by reducing the number of generators and network nodes. Alternatively, the dimension of the problem can be reduced by extracting only the relevant modes of oscillation from the dynamic model.

There are three main approaches reported in the literature:

1. modal methods, where the external system is represented by an approximate linear model
2. coherency methods, where coherent groups of generators are identified and the generators in coherent groups are represented by an equivalent generator
3. measurement or simulation-based methods, where the external system response is either measured or simulated and curve-fitting techniques are used to determine the model parameters

Some methods are combinations of the three.

B.3.2 Modal Methods

Modal methods are based on the linearized state-space model (B.19), derived from (B.1), (B.17) and (B.18):

$$[\dot{X}] = [A][X]+][B][u] \tag{B.19}$$

Eigenvalues of the system matrix $[A]$ give the modes of the dynamic system. The complex conjugate eigenvalues give oscillatory modes, and the real eigenvalues give non-oscillatory modes.

When a system undergoes a transient subsequent to a disturbance, the oscillation modes with high damping decay faster than the modes with lower damping. Modal methods try to extract the relatively less damped modes (represented by eigenvalues of $[A]$ which are closer to the origin) and remove the highly damped modes (represented by eigenvalues of $[A]$ which are the farthest away from the origin). The relatively less damped modes are present in the responses over a longer period and hence determine the overall response [36–44].

A comprehensive framework known as selective modal analysis (SMA) for the analysis of selected parts of linear dynamic systems is presented in [39–41]. The method employs the eigenvalues, eigenvectors and participation factors of the linear system to reduce the less relevant part of the network.

Modal methods have also been used to supplement the coherency methods where coherent groups are identified using modal methods [45]. A special class of modal methods is the structure-preserving techniques where the zero entries of the device matrices are still retained as zero entries in the equivalent system matrix [46, 47].

B.3.3 Coherency Methods

In coherency methods [48–51], coherent groupings of machines are obtained by analysing the system response to a perturbation. An equivalent of the external system is then obtained by replacing each such coherent group of machines by a large equivalent machine. Unlike the modal method, this approach retains the physical models of the generators in an equivalent form. The equivalent generator models are nonlinear. Coherency methods involve the following steps:

1. identification of the groups of coherent generators
2. aggregation of the generator busses
3. aggregation of generator models and their associated control devices [47, 48, 52]
4. reduction of load buses

An application of coherency-based dynamic reduction to a large power system using the DYNRED program developed by EPRI [53] is reported in [54]. In [55], coherency identification is performed by using the eigenvectors of the system matrix $[A]$ in (B.19). The method is based on the identification of a slow eigenbasis matrix corresponding to the electromechanical model of the power system (i.e. only

the swing equations are modelled in (B.19)). The *r* number of the most linearly independent rows of the eigenbasis matrix becomes the corresponding reference generator. A grouping algorithm is then applied to group non-reference generators to reference generators. Finally, an eigenvector method is used to include load buses into coherent areas. This approach is referred to as the two-time scale method because it is based on the separation of system dynamics into fast and slow modes [38]. A combination of a modal and coherency methods is presented in [56, 57].

B.3.4 Measurement or Simulation-Based Methods

Measurement or simulation-based techniques use either real-time measurements or simulated responses of the power system. System identification techniques are used to identify the parameters of an equivalent model [58–61].

In [58], parameter identification is carried out using a least-squares algorithm with an adaptive step-size scheme. To start with, an equivalent model is first estimated. It is re-evaluated against the original system, until the cost function has reached the minimum and all equivalent parameters have been identified. A similar principle is suggested in [59, 60]. The main attempt here is to search for the best parameter vector which minimizes an error index that is taken to be a square function of the difference between the measured output and the calculated output. In [61], recorded disturbances are analysed and equivalent parameters are identified and then applied in dynamic simulations.

B.4 Wideband Equivalents

Unlike HFEs and LFEs, which are valid in specific frequency ranges, wideband system equivalents model the behaviour of the equivalenced external system over the entire frequency spectrum ranging from sub-Hertz electromechanical phenomena to several tens or hundreds of kilohertz electromagnetic phenomena. These tools are particularly of interest in real-time simulators. Real-time digital simulators are real-time implementations of EMT-type simulation on a parallel computation platform. Using these tools, a wideband EMT model of a power system with up to several hundred buses can be simulated in real time [62]. Since the simulation can be kept running continuously (over hours or days) in real time, it becomes possible to use the same tool for the study of very low- and high-frequency system behaviours. However, the size of the real-time hardware (counted in terms of processor racks), and subsequently its monetary cost, is proportional to the size of the modelled system. Hence, it makes economic sense to model in full nonlinear detail only that part of the network which is of great interest (referred to as the internal system) and formulate the remainder (external system) of the network into an appropriately accurate equivalent. It should be noted that the equivalent must be able to properly represent the high-frequency electromagnetic as well as the low-frequency electromechanical transient behaviour.

The implementation of wideband equivalents in a real-time environment has been reported in [62, 63]. This method uses a multiport FDNE to represent the high-frequency behaviour and uses a specially adapted real-time transient stability (TSA) simulator to calculate the lower-frequency behaviour.

B.5 Conclusions

A brief review of techniques available for obtaining dynamic system equivalents has been presented in this annex. The need for equivalent models has been driven by the demand for fast and accurate simulation tools. For EMT simulations, large networks need to be modelled using equivalent network models that accurately represent the high-frequency response of the original network. The generators are represented by voltage sources in these studies. For transient stability simulations, the high-frequency response is not important. The system reduction is achieved by grouping the generators together and eliminating the load

buses to reduce the size of the network. The transmission network is modelled as constant impedances calculated at the power frequency. Wideband models that accurately model the high-frequency as well as low-frequency response are required in some applications of real-time simulation.

References

[1] Soysal, A.O. and Semlyen, A. (1993) Practical transfer function estimation and its application to wide frequency range representation of transformers. *IEEE Transactions on Power Delivery*, **8**(3), 1627–1637.

[2] Noda, T. (2005) Identification of a multiphase network equivalent for electromagnetic transient calculations using partitioned frequency response. *IEEE Transactions on Power Delivery*, **20**(2 pt. 1), 1134–1142.

[3] Noda, T. (2007) A binary frequency-region partitioning algorithm for the identification of a multiphase network equivalent for EMT studies. *IEEE Transactions on Power Delivery*, **22**(2), 1257–1258.

[4] Hong, J. and Park, J. (1995) A time-domain approach to transmission network equivalents via Prony analysis for electromagnetic transients analysis. *IEEE Transactions on Power Systems*, **10**(4), 1789–1797.

[5] Singh, H. and Abur, A. (1995) Multiport equivalencing of external systems for simulation of switching transients. *IEEE Transactions on Power Delivery*, **10**(1), 374–382.

[6] Abur, A. and Singh, H. (1993) Time domain modelling of external systems for electromagnetic transients programs. *IEEE Transactions on Power Systems*, **8**(2), 671–679.

[7] Morched, A.S., Ottevangers, J.H. and Martí, L. (1993) Multi-port frequency dependent network equivalents for the EMTP. *IEEE Transactions on Power Delivery*, **8**(3), 1402–1412.

[8] Do, V.Q. and Gavrilovic, M.M. (1984) An iterative pole removal method for synthesis of power system equivalent networks. *IEEE Transactions on Power Apparatus and Systems*, **103**(8), 2065–2070.

[9] Do, V.Q. and Gavrilovic, M.M. (1986) A synthesis method for one-port and multiport equivalent networks for analysis of power system transients. *IEEE Transactions on Power Systems*, **1**(2), 103–113.

[10] Gustavsen, B. and Semlyen, A. (1999) Rational approximation of frequency domain responses by vector fitting. *IEEE Transactions on Power Delivery*, **14**(3), 1052–1061.

[11] Gustavsen, B. (2002) Computer code for rational approximation of frequency dependent admittance matrices. *IEEE Transactions on Power Delivery*, **17**(4), 1093–1098.

[12] Gustavsen, B. and Semlyen, A. (1998) Application of vector fitting to state equation representation of transformers for simulation of electromagnetic transients. *IEEE Transactions on Power Delivery*, **13**(3), 834–842.

[13] Gustavsen, B. and Semlyen, A. (2001) Enforcing passivity for admittance matrices approximated by rational functions. *IEEE Transactions on Power Systems*, **16**(1), 97–104.

[14] Deschrijver, D., Gustavsen, B. and Dhaene, T. (2007) Advancements in iterative methods for rational approximation in the frequency domain. *IEEE Transactions on Power Delivery*, **22**(3), 1633–1642.

[15] Gustavsen, B. and Mo, O. (2007) Interfacing convolution based linear models to an electromagnetic transients program. Proceedings of International Conference on Power Systems Transients, Lyon, France, June 2007.

[16] Morched, A., Gustavsen, B. and Tartibi, M. (1999) A universal model for accurate calculation of electromagnetic transients on overhead lines and underground cables. *IEEE Transactions on Power Delivery*, **14**(3), 1032–1038.

[17] Abdel-Rahman, M., Semlyen, A. and Iravani, M.R. (2003) Two-layer network equivalent for electromagnetic transients. *IEEE Transactions on Power Delivery*, **18**(4), 1328–1335.

[18] Nie, X. and Dinavahi, V. (2005) A robust two-layer network equivalent for transient studies. Proceedings of International Conference on Power System Transients, Montreal, QC, Canada, June 2005.

[19] Nie, X., Chen, Y. and Dinavahi, V. (2007) Real-time transient simulation based on a robust two-layer network equivalent. *IEEE Transactions on Power Systems*, **22**(4), 1771–1781.

[20] Pak, L., Faruque, M.O., Nie, X. and Dinavahi, V. (2006) A versatile cluster-based real-time digital simulator for power engineering research. *IEEE Transactions on Power Systems*, **21**(2), 455–465.

[21] Semlyen, A. and Iravani, M.R. (1993) Frequency domain modeling of external systems in an electromagnetic transients program. *IEEE Transactions on Power Systems*, **8**(2), 527–533.

[22] Martí, J.R. (1982) Accurate modeling of frequency-dependent transmission lines in electromagnetic transient simulations. *IEEE Transactions on Power Apparatus and Systems*, **101**(1), 147–157.

[23] Matar, M. and Iravani, R. (2010) A modified multi-port two-layer network equivalent for the analysis of electromagnetic transients. *IEEE Transactions on Power Delivery*, **25**(1), 177–186.

[24] Graimger, J. and Stevenson, W.D. (1994) *Power System Analysis*, McGraw-Hill, New York.

[25] EMTDC User's Guide. Winnipeg, MB, Canada, Manitoba HVDC Res. Ctr., 2004.

[26] Matar, M. and Iravani, R. (2009) FPGA implementation of a modified two-layer network equivalent for real-time simulation of electromagnetic transients. Proceedings of International Conference on Power System Transients, Kyoto, Japan, June 2009.

[27] Reeve, J. and Adapa, R. (1988) A new approach to dynamic analysis of AC networks incorporating detailed modeling of DC systems. I. Principles and implementation. *IEEE Transactions on Power Delivery*, **3**(4), 2005–2011.

[28] Adapa, R. and Reeve, J. (1988) A new approach to dynamic analysis of AC networks incorporating detailed modeling of DC systems. II. Application to interaction of DC and weak AC systems. *IEEE Transactions on Power Delivery*, **3**(4), 2012–2019.

[29] Stankovic, A.M. and Aydin, T. (2000) Analysis of asymmetrical faults in power systems using dynamic phasors. *IEEE Transactions on Power Systems*, **15**(3), 1062–1068.

[30] Stankovic, A.M., Sanders, S.R. and Aydin, T. (2002) Dynamic phasors in modeling and analysis of unbalanced polyphase AC machines. *IEEE Transactions on Energy Conversion*, **17**(1), 107–113.

[31] Gustavsen, B. and Heitz, C. (2009) Fast realization of the modal vector fitting method for rational modeling with accurate representation of small eigenvalues. *IEEE Transactions on Power Delivery*, **24**(3), 1396–1405.

[32] Boyd, S. and Chua, L.O. (1982) On the passivity criterion for LTI *n*-ports. *Circuit Theory App.*, **10**, 323–333.

[33] Boyd, S., Ghaoui, L.E., Feron, E. and Balakrishnan, V. (1994) Linear matrix inequalities in system and control theory, SIAM, Singapore, vol. 15, Studies in applied mathematics. [Online]. Available: http://www.stanford.edu/boyd/lmibook/.

[34] Grivet-Talocia, S. (2004) Passivity enforcement via perturbation of Hamiltonian matrices. *IEEE Transactions on Circuits and Systems*, **51**(9), 1755–1769.

[35] Gustavsen, B. (2008) Fast passivity enforcement for pole-residue models by perturbation of residue matrix eigenvalues. *IEEE Transactions on Power Delivery*, **23**(4), 2278–2285.

[36] Davison, E. (1966) A method for simplifying linear dynamic systems. *IEEE Transactions on Automatic Control*, **11**(1), 93–101.

[37] Undrill, J.M. and Turner, A.E. (1971) Construction of power system electromechanical equivalents by modal analysis. *IEEE Transactions on Power Apparatus and Systems*, **90**(5), 2049–2059.

[38] Chow, J.H. (1982) *Time Scale Modelling of Dynamic Networks with Applications to Power Systems*, Springer-Verlag, New York.

[39] Perez-Arriaga, I.J. (1981) Selective modal analysis with applications to electric power systems. Ph.D. dissertation, Electrical Eng., Mass. Inst. Technol., Cambridge, MA, 1981.

[40] Perez-Arriaga, I.J., Verghese, G.C. and Schweppe, F.C. (1982) Selective modal analysis with application to electric power systems, Part I: Heuristic Introduction. *IEEE Transactions on Power Apparatus and Systems*, **101**(9), 3117–3125.

[41] Perez-Arriaga, I.J., Verghese, G.C. and Schweppe, F.C. (1982) Selective modal analysis with application to electric power systems, Part II: The Dynamic Stability Problem. *IEEE Transactions on Power Apparatus and Systems*, **101**(9), 3126–3134.

[42] Altalib, H.Y. and Krause, P.C. (1976) Dynamic equivalents by combination of reduced order models of system components. *IEEE Transactions on Power Apparatus and Systems*, **95**(5 pt. 1), 1535–1544.

[43] de Oliveira, S.E.M. and Massaud, A.G. (1988) Modal dynamic equivalent for electric power systems I: Theory. *IEEE Transactions on Power Systems*, **3**(4), 1731–1737.

[44] de Oliveira, S.E.M. and Massaud, A.G. (1988) Modal dynamic equivalent for electric power systems. II: Stability simulation tests. *IEEE Transactions on Power Systems*, **3**(4), 1731–1737.

[45] Troullinos, G., Dorsey, J.F., Wong, H. *et al.* (1985) Estimating order reduction for dynamic equivalents. *IEEE Transactions on Power Apparatus and Systems*, **104**(12), 3475–3481.

[46] Nath, R. and Lamba, S.S. (1986) Development of coherency-based time-domain equivalent model using structure constraints. *Proc. Inst. Elect. Eng., Gen., Transm. Distrib.*, **133**(4), 165–175.

[47] Ourari, M.L., Dessaint, L.-A. and Do, V.-Q. (2006) Dynamic equivalent modelling of large power systems using structure preservation technique. *IEEE Transactions on Power Systems*, **21**(3), 1284–1295.

[48] Galarza, R.J., Chow, J.H., Price, W.W. *et al.* (1998) Aggregation of exciter models for constructing power system dynamic equivalents. *IEEE Transactions on Power Systems*, **13**(3), 782–788.

[49] Newell, R.J., Risan, M.D., Allen, L. *et al.* (1985) Utility experience with coherency-based dynamic equivalents of very large systems. *IEEE Transactions on Power Apparatus and Systems*, **104**(11), 3056–3063.

[50] Wang, L., Klein, M., Yirga, S. and Kundur, P. (1997) Dynamic reduction of large power systems for stability studies. *IEEE Transactions on Power Systems*, **12**(2), 889–895.

[51] Lei, X., Povh, D. and Ruhle, O. (2002) Industrial approaches for dynamic equivalents of large power systems. Proceedings of IEEE Power Eng. Soc. Winter Meeting, 2002, pp. 1036–1042.
[52] Germond, A.J. and Podmore, R. (1978) Dynamic aggregation of generating unit models. *IEEE Transactions on Power Apparatus and Systems*, **97**(4), 1060–1069.
[53] Dynamic reduction, Final report. EPRI, EPRI TR-102234, Project 2447-01, 1993, 1.
[54] Price, W.W., Hargrave, A.W., Chow, J.H. *et al.* (1998) Large-scale system testing of a power system dynamic equivalencing program. *IEEE Transactions on Power Systems*, **13**(3), 768–774.
[55] Yusof, S.B., Rogers, G.J. and Alden, R.T.H. (1993) Slow coherency based network partitioning including load buses. *IEEE Transactions on Power Systems*, **8**(3), 1375–1382.
[56] Geeves, S. (1988) A modal-coherency technique for deriving dynamic equivalents. *IEEE Transactions on Power Systems*, **3**(1), 44–51.
[57] Nath, R., Lamba, S.S. and Prakasa Rao, K.S. (1985) Coherency based system decomposition into study and external areas using weak coupling. *IEEE Transactions on Power Apparatus and Systems*, **104**(6), 1443–1449.
[58] Yu, Y.-N. and El-Sharkawi, M.A. (1981) Estimation of external dynamic equivalents of a thirteen-machine system. *IEEE Transactions on Power Apparatus and Systems*, **100**(3), 1324–1332.
[59] Stankovic, A.M. and Saric, A.T. (2004) Transient power system analysis with measurement-based gray box and hybrid dynamic equivalents. *IEEE Transactions on Power Systems*, **19**(1), 455–462.
[60] Ju, P., Ni, L.Q. and Wu, F. (2004) Dynamic equivalents of power systems with online measurements. Part 1: Theory. *Proc. Inst. Elect. Eng., Gen., Transm. Distrib.*, **151**(2), 175–178.
[61] Ju, P., Li, F., Yang, N.G. *et al.* (2004) Dynamic equivalents of power systems with online measurements Part 2: Applications. *Proc. Inst. Elect. Eng., Gen., Transm. Distrib.*, **151**(2), 179–182.
[62] Lin, X., Gole, A.M. and Yu, M. (2009) A wideband multi-port system equivalent for real time digital power system simulators. *IEEE Transactions on Power Systems*, **24**(1), 237–249.
[63] Liang, Y., Xi, L., Gole, A.M. and Yu, M. (2011) Improved coherency-based wideband equivalents for real time digital simulators. *IEEE Transactions on Power Systems*, **26**(3), 1410–1417.

Index

Transient Analysis of Power Systems: Solution Techniques, Tools and Applications, First Edition.
Edited by Juan A. Martinez-Velasco.

WILEY END USER LICENSE AGREEMENT

Go to www.wiley.com/go/eula to access Wiley’s ebook EULA.